

13th Scandinavian International  
Conference on Fluid Power

Linköping, Sweden, June 3–5, 2013

Editors

Petter Krus, Magnus Sethson and Liselott Ericson

## Copyright

The publishers will keep this document online on the Internet – or its possible replacement – from the date of publication barring exceptional circumstances.

The online availability of the document implies permanent permission for anyone to read, to download, or to print out single copies for his/her own use and to use it unchanged for non-commercial research and educational purposes. Subsequent transfers of copyright cannot revoke this permission. All other uses of the document are conditional upon the consent of the copyright owner. The publisher has taken technical and administrative measures to assure authenticity, security and accessibility. According to intellectual property law, the author has the right to be mentioned when his/her work is accessed as described above and to be protected against infringement.

For additional information about Linköping University Electronic Press and its procedures for publication and for assurance of document integrity, please refer to its www home page: <http://www.ep.liu.se/>.

Linköping Electronic Conference Proceedings, No. 92  
Linköping University Electronic Press  
Linköping, Sweden, 2013  
ISSN: 1650-3686  
eISSN: 1650-3740  
ISBN: 978-91-7519-572-8  
URL: [http://www.ep.liu.se/ecp\\_home/index.en.aspx?issue=092](http://www.ep.liu.se/ecp_home/index.en.aspx?issue=092)

# Table of Contents

## Mobile Systems 1

Eco-Efficiency Analysis for Hydraulic and Hybrid Concepts for Mobile Working Machines <i>C. Schindler, M. Eigner, C. Scholler and P. Schaefer</i> .....	1
Design Rules for High Damping in Mobile Hydraulic Systems <i>Mikael Axin and Petter Krus</i> .....	13
Modelling and Control of a Complementary Energy Recuperation System for Mobile Working Machines <i>Hugo, K. Pettersson, K. Heybroek and P. Krus</i> .....	21
A Series-Parallel Hydraulic Hybrid Mini-Excavator with Displacement Controlled Actuators <i>Rohit Hippalgaonkar and Monik Ivantysynova</i> .....	31

## Industry Applications 1

Universal Energy Storage and Recovery System - A Novel Approach for Hydraulic Hybrid <i>M. Erkkilä, F. Bauer and D. Feld</i> .....	45
Modeling and Verification of An Excavator System - Axial Piston Pump, Kinematics and Load Sensing Flow Sharing Valve Block <i>Paolo Casoli, Luca Riccò and Dolcin Cesare</i> .....	53
New PTFE-based Material for Hydraulic Seal Applications <i>Thomas Larsen, Siereb Roepstorff and Holger Jordan</i> .....	65
Prestudy of a Power Management of a Cut-To-Length Forest Harvester with a Hydraulic Hybrid System <i>Kalle Einola</i> .....	71

## Mobile Systems 2

Investigation and Energetic Analysis of a Novel Hydraulic Hybrid Architecture for On-Road <i>Michael Michael Sprengel and Monika Ivantysynova</i> .....	87
Development of Power Train of Hybrid Power Excavator <i>Qingfeng Wang and Hong Yao</i> .....	99
Modeling of a Series Hybrid Hydraulic Drivetrain for a Light-Duty Vehicle in Hopsan <i>Katharina Baer, Liselott Ericson and Petter Krus</i> .....	107
Modular Design of Hydromechanical Transmissions for Mobile Working Machines <i>Karl Pettersson and Petter Krus</i> .....	113

## Industry Application 2

Energy-Saving Design for Hydraulic Tube Bender <i>J. C. Renn, C. Y. Cheng and M. H. Lin</i> .....	123
Thermo-Energetic Analysis and Simulation of the Fluidic Cooling System of Motorized High-Speed Spindles <i>Juliane Weber and Jürgen Weber</i> .....	131

Modeling of EHA Module Equipped with Fixed-Displacement Vane Pump <i>Emanuele Gnesi, Jean-Charles Maré and J. Bordet</i> .....	141
Model Predictive Control for Power Optimization in a Hydrostatic Wind Turbine <i>Feng Wang and Kim A. Stelson</i> .....	155
<b>Pumps and Motors</b>	
Swash Plate Oscillation in A Variable Displacement Floating Cup Pump <i>P.A.J. Achten, S. Eggenkamp and H.W. Potma</i> .....	163
A Novel Approach to Predict the Steady State Temperature in Ports and Case of Swash Plate Type Axial Piston Machines <i>M. Zecchi, M. Ivantysynova and A. Mehdizadeh</i> .....	177
Performing and Interpreting Experiments Towards Understanding Noise Generation in Displacement Machines <i>T. Opperwall and A. Vacca</i> .....	189
Optimization of Process Parameters in Series Hydraulic Hybrid System through Multi-Objective Function <i>Somashekhar S. Hiremath, R. Ramakrishnan and M. Singaperumal</i> .....	199
<b>Aerospace Applications</b>	
A Robust Adaptive Hydraulic Power Generation System for Jet Engines <i>Giovanni Jacazio, Andrea Mornacchi, Pierantonio Ronco and Massimo Sorli</i> .....	209
The Influence of Fuel Pressure Ripple on Performances of Engine Control System <i>V. Shorin, A. Gimadiev and V. Sverbilov</i> .....	225
Test Rig Landing Gear Free-Fall System Model Simulation and Design Optimization Using Matlab <i>Mário Maia Neto and Luiz Carlos Sandoval Góes</i> .....	229
<b>Valve Technology 1</b>	
Investigation on the Dynamic Behavior of a Solenoid Hydraulic Valve for Automotive Semi-Active Suspensions Coupling 3D and 1D Modeling, <i>Matteo Pelosi, Kashyap Subramanya and Jonas Lantz</i> .....	241
Cylinder Pressures in a Position Controlled System with Separate Meter-in and Meter-out <i>Gerhard Ruth and Emil Zaev</i> .....	251
Structural Design of Independent Metering Control Systems <i>A. Sitte and J. Weber</i> .....	261
<b>Innovative Studies</b>	
Electrostatic Charge Measurement in Hydraulic Circuits <i>Michael Kuehnlein, T. Wendel and H. Murrenhoff</i> .....	273
Basic Theory and Experiment Study on New Electro-hydraulic Exciter <i>Dong Han, Guofang Gong, Yi Liu and Huayong Yang</i> .....	285
A Case Study on Quantifying the Workload of Working Machine Operators by Means of Psychophysiological Measurements <i>Reno Filla, Erik M. G. Olsson, Bo H. C. von Scheéle and Kjell Ohlsson</i> .....	293

## Effective Use

Optimizing the Trajectory of a Wheel Loader Working in Short Loading Cycles  
*Reno Filla* ..... 307

Measurements and Simulations to Evaluate Strategies for Improved Energy Efficiency of a Reach Stacker, Forwarder and Wheel Loader  
*Olof Noréus, Magnus Hägglund and Mats Emlén* ..... 319

Modeling Hydraulic Accumulators for use in Wind Turbines  
*Henrik Brun Hansen and Peter Windfeld Rasmussen* ..... 327

## Valve Technology 2

Numerical and Experimental Study of Motion Control Using Pressure Feedback  
*Magnus B. Kjellander and Michael R. Hansen* ..... 337

Lubricity of new Tailor-Made Fuels from Biomass  
*Alexander Weinebeck and Hubertus Murrenhoff* ..... 345

Energy Efficient Active Vibration Damping  
*Eemil Zaev, Gerhard Rath and Hubert Kargl* ..... 355

Geometrical Design and Operability Verification of a Proportional Pressure Relief Valve  
*M. Erhard, J. Weber and Georg Schoppel* ..... 365

## Diagnostics

Recognition of Operating States of a Medium-Sized Mobile Machine  
*Tomi Krogerus, Mika Hyvönen and Kalevi Huhtala* ..... 379

Model-Based Fault Detection for Hydraulic Servoproportional Valves  
*José Roberto Branco Ramos Filho and Victor Juliano De Negri* ..... 389

Guidelines for Modeling Hydraulic Components and Model Based Diagnostics of Hydraulic Applications  
*Sebastian Adén and Kenny Stjernström* ..... 399

Comparison of Optical and Magnetic Particle Detection Systems for Detection of Pitting Damage in Low Speed Hydraulic Motors  
*E. Sjödin and Per-Oskar Westin* ..... 409

## Low Viscosity

Investigation on Velocity Response and Energy Saving Performance of Water Hydraulic Systems Without Using Servo Valve  
*Pha N. Pham, Kazuhisa Ito and Shigeru Ikeo* ..... 419

Effects of Design Parameters on Response Characteristics of Water Hydraulic Proportional Control Valves  
*F. Yoshida AND S. Miyakawa* ..... 429

Simulative Analysis and Experimental Investigation of Common Rail Injection Pumps Lubricated with Tailor-Made Biofuels  
*Stefan Heitzig, S. Drumm AND Hubertus Murrenhoff* ..... 437

Hydraulic Fluid Properties and their Impact on Energy Efficiency  
*Karl-Erik Rydberg* ..... 447

## Pneumatics

Fast Switching Pneumatic Valves: Experimental Bench for Flow and Pulsed Air Jet Characterizations <i>Thiago Ferreira, Sylvie Sesmat, Eric Bideaux and Fabien Sixdenier</i> .....	457
Statistical Approach To Energy Efficiency Issue In Industrial Pneumatic Systems <i>Jyrki Parkkinen, Kai Zenger adn Joonas Ollila</i> .....	465
Energy Saving Measures on Pneumatic Drive Systems <i>J. Hepke and J. Weber</i> .....	475
A Scheme for Compressed Air Saving in Pneumatic Positioning Systems for High Loads <i>Luciano Endler, Victor Juliano De Negri and Eugênio B. Castelan</i> .....	485

## Digital Hydraulics

Control of a Fast Switching Valve for Digital Hydraulics <i>N. P. Sell, D. N. Johnston, A. R. Plummer and S. Kudzma</i> .....	497
Investigation of a Digital Hydraulic Actuation System on an Excavator Arm <i>Alessandro Dell'Amico, Marcus Carlsson, Erik Norlin and Magnus Sethson</i> .....	505
Hydraulic Energy Recovery in Displacement Controlled Digital Hydraulic System <i>Mikko Heikkilä and Matti Linjama</i> .....	513

## Control

Robustness Study on the Model-Free Control and the Control with Restricted Model of a High Performance Electro-Hydraulic System <i>Yaozhong Xu, Eric Bideaux and Daniel Thomasset</i> .....	523
Contribution on Control Strategies of Flow-On-Demand Hydraulic Circuits <i>Martin Scherer, Marcus Geimer and B. Weiss</i> .....	531
Novel Energy-Saving Steer-by-Wire System for Articulated Steering Vehicles: A Compact Wheel Loader Case Study <i>Naseem Daher, Chuang Wang and Monika Ivantysynova</i> .....	541

## Program Committee

Prof. Peter **Krus**, Linköping University, Chairman  
Prof. Jan-Ove **Palmberg**, Linköping University, Vice Chairman  
Dr. Magnus **Sethson**, Linköping University, Program Secretary  
Prof. Bo R. **Andersson**, Linköping University  
Prof. Eric **Bideaux**, INSA de Lyon  
Prof. Richard **Burton**, University of Saskatchewan  
Prof. Victor Juliano **De Negri**, Federal University of Santa Catarina  
Dr. Liselott **Ericson**, Linköping University  
Prof. Ludger **Frerichs**, TU-Braunschweig  
Prof. Emanuele **Guglielmino**, Istituto Italiano di Tecnologia  
Prof. Kalevi **Huhtala**, Tampere University of Technology  
Prof. Monika **Ivantysynova**, Purdue University  
Prof. Toshiharu **Kagawa**, Tokyo Institute of Technology  
Prof. Kari **Koskinen**, Tampere University of Technology  
Prof. Dieter **Krause**, Technical University of Hamburg-Harburg  
Prof. Jean-Charles **Mare**, INSA de Toulouse  
Prof. Hubertus **Murrenhoff**, RWTH Aachen  
Prof. Mariusz **Olszewski**, Warsaw University of Technology  
Prof. Peter **Pelz**, TU-Darmstadt  
Prof. Andrew **Plummer**, University of Bath  
Prof. Karl-Erik **Rydberg**, Linköping University  
Prof. Rudolph **Scheidl**, Johannes Kepler University Linz  
Prof. Kim **Stelson**, University of Minnesota  
Prof. Jürgen **Weber**, TU Dresden  
Prof. Huayong **Yang**, Zhejiang University



# Mobile System 1



## **Eco-Efficiency Analysis for Hydraulic and Hybrid Concepts for Mobile Working Machines**

C. Schindler<sup>1</sup>, M. Eigner<sup>2</sup>, C. Scholler<sup>1</sup>, and P. Schaefer<sup>2</sup>

<sup>1</sup>Chair of Design in Mechanical Engineering, University of Kaiserslautern, Kaiserslautern, Germany

<sup>2</sup>Institute for Virtual Product Engineering, University of Kaiserslautern, Kaiserslautern, Germany

E-mail: [schindler@mv.uni-kl.de](mailto:schindler@mv.uni-kl.de), [eigner@mv.uni-kl.de](mailto:eigner@mv.uni-kl.de), [scholler@mv.uni-kl.de](mailto:scholler@mv.uni-kl.de), [schaefer@mv.uni-kl.de](mailto:schaefer@mv.uni-kl.de)

### **Abstract**

The sector of construction equipment is currently in change. The scarcity of fossil resources and raw materials as well as rising energy costs in the last years and new political and technical requirements has brought the industry to a massive rethinking. A reduction of energy consumption is one of the most important innovation topics in this industry branch. In order to fulfill high energy requirements in the near future, extensive concepts, new structures and innovative technical approaches increasing the total energy efficiency of the product are needed. Therefore the importance of life cycle based eco-efficiency analysis must be considered. Life Cycle Assessment (LCA) and Eco-efficiency assessment are powerful tools for achieving design for life cycle. An LCA examines all stages of a product's life cycle and gives a quantitative assessment of its potential environmental impact. In addition, the results of an Eco-efficiency assessment help to identify priority areas for ecological improvement which are economically worthwhile. This paper presents a comprehensive approach integrating technical analyses to recognize and evaluate possible improvement areas within the machine's construction for doing a quantitative assessment of the environmental impact of the improved technical concepts. The paper describes how LCA and Eco-efficiency assessment can be applied for hydraulic and hybrid concepts and how it can be used to improve the environmental performance of a product in an early step of the life cycle. The approach is demonstrated on the example of a wheeled excavator.

**Keywords:** Hydraulic and Hybrid Optimization, Eco-Efficiency Assessment, Life Cycle Assessment, Product Lifecycle Management, Modular Based Simulation.

### **1 Introduction**

The awareness of limited resources availability, environmental problems and pollution, the increasing demand for goods, energy and materials, as well as the increase of costs of scarce resources, all are calling for a new paradigm of life, overcoming the obsolete consumerist model of modern societies. The reduction of energy consumption and successive use of renewable energy are one of the most important innovation topics in the automotive industry. New and further developments for reducing fuel consumption and CO<sub>2</sub> emissions can be seen mainly in the passenger cars sector, where political requirements on technical developments are already very high. In the field of construction equipment, with well-established hydraulic and hybrid systems, the further increase of energy costs, the need of sustainable production models and the growing competitive pressure will increase significantly because of energetic requirements, too. Therefore extensive concepts, new structures just as innovative and integrated technical approaches for increasing the total energy efficiency of construction

equipment are needed [1][2]. This demand of high flexibility leads to complex systems which contain mechanic, hydraulic electric and even hybrid subsystems. The overall effect of energy and resource reduction of these new technical concepts is often hard to predict, especially within a life cycle view taken into account. Already promising technical concepts are in pre-commercial development, but their performance is frequently designed for the operation efficiency at a specific load scenario. Often, they are not tested within a total life cycle perspective. [3] This paper presents a comprehensive approach to estimate the life cycle based eco-efficiency for future hydraulic and hybrid concepts of construction equipment. The approach involves an implementation of Life Cycle Assessment (LCA) and Eco-efficiency assessment as fully integrated within the Product Lifecycle Management (PLM) supporting the engineering in terms of sharing relevant product data across modules and life cycle phases. The capabilities of the proactive Life Cycle Assessment and Eco-efficiency assessment solution for a sustainable management are examined and presented on the example of a wheeled excavator.

## 2 Sustainable Management

Moreover, to be competitive on the global market in time of an increasing shortage of resources, companies have to develop not only good products but have to make them also more sustainable. Sustainable Development, conceptually founded on the three dimensions economical, ecological and social sustainability, is the main paradigm for future improvement of humankind in the 21<sup>st</sup> century [4]. One of the guiding principles for engineering design is to develop products that conform to the sustainability paradigm [5]. In the discourse on sustainable management, the potential of the product development process is currently inadequately treated [6] [7]. A sustainable product development aims at the real goods, but also on the assessment of environmental, ecological and social issues over its entire life cycle. Therefore, a total approach is necessary, accompanying the product from the initial idea, through the development and manufacturing phases, the usage and all end-of life treatments. Already in the early phases of the life cycle, the engineer defines key properties of a product, implicitly including the definition of the resulting life cycle costs as well as environmental and social effects: The product shape is clearly determined by the product development [5]. A central problem for those companies interested in sustainable management is to analyze, to optimize and to communicate its product portfolio with as low as possible effort. Therefore the process of creating a more sustainable product needs to be monitored and managed from the very first beginning, whether a new product is to be designed or an existing one is to be improved [8]. This is also of importance for companies producing construction equipment [3] [8]. To address a sustainable product development or engineering design process, appropriate methods and tools are required. Internationally standardized tools for the assessment of environmental-economical sustainability of a product system do already exist – Life Cycle Assessment [9] and Eco-efficiency assessment [10].

### 2.1 Regarding the Environmental Impact

The ISO 14040 standardized Life Cycle Assessment (LCA) [9], as part of a sustainability assessment, provides a meaningful methodological framework for the ecological dimension [11]. The product related Life Cycle Assessment (LCA) with an emphasis on energy, resource and waste, first started back in the 1970s, in time of the famous report ‘The Limits to Growth’, addressed to the Club of Rome and the first worldwide oil crisis, which brought awareness of the finiteness of oil and revealed the vulnerability of the global economic system. In the 1990s LCA was developed as method, mainly driven by the Society of Environmental Toxicology and Chemistry (SETAC), and standardized by the International Organization for Standardization (ISO). Later on, in 2006 the international series of LCA standards have been slightly revised to their current version of ISO 14040 and ISO 14044 [12]. [13] The basic principles of any Life Cycle Assessment are the cradle-to-grave analysis and the use of functional unit. All mass and energy flows, resource and land use, and even the potential impacts and probable interventions are set in relation to the functional

unit as quantitative measures of the benefit. Life Cycle Assessment is a method to analyze environmental parameters out of the environmental profile of a product system and across its life cycle. The environmental profile of a product system is thereby determined and dependence on five categories [14]:

- Energy use
- Material use
- Emissions in air, water and soil
- Toxic potential of used and released substances
- Compliance to environmental laws and regulations

Life Cycle Assessment can systematically identify key areas to improve environmental performance, even applied to the sector of construction equipment. The main characteristic of the standards ISO 14040 and ISO 14044 is the clear framework which consists in four components [9] [12]:

- Goal and Scope Definition
- Inventory analysis
- Impact Analysis
- Interpretation

The definition of the goal and the scope of any LCA is crucial, since this is the phase of essential determinations. According to the aims and the insight interest, a survey framework is defined and demands on further phases are determined. This may concern the intensity of a survey, the necessary quality of data, a selection of the effect parameters with regard to the impact assessment, and the interpretive possibilities within the framework of an evaluation. In the inventory analysis, all material and energy flows are grasped and listed during their entire life cycle. In a first step, process structures are modeled in order to have a basis for assembling data. All material and energy flows are determined as input-/output-sizes for every partial process with regard to the system boundary. By connecting all partial processes, the relations between the modules and the environment are represented, and the mass/energy balance is drawn up as the inventory of the total system. All material and energy streams which pass the system borders are listed as quantities in physical units. The data refer to the functional unit. The task of the impact assessment is the evaluation of all material and energy flows raised in the inventory analysis according to certain environmental effects. Thus, an impact assessment serves the recognition, summarization, and quantification of the potential environmental effects of the examined systems and delivers essential information for the evaluation. [13] The following impact categories are usually included into a LCA [15]:

- Global warming Potential (GWP)
- Stratospheric ozone depletion (ODP)
- Tropospheric photochemical ozone creation (POCP)
- Acidification (AP)
- Eutrophication (NP)
- Human toxicity (HTP)
- Ecotoxicity (ETP) and
- Land use

The impact categories describe potential effects on human and environment. Among other things, they differ according to their spatial references (global, regional and local effects). In principle, every environmental effect can be included into the survey, as long as the necessary data and a suitable model for the description and parameterization of the effect are available. The task of the interpretation step is the analysis of the results as well as the explanation of the meaningfulness and the restrictions. The essential facts, based on the results of the inventory analysis and the impact assessment, are to be determined and checked with regard to their completeness, sensitivity, and consistency of the results. The assumptions made in the phase of the goal and scope definition have to be considered. Based on this, conclusions have to be drawn and recommendations are to be made. [13] The Life Cycle Assessment is an essential comparative method to estimate the environmental aspects of a product system. It explores environmental performance and potential environmental impacts across the product life cycle, from raw material extraction, across production, to reuse of recyclates and waste disposal. A LCA can assist engineers and decision-makers in industry by identifying opportunities to improve the environmental performance of product systems and providing them with a platform for observing the environmental product declarations and environmental compliance, thus support the design of more eco-efficient products.

## 2.2 From LCA to Eco-Efficiency Assessment

A first step towards an integrated sustainability assessment provides the link between economic and ecological issues and is represented in the international standard ISO 14045 - Eco-efficiency assessment of product systems: principles, requirements and guidelines, adopted in 2012 [10]. The principles relate to the ISO 14040 - 14044 for product systems, and are translated into specific objectives [16]:

- Minimize energy intensity
- Minimize material intensity of goods and services
- Maximize the use of renewable resources
- Minimize toxic dispersion
- Extend product durability
- Increase product efficiency
- Promote recycling

The objective of an Eco-efficiency assessment is to support the economical-ecological evaluation of different product systems by providing an overall life cycle view.

## 2.3 Beyond an Eco-Assessment

To arrange an LCA or an Eco-efficiency assessment, it is a very complex, time-intensive and cost-intensive task. This is based on the fact that an extensive data base of a product system with its processes is needed [17][18]. The practice of the standards ISO 14040-14044 and ISO 14045 is, due to a high complexity, often carried out with special software tools [17][19]. It becomes apparent that the analysis of an existing product system is retrospective. But especially for complex products, like for construction equipment, the application of Life Cycle Assessment and Eco-efficiency in

product development is very interesting [20]. The product development determines all other phases in life cycle, like the manufacturing, the usage and the end-of-life [21] [22]. Decisions in this early phase play a key role in terms of economic-ecological product design. According to [29] up to 70% of the total cost of ownership is set in the early phase of product development. In the same extent according [23] the environmental impacts of the final product system are determined. With a proactive Life Cycle Assessment and Eco-efficiency solution, a company can identify priority areas for improvement and become preemptive in its sustainability initiatives. This was the trigger for the research project ERMA underlying the following case study.

## 3 Improving the Environmental Performance of Construction Equipment

In order to fulfill the pressing problems of a sustainable management within the product development of construction equipment, four institutes at University of Kaiserslautern initiated the research project Energy and Resource Efficient Mobile Working Machines (ERMA). [3] Main objectives are the further development and application of methods and tools to estimate and evaluate the overall eco-efficiency of a wheeled excavator [20][24][25][26][27]. The advancement of new concepts for less energy and resource using subsystems is directed to improve the chosen product system with this consideration.

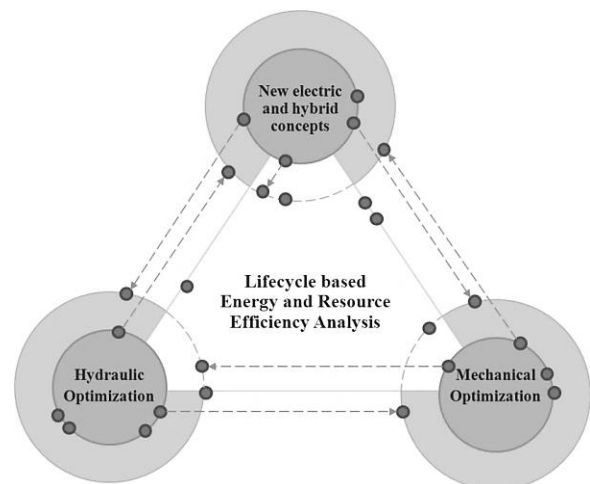


Figure 1: Interdisciplinary Optimization Supported by Life Cycle Based Eco-Efficiency Analysis (adapted from [3]).

In the first step, a modular simulation model of the wheeled excavator is created, followed by a verification of the full simulation model. The focus of the model is to calculate the energy consumption for specific load cycles, which can also be configured to specific customer usage profiles. Because of this, modular subsystems can easily be implemented in the model. This way the overall energy consumption of an improved technical system can be estimated as well. In a second step, the objective is to improve the current product system itself with respect to energy savings. Starting with the analysis and the minimization of friction losses of the

existing bearings and seals, more efficient hydraulic solutions are developed. New concepts of electric or hybrid subsystems will be developed and introduced to substitute parts of the current hydraulic system for reducing the energy consumption. Same time, new methods and a concept for an integrated product life cycle based proactive eco-efficiency assessment are developed, and will be tested and verified. The project structure is shown in *Figure 1*. The interdisciplinary tasks within ERMA cover both: the technical improvements of construction equipment and an eco-analysis of the improved concepts. Therefore the results of the technical evaluations are used in the eco-efficiency analysis to get an overall result of single concepts including customer usage profiles for specific life cycles.

### 3.1 Technical Evaluation

The technical evaluation of ERMA aims to estimate the energy consumption and the system behavior of concepts during operation. With this, different concepts are comparable concerning for example the reliability of the concept, the operability of the machine as well as variable costs due to fuel consumption. For the evaluation process many influences have to be considered like proper reference data or the customer usage profile. Due to cost reduction a simulation model was used to estimate the energy consumption. The excavator was modeled along the common V-Model [28]: The hydraulic structure was reproduced in the numeric Simulation tool AMESim and with the help of measurement data and data sheets, the important parameters were defined and valued. The verification and validation process confirms the correctness of the model (see *Figure 2*). After that, an overall model of the excavator in its current state exists.

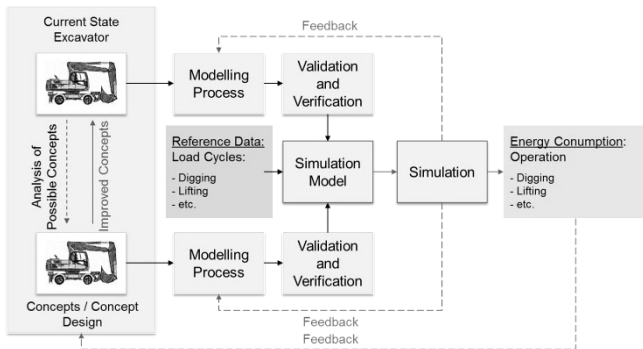


*Figure 2: Technical Evaluation of new Hydraulic and Hybrid Concepts for a Wheeled Excavator.*

If a new concept is modeled and implemented in the overall model, inevitably the model will change and a new model of the excavator comes into existence. If this is done with many concepts and maybe different parameter variations, the amount of different simulation models of the excavator will increase and the maintenance effort due to synchronization issues will rise exponentially. This will make it difficult to compare different technical concepts. To avoid that, a modular structure was implemented in the model. If the modules are suitable designed, it is possible to exchange only one or two modules to implement a new

technical concept. With this, the overall structure of the simulation model is unchanged and no new simulation model will come into existence. Also the maintenance effort is restricted to the single modules. This approach was published in [27]. For the technical evaluation of a concept, a customer-usage-profile has to be defined. This is normally done by reducing the usage of the machine to a certain amount of load-cycles in combination with a weighting according to the amount of time a certain user operates the machine the specific load cycles [30][31]. But often, the usage of the machine is not known or differs from customer to customer. Hence, it is hardly possible to make an exact statement if a technical concept is eco-efficient or not related to its whole work cycle or even life cycle. For example, if a wheeled excavator is used for mass excavation, a regeneration device for the swing will generate a much better result as if the wheeled excavator is only used for driving or trench digging. Because of this issue, for ERMA we decided to expand the approach and take a variable user-profile into account. For that, the technical evaluation only considers different load-cycles without a weighting. The weighting will follow after the eco-efficiency analysis, see chapter 4. This procedure has the advantage that the design of the machine is related to its purpose and a customer can get the ideal machine for his individual usage. In summary, the result of this approach calculates the unweighted energy consumption of concepts with respect to the defined load-cycles. With the modular structure of the simulation model, a comparison of the results between the single technical concepts is possible. The results will be forwarded to the product life cycle management solution, where they are used in the eco-efficiency analysis.

### 3.2 Eco-Efficiency Analysis

Complex products like construction equipment are characterized by a large number of constituent parts, complex processes and referring to the life cycle, high fuel consumption throughout a long life cycle [3][22]. Regarding the life cycle of a mobile working machine [8] or an agricultural machine [15] for example, an eco-efficiency analysis helps to identify environmental key factors and cost drivers within the use phase where CO<sub>2</sub> emissions, resulting from fuel consumption, are very high. The operational eco-efficiency analysis of ERMA demonstrates how much environmental impact is caused by a product and its processes and how different life cycle phases as well as product subsystems contribute to the total impact [22]. The eco evaluation concept shown in *Figure 3* is in addition to it closely linked to a product life cycle management solution. It extends the product model as well as the process model by technical-economical attention of ecological parameters, thus it allows an aggregated evaluation of energy and resource efficiency of the product system over the entire life cycle. Energetically improved technical products will assert themselves in enterprise practice only if they are advantageous in economic regard. Hence, the deliberate design of eco-efficient products is as important as both, economic balance and Life Cycle Assessment. The approach deals with this and is outlined in a way, that it corresponds

to a multidimensional, interdisciplinary and federated life cycle management. Integrated funds on a solution that handles the whole life cycle of the product system, starting with a first idea up to the end-of-life. Federated calls for an engineering collaboration in distributed enterprises as well as within suppliers, customers or even the whole supply chain, and Multidisciplinary refers to the cooperation of different disciplines or specialized divisions which are involved in the product development. [22]

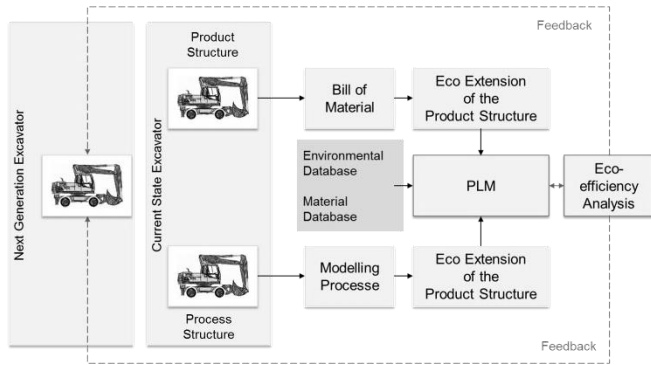


Figure 3: Eco Evaluation of new Technical Concepts for a Wheeled Excavator.

To achieve best practice, all concerned parties have to cooperate and tap into the know-how of all phases of a product life cycle. This leads to the need for an entire system solution.

#### 4 Comprehensive Approach

The prospective view within ERMA requires the application of an eco-efficiency analysis in a proactive view for product development as well as an analysis which has to be applied

to a complex system. This paper considers Product Lifecycle Management (PLM) [21] as one key concept for the establishment of sustainable engineering design processes. Product Lifecycle Management is based on the idea of connecting knowledge. It represents a concept rather than a monolithic IT-system. [31][32] PLM is an integrated, information-driven approach to improve the product performance over the entire life cycle. It achieves efficiency by using a shared information core system that helps business to efficiently manage complexity in the product life cycle from design to end-of-life. [21][31][33] Thus, PLM does not provide innovative products, but it is a concept that can contribute engineering at the administrative level by providing the right information at the right time in the right context [18]. As a consequence, Product Lifecycle Management can help to improve the environmental and sustainability performance of a product [34] [35] [36] [37].

#### 4.1 Identifying Priority Areas for Eco-Efficiency Improvements

Regarding the material flow and the information flow on the entire life cycle, the most pertinent issues and important elements of an eco-efficient product strategy are highlighted (see Figure 4): As shown the relevant material flow consists of the three phases: manufacturing, usage and end-of-life treatment. Within the manufacturing, sub phases like extraction of raw material and the production of intermediate products as well as the entire product system are included. The usage includes the operation and maintenance, in our case, of a wheeled excavator. Here, fuel consumption and emissions from machine operation as well as the replacement of spare parts, filters, oils and fluids are all relevant targets and are taken into account. The end of life phase involves all recycling and disposal activities. [22]

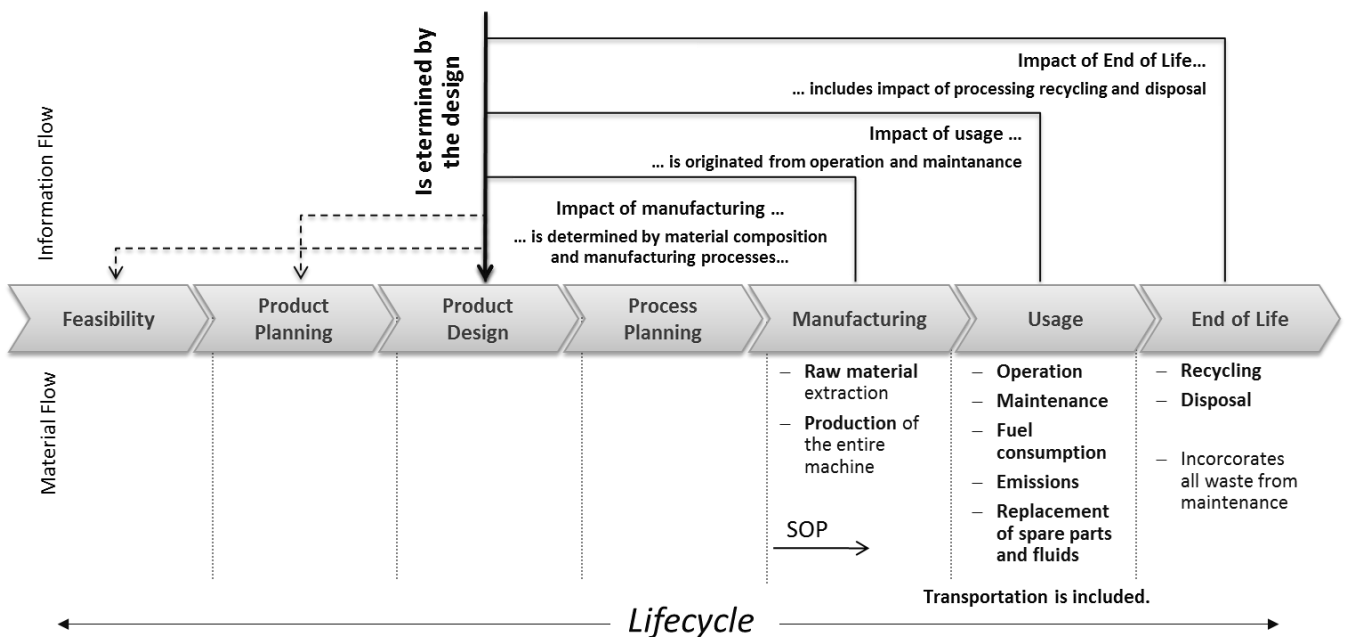


Figure 4: The Early Phase of the Product Development Takes a Key Role (adapted from [22]).

As shown in the information flow, the impact of the manufacturing is determined by the design of the product system. It is defined by the composition of the assembly and sub-assembly, even so hydraulic, electric and hybrid components as well as their production processes and the production process of the entire product system, to be exact. Relevant sub-processes within the phases of manufacturing, usage and end-of-life, such as transportation are included. The impact of usage is originated as shown in *Figure 4* from operation and maintenance. Main driver with the most impact on eco-efficiency does have the operation. New hydraulic and hybrid technical concepts will make a contribution and help to improve the impact of fuel consumption as well as the associated impact of emissions of the whole product system. [22] Even strategies to reduce the energy demand are an essential factor for future construction equipment. The increasing diversification of alternative technical concepts offers a great potential for electric and hybrid solutions and also further improved hydraulic solutions. [38] The impact of end-of-life treatment includes the impacts of processing the end-of-life product system and processing all replacement parts and fluids consumed over the lifetime of the wheeled excavator [22]. Even for construction equipment, regarding the cumulated energy demand of different used materials and in relation to their mass, it turns out that in future the use of recyclates will play an essential role [38]. The known information about the life cycle including material the flow, it applies making it available for new product design and improvements for current product. In order to address these potentials for engineering design, appropriate methods and tools are required. Several software solutions to assist decision-makers in the product development phase regarding the environmental impact do already exist. The selection exemplifies the degree of integration depth:

- GaBi Software  
*Stand-alone software solution LCA at the product level.*
- SimaPro Software  
*Stand-alone software solution LCA at the product level.*
- Sustainability Pro from Dassault Systèmes  
*Software solution embedded into the CAD of SolidWorks*
- Teamcenter Sustainability and Environmental Compliance  
*Semi-integrated in PLM solution.*
- Windchill Product Analytics  
*Stand-alone software solution but in practice mainly semi-integrated in PLM solution.*

It lacks to a fully integrated eco-efficiency solution into the Product Lifecycle Management. Below, the argument of how eco-efficiency analysis is integrated into Product Lifecycle Management is presented with a comprehensive approach for ERMA.

#### 4.2 A Concept of an Eco-Efficiency Analysis as Part of Product Lifecycle Management

Within the research project ERMA, the existing Product Lifecycle Management solution is extended by enabling the monitoring of a product life cycle already in the early phases of an engineering design process. The total concept is shown in *Figure 5*. The objective of the eco-efficiency analysis is to support the evaluation of different optimized technical concepts by providing an overall life cycle view. The approach refers to Eco-efficiency assessment and is linked to the Product Lifecycle Management [34] [39]. It extends the product model as well as the process model by technical-economical attention of ecological parameters, thus it allows an aggregated evaluation of energy and resource efficiency of the product over the entire life cycle. Energetically improved technical products will assert themselves in enterprise practice only if they are advantageous in economic regard. Hence, the deliberate design of eco-efficiency products is as important as both economic balance and life-cycle assessment. The concept deals with both and is outlined in a way, that it corresponds to a multidimensional, interdisciplinary and federated lifecycle management. Aim of the analysis made with the Product Lifecycle Management solution is to measure multiple dimensions of the product performance in two of the three sustainability areas – ecological and economical. The modules share common, scalable infrastructure and support multiple methods for supplier data acquisition. Bi-directional integrations with multiple enterprise systems such as authoring systems and the PLM solution are also supported. The extended Product Lifecycle Management solution forecasts the eco-efficiency performance of the product system. Beside this, the solution audits the conformity to current environmental legislation. Just for the development of electric and hybrid solutions, this is of central importance. Environmental regulations influence companies to follow environmental procedures. They have to comply with governmental regulations or face immediate and serve consequences [33] [34]. The selection shows a summary of some current environmental legislation [18]:

- EuP  
*Energy using Product*
- REACH  
*Registration, Evaluation, and Authorization of Chemicals*
- RoHS  
*Restriction of use of certain Hazardous Substances*
- WEEE  
*Waste Electrical and Electronic Equipment*
- ELV  
*End of Life Vehicle*

To reach the goal, the design of eco-efficient construction equipment not only the need to choose materials that are compliant with regulations is necessary, but also the need to move beyond basic eco-compliance with a sustainability strategy that phases out or replaces current hydraulic components with new electric and hybrid ones.

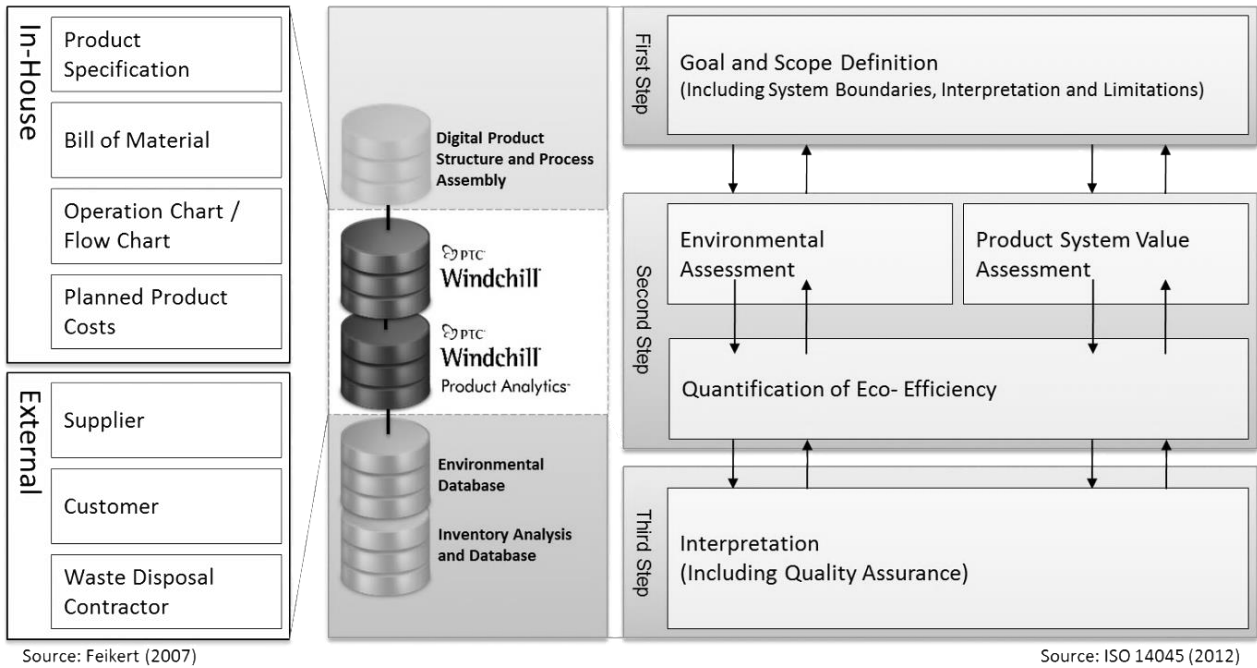


Figure 5: Concept of an Eco-Efficiency Analysis as Part of Product Lifecycle Management (adapted from [39])

The introduced Product Analytics module (see Figure 6) uses a streamlined Life Cycle Assessment approach for qualifying the environmental impact over the entire life cycle of a product. This means that relies primarily on secondary existing life cycle impact data from the wheeled excavator and, but not necessarily, third party data such as theecoinvent eco-balance data base, to produce quick, relatively robust information. It has the capabilities to model and analyze embodied environmental impacts throughout the life cycle utilizing supplier material disclosures for that, it can identify highest impact areas among products, parts, material, suppliers as well as the choice of hydraulic and hybrid options. It provides relevant eco-efficiency data in report dashboards, which are of help for design engineers in the evaluation of improvement opportunities. [20]

intellectual product system to multiple standardized regulations and requirements such as EuP, REACH, RoHS, WEEE, and ELV using supplier material declarations as data source. It helps to measure and manage compliance risk early in the product development phase of next generation construction equipment. [20]

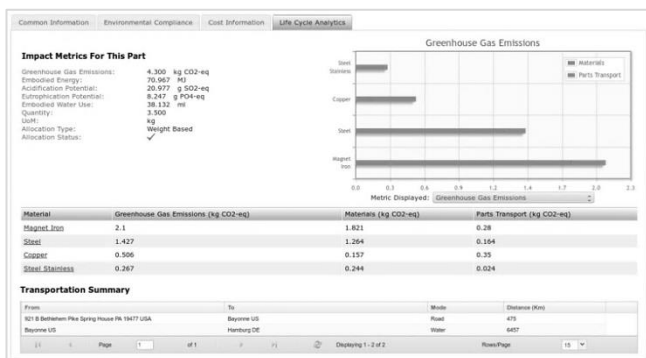


Figure 6: Life Cycle Analysis Dashboard of the Product Lifecycle Management Solution (adapted from [39])

The Environmental Compliance module (see Figure 7) is used to analyze and report compliance of company products or even chosen hydraulic and hybrid options of the

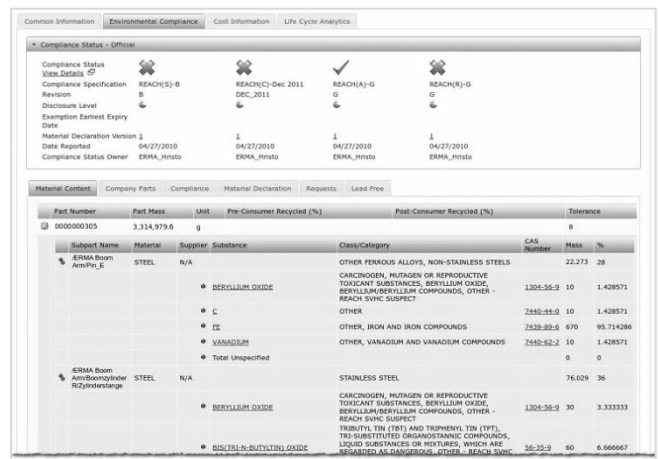


Figure 7: Environmental Compliance Dashboard of the Product Lifecycle Management Solution (adapted from [39])

The Lifecycle Cost Module (see Figure 8) enables users to easily estimate and display cost information for company or supplier parts or product systems based on different estimation model to maintain them as dynamical database. It supports cost breakdowns as well as cost confidence levels and gives an overview of the cost history of a part, assembly, product system or even chosen hydraulic and hybrid alternatives. [20]

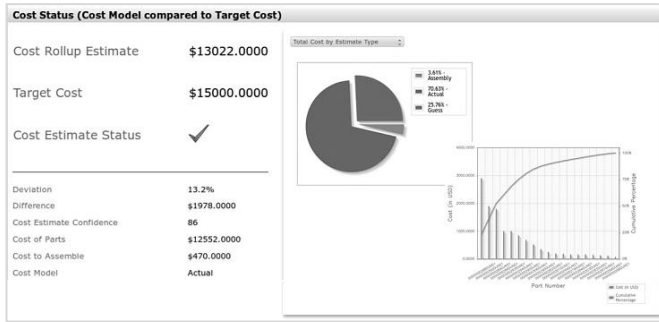


Figure 8: Life Cycle Costing Dashboard of the Product Lifecycle Management Solution (adapted from [39])

### 4.3 Dependent Opportunities for Reducing Environmental Impact

In the following, range opportunities [22] for reducing the environmental impact referring construction equipment are investigated, and are proposed as potentials for ERMA:

- Reduced fuel consumption rate
- Reduced emission rates
- Improved durability
- Improved machine productivity
- Reduced Idling
- Use of biodiesel

The first cluster of solutions relate to the product design while the second cluster relate to the usage behavior. Both directions are investigated for a customer related assessment.

### 4.4 Integration of Technical Evaluation and Eco-Efficiency Analysis based on Product Lifecycle Management

As consequences of technical evaluations (shown in chapter 3.1) and eco-efficiency analysis (shown in chapter 3.2) the comprehensive approach of ERMA includes integration, shown in Figure 9. Based on this, it becomes possible to analyze and optimize the current wheeled excavator focusing on new, innovative mechanical, hydraulic and electric/electronic as well as hybrid components and system solutions. The introduced Product Lifecycle Management solution is proposed as a guiding approach of the whole analysis and optimization process, with the aim of measuring multiple dimensions of the product performance in two of the three sustainability areas – ecological and economical as well as providing the data relevant for technical analysis to external software tool. Thereby existing PLM concepts will be extended by enabling the monitoring of a product life cycle already in the early phases of an engineering design process. On the technical side main topic is the analysis of hydraulic and hybrid optimizations with a digital simulation model in regard to energy loss and consumption, with consequent energy optimization of the wheeled excavator. The calculation of the energy consumption and the energy efficiency do have many

versatile requirements. Here, the objective is to analyze the benefits of new technologies on the energy consumption. For the evaluation of different subsystem variants, a comprehensive system solution is required. It is necessary to evaluate the impact of different customer usage profiles on these subsystems with respect to the total energy consumption. To meet these demands, the numerical simulation model of the wheeled excavator is developed in a modular design. The model is structured in exchangeable modular sub-systems, where existing modules can be simply replaced by new ones with improved functions. In this way a direct comparison of the function, the dynamic behavior and the energy consumption of different technical solutions with respect to the used load-cycle can be accomplished.

## 5 Conclusion

The paper shows a first approach of an eco-efficiency analysis concerning economical attention of ecological parameters and technical evaluation of hydraulic and hybrid concepts for mobile working machines. New functions are developed to evaluate the technical behavior as well as the resources consumption using environmental databases. Hereby the main focus is on the structure of the system, interfaces of the functions and the implementation within a Product Lifecycle Management solution. Furthermore, a method is given, how to use a numerical simulation model for the technical evaluation of concepts. The topics are the modular structure of the simulation model and about how to deal with different customer usage profiles. The need for a linkage between the Product Lifecycle Management solution and the numerical simulation software is shown and by a comprehensive approach. The importance of lifecycle based energy and resource efficiency analysis in the sector of construction equipment is very high. A reduction of energy consumption is one of the most important innovation topics for construction equipment. In order to fulfill high energy requirements in the near future, extensive concepts, new structures and innovative technical approaches increasing the total energy efficiency of the product are needed. Therefore the importance of lifecycle based eco-efficiency analysis must be considered. Life cycle assessment (LCA) and Eco-efficiency assessment are powerful tools for achieving design for life cycle. An LCA examines all phases of the life cycle of a product system and gives a quantitative assessment of its potential environmental impact. In addition, the results of an eco-efficiency analysis help to identify priority areas for ecological improvement which are economically worthwhile. This paper presents an approach of eco-efficiency analysis as fully integrated into Product Lifecycle Management.

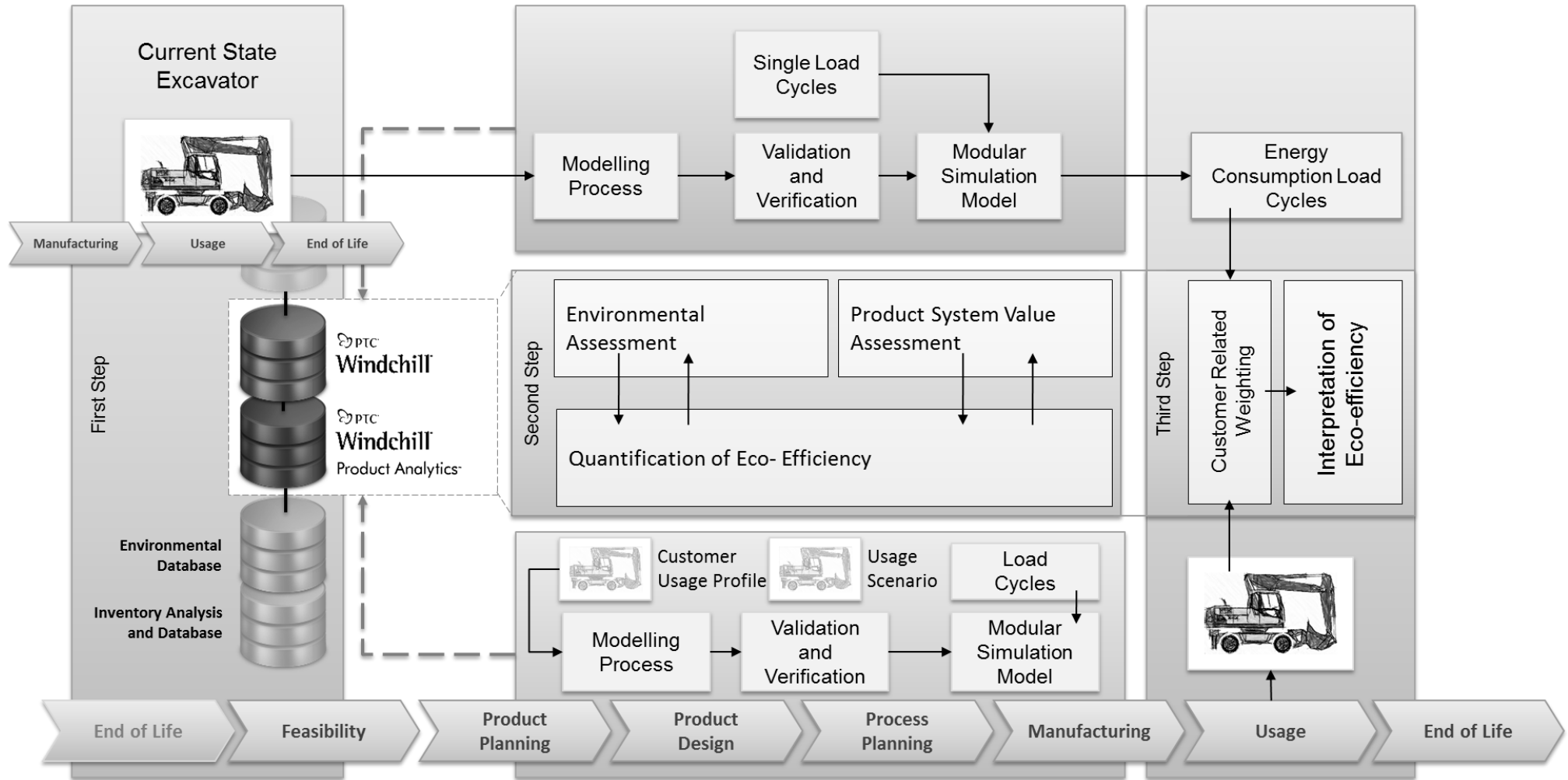


Figure 9: Integration of Technical Evaluation and Eco-Efficiency Analysis based on Product Lifecycle Management.

## Acknowledgments

The research project ERMA is funded by the Foundation for Innovation of the German state Rhineland-Palatinate. We extend our sincere thanks to all partners at the product design group at the Center of Commercial Vehicle Technology at the University of Kaiserslautern who contribute in preparing the project.

## References

- [1] C Holländer. *Untersuchungen zur Beurteilung und Optimierung von Baggerhydrauliksystemen*. Fortschritt-Berichte VDI Reihe 1(307). VDI, Düsseldorf, 1998.
- [2] R Finzel, H Jähne, and S Helduser. Energieeffiziente Antriebssysteme mobiler Arbeitsmaschinen. *Proc. of 4. Fachtagung Baumaschinentechnik*. Dresden, 2009.
- [3] S Pick, M Mohr, P Schaefer, C Scholler, M Eigner, S Mueller, B Sauer, and C Schindler. Lifecycle based Evaluation of new Energy- and Resource-Efficient Concepts for Mobile Working Machines. *Proc. of the 2nd Commercial Vehicle Technology Symposium*. Shaker, Aachen, 2012, pp. 319-328.
- [4] J Blank. Sustainable Development. *Lexikon Nachhaltiges Wirtschaften*. Oldenbourg, München, Wien, 2001, pp. 374-385.
- [5] M Eigner, M von Hauff, and P Schaefer. Sustainable Product Lifecycle Management - A Lifecycle based Conception of Monitoring a Sustainable Product Development. *Glocalized Solutions for Sustainability in Manufacturing*. Springer, Berlin, Heidelberg, 2011, pp. 501-506.
- [6] S Terzi, A Bouras, D Dutta, M Garetti, and D Kiritsis. Product Lifecycle Management – from its history to its new role. *Int. J. Product Lifecycle Management*, 4(4), pp. 360-389. 2010
- [7] B Bras. Sustainability and product life cycle management - issues and challenges. *Int. J. Product Life Cycle Management*, 4(1/2/3), pp. 23-48. 2009
- [8] M Eigner, and P Schaefer. Sustainable Product Lifecycle Management - A Lifecycle based Conception of Monitoring a Global Product Development in a Sustainability-Driven Century. *Openness for Global Success - ProSTEP iViP Symposium 2013*. Hannover, 2013, p. 70.
- [9] ISO 14040. *Environmental management - Life cycle assessment - Principles and framework*. Beuth, Berlin, 2006.
- [10] ISO 14045. *Environmental management - Eco-efficiency assessment of product systems - Principles, requirements and guidelines*. Beuth, Berlin, 2012.
- [11] W Kloepffer. Life Cycle based methods for sustainable product development. *Int. J. of Life Cycle Assessment*, 8(3): pp. 157-159, Springer, Berlin, 2003.
- [12] ISO 14044. *Environmental management - Life cycle assessment - Requirements and guidelines*. Beuth, Berlin, 2006.
- [13] W Kloepffer, and B Grahl. *Oekobilanz (LCA) – Ein Leitfaden für Ausbildung und Beruf*. Wiley-Vch, Weinheim, 2009.
- [14] E Baroulaki, and A Veshagh. Eco-Innovation – Product Design and Innovation for the Environment. *Advances in Life Cycle Engineering for Sustainable Manufacturing Businesses*. Springer, London, 2007.
- [15] P Pickel, M Eigner. Life Cycle Assessment (LCA) and its importance for the agriculture sector. *Proc. of the 23rd Annual Meeting of the Club of Bologna*. Bologna, 2012.
- [16] World Business Council for Sustainable Development. *Eco-efficiency – Creating more value with less impact*. 2000.
- [17] S Feickert. *Oekologisches Product Lifecycle Management – Ein Integrationskonzept der oekologischen Produktbilanzierung in betrieblichen ERP-Systemen*. Aachen, 2007.
- [18] N Ciceri, M Garetti, and S Terzi. Product Lifecycle Management Approach for Sustainability. *Proc. of the 19th CIRP Design Conference*. Cranfield, 2009, pp. 147-154.
- [19] K Ramani, D Ramanujan, W Bernstein, F Zhao, J Sutherland, C Handwerker, J Choi, H Kim, and D Thurston. Integrated Sustainable Life Cycle Design – A Review. *J of Mechanical Design*, 132. 2010
- [20] M Eigner, P Schaefer, and H Apostolov. Leveraging Product Development for a Sustainable Future - Energy and Resource Efficiency in Lifecycle Analysis. *Smart Product Engineering, Proc. of the 23rd CIRP Design Conference*. Springer, Berlin, Heidelberg, 2013, pp. 725-734.
- [21] M Eigner, and R Stelzer. *Product Lifecycle Management - Ein Leitfaden für Product Development und Life Cycle Management*. 2. Ed., Springer, Berlin, Heidelberg, 2009.

- [22] M Kwak, and H Kim. Exploring Opportunities to Improve Life Cycle Environmental Performance of a Complex Product. *Smart Product Engineering, Proc. of the 23<sup>rd</sup> CIRP Design Conference*. Springer, Berlin, Heidelberg, 2013, pp. 735-744.
- [23] A Posch, and E Perl. Regionale Verwertungsnetze und industrielle Symbiose. *Industrial Ecology - Mit Oekologie zukunftsorientiert wirtschaften*. Elsevier, München, 2007, pp. 265-276.
- [24] C Scholler, and C Schindler. Simulation der Energieverteilung innerhalb eines Load-Sensing-Ventils im Mehrverbraucherbetrieb am Beispiel eines Mobilbaggers. *Proc. of the 5. Fachtagung Bau-maschinentechnik 2012*. Dresden, 2012, pp- 309 - 324.
- [25] S Pick, S Mueller, P Bach, and U Fass. Future Wheeled Excavator - Higher Efficiency by Electrification. *Proc. of the Aachener Colloquium Automobile and Engine Technolog.* Aachen 2012, pp. 1577-1594.
- [26] M Mohr, and B Sauer. Optimierung der Energie- und Ressourceneffizienz eines Mobilbaggers im Rahmen von ERMA. *Proc. of the Antriebstechnisches Kolloquium ATK 2013*. Aachen, 2013, pp. 193-220.
- [27] C Scholler, C Schindler, S Pick, and S Mueller. Modularer Simulationsbaukasten zur Potenzialabschätzung hydraulischer und hybrider Konzepte. *Hybridantriebe für mobile Arbeitsmaschinen, Proc. of the 4. Fachtagung des VDMA und des Karlsruher Instituts für Technologie*. KIT Scientific Publishing, Karlsruhe, 2013, pp. 61-72.
- [28] VDI 2206. *Design methodology for mechatronic systems*. Beuth, Berlin, 2004.
- [29] R Finzel, S Helduser, and D Jang. Electro-hydraulic Dual-Circuit System to improve the energy efficiency of Mobile Machines. *Proc. of the 7th International Fluid Power Conference Aachen*. Aachen, 2010.
- [30] M Kagoshima, M Komiyama, T Nanjo, and A Tsutsui. *Development of New Hybrid Excavator*. Kobelco Technology Review, 2007, pp. 39-42.
- [31] J Stark. *Product Lifecycle Management – 21st Century Paradigm for Product Realisation*. Springer, London, 2011.
- [32] U Sandler. *Das PLM Kompendium – Referenzbuch des Produktlebenszyklus Management*. Springer, Berlin, Heidelberg, 2009.
- [33] M Grieves. *Product Lifecycle Management – Driving the next generation of lean thinking*. New York, 2006.
- [34] L Barreto, H Anderson, A Anglin, and C Tomovic. Product Lifecycle Management in support of green manufacturing – Addressing the challenges of global climate change. *Int. J. of Manufacturing Technology and Management*, 19(3/4), pp. 294-305. 2010.
- [35] A Moeller, and A Rolf. Eco Product Lifecycle Management. *Proc. of the 2<sup>nd</sup> International Symposium on Environmentally Conscious Design and Inverse Manufacturing*. Tokyo, 2001, pp. 739-744.
- [36] A Abele, S Feickert, D Kuhrke, and F Clesle. Environmental Product Lifecycle Management – Customizing the Enterprise Specific Manufacturing Processes. *Proc. of the 13<sup>th</sup> CIRP International Conference on Life Cycle Engineering*. Leuven, 2006, pp. 651-656
- [37] A Staisch, G Peters, T Stueckl, and J Sergua. Current Trends in Product Lifecycle Management. *Proc. of the 23<sup>rd</sup> Conference on Information Systems*. Geelong, 2012.
- [38] H Demel. Comparison of the well-to-wheel energy efficiency of different vehicle concepts. *Proc. of the 30<sup>th</sup> International Wiener Motorensymposium*. Wien, 2009.
- [39] M Eigner, and P Schaefer. Nachhaltige Produktentwicklung im Bau von mobilen Arbeitsmaschinen mit PTC Windchill und PTC Windchill Product Analytics. *PTC Live 2012*, Stuttgart, 2012.

## Contact

University of Kaiserslautern  
 Research Project "ERMA"  
 c/o Chair of Design Engineering  
 P.O. Box 3049  
 D-67653 Kaiserslautern

Email: [erma@mv.uni-kl.de](mailto:erma@mv.uni-kl.de)  
 www: <http://www.uni-kl.de/erma>



## **Design Rules for High Damping in Mobile Hydraulic Systems**

Mikael Axin and Petter Krus

Division of Fluid and Mechatronic Systems, Department of Management and Engineering, Linköping University, Sweden  
E-mail: mikael.axin@liu.se, petter.krus@liu.se

### **Abstract**

This paper analyses the damping in pressure compensated closed centre mobile working hydraulic systems. Both rotational and linear loads are covered and the analysis applies to any type of pump controller. Only the outlet orifice in the directional valve will provide damping to a pressure compensated system. Design rules are proposed for how the system should be dimensioned in order to obtain a high damping. The volumes on each side of the load have a high impact on the damping. In case of a small volume on the inlet side, the damping becomes low. However, the most important thing is to design the outlet orifice area properly. There exists an optimal orifice dimension for maximized damping; both smaller and larger orifice areas give lower damping independently of the volumes. This paper presents a method to dimension the outlet orifice area and the load volumes in order to obtain a desired system damping. Experimental results, which confirm the theoretical expectations, are also presented. The conclusions are that it is possible to obtain a high damping contribution from the outlet orifice if the system is dimensioned correctly. However, the energy efficiency needs to be considered while improving the damping.

**Keywords:** Damping, compensator, outlet orifice, efficiency

### **1 Introduction**

In most fluid power systems, directional valves control the speed of the actuators. Two different types of valves are commonly used in mobile machines; open centre and closed centre. This paper addresses closed centre valves. Closed centre valves are commonly used in systems where the pump is actively controlled, for example in constant pressure and load sensing systems [1] [2] [3].

Several loads often share one common pump in mobile machines. If the system pressure level is adapted to the highest load and several functions are operated simultaneously, load interference challenges will occur. This means that the pressure level at the highest load will affect the velocity of the lighter loads. In applications where velocity control is an important property, the valves are often equipped with pressure compensators. The pressure drop across all directional valves will then be constant and the flow will be proportional to the opening area of the valve.

A drawback with pressure compensators is that the load will be poorly damped [4]. To obtain damping from a valve, the flow has to increase when the pressure drop across the valve increases and vice versa. A pressure compensated valve endeavours to achieve low influence on the flow from the load pressure. Except for secondary effects such as leakage, stiffness of the compensator spring and load friction, only the outlet orifice in the directional valve will provide damping to a pressure compensated actuator. A hydraulic system with poor

damping has a tendency to oscillate, which has a negative impact on both the productivity of the application and the comfort of the operator [5].

This paper analyses the damping in systems using pressure compensated closed centre valves. Both rotational and linear loads are covered. The pump controller can be of any type; it does not affect the analysis. Design rules for how the system should be dimensioned in order to obtain a high damping are proposed. Experimental results, which confirm the theoretical expectations, are also presented.

### **2 Damping**

A valve will contribute damping if the flow increases when the pressure drop across the valve increases and vice versa. An example of a hydraulic system with high damping is the constant pressure system, see figure 1. The pump is controlled to maintain a constant pressure before the valve. If the load starts to oscillate, the pressure in the cylinder will also oscillate. Increased cylinder pressure, which means an accelerating force on the piston, results in decreased pressure drop across the valve and consequently also decreased flow through the valve. The acceleration will then be slowed down and the oscillations will decrease, as shown in figure 1.

If the directional valve is complemented with a pressure compensator, a constant flow valve is realized. The function of the pressure compensator is to maintain a constant pressure drop across the directional valve, regardless of pressure variations

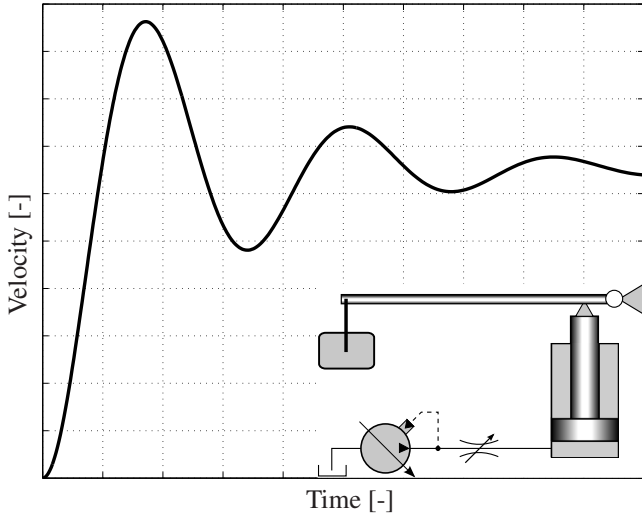


Figure 1: Simulation of a constant pressure system. The oscillations are decreased relatively fast which means that the damping is high.

on the pump and load side. The flow through the valve will then not change when the cylinder pressure oscillates. Therefore, nothing will dampen the accelerating force. An ideal pressure compensated hydraulic system with a closed centre valve is therefore completely undamped, which means that the oscillations will not decrease, see figure 2.

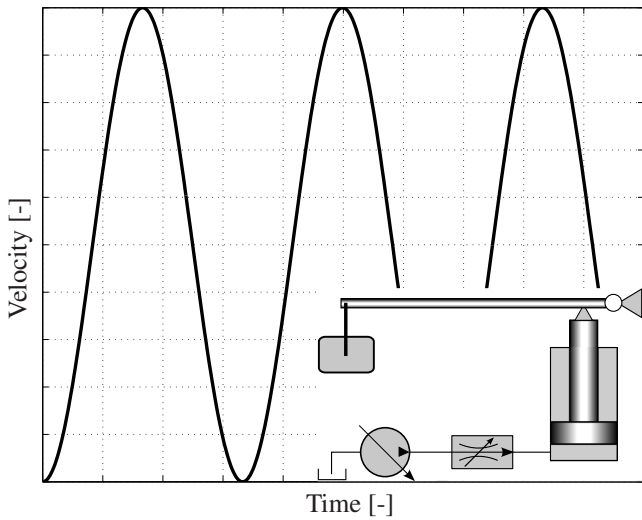


Figure 2: Simulation of a system with a constant flow valve. The pump controller can be of any type; it does not affect the results. Ideally, the system is completely undamped.

The simulation model in figure 2 is simplified to a pressure source, a constant flow valve, a cylinder and a load. The outlet orifice in the directional valve is thus missing. If an outlet orifice is included in the simulation, it is possible to obtain a high damping, see the solid line in figure 3. However, a bad system design results in a low damping according to the dashed line in figure 3.

It is important to design the system correctly in order to ob-

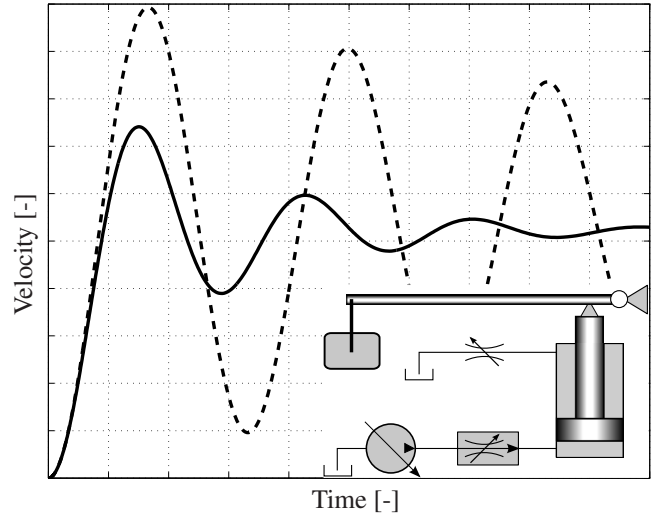


Figure 3: Simulation of a system with a constant flow valve and an outlet orifice. A good system design results in a high damping and a bad design results in a low damping.

tain a high damping from the outlet orifice. This paper will systematically describe how to design the system and propose design rules for how to achieve a high damping. Rotational and linear loads will be discussed. The difference between rotational and linear loads is that the volumes on the inlet and outlet side of the load will change during the stroke in case of a linear load. A rotational load has constant volumes. Experimental verifications of the findings are presented in section 5.

### 3 Rotational Load

A system consisting of a constant flow valve, a rotational inertia load and an outlet orifice, see figure 4, can be described by equations (1)-(4). The viscous friction has been ignored to simplify the analysis and the valve is considered to be much faster than the rest of the system. The valve dynamics are therefore ignored. The dynamics of pressure compensated valves have been studied in, for example, [6] and [7].

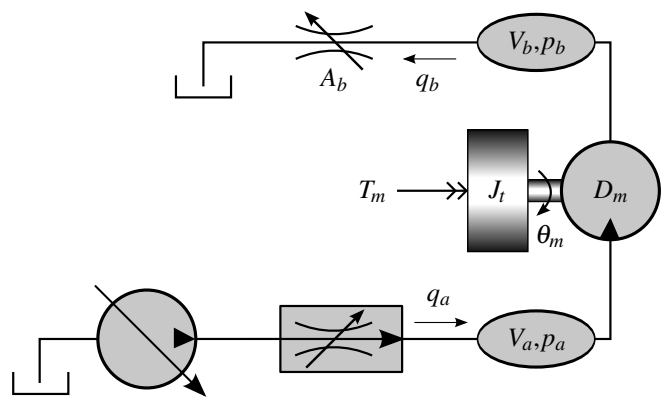


Figure 4: The system analysed in this section, a constant flow valve, a rotational inertia load and an outlet orifice.

$$q_a - D_m \frac{d\theta_m}{dt} = \frac{V_a}{\beta_e} \frac{dp_a}{dt} \quad (1)$$

$$J_t \frac{d^2\theta_m}{dt^2} = D_m(p_a - p_b) - T_m \quad (2)$$

$$D_m \frac{d\theta_m}{dt} - q_b = \frac{V_b}{\beta_e} \frac{dp_b}{dt} \quad (3)$$

$$q_b = q_a = C_q A_b \sqrt{\frac{2}{\rho} p_b} \quad (4)$$

Linearized and Laplace transforming equations (1)-(4) result in equations (5)-(8). The derivation of the equations is shown in [8].

$$Q_a - D_m s \theta_m = \frac{V_a}{\beta_e} s P_a \quad (5)$$

$$J_t s^2 \theta_m = D_m (P_a - P_b) - T_m \quad (6)$$

$$D_m s \theta_m - Q_b = \frac{V_b}{\beta_e} s P_b \quad (7)$$

$$Q_b = K_{c_b} P_b \quad (8)$$

where

$$K_{c_b} = \frac{\partial q_b}{\partial p_b} = \frac{C_q A_b}{\sqrt{2\rho p_b}} \quad (9)$$

An expression for  $K_{c_b}$  where maximum damping is obtained has been derived in [9] for a linear load. Substituting to a rotational load gives the expression in equation (10).

$$K_{c_{b_{opt}}} = D_m \sqrt{\frac{V_b}{\beta_e J_t (\gamma - 1)}} \gamma^{3/4} \quad (10)$$

where

$$\gamma = 1 + \frac{V_a}{V_b} \quad (11)$$

The maximum damping of the system can be calculated using equation (12), also derived in [9].

$$\delta_{h_{max}} = \frac{1}{2} (\sqrt{\gamma} - 1) \quad (12)$$

The most common system design is that the volumes on each side of the load are equal. In that case, the maximum damping of the system is  $\delta_h = 0.21$  according to equations (11) and (12). To obtain the optimal damping, the required outlet orifice area can be calculated using equations (4), (9) and (10), resulting in equation (13).

$$A_{b_{opt}} = \sqrt{\frac{q_a K_{c_{b_{opt}}} \rho}{C_q^2}} \quad (13)$$

The outlet orifice opening area should according to equation (13) increase with the square root of the inlet flow rate; all other parameters are constant. Since the valve is assumed to be pressure compensated, the inlet flow is directly proportional to the inlet orifice opening area. The damping as a function of the outlet orifice area is shown in figure 5.

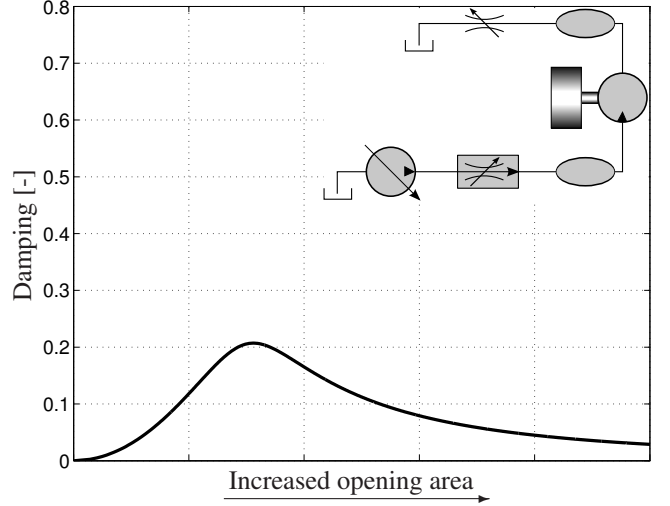


Figure 5: The damping as a function of the opening area for the outlet orifice. The volumes on each side of the load are assumed to be equal.

It is possible to obtain a higher damping than  $\delta_h = 0.21$  by changing the volumes on each side of the piston. To increase the damping, the volume on the inlet side should be large compared to the volume on the outlet side according to equations (11) and (12). As can be seen in figure 6, it is possible to obtain a high damping contribution from the outlet orifice by increasing the volume on the inlet side. For example, the maximum damping becomes  $\delta_h = 0.72$  if the inlet volume is five times larger than the outlet volume.

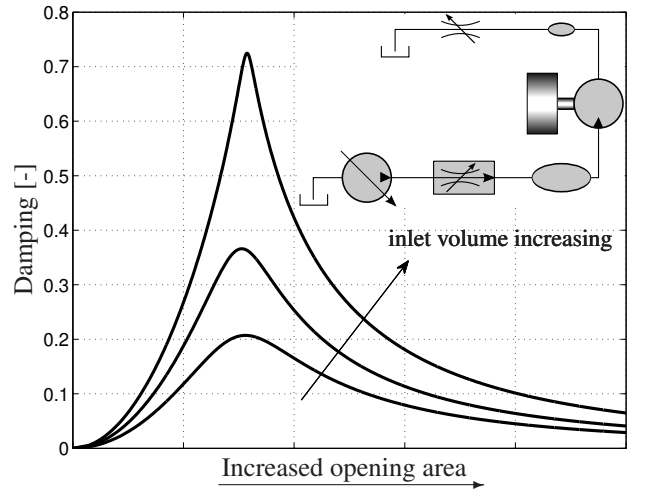


Figure 6: A higher damping can be obtained if the inlet volume is large compared to the outlet volume.

Increasing the inlet volume will increase the damping. However, there are drawbacks with this approach. In case of changing the flow direction, and thereby the direction of the rotation, there will be a large volume at the outlet side instead. Consequently, the damping will be low, see figure 7. If the outlet volume is five times larger than the inlet volume, the maximum damping is  $\delta_h = 0.05$ .

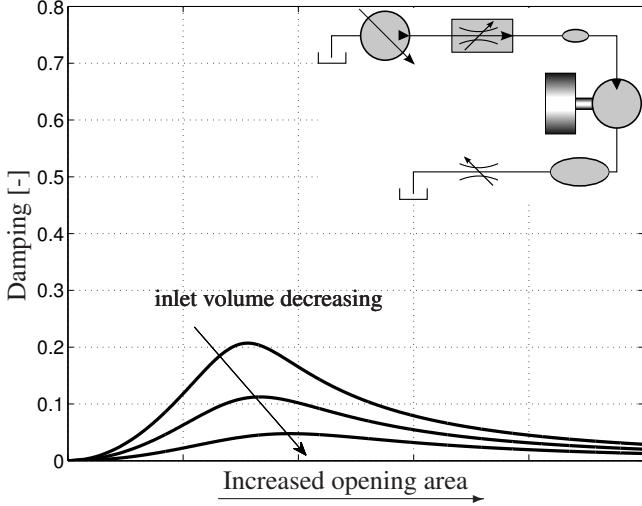


Figure 7: The damping will be low if the inlet volume is small compared to the outlet volume. This will be the case if the flow direction changes compared to figure 6.

To dimension the outlet orifice area in order to get a desired damping, the load needs to be known, see equation (10). In mobile hydraulic applications, the load situation varies greatly over time in a typical working cycle. It is therefore important to consider the load when designing the outlet orifice area. It is only possible to optimize the damping for a specific load. The damping will no longer be optimal if the load situation alters. In figure 8, it is shown how a load change will influence the damping. It is assumed that the outlet orifice area is dimensioned to obtain the highest possible damping for a nominal load. It is then shown how an increased/decreased load will affect the damping.

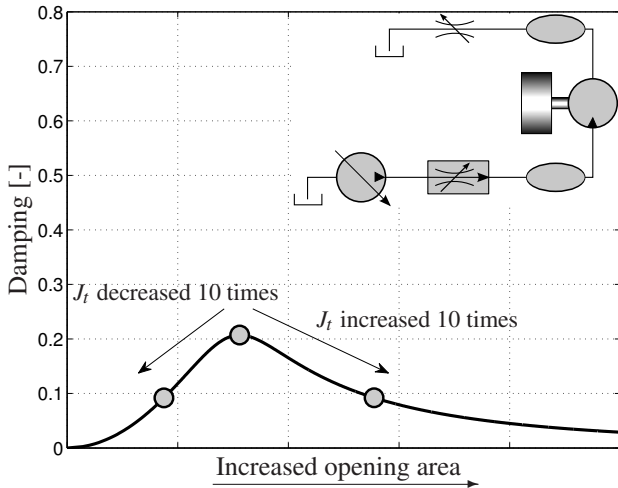


Figure 8: The outlet orifice area is designed to obtain the optimal damping for a nominal load. It is then shown how the damping will change if the load situation alters.

As can be seen in figure 8, the damping will decrease if the load changes. From an efficiency point of view, it is advantageous to have as large opening area of the outlet orifice as

possible. The pressure drop across the valve can then be kept small, resulting in low losses. It is therefore recommended to design the opening area to be optimal for the minimum load. By doing so, the damping will be optimal for that load and then decrease for higher loads. Designing the opening area optimally for the minimum load maximizes the optimal outlet orifice area according to equations (10) and (13).

#### 4 Linear Load

A system consisting of a constant flow valve, a linear load with a gear ratio and an outlet orifice, see figure 9, can be described by similar equations as the rotational load in section 3. Equations (14)-(17) describe the linearized system. The viscous friction in the cylinder has been ignored to simplify the analysis.

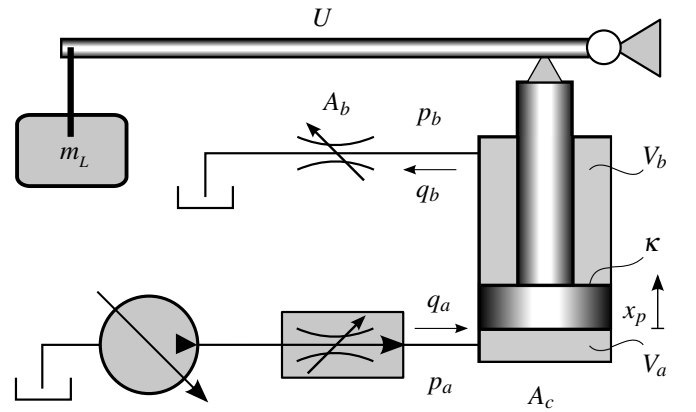


Figure 9: The system analysed in this section, a constant flow valve, a linear load with a gear ratio and an outlet orifice.

$$Q_a - A_c s X_p = \frac{V_a}{\beta_e} s P_a \quad (14)$$

$$U^2 m_L s^2 X_p = A_c P_a - \kappa A_c P_b - F_p \quad (15)$$

$$\kappa A_c s X_p - Q_b = \frac{V_b}{\beta_e} s P_b \quad (16)$$

$$Q_b = K_{c_b} P_b \quad (17)$$

The expression for  $K_{c_b}$  where maximum damping is obtained is shown in equation (18) and the maximum damping is calculated in the same way as for a rotational load, see equation (12) [9].

$$K_{c_{b_{opt}}} = \kappa A_c \sqrt{\frac{V_b}{\beta_e U^2 m_L (\gamma - 1)}} \gamma^{3/4} \quad (18)$$

where

$$\gamma = 1 + \kappa^2 \frac{V_a}{V_b} \quad (19)$$

The outlet orifice area where optimal damping is obtained is derived according to equation (20).

$$A_{b_{opt}} = \sqrt{\frac{\kappa q_a K_{c_{b_{opt}}} \rho}{C_q^2}} \quad (20)$$

The difference between rotational and linear loads is that the volumes on the inlet and outlet side of the load will change during the stroke in case of a linear load. In the following example, a dead volume of 20% is assumed on each side of the piston. While the piston moves upwards, the inlet volume will increase and the outlet volume decrease. The damping will therefore increase during the stroke. In figure 10, the damping as a function of the outlet orifice opening area is shown during a whole stroke.

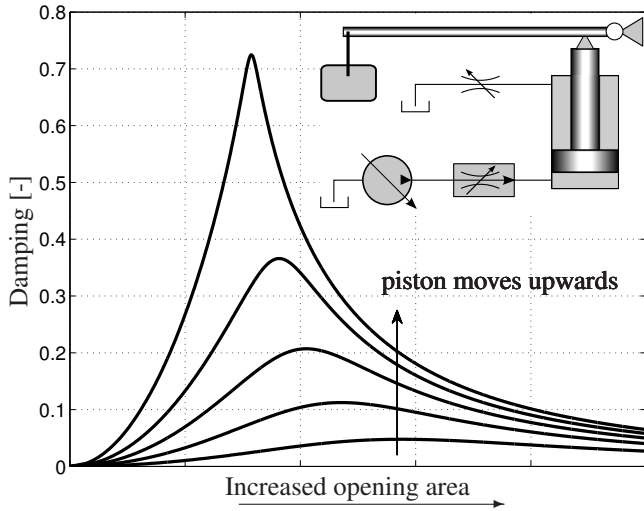


Figure 10: The damping will increase during the cylinder stroke. A dead volume of 20% on each side of the piston is assumed.

One design approach is to maximize the damping in the worst case scenario. In that case, the outlet orifice area should be dimensioned optimally at the piston's lower end position. The damping will then increase while the piston moves upwards, see the solid line in figure 11. It is possible to design the outlet orifice area smaller if a higher damping is required. However, drawbacks with that approach are slightly lower damping at the piston's lower end position, see the dashed line in figure 11, and higher losses across the orifice. A large opening area will reduce the losses at the outlet orifice. This, however, is at the expense of a lower damping, see the dashed-dotted line in figure 11. There is no point in designing the opening area to the left of the peaks in figure 10, since the damping will then be low while the losses are large. In applications where damping is important, it is appropriate to design the outlet orifice somewhere between the optimal area at the piston's lower end position and the optimal area at the piston's higher end position.

It is possible to obtain a higher damping than  $\delta_h = 0.05$  at the piston's lower end position by increasing the dead volumes in the cylinder. For example, in case of 50% dead volume, the optimal damping would increase to  $\delta_h = 0.11$  at the lower end position, see figure 12. Drawbacks with this approach are that the system response will decrease and that more space will be required. By increasing the dead volumes further, the volume change can eventually be ignored and the damping becomes constant, similar to the rotational load in figure 5.

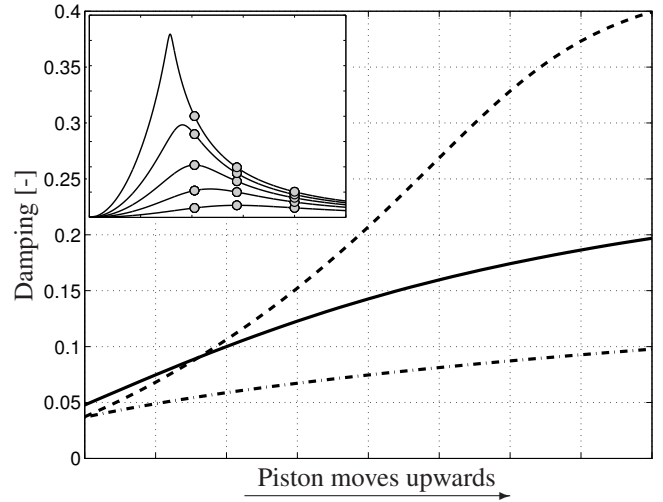


Figure 11: Three different designs of the outlet orifice area. The solid line shows an orifice area where the damping is optimized at the piston's lower end position, the dashed line shows a smaller orifice area and the dashed-dotted line a larger orifice area. The losses will increase with a decreased orifice area.

Similar to the rotational load case, the load needs to be taken into consideration when designing the outlet orifice, see equation (18). It is shown how a load change affects the damping in figure 13. The damping is assumed to be optimized for a nominal load when the piston is at its lower end position. It is then shown how an increased/decreased load will affect the damping.

For the linear load case, it is not obvious to design the opening area to be optimal for the minimum load. This is because the optimal opening area will change while the piston moves upwards. Designing the opening area to be optimal for the minimum load will minimize the losses since the opening area can be designed large, see equations (18) and (20). However, the damping will become small in case of higher loads according to figure 13. If the opening area is designed to be optimal for a higher load, it is possible to obtain a higher damping when the load decreases. It is, however, important to ensure that the damping does not shift to the left of the peaks in figure 13 when the load decreases. Drawbacks with designing the opening area optimally for a higher load are a larger pressure drop across the outlet orifice and lower damping at the piston's lower end position. To obtain the highest possible overall damping during the cylinder stroke, the outlet orifice area should be designed to be optimal somewhere between the minimum and maximum load.

## 5 Experimental Results

A test rig has been constructed to validate the damping contribution of the outlet orifice. It consists of a traditional pressure compensated valve on the inlet side, a cylinder with a mass load and a servo valve on the outlet side, see figure 14. Different designs of the outlet orifice can be achieved by controlling the opening area of the servo valve. A constant pressure pump

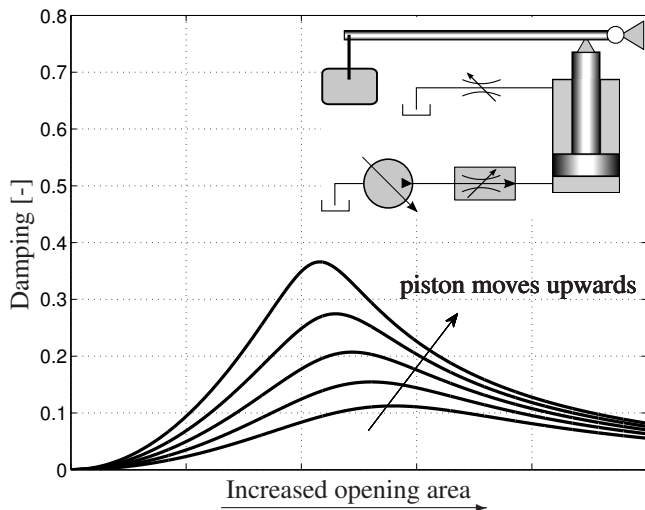


Figure 12: The damping in the worst case scenario can be increased by increasing the dead volumes in the cylinder. A dead volume of 50% on each side of the piston is assumed.

supplies the system. Pressure sensors are attached on the supply side and on both cylinder chambers. The cylinder and the servo valve are equipped with position sensors. External volumes are mounted on both sides of the piston. By using either one, it is possible to manipulate the dead volumes on either side of the piston.

In the experiments, a step is made in the flow by opening the inlet valve. Oscillations in the cylinder velocity are then studied. The experimental results are presented in figures 15-18. In tests (a) and (b), there is a large volume on the inlet side, which means that a relatively high damping can be expected. In test (a), the outlet orifice area is dimensioned close to the maximized damping. As can be seen in figure 15, there are almost no oscillations in the cylinder velocity. In test (b), the outlet orifice area is larger than in test (a) and the damping becomes lower, see figure 16.

In test (c), there is a large volume on the outlet side of the cylinder, which means that the damping is expected to be low. The outlet orifice area is dimensioned close to the maximized damping. Nevertheless, the damping is still low according to figure 17. This is consistent with the mathematical analysis according to equations (12) and (19).

In test (d), the outlet orifice area is so large that it can be equated with having no outlet orifice at all. Theoretically, the hydraulic system will not contribute any damping without an outlet orifice, as shown in figure 2. This is almost the case in the measurements as can be seen in figure 18. The damping that is still obtained is due to secondary effects ignored in the mathematical analysis, such as friction and leakage.

## 6 Design Rules

This section summarizes the findings from sections 3 and 4 concerning how a pressure compensated hydraulic system should be designed in order to obtain a high damping contribution from the outlet orifice in the directional valve. Some

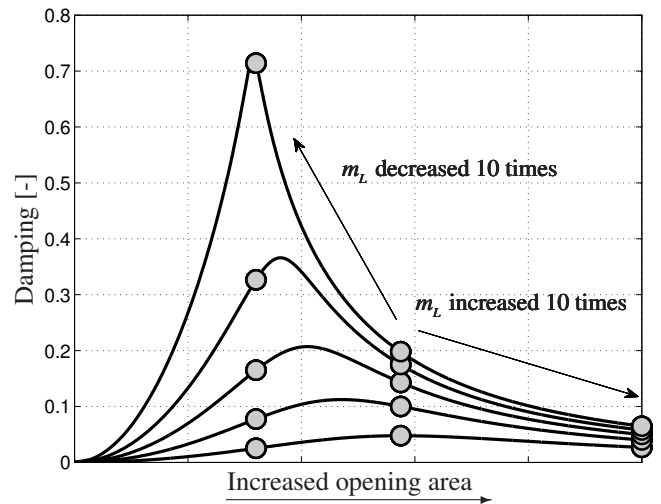


Figure 13: The outlet orifice area is designed to give the highest possible damping when the piston is at its lower end position. It is then shown how the damping will change if the load situation alters.

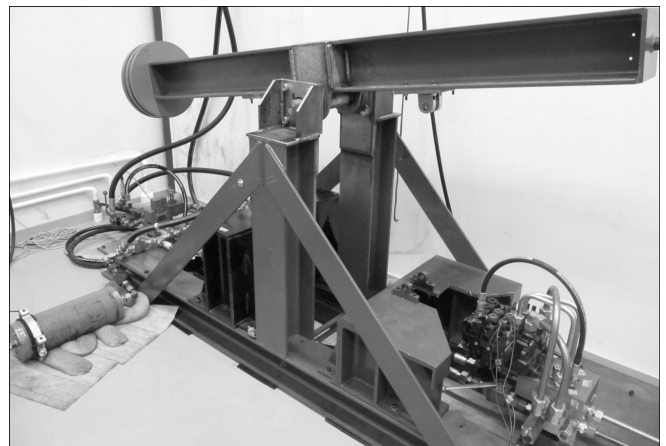


Figure 14: The experimental test stand. The pressure compensated valve can be seen at the lower right and one of the volumes to the left.

design rules are general and some are specific depending on whether the load is rotational or linear.

**Design the outlet orifice area correctly** There exists an optimal orifice dimension; both smaller and larger orifice areas give lower damping. The outlet orifice area which gives the highest possible damping can be calculated using equations (10) and (13) for a rotational load and equations (18) and (20) for a linear load.

**Consider the volumes on each side of the load** The damping will be higher if the inlet volume is large compared to the volume on the outlet side of the load. In case of a linear load, the volumes will change during the cylinder stroke. The outlet orifice can only be designed optimally for a specific volume. It is appropriate to design the outlet orifice optimally somewhere between the piston's lower and higher end positions.

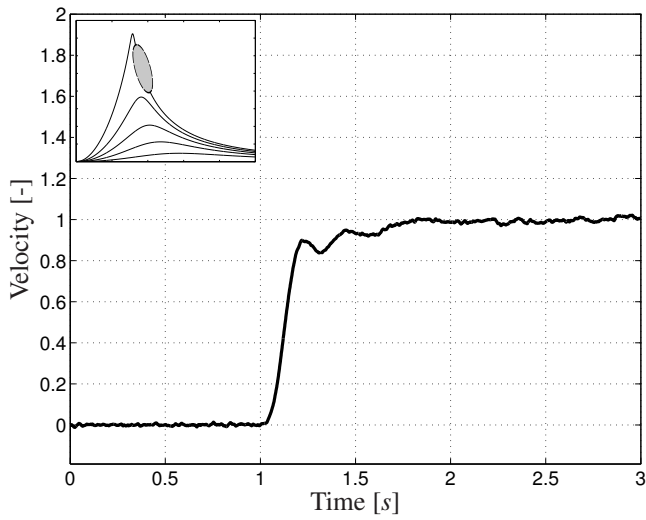


Figure 15: Test (a): A high damping is obtained when there is a large volume on the inlet side of the cylinder and the outlet orifice is designed close to its optimum.

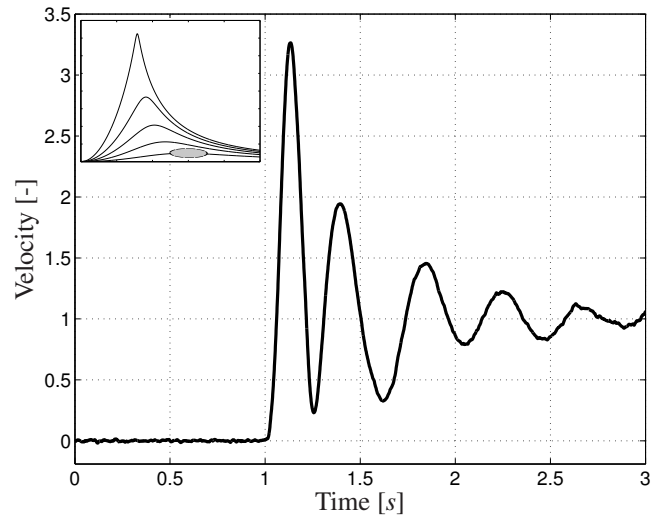


Figure 17: Test (c): When there is a large volume on the outlet side of the cylinder, the damping becomes low even if the outlet orifice is designed close to its optimum.

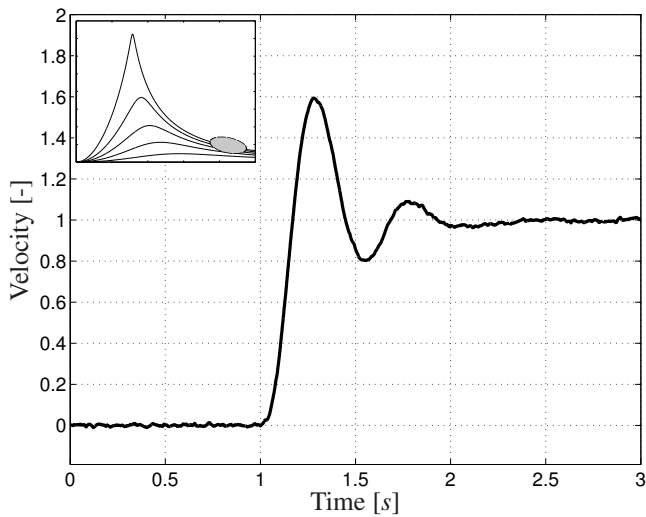


Figure 16: Test (b): The damping becomes lower when there is a large volume on the inlet side and the outlet orifice area is too large.

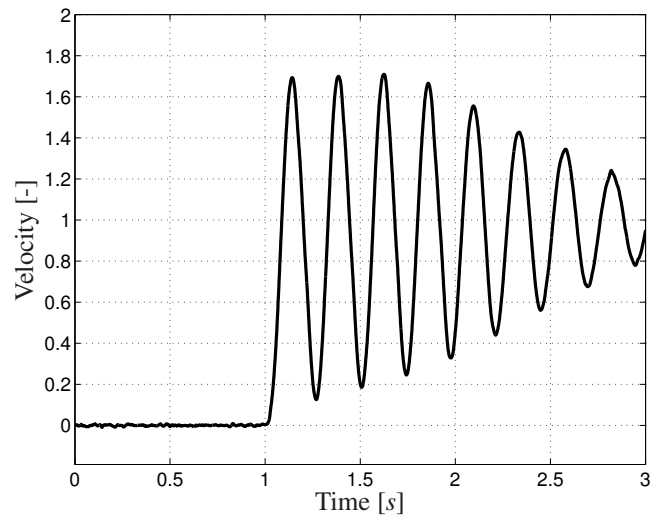


Figure 18: Test (d): Without an outlet orifice, only secondary effects such as friction and leakage will contribute to the damping.

**Consider load changes** The size of the load will affect the optimal orifice area. For a rotational load, the orifice should be designed optimally for the minimum load. For a linear load, the orifice should be designed optimally somewhere between the minimum and maximum load.

**Consider the losses** When improving the damping, it is important to consider the losses. The final valve design will always be a compromise between high damping and low losses.

## 7 Conclusions

A hydraulic system consisting of a pressure compensated valve, a load and an outlet orifice has been studied in this paper. Without the outlet orifice, the hydraulic system will not contribute with any damping at all. Also with an outlet orifice, the damping might become low. However, it is possible to obtain a high damping contribution from the outlet orifice in the directional valve if the system is designed correctly.

To obtain a high damping, the outlet orifice area should be designed properly. There exists an optimal orifice dimension; both smaller and larger orifice areas give lower damping. It is also important to consider the volumes on each side of the load. The damping will be higher if the volume on the inlet side of the load is large compared to the outlet volume. It is possible to obtain a high damping in one flow direction by having a large inlet volume. However, the damping will be low for the other flow direction since the outlet volume is large in that case.

It is important to consider the losses while improving the damping. Some combinations of system parameters might give a high damping but also unrealistically high power losses. This is a well-defined optimization problem which will give different optimal system designs depending on the penalty factors for the damping and the energy efficiency.

## References

- [1] B.R. Andersson. A survey of load-sensing systems. *The BFPR Journal*, 13:103–115, 1980.
- [2] P. Krus. *On Load Sensing Fluid Power Systems - With Special Reference to Dynamic Properties and Control Aspects*. PhD thesis, Linköping University, 1988.
- [3] B. Lantto. *On Fluid Power Control with Special Reference to Load-Sensing Systems and Sliding Mode Control*. PhD thesis, Linköping University, 1994.
- [4] B.R. Andersson. Valves contribution to system damping. In *The 5th Scandinavian International Conference on Fluid Power (SICFP'97)*, Linköping, Sweden, 1997.
- [5] R. Rahmfeld and M. Ivantysynova. An overview about active oscillation damping of mobile machine structure. *International Journal of Fluid Power*, 5(2):5–24, 2004.

- [6] H. Pettersson, P. Krus, A. Jansson, and J.-O. Palmberg. The design of pressure compensators for load sensing hydraulic systems. In *UKACC International Conference on Control'96*, 1996.
- [7] D. Wu, R. Burton, G. Schoenau, and D. Bitner. Analysis of a pressure-compensated flow control valve. *Journal of Dynamic Systems, Measurement, and Control*, 129:203–211, 2007.
- [8] H.E. Merritt. *Hydraulic Control Systems*. John Wiley & Sons, Inc., 1967.
- [9] M. Axin, J.-O. Palmberg, and P. Krus. Optimized damping in cylinder drives using the meter-out orifice - design and experimental verification. In *8th International Fluid Power Conference (IFK)*, volume 1, pages 579–591, Dresden, Germany, 2012.

## Nomenclature

The quantities used in this paper are listed in the table. Capital letters are used for linearized and Laplace transformed variables.

Quantity	Description	Unity
$A_b$	Outlet orifice opening area	$m^2$
$A_{b_{opt}}$	Outlet orifice opening area which gives the highest damping	$m^2$
$A_c$	Cylinder area	$m^2$
$C_q$	Flow coefficient	-
$D_m$	Hydraulic motor displacement	$m^3/\text{rad}$
$F_p$	External force	N
$J_t$	Rotational inertia load	$\text{kg } m^2$
$K_{c_b}$	Flow-pressure coefficient for the outlet orifice	$m^3/\text{Pa } s$
$K_{c_{b_{opt}}}$	$K_{c_b}$ which gives the highest damping	$m^3/\text{Pa } s$
$m_L$	Load mass	kg
$p_a$	Pressure on the inlet side of the load	Pa
$p_b$	Pressure on the outlet side of the load	Pa
$q_a$	Flow into the load	$m^3/s$
$q_b$	Flow out of the load	$m^3/s$
$T_m$	External torque	Nm
$U$	Mechanical gear ratio	-
$V_a$	Volume on the inlet side of the load	$m^3$
$V_b$	Volume on the outlet side of the load	$m^3$
$x_p$	Piston position	m
$\beta_e$	Bulk modulus	Pa
$\gamma$	Parameter	-
$\delta_h$	Damping	-
$\delta_{h_{max}}$	Maximum damping	-
$\theta_m$	Rotational angle	rad
$\kappa$	Cylinder area ratio	-
$\rho$	Density	$\text{kg}/m^3$

# Modelling and Control of a Complementary Energy Recuperation System for Mobile Working Machines

A. Hugo , K. Pettersson , K. Heybroek\* , and P. Krus

Division of Fluid and Mechatronic Systems, Department of Management and Engineering, Linköping University, Sweden

E-mail: anton\_hugo@hotmail.com, karl.pettersson@liu.se, kim.heybroek@volvo.com, petter.krus@liu.se

\*Volvo Construction Equipment AB, SE-631 85 Eskilstuna, Sweden

## Abstract

The concept of hybrid technologies for mobile working machines has gained increased attention in recent years. This paper deals with a parallel hybrid system for energy recuperation based on a two-machine hydraulic transformer. The system can be connected hydraulically to an existing hydraulic circuit as a complementary add-on system. The linear analysis of the system visualises the control difficulties coming from a low inertia, slow control dynamics of the machines and the non-linear stick-slip friction during low speeds. A control strategy based on linear control methods is proposed and evaluated in a hardware test bench. It is shown that an acceptable performance can be achieved even with fairly simple models. Additionally, a start-up procedure is proposed to start the transformer from zero speed.

**Keywords:** Parallel hybrid, Energy recuperation, Hydraulic transformer

## 1 Introduction

If hydraulic power would let itself be transformed from one pressure level to another as easy, cheap and efficient as electric power does, a great roadblock for the future of hydraulics would be out of the way. Within electrics the transistor technology has revolutionised the switching transformers in terms of size, efficiency and cost. In hydraulics, the digital approach is still in its cradle and so far mainly exists on an academic level. Some of the research carried out in this field tries to mimic the behaviour of electric buck and boost converters by applying fast switching valves taking advantage of the fluid inertia effects to create oscillator circuits [1], [2]. In other research, inertial effects are added by mechanical means [3], [4], e.g. a series connected hydraulic machine driving a flywheel. Other work instead focus on transformation through the mechanical domain, using either rotary or linear digital controlled machines [5], [6]. The linear transformer has the advantage of only two domain transformations; from hydraulic to linear mechanic and back to hydraulic. The rotary machine normally takes four steps also counting the transformation between linear moving pistons to rotary movement of the shaft and back again. On the other hand, the linear transformer has a finite stroke and requires continuous switching in direction.

The idea of transforming hydraulic energy via the mechanical domain is nothing new. Already in the early 80's significant research was done on very similar concepts [7], [8], but at that time using conventional variable displacement machines rather than digital hydraulic machi-

nes. An interesting challenge here is controllability. Since the machine has a free rotating axle with very low inertia, it is highly sensitive to torque disturbances. To keep a stable operation, good hardware as well as intelligent controls are needed. Due to the finite number of pistons, torque ripple is a problem making low speed operation a challenge. From the late 90's up until today much research was done on alternative transformer principles where one machine may be used instead of two in an endeavour to make the component easier to control, more energy efficient and commercially viable, see [9]. However, less research is found on how modern control theories may be applied to overcome the known hurdles in control of these transformers.

From the hydraulic system point of view the hydraulic transformer may be applied in several different ways. Some examples can be found in [10], [11] and [12]. One way is to use one transformer per function, where each transformer controls the flow to one actuator, see fig. 1. Alternatively, the transformer may be used as a load-sensing pump supplying flow to a load-sensing control valve. Another option is to place the transformer in parallel to a conventional circuit, as shown in fig. 2. This allows energy to be recuperated and stored when possible and energy reused when needed. In this paper, the "parallel" transformer concept is targeted, even though the presented control theories also applies to the other two concepts with minor modifications. The transformer is built up by two variable displacement machines, as previously described in [13]. With standard hydraulic machines, this configuration gives a rather poor round-trip efficiency, which limits its use for energy recuperation. With new technology

and high-efficient hydraulic machines, however, this may change. Another important contribution of an add-on energy storage system might be that it can allow for downsizing of the engine. This paper analyses the described system dynamically and suggests a control strategy based on linear techniques. A control algorithm is tested and evaluated both in simulation and in hardware tests.

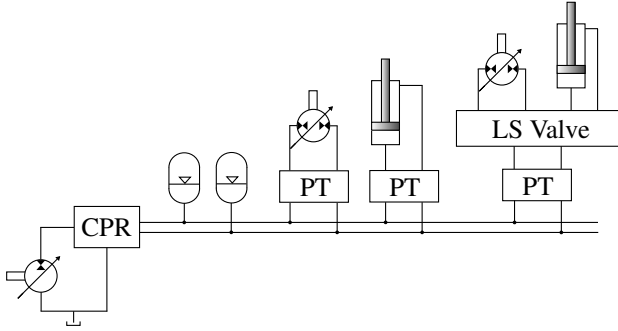


Figure 1: One possible configuration of a transformer based system. A common pressure rail (CPR) supports the applications with pressure. The flow to each actuator and the load sensing (LS) valve control system is controlled by separate pressure transformers (PT).

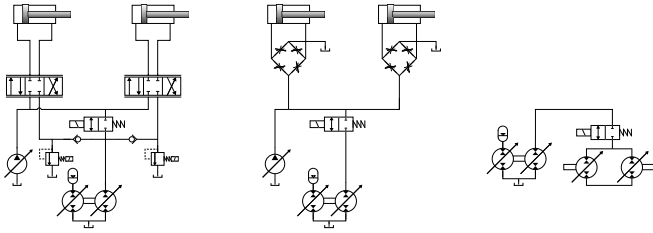


Figure 2: Examples of how the transformer-based system can be connected to standard hydraulic systems in a parallel structure, from [13].

## 2 Modelling

The model of the system is used both in the proposed model-based controller and also to evaluate the proposed control approach. The model is kept relatively simple to achieve a robust and reliable controller. The suggested level of detail serves this purpose, although additional modelling effort would of course increase the precision. The system is modelled as a rotating mass with inertia  $J$ , connected to the two displacement machines according to fig. 3. The shaft torque on the transformer is generated from the pressure on the load and accumulator side,  $p_L$  and  $p_A$ , in reference to the low side pressure  $p_T$ . The relative displacement of the displacement machines are determined by the control signals  $\epsilon_A$  and  $\epsilon_L$ . The losses in flow and torque has been modelled with separate efficiency models ( $\eta_A, \eta_L$ ) for the two displacement machines. The dynamic equations for the system are shown in eq. (1). The net torque (ideal torque minus torque losses) affects the acceleration of the transformers inertial load. The control dynamics of the the displacement machines are modelled with

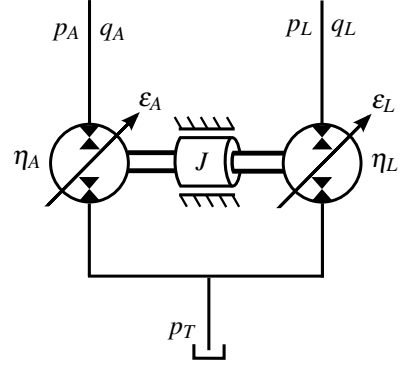


Figure 3: Transformer model.

a first order system with time constants  $\tau_L$  and  $\tau_A$ . The load side flow is dependent on the rotational speed and the load side displacement.

$$J\dot{\omega} = T_{L,ideal} - T_{A,ideal} - T_{loss}(\epsilon, p, \omega) \quad (1a)$$

$$\dot{\epsilon}_L = -\frac{\epsilon_L}{\tau_L} + \frac{\epsilon_{L,ref}}{\tau_L} \quad (1b)$$

$$\dot{\epsilon}_A = -\frac{\epsilon_A}{\tau_A} + \frac{\epsilon_{A,ref}}{\tau_A} \quad (1c)$$

$$q_L = \epsilon_L D_L \omega \pm q_{loss}(\epsilon_L, \omega) \quad (1d)$$

where

$$T_{i,ideal} = \frac{\epsilon_i D_i}{2\pi} \Delta p_i, \text{ for } i = L, A \quad (2a)$$

$$\Delta p_i = p_i - p_T, \text{ for } i = L, A \quad (2b)$$

### 2.1 Loss modelling

The loss modelling of the displacement machines are quite critical to the performance of the controller, since both torque and flow losses are dependent on the surrounding operating conditions. Different modelling approaches have been suggested over the years with different level of complexity and accuracy [14]. Rydberg [15] suggested a physical model of the torque and flow losses of axial piston machines. The proposed models in this paper is based on Rydberg's models, with modifications to reduce the complexity of the expressions.

#### 2.1.1 Flow losses

The flow losses on the load side has been modelled with a two parameter model according to eq. (3). The model consists of one constant term and one term depending on the relative displacement. No bias is assumed for zero speeds. This model is able to capture the flow losses in the limited operating area that has been tested in this paper. To increase the quality of the model in a larger operating area, additional terms are necessary.

$$q_{loss} = a_0 \epsilon_L D_L \omega + a_1 \epsilon_L^2 D_L \omega \quad (3)$$

#### 2.1.2 Torque losses

The torque losses for the complete transformer are modelled as a function of relative displacement, pressure and rotational

speed, according to eq. (4).

$$T_{loss} = (b_0 + b_1 \varepsilon_L) \frac{D_L}{2\pi} \Delta p_L + (c_0 + c_1 \varepsilon_A) \frac{D_A}{2\pi} \Delta p_A + (C_{d1} \varepsilon_L + C_{d2} \varepsilon_A) \omega + T_C \quad (4)$$

The temperature is also an important parameter affecting the friction of the transformer. To reduce the degrees of freedom, the system is evaluated for a fixed temperature.

### 3 Control Approach

The control strategy for the system is a feed forward link based on the non-linear system model in section 2. The control signals of the transformer are calculated to get the requested flow,  $q_{L,ref}$  (see fig. 4). To compensate for model errors, the measured and estimated states are used in a feedback link that compensates the control signal. Since the flow cannot be measured directly, it is estimated through an observer that uses the modelled flow losses. Previous research of the system can be found in [13], where a similar control strategy was evaluated for the accumulator side displacement machine, together with a fixed value for the load side displacement.

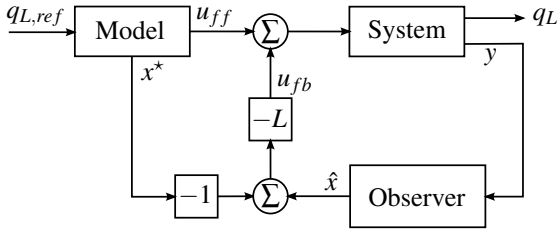


Figure 4: Overview of the control strategy for the system. The model of the system calculates the desired states and inputs. Feedback of state error is used to compensate for model errors. The flow cannot be measured directly and is estimated by an observer.

#### 3.1 Feed forward

The feed forward link used two separate control loops to control the relative displacement on each displacement machine (see fig. 5). An inner control loop uses the reference flow to control the relative displacement on the load side,  $\varepsilon_{L,ff}$ . The goal is to choose a displacement that gives a suitable rotational speed,  $\omega_{ref}$ , of the transformer. Due to the limited conversion range of the transformer it is not always possible to run at the requested angular velocity for all reference flows. Based on the load side control signal from the inner control loop, a secondary loop uses the non-linear torque loss model to control the relative displacement on the accumulator side,  $\varepsilon_{A,ff}$ .

#### 3.2 Feedback

To compensate for model errors, the controller uses the measured and estimated states to compensate the control signals

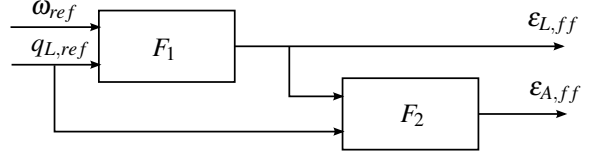


Figure 5: Overview of the control loops for the feed forward link. The control block  $F_1$  controls the relative displacement on the load side and  $F_2$  controls the relative displacement on the accumulator side.

on both displacement machines. This is done by applying a feedback gain matrix,  $L$ , on the controlled state which results in a control signal that is added as input to the system. The static feedback gain cannot fully compensate for stationary errors. For this reason, an additional, integrated state can be introduced (see [16]). For this system, the integrated state feedback is activated within a finite area around the requested flow so that it will not affect the behaviour during transients in the flow.

#### 3.3 Extra degree of freedom

The inner control loop for the load side displacement provides an extra degree of freedom, where the working speed of the transformer can be controlled. Working at a low rotational speed can minimize the torque losses but also compromises the performance since the stick-slip effect are prominent for low speeds. Working at higher speeds reduces these effect and improves the performance, but may lead to larger torque losses. Additional studies of this control aspect can be found in [10] where the transformer speed and load side flow of a two-machine transformer are controlled by separate PI-controllers.

### 4 Linear analysis

To investigate the properties of the system in different parts of its operating area, the non-linear model of the system is linearised in different operating points and analysed. For each operating point, a state space model of the system is created.

$$\begin{aligned} \dot{x} &= Ax + Bu \\ y &= Cx \end{aligned} \quad (5)$$

where

$$x = [\Delta q_L, \Delta \varepsilon_L, \Delta \varepsilon_A, \Delta \omega]^T \quad (6a)$$

$$u = [\Delta \varepsilon_{L,ref}, \Delta \varepsilon_{A,ref}]^T \quad (6b)$$

Using the friction model previously described in section 2.1.2, the mathematical equations are used to form the state space matrices. The dynamics of the pressures are assumed to be small enough for the pressures to be treated as constants at each operating point. The performance for different feedback gains has been investigated by forming the state space model of the closed loop system. With feedback, the input to the system is a function of the state, as in eq. (7).

$$u = -Lx \quad (7)$$

This results in the closed loop system in eq. (8).

$$\begin{aligned} \dot{x} &= (A - BL)x \\ y &= Cx \end{aligned} \quad (8)$$

Depending on the design of the matrix  $L$  it is possible to control the impact of each state on the control signals. In this paper, the feedback link is designed to compensate both the load side and the accumulator side displacement based on the estimated flow. By letting both displacement machines be affected instead of just one, the performance is increased.

To find a suitable value for the gain, the pole placement with respect to the feedback gain is analysed. Figure 6 shows the placement of the poles for an increasing feedback gain. The system has four poles. Two of them are placed on the

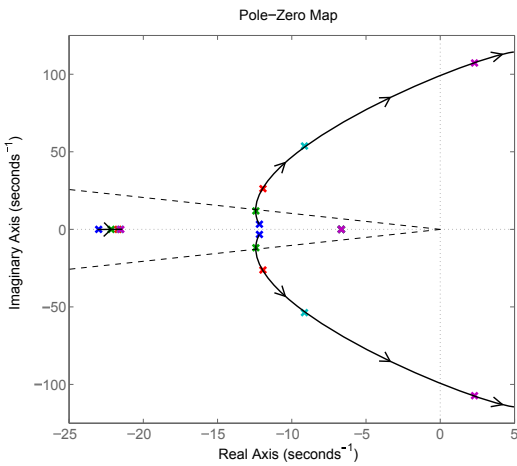


Figure 6: The poles of the closed loop system in a common operating point for different values of feedback gain. The dashed lines indicates the area in which the poles should be placed to avoid large oscillations.

real axis and the other two are complex-conjugated with both a real and an imaginary part. An increased feedback gain pushes the complex-conjugated pair of poles along the positive real axis and increases the imaginary part. This leads to increased oscillations for the system and ultimately instability when the poles reaches the right half plane. The dashed lines represents a damping of 0.7. A common demand is to keep the poles within this area to prevent to large oscillations in the system. It is clear that the poles for the closed loop system are quickly moved out of this area even for small values of feedback gain. Since the load side pressure source on the hardware test bench is based on a flow source and a pressure control valve, it is extra sensitive to oscillations in the system. The oscillations cause pressure disturbances which can lead to instability if they are too large.

#### 4.1 Variance between operating points

The sensitivity of feedback gain is different between operating points. Figure 7 and 8 shows the effect of an increased

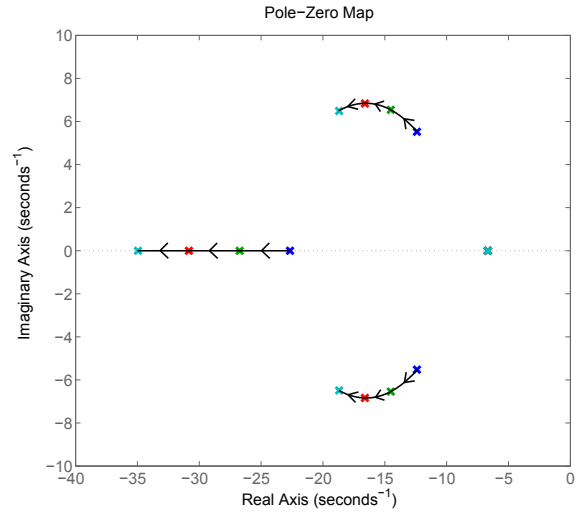


Figure 7: Increasing load pressure.

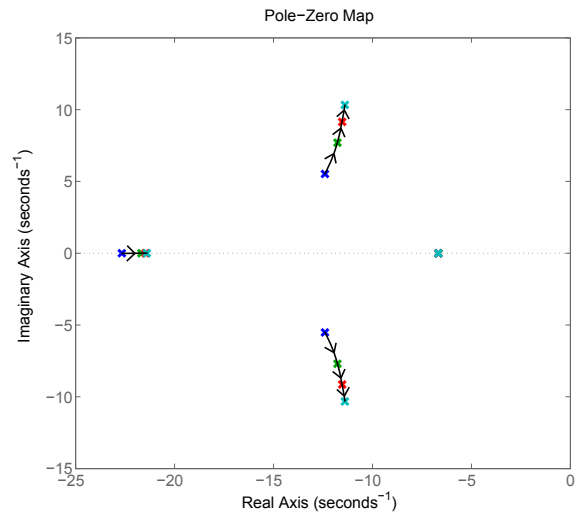


Figure 8: Increasing accumulator pressure.

load and accumulator pressure on the closed loop system. An increased load side pressure moves three of the poles along the negative real axis with a small effect on the imaginary part of the poles. This causes faster dynamics for the system. Increasing accumulator pressure pushes two of the poles along the imaginary axis which leads to larger oscillations in the system. The behaviour of the closed loop system in different operating points can be optimised by changing the feedback gain based on the the current operating point. This will be discussed briefly in section 5.

#### 4.2 Dynamics of the control units

The performance of the closed loop system is highly dependent on the dynamics of the control units which control the relative displacements of the transformer. The low inertia of the transformer shaft makes the system sensitive to disturbances which immediately impacts the performance. To compensate

for these disturbances, fast response time is needed from the displacement machines. Figure 9 and 10 shows the normalized frequency response between the relative displacement on load and accumulator side respectively and the load side flow for different dynamics. The time constants for the swash plate servo is varied from 0.05 to 0.5 seconds. The frequency re-

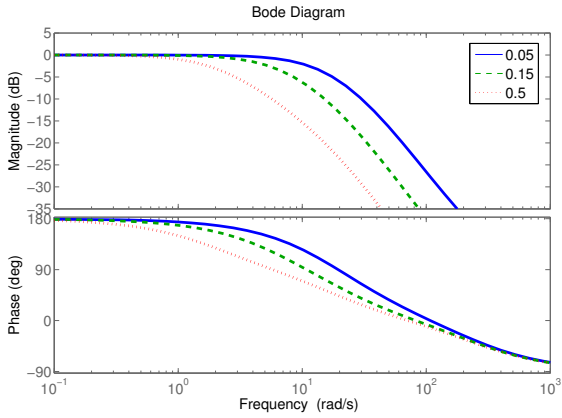


Figure 9: The frequency response between  $\epsilon_L$  and  $q_L$  for different dynamics in the swash plate setting.

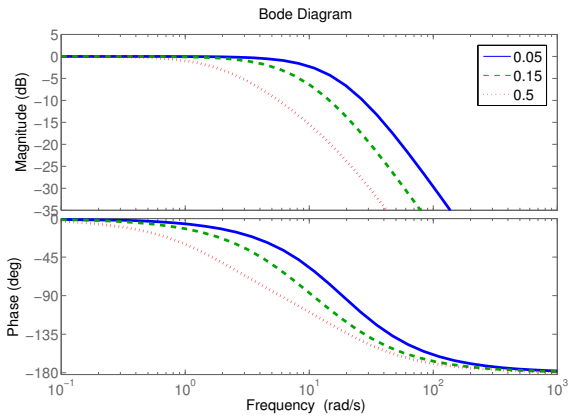


Figure 10: The frequency response between  $\epsilon_A$  and  $q_L$  for different dynamics in the swash plate setting.

sponse from the control signals to the load side flow is directly affected by the dynamics of the control unit. The required response times of the machines are of course coupled to the inertia of the transformer.

#### 4.3 Dynamics for an increased inertia

As previously discussed, the small inertia of the system is problematic since it leads to quick changes in the rotational speed while the control dynamics are comparatively slow. For this reason, a study of the pole placement is made for an increasing inertia on the transformer, with the inertia increased 2, 5 and 10 times the original value. This is shown in fig. 11. As expected, an increased inertia decreases the imaginary part of the poles which reduces the oscillations in the system. At the same time, it pushes the poles closer to the origin which leads to slower dynamics. It is clear that while a high inertia

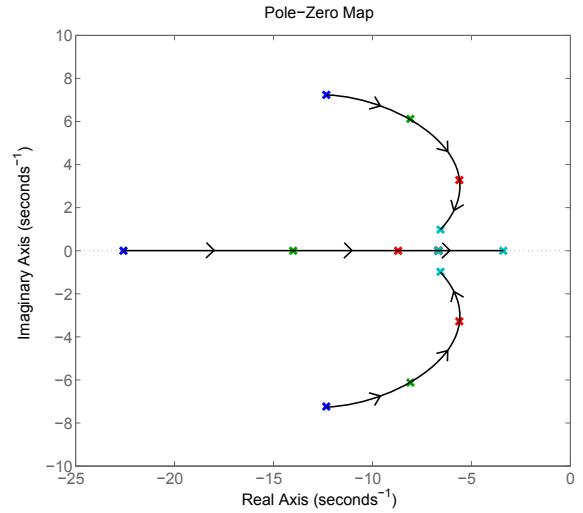


Figure 11: The pole placement of the closed loop system for an increasing inertia. Starting with the original value of  $J$  the inertia is then increased 2, 5 and 10 times.

could allow for an increased feedback gain and less sensitivity to disturbances, it will slow down the response time for the system as well.

## 5 Gain scheduling

To compensate for the varying feedback sensitivity between operating points, the feedback gain can be implemented as a function of the variables in the system. This makes it possible to achieve optimal performance for the feedback link in the full operating area of the transformer. One way to accomplish this is to scale the feedback gain matrix  $L$ , with an operating point dependent function  $K_{gain}$ . For this system, the function is chosen as a function of accumulator and load side pressure, according to the analysis in section 4.1.

$$K_{gain} = f(p_A, p_L) \quad (9)$$

## 6 Start-up procedure

Achieving a requested load flow from zero-speed operation is problematic due to large stick-slip effects on the transformer for low speed operations [17]. Figure 12 shows the magnitude of the friction torque on the transformer as a function of the rotational speed. For zero speed, a large torque is needed to overcome the stiction torque,  $T_{st}$ . Once the transformer is in motion, the stick-slip effects still have great influence on the torque losses for lower speeds but are reduced for higher speeds where the Coulomb friction ( $T_c$ ) and viscous friction is dominating. To compensate for the stiction torque it is necessary to create an overshoot in the torque on the displacement machines, that sets the transformer into motion. Once the transformer is running, the stick-slip effects are reduced and the overshoot torque is no longer necessary. One way to implement this overshoot is to add a term,  $u_{start-up}$ , to the original feed forward control signal,  $u_{ff0}$  (see [17]). This results

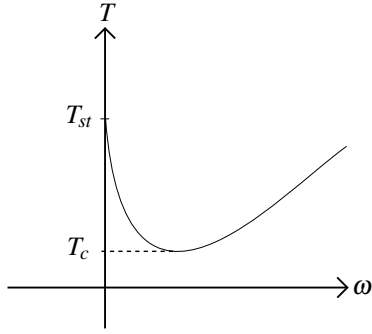


Figure 12: Principle of the stiction torque acting on the transformer. During low speed operations, the transformer is subject to large stick-slip effects. These are reduced for higher speeds.

in the feed forward control signal described by eq. (10).

$$u_{ff} = u_{start-up} + u_{ff0} \quad (10)$$

The term  $u_{start-up}$  creates a peak in the control signals while the transformer speed is zero, which rapidly declines after the transformer starts to rotate. For the system described in this paper, such a peak will be used as the control signal on one side of the transformer while the control signal on the other side is set to zero. The peak is generated by eq. (11).

$$u_{start-up} = \pm K^{-\frac{\omega}{\omega_0}} \quad (11)$$

The sign of the function is depending on the direction of the requested flow. For zero speed, the control signal is  $u_{start-up} = -1$ , when a negative flow is requested. This value moves quickly towards zero for increasing rotational speeds. The fix value  $\omega_0$  is a speed where the stick-slip effects are assumed to no longer affect the transformer. At this speed, the control signal is  $-\frac{1}{K}$  and declines further towards zero for increasing speeds. Figure 13 shows the output from this function as a function of the rotational speed.

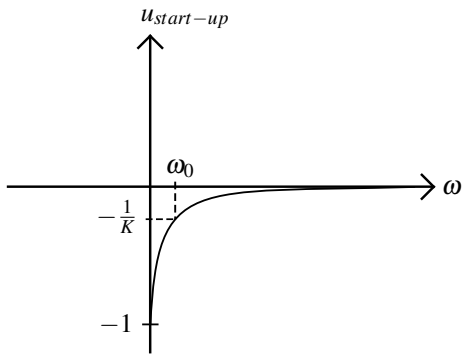


Figure 13: The extra control signal used to set the transformer into motion.

## 7 Hardware

A hardware test bench has previously been developed (see [13] and [18]) to evaluate the system concept and control strategy. The test bench is shown in fig. 14 and consists of two Bosch Rexroth (A4VG) displacement machines connected via a mechanical shaft. The relative displacement and pressure at each machine is measurable as well as the rotational speed of the shaft. Figure 15 shows the schematic overview of the test bench. Further details can be found in the above referenced documents.



Figure 14: The hardware test bench used to evaluate the controller.

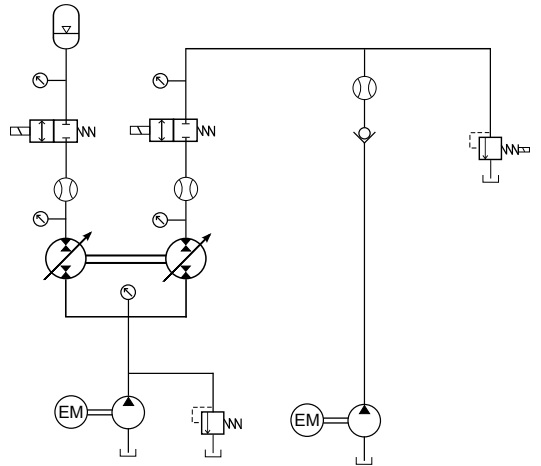


Figure 15: Schematic overview of the test bench. The pressures on the load side and the low-pressure side of the transformer are controlled by two separate pump systems and pressure relief valves. The flow sensors are used for validation and not for controlling.

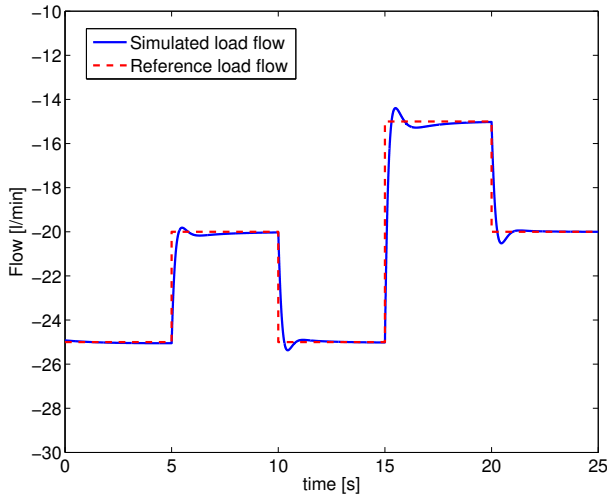
## 8 Results and Discussions

The performance of the controller has been evaluated on both a simulation model and the hardware test bench. The simulation model is implemented in the modelling software AMESim. The standard library components have been modified according to the above described system model.

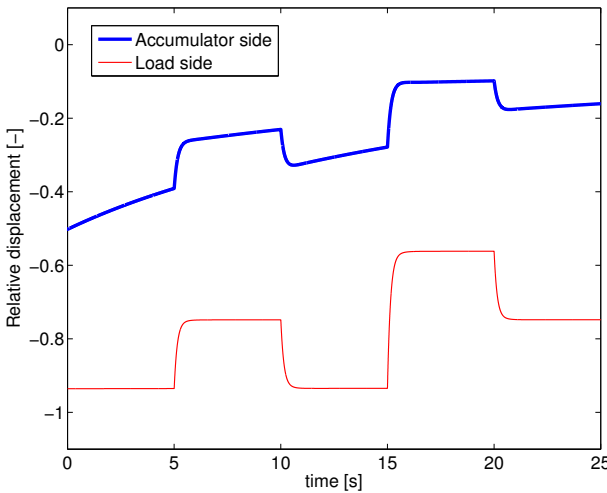
The evaluation is performed through cosimulation between MATLAB Simulink and AMESim [19].

### 8.1 Reference tracking

The controller's ability to follow a reference flow has been evaluated on the simulation model as well as the hardware test bench. Figure 16a shows the simulation results with the corresponding displacement shown in fig. 16b. The control-



(a) Load side flow.

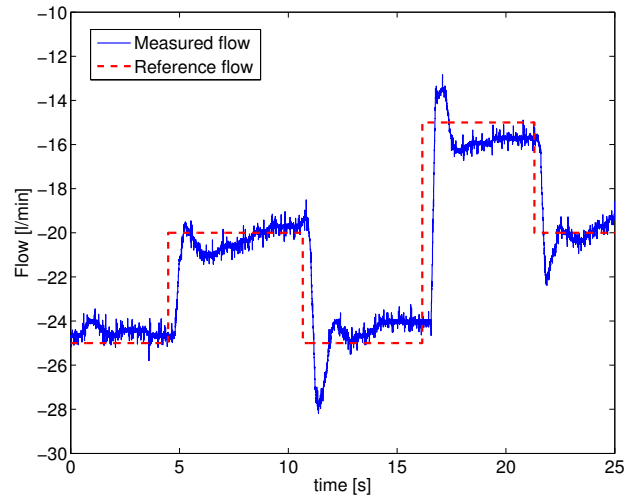


(b) Relative displacement.

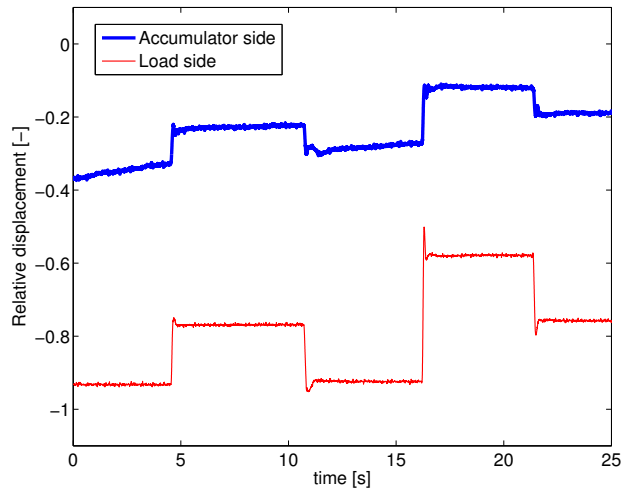
Figure 16: Reference tracking experiment on the simulation model.

ler causes both displacement machines to react to steps in the load side flow. The feedback link adjusts the control signal on both sides which provides for superior compensation for model errors. This does, however, lead to a small overshoot in the flow before the stationary value is reached. Figure 17 shows an equivalent evaluation on the hardware test bench. The feed forward link is highly dependent on an accurate model of the torque losses, which are harder to estimate in the

hardware experiments. Unmodelled non-linearities and temperature dependency cause stationary errors which are partly compensated by the feedback link.



(a) Load side flow.

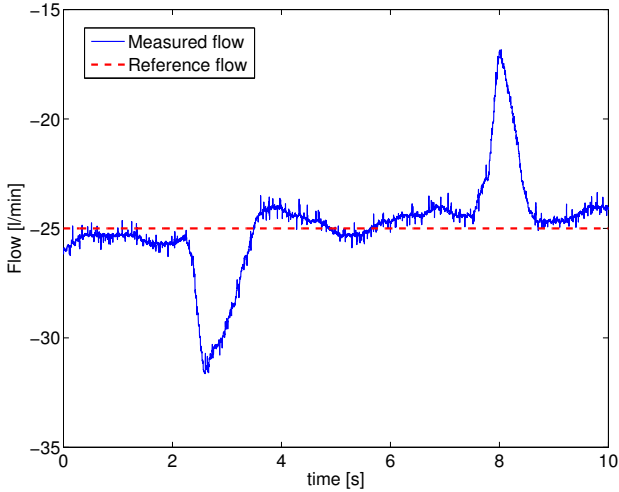


(b) Relative displacement.

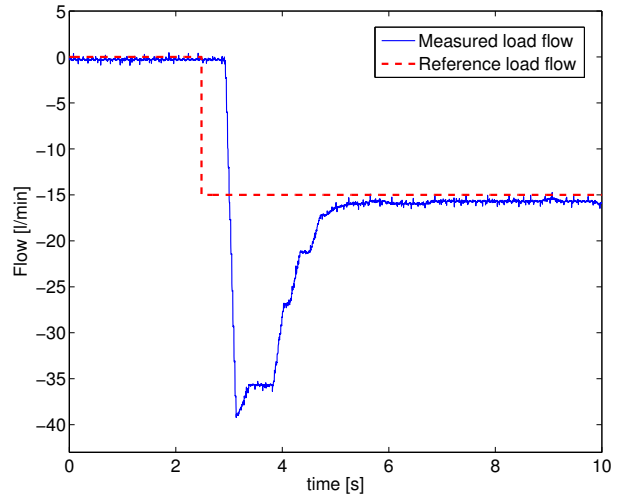
Figure 17: Reference tracking experiment on the hardware test bench.

### 8.2 Suppression of load disturbances

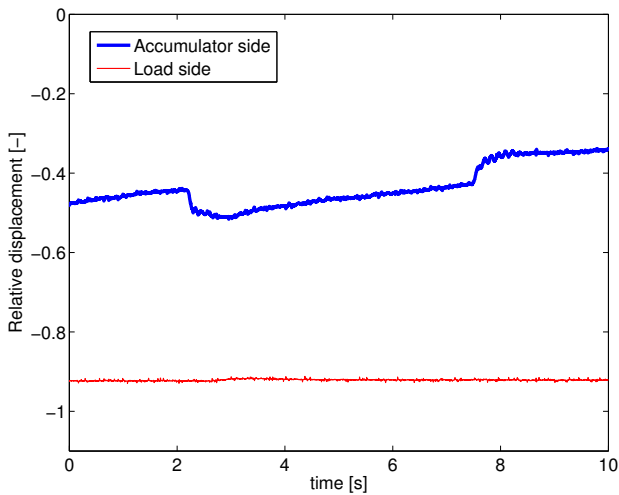
Another important aspect of the controller is the ability to compensate for disturbances in the load side pressure. Figure 18 shows a hardware test result of a 10% step in load side pressure in each direction. The feed forward link is able to compensate for the pressure disturbances by adjusting the relative displacement on the accumulator side. However, the relatively slow dynamics of the displacement machines cause an unsatisfactory high flow disturbance. In a real application, e.g. with the transformer connected to a hydraulic crane, the force from the lift load would create pressure oscillations that need to be suppressed. The problem with slow displacement



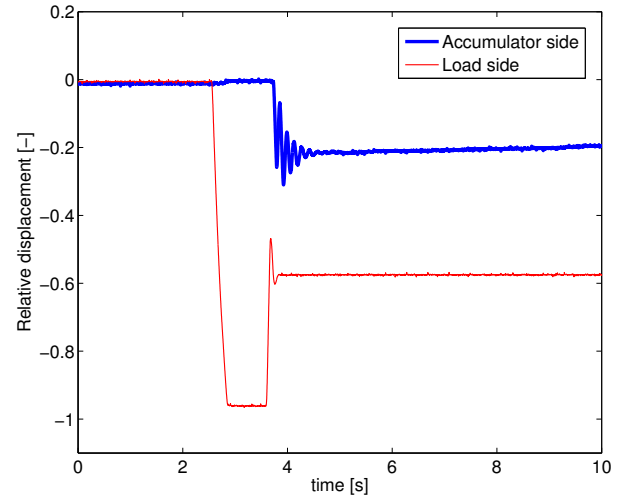
(a) Load side flow.



(a) Load side flow.



(b) Relative displacement.



(b) Relative displacement.

Figure 18: Hardware experiment where a step in the load side pressure of 10% is made in each direction.

Figure 19: Evaluation of the start-up procedure on the hardware test bench.

machines is also treated in [10], where a crane arm is controlled by a similar system.

### 8.3 Start-up procedure

An evaluation of the start-up procedure on the test bench is shown in fig. 19. Both the reference and actual flow is presented, as well as the relative displacement on each side. A step in reference flow is made from 0 l/min to -15 l/min at a point where the transformer speed is zero. To overcome the stiction torque, an overshoot in the relative displacement is given until the transformer starts to rotate. This leads to an overshoot in the load flow before the flow is controlled to the requested value. The transformer shaft is accelerated to a high speed before the system is able to react and adjust the control signal. Certain delays in the measurement equipment also contributes to the magnitude of the overshoot.

## 9 Conclusion

A control strategy for a transformer-based energy recuperation system has been proposed and evaluated. The control strategy is based on a non-linear feed forward link and a state feedback link that compensates for model-errors and disturbances. The implementation of separate control loops for each displacement machine reduces the control problem to a single input single output system. This simplifies the control algorithm and provides the possibility to affect the working speed of the transformer as well. The model based feed forward control signal allows for good reference tracking, but it is highly dependent on correct estimations of the torque losses. Due to strong non-linearities in the friction between operating points, this is a major issue in the control problem. Another issue is the small inertia and slow control dynamics, which cause challenges for the start-up process

and difficulties when compensating for disturbances.

The fundamental properties of the system has been investigated through linear methods. The problem with low inertia and slow control dynamics is visualised by the frequency response and the pole placement of the closed loop system. The ability to react to changes in the load flow is directly affected by the response time for the control units. The small margin for feedback gain is another consequence, where oscillations and instability follows an increasing feedback gain.

## Nomenclature

### Quantities

Designation	Denotation	Unit
$p$	Pressure	[Pa]
$q$	Flow	[m <sup>3</sup> /s]
$\varepsilon$	Relative displacement	[-]
$\omega$	Rotational velocity	[rev/s]
$J$	Moment of inertia	[kgm <sup>2</sup> ]
$T$	Torque	[Nm]
$T_C$	Coulomb torque	[Nm]
$T_{st}$	Stiction torque	[Nm]
$\eta$	Efficiency	[-]
$\tau$	Time constant	[s]

### Subscripts

Designation	Denotation
$T$	Low pressure (Tank) side
$L$	Load side
$A$	Accumulator side
$loss$	Machine losses
$ref$	Reference value
$ff$	Feed forward
$fb$	Feedback

## References

- [1] E. Guglielmino, C. Semini, H. Kogler, R. Scheidl, and D. G. Caldwell, "Power Hydraulics - Switched Mode Control of Hydraulic Actuation," in *The 2010 IEEE/RSJ International Conference on Intelligent Robots and Systems*, pp. 3031–3036, 2010.
- [2] R. Scheidl, B. Manhartgruber, and B. Winkler, "Hydraulic Switching Control - Principles and State of the Art," in *1st Workshop on Digital Fluid Power*, (Tampere, Finland), pp. 31–49, 2008.
- [3] F. Wang, L. Gu, and Y. Chen, "A Continuously Variable Hydraulic Pressure Converter Based on High Speed On-Off Valves," *Mechatronics*, vol. 21, no. 8, pp. 1298–1308, 2011.
- [4] M. B. Rannow, H. C. Tu, P. Y. Li, and T. R. Chase, "Software Enabled Virtually Variable Displacement Pumps - Theoretical and Experimental Studies," *ASME Journal of Dynamic Systems, Measurement, and Control*, no. April, 2007.
- [5] M. Linjama and J. Tammisto, "New Alternative for Digital Pump-Motor-Transformer," in *The Second Workshop on Digital Fluid Power*, (Linz, Austria), pp. 49–61, 2009.
- [6] E. D. Bishop, "Digital Hydraulic Transformer - Approaching Theoretical Perfection in Hydraulic Drive Efficiency," in *The 11th Scandinavian International Conference on Fluid Power*, (Linköping, Sweden), 2009.
- [7] M. Shih, *Untersuchung Einer Zylinderansteuerung durch Hydro-Transformator am Konstant Drucknetz*. PhD thesis, Rheinisch-Westfälischen Technischen Hochschule Aachen, 1984.
- [8] R. Kordak, *Hydrostatische Antriebe mit Sekundärregelung*. 1996.
- [9] P. A. J. Achten, Z. Fu, and G. E. M. Vael, "Transforming future hydraulics : a new design of a hydraulic transformer," in *5th Scandinavian International Conference on Fluid Power*, (Linköping, Sweden), pp. 1–24, 1997.
- [10] S. Wei, *On Studies of Energy Regeneration System for Hydraulic Manipulators*. PhD thesis, Tampere University of Technology, 2004.
- [11] P. A. J. Achten, G. E. M. Vael, H. Murrenhoff, T. Kohmäscher, and M. Inderelst, "Low-emission Hydraulic Hybrid for Passenger Cars," *ATZ*, vol. 5, pp. 378–384, 2009.
- [12] M. Inderelst, "Energy Efficient System Layout for Work Hydraulics of Excavators," in *The 12th Scandinavian International Conference on Fluid Power*, (Tampere, Finland), 2011.
- [13] K. Pettersson, K. Heybroek, A. Klintemyr, and P. Krus, "Analysis and control of a complementary energy recuperation system," in *The 8th International Fluid Power Conference*, (Dresden, Germany), 2012.
- [14] T. Kohmäscher, "Improved Loss Modeling of Hydrostatic Units - Requirement for Precise Simulation of Mobile Working Machine Drivelines," in *ASME International Mechanical Engineering Congress and Exposition, Seattle, Washington, USA*, vol. 4, (Seattle, Washington), 2007.
- [15] K.-E. Rydberg, *On Performance Optimization and Digital Control of Hydrostatic Drives for Vehicle Applications*. PhD thesis, Linköping University, 1983.
- [16] J. Lennevi, *Hydrostatic Transmission Control*. PhD thesis, Linköping University, 1995.

- [17] R. Werndin and J. Palmberg, "Hydraulic Transformers in Low Speed Operation - A Study of Control Strategies," in *The 5th International Symposium of Fluid Power*, (Nara, Japan), 2002.
- [18] A. Klintemyr and R. Bergström, "Analysis and Sizing of a System for Hydraulic Energy Recovery," Master's thesis, Linköping Univeristy, Linköping, 2011.
- [19] LMS International, "LMS Imagine.Lab AMESim Rev 11 User Manual and Software."

# A Series-Parallel Hydraulic Hybrid Mini-Excavator with Displacement Controlled Actuators

Rohit Hippalgaonkar\* and Monika Ivantysynova<sup>†</sup>

<sup>†</sup>Department of Agricultural & Biological Engineering, Purdue University, West Lafayette, IN/ USA

E-mail: rohit@purdue.edu, mivantys@purdue.edu

\*School of Mechanical Engineering, Purdue University, West Lafayette, IN/ USA

## Abstract

A displacement-controlled (DC) prototype mini-excavator built at the Maha Fluid Power Research Center at Purdue University, had previously demonstrated 40% fuel savings over a standard mini-excavator with load-sensing architecture, in independent side-by-side testing. A DC series-parallel (DC S-P) hydraulic hybrid architecture has since been conceptualized where the braking energy of the swing can be stored in an accumulator. This architecture promises further efficiency gains over the DC architecture by taking advantage of four-quadrant operation enabled by DC actuation, swing kinetic energy storage capability, and enables 50% reduced engine power, through load-leveling and power management, while exploiting the cyclical nature of excavator work cycles. In simulation, feasibility studies for the DC S-P hybrid excavator with reduced engine power, showed 51% fuel savings over the standard excavator without loss of performance for an expert truck-loading cycle. Conservative power management was used for these studies, with the downsized engine operated efficiently at a single point (maximum governed speed and torque).

This work will focus on: a) the high-fidelity co-simulation model used to model dynamic behavior and evaluate various power management strategies, b) working hydraulic schematics for the series-hybrid swing drive, c) the controller in use on the prototype, and d) measurements for proof-of-concept.

**Keywords:** DC actuation, hydraulic hybrid, multi-actuator machines, engine management and downsizing, secondary-controlled swing motor.

## 1 Background

Rising fuel costs, more stringent emission restrictions and increasing use of electronic controls and sensors have recently accelerated research and development of efficient hydraulic actuation technologies. In multi-actuator machines, DC actuation is a relatively recent technology that eliminates the use of throttling valves that are used in the current standard valve-controlled versions of these machines.

In DC actuation, one variable displacement over-center hydraulic unit is used for each actuator to control the actuator motion ([1]). For differential cylinders, pilot-operated check valves are used to ensure balancing the unequal cylinder flow. The DC prototype mini-excavator (5-t) built at the Maha Fluid Power Research Center at Purdue University uses four variable displacement pumps to power the four main actuators of the excavator, the boom, arm, bucket and swing drive. Switching valves allow switching of all four pumps to power the remaining four actuators, also

utilizing the efficient displacement controlled actuation concept.

Simulations were performed using detailed, dynamic co-simulation models of both the standard, load-sensing (LS) architecture as well as the DC architecture for the 5-t excavator system [2], [3]). It was found that throttling losses accounted for 50% of the energy consumption in the LS machine, and that the DC system could provide 40% fuel savings over the LS system. A prototype DC excavator was built at the Maha Fluid Power Research Center, and this validated the prediction made using simulations, during independent, side-by-side testing with an LS excavator ([4], [5]) at a Caterpillar testing facility.

A novel hybrid hydraulic architecture ([6]) builds on the success of the DC prototype excavator, by enabling storage (and reuse) of braking energy of the cabin in a high-pressure hydraulic accumulator, via a series hybrid swing drive as shown in Figure 1.1.

The DC S-P architecture retains the circuits for the linear actuators in the prototype DC excavator. The DC S-P hybrid enables 50% engine downsizing through appropriate power

management, relying on typical cyclical operation of excavators, and in the process further fuel savings over the

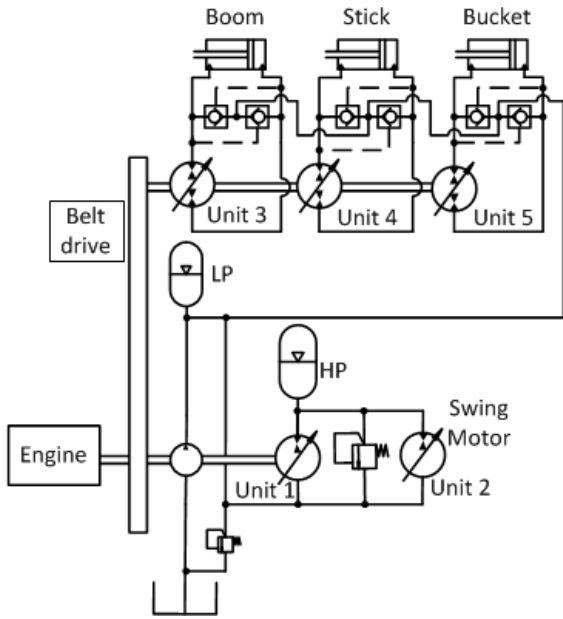


Figure 1.1 : DC S-P Hybrid Excavator

demonstrated previously in [6], for an aggressive, expert-operated truck-loading cycle, by using a conservative power management strategy that forces the downsized engine to operate at its maximum governed speed and maximum

## 2 Simulation of the DC S-P Hybrid

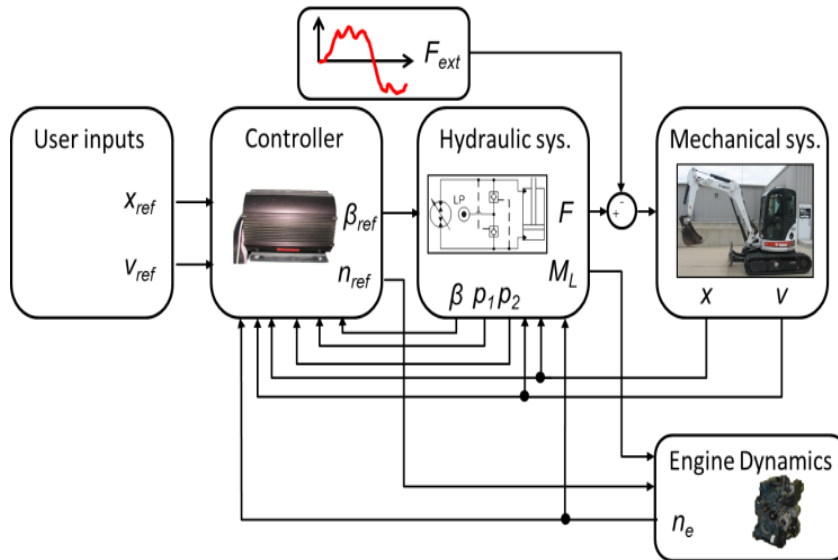


Figure 2.1: Simulation Model Structure

A co-simulation model (Figure 2.1) has been used to model the system dynamics, including both hydraulic and mechanical behavior, for both the non-hybrid and hybrid excavator architectures. The model accurately estimates energy and fuel consumption and was the basis for prediction of the fuel savings with the non-hybrid DC prototype. This model will be used to evaluate the energy consumption of the hybrid excavator as well, before measurements are made.

DC prototype excavator in simulation. This was power (near its maximum efficiency). Appropriate control of the primary unit (1) in the series-hybrid swing actuation system is necessary in order to allow charging of the accumulator with excess engine power and discharging the accumulator when power requested by the actuators is greater than the peak engine power.

In Section 2, the dynamic model that has been extensively used to simulate the dynamic behavior and fuel consumption of the DC S-P hybrid architecture will be briefly described. Further, an implementable power management strategy that exploits all available system degrees of freedom as well as achieving near-optimal behavior (in terms of replicating the optimal system state trajectories and control histories) is presented. This sheds light on what is possible with the DC S-P hybrid architecture with reduced engine power, when used with the appropriate power management strategy.

The transition from the non-hybrid DC demonstrator machine to the DC S-P hybrid demonstrator machine has been completed and will be reported in this paper. Section 3 will outline the transition, with particular focus on the working hydraulic schematic and the controller in use for the excavator. Preliminary measurements on the excavator are presented in Section 4. Future work planned on the prototype hybrid excavator is also outlined.

The simulation model is built to ensure tracking of a given excavator cycle, by providing inputs such as measured actuator positions ( $x_{ref}$ ) and loads ( $F_{ext}$ ). The user of the model must also input reference velocities,  $v_{ref}$ , for the actuators (which are generated from measured joystick signals).

The first level of the ‘Controller’ in the simulation model is shown in Figure 2.2. Here, supervisory power management

schemes are implemented. The outputs are commands for engine speed ( $n_{PM,CE}$ ) and the various units,  $\beta_{PM,i}$ . These are interpreted as a speed command for the swing motor and flow commands for the DC actuators (boom, stick and bucket).

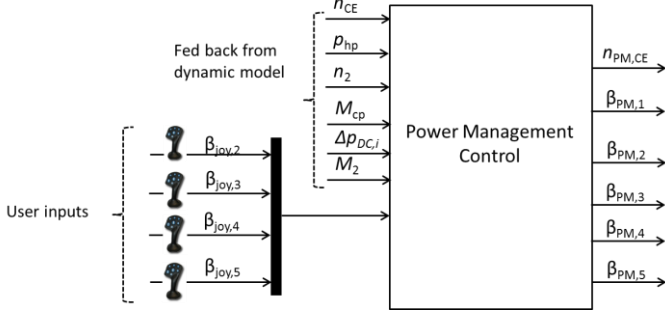


Figure 2.2 : Supervisory Level Power Management Control

### 2.1 Rule-Based ‘Minimum-Speed’ Power Management Strategy

This implementable strategy was designed to replicate optimal state trajectories and control histories obtained from dynamic programming. From analysis of the optimal results for an expert truck-loading cycle (Fig. 2.3), it was found that for most part of the cycle, the engine stayed at minimum allowable speeds to meet flow requirements at the DC (linear) actuators.

<b>I. <math>P_{DC} &lt; 0</math></b>	<b>II. <math>P_{CE,max} \geq P_{DC} \geq 0</math></b>	<b>III. <math>P_{CE,max} &lt; P_{DC}</math></b>
$n_{PM,CE} = n_{CE,min}$	$n_{PM,CE} = n_{CE,min}$	$n_{PM,CE} = n_{CE,min}$
$P_{CE} = \min\{P_{ref}, M_1 \omega_{CE} + P_{load}\}$	$P_{CE} = P_{ref}$	$P_{CE} = P_{CE,max}$
$M_1 = M_{1,max}$	$M_1 = (P_{CE} - P_{load})/\omega_{CE}$	$M_1 = (P_{CE} - P_{load})/\omega_{CE}$

Table 2.1: Rules Used in Minimum-Speed Strategy

The terms,  $P_{DC}$  and  $P_{load}$  – respectively, the total power requirement purely from DC units and the total power requirement from the engine shaft (DC power plus power required to accelerate engine) at any instant, are given by Eq. 2.1.

$$P_{load} = \left( M_{DC} + \frac{I_{CE} (\omega_{CE,min}(k+1) - \omega_{CE}(k))}{T_s} \right) \omega_{CE}(k) \quad Eq. 2.1$$

$$P_{DC}(k) = M_{DC}(k) \omega_{CE}(k)$$

$$M_{DC}(k) = M_{cp}(k) + i_{belt} \sum_{i=3}^5 \left( \frac{\beta_{PM,i} V_{d,i} \Delta p_i}{2\pi} + M_{s,i} \right)$$

The engine was commanded to be at  $n_{CE,min}$ , the minimum allowable engine speed based on flow requirements at all instants in time (Eq. 2.2).

$$n_{CE,min} = \min \left\{ abs \left[ \frac{Q_{req,i}}{0.95 V_{d,i}} \right], i = 3, 4, 5 \right\} \quad Eq. 2.2$$

At moderate DC loads, the engine was kept at a reference power  $P_{ref}$  ( $= 18kW$ ), which was in a high-efficiency area of the engine (but below the peak engine power), whereas for high loads above the peak engine power, the engine was kept at peak power (20.7 kW). For aiding loads ( $P_{DC} < 0$ ), unit 1 was kept at 100% to charge the accumulator up as fast as possible, whereas the engine was operated at a power which was the lower among the reference power or the power required to simply meet the total load as well as the storage pump torque.

For the linear actuators, these are processed in a feed-forward manner ([9], not shown) by the low-level controller, together with a correction for transient pressure feedback. For the swing motor, the low-level control structure generates swash-plate commands based on error in speed of swing motor. The errors between the final unit displacement and engine speed commands (outputs of the lower-level controller) and the measured unit displacements and engine speed, are processed and sent as voltage commands to hardware, which is modeled in the ‘hydraulic system’ model, ‘engine dynamics’ and ‘mechanical system’ modules of the simulation model.

The rules presented in Table 2.1 replicate the optimal control results reasonably well, as can be seen from Figure 2.3.

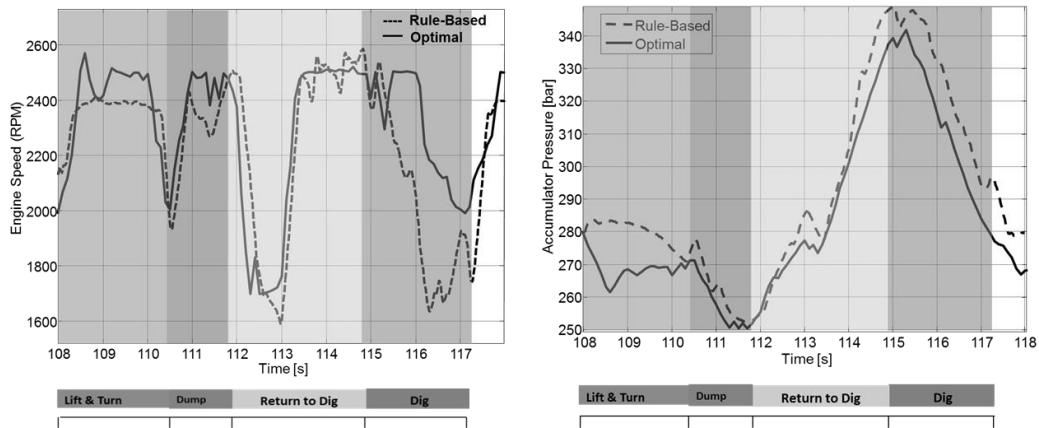


Figure 2.3: Replication of Optimal Accumulator Pressure and Engine Speed by Rule-Based Strategy

The accumulator steps in to meet peak actuator power requirements (where the engine could not meet them by itself, such as during the dig-phase or the ‘dump’ phase), and is charged during the ‘return-to-dig phase’, where the power requirement is moderate throughout and toward the end swing comes to rest and the boom is lowered (aiding DC load). The rule-base leads to slightly more aggressive charging of the accumulator than in the optimal case.

The controls,  $\beta_i$ ,  $i = 2,3,4,5$  are plotted in Figure 2.4. The DC pump displacements ( $i = 3,4,5$ ) rise and fall with the corresponding flow requirements. There is a disagreement between the rule-based and optimal displacements in the digging phase – the rule-base enforces the engine speed to be at the minimum allowable speed (and thus both stick and bucket are at 100%), whereas the optimal power management raises the engine speed a little and keeps the stick and bucket displacements just below 100%.

The unit 2 displacement  $\beta_2$ , is adjusted to match the torque requirement at the swing motor and matches the optimal displacement reasonably well.

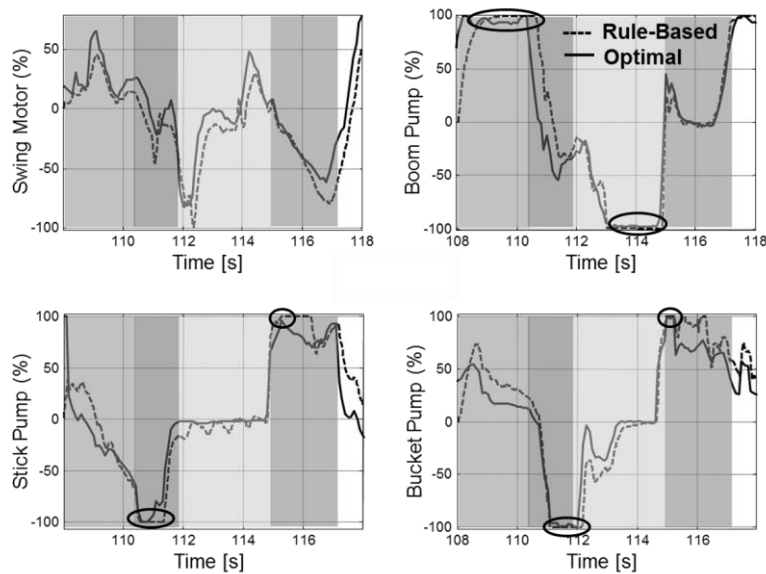


Figure 2.4: Replication of Optimal DC Pump and Unit 2 Displacements by Minimum-Speed Strategy

A comparison of the fuel consumption results is also provided between the DC non-hybrid with a constant speed strategy, and the DC hybrid, using both the minimum-speed strategy as well as the optimal power management results.

Expert-Truck Loading Cycle Results	DC Non-Hybrid (Constant Speed)	DC Hybrid (Min. Speed)	DC Hybrid (Optimal)
Fuel Consumed (g)	42	34.5	33.8
% Improvement	(Baseline)	+17.9%	+19.5%*

Table 2.2 : Fuel Consumption Comparison

### 3 DC S-P Hybrid Excavator Prototype

The detailed circuit for the swing drive is explained in this section, including all the logic valves that are necessary for operation. The units 3, 4, 5 (Figure 1.1) are also shared by the auxiliary actuators (offset, left and right travel motors respectively), not shown here. Unit 1 is also used to provide flow to the blade.

#### 3.1 Series-Hybrid Swing Drive: Detailed Circuit Configurations

Apart from the components shown in the simplified schematic of the DC S-P hybrid the detailed working hydraulic circuit of the series-hybrid swing drive is shown in Figure 3.1. There is an electrically-operated shut-off valve SF to isolate unit 2 from the accumulator as desired. An integrated safety block has also been added which contains - a manually-operated ball valve 'NO' that is always open (to connect accumulator to either of the units), another ball valve NC that is normally closed and used only to bleed off HP after operation, and a high-pressure relief valve RV HP. The two valves CV2 and ACV together perform the function of anti-cavitation of unit 2 when ACV is energized (during swing motor operation) and the function of load-holding (swing motor is stationary) when ACV is de-energized. The secondary controlled displacement unit (2) uses a high pressure swash plate control system.

The on-off valves A1, A2, B1 and B2 are responsible for switching unit 1 to provide flow either to the blade or to the series-hybrid swing drive. The pilot-operated check valves (PO CV-A, PO CV-B) are responsible for balancing flow when unit 1 is used for operation of the blade (which uses a differential cylinder), and the relief valves RV-A and RV-B limit pressures to acceptable levels.

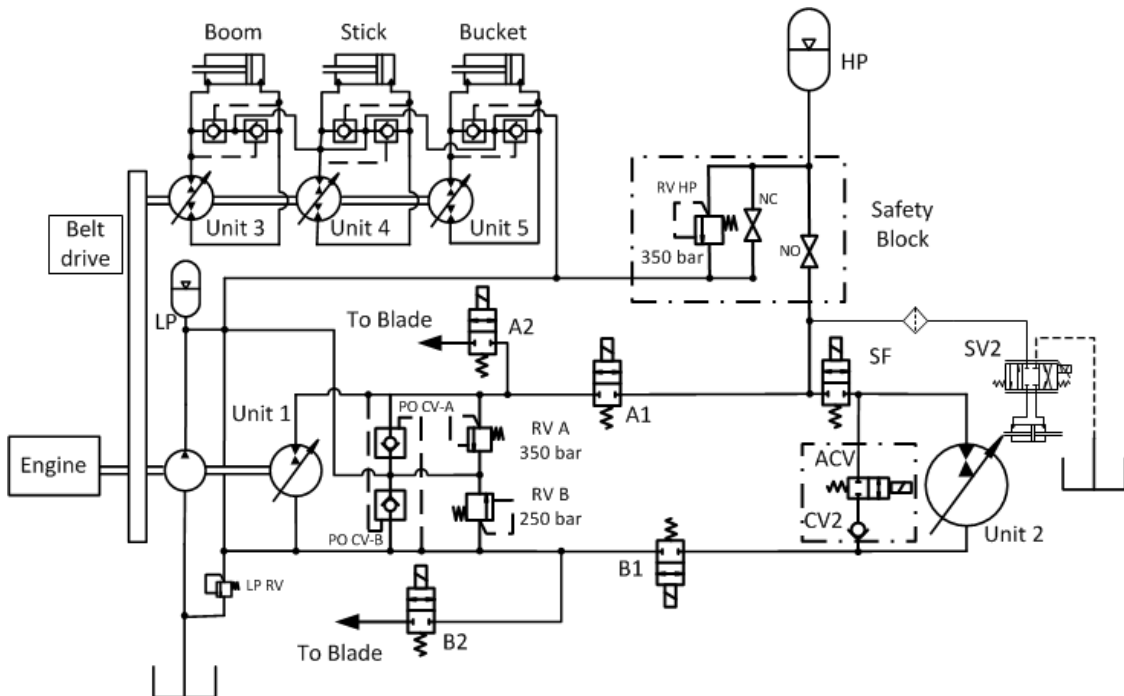


Figure 3.1: Closed-Circuit Series-Hybrid Swing Drive-Option A



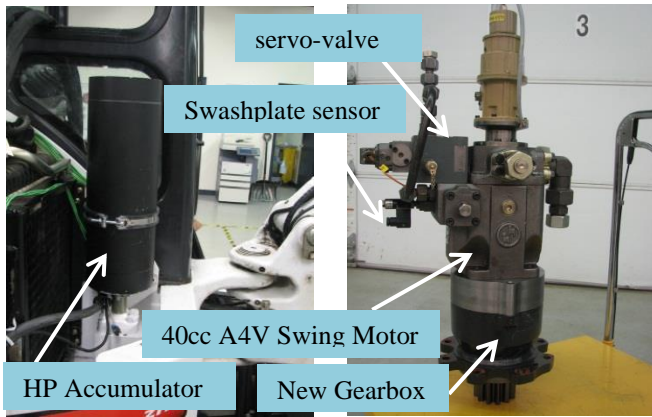


Figure 3.3: System Integration with Hybrid Components

The prototype excavator has been instrumented with appropriate sensors for motion control of the various actuators (Figure 3.4) and to advanced power management strategies.

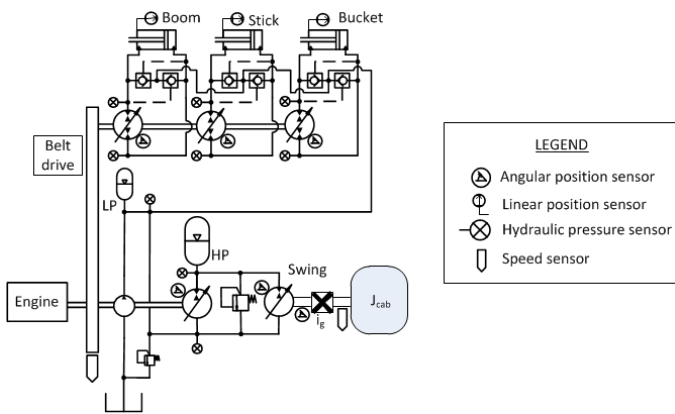


Figure 3.4: Sensors Instrumented on Prototype Excavator

Angle sensors are used to measure swashplate angles of all units. A rate gyroscope measuring cabin speed is used for

### 3.3 Excavator Controller

The overall structure of the excavator controller is summarized in Figure 3.5. The controller takes in the operator inputs (such as the joystick and lever positions), interprets them in terms of physical quantities (engines speed and % displacement commands for the units) and also needs various measured quantities (pump displacements, accumulator pressure, engine speed, swing motor speed) as inputs. The final outputs of the controller are electrical signals (voltages or currents) that are directly applied to the hardware (servovalves in the swashplate control systems and engine actuator commands).

The swing motor is closed-loop speed-controlled, meaning that the joystick signal is interpreted as a speed command for the swing motor. The linear actuators (boom, stick and bucket and auxiliary functions) are open-loop, flow-controlled during motion meaning that respective joystick signals are interpreted as flow commands (swashplate angle) for the corresponding unit (3, 4, 5). Position control will be used to keep the actuators at rest when no motion is commanded.

closed-loop speed-control of unit 2 during motion. A Hall-effect angle sensor measuring unit 2 shaft position (converted online to cab position) is used for closed-loop position control of the cabin, when no motion is commanded by the operator. The prototype has also been instrumented with pressure sensors to measure HP and LP accumulator pressures, as well as pressures at both ports of each unit (1, 3, 4 and 5) on the engine shaft. These are all diaphragm-type strain gages. Linear position sensors are integrated with the cylinders, and are necessary when no motion is commanded by the operator, to hold position. A linear motor (or 'engine speed actuator') that is directly linked to the diesel engine governor, is moved to change engine speed. A particular position of the linear actuator corresponds to a particular speed at which the governor cuts off fuel to the combustion chamber. Thus, an engine speed sensor and a position sensor for the engine speed actuator, are required to ensure speed control of the engine. Appropriate signal amplification hardware has also been incorporated to amplify controller output signals to the servo-valves (in swashplate control systems) and linear motor.

National Instruments' (NI) cRio control hardware is currently in use on the excavator to deploy the controller as well as for data acquisition. Controller development is done in Matlab Simulink and the NI Veristand software provides the user-interface for online controller tuning and signal monitoring.

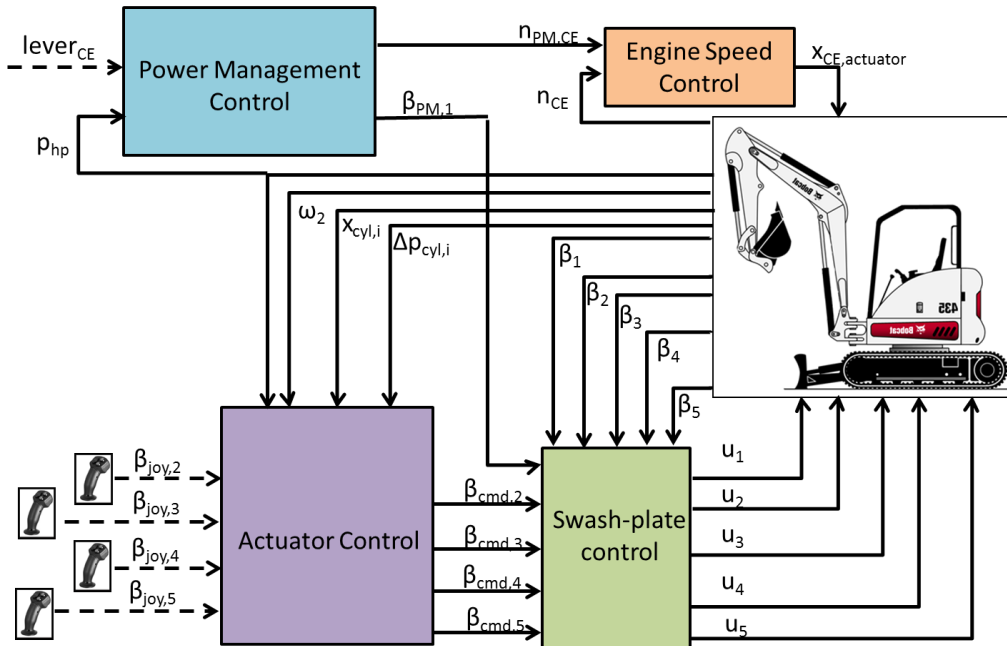


Figure 3.5: Structure of Controller on Prototype Excavator

The two controls,  $\beta_{PM,1}$  (unit 1 displacement command) and engine speed  $n_{CE,cmd}$  are determined by the power management routine. The other controls ( $\beta_{cmd,i}$ ,  $i = 2,3,4,5$ ) are manipulated to meet actuator requirements – i.e.  $\beta_{cmd,2}$  should be high enough to swing motor torque requirement at the current accumulator (HP) pressure, and  $\beta_{cmd,3}$ ,  $\beta_{cmd,4}$ ,  $\beta_{cmd,5}$  to meet cylinder velocity requirements at the current engine speed.

### 3.3.1 Power Management Control

In our first study which is reported in this paper, the engine is simply operated at a constant speed of 2500 rpm (the maximum governed speed of this engine). Unit 1 is controlled in order to maintain a constant, desired accumulator pressure during operation – it is held at a constant value (40%) when HP accumulator pressure is between 190 bar and 220 bar, and de-stroked close to zero as it nears 225 bar.

### 3.3.2 Actuator Control

The actuator controller is responsible for translating the various operator inputs to swashplate angle commands for the respective units (2, 3, 4, 5). As was explained before and evident from Figure 3.6, unit 2 (swing motor) is closed-loop speed controlled when motion is commanded and closed-loop position controlled when there is no joystick command. The joystick input is interpreted as a speed command when it is not zero.

When the operator commands motion, a combination of feed-forward and feedback control is used. A feed-forward term that accounts for accumulator pressure is also present, which computes the desired displacement required to meet a particular acceleration (using a nominal inertia term) at the measured accumulator pressure. This is added to a feedback term – which is the result of a PI controller acting on the error in speed. The sum of these two terms determines the final unit 2 displacement command,  $\beta_{cmd,2}$ .

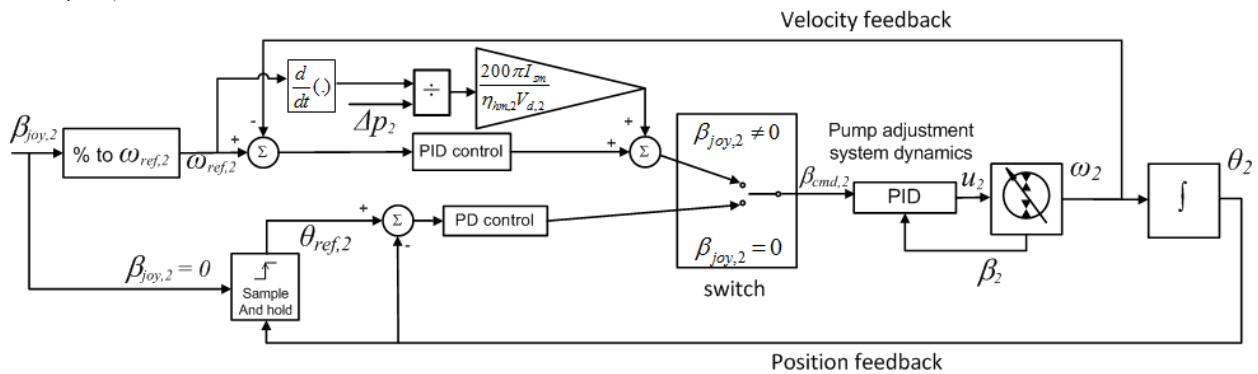


Figure 3.6: Actuator Control for Unit 2

Figure 3.7 summarizes the results of simulation of the closed-loop speed control of the swing motor. The swing motor is commanded to follow speed profiles expected in a typical digging cycle in the first 10 seconds. The swing is at rest in the first 3 seconds (the ‘dig’ phase of the cycle), following which it accelerates gradually (and then cruises) toward the truck, from  $t = 3$  to 6.5 s (this phase is slow due to the high inertia of rotation due to an extended arm and a loaded bucket). Braking is fast and short (from  $t = 6.5$ s to  $t = 7$  s), followed by a short phase at rest wherein the bucket is emptied in the truck. Following this, the cab accelerates rapidly back toward the digging trench (from  $t = 7.2$ s to  $t = 8.1$ s), cruises at maximum speed and brakes (slower compared to braking before emptying of accumulator). It can be seen that the simulated swing motor speed follows the commanded swing motor speed very well throughout the first 10 seconds.

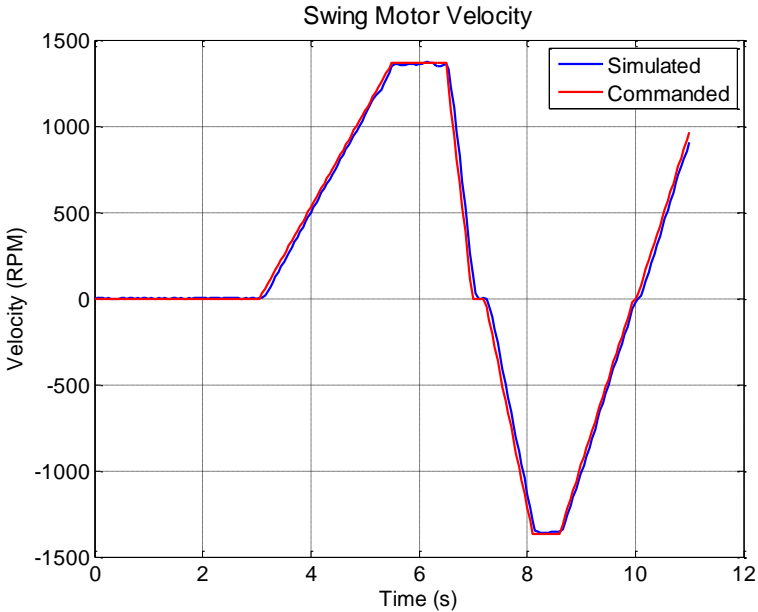


Figure 3.7: Simulated Results of Swing Motor Closed-Loop Speed Control

When the boom, stick or bucket are to be moved, they are done so in an open-loop or flow-controlled manner (Figure 3.8). The joystick command translates directly to a swashplate command (with some regulation using pressure-feedback to avoid un-commanded actuator oscillations) for the corresponding unit. There is no velocity or position feedback, during motion. Once the joystick is centered, it is desired that the corresponding actuator hold its position.

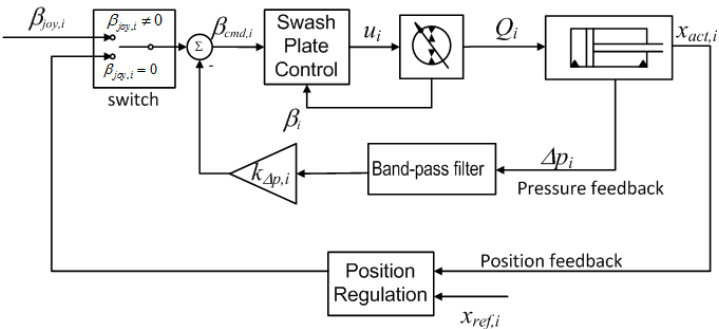


Figure 3.8: Actuator Control for DC Units (supplying boom, stick, bucket)

The position controller currently being used for all linear actuators (when no motion is commanded) is the limited semi-integrator (Berg, 1999). The velocity control for the swing motor is simply a PID controller at this stage, although a more sophisticated controller will be required once better power management strategies are implemented (accumulator pressure will not be constant).

### 3.3.3 Unit Displacement Control

Swash-plate commands ( $\beta_{cmd,i}, i = 1,2,3,4,5$ ) from the actuator controller are inputs to the swashplate controller. The swashplate controller acts on the error between the commanded and measured displacements, to provide an output current or voltage signal for the servo-valve. These are the final outputs of the excavator controller. PI controllers are used as the swashplate control law.

Discrete PI controllers are also used for the engine controller, which generates a command for the linear motor (or engine speed actuator) based on the error in commanded and actual engine speeds. An aspect of the excavator controller that has not been shown here is the anti-stall controller. Here the displacement commands for the units on the engine shaft (1,3,4,5) are reduced if the engine speed is significantly below the engine speed command.

### 4 Preliminary Measurements on Prototype

A video of the prototype hybrid DC excavator being operated in a 90-degree digging cycle (Fig. 4.1) can be found at the following website: <https://engineering.purdue.edu/Maha/ccefp/>.



Figure 4.1: DC S-P Hybrid Excavator Prototype in a Digging Operation

Measurement results during an artificial digging maneuver (about two scoops or cycles) are plotted in Figure 4.2, Figure 4.3 and Figure 4.4. In Figure 4.2, commanded and measured pump displacement (%) are plotted. These plots show the effectiveness of the pump displacement controller being used.

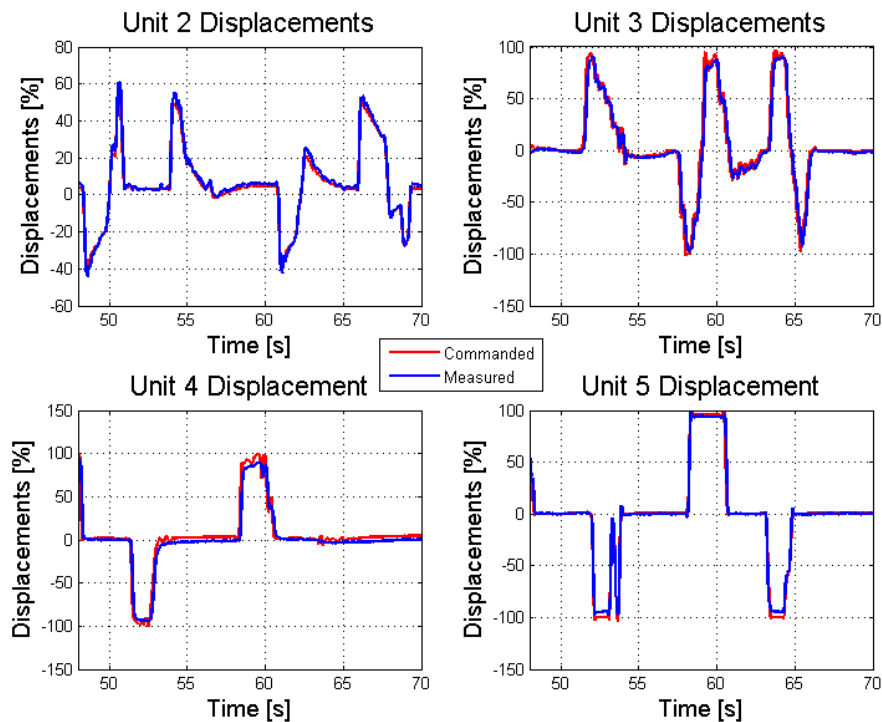


Figure 4.2: Unit Swashplate Angle Commands and Measurements during Artificial Dig Maneuver

Analyzed together with Figure 4.3, it can be seen that a change in the position of the actuators (boom, stick and bucket only) occurs when the displacements of the corresponding units are non-zero. Also, the actuator positions (especially the boom) do not change in an exactly cyclical fashion since this artificial dig cycle was performed by a novice operator.

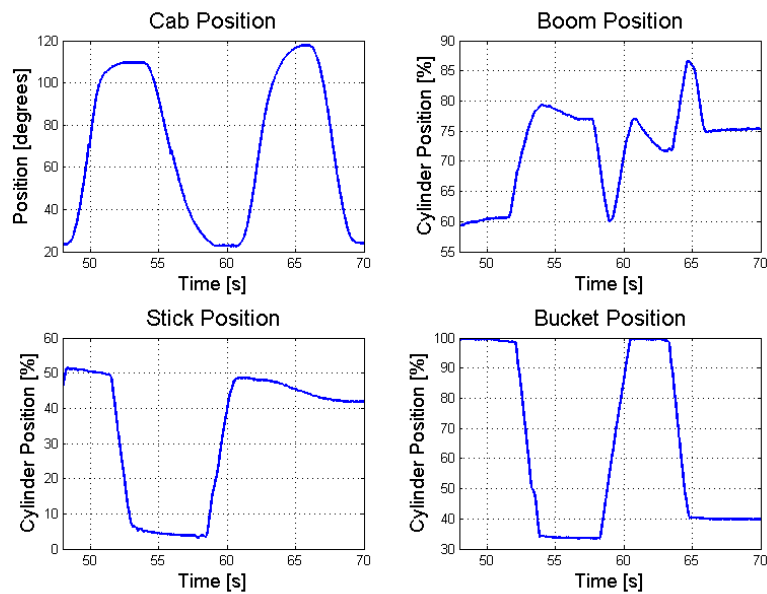


Figure 4.3: Actuator Positions during Artificial Dig Maneuver

Engine speed and pressure (of the accumulator HP) are plotted in Figure 4.4. The engine speed is commanded to stay near 1900 rpm while unit 1 is commanded to ensure that the accumulator pressure stays at 225 bar. It can be seen that when the cabin accelerates, HP is drained slightly (to 220 bar) from  $t = 48$ s to 50s, whereas during deceleration of the swing (from  $t = 50$ s to 52s), there is a slight increase in accumulator pressure above 225 bar. Once at rest ( $t = 52$  s to 54 s) the pressure drops back to 225 bar.

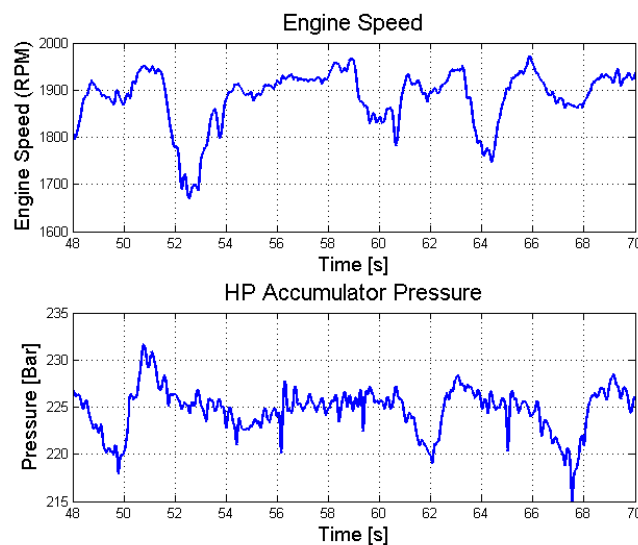


Figure 4.4: Engine Speed and Accumulator Pressure During Artificial Dig Maneuver (with Preliminary Power Management)

## 5 Conclusions and Future Work

A prototype DC S-P hybrid excavator has been realized at the Maha Fluid Power Research Center at Purdue University and instrumented with electronic equipment necessary for implementation of actuator motion control and advanced power management schemes. Closed-loop speed control has been demonstrated for the secondary-controlled swing

motor on the prototype, and working open-loop flow control demonstrated for the other actuators as well.

Based on a high-fidelity dynamic co-simulation model, the novel hydraulic hybrid architecture is predicted to have substantially higher energy efficiency than state-of-the-art valve-controlled excavators, as well as to show a significant improvement over the non-hybrid prototype DC excavator,

while enabling up to 50% engine downsizing. The simulation model has also been utilized to demonstrate the ability of a rule-based power management strategy to replicate optimal control results.

In the future, the single-point power management strategy ([4], [6]) will be implemented on the excavator to demonstrate the feasibility of using reduced engine power and productivity measurements will be made for an expert truck-loading cycle. Just as in the case of the non-hybrid DC prototype, these will be made following system simulations of the DC S-P hybrid concept (actual engine downsizing is not planned on the prototype). Implementation of advanced power management strategies will also be performed, to investigate power management schemes that yield near-optimal results independent of duty cycle.

## Nomenclature

Designation	Denotation	Unit
$\beta_{\text{joy},i}$	$i^{\text{th}}$ joystick command	(%)
$\beta_{\text{PM},i}$	displacement command for $i^{\text{th}}$ unit	(%)
$\beta_i$	measured displacement of $i^{\text{th}}$ unit	(%)
$n_{\text{CE}}$	Engine speed	[rpm]
$n_{\text{CE,cmd}}$	Commanded engine speed	[rpm]
$n_i$	Speed of $i^{\text{th}}$ hydraulic unit	[rpm]
$\Delta p_i$	Pressure difference across $i^{\text{th}}$ unit	[bar]
$M_{1,\text{des}}$	Storage pump torque	[N.m]
$M_{\text{cp}}$	Charge pump torque	[N.m]
$M_{\text{des}}$	Desired engine output torque	[N.m]
$V_{\text{d},i}$	Displacement of $i^{\text{th}}$ hydraulic unit	[cc/rev]

## References

- [1] Rahmfeld, R. and Ivantysynova, M. 2001. Displacement Controlled Linear Actuator with Differential Cylinder - A Way to Save Primary Energy in Mobile Machines. *Proc. of 5th International Conference on Fluid Power Transmission and Control (ICFP'2001)*, Hangzhou, China, pp. 316 - 322.
- [2] Zimmerman, J., Pelosi, M., Williamson, C., and Ivantysynova, M. 2007. Energy Consumption of an LS Excavator Hydraulic System. *2007 ASME International Mechanical Engineering Congress and Exposition*, Seattle, WA, USA. IMECE2007-42267.
- [3] Williamson, C., Zimmerman, J. and Ivantysynova, M. 2008. Efficiency Study of an Excavator Hydraulic System Based on Displacement-Controlled Actuators. *Bath ASME Symposium on Fluid Power and Motion Control (FPMC2008)*, pp.291-307
- [4] Williamson, Christopher A. *Ph.D. Thesis*, Purdue University. December 2010. Power Management for Multi-Actuator Mobile Machines with Displacement Controlled Hydraulic Actuators.
- [5] Zimmerman, J., Busquets, E. and Ivantysynova, M. 2011. 40% Fuel Savings by Displacement Control Leads to Lower Working Temperatures - A Simulation Study and Measurements. *Proceedings of the 52nd National Conference on Fluid Power 2011*, NCFP I11-27.2.
- [6] Zimmerman, J. and Ivantysynova, M. 2011. Hybrid Displacement Controlled Multi-Actuator Hydraulic Systems. *Proceedings of the 12th Scandinavian International Conference on Fluid Power*, May 18-20 2011, Tampere, Finland, pp 217 - 233.
- [7] Zimmerman, J., Hippalgaonkar, R. and Ivantysynova, M. 2011. Optimal Control for the Series-Parallel Displacement Controlled Hybrid Excavator. *ASME/Bath Symposium on Fluid Power and Motion Control*, Arlington, VI, USA.
- [8] Hippalgaonkar, R., Zimmerman, J. and Ivantysynova, M. 2011. Investigation of Power Management Strategies for a Multi-Actuator Hydraulic Hybrid Machine System. SAE 2011 Commercial Vehicle Engineering Congress, Rosemont, IL, USA.
- [9] Hippalgaonkar, R., Ivantysynova, M. and Zimmerman, J. 2012. Fuel-Savings of a Mini-Excavator through a Hydraulic Hybrid Displacement Controlled System. 8<sup>th</sup> International Fluid Power Conference (IFK) Dresden. Dresden, Germany.
- [10] Zimmerman, Joshua D. Ph.D., Purdue University, May 2012. Toward Optimal Multi-Actuator Displacement Controlled Mobile Hydraulic Systems.

# Industry Applications 1



## Universal Energy Storage and Recovery System – A Novel Approach for Hydraulic Hybrid

M Erkkilä, F Bauer\*, D Feld\*

Hydac Oy, Tampere, Finland

\*Hydac International GmbH, Sulzbach/Saar, Germany

E-mail: [mikko.erkkila@hydac.fi](mailto:mikko.erkkila@hydac.fi), [frank.bauer@hydac.com](mailto:frank.bauer@hydac.com), [daniel.feld@hydac.com](mailto:daniel.feld@hydac.com)

### Abstract

The paper presents the basic principles of hybrid systems. It gives a rough approximation of factors that can affect the efficiency of a hybrid system. A Short comparison between hydraulic, mechanic and electric energy storing system is presented.

In a mobile working machine, there are mainly three possible sources for energy storage or recovery which are: energy of the combustion engine, when it is working on part load, braking energy of a vehicles kinetic energy and its hydraulic system.

A novel hydraulic system is introduced that is capable to store and recover energy from all energy sources of mobile working machine. The power peaks during the working cycles of the machine can be covered with energy stored in the hydraulic accumulator and so the size of the combustion engine can be reduced and dimensioned according to the average power. It also reduces the energy conversion losses. Simple and cost effective design makes it an attractive alternative for many applications.

**Keywords:** Hydraulic hybrid

### 1 Introduction

In mobile working machines the loading of the combustion engine is often not constant during the working cycle. Maximum power is in many cases needed only for short periods. Normally the combustion engine must be dimensioned according to the maximum peak power, which leads to oversized engines compared to the average power during the working cycle and to low efficiency, because the engine is running most of the time on part load. In the past it has not been a problem to increase the engine size, but the tightening of engine exhaust regulations like Euro/TIER and increased fuel cost will force the equipment manufacturer to search for new solutions.

During movements kinetic energy is charged in the vehicle and it is normally extinguished and wasted in the brakes, causing wear and thermal loading. More sophisticated transmissions, like Continuously Variable Transmissions (CVT) [1], hydrostatic, or electrical transmissions are able to transmit the braking energy back to the combustion engine. Unfortunately the braking capacity of the new low emission diesel engines is limited. In some applications, like in city busses or package delivery or garbage vehicles, in which the amount of braking energy is sufficient; energy recuperation systems have been tested and are in use.

By lifting of a load, potential energy is accumulated in the own mass of the lifting equipment. In a traditional hydraulic

system, when the equipment is lowered, this energy is lost in the return notch of the control valve. Balancing systems can be used to compensate the dead weight. There are also proposals how the returning energy could be recovered.

In most of the studies only one of these three possible energy storing sources has been considered and the energy recuperation systems have been individually developed.

### 2 Hybrid systems

In the past years a lot of effort has been focused to the development of hybrid drives. Car industry has already taken hybrid solutions in mass production, in order to reduce fuel consumption.

In the branch of mobile working machines many studies and investigations have been carried out, regarding the possibility to use hybrid technology.

By side of energy saving one interesting chance for mobile working machines is the possibility to reduce the engine size.

Traditionally the engine has to be dimensioned according to the peak power of the machine. In many mobile machines there is a big difference between required average and peak power. Figure 1 show the so called Y-working cycle for a

wheel loader, for filling a lorry C from a pile B. And figure 2 the correspondent power demand from the engine during this cycle.

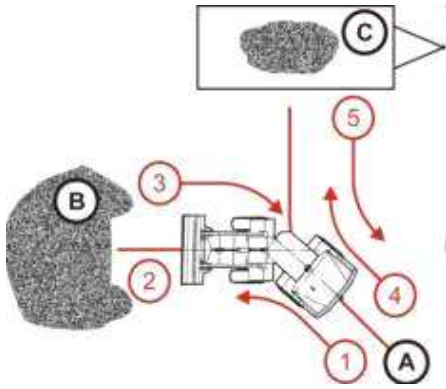


Figure 1: Y- working cycle of a wheel loader

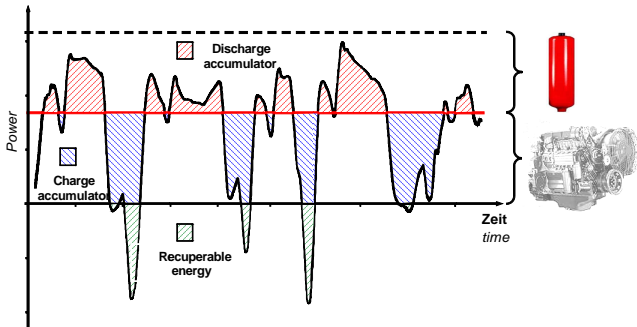


Figure 2: Power demand during the Y- working cycle [2]

From figure 2 we can see that the amount of recoverable energy is moderate. The main benefit for hybrid system in this kind of machines is to dimensioning the engine according to the average power and covers the peak power demand with the stored energy.

Hybrid drives can roughly be divided into two categories: parallel and serial hybrids

**2.1 Serial hybrid**

In the serial hybrid the total engine power is transformed to electrical or hydraulic power, from which the energy is stored and re-used. Figure 5 shows a typical hydraulic serial hybrid design.

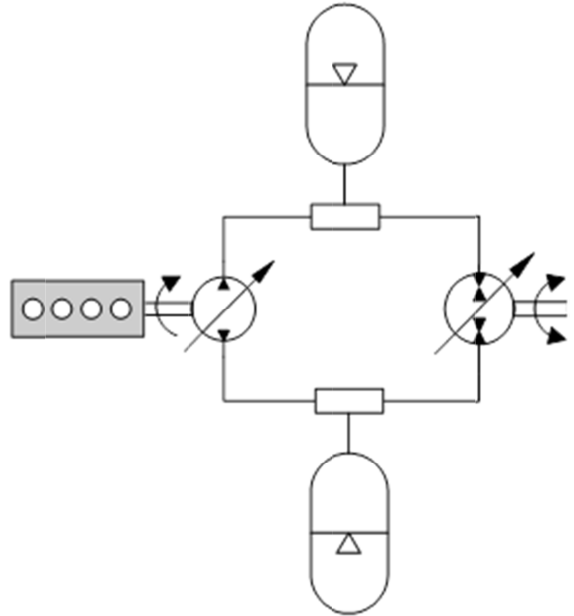


Figure 5: Serial hybrid system

In serial hybrid the engine is decoupled from the power consumers like powertrain or working hydraulics, which utilizes the possibility to optimize the engine control and efficiency only according to optimal energy production.

The disadvantage of a serial hybrid is that the complete power in the main power train has to be transformed first to electrical or hydraulic power and then back to mechanical power. The main power line power loss is then:

$$P_l = P_e(1 - \eta_{transfer1})(1 - \eta_{transfer2}) \quad (1)$$

,where:

P<sub>l</sub> is power loss

P<sub>e</sub> is actual engine power

$\eta_{transfer1}$  ,and  $\eta_{transfer2}$  are the power transform efficiencies.

**2.2 Parallel hybrid**

In parallel hybrid system the energy storing device is arranged in parallel to the main power line, and it has no influence to the basic function of it. Figure 6 shows the typical hydraulic parallel hybrid design.

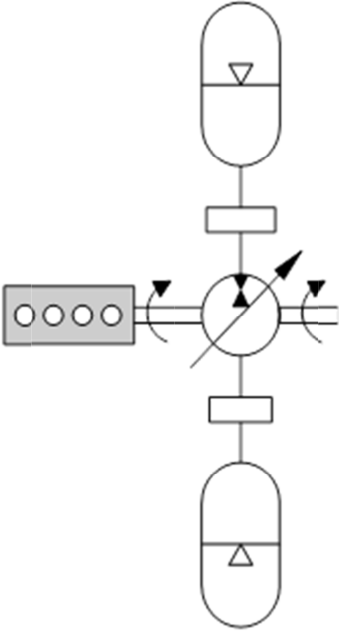


Figure 4: Parallel hybrid system

In parallel hybrid system the speed of the engine has to be controlled due to the requirements of the main power line. The parallel hybrid can only increase or decrease the engine torque.

If the accumulator is not charged or discharged, the main power line efficiency is only affected by the idle power loss of the energy storage device. The main power line power loss is then

$$P_l = P_{idle(p,n)} \quad (2)$$

, where

$P_l$  is power loss.

$P_{idle}$  is power loss of the energy storing device, which normally depends on the pressures in high and low pressure accumulators and running speed of the engine.

When the accumulator is charged and discharged, the power loss can be defined as:

$$p_l = Q(p_{ha} - p_{la})(1 - \eta_{transfer}) + P_{idle(p,n)} \quad (3)$$

where:

$Q$  is the flow that is charged or discharged from or to the accumulator, and

$p_{ha}$  is the pressure in high pressure accumulator and

$p_{la}$  is the pressure in low pressure accumulator.

### 3 Hydraulic accumulator as energy storage

#### 3.1 Characteristics of a hydraulic accumulator compared with other energy storage devices

Figure 3 shows the energy and power densities for different kind of energy storing devices.

The energy storing capacity of hydraulic accumulators is limited, but they are able to restore and discharge high power.

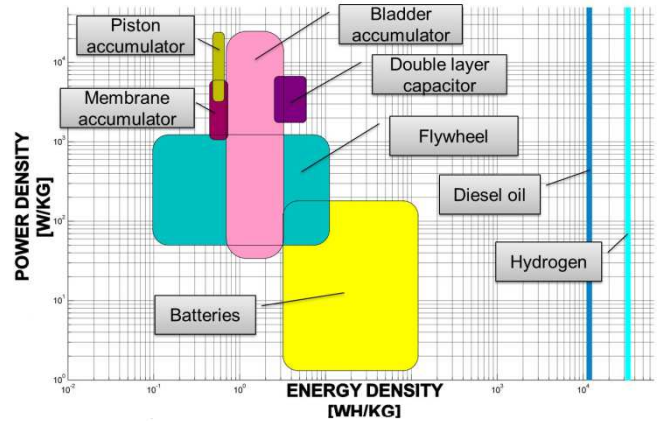


Figure 6: Energy and power densities of energy storage device [3]

Table 1 shows a comparison of the characters of electrical, mechanical and electrical power storing devices

Technology	Electrical		Mechanical	Hydraulic
Energy storage device	Double layer capacitor	Lithium ion battery	Flywheel	Hydraulic accumulator
Energy density	-	+	o	-
Power density	+	o	o	+
Ageing / Capacity loss	o	-	o	+
Temperature sensitivity	-	-	o	+
Self discharge	-	o	-	+
Packaging	o	o	o	o
Cost effectiveness	-	o	o	+
Safety / Service	-	-	o	+

Table 1: Comparison of energy storing devices

In the past the main focus of hybrid drives has been concentrated to the development of electric hybrids due to the better efficiency of the electric components. A study made by Liebherr [4] shows that due to the high number of required energy transformations the total efficiency of electric hybrid systems can drop on the level of the hydraulic systems. See figure 7.

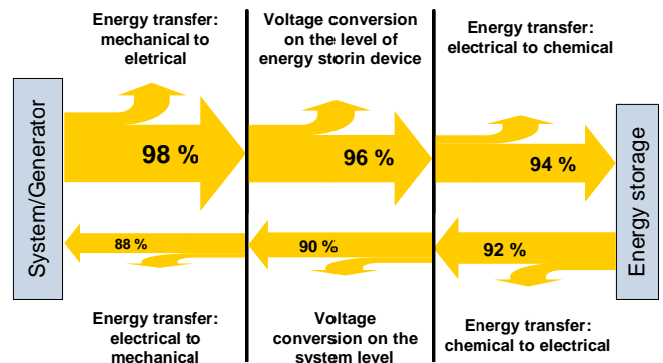


Figure 7: Power losses in electrical energy storage [4]

On the other hand electric energy transfer can be dangerous in mobile machines which are working in rough environment. For example 60 kW means 600 V and 100 A or 100 V and 600 A. Cable breaks or damaged cable isolations can cause far bigger problems than hydraulic hose breaks.

Hydraulic accumulators have been used several decades in mobile working machines. Security standards have been developed on a high level and security devices are well known and available.

In mobile working machines the required power is typically changing extremely during the working cycles and those are typically short. Due to the good power density hydraulic accumulators are suitable to compensate rapid power peaks.

### 3.2 The energy storing capacity of a hydraulic accumulator

The Energy capacity of a hydraulic accumulator for an ideal gas can be defined as [5]:

$$E = \frac{p_{min} V_0 \left(\frac{p_0}{p_{min}}\right)^{\frac{1}{K}}}{1-K} \left[ 1 - \left(\frac{p_{min}}{p_{max}}\right)^{\frac{1-K}{K}} \right] \quad (4)$$

Where;

E is the energy capacity of the accumulator,

V<sub>0</sub> is the volume of the accumulator,

p<sub>min</sub> is the minimum pressure

p<sub>max</sub> is the maximum pressure

p<sub>0</sub> is the pre charge pressure of the accumulator

K is the adiabatic constant for nitrogen.

The figure 8 shows the energy capacity for a 10 Liter accumulator, with a maximum pressure of 350 bar as a function of P<sub>min</sub>, when the pre charge pressure is 0.9 \* P<sub>min</sub>.

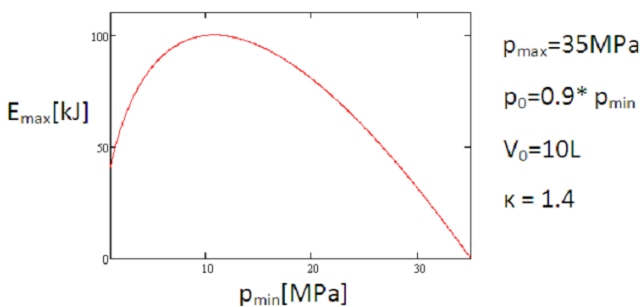


Figure 8: Theoretical energy storing capacity of a 10 L accumulator

In practice the accumulator has to operate on wide temperature range, which limits the theoretical power charging capacity. Hydac's ASP Accumulator Simulation Program is an excellent tool for dimensioning accumulators for hybrid solutions. It is based to real gas characteristics and thermo dynamical processes during loading and unloading.

In praxis a 50 L accumulator with operating pressure range maximum 330 bar and minimum 100 bar is able to store about 360 kJ energy. Figure 9 shows that with 360 kJ energy can be loaded, when a vehicle with weight of 10 ton is braked from a velocity of 36 km/h to 19 km/h. With this stored energy it is possible to lift a load of 3,6 ton in a height of 10 m.

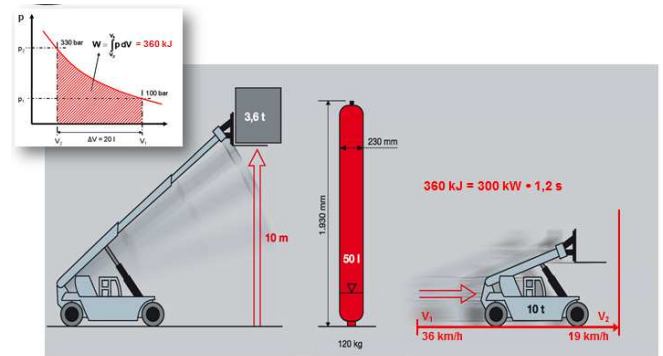


Figure 9: Practical energy capacity of a 50L accumulator

## 4 Conventional hydraulic energy storing systems

In the following some known hydraulic hybrid systems are shown.

### 4.1 Adding an accumulator to a hydraulic system

The easiest possibility to store energy is to add an accumulator to the hydraulic system as shown in figure 10.

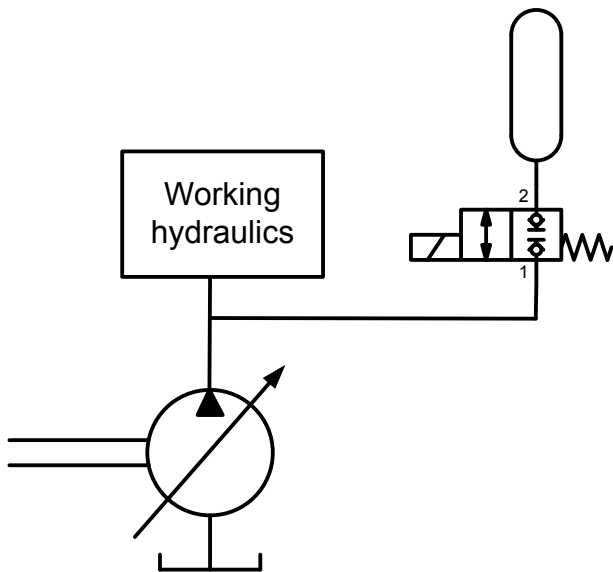


Figure 10: Simple energy storing system

This kind of system is used in a forestry machine application by the company HSM. Where energy is stored in the accumulator and used to accelerate the feeding rolls in a harvester head [6] see figure 11. According to HSM it was possible to reduce 20% fuel consumption with this system.

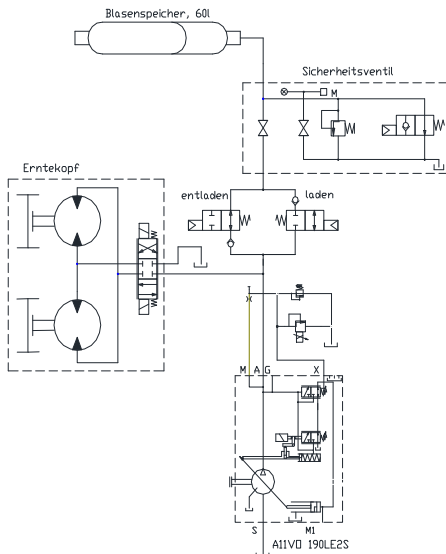


Figure 11: Serial hybrid system [6]

The main disadvantage for the general use of this kind of system is that the energy from the accumulator can only be used, when the pressure in the accumulator is higher than the load pressure, see figure 12. The preloading and the minimum operating pressure of the accumulator can of course be chosen so that the accumulator pressure is always higher than the maximum load pressure, but also then the accumulator energy capacity is limited. Also the pressure difference between accumulator and system pressure is lost.

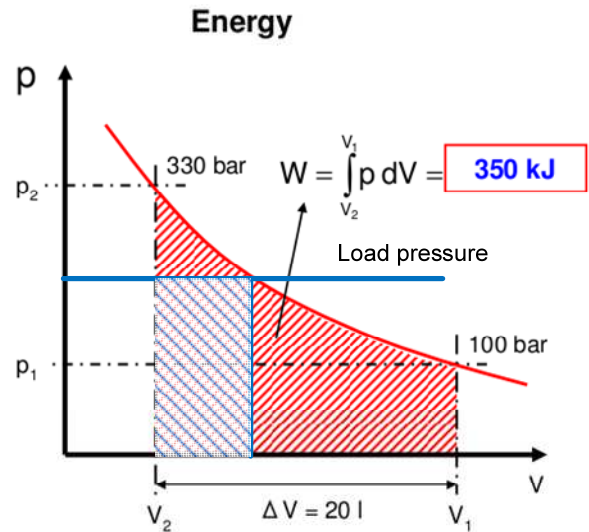


Figure 12: Usable energy capacity in a simple system, marked as blue

#### 4.2 Using an extra pump

Figure 13 shows a hydraulic system, where an extra pump is used to charge and discharge the accumulator. The pump is mechanically driven from the engine and the transmission. It is then able to store braking energy and also energy from the engine, when the engine is not fully loaded.

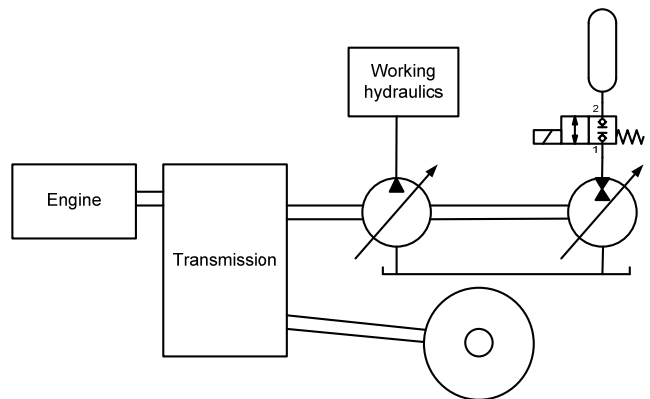


Figure 13: Additional pump/motor unit with accumulator as energy storing unit

This kind of energy storing system has been proposed by the Purdue university research team for the Multi-Actuator Hydraulic Hybrid Machine Systems [6] see figure 14.

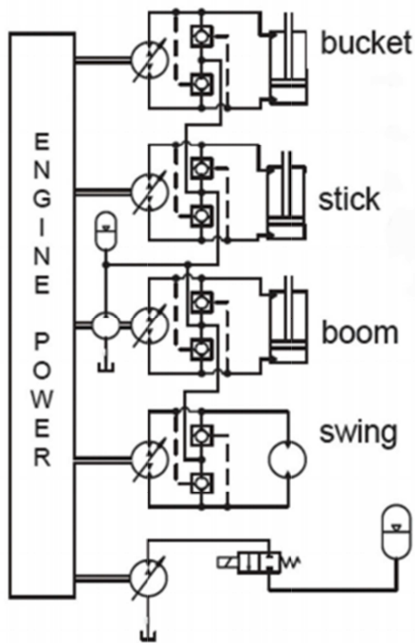


Figure 13: Additional pump/motor unit with accumulator as energy storing unit in Multi-Actuator Hydraulic Hybrid Machine System [7]

The main disadvantage of this system is that the energy from accumulator has to be first converted to mechanically energy, and then with the working hydraulic pump back to hydraulic energy. Due to the required energy conversions the energy losses are high and the overall efficiency is poor.

## 5 A Novel Approach for Hydraulic Hybrid

### 5.1 System design

In the new proposed system (see figure 15) a pump/motor unit that can be pressurized on both sides A and B is added to feed a hydraulic accumulator from the working hydraulic system. This kind of unit is normally used as pump in a closed loop power transmission system

The pump/motor unit can be driven as shown on the picture, direct or via through drive from the main engine or from gearbox that is connected to drive wheels.

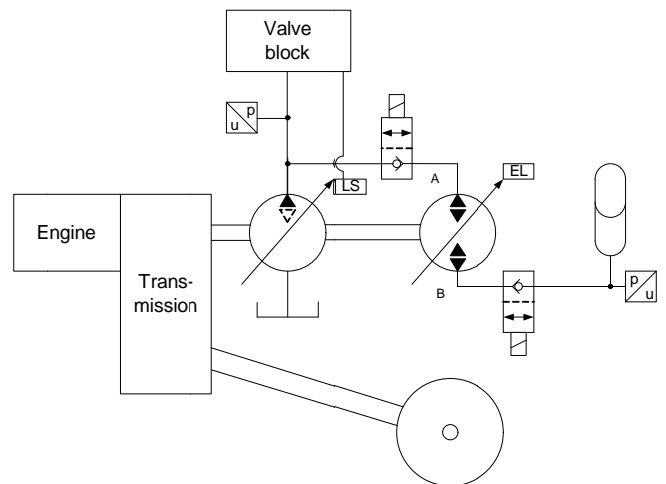


Figure 15: A new approach for hydraulic hybrid

### 5.2 Function principle

The hydraulic system can be designed as a normal Load Sensing system, where only a pump/motor unit and an accumulator are added.

The function of the pump/motor unit is to control the flow for charging the accumulator and controlling the flow from the accumulator to working hydraulics. It also works as pressure transformer between the accumulator and system pressure.

In the system there are also 2/2-valves on the both sides of the pump/motor unit. With those valves it is possible disconnect the energy storing system from the working hydraulic system to avoid power losses, when the energy storing system is not activated during the operation of the machine. So the high pressure in accumulator or in working hydraulics is not increasing the hydromechanical or volumetric losses of the pump/motor unit.

The valves are working also as safety devices, when the A side valve is opened only accumulator loading is possible. When B side valve is opened the accumulator can be discharged.

### 5.3 Energy storing

The open loop Load Sensing pump keeps the A side of the pump/motor unit pressurized. When there is no flow consumption for the working hydraulics the Load Sensing pump is on Stand By pressure, normally on the level of about 20 bar. This is enough to assure the needed suction pressure and flow for the pump/motor unit.

If there is a parallel need for working hydraulics the Load Sensing pump pressure is controlled according to the needed load pressure. In this case the pump/motor unit works as a pressure transformer between the Load Sensing pump and accumulator pressure. The pump/motor unit can use the rest of the available flow capacity of the main pump to charge the accumulator.

The amount of the stored energy is controlled with the displacement control of the pump/motor unit.

### 5.3.1 Energy storing from the engine

When during the working cycles of the machine, there are periods, when the engine power is not fully used, the remaining energy can be stored to the accumulator.

The amount of stored power can be controlled with the displacement control of the pump/motor unit.

### 5.3.2 Braking energy

Modern driveline designs, like hydrostatic transmissions, or CVT are able to transmit the braking energy from the drive wheels back to the diesel engine. The braking capacity of modern diesel engines is limited, and the braking energy cannot be stored.

With the proposed system the braking energy from the driveline can be stored to the accumulator.

The braking force and power can be controlled by the displacement control of the pump/motor unit.

One big advantage of the braking energy storing system is that the wear and the heating of the vehicle brakes can be reduced.

### 5.3.3 Energy storing from the hydraulic system

If the hydraulic system is capable to return pressurized flow from the working hydraulic system, the returning oil flow from the main valve block can be restored to the accumulator.

### 5.4 Re-use of stored energy

Stored energy can be used for the working hydraulics.

The pressure level of the hydraulic system is controller with the Load Sensing pressure. With the displacement control of the pump/motor unit the amount of oil that is taken from the accumulator or from the LS-pump can be controlled.

The flow from the accumulator is used via the pump/motor unit to the main hydraulic system.

The motor/pump unit transforms the pressure between system and accumulator pressure. When the pressure in the system is higher, than that in the accumulator the closed loop unit works as pump and takes the needed extra power from the engine. When the system pressure is lower, than the one in the accumulator the closed loop unit works as motor and releases energy to the engine, driveline or auxiliary devices.

The whole accumulator capacity can then be utilized.

Figure 16 shows the usability of the stored energy of a 50 liter accumulator, with a total energy storage capacity of 350 kJ.

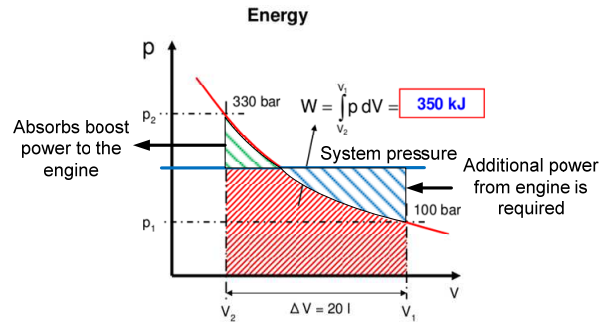


Figure 16: Energy usability in the proposed hydraulic hybrid system

If the LS-pump is a unit that can work as a motor (mooring unit) the stored energy can be used for boosting the drive line or for auxiliary units.

### 5.5 Power losses and efficiency

The power losses of the proposed system can be defined as follows:

$$P_l = P_{idle(p,n)} + Q(p_s - p_a), \quad (5)$$

where:

$P_l$  is power loss

$P_{idle(p,n)}$  is constant power loss, depending of the pressure and rotation speed.

$Q$  is flow to (or from) the accumulator,

$p_s$  is system pressure and

$p_a$  is accumulator pressure.

The main power loss:

$$Q(p_s - p_a),$$

depends only on the flow, which is stored or taken out of the accumulator and the pressure difference between accumulator and system pressure.

This offers a remarkable advantage compared with traditional serial or parallel hybrid systems.

### 5.6 Benefits

The size of the engine can be reduced, because it only needs to deliver the average power, not the max peak power during the working cycle.

The hydraulic system can be designed as a normal Load Sensing system, where the main pump pressure is controlled by the LS pressure.

The flow from the accumulator is used via the pump/motor unit to the hydraulic system. The LS pump size can then be chosen smaller or the working speed of the machine can be increased.

The motor/pump unit controls the flow rate that is stored or taken out from the accumulator.

The main advantages of the system are listed as follows:

- Simple system design
- Universally usable for restoring energy
- No pressure losses, as in a valve controlled system
- Min. energy transformation losses
- Flow from the accumulator can be directly used for the working hydraulics:
- Smaller main pump can be used
- Reduced tank flow: smaller tank can be used
- The accumulator energy storing capacity can be used on a wide pressure variation range and the full energy storage capacity of the accumulator can be used.

## 6 Outlook and conclusions

Hydraulic hybrid is a good alternative to improve total efficiency and to reduce the size of the engine in a mobile working machine.

In the design of hybrid systems, it is important to reduce energy transforming losses to the minimum.

The proposed new hydraulic hybrid system can fulfill all requirements regarding energy storing from different restorable sources. It is also capable to use the full accumulator capacity. And can minimize energy transformation losses.

The novel system design has only been shown on a principle level. For real system some kind of power management system is needed to control the charging and the discharging functions.

## References

- [1] Erkkilä M, Model-Based Design of Power-Split Drivelines, *Dissertation*, September 2009 Tampere Finland
- [2] Bauer, F., Feld, D. Warum hydraulische Hybridsysteme? *Het Hydrauliek Symposium, Delft*, 87-104, 2010
- [3] Thiebes, P., Geimer, M., Energy storage devices for industrial vehicles with hybrid drive trainsQuelle: 1. VDI Fachkonferenz: "Getriebe in

*mobilen Arbeitsmaschinen"* 07./08. Juni 2011 in Friedrichshafen

- [4] Boehm, D. , Holländer, C., Landman, T., Hybrid-Antriebe bei Raubenbaggern - Konzepte und Lösungen, *Hybridantriebe für Arbeitsmaschinen, Karlsruher Schriftenreihe Fahrzeugsystemtechnik*, 7:117-124, 2011.
- [5] Sahlman, M., Valve controlled multi-chamber cylinder, *Master's theses Tampere University of Technology*, 2012
- [6] Prinz zu Hohenlohe, F., Phlegmatisierung als Tugend in der Mobilhydraulik - Das Energiespeichersystem des Kranvollernters HSM 405H2, *Hybridantriebe für mobile Arbeitsmaschinen, Karlsruher Schriftenreihe Fahrzeugsystemtechnik*, 7:151-163, 2011
- [7] [http://www.ccefp.org/sites/all/files/documents/Info\\_1A.2\\_MultiActuator\\_Hybrid.pdf](http://www.ccefp.org/sites/all/files/documents/Info_1A.2_MultiActuator_Hybrid.pdf) Downloaded 8.4.2013

## **Modeling and verification of an excavator system – Axial Piston Pump, Kinematics and Load Sensing Flow Sharing Valve Block**

Professor Dr.-Ing. Paolo Casoli, Dr.-Ing. Luca Riccò, Dr.-Ing. Dolcin Cesare\*

Industrial Engineering Department, University of Parma (Italy)

\*Walvoil S.p.A., Reggio Emilia (Italy)

E-mail: paolo.casoli@unipr.it

### **Abstract**

This paper presents the results of a study focused on mathematical modeling of an excavator hydraulic system, composed by: the pump gray box model, the kinematics model and the valve white box model. The kinematics model has been realized using the planar mechanical library of AMESim<sup>®</sup> and is composed by the front excavation tool: the arm, the boom and the bucket. The valve section white box model has been validate with the comparison between the numerical and experimental result obtained during the laboratory tests. The excavator is equipped by a full flow sharing valve, that is very useful in this kind of machinery when during a digging cycle all the valve sections are used at the same time. In this paper the excavator mathematical model system will be composed by the pump, the kinematics and two valve sections. The new system will be validated with the comparison between the experimental results, obtained with two sections working at the same time, and the numerical results provided by the simulation. The experimental results will be obtained in two different working conditions: standard operation condition and flow saturation condition. This will show the mathematical model capability in the study of the interaction between all the system components and could be useful in the study of alternative control strategies towards energy efficient systems and new control system designs.

**Keywords:** Hydraulic Excavator, Load Sensing, Mathematical Model, Energy Saving.

### **1 Introduction**

In the last years, the simulation of the kinematics and dynamics of multi-body systems is a topic of increasing importance in many industrial branches, due to its potential for providing insight into inherent effects governing the systems' behavior and for reducing manufacturing costs. Furthermore with the continuous petrol price rising the higher interest in energy saving is rising as well. Lots of researchers have been studying for years these topics.

Focusing on mobile machineries, one of the primary needs is that of consume the less energy possible to complete a working cycle, like a standard digging cycle[1]. In other words one of the principal target being that of achieving more efficient machinery. Due to this, one of the first goals for machinery producers

is the energy saving toward the optimization of their products, the system components interaction, and also with the introduction of energy recovery systems. Study such a complex system (like an excavator) require time, know-how and lot of money. Thus mathematical models are always more used.

Typically, mobile machineries hydraulic system are composed by a variable displacement axial piston pump [2] and proportional directional valves [3]. The hydraulic system controls the kinematics movements, under user needs.

An excavator system is a very complex nonlinear plant, and for this reason a suitable mathematical model is needed as well as a good simulation tool.

Many qualities are required from mathematical models, including accuracy, predictability for the simulated

system behaviors (stationary and transient) as well as low computation time.

The research reported in this paper describes the mathematical model, for a middle size excavator, that is under developing using AMESim<sup>®</sup> modeling environment. The mathematical model has been developed to be as simple as possible while ensuring the original elements functions.

The following sections present the modeling of the pump, the flow sharing valve, the excavator kinematics and validated results of the pump model and valve models.

## 2 Physical Modeling

As already described in the introduction, the most important qualities required from a mathematical model of complex systems are: result accuracy, predictable of transient and stationary behaviors and at last but not least short calculation time.

Certainly in the individual components optimization study the first two characteristics play a predominant role, but in the complete system study, focused on the interaction between all the components, such as the pump, the valve and the kinematics a short computational time becomes very important.

Taking this into account, the mathematical model under development, has the skill of a short calculation time while maintaining a satisfactory accuracy and behaviors predictability.

The mathematical model is composed by: the pump graybox model, the kinematics model and the valve white box model.

### 2.1 Pump Model

The pump, mounted on the excavator, is a load sensing variable displacement axial piston pump [2] developed by Casappa<sup>®</sup> S.p.A. and belongs to the MVP series.

Its mathematical model has been validated, at steady state conditions, with the comparison between experimental and numerical results in previous work [4]. The validation of the model in transient condition is in progress. The pump mathematical model, depicted in fig.1, has been defined gray box because it is composed by the combination of white box model for its regulators, such as the pressure compensator (PC) and the flow compensator (FC), and the black box model of the pump's flow characteristic.

### 2.2 Kinematics Model

The kinematics model, shown in fig.2, is composed by the front excavation tool only: arm, boom and bucket.

The kinematics model is used to create realistic forces on the hydraulic actuators.

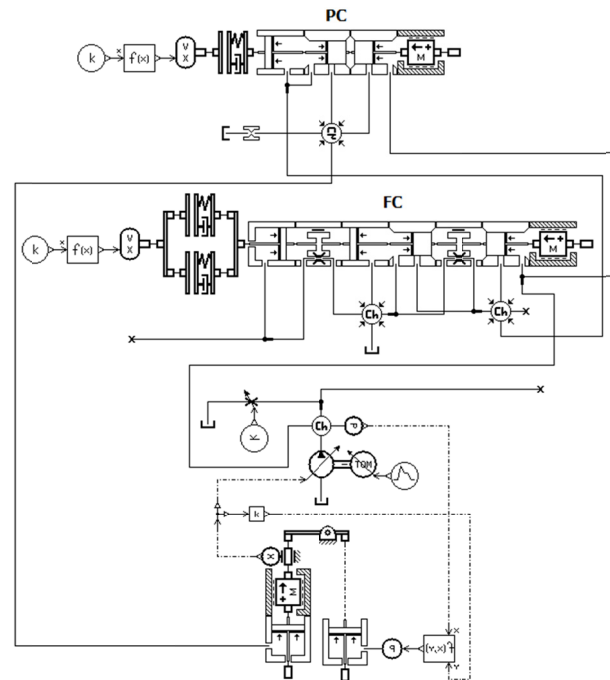


Figure 1: AMESim<sup>®</sup> Pump Mathematical Model

Considering the benefits of having the kinematic model integral with the hydraulic model, the linkage parameters were coupled to the hydraulic model using the Planar Mechanics library of AMESim<sup>®</sup> [5]. This facilitates the understanding of dynamic loads on the hydraulic cylinder. The driving joint torques of the boom, arm and bucket are generated by the forces of the hydraulic ram actuators. The equations of motion can be derived by applying the Euler-Lagrange equations to a Lagrangian energy function. The revolute pairs have been modeled as Lagrange multipliers and are calculated from the Baumgarte stabilization method applied to the constraint equations [6]. The model is not yet set to simulate the forces acting on the bucket during the interaction with the soil [7].

### 2.3 Valve Section Model

The valve section is a full flow sharing valve by Walvoil<sup>®</sup> S.p.a. and belongs to the DPX series.

Its mathematical model has been validated in [8], considering only one section working, with the comparison between the simulation and experimental results obtained during laboratory tests.

In a mobile machinery, such an excavator under study, the use of this kind of valve is very useful because during a standard digging cycle [1] are almost used all the valve sections at the same time. When this situation occur, the pump could work in flow saturation

condition, i.e. the pump flow is less than the flow required by the valve block.

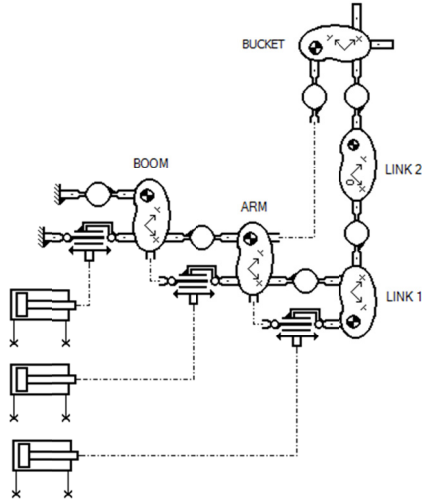


Figure 2: AMESim® Kinematics Mathematical Model

If this situation occur, the operator can lose the direct control on the moving parts, that could be very dangerous, but with this kind of valve the operator still maintains the control on the parts movements losing the control on their movements velocity only.

The principal working condition of a valve section, keeping in mind that the complete valve could be composed by lots of sections (defined valve block), is that of define the outlet flow through the section to its actuator, maintain the pressure drop constant between the main spool metering area, define the LS pressure and provide the flow sharing operation condition when needed. It's easy understandable that a simple mathematical model for the valve cannot be able to recreate all of this functioning conditions.

For this reason the valve mathematical model has been developed not like a simple valve, but like a demi complex valve, the AMESim® sketch is reported in fig.3, able to recreate the working functioning of the real valve. This has increased the simulation time if compare by an ideal valve model but has allowed to retain all the original working conditions, of the real valve section. This is the plus of this kind of mathematical model, able to recreate the interaction of all the valve sections.

## 2.4 Governing Equations

The governing equations are described by the interaction between a fluid-dynamic model (FDM) and a mechanical-geometrical model (MGM). The FDM calculates the pressures inside the chambers and the flow rate between adjacent chambers, while the MGM

calculates the forces acting on the spool and determines its dynamics and the flow areas.

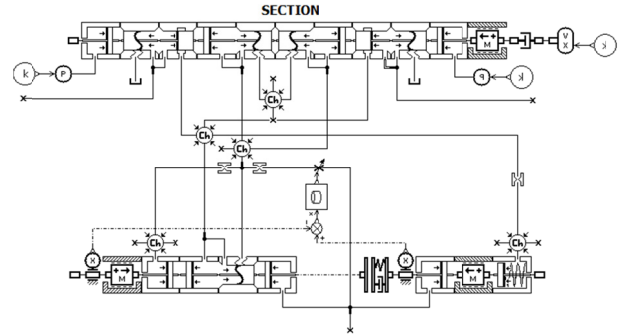


Figure 3: AMESim® Valve Section Mathematical Model

The FDM is based on a lumped parameter framework. The pressure inside each control volume is assumed uniform and time dependent, and is determined by the pressure-rise rate equation:

$$\frac{dp_i}{dt} = \frac{\beta}{\rho_i} \frac{1}{V_i(x)} \left( \sum \dot{m} - \rho_i \frac{dV_i(x)}{dt} \right) \quad (1)$$

The model assumes a constant value of fluid temperature. The fluid density is evaluated as a function of pressure as described in [9]. The summation term represents the net mass flow rate entering or leaving the volume. This is obtained by considering the contribution of all orifices connected with the considered volume. The mass exchange occurring through the orifices is calculated using the generalized Bernoulli's equation under quasi-steady conditions, Eq. (2):

$$\dot{m} = \rho C_d A(x) \sqrt{\frac{2 |\Delta p|}{\rho}} \quad (2)$$

The user sets an appropriate saturated value for the coefficient of discharge of each connection, on the basis of experimental data or using values reported in literature, such as [10]; thereafter the instantaneous coefficient of discharge value is evaluated as a function of Reynolds number, to account for partially developed or fully turbulent conditions. The mechanical model calculates the instantaneous position and velocity of the spool using Newton's second law.

The forces acting on the spool are: hydrostatic forces, spring force, friction forces, hydrodynamic forces. Static and dynamic friction forces are evaluated by use of the Karnopp friction model and considering the Stribeck effect; static and dynamic friction coefficients are assumed constant; in this simplified version of the model the hydrodynamic forces are neglected.

### 3 Experimental Setup

Figure 4 represents the ISO schematic of the test bench setup that has been used to verify the valve block functioning as a double sections. In table 1 are reported the features of the used sensors.

Sensor	Type	Main features
M	Prime mover	ABB <sup>®</sup> , 4-quadrant electric motor, 75 kW
P	Pump	CASAPPA <sup>®</sup> MVP60, 84 cm <sup>3</sup> /r
P1 – P8	Strain gage	Trafag <sup>®</sup> , Scale 0..400 bar, 0.3% FS accuracy
Q1 – Q2	Flow meter	VSE <sup>®</sup> VS1, Scale 0.05..80 l/min, 0.3% measured value accuracy
T	Torque/speed meter	HBM <sup>®</sup> T, Scale: 0..500 Nm, 0.05 Accuracy Class
Θ	Incremental encoder	HEIDENHAIN <sup>®</sup> ERN120, 3600 imp./r, 4000 r/min Limit velocity, 1/20 period accuracy
LVDT	Linear variable differential transducer	Magnet Schuz AVAX 015

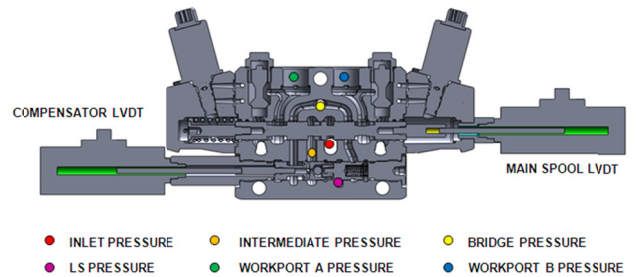
**Table 1:** Features of sensors and main elements of the apparatus used in the present research

The tests were carried out using the valve block, composed by two valve sections coupled with the variable displacement pump.

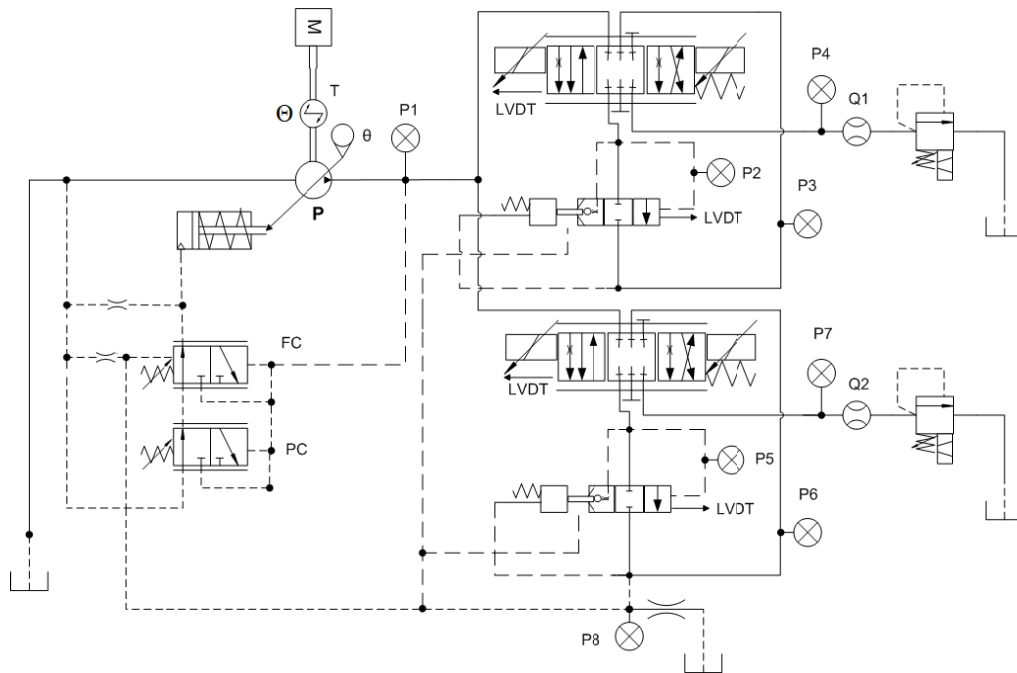
The pump has been instrumented by an angular sensor directly connected with the swash plate.

Figure 5 illustrates the cross section of the valve along with the pressure mapping points and the mounting positions of the two LVDT's connected to the main spool and the pressure compensator.

Figure 6 show the test bench picture before starting the experimental test.



**Figure 5:** Valve with LVDT mounted and Pressure Mapping Points



**Figure 4:** Test setup for Load Sensing Flow Sharing Valve Block

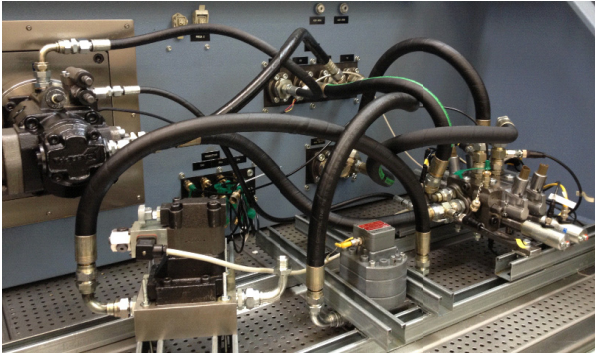


Figure 6: Test Bench Layout

### 3.1 Experimental Setting condition

As mentioned before, two different type of tests were carried out:

- Double pressure compensation, without flow saturation;
- Double pressure compensation, with flow saturation.

The first operating condition has been performed in standard condition, i.e. without flow saturation, defined as double pressure compensation, where the section 1 has a constant load and the section 2 has a variable load. The two loads pressure are display in fig.7.

The pump speed has been set at 1500 rpm and the main spools opening position has been reported in fig.8. The pump margin has been set at 20 bar and the oil temperature at 50 °C.

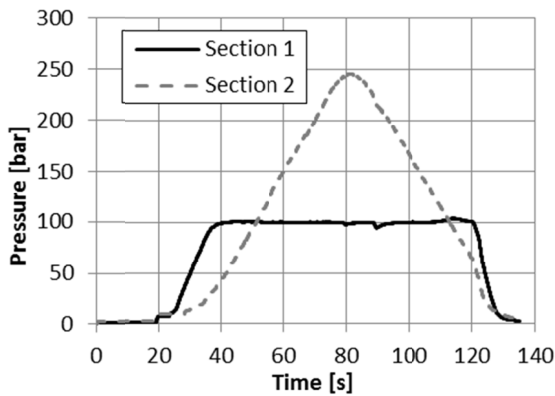


Figure 7: Sections Imposed Loads

The second operation condition has been performed in flow saturation, i.e. the required flow rate by the circuit is higher than the pump's outlet flow. The two sections load are represented in fig.9, the pump speed has been set at 1000 rpm and the opening position law for the two main spools are depicted in fig.10. The pump margin has been set at 15 bar and the oil temperature maintained constant at 50 °C.

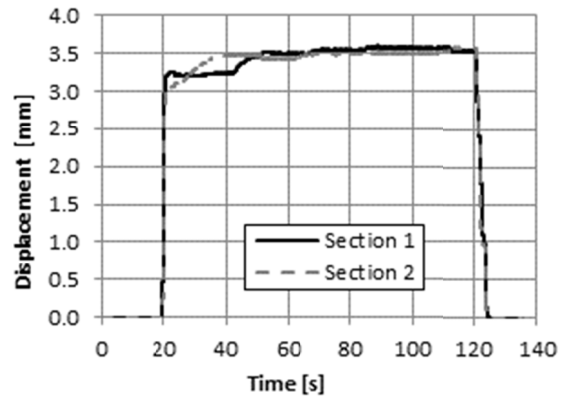


Figure 8: Main Spools Displacement

The transient pressure peaks, visible in fig. 9, are due to the test bench pressure proportional relief valve feedback control system setting. The transient does not introduce problem, rather if the mathematical model is able recreate this actual condition, will be very useful to prove the model accuracy.

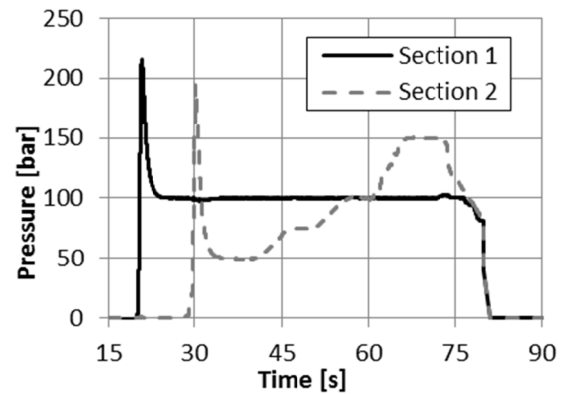


Figure 9: Sections Imposed Load

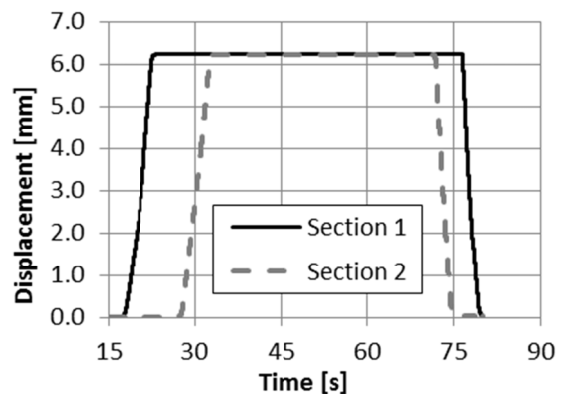


Figure 10: Main Spools Displacement

## 4 Comparison between experimental and simulation result

Figure 11 depicts the AMESim<sup>®</sup> sketch of the system comprising of the pump and valve used to recreate the layout mounted on the test bench, as shown in fig.4.

### 4.1 Double pressure compensation, no flow saturation

In this paragraph are compared the numerical and experimental result obtained during the first type of test.

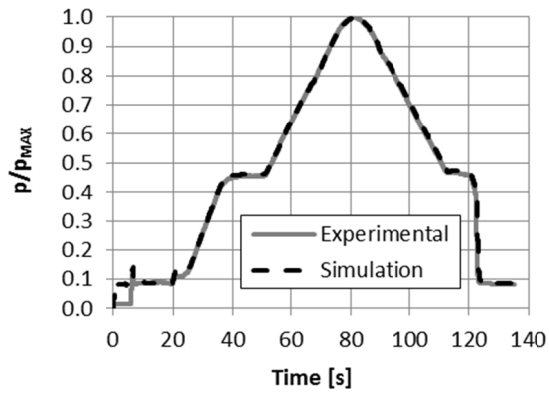


Figure 12: Inlet Pressure

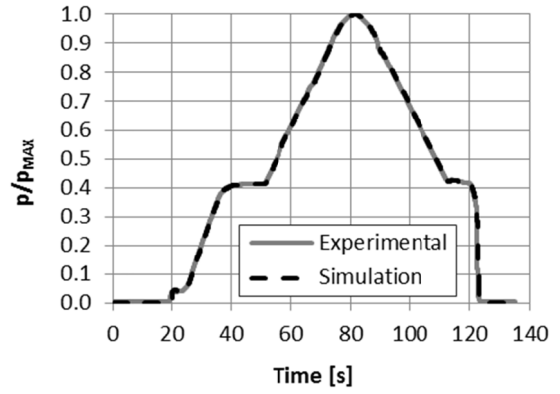


Figure 13: Load Sensing Pressure

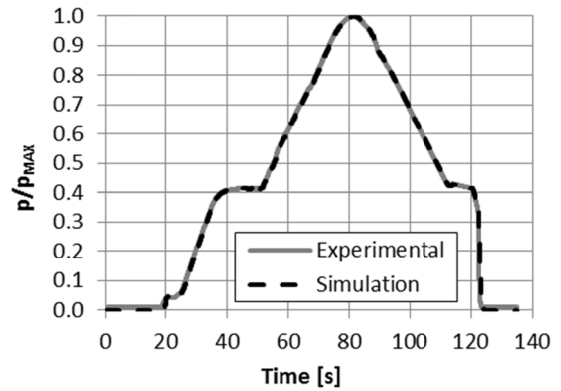


Figure 14: Intermediate Pressure Section 1

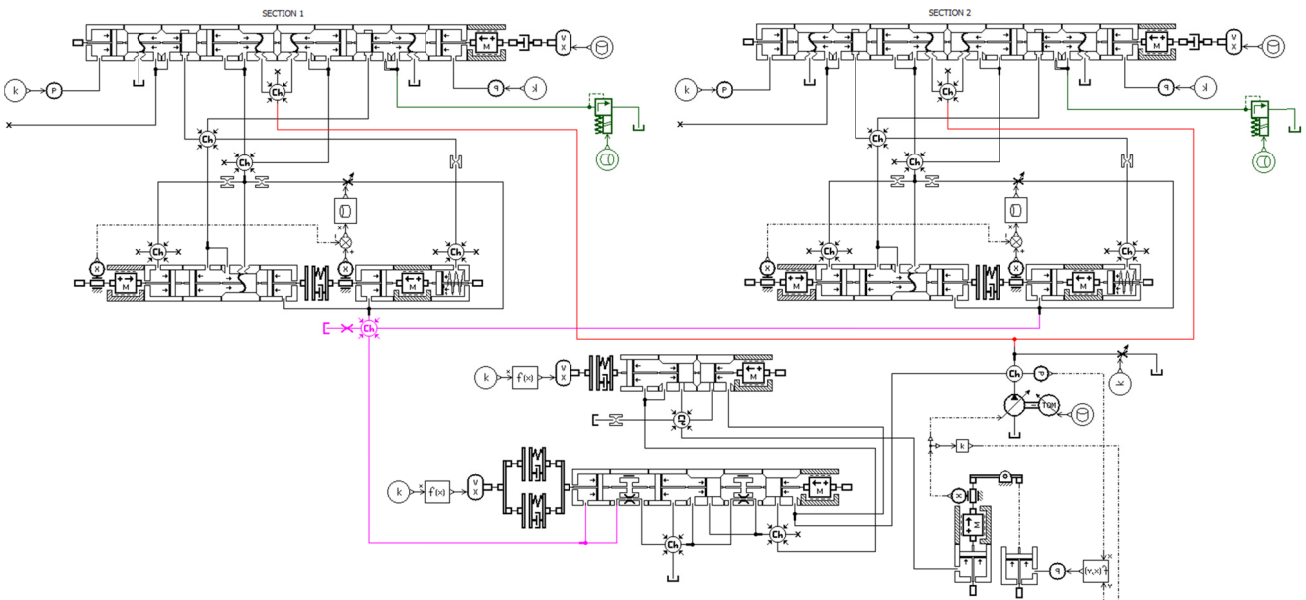


Figure 11: Test setup for Load Sensing Flow Sharing Valve Block

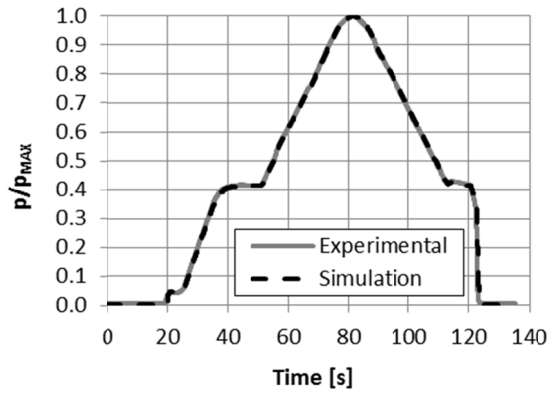


Figure 15: Intermediate Pressure Section 2

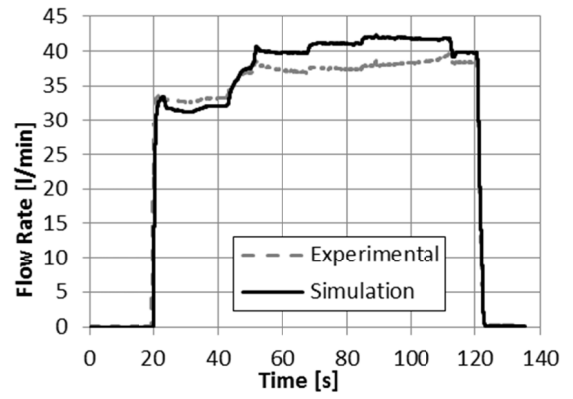


Figure 18: Outlet Flow Rate Section 1

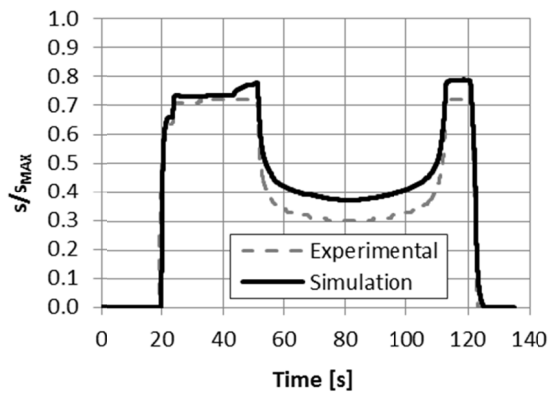


Figure 16: Compensator Displacement Section 1

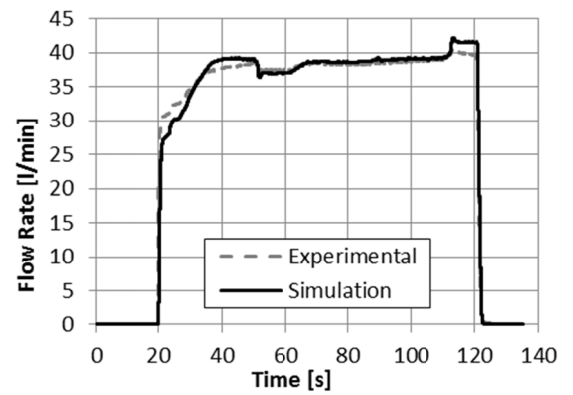


Figure 19: Outlet Flow Rate Section 2

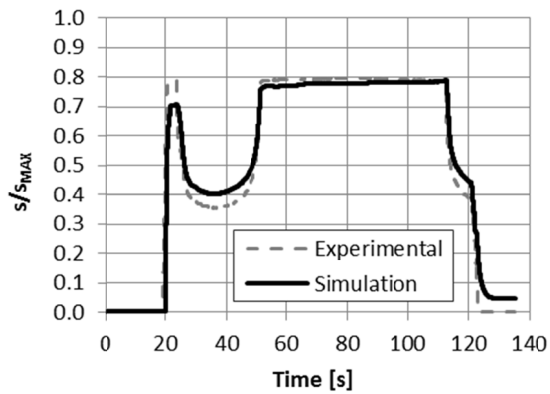


Figure 17: Compensator Displacement Section 2

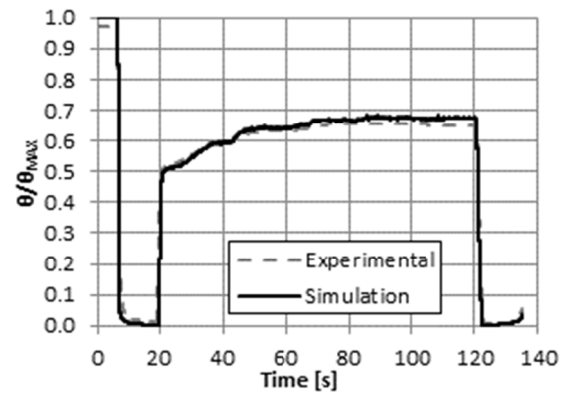


Figure 20: Pump Swash Plate Position

Figures 12, 13 show the comparison of the inlet and the load sensing pressure. This two pressures are common for all the valve sections.

Figure 14, 15 refer to section 1 and 2 intermediate pressures (see fig. 5). The comparison between section 1 and 2 pressure compensators displacement are showed in figures 16 and 17.

Figures 18, 19 depict the comparison between the experimental and simulation outlet flow rates from section 1 and the section 2.

As can be seen the model has the capability to recreate all the pressures inside the chambers with errors under 2% if compare with the experimental data; further the mathematical model is able to recreate the outlet flow rates with a maximum error among 10%, acceptable for a simplified model.

It's possible to observe that the model has also a good capability to calculate the actual compensators position.

Figure 20 reports the pump swash plate position, where the simulation data match the experimental position accurately.

#### 4.2 Double pressure compensation, with flow saturation

In this paragraph are compared the numerical and experimental result obtained during the second type of test. Figures 21 – 24 show the pressure inside the chambers in the valve block: the inlet and LS pressure, common for the valve block and the intermediate pressures. Figures 26, 27 show the sections outlet flow rates comparison. When the flow saturation occur, between 30s and 70s, the outlet flow rate from section 1 decreases until the section 2 main spool remains open.

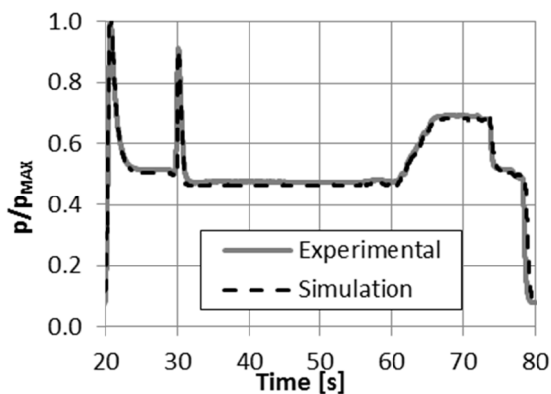


Figure 21: Inlet Pressure

Figure 25 depicts the displacement of the section 2, unfortunately is not possible compare it with the section 1 pressure compensator position due to the LVDT absence when this test has been carried out. As already seen in the double pressure compensation test without flow saturation condition, the model of the valve section has the capability to perform good result

for the two working conditions. The outlet flow rates and the pressure compensator position are recreated in an acceptable way by the model and the pressures match the experimental one satisfactorily.

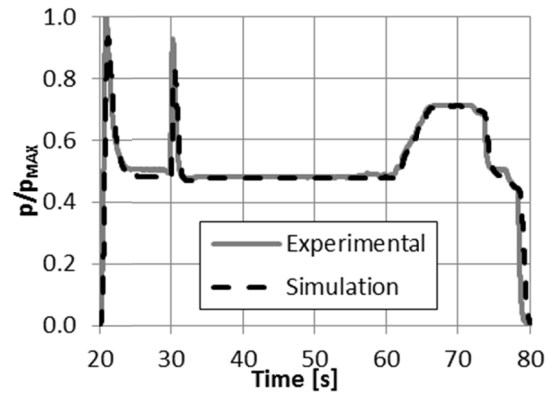


Figure 22: Load Sensing Pressure

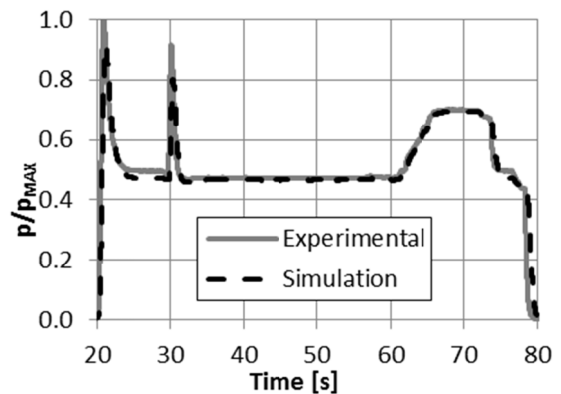


Figure 23: Intermediate Pressure Section 1

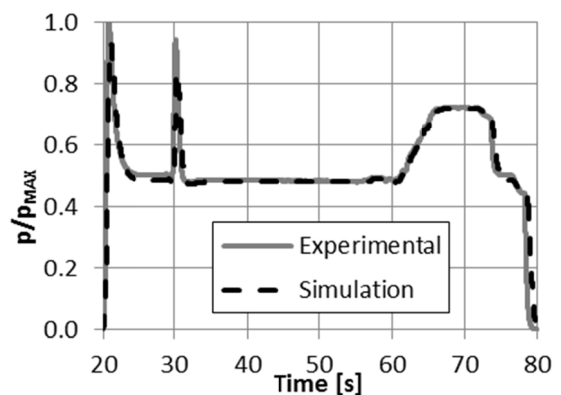


Figure 24: Intermediate Pressure Section 2

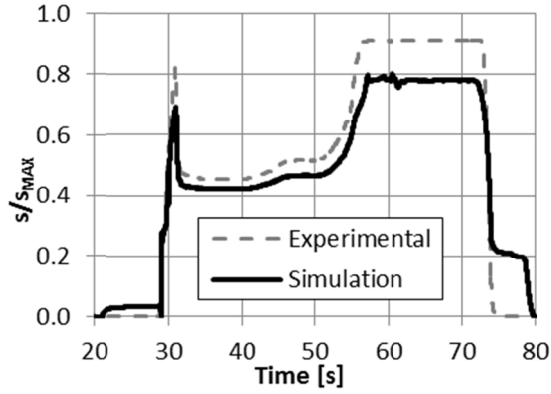


Figure 25: Compensator Displacement Section 2

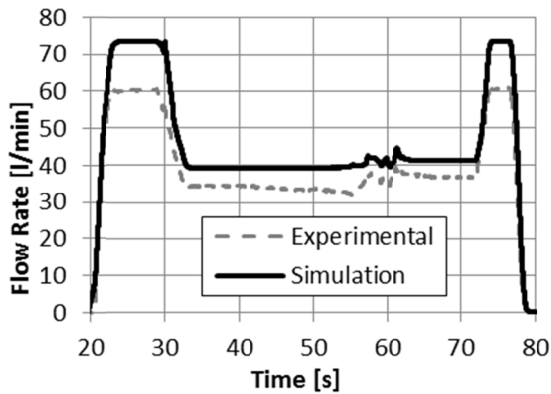


Figure 26: Outlet Flow rate Section 1

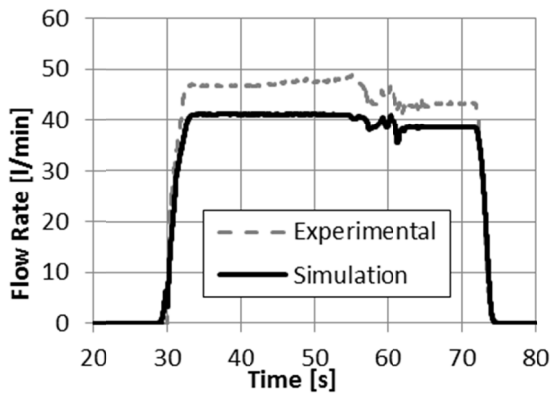


Figure 27: Outlet Flow rate Section 2

## 5 Excavator Model and cycle simulation

The excavator under study is a middle size one and is depicted in fig 28. Its operating weight is 9500 kg and the engine power is 46.5 kW at 2200 rpm.



Figure 28: Photograph of the excavator

Based on the analysis of results presented in the previous section, it is evident that the pump and valve models are capable of reproducing actual conditions. Thus to widen the model capabilities the kinematics has been included as illustrated in fig 34.

The complete system was subjected to a duty cycle as described in fig 29. The pump speed has been set at 1500 rpm. Figure 30 shows the simulated system and LS pressures. The sections inlet flow rates are depicted in fig 31. Figure 32 reports the section compensators position during the cycle and it's possible observe the model capability to recreate the compensating mode. Figure 33 depicts the pump swash plate position. The figures in this section provides to the system developers an insight into the internal functioning of the pump and the valve. These information are needful for studying new control strategies or proposing improvements in the design of these components.

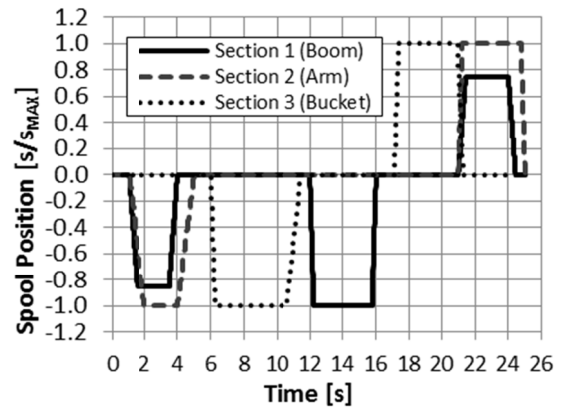


Figure 29: Valve section spools position

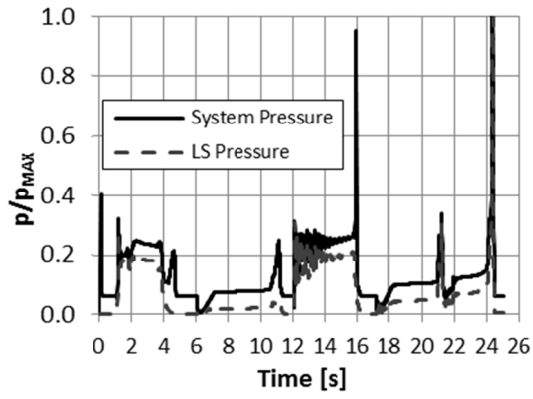


Figure 30: System and Load Sensing pressure

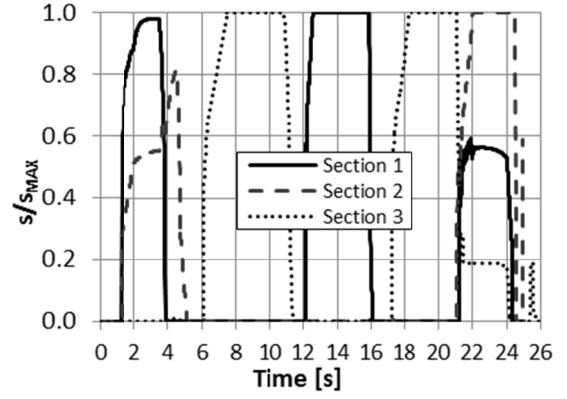


Figure 32: Sections compensator displacement

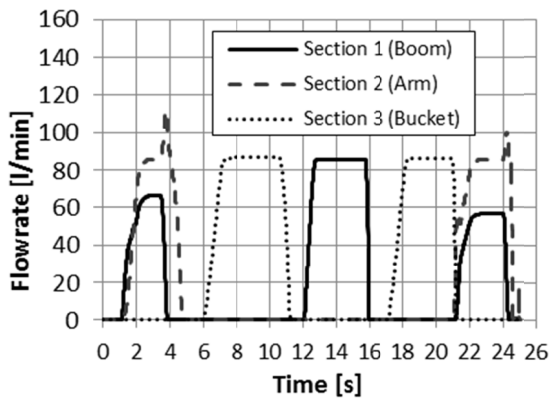


Figure 31: Sections inlet flow rate

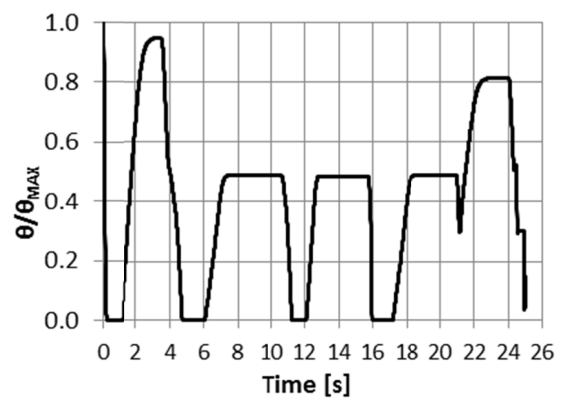


Figure 33: Pump swash plate position

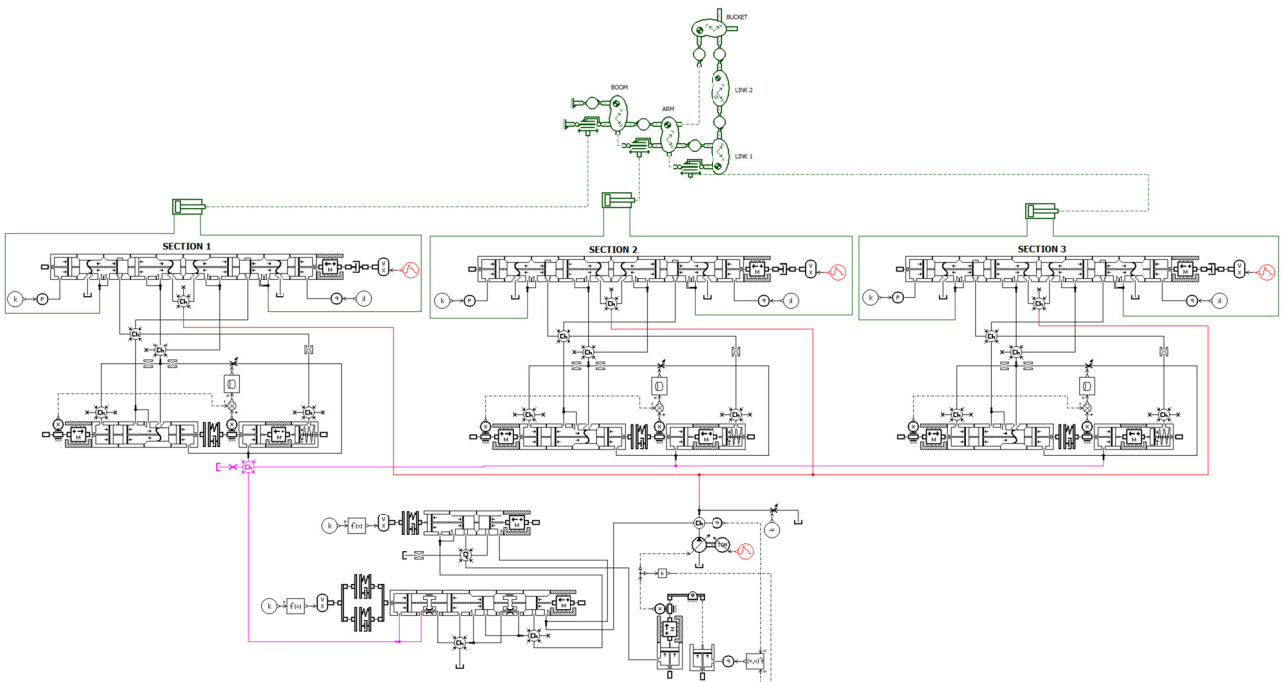


Figure 34: AMESim<sup>®</sup> sketch of the front excavator tool and hydraulic circuit.

## 6 Conclusion

This paper has presented the analysis of an excavator system. A nonlinear mathematical model of an excavator has been developed using the AMESim<sup>®</sup> modeling environment to replicate real operating conditions. The model is described by hydraulic model comprising of a load sensing pump, a flow sharing valve model and a 2D kinematic model to simulate the excavator front excavation tool. This approach has enabled the study of the dynamic behavior and interaction of the pump and valve with a completely developed kinematic model of the excavator. The detailed hydraulic model described regard a load sensing flow sharing valve block, composed by two valve sections model working at the same time. The mathematical model of the valve has been validated against experimental results in different conditions: standard operating without flow saturation and flow sharing condition, i.e. with flow saturation. The pump and valve models and their verification, as represented in this paper, offer a great deal of confidence in the individual models capabilities of recreating the functioning of an excavator. The last section of the paper provides an overall view of the hydraulic model capability coupled with the kinematics of the system, with the simulation of an arm-bucket movement. The results presented show the paramount of advantages that this model possess in aiding a pump and valve designers in analyzing/assessing the behavior of the components as a part of a complex system. The mathematical model of the excavator could be useful in future study of both new control system and new energy saving solutions.

## Acknowledgments

The authors would like to acknowledge the active support of this research by Casappa S.p.A., and Walvoil S.p.A (ITALY).

## Nomenclature

$A$	flow area	[m <sup>2</sup> ]
$C_d$	discharge coefficient	-
$i$	volume index	-
$\dot{m}$	mass flow rate	[kg/s]
$p$	pressure	[bar]
$V$	volume	[m <sup>3</sup> ]
$t$	time	[s]

## Greek Letters

$\beta$	bulk modulus	[Pa]
---------	--------------	------

$\rho$	density	[kg/m <sup>3</sup> ]
<b>Acronyms</b>		
FC	Flow compensator	
PC	Pressure compensator	
PS	System Pressure	
PLS	Load Sensed Pressure	

## References

- [1] JCMAS H 020 – Earth Moving machinery – Test methods for energy consumption – Hydraulic excavators, 2010.
- [2] J Ivantysyn , M Ivantysynova. Hydrostatic Pumps and Motors, Tech Books International, New Delhi,2003, India. ISBN 81-88305-08-
- [3] Blakburn J. F., Reethof G. & Shearer J. L. (1966) “Fluid Power Control”. USA: MIT Press, 1966. ISBN 0262520044
- [4] P. Casoli, A. Anthony (2013) “Gray box modeling of an excavator’s variable displacement hydraulic pump for fast simulation of excavation cycles” *Control Engineering Practice* 21 (2013) pp.483-494. Elsevier Ltd. <http://dx.doi.org/10.1016/j.conengprac.2012.11.011>
- [5] LMS Imagine – AMESim<sup>®</sup> Reference manual 2011
- [6] Shih-Tin Lin, Jiann-Nan Huang. (2002) .Stabilization of Baumgarte’s Method Using the Runge-Kutta Approach. In *ASME Journal of Mechanical Design*, vol. 124, n.4, pp. 633-641. December 2002.
- [7] Grzesikiewicz, W. (1998). Dynamics of a ground digging tool. XI scientific Conference Problems of Work Machines, konferencja Naukowa Problem Maszyn Roboczych) Polska: Zakopane, 1998.
- [8] P. Casoli, A. Anthony, L. Riccò (2012) “Modeling of an Excavator System – Load sensing flow sharing valve model” SAE 2012 Commercial Vehicle Engineering Congress, Rosemont, Illinois, USA, 13-14 September 2012. doi:10.4271/2012-01-2042H
- [9] E Merritt. *Hydraulic Control Systems*. John Wileys and Sons, Cincinnati, Ohio, 1967. ISBN 0-471-59617-5.
- [10] McCloy, D., Martin, H. M. (1973). “The control of Fluid Power”, Longman, London, 1973.



## New PTFE-based Material for Hydraulic Seal Applications

T. Larsen<sup>1</sup>, S. Roepstorff<sup>2</sup>, and H. Jordan<sup>3</sup>

<sup>1,2</sup>Trelleborg Sealing Solutions, R&D, Helsingør, Denmark

E-mail: [thomas.larsen@trelleborg.com](mailto:thomas.larsen@trelleborg.com), [soeren.roepstorff@trelleborg.com](mailto:soeren.roepstorff@trelleborg.com), [holger.jordan@trelleborg.com](mailto:holger.jordan@trelleborg.com)

<sup>3</sup>Trelleborg Sealing Solutions, R&D, Stuttgart, Germany

### Abstract

PTFE-based materials are widely applied for seals and are chemically compatible with almost all media and tolerate a wide temperature range. The weaknesses of virgin PTFE are the wear and deformational properties, which however can be improved significantly by incorporating suitable fillers. A range of PTFE-based seal materials exists on the market today, each with their strengths and short-comings. The idea of a universally applicable seal material is probably unrealistic. However, this paper reports the outcome of a project aimed at developing a new PTFE-based material (Turcon<sup>®</sup> M12), which covers a significantly wider range of applications compared to existing PTFE materials. Shown results compare this new material with traditional PTFE seal materials using different types of hydraulic test-rigs, operating conditions and media. The results show that the new PTFE material matches the good extrusion, wear and deformational properties of PTFE/Bronze while being able to cope with conditions of starved lubrication without damaging the counter surface.

**Keywords:** hydraulic seals, PTFE materials, test-benches, friction, wear, abrasiveness

### 1 Introduction

PTFE-based materials as a group are a well known standard for seal materials, which are applied in various hydraulic equipment [1-2]. PTFE is superior with respect to chemical and thermal resistance as well as low friction. Thus, PTFE is chemically compatible with almost all media and can operate in a wide temperature range [3]. The weaknesses of virgin PTFE are the wear and deformational properties. However, these properties can be improved dramatically by incorporating suitable fillers, which makes it possible to develop PTFE-based sealing materials with overall excellent properties.

Glass and bronze are widely applied as fillers for PTFE under well-lubricated conditions. PTFE/Glass fiber materials have high seal efficiency but moderate extrusion strength, and require a hard counter surface in order to avoid hardware damage due to the abrasiveness of glass fibers. PTFE/Bronze materials combine high extrusion resistance, high wear resistance and high seal efficiency, but in critical applications scratches can in principle be created in two different ways: 1) bronze is a relatively soft material but in demanding applications, a high contact temperature may lead to tribo-oxidation generating hard abrasive particles (sulphides and oxides) and 2) bronze particles may offer a good substrate for hard particles to attach to thereby increasing their grinding action.

Carbon/graphite particles and carbon fibers are widely applied fillers for PTFE under poorly lubricated conditions.

Carbon/graphite is mild against the counter surface, and depending on the specific filler type, a good extrusion resistance can be achieved. However, Carbon/graphite tends to suffer from a low wear resistance. PTFE/Carbon fiber materials typically have a good wear resistance but a lower extrusion resistance relative to PTFE/Bronze. PTFE/Carbon fibers maintain a porous surface in service, giving good lubrication of the contact area but also somewhat reduced seal efficiency.

In short, the typical fillers mentioned above all have their specific strengths and short-comings. Why, one might ask, should a new PTFE-based material be introduced to the market when a line of materials are available, which covers a wide range of applications? The answer: One sealing material, which combines the specific advantages of several existing materials, can bring a range of substantial advantages.

The task presented to R&D was to develop a PTFE-based material for linear seals and scrapers, that would combine high seal efficiency with low friction, low wear on seal and hardware, as well as high extrusion resistance. On top of this it should not contain bronze, and be price-wise competitive. Needless to say this was no easy task, and it took years of analysis, testing and evaluation to develop the final candidate for field testing.

This paper shows several seal test results obtained with this new material Turcon<sup>®</sup> M12. The results are obtained using different types of test-rigs, which makes it possible to compare the performance with traditional seal materials

based on the following parameters: friction, wear, deformation, extrusion, seal ability and hardware damage under well-lubricated and poorly lubricated conditions, respectively.

## 2 Experimental

Turcon<sup>®</sup> M12 consists of a complex blend of reinforcing, wear-reducing and non-abrasive mineral fibers together with friction reducing additives. The nature of the fillers, the particle distribution of the applied fillers and the final composition are carefully adjusted with the aim of obtaining the best balance between properties such as wear resistance, extrusion strength, seal efficiency, low friction, low abrasiveness and fatigue resistance. Specific fillers are typically capable of improving certain of the mentioned properties but at the expense of others. The same also applies to particle distributions and the degree of filling. Thus, the challenge has been to find a balance between these adjustable parameters in order to obtain the best overall performance.

Turcon<sup>®</sup> M12 is compared with traditional PTFE-based seal materials, which are shown in the table 1.

Table 1: traditional seal materials included for reference

Material	Degree of filling	Abbreviations
PTFE added pigment	Very low	PTFE/pigment
PTFE filled with carbon fibers	Medium	PTFE/CF
PTFE filled with glass fibers	Medium	PTFE/GF
PTFE filled with bronze	Medium	PTFE/bronze
PTFE filled with carbon particles	High	PTFE/carbon

The data presented in this paper are obtained using four different test-rigs, which will be briefly introduced in the following.

### 2.1 Standard Rod-Seal Test

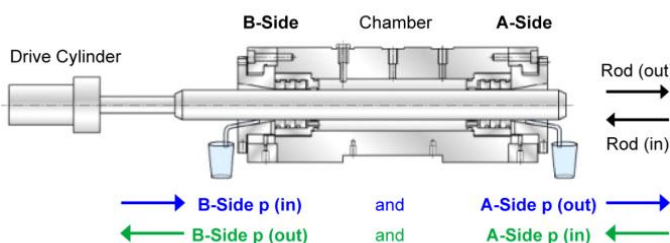


Figure 1: illustration of the applied Rod-Seal Test-Rig

Table 2: parameters applied for the standard rod-seal testing. Note, the A-side works as a rod seal normally operates

Test parameters:	
Pressure cycle (A-side)	: p (out) = < 0.5 MPa p (in) = 30MPa
Pressure cycle (B-side)	: p (out) = 30 MPa p (in) = < 0.5 MPa
Stroke length	: 280 mm
Velocity	: 0.20 m/s
Rod	: $\phi$ 50 mm hard chrome plated
Medium no. 1	: HV 46, Mineral oil, Equivis ZS
Medium no. 2	: HEES 46, Ester oil, Biohydran
Temperature	: 55 °C
Duration	: 200,000 cycles (112 km)
Test specimen	: Rod seal, Turcon <sup>®</sup> Stepseal <sup>®</sup> 2K

### 2.2 Rod Seal Short Stroke / High Frequency Test



Figure 2: picture of the Hydro-Pulse (short stroke/high frequency) Test-Rig

Table 3: Parameters applied for the Hydro-Pulse (short stroke/high frequency) test

Test parameters:	
Pressure	: 15 MPa (constant)
Stroke length	: 5 mm
Frequency	: 15 Hz
Temperature	: 60 °C
Duration	: 24 h (1.3 million cycles)
Medium	: HLP 46, zinc free mineral oil, 46 cSt.
Test specimen	: Rod seal, special Turcon <sup>®</sup> Twinseal
Rod	: $\phi$ 50 mm hard chrome plated steel

### 2.3 Rod Seal Wear and Endurance Test

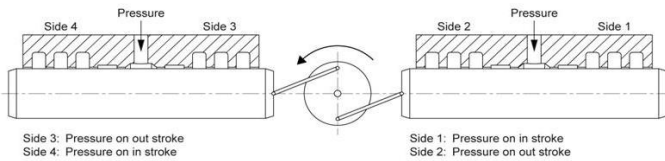


Figure 3: illustration (top) and picture (bottom) of the rod seal wear and endurance tester

Table 4: parameters applied for the rod seal wear and endurance tester

Test parameters:	
Pressure	: 20 MPa (constant)
Stroke length	: 10 mm
Velocity	: 1 Hz
Rod	: $\varnothing$ 50 mm hard chrome plated steel
Medium	: HLP 46, zinc free mineral oil, 46 cSt.
Temperature	: 80 °C
Duration	: 1,000,000 Cycles
Test specimens	: Pri. rod seal Turcon® Stepseal® V : Sec. rod seal Turcon® Stepseal® 2K

### 2.4 Side-Load Wear Ring Test

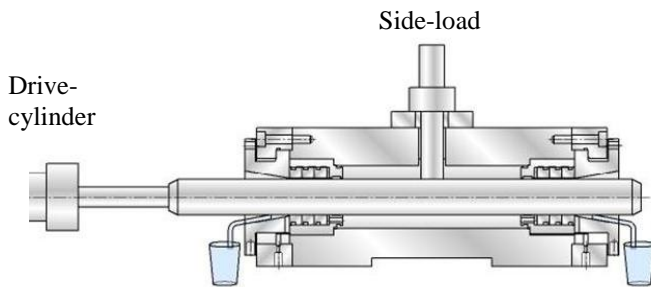


Figure 4: illustration of the side-load test-rig

Table 5: parameters applied for the side-load test

Test parameters:	
Pressure	: 2.5 MPa (constant)
Side-Load	: 8 N/mm <sup>2</sup> (on the wear rings)
Stroke length	: 250 mm
Velocity	: 0.20 m/s
Rod	: $\varnothing$ 50 mm hard chrome plated steel
Medium	: HV 46, Mineral oil, Equivis ZS, 46 cSt.
Temperature	: 50 °C (fluid temperature)
Duration	: 100,000 Cycles (50 km)
Test specimen	: Wear rings, Slydring®

## 3 Results

### 3.1 Friction during Standard Rod-Seal Testing

The friction data shown in this section is obtained using the standard rod seal test described in section 2.1. The friction values are for two rod seals at 30 MPa and are shown as a function of the number of cycles completed.

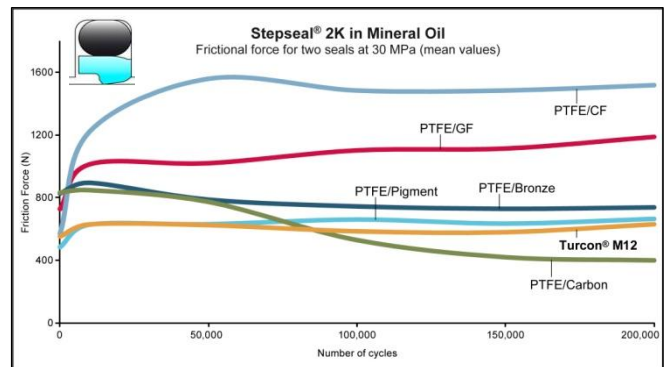


Figure 5: friction for two Stepseal® 2K rod seals placed opposite each other in the same test-chamber. The hydraulic fluid is traditional mineral oil. Data is collected on the rod-seal test-rig described in section 2.1

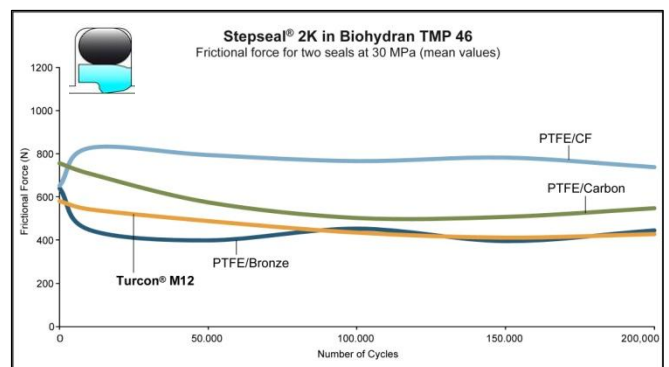


Figure 6: friction for two Stepseal® 2K rod seals placed opposite each other in the same test-chamber. The hydraulic fluid is a bio degradable synthetic ester fluid. Data is collected on the rod-seal test-rig described in section 2.1

Addition of fillers to PTFE typically increases friction, which is also seen in figure 5 when comparing the very low filled PTFE/pigment material with PTFE/CF, PTFE/GF and PTFE/bronze. Note that Turcon® M12 has the same low friction as PTFE/pigment, which demonstrates the ability of the incorporated fillers to maintain a low level of friction. The friction of PTFE/carbon drops to a surprisingly low level after about 100,000 cycles, which is explained by a rapid increase in leak rate observed midway through the test. The Stepseal® 2K rod seal test is repeated for some of the materials using a biodegradable fluid as medium instead of mineral oil, cf. figure 6. Turcon® M12 has lower friction than PTFE/carbon, which is normally recommended for fluids with reduced lubricity, and is on level with, but more stable than PTFE/bronze. PTFE/CF shows the highest friction, which was also the case when operating in mineral oil.

### 3.2 Friction of Wear Rings

Table 6 shows measured coefficients of friction when testing wear rings as described in section 2.4.

Table 6: coefficients of friction measured for Slydring® wear rings after 100 and 100,000 cycles, respectively. Data is collected on the side-load test-rig described in section 2.4

Material	100 cycles	100,000 cycles
Turcon®M12	$\mu = 0.13$	$\mu = 0.14$
PTFE/carbon	$\mu = 0.11$	$\mu = 0.18$
PTFE/CF	$\mu = 0.08$	$\mu = 0.23$
PTFE/bronze	$\mu = 0.15$	$\mu = 0.20$

PTFE/CF shows the lowest run-in friction of the four tested materials. The coefficient of friction for Turcon® M12 has the same low value after 100,000 cycles as it had during run-in, whereas the friction for all the other materials increased significantly at the end of test.

### 3.3 Leakage during Standard Rod-Seal Testing

Rod seals are typically installed as systems rather than as single elements. At high system pressures the back-pumping ability of a single rod-seal may be hampered. Therefore, a secondary rod seal or a double-acting scraper is often installed behind the primary seal. This secondary seal operate at a lower pressure and will assist in maintaining hydrodynamic back-pumping and thus good seal-ability. Figure 7 shows the leakage behaviour for the two materials Turcon® M12 and PTFE/Bronze when installed as a system consisting of two identical rod seals acting as a primary and a secondary seal, respectively.

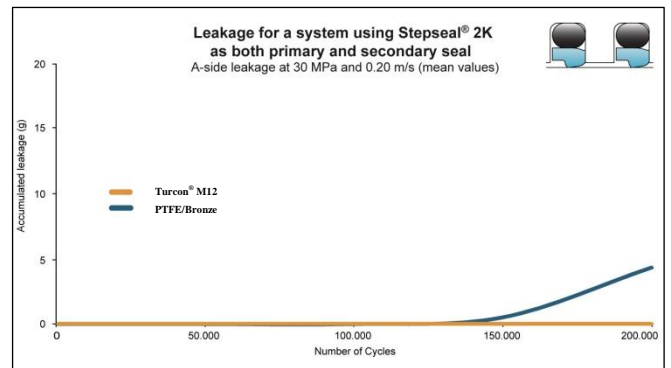


Figure 7: accumulated leakage versus the number of cycles completed for a seal system consisting of two Stepseal® 2K rod seals acting as a primary and a secondary seal, respectively. Data is collected on the rod-seal test-rig described in section 2.1

It is seen that the Turcon® M12 seal system is completely tight during the 200,000 cycles at 30 MPa. The PTFE/Bronze system also shows a good performance despite a small amount of leakage at the end of the test.

### 3.4 Wear and Deformation of Wear Rings

The reduction in w-measure (thickness) of wear rings after testing shows the combined effect of deformation and wear, cf. figure 8. It is seen that Turcon® M12 has the lowest wear of the tested materials. The remaining (plastic) deformation is on the same level for Turcon® M12, PTFE/bronze and PTFE/CF. The higher filled PTFE/carbon material has the lowest deformation but the wear is high, which is a frequently occurring weakness of this type of material.

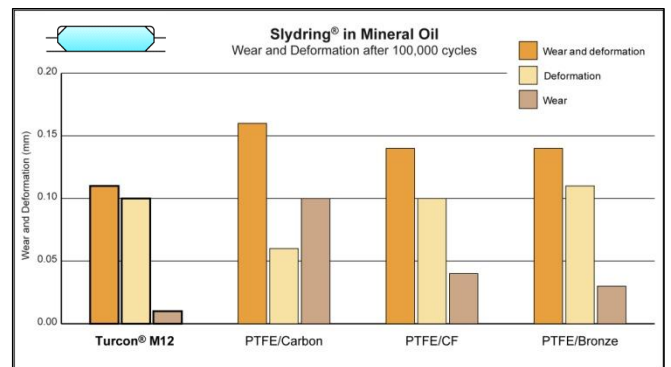


Figure 8: wear and deformation of Slydring® wear rings. In order to separate the contribution from wear and deformation, respectively, the tested wear rings have been resintered. During resintering the reduced thickness caused by deformation is recovered and the remaining reduction in thickness is due to wear. Data is collected on the side-load test-rig described in section 2.4

### 3.5 Deformation and Wear of Rod-Seals

Figure 9 shows the reduction of radial height of the seal profile (W) after testing, which is caused by deformation

and wear. The lowest measured value is seen for Turcon<sup>®</sup> M12 both in mineral oil and in biodegradable oil. This result agrees well with the Slydring<sup>®</sup> test shown in figure 8. In biodegradable oil the normally very wear resistant PTFE/bronze material clearly shows the highest wear-reduction. This high level is due to wear of the seals and indicates that the applied fluid does not have as high a lubricity as the applied mineral hydraulic oil.

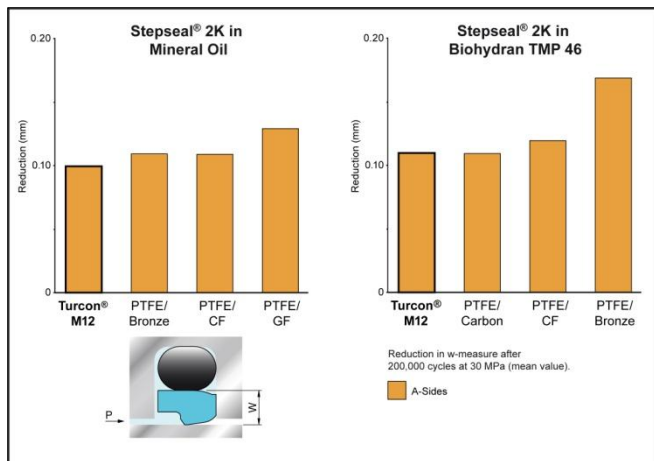


Figure 9: reduction of radial height of the seal profile, W (a combination of deformation and wear) after testing in mineral oil and biodegradable oil, respectively. Data is collected on the rod-seal test-rig described in section 2.1

### 3.6 Wear and endurance test of a rod seal system

Figure 10 shows cross-sections and seal faces of the examined rod seal system after the wear and endurance test described in section 2.3. Furthermore, the roughnesses of the countersurface before and after testing are shown in figure 11. The short stroke movement combined with zinc free oil is considered especially critical from a lubrication and wear point of view. However, despite of this, the turning grooves from production of the seals can still be seen after one million cycles indicating a very low level of wear. The seal profiles look almost as new without any signs of extrusion. Furthermore, the roughness of the counter surface is basically unchanged. This shows a stable and constant tribosystem with long lasting potential.

### 3.7 Extrusion of Rod-Seals

The level of seal extrusion measured after the standard rod seal test (described in section 2.1) is shown in figure 12. In mineral oil, Turcon<sup>®</sup> M12 and PTFE/bronze have an equal performance, while PTFE/GF and PTFE/CF show higher extrusion. The lowest value is seen for the high filled PTFE/carbon. In biodegradable oil, the lowest extrusion is seen for PTFE/bronze but the fact that it also has the highest wear rate in this fluid may interfere with the result. Material at the contact surface, which could have extruded may be worn away. The extrusion of Turcon<sup>®</sup> M12 is close to the

level seen for the high filled PTFE/carbon and significantly lower compared to PTFE/CF.

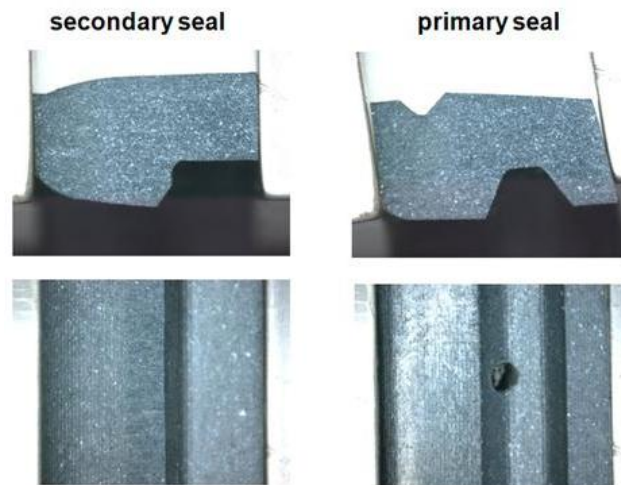


Figure 10: seal profiles (top) and seal faces (bottom) after wear and endurance testing shown for the primary and the secondary seal, respectively. Data is collected on the rod seal wear and endurance tester described in section 2.3

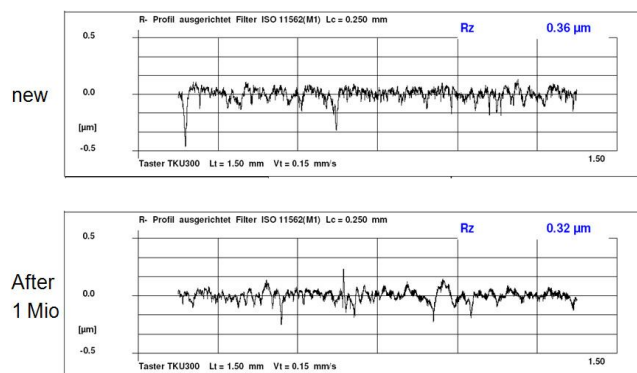


Figure 11: roughness of the hard chrome surface before and after wear and endurance testing

### 3.8 Hardware Scratching - Hydro Pulse Test

In order to compare the tendency of PTFE/bronze and Turcon<sup>®</sup> M12 to scratch the counter surface under poorly lubricated conditions, a test is conducted using short strokes, high frequency and Zinc free oil, cf. figure 13. In the case of PTFE/bronze, there are relatively heavy axial scratches at the complete seal contact area. This may be initiated by hard metal particles either released from the rod or present in the system, which subsequently get caught by bronze in the seal material and thereby accelerate wear on the rod. Tribo-oxidation may also play a role due to frictional heating. In the case of Turcon<sup>®</sup> M12, a completely different result is obtained. Micro-scratching did not occur, and the grinding pattern from the manufacturing process of the rod is still visible even after 1.3 million strokes. Only a slight polishing of the metal surface has taken place.

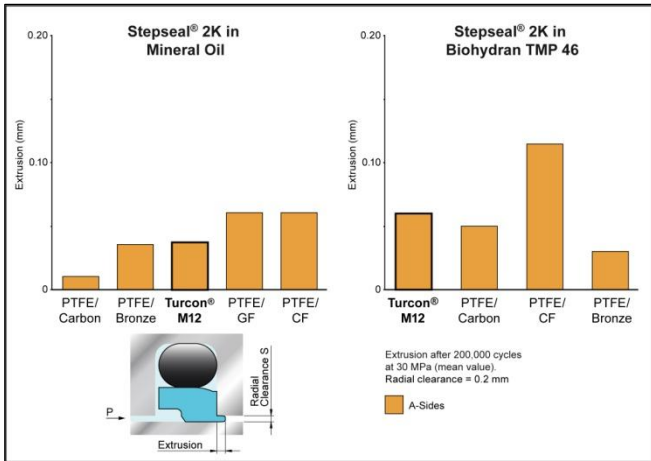


Figure 12: extrusion of Stepseal® 2K rod seals in mineral oil and biodegradable oil, respectively. Data is collected on the rod-seal test-rig described in section 2.1

seal test shows that Turcon® M12 is among the PTFE materials running with lowest friction.

## References

- [1] H K Müller and B S Nau. *Fluid Sealing Technology Principles and Applications*. Marcel Dekker, Inc. New York 1998, ISBN: 0-8247-9969-0
- [2] R Flitney *Seals and Sealing Handbook*. Butterworth-Heinemann, imprint of Elsevier, Oxford 2007, ISBN: 9781856174619
- [3] S Ebnesajjad and P R Khaladkar. *Fluoropolymers Applications in Chemical Processing Industries*. William Andrew, Inc. 2005, ISBN: 0-8155-1502-2

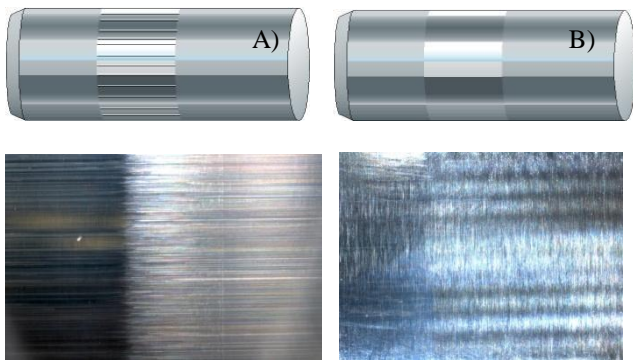


Figure 13: evaluation of micro-scratching after testing with short strokes and high frequency in Zinc free oil. Illustration (top) and picture (bottom) of the steel surface after testing: A) PTFE/bronze and B) Turcon® M12. Data is collected using the Hydro-Pulse test-rig described in section 2.2

## 4 Conclusions

The aim with this new PTFE-based material, Turcon® M12, has been to develop a material, which covers a significantly wider range of applications compared to existing PTFE materials. The results given in this paper show that Turcon® M12 matches the good extrusion, wear and deformational properties of medium filled bronze materials. The latter have limitations under conditions of starved lubrication or in media with reduced lubricity. Turcon® M12 is significantly better suited to cope with such conditions due to excellent wear properties and its ability to prevent damage to the counter surface. Furthermore, Turcon® M12 out-performs materials such as PTFE/carbon and PTFE/CF, normally recommended for fluids with reduced lubricity, on a number of parameters. Finally, both the wear ring test and the rod

# Prestudy on Power Management of a Cut-To-Length Forest Harvester with a Hydraulic Hybrid System

K. Einola

Ponsse Plc, Vieremä, Finland  
E-mail: [kalle.einola@ponsse.com](mailto:kalle.einola@ponsse.com)

## Abstract

A Cut-To-Length (CTL) forest harvester is used for felling, delimiting and bucking of the tree stems as forwarder is used to forward the logs cut to length to roadside landing for highway transport to the refining facilities like saw- and pulp & paper mills. Fuel consumption of forest harvesting operation is becoming a more and more important cost factor as the fuel prices are raising constantly.

A number of studies exist on various hybrid systems related to on- & off-highway vehicles and work machines. This paper deals with technological possibilities and potential to cut down fuel consumption of a CTL harvester by implementation of a hydraulic hybrid system that is mainly designed to take care of the highest power demands. In order to be successful in this aim, a detailed analysis of the work cycle and present power management and transmission systems are needed. Engine load data together with relevant Arcnet and CAN bus messages as well as needed hydraulic system parameters are logged during actual work in order to understand the actual nature of the application in terms of work cycle.

This study is focusing on a hydraulic hybrid system, as it seems to be an applicable solution to mobile work machinery in question. However – a background review of other hybrid solutions is also given. Some of the relevant advantages of a hydraulic hybrid system in forest machine application are also explained in this paper.

Based on the pre-study and analysis on the work cycle – a promising potential for hydraulic hybrid system can be seen in a CTL harvester. Future work to be done is proposed to include simulations to make a more detailed dimensioning of the components and design of the system possible already before building an actual test setup.

**Keywords:** Hydraulic hybrid, forest machinery, cut-to-length harvester

## 1 Introduction

Steadily growing percentage of industrial wood raw material is harvested mechanically and increasingly carried out with modern Cut-To-Length (CTL) machines. Typical CTL forestry operation is carried out with two principal machine units, a harvester and a forwarder. A CTL harvester is used for mechanized felling, delimiting and bucking of the tree stems whereas forwarder is used to forward the logs already cut-to-length to roadside landing for highway transport to the forest industry facilities like saw- and pulp/paper mills. In the competing TL method a larger number and variety of equipment is typically needed on one site and often four individual machine types are used[14]: feller-buncher, skidder, loader and processor.

Despite of the fact that CTL machinery is often considered more fuel efficient than Tree-Length (TL) method and machinery used - the fuel consumption of CTL machinery is also becoming a more and more important cost factor. Fuel prices are supposed to continue rising globally which is coming into a conflict with the forest industry's objective

of still lowering the harvesting cost per timber cubic meter in the future.

## 2 Review on the recent development on hybrid systems – both in industry and research

A brief review on the development of various hybrid solutions in both on- and off-highway vehicles and mobile work machines is given. Many of the discussed hybrid systems are still in prototype or demonstration phase but some of them already in serial production. In this study the term *hybrid* is widely understood as a system with more than one power source – even though only a single primary power source typically exist in vehicles and mobile work machines.

### 2.1 On-highway vehicle hybrids

During the last decade, a number of electric hybrid driven on-highway vehicles have entered serial production. In these vehicles the fuel economy has typically been

improved by accompanying an internal combustion engine (ICE) with one or more suitable assisting electric motors that are connected to the energy storage system like Lithium-ion battery pack. Typically a suitable battery management system (BMS) is also needed. This way the ICE can be dimensioned for lower peak load in a more optimal way to suit the average drive conditions. Of course the other approach is to use the stored hybrid power as a hybrid-boost functionality, often both functionalities can be incorporated into the same system. Brake energy can also effectively be recovered into the energy storage of the system. The electric motor can take care of the highest power demands and on the other hand make it possible to use start/stop functionality which is very useful in stop-and-go urban traffic. Remarkable fuel savings and CO<sub>2</sub> emission reduction have been proven especially in urban driving – also some all-electric range can be provided with large enough energy storage.

Both series and parallel hybrid designs exist in passenger car segment and all the time more models will be available. Earlier the ICE of electric hybrid passenger cars was typically chosen to be petrol driven, but more recently some European car manufacturers have started to turn towards diesel-electric hybrids also in passenger cars [13]. Mercedes-Benz is also introducing a new functionality named “sailing” in this E300 Bluetec Hybrid model which means that diesel engine is automatically shut down and disengaged from the powertrain also on higher speeds up to 160 km/h when the electric drive is able to maintain the constant speed. In other words on flat gradient or decline, like motorway conditions an all electric drive is used as long as there is stored energy available or the driver wants to take over.

Hydraulic hybrids in on-highway applications have so far been mainly tested and used in heavier commercial vehicles that typically drive in urban conditions and a remarkable amount of acceleration and braking of the vehicle – with relatively heavy vehicle gross weight is included in the daily work cycle. In this kind of application the payback time for a hybrid drive system can easier be short enough to make it also commercially viable. As an example garbage and delivery trucks have been the most potential application environments for this kind of technology. A well known commercial hydraulic launch assist (HLA) system is delivered by Eaton Corporation. This system is claimed to deliver 15 to 30% better fuel economy and simultaneously more than four times longer brake life [21]. These numbers have obviously convinced a number of large logistics companies and the HLA system is already in use in commercial vehicles.

Interestingly - more attention is given on hydraulic hybrids also on small passenger cars as the cost level hydraulic hybrid seems to be very competitive yet an excellent fuel efficiency can be expected. PSA Peugeot Citroen launched recently a hydraulic hybrid platform called Hybrid Air and states that it will be available on B and C segment passenger cars as well as some commercial vehicles [20]. This platform including hydraulic hybrid components like high and low pressure accumulators as well as hydraulic

pump and motor with the needed hydraulic lines can be seen in fig 1.

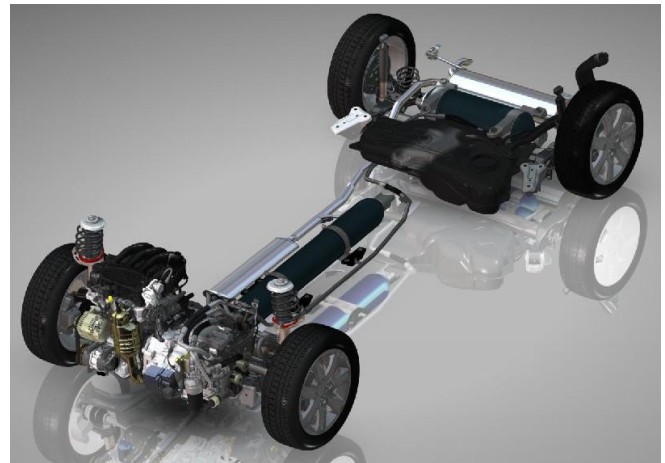


Figure 1. “Hybrid Air” petrol full-hybrid – by PSA Peugeot Citroen. A hydraulic hybrid shows great potential in passenger cars as well. [20]

The manufacturer of Hybrid Air is claiming that the technology will be affordable and provide up to 45% fuel savings in city traffic when compared to conventional engines with the same power rating. Furthermore it is emphasized that the environmental footprint is significantly reduced and the materials used throughout the power system are plentiful and easily recyclable for a lower overall impact on the environment. In contrast to hydraulic hybrid this is not the case with e.g. rare-earth elements typically used in modern high power electric energy storage systems. It is also stated that hydraulic hybrid technology is viable in all markets and climates regardless of the extent of the service network, which is a great advantage. According to the manufacturer more than 80 patent applications have been filed related to this technology [20].

In fig 2 vehicle power systems price is compared with CO<sub>2</sub> emissions. Manufacturer is claiming that the trade-off between CO<sub>2</sub> and power system price is simply unmatched by any of the current other hybrid technologies.

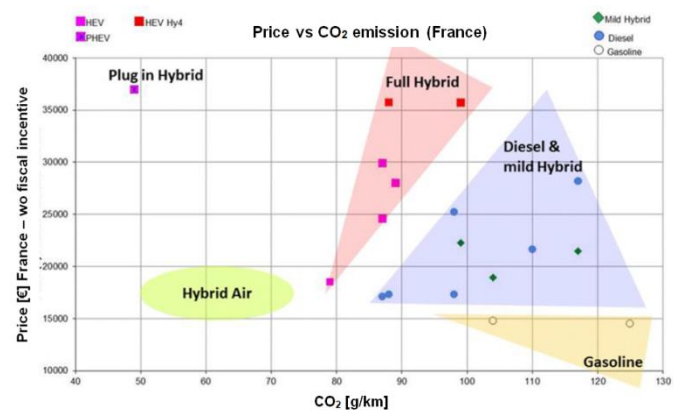


Figure 2. Price vs. CO<sub>2</sub> emission comparison by PSA Peugeot Citroen. [20]

Furthermore an interesting electro hydraulic hybrid has been proposed to be used in a commuter car in a study by Innas BV [18]. The vehicle driveline concept is based on a serial hydraulic hybrid replacing the mechanical drive transmission. Studied driveline is based on a hydraulic grid which makes the implementation of an electric power source easy. The concept is said to combine the optimal capabilities of both hydraulic and electric driveline and energy storage. These capabilities include reasonably long all-electric operating range of up to 25 km that gets very useful in urban zero emission traffic, and on the other hand performance characteristics comparable with reference car thanks to the hydraulic hybrid system which works as the backbone of the drive system. Fuel consumption as well as CO<sub>2</sub> emission were stated to be more than 30% lower than the values with respective reference car – even with the hydraulic driving in use only.

## 2.2 Off-highway vehicle and work machine hybrids

Various hybrid systems are also entering mobile work machine business and the most popular application for the hybrid drive seems to be a hydraulic excavator with rotatable upper structure. This design can generally be taken as a machine type with a high production volume in the industry and where the fuel saving potential is thus remarkable. Typically in the hybrid excavators the swing function of the upper structure is driven with an electric motor and this way swing function braking energy can be recovered to energy storage system like ultra capacitor or battery pack or their combination. A large number of patents publications exist related to electrical hybrid systems and especially control of such systems [4]. The hybrid system usually also includes a power generation electric motor that is typically mounted on the pump divider gear connected to the main drive train. This way also parallel hybrid functionality can be added to the machine in a feasible way and extra power is available to all or most of the power train of the machine if needed.

In fig 3 below the working principle of a Komatsu hybrid excavator is explained.

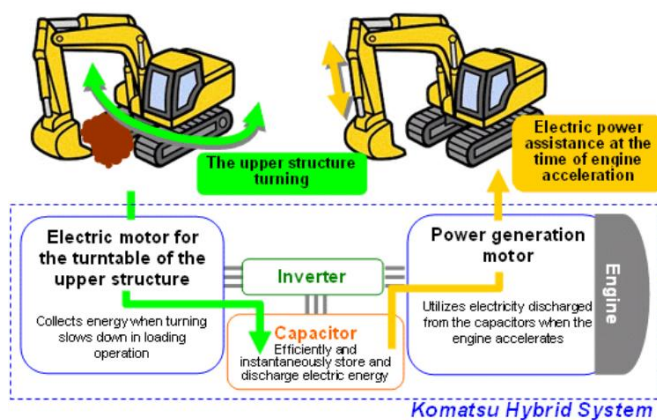


Figure 3. Working principle of the electric hybrid system of a Komatsu hybrid excavator.[9]

Mobile work machine manufacturer Komatsu Ltd. [9] claims that their PC200-8 Hybrid excavator achieves 25% fuel savings on average use. Fuel saving potential is however strongly linked to the actual work cycle of such an excavator and as the manufacturer is stating, savings can also be remarkably higher if upper structure swing function has a more important role in the work cycle. This is quite natural as swing function is the only function with energy recovery functionality. This is emphasized in fig 4.

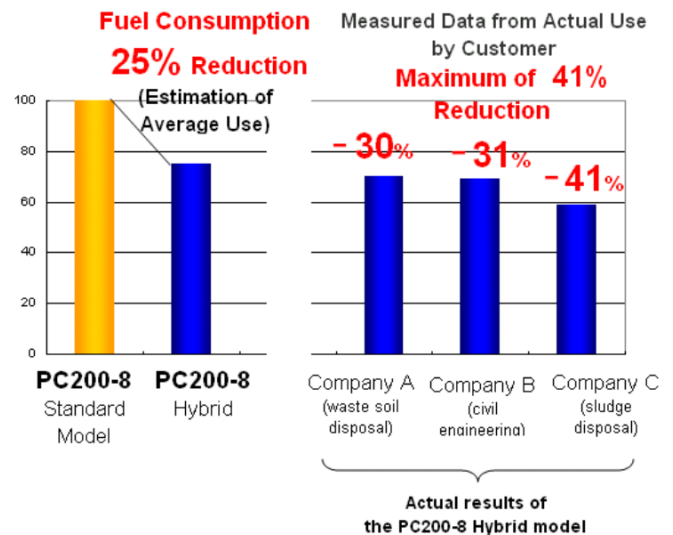


Figure 4. Claimed fuel consumption reductions of a Komatsu PC200-8 Hybrid Excavator.[9]

Electric hybrid systems are tested also in recent CTL forest machinery, for example a Swedish manufacturer El-Forest Ab has already for a number of years tested and developed forwarder with electric hybrid system for both drive transmission [3] in serial hybrid design as well as boom system with parallel hybrid functionality. El-Forest B12 forwarder is stated [10] to provide 25% lower fuel consumption than respective machine with traditional power transmission. A little later this same electric hybrid technology by El-Forest Ab has also been fitted to a CTL harvester manufactured by a Finnish company ProSilva Plc. In this harvester application the electric hybrid system is only driven in parallel mode, assisting the diesel engine serving as the prime mover of the hydraulic systems of the machine. ProSilva is claiming [11] that in their 910EH harvester the diesel engine was downsized from 155kW 6-cylinder engine to a 60kW 4-cylinder unit without compromising the harvesting power. If this is taken as a matter of fact it can be concluded that a remarkable downsizing potential really exists.

A simple hydraulic hybrid solution for a CTL harvester was studied and tested by a German company HSM GmbH [5]. In this machine a hydraulic accumulator with volume of 60 liters was connected in parallel with the variable displacement pump in order to feed the same harvester head hydraulic circuit. Hydraulic accumulator was connected to the standard hydraulic system via safety valve block and 2/2 charge and discharge on/off valves as seen in fig 5 [5].

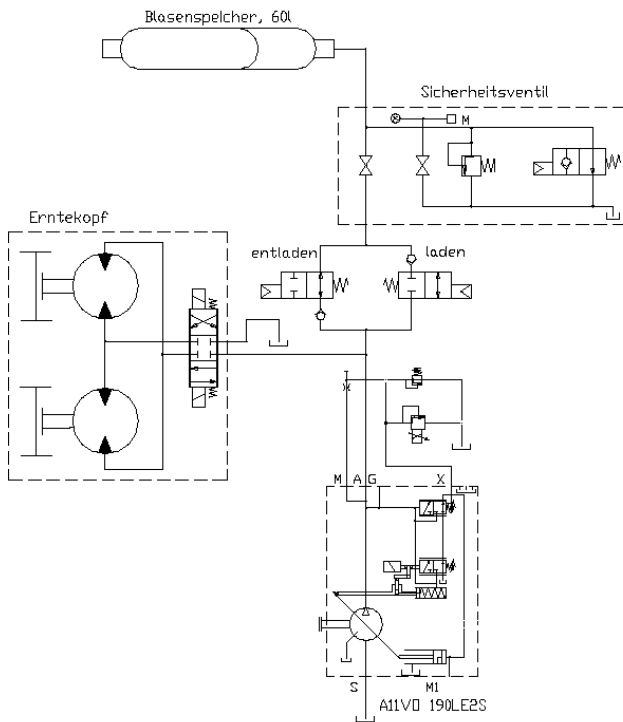


Figure 5. Hydraulic diagram of HSM 405H2 harvester with the studied energy storage system. [5]

The following aims were addressed for the studied system: more even engine load, higher delimiting power, better dynamics for delimiting feed start, lower pressure peaks during deceleration of delimiting and finally the shifting of the engine operation point to best efficiency area. The energy storage capacity of the used hydraulic accumulator, ca. 360 kJ was in the study used for a hybrid boost which was roughly calculated to be able to increase the available power from 175 kW diesel engine ca. 50% say 90kW for a maximum period of four seconds. On the other hand it would have been possible to do downsizing on diesel engine as well as on the hydraulic pump maximum displacement and achieve e.g. fuel savings that way. However, even with the studied hybrid boost functionality, up to 20% fuel efficiency improvement was observed as the fuel consumption was measured in liters per harvested cubic meter of timber. In other words also increased production possibly had an effect on the fuel consumption comparison. The main drawback of such a simple energy storage system is however that not all of the energy storage capacity can be effectively used in the application, because as the accumulator pressure is lowered to the same level or under the actual circuit pressure – the stored energy is no more really useful. In mobile work machines as well as in vehicles in general it is not easy or economical to oversize the energy storage but on the contrary the installed capacity should be exploited in its entirety. This problem needs to be addressed with a more advantageous connection of the hydraulic accumulator to the hydraulic system. In a good solution most of the energy storage capacity of a hydraulic accumulator can be used in parallel also with the full system pressure in the work hydraulics.

Research related to hydraulic hybrids is often concentrating to vehicle propulsion and drive transmission systems as industrial production volumes and on the other hand also braking energy recovery possibilities there are remarkable. Rydberg is comparing electric and hydraulic hybrids, especially in the field of vehicle propulsion in his study [12] and states that hydraulic hybrid systems create a unique opportunity to optimize the engine loading at all speeds. Furthermore hydraulic machines are told to have around five times higher power density than electric machines, which is a great advantage when manufacturers are packing the components to limited space in the vehicles. Often the situation is also that the same machine layout should be possible to deliver with the hybrid solution as well as with the more traditional power train and this means that possibly needed extra room for hybrid system components can be hard to find. Higher power density is also stated to give the opportunity to use direct hydraulic drive and leave out mechanical gearing that is typically needed in electric hybrid systems. Interestingly, the round-trip efficiency of a hydraulic accumulator is known to be higher than for the electric battery, especially in applications with frequent acceleration and braking. On the other hand it is quite obvious that an ultra-capacitor (UC) or a combination of batteries and UC would most likely make a better alternative to serve as energy storage of a highly dynamic electric hybrid application. However the cost level of ultra-capacitors is known to be relatively high.

One recent and interesting commercial activity on the narrow area of work machine hydraulic hybrids seems to be Caterpillar Inc. releasing its new 336E H Hydraulic hybrid excavator [19]. In this machine weighing 37.200 kg and having installed engine power of 230 kW, the upper structure swing brake energy is stored to hydraulic accumulators and reused at the time of next swing acceleration. Not much technical facts are unfortunately available at the moment, but the manufacturer claims fuel savings as high as 25% compared to a respective machine unit with traditional hydraulic system. The improved fuel efficiency is said to give return on investment in as short time as one year, more typically in 18 months. Caterpillar is also stating that more than 300 patent applications were filed for the technology developed in the 336E H.

Also a number of other studies to improve the energy efficiency of hydraulically driven mobile work machines have been carried out earlier. Many of them have concerned various hydraulic energy recovery or boom balancing [5, 8] solutions that aim to increase hydraulic system efficiency by directly reusing potential or kinetic energy to other functions or storing the energy for later use. However these studies have been earlier discussed as boom dead weight balancing systems or potential energy recovery or reuse systems – more than hydraulic hybrid systems.

### 3 Power transmission system of a CTL harvester

In a typical CTL harvester the harvester head is supported and moved with a purpose built hydraulic boom system in order to reach the trees to be felled and processed. Actually almost all power transmission in the machine is implemented by a hydraulic system and its actuators. In case of PONSSE Ergo harvester that can be seen in fig 6 - two independent open circuit hydraulic systems are used, one for the boom and another for the harvester head. The harvester head circuit is being fed by a 190 cm<sup>3</sup> variable displacement pump with electrical maximum displacement control, the pressure level also being electrically adjustable in order to match these parameters accurately for each work phase and function. This way excess system flow and pressure can be satisfactorily avoided in most cases. By adjusting the maximum pump displacement the actuator speed can be controlled in a more efficient way than using throttling in proportional directional valves. One example of this is that the maximum feed speed of the log is limited with pump displacement and valve control is only used for more accurate positioning when approaching the desired cutting position on the tree stem.



Figure 6. A Cut-To-Length harvester felling a tree on a full boom reach. Functions of crane and harvester head are often activated simultaneously and this creates high intermittent power demand. Photo: Ponsse Plc.

An embedded Arcnet / CAN bus based control system is managing these pressure and volume flow settings as well as reading the operator input and controlling the actuators of the system and the diesel engine that serves as the prime mover of the whole machine.

Variable displacement pump driving the boom system has a maximum displacement of 145 cm<sup>3</sup> and is controlled with a Load Sensing (LS) governor as very typically in mobile work machine boom systems like this in order to achieve state of the art efficiency.

The hydraulic pumps of these circuits are driven with an Euromot Stage 3B compliant diesel engine with nominal power of 210 kW (@2200RPM) and torque of 1120 Nm (@

1200 to 1600 RPM) via a pump divider gear with two parallel outputs.

These two main hydraulic systems of a CTL harvester can generate remarkable power demand to the diesel engine especially when both boom and harvester head functions are utilized simultaneously during harvesting work. Other hydraulic circuits and functions are as well present within the machine, including hydrostatic drive transmission for example as well as hydraulic fluid filtration & cooling circuits. More rarely also drive transmission can be used at the same time with harvester head and boom functions. The main hydraulic systems and their pump placement on the pump divider gear are generally shown in the fig. 7.

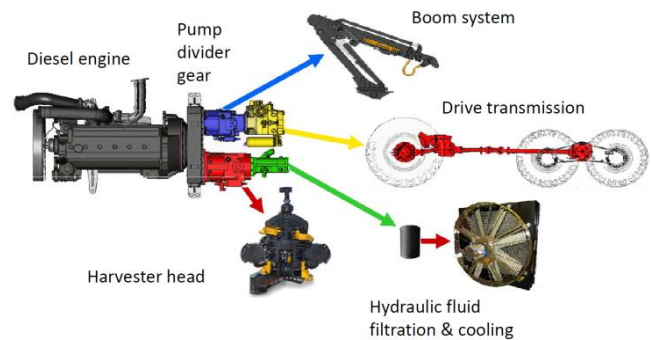


Figure 7. The main hydraulic system of a PONSSE Ergo harvester. Schematic figure by Ponsse Plc.

#### 3.1 Power demand and how to manage it

The power demand from the prime mover is typically highly dynamic in a CTL harvester and for this reason the diesel engines typically need to be dimensioned for remarkably higher maximum power than the average harvesting work load. Furthermore diesel engines typically have their most fuel efficient working point in lower RPM range, in case of PONSSE Ergo between 1200 to 1400 RPM where the highest nominal power is not available and thus even more oversizing may be needed.

As the challenges caused by the harvester work cycle have been around for a while - there are a number of different approaches to manage these high-power, but typically short-duration power peaks, some of which being the following:

- dimensioning of the primary mover, typically diesel engine simply for the highest possible intermittent power demand
- use of power limiting governor and/or control approach on one or more of the variable displacement hydraulic pumps

- forecasting and estimation of foreseeable power demand changes based on the knowledge on a typical work cycle and controlling the engine in beforehand and taking the advantage of the hydraulic system delays [6]
- Power demand estimation based on measured signals like tree stem diameter indirectly describing the needed power level for each individual tree to be processed [7]

However, measurements and experience has shown that the maximum power needed can be easily over twice the average power in a Cut-To-Length harvesters work cycle. In other words the present solution can not be the optimal one in terms of fuel efficacy or component dimensioning.

In history when engine exhaust emission regulations were not as strict as today, one way to improve engine dynamics in front of high step-like loads was to choose as heavy flywheel option for the engine as possible. This way the engine could a little easier go over rapid load transients. The drawback of this approach was of course excess weight and the fact that that engine RPM recovery was inconveniently slow if the engine was stalling after a little longer power demand. The prevailing diesel engine exhaust emission regulations [1] are however making the use of this approach practically impossible.

It is also possible to use power limiting governors on variable displacement pumps, but this is typically compromising the productivity and ruining the smooth and fast operation of a hydraulic boom system with expected high dynamic performance. On the other hand especially in harvester head circuit high intermittent power is simply needed in order to be able to cut through the thick tree branches with delimiting knives. This dynamical requirement of delimiting process and especially the acceleration phase at the start of the function are also depicted in the study by company HSM [2]. Also cross cutting process is very critical in terms of time and maximum power available as if the cut starting from the upper side of a log is too slow, the log will have too much time to be bent and this will damage the valuable sawmill logs with longitudinal splitting, so called end checks [15] that are known to be specially harmful problem for sawmill and veneer industry.

Also different ways to more intelligently control the engine of a forest machine exist on the market. Modern diesel engines with electronic engine control units (ECU) can be controlled with reasonably quick response. This way it may be advantageous to deliver a short extra RPM or fuel injection request to the engine as soon as it is clear that increase in engine load will take place soon. Typically in a harvester for example it takes some hundred milliseconds for the system pressure level to rise in harvester head circuit – after the feed or saw function is activated by the operator or an automatic control sequence. This delay gives the control system a possibility to tell the engine shortly

beforehand that a load peak will be coming soon and the engine can prepare for that event with a more dynamic response [6].

Another proposed system is to measure the tree diameter when the harvester head grabs the tree to be processed [7]. Tree diameter value and possibly operator entered tree species could for example be the basis for engine control which basically could ask for more engine RPM or torque if the tree to be processed is bigger and thus most likely heavier to process than the earlier ones.

It is quite obvious that a suitable parallel hybrid system could be very useful in tackling these problems in an intelligent way. Therefore - parallel hybrid systems capable of evening out the power peaks of the work cycle are of great interest among forest machine manufacturers.

## 4 Motivation

As fuel prices have been rising remarkably, the fuel cost of a Cut-To-Length harvesting operation have already reached a level that can be compared to other factors of production in the harvesting process, for example operator labor cost on at least some market areas. Therefore more and more interest to novel solutions reducing the fuel consumption is brought to discussion. For example a Cut-to-length harvester can yearly run 1500 to 7000 work hours in the forest with a average fuel consumption of 10 to 15 liters per hour which will mean yearly fuel consumption of 15.000 to 105.000 liters. With diesel fuel prices exceeding of 1 Euro for liter, this clearly has a remarkable effect on the operating costs of such piece of work machinery.

Also in forestry sector - hybrid solutions are found attractive at seen at least from two different points of view, them being the one of an end user of the machinery as well as the one of the original equipment manufacturer (OEM).

### 4.1 Motivation of engine downsizing for the forestry contractor and machine owner

A machine with downsized engine and a hybrid system taking care of the short-duration, high-power peaks - will most likely be able to deliver better fuel economy of the logging operation. It is also possible that the engine response and dynamics can be even better than with a traditional solution – as hybrid system can provide high power to the system for the needed short times. This would help the operators to achieve higher productivity and in some cases also higher work quality. Especially cross-cutting and delimiting quality is often compromised if the needed power and dynamics is not available during the work.

Furthermore - the use of a downsized engine will possibly result to more compact machine layout and for example better visibility and agility of the machinery as well as lowered noise and vibration levels at the operator's station. Typically - downsizing from a 6-cylinder diesel engine to 4-cylinder engine cuts already 200...300 mm of the engine length which actually could have an effect on the engine

hood that is typically compromising the visibility as well as affecting the maneuverability of the machine.

Service and maintenance cost can also be lower for downsized smaller diesel engine which works assisted by a hybrid system evening out the heaviest loads.

#### 4.2 Motivation for the forestry equipment OEM

Especially with the diesel engines meeting the latest exhaust regulations it has been noticed that not only the engine itself causes costs related to the power generation system. Also cooling system, exhaust after treatment (EGR, SCR, DPF etc.) systems etc. cause remarkable costs and require lot of room on the machine layout. These costs and component dimensions seem to be in relation in the first place to the engine displacement and on the other hand to the engine nominal power rating.

In other words a possibility to replace a 6-cylinder engine with a shorter, say 4-cylinder unit would not only free up the room right next to the engine, but also from other parts of the engine bay as engine cooler and exhaust systems will be smaller on the machine. With the right hybrid system design a small diesel engine combined with a hybrid system could perform as good as a larger displacement diesel engine without hybrid. Hybrid solution can also be attractive in terms of component and manufacturing costs but this is more case specific.

On the other hand a hybrid system could of course be used to provide power boost functionality to a present solution and make a higher productivity and performance possible without the need to increase the engine displacement and dimensions.

### 5 Work cycle of a CTL harvester

In order to evaluate the potential of a hybrid system in a harvester it is very important to know the work cycle in as many detail as possible. Therefore a set of measurements in actual harvesting work were carried out. Some details of the measurements are presented in the following.

#### 5.1 Work cycle measurements

A large number of Arcnet/CAN bus signals were logged via the machine control system. Also some separately instrumented flow and pressure measurements were collected. An overview of over 60 signals altogether, logged or measured can be seen below:

- all operator entered input signals to the machine control system (boom control lever and harvester head function key signals, drive direction, drive speed etc.)
- a number of CANbus messages from the diesel engine (RPM, engine load percent, intermittent and cumulative fuel consumption data)

- system pressure and volume flow data (boom circuit volume flow, LS pressure and circuit pressure, harvester head circuit volume flow and pressure)

Measured work cycles were also captured on video in the same time domain in order to be able to trace each measured work phase also on the video for checking the actual work done with the machine.

Measured harvesting work included harvesting of different size trees in actual harvesting work. Diameter and length of each tree and log among other operator input data (log assortments, tree species etc.) was measured and automatically saved for each tree in a .stm file per StanForD standard (Standard for Forest machine Data and Communication) [17] with the harvester measurement system.

#### 5.2 Work cycle analysis

It is well known that the work cycle of a CTL harvester typically consists of rather short duration duty cycles - that are - quite naturally linked to short phases of the actual harvesting work. This means processing the trees with the crane and the harvester head, in more detail including the following sub cycles:

- if needed - driving the machine to the next working position on the logging site
- moving the harvester head with the crane to the next tree and grabbing it
- felling the tree by cutting it with the high speed chain saw an directing the tree to fall to the desired direction
- feeding the tree trunk through the harvester head with the feed rollers and at the same time
- delimiting the tree with the delimiting knives
- as well as measuring and bucking the tree in desired dimensions with the cutting saw
- dropping the tree top to the ground by opening the feed rollers and delimiting knives and tilting the harvester head into the upright position
- moving the harvester head with the crane to the next tree and grabbing it

This work cycle related to processing of one tree is then normally repeated hundreds or thousands of times a day or during each work shift.

In fig 8 it can be seen how ten different main functions of a harvester machine are used during processing of two consecutive trees.

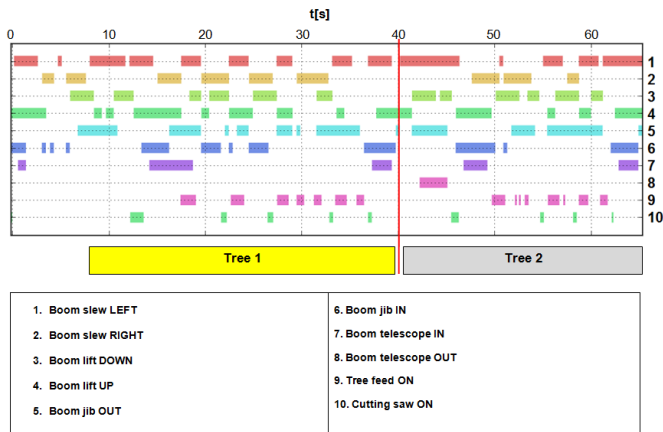


Figure 8. Processing of two consecutive trees with a Ponsse Ergo harvester. Activation of 10 different harvester functions shown as a Gantt chart.

For example slightly longer cutting saw activations (function 10) are needed when the tree is being felled. These moments can be seen on the  $t[s]$  axis at  $\sim 12$  seconds and  $\sim 47$  seconds. The cross-cuts and feeding of the tree (function 9) are then taking turns as long as the whole tree is processed. In this case tree 1 obviously comprised of four logs and tree 2 of three logs. It can be seen that during cutting and feeding also boom functions are used. Sometimes several functions simultaneously.

Of course the CTL harvester machine needs to be moved a short distance between work positions once in a while – but this propel function implemented with a hydrostatic-mechanical drive transmission is not really important in typical work cycle of the machine type in terms of power demand or lifecycle fuel consumption. Thus the drive transmission is so far excluded in the study even if transmission data was also logged. On the other hand propelling of the machine is typically not used simultaneously with the tree processing functions – even if it is actually possible with some limitations.

It is clear that harvester head cutting saw as well as tree feeding roller rotation functions are the most important power consumers in a CTL harvester, also crane functions having a remarkable power need. Especially when two or more of these functions are activated at the same time – high power peaks can be observed in the hydraulic system as well as high torque values at the diesel engine.

Very typically these loads can be almost step-like load transients, which are difficult to handle for a diesel engine without compromising the exhaust emission levels. Especially the latest diesel engine exhaust emission regulations like the Euromot Stage 3A and 3B [1] have caused that the fact that engines have to be dimensioned to remarkably higher power level than the average power demand in a CTL harvester application.

Of course the actual power demand depends on the trees and the forest to be cut and processed but typical average power demand from PONSSE Ergo harvester can be lower than 100 kW even on a regeneration harvesting site – despite of which the engine is dimensioned to 210kW in order to be

able to handle the highest power peaks without compromising the productivity or processing quality. Also work methods of the operator and operator set system settings can have a remarkable influence on this power demand

In fig. 9 a measured typical power demand curve for harvesting work is shown. The maximum peak power demand level at this harvesting site seems to stay mainly below 180 kW level as the average power level is slightly over 80 kW. Power peaks exceeding the average power are coded with red colour and power levels below average power is coded with blue colour. In other words the 210 kW engine is pretty much required to take care of these loads even if it is heavily oversized when compared to the average load. On the other hand tree size during the measurements was not the absolute maximum for this machine and the power demand will still be higher when working with larger timber.

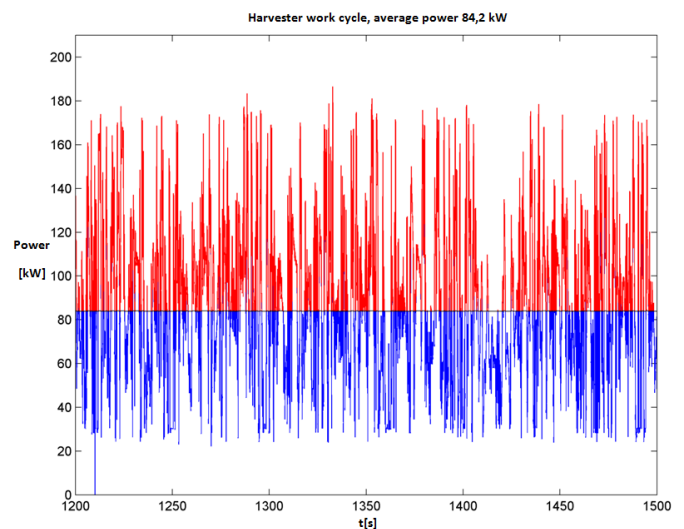


Figure 9. Actual power demand from the 210 kW diesel engine of a PONSSE Ergo harvester during 300 seconds of harvesting.

On the other hand if a constant output power of approximately 80 kW is taken from the diesel engine, the excess power needs to be taken care with the secondary power source, the hybrid system and its energy storage.

In fig. 10 a shorter seven second long section of the harvesting work zoomed in. It can be seen that power peaks typically last only short time, typically 1 to 2 seconds a couple at the time and then the power level comes down – which would give us a chance of engine downsizing with reasonable energy storage dimensioning.

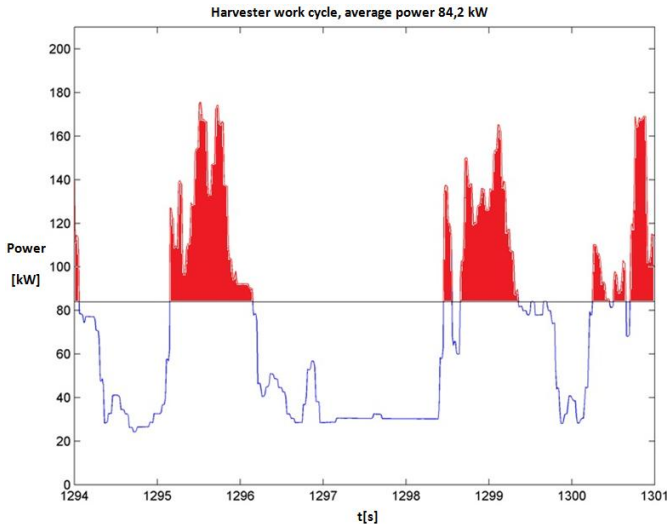


Figure 10. Actual power demand in kW from the 210kW diesel engine of a PONSSE Ergo harvester during seven seconds of harvesting.

The energy / work of a single power peak can be determined as an area between the given constant (here average) power level and actual power curve. In other words by integrating the power curve over time from point *a* to *b* as shown in equation 1.

$$A = \int_a^b f(t)dt \quad (1)$$

Trivially - the basic principle to dimension a hybrid system to take care of the power peaks is to dimension its energy storage capacity as well as power transforming means to be able to handle the energy flows in an adequate manner.

Based on the measurements done in this study, a typical amount of energy needed from the hybrid system for a single power peak is typically around 100 kJ, when calculated based on the average power. In this rough estimation hybrid system component losses are not considered. However in some parts of the work cycle there is not enough time available to keep the energy balance on the positive side with energy storage capacity of 100 kJ, but more energy storage capacity is needed.

Energy balance of the energy storage and the hybrid system in general is discussed in fig. 11 which shows the calculated cumulative energy needed from the energy storage during the measured harvesting work cycle. This curve is calculated based on the assumption that the diesel engine only provides a constant power of 84,2 kW and all power exceeding this level is taken from the energy storage. From the curve in fig. 11 it can be seen that there are periods when the energy demand stays high for extended period of time. For example the part of the work cycle between moments *t*[s] ~ 470 seconds and ~ 620 seconds seems to require almost 1200 kJ of energy.

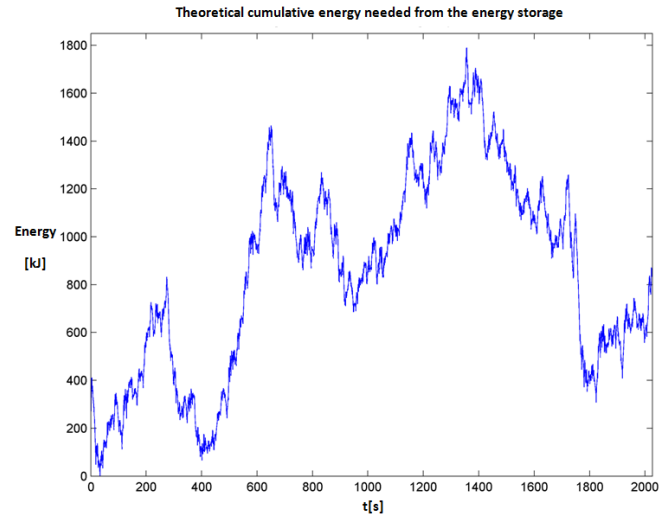


Figure 11. Theoretical cumulative energy needed from the energy storage during measured harvesting work cycle – based on the assumption that diesel engine provides constant power of 84,2 kW and everything exceeding that is taken from the energy storage.

On the other hand if the aim is to look for engine downsizing from the starting point of 210 kW 6-cylinder engine, we can choose for example 145 kW or 129 kW 4-cylinder engine and still take away two cylinders as well as downsize engine displacement dependent add-on systems like cooling system and exhaust gas after treatment. Anyhow - this extra power margin over the average power level allows the engine load to be higher also for little longer times – and still keep the energy balance of the hybrid drive on the positive side. It may also be a good idea to think about allowing the diesel engine to operate on variable or adaptive power level depending on the actual work conditions. Also different kind of hybrid operation modes can possibly be taken into implementation – for example one setting or mode could aim for lowest fuel consumption but as a drawback, performance would be possibly more or less limited. Respectively another setting could aim for maximum performance or “power boost” functionality, but most likely compromising the fuel efficiency.

However a rough estimate for the needed energy storage capacity for engine downsized PONSSE Ergo hybrid harvester could be about 300kJ to 500 kJ, which is still reasonable to implement also with hydraulic accumulators as well as with electric energy storage systems.

## 6 Choosing the hybrid system

Choosing the right hybrid solution for a CTL forest machine needs to be done based on the work cycle. First of all in this study a harvester machine is only considered as it seems to be the more interesting machine type in terms of load cycle. In other words harvester load cycle is thought to be more difficult and dynamic than the one of a forwarder and thus the potential for hybrid system payback would be better.

Then choosing between electric and hydraulic hybrids is the next question. Hydraulic hybrid seems to have a number of clear advantages compared to electric hybrids. Some facts that stand for hydraulic hybrid in CTL harvester application are discussed hereinafter.

Naturally it is a good idea to avoid all unnecessary energy conversions if possible, because every conversion causes losses. Almost all of the functions in a CTL harvester are implemented hydraulically and with hydraulic actuators mainly because of the high power to size & weight ratio. If an electric hybrid system would be chosen that would naturally mean more energy conversions between electric and hydraulic energy which should be avoided. Possibly some of the forest machine functions could be direct electric drive, but not the majority. For example replacement of hydraulics in forest machine boom systems and especially in the harvester head simply does not seem to be realistic in the near future.

On the other hand forest machinery manufacturers as well as their dealer and service network are familiar with hydraulic power transmission and also energy storing into hydraulic accumulators as on the opposite – high current and voltage electric hybrid drives are often totally unknown technology in the business. This would mean very high requirements on service people training and most likely demand for officially qualified electricians in the service organization.

On the other hand it is a fact that forest machines rarely work close to infrastructure like power grid – where electrical energy could be available to introduce plug-in functionality. This possibility for example by charging energy storage from grid could be an interesting topic for mining, earthmoving or material handling machinery that may operate extended times close to energy available from the electric grid and sufficient energy storage capacity could be mounted on board.

Forest machines also work in really harsh circumstances and also service often has to be possible on site in the forest. A special requirement for all forest machine systems is that they need to be performing in both cold and hot ambient temperatures, say from -40°C to +40°C. On the northern hemisphere the most important logging season is during the mid winter when ground frost makes the access to thinning sites and wetlands possible. On the other hand fast growing eucalypt plantations are typically located in the southern hemisphere where high ambient temperatures ask for the maximum cooling capacity from the machine. Cold start

does not need to be possible in the coldest weather but as the machine have been started the continuation of the –logging operation has to be possible. Concerning hybrid systems - especially electric battery system performance seem to be a problem in cold temperatures. Also a hydraulic accumulator needs to be assembled with the right materials and taken into use the right way in cold start – but these problems seem to be a little easier to overcome.

Finally the cost factors also seem to be advantageous for hydraulic hybrid – at least in harvester application where the nature of hybrid system is power peak management with reasonably small energy storage capacity needed. The costs between electric and hydraulic hybrids have been compared in a number of studies and typically hydraulic hybrid is considered to be remarkably more economical. According to hydraulic accumulator manufacturers cost effectiveness is better on hydraulic energy storage as seen in fig 12. Also other main characteristics seem to be positive.

Technology	Electrical	Mechanical	Hydraulic	
Energy storage device	Double layer capacitor 	Lithium ion battery 	Flywheel 	Hydraulic accumulator 
Energy density	-	+	o	-
Power density	+	o	o	+
Ageing / Capacity loss	o	-	o	+
Temperature sensitivity	-	-	o	+
Self discharge	-	o	-	+
Packaging	o	o	o	o
Cost effectiveness	-	o	o	+

Figure 12. Comparison of energy storage devices by Hydac. [16]

The main drawback of a hydraulic hybrid seems to be the somewhat limited energy storage capacity of hydraulic accumulators. Possibly also controlling of the hydraulic energy flow between the work hydraulic system and the energy storage, especially in highly dynamic operation can be more challenging than in electric hybrid systems. Both these drawbacks are however much related to the actual application. For example a somewhat limited energy storage capacity is not a crucial problem if full hybrid driving is not needed at all which is the case in this study.

The energy storage capacity of a hydraulic accumulator is demonstrated in fig 13 [16]. The size of the hydraulic accumulator in this example could roughly provide the energy storage capacity needed in the CTL harvester discussed in this paper. The energy capacity of 360 kJ can be used in 6 seconds at constant power of 60 kW. On the other hand this 50L accumulator can provide a power of 100 kW for 3,6 seconds – which should be long enough time to handle most of the power peaks in the measured harvesting work cycle.

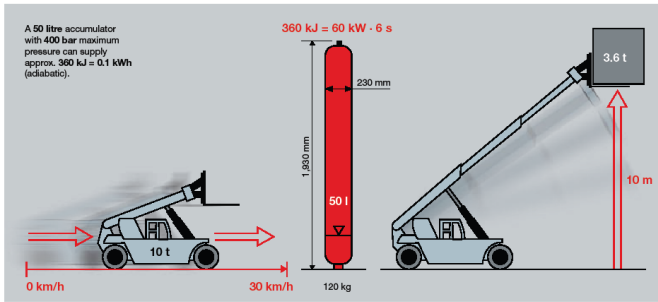


Figure 13. Demonstration of energy storage capacity of a hydraulic accumulator of volume 50L and maximum pressure of 400 bar. [16]

The charge – discharge rate of the energy storage will be an important issue as we know the load cycle being very dynamic. From fig 9 we could see that a typical charge – discharge cycle of a CTL harvester only lasts about two seconds. With electrical energy storage this kind of dynamics seems to be achievable only with ultra capacitor at least as a part of the energy storage system. A comparison of various energy storage systems is telling that different designs of hydraulic accumulators are very competitive with electrical ultra capacitors in terms of charge – discharge rate. Electrical batteries are told to have a cycle time starting from one minute so they can not be a good solution, definitely not as the only energy storage. Also round trip efficiency of an electric battery is stated to be lower than the one of a hydraulic accumulator [5].

In other words hydraulic accumulator should be well able to cope with the dynamical requirements set by the short cycle time of this CTL harvester application under the study.

### 6.1 Proposed hydraulic hybrid system

Finally a very simple hydraulic hybrid system for a Cut-To-Length harvester is proposed in fig. 14. The hybrid system pump-motor 2 is added on the same driveline as present pump 1 serving the harvester work hydraulics. A separate over-center controllable closed circuit pump-motor 2 is needed to control the oil and energy flow between the hydraulic system and the energy storage that is a pressure accumulator or set of them.

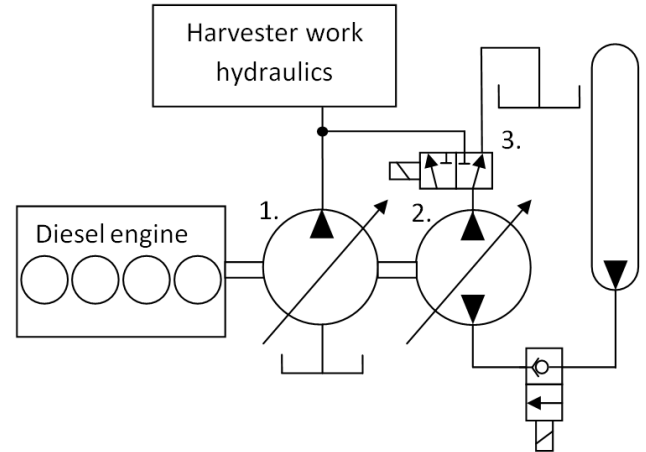


Figure 14. A simplified hydraulic hybrid system of a CTL harvester.

During low power demand of the actual work cycle the pump-motor 2 is delivering the hydraulic energy into a higher pressure to the hydraulic accumulator and during high power demand - respectively feeding the power from the hydraulic accumulator into the harvester work hydraulics through the pump-motor 2.

Pump-motor 2 could also be connected directly to the tank from the work hydraulics side with e.g. a 2/3 directional valve 3 for example - and this way stored energy could simply be used to feed assist torque and power to drive pump 1 and the diesel engine as well as any other pumps and devices on the same mechanical drive train.

The proposed system is expected to be able to effectively use the installed energy storage capacity thanks to the variable displacement pump-motor 2 used also as a pressure converter unit. Furthermore this same unit, principally a standard pump more typically used in closed loop hydrostatic drive transmissions, has good possibilities to control the charge-discharge process accurately without needed extra valves. However the dynamics of the pump-motor 2 as a component as well as its control approach will possibly pose challenges as the cycle time in a CTL harvester application is rather short, presumably less than two seconds. If the dynamic properties of pump-motor turn out to be inadequate - one possibility also worth studying could be to look for direct discharge or boost valve directly from the pressure accumulator to the system - bypassing pump-motor 2.

As downsizing is discussed - in addition to the diesel engine downsizing - also the original variable displacement pump 1 should be downsized as volume flow demand in the proposed system is divided for two pumps in place of earlier single pump.

Energy recovery functionality from different subsystems of the CTL harvester can also be discussed in the future as remarkable energy storage capacity is installed on the machine.

## 7 Conclusions

There seems to be promising possibilities for a hydraulic hybrid system to help the machine manufacturers with the power management of a CTL harvester machine.

Hydraulic accumulator seems to be a suitable energy storage for CTL harvester application because the overall nature of power peaks in the work cycle seem to be short-duration and high-power.

The dimensioning as well as control principle of the hydraulic hybrid system needs to be discussed in more detail in the future. It is clear that simulation can be a useful tool in order to determine the energy balance of various work cycles and machine configurations as well as to study the dynamical behavior of the pump-motor connecting the energy storage to the hydraulic system.

## 8 Proposed future work

Next phases of this ongoing study will include simulation of the hydraulic hybrid system of a harvester. Diesel engine model is possibly also needed to take into consideration and interaction with the hybrid power transmission system. Then, based on the simulations the system components can be dimensioned and chosen. System will need hydraulic energy storage like set of hydraulic accumulators as well as suitable over-center closed circuit pump-motor for connecting the energy storage to the hydraulic system. Simulation can also give important information about the dynamical requirements that are set by the work cycle to the pump-motor and its control. So far the efficiency of the components needed in the hydraulic hybrid have been more or less ignored and they have to be taken into account in future work.

After the simulations and component selection – possibility of test / prototype machine assembly is to be considered. With the actual machine real scale fuel economy measurements could be done in harvesting work and compared to a respective machine with traditional power system.

The right design of the energy storage, say hydraulic accumulators also need to be chosen carefully taking the performance, cost and room as well as placement constraints into account. For example the installation position of large bladder accumulators is more limited than the one of piston accumulators for example.

## References

- [1] N.N. *Directive 97/68/EC of the European Parliament and of the Council of 16 December 1997 on the approximation of the laws of the Member States relating to measures against the emission of gaseous and particulate pollutants from internal combustion engines to be installed in non-road mobile machinery. Official Journal L 059 , 27/02/1998 P. 0001 – 0086.* 1998.
- [2] Felix Prinz zu Hohenlohe. *Phlegmatisierung als Tugend in der Mobilhydraulik – Das Energiespeichersystem des Kranvollernters HSM 405H2.* Karlsruher Schriftenreihe Fahrzeugsystemtechnik 3. Fachtagung - Hybridantriebe für Arbeitsmaschinen. Karlsruhe, 2011.
- [3] L.Lundström, *Electrically propelled vehicle,* International Patent Application WO2005/047042, 2005.
- [4] J. Morinaga, T. Kawaguchi, H. Inoue. *Power generation control method of hybrid construction machine and hybrid construction machine,* US Patent 8,207,708B2, 2012.
- [5] R. Späth, T. Landmann, D. Boehm. *Energierückgewinnungskonzepte bei Hydraulikbaggern.* 5. Fachtagung Baumaschinentechnik 2012. 2012.
- [6] K. Einola, V. Rintamäki. *Method for controlling a power source of a forest machine,* US Patent 7,802,595B2, 2010.
- [7] J. Järvinen, O. Hankamäki, P. Karjalainen. *A Method in controlling an engine of a forest machine and a forest machine.* International Patent Application WO03/096794, 2003.
- [8] W. Sun, T. Virvalo. *Simulation study on a hydraulic-accumulator-balancing energy-saving system in hydraulic boom. Proceedings of the 50<sup>th</sup> National Conference on Fluid Power.* March 16-18 2005, Las Vegas, Nevada USA pp. 371-381.
- [9] N.N. Komatsu Ltd. *Press Release 2008/05/13.* 2008. Komatsu Corporate Communications. Retrieved 25.3.2013 from: <http://www.komatsu.com/CompanyInfo/press/2008051315113604588.html>
- [10] Jönsson A. *Weg vom Öl, Forstpraxis.de, Forst & Technik* 21.01.2013. 2013. Retrieved 25.3.2013 from: <http://www.forstpraxis.de/weg-vom-oe>
- [11] N.N. ProSilva Plc. *Press Release 31.8.2013.* Finland. Retrieved 25.3.2013 from: <http://www.prosilva.fi/images/stories/pdf/pressrelease.pdf>
- [12] Rydberg K-E. *Energy Efficient Hydraulic Hybrid Drives. The 11th Scandinavian International Conference on Fluid Power.* Linköping, Sweden June 2-4. 2009. Linköping University, Department of Management and Engineering.
- [13] N.N. Mercedes-Benz UK Ltd. *Press release 03-JAN-2013.* United Kingdom. Retrieved 25.3.2013 from: <http://www.mercedes-benz-media.co.uk/doc/2367/70121mer.doc>

- [14] Abebayo B. *Productivity and cost of Cut-to-Length and Whole-Tree harvesting in a mixed-conifer stand*. July 2006. University of Idaho. USA.
- [15] J. Inberg, J. Mattila, T. Virvalo. *Harvester boom tip acceleration control during a crosscutting – Theoretical background*. International Journal of Forest Engineering, Volume 13, Number 1. 2002 . Tampere University of Technology, Finland.
- [16] N.N. Hydac International GmbH. *Hydraulic accumulators in hybrid technology*. E 10.140.0/05.12. Retrieved 25.3.2013 from: [www.hydac.com](http://www.hydac.com)
- [17] N.N. Skogforsk. *StanForD – Listing of variables by category, Version 2012-04-18*. Retrieved 27.4.2013 from: [http://www.skogforsk.se/PageFiles/60712/AllVarGrp\\_ENG\\_120418.pdf](http://www.skogforsk.se/PageFiles/60712/AllVarGrp_ENG_120418.pdf)
- [18] P. Achten, S. Eggenkaemp, V. Georges. *THE E-HYDRID*. – The Twelfth Scandinavian International Conference on Fluid Power, May 18-20, 2011, Tampere, Finland.
- [19] N.N. Caterpillar Inc. *Press release 15-APR-2013. CAT® 336E H Hydraulic Hybrid Excavator Delivers No-Compromise, Fuel-Saving Performance*. Retrieved 27.4.2013 from: <http://www.cat.com/cda/layout?m=343975&x=7&id=4375050>
- [20] N.N. PSA Peugeot Citroen. Dossier de Presse 22.1.2013. *Hybrid Air – an innovative petrol full-hybrid solution*. Retrieved 27.4.2013 from: [http://www.psa-peugeot-citroen.com/sites/default/files/content\\_files/press-kit\\_hybrid-air\\_en.pdf](http://www.psa-peugeot-citroen.com/sites/default/files/content_files/press-kit_hybrid-air_en.pdf)
- [21] N.N. Eaton Corporation. *Hydraulic Launch Assist Refuse Truck*. 2009. Retrieved 27.4.2013 from: [http://www.eaton.com/ecm/groups/public/@pub/@eaton/@hyd/documents/content/ct\\_234114.pdf](http://www.eaton.com/ecm/groups/public/@pub/@eaton/@hyd/documents/content/ct_234114.pdf)



# Mobile Systems 2



# **Investigation and Energetic Analysis of a Novel Hydraulic Hybrid Architecture for On-Road Vehicles**

Michael Sprengel and Monika Ivantysynova

Dept. of Mechanical Engineering, Purdue University  
225 S. University Street, West Lafayette, IN 47907, USA  
E-mail: msprengel@purdue.edu, mivantys@purdue.edu

## **Abstract**

Hydraulic hybrid transmissions in on-road vehicles have been proven to significantly reduce fuel consumption. Existing hydraulic hybrid transmissions have shown fuel savings of 30-50% [1] with higher savings predicted when using advanced architectures [2]. However while these results are promising there exists room for improvement. Consider the series hybrid architecture which is currently the most common full hydraulic hybrid configuration. This system requires over-center units which increase expense and are relatively uncommon especially for high performance bent axis units. Series hybrids may also possess a synthetic feel due to the high compliance inherent in their accumulators. Further efficiency suffers as the hydraulic units in series hybrids are often forced to operate at high pressures and low displacements. A novel hydraulic hybrid configuration is analyzed in this paper which may reduce costs, improve response, and increase efficiency under certain conditions. An automatic transmission, a series hydraulic hybrid, and the novel blended hybrid architecture were simulated for a class II truck and fuel consumption rates compared. Dynamic programming was used to optimally control all three transmissions thereby removing the effect of controller design of fuel consumption. Simulation results show a 44.8% increase in fuel efficiency for the series hybrid and a 37.0% increase with the proposed system architecture. While the proposed architectures currently lags the series hybrid in fuel economy, there exists sufficient benefits to merit further studies.

**Keywords:** hydraulic hybrids, blended hybrid, dynamic programming

## **1 Introduction**

In a world of rapidly expanding population and diminishing oil reserves, increasing the efficiency of on-road vehicles is now more of a priority than ever. One approach that has shown considerable potential is vehicle hybridization through a hydraulic hybrid transmission. Existing hydraulic hybrid transmissions have shown fuel savings of 30-50% [1] with higher savings predicted when using advanced architectures [2]. Further research has shown that the benefits gained from hydraulic hybridization increase as vehicle mass grows due to the increased availability of braking energy [3].

Today hydraulic hybrid transmissions can be grouped into three main categories: parallel, series, and power split. And while each of these architectures has advantages in specific applications, there exists room for improvement. Consider the series hybrid, currently the most popular architecture for full hybrids. This transmission requires over-center units which are less common and more expensive than non over-center units and especially true of the more efficient bent axis variety. Series hybrids are also often forced to operate inefficiently at high pressures and low displacements due to the accumulator's state of charge. Another drawback of

series hybrids is the potential for a "synthetic" or "spongy" feel which becomes more pronounced as vehicle, and consequently accumulator size, increases. This spongy feel originates in the relationship between maximum wheel torque and current system pressure. In order to increase system pressure, more flow must enter the accumulator than exits. In series hybrids a considerable delay may be felt in achieving desired wheel torque when system pressure is below what is required resulting in a spongy feel. This inherent delay in increasing system pressure is in contrast to hydrostatic transmissions which increase pressure virtually instantaneously, a property that forms the basis for a novel system architecture presented in this paper.

In order for a new transmission to gain acceptance it must possess a similar feel and response to current systems [1]. To improve response, i.e. stiffness, to that of a mechanical transmission a new hydraulic hybrid architecture was created. This Blended Hybrid is so named for the blending of a hydrostatic transmission with a parallel hybrid. Because fuel economy is of principle concern, this paper will focus on overall vehicle efficiency. Simulation models have been created of a conventional automatic transmission, a series hybrid transmission, and the new blended hybrid and fuel consumption rates compared on a standard driving cycle.

Dynamic programming was used to optimally control all three transmissions thereby removing the effect of controller design of fuel consumption and ensuring a fair comparison between all three transmission architectures.

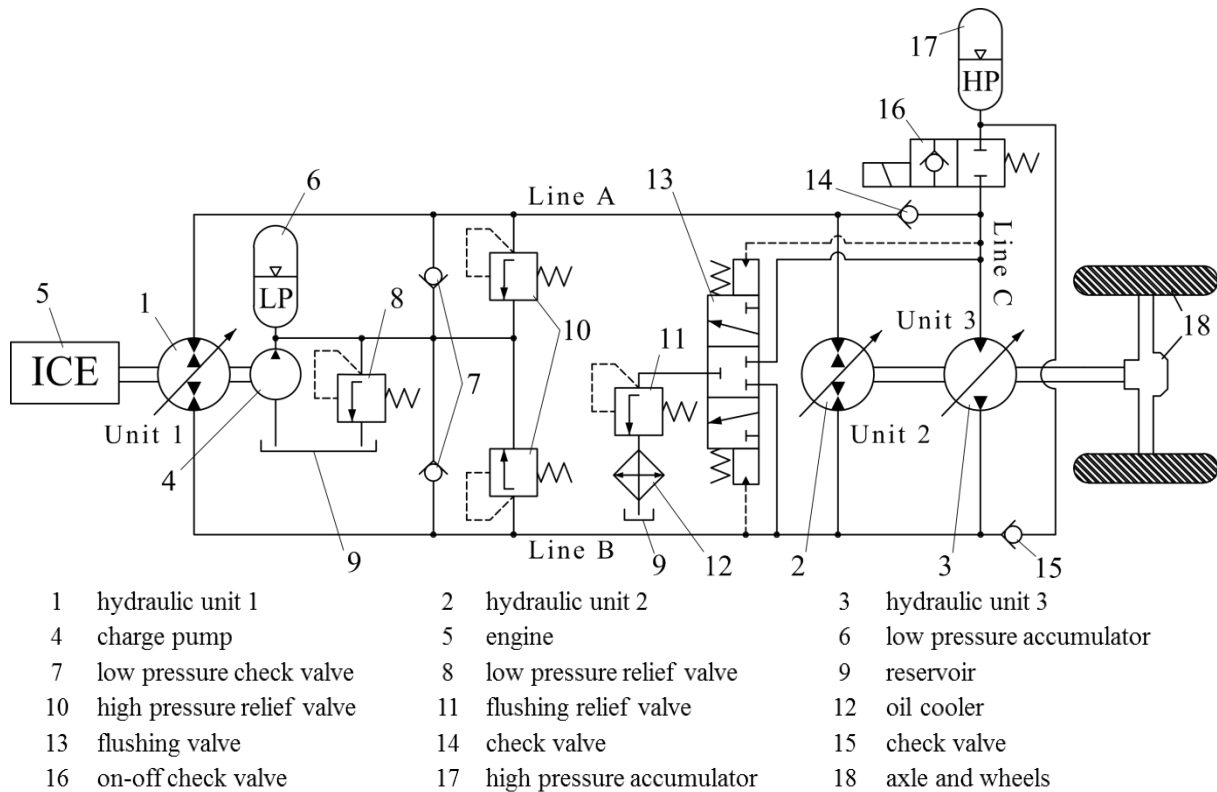


Figure 1: Blended hybrid circuit

## 2 Blended Hybrid

A detailed description of the blended hybrid architecture was first proposed by Sprengel and Ivantysynova in [4]. A schematic of the blended hybrid is located in fig. 1. The blended hybrid is in essence a hydrostatic transmission with an additional unit attached to the transmission output shaft. A series of check valves connects this third unit to either Unit 1 thereby increasing the hydrostatic transmission's displacement, or to a high pressure accumulator which allows for secondary control of the unit. An additional check valve connects Line B to the high pressure accumulator while braking thereby permitting energy recovery without the need for over-center units.

The blended hybrid can operate in several distinct modes:

### 2.1 Forward driving without using the high pressure accumulator

The engine provides power to Unit 1 which supplies flow to Line A. With on-off check valve (16) closed, check valve (14) opens and connects Line C to Line A. Both Units 2 and 3 use this flow to rotate at a speed determined by a combination of their displacement. In effect both units operate as a single motor.

### 2.2 Forward driving using the high pressure accumulator

With on-off check valve (16) enabled, Line C is exposed to the high pressure accumulator's (17) pressure. As long as the pressure in Line C is higher than Line A, check valve (14) remains closed. Unit 3 is then able to use energy from the accumulator to supply torque to the wheels. Power can also be supplied from the engine by increasing Unit 1's displacement above zero. Flow from Unit 1 is then used to turn Unit 2. Pressure in Line A is a function of Unit 2's displacement and the resistive load on the wheels minus the torque contribution made by Unit 3. If pressure in Line A exceeds that of the high pressure accumulator, check valve (14) opens and on-off check valve (16) closes causing both Units 2 and 3 to behave as a hydrostatic transmission.

### 2.3 Braking while in forward motion

While braking high pressure automatically switches from Lines A and C to Line B (a feature inherent of hydrostatic transmission). Flow from Units 2 and 3 in Line B can leave through Unit 1, thereby powering parasitic loads, or through check valve (15). Pressure in Line B is a function of flow between all three hydraulic units. If flow from Units 2 and 3 exceeds that removed by Unit 1, pressure will rise. When

the pressure exceeds that of the high pressure accumulator, check valve (15) opens allowing flow from Units 2 and 3 into the high pressure accumulator.

### 2.4 Reverse operation

To reverse Unit 1 moves over-center and supplies flow to Line B. Unit 2 then uses this flow to drive the wheels. If Unit 2 requires a pressure in Line B higher than that of the high pressure accumulator, check valve (15) opens and flow from Unit 1 is used to charge the accumulator until a suitable pressure for Unit 2 is achieved. When braking in reverse high pressure switches to Line A and can be used to power patristic loads on the engine or pass through relief valve 10.

## 3 Investigation Vehicle

A class II pickup truck was used as a base vehicle in which to test the three transmissions. Vehicle parameters can be found in tab. 1.

Table 1: Investigation vehicle parameters

Engine:	225 kW	Vehicle mass:	2525 kg
Axle ratio:	3.55:1	Tire rolling radius:	0.364 m
Frontal area:	3.6 m <sup>2</sup>	Coefficient of drag:	0.416
Rolling resistance:	0.01		

Simplifications and assumptions were made in all three transmission models to either remove components that were not directly related to this paper’s investigation or estimate the values of parameters which were not available. Modifications to all three models include the use of an engine map from a similarly size, although different, engine. Additionally all auxiliary loads on the engine such as the alternator and water pump were omitted.

It should be noted that the authors’ purpose in this paper is not to predict fuel economy for a given transmission in the reference vehicle, but instead use the results to fairly compare all three transmission against each other. As such, simplifications which have been made hold valid because they have been applied to all three transmissions equally.

### 3.1 Automatic Transmission

An automatic transmission is the style of transmission typically found in class II pickup trucks and will serve as a baseline for comparing the fuel consumption rates of the two hybrid transmissions. A schematic of the automatic transmission is located in fig. 2.

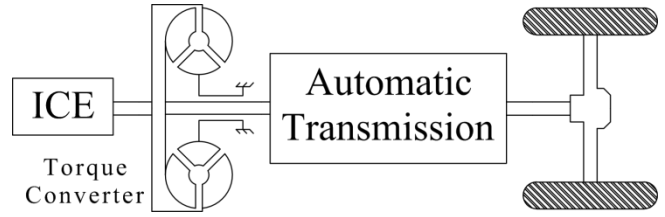


Figure 2: Automatic transmission architecture

Gear ratios for the automatic transmission are located in tab. 2.

Table 2: Automatic transmission parameters

1 <sup>st</sup>	4.17:1	2 <sup>nd</sup>	2.34:1
3 <sup>rd</sup>	1.52:1	4 <sup>th</sup>	1.14:1
5 <sup>th</sup>	0.86:1	6 <sup>th</sup>	0.69:1

Due to a lack of information the torque converter was modeled after a torque converter from a similarly sized vehicle. A lock-up clutch was not included in the torque converter model which would serve to rigidly couple the impeller and turbine. Additionally the hydraulic pump for the automatic transmission has been omitted.

### 3.2 Series Hybrid

A series hybrid with two units connected to the output shaft was used for the presented research study. This dual configuration is common in series hybrids and allows for a better comparison between it and the blended hybrid. A schematic of the series hybrid is located in fig. 3.

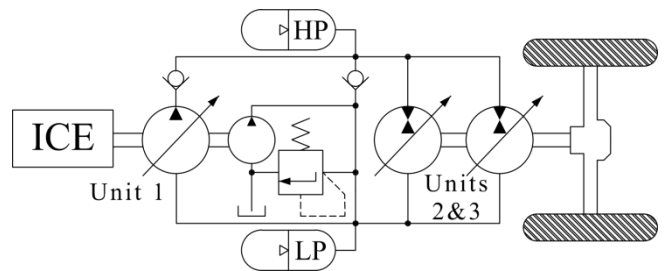


Figure 3: Series hybrid architecture

Parameters for the series hybrid are located in tab. 3.

Table 3: Series hybrid transmission parameters

Unit 1:	65 cc	Unit 2:	45 cc
Unit 3:	45 cc	Charge pump:	10 cc
Max pressure:	360 bar	Low pressure:	10 bar
HP accumulator pre-charge:	100 bar	HP accumulator volume:	30 l
HP accumulator min pressure:	130 bar	Polytropic coefficient:	1.3

Unit 1 was modeled using a 42 cc swashplate style unit while Units 2 and 3 were based on a 110 cc bent axis unit. Linear scaling laws were applied to all three units' empirically derived loss models.

### 3.3 Blended Hybrid

System parameters for the blended hybrid were kept as close to the series hybrid as practical for comparison purposes. While both hybrid architectures may benefit from somewhat different sizing's, by maintain identical unit sizes any differences in fuel economy can be attributed exclusively to differences in their architectures.

Parameters for the blended hybrid are located in tab. 4.

Table 4: Blended hybrid transmission parameters

Unit 1:	65 cc	Unit 2:	45 cc
Unit 3:	45 cc	Charge pump:	10 cc
Max pressure:	360 bar	Low pressure:	10 bar
HP accumulator pre-charge:	100 bar	HP accumulator volume:	30 l
HP accumulator min pressure:	130 bar	Polytropic coefficient:	1.3

## 4 Reference Cycle

All three transmissions were simulated using the industry standard UDDS driving schedule seen in fig. 4.

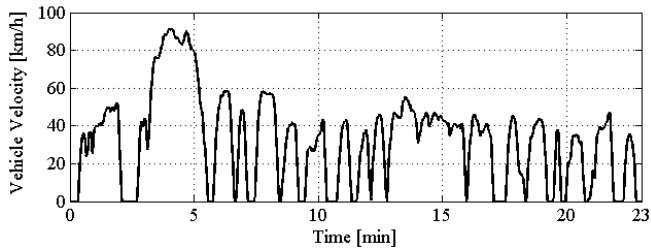


Figure 4: UDDS driving schedule

## 5 System Modeling

The transmissions were modeled in Matlab Simulink using governing equations.

Engine dynamics are modeled as a force balance between combustion torque, inertia, and load torque.

$$J_{\text{eng}} \dot{\omega}_{\text{eng}} = u_{\text{eng}} M_{\text{eng,max}}(\omega_{\text{eng}}) - M_1 \quad (1)$$

where  $J_{\text{eng}}$  is the engine's inertia,  $\dot{\omega}_{\text{eng}}$  is the engine's acceleration,  $u_{\text{eng}}$  is the throttle,  $M_{\text{eng,max}}(\omega_{\text{eng}})$  is the engine's wide open throttle curve, and  $M_1$  is Unit 1's torque or the torque converter's torque depending on the transmission. The engine's wide open throttle (WOT) curve and fuel consumption map are based on measured data for a

201 kW engine which has been scaled up to 225 kW. Friction is included within the engine's WOT curve and therefore not considered separately.

Vehicle dynamics are modeled as a force balance between propulsion torque provided by the driveline and the load torque generated by vehicle's inertia, rolling resistance, and aerodynamic drag.

$$m_{\text{veh}} r_{\text{roll}}^2 \dot{\omega}_{\text{wheel}} = M_{\text{axle}} - (F_{\text{aero}} + F_{\text{roll}}) r_{\text{roll}} \quad (2)$$

where  $m_{\text{veh}}$  is the vehicle's mass,  $r_{\text{roll}}$  is the tire's dynamic rolling radius,  $\dot{\omega}_{\text{wheel}}$  is the wheel's acceleration,  $M_{\text{axle}}$  is the torque provided to the wheels by the axle,  $F_{\text{aero}}$  is the vehicle aerodynamic drag, and  $F_{\text{roll}}$  is the tire's rolling resistance.

The torque converter is modeled using a K-Factor modeling approach [6]. Torque on the engine from the impeller is calculated using eq. (3). While torque on the transmission from the turbine is calculated using eq. (4).

$$M_{\text{eng}} = M_{\text{ratio}} \left( \frac{\omega_{\text{trans}}}{\omega_{\text{eng}}} \right) \cdot \left( \frac{\omega_{\text{eng}}}{K_{\text{fact}} \left( \frac{\omega_{\text{trans}}}{\omega_{\text{eng}}} \right)} \right)^2 \quad (3)$$

where  $M_{\text{eng}}$  is the torque on the engine,  $M_{\text{ratio}}$  is a torque converter characteristic and a function of the torque converter's turbine speed  $\omega_{\text{trans}}$  and the impeller speed  $\omega_{\text{eng}}$ . The torque converter's second characteristic parameter is  $K_{\text{fact}}$  and also a function of  $\omega_{\text{trans}}$  and  $\omega_{\text{eng}}$ .

$$M_{\text{trans}} = \left( \frac{\omega_{\text{eng}}}{K_{\text{fact}} \left( \frac{\omega_{\text{trans}}}{\omega_{\text{eng}}} \right)} \right)^2 \quad (4)$$

The automatic transmission is modeled as a set of gear ratios using eq. (5) and (6).

$$M_{\text{prop}} = M_{\text{trans}} \zeta_i \eta_{\text{trans}} \quad (5)$$

where  $M_{\text{prop}}$  is the torque on the propeller shaft,  $M_{\text{trans}}$  is the torque from the transmission,  $\zeta_i$  is the current gear ratio of the transmission, and  $\eta_{\text{trans}}$  is the transmission efficiency.

$$\omega_{\text{prop}} = \frac{\omega_{\text{trans}}}{\zeta_i} \quad (6)$$

Equation (6) provides the propeller shaft speed  $\omega_{\text{prop}}$ , the transmission speed  $\omega_{\text{trans}}$ , and the current transmission gear ratio  $\zeta_i$ .

Similarly the axle is modeled using eq. (7) and (8).

$$M_{\text{axle}} = M_{\text{prop}} \zeta_{\text{axle}} \eta_{\text{axle}} \quad (7)$$

where  $M_{\text{axle}}$  is the axle torque,  $M_{\text{prop}}$  is the propeller shaft torque,  $\zeta_{\text{axle}}$  is the axle ratio, and  $\eta_{\text{axle}}$  is the axle efficiency.

$$\omega_{\text{axle}} = \frac{\omega_{\text{prop}}}{\zeta_{\text{axle}}} \quad (8)$$

where  $\omega_{\text{axle}}$  is the axle speed,  $\omega_{\text{prop}}$  is the propeller shaft speed, and  $\zeta_{\text{axle}}$  is the axle ratio.

The hydraulic units are modeled using governing equations and empirically derived loss models. Effective unit flow is given by:

$$Q_{\text{eff}} = \frac{V \omega \beta}{2\pi} \pm Q_s \quad (9)$$

where  $Q_{\text{eff}}$  is the effective flow,  $V$  is the unit displacement,  $\omega$  is the unit speed,  $\beta$  is the percentage of maximum unit displacement, and  $Q_s$  is the empirically derived leakage.

Effective torque is given by:

$$M_{\text{eff}} = \frac{V \Delta p \beta}{2\pi} \pm M_s \quad (10)$$

where  $M_{\text{eff}}$  is effective torque,  $V$  is the unit displacement,  $\Delta p$  is differential pressure,  $\beta$  is the percentage of maximum unit displacement, and  $M_s$  is the empirically derived torque losses.

Pressure build up in the lines is calculated using:

$$\Delta \dot{p} = \frac{1}{C_H} (\Delta Q) \quad (11)$$

where  $\Delta \dot{p}$  is the change in pressure,  $C_H$  is the hydraulic capacitance, and  $\Delta Q$  is the change in fluid volume within the line.

Accumulator capacitance is given by:

$$C_{\text{accu}} = \frac{V_0}{n} \left( \frac{P_0}{\Delta p^{n+1}} \right)^{\frac{1}{n}} \quad (12)$$

where  $C_{\text{accu}}$  is the accumulator's capacitance,  $V_0$  is the initial gas volume,  $n$  is the polytropic coefficient,  $p_0$  is the pre-charge pressure, and  $\Delta p$  is the change in pressure.

## 6 System Control

How a transmission is controlled has a major impact on its fuel economy. A poor system architecture with a good control scheme can outperform a superior system architecture with a substandard controller, thereby obscuring which system is truly better. One means of counteracting this problem is to optimally control the system essentially removing control as a factor affecting fuel economy [7]. In this paper the authors have used Dynamic Programming (DP) to optimally control all three transmission architectures.

### 6.1 Dynamic Programming

Dynamic programming is a powerful technique for solving dynamic optimization problems. DP's strength lies in its ability to easily handle non-linear dynamics and constrains while insuring a global optimal solution is reached. DP is based on the principle of optimality as proposed by Bellman in [5]: "An optimal policy has the property that, whatever the initial state and optimal first decision may be, the remaining decisions constitute an optimal policy with regard to the state resulting from the first decision".

Discrete time Dynamic Programming utilizes a state space modeling approach and requires both the continuous time and state spaces to be discretized. The granularity by which the system is divided has a direct impact on both solution accuracy and computational expense [8]. And while DP ensures a global optimal control strategy, it only holds true down to the level the system is discretized. Computational expense is a key drawback of DP which can be attributed to the "Curse of Dimensionality". As the number of states variables and their discretization increases, the required computation expense grows exponentially.

While DP's computational expense grows exponentially with the number of states, it grows linearly with the number of time steps to be simulated. However a caveat applies to the previous statement. DP requires that a state be capable of fully transitioning from one state to another during a single time step. If not, a state once inadmissible will remain inadmissible until it can fully project to an admissible state. A smaller DP time step reduces flow into the accumulator and consequently limits the maximum change in pressure. To satisfy the previously mentioned requirement, as the DP time step decreases the accumulator pressure discretization must proportionally increase. Balancing these requirements a one second primary DP time step was used in this paper.

Two distinct time steps and a solver were employed within the DP algorithm. First optimal controls were evaluated and held constant for the aforementioned one second primary DP time step. However one second is too long of a time step

for accurate integration of rapid system dynamics. Therefore a 0.25 second simulation time step was used to increase numerical accuracy. Finally the differential equations were solved using Heun's Method (ODE2) which contains an internal time step of 0.125 seconds. The two time steps and solver were chosen to balance solution accuracy, numerical accuracy, and computational expense.

Formulating the DP problem begins by creating a cost function to optimize. As fuel economy is the principle metric by which these three transmissions are being compared, the cost function to be minimized consists primarily of the fuel consumed during the drive cycle.

$$J_{N-k,N}^* = \min_{u_{k,i} \in U_k} \left[ \underbrace{g(X_{N-k}, U_{N-k})}_{\text{transitional cost}} + \underbrace{J_{N-k-1,N}^*(L(X_{N-k-1}, U_{N-k-1}))}_{\text{optimal cost from k-1 to final stage}} \right] \quad (13)$$

where  $J^*$  is the optimal cost,  $N$  is the number of stages,  $k$  is a stage counter,  $u$  is a control effort,  $i$  is a control space counter,  $U$  is the control space,  $g$  is the transitional cost function,  $X$  is the state space, and  $L$  is the cost to finish.

Constraint functions are included in the cost function to ensure the cycle is met. While required wheel torque is cycle defined, the torque applied by the transmission is unlikely to exactly match. Therefore a constraint function is applied which increases cost the further apart the required and actual torque are, up to a point where the control effort is considered inadmissible.

The cost function also includes certain penalty functions which act to shape system response. One example is a penalty function imposed on changing engine speed. This function discourages the DP algorithm from applying a high throttle at one time step, thereby efficiently storing energy in the engine's inertia, and then low throttle at the next time step dropping engine speed and recovering the stored energy. Care must be taken when crafting penalty functions that shape system control. Fuel economy is highest when the DP algorithm is unconstrained and free to operate as desired. However such operation may lead to control actions which are impractical or infeasible due to effects not captured in the model. Therefore the influence of penalty functions should be minimized to prevent obscuring control strategies which are valid but unorthodox.

## 6.2 System Modeling for Dynamic Programming

All three transmissions are modeled in Simulink and represented in the state space form. This approach is a departure from the more commonly applied method of modeling the system in lines of code. Using Simulink offers several benefits including many engineers increased comfort with graphical programming languages (an attribute which should not be over looked). Additionally many system models for which DP is well suited are already constructed in Simulink and converting these models into line of code is

a laborious and error-prone task. Finally Simulink features an advanced ODE solver which increases the fidelity of the simulation results.

Coupling Simulink to the DP driving algorithm requires using Simulink in a somewhat unconventional manner. The DP algorithm determines the current time step, states, and controls. Then the Simulink model is initialized at these states with the appropriate control efforts and simulated for a single time step.

Simplifications have been made to the Simulink models to reduce complexity and computational expense. The simplifications made are detailed below but generally involve either neglecting dynamics which are faster than the DP time step, or imposing certain deterministic properties.

Deterministic properties result from the assumption that the drive cycle is being tracked. Consequently the wheel speed is known at every instance in time. Similarly required wheel torque is calculated using the change in vehicle speed over the next time step along with other vehicle loads.

### 6.2.1 Automatic Transmission

The automatic transmission's state space representation is given by:

$$X \equiv \begin{bmatrix} \omega_{\text{eng}} \\ \omega_{\text{wheel}} \end{bmatrix} \quad U \equiv \begin{bmatrix} u_{\text{eng}} \\ i_{\text{gear}} \end{bmatrix} \quad (14)$$

where  $\omega_{\text{eng}}$  is the engine speed,  $\omega_{\text{wheel}}$  is the wheel speed,  $u_{\text{eng}}$  is the engine throttle, and  $i_{\text{gear}}$  is the transmission gear.

The reduced state space representation used in the DP algorithm is given in eq. (15).

$$X \equiv \begin{bmatrix} \omega_{\text{eng}} \end{bmatrix} \quad U \equiv \begin{bmatrix} \omega_{\text{eng,des}} \\ i_{\text{gear}} \end{bmatrix} \quad (15)$$

where  $\omega_{\text{wheel}}$  has been removed due to being cycle defined.

Engine throttle  $u_{\text{eng}}$  has also been replaced with the desired engine speed  $\omega_{\text{eng,des}}$ . This simplification has been made to reduce computational expense by decreasing the size of the throttle control mesh. Engine speed changes based on the difference between combustion and load torques (eq. (1)). Over a time step even a minor difference in the torques can lead to a significant change in engine speed. Due to the system's stiff nature the throttle would need to be highly discretized in order to correctly match required torque thereby significantly increasing computation expense.

A different approach is used in this paper in which the desired engine speed is the control input. An equation within the simulation model then calculates the required throttle based on the initial and desired engine speeds. This method remains valid because it is based only on the control input and current states. Therefore when the optimal control path

is eventually generated, the desired engine speed control will generate the same throttle input as was done during the recursive operation. This method of using feed forward control coupled with the control space is used in all three simulation models to overcome issues related to stiff systems and large time steps.

### 6.2.2 Series Hybrid

The low pressure system in the series hybrid is neglected (charge pump losses remain). Instead it is assumed that the low pressure line remains at 10 bar. Similarly the high pressure relief valve is ignored by saturating the high pressure at the high pressure relief valve's cracking pressure.

Pump dynamics are neglected with the pump's displacement being set by the DP algorithm. Pump dynamics are generally much faster than the DP time step so including these dynamics is unnecessary. Similarly engine throttle dynamics are much faster than the DP time step and are not included for any of the models.

The series hybrid's state space representation is given by:

$$X \equiv \begin{bmatrix} \omega_{\text{eng}} \\ \omega_{\text{wheel}} \\ p_{\text{acm}} \end{bmatrix} \quad U \equiv \begin{bmatrix} u_{\text{eng}} \\ \beta_1 \\ \beta_2 \\ \beta_3 \end{bmatrix} \quad (16)$$

where  $\omega_{\text{eng}}$  is the engine speed,  $\omega_{\text{wheel}}$  is the wheel speed,  $p_{\text{acm}}$  is the accumulator's pressure,  $u_{\text{eng}}$  is the engine throttle, and  $\beta_1, \beta_2, \beta_3$  are the percentage of maximum unit displacement for Units 1-3 respectively.

The reduced state space representation used in the DP algorithm is given in eq. (17).

$$X \equiv \begin{bmatrix} \omega_{\text{eng}} \\ p_{\text{acm}} \end{bmatrix} \quad U \equiv \begin{bmatrix} \omega_{\text{eng,des}} \\ \beta_1 \end{bmatrix} \quad (17)$$

where  $\omega_{\text{wheel}}$  has been removed due to being cycle defined.

As was done in the automatic transmission  $u_{\text{eng}}$  was replaced with desired engine speed  $\omega_{\text{eng,des}}$ . Required wheel torque is defined by the cycle, however the manner in which this torque is split between Units 2 and 3 is not. To reduce computational expense, especially for the blended hybrid, both units are controlled to provide 50% of the required torque. A feed forward controller within the Simulink model calculates the required Unit 2&3 displacement based on pressure, speed, and desired torque. If insignificant torque is generated the state is considered inadmissible.

### 6.2.3 Blended Hybrid

Modeling the blended hybrid in a form suitable for dynamic programming required a number of simplifications to be made. These simplifications were required due the stiff nature of the hydrostatic transmission and the presence of hydraulic logic elements (i.e. check and flushing valves).

First, as with the series hybrid, the low pressure system dynamics were neglected and assumed to maintain a 10 bar setting. Next only two pressure build-up equations were used: one for Line A, and one for the high pressure accumulator. Line C's pressure was set to either Line A's pressure or the HP accumulator's pressure depending on the on-off valve's position and related check valves' states. Line B's pressure was normally set to 10 bar unless both Line C was at 10 bar (due to the flushing valve) and the net flow between all three units in Line B was positive (i.e. braking). While these conditions were met Line B's pressure was set to the HP accumulator's pressure. This simplification assumes that Line B is infinitely stiff and therefore immediately transitions between 10 bar and the accumulator's pressure while braking. For an energetic comparison this is a valid assumption. Flow in and out of the two control volumes follows the same logic as the pressures.

The blended hybrid's state space representation is given by:

$$X \equiv \begin{bmatrix} \omega_{\text{eng}} \\ \omega_{\text{wheel}} \\ p_A \\ p_{\text{acm}} \end{bmatrix} \quad U \equiv \begin{bmatrix} u_{\text{eng}} \\ \beta_1 \\ \beta_2 \\ \beta_3 \\ u_{\text{enab}} \end{bmatrix} \quad (18)$$

where  $\omega_{\text{eng}}$  is the engine speed,  $\omega_{\text{wheel}}$  is the wheel speed,  $p_A$  is Line A's pressure,  $p_{\text{acm}}$  is the accumulator's pressure,  $u_{\text{eng}}$  is the engine throttle,  $\beta_1, \beta_2, \beta_3$  are the percentage of maximum unit displacement for Units 1-3 respectively, and  $u_{\text{enab}}$  is the on-off check valve's setting.

Hydrostatic transmissions are generally considered to be flow controlled, that is flow from Unit 1 must pass through Unit 2 and the system pressure is set by the wheel load. However numerically there is no difference between a HST and a series hybrid. The line's equivalent capacitance does not fundamentally change the system's nature. The conventional method of thinking can be explained by realizing flow control is only a deterministic control when an additional constraint that constant pressure be maintained is applied to the system. In order to increase pressure additional energy must be placed into the system. During normal operation only the engine, and not the wheels, can accomplish this. Therefore the displacement of Unit 1 should be a control variable and not a deterministic quantity.

Line A's stiffness does increase complexity when using Unit 1's displacement as a control variable. A displacement even several hundredths of a percent off of that required to maintain a constant pressure will significantly alter the system pressure over a single time step. Consequently applying a finite range of displacements (as done with the series hybrid) will never yield satisfactory results in the DP algorithm.

For the blended hybrid Unit 1's control variable indicated the desired pressure. The flow required to maintain the current Line A pressure was first calculated. Next the flow required to change Line A from its current pressure to the desired pressure was determined. This value was then added to the flow required to maintain the initial pressure. Finally a feed forward controller was used to calculate the required displacement of Unit 1.

The reduced state space representation used in the DP algorithm is given in eq. (19).

$$X \equiv \begin{bmatrix} \omega_{\text{eng}} \\ p_A \\ p_{\text{acm}} \end{bmatrix} \quad U \equiv \begin{bmatrix} u_{\text{eng}} \\ p_{A,\text{des}} \\ u_{\text{enab}} \end{bmatrix} \quad (19)$$

where  $\omega_{\text{wheel}}$  has been removed due to being cycle defined. As was done in the automatic transmission,  $u_{\text{eng}}$  was replaced with desired engine speed  $\omega_{\text{eng,des}}$  and  $\beta_2$  and  $\beta_3$  were removed and treated as deterministic quantities.  $\beta_1$  is also replaced with the previously discussed  $p_{A,\text{des}}$  which indicates desired Line A pressure.

### 6.3 Dynamic Programming Algorithm

Dynamic programming is a recursive algorithm which starts at the final stage to be simulated and steps backwards through time while projecting forwards. DP decomposes the optimal control problem into a series of one stage (time step) sub-problems; each containing the model's discretized state space representation.

Beginning at the final time step a series of control efforts are applied to each state within the stage. The goal of which is to determine the optimal control effort for a given state that minimizes the one stage sub problem's cost. At the final stage the sub problem's cost is equal to the transitional cost between the final stage and the final time. Included in the transitional cost is the fuel consumed during the time step along with any other constraint or penalty functions which were applied. After the optimal control efforts and cost have been determined for every state the DP algorithm steps backwards in time to the previous time step.

In the intermediate time step a similar process is performed to determine the optimal controls with one additional cost function. Along with the transitional cost, there is now a cost to finish. As the simulation model runs it determines the

amount of fuel consumed as well as the states at the end of the time step. These final states are projected onto the next stage and used to determine the cost to finish the entire cycle. It is precisely this idea of a cumulative cost function which is at the heart of DP and eliminates the need for full cycle enumeration.

DP's recursive method of stepping backwards though time repeats until the initial time step is reached. DP records the optimal control effort at every state but does not save where each state is projected. To determine the optimal path, control efforts, and fuel consumption, the simulation model is ran forward in time. Optimal controls at each state and time step are provided by look up tables generated through the recursive DP algorithm.

DP's computation expense is most clearly illustrated with the blended hybrid requiring over 35 billion dynamic simulations. Consequently any technique which decreases runtime is valuable. One approach taken was to use matrix operations whenever possible. MATLAB (MATrix LABoratory) is optimized for such operations which resulted in significant time savings compared against the commonly used method of nested loops. Simulink also benefits from matrix operations. Simulink requires significant overhead to initialize, consequently individually running each simulation would be infeasible. Instead the entire transmission model is placed within a repeating subsystem block in Simulink (proposed in [9]). An array is then created that contains all combinations of states and controls for a given time step and then subdivided into sets which contain ~500,000 simulations. Simulink is then run for each subset with all 500,000 simulations running simultaneously. Once complete, Simulink outputs an array containing the cost for each simulation run. Finally the DP algorithm records the minimum cost and respective control effort for each state, thereby generating the optimal control history. Another benefit of this approach is that each simulation subset is independent. Therefore each can be simulated concurrently on multiple processors using parallel computing which significantly reduces runtime.

Previous research using nested Matlab loops for performing DP on a series hybrid achieved a simulation rate of ~740 dynamic simulations per second [10]. Using the technique proposed in this paper simulation rates of up to 45,000 dynamic simulations per second were achieved using a single processor core.

## 7 Simulation Results

Dynamic programming determines the optimal control effort for every state during each time step. However it is the optimal control path and efforts which are of the most interest and presented in the results.

### 7.1 Automatic Transmission

An automatic transmission was modeled then simulated with dynamic programming for two functions. First simulation results provide a baseline by which to compare the two

hybrid transmissions. Second modeling the transmission and comparing fuel economy results with published values serves to validate the simulation model and methodology. Understandably the results were somewhat different due to optimal control and simplifications that have been made. However the relatively close correlation with published values seen in this paper indicates a sufficiently accurate model has been constructed.

Running the automatic transmission on the 7.45 mile UDDS cycle consumed 0.4838 gallons of fuel corresponding to a fuel consumption rate of 15.4 mpg (miles per gallon). Published measurements certified by the US Environmental Protection Agency for the investigation vehicle following the UDDS cycle yielded 17 mpg. It was expected that the DP approach would yield a better fuel consumption rate than the sub optimally controlled measured value. However a portion of this discrepancy can be attributed to using a fuel consumption map from an older, and presumably less efficient, engine. Additionally the lack of a lock-up clutch, and a control law prohibiting aiding torque from being placed on the engine (common to all three transmissions), also explain the reduced fuel economy. Regardless the simulated and published values are close enough to consider the simulation model and methodology reasonable.

Figure 5 shows a plot of the automatic transmission's vehicle speed, engine speed, throttle, and transmission gear.

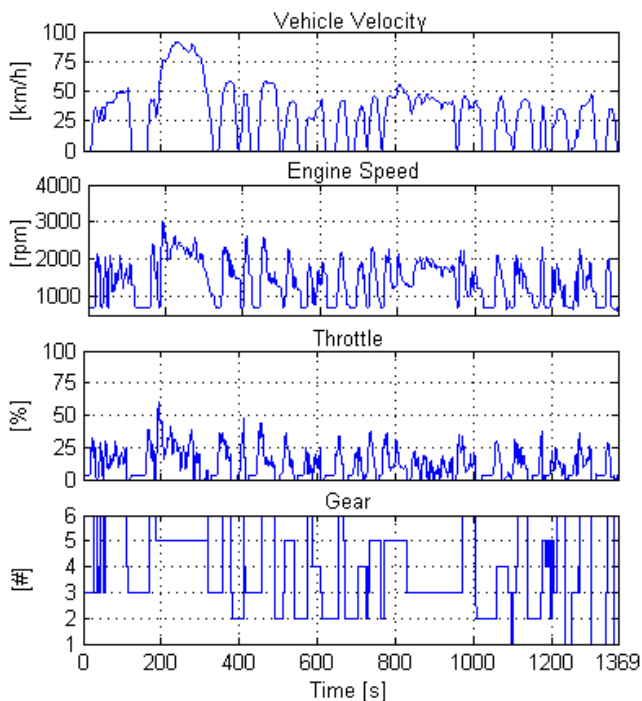


Figure 5: Automatic transmission DP results

It can be seen that the DP controller prefers to minimize engine speed by normally running in as high of a gear as possible. However the engine and wheels are linked by a mechanical ratio which restricts the engine's freedom of operation.

An engine operation map for the automatic transmission during the UDDS cycle is located in fig. 6. The white circles denote where the engine operated with their size proportional to the operation's duration. Contour lines indicate the engine's efficiency in terms of grams of fuel consumed per kWh. Like most gas engines the engine used in this paper is most efficient at low to medium speeds and medium to high throttle. However due to the finite gear ranges, and the nature of the torque converters operation, the automatic transmission's engine is often forced to operate in an inefficient manner. It is partially this poor engine management that allows the series hybrid to significantly outperform the baseline automatic transmission.

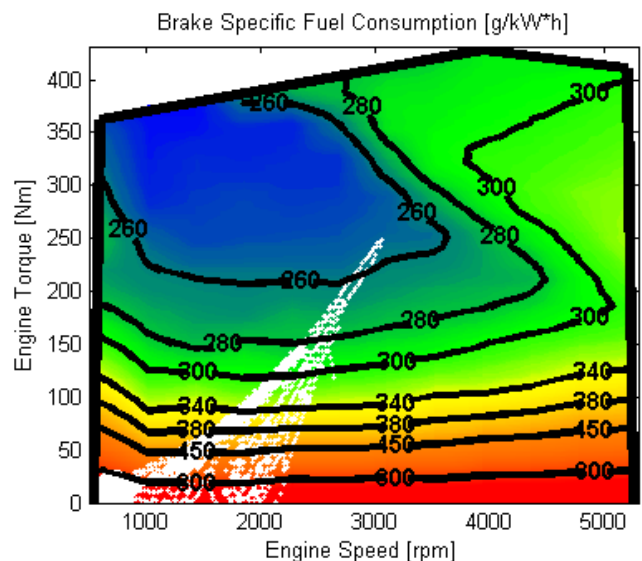


Figure 6: Automatic transmission engine operation map

## 7.2 Series Hybrid

Dynamic programming naturally determines the optimal control path for the series hybrid begins with a full accumulator. However because the fuel which would have been consumed to fill the accumulator is never accounted for, the resulting fuel economy would be artificially increased. Therefore both the series and blended hybrids are started with an empty accumulator and minimum engine speed.

During the UDDS cycle the series hybrid consumed 0.3341 gallons of fuel corresponding to a fuel consumption rate of 22.3 mpg. This represents an improvement of 44.8% over the baseline automatic transmission.

Figure 7 shows a plot of the series hybrid's vehicle speed, engine speed, throttle, accumulator pressure, and unit displacements. Clearly apparent are the differences in engine speed and throttle between the series hybrid and the automatic transmission. One of the series hybrids key advantages is the decoupling of the engine and wheel speeds. This permits increased control over engine management allowing the engine to operate in a more efficient manner.

It can be seen from fig. 7 that the series hybrid uses the entire range of accumulator pressures from 130 to 360 bar. The series hybrid's efficiency is directly related to the accumulator pressure with low pressures and high displacements being favored over high pressures and low displacements. However in order to recover energy while braking a certain minimum pressure is needed to provide the requisite braking torque. Dynamic programming has a priori knowledge of the future cycle which permits it run the accumulator at low pressures when possible. Before braking the DP algorithm will increase accumulator pressure to ensure full recovery of the available kinetic energy. Such a control strategy may be difficult to include in an implementable controller.

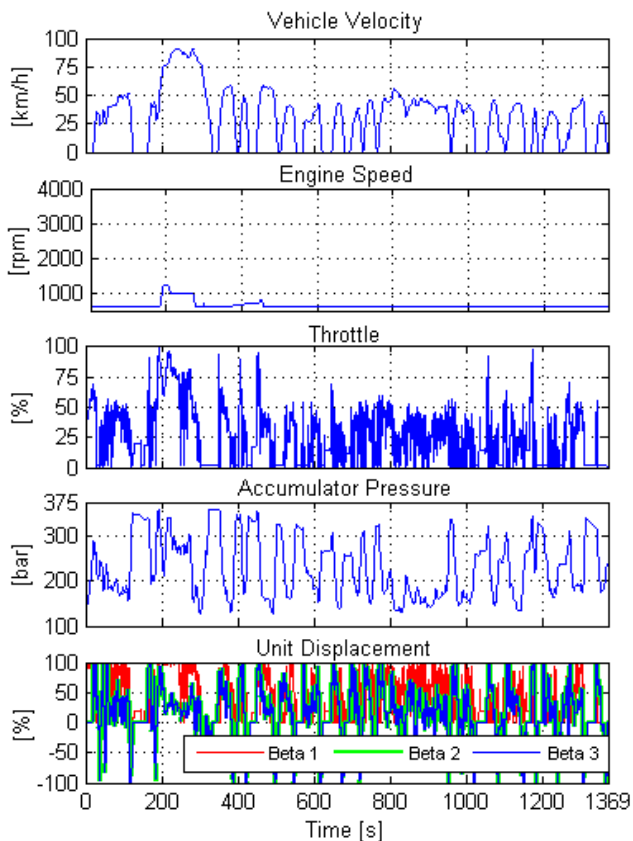


Figure 7: Series hybrid DP results

The series hybrid generally operates at the lowest allowable engine speed with a low to medium throttle (fig. 8). This is in stark contrast to the automatic transmission's operation and partially explains the series hybrids increase in fuel economy.

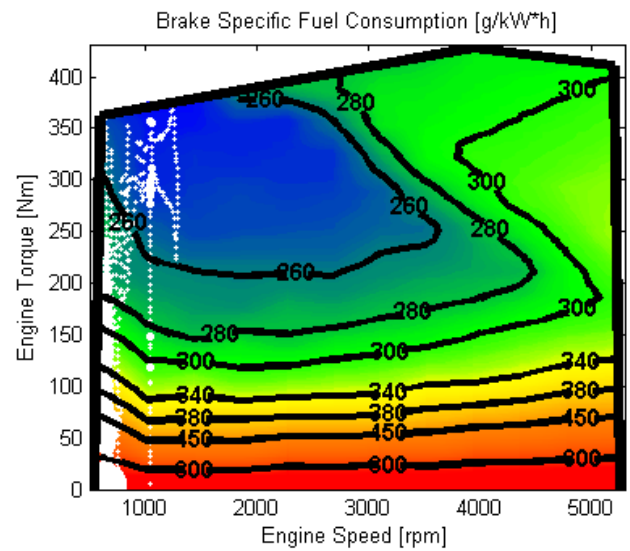


Figure 8: Series hybrid engine operation map

### 7.3 Blended Hybrid

Under the UDDS cycle the blended hybrid consumed 0.3526 gallons of fuel equating to a fuel consumption rate of 21.1 mpg. This represents a 37.0% improvement over the automatic transmission.

Figure 9 shows a plot of the blended hybrid operation during the UDDS cycle.

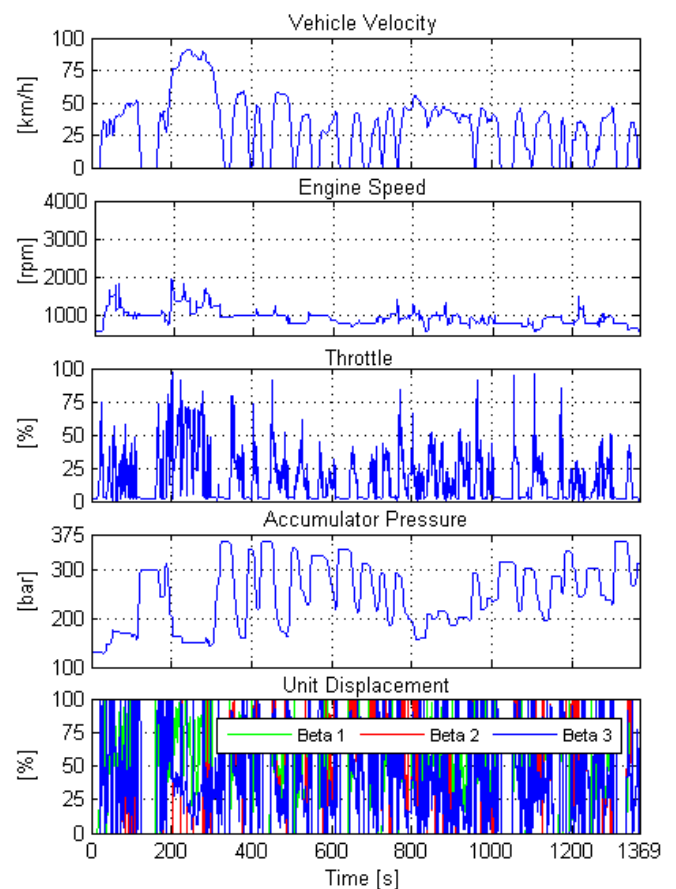


Figure 9: Blended hybrid DP results

The blended hybrid's accumulator maintains a generally higher pressure than the series hybrid. This is partially because the blended hybrid is not required to always operate at the accumulator's current pressure. Therefore there is not a need to increase efficiency by reducing pressure during extended periods of low torque requirement. The blended hybrid also maintains a higher minimum pressure to ensure all of the available braking energy is captured.

Unlike the series hybrid, the blended hybrid is not capable of increasing accumulator pressure while driving. This is due to a lack of a direct connection between Unit 1 and the accumulator. A characteristic which also prevents the transmission from storing excess energy from the engine in the accumulator. The diminished potential for engine management in the blended hybrid helps to explain the 5.4% decrease in fuel efficiency when compared to the series hybrid.

The blended hybrid's engine operation map is shown in fig. 10.

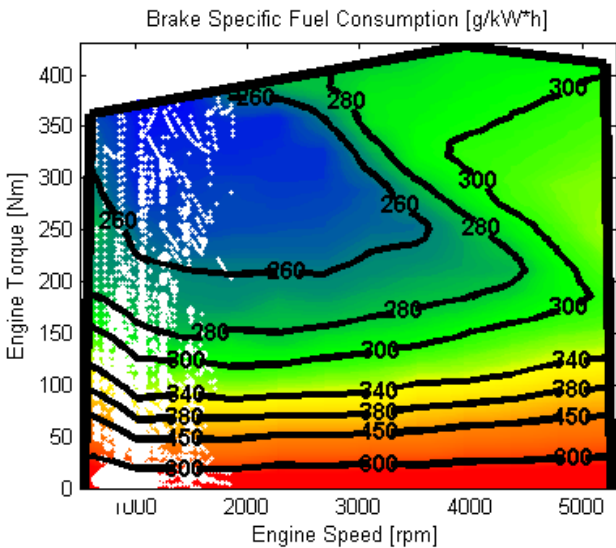


Figure 10: Blended hybrid engine operation map

A deeper understanding of the blended hybrid's operations can be gained by examining the braking and acceleration event shown in fig. 11. While braking both Units 2&3 are at Line B's (i.e. accumulator) pressure. Both units are also at the same displacement because of a control law in place which dictates both units provide 50% of the required torque. Around 728s the enabling valve opens and the vehicle begins to accelerate. Initially both Line's A & C are above the accumulator pressure and the transmission is operating in the HST mode. As the required torque decreases the pressures falls until Line's A & C are equal to the accumulator's pressure. At this point Unit 3 (Line C) connects to the accumulator and operates under secondary control while Unit 2 (Line A) remains connect to Unit 1 and operates as a stiff HST. At 746s the enabling valve closes and both Units 2 & 3 are once again operating as a HST, albeit at a pressure lower than is possible with the series hybrid.

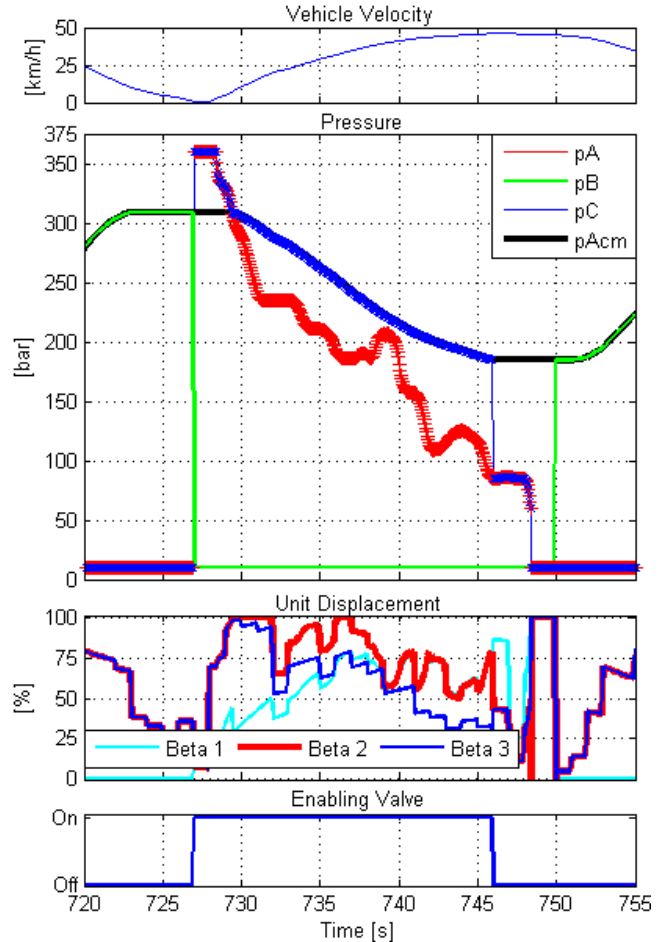


Figure 11: Detailed blended hybrid operation

Clearly apparent are the complexities of design and control which have not been fully explored through the optimal control study presented herein. There remains a question of the impact of sizing on the hybrid architectures. Both architectures will likely benefit from different unit sizes, accumulator sizes, and precharge pressures. There also remains a question of whether both Units 2 & 3 should be same size or would different unit sizes benefit the blended hybrid. In order to reduce computational expense by avoiding an additional control, the percentage of torque supplied by each unit was set to 50%. However the blended hybrid would likely benefit from being able to supply all of the required torque from the accumulator under certain circumstances. Finally there remains a question of how close an implementable controller can match each of these optimally controlled designs, a problem discussed in [11].

## 8 Conclusion

In this paper a novel architecture for a hydraulic hybrid transmission was presented. A class II pickup truck was used as a reference vehicle following the UDSS driving schedule. A baseline automatic transmission, a series hybrid, and the novel blended hybrid were modeled and simulated in the reference vehicle. Dynamic programming was then used to optimally control all three transmissions in order to remove control as a factor affecting fuel economy. The automatic transmission achieved a fuel economy of 15.4

mpg. The series hybrid reached 22.3 mpg which represents a 44.8% improvement over the baseline automatic transmission. Finally the blended hybrid achieved a fuel economy of 21.1 mpg which is 37.0% better than the automatic transmission.

While the blended hybrid achieved a fuel economy 5.4% lower than the series hybrid there remains a number of questions regarding sizing and implementable control of both architectures which will surely alter the efficiencies. Fuel economy, while important, is not the sole consideration. The blended hybrid architecture shows considerable potential in other areas over existing series hybrid configurations. The blended hybrid's stiff nature improves user response and feel to that of a traditional mechanical transmission. Removing the requirement for over-center units attached to the wheels lowers cost and permits the use of more bent-axis units. Finally the blended hybrid increases efficiency under certain lower power operations such as driving at a constant moderate speed. During this operation the line pressure can be reduced below the accumulator's minimum pressure, a behavior not possible with series hybrids.

## References

- [1] Johansson, A. and Ossyra, J.-C. 2010. Hydraulic Hybrid Transmission Design Considerations for Optimal Customer Satisfaction. *Proceedings of the 7th International Fluid Power Conference*. Aachen, Germany.
- [2] Stecki, J. and Matheson, P. 2005. Advances in Automotive Hydraulic Hybrid Drives. Proceedings of the 6th JFPS International Symposium on Fluid Power. Tsukuba, Japan.
- [3] Buchwald P., Christensen H., Larsen H., Pedersen P.S. 1979. Improvement of City Bus Fuel Economy Using a Hydraulic Hybrid Propulsion System – A Theoretical and Experimental Study. SAE Paper 790305, Warrendale, PA USA.
- [4] Sprengel, M. and Ivantysynova, M. Novel Transmission Configuration for Hydraulic Hybrid Vehicles. Proceedings of the International Sci-Tech Conference "Machine Dynamics and Vibro Acoustics", Samara, Russia, pp. 207 - 209. 2012.
- [5] Bellman R.E. 1957. *Dynamic Programming*. Princeton University Press, NJ, USA.
- [6] Kotwicki, A., 1982, "Dynamic Models for Torque Converter Equipped Vehicles," SAE Technical Paper 820393
- [7] Lin C., Kang J., Grizzle J.W. and Peng H. 2001. Energy Management Strategy for a parallel Hybrid Electric Truck. Proceedings of the 2001 American Control Conference, Arlington, VA USA.
- [8] Bertsekas, D.P., 1975. "Convergence of discretization procedures in dynamic programming," *Automatic Control, IEEE Transactions on* , vol.20, no.3
- [9] Liu, J. and Peng, H. 2006. "Control optimization for a power-split hybrid vehicle," American Control Conference.
- [10] Cross, M. 2011. Optimal Control: An Effective Method for Designing Hydraulic Hybrid Vehicles. M.S. thesis. Purdue University, West Lafayette, IN, USA
- [11] Wu, B., Lin, C. C., Filipi, Z., Peng, H., & Assanis, D. 2004. Optimal power management for a hydraulic hybrid delivery truck. *Vehicle System Dynamics* 42

# Development of Power Train of Hybrid Power Excavator

Hong Yao\*, Qingfeng Wang

State Key Lab of Fluid Power Transmission and Control/Zhejiang University, Yuquan Campus, Zhejiang, China

E-mail: [yaohong7901@hotmail.com](mailto:yaohong7901@hotmail.com), [qfwang@zju.edu.cn](mailto:qfwang@zju.edu.cn)

## Abstract

In this paper, a 20-ton prototype compound hybrid excavator is presented which includes assisting electric motor, swing electric motor, a super capacitor pack, an engine and negative flow hydraulic system. The energy-saving principle of hybrid excavator is introduced as well. The development rules of power train which include parameter design rules of key components and hierarchical structure of control strategy of hybrid power system are presented. By developing the electric swing control strategy and power management algorithm, experiments show that the developed hybrid power system can significantly improve the fuel economy of the excavator.

Key words: hybrid power, excavator, power train, swing system

## 1 Introduction

Energy is consuming up and pollution is more and more serious nowadays, so research on energy saving of hydraulic excavators has great significance because of their large application quantities, high energy consumption and bad exhaust. The efficiency of hydraulic excavators is only 22% [1], because of the lower efficiency of the engine and hydraulic system. To raise the system efficiency of excavators, hybrid power system, which is successfully applied in automobile industry, has been already introduced into construction machinery. In construction machinery industry, researchers also actively developed various kinds of construction machines based on hybrid concept. KOMATSU construction machinery company is the first one which promoted hybrid excavator into the market in 2008.

A lot of research work has been conducted in automobile industry, but those research achievements cannot be directly applied in the development of hybrid excavators because of the difference of working condition and load. However, only a few literatures on hybrid excavators which focus on the research of power train system configuration [2], simulation research [3] and control strategy [4,5,6] can be retrieved. Few reports on the development rules of hybrid excavators can be found.

In this paper, the development rules of parameters design and control strategy in hybrid excavator are presented. A 20-ton hybrid excavator is the design target, in which a compound hybrid power configuration is applied, a negative flow hydraulic system is adopted, the hydraulic swing motor is substituted by an electric motor and the super capacitor pack is used as an energy accumulator. According to the

typical work condition of heavy mode and the measured load profile, the key parameters design of the power train is proposed and a control strategy characterized by hierarchical structure is presented. Experiments show that the designed compound hybrid excavator can effectively reduce fuel consumption and emission.

## 2 Configuration and principle

Several kinds of power train architectures of hybrid excavator are presented in [6,7,8,9]. According to the power flow structure of drive train, the hybrid drive train can be classified into three categories such as parallel, series and compound type. The most popular structure is shown in fig. 1 and also adopted as the target excavator structure in this paper. The hybrid excavator includes an engine, a hydraulic pump connected to an output shaft of the engine, hydraulic actuators (bucket cylinder, arm cylinder, boom cylinder and traveling motors) driven by the hydraulic pump, a generator motor connected in parallel to an output shaft of the engine to perform both a generator function and a motor function, a swing motor driving the upper structure of the hybrid excavator, an electric storage device (super capacitor pack) which supplies and receives electric power to and from the generator motor and the swing motor, and a hybrid power controller for coordinating the entire power train composed of the engine, the hydraulic pump, electric actuators and the capacitor pack. The engine, engine assist motor, pump and super capacitor constitutes the parallel hybrid power train; the engine assist motor, swing motor and capacitor constitutes the serial hybrid power train. So this kind of power train is called compound hybrid power system.

The negative flow hydraulic system is adopted in this paper and shown in fig. 2. The pump displacement is controlled by

the negative flow pressure  $p_{m1}$ ,  $p_{m2}$ , pump output pressure  $p_1$ ,  $p_2$  and proportional valve pressure  $p_{f1}$ ,  $p_{f2}$ . The limit displacement of the pump is determined by  $p_{f1}$  and  $p_{f2}$  which are controlled by the current  $I$ . And the relationship of limit input torque and current is depicted in fig. 3.

Negative control metering valve PN1 and PN2 are placed between the control valve and the tank for reducing the loss of the discharge flow rate of the hydraulic pump1 and pump2 returning to the tank. Specifically, in a case where the hydraulic load is not in an operating state, said differently, there is no supplying the operating oil to the cylinders, the amount of the operating oil to be recovered to the tank without being used for the operation becomes great. In this case, because the oil passage is choked by the negative control metering valve PN1 and PN2, the negative control pressure  $P_{m1}$  and  $P_{m2}$  becomes higher than a predetermined value, the operating oil is supplied to the regulator to reduce the swash plate of the hydraulic pump. With this, when the hydraulic load is not in the operation state, the flow rate  $Q$  of the hydraulic pumps is decreased to restrict circulation of useless operating oil.

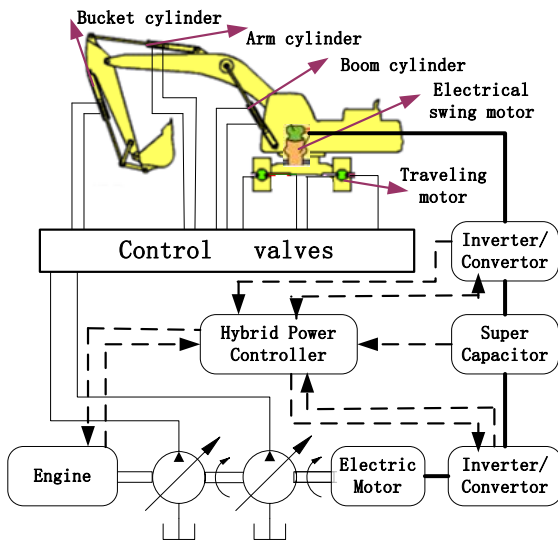


Figure 1: Configuration of hybrid powertrain

According to different working condition and requirements, excavators have various operation modes such as a heavy digging mode(H mode), a standard digging mode(S mode), and a finishing leveling mode(L mode). For different operation mode, excavators have different maximum output power. So the power output of the engine and hydraulic pumps are adjustable according to the operation mode.

The rotational speed of the engine is set by the engine controller which is mounted on the engine. Further, an electromagnetic proportional valve which controls the pressure  $P_{f1}$  and  $P_{f2}$ , is connected to pump regulators, and the regulators control the displacement of the hydraulic pumps. A pump control current  $I$  for adjusting the tilting angle of the swash plates of the hydraulic pumps is controlled by the hybrid power controller.

In the case of performing a light-load operation, the motor-generator is operated to generate power to charge the super capacitor pack using a portion of the engine output, while in the case of performing a heavy-load operation, electric energy is provided from the super capacitor to supplement the engine. At a time of a driving operation, the swing motor works in the motor operation and the super capacitor pack supplies energy to the swing motor to drive the upper structure. At a time of braking revolution, the controller switches the swing motor into the power generating operation and inertia energy of the upper structure is regenerated and charged into the super capacitor pack. In such a way, the load exerted on the engine is leveled into the economical area and kinetic energy of upper structure is regenerated, so the hybrid excavator should work more efficiently than hydraulic excavators. But the system is also more complex, so how to design the key parameters of components and control strategy is a puzzling problem.

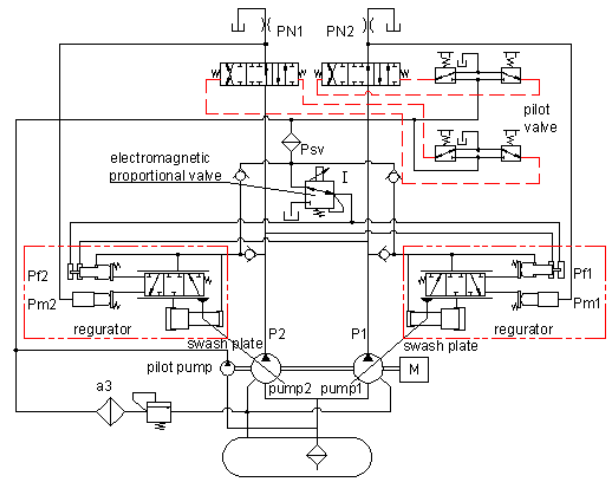


Figure 2: Negative flow hydraulic system

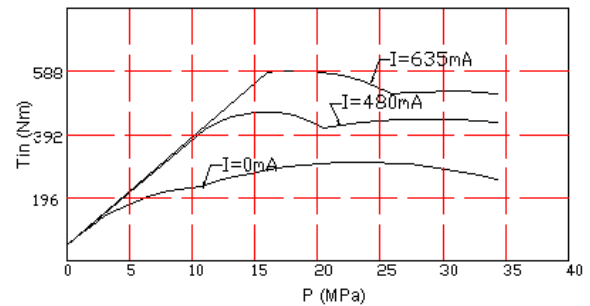


Figure 3: Relationship of torque and pressure of pump

### 3 Key parameters design

Fig. 4 is a graph showing a transition of absorption power of the hydraulic pump in one cycle when “an excavating and loading operation” in which excavated earth and sand are rotated and loaded into a damp vehicle is carried out in “H mode”. The red solid line is the total power output used for boom, arm, bucket, and swing motor; and the blue dash line is the power output for driving the upper structure. The characteristics of the load profile: (1) Load change is very sharp as compared with a passenger car; (2) Work capacity

of the excavator is not fully utilized at all time; (3) Kinetic energy of upper structure is substantial and occupies 12% of the total energy. How to design the key parameters according to the load profile is described below.

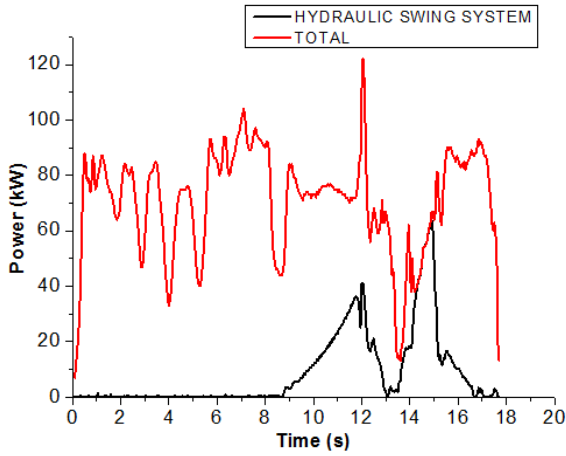


Figure 4: Load profile of 20-ton hydraulic excavator

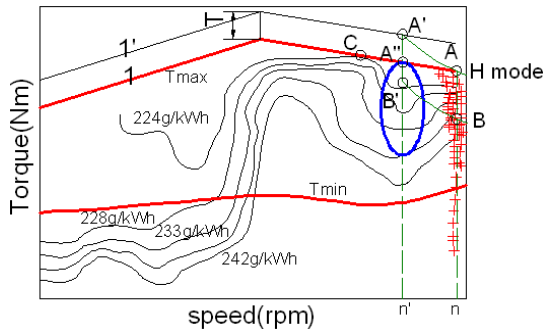


Figure 5: Operation points of engine

### 3.1 Engine

Engines of excavators are usually constantly rotated at a predetermined speed which set by operators manually according to the excavating job at hand. Usually, there are five engine speeds or five operating modes. It should be emphasized that load torque is distributed widely from very low torque to very high torque for each operating mode. In fig. 5, the operation points of the engine of hydraulic excavators during a cycle of “excavation and loading” in H mode are plotted on the brake specific fuel consumption map. In this case, the operators set the engine speed at its rated point, namely  $n$ , to utilize the full extent of working capability of the conventional excavators. The red-cross signs indicating operation points are strayed from the optimum area which is indicated by blue ellipse. The objective of the hybrid power is to improve the fuel consumption rate during the whole excavating operation. So, moving the engine operating region to high efficiency region on the fuel map from the low efficiency region operation via elaborate use of the hybrid structure is natural and reasonable. Therefore, setting the engine speed at  $n'$  is more reasonable.

The maximum system power of the hybrid excavator is determined based on the maximum power (i.e., maximum

engine power)of the hydraulic excavator with equivalent operating capabilities and is typically set to be higher than the maximum power of the hydraulic excavator due to the efficiency of energy transfer. As shown in fig. 5, AA' and BB' are equal power curves. Point A is the maximum power and Point B is the average power for the engine operation in H mode of hydraulic excavators. In order to retain the same operating capabilities, Point A and Point B are shifted to Point A' and Point B'. The engine torque at the speed  $n'$   $T(A')$  should conform to Equation (1).

$$T_{B'} < T_{A'} < T_A \quad (1)$$

The hybrid excavator can assist the engine by the electric motor, Therefore, the maximum output required by the engine can be decreased. Thus, a small engine or smaller power may be utilized.

### 3.2 Pump

In order to retain the same output power of the pump, the set engine speed is lowered to  $n'$ , meanwhile the limit input torque point is shifted from A to A'. Therefore the limit displacement of the pump is increased according to Equation (2).

$$D' = D \frac{n}{n'} \quad (2)$$

### 3.3 Engine assisting motor

By enlarging the pump displacement, the maximum absorbed torque of the pump is increased beyond the maximum available torque of the engine at the speed  $n'$ , therefore the generator /motor torque should compensate for the excessive power. Besides, the dynamics of the power train has to be taken into consideration. For example, the engine operation is to set engine to the point shown as A''. When load occurs, the engine operation droops to Point C, due to the delay of the compensation and the dynamics of drive train, which causes the machine response to suffer, excessive fuel consumption and more emission. In such a case, if the generator/motor performs a “transient torque assist” function, the engine can operate at a more fuel efficient speed and maintain machine response. Therefore  $T_m$  should satisfy Equation (3) and Equation (4).

$$T_m = T + J\alpha \quad (3)$$

The first term on the right side of Equation (3) is the increased torque, and the second term is determined by the acceleration and equivalent inertia when the engine decelerates.

For a typical excavation and dumping operation, energy balance equation (4) also should be conformed to.

$$\int_0^{t_f} T_g \omega dt \eta_g \eta_c = \frac{\int_0^{t_f} T_m \omega dt}{\eta_m \eta_d} + \frac{\int_0^{t_f} T_s \omega_s dt}{\eta_{sm} \eta_d} - \int_0^{t_f} T_s \omega_s dt \eta_{sg} \eta_c \quad (4)$$

### 3.4 Swing motor

The maximum equivalent inertia of the upper structure can be obtained through the hydraulic motor displacement, the cracking pressure of the relief valves installed in the swing circuit and the acceleration time. Therefore, the maximum torque and speed of the swing motor can be estimated as in Equation (5) and Equation (6).

$$T_{s\max} = \frac{P_r q_m}{2\pi} \quad (5)$$

$$n_{s\max} = \frac{n_{\text{rated}} q_p}{q_m} \quad (6)$$

### 3.5 Super capacitor

In order to meet the demand of supplying or receiving electric energy to generator/motor and swing motor together, the power of super capacitor should satisfy Equation (7).

$$P_c \geq P_s + P_a \quad (7)$$

During a working cycle, the energy charged into super capacitor is shown in Equation (8), therefore the capacity of has to satisfy Equation (9).

$$E_{c\max} = \int_0^t T_g \omega dt \eta_g \eta_c + \int_0^t T_s \omega_s dt \quad (8)$$

$$C = \frac{2E_{c\max}}{V_{\max}^2 - V_{\min}^2} \quad (9)$$

According to the rules and load profile, key parameters are shown in table 1:

Component	Parameter	Value
Engine	Rating power	113kW
	Rating speed	2000rpm
Assist motor	Rating power	30kW
	Rating speed	2000rpm
Swing motor	Rating power	60kW
	Rating speed	3800rpm
Super capacitor	Rating capacity	10F
	Maximum voltage	350V
	Minimum voltage	280V

## 4 Control strategy

The hybrid excavator is an integrated system that consists of many sub-systems including engine, generator/motor, capacitor pack, swing motor and pump. Each sub-system is also a complex system that has its own functionality and desired performance. In this case, almost every subsystem is equipped with its behavior. Moreover, all sub-systems need to be coordinated in an optimal manner to achieve different objectives, e.g. fuel economy, emissions reduction, charge

balance, and drivability. With this increasing complexity of power train system and the need of achieving multiple objectives, an integrated machine-level controller is required to accomplish the task.

### 4.1 Hierarchical structure

The hierarchical structure of control strategy is proposed in fig. 5. It is decomposed into three layer, management layer, control layer and executor layer.

Based on the working condition and driver's expectation, drivers operate the excavator, such as pilot handles, and mode selection switch and increase power button, which produce corresponding signals. The hybrid power controller represents a high-level control system that can coordinate the overall power train to satisfy certain performance target such as fuel economy and emissions reduction. The high-level power controller must determine the desired output to be generated by the sub-systems (e.g. engine speed, motor torque, proportional valve current for pump, etc.). These desired output signals are sent to the corresponding sub-systems and become the commands for the lower-level control system of each sub-system. The executor layer controller include engine electronic control unit, generator/motor controller, swing motor controller, and super capacitor monitor unit, which are normally provided by sub-system supplier. The data exchange between control layer and executor layer is implemented through CAN BUS communication.

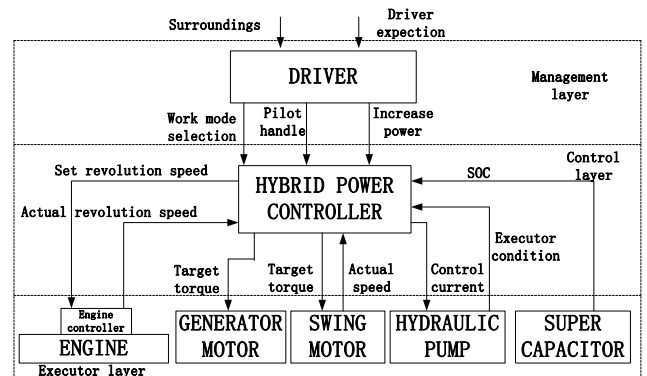


Figure 6: Hierarchical structure of control strategy

The hierarchical structure makes it possible to simplify and expedite the control design. However, a systematic design approach for the high-level control system in hybrid excavator is still lacking and needs to be developed.

### 4.2 Power management strategy

The term “power management” refers to the design of the higher-level control algorithm that determines the proper power (torque) level to be generated, and its split between the generator/motor and the engine while satisfying the power (torque) demand from the pump and the swing motor, maintaining adequate energy in the super capacitor.

The intuition of “hybrid power” is based on the concept of “load leveling”, which attempts to operate the irreversible

energy conversion device such as engine in an efficient region and uses the reversible energy storage device as a load-leveling device to compensate the rest of the power demand. However, due to the unknown nature of future power demand, a charge sustaining strategy is needed to maintain the SOC level of the super capacitor. The voltage range of super capacitor is separated into three regions, as shown in (9), and the normal range is from  $SOC_L$  to  $SOC_H$ . The other two regions are retained for swing motor in such cases that the generator/motor and the swing motor work together. Control strategy based on rules is designed below.

$$SOC_{\min} < SOC_L < SOC_H < SOC_{\max} \quad (9)$$

(1) If  $SOC > SOC_H$ , then

$$\text{If } T_{pump} > T_{\max}, \text{ then } T_m = T_{pump} - T_{\max} + a \cdot \Delta\omega;$$

$$\text{If } T_{\max} > T_{pump} > T_{\min}, \text{ then } T_m = a \cdot \Delta\omega;$$

$$\text{If } T_{pump} < T_{\min}, \text{ then } T_m = 0;$$

(2) If  $SOC_H > SOC > SOC_L$ , then

$$\text{If } T_{pump} > T_{\max}, \text{ then } T_m = T_{pump} - T_{\max} + a \cdot \Delta\omega;$$

$$\text{If } T_{\max} > T_{pump} > T_{\min}, \text{ then } T_m = a \cdot \Delta\omega;$$

$$\text{If } T_{pump} < T_{\min}, \text{ then } T_g = T_{\min} - T_{pump};$$

(3) If  $SOC < SOC_L$ , then

$$\text{If } T_{pump} > T_{\min}, \text{ then } T_m = 0;$$

$$\text{If } T_{pump} < T_{\min}, \text{ then } T_g = T_{pump} - T_{\min};$$

### 4.3 Control strategy of swing system driven electrically

The upper structure is characterized by the large and variable swing inertia which varies with the posture of the upper structure and payload in the bucket. Most researchers are only interested in the swing speed control of the upper structure [5,6]. But some occasions on which the motor torque need also to be controlled are neglected, therefore in this paper a compound(speed mode and torque mode) control strategy is proposed, and the control scheme is shown in fig. 7.

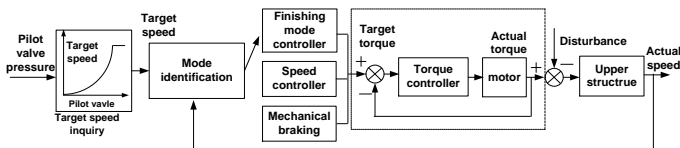


Figure 7: Control strategy of swing system driven by electric motor

Mode identification method and corresponding controller are shown below:

1, If  $n_0 - n > \varepsilon$ , then torque control mode is applied;

$$T_0 = (n_0 - n)k;$$

2, If  $n_0 - n < \varepsilon$ , then PI(proportional integral) is applied;

3, If  $P_1 = 0$  and  $P_2 = 0$  and  $n < n_m$  then mechanical braking is applied;

## 5 Experiment results

The prototype of 20-ton hybrid power excavator and power train are shown in fig. 8 and fig. 9 respectively. The prototype excavator is equipped with the aforementioned electrical components, which are a generator/motor, an electric swing motor, a super capacitor pack and a hybrid power controller.



Figure 8: Prototype of 20-ton hybrid power excavator

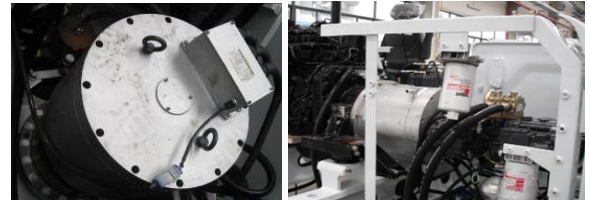


Figure 9: Swing motor and engine assisting motor

Fig. 10 shows the swing control performance for PI controller and the presented compound strategy. It is obvious that during the acceleration the speed overshoot is produced for PI controller while for the compound strategy it accelerates smoothly. Moreover, the swing motor is controlled to stop more smoothly than the hydraulic swing motor, without any jerks that a driver might feel discomfort. fig. 11 shows the experiment results for 180° swing operation. The motor speed and torque are shown in (a), and the current and voltage of super capacitor are shown in (b). The swing motor accelerates and decelerates smoothly and the kinetic energy can be recovered during the deceleration.

For the excavation and dumping operation, engine operation points of the 20-ton hybrid power excavator are shown in fig. 12. Compared to the operation points in fig. 5, the operation points of hybrid excavator engine are converged around the high efficiency area. Except that, for the same capacity, the energy used to drive the auxiliary components such as

cooling fan, cooling pump, etc also can be reduced due to engine speed is lowered.

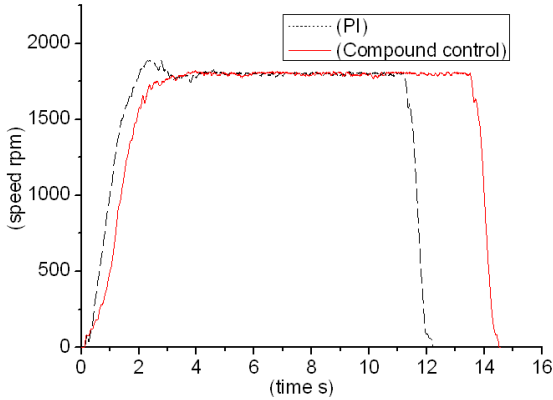
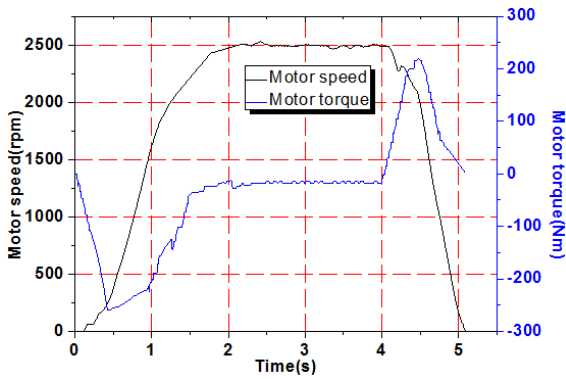
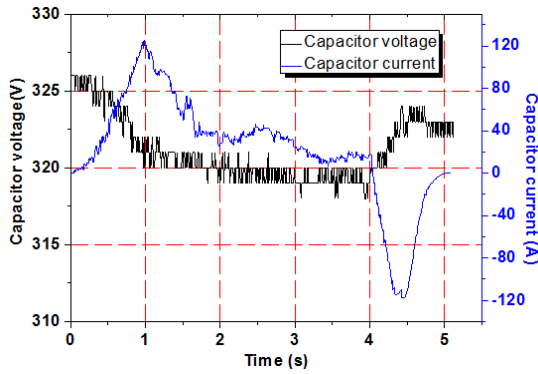


Figure 10: Swing motor speed



(a) Speed and torque of motor



(b) Voltage and current of super capacitor

Figure 11: 180° swing operation

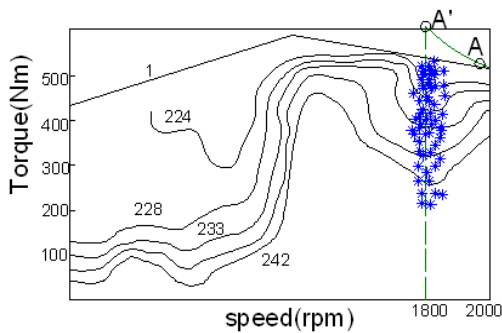


Figure 12: Engine operation point

## 6 Conclusion

In this paper, a 20-ton prototype compound hybrid excavator is presented which includes assisting electric motor, swing electric motor, a super capacitor pack, an engine and negative flow hydraulic system. The energy-saving principle of hybrid excavator is introduced as well. The development rules which include parameter design rules of key components and hierarchical structure of control strategy of hybrid power system are presented. By developing the electric swing control strategy and power management algorithm, experiments show that the swing motor accelerates and decelerates smoothly and the kinetic energy can be recovered during the deceleration, the developed hybrid power system can significantly improve the fuel economy of the excavator without any performance degradation or drivability deterioration.

## Nomenclature

Designation	Denotation	Unit
$D'$	limit displacement of hybrid excavator	$[cm^3/r]$
$D$	limit displacement of hydraulic excavator	$[cm^3/r]$
$T_m$	maximum torque as motor	[Nm]
$J$	equivalent rotary inertia of drive train	$[kgm^2]$
$\alpha$	acceleration of drive train	$[rad/s^2]$
$T_g$	maximum torque as generator	[Nm]
$\omega$	engine revolutionary speed	[rpm]
$\eta_g$	mean efficiency as generator	[%]
$\eta_m$	mean efficiency as motor	[%]
$\eta_c$	mean charge efficiency of super capacitor	[%]
$\eta_d$	mean discharge efficiency of super capacitor	[%]
$T_s$	torque of swing motor	[Nm]
$\omega_s$	rotary speed of swing motor	[rpm]
$\eta_{sm}$	mean efficiency as swing motor	[%]
$\eta_{sg}$	mean efficiency as swing generator	[%]
$T_{smax}$	maximum torque of swing motor	[Nm]
$n_{smax}$	maximum rotary speed of swing motor	[rpm]
$P_r$	cracking pressure of relief valve	[Mpa]

$q_p$	displacement of pump	$[cm^3/r]$
$q_m$	displacement of hydraulic motor	$[cm^3/r]$
$P_c$	power of super capacitor	[kW]
$P_s$	power of swing motor	[kW]
$P_a$	power of generator/motor	[kW]
$E_{c,max}$	Maximum storage energy	[J]
$C$	Capacity of super capacitor	[F]
$V_{max}$	Maximum voltage of super capacitor	[V]
$V_{min}$	Minimum voltage of super capacitor	[V]
$n_0$	Target speed of swing motor	[rpm]
$n$	Actual speed of swing motor	[rpm]
$n_m$	Mechanical braking speed	[rpm]
$\varepsilon$	Swing speed threshold	[rpm]
$P_1$	Pilot valve1 pressure	[Mpa]
$P_2$	Pilot valve2 pressure	[Mpa]

excavator. Journal of Zhejiang university science A, 9(5).

- [8] Ahn K. K., Yoon J. H., Cho Y. R., Kim J. S., A study on basic of hybrid excavator. KSME 2006 fall conference proceedings, 2006
- [9] Ahn K. K., Cho Y. R.,(2006) . Hybrid excavator using electro-hydraulic hybrid actuator. Journal of korea fluid power system society, 6(1)
- [10] Seungjin Yoo, Sangjun An, Cheol-Gyu Park and Nagin Kim. Design and Control of Hybrid Electric Power System for a Hydraulically Actuated Excavator (2008).

## References

- [1] Kagoshima Masayuki, Takao NANJO, Akira TSUTSUI, development of new hybrid excavator, KOBELCO Technology Review, NO. 27, NOV.2007, pp.39-42;
- [2] Yoo S. Design and control of hybrid electric power system for a hydraulic actuated excavator. SAE Int. J. Commercial Vehicles 2010; 2(2): 264-273.
- [3] Qiang Feng, Research on hardware-in-the-loop simulation system of hydraulic excavators. Proc. of the 8th JFPS International Symposium on Fluid Power, pp.318-323, 2011.
- [4] Zhang Y.,Wang Q., Constant work-point control for parallel hybrid system with capacitor accumulator in hydraulic excavator. Chinese journal of mechanical engineering. 19(4):132-139,2006.
- [5] Lin X., Pan S., Dynamic simulation and optimal control strategy for parallel hybrid hydraulic excavator. Journal of Zhejiang university science A.9(5):624-632,2008.
- [6] Xiao, Q., Wang, Q., Control strategies of power system in hybrid hydraulic excavator. *Automation in Construction*, 17(4), pp. 361–367,2008.
- [7] Lin X., Pan S. X., Wang D. Y., Dynamic simulation and optimal control strategy for parallel hybrid hydraulic



# **Modeling of a Series Hybrid Hydraulic Drivetrain for a Light-Duty Vehicle in Hopsan**

K. Baer, L. Ericson, and P. Krus

Division of Fluid and Mechatronic Systems, Department of Management and Engineering,  
Linköping University, Linköping, Sweden  
E-mail: katharina.baer@liu.se, liselott.ericson@liu.se, petter.krus@liu.se

## **Abstract**

Hydraulic hybrids continue to receive attention as a possible solution in the search for improved fuel economy for different vehicle types. This paper presents the development of a framework for hybrid hydraulic vehicles, using the Hopsan simulation tool of Linköping University's Division of Fluid and Mechatronic Systems (Flumes). This framework is then used on a series hydraulic hybrid transmission which employs a pump control based on the hydraulic accumulator's state-of-charge (SoC). Several simplifications were made, especially concerning mechanical components. Simulation over two urban standard cycles shows promising results concerning velocity error and energy recuperation potential, provided the components are sized appropriately to compensate for the mechanical limitations. This paper lays the foundation for the further development of a design framework suitable for optimizing the full drivetrain, including component sizing and controller parameterization.

**Keywords:** Series hydraulic hybrid model, Hopsan modeling

## **1 Introduction**

Fuel economy continues to be a major challenge and focus in vehicle technology, both for economic and environmental reasons. As a possible solution, hybrid architectures keep being investigated for both passenger and larger vehicles. They have in common that another power source is added to the existing combustion engine including an energy storage component to allow for some form of energy recuperation; in the case of hybrid drivetrains it is the kinetic energy of the vehicle that would be lost in form of heat when braking. While this implies the addition of a number of components to the drivetrain, it potentially allows for down-sizing, and depending on the configuration, also optimized operation of the internal combustion engine.

Commercially available hybrid passenger vehicles are typically electric hybrids, one of the best-known examples being the Toyota Prius. These hybrids use batteries for storing the recuperated energy, which are advantageous in comparison to hydraulic accumulators in terms of energy density, allowing more energy to be stored. In comparison to that, hydraulic hybrids allow for a higher power density [1], which makes them especially interesting when frequent starts and stops occur, and a large vehicle mass is moved. Typical applications are heavier vehicles in urban traffic, such as busses [2], refuse vehicles [3] or delivery trucks [4]. But also passenger and light-weight vehicles are considered suitable for hydraulic hybrids [5][6].

To provide a framework for future research, a simulation model of a series hydraulic hybrid light-duty vehicle has been developed which will be presented in this paper. It is to be enhanced further to allow for a comprehensive optimization of the complete hybrid vehicle, and to be compared to other hydraulic hybrid architectures.

## **2 Hybrid hydraulic drivetrains**

Three principle architectures can be found for hybrids: series, parallel and power-split. Their differences concern how the internal combustion engine is operated and whether highly efficient mechanical power transfer is possible. In hydraulic hybrids, at least one hydrostatic reversible unit (pump/motor) is used, acting as a motor on the wheels during acceleration and as a pump for energy recuperation during braking.

In a series hydraulic hybrid configuration, the engine drives a pump, which in turn drives the pump/motor and charges the system's accumulator if necessary. The pump/motor is then connected to the vehicle's axle. This way, the engine speed is decoupled from the wheel speed, allowing for a more efficient operating point. The engine can also be completely decoupled when including a clutch. Because of the energy conversion from mechanical to hydraulic to mechanical, the transmission is less efficient than an entirely mechanical drivetrain.

This mechanical connection between the internal combustion engine and the vehicle exists in the parallel hybrid ar-

chitecture. The pump/motor is mounted between the engine and a mechanical transmission, and can provide additional torque to the wheels. The speeds of the engine and the wheels are coupled, and consequently optimal engine management is not possible. As the drivetrain does not require a complete redesign, the parallel hybrid architecture offers the possibility for reconfiguration of existing vehicles and drivetrains (e.g. as so-called add-on hybrids) [7][2].

A power-split configuration, sometimes also referred to as “hydro-mechanical hybrid”, aims to combine the advantages of both series and parallel hydraulic hybrids through planetary gear sets. The engine power is split into a hydraulic and a mechanical path. The hydraulic system can add or take power from the drivetrain, and hydraulic and mechanical power are recombined before the wheels. This way, both optimal engine management and efficient mechanical power transfer can be realized. Depending on the number and location of the planetary gear sets, there are different configurations for power-split hydraulic hybrids [3] [4].

### 3 Framework for a hybrid hydraulic drivetrain system design in Hopsan

The model of the series hybrid hydraulic drivetrain is developed in Hopsan [8], a multi-domain system simulation tool. Its current generation is continuously being developed at the Division of Fluid and Mechatronic Systems in Linköping since 2009. Just like its predecessor, now referred to as “Hopsan Classic”, Hopsan utilizes the transmission line modeling (TLM) technique and is available for download free of charge. For this paper, a development version has been used together with customized components.

The primary focus of the model is the hydraulic part of the drivetrain together with the vehicle, while the combustion engine driving the pump will be considered in the future. Here it is assumed to run at a constant speed. Furthermore, gearing is limited to the gear ratio of the vehicle’s differential, without an additional gearbox. The lack of a gearbox does increase the system’s efficiency due to reduced losses [1], but its inclusion could be beneficial for reducing the component sizes. The general structure of the model is given in Figure 1; the volumes and the rotary shaft used are connecting elements required by the underlying modeling technique. The main components will be explained below.

The vehicle is represented by a one-dimensional component model and described by the parameters total vehicle mass  $M_{veh,total}$ , effective front area  $c_d \cdot A$  and wheel radius  $r_{wheel}$ , the latter being combined with the differential gear ratio  $i_{diff}$  into what is referred to here as effective wheel radius  $r_{wheel,e}$ :

$$r_{wheel,e} = r_{wheel} / i_{diff}. \quad (1)$$

The component model takes into account the aerodynamic drag and rolling resistance acting on the vehicle, but neglects factors such as gradeability and driving turns. There is no difference between supplying power to the front or rear axle of the vehicle.

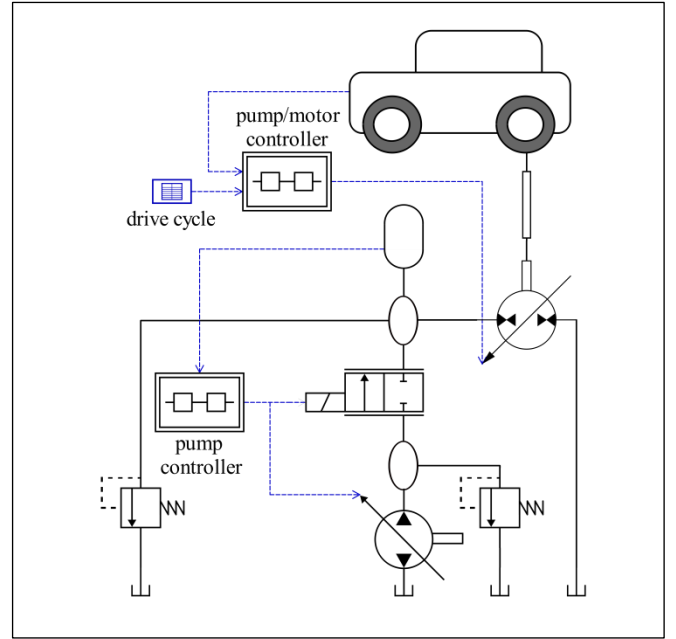


Figure 1: Basic model structure

$$T_{veh,1} + T_{veh,2} = r_{wheel,e} \cdot (M_{veh,total} \cdot \dot{v}_c + 9.82 \cdot M_{veh,total} \cdot c_{fr} + c_d \cdot A \cdot \rho \cdot v_c^2 / 2), \quad (2)$$

with  $T_{veh,1}$  and  $T_{veh,2}$  being the torques acting on the vehicle’s axles,  $v_c$  being the vehicle’s current velocity,  $c_{fr}$  the rolling resistance coefficient and  $\rho$  the air density.

For the transmission, a variable pump and a variable pump/motor are used. Both components contain a mathematical efficiency model by Rydberg [9], which determines the efficiency based on angular velocity, pressure, and displacement setting angle.

The model of the accumulator component is based on the polytropic law for a perfect gas, and further idealized assuming a loss-free component. For this model, an adiabatic process is assumed, and the accumulator not to be charged at the beginning of the operation.

The pump/motor’s displacement setting angle is determined through a PI-controlled velocity feedback, with the drive cycle being simulated as reference input. The pump charging the system is switched on and shut off according to the accumulator’s current state-of-charge (SoC) [10]: in the case of the accumulator state-of-charge  $SoC_{Acc}$  falling below a defined minimum state-of-charge  $SoC_{low}$ , the pump delivers a charge flow. It is shut down once an upper limit state-of-charge  $SoC_{high}$  is reached in order to reserve accumulator capacity for energy recuperation. In the current accumulator model, this state-of-charge can be equivalently expressed as a function of the current filling volume, or of the pressure in the accumulator (cf. for example [11]). While Kim and Filipi [6] define an engine power corresponding to the state-of-charge, here the power input is determined through the load on the pump and its constant speed. Even though the pump is fully variable, it is effectively either fully closed or fully opened, thus avoiding an operation in the low-efficiency low

displacement setting angle range. The same controller also actuates a 2/2 directional valve for the pump's protection.

The main hydraulic components' contribution to the vehicle's total weight  $M_{veh,total}$  is considered in order for the model to be ultimately used in a full system optimization. For the variable pump and the accumulator, data of commercially available components are extrapolated continuously, while the pump/motor is described with discrete values of the next bigger available component size.

#### 4 Application example: Simulation of two urban drive cycles

In this paper, a light-duty vehicle is modeled with the parameters according to Table 1. As reference velocity profiles, two EPA driving schedules [12] were chosen in order to ensure the model is not only parameterized for one single drive cycle, cf. Figure 2. They are different in respect to duration, maximum and average speed, as well as the total distance traveled, even though both are representing urban velocity profiles.

Table 1: Light-duty vehicle data.

Vehicle parameter	Value
Vehicle mass $M_{veh}$ (half-loaded, without main hydraulic components)	2700 kg
Frontal area $A$	3.75 m <sup>2</sup>
Aerodynamic drag coefficient $c_d$	0.475
Effective wheel radius $r_{wheel,e}$	0.1 m

The sizes of the main components of the drivetrain, i.e. the hydraulic machines and the accumulator, as well as the controller settings are the same for both drive cycles. When evaluating the results of simulating the drive cycles, two different values are considered. On the one hand, as a measure of the accumulated relative velocity error, ARVE, the accumulated velocity deviation relative to the drive cycle's total covered distance is given, i.e.

$$ARVE = \int_{t_{start}}^{t_{end}} |v_c - v_{ref}| dt / x_{max}, \quad (3)$$

with  $v_{ref}$  as the reference velocity according to the simulated drive cycle, and  $x_{max}$  as the total distance covered by the respective drive cycle.

As an example, the results for simulating the FTP-72 cycle are given in Figure 3, showing that the vehicle follows the reference velocity very well, with the largest deviations occurring in acceleration phases.

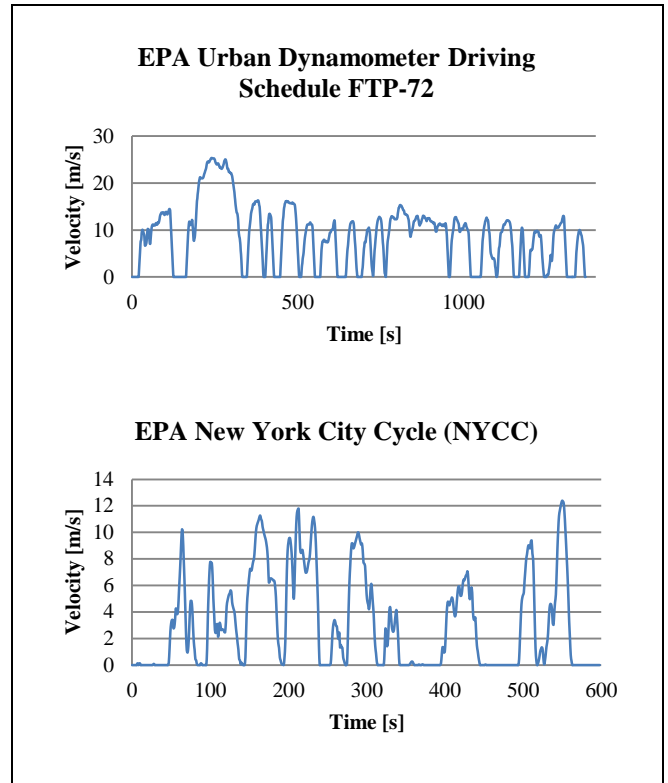


Figure 2: EPA Driving Schedules

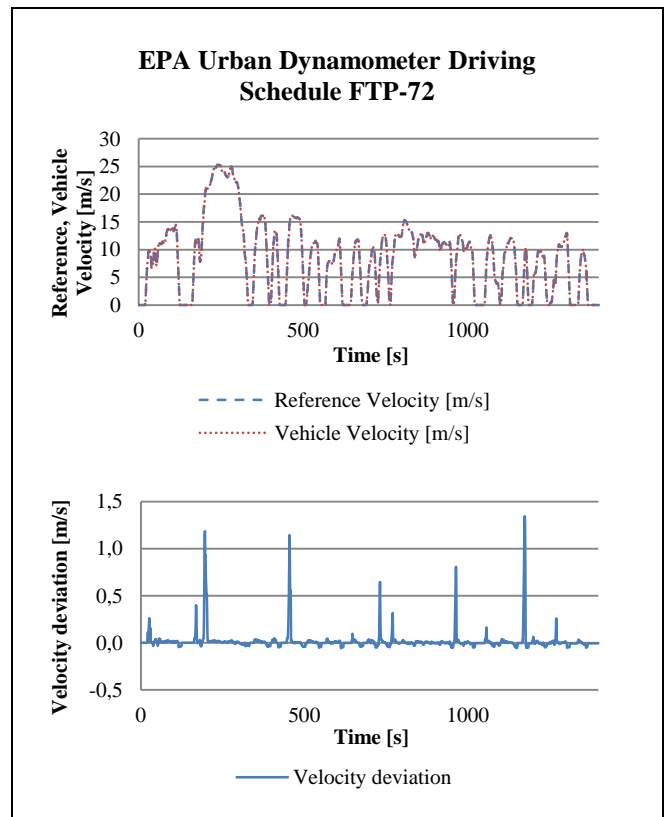


Figure 3: Simulation results for EPA UDDS FTP-72: Actual vehicle velocity vs. reference velocity; velocity deviation

The effect of the accumulator's inclusion in the system on the energy consumption is expressed as the energy input ratio

$$EIR = E_{in,pump} / (E_{in,veh} + E_{loss}), \quad (4)$$

with  $E_{in,pump}$  as the energy provided to the pump,  $E_{in,veh}$  as the (positive) energy input into the vehicle, not accounting for the recuperated energy, and  $E_{loss}$  accounting for losses in the charge pump, the valve and the pump/motor when operating in motor mode. If there was no accumulator allowing for energy recuperation, this ratio would equal 1; the more energy recuperation occurs, the lower this value becomes.

The results for the simulation over both cycles are summarized in Table 2. As the values show, different driving schedules will lead to varying results.

Table 2: Simulation results for ARVE and EIR

Drive Cycle	Accumulated relative velocity error	Energy input ratio
FTP-72	0.385 %	68.81 %
NYCC	3.259 %	75.65 %

It should be noted that after completing the driving schedule, the final state-of-charge  $SoC_f$  differs for both drive cycles (see Table 3). This effect has been neglected in the energy efficiency considerations so far, as the focus with the EIR calculations is the energy efficiency in the drive cycle. The energy at the end of drive cycle can be accounted for by adjusting the energy input ratio to

$$EIR_a = (E_{in,pump} - E_{Acc,f}) / (E_{in,veh} + E_{loss}), \quad (5)$$

with  $E_{Acc,f}$  as the energy content of the accumulator at the end of the drive cycle.

Table 3: Simulation results for accumulator's  $SoC_f$  and  $EIR_a$

Drive Cycle	Final state of charge	Adjusted EIR
FTP-72	0.7671	65.39 %
NYCC	0.8524	52.44 %

As the New York City Cycle is shorter and the accumulator's final state-of-charge is higher, taking the energy content of the accumulator at the end of the drive cycle into account affects the energy considerations for this cycle much more than for the FTP-72 cycle.

## 5 Study of parameter variation

The parameter values used in the simulations presented in chapter 4,  $SoC_{low}=0.71$  and  $SoC_{high}=0.55$ , were chosen based on pressure considerations, in an attempt to allow for complete braking energy recuperation.

Typically, the controller parameterization for specific vehicle configurations is achieved via optimization. In literature, a number of approaches can be found using different optimi-

zation algorithms [2][4][5][13]. The results will be influenced by the chosen objectives, the weighing of the multiple objective functions, and underlying drive cycles, amongst others. In order to study the pump controller parameterization, this chapter will instead present the results for the individual objectives and drive cycles.

Figure 4, Figure 5 and Figure 6 show the results for the objectives separately. Cases of  $SoC_{low} > SoC_{high}$  are not considered, as with the implemented control strategy this would effectively eliminate the control variable  $SoC_{high}$ , and cause the hydraulic accumulator to always be charged to a predefined state-of-charge. For both drive cycles, the velocity error can be lowered by increasing the control parameters, with the result for the New York City Cycle being affected more by the choice of  $SoC_{high}$  for a given  $SoC_{low}$  than the FTP-72 cycle. Analyzing the energy input ratio, little variation can be observed for the FTP-72 cycle, while for the New York City Cycle a tendency towards improvement can be observed for lower values of the control parameters. For a number of outlier parameter pairs, the charging of the accumulator occurs from a rather low state-of-charge to a high one, though, resulting in a low energy input ratio. The adjusted energy input ratio explains this variation through the accumulator energy content at the end of the drive cycle. While there is little difference between EIR and  $EIR_a$  for the FTP-72 cycle, the adjusted energy input ratio for the New York City Cycle is lower, and shows less variation.

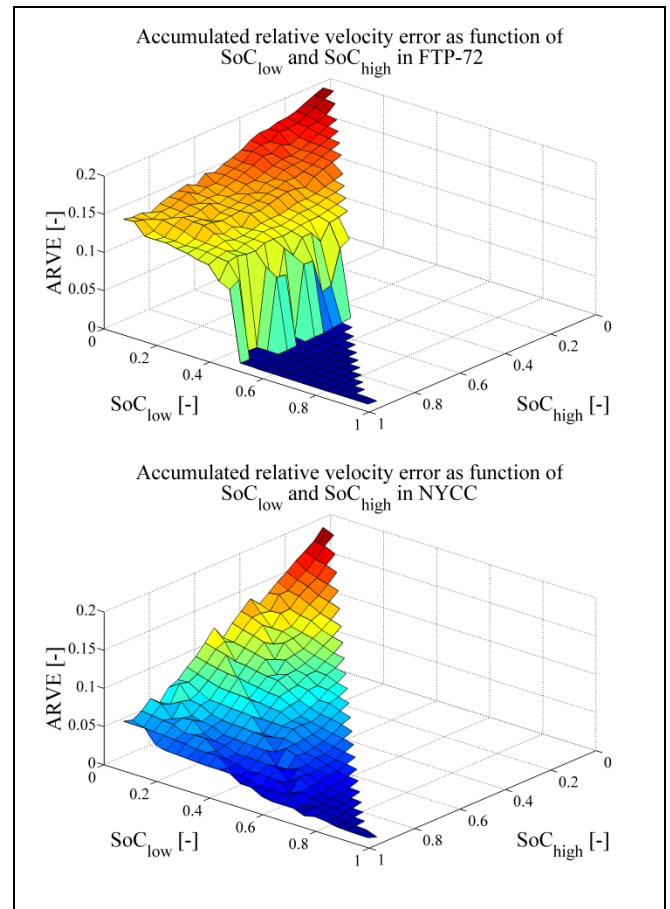


Figure 4: Accumulated relative velocity error as function of  $SoC_{low}$  and  $SoC_{high}$

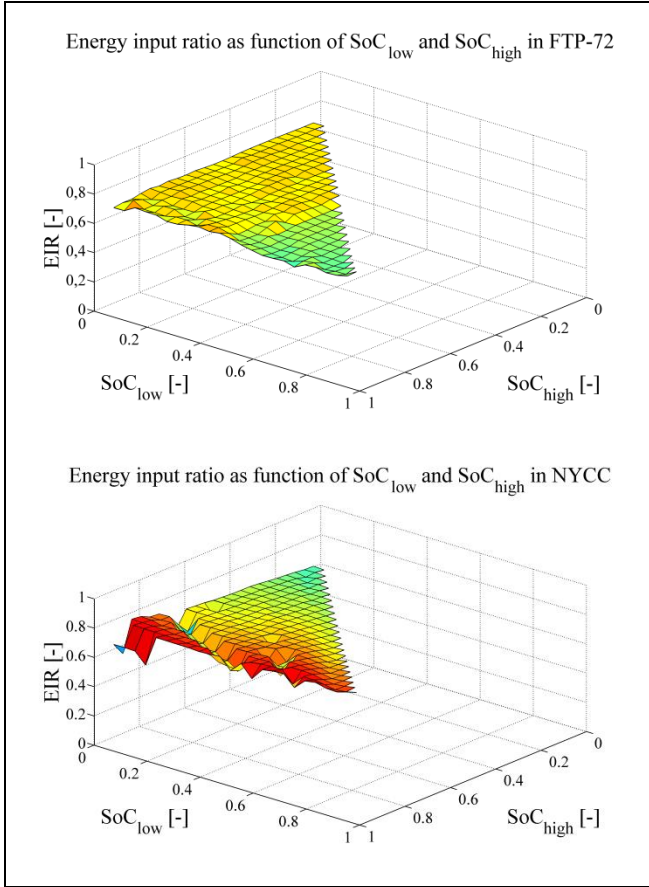


Figure 5: Energy input ratio as function of  $SoC_{low}$  and  $SoC_{high}$

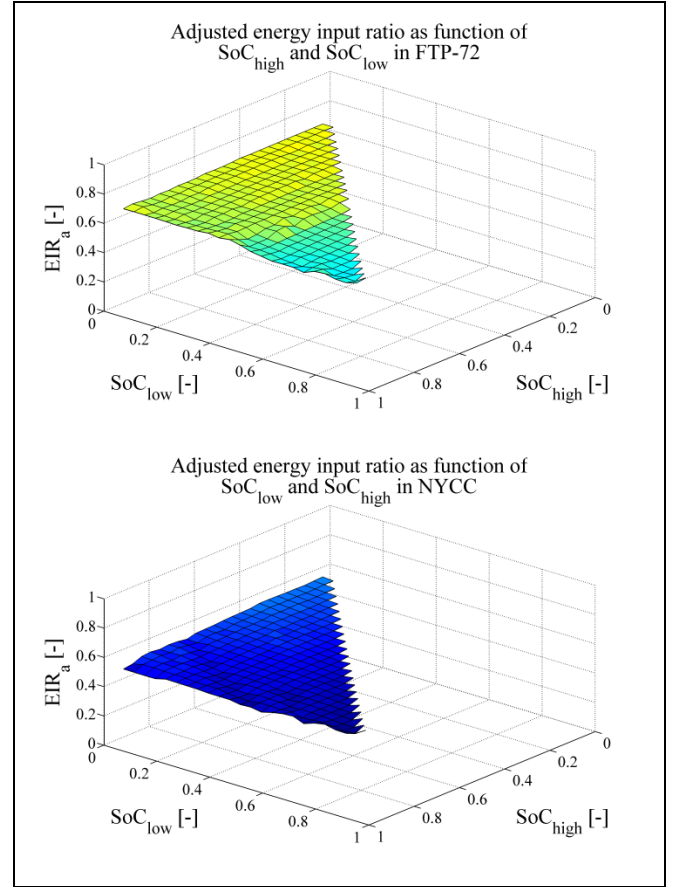


Figure 6: Adjusted energy input ratio as function of  $SoC_{low}$  and  $SoC_{high}$

## 6 Conclusion

This paper presents a framework for the design of hybrid hydraulic vehicles. This framework has been tested for a series hydraulic hybrid light-weight vehicle. Simulation over two different urban drive cycles has given reasonable results concerning the velocity error, and indicates a potential to reduce the energy input into the system in comparison to running the vehicle with the same transmission, but without the possibility to recuperate energy during braking. Overall, the results show the potential of the framework for more advanced systems.

However, in its current version the model contains a number of significant simplifications which need to be tackled in the future. One extension would be the inclusion of a scalable combustion engine component model, as its fuel consumption characteristics are neglected so far. It could allow for studying downsizing possibilities through hybridization. Furthermore, the current lack of a mechanical gearbox leads to relatively big hydraulic machines, which are not suitable especially for a vehicle of this size.

The goal for the model is to allow a full optimization of the vehicle's drivetrain, including component sizing and controller parameterization, based on a vehicle's specifications and a reference drive cycle. This optimization could also include a limitation for the component sizing to a discrete number of available sizes instead of a continuum of options,

and further respective parameter variations in other components to account for component-size specific limitations.

Similar models will be developed for the parallel and power-split hydraulic hybrid architectures to run comparisons between the different models. This set of models should be able to give a comprehensive understanding of hydraulic hybrids for future projects.

## Nomenclature

Designation	Denotation	Unit
$A$	Frontal area of vehicle	$[m^2]$
$ARVE$	Accumulated relative velocity error	$[-]$
$c_d$	Aerodynamic drag coefficient	$[-]$
$c_d A$	Effective front area	$[m^2]$
$c_{fr}$	Rolling resistance coefficient	$[-]$
$E_{Acc,f}$	Final accumulator energy content	$[J]$
$E_{in,pump}$	Energy input to pump (system)	$[J]$
$E_{in,veh}$	Energy input to vehicle	$[J]$
$E_{loss}$	Energy losses	$[J]$

$EIR$	Energy input ratio	[-]
$EIR_a$	Adjusted energy input ratio	[-]
$i_{diff}$	Differential gear ratio	[-]
$M_{veh}$	Vehicle mass (half-loaded, without main hydraulic components)	[kg]
$M_{veh,total}$	Total vehicle mass	[kg]
$r_{wheel}$	Wheel radius	[m]
$r_{wheel,e}$	Effective wheel radius	[m]
$SoC_{Acc}$	Accumulator state-of-charge	[-]
$SoC_f$	Final state-of-charge	[-]
$SoC_{low}$	Lower state-of-charge boundary	[-]
$SoC_{high}$	Higher state-of-charge boundary	[-]
$t_{end}$	End time of drive cycle	[s]
$t_{start}$	Start time of drive cycle	[s]
$T_{veh,1}, T_{veh,2}$	Torque on vehicle's axle	[Nm]
$v_c$	Actual vehicle velocity	[m/s]
$v_{ref}$	Reference velocity	[m/s]
$x_{max}$	Total drive cycle distance	[m]

## References

- [1] K-E Rydberg. Energy Efficient Hydraulic Hybrid Drives. Proc. of the *11th Scandinavian International Conference on Fluid Power*, Linköping, Sweden, 2009.
- [2] Y Yan, G Liu, and J Chen. Integrated Modeling and Optimization of a Parallel Hydraulic Hybrid Bus. *International Journal of Automotive Technology*, 11(1):97-104, 2010.
- [3] S Baseley, C Ehret, E Greif, and M G Kliffken. Hydraulic Hybrid Systems for Commercial Vehicles. Proc. of *SAE 2007 Commercial Vehicle Engineering Congress and Exhibition*, Rosemont, Illinois, United States, 2007.
- [4] C-T Li, and H Peng. Optimal Configuration Design for Hydraulic Split Hybrid Vehicles. Proc. of *2010 American Control Conference*, Baltimore, Maryland, United States, 2010.
- [5] K A Stelson, J J Meyer, A G Alleyne, and B Hency. Optimization of a Passenger Hydraulic Hybrid Vehicle to Improve Fuel Economy. Proc. of the *7th JFPS International Symposium on Fluid Power*, Toyama, Japan, 2008.
- [6] Y J Kim, and Z Filipi. Simulation Study of a Series Hydraulic Hybrid Propulsion System for a Light Truck. Proc. of *SAE 2007 Commercial Vehicle Engineering Congress and Exhibition*, Rosemont, Illinois, United States, 2007.
- [7] K L Cheong, P Y Li, S Sedler, and T R Chase. Comparison between Input Coupled and Output Coupled Power-split Configurations in Hybrid Vehicles. Proc. of the *52nd National Conference on Fluid Power*, Las Vegas, Nevada, United States, 2011.
- [8] B Eriksson, P Nordin, and P Krus. Hopsan NG, A C++ Implementation using the TLM Simulation Technique. Proc. of the *51st Conference on Simulation and Modelling*, Oulu, Finland, 2010.
- [9] K-E Rydberg. On Performance Optimization and Digital Control of Hydrostatic Drives for Vehicle Applications, *PhD thesis*, Linköping University, 1983.
- [10] J D Van de Ven, M W Olson, and P Y Li. Development of a Hydro-Mechanical Hydraulic Hybrid Drive Train with Independent Wheel Torque Control for an Urban Passenger Vehicle. Proc. of *International Fluid Power Exhibition*, Las Vegas, Nevada, United States, 2008.
- [11] F Wang, M I Ramdan, and K A Stelson. Comparison between Hydraulic Hybrid and Electric Hybrid Passenger Vehicle using ADVISOR 2004. Proc. of the *52nd National Conference on Fluid Power*, Las Vegas, Nevada, United States, 2011.
- [12] United States Environmental Protection Agency. Dynamometer Drive Schedules. Available at: <http://www.epa.gov/nvfel/testing/dynamometer.htm> (Accessed 2013-05-23).
- [13] H Sun. Multi-objective optimization for hydraulic hybrid vehicle based on adaptive simulated annealing genetic algorithm. *Engineering Applications of Artificial Intelligence*, 23(1):27-33, 2010.

# **Modular Design of Hydromechanical Transmissions for Mobile Working Machines**

K. Pettersson and P. Krus

Division of Fluid and Mechatronic Systems, Department of Management and Engineering, Linköping University, Sweden  
E-mail: karl.pettersson@liu.se, petter.krus@liu.se

## **Abstract**

This paper demonstrates an optimisation-based method of designing modular gearboxes scalable for a range of applications. The design is adapted to the typical operating behaviours of the reference vehicles and considers the manufacturing costs of the gearboxes. Hydromechanical continuously variable transmissions (CVTs) are today strong candidates to replace drive line transmissions based on fuel-thirsty torque converters in many mobile working machines. The advantages include a wide range of torque/speed ratios, high energy efficiency throughout the speed range and decoupling of engine speed and vehicle speed. Advanced multiple mode CVTs, however, are difficult to evaluate early in the product development process due to their complex architectures and the great variety of possible concepts. There is consequently an increased need for methods to design, compare and evaluate the transmission concepts. To decrease the development and manufacturing costs, there is also a need for scalable transmission concepts that can be used in several applications of different classes. The results show the proficiency of the methodology compared to a manual design process and that the energy efficiency of the transmissions are strongly linked to the designs.

**Keywords:** Hydromechanical transmissions, Power-split, Design optimisation

## **1 Introduction**

A multiple-mode hydromechanical transmission provides a wide torque/speed range with a high efficiency throughout the speed range and is today a strong candidate to replace the torque converter in many heavy mobile working machines. Furthermore, the continuously variable torque/speed ratio allows for decoupling of engine speed and vehicle speed which enables more energy savings through engine management. With single-mode configurations, such as pure hydrostatic transmissions, very large displacement machines (hydraulic pump/motors) are required to meet the high power demands of heavier applications. By using synchronised shafts, multiple hydromechanical configurations can be combined to improve the energy efficiency and decrease the necessary sizes of the displacement machines. In recent years, a number of commercial concepts have been released for construction machines and off-highway applications, see for instance [1].

The combination of configurations leads to great many possible multiple-mode concepts. Furthermore, complex multiple-mode transmissions contain large numbers of mechanical gears and are more difficult to design. The notion of designing the transmission means, in this paper, the process of sizing the transmission components, i.e. the gear ratios and the displacement machines. For complex transmission architectures, there is a design space in which the transmission has the same performance, i.e. two different designs can

result in the same performance. A fair comparison between concepts is consequently only valid for optimised designs.

Much research has been done on developing simulation models for hydromechanical transmissions with the purpose of evaluating different transmission concepts, see for instance [2], [3] and [4]. Comparisons and evaluations of different transmission concepts can be found in for instance [5] and [6]. Fewer works, however, can be found on the design process of hydromechanical transmissions. Volpe et al. [7] suggested an optimisation-based design method using only kinematic models of the transmission components. Macor and Rosetti formulated a simulation-based optimisation method using more detailed loss models in [8] and [9]. The authors of this paper have proposed a design methodology for complex hydromechanical transmissions based on numerical optimisation in [10]. The methodology adapts the design in order to minimise the energy consumption for a predefined operating behaviour of the considered application. The studies have shown that the design of the transmission is strongly linked to the energy consumption of the application. It is also shown that an optimal design may be difficult to find manually, underlining the need for an automated design process.

### 1.1 Modular Design

The concept of modularity and platform design within product development is a well-recognised methodology to decrease the variety of components in a product family. The main advantages include lower manufacturing costs and lower development costs due to the increased communality of the products. The trade-off for the company lies instead in the decreased individual performance of the products. [11]

### 1.2 Problem Outline

There are a number of plausible desired characteristics of a gearbox, e.g. energy efficiency, manufacturing cost, controllability, low volume and weight. For the industrial designer these are most likely all aspects to consider when designing the transmission. For an OEM with a range of vehicles in its product portfolio, more than one application needs to be considered in the development process. A scalable (modular) gearbox with collective characteristics can reduce both the development costs and the manufacturing costs of the transmissions. This paper focuses on the design process of a modular gearbox suitable for a range of applications. The modularity is here confined to the use of the same transmission concept with the same hydraulic variator, but with varying number of modes. The modular design targets a wide range of wheel loader applications of different power classes.

## 2 Transmission Concept

The concept considered in the design methodology is the so called "Jarchow-concept" with an arbitrary number of modes, shown in fig. 1.

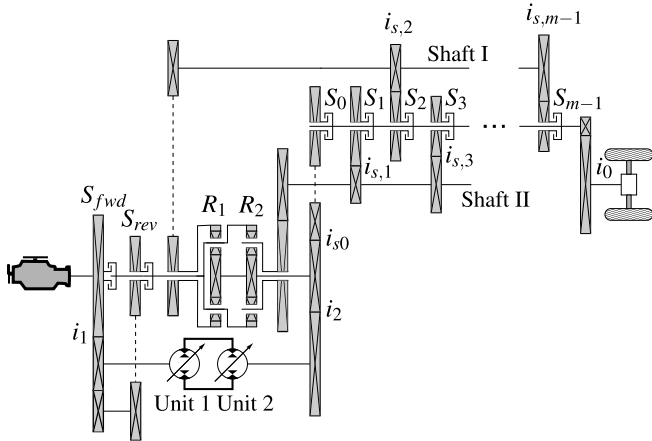


Figure 1: The "Jarchow-concept" with an arbitrary number of modes. The dimensions of the gear wheels are not necessarily proportionally correct; the figure merely shows the principle of the concept. In the figure, the number of modes,  $m$ , is an odd number.

The starting mode (H) is purely hydrostatic and the subsequent modes are input-coupled power-split modes. The number of modes,  $m$ , is defined as the number of forward power-split-modes plus the hydrostatic mode, i.e.  $m = 3$  means one hydrostatic mode and two power-split modes for

the forward motion. There are also  $m - 1$  power-split modes for the reverse motion. In the odd power-split modes (F1, F3 etc), the second planetary gear ( $R_2$ ) actively transfers power to Shaft II and in the even power-split modes (F2, F4 etc) the first planetary gear ( $R_1$ ) actively transfers power to Shaft I. The complete clutch configuration is shown in Table 1. An ar-

Table 1: Clutch arrangement

Mode	$S_{fwd}$	$S_{rev}$	$S_0$	$S_1$	$S_2$	$S_{m-1}$
Rm-1		•				•
R2		•			•	
R1		•		•		
H			•	•		
F1	•			•		
F2	•				•	
Fm-1	•					•

bitrary number of modes makes it possible to scale the transmission up or down depending on the power class of the application. The principle of this architecture can be found in several commercial hydromechanical CVTs and it has been treated previously in some of the papers referenced above.

## 3 Reference Vehicles

This study focus on the design of a modular gearbox for three wheel loader applications to demonstrate the design methodology. All three wheel loader sizes are traditionally equipped with a torque converter and a powershift gearbox making them suitable applications for hydromechanical transmissions. Table 2 shows the main parameters of the considered wheel loaders, denoted A-C, where A is the largest and C is the smallest. Figure 2 shows the tractive force requirements.

Table 2: Wheel loader parameters.

Wheel loader	A	B	C	Unit
$P_{max}$	219	161	96	kW
$F_{max}$	245	181	130	kN
$v_{max}$	40	40	40	km/h

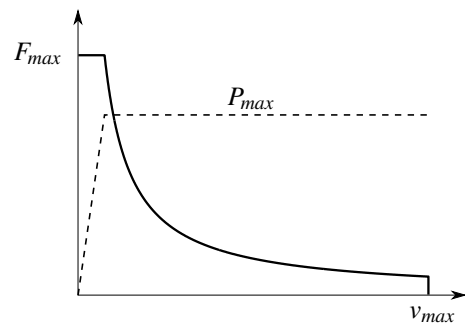


Figure 2: The tractive force requirements of a wheel loader.

To evaluate the energy consumption of a transmission design, pre-recorded data from typical operating cycles are used. By simulating the operating cycles, the energy consumption of a transmission design can be evaluated. This is a common way of evaluating system concepts and allows for an optimised system design specifically for the typical operating behaviour of the vehicle [12]. Wheel loaders are versatile machines and have many different application areas. Many machines are sold as multi-purpose machines although operating with a bucket in a production site is the most common task [13]. Two operating cycles are often used to characterise the operating behaviour of the wheel loader; the short loading cycle and the load-carry cycle, see fig. 3. For details of the operation of these cycles see [14].

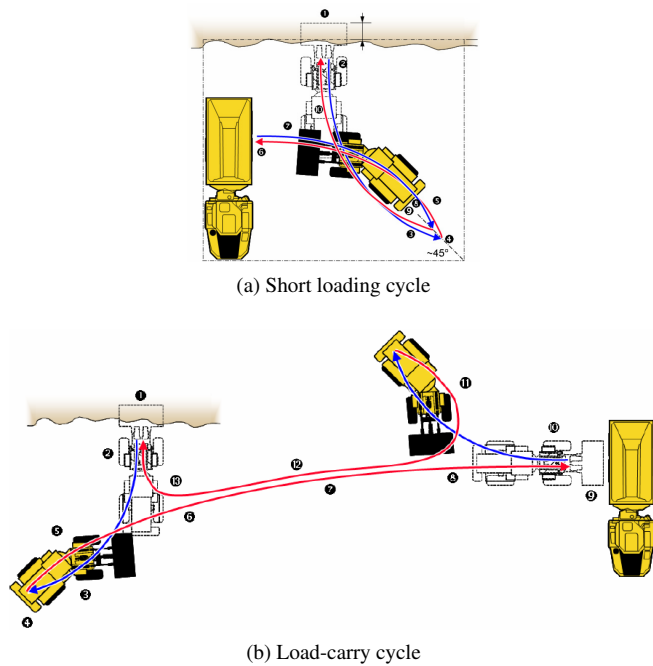


Figure 3: Typical operating cycles of the wheel loader, from [14].

Two examples of the cycles above have been recorded in real world operation for all three wheel loaders. For both cycles, gravel is loaded from a pile on to a load receiver of appropriate height for each wheel loader. Two trained operators each performed nine cycles each for every wheel loader application in every operating cycle. Data was recorded for the output axle of the transmission. The data was then analysed and one representative data set was selected for every wheel loader and cycle. This data is then used to represent the typical operating cycles for each wheel loader application.

Normally, larger wheel loaders are used to a greater extent in short loading cycles whereas smaller machines more often operate in transportation phases. The complete operating behaviour of the wheel loader is therefore achieved by weighing each cycle according to its significance for each wheel loader application. The weight factors are supplied by an OEM and represent approximate values of the distribution

for the average wheel loader. Figure 4 shows the operating point distribution over the speed range for the complete operating behaviour of the wheel loaders. The suggested

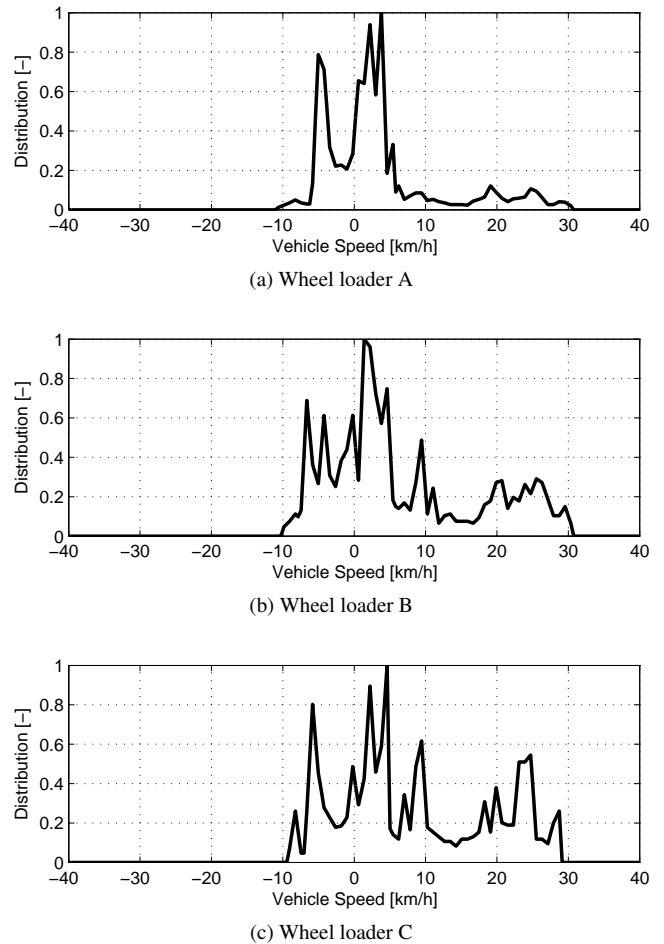


Figure 4: Distribution of the operating speeds for the typical operating behaviour of the considered wheel loaders

operating cycles represent a typical behaviour of the machine and, as stated earlier, are not true for every (any) wheel loader in the field. The use of typical operating cycles, however, is still helpful in the design process [12].

#### 4 Transmission Design

When dealing with multiple-mode hydromechanical transmissions, much can be gained from using similar concepts for many applications, including different power classes of the same type of vehicle. The development costs are significantly reduced if the gearbox can be scaled up and down or at least easily adapted to each application. Additionally, manufacturing costs can be reduced by producing or buying larger quantities of the same component.

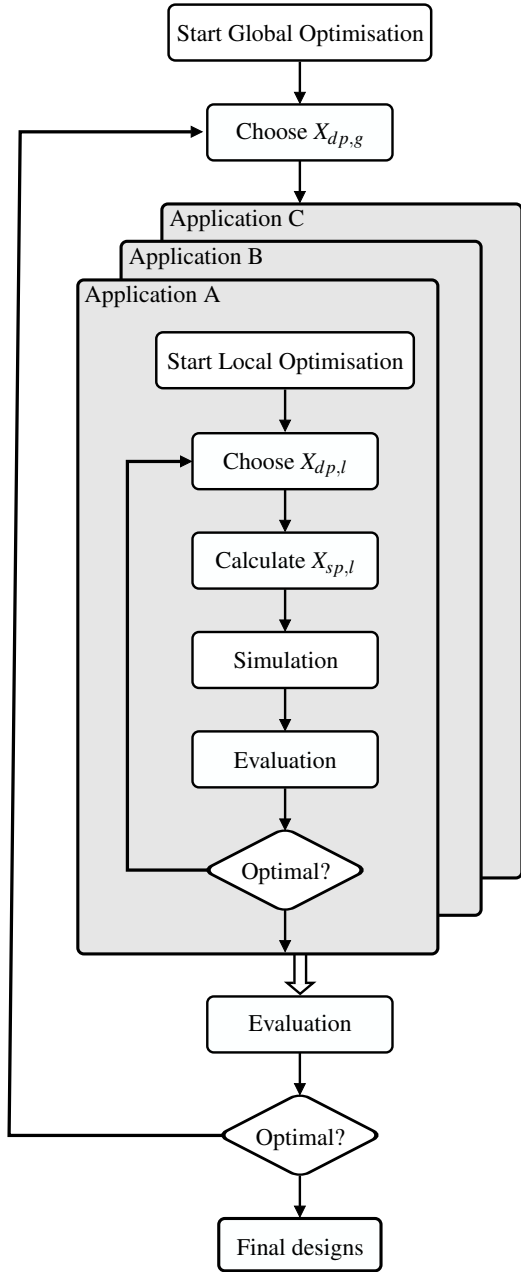


Figure 5: The design process for the modular gearbox. The inner loop optimises the transmission designs for all wheel loaders individually given a number of modes and a variator size. The outer loop sets the number of modes and variator size optimally for the considered range of applications.

The tractive force requirements and the demands of the gearbox characteristics naturally vary between applications. The demand for low cost and high energy efficiency may vary greatly also within different sizes of the same type of vehicle. One approach to achieve a modular gearbox is to use the same number of modes in each transmission and to vary the sizes of the displacement machines to match the tractive force requirements of each application, as shown in [1]. Another approach is to use the same hydrostatic variator, i.e. the same sizes of displacement machines, but with different numbers of modes depending on tractive power demands.

The advantages include lower manufacturing costs for the gearboxes since the variator can be bought or manufactured in larger series. The development costs may also be reduced and robustness increased if similar control software can be used for all transmissions. This is the design approach further examined in this paper. The trade-off for this scenario is that transmissions with a small hydraulic variator, leading to lower power losses, requires a higher number of modes, leading to higher costs.

The proposed design methodology is an extension of the previously developed methodology for designing complex hydromechanical transmissions [10]. Briefly explained, the design is achieved by identifying the degrees of freedom for the concept and letting an optimisation routine set the design parameters to minimise the energy consumption during simulated work cycles. The modular transmission is achieved when the design of each application is optimised with a collective hydraulic variator. The choice of hydraulic variator and number of modes for each application should consequently also be the subject of a design optimisation. Figure 5 shows the proposed methodology for the design process.

#### 4.1 Local Optimisation

The local optimisation loop optimally designs each application one by one, with a given number of modes  $m$  and a given variator size  $D_{var}$ . The explicit design relations have previously been derived in [10] for the same concept, but with Unit 2 as a fixed displacement machine. The two degrees of freedom are shown in eq. (1):

$$x_1 = \frac{v_{shift,k+1}}{v_{shift,k}} \text{ for } k = 1, 3, 5, \dots \quad (1a)$$

$$x_2 = \frac{v_{shift,k+1}}{v_{shift,k}} \text{ for } k = 2, 4, 6, \dots \quad (1b)$$

The degrees of freedom are hence the freedom of positioning the mode shifts within the speed range of the vehicle. With a variable Unit 2, smaller displacement machines may be required, since the hydrostatic speed range increases. For this study, the minimum displacement of Unit 2,  $\epsilon_{2,min}$ , is left as a design parameter, since it is unclear whether a lower  $\epsilon_{2,min}$  will lead to higher energy efficiency. Generally, the efficiency of the displacement machine is reduced when operating with low relative displacements. The system parameters and the design parameters for the local optimisation are consequently:

$$X_{sp,l} = [D_1 D_2 R_1 R_2 i_1 i_2 i_{s,0} i_{s,1} i_{s,2} \dots i_{s,m-1}]^T \quad (2a)$$

$$X_{dp,l} = [x_1 x_2 \epsilon_{2,min}]^T \quad (2b)$$

The simulation of the transmission is based on backward calculation with known steady-state models of the components. The greatest power losses come from the displacement machines, which require detailed loss models with dependency on all operating conditions [4]. The hydraulic variator also requires a charge pump for anti-cavitation and cooling and to supply the control circuit. For details of the simulation models used in this paper, see [10].

#### 4.1.1 Objective Function

The objective function for the local optimisation is simply the simulated equivalent energy consumption of the transmission for the specified operating cycles, shown in eq. (3):

$$f_l = \sum_k w_{l,k} \int_0^{t_{end,k}} P_{tot,k}(t) dt \quad (3)$$

where  $w_k$  is the weight factor for the operating cycle, as described in section 3.

#### 4.1.2 Constraints

Two constraints are used in the local optimisation to restrict the freedom of positioning the mode shifts in the speed range, see eq. (4).

$$v_{shift,1} \geq 5 \text{ km/h} \quad (4a)$$

$$v_{shift,k+1} - v_{shift,k} \geq 2 \text{ km/h for } k = 1, 2, \dots, m-1 \quad (4b)$$

The first constraint relates to the need to avoid mode shifts during the bucket fill operation, which normally takes place at under 5 km/h, see fig. 4. The second constraint prevents the mode shifts to be positioned too closely together. Between two mode shifts, the relative displacement of Unit 1 is controlled from -1 to 1 or vice versa. During quick accelerations and decelerations, there are consequently high demands on the control speed of the displacement machines.

#### 4.2 Global Optimisation

The global optimisation loop sets the optimal size of the variator and the number of modes for each wheel loader. The design parameters for the global optimisation are consequently:

$$X_{dp,g} = [m \ D_{var}]^T \quad (5)$$

where

$$m = [m_A \ m_B \ m_C]^T \quad (6a)$$

$$D_{var} = D_1 + D_2 \quad (6b)$$

#### 4.2.1 Objective Function

The target for the global optimisation problem is a multi-objective one. Since energy efficiency normally increases with number of modes, it is unreasonable only to optimise the vehicles' energy efficiency. The objective should instead formulate the trade-off between energy efficiency and the manufacturing cost of the gearbox.

$$f(X_{dp,g}) = \lambda_1 f_{g1} + \lambda_2 f_{g2} \quad (7)$$

The first objective,  $f_{g1}$ , is the weighted sum of equivalent energy consumptions from the local optimisation results according to eq. (8).

$$f_{g1} = \sum_k w_{g1,k} E_{k,equiv} \text{ for } k = A, B \text{ and } C \quad (8)$$

The weight factors  $w_{g1,k}$  specify the importance of energy efficiency for one application versus another. These values relate to factors such as number of sold vehicles, cost margins, fuel price, customer demands, acceptable payback period, etc. This type of analysis is beyond the scope of this paper; instead, the equivalent energy consumption is evenly weighted for the considered wheel loaders. The second objective,  $f_{g2}$ , is the weighted manufacturing costs of the gearboxes, according to eq. (9).

$$f_{g2} = \sum_k w_{g2,k} C_k \text{ for } k = A, B \text{ and } C \quad (9)$$

The weight factors  $w_{g2,k}$  also relate to the above mentioned market-related factors and are here assumed to be equal. The manufacturing costs are simply modelled as the sum of all component costs plus a fixed cost for the housing, additional hydraulic components, etc. See [15].

#### 4.2.2 Constraints

In previous studies, the sizes of the displacement machines are calculated and can take any continuous value. A more realistic approach for an industrial designer is to choose from a discrete series of sizes. To represent this scenario, the listed sizes of the Bosch Rexroth standard displacement machines A4VG/40 (Unit 1) and the A6VM/71 (Unit 2) [16] are used as possible variator sizes. One variator size means, for this case, only one combination of machine sizes, according to eq. (10).

$$\begin{bmatrix} D_1 \\ D_2 \end{bmatrix} \in \left( \begin{bmatrix} 145 \\ 170 \end{bmatrix}; \begin{bmatrix} 175 \\ 215 \end{bmatrix}; \begin{bmatrix} 210 \\ 280 \end{bmatrix} \right) \quad (10)$$

The number of modes for every transmission is naturally also a discrete value, which in this study is limited according to eq. (11).

$$2 \leq m_k \leq 6 \text{ for } k = A, B \text{ and } C \quad (11)$$

#### 4.3 Optimisation Algorithm

The Complex-RF method is used in the design process for both the global and the local optimisation. Briefly explained, the algorithm generates a certain number of random points in the design space and reflects the worst point towards the centroid of the other points until it is no longer the worst point. This process is iterated until the minimum function value is found or the maximum number of evaluations is reached. The Complex-RF method has previously been proved to be suitable to use in simulation-based design optimisation. [17]

### 5 Results and Discussions

Figure 6 shows optimisation results for consecutive runs with linearly changed weight factors  $\lambda_1$  and  $\lambda_2$  to form the Pareto optimal front. The solution will generally travel to the bottom right corner of the graph with an increased number of modes for the transmissions. A suitable weight between the two objectives is probably found somewhere in the middle, where a higher number of modes for a larger application is a reasonable choice. The awkward selections of  $m$  on the Pareto front shows that an optimised manual design would be

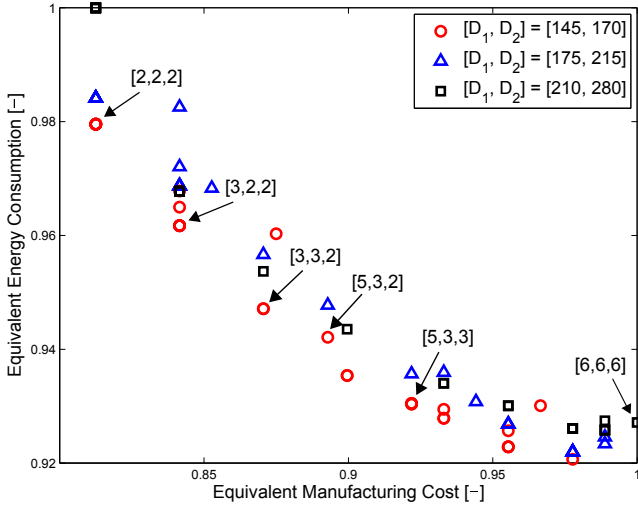


Figure 6: The Pareto front for the multi-objective design optimisation. Each marker represents a set of numbers of modes as indicated, according to  $[m_A, m_B, m_C]$ . The top left corner represents low energy efficiency and low costs, whereas the bottom right corner represents high costs and high energy efficiency.

difficult to achieve. The absence of the 4-mode transmission can also be seen in the graph. The 4-mode transmission seems to be only slightly better than the 3-mode transmission that dominates the Pareto front. This can also be seen in fig. 7 where the optimised designs of the transmissions for wheel loader C are simulated with the lowest variator size. The

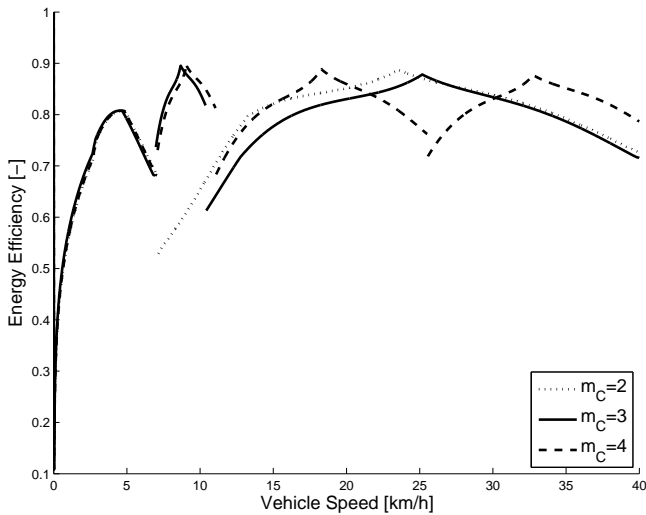


Figure 7: Simulation of an acceleration from 0 to maximum speed during maximum load conditions for wheel loader C. The peak efficiencies represent the full mechanical points where all power flows through the mechanical branch.

figure shows how the positioning of mode shifts is handled by the optimisation algorithm. The constraint for the bucket fill operation (eq. (4)) is often a limiting factor and most designs have the first mode shift close to 5 km/h. The other mode shifts are more cleverly positioned to match the full

mechanical points at the same speeds as the peaks in fig. 4. For the depicted case,  $m=3$  has even better capabilities to match the typical operating behaviour than  $m=4$ , which is a remarkable result.

To identify the decreased individual energy efficiency of the applications, the optimised designs are simulated with two different variator sizes. Table 3 compares the equivalent energy consumption for the wheel loaders using a larger variator than actually needed to achieve the specified performance.

Table 3: Percentage of increase in energy consumption when using the largest variator instead of the smallest one.

Wheel loader	A	B	C
$m = 2$	2.6%	1.9%	2.5%
$m = 3$	-1.4%	2.1%	3.3%
$m = 4$	-1.1%	1.1%	2.9%
$m = 5$	-1.0%	1.5%	3.0%
$m = 6$	-2.3%	0.5%	2.6%

Normally, a transmission with a smaller variator suffers from lower power losses, as the parasitic losses from the hydrostatic transmission are reduced. This seems to be the case for wheel loaders B and C. A small variator used in a large application, however, is forced to operate with smaller relative displacements which lowers the efficiency of the transmission. This is the reason why wheel loader A has a lower energy consumption when a larger variator is chosen. A special case is  $m = 2$  for wheel loader A, which suffers from poor energy efficiency in both cases. Table 4 displays the above discussed phenomenon for wheel loader A.

Table 4: Optimal  $\varepsilon_{2,min}$  for wheel loader A.

$[D_1, D_2]$	[145, 170]	[175, 215]	[210, 280]
$m = 2$	0.45	0.44	0.61
$m = 3$	0.76	0.47	0.96
$m = 4$	0.75	0.84	0.95
$m = 5$	0.74	0.83	0.96
$m = 6$	0.58	0.83	0.94

## 6 Conclusions

In this paper, a design methodology for modular multiple-mode hydromechanical transmissions has been proposed and implemented on the design of the "Jarchow-concept" for a range of wheel loader applications. The problem has been formulated into a multi-objective optimisation problem where energy efficiency and manufacturing costs of the product family are antithetic objectives. The implementation indicates that an optimised design of the modular transmission is difficult to achieve manually. Moreover, the number of degrees of freedom for the design increases when using a collective hydraulic variator, which further complicates the design task. This increases the need for an automated design process for the industrial designer.

## Nomenclature

### Quantities

Designation	Denotation	Unit
C	Cost	[–]
D	Hydraulic displacement	[ $cm^3/rev$ ]
F	Force	[ $kN$ ]
i	Gear ratio	[–]
m	Number of modes	[–]
P	Power	[ $kW$ ]
R	Planetary gear ratio	[–]
v	Vehicle speed	[ $km/h$ ]
w	Weight factor	[–]
$\epsilon$	Relative displacement	[–]
$\lambda$	Weight factor	[–]

### Indices

Designation	Denotation
g	Global
l	Local

## References

- [1] Thomas Anderl, Jürgen Winkelhake, and Marcus Scherer. Power-split Transmissions For Construction Machinery. In *8th International Fluid Power Conference*, pages 189–201, Dresden, Germany, 2012.
- [2] D Mikeska and M Ivantysynova. Virtual Prototyping of Power Split Drives. In *Workshop on Power Transmission and Motion Control*, pages 95–111, Bath, UK, 2002.
- [3] P Casoli, A Vacca, G L Berta, S Meleti, and M Vescovini. A Numerical Model for the Simulation of Diesel / CVT Power Split Transmission. In *8th International Conference on Engines for Automobiles*, Capri, Naples, Italy, 2007.
- [4] Torsten Kohmäscher. *Modellbildung, Analyse und Auslegung Hydrostatischer Antriebsstrangkonzepete*. PhD thesis, RWTH Aachen, Aachen, Germany, 2009.
- [5] Alexander Krauss and Monika Ivantysynova. Power Split Transmissions Versus Hydrostatic Multiple Motor Concepts - A Comparative Analysis. *SAE Transactions*, 113(2), 2004.
- [6] Blake Carl and Monika Ivantysynova. Comparison of Operational Characteristics in Power Split Continuously Variable Transmission. In *Commercial Vehicle Engineering Congress and Exhibition*, Chicago, Illinois, USA, 2006.
- [7] S. Schembri Volpe, G. Carbone, M. Napolitano, and E. Sedoni. Design Optimization of Input and Output Coupled Power Split Infinitely Variable Transmissions. *Journal of Mechanical Design*, 131(11):111002, 2009.
- [8] Alarico Macor and Antonio Rossetti. Optimization of Hydro-mechanical Power Split Transmissions. *Mechanism and Machine Theory*, 46(12):1901–1919, 2011.
- [9] Antonio Rossetti and Alarico Macor. Multi-objective optimization of hydro-mechanical power split transmissions. *Mechanism and Machine Theory*, 62:112–128, April 2013.
- [10] Karl Pettersson and Petter Krus. Design Optimization of Complex Hydromechanical Transmissions. *ASME Journal of Mechanical Design*, 2013. Accepted for publication.
- [11] Alberto Jose and Michel Tollenaere. Modular and Platform Methods for Product Family Design : Literature Analysis. *Journal of Intelligent Manufacturing*, 16(3):371–390, 2005.
- [12] K Steindorff. Methods for benchmarking the efficiency of mobile working machines and heavy duty vehicles. In *6th International Fluid Power Conference*, pages 197–207, Dresden, Germany, 2008.
- [13] Bobbie Frank, Lennart Skogh, and Mats Alaküla. On Wheel Loader Fuel Efficiency Difference Due To Operator Behaviour Distribution. In *2nd International Commercial Vehicle Technology Symposium, CVT2012*, Kaiserslauten, Germany, 2012.
- [14] Reno Filla. *Quantifying Operability of Working Machines*. PhD thesis, Linköping University, Linköping, Sweden, 2011.
- [15] Karl Pettersson and Petter Krus. Optimisation and Concept Sensitivity of Continuously Variable Hydromechanical Transmissions. In *8th International Conference on Fluid Power Transmission and Control, ICFP13*, Hangzhou, China, 2013.
- [16] Bosch Rexroth AG. Produktkatalog Mobilhydraulik. <http://www.boschrexroth.com/mobile-hydraulics-catalog/>, 2013.
- [17] Petter Krus and Johan Andersson. Optimizing Optimization for Design Optimization. In *ASME Design Engineering Technical Conferences and Computers and Information in Engineering Conference*, Chicago, Illinois, USA, 2003.



## Industry Application 2



## Energy-Saving Design for Hydraulic Tube Bender

J C Renn, C Y Cheng, and M H Lin,

Department of Mechanical Engineering,  
National Yunlin University of Science and Technology,  
Douliou, Yunlin, Taiwan

E-mail: rennjc@yuntech.edu.tw, g9511706@yuntech.edu.tw, m10011004@yuntech.edu.tw

### Abstract

Generally speaking, hydraulic control systems can be divided into two different driving concepts. The first one is the well-known valve-controlled system and the second one is the pump-controlled system. The former possesses the feature of fast dynamic response. However, the poor energy-saving performance is its major fault. On the contrary, the pump-controlled hydraulic system has the significant advantage of energy-saving which meets the current demand in modern machine design. In this paper, the simulation analysis using MatLab/SimuLink and DSHplus for a newly developed energy-saving hydraulic tube bender is conducted. Instead of the conventional fixed displacement hydraulic pump, the new hydraulic tube bender utilizes an internal gear pump with AC servomotor as its driving power source. In the new energy-saving hydraulic circuit, the use of conventional pressure relief valve and unloading valve are no longer necessary since the demanded flow-rate and pressure output can be precisely obtained by continuously changing the speed of the AC servomotor. In addition, two closed-loop control schemes using fuzzy sliding-mode controller are adopted and compared. From the simulation results, it is shown that the energy-saving performance of constant pressure control scheme is somewhat better than that of load-sensing control scheme. Furthermore, the simulation results also show that the newly developed hydraulic tube bender can save up to 42 % of energy consumption in a working cycle as compared to the conventional hydraulic tube bender.

**Keywords:** Hydraulic Energy-Saving, Pump-Controlled System, Fluid Power, Tube Bender

### 1 Introduction

Nowadays, hydraulic systems still play a very important role in modern industry due to the large output force, high power/weight ratio and excellent stiffness. In this paper, a conventional hydraulic tube bender shown in Fig. 1 is chosen for the study of implementing the hydraulic energy-saving design. Figure 2 shows a typical working cycle of the chosen hydraulic tube bender [5]. It is observed that eight sequential steps are required to complete the bending of a straight tube. They are: (A) advancing the main pushing unit, (B) clamping the tube, (C) advancing the bending unit together with auxiliary pushing unit and bending the tube (90 degrees), (D) retracting the main pushing unit, (E) releasing the clamping of tube, (F) retracting the auxiliary pushing unit, (G) removal of tube and (H) retracting the bending unit. In the hydraulic circuit of a conventional tube bender, a fixed-displacement vane pump is generally utilized as shown in Fig. 3. In addition, a pilot-operated pressure balanced relief valve together with a two-way solenoid operated valve is used as well to construct the unloading circuit. However, the hydraulic supply pressure of the conventional tube bender has to be set at the maximal demanded pressure of 120 bar to ensure the proper function of all 8 steps. Thus, from Fig. 2, it is clear that huge energy lost in the working cycle is inevitable since only the step C requires the maximal supply pressure of 120 bar. For the rest 7 steps, however, the actually demanded supply pressure is

much lower than the maximal pressure of 120 bar. On the other hand, recent performance improvements in the AC servomotor provide a promising alternative to design the energy-saving hydraulic circuit [2, 3, and 4]. In details, the demanded flow-rate and pressure output of the hydraulic pumping unit can be precisely obtained by continuously changing the speed of the AC servomotor. In this paper, therefore, the implementation of energy-saving design is mainly based on the AC servomotor-controlled scheme. In the following, the proposed energy-saving control scheme is firstly outlined.



Figure 1: A hydraulic tube bender [5].

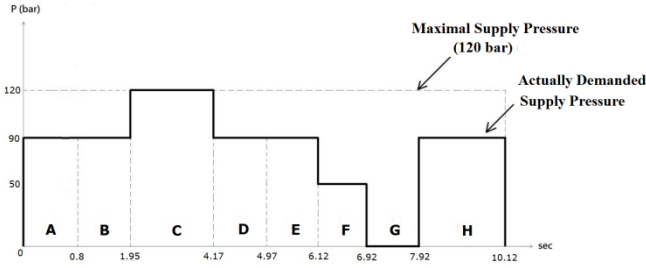


Figure 2: Demanded pressure in a working cycle.

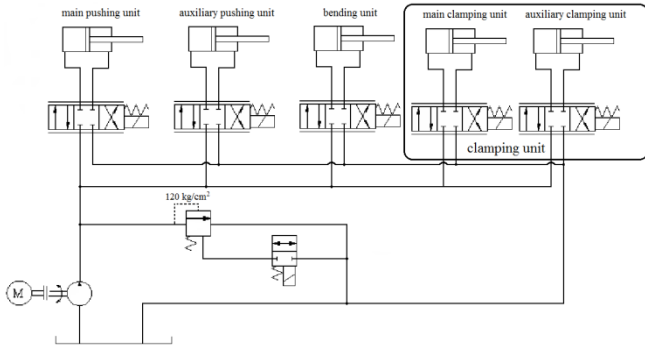


Figure 3: Schematic circuit diagram of a conventional hydraulic tube bender.

## 2 Energy-saving control scheme

In this paper, two closed-loop control schemes using fuzzy sliding-mode controller are adopted and compared. The first one is load-sensing control strategy and the other one is constant pressure control scheme [4]. Figure 4 shows the block diagram of the load-sensing control. A fixed pressure drop,  $\Delta p_{set}$ , across the control solenoid valve serves as the reference input. The load pressure,  $p_{Ls}$ , is measured by a pressure sensor and feedback to the closed-loop control system to ensure that the supply pressure,  $p_s$ , can be real-time adjusted according to the variable load pressure. Consequently, the actual pressure drop,  $\Delta p = p_s - p_{Ls}$ , can be maintained as a constant by the closed-loop control. On the other hand, Figure 5 shows the block diagram of constant pressure control. In this configuration, the reference supply pressure input,  $P_{sset}$ , is varied according to the different demanded pressure levels at various steps as shown in Fig. 2. Thus, the reference supply pressure input is actually not a constant and has to be changed at different steps. Besides, it is worth mentioning that the fuzzy sliding-mode scheme is chosen as the closed-loop controller because it provides a dither-like chattering signal. Such a signal is proven to be effective to overcome the nonlinear friction disturbances [1].

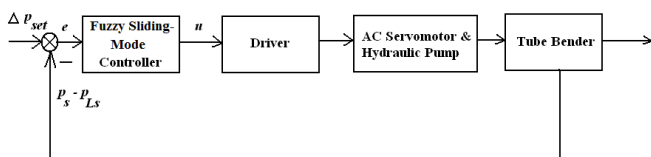


Figure 4: Load-sensing control block diagram.

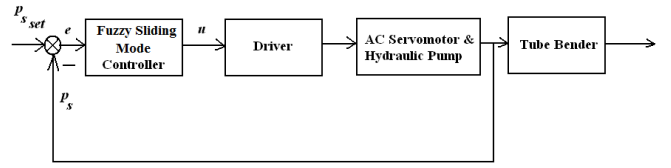


Figure 5: Constant pressure control block diagram.

The combination of fuzzy-logic-controller with sliding mode controller results in the fuzzy sliding-mode controller. As an example, the constant pressure control scheme combining the fuzzy sliding-mode controller is illustrated as follows. Figure 6 shows the schematic block diagram of the fuzzy sliding-mode controller. The error signal,  $e(k)$ , and the error signal change,  $\Delta e(k)$ , are denoted by  $x_1$  and  $x_2$  respectively, that is

$$x_1 = e(k) = p_{sset} - p_s, \quad (1)$$

$$x_2 = \Delta e(k) = e(k) - e(k-1), \quad (2)$$

where  $p_{sset}$  : reference supply pressure input,

$p_s$  : actual supply pressure.

Unlike the conventional controller, there are four procedures involved in the implementation of a fuzzy sliding-mode controller, fuzzification of the input, fuzzy inference based on the knowledge, the defuzzification of the rule-based control signal and the determination of the scaling factors.

### 2.1 Fuzzification

The proposed fuzzy sliding-mode controller requires only one input signal,  $s$ , which is exactly the combination of the parameters  $x_1$  and  $x_2$ .

$$s = \lambda x_1 + x_2. \quad (3)$$

Figure 7 shows the usual triangular fuzzy membership function for the input signal,  $s$ , and for the output signal,  $u$ . The input signal also represents the switching surface of the sliding mode controller.

### 2.2 Inference

The inference process consists of nine typical rules driven by the linguistic values of the input signal,  $s$ . There are:

If  $S$  is very large-positive, then  $u$  is very large-positive.

If  $S$  is large-positive, then  $u$  is large-positive.

If  $S$  is medium-positive, then  $u$  is medium-positive.

If  $S$  is small-positive, then  $u$  is small-positive.

If  $S$  is zero, then  $u$  is zero.

If  $S$  is small-negative, then  $u$  is small-negative.

If  $S$  is medium-negative, then  $u$  is medium-negative.

If  $S$  is large-negative, then  $u$  is large-negative.

If  $S$  is very large-negative, then  $u$  is very large-negative.

### 2.3 Defuzzification

The defuzzification is to transform control signal into exact control output. In the defuzzification, the method of center of gravity is used.

$$u = \frac{\sum_{i=1}^n W_i B_i}{\sum_{i=1}^n W_i}, \quad (4)$$

where  $u$  : output of the fuzzy sliding-mode controller,

$W_i$  : the degree of firing of the  $i_{th}$  rule,

$B_i$  : the centroid of the consequent fuzzy subset of the  $i_{th}$  rule.

### 2.4 Determination of scaling factors, $GS$ and $GU$

Before the input signal,  $s$ , is fed into the fuzzy-sliding mode controller, it has to be multiplied by the scaling factor,  $GS$ , so that the product is normalized in the interval  $[-1, 1]$ . Similarly, the output signal of the fuzzy-sliding mode controller,  $u$ , is multiplied by the scaling factor,  $GU$ , to meet the actual operating voltage range,  $-10$  V to  $10$  V, of the AC servomotor. It is also worth mentioning that the values of the factors,  $GS$  and  $GU$ , affect the system response greatly.

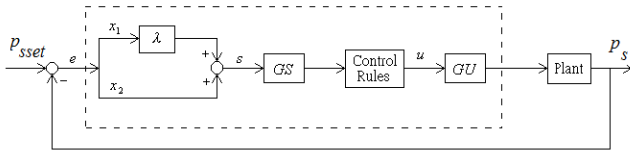


Figure 6: Scheme of the proposed fuzzy sliding-mode control.

## 3 Modeling, Simulation results and Discussion

In this paper, two commercial software packages, the MatLab/SimuLink and DSHplus, are chosen as simulation tools to analyze the energy-saving performance. Firstly, the modeling procedure by MatLab/SimuLink will be outlined.

The dynamics of the utilized AC servomotor can be simplified as a first-order function. In addition, a simplified model for a typical single-acting hydraulic cylinder is shown in Fig. 8. The volumetric flow-rate output of the hydraulic pump is given by [2]

$$Q_s = Vp \times (1 - e^{-t/T})N, \quad (5)$$

where  $Vp$  : displacement of pump,

$T$  : time constant of AC servomotor,

$N$  : reference rotational speed input.

In practice, the time constant,  $T$ , can be derived from the data sheet of the AC servomotor and is estimated to be 50 ms [6].

From continuity equation, the dynamic model for the supply pressure can be simplified as

$$\frac{dP_s}{dt} = \frac{E_{oil}}{V_{pipe}} (Q_s - Q_a), \quad (6)$$

where  $Q_a$  denotes the volumetric flow-rate going into the chamber A of cylinder and can be described by

$$Q_a = BX_v \sqrt{(P_s - P_a)}. \quad (7)$$

Similarly, the volumetric flow-rate coming out of the chamber B of cylinder can be obtained as

$$Q_b = BX_v \sqrt{P_b}, \quad (8)$$

where  $X_v$  : spool displacement,

$B$  : flow constant.

Since the switching directional control valve is utilized in the circuit design, the spool displacement,  $X_v$ , is set to be the maximal stroke  $+3$  or  $-3$  mm.

The flow constant,  $B$ , in Eq. (8) can further be expressed as

$$B = C_d \pi d_v \sqrt{2/\rho}, \quad (9)$$

where  $C_d$  : flow coefficient,

$d_v$  : diameter of the valve spool,

$\rho$  : density of the hydraulic oil.

If the internal and external leakages of the cylinder are both negligible, the simplified dynamic pressure equations for both chambers of the cylinder are

$$\frac{dP_a}{dt} = \frac{E_{oil}}{V_a + V_{pipe}} (Q_a - A\dot{Y}), \quad (10)$$

$$\frac{dP_b}{dt} = \frac{E_{oil}}{V_b + V_{pipe}} (-Q_b + A\dot{Y}), \quad (11)$$

where  $E_{oil}$  : bulk modulus of oil,

$V_a$  : volume of chamber A,

$V_b$  : volume of chamber B,

$V_{pipe}$  : volume of connecting pipe,

$A$  : average area of piston,

$\dot{Y}$  : velocity of the piston.

Finally, the equation of motion gives

$$M\ddot{Y} + b\dot{Y} = A_a P_a - A_b P_b - F_L, \quad (12)$$

Where  $M$  : mass of load,

$\ddot{Y}$  : acceleration of piston,

$b$  : Newton's friction coefficient,

$A_a$  : actuating area of piston in chamber A,

$A_b$  : actuating area of piston in chamber B,

$F_L$  : disturbance load.

Thus, the MatLab/SimuLink model for the single-acting hydraulic cylinder is shown in Fig. 8. Since there are totally five hydraulic cylinders in the conventional tube bender, the whole hydraulic circuit model containing five single-acting hydraulic cylinders built by MatLab/SimuLink is shown in Fig. 9. On the other hand, to double check the validity of the above mentioned modeling and simulation, the hydraulic circuit model using the second software package DSHplus for the same conventional tube bender is established as shown in Fig. 10. Figure 11 shows the simulation displacements of the main pushing cylinder by two different software packages respectively. Similarly, two calculated actuating pressure curves of the main pushing cylinder are also depicted in Fig. 12. Obviously, from Figures 11 and 12, the calculated cylinder displacements as well as actuating pressure curves derived from MatLab/SimuLink and DSHplus respectively are almost identical. It can therefore be verified that the modeling procedure and simulation results by MatLab/SimuLink are reliable and can be used for further energy-saving analysis.

It is worth mentioning that the block diagram shown in Fig. 9 is actually an open loop control scheme. It is necessary to incorporate the proposed fuzzy sliding-mode controller into

the control structure and form a closed-loop control block diagram. In addition, two proposed control schemes, the constant pressure control and load-sensing control, have also to be implemented. Thus, based on the simplified block diagrams shown in Figures 4 and 5, two comprehensive closed-loop control block diagrams can be obtained as shown in Figures 13 and 14 respectively. In the following, the control performances of these two closed-loop control schemes will be discussed and compared.

After adequate simulations, all important data and information of the whole tube bender system, like the pressure and flow-rate etc., can be obtained. The power consumption of the pumping unit can easily be calculated by the following equation (13).

$$P_{pump} = \frac{p_s \times Q_s}{600}, \quad (13)$$

where  $P_{pump}$  : power consumption of the pump,

$p_s$  : supply pressure,

$Q_s$  : supply flow-rate.

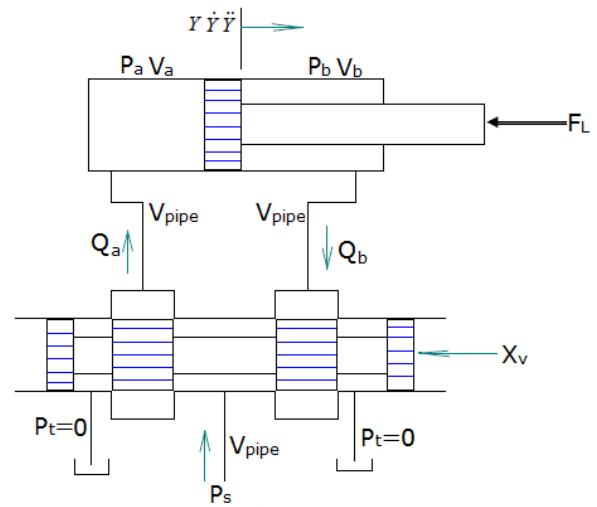


Figure 7: A simplified model for a single-acting hydraulic cylinder [2].

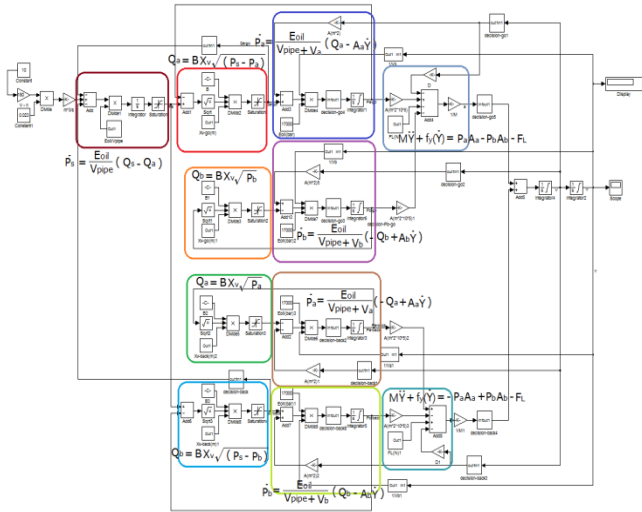


Figure 8: MatLab/SimuLink model for the single-acting hydraulic cylinder.

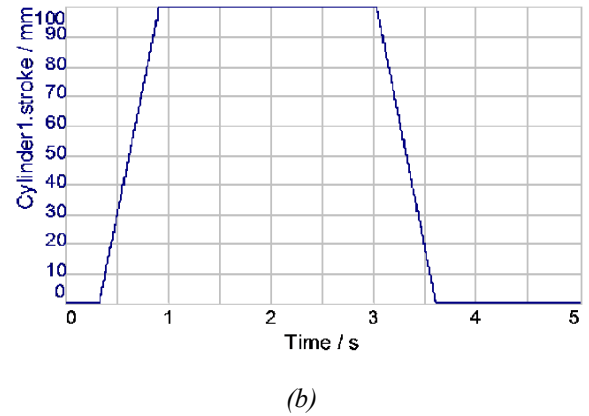
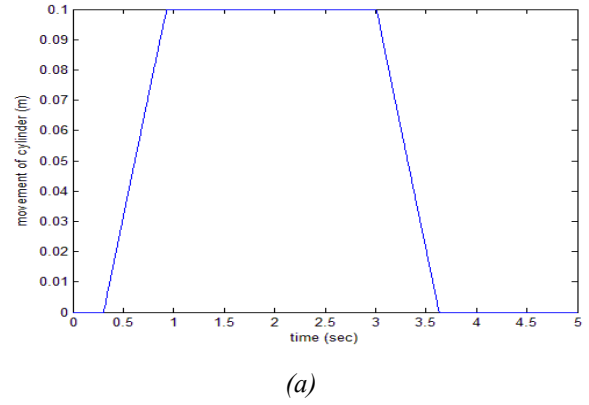


Figure 11: Simulation cylinder displacements of the main pushing unit by two different software packages (open loop). (a) MatLab/SimuLink results; (b) DSHplus results

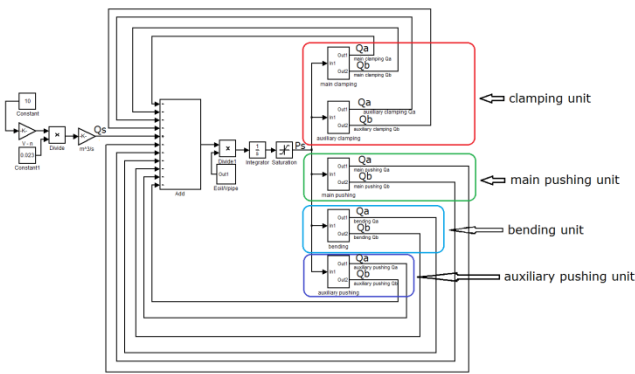


Figure 9: MatLab/SimuLink model for the conventional hydraulic tube bender.

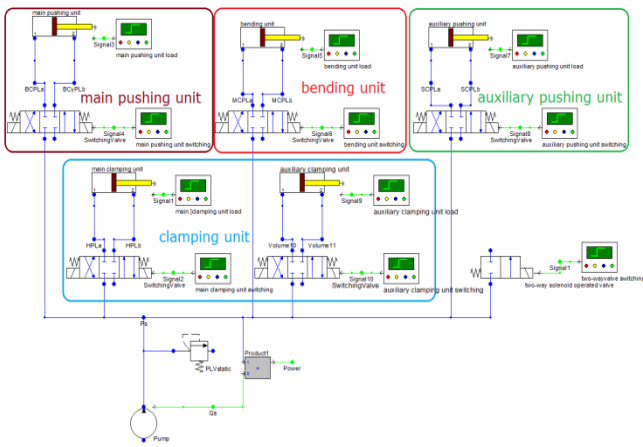
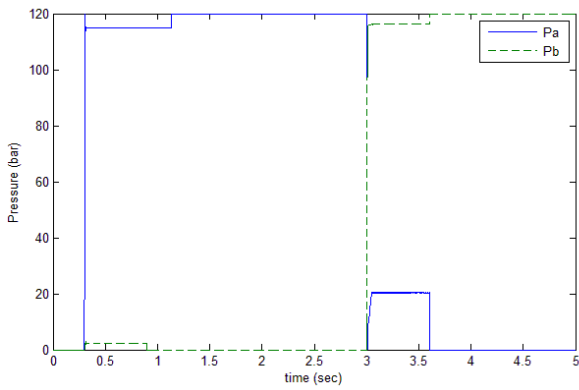


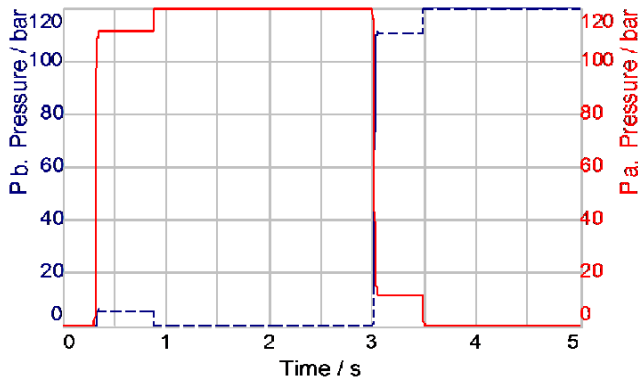
Figure 10: Hydraulic circuit model built by DSHplus for conventional tube bender.

As an illustrated example, the simulation results of supplied actuating pressure and volumetric flow-rate by load-sensing control for the main pushing cylinder are shown in Fig. 15, where the pressure drop,  $\Delta p_{set}$ , is set to be 3 bar. It is noticeable that both the pressure and flow-rate curves for the advance and retraction of the main pushing cylinder are depicted. In addition, Figure 16 shows the similar simulation results by constant pressure control scheme, where the reference supply pressure input,  $P_{set}$ , is set to be 90 bar according to the demanded pressure level at step A shown in Fig. 2. Comparing Fig. 15 and Fig. 16, it is actually not easy to tell the differences of the pressure and volumetric flow-rate signals during the advance and retraction phases of the main pushing cylinder. However, if Eq. (13) and appropriate numerical calculations are applied to evaluate the power consumption, the difference of driving power between two utilized closed-loop control strategies for the main pushing cylinder in one working cycle is more obvious as shown in Fig. 17.

It is worth mentioning that the energy-saving analysis using DSHplus is not executed in this paper because the proposed fuzzy sliding-mode controller is not available in the current library of the commercial software package DSHplus.



(a)



(b)

Figure 12: Simulation actuating pressure curves of the main pushing unit by two different software packages (open loop.)  
 (a) MatLab/SimuLink results; (b) DSHplus results

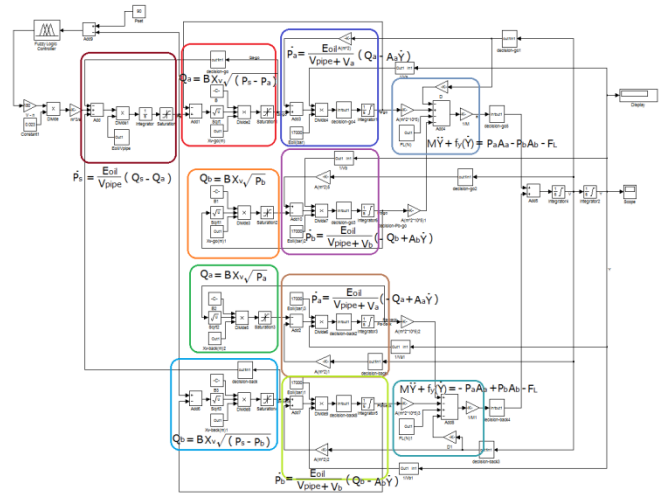
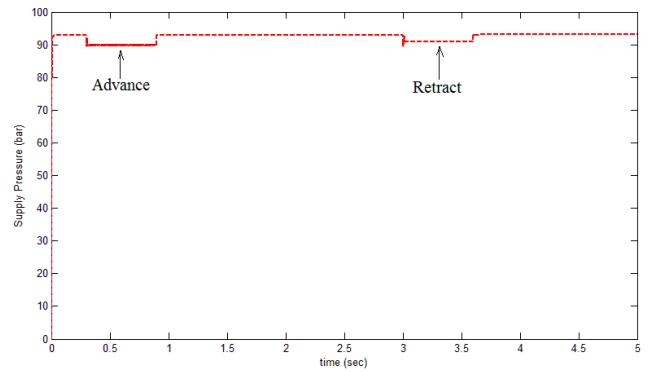
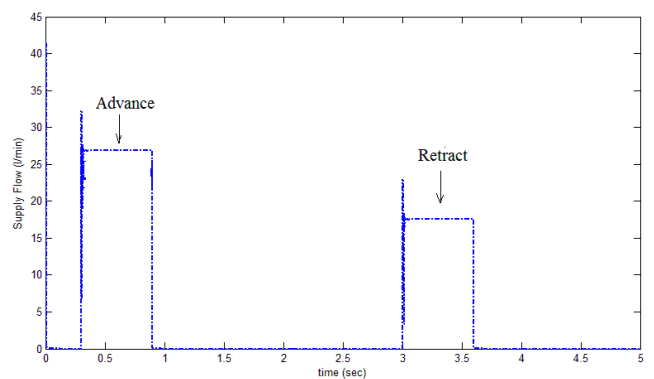


Figure 14: Closed-loop constant pressure control block diagram for the main pushing cylinder.



(a)



(b)

Figure 15: Simulation results of (a) supplied actuating pressure and (b) volumetric flow-rate by load-sensing control for the main pushing cylinder.

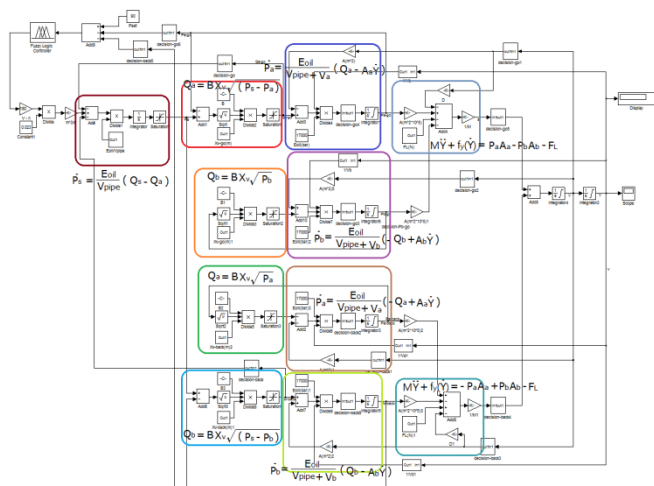
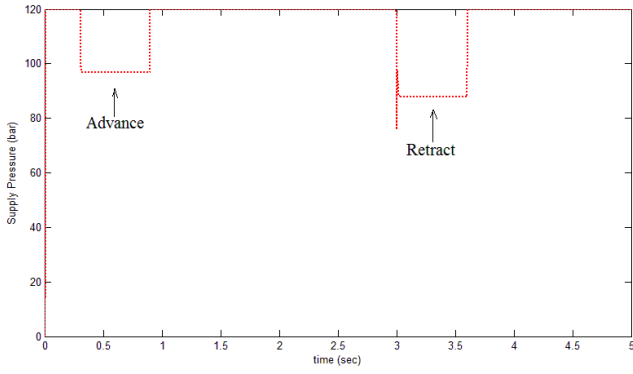
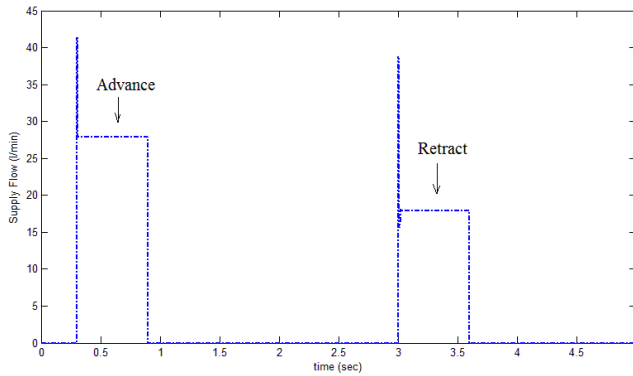


Figure 13: Closed-loop load-sensing control block diagram for the main pushing cylinder.



(a)



(b)

Figure 16: Simulation results of (a) supplied actuating pressure and (b) volumetric flow-rate by constant pressure control for the main pushing cylinder.

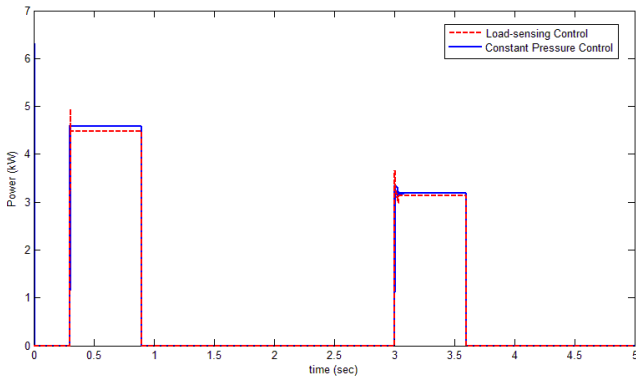


Figure 17: Simulation results of power consumption between two utilized closed-loop control strategies for the main pushing cylinder.

Table 1 shows the comparisons of overall energy consumption of pumping unit between the conventional and newly designed energy-saving hydraulic tube bender. It is observed that the energy-saving performance of constant pressure control scheme is somewhat better than that of load-sensing control scheme. Furthermore, the simulation results also show that the newly designed hydraulic tube bender can save up to 42 % of energy consumption in a working cycle as compared to the conventional hydraulic

tube bender. These results prove the validity of the proposed energy-saving hydraulic circuit design as well as the effectiveness of proposed closed-loop control schemes.

Table 1: Comparisons of energy consumption between conventional and new energy-saving hydraulic tube bender

Step	Conventional			Load-sensing control			Const. pressure control		
	$P_s$ (bar)	$Q_s$ (l/min)	$P_{pump}$ (kW)	$P_s$ (bar)	$Q_s$ (l/min)	$P_{pump}$ (kW)	$P_s$ (bar)	$Q_s$ (l/min)	$P_{pump}$ (kW)
A	120	41.4	8.28	89.36	31.41	4.68	89.6	32.58	4.86
B	120	41.4	8.28	89.97	33.08	4.96	89.6	32.43	4.84
C	120	41.4	8.28	119.04	38.04	7.55	119.54	38.37	7.64
D	120	41.4	8.28	89.96	22.06	3.31	89.71	23.93	3.58
E	120	41.4	8.28	89.84	26.26	3.93	89.59	23.23	3.47
F	120	41.4	8.28	51.04	17.42	1.48	49.82	14.38	1.19
G	0	41.4	0	0	0	0	0	0	0
H	120	41.4	8.28	89.94	27.51	4.12	89.6	28.2	4.21
Total Energy(kJ)	75.51			43.62			43.46		
Energy-Saving Percentage	0%			42.23%			42.44%		

## 4 Conclusions

In this paper, a new energy-saving hydraulic tube bender is successfully designed based on the simulation analysis using MatLab/SimuLink and DSHplus. The introduction of the additional commercial software package DSHplus is merely to verify the validity of proposed modeling procedure and simulation results. In addition, three conclusions may also be drawn from this research.

- (1) The simulation results derived from MatLab/SimuLink and DSHplus respectively are nearly identical. It can therefore be verified that the modeling procedure and simulation results by MatLab/SimuLink are reliable and can be used for further energy-saving analysis.
- (2) Simulation results show that the newly designed hydraulic tube bender can save up to 42 % of energy consumption in a working cycle as compared to the conventional hydraulic tube bender. This result not only shows the potential of energy-saving design but also encourages the future real implementation of the new tube bender.
- (3) The energy-saving performance of constant pressure control scheme is somewhat better than that of load-sensing control scheme. Besides, the former utilized only one pressure sensor while the latter requires two pressure sensors to calculate the actual pressure drop. Therefore, the better choice would be undoubtedly the constant pressure control scheme which will be suggested to be implemented in the future real layout of the new hydraulic tube bender.

## 5 Acknowledgement

The financial support of the National Science Council under grant number NSC-101-2622-E-224-014-CC3 is greatly appreciated. In addition, the industrial project supported by SOCO Machinery Co., LTD. is also acknowledged.

## Nomenclature

Designation	Denotation	Unit
$A$	Piston Average Area	[m <sup>2</sup> ]
$A_a$	Piston Actuating Area (Chamber A)	[m <sup>2</sup> ]
$A_b$	Piston Actuating Area (Chamber B)	[m <sup>2</sup> ]
$B$	Flow Constant	[m <sup>2</sup> /min √bar]
$b$	Newton's Friction Coefficient	[N s/m]
$C_d$	Flow Coefficient	[-]
$d_v$	Spool Diameter	[mm]
$E_{oil}$	Oil Bulk Modulus	[bar]
$F_L$	Disturbance Load	[N]
$M$	Mass of Load	[kg]
$N$	Reference Rotational Speed Input	[rpm]
$p_{Ls}$	Load-sensing Pressure	[bar]
$p_s$	Supply Pressure	[bar]
$Q_a$	Volumetric Flow-rate going into the Chamber A	[l/min]
$Q_b$	Volumetric Flow-rate coming out of the Chamber B	[l/min]
$Q_s$	Supply Flow-rate	[l/min]
$\Delta p_{set}$	Reference Pressure Drop Input	[bar]
$P_{sset}$	Reference Supply Pressure Input	[bar]
$P_{pump}$	Power Consumption of Pump	[kW]
$T$	time constant of AC servomotor	[s]
$u$	Actuating Signal	[Volt]
$V_p$	Pump Displacement	[cc]
$V_a$	Volume of Chamber A	[m <sup>3</sup> ]
$V_b$	Volume of Chamber B	[m <sup>3</sup> ]
$V_{pipe}$	Volume of Connecting Pipe	[m <sup>3</sup> ]
$X_v$	Spool Displacement	[mm]
$Y$	Displacement of Cylinder Piston	[m]
$\dot{Y}$	Velocity of Cylinder Piston	[m/s]

$\ddot{Y}$	Acceleration of Cylinder Piston	[m/s <sup>2</sup> ]
$\rho$	Oil Density	[kg/m <sup>3</sup> ]

## References

- [1] J C Renn, Position Control of A Pneumatic Servo-cylinder Using Fuzzy-sliding Surface Controller, *Int. J. of Fluid Power*, 3(3): 19-25, 2002.
- [2] H E Merritt, *Hydraulic Control Systems*, John Wileys and Sons, Cincinnati, Ohio, 1967. ISBN 0-471-59617-5.
- [3] H Murrenhoff, Systematic approach to the control of hydrostatic drives, *Proc. of the Institution of Mechanical Engineers*. Part I: Journal of Systems & Control Engineering, 213(15): 333-347, 1999.
- [4] M H Chiang, Y W Chien and D D Yu, Implementation of integrated control of path control and energy-saving control for hydraulic servo systems," *J CSME*, 24(2): 50–58, 2003.
- [5] N N, Hydraulic Tube Bender, Catalogue of SOCO machinery Co., LTD, [www.soco.com.tw](http://www.soco.com.tw), 2012.
- [6] N N, HES Series AC Servomotor, Catalogue of Delta Electronics, Inc., <http://www.delta.com.tw>, 2012.

## **Thermo-energetic analysis and simulation of the fluidic cooling system of motorized high-speed spindles**

Juliane Weber, and Jürgen Weber

Institute of Fluid Power, Dresden University of Technology, 01062 Dresden, Germany  
E-mail: juweber@ifd.mw.tu-dresden.de, weber@ifd.mw.tu-dresden.de

### **Abstract**

Beside drive tasks for feeding movements and tool clamping, fluid power systems especially permit the temperature control in machine tools: They allow cooling or pre-heating of both single components and complete assemblies (e.g. frame components, drive motors and spindles). In this respect, fluid power systems are an important element for controlling and managing the thermo-elastic behaviour of machine tools. As an essential part of the machine, they must be included from the beginning of the design studies of machine tools – particularly in terms of accuracy under conditions of energy-efficient manufacturing.

The increasing complexity and performance of fluid power systems generally lead to an increased use of auxiliary power. This has to be critically examined from an economic and environmental point of view. Focusing especially on the optimum thermal performance with minimum power supply, existing simulation models are not adequate for a scientifically based design. The complex system structures as well as the lack of basic investigations and design tools lead to a thermal optimization problem that is not solved satisfactorily today. For this purpose the Institute of Fluid Power (IFD) develops principles and simulation models with a holistic approach.

Based on the analysis of general tooling machines fluidic subsystems are identified and essential modelling requirements are specified. From a fluid-technical perspective the motor spindle represents an important principal component, and therefore, is a particular focus of current investigations. Starting from the basic technical structure of the motor spindles an abstract model is derived. This model represents the basis for different simulation strategies such as network-based or numerical ones. To study the thermal behaviour of cooling sleeves in motor spindles – especially with regard to the parameter identification and the validation of simulation models – a test rig was developed. The modular construction of the test rig ensures a simple replacement of the cooling sleeve allowing the examination of different flow geometries.

**Keywords:** heat transfer, high-speed spindle, numerical simulation, network-based simulation

# 1 Introduction

In machine tools, a variety of fluid power systems are used such as pumps, heat exchanger or cooling components in motors and spindles (see fig. 1). Beside drive tasks for feeding movements and tool clamping, they especially facilitate the temperature control in machine tools. In this respect, fluid power systems are an important element for controlling and managing the thermo-elastic behaviour of machine tools.

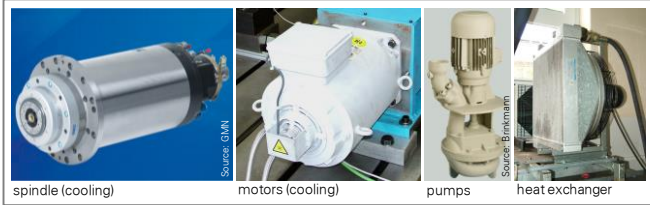


Figure 1: Examples of important fluid power components in machine tools.

The working precision of cutting machine tools depends to a significant degree on the relative motion between the workpiece and the tool. Machine disturbances such as temperature gradients occurring in the feed units and the working spindle limit the overall precision, both dimensional and geometrical, and the surface quality of the machined workpiece. For example, heat losses in the bearings and the motor of the working spindle result in reduced bearing stiffness and thermal deformations. This causes a displacement of the tool centre point (TCP) and, consequently, has a negative effect on the production quality. Thus, knowledge of the sources of losses, the heat flow paths and the resulting temperature distribution in motor spindles or feed units represents an essential basis for the characterization of the thermal behaviour of these main components – aiming at the improvement of the manufacturing quality and the process.

To reduce the displacement of the TCP fluid-technical spindle cooling systems are used. The cooling liquid circuit is realized by a cooling jacket or by directly flowing through the spindle shaft [1]. In [2] cooling systems with helical channel structures were examined. The main focus was to increase the efficiency by adjusting the channel slope and width. Cooling the spindle can also be realized by means of a heat pipe [3]. By local evaporation and condensation of a fluid within a closed volume this element allows an efficient evacuation of heat. With the aim of enhancing the displacement of the spindle and the life cycle of spindle bearings, Gebert developed an approach describing the thermal processes occurring in high-frequency spindle motor systems [4]. In [5] the heat transfer in high-speed spindle housings with helical cooling channels is analyzed. By numerical simulations the temperature distribution in the fluid flow was determined and experimentally verified.

The purpose of this paper is to develop a network-based computation model that describes the transient, three-dimensional energy exchanging processes in built-in motorized spindles – especially in a cooling sleeve with a single helical rectangular water-cooling channel (see variant

d in fig. 4). Since tool machines are high-precision plants, an outstanding level of accuracy is required for the thermo-energetic calculation. Regarding future combinations of component models for the description of complete system structures the network-based model benefits from less modelling effort and computation time.

# 2 Methodology and modelling approach

The aim of the research activities is the development of system-describing thermo-fluidal models. Therefore the modelling approach is divided in four parts: The experimental investigation of systems and of components as well as the development of numerical and network-based simulation models – as depicted in fig. 2.

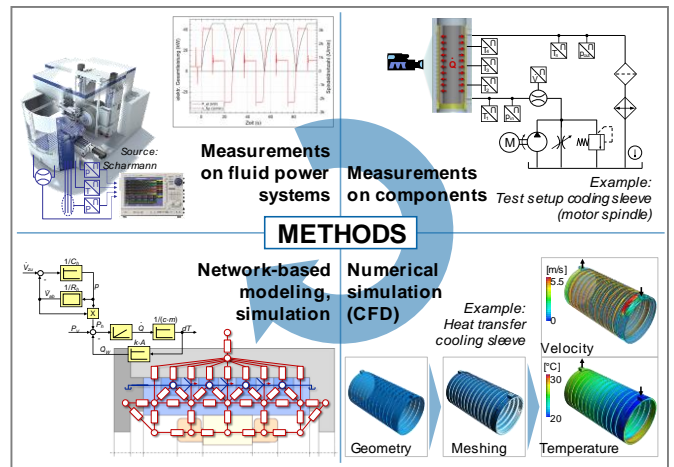


Figure 2: Overview of the methodology for the development of holistic fluidic simulation models.

In the first step fluid technical cooling systems are investigated experimentally in the tooling machine directly. On this basis, information concerning the physical active structures and the machine operations are received. Thus, the crucial main components are identified. Secondly, these main components have to be analyzed experimentally. The aim is to extract key figures and reference variables for the simulation models from these measurement data. The development of thermo-energetic component models with help of network-based modelling techniques starts with the analysis of existing simulation tools and the identification of the specific modelling requirements. Subsequently, extensive numerical simulations (CFD) are carried out in the third step. These simulations make the thermo-energetic exchange processes visible in a high temporal and spatial resolution, even inside the components. They support significantly the derivation of structures as well as parameters for the network modelling and represent an additional basis for comparison beside the measured data. Within the last step abstract component models are derived by the use of network-based modelling techniques. In contrast to numerical models they promote a fast calculation, even on lower performance machines. Consequently it is of great advantage to combine single component models to whole system describing models. Thus, the acting physical relationships and interactions

between the components can be characterized precisely at the system level. To check the suitability of component models for the precise calculation of the real system and to exclude an unacceptable adding up of individual errors, a further verification using measurement data is necessary.

In this paper, the development of a network-based simulation model is illustrated – especially for the stator cooling sleeve of a motorized high-speed spindle. Therefore, the focus is on the experimental investigations as well as the numerical simulation model used for the extraction of important key figures and reference data.

### 3 Design of motorized high-speed spindles

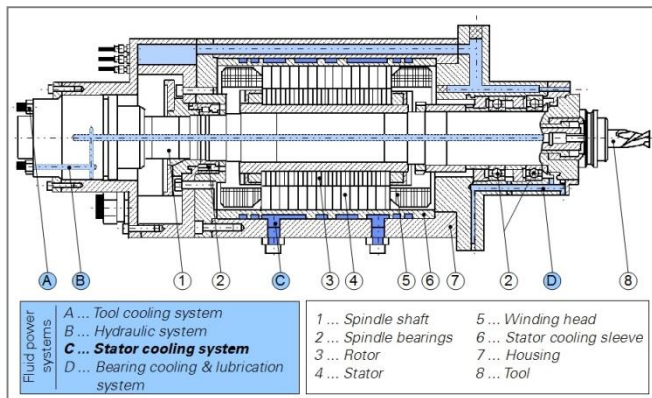


Figure 3: Principle structure of a motor spindle, adapted from [4].

Motor spindles are specifically used in high-speed cutting (HSC) machining centres and milling machines. As a result of the rapid tool rotation high centrifugal forces occur and thus power transmission devices such as belts or gears cannot be utilized. Consequently, the spindle is directly driven by a built-in motor. Figure 3 illustrates the basic structure of a built-in motorized spindle with a helical rectangular water-cooling channel. The main fluid systems are highlighted in blue. The hydraulic system (B) serves for the tool clamping. The cooling system can be divided regarding the components that needed to be cooled: the tool (A), the stator (C) and the bearings (D).

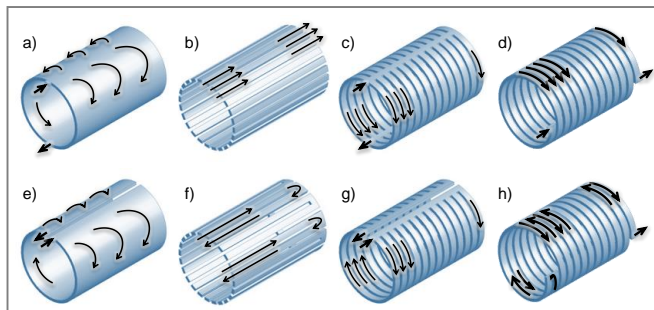


Figure 4: Typical types of flow geometries within the stator cooling sleeve.

Hence, one subject of current research is the cooling of the motor – especially the stator – via a cooling sleeve. This

cooling sleeve is press-fitted into the stator and a cooling liquid flows around its outer radius. The sleeve itself is made of a highly thermally conductive material (e.g. brass), and may additionally comprise rib structures at the outer radius improving the heat transfer into the fluid. In Figure typical flow paths resulting from different geometries of the cooling sleeve are depicted, where the single helical and the double helical channel structure (variants d and h) are the most common ones [4]. The current research focuses on the single helical channel variant d.

### 4 Experimental test set-up

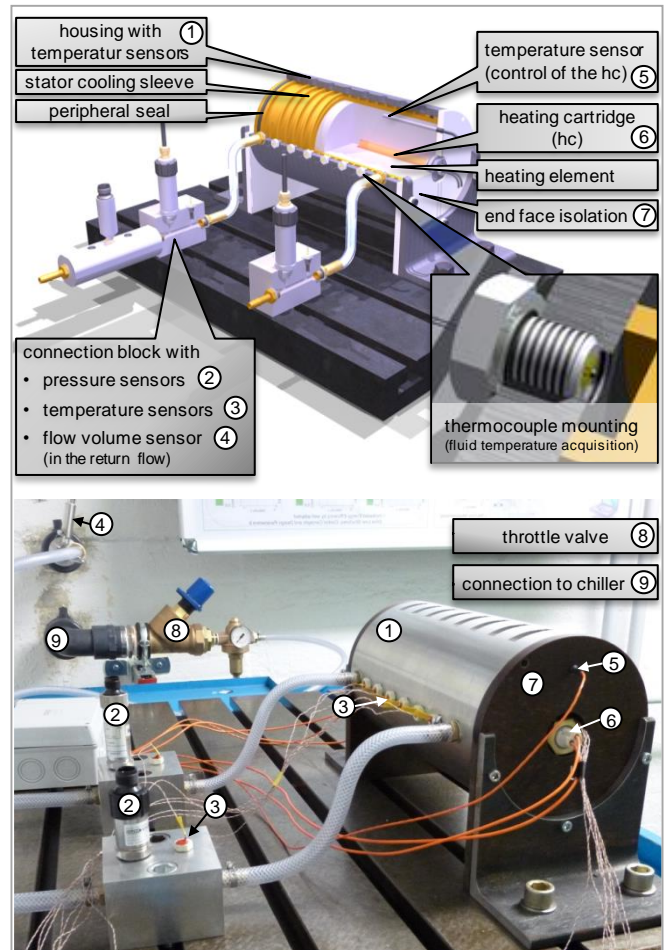


Figure 5: CAD model and real experimental set-up for the investigation of the thermal behaviour of stator cooling sleeves with different flow geometries.

A test stand (see fig. 5) has been developed allowing measurement of both fluid and surface temperatures of the stator cooling sleeves under defined conditions. In parallel, the upstream and downstream pressure as well as the throttle flow rate is measured. The modular design of the test stand permits a simple replacement of the cooling sleeve to examine different flow geometries in detail. The energy input into the cooling sleeve is realized due to two heating cartridges centrally introduced into an aluminium cylinder whose power can be controlled separately. The temperature is locally measured at defined intervals in the axial direction at the inner wall of the cooling sleeve, on the housing wall

and in the fluid. They mainly depend on the supplied amount of heat, the flow rate and the composition of the cooling liquid. In addition, an infrared camera is used for an area-wise detection of the temperature of the housing surface and the investigation of the temperature distribution.

First measurements were done with chilled water as working medium in the helical channel. The inlet temperature was set to 20°C and controlled by the temperature sensor integrated in the chiller. The fluid temperatures were measured by 8 thermocouples embedded in the helical channel along the axial direction, including the inlet and outlet temperatures. The used thermocouple type was T with a class 1 calibration, so that the minimum accuracy was within ±0.5 K. The volumetric flow rate was measured by a turbine flow meter with an accuracy within ±0.5%FS. Furthermore, the pressure was measured in the flow and return flow pipes. The accuracy of the installed electronic pressure transmitters was within ±0.123%FS. All signals were connected to a junction terminal block and recorded by a NI M Series multifunction data acquisition device.

## 5 Modelling and simulation

### 5.1 Basic concepts of modelling

Figure 6 illustrates the flow diagram of a fluid-technical component model, whereby the investigation scope is strictly limited to the component's inner wall. The focus is on network-based computing models. The input parameters (e.g. flow rate, wall temperature, and thermal conductivity) characterize the thermal behaviour and the flow, and are directly ascertained from existing design and material data, numerical simulations or experimental studies. The results of the network-based calculation are for instance the transferred heat flux, the fluid temperature and the amount of auxiliary energy required for driving the flow.

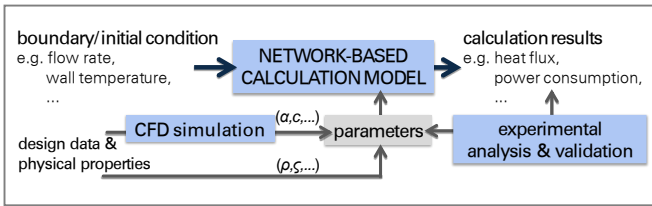


Figure 6: Flow of information within a fluid-technical component model.

In table 1 the basic dynamic relationships of hydraulics, pneumatics, thermodynamics, mechanics and electric engineering are depicted. The behaviour of systems of various types of energy is describable in the same way using these basic dynamic relationships. They form the basis for a cross-system simulation in a computational model.

Furthermore, the figure shows a categorization of the basic dynamic relationships of various forms of energy with respect to the calculation of flow and potential variables. On this basis, the basic relationships are attributed to nodes and elements. The potential variable is calculated in a node from the sum of the flow variables. The flow variable is

determined by the difference of potential variables at the element.

The model structure is basically set up in alternating arrangement, because of the correlation between the input and output variables of nodes and elements. Due to the summation of the flow variables in the node, any number of elements can be connected to a node. However, at each connection of an element only one node can be located. Thus, the nodes are used to extend the scope of the model and to structure the network-based system or component model. [6, 7, 8]

Table 1: Analogy of basic dynamic elements, adapted from [6, 7, 8]

	NODE computation of potential variables	ELEMENT	ELEMENT computation of flow variables
<b>ELECTRICAL</b>	 $u = \frac{1}{C_e} \int \sum_{i=1}^n i_i \cdot dt$	 $i = \frac{1}{L_e} \int u_{21} \cdot dt$	 $i = \frac{1}{R_e} \cdot u_{21}$
<b>MECHANICS</b>	 $\dot{x} = \frac{1}{m} \int \sum_{i=1}^n F_i \cdot dt$	 $F = c_m \int \dot{x}_{21} \cdot dt$	 $\dot{m} = d \cdot \dot{x}_{21}$
<b>PNEUMATICS</b>	 $\rho = \frac{1}{C_p} \int \sum_{i=1}^n \dot{m}_i \cdot dt$	 $\dot{m} = \frac{1}{L_p} \int p_{21} \cdot dt$	 $\dot{m} = \frac{1}{R_p} \cdot f(p_1, p_2)$
<b>HYDRAULICS</b>	 $\rho = \frac{1}{C_h} \int \sum_{i=1}^n \dot{V}_i \cdot dt$	 $\dot{V} = \frac{1}{L_h} \int p_{21} \cdot dt$	 $\dot{V} = \frac{1}{R_h} \cdot f(p_1, p_2)$
<b>THERMAL</b>	 $T = \frac{1}{C_t} \int \sum_{i=1}^n \dot{Q}_i \cdot dt$	 <p>* a thermal inductivity does not exist</p>	 $\dot{Q} = \frac{1}{R_t} \cdot T_{21}$

Figure 7 shows a simple example of a network-based model using the basic hydraulic and thermal elements described in

the table above. The mass or volume is concentrated in the node which is defined by the thermal and/or hydraulic capacity. The nodes are connected to one another via thermal or hydraulic resistances. The input and output parameters of each element as well as the appropriate calculation formulas are depicted in the figure.

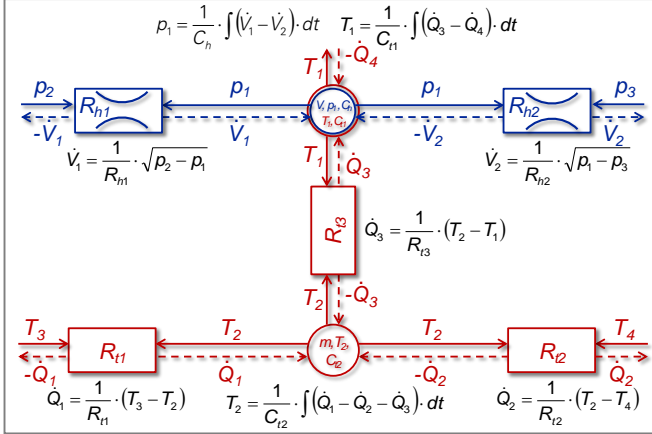


Figure 7: Mathematical description of the basic hydraulic and thermal elements used in a network-based model.

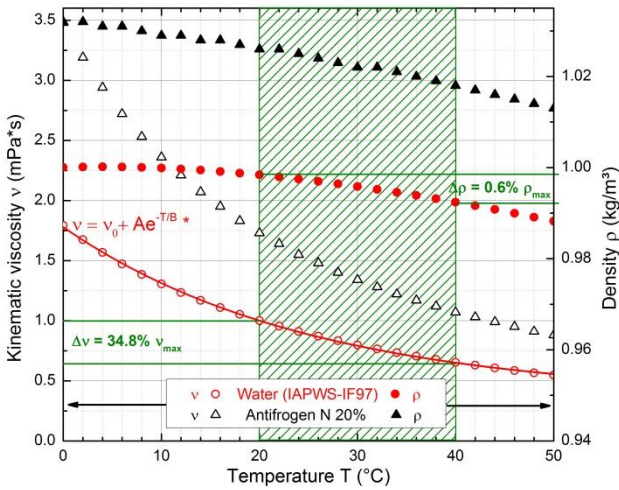


Figure 8: Selection of temperature dependent fluid properties for water and Antifrogen@N.

Figure 8 shows a selection of temperature dependent fluid parameters for water and a typical water-glycol-mixture. It can be seen exemplarily for water that the density only changes slightly in the temperature range of interest from 20 to 40°C. Since the density only changes by 0.6% the temperature dependency is negligible. On the other hand the kinematic viscosity changes by 34.8% in the same temperature range and has to be considered in the simulation models. This can be done by implementing the ascertained expression

$$v = v_0 + A \cdot e^{-\frac{T}{B}} \quad (1)$$

with the fitting parameters

$$v_0 = 0.36 \text{ mPa} \cdot \text{s} \quad (2)$$

$$A = 1.41 \text{ mPa} \cdot \text{s} \quad (3)$$

$$B = 25.4 \text{ } ^\circ\text{C}. \quad (4)$$

A similar approach can be used to extract the relevant parameters for Antifrogen®N and all other cooling fluids. Furthermore the following assumptions are made to simplify the modelling:

- The thermal capacity and the density of the fluid are temperature independent, whereas the temperature dependency of kinematic viscosity has to be considered.
- The physical properties of the solids (heating element, cooling sleeve, housing, isolation and mounting) are assumed to be isotropic and temperature independent.
- The flow is considered to be steady and turbulent with no viscous dissipation.
- Gravity and buoyancy effects are neglected.

## 5.2 Numerical simulation model and parameter identification

The development of a numerical simulation model of the stator cooling sleeve is a first approach for the characterization of its thermo-energetic behaviour and its flow as well as the determination of required model parameters. For this purpose the shear stress transport formulation (SST model) was used.

Turbulence models are used to approximate the effects of turbulence without resolving the smallest turbulent fluctuations. The SST model is one of various turbulence models based on the Reynolds Averaged Navier-Stokes (RANS) equations. The SST model is a hybrid two-equation eddy-viscosity model that combines the advantages of both the k- $\omega$  and k- $\epsilon$  model. Since the advantage of the near wall treatment for low Reynolds number computations the k- $\omega$  model performs much better for boundary layers. Therefore, computations are more accurate and robust. However, the common k- $\omega$  problem is its strong sensitivity to the inlet free-stream turbulence properties, while the k- $\epsilon$  model is not susceptible to such problems. To overcome this drawback the SST model switches between the k- $\omega$  model near the surface and the k- $\epsilon$  model in the outer region. Accordingly, in free shear flows the SST model is identical with the k- $\epsilon$  model. The SST model is recommended for applications that require a high accuracy in the boundary layer, whereby the minimum resolution is 10 cells. Thus, an automatic near-wall treatment method is applied to model the flow near the wall. The near wall region can be subdivided into two layers. In the innermost, the laminar (viscous) sublayer the viscosity plays a major role in momentum and heat transfer. Further away from the wall, in the logarithmic layer the mixing process is dominated by turbulence. The region between the laminar sublayer and the logarithmic layer is called buffer layer. Effects of molecular viscosity and turbulence are of equal importance here. For more information on the solver and modelling theory, refer to [9, 10, 11].

To predict the temperature throughout the flow heat transfer has to be taken into account. The heat transfer in the fluid domain is ascertained by the energy transport equation

$$\frac{\partial(\rho h_{tot})}{\partial t} - \frac{\partial p}{\partial t} + \nabla(\rho U h_{tot}) = \nabla(\lambda \nabla T) + \nabla(U \cdot \tau) + S_E. \quad (5)$$

Since the flow is considered to be steady and the viscous dissipation is neglected the expression can be simplified

$$\nabla(\rho U h_{tot}) = \nabla(\lambda \nabla T) + S_E. \quad (6)$$

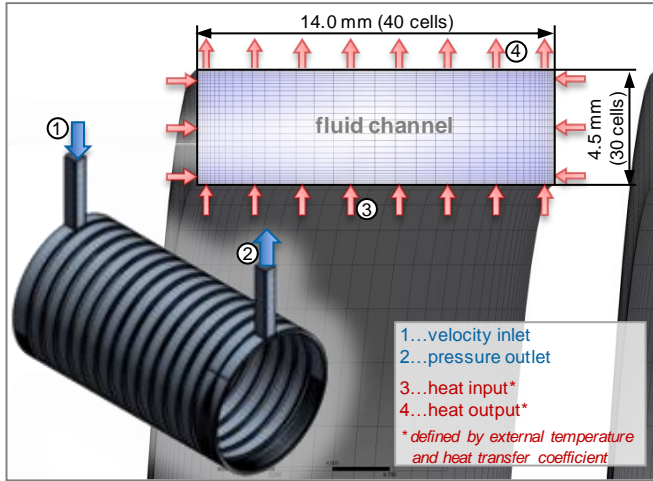


Figure 9: Fluid volume's total grid and cross-section through one turn of the helical channel.

Figure 9 shows the discretized fluid volume that is used in the computational domain. The grid comprises up to around 2.097 million hexahedral elements where the minimum quality of the elements is 0.66 and the mean quality 0.97. The grid is structured and was generated by using the blocking method and edge bunching laws in ANSYS ICEM. To minimize the computing time disparate time-scales of heat transfer and fluid flow are utilized. The computations are performed in parallel on four cores and lasted about eight hours until residuals of all the variables were less than  $1.0 \times 10^{-5}$ .

Since the heat transfer in the solids is actually not considered in the numerical simulation it is necessary to specify a so-called alternative heat transfer coefficient  $\alpha_{alt}$  in relation to the fluid temperature difference  $\Delta T_F$  between the inlet and outlet. This coefficient describes the heat transfer consisting of the heat transfer between the heating element, the cooling sleeve and the fluid as well as the heat conduction in the heating element and the cooling sleeve. In order to identify this alternative heat transfer coefficient  $\alpha_{alt}$  several simulations were performed. In fig. 10 the characteristic map of  $\alpha_{alt}$  as a function of the fluidic temperature difference  $\Delta T_F$  is depicted for varying volume flow rates (5 l/min, 10 l/min and 14 l/min) and two constant temperatures  $T_H$  in the heating element (30°C and 40°C).

By analogy, the cooling capacity  $P_Q$  of the fluid depending on the fluids temperature difference  $\Delta T_F$  is determined by

several numerical simulations. Its characteristic map is shown in fig. 11.

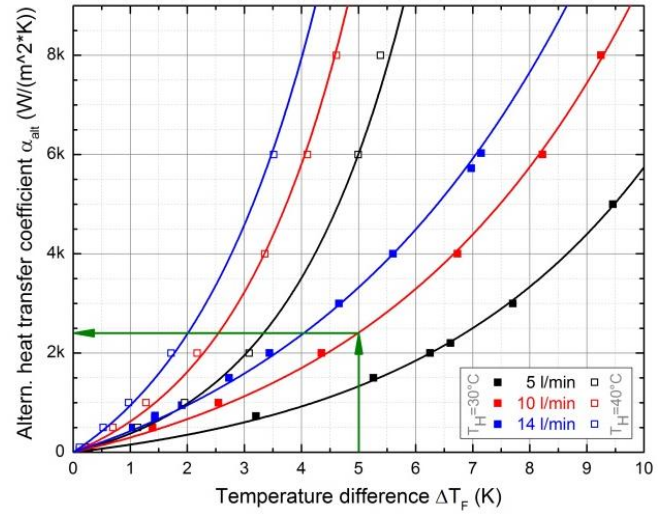


Figure 10: Alternative heat transfer coefficient  $\alpha_{alt}$  depending on the fluid temperature difference  $\Delta T_F$  between inlet and outlet.

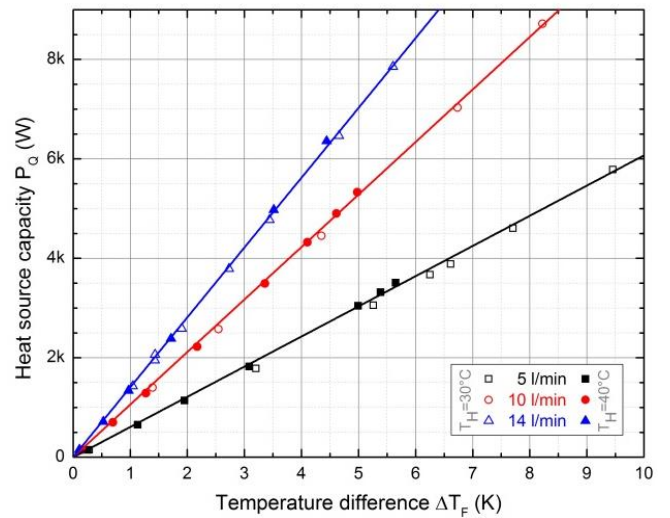


Figure 11: Cooling capacity  $P_Q$  depending on the fluid temperature difference  $\Delta T_F$  between inlet and outlet.

### 5.3 Network-based simulation

Simulation models based on concentrated parameters feature a wide range of interfaces to external CAX- and database programs, and short computing times with resulting cost savings. Therefore, the applicability of existing modelling tools (like SimulationX) is examined for the description of a real component. As can be seen from fig. 12, the network-based model of a cooling system for motor spindles is composed of blocks describing the physical correlations of single elements. The potentials required for the computation are transported by thermal or hydraulic connections between the individual blocks. The overall model consists of geometrically simple subcomponents whose behaviour can

be described by general equations of thermodynamics and fluid power [11, 12, 13, 14].

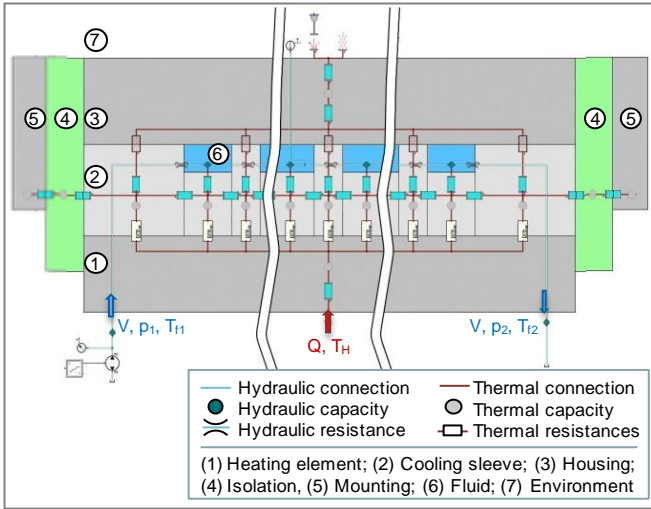


Figure 12: Network-based simulation model of the stator cooling sleeve according to the test set-up.

The power dissipation of the motor spindle is either represented by a heat input or by a fixed temperature that is higher than the ambient temperature. The difference between the induced and ambient temperature causes a heat flow in the system. This heat flow is transported through the model of the cooling system by heat conduction in the parts and heat transfer between the parts. The heat transport essentially propagates through cylindrical layers. The used blocks describe the physical correlations of heat conduction and heat transfer with thermal resistances.

$$R_t = \frac{\ln(d_o/d_i)}{(2\pi - \varphi) \cdot l \cdot \lambda} \quad (6)$$

$$R_t = R_{contact} \quad (7)$$

It is especially challenging to compute the thermal resistances of heat transfer between two solids (i.e. between the heating element and the cooling sleeve), because the modelling of the contact points is afflicted with some degree of uncertainty. Due to a comparison of the computational results with the experimental results this uncertainty may be reduced. The thermal capacities describe the characteristic heating of the solids due to heat supply.

The central process in the simulation of the cooling system is the forced convection of the heat due to the fluids motion. In this context the two disciplines thermodynamics and fluid power mutually influence each other.

The flow through the cooling channel, embedded in a cooling sleeve, exhibit a constant volume flow rate. Moreover, the cooling channel is subdivided into multiple parts and represented by hydraulic capacities in the model. An individual element corresponds to exactly one turn of the helical channel. Here, the model is simplified to describe the complex geometry of the cooling channel at the inlet and the outlet with the available tools. Hence, the slope of the

helical cooling channel is neglected, whereby the real heat exchanging surface coincides with the surface in the model. The flow rate is adapted with the help of a correction factor so that the flow conditions are not influenced by the neglected slope. Throttle resistances are located between the hydraulic capacities to describe the resulting pressure drop. The heat transfer from the solid into the cooling fluid is taken into account by the hydraulic capacity with the following relation.

$$R_t = \frac{1}{\alpha \cdot \pi \cdot d \cdot l} \quad (8)$$

The heat transfer coefficient  $\alpha$  is characterized by the dimensionless quantities  $Nu$ ,  $Re$  and  $Pr$  of the flow and has a major influence on the heat resistance. The model delivers the possibility to compute laminar as well as turbulent flows. The transition zone between turbulent and laminar is interpolated, so that all flow conditions are possible. The part of the heat flow that is not absorbed by the fluid is transferred to the environment by free convection and heat radiation.

Due to an external database link, the network-based model provides a uniform and clear parameterization, based on the geometry of the cooling system and the physical properties.

The parameterization of the heat transfers coefficients between two solids and the parameterization of forced convection are a great challenge within the modelling of cooling systems of motorized spindles with network-based models. Therefore, it is necessary to compare and optimize these computation models with experimental measurements.

## 6 Results and discussion

In fig. 13a-c the numerical results of the pressure, the velocity and the temperature distribution along the fluids flow path with a heating element temperature  $T_H = 40^\circ\text{C}$ , a flow rate  $\dot{V} = 14 \text{ l/min}$  and a fluid inlet temperature  $T_{f1} = 20^\circ\text{C}$  are presented. The inlet and outlet ports are attached at opposite ends of the spindle housing because the helical channel structure only consists of one pass. Due to production requirements the inlet and outlet channel (see fig. 13 position 1 and 8, respectively) differ in size and geometry from the other helical channels. These geometrical features are taken into account in the numerical and network-based model as well, in order to achieve a good congruence between experimental data and simulation results. It is obvious from fig. 13 that the almost 180-degree turnaround at the inlet channel causes a necking of the flow. This leads to an increased velocity of about 7 m/s accompanied by a pressure drop of about 0.5 bar at the same position. Due to the larger cross section at the inlet and outlet channel the velocity is kept slightly lower than the average velocity of about 4.1 m/s in the other helical channels (see fig. 13b). Except the deviations in the inlet and outlet region the fluid velocity distributions are mixed well and become nearly uniform. Furthermore, it can be seen from fig. 13c that the fluid temperature is constantly increasing in the axial direction from the inlet to the outlet.

Figure 14a depicts the calculated and measured average temperatures of the fluid along the spindle axis with different values of the volume flow rate of  $\dot{V}=5$  l/min, 10 l/min and 14 l/min, and with a constant heating element temperature of  $T_H=40^\circ\text{C}$ . As expected, the fluid temperature is decreased as the volume flow rate is increased. Since the fluid temperature is increasing along the spindle axis the maximum temperatures are reached at the outlet region. The averaged maximum temperatures at the outlet are  $21.6^\circ\text{C}$ ,  $22.2^\circ\text{C}$  and  $23.5^\circ\text{C}$  for  $\dot{V}=14$  l/min, 10 l/min and 5 l/min. Controlled by a chiller, the fluid inlet temperature was fixed at  $20^\circ\text{C}$ . Thus, the temperature differences are 1.5 K, 2.2 K and 3.5 K for  $\dot{V}=14$  l/min, 10 l/min and 5 l/min. In this respect it is noted that the temperature accuracy of the used chiller was within  $\pm 0.5$  K. This can also be seen in fig. 14, where the inlet temperature differs by  $-0.5$  K for a volume flow rate of 5 l/min.

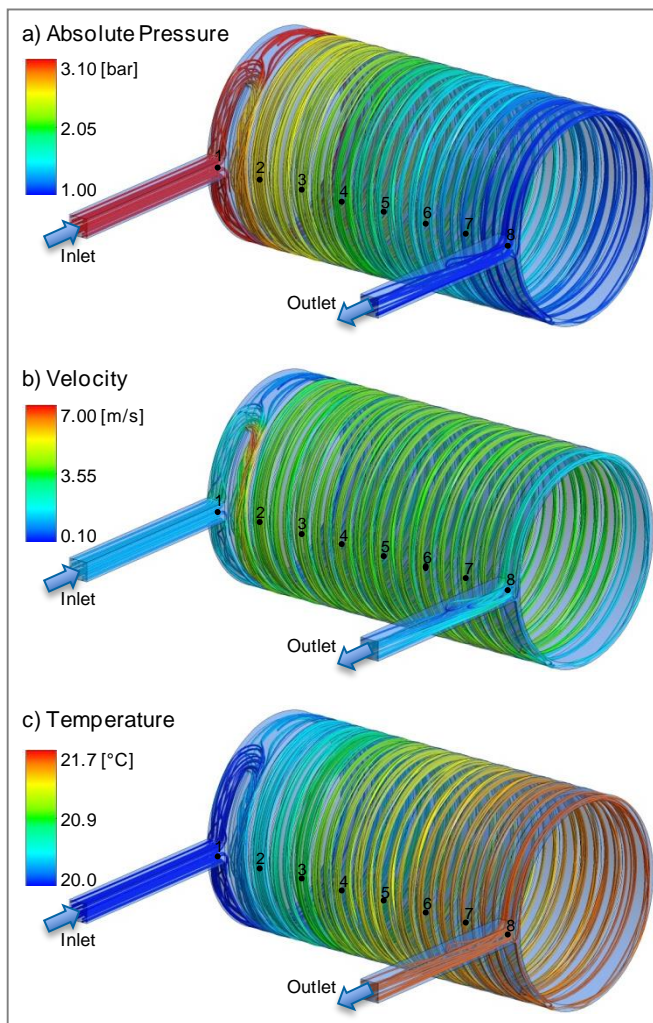


Figure 13: The pressure, velocity and temperature distribution along the fluids flow path with heating element temperature  $T_H = 40^\circ\text{C}$  and flow rate  $\dot{V} = 14$  l/min.

Concerning fig. 14a one can see that the network-based modelling results of the single helical cooling channel are in good agreement with the numerical simulation as well as the experimental data. In the both upper diagrams of fig. 14a the relative deviations for the network-based model to the two

other ones are depicted. The deviation amounts to a maximum of 2.4 % compared with the experimental data and a maximum of 2.1 % compared with the numerical simulation.

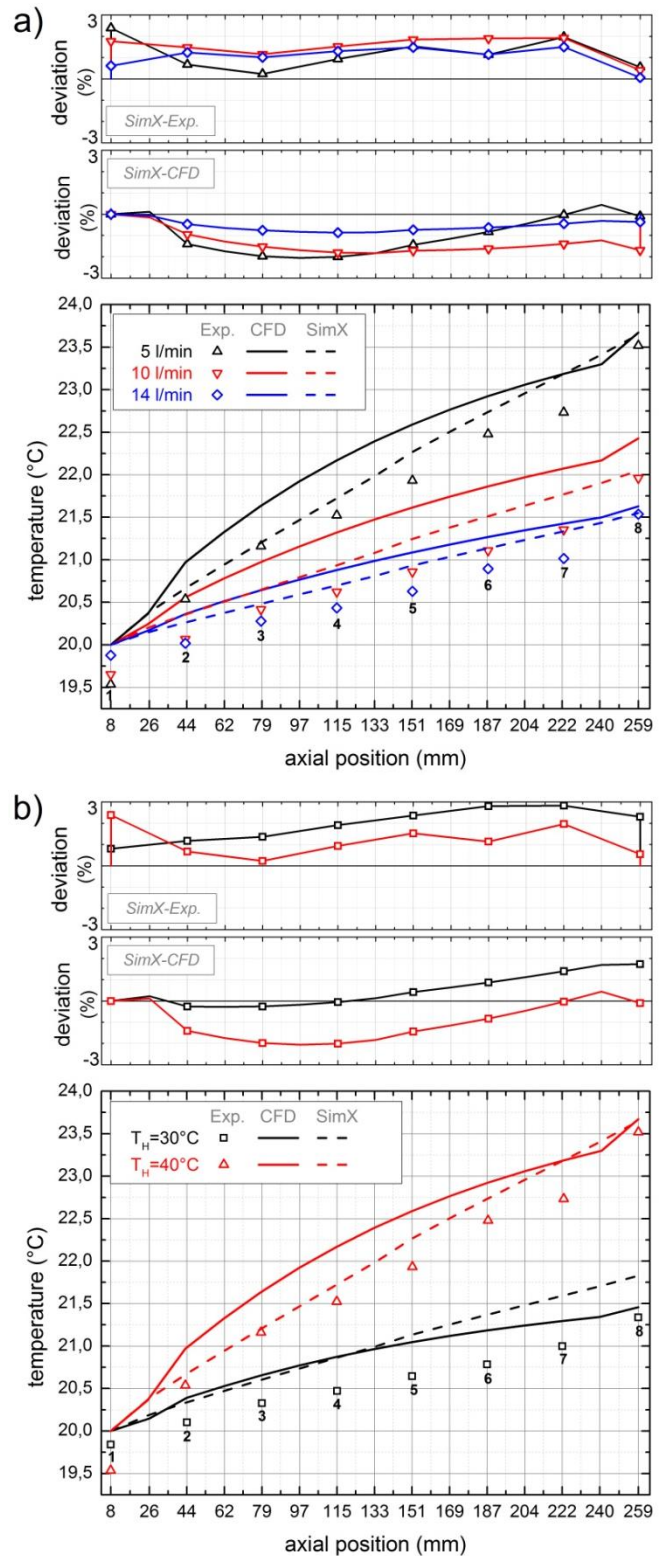


Figure 14: Simulation results showing the fluid warming along the spindle axis; a) with a constant heating element temperature  $T_H = 40^\circ\text{C}$  concerning different volume flow rates; b) with a constant volume flow rate  $\dot{V} = 5$  l/min concerning different heating element temperatures.

The results in fig. 14b show the fluid warming in the axial direction with different heating element temperatures,  $T_H=30^\circ\text{C}$  and  $40^\circ\text{C}$ , with a constant volume flow rate  $\dot{V}=5\text{ l/min}$ . It is observed that the fluid temperature increases with the heating temperature. Furthermore, the simulation results are in good agreement with the experimental and numerical data. The maximum deviation of the network-based results is about 2.8 % (for a heating element temperature  $T_H=30^\circ\text{C}$ ) in comparison with the experimental data and about 2.1 % (for  $T_H=40^\circ\text{C}$ ) in comparison with the numerical results.

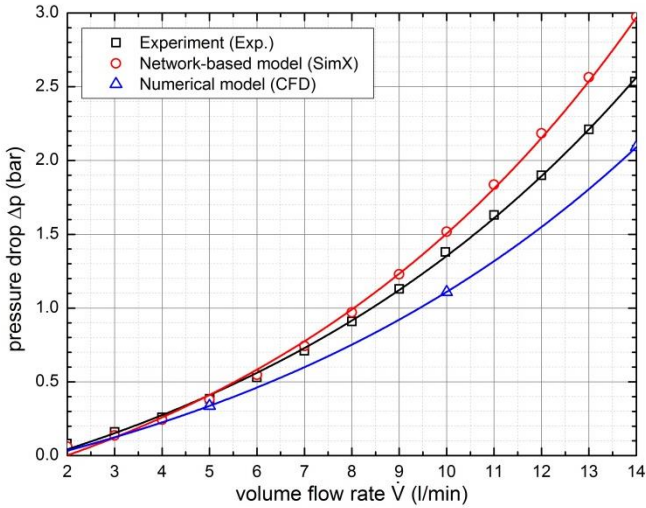


Figure 15: Pressure drop - flow rate characteristic, comparison between network-based model, numerical model and experimental data.

Figure 15 presents the calculated and measured pressure drop in the single helical cooling sleeve for varying volumetric flow rates from 2 l/min to 14 l/min. It is seen that the simulated data are in good agreement with the measured ones. The error constantly rises with the volume flow rate to its maximum of about 0.5 bar. In case of the network-based model the calculated value exceeds the measured one. Whereas the numerical simulation model predicts a value of approximately 0.5 bar less for a volume flow rate of 14 l/min. The reason for the smaller value in case of the numerical simulation is the simplification of the flow and return flow pipe. In case of the network-based model the causes for the deviations could not be conclusively clarified.

## 7 Conclusion and outlook

Especially in high-speed cutting applications heat dissipation and expansions of the spindle components have a negative impact on the manufacturing accuracy and quality. A selective control of the temperature distribution of a spindle is therefore a basic requirement for a high-precision machining. Thus, a network-based thermal model of heat transfer and fluid flow was developed to characterize the forced convection of cooling water within a single helical cooling channel of a high-speed spindle, and furthermore, to better control its temperature distribution and machining precision. Comparing a numerical with a network-based simulation model the second benefits from less modelling

efforts and computing times. By combining network-based component models it is possible to develop complete system structures. This allows a precise description of the acting physical principles and interactions between the components at the system level. Furthermore integration into the machine control is conceivable in order to estimate or control the machines thermal behaviour.

Therefore, this paper explains a modelling approach enabling the computation of thermal and fluidic characteristics of the fluid within a single helical cooling sleeve of a motorized high-speed spindle. This modelling approach includes a numerical simulation and a network-based simulation model as well. It is demonstrated that the averaged maximum temperatures along the spindle axis are decreased when the volume flow rates are increased. Furthermore the fluid temperature increases when the temperature of the heating element increases. The simulation results were validated through comparison with experimental data. It is shown that the network-based results agreed with the experimental data within 3% and with the numerical results, too. Concerning further investigations it is necessary to examine whether this deviations result from the simulation models or the experimental test set-up. Therefore, the accuracy of the chiller and the temperature sensors has to be improved, e.g. by the use of resistance thermometers instead of thermocouples.

However, the numerical simulation model can be extended by modelling the conjugate heat transfer (CHT). Therefore the conduction equation is additionally solved within the numerical model.

$$\frac{\partial(\rho h)}{\partial t} + \nabla(\rho U_s h) = \nabla(\lambda \nabla T) + S_E \quad (8)$$

Considering the heat transfer in solid domains, especially for the cooling sleeve and the housing, is particularly advantageous for the parameterization of each heat transfer coefficient in the network-based model [9, 10].

## 8 Acknowledgements

The presented research activities are part of the Collaborative Research Centre Transregio 96 “Thermo-energetic design of machine tools. A systematic approach to solve the conflict between power efficiency, accuracy and productivity demonstrated at the example of machining production”, sub-project A04 “Thermo-energetic description of fluid systems”. The authors would like to thank the Deutsche Forschungsgemeinschaft (DFG, German Research Foundation) for the financial support.

Supported by:



## Nomenclature

Designation	Denotation	Unit
$C_h$	Hydraulic capacity	[m <sup>3</sup> /Pa]
$C_t$	Thermal capacity	[J/K]
$d_{(o/i)}$	(Outer/inner) Diameter	[mm]
$h_{(tot)}$	(Mean total) Enthalpy	[J/kg]
$k$	Turbulence kinetic energy	[m <sup>2</sup> /s <sup>2</sup> ]
$l$	Length	[mm]
$m$	Mass	[kg]
$Nu$	Nusselt number	[-]
$p$	Pressure	[bar]
$P_Q$	Cooling capacity	[W]
$Pr$	Prandtl number	[-]
$Q$	Heat quantity	[J]
$\dot{Q}$	Heat/cooling in-/output	[W]
$Re$	Reynolds number	[-]
$R_h$	Hydraulic resistance	[Pa/(m <sup>3</sup> ·s)]
$R_t$	Thermal resistance	[K/W]
$S_E$	External energy source	[W]
$T$	Temperature	[°C]
$t$	Time	[s]
$T_H$	Heating element temperature	[°C]
$U$	Velocity	[m/s]
$V$	Volume	[m <sup>3</sup> ]
$\dot{V}$	Volume flow rate	[l/min]
$\alpha_{(alt)}$	(Alternative) Heat transfer coefficient	[W/(m <sup>2</sup> ·K)]
$\Delta p$	Pressure drop/pressure loss	[bar]
$\Delta T_F$	Fluid temperature difference	[K]
$\varepsilon$	Turbulence dissipation rate	[m <sup>2</sup> /s <sup>3</sup> ]
$\lambda$	Thermal conductivity	[W/(m <sup>2</sup> ·K)]
$\nu$	Kinematic viscosity	[Pa·s]
$\rho$	Density	[kg/m <sup>3</sup> ]
$\tau$	Wall shear stress	[MPa]
$\varphi$	Angle	[rad]
$\omega$	Specific turbulence dissipation	[1/s]

## References

- [1] R. Walter. *Mit direkter Kühlung zu mehr Genauigkeit.* Werkstatt und Betrieb, 139(6):129-130, 2006

- [2] I. S. Javelov. *Projektierung von Kühlsystemen für Elektroschneideln.* Stanki i Instrument, 54(4):25-26, 1983.
- [3] R. L. Judd, K. Aftab, M. A. Elbestawi. *An Investigation of the Use of Heat Pipes for Machine Tool Spindle Bearing Cooling.* International Journal of Machine Tools and Manufacture, 34(7): 1031-1043, 1994.
- [4] K. Gebert. *Ein Beitrag zur thermischen Modellbildung von schnell-drehenden Motorschneideln.* Darmstädter Forschungsberichte für Konstruktion und Fertigung. Shaker Verlag, Aachen, 1997. ISBN 978-3-8265-2881-1.
- [5] C. H. Chien, and J. Y. Jang. *3-D numerical and experimental analysis of a built-in motorized high-speed spindle with helical water cooling channel.* Applied Thermal Engineering, 28: 2327-2336, 2008.
- [6] J. Weber. *Ein geräteorientiertes Modellierungskonzept mit Berücksichtigung der Fluideigenschaften für die dynamische Simulation in der Hydraulik.* Dissertation, Technische Universität Dresden, 1990.
- [7] E. Lautner, and F. Röpke. *Simulationsmodul Fluidtechnik für systemübergreifende dynamische Analysen.* Sonderdruck aus O+P Ölhydraulik und Pneumatik, 41(6), 1997.
- [8] G. Jungnickel. *Simulation des thermischen Verhaltens von Werkzeugmaschinen. Modellierung und Parametrierung.* Schriftenreihe des Lehrstuhls für Werkzeugmaschinen, Addprint AG, Dresden, 2010. ISBN 978-3-86780-172-0.
- [9] ANSYS Inc. (ed.). *ANSYS CFX-Solver Modeling Guide.* Canonsburg, U.S.A., 2010.
- [10] ANSYS Inc. (ed.). *ANSYS CFX-Solver Theory Guide.* Canonsburg, U.S.A., 2010.
- [11] H. Sigloch. *Technische Fluidmechanik.* Springer-Verlag, Berlin, Heidelberg, 2009. ISBN 978-3-642-03089-5.
- [12] VDI (ed.). *VDI-Wärmeatlas. Berechnungsunterlagen für Druckverlust, Wärme- und Stoffübertragung.* Springer-Verlag, Berlin, Heidelberg, 2006. ISBN 3540255044.
- [13] E. F. Schmidt. *Wärmeübergang und Druckverlust in Rohrschlangen.* Zeitschrift für Technische Chemie, Verfahrenstechnik und Apparatewesen, 39(13):781-832, 1967.
- [14] J. Hak. *Lösung eines Wärmequellen-Netzes mit Berücksichtigung der Kühlströme.* Archiv für Elektrotechnik. 42(3):137-154, 1956

## Modeling of EHA Module Equipped with Fixed-Displacement Vane Pump

E. Gnesi, J-C. Maré\*, J. L. Bordet

Parker Hannifin Manufacturing France S.A.S., Vane Pump Division, 14 route du Bois Blanc  
CS 50601, 18106 Vierzon Cedex, France

E-mail: emanuele.gnesi@parker.com, jean-charles.mare@insa-toulouse.fr, JBordet@parker.com

\* Université de Toulouse; INSA-UPS, Institut Clément Ader, 135 Avenue de Ranguéil  
31077 Toulouse Cedex, France

### Abstract

The present communication deals with the development of new EHA modules for injection molding machines, which involve industrial motor power drive, brushless motor and vane pump for downsizing and energy saving when actuators are used in sequence. Once introduced the evolution in actuation for such applications, the interest of EHA architecture is pointed up. In a second part, a simple control model is developed, highlighting explicitly the functional and parasitic effects for the different mode of use: motor speed control, cylinder pressure control and cylinder position control. The last part is dedicated to the virtual prototyping with special focus on energy losses within the module. Model structures and their implementation are proposed for pump frictions and internal leakages that use standard components of the LMS-AMESim libraries. The influence of speed and pressure are introduced either through look-up tables or simple parametric model which parameters are identified from real experiments.

**Keywords:** Actuator, EHA, energy saving, efficiency, injection molding machine, vane pump, AMESim

### 1 Introduction

The paper deals with the model based design of an electrohydrostatic actuator (EHA) module for industrial applications, with special focus on modeling and simulation. The last years growing interest to environmental issues has turned companies policy's attention to research of more eco-friendly solutions with lower environmental impact and energy saving. Thus the energy consumption, the CO<sub>2</sub> and acoustic emissions have become essential requirements, in addition to functionality and productivity demands, that the industrial engineering has to take into account during conceptual and preliminary phases.

Within the framework of environment respect, a significant improvement has been put concerning the actuation technology. Initially hydraulically-powered and valve-controlled, the actuators have been or are being replaced by electrically supplied, power-on-demand solutions, thanks to the increasing maturity of high power electronics and the progress of rare earth electric motors and their controls. An example is represented by the aerospace industry which in last decade has dedicated itself to development of greener aircrafts: in the commercial transport the recent A380 and the Boeing 787 are considered the first "more electric aircrafts" due to adoption of power-by-wire actuators such

as EHAs, electro-backup hydrostatic actuators (EBHAs) and electromechanical actuators (EMAs) principally in backup mode for primary and secondary flight controls, in place of the conventional servohydraulic actuators (SHAs) [1].

The trend has affected the stationary machinery in the industrial automation too. It includes the drive technology for motion control in the injection molding machines. As this is one of the highest energy consuming sector, the design studies do focus more and more on energy efficiency improvement. The injection molding machine is a cyclical machine producing plastic or rubber parts: it generally consists of some axes (at least six) moved sequentially by a drive module, the machine's heart, which was usually in the conventional design operated using a centralized pressure/flow control. Today the demands on drive systems and control are pressing to increase service pressure, velocities and repeatability over a long period of time. This enables increasing productivity while saving energy and reducing noise and maintenance costs [2], [3].

All these requirements have led the drive technology to evolve by increasing the interest for the electromechanical and electrohydrostatic modules.

Common practice in the past was the employment of hydraulically driven injection molding machines where the

axes' control was achieved through proportional valves supplied at a constant pressure. In the nineties, high dynamics response valves with load-sensing features were introduced (fig. 1). The electrohydraulic drives and controls manufactures development started in those years and, for the 2000's decade, a step forward was achieved by using pressure/flow variable displacement pump controls (fig. 1): the new solution was based on a constant-speed electric motor driving a variable-displacement pump which represented a favorable alternative to valve controlled drives towards reduction of energy losses [4]. Since these years, the electromechanical machines popularity has been increasing, in particular in the Japanese manufactures. The electromechanical module is typically constituted by an AC servomotor controlled by a frequency converter and driving the translating load through a ball-screw (fig. 1). For an average production cycle, this design can potentially save around 30% energy compared with the most efficient hydraulic machines due to improved efficiency of electric drive modules. Shorter cycle time and higher accuracy are obtained with simpler control [3]. The drawbacks of this technology mainly concerns cost (about 20-30% higher than comparable hydraulically driven machines) [4], low capability to dispose the heat generated by the energy losses, high kinetic energy of rotating parts and low tolerance to jamming of mechanical components. This last fault involves a frequent need of maintenance and further cost increase [5].

Recently the demand for drive solutions with higher force density has again pushed to the fore the electrohydraulic ones. In particular the interest concerns the EHA module concept of speed-controlled fixed-displacement pump driven by a permanent magnet synchronous machine with its inverter (fig. 1). By combining the advantages of power-by-wire (energy saving) and hydraulics (fluid as a heat conveyor) without requiring a motor power drive per axis, this design makes the injection molding machines more competitive than before [6]. Compared with constant-speed variable-displacement pump, it reveals its advantages of drastic reduction of energy consumption, especially in processes characterized by long phases with no or little oil flow [3]. Therefore, it appears as the principal competitor of the electromechanical modules when accuracy, reliability, flexibility and noise are considered. In particular, maintenance costs are significantly cut as it is cheaper to replace hydraulic seals than ball-screws and bearings.

Several studies have been achieved concerning possible EHA module configurations, just mention modeling of variable-speed electric motor driving gear pump [7] and [8], and solutions are already existing for various application fields as for light industrial and domestic one [9]. Other configurations constituted by variable-speed electric motor driving fixed-displacement axial piston pump that are present on global market as the designs of Liebherr Aerospace (bent axis) or Messier-Bugatti (in-line) for the recent Airbus A380 [10].

In this communication an innovative Parker solution of EHA module is proposed that associates an inverter, a brushless DC motor and a fixed-displacement low-noise vane pump.

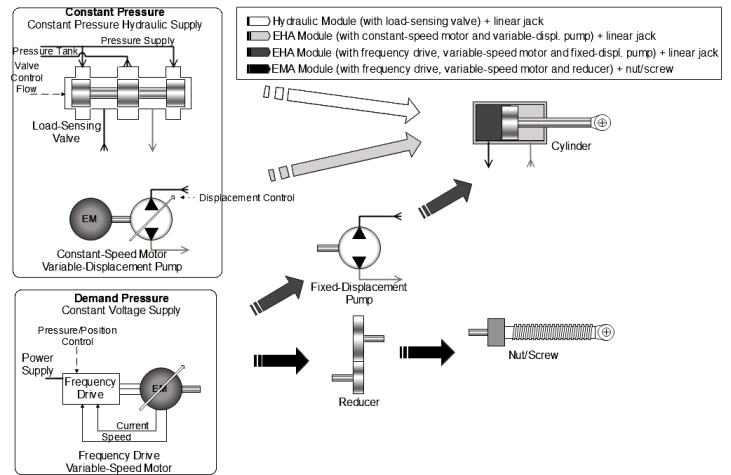


Figure 1: Architecture of modules: hydraulic, EHA and EMA

Depending on the phase of the molding cycle, injection molding machines require the module to be closed-loop controlled either in position, speed or pressure.

The EHA module integrates the advantages of both conventional technologies: easiness of integration (compactness, simplicity), reduced maintenance cost (very few rolling components), resistance to harsh conditions, high power density of hydraulics and high energy efficiency of control electric of power, high speed response, low noise level, flexibility and easiness of vector control. Parker proposes to immerse the motor-pump monobloc unit inside oil tank. This improves motor cooling and pump suction and reduces the noise level. Figure 2 shows an example of NX Series servomotor and T7 Series vane pump constituting the motor-pump unit of EHA module.

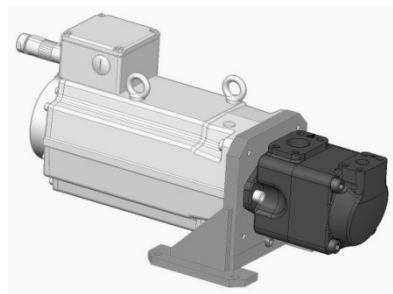


Figure 2: Example of Motor-pump unit of EHA module with NX Series servomotor and T7 Series vane pump

Recent fixed-displacement Parker vane pumps are well-known for their high performances (operating pressure up to 280 bars in a speed range from 600 to 3600 rpm), high efficiency, low noise levels, low ripple pressure, good compactness, mounting flexibility and good reliability. The plenty of possible configuration (workable thanks to cartridge concept) makes EHA module versatile and adapted to market requirements.

Section 2 of this paper describes the reference architecture of EHA module while in section 3 preliminary analysis is carried out by developing functional and architectural analytical models (paragraphs 3.1 and 3.2). In paragraph 3.3 control synthesis of the three types of closed loop operation

(position, pressure and speed) is addressed in a formal way. Paragraph 3.4 concerns the evaluation of parasitic effects on open loop natural dynamics. In section 4 a detail vane pump model with characterization of frictional torques and internal leakages is developed through virtual prototyping in LMS-AMESim environment. The non-linear phenomena are also parameterized by getting parametric linear models useful in the control unit design phase of EHA module. Section 5 concerns conclusions and future work planning.

## 2 Reference architecture of EHA module

A reference architecture is identified and showed in fig. 3: a frequency drive (control electronic unit and motor power unit), a variable speed electric motor (brushless DC Motor, BLDC), a fixed displacement pump (vane pump) and a linear hydraulic jack. The control electronic unit performs closed-loop on either rod position or on cylinder pressure. The motor power unit operates in closed-loop on motor shaft speed and an inner closed-loop motor torque control. The external position controller provides the command value for the cylinder pressure controller and its output represents the command for the motor speed control loop. The last one forms then the input for the motor torque loop.

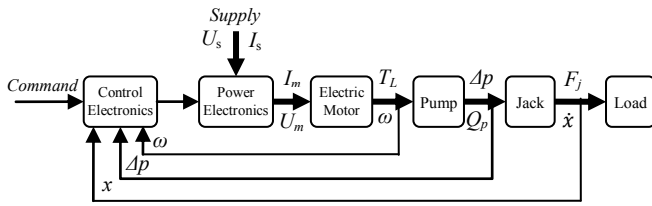


Figure 3: EHA reference architecture schematic diagram

In reference to fig. 3:  $x$  is the rod position,  $\Delta p$  is the cylinder pressure,  $\omega$  is the motor shaft speed,  $U_s$  and  $I_s$  are respectively the supply voltage and current,  $U_m$  and  $I_m$  the electric motor voltage and current,  $T_L$  is the load torque acting on the motor shaft,  $Q_p$  is the output volume flow rate generated by pump,  $F_j$  is the external load force acting on jack rod and  $\dot{x}$  is the translational rod speed.

## 3 Model-Based Design

The scientific approach proposed to develop the research subject, is characterized by a preliminary design based on analytical models (Model-based design) and on virtual prototypes at subsystem level. The EHA study is complex because it is multi-domain, multi-criteria and strong coupling between domains (reflected inertia of the rotor and thermal issues). Multi-domain feature is about to the presence of several physical phenomena coexistent and to be taken into account: a transversal vision is required to work with solid/fluid mechanics, power electronics, electrotechnics, thermal exchanges, control, etc. It has also multi-criteria features: requirements to be fulfilled, are about power capacity, energy consumption, reliability, natural dynamics, control performance, etc.

In detail, a preliminary analysis has been carried out by means of an analytical model at architectural level, obtained

by reducing a more detailed model at functional level to a simple ordinary differential equations' system (ODE). It permits to: understand the constraints between variables, the fundamental parameters effects on performance, all aspects which characterize the actuator physical operation principle and address control synthesis in a formal way. Successfully the analysis has been concerned with the advanced model that evaluates the parasitic effects associated to each component: open-loop transfer functions have been analyzed to provide the designer with key relationships between open-loop performance and parasitic effects. Virtual prototypes have been developed in LMS-AMESim environment to validate the theoretical results got from the linear analysis.

### 3.1 System level modeling

The advanced model exposed in this paragraph is represented by a linear functional model that describes the EHA module dynamics with the major parasitic effects. It is the starting point to get the simplified model that will be exposed in 3.2. With reference to fig. 3, the equations relative to electric motor, vane pump and hydraulic jack are introduced.

The BLDC is described by the mathematical equations concerning the Motor Electric Equation and the Momentum Balance referred to motor shaft axis [11]:

$$\begin{cases} U_m = K_m \omega + R I_m + L \frac{dI_m}{dt} \\ T_L = K_m I_m - J_m \dot{\omega} - T_{fm} \end{cases} \quad (1)$$

where  $K_m$  is the back-electromotive force coefficient,  $R$  is the motor winding resistance,  $L$  is the motor winding inductance,  $J_m$  is the motor inertia and  $T_{fm}$  is the frictional motor torque.

By observing the eq.s (1), first terms of second members represent the functional contributions while the remainders represent the parasitic contributions. In order to get the eq.s (1), the following assumptions have been added:

- The frictional torques of motor are considered linear functions of motor shaft speed

$$T_{fm} = B_m \omega \quad (2)$$

where  $B_m$  is the motor viscous friction coefficient.

The vane pump dynamics is described by the Flow Conservation Equation, written in reference to Control Volume and the Momentum Balance referred to pump shaft axis:

$$\begin{cases} Q_p = V_0 \omega - Q_{lp} - \frac{V_p}{\beta} \Delta \dot{p} \\ V_0 \Delta p = T_L - J_p \dot{\omega} - T_{fp} \end{cases} \quad (3)$$

where  $V_0$  is the pump displacement,  $V_p$  is the pump volume,  $\beta$  is the apparent Bulk modulus of the fluid,  $J_p$  is the pump

rotor inertia while the variable  $Q_{lp}$  is the internal pump leakage flow and  $T_{fp}$  is the frictional pump torque.

Similarly to eq.s (1), first terms of second members represent the functional contributions while the remainders represent the parasitic contributions. In order to get the eq.s (3), the following assumptions have been added:

- The Control Volume is considered rigid (no wall deformations)
- The flow conditions are assumed laminar (all mating pump clearances are made small, leading to laminar flow conditions, [12]). The internal pump leakage is so a linear function of pressure drop:

$$Q_{lp} = a_p \Delta p \quad (4)$$

where  $a_p$  is the internal pump leakage coefficient.

- The frictional torques of pump are considered linear functions of motor shaft speed:

$$T_{fp} = B_p \omega \quad (5)$$

where  $B_p$  is the pump viscous friction coefficient.

The hydraulic conduit, that links pump and jack, has to be taken into account because its length can reach several meters in plastic injection machines and the flow variations due to fluid compressibility can be relevant. By applying the Flow Conservation Equation for the Control Volume and by adding an empiric equation that describes the pressure drop dependent on laminar/turbulent flow type [12], it results:

$$\begin{cases} Q_j = Q_p - \frac{V_c}{\beta} \Delta p_c \\ \Delta p_c = \lambda(Re) \frac{L_c \rho \left(\frac{Q_p}{A_c}\right)^2}{D_c} \end{cases} \quad (6)$$

where  $V_c$  is the volume of pipe,  $\lambda(Re)$  is the friction factor (that depends on Reynolds number  $Re$  and pipe roughness),  $L_c$  is the pipe length,  $D_c$  is the pipe diameter and  $A_c$  is the transversal section pipe area. The variable  $Q_j$  is the flow rate coming into jack chamber,  $\Delta p_c$  is the pressure drop between the extremes of pipe and  $\rho$  is the fluid density.

In order to get the eq.s (6), the following assumptions have been added:

- The Control Volume is considered rigid (no wall deformations). In practice its compliance is implicitly considered in the apparent Bulk modulus of the fluid
- Leakage flow rates due to presence of hydraulic valves are neglected

The hydraulic jack is asymmetrical (the jack chambers symmetry is not needed because injection molding machines require unidirectional forces to be generated by each axis unit and they consider the motion inversion only as a return to initial condition). However, for linear analysis it is considered as an equivalent symmetrical cylinder [13]. The Mass Conservation equation applied to jack chamber and the Second Newton's Law equation applied to rod are:

$$\begin{cases} S\dot{x} = Q_j - Q_{lj} - \frac{V_j}{\beta} \Delta \dot{p} \\ F_j = S\Delta p - M\ddot{x} - F_{fj} \end{cases} \quad (7)$$

where  $S$  is the active area of the piston,  $V_j$  is the jack chamber volume,  $M$  is the total mass of piston and load. The variable  $Q_{lj}$  is the jack chamber leakage and  $F_{fj}$  is the piston/cylinder frictional force.

First terms of second members of the eq.s (7) represent the functional contributions while the remainders represent the parasitic contributions. In order to get the eq.s (7), the following assumptions have been added:

- The jack chamber volume is considered rigid (no wall deformations)
- The fluid conditions are assumed laminar and so the internal leakage is so a linear function of pressure drop [12]:

$$Q_{lj} = a_j \Delta p \quad (8)$$

where  $a_j$  is the cross-chamber leakage coefficient.

- The piston/cylinder friction is assumed to be a linear function of rod speed:

$$F_{fj} = f\dot{x} \quad (9)$$

where  $f$  is the piston/cylinder viscous friction coefficient.

Concerning the power electronics, the motor voltage and current are correlated to supply voltage and current through the simplified following expressions:

$$\begin{cases} U_m = \alpha U_s \\ I_m = \frac{1}{\alpha} I_s \end{cases} \quad (10)$$

where  $\alpha$  is power modulation factor and the assumption of ideal power electronics is made (no voltage drop through closed switch and no current leak through opened switch).

Before evaluating the parasitic effects on actuator performance, a simplification of the equations' system has been carried out in next paragraph in order to: understand the constraints between variables, the fundamental parameters effects on performance and all aspects which

characterize the actuator physical operation principle and address control synthesis in a formal way.

### 3.2 Architectural model

In first design phase, a preliminary analysis at “architectural level” has been carried out in order to evaluate the EHA module physical operation principle without taking into account parasitic effects. Under these assumptions, the eq.s (1) of the electric motor reduce to:

$$\begin{cases} U_m = K_m \omega \\ T_L = K_m I_m \end{cases} \quad (11)$$

The eq.s (3) of pump are reduced to:

$$\begin{cases} Q_p = V_0 \omega \\ V_0 \Delta p = T_L \end{cases} \quad (12)$$

The eq.s (6) of hydraulic lines are reduced to:

$$Q_j = Q_p \quad (13)$$

The eq.s (7) of hydraulic jack are reduced to:

$$\begin{cases} Q_j = S \dot{x} \\ F_j = S \Delta p \end{cases} \quad (14)$$

This enables relating the steady-state operation with fundamental parameters to be defined during the early design phase, in particular for sizing and component reference selection:  $K_m$ ,  $V_0$  and  $S$ .

### 3.3 Control synthesis: system performance in closed-loop operation

The controller is designed for three types of closed loop operation (position, pressure and speed). A study is conducted on major requirements (accuracy, rapidity and stability) the controlled dynamical system has to satisfy. The controllers taken into account are: proportional (P), proportional integral (PI), proportional derivative (PD) and proportional integral derivative (PID) because of their availability in industrial motor drives. In order to accomplish correctly its functions, the controlled system has to be developed assuring some requirements on both steady-state and transient condition. In time domain, the closed loop system response is analyzed by means of accuracy and rapidity proprieties while in frequency domain by means of the stability propriety [14]: the accuracy is evaluated through static error calculation  $\varepsilon_s$ , the rapidity through response time  $t_s$  and the asymptotic stability through the poles locations in the Complex Plane (Real, Imaginary). All controllers are initially considered proportional that aims at providing a performance reference and at pointing out the effort in controller design to be done for meeting the performance requirements. An analysis more accurate has to be conducted about system robust stability [15].

Concerning the rod position control, the load position ( $x$ ) signal is achieved by a voltage control signal  $U_m$ : it is obtained by integration of rod speed  $\dot{x}$  in the eq. (14):

$$x(s) = \frac{V_0}{SK_m s} U_m(s) \quad (15)$$

where  $\frac{V_0}{SK_m}$  represents the ideal speed gain of the process for load position control and  $s$  is the Laplace variable.

Concerning the cylinder pressure control synthesis, the pressure ( $\Delta p$ ) is varied by a motor current control signal  $I_m$ , leading to:

$$\Delta p(s) = \frac{K_m}{V_0} I_m(s) \quad (16)$$

where  $\frac{K_m}{V_0}$  is the ideal static gain of the process for pressure control.

Concerning the motor shaft speed control synthesis, the angular velocity  $\omega$  signal is varied by a voltage control signal  $U_m$  leading to:

$$\omega = \frac{1}{K_m} U_m \quad (17)$$

where  $\frac{1}{K_m}$  is the ideal static gain of the process for motor speed control.

Finally the EHA actuation system for position control is ideally once integrator in open loop while it is only a pure gain for pressure and speed control.

### 3.4 Natural Dynamics Analysis

The analysis executed in last paragraph 3.3, has permitted to provide the designer with key relationships between closed loop performance and fundamental parameters. Next step concerns the addition of the parasitic parameters and their modification effects on natural system dynamics. The functional model described in 3.1, has so been analyzed through its open-loop transfer functions characterization. In order to simplify the treatise, the following assumptions are made:

- The mechanical transmission between motor and pump is considered perfectly rigid: the motor and pump inertia and frictional torques have so been merged as single inertia and friction torque
- The pump volume is considered small making the compressibility flow negligible on the actuator behaviour
- The pressure drop in the pipe between pump and jack is neglected and so the output pump flow rate corresponds to input jack chamber flow rate

- There is no leakage at jack level due to the presence of seals
- a separation in frequency domain has been fulfilled by deciding to reproduce only the lowest natural frequencies, lower than 600 Hz. So the motor currents loop dynamics have been neglected

Consequently motor inductance and resistance were removed from the model. The modelled motor electromagnetic torque  $T_m$  is therefore assumed to be coincident with the torque demand  $T_m^*$ :

$$T_m = T_m^* \quad (18)$$

A representation in state-space domain has been used in order to reduce the functional model to four first order equations in the four variables: rod position, rod speed, cylinder pressure and motor shaft speed.

$$\dot{X} = \begin{bmatrix} 0 & 1 & 0 & 0 \\ 0 & -\frac{f}{M} & \frac{S}{M} & 0 \\ 0 & -\frac{\beta S}{V} & -\frac{\beta a_p}{V} & \frac{\beta V_0}{V} \\ 0 & 0 & -\frac{V_0}{J} & -\frac{B}{J} \end{bmatrix} X + \begin{bmatrix} 0 & 0 \\ 0 & -\frac{1}{M} \\ 0 & 0 \\ \frac{1}{J} & 0 \end{bmatrix} u \quad (19)$$

where  $B$  is the sum of motor and pump viscous coefficient,  $V$  is the sum of pipe and jack chamber volume and  $J$  is the sum of motor and pump inertia.

The derivative state vector  $\dot{X}$ , the state vector  $X$  and the input system vector  $u$  are respectively given by:

$$\dot{X} = \begin{bmatrix} \dot{x} \\ \ddot{x} \\ \Delta p \\ \omega \end{bmatrix}; \quad X = \begin{bmatrix} x \\ \dot{x} \\ \Delta p \\ \omega \end{bmatrix}; \quad u = \begin{bmatrix} T_m^* \\ F_j \end{bmatrix} \quad (20)$$

leading to the state space model of eq. (19). This permits getting the natural frequencies and to associate them with the hydraulic and hydromechanical modes.

### 3.4.1 Rod position transfer function

The open-loop transfer function, which describes the rod position dynamics in function of motor shaft speed control signal and of jack force disturbance signal, has been got by reducing the system (19). It results:

$$x(s) = G_{\omega}^x(s)\omega(s) + G_F^x(s)F_j(s) \quad (21)$$

$$\text{with } G_{\omega}^x(s) = \frac{\frac{\beta V_0 S}{VM}}{s \left[ s^2 + s \left( \frac{\beta a_p}{V} + \frac{f}{M} \right) + \frac{\beta S^2}{VM} \left( \frac{a_p f}{S^2} + 1 \right) \right]}$$

$$G_F^x(s) = \frac{-\frac{1}{M} \left( s + \frac{\beta a_p}{V} \right)}{s \left[ s^2 + s \left( \frac{\beta a_p}{V} + \frac{f}{M} \right) + \frac{\beta S^2}{VM} \left( \frac{a_p f}{S^2} + 1 \right) \right]}$$

It is possible to simplify the expressions by adding the following hypothesis:

- The ratio  $\frac{a_p f}{S^2}$  is negligible compared to unit [12]:  $\frac{a_p f}{S^2} \ll 1$

As the denominator in common between the two transfer functions,  $DG^x(s)$  reduces to:

$$DG^x(s) = s \left[ s^2 + s \left( \frac{\beta a_p}{V} + \frac{f}{M} \right) + \frac{\beta S^2}{VM} \right] \quad (22)$$

where the pair of poles is characterized by an hydraulic undamped natural pulsation  $\omega_h$  and damping ratio  $\xi_h$  respectively equal to:

$$\omega_h = \sqrt{\frac{\beta S^2}{VM}} \quad (23)$$

$$\xi_h = \frac{a_p}{2S} \sqrt{\frac{\beta M}{V}} + \frac{f}{2S} \sqrt{\frac{V}{\beta M}}$$

In order to increase hydraulic mode natural frequency  $f_h = \frac{\omega_h}{2\pi}$ , it is necessary: to increase the compressibility coefficient  $\beta$ , the jack piston surface  $S$  and to reduce the volume  $V$  and the total mass  $M$ . The natural frequency increase permits to reduce rise time ( $\propto \frac{1}{\omega_h}$ ) and response time ( $\propto \frac{1}{\xi_h \omega_h}$ ).

In order to increase  $\xi_h$ , it is necessary to increase both  $a_p$  and  $f$ : it permits to reduce the maximum peak of rod position temporal response and to reduce response time ( $\propto \frac{1}{\xi_h \omega_h}$ ). The increase of  $a_p$  is possible for example by means of a voluntary leakage but paying attention to reduction of volumetric efficiency and increase of tracking and load disturbance error.

In steady-state condition the eq. (21) is reduced to eq. (24) by means of assumption  $\frac{a_p f}{S^2} \ll 1$ :

$$x(s) = \frac{V_0}{Ss} \omega(s) - \frac{a_p}{S^2 s} F_j(s) \quad (24)$$

On the one hand the pump leakage increase, through the coefficient  $a_p$ , improves temporal response rapidity through the increase of  $\xi_h$ . On the other hand it makes worse the accuracy (static error) in confront to a motor shaft speed signal due to increase of disturbance contribution associated to jack force signal.

### 3.4.2 Cylinder pressure transfer function

In the same manner as for position control, the open-loop transfer function which describes the cylinder pressure dynamics in function of motor torque signal and of rod

speed disturbance signal has been got by reducing the system (19) and by getting the expression:

$$\Delta p(s) = G_{T_m}^{\Delta p}(s)T_m(s) + G_{\dot{x}}^{\Delta p}(s)\dot{x}(s) \quad (25)$$

$$\text{with } G_{T_m}^{\Delta p}(s) = \frac{\frac{\beta V_0}{VJ}}{\left(s^2 + s\left(\frac{B}{J} + \frac{\beta a_p}{V}\right) + \frac{\beta V_0^2}{VJ}\left(1 + \frac{a_p B}{V_0^2}\right)\right)}$$

$$G_{\dot{x}}^{\Delta p}(s) = \frac{-\frac{\beta S}{V}\left(s + \frac{B}{J}\right)}{\left(s^2 + s\left(\frac{B}{J} + \frac{\beta a_p}{V}\right) + \frac{\beta V_0^2}{VJ}\left(1 + \frac{a_p B}{V_0^2}\right)\right)}$$

It is possible to simplify the expressions by adding the following hypothesis:

- The ratio  $\frac{a_p B}{V_0^2}$  is negligible compared to unit [12]:  

$$\frac{a_p B}{V_0^2} \ll 1$$

As the denominator in common between the two transfer functions,  $DG^{\Delta p}(s)$ , reduces to:

$$DG^{\Delta p}(s) = \left(s^2 + s\left(\frac{B}{J} + \frac{\beta a_p}{V}\right) + \frac{\beta V_0^2}{VJ}\right) \quad (26)$$

where the pair of poles is characterized by an hydromechanical undamped natural pulsation  $\omega_{hm}$  and damping ratio  $\xi_{hm}$  respectively equal to:

$$\omega_{hm} = \sqrt{\frac{\beta V_0^2}{VJ}} \quad (27)$$

$$\xi_{hm} = \frac{a_p}{2V_0} \sqrt{\frac{\beta J}{V}} + \frac{B}{2V_0} \sqrt{\frac{V}{\beta J}}$$

In order to increase the hydromechanical mode natural frequency  $f_{hm} = \frac{\omega_{hm}}{2\pi}$ , it is necessary: to increase the compressibility coefficient  $\beta$ , the pump displacement  $V_0$  and to reduce the volume  $V$  and the motor-pump inertia  $J$ . The natural frequency increase permits to reduce rise time and response time.

In order to increase  $\xi_{hm}$ , it is necessary to increase both  $a_p$  and  $B$ : it permits to reduce the maximum peak of pressure temporal response and to reduce response time.

In steady-state condition the eq. (25) is reduced to eq. (28) by means of assumption  $\frac{a_p B}{V_0^2} \ll 1$ :

$$\Delta p(s) = \frac{1}{V_0} T_m(s) - \frac{SB}{V_0^2} \dot{x}(s) \quad (28)$$

If on the one hand the  $B$  viscous friction increase improves temporal response rapidity through the increase of  $\xi_{hm}$ , on the other hand it makes worse the accuracy (static error) in confront to a motor torque signal due to increase of disturbance contribution associated to rod speed signal.

The theoretical results got by linear analysis until this time, have been validated through simulation tests performed in AMESim environment consisting of a simple model stimulated with different inputs magnitude and in which the several parasitic phenomena have been added progressively.

#### 4 Detail model: vane pump

The limitations of the linear approach proposed in 3.4.1 and 3.4.2, provide results not completed realistic. The motivation depends on fact that the parasitic phenomena modeling is not sufficiently representative of all effects correlated to them. Concerning the motor-pump frictions, the viscous coefficient  $B$  represents the simplest model to describe the frictions as function of speed. For getting higher accuracy, a more detailed friction model could be expressed as follows:

$$T_f(\omega) = \left[ T_c + (T_s - T_c)e^{-\frac{|\omega|}{\alpha_k}} + B|\omega| \right] \text{sign}(\omega) \quad (29)$$

where  $T_c$  is the Coulomb friction,  $(T_s - T_c)e^{-\frac{|\omega|}{\alpha_k}}$  is the Stribeck friction and  $B|\omega|$  the viscous friction [16]. The friction contribution due to pressure drop could be relevant too. Same considerations can be done about the Bulk modulus  $\beta$ : its effective value varies in function of pressure and temperature and it depends also on: presence of bubbles of free gas present inside fluid and deformability of the hydraulic components. The pump leakages are variable in function of operation conditions (pressure, pump speed and temperature) too and a constant coefficient  $a_p$  results limitative to characterize adequately the phenomena.

In order to improve the EHA module analysis, it is so necessary to evaluate the non-linearities that have not been taken into account in the architectural and functional models. The progressive improvement of the EHA module modeling concerns the evaluation of major non-linearities effects that may alter performance. Therefore a detail model has to be developed, for each component constituting the module, that permits analyzing phenomena in a more realistic way. At this modeling level, a virtual prototype has been developed.

In the present work, the Parker vane pump dynamics have been analyzed through the development of an AMESim virtual test bench which aimed at simulating the frictional torques and the leakage flow rates in accordance to experimental data. The purpose has been to insert the experimental curves directly in the AMESim model so that it is made as much as lookup tables. Specific mechanical and hydraulic submodels of the AMESim libraries have been identified and simulation tests have been performed in order to select the more adapted ones to reproduce the friction and leakage effects. Figure 4 shows the virtual prototype which simulates the vane pump performance using a generic implementation of its energy losses. At hydraulic ports 1 and 2, the line pressure is the input signal while at port 3 the input signal is represented by motor torque.

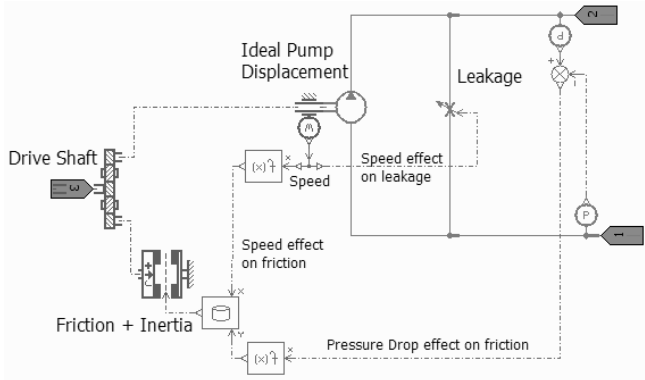


Figure 4: Virtual prototype of vane pump

The effective frictional torques and the leakage flow rates of the vane pump, are expressible through non-linear functions of operating conditions: pressure drop, pump speed and fluid temperature. The fluid temperature influences both frictional torques and leakages by means of variations of the dynamic viscosity of hydraulic fluid. At this modeling level and as a first step, it was assumed that:

- the operating temperatures are maintained constant. So the dependence to viscosity is not taken into account and postponed to next modeling level

Therefore the frictional torques and leakages are considered dependent only on hydraulic lines pressure drop and on the pump speed. The frictional torque is expressed in general form by eq. (30):

$$T_{fp} = f_f(\Delta p, \omega) \quad (30)$$

while the leakage flow rates got from eq. (31):

$$Q_{lp} = f_l(\Delta p, \omega) \quad (31)$$

In order to simulate the frictional torques in the form of the eq. (30), the component *FRIRK000* in the mechanical library of AMESim has been selected (fig. 5) for its ability to vary friction versus operating conditions. It is a rotary friction torque generator based on Karnopp model that deals and solves efficiently the numerical implementation of transition between sticking and sliding conditions [17]. As required by the Karnopp model, the motor-pump rotor inertia is included in the friction component.

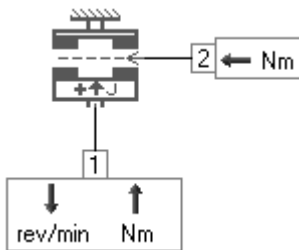


Figure 5: Component for pump frictions simulation, *FRIRK000*, from [18]

The experimental data of frictions torques, implemented in AMESim by means of an ASCII file in the format multi 1D tables [18], represent the input signal at port 2 of the component in fig. 5 and they permit to produce the desired friction versus pressure, velocity and even later temperature. A comparison between results provided by component and experimental curves has been carried out in order to verify the quality of the simulation (fig. 6).

△ p = 10 [bar], experimental curve	— p = 10 [bar], simulated curve
□ p = 50 [bar], experimental curve	- - - p = 50 [bar], simulated curve
◇ p = 100 [bar], experimental curve	⋯ p = 100 [bar], simulated curve
× p = 140 [bar], experimental curve	- · - p = 140 [bar], simulated curve
+ p = 180 [bar], experimental curve	— p = 180 [bar], simulated curve
○ p = 210 [bar], experimental curve	- - - p = 210 [bar], simulated curve
▲ p = 240 [bar], experimental curve	⋯ p = 240 [bar], simulated curve
■ p = 280 [bar], experimental curve	- · - p = 280 [bar], simulated curve

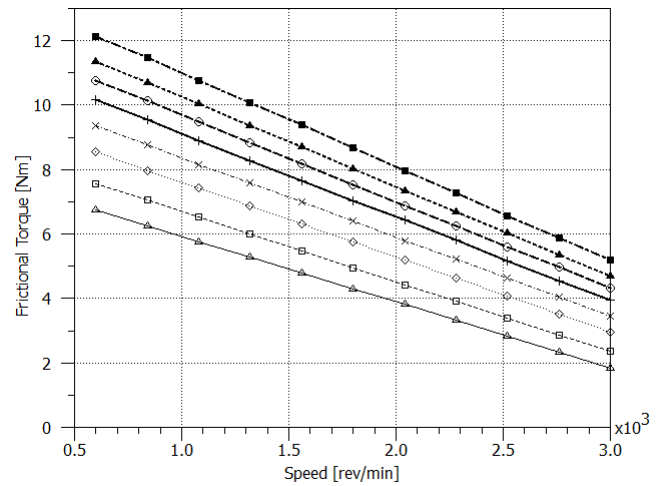


Figure 6: Frictional pump torques: experimental curves and curves obtained by AMESim model @45°C

Figure 6 shows that the simulation results agree well with experimental data inside the range of operating conditions performed in laboratory. In order to extend the range of operating conditions where the AMESim model is capable to provide values of frictional torques, an extrapolation of data has been proposed. A linear extrapolation has been carried out by the component *FRIRK000* in the range of pump speed from -3500 to 3500 *rev/min* and for positive pressure drop values. Figure 7 shows both the experimental curves in the range of laboratory tests and the extrapolated curves.

It is interesting to mention that at zero speed the frictional torques are not null but they correspond to stiction. This would not have been possible if using *tanh* models. However, the Karnopp model requires defining a region around the exact condition of zero speed, where a threshold speed value is provided by user for transition between sticking and sliding conditions. In this context the value entered is of 0,36 *rev/min*, 1/10000 of the rated velocity.

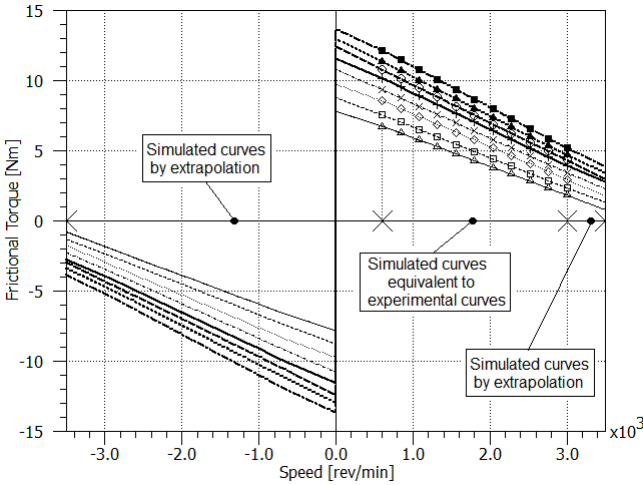
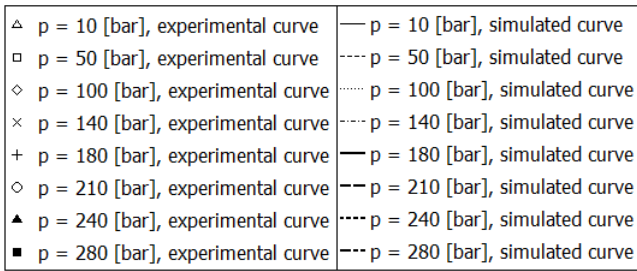


Figure 7: Frictional pump torques: extrapolation in the pump range: [-3500, 3500] rev/min provided by component FR1RK000

It is not easy to validate the extrapolated results provided at low speed near to zero through laboratory tests under constant operating temperature: in condition of low speed, the volumetric flow coming into pump is not sufficient to produce an adequate recirculation of fluid necessary to guarantee constant temperature inside pump. The AMESim model of frictional torques can be then improved by adding the dependence of friction to fluid temperature and by allowing testing the pump in those processes in which the evolution of temperature plays a fundamental role on performance degradations.

Concerning the leakages flow rates, the component VOR001 has been selected in the hydraulic AMESim library in order to simulate them by non-linear functions of pressure drop, pump speed (fig. 8) and later fluid temperature.

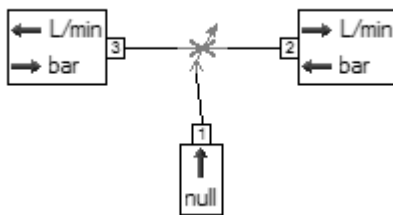


Figure 8: Component for pump leakages simulation, VOR001, from [18]

It represents a variable hydraulic orifice which provides, as outputs (ports 2 and 3), the leakage flow rate. In the component parameters table it is possible to insert directly the experimental data file. The signal at port 1 is the pump speed. Like for the frictional torques, the experimental data have been implemented in AMESim model. A comparison between results provided by component and experimental curves has been carried out in order to verify the quality of the simulation (fig. 9).

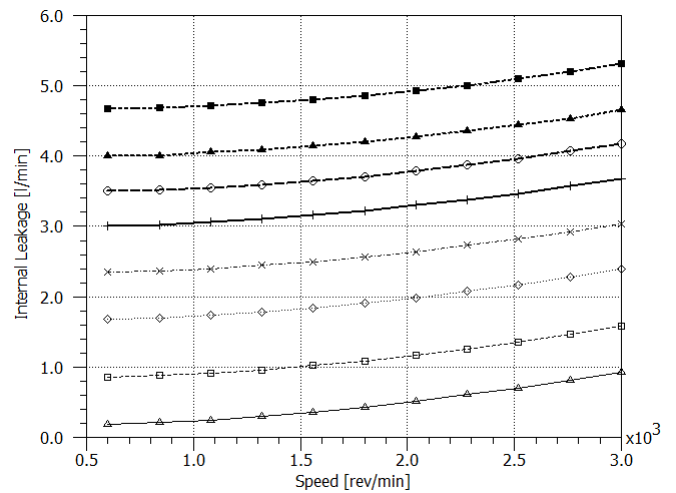
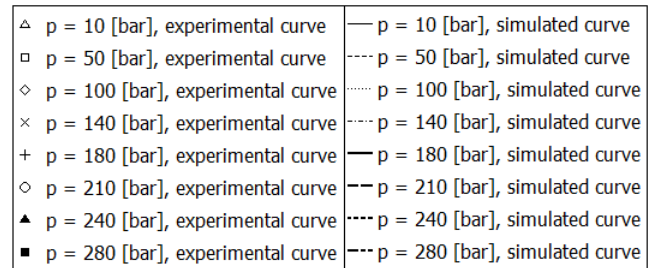


Figure 9: Internal pump leakages: experimental curves and curves obtained by AMESim model @45°C

Figure 9 shows that the simulation results agree well with experimental data inside the range of operating conditions performed in laboratory. In order to extend the range of operating conditions where the AMESim model is capable to provide values of leakage flow rates, an extrapolation of data has been proposed.

A linear extrapolation has been carried out by the component VOR001 in the range of pump speed from -3500 to 3500 rev/min and for positive pressure drop values. In addition, even if the vane pumps do not accept negative values of pressure drop because they are designed to operate in 2 quadrants only, the AMESim model enables reaching these conditions. Figure 10 shows both the experimental curves in the range of laboratory tests and the extrapolated curves.

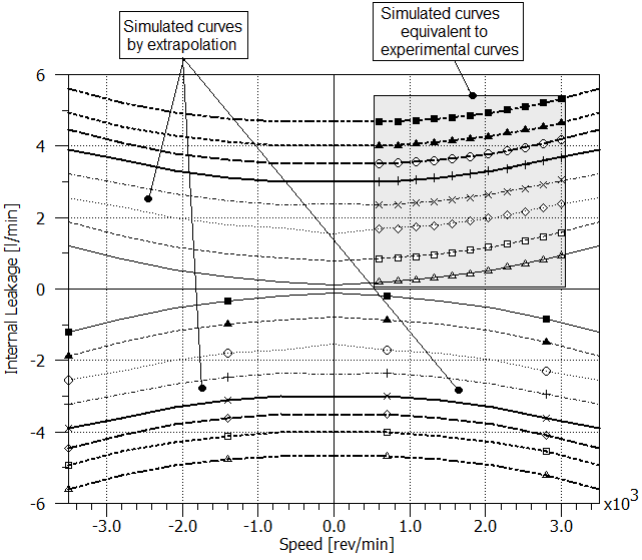
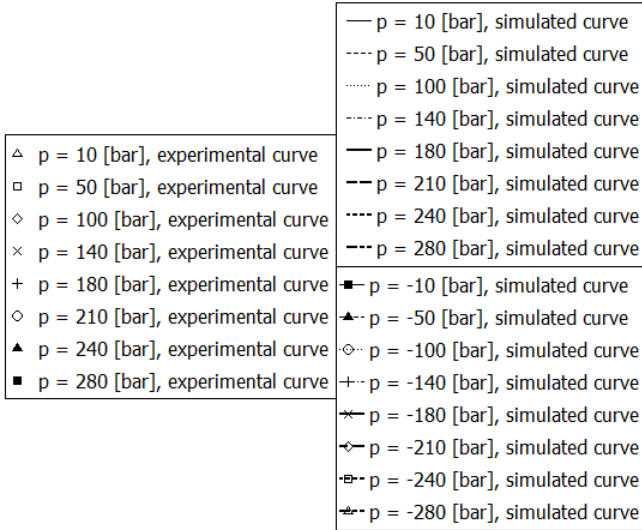


Figure 10: Internal pump leakages: extrapolation in the pump range: [-3500, 3500] rev/min provided by component VOR001

Due to difficulty to maintain constant the operating temperature during laboratory tests, as already described for frictional torques, it is not an easy task to validate the extrapolated results provided at low speed near to zero. The AMESim model of internal pump leakages can be then improved by adding the dependence to the fluid temperature.

#### 4.1 Parametric model of pump frictions and leakages

A linear parametric representation model of energy losses has also been developed, capable to approximate the experimental curves of pump frictions and leakages, in accordance with the Linear Gap Theory for radial gap (LGT) [19]. This model represents a useful tool in the control unit design of the EHA module in order to assure system performance requirements.

The parametric model proposes a solution of the first degree polynomial type for both frictional torques and internal pump leakages:

$$T_{fp} = \alpha_{fp} + \beta_{fp}\omega + \gamma_{fp}\Delta p \quad (32)$$

$$Q_{lp} = \beta_{lp}\omega + \gamma_{lp}\Delta p \quad (33)$$

where  $\alpha_i$ ,  $\beta_i$  and  $\gamma_i$  are the parameters determined through the Least Square Method (LSM).

The LSM's objective is to find a good estimation of parameters, in order to fit the set of experimental data, by minimizing the sum of squared residuals (SSR). By varying the values of the parameters  $\alpha_i$ ,  $\beta_i$  and  $\gamma_i$  of the eq.s (32) and (33), it has been possible to obtain the values of them which makes SSR minimum.

Figure 11 shows the comparison between experimental curves and parametric model curves of the frictional pump torques.

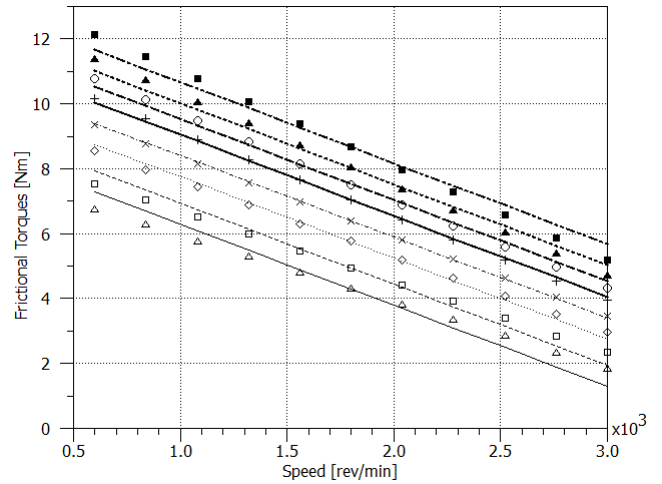
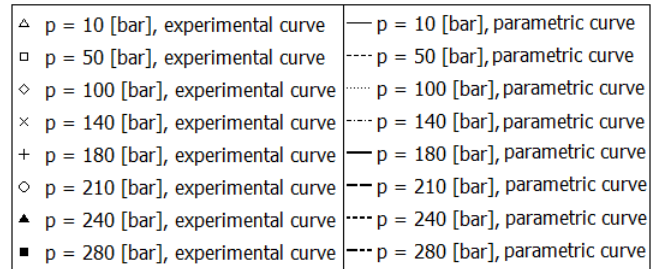


Figure 11: Frictional pump torques: experimental curves and curves obtained by parametric model @45°C

The relative error in percentage of frictional torques has been computed as:

$$e_{rel}^T \% = \frac{(T_{fp}^{experimental} - T_{fp}^{model})}{T_{fp}^{experimental}} 100 \quad (34)$$

It is possible to assert that the major region is characterized by an error  $e_{rel}^T$  less than 5% while only in a small region of high speed ( $> 2600 \text{ rev/min}$ ) and low pressure ( $10 \text{ bar} < \Delta p < 50 \text{ bar}$ ) the  $e_{rel}^T$  overcomes 15% but never exceed 29%.

Figure 12 shows the comparison between experimental curves and parametric model curves of the internal pump leakages.

△ p = 10 [bar], experimental curve	— p = 10 [bar], parametric curve
□ p = 50 [bar], experimental curve	- - - p = 50 [bar], parametric curve
◇ p = 100 [bar], experimental curve	⋯ p = 100 [bar], parametric curve
× p = 140 [bar], experimental curve	- · - · p = 140 [bar], parametric curve
+ p = 180 [bar], experimental curve	— p = 180 [bar], parametric curve
○ p = 210 [bar], experimental curve	- - - p = 210 [bar], parametric curve
▲ p = 240 [bar], experimental curve	⋯ p = 240 [bar], parametric curve
■ p = 280 [bar], experimental curve	- · - · p = 280 [bar], parametric curve

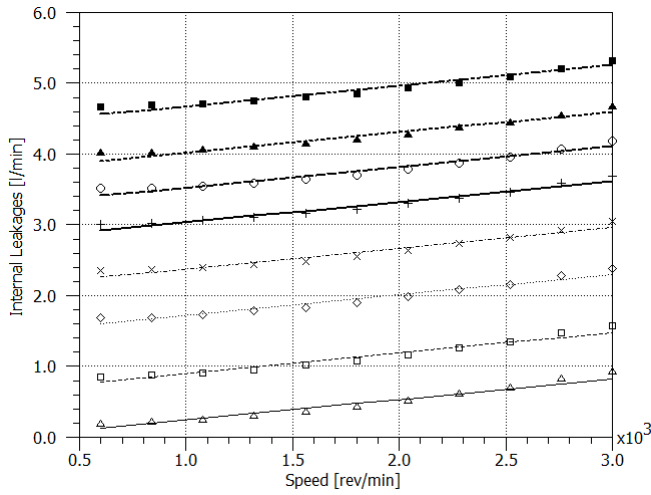


Figure 12: Internal pump leakages: experimental curves and curves obtained by parametric model @45°C

The relative error in percentage of internal leakages has been computed as:

$$e_{rel}^Q \% = \frac{(Q_{lp}^{experimental} - Q_{lp}^{model})}{Q_{lp}^{experimental}} 100 \quad (35)$$

Also in this case, the major region is characterized by  $e_{rel}^Q$  less than 5% while only in a small region of low speed ( $< 800 \text{ rev/min}$ ) and low pressure ( $10 \text{ bar} < \Delta p < 50 \text{ bar}$ ) the error overcomes 15% but never exceed 29%.

In conclusion, the parametric model based on the linear gap theory is able to reproduce the pump frictional torques and leakages experimental curves in the speed range [600, 3000]  $\text{rev/min}$  and pressure drop range [10, 280]  $\text{bar}$ , with relative errors in percentage of experimental data under the 5% in the majority of operating conditions. In next analysis, it will be necessary to extend the model capability and check its validity in a wider range of speed by taking into account also starting pump conditions.

## 5 Conclusion

The paper has dealt with modeling and simulation at three level of accuracy of an EHA module for industrial applications. An EHA innovative solution has been showed that takes advantage of fixed-displacement vane pump and of closed-loop control respectively on: rod position, cylinder pressure and motor shaft speed. A preliminary analysis has been achieved by means of architectural model that has permitted to relate the steady-state operation with fundamental parameters to be defined. An initial approach to control synthesis has been exposed by providing the designer with key relationships between open loop statics and dynamics and fundamental parameters. The parasitic effects have been added and their influence on hydraulic and hydromechanical modes has been analyzed. In order to get a realistic representation of losses that play role for power sizing and temperature management, two types of models were implemented using standard components of the LMS-AMESim libraries. Both frictional torque and internal leakage at vane pump level have been reproduced well using either look-up tables or parametric models of low complexity.

A complete virtual prototype, got by adding the detail model of the vane pump, exposed in this paper, and the models of other components constituting the EHA module, would represent an useful instrument to evaluate the energy consumption during a typical mission of injection molding machines and to optimize the EHA module design by simulating the influence of design choices on energy saving, closed loop performance and heat balance.

Another important aspect in the modelling of the EHA module to be taken into account is the thermo-hydraulic coupling: the system performances are hugely dependent on operating temperature because it strongly influences the hydraulic fluid properties. These effects become key design drivers in specific operating conditions, e.g. when pressure has to be accurately controlled without jack displacement phase of plastic injection. As the pump has no case drain to collect internal leakage and to take away heat coming from internal energy losses even a small error in modeling friction and leakage will alter the predictability of the EHA model and therefore not reproduce the potential issue of thermal divergence. For this reason, the ongoing work consists in improving accuracy of the EHA virtual prototype by developing thermal-hydraulic simulation at system level and generating expert tools for component selection from catalogues and controller setting.

## Nomenclature

Designation	Denotation	Unit
$A_c$	Section pipe area	$[m^2]$
$a_j$	Jack cross-chamber leakage coefficient	$[m^4s/kg]$

$a_p$	Internal pump leakage coefficient	$[m^4s/kg]$	$t_s$	Response time	$[s]$
$B$	Total viscous friction coefficient	$[Nm\ s/rad]$	$U_m$	Motor voltage	$[V]$
$B_m$	Motor viscous friction coefficient	$[Nm\ s/rad]$	$U_s$	Supply voltage	$[V]$
$B_p$	Pump viscous friction coefficient	$[Nm\ s/rad]$	$V$	Total volume of pipe and jack chamber	$[m^3]$
$D_c$	Pipe diameter	$[m]$	$V_c$	Conduit Volume	$[m^3]$
$F_{fj}$	Cylinder/piston frictional force	$[N]$	$V_j$	Jack chamber volume	$[m^3]$
$F_j$	Jack force	$[N]$	$V_0$	Pump displacement	$[m^3/rad]$
$f$	Jack viscous friction coefficient	$[kg/s]$	$x$	Rod position	$[m]$
$f_h$	Hydraulic natural frequency	$[Hz]$	$\dot{x}$	Rod speed	$[m/s]$
$f_{hm}$	Hydromechanical natural frequency	$[Hz]$	$\ddot{x}$	Rod acceleration	$[m/s^2]$
$J$	Total inertia	$[kg\ m^2]$	$\alpha$	Power modulation factor	$[-]$
$J_m$	Motor inertia	$[kg\ m^2]$	$\alpha_{fp}$	Static friction coefficient	$[Nm]$
$J_p$	Pump inertia	$[kg\ m^2]$	$\alpha_k$	Stick-slip coefficient	$[rad/s]$
$K_m$	Back-electromotive force coefficient	$[Nm/A]$	$\beta$	Bulk modulus	$[Pa]$
$I_m$	Motor current	$[A]$	$\beta_{fp}$	Viscous friction coefficient	$[Nm\ s/rad]$
$I_s$	Supply current	$[A]$	$\beta_{lp}$	Speed coefficient for leakage	$[m^3/rad]$
$L$	Motor inductance	$[H]$	$\gamma_{fp}$	Pressure coefficient for friction	$[m^3]$
$L_c$	Pipe length	$[m]$	$\gamma_{lp}$	Pressure Coefficient for leakage	$[m^4s/kg]$
$M$	Total mass	$[kg]$	$\Delta p$	Cylinder pressure	$[Pa]$
$Q_j$	Input jack flow rate	$[m^3/s]$	$\Delta p_c$	Pipe pressure drop	$[Pa]$
$Q_{lj}$	Jack chamber leakage	$[m^3/s]$	$\Delta \dot{p}$	Cylinder pressure variation in time	$[Pa/s]$
$Q_{lp}$	Internal pump leakage	$[m^3/s]$	$\lambda$	Friction factor	$[-]$
$Q_p$	Output pump flow rate	$[m^3/s]$	$\rho$	Fluid density	$[kg/m^3]$
$R$	Motor resistance	$[Ohm]$	$\omega$	Motor shaft speed	$[rad/s]$
$Re$	Reynolds number	$[-]$	$\omega_h$	Hydraulic undamped natural pulsation	$[rad/s]$
$S$	Active area of piston	$[m^2]$	$\omega_{hm}$	Hydromechanical undamped natural pulsation	$[rad/s]$
$T_c$	Coulomb torque	$[Nm]$	$\dot{\omega}$	Motor shaft acceleration	$[rad/s^2]$
$T_{fm}$	Frictional motor torque	$[Nm]$	$\xi_h$	Hydraulic damping ratio	$[-]$
$T_{lp}$	Frictional pump torque	$[Nm]$	$\xi_{hm}$	Hydromechanical damping ratio	$[-]$
$T_L$	Load torque	$[Nm]$			
$T_m$	Effective motor torque	$[Nm]$			
$T_m^*$	Requested motor torque	$[Nm]$			
$T_s$	Static torque	$[Nm]$			

---

## References

- [1] J-C Maré. Towards more electric drives for embedded applications: (re)discovering the advantages of hydraulics. *7<sup>th</sup> International Fluid Power Conference, Aachen, Germany, 2010.*

- [2] S Helduser. Development trends in electrohydraulic drives and controls. *6<sup>th</sup> International Fluid Power Conference, Dresden, Germany, 2008.*
- [3] K Muller, and U Dorn. Variable speed drives – customer benefits in injection molding machines and presses. *7<sup>th</sup> International Fluid Power Conference, Aachen, Germany, 2010.*
- [4] S Helduser. Improved energy efficiency in plastic injection moulding machines. *8<sup>th</sup> Scandinavian International Conference of Fluid Power, Tampere, Finland, 2003.*
- [5] J-C Maré. Combining hydraulics and electrics for innovation and performance improvement in aerospace actuation. *12<sup>th</sup> Scandinavian International Conference of Fluid Power, Tampere, Finland, 2011.*
- [6] A Feuser. Modern electrohydraulic drive technology for stationary machinery in industrial automation. *7<sup>th</sup> International Fluid Power Conference, Aachen, Germany, 2010.*
- [7] K R McCullough. Design and characterization of a dual electro-hydrostatic actuator. *Department of Mechanical Engineering, McMaster University, Hamilton, Canada, 2011.*
- [8] S Habibi, and A Goldenburg. Design of a new high performance electrohydraulic actuator. *IEEE/ASME Transactions on Mechatronics, Vol.5, 2000.*
- [9] Parker Catalogue. *Compact electro-hydraulic actuator (EHA).* Bulletin HY22-3200A/US.
- [10] D van den Bossche. The A380 flight control electrohydrostatic actuators, achievements and lessons learnt. *25<sup>th</sup> International Congress of the Aeronautical Sciences, Hamburg, Germany, 2006.*
- [11] A E Fitzgerald, C Jr Kingsley, and S D Umans. *Electric Machinery.* 6<sup>th</sup> edition, McGraw Hill, 2003.
- [12] H E Merritt. *Hydraulic Control Systems.* John Wileys and Sons, Cincinnati, Ohio, 1967. ISBN 0-471-59617-5.
- [13] J-C Maré. Actionneurs hydrauliques - commande. *Article S7531, série Mesure et Régulation, Encyclopédie des Techniques de l'Ingénieur, page 17, Septembre 2002.*
- [14] F H Raven. *Automatic Control Engineering.* 5<sup>th</sup> edition, McGraw Hill, 1995.
- [15] J-C Maré. Considerations pratiques sur les correcteurs PID dans le domaine de l'énergie fluide. *Revue Fluides, pp 8-17, Numéro Spécial Matériels, Septembre 2000*
- [16] E G Papadopoulos, and G C Chasparis. Analysis and model-based control of servomechanisms with friction. *Proceedings of the IEEE/RSJ International Conference on Intelligent Robots and System, Lausanne, Switzerland, 2002.*
- [17] D Karnopp. Computer simulation of stick-slip friction in mechanical dynamic systems. *Journal of Dynamic Systems, Measurement and Control. Vol. 7, March 1985.*
- [18] LMS-AMESim. *AMEHelp*
- [19] P Krus. *Formula Book For Hydraulics and Pneumatics.* Fluid and Mechanical Engineering Systems, Department of Management and Engineering, Linköping University, Sweden. Revised 2008-10-27.



# Model Predictive Control for Power Optimization in a Hydrostatic Wind Turbine

Feng Wang and Kim A. Stelson

Center for Compact and Efficiency Fluid Power  
Department of Mechanical Engineering, University of Minnesota  
Minneapolis, MN 55455 USA  
E-mail: wang2148@umn.edu, kstelson@umn.edu

## Abstract

Model predictive control (MPC) is applied to a mid-sized hydrostatic (HST) wind turbine for maximizing power capture in this paper. This study focuses on the torque control in region 2, which tracks the desired rotor speed so that the turbine can operate at the optimum tip-speed ratio (TSR) for maximum power. Preliminary study shows that the widely used  $K\omega^2$  control law has a good control performance in steady-state wind conditions. However due to wind turbulence, the turbine operates at tip-speed ratios far away from the optimal point. This deviation is not only due to the large rotor inertia, but also due to the characteristics of the  $K\omega^2$  control. An MPC controller is proposed to track the desired rotor speed by using the future prediction of wind speed. To consider the potential advantage, the MPC controller is applied to a 50 kW HST wind turbine. A wind speed step change is selected as a basic test of transient response. The control performance of the MPC is evaluated and compared with the  $K\omega^2$  control law. Results show that the MPC controller in a smaller wind speed step change shows a faster response than  $K\omega^2$  control law, but a large overshoot is observed. In a larger wind speed change, the MPC controller loses control when the wind speed steps down. This indicates the MPC controller in this study has limited effective operation range since it uses a linearized plant model and the wind turbine is a highly nonlinear system. Future work includes the optimization of MPC controller parameters to reduce the overshoot during the wind speed change and the design of multiple MPC controllers for wide operation range.

**Keywords:** Mid-sized wind turbine, hydrostatic transmission, wind turbulence, power optimization, model predictive control

## 1. Introduction

Wind power is a plentiful, renewable source of energy, able to produce emission-free power in the kilowatt to megawatt range. Land-based or off-shore wind farms can connect several hundred wind turbines to the grid. However, these facilities require expensive power transmission lines and typically incur significant construction and maintenance costs. For areas with smaller power needs, such as farms or factories, a small wind facility is a cost-effective method of power generation. These mid-sized wind turbines often have a fixed rotor speed which reduces cost by eliminating the power converter. However, since the tip-speed ratio (TSR) cannot be optimized, fixed speed operation does not allow the rotor to capture the maximum energy as the wind speed varies. To capture wind energy more efficiently, a continuously variable transmission (CVT) is required.

A hydraulic CVT in the form of a hydrostatic transmission (HST) provides a competitive solution for a

mid-sized wind turbine. With a hydrostatic transmission, the generator speed is decoupled from the rotor speed, making it possible to use a synchronous generator. The generator can run at synchronous speed at different wind speeds and rotor speeds, eliminating the use of a power converter. There are also some other advantages of using an HST in a wind turbine, such as more damping to reduce shock loading, flexible system configuration, low cost and high reliability [1].

There are four control regions in a wind turbine. In region 1 where the wind speed is below cut-in speed, the turbine is in stand-by mode. In region 2 where the wind speed is between the cut-in and the rated speed, the turbine is controlled so that it runs at the optimum TSR to achieve maximum power. In region 3 where the wind speed is above the rated but below the cut-out speed, the turbine output is limited to the rated power. In region 4 where the wind speed is above the cut-out speed, the turbine is shut down to avoid damage. To achieve maximum energy capture in region 2, a widely used control strategy in the wind industry, referred to as the

$K\omega^2$  control law, is used. The beauty of the  $K\omega^2$  law is that it only needs rotor speed information and does not require the wind speed information. The control law can automatically bring the turbine to the optimum operation point by controlling the rotor reaction torque [2, 3].

Preliminary study shows that the  $K\omega^2$  law gives good control performance in steady-state wind conditions [4]. However in the real world, wind speed varies both temporally and spatially. Wind turbulence in the form of wind gusts, happen unexpectedly. During wind turbulence, the turbine operates at tip-speed ratios far away from the optimum TSR even with the  $K\omega^2$  law. This is not only due to the large inertia of the blade, but also due to the characteristics of the  $K\omega^2$  law in which the rotor speed is regulated indirectly by controlling the rotor reaction torque. In a wind gust, the large inertia of the rotor prevents the rotor speed from changing fast enough to adapt to the increased wind speed. On the other hand, the rotor reaction torque increases slowly due to slowly increasing rotor speed according to  $K\omega^2$  law, which tends to slow down the rotor angular acceleration.

Various control methods for wind turbines have been recently studied. A typical feedback controller adjusts the rotor angular speed to desired values based on the wind speed information. However, even if the feedback controller can use the wind speed information, the delay between the control action and the resulting response cannot be avoided since the inertia of the blade is fairly large. The use of the future wind information has been discussed to further improve the control performance in some studies. If the controller can preview the wind speed information, this would lead to significant improvements in the control performance.

In this paper we consider applying model predictive control to rotor speed control. An MPC controller is designed to track desired rotor speed by using estimates of future wind speed. In the design it is assumed that the MPC controller can use wind speed over some future time horizon from a few seconds to minutes. The future prediction of wind speed can be obtained using a statistical model. Also, the use of Light Detection And Ranging (LIDAR) technology to measure the wind speed is possible. MPC has been considered for control of conventional gearbox turbines for power optimization and load reduction [5, 6, 7, 8, 9]. This is the first study to consider MPC control of a hydrostatic wind turbine.

## 2. Hydrostatic wind turbine control - baseline

### 2.1 Control hierarchy

A modern gearbox turbine has several levels of control systems. In the high level, a supervisory controller monitors the wind speed and determines when the wind speed is sufficient to start up the turbine and when the turbine must be shut down for safety due to high wind speeds. The middle level control mainly includes the torque control and the blade pitch control. Torque control, controlled through the power electronics in gearbox turbines, determines how much torque is extracted from

the rotor shaft. The extracted torque opposes the rotor aerodynamic torque provided by the wind and thus indirectly regulates the rotor speed. The low control level includes the generator, power electronics and pitch actuator controllers, which operate much faster than the middle-level control. The control hierarchy of the gearbox wind turbine is shown in Figure 1.

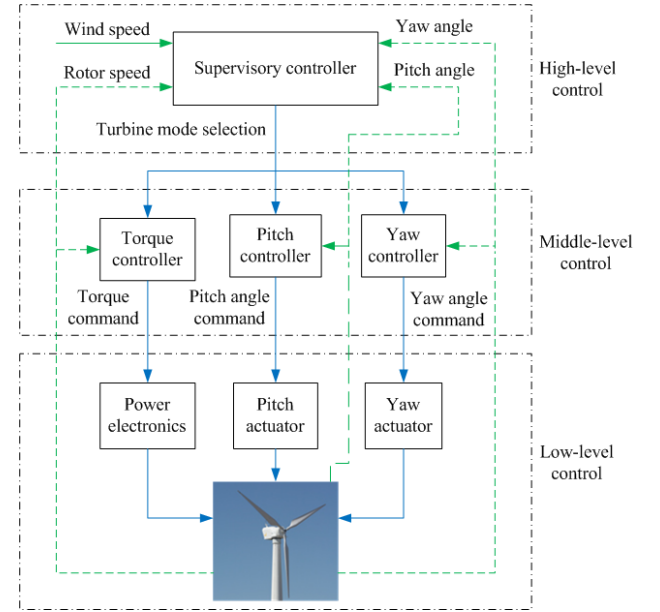


Figure 1 Control hierarchy of gearbox wind turbine

For variable-speed turbines operating in region 2, the control objective is to maximize energy capture by operating the turbine at the optimum TSR. This is achieved by the torque controller. The pitch controller is not active in this region. The focus of this study is torque control in region 2. The  $K\omega^2$  control law is used as the baseline in this study.

### 2.2 Baseline $K\omega^2$ control law

The power coefficient  $C_p$  is a function of the tip-speed ratio  $\lambda$  and the blade pitch angle  $\beta$ , which is represented by a surface. The optimum TSR to reach the maximum power coefficient shifts with the blade pitch angle. In region 2 where the blade is at a fine pitch angle, the optimum TSR is fixed. The TSR,  $\lambda$ , is defined as:

$$\lambda = \frac{\omega R}{v}$$

where  $\omega$  is the rotor angular speed,  $R$  is the radius of the blade and  $v$  is the wind speed.

In  $K\omega^2$  control, the control torque (rotor reaction torque),  $\tau_c$ , is given by:

$$\tau_c = K\omega^2$$

where  $K$  is the control gain given by:

$$K = \frac{1}{2} \rho A R^3 \frac{C_{p\max}}{\lambda_*^3}$$

where  $\rho$  is the air density,  $A$  is the blade swept area and  $\lambda_*$  is the optimum TSR at which the maximum power coefficient  $C_{pmax}$  occurs.

The beauty of the  $K\omega^2$  law is that it only needs rotor speed information and does not require wind speed information. The control law can automatically bring the turbine to the optimum operation point since the optimum operation parameters,  $\lambda_*$  and  $C_{pmax}$ , are included in the control gain,  $K$ . The  $K\omega^2$  law can track the optimum TSR well if accurate turbine parameters,  $\lambda_*$  and  $C_{pmax}$ , are given.

### 2.3 Hydrostatic wind turbine control

The schematic diagram of a hydrostatic wind turbine is shown in Figure 2. The low-speed rotor shaft drives a fixed displacement pump and the high-speed generator is driven by a variable displacement hydraulic motor.

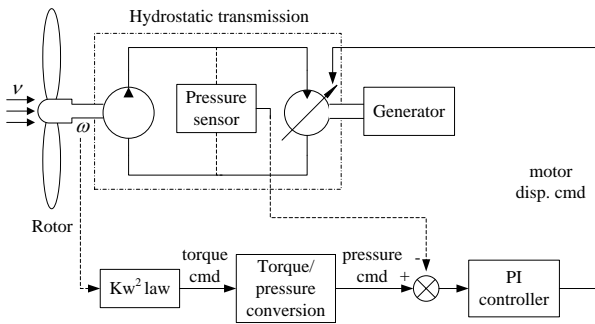


Figure 2 Schematic diagram of a hydrostatic wind turbine

The control of an HST turbine is similar to a gearbox turbine except for the torque control in the middle-level. In an HST turbine, instead of controlling the generator torque through power electronics, the rotor reaction torque (pump torque) is determined by the line pressure which is controlled by varying the motor displacement. By using a PI controller to track the desired line pressure, the desired control torque can be achieved.

The relationship between the control torque,  $\tau_c$ , and the line pressure,  $p_c$ , is:

$$p_c = \frac{\tau_c \eta_{pm}}{D_p}$$

where  $D_p$  is the pump displacement and  $\eta_{pm}$  is the pump mechanical efficiency.

A simulation model of the hydrostatic wind turbine is built in Simulink. The model is a physical equation based dynamic simulation model which simulates both the quasi-static and the dynamic conditions. The input and output causality of each component is verified by the bond graph method. The detailed system modeling can be found in our previous work [10].

## 3. Model predictive control for HST wind turbine

### 3.1 Overview

The fundamental idea of MPC is illustrated in Figure 3. At current time  $k$ , the MPC controller predicts the future behavior of a plant over a prediction horizon by using a plant model and computes a control input sequence which minimizes a certain performance cost function by solving an optimization problem. Only the first element of the control input sequence is applied to the plant. At next time step  $k+1$ , based on the new measurements, the MPC controller predicts the future behavior over the shifted prediction horizon and computes a new control input sequence. Similarly, only the first element of the newly computed control input sequence is applied to the plant. The above procedure is repeated as time shifts. During solving the optimization problem, MPC also takes the input and output constraints into considerations.

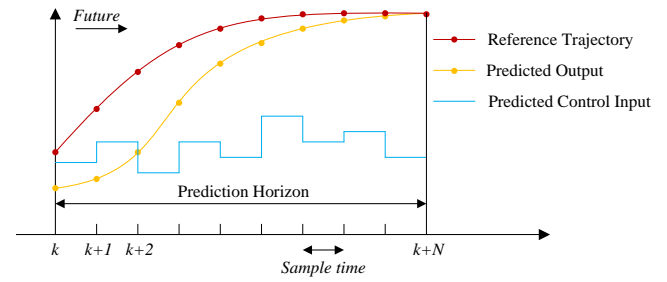


Figure 3 Scheme of model predictive control

While applying MPC to an HST wind turbine, the reference signal of the MPC controller is the desired rotor speed based on the future wind speed information. The system output, rotor speed, is feedback to the MPC controller. The wind speed is input to the MPC controller as a measured disturbance. The MPC controller uses an internal plant model and optimizer to calculate the control input to the plant, which is in the current case the pump torque command. The MPC controller in the hydrostatic turbine is shown schematically in Figure 4.

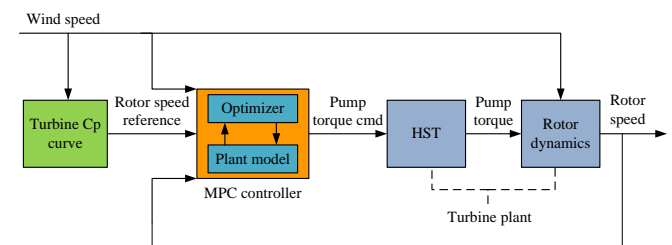


Figure 4 MPC controller in hydrostatic wind turbine

The objective function over the prediction horizon  $N$  is:

$$J = \sum_{i=0}^{N-1} \left[ Q(\omega_{r|k+i} - \omega_{k+i})^2 + S(\delta\tau_{c|k+i})^2 \right]$$

where  $Q$  and  $S$  are weighting factors.

The optimization minimizes the rotor speed tracking error  $\omega_{r|k+i} - \omega_{k+i}$  and the pump torque command variation  $\delta\tau_{c|k+i}$  over the prediction horizon while satisfying the input and output constraints. In an HST

wind turbine, the maximum rotor speed is limited by the blade design. The maximum pump torque is determined by the pump displacement and maximum line pressure. The second term of the cost function is to penalize the pump torque variation since there are physical limitations on how fast the pump torque can change.

The MPC controller uses a linearized plant model to calculate control inputs. Therefore the MPC controller is an approximation of the system behavior since there is discrepancy between the linearized model and the actual plant. If the plant is highly nonlinear within the operation range, the MPC controller designed for the specific operation point may not have satisfactory control performance throughout the operation range. The wind turbine system is such a system where the rotor torque increases nonlinearly with wind speed and rotor speed.

#### 4. Simulation study

##### 4.1 Simulation parameters

The case studied in this paper is a mid-sized wind turbine. The rotor aerodynamic model is from AOC 15/50, which is a 50 kW wind turbine manufactured by Atlantic Orient Corporation. The rotor aerodynamic model of AOC 15/50 is generated using FAST code. FAST is a multi-body wind turbine dynamics code developed by NREL [11]. In the simulation model, the rotor aerodynamic torque is generated by a 2D loop-up table taking the wind speed and rotor speed as input indexes.

Instead of designing an MPC controller for the entire operation range, the current study considers one operation point and the plant model is linearized at this point. In the simulation, the selected operation point is at the wind speed of 6 m/s. To compare the MPC controller with the  $K\omega^2$  control law, a step change on the wind speed is considered. The main simulation parameters are shown in Table 1.

Table 1 Main simulation parameters

Property	Value	Unit
Blade radius	7.5	m
Rotor swept area	176.7	m <sup>2</sup>
Rated rotor speed	88	rpm
Optimum TSR	6.1	-
Maximum Cp	0.45	-
Air density	1.225	kg/m <sup>3</sup>
Pump displacement	1570	cc/rev
Motor displacement	71	cc/rev
Pipeline internal diameter	32	mm
Pipeline length	2	m
Wind speed at operation point	6	m/s
Rotor speed setpoint at 6 m/s	4.88	rad/s
Pump torque at 6 m/s	2156	Nm
Control interval	0.02	s
Prediction horizon	200	-
Control horizon	50	-
Pump torque rate weight, $S$	0.1	-
Rotor speed weight, $Q$	20	-

#### 4.2 Simulation results

The wind turbine system is linearized at the wind speed of 6 m/s using the Matlab linearization toolbox. This linearized model is then used in the MPC controller to solve the optimization problem. Figure 5 shows the wind speed changes and the corresponding rotor speed changes using the  $K\omega^2$  and MPC controllers. The wind speed steps up from 6 to 7 m/s at 60 s and steps down from 7 to 6 m/s at 120 s.

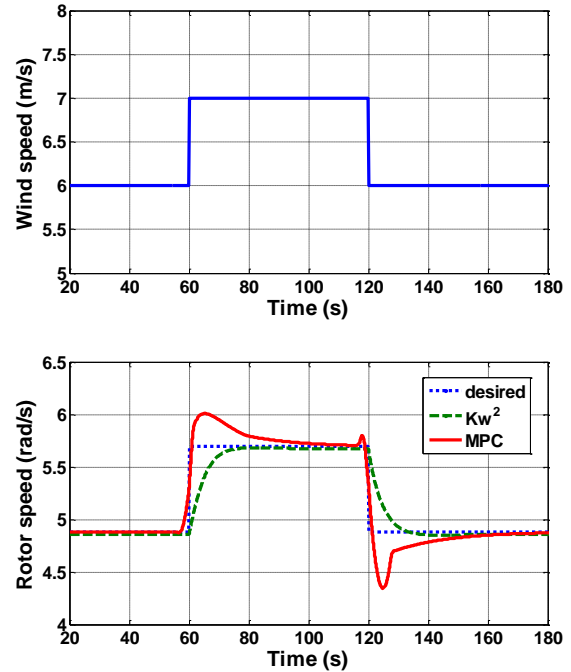


Figure 5 Wind speed change from 6 to 7 m/s and the corresponding rotor speed changes using the  $K\omega^2$  and MPC controllers

The desired rotor speed is calculated using the wind speed information. It is shown that the rotor speed using  $K\omega^2$  controller slowly approaches the desired point without overshoot. The rotor speed using MPC controller changes before the wind speed change because it uses future wind speed information. The MPC controller shows a shorter rise time than the  $K\omega^2$  controller. However a large overshoot is observed and the settling time is longer. Since the 1 m/s wind speed change is within the linear range of the model, the same response will be seen for smaller steps.

To show the response of the controller in the nonlinear range, a 2 m/s wind speed step change is simulated. Figure 6 shows the response using the  $K\omega^2$  and MPC controllers. The wind speed steps up from 6 to 8 m/s at 60 s and steps down from 8 to 6 m/s at 120 s. When the wind speed steps up, the results are similar to previous simulation results. However, the MPC controller loses control when the wind speed steps down from 8 to 6 m/s. This indicates the MPC controller in the wind turbine system has a limited effective operation range since the linearized plant model at the wind speed of 6 m/s may not work well when the wind speed is too far away from

that wind speed. To solve this problem, multiple MPC controllers at different operation points are required and the control may switch among different MPC controllers according to the wind speed.

Comparing the simulation results in Figure 5 and Figure 6, it is also shown that the MPC controller has an asymmetric behavior when the wind speed steps up and down. In Figure 5, the overshoot when the wind speed steps down is larger than the overshoot when the wind speed steps up. While in Figure 6, the situation when the wind speed steps down is even worse.

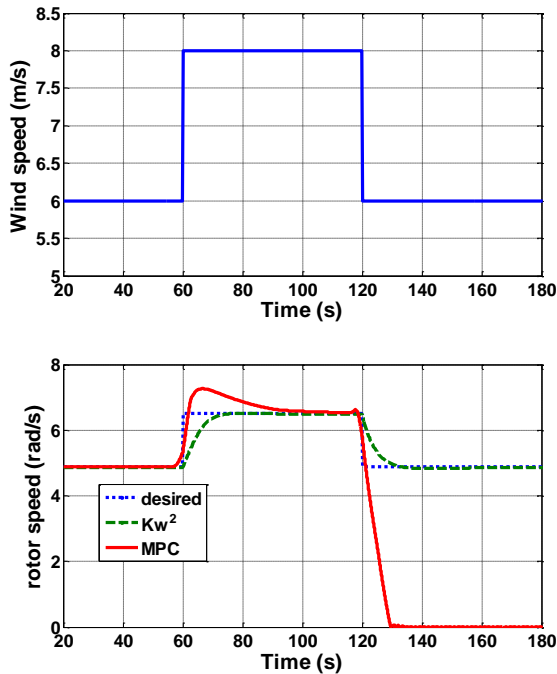


Figure 6 Wind speed change from 6 to 8 m/s and the corresponding rotor speed changes using the  $K\omega^2$  and MPC controllers

## 5. Conclusions and discussions

In this paper a model predictive control is proposed for maximizing power capture in a mid-sized hydrostatic wind turbine. The study focuses on the torque control in region 2, which tracks the desired rotor speed so that the turbine can operate at the optimal tip-speed ratio for maximum power. Preliminary study shows that the well developed  $K\omega^2$  law has a good control performance in steady-state wind conditions. However during wind turbulence, the turbine operates at tip-speed ratios far away from the optimum TSR. This is not only due to the large rotor inertia, but also due to the characteristics of the  $K\omega^2$  law itself.

An MPC controller is proposed to track the desired rotor speed by using the future prediction of wind speed. The controller uses a linearized plant model to solve an optimization problem that minimizes the rotor speed tracking error and the control input variation over the prediction horizon while satisfying the input and output constraints. To consider the potential advantage, the

MPC controller is applied to a 50 kW HST wind turbine. The plant model is linearized at the wind speed of 6 m/s and then used in the MPC controller.

The control performance of the MPC is evaluated and compared with the  $K\omega^2$  control law in the simulation. Two wind speed step changes (1 and 2 m/s) are studied. Results show that the MPC controller in a smaller wind speed change has a faster response than  $K\omega^2$  control law, however a large overshoot is observed. In a larger wind speed change, the MPC controller loses control when the wind speed steps down. This indicates the MPC controller in this study has a limited effective operation range since the linearized plant model at the wind speed of 6 m/s may not work well when the wind speed is far away from that wind speed.

Based on the results of this study, there are still many improvements needed before applying the MPC controller to wind turbines. One future task is to optimize the MPC control parameters to reduce the overshoot during the wind speed change. Another task is to design multiple MPC controllers and switch among different MPC controllers at different wind speeds.

## Acknowledgments

This research was supported by the Center for Compact and Efficient Fluid Power, a National Science Foundation Engineering Research Center funded under cooperative agreement number EEC-0540834.

## References

- [1] Thul, B., Dutta, R., Stelson, K. A., Hydrostatic transmission for mid-sized wind turbines. 52<sup>nd</sup> National Conference on Fluid Power, Las Vegas, USA, 2011.
- [2] Johnson, K. E., Pao, L. Y., Balas, M. J., Fingersh, L. J., Control of variable-speed wind turbines: standard and adaptive techniques for maximizing energy capture. IEEE Control Systems Magazine, vol.26, no.3, pp.70–81, 2006.
- [3] Pao, L. Y., Johnson, K. E., A tutorial on the dynamics and control of wind turbines and wind farms. American Control Conference, pp. 2076-2089, St. Louis, Missouri, USA, 2009.
- [4] Wang, F., Trietch, B., Stelson, K. A., Mid-sized wind turbine with hydro-mechanical transmission demonstrates improved energy production. The 8th International Conference on Fluid Power Transmission and Control (ICFP 2013), Hangzhou, China, 2013.
- [5] Henriksen, L. C., Model predictive control of a wind turbine, master thesis, Technical University of Denmark, 2007.
- [6] Soltani, M., Wisniewski, R., Brath, P. and Boyd, S., Load reduction of wind turbines using receding horizon control, Proceedings IEEE Multi-Conference on Systems and Control, pp. 852–857, 2011.

- [7] Zhongzhou, Y., Yaoyu, L., and Seem, J. E., Model predictive control for wind turbine load reduction under wake meandering of upstream wind turbines, American Control Conference, 2012.
- [8] Mostafa, S., Malik, O. P., and Westwick, D. T., Multiple model predictive control for wind turbines with doubly fed induction generators. IEEE Transactions on Sustainable Energy, vol.2, no.3, 2011.
- [9] Khalid, M., Savkin, A.V., A model predictive control approach to the problem of wind power smoothing with controlled battery storage, Renewable Energy, vol.35, pp.1520-1526, 2010.
- [10] Dutta, R., Wang, F., Bohlmann, B., Stelson, K. A., Analysis of short-term energy storage for mid-size hydrostatic wind turbine. ASME Dynamic Systems and Control Conference, Fort Lauderdale, FL, USA, 2012.
- [11] NWTC design codes (FAST by Jason Jonkman). <http://wind.nrel.gov/designcodes/simulators/fast/>

# Pumps and Motors



## Swash plate oscillation in a variable displacement floating cup pump

P.A.J. Achten, S. Eggenkamp, H.W. Potma  
Innas, Breda, the Netherlands  
E-mail: pachten@innas.com

### Abstract

The oscillation of a swash plate has been studied in a variable displacement floating cup pump. Servo valves have been designed and built into the pump. These so called  $\beta$ -valves define a certain operating angle, while leaving the swash plate free to oscillate, in the same way as during real pump operation. Measurements have been performed in a wide range of operating conditions. A simulation model has been built to get a better understanding of the dynamic behaviour. The study has proven the large impact of the swivel torque of the swash plate on the pump behaviour. The swash plate oscillation creates an additional displacement of the pump, especially during commutation, which is often larger than the original sinusoidal movement. The dynamic oscillation of the swash plate therefore dominates the commutation phenomena. It has also been proven that the overall efficiency is substantially reduced if the swash plate is free to oscillate, like in real pump operation. Although this study is performed on a floating cup pump, the authors of this paper believe that these effects also occur in conventional types of pumps and motors. It is recommended that a similar study should be performed on slipper type and bent axis pumps and motors.

**Keywords:** Variable displacement pump, floating cup principle, oscillation of the swash plate

### 1 Introduction

When analysing variable displacement pumps or motors, it is often convenient to set the displacement at a constant value. In for instance a slipper type pump, this condition can be realised by locking the swash plate position by means of a screw or bolt. This way, a certain swash angle and pump displacement can be defined and reproduced during experiments. In simulations, the same 'locked' position is simply realised by defining the angular position of the swash plate as a constant. These procedures and assumptions are so common that they are often not even mentioned in publications.

This paper discusses the validity of these procedures and assumptions. Evidently, in real operation, a variable displacement pump does not have a constant displacement. In most cases the swash plate position is controlled dynamically by means of hydraulic cylinders. These cylinders not only set the swash angle but also act as shock absorbers for counteracting the oscillating torque load of the pistons on the swash plate. From previous literature [1-6] it is already known that the oscillating torque load results in an oscillating rotation of the swash plate. However, the vibration of the swash plate also results in an extra movement of the pistons of the rotating group, which is superimposed on the general, sinusoidal movement [1, 2].

The extra oscillating displacement is largest in the top and bottom dead centres [7]. In these commutation zones, the base sinusoidal movement is minimal. The oscillating movement of the swash plate and the resulting movement of the pistons could therefore have a larger effect on the commutation than the base sinusoidal movement of the

pistons. This is of importance for the design and dimensioning of the port plates, in particular of the silencing grooves.

This paper investigates the oscillating movement of the swash plates in a 28 cc variable displacement floating cup pump. A special servo valve has been introduced which controls the pressure level in the actuator cylinders and, more or less, defines a constant and reproducible operating condition, while keeping the swash plates free to vibrate. A simulation model has been developed which describes the vice versa relationship between the commutation and the swash plate movement. The results from the simulation have been compared to measurements in a wide range of operating conditions. Finally the effect of the swash plate oscillation on the piston movement, the commutation and the efficiency will be discussed.

### 2 Variable displacement floating cup pump

In the floating cup principle [8, 9] the pistons are not free to move, but are press fitted into a rotor. Each piston has its own cup-like cylinder, which is supported by and floating on a tilted 'barrel plate'. The floating cup principle is a multi-piston principle. Typically, 2 rings of 12 pistons are mounted side by side on a rotor, resulting in a total number of 24 pistons.

The rotation of the barrel plates and the cups is synchronised with the main shaft by means of a pin and slot mechanism. In the variable displacement design [10], the pump displacement is defined by the angular position of the swash plates (see Figures 1 and 2).

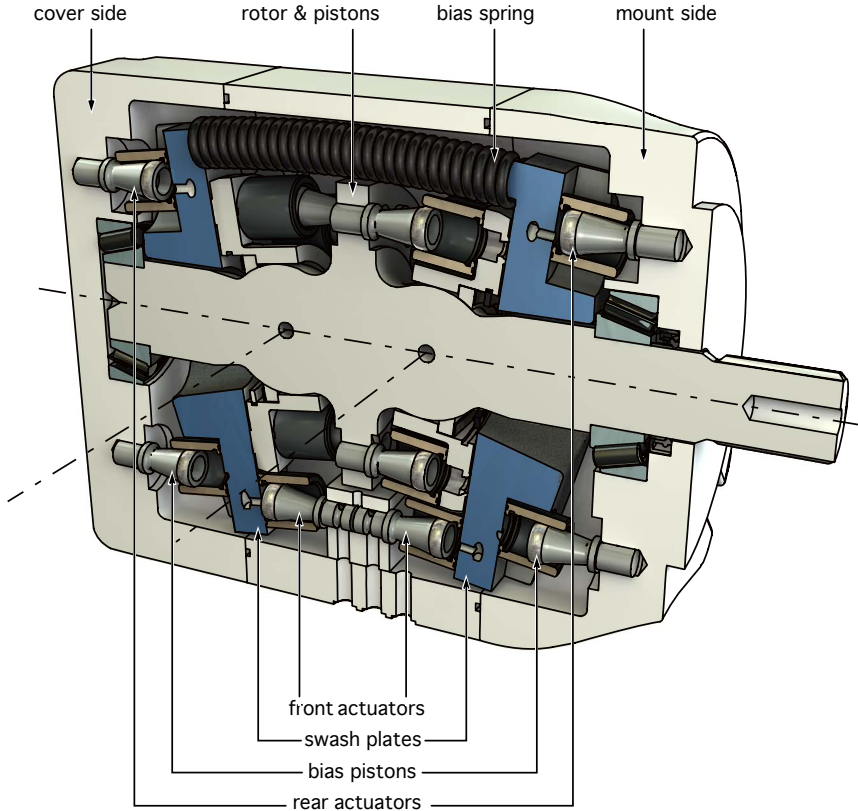


Fig. 1: Cross section of the variable displacement floating cup pump (FCVP28). The right side, where the pump is mounted, is called the mount side, the left side the cover side.

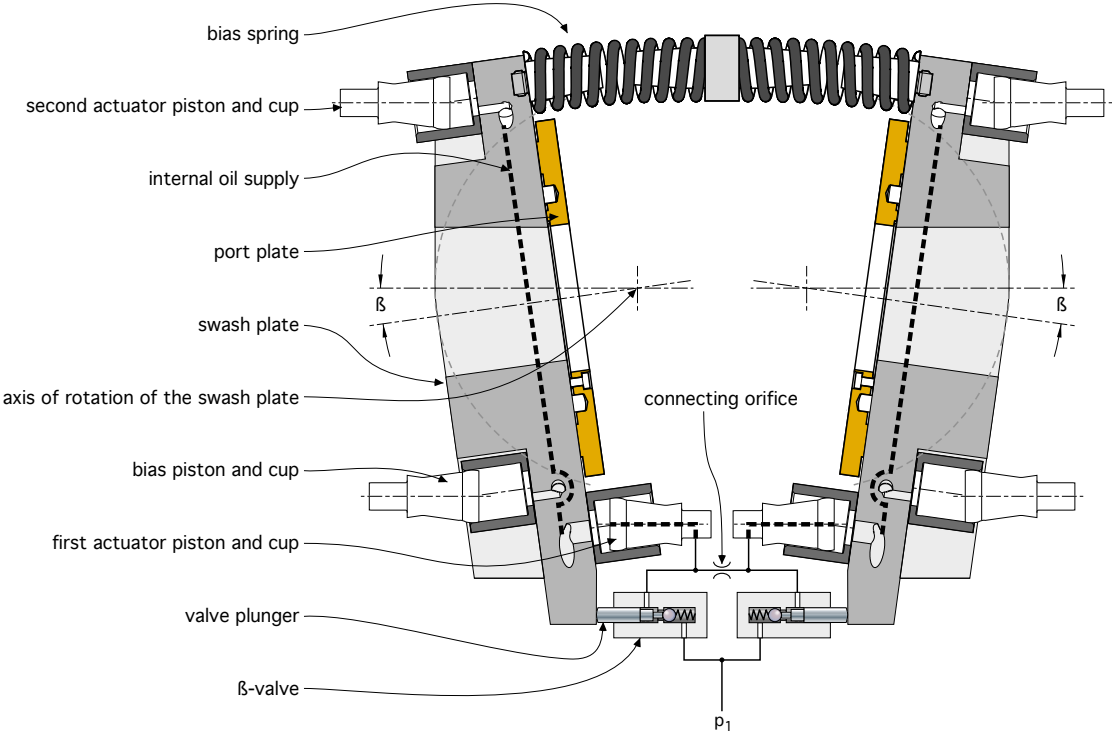


Fig 2: Cross section of the swash plates and actuator systems

Figure 2 shows a detailed cross section of the swash plates. A bias spring sets the swash angle to a maximum at the start of the pump operation. Furthermore, for each swash plate, one bias piston and two actuator pistons are used to control the swash angle  $\beta$  i.e. the displacement of the pump. The bias and actuator pistons are the same as of the rotating group. Like in conventional slipper type pumps, the cylinder of the bias piston is always connected to the high-pressure side of the pump. The bias piston and one of the actuator pistons are positioned at the backside of the swash plate, thereby supporting and reducing the deformation of the swash plate.

Unlike conventional pumps, in which only one actuator piston is applied, each swash plate has two actuator pistons to control the angular position  $\beta$  of the swash plate. The two actuators push in opposite directions (Figures 1, 2 and 12). As a result the two actuators together create a pure operating moment, thereby eliminating any axial force load on the swash plate and its hydrostatic bearings.

The average pressure level in the actuators determines the average position of the swash plate. A control valve sets the actuator pressure. Like in normal pumps, this control valve can be a pressure control, a flow control, a power control or a combination of these controls. For testing the pump at specific predefined and reproducible swash plate conditions, the normal procedure is to connect the actuators to the low-pressure side of the pump. The bias spring and the bias pistons will then rotate the swash plate to a larger angle until a mechanical end stop is hit.

The mechanical lock up not only defines the swash angle; it also stops the oscillation of the swash plate. This is unlike real pump operation in which the swash angle is controlled by means of hydraulic cylinders.

The aim of this study is to measure the pump performance and characteristics like in real operation. On the other hand, a system is needed which allows a clearly defined and reproducible swash angle. This is achieved by implementing small so-called  $\beta$ -valves (see Figure 2). When the bias piston forces the swash plate to move to a larger angle, the  $\beta$ -valve opens and supplies oil to the actuators. The pressure in the actuator cylinders increases, which counteracts the torque from the bias piston and cylinder. The  $\beta$ -valve is operated by a pin, which pushes the check valve of the  $\beta$ -valve to an open position. The length of the valve pin defines the angle at which the pump is operated. In this study 4 different pin pairs are used defining swash angles of about  $2^\circ$ ,  $4^\circ$ ,  $6^\circ$  and  $8^\circ$ .

The actuators are not only used to set the swash angle but also counteract the torque load of the rotating group on the swash plate. The strong and dynamic variation of the torque load results in an equally strong and dynamic variation of the pressure level in the actuators. This is the reason why the swash plates need to oscillate. The movement of the swash plate results in a displacement of the actuator volume, which is then used to change the pressure level in the actuators.

The variable displacement floating cup pump has two of these oscillating swash plates. Since the pistons of the left

side of the rotor are positioned in between the pistons of the right side of the rotor, the two sides of the pump are operated in counter phase. This counter phase operation is used to connect the actuator systems on the left and right side of the pumps. Whenever the actuators of the left side of the pump make a delivery stroke, the actuators on the right side make a suction stroke, and vice versa. Via the connecting orifice, oil is simply transferred from one side to the other (Figure 2). The orifice in the connecting line ( $2 \times \text{Ø}0.7$  mm in series) determines the pressure variation in the actuators in relation to the rocking movement of the swash plates.

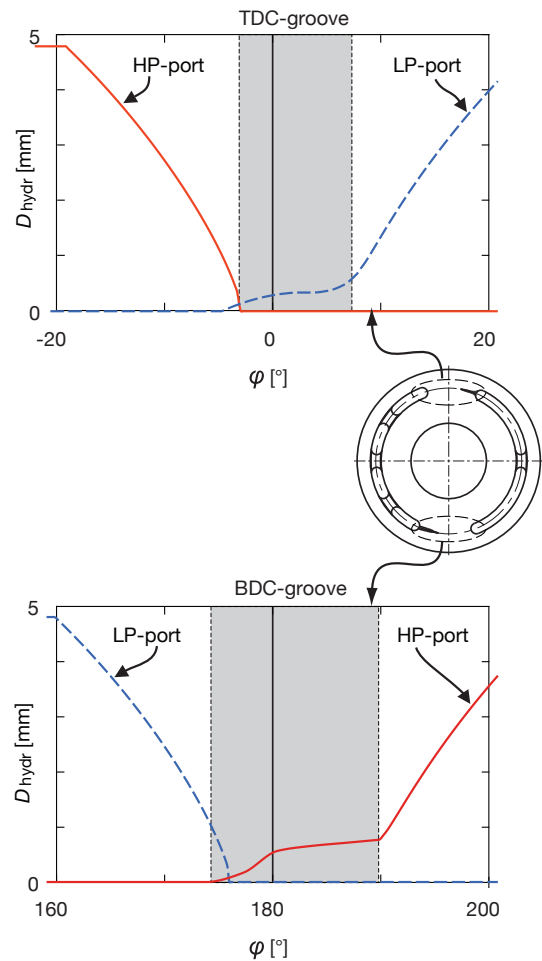


Fig. 3: Hydraulic diameter of the opening area between the ports of the barrel and the ports and silencing grooves of the port plate. The grey areas in the middle indicate the position of the silencing grooves

Like in conventional pumps and motors, silencing grooves are applied to soften the commutation in the top and bottom dead centres. Figure 3 shows the hydraulic diameter of the opening area between the ports of the barrel and the ports and grooves of the port plate. The dimensions and geometry of the silencing grooves have a strong effect on the torque load, which the barrel exerts on the swash plate. The design shown in figure 3 is optimised assuming a locked swash angle  $\beta$ .

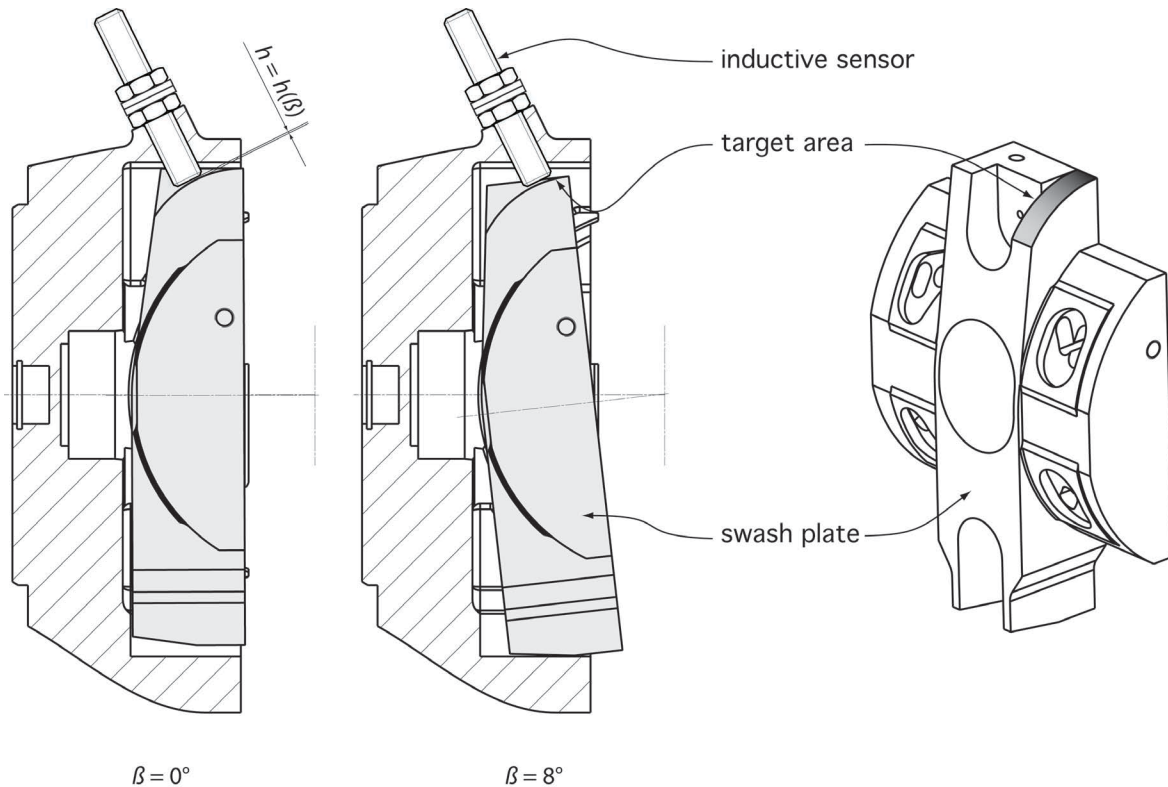


Fig. 4: Cross section of part of the housing (at  $\beta = 0^\circ$  and  $\beta = 8^\circ$ ), showing the position of the inductive sensors and the curved target area on the swash plate. The gap height  $h$  varies as a function of the swash plate angle  $\beta$

Of this pump, the movement of the swash plates and the pressure in the actuator systems have been measured at 4 different swash angles ( $2^\circ$ ,  $4^\circ$ ,  $6^\circ$  and  $7.8^\circ$ ), 6 different operating speeds (500, 1000, 1500, 2000, 2500 and 3000 rpm) and 7 different pump pressures (50, 100, 150, 200, 250, 300 350 bar). The FCVP is designed for a maximum swash angle of  $8^\circ$ . This is the angle where the swash plates will be stopped mechanically. Since the objective of this study was to study the pump behaviour when the swash plates are oscillating, the maximum swash angle is reduced to about  $7.8^\circ$ , thereby pushing the swash angle away from the mechanical end stop at  $8^\circ$ .

The movement of the swash plates has been measured by means of inductive sensors (one for each swash plate), as is illustrated in Figure 4. The pressure in the actuator cylinders has been measured by means of fast response piezoresistive pressure sensors.

In all operating points, the efficiency of the pump has been measured at Eindhoven University of Technology, for two different conditions:

- the swash plates are locked mechanically and the swash plates can't oscillate
- the swash angle is set by means of the  $\beta$ -valves and the swash plates are free to oscillate

At the end of this paper the two sets of measurements are compared. The measured swash angle and pressure level of the actuators is compared to the results from a simulation model.

### 3 Simulation model

In most analysis of variable displacement axial piston pumps, the swash angle is considered to be a constant. The calculation of the pressure in each of the cylinders of the rotating group is a matter of combining the sinusoidal movement of each piston with a detailed model of the port plate geometry (the upper part of Figure 5).

The variation of the displacement volumes of the rotating group is also a function of the swash angle  $\beta$ . If the swash angle varies during one revolution –as is postulated in this study– the variation of the displacement volumes is no longer sinusoidal. An extra movement is added to the sinus curve. The source of this extra movement is the torque load of the pistons of the rotating group acting on the swash plate. The rotational speed and the number of pistons rotating on the barrel determine the prime frequency of the variation of the torque load. In case of 12 pistons per barrel (as is the case in the floating cup pump) the swash plate torque will change periodically 12 times per revolution.

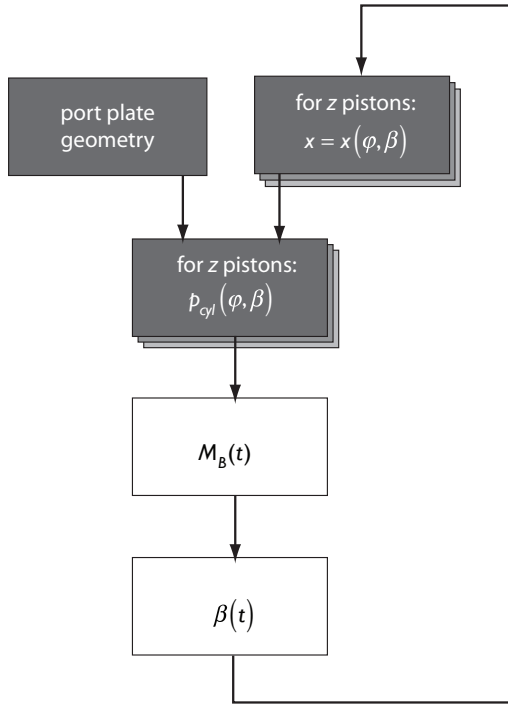


Fig 5: Model of the cylinder pressure assuming a constant swash angle  $\beta$  (the grey boxes). The white boxes show the extension of the model in case the swash plates are free to oscillate and create an additional oscillation of the displacement volumes of the rotating group.

The torque load causes a rocking movement of the swash plate and the swash angle  $\beta$  will no longer be constant but vary as a function of time. The actuators counteract this rocking movement. The amplitude of  $\beta(t)$  is, amongst others, determined by the amplitude of the torque load on the swash plate, which in turn is strongly dependent on the commutation of the displacement volumes in the top and bottom dead centres. As a result, there is a circular dependency in which the commutation influences the oscillating movement of the swash plate, and the oscillating movement influences the commutation.

The interaction between swash plate oscillation and commutation has a significant effect on the behaviour of the pump. Figure 6 shows, for four different operating speeds and a pump pressure of 300 bar, a comparison of the calculated torque load of the barrel on the swash plate in case of a constant swash angle compared to the situation in which the swash plate is free to oscillate.

The oscillation of the swash plate softens the saw tooth shaped torque curve, which is typical for a situation in which the swash plate is not free to oscillate but is locked mechanically. This is also of importance for all studies in which the torque load on the swash plate is averaged during one revolution of the barrel. The oscillation of the swash plate creates a lower average value at low rotational speeds and a higher average torque load at high operating speeds.

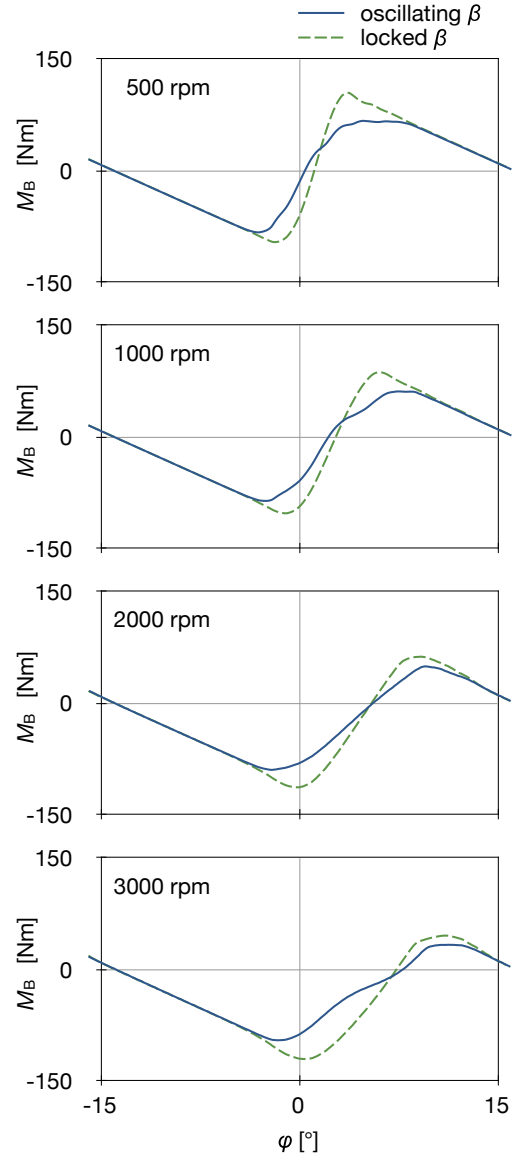


Fig. 6: Calculated torque load  $M_B$  of the barrel on the swash plate for a locked swash plate at an absolutely constant swash angle and a free oscillating swash plate ( $p_1 = 300$  bar,  $p_0 = 10$  bar,  $T_0 = 55^\circ\text{C}$ ,  $\beta = 7.8^\circ$ )

#### 4 Validation of the simulation model

The simulation model is validated by comparing the measured and calculated results of the swash angle and the pressure in the actuator system in a wide range of operating conditions. Figures 7 and 8 show the outcome for the maximum swash angle at a pump pressure of 300 bar. The pump was operated with a supply pressure of 10 bar and an oil temperature at the inlet of  $50^\circ\text{C}$ . The time scale shown on horizontal axis is made dimensionless by dividing the time by the characteristic period  $T$  of  $1/12$  of a revolution (12 being the number of pistons per barrel):

$$T = \frac{60}{12 \cdot n} \quad (1)$$

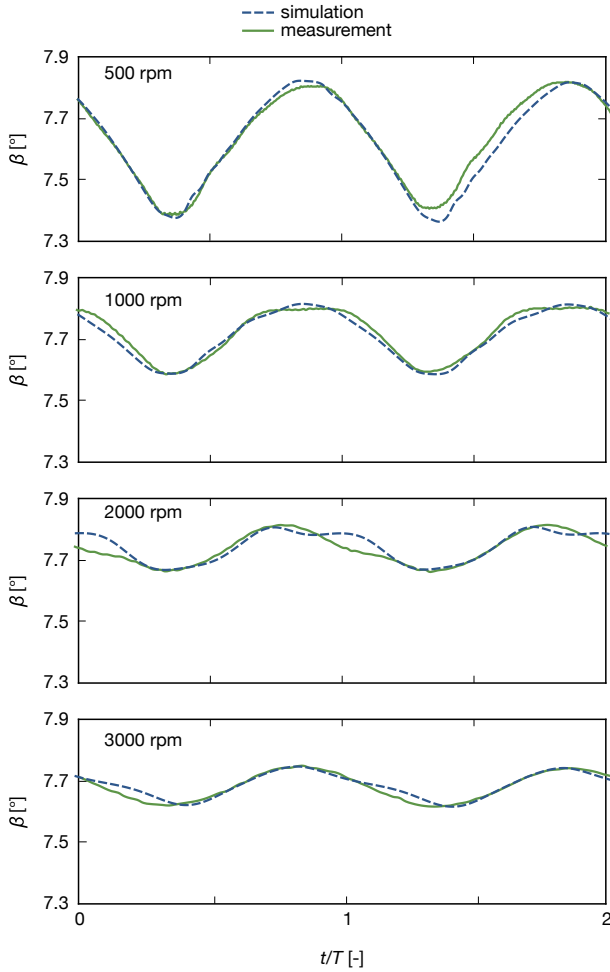


Fig. 7: Calculated and measured swash angle ( $p_1 = 300$  bar,  $p_0 = 10$  bar,  $T_0 = 50^\circ\text{C}$ ,  $\beta' = 7.8^\circ$ ).

There is a good correlation between the simulations and the measurements. The simulation model allows an adequate prediction of the dynamic behaviour of the swash plate and the pressure variation in the actuator system in a wide range of operating conditions. The model correctly calculates a larger amplitude of the swash plate oscillation at lower operating speeds of the pump. The most important difference between the simulation and measurement results occurs around 2000 rpm, where the simulation model forecasts a larger amplitude of the actuator pressure and a somewhat different swash angle variation.

## 5 Influence of pump pressure, operating speed and swash angle

The variable displacement floating cup pump has two swash plates, one on the mount side and one on the cover side. The pistons on the cover side are positioned in between the pistons on the mount side. As a result, the commutation, the torque load on the swash plates and the resulting dynamic behaviour of both actuator systems are all out of phase.

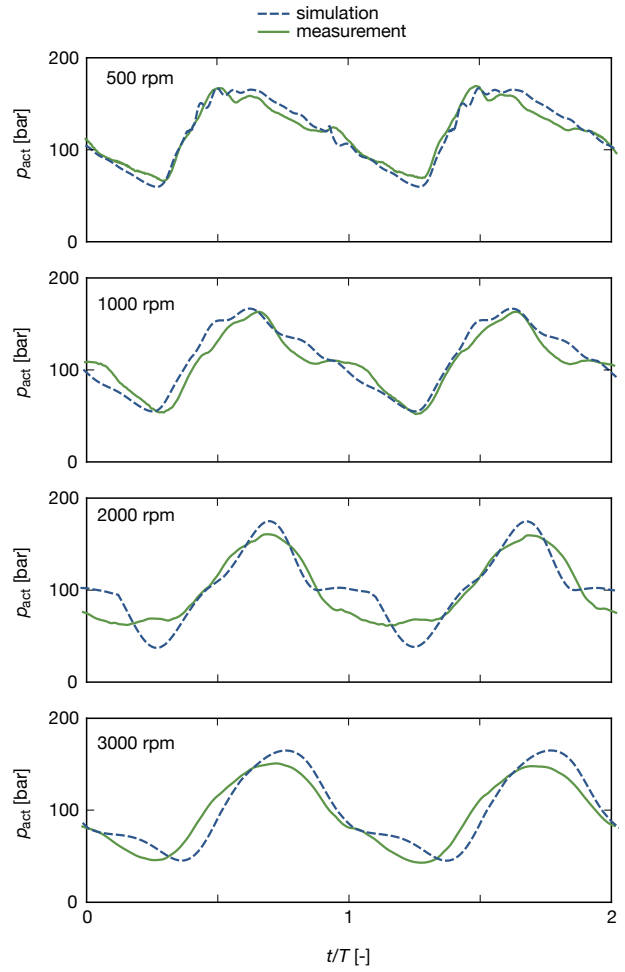


Fig. 8: Calculated and measured pressure in the actuator system ( $p_1 = 300$  bar,  $p_0 = 10$  bar,  $T_0 = 50^\circ\text{C}$ ,  $\beta' = 7.8^\circ$ ).

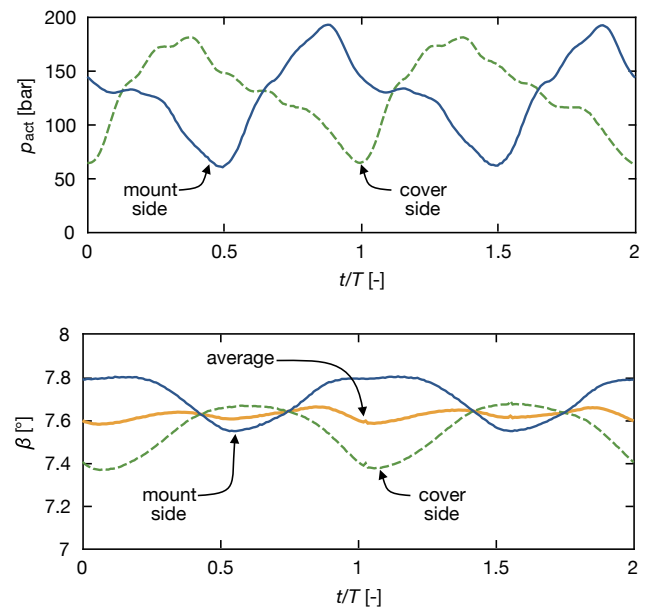


Fig. 9: Measured actuator pressure and swash angle for both sides of the pump ( $n = 1000$  rpm,  $p_1 = 350$  bar,  $p_0 = 10$  bar,  $T_0 = 50^\circ\text{C}$ ,  $\beta' = 7.8^\circ$ ).

This can clearly be seen in the measurement of the actuator pressure and the swash angle (Figure 9). The experiment is performed for an opening position of the  $\beta$ -valve, at  $\beta' = 7.8^\circ$ . Although each swash plate is oscillating with an amplitude of about  $0.3^\circ$ , the average swash angle of the two sides of the pump is much more constant. This is an advantage of the mirrored out-of-phase operation of the floating cup principle.

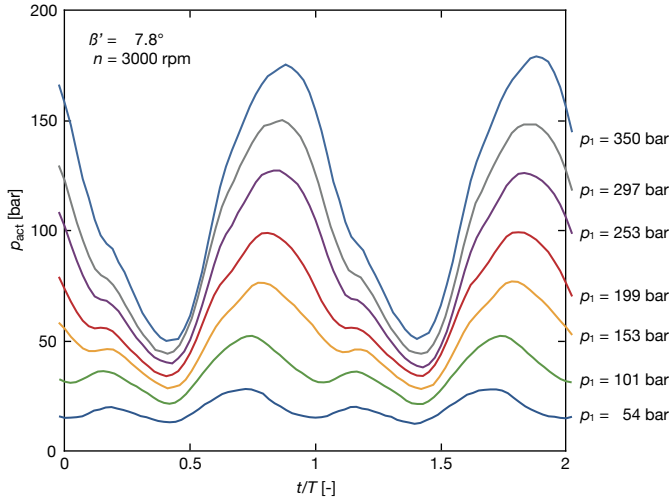
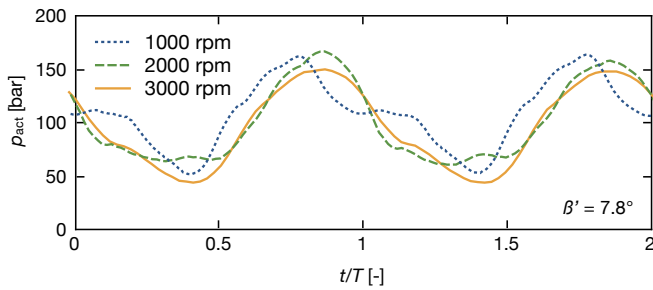
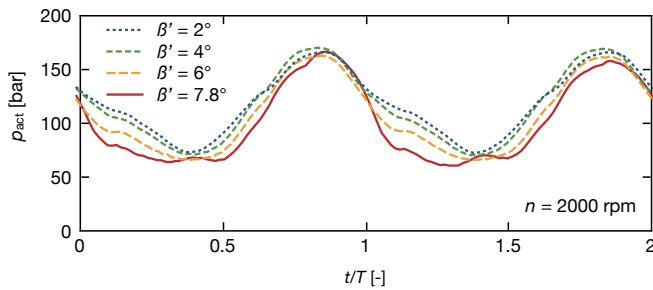


Fig. 10: Measured influence of the delivery pressure of the pump on the pressure in the actuator system ( $n = 3000 \text{ rpm}$ ,  $p_0 = 10 \text{ bar}$ ,  $T_0 = 50^\circ\text{C}$ ,  $\beta' = 7.8^\circ$ )



a) Influence of the operating speed  $n$



b) Influence of the swash angle  $\beta$

Fig. 11: Measured influence of the rotational speed (a) and the swash angle (b) on the pressure in the actuator system ( $p_1 = 300 \text{ bar}$ ,  $p_0 = 10 \text{ bar}$ ,  $T_0 = 50^\circ\text{C}$ )

The pressure variation in the actuator system is strongly influenced by the delivery pressure of the pump (see Figure 10). This is to be expected: a higher pump pressure creates a larger torque load on the swash plate, which has to be counteracted by a higher pressure and pressure variation in the actuator system. The rotating pressurised cylinders of each barrel determine the torque load of the rotating group. Aside from the commutation, the hydrostatic forces from the barrel are to a much lesser extent related to the operating speed or the swash angle. As a result the amplitude of the actuator pressure is almost independent of the operating speed  $n$  and the swash angle  $\beta$ , as can be seen in Figures 11a and 11b.

The relationship between the oscillating pressure in the actuator system and the hydrostatic force generated by the barrel can be explained by means of the forces shown in Figure 12. There are many forces acting on the swash plate, such as the force from the bias spring, the hydrostatic force from the  $\beta$ -valve and the friction force in the swash plate bearing, but the most dominating forces are the hydrostatic force  $F_b$  from the barrel, the force  $F_{\text{bias}}$  from the bias cup, and the two actuator forces  $F_{\text{act}}$ . All of these forces create a moment around the swivel axis of the swash plate. The torque generated by the barrel fluctuates around zero, being alternating positive and negative. The bias cup adds an almost constant torque load and pushes the total moment of the barrel and the bias cup above the zero axis. The calculated effects of the operating pressure and speed on the torque load of the swash plate can be seen in Figure 13. Both the average torque and the torque variation have an almost linear relationship with the delivery pressure of the pump. The operating speed only has a mild influence on the torque load, most and for all because of the influence of the pump speed on the commutation.

The actuator system has to counteract the load from the barrel and the bias piston. There are three parameters that determine the torque created by the actuators:

- the effective arm length of the actuators
- the hydrostatic area of the actuator cups
- the pressure level in the actuators

Both the cup area and the arm length can be considered to be constant. Therefore, a variation of the torque created by the actuators can only be achieved by a variation of the pressure level in the actuator system. This variation needs to correspond with the strong and dynamic variation of the torque created by the bias cup and the barrel. Figure 15 shows the average and the amplitude of the measured values of the pressure in the actuator system. The measured values show the same trend as the calculated values for the torque load (Figure 14).

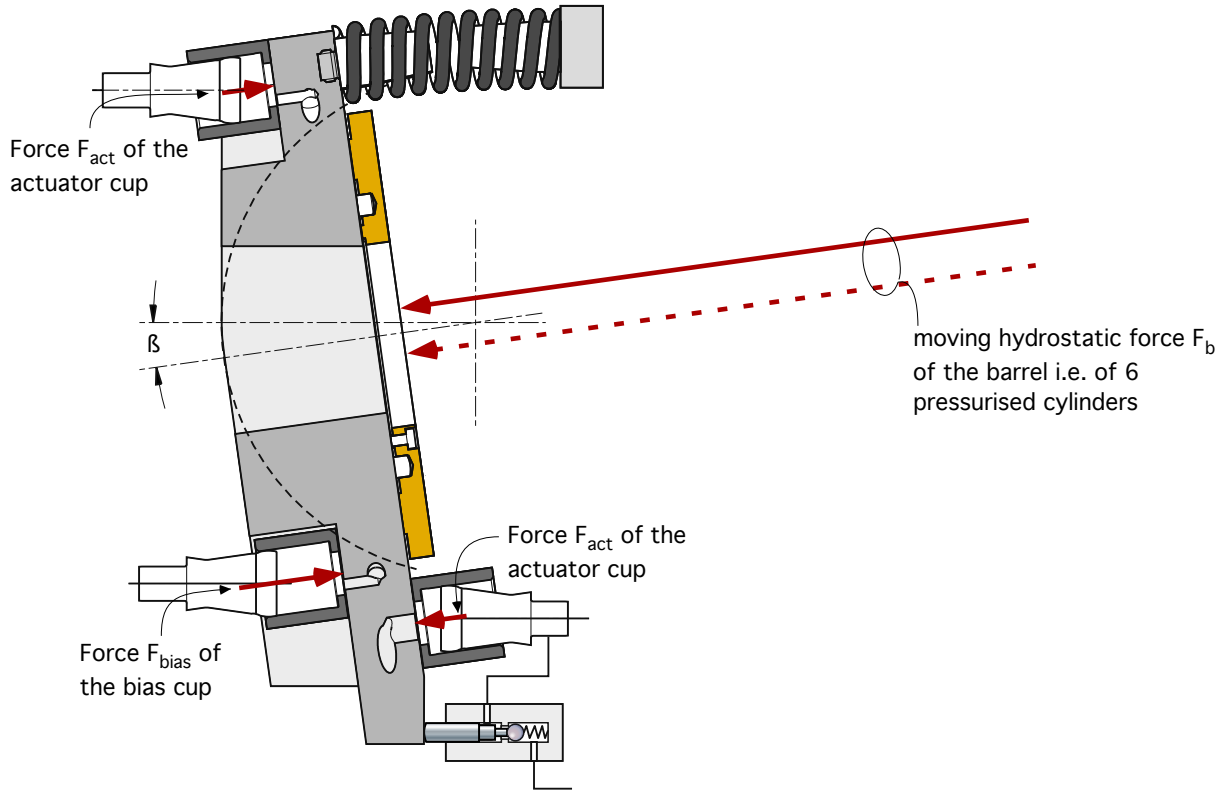


Fig. 12: Most important forces that determine the torque balance of the swash plate

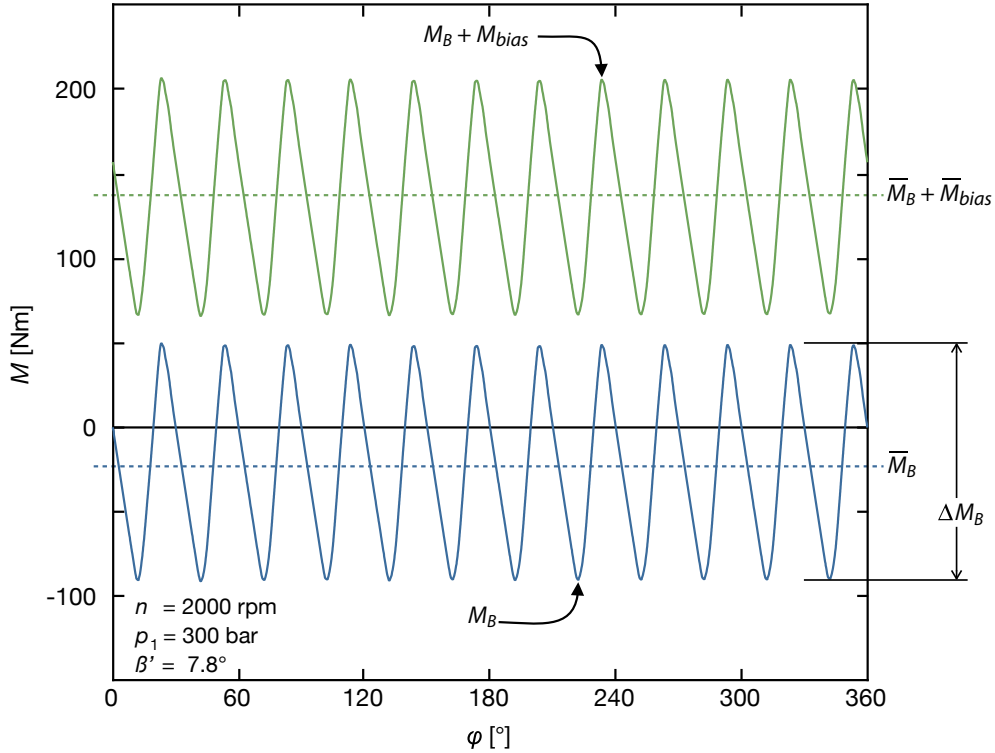


Fig. 13: Calculated torque load of the barrel  $M_B$  and of the barrel plus the bias cup ( $M_B + M_{bias}$ ) for one barrel revolution ( $n = 2000 \text{ rpm}$ ,  $p_1 = 300 \text{ bar}$ ,  $p_0 = 10 \text{ bar}$ ,  $\beta' = 7.8^\circ$ )

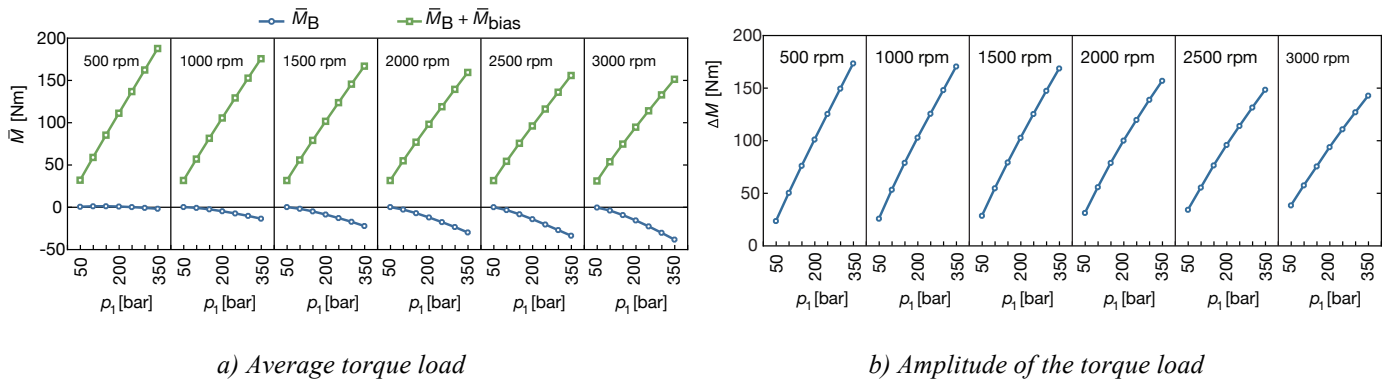


Fig. 14: Calculated effect of the operating speed and delivery pressure of the pump on the average torque load and the amplitude of the torque load on the swash plate ( $p_0 = 10$  bar,  $\beta' = 7.8^\circ$ ).

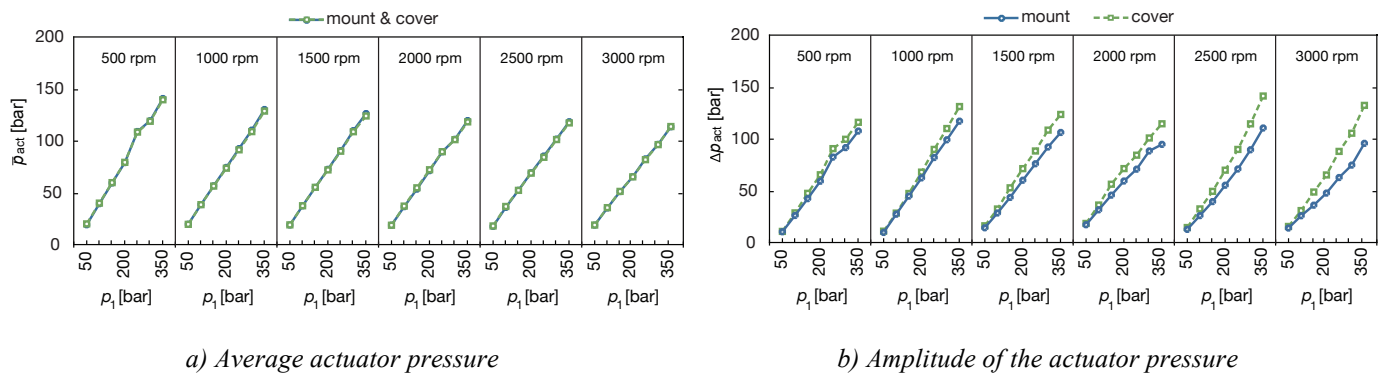


Fig. 15: Measured mean pressure and pressure amplitude of the actuator system for various operating pressures and speeds ( $p_0 = 10$  bar,  $T_0 = 50^\circ\text{C}$ ,  $\beta' = 7.8^\circ$ ).

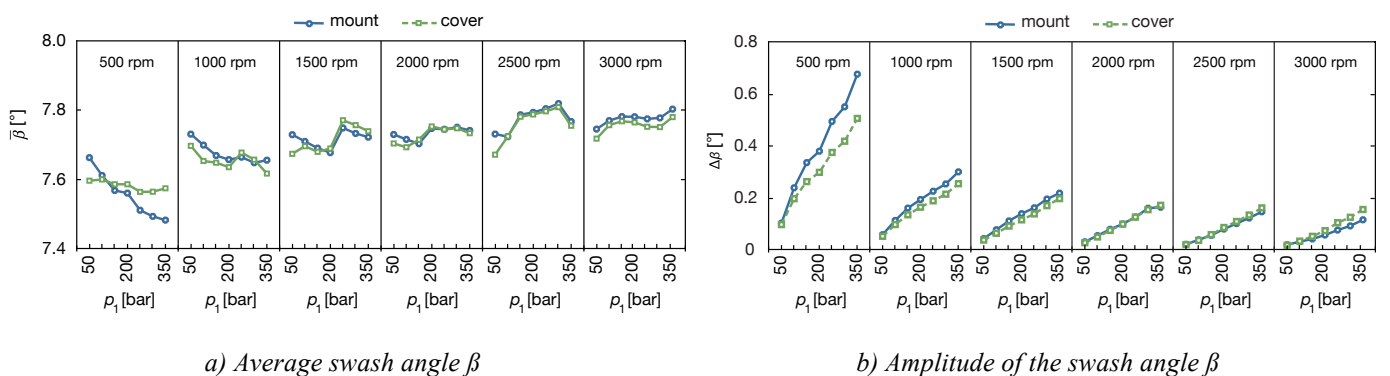


Fig. 16: Measured influence of the delivery pressure and the operating speed on the average swash angle and the peak-to-peak amplitude of the swash angle ( $p_0 = 10$  bar,  $T_0 = 50^\circ\text{C}$ ,  $\beta' = 7.8^\circ$ ).

In order to generate a strong and dynamic variation of the pressure level in the actuator system, the swash plates have to oscillate, thereby forcing oil in and out of the actuator cups, through the centre restriction in the line that connects both actuator systems (see Figure 2). The  $\Delta p$  of the resistance is dependent on the flow, which is generated by the rocking movement of the swash plates. This flow is directly related to the operating speed of the pump. To

compensate for the reduced frequency at lower speeds, the swash plate system responds by increasing the amplitude of the swash plate (Figure 16b), thereby creating again the desired flow through the connecting orifice. This effect can be seen in Figure 17, which shows the oscillation of the swash plate relative to the setting point of the  $\beta$ -valve for three different operating speeds of the pump.

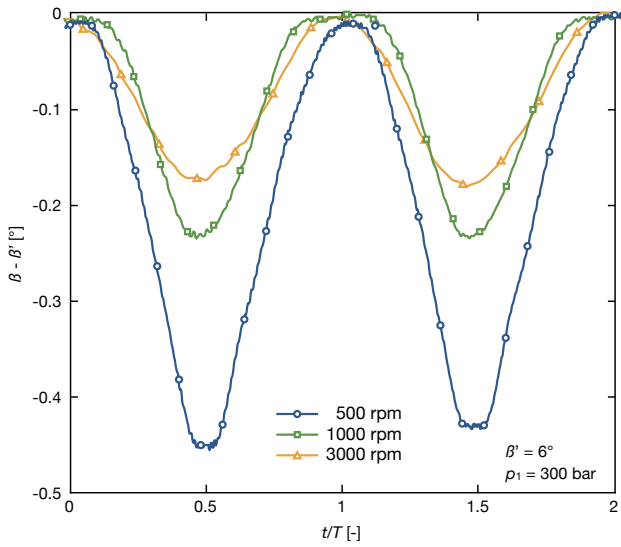


Fig. 17: Measured swash plate oscillation, relative to the opening position  $\beta'$  of the  $\beta$ -valve, for three different pump speeds ( $p_1 = 300$  bar,  $p_0 = 10$  bar,  $\beta' = 6^\circ$ ,  $T_0 = 50^\circ\text{C}$ )

The effect of the increased amplitude of the swash plate oscillation at reduced pump speeds can also be seen in Figure 16b. Since the  $\beta$ -valves define the maximum value of the oscillation, the average swash angle (Figure 16a) reduces when the oscillation amplitude increases, i.e. at low operating speeds. This implies that the pump displacement, when operated with the  $\beta$ -valves, is not a constant value, despite the mechanically defined opening position of the  $\beta$ -valves.

## 6 Effects on the commutation

The oscillating movement of the swash plate also creates an additional movement of the barrel, and therefore affects the cylinder volume of each cup of the rotating group. The effect of the swash plate oscillation is largest in the top and bottom dead centres where the commutation occurs. Consequently, the swash plate oscillation also influences the compression and expansion of the oil in the cups. Figures 18 and 19 show the results of the simulation for two pump speeds (500 and 3000 rpm) and for two different operating conditions:

- Assuming a fixed swash plate, locked at a constant swash angle of  $\beta = 7.8^\circ$
- Simulating a real pump operation with an oscillating swash plate, having an opening position of the  $\beta$ -valve of  $\beta' = 7.8^\circ$

Both simulations have been performed for a delivery pressure of 300 bar. The grey area in the middle of each diagram shows the position of the silencing grooves (see Figure 3).

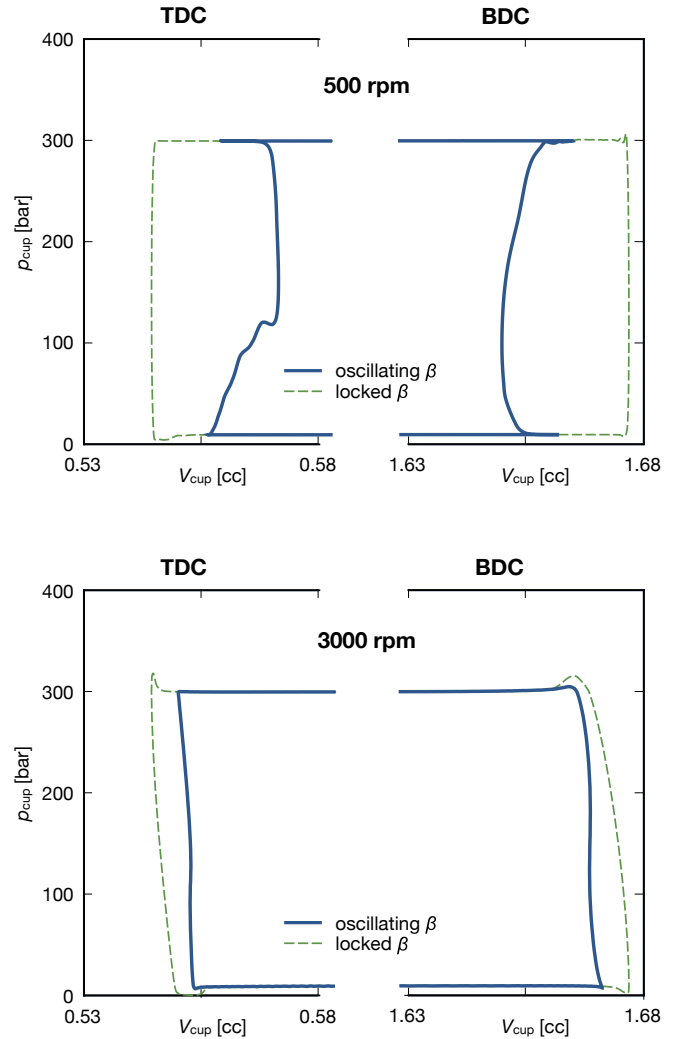
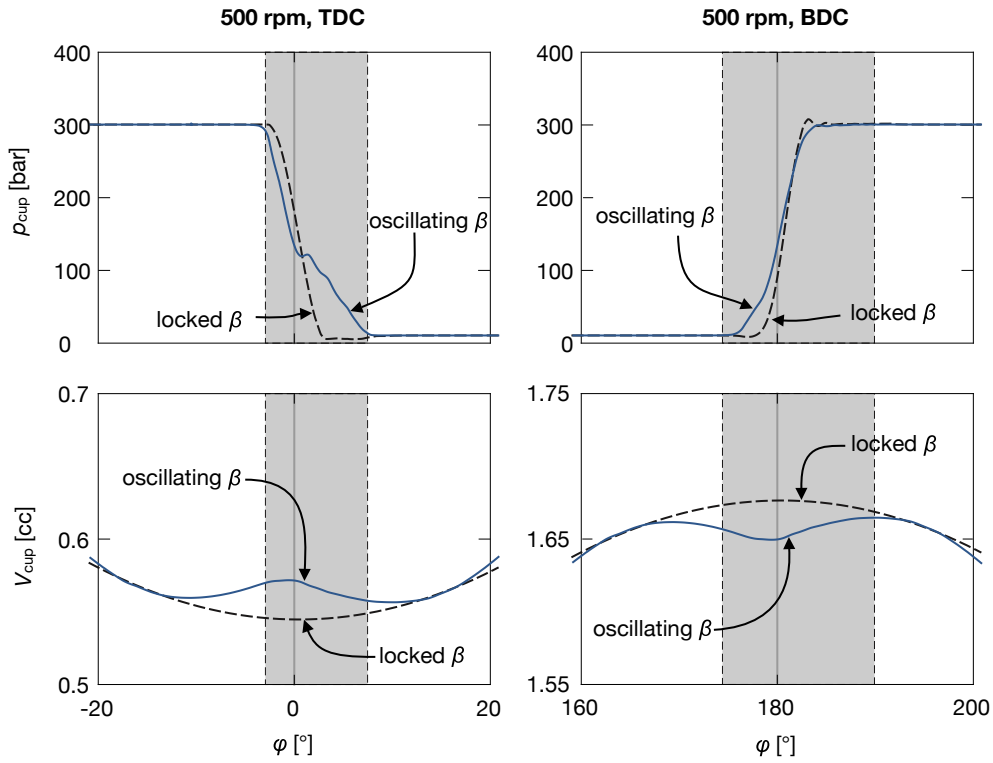
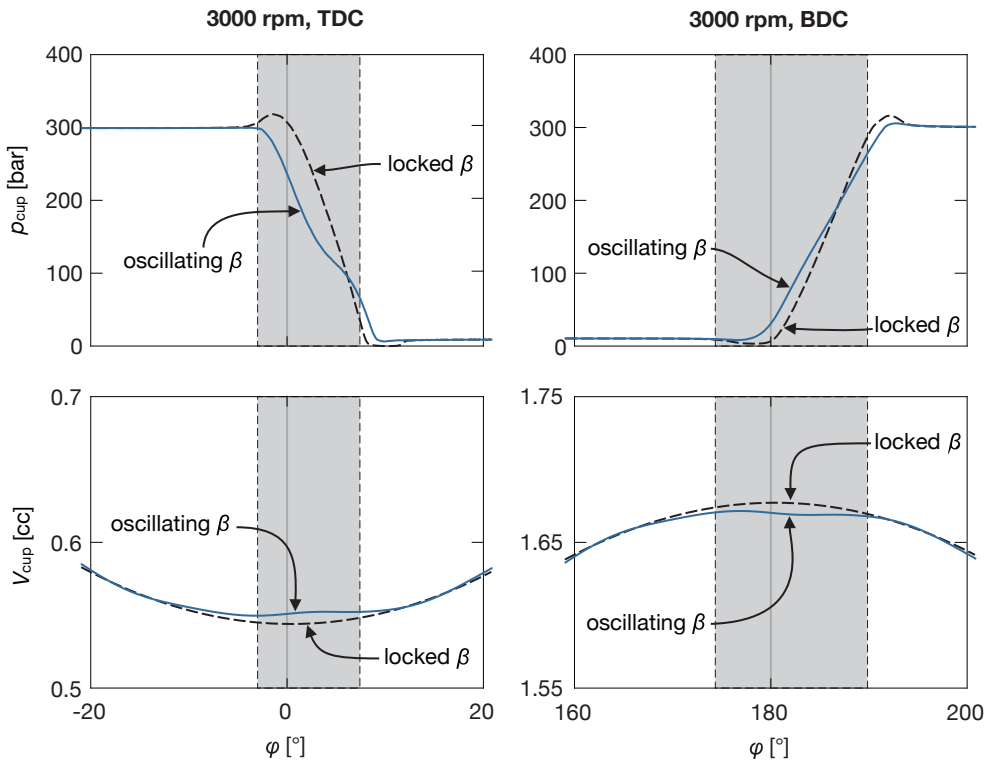


Fig. 18: Calculated effect of the swash plate oscillation on the  $pV$ -diagram in and around the top and bottom dead centres at two different pump speeds ( $p_1 = 300$  bar,  $p_0 = 10$  bar,  $\beta' = 7.8^\circ$ ,  $T_0 = 50^\circ\text{C}$ )

In the areas where the commutation occurs, the additional displacement, which is created by the swash plate oscillation, is in most operating points larger than the base sinusoidal movement. The results shown in Figures 18 and 19 are calculated for a situation in which the pump is operated at full displacement. At smaller displacements, the sinusoidal movement will be further reduced, whereas the swash plate oscillation is hardly affected by the swash angle. As a result the effect of the swash plate oscillation is even larger at smaller swash angles. Generally, the effect of the swash plate oscillation is largest at low operating speeds, high pump pressures and small swash angles. The influence of the swash plate oscillation should be taken into account in the design of the port plates and the silencing grooves. This has not yet been considered in the design of the port plates shown in this paper.

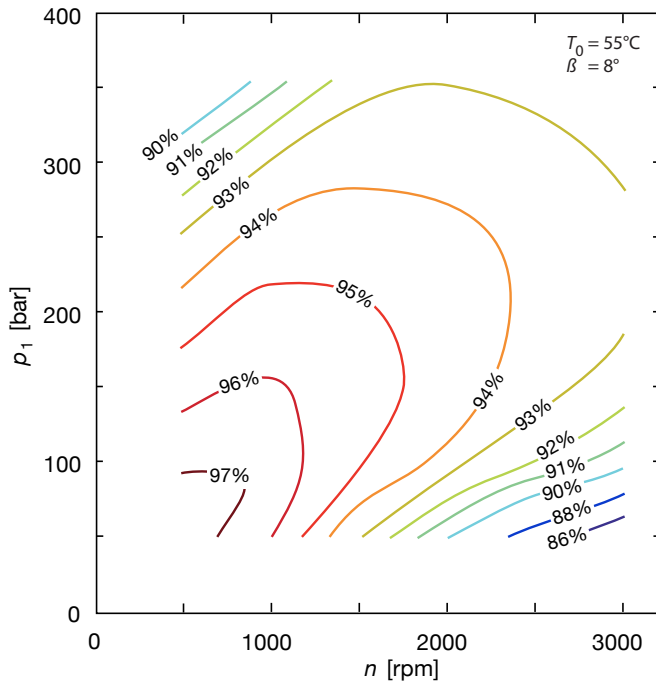


a) pump speed  $n = 500$  rpm

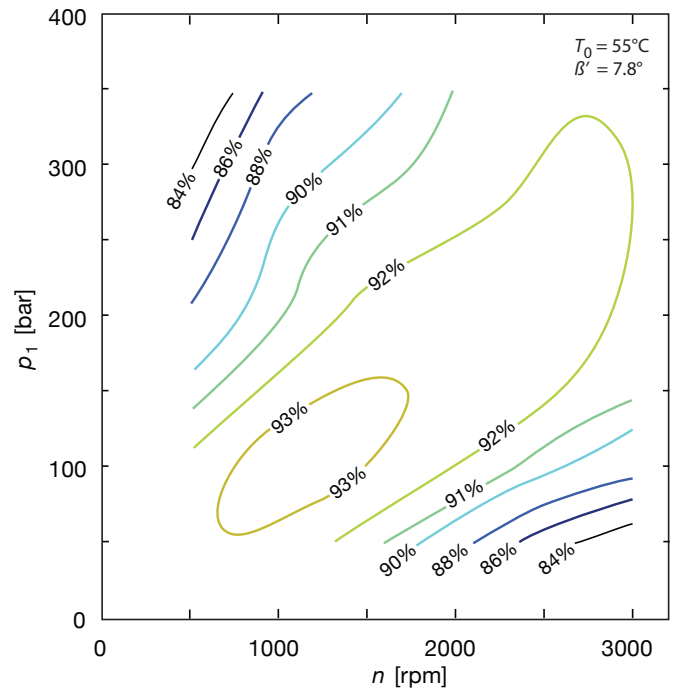


b) pump speed  $n = 3000$  rpm

Fig. 19: Calculated cup pressure and volume in case of a locked swash angle  $\beta$  and in case of a free oscillating swash angle  $\beta$ . The grey areas in the middle of each diagram indicates the position of the silencing grooves ( $n = 3000$  rpm,  $p_1 = 300$  bar,  $p_0 = 10$  bar,  $\beta' = 7.8^\circ$ )



a) Locked swash plate with constant  $\beta$  ( $\beta = 8^\circ$ )



b) Oscillating swash plate ( $\beta' = 7.8^\circ$ )

Fig. 20: Measured total efficiency of the variable displacement floating cup pump (Measurements performed at Eindhoven University of Technology)

## 7 Effects on the efficiency

The efficiency and performance of the pump have been tested in a wide range of operating conditions and swash angles at Eindhoven University of Technology. The results for the total efficiency of the pump at full displacement are presented in Figure 20. Two situations have been examined:

- the pump is operated as conventional against a mechanical end stop,
- the swash plates were free to oscillate and the swash plate position was controlled by means of the  $\beta$ -valves.

The oscillation of the swash plate and the opening position of the  $\beta$ -valve at  $\beta' = 7.8^\circ$  resulted in an average swash angle of  $7.7^\circ$ , which is about 4% smaller than the situation in which the pump was operated at a constant non-oscillating swash angle of  $\beta = 8^\circ$ . Nevertheless, the two measurements will be compared further on.

Figure 21 presents the difference between the total efficiency of the two measurements. According to the test results, the oscillation of the swash plates results in a reduction of the efficiency of up to 6%.

About half of the efficiency reduction is due to increased leakage, possibly of the actuator pistons (which are pressurised in situation b.), but also because of leakage of the  $\beta$ -valves. The other half is for the largest part due to the flow restriction of the orifices in between both actuator systems. Both power losses are approximately linearly dependent of the pump pressure but nearly independent of the rotational speed.

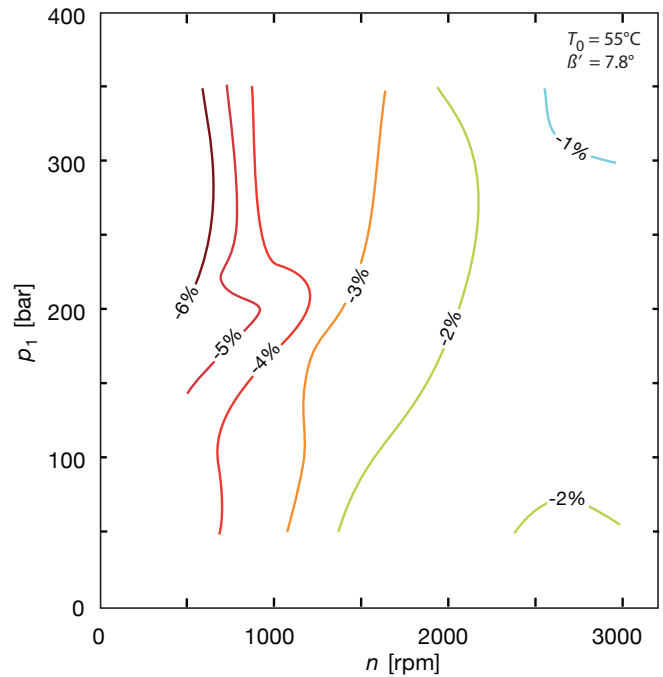


Fig. 21: Effect of the swash plate oscillation on the total efficiency of the pump, measured at full pump displacement ( $\beta \approx 8^\circ$ )

This corresponds with the measured reduction of the overall efficiency (Figure 21): a reduced pump speed results in a reduced pump power, whereas the additional power losses due to the pump oscillation are nearly independent of the pump speed.

The simulation model also allows a calculation of the flow losses in the restriction of the silencing grooves of the port plates. However, the simulations show no significant influence of the swash plate oscillation on the dissipation in the silencing grooves.

The data of Figures 20 and 21 were acquired for a pump running at full displacement. The measurements and simulations show that the extra leakage and flow losses from the actuator system are not influenced by the pump displacement i.e. the swash angle of the pump. However, the pump power is linearly dependent on the pump displacement. Therefore, the relative effect of the swash plate oscillation (i.e. the effect on the overall efficiency) is much stronger at small displacements. This can be seen in Figure 22, which is the same diagram as in Figure 21, but now based on a pump operation at 25% displacement, i.e. at  $\beta' = 2^\circ$ . Now, the efficiency reduction, which is caused by the operation of the actuator system, is about four times as high as at maximum pump displacement.

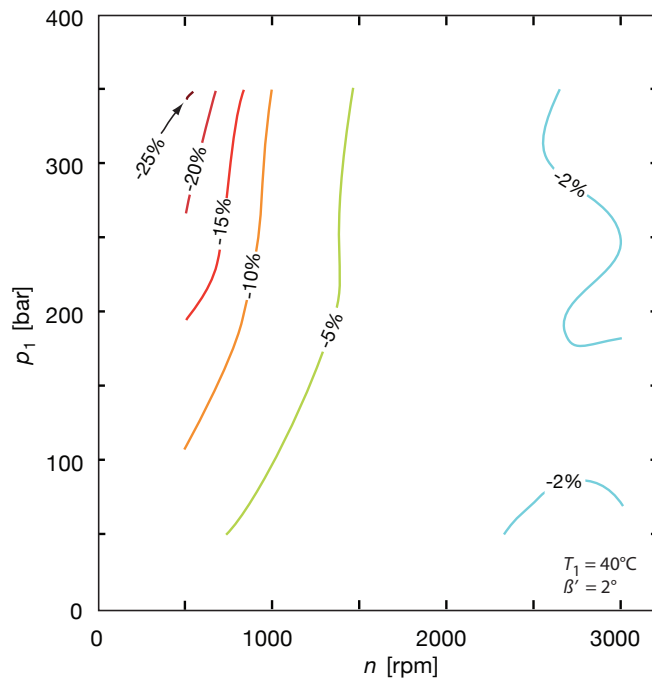


Fig. 22: Effect of the swash plate oscillation on the total efficiency of the pump, measured at 25% pump displacement ( $\beta' = 2^\circ$ )

It will certainly be possible to reduce the extra leakage of the actuator system and the  $\beta$ -valves. It is estimated that the additional losses can be halved. But even then, the displacement control and oscillation of the swash plate will have a significant effect on the efficiency, especially at low operating speeds and reduced pump displacements.

## 8 Conclusions

In variable displacement pumps and motors, the swash plate oscillates during normal operation. Yet, it is common to treat the variable displacement machine as a constant displacement machine when analysing the efficiency, noise or pulsations. The swash plate is then rotated until a

mechanical end stop is reached. As a consequence, the normal dynamic oscillation of the swash plate is suppressed and the losses and effects caused by the oscillation and the swash plate control are disregarded.

In this study, the performance of a variable displacement floating cup pump is measured and analysed, while allowing the swash plate to respond to the dynamic torque loads. A simulation model has been created to get a better understanding of the dynamic behaviour of the swash plate oscillation and its effects on commutation and pump efficiency.

From the study it can be concluded:

- The amplitude of the oscillation of the swash plate increases proportionally with the delivery pressure of the pump. The amplitude is largest at low pump speeds and high pump pressures. The pump displacement (i.e. the average swash angle) does not influence the swash plate oscillation.
- The oscillation of the swash plate causes an additional displacement of the individual cylinders of the rotating group. While passing the silencing grooves this additional movement is larger than the base sinusoidal movement. In the design of port plates and silencing grooves the effect of the swash plate oscillation should therefore be taken into account.
- The oscillations of the swash plate and the control system of the swash angle have a significant effect on the overall efficiency of the pump, especially at low pump speeds and reduced displacements.

Although not reported in this paper, the noise and pulsation levels of the pump are also strongly influenced by the new test procedure.

There are many differences between the floating cup pump –which is studied in this paper– and conventional state-of-the-art slipper type and bent axis pumps and motors. However, previous research [1-6] has already proven that also in conventional pumps and motors a similar dynamic behaviour occurs. It is strongly recommended to investigate the effects of the swash plate oscillation and the swash plate control system in these conventional pumps and motors.

If, as expected, the swash plate oscillation influences the commutation, the efficiency, the noise level and the pulsation level, then the common procedure to lock the swash plate must be abandoned, also for the analysis of conventional piston pumps and motors. It is also certain that the power losses of the control valves should be included in the determination of the efficiency. The standards, which describe the general procedure for determine the performance of hydrostatic machines, should be changed accordingly.

## Nomenclature

Designation	Denotation	Unit
$D_{hydr}$	hydraulic diameter of the opening area between the barrel port and the ports and silencing grooves of the port plate	[mm]
$F_b$	axial barrel force	[N]
$F_{bias}$	force bias cup	[N]
$F_{act}$	force actuator cup	[N]
$n$	rotational speed of the pump shaft	[1/min]
$p_0$	supply pressure of the pump	[bar]
$p_1$	delivery pressure of the pump	[bar]
$p_{act}$	pressure actuator system	[bar]
$p_{cup}$	pressure in a cup of the rotating group	[bar]
$M_B$	torque load of the barrel on the swash plate	[Nm]
$t$	time	[s]
$T_0$	oil temperature at the supply side	[°C]
$T$	duration of 1/12 of a revolution	[s]
$V_{cup}$	oil volume in the cup of the rotating group	[cm <sup>3</sup> ]
$x$	displacement	[mm]
$z$	Number of pistons of the pump	[-]
$\beta'$	swash angle were the $\beta$ -valve opens	[°]
$\beta$	swash angle	[°]
$\varphi$	rotational position of the barrel	[°]

## References

- [1] K. Inoue, and M. Nakasato, Study of the operating moment of a swash plate type axial piston pump, First report: Effects of dynamic characteristics of a swash plate angle supporting element on the operating moment, *The Journal of Fluid Control*, Vol. 22, Issue 1, p 7-27, 1994
- [2] K. Inoue, and M. Nakasato, Study of the operating moment of a swash plate type axial piston pump, Second report: Effects of dynamic characteristics of a swash plate angle supporting element on the cylinder pressure, *The Journal of Fluid Control*, Vol. 22, Issue 1, p 30-45, 1994
- [3] J.W. Dobchuk. Sub-component Level Modeling of a Variable Displacement Axial Piston Pump, Thesis

University of Saskatchewan, Saskatoon, Canada, December 2000

- [4] J.W. Dobchuk, P.N. Nikiforuk, P.R. Ukrainetz, R.T. Burton. "Effect of internal pump dynamics on control piston pressure ripple, Proc. of the 6th Triennial International Symposium on Fluid Control, Measurement and Visualization, Sherbrooke, Canada, August 13-17, 2000
- [5] S.A. Kassem, M.K. Bahr. On the dynamics of swash plate axial piston pumps with conical cylinder blocks", Proc. of the 6th Triennial International Symposium on Fluid Control, Measurement and Visualization, Sherbrooke, Canada, August 13-17, 2000
- [6] M.K. Bahr, J. Svodoba, R.B. Bhat. Vibration analysis of constant power regulated swash plate axial piston pumps", *Journal of sound and vibration*, 2003, Vol 259(5), p. 1225-1236, Elsevier Science Ltd.
- [7] P.A.J. Achten, T.L Van den Brink, T. Paardenkooper, T. Platzer, H.W. Potma, M.P.A. Schellekens and G.E.M. Vael. "Design and testing of an axial piston pump based on the floating cup principle", *Proc. 8th Scandinavian Int. Conf. on Fluid Power SICFP'03*, Vol. 2, Tampere University of Technology, pp. 805-820, 2003
- [8] P. Achten. Dynamic high frequency behaviour of the swash plate in a variable displacement, axial piston pump, *Proc. of the IMechE, Part I: Journal of Systems and Control Engineering*, Volume 227 Issue 6 July 2013 pp. 529 – 540, doi: 10.1177/0959651813483419
- [9] P.A.J. Achten, "Designing the impossible pump", *Proc. Hydraulikdaggar 2003*, Linköping University, Sweden 2003
- [10] P.A.J. Achten, T. van den Brink, M. Schellekens, (2005) Design of a variable displacement floating cup pump, *Proc. 9th Scandinavian Int. Conf. on Fluid Power, SICFP'05*, Linköping, Sweden, 2005

# A novel approach to predict the steady state temperature in ports and case of swash plate type axial piston machines

M. Zecchi, A. Mehdizadeh, and M. Ivantysynova

Maha Fluid Power Research Center, Purdue University, 1500 Kepner Dr. Lafayette, IN, USA 47905

## Abstract

This paper presents a model able of predicting the working temperature of the hydraulic fluid in the case volume and outlet port of axial piston machines. For the first time the working temperature is estimated accounting for the power losses associated with the fluid flow in the lubricating interfaces, the churning motion of the oil in the machine case and the losses due to the compressibility of the hydraulic fluid. The paper illustrates a thorough comparison between the calculated and the measured case and outlet port temperatures for steady state operation of the axial piston machine.

**Keywords:** Axial piston machines, Heat transfer, Churning losses, Case temperature

## 1 Introduction

Current advanced developments in the fluid power systems technology, such as displacement controlled actuation, power split and hydraulic hybrid transmissions, use variable displacement axial piston units directly as control element. The units are therefore forced to operate over a much wider range of operating conditions compared to standard load sensing and similar systems, in terms of speed, displacement and differential pressure. These types of applications expect the axial piston unit to maintain a very high efficiency under extremely varying operating conditions, introducing a significant challenge for the designers. The performance and level of energy dissipation in axial piston machines is determined by the design of the rotating group and the design of the three main lubricating interfaces between piston and cylinder, cylinder block and valve plate and slipper and swash plate.

A cross section of the rotating group of a swash plate type axial piston machine is represented in 1. The main lubricating interfaces between parts in relative motion are highlighted. The lubricating interfaces represent a key design element, because they have to fulfill simultaneously a bearing and a sealing function: the film of lubricant is fundamental to properly support the high oscillating external loads, avoiding metal to metal contact, but the clearance between the parts is subjected to leakages of lubricant from high to low pressure regions and also to viscous dissipation associated with the fluid flow. The lubricating interfaces are most of the times the major source of power losses. A deep understanding of the behavior of the fluid film in these interfaces will allow for improved designs, which can rise the overall axial piston machine efficiency especially at partial load conditions, through computational design. Research towards computational design of positive displacement machines has made major progresses in the recent years. The computer aided

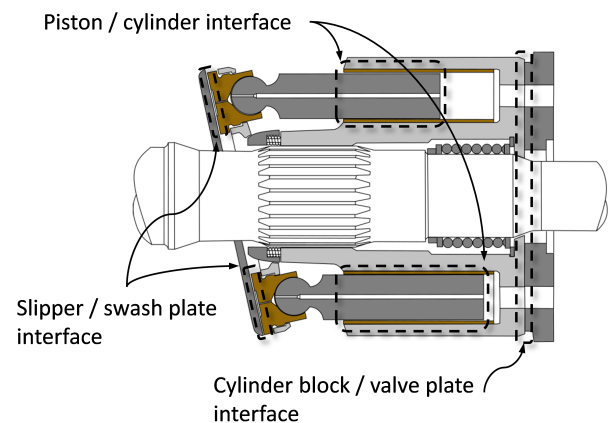


Figure 1: Three main lubricating interfaces in swash plate type axial piston machines.

design of axial piston machines has seen substantial developments and it is starting to gain a fundamental importance in industry. Nevertheless, recent studies ([1], [2]) have demonstrated that a reliable and accurate prediction of the lubricating interfaces performance can be achieved only if different physical phenomena are coupled together. Moreover, latest studies pointed out that the thermal behavior of the lubricating interface is particularly critical for two reasons. First, the solution of the non-isothermal fluid flow is fundamental to correctly estimate the viscosity of the lubricant and therefore the load carrying ability of the interface; second the temperature distribution in the machine solid parts during operation of the units causes thermal deflections which are of the same order of magnitude of the fluid film thickness, leading to substantial modifications of the geometry of the resulting fluid film. Advanced fluid structure interaction models are able of

capturing the described phenomena, but one of their current limits is the definition of the boundary conditions to be applied in the thermal analysis. The prediction of the lubricating interfaces performance is extremely sensitive to the temperatures of the surrounding material and depends strongly on the temperature of the case and machine ports. Usually these temperatures are known from measurements, but during the design of new units such information is not available. The goal of the author's research study was to develop a model, which can predict the temperature of the fluid in the case and at the outlet port of the machine for a given inlet temperature of the fluid while the machine runs under steady state conditions. The in this paper presented model represents a new important step towards computational design of pumps and motors.

## 2 Heat exchange in the axial piston machine

The case and the outlet volumes are represented in Fig. 2. The case volume is defined by the hydraulic fluid filling the machine's housing, the outlet control volume by the hydraulic fluid in the high pressure port and in all the displacement chambers connected with it. The temperature is assumed to be

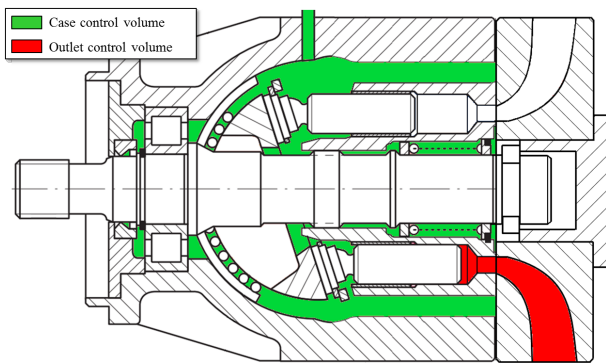


Figure 2: Definition of the control volumes

uniform throughout the volumes and since steady state conditions apply, the time variation is not of interest. The overall heat exchange can therefore be reduced to a lumped parameter representation. Each control volumes, exchanges mass, work and heat with the exterior, as illustrated schematically in Fig. 3. The mass flow rate  $\dot{m}_i$  entering in the machine through the inlet port is then transferred to the outlet volume. If the unit works as a pump, and some load is applied, work is made by the displacement volume to pressurize the fluid. When a pressure difference is present between the two ports, the outlet mass flow rate  $\dot{m}_o$  will differ from the inlet mass because of different source of volumetric losses. The mass flow  $\dot{m}_{l,e}$  represents the total external leakage (or case flow) resulting from leakage flow between pistons and cylinders, cylinder block and valve plate and between slippers and swash plate. Another important source of loss impacting the effective outlet flow is caused by the non ideal timing of the valve plate combined with the compressibility of the fluid, which generates a backflow from the outlet port to the displacement chamber, as illustrated in . The dotted line indicates the theoretical

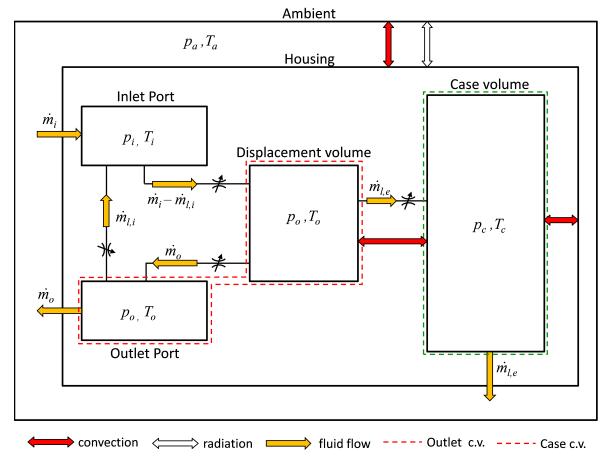


Figure 3: Schematic of the heat and mass transfer in the axial piston machine.

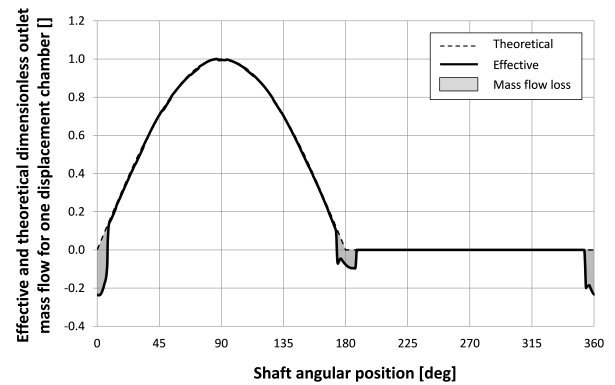


Figure 4: Effect of oil compressibility on the outlet mass flow rate associated to one displacement chamber.

dimensionless outlet mass flow associated with one displacement chamber, which is just a function of the kinematics of the machine; the solid line depicts the actual dimensionless mass flow. The difference between the two lines is due to the fact that when the displacement chamber opens to the valve plate port the fluid is at lower pressure and therefore a back-flow occurs with an impact on the effective outlet mass flow rate. Furthermore, depending on the valve plate design, the inlet and outlet ports can be connected through the displacement chamber; in this case an amount of fluid is not properly delivered because it flows back from the high to the low pressure port; this volumetric loss is called internal leakage. The rate of mass associated with compressibility and internal leakage is indicated with  $\dot{m}_{i,l}$  in Fig. 3

The heat transfer is included with a quite simple approach, considering forced convection between displacement and case volumes, natural convection and radiation between machine's housing and ambient. The governing equation is the expression of the energy conservation for an open system: with reference to the schematic of Fig. 5, the following equation applies for each control volume

$$\sum \dot{m}_i h_i - \sum \dot{m}_o h_o + \dot{Q} - \dot{W} = 0 \quad (1)$$

In Eq. 1  $\dot{m}$  is the mass flow rate,  $h$  the enthalpy,  $\dot{Q}$  is rate of heat flow into the control volume and  $\dot{W}$  is the rate of work done by the control volume. Figure 3 illustrates a schematic representation of the heat and mass flows associated with the axial piston machine operation. In the next two sections Eq.

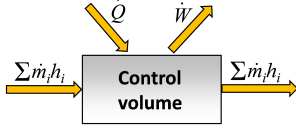


Figure 5: Schematic representation of the mass, heat and work exchanged by a control volume

1 will be applied to the outlet and case control volumes, generating a system of two equations in the two unknown temperatures in the case  $T_c$  and outlet volumes  $T_o$ .

## 2.1 Energy balance for the outlet control volume

The outlet control volume is defined as the volume enclosed by the outlet port and the volume of all the displacement chambers connected with it. Assuming pumping operation, after being compressed, the mass flow taken from the inlet is partially lost through leakages in the lubricating interfaces and is then delivered at the outlet. Regardless of whether the mass flow leaves the volume as leakage or actual discharge flow its thermodynamic state is the same, being defined by the conditions at the outlet. Therefore, the two summations in Eq. 1 can be written as follows:

$$\dot{m}_i (h_i - h_o) \quad (2)$$

The enthalpy's differential can be expressed as follows

$$dh = \left( \frac{\partial h}{\partial T} \right)_p dT + \left( \frac{\partial h}{\partial p} \right)_T dp \quad (3)$$

The first term in Eq. 3 is the definition of specific heat capacity at constant pressure, while it can be demonstrated [3] that the second term is related to the volumetric expansion of the fluid. Equation 3 can therefore be rewritten as a function of pressure and temperature as follows

$$dh = c_p dT + (1 - \gamma T) \frac{dp}{\rho} \quad (4)$$

where  $c_p$  is the specific heat capacity at constant pressure,  $\gamma$  is the fluid's coefficient of volumetric expansion and  $\rho$  is the fluid's density. Equation 4 can be approximated to express a finite difference and applied to the case of Eq. 2 as follows

$$h_i - h_o \approx c_p (T_i - T_o) + (1 - \gamma T_i) \frac{(p_i - p_o)}{\rho_i} \quad (5)$$

The outlet control volume also exchanges work with the fluid: if the unit operates as a pump, work is made on the fluid by the pumping action of the pistons; if the unit operates as a motor, work is done by the pressurized fluid on the pistons. In both cases the rate of work can be expressed as follows

$$\dot{W} = \beta V_o n (p_i - p_o) = \dot{m}_i \frac{p_i - p_o}{\rho_i} \quad (6)$$

where  $p_o$  is the pressure in the displacement volume,  $\beta$  is the displacement angle (in percentage with respect to the maximum value),  $V_o$  is the geometric displacement of the unit and  $n$  is the speed of the unit. The work is negative in pumping mode and positive in motoring mode. In this way, according to Eq. 1, the energy content of the fluid in the control volume increases in the first case and decreases in the second case. In Eq. 6 it is assumed that exactly half of the  $z$  displacement chambers are actually part of the outlet control volume.

Regarding the heat transfer, it is assumed that the heat is exchanged with the cylinder block and the end case through forced convection. The rate of heat flow has been expressed through the Newton's law of cooling as follows:

$$\dot{Q}_{fcv} = z \alpha_{DC} (A_{DC}^- + A_{oc}) (T_c - T_o) \quad (7)$$

where  $A_{DC}^-$  is the average area of one displacement chamber which exchanges heat with the cylinder block body over one shaft revolution and  $A_{oc}$  is the inner surface of the outlet port;  $\alpha_{DC}$  is the average convection coefficient associated with the fluid flow in these surfaces. The fluid temperature is  $T_o$  and  $T_c$  is the temperature of the wall. The temperature of the inner surface of the displacement chambers and outlet port is indeed unknown, but it is reasonable approximation to assume that they are at the same temperature of the fluid in the case.

By combining Eq. 5, 6 and 7 the energy balance for the outlet control volume yields:

$$\begin{aligned} \dot{m}_i \left[ c_p (T_i - T_o) + (1 - \gamma T_i) \frac{(p_i - p_o)}{\rho_i} \right] + \\ + z \alpha_{DC} A_{DC}^- (T_c - T_o) - \dot{m}_i \frac{p_i - p_o}{\rho_i} = 0 \end{aligned} \quad (8)$$

In case of motoring mode operation, the pressurized region is the inlet and the leakage will occur mostly there. Therefore, the mass flow of interest is the outlet one and Eq. 9 changes as follows:

$$\begin{aligned} \dot{m}_o \left[ c_p (T_i - T_o) + (1 - \gamma T_i) \frac{(p_i - p_o)}{\rho_i} \right] + \\ + z \alpha_{DC} A_{DC}^- (T_c - T_o) - \dot{m}_o \frac{p_i - p_o}{\rho_i} = 0 \end{aligned} \quad (9)$$

It shall be noticed that the work done on the fluid has an opposite sign in case of pumping or motoring mode operation. In the first case that contributes to raising the outlet temperature, while in the second case to lower it.

## 2.2 Energy balance for the case control volume

The case control volume is subjected to two major heat sources: the heat coming from the viscous dissipation associated with the fluid flow in the lubricating interfaces and in the heat generated due to the rotation of the cylinder block and pistons in the oil filled case. On the other hand, heat is removed from the case volume thanks to different heat transfer phenomena.

The first cooling effect is determined by the external leakage  $\dot{m}_{l,ext}$ ; the situation is sketched in Fig. 6 in the case of

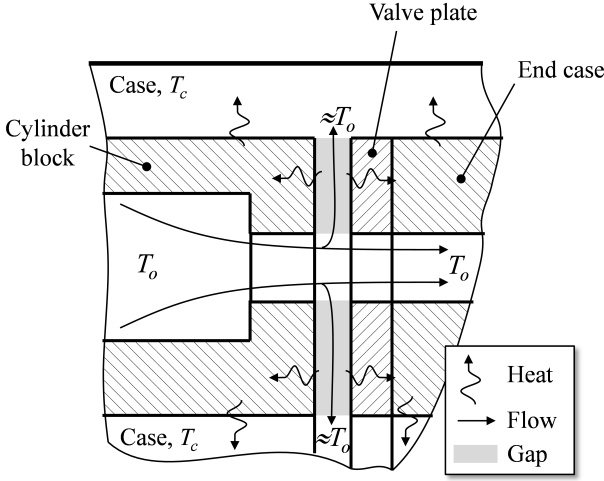


Figure 6: Schematic representation of the external leakage flow through the cylinder block valve plate interface and the heat exchange between solid parts and the hydraulic fluid in the case.

the cylinder block valve plate interface. When the leakage flow enters in the case, its temperature is different from the temperature in the high pressure port, because during its path through the lubricating interfaces it is heated up by the viscous friction. However, for practical calculation, it is reasonable to assume that the temperature of the leakage flow is not affected by the viscous dissipation and therefore that the hydraulic fluid enters into the case volume at the same temperature of the outlet port,  $T_o$ ; to compensate for this approximation it is assumed that all the heat generated in the lubricating interfaces is transferred to the solid parts. The rate of heat flow carried out by the external leakage is expressed as follows

$$\dot{Q}_{l,ext} = \dot{m}_{l,ext} [c_p (T_o - T_c)] \quad (10)$$

The case volume is subjected to natural and forced convection. The forced convection is generated by the fresh oil flowing from the inlet to the outlet port through the displacement chambers and it was already introduced in the previous section during the analysis of the heat exchange of the displacement volume, Eq. 7. This second cooling effect actually takes place inside the cylinder block, valve plate and end case bodies, rather inside the oil in the case. Nevertheless, since it was assumed that all the heat generated by viscous friction in the lubricating interfaces is transferred to the solid parts in the rotating kit, it is reasonable to think this convection effect just as part of the total heat which is not transferred to the fluid in the case. In this way the rate of heat flow associated with this cooling action is expressed with Eq. 7, but with opposite sign

$$\dot{Q}_{fcv} = -\frac{z}{2} \alpha_{DC} (A_{DC}^- + A_{oc}) (T_c - T_o) \quad (11)$$

Natural convection is assumed for the heat exchange of the outer surface of the machine case with the ambience. The associated rate of heat flow is expressed as follows:

$$\dot{Q}_{ncv} = -\alpha_h A_h (T_c - T_a) \quad (12)$$

The natural convection coefficient can be estimated with the correlation for natural convection over a vertical plane [3].

$$\alpha_h = 0.478 Gr^{0.25} \quad (13)$$

where the Grashof number is defined as follows

$$Gr = \frac{gL^3 (T_c - T_a)}{\nu^2 T_a} \quad (14)$$

where  $L$  is a characteristic dimension of the housing,  $g$  the gravity acceleration and  $\nu$  the kinematic viscosity of the air. A value of about  $25 \text{ W/m}^2\text{K}$  is usually a good estimate for natural convection.

Thermal radiation is the last effect which impacts the case temperature. Even though radiation heat transfer is proportional to the difference of the fourth power of the absolute temperatures, it is usually the smallest contribution to the overall heat exchange, but it is not small enough to be totally neglected. The expression for the radiation heat transfer is the following:

$$\dot{Q}_R = -\sigma \epsilon A_h (T_c^4 - T_a^4) \quad (15)$$

The energy balance for the case control volume becomes therefore the following:

$$\begin{aligned} & \dot{m}_{l,ext} [c_p (T_o - T_c)] - \alpha_h A_h (T_c - T_a) \\ & - z \alpha_{DC} A_{DC}^- \left( T_c - \frac{T_i + T_o}{2} \right) - \sigma \epsilon A_h (T_c^4 - T_a^4) \\ & + \Phi_{c,v} + \Phi_{s,s} + \Phi_{p,c} + \Phi_{ch} = 0 \end{aligned} \quad (16)$$

The rate of heat flow associated with the viscous dissipation in the piston / cylinder interface is represented by  $\Phi_{p,c}$ ; analogous definitions apply for  $\Phi_{s,s}$  and  $\Phi_{c,v}$  for the slipper / wash plate and the cylinder block / valve plate interface, respectively. The rate of heat flow associated with churning losses were instead indicated with  $\Phi_{ch}$ . The calculation of these sources of heat will be discussed in detail in sections 3.2 and 3.3. Furthermore it shall be noticed that the enthalpy difference does not include the term related with the fluid compression, since the oil enters and exits from the case volume at the same pressure.

### 2.3 Calculation of the case and outlet temperatures

Equations 9 and 16 define a system of two equations with the two unknowns  $T_c$  and  $T_o$ . Due to the non-linearity of the equations an iterative procedure has been used to solve the problem.

## 3 The estimation of the power losses in the axial piston machine

Axial piston pumps and motors are affected by two sources of power loss: mechanical and volumetric losses. As already anticipated in section 2 volumetric losses are represented by external and internal leakage and by the effect of the oil compressibility. Mechanical losses occur due to friction in the lubricating interfaces, churning losses, drag due fluid flow from inlet to outlet and losses in shaft bearings and seals. In

this study the losses associated with drag and the losses in shaft bearings and seals are neglected, i.e. only the two major sources of mechanical losses are considered; losses due to friction in lubricating interfaces and churning losses.

Since the oil temperature in the case and displacement volume is affected by many of the aforementioned losses, this section illustrates how they are calculated through computer simulation. In this way the results of this study can be presented into a bigger picture, which extends to the prediction of the machine's overall efficiency.

### 3.1 Prediction of the effective outlet flow and associated volumetric losses

The prediction of the effective volumetric flow rate and volumetric losses due to compressibility, non ideal timing and internal leakage are based on a lumped parameters approach. The control volume in this case is defined just by the fluid in the displacement chamber, as illustrated in Fig. 7. The actual

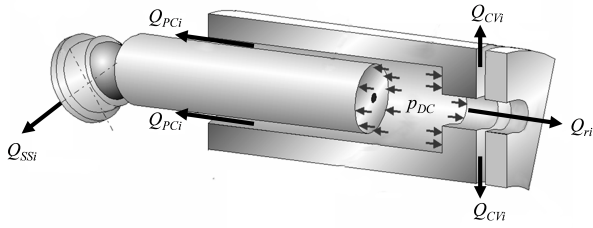


Figure 7: Modeling approach used to predict the lubricating interface performance in axial piston machines.

volumetric flow delivered by the displacement action of the pistons is  $Q_{ri}$ . However, additional volumetric flows leave the control volume in form of leakage through the piston / cylinder interface  $Q_{PCi}$ , cylinder block / valve plate interface  $Q_{CVi}$  and and slipper / swash plate interface  $Q_{SSi}$ . The sum of these leakage flows for all the displacement chambers determines the volumetric external leakage flow:

$$Q_{l,e} = \sum_{i=1}^z (Q_{PCi} + Q_{CVi} + Q_{SSi}) \quad (17)$$

Changes in the amount of fluid in the control volume lead to changes in the displacement chamber pressure  $p_{DC}$  as indicated by the pressure build-up equation:

$$\frac{dp_{DC}}{dt} = \frac{K}{V} (Q_{ri} - Q_{PCi} - Q_{CVi} - Q_{SSi}) \quad (18)$$

where  $K$  is the bulk modulus of the hydraulic fluid and  $V$  is the instantaneous volume of the chamber. The volumetric flow  $Q_{ri}$  can be thought as a sum of the volumetric flow coming from the inlet  $Q_i$  and the volumetric flow heading to the outlet  $Q_o$ . These two volumetric flows depend on the pressure differentials between the displacement chamber and the relative ports and are modeled with the equation describing the

turbulent flow through an orifice

$$\begin{aligned} Q_{ri} &= Q_{ri,i} + Q_{ri,o} = \\ &= A_i \alpha_{D,i} \sqrt{\frac{2(p_{DC} - p_i)}{\rho}} \text{sgn}(p_{DC} - p_i) + \\ &+ A_o \alpha_{D,o} \sqrt{\frac{2(p_{DC} - p_o)}{\rho}} \text{sgn}(p_{DC} - p_o) \end{aligned} \quad (19)$$

In Eq. 19  $\alpha_{D,i}$  and  $\alpha_{D,o}$  are the discharge coefficients, while  $A_i$  and  $A_o$  are the orifice areas, determined by the geometry of the valve plate.

The combination of Eq. 18 and 19 allows the instantaneous pressure in the displacement chamber and the effective outlet flow to be calculated over one shaft revolution. More details about the modeling approach and the solution method can be found for example in [4]. Figure 8 illustrates the predicted volumetric outlet flow for a 75 cc unit at 2000 rpm and 300 bar of differential pressure. The combined effect of

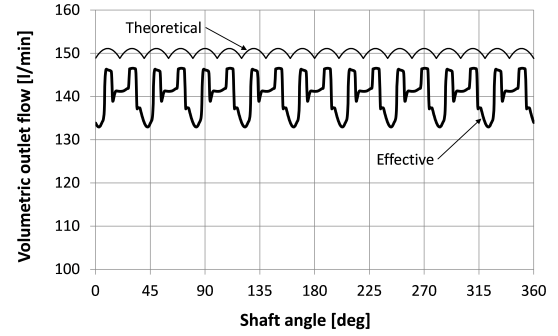


Figure 8: Effective and theoretical outlet flow for a 75 cc unit, at 2000 rpm, maximum displacement angle and 300 bar of differential pressure.

compression loss, internal leakage and backflow due to non ideal timing (shown in Fig. 4 for one displacement chamber), determines an average volumetric outlet flow rate  $Q_{o,e}$  that is lower than the theoretical  $Q_{o,th}$ . The power loss associated with this lower volumetric flow rate is calculated as follows

$$P_{l,ci} = (Q_{o,th} - Q_{l,e} - Q_{o,e}) \Delta p \quad (20)$$

### 3.2 Prediction of power losses in the lubricating interfaces of axial piston machines

The prediction of the energy dissipation and leakage flows in the three lubricating machine interfaces (piston/cylinder, cylinder block/valve plate and slipper/swash plate) represents an extremely difficult problem because the fluid film thickness is determined by the combined effect of a variety of physical phenomena. Recent works of the author's research group have demonstrated that the fluid film behavior can be predicted with good level of accuracy only when multiphysics simulation model are introduced [1], [5], [6] for the piston / cylinder interface, [7], [8] for the slipper / swash plate interface and [9], [10], [2] for the cylinder block / valve plate

interface. The three interfaces are subject to the same physical phenomena and therefore can be modeled using the same basic structure.

An overview of the modeling approach is represented in Fig. 9. Four main modules, coupled together, account for all the

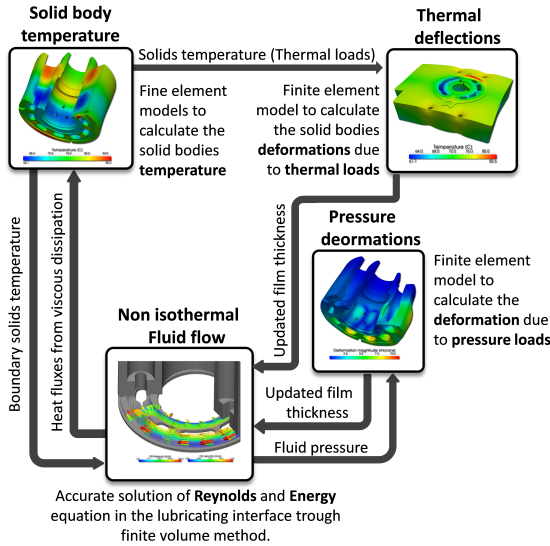


Figure 9: Modeling approach used to predict the lubricating interface performance in axial piston machines.

main physical phenomena in the lubricating interfaces. The first module solves for the non-isothermal fluid flow in the lubricating interfaces, the governing equations are the Reynolds and the Energy equations. The Reynolds equation is solved iteratively by changing the normal squeeze term until the external loads on the solid parts are balanced by the pressure field in the lubricant. A modified version of the standard Reynolds equation has been derived, in order to account for any alteration of the surfaces in contact with the clearance and to allow the viscosity to change along the film. Furthermore, the fluid viscosity is calculated with experimentally derived correlation and it is estimated as a function of pressure and temperature. The energy equation accounts for conductive heat transfer between fluid film and solid parts, convective effects determined by the fluid velocity field and heat generation due to the viscous dissipation; this last term is fundamental for the present work and it will be discussed with more detail later. Thanks to the solution of the non-isothermal fluid flow, the main oil properties (pressure, temperature, viscosity, velocity) can be calculated as function of the operating condition; this allows for the load carrying ability, leakages and torque losses to be estimated for all the three lubricating interfaces.

From the knowledge of the pressure field, the elastic deformations of the solid parts are calculated using an in house finite element solver. The deformations of the surfaces in contact with the lubricant are extracted and used to correct the film thickness in the fluid flow module. However, pressure and deformation mutually influence each other and therefore a converged solution can be found only by solving a fluid structure interaction problem or, more precisely, an elasto-hydrodynamic lubrication problem. This is achieved thanks to

a partitioned fluid structure interaction algorithm: two separate solver are used for the fluid mechanic and the solid mechanic problems and the solutions are coupled together through the interface between fluid and structure; an under-relaxed iterative procedure ensures the convergence of the solution.

Also the heat transfer is characterized by an interaction between the lubricating interface and the solids. In the solution of the Energy equation the surface temperatures of the solid parts are important boundary conditions that strongly affect the calculated temperature field. On the other hand, the mechanical dissipated in the fluid flow generates heat, which heads to the solid parts. The rate of heat flow released by the viscous friction can be calculated using the mechanical dissipation function for a Newtonian fluid [3]. The typical assumptions that the lubrication theory allows to make, simplify the expression of the mechanical dissipation as follows:

$$\Phi_d = \mu \left[ \left( \frac{\partial u}{\partial z} \right)^2 + \left( \frac{\partial v}{\partial z} \right)^2 \right] \quad (21)$$

$$\Phi_d = \mu \left[ \left( \frac{\partial u}{\partial z} \right)^2 + \left( \frac{\partial v}{\partial z} \right)^2 + \frac{4}{3} \left( \frac{u}{r} \right)^2 + \left( \frac{v}{r} \right)^2 \right]$$

In Eq. 21 the first expression is used for a Cartesian reference frame, the second for a cylindrical reference frame;  $u$  and  $v$  are fluid velocity components along the film and  $z$  is the direction of the film thickness.

From Eq. 21, the heat fluxes towards the solid parts can be calculated and applied as boundary conditions to solve for the temperature fields in all the parts of the rotating kit. A finite element solver based on the Galerkin formulation of the finite element method has been specifically developed for this purpose. From the knowledge of temperature fields in the solids, the thermal loads associated to the temperature induced strains are calculated through the coefficient of linear expansion of the materials. The resulting thermal deflection of the solid parts are determined thanks to finite element calculation. Likewise the elastic deformation due to pressure, the deflections deriving from the thermal expansion affect the fluid film thickness with substantial modification of the fluid film behavior.

The whole model requires many iterations to reach a converged solution, because just the external loads on the parts can be calculated a priori; all the other variables have to be guessed and updated iteration after iteration. The described modeling approach is quite complex and certainly a thorough description is out of the scope of this paper; more detailed information is addressed to the publications mentioned above.

Using the above very briefly described modeling approach the energy dissipation taking place during steady state operation of the machine can be calculated for all three interfaces according to Eq. 19. In addition the case flow resulting from all three interfaces can be accurately predicted. These values are used as inputs for the in this paper presented model.

### 3.3 Prediction of the churning losses in the machine case

The rotation of the cylinder block together with the reciprocating motion of the pistons in the case filled with hydraulic

fluid generate power loss, which is usually referred as churning loss. The two major contributions to churning losses are illustrated in Fig. 10.

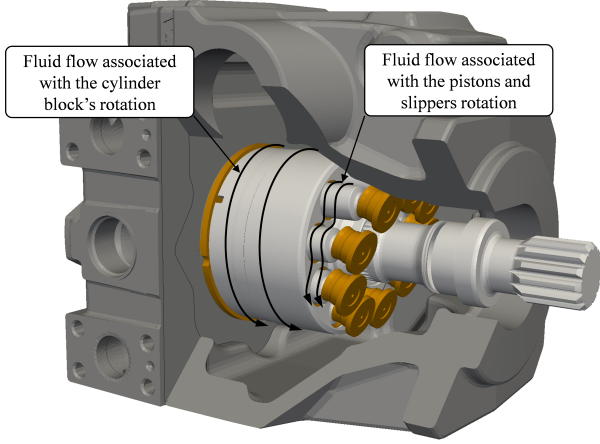


Figure 10: Two main sources of churning losses.

In order to estimate churning losses as a function of the pump design and the working speed, the following model is proposed.

### 3.3.1 Churning losses due to the cylinder block rotation

To determine the power loss due to the rotating cylinder block in the oil filled case, the following assumptions have been made:

- the internal shape of the housing can be well approximated with a cylinder or, in other words, the cylinder block and the internal region of the housing are conformal surfaces;
- the flow is laminar and no major eddies are present. In this way, since the fluid flow is determined by the dragging effect of the cylinder block rotation, the only non zero component of the fluid velocity is in the circumferential direction.

These conditions are usually a reasonable simplification of the problem and lead to acceptable results. With reference to Fig. 11, recalling Eq. 21, when the above mentioned conditions are applied the expression of the viscous dissipation becomes

$$\Phi_d = \mu \left[ r \frac{\partial}{\partial r} \left( \frac{v}{r} \right) \right]^2 \quad (22)$$

Furthermore, the expression of the oil velocity is

$$v = \omega R_B \left( \frac{R_B + t - r}{t} \right) \quad (23)$$

where  $\omega$  is the cylinder block's angular velocity and  $t$  the thickness of the gap between cylinder block and internal surface of the case. The mechanical dissipation per unit volume can therefore be defined as

$$\Phi_d = \mu \omega^2 R_B^2 \left( \frac{R_B + t}{R_B t} \right)^2 \quad (24)$$

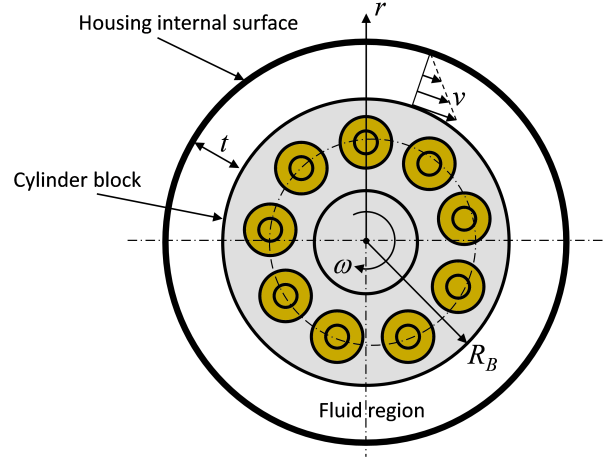


Figure 11: Schematic representation of the flow field between cylinder block's outer surface and housing's inner surface.

The dissipation associated with all the volume of the fluid enclosed by the cylinder block and the housing is determined by the following integral

$$\Phi_{ch,cb} = \int_{R_B}^{R_B+t} 2\pi L \mu \omega^2 R_B^2 \left( \frac{R_B + t}{R_B t} \right)^2 r dr \quad (25)$$

The result of the integration is the following expression

$$\Phi_{ch,cb} = -2\pi L \mu \omega^2 R_B^2 \left( \frac{R_B + t}{t} \right)^2 \ln \left( 1 - \frac{t}{R_B + t} \right) \quad (26)$$

By defining the Reynolds number as

$$Re = \frac{\omega R_B t \rho}{\mu} \quad (27)$$

Eq. 26 becomes

$$\Phi_{ch,cb} = -\frac{2\pi L \rho \omega^3 R_B^3}{Re} \left( \frac{R_B + t}{t} \right)^2 \ln \left( 1 - \frac{t}{R_B + t} \right) \quad (28)$$

The thickness of the gap  $t$  is usually small and Eq. 26 reduces to the following expression

$$\Phi_{ch,cb} \approx \frac{2\pi L \rho \omega^3 R_B^4}{Re} \quad (29)$$

### 3.4 Churning losses due to the pistons and slippers motion

The fluid flow determined by the motion of the pistons and slippers is less likely to meet the conditions listed in the previous section. The pistons and slippers are subjected to friction and pressure drag. However, since the pistons are very closed to each other in circumferential direction, the pressure drag component can be neglected in first approximation, because each piston is shielding the next, located downstream with respect to the rotation direction. This effect is shown schematically in Fig. 12. The problem can be addressed by following

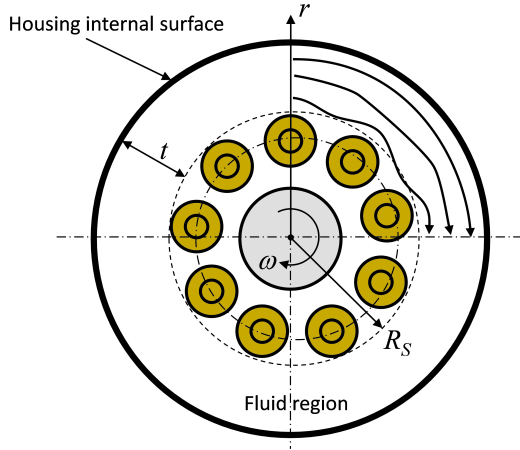


Figure 12: Schematic representation of the flow field between piston & slipper assemblies and the housing's inner surface.

the same procedure illustrated for the cylinder block churning losses, by defining the radius  $R_S$  as the outer radius of the slippers, as shown in Fig. 12. Nevertheless, in this situation is reasonable to expect that turbulence is likely to occur.

As suggested by [11], a modified version of Eq. 29 can still be applied for the calculation of the mechanical dissipation under turbulent flow, if the skin friction coefficient  $C_d(Re)$  is properly estimated. For the laminar case it was  $C_d = Re/2$ , while in general

$$\Phi_{ch,cb} \approx C_d \pi L \rho \omega^3 R_S^4 \quad (30)$$

In this work the skin friction coefficient was calculated according with the correlation proposed by [12]:

$$\frac{1}{\sqrt{C_d}} = 2.04 + 1.78 \ln(Re \sqrt{Cd}) \quad (31)$$

The combination of Eq. 30 and 31 allowed reasonable results to be achieved; however, the effect of turbulence will be further investigated in future studies.

Figure 13 illustrates the dependence of churning losses upon the speed of the machine for a 75cc swash plate type axial piston pump. The trend in Fig. 13 is in very good agreement

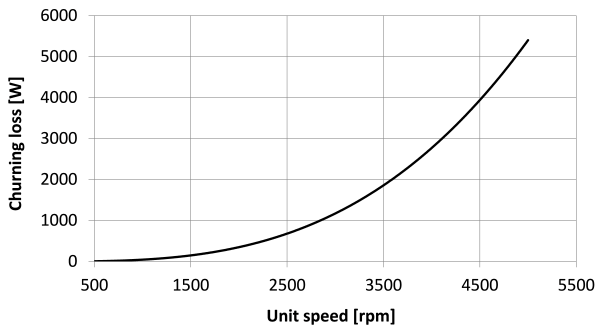


Figure 13: Total churning losses versus machine's speed for a 75 cc swash plate axial piston unit.

with the results found in [13], where the authors measured the

difference in input power between full and dry case operation for 233 cc bent axis unit with 45° angle.

## 4 Results

This section presents a simulation study for a 75 cc unit of current production. The steady state performance of the unit, together with the case and outlet temperature were predicted for the two operating conditions listed in Table 1 and compared with steady state measurements.

Table 1: Definition of the operating conditions considered in the present study.

OC	$T_i$ [C]	n [rpm]	$p_i$ [bar]	$p_o$ [bar]	$\Delta p$ [bar]	$\beta$ [%]
1	52.5	1000	20	320	300	100
2	52.5	2000	20	320	300	100

Before the presentation of the simulation results, a brief discussion about the estimation of the performance parameters from the steady state measurements is given in the next section.

### 4.1 Steady state measurements and data analysis

Tables 2 and 3 summarize the results of the steady state measurements for the two operating conditions listed in Table 1. The measurements were conducted following the specifications found in [14].

Table 2: Steady state measurement data for OC1.

Measured quantities		Value	Unit
$\Delta p$	Pressure differential	299.8	bar
$n$	Speed	1006	rpm
$Q_o$	Effective volumetric outlet flow rate	66.4	l/min
$Q_c$	Case volumetric flow rate (external leakage)	1.8	l/min
$M_i$	Input torque	371.4	Nm
$T_i$	Inlet temperature	52.5	°C
$T_o$	Outlet temperature	57.1	°C
$T_c$	Case temperature	64.9	°C
Derived quantities		Value	Unit
$V_d$	Derived displacement	72.8	cc/rev
$P_{i,th}$	Theoretical input power	36.6	kW
$Q_{o,th}$	Theoretical volumetric flow rate	73.2	l/min
$M_{1,th}$	Theoretical torque	347.3	l/min
$P_o$	Output power	33.2	kW
$P_{l,Q}$	External leakage power loss	0.90	kW
$P_{l,mh}$	Mechanical power loss	2.54	kW
$P_{l,ci}$	Power loss due to Compressibility & internal leakage	2.4	kW
$P_{l,tot}$	Total power loss	5.9	kW

The derived displacement was determined through the Toet method, for more details see [15]. The theoretical input torque and the theoretical volume flow rate were calculated through the derived displacement volume as follows

$$M_{i,th} = \frac{\Delta p V_d}{2\pi} \quad Q_{o,th} = \frac{\omega V_d}{2\pi} \quad (32)$$

Table 3: Steady state measurement data for OC2.

Measured quantities		Value	Unit
$\Delta p$	Pressure differential	299.8	bar
$n$	Speed	2008	rpm
$Q_o$	Effective volumetric outlet flow rate	139.2	l/min
$Q_c$	Case volumetric flow rate (external leakage)	2.5	l/min
$M_i$	Input torque	376.9	Nm
$T_i$	Inlet temperature	53.2	°C
$T_o$	Outlet temperature	57.3	°C
$T_c$	Case temperature	72.5	°C
Derived quantities		Value	Unit
$V_d$	Derived displacement	74.1	cc/rev
$P_{i,th}$	Theoretical input power	74.3	kW
$Q_{o,th}$	Theoretical volumetric flow rate	148.8	l/min
$M_{1,th}$	Theoretical torque	353.5	l/min
$P_o$	Output power	69.7	kW
$P_{l,Q}$	External leakage power loss	1.2	kW
$P_{l,mh}$	Mechanical power loss	4.9	kW
$P_{l,ci}$	Power loss due to Compressibility & internal leakage	3.4	kW
$P_{l,tot}$	Total power loss	9.6	kW

The theoretical input power and the actual output power were derived according to Eq. 33:

$$P_{i,th} = \omega M_{i,th} \quad P_o = \Delta p Q_o \quad (33)$$

The external leakage and mechanical losses were calculated as follows

$$P_{l,l,e} = \Delta p Q_c \quad P_{l,mh} = \omega (M_i - M_{i,th}) \quad (34)$$

The power loss due to compressibility and internal leakage were calculated using Eq. 35 considering the difference between the theoretical volumetric flow rate

$$P_{l,ci} = \Delta p (Q_{o,th} - Q_l - Q_o) \quad (35)$$

## 4.2 Simulation results

Tables 4 and 5 summarize the simulation results for the two operating conditions listed in Table 1. The simulation were run with the same inlet temperature, speed and differential pressure of the corresponding measurement. For both the operating conditions the prediction of the overall performance of the axial piston unit is in excellent agreement with the measurements.

The simulation model tends to underestimate the case flow with an error of about 20%, which is reasonable considering the complexity of the prediction of the fluid film thickness discussed in Sec. 3.2. The outlet flow is predicted almost exactly; the simulation model also matches quite well the compressibility and internal leakage losses, which represent a very important source of power loss of the unit.

Looking at the total mechanical loss, the simulation predictions are lower than the values derived from the measured data, but this is justified by the fact that the simulation model does not account for the additional mechanical losses in the machine. Moreover, the value calculated from the measurements is affected by the derived displacement in Eq. 32,

Table 4: Simulation results for OC1.

Simulation input		Value	Unit
$\Delta p$	Pressure differential	300.0	bar
$n$	Speed	1000.0	rpm
$T_i$	Inlet temperature	52.5	°C
Simulation predictions		Value	Unit
$Q_o$	Volumetric outlet flow rate	67.2	l/min
$P_{l,mh,PC}$	Mechanical loss p/c	0.610	kW
$P_{l,mh,SS}$	Mechanical loss s/s	0.250	kW
$P_{l,mh,CV}$	Mechanical loss c/v	0.430	kW
$P_{l,ch}$	Churning losses	0.052	kW
$P_{l,mh}$	Total mechanical loss	1.375	kW
$Q_{l,e}$	Total external leakage	1.34	l/min
$P_{l,l,e}$	External leakage loss	0.67	kW
$P_{l,ci}$	Compressibility & internal leakage loss	3.32	kW
$P_{l,tot}$	Total power loss	5.36	kW
$T_o$	Outlet temperature	56.3	°C
$T_c$	Case temperature	63.4	°C

Table 5: Simulation results for OC2.

Simulation input		Value	Unit
$\Delta p$	Pressure differential	300.0	bar
$n$	Speed	2000.0	rpm
$T_i$	Inlet temperature	53.2	°C
Simulation predictions		Value	Unit
$Q_o$	Volumetric outlet flow rate	140.5	l/min
$P_{l,mh,PC}$	Mechanical loss p/c	0.97	kW
$P_{l,mh,SS}$	Mechanical loss s/s	0.55	kW
$P_{l,mh,CV}$	Mechanical loss c/v	1.06	kW
$P_{l,ch}$	Churning losses	0.340	kW
$P_{l,mh}$	Total mechanical loss	2.92	kW
$Q_{l,e}$	Total external leakage	2.00	l/min
$P_{l,l,e}$	External leakage loss	1.00	kW
$P_{l,ci}$	Compressibility & internal leakage loss	3.92	kW
$P_{l,tot}$	Total power loss	7.84	kW
$T_o$	Outlet temperature	56.0	°C
$T_c$	Case temperature	74.0	°C

which is just an approximation of the actual displacement of the machine, not an exact number. For example, just 1 cc/rev of difference in the derived displacement can change the derived mechanical loss of more than 500 W. The maximum error on the outlet and case temperature predictions is below the 2 °C overall, which confirms a remarkable accuracy of the thermal model.

In order to further confirm the fidelity of the developed model, the case and outlet temperatures were predicted for a fixed speed of 2000 rpm and a variety of differential pressures. The comparison between the measurements and the simulation results are illustrated in Fig. 14 and 15.

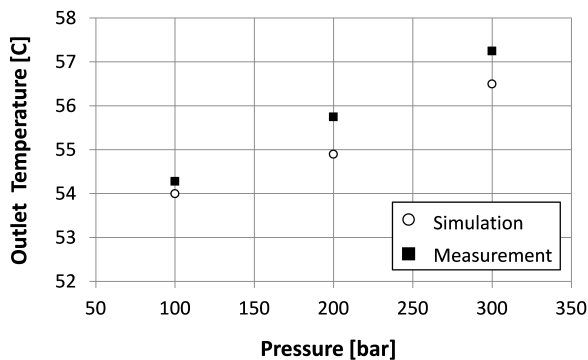


Figure 14: Comparison of the predicted and measured outlet temperature for maximum displacement, 2000 rpm and different operating pressures.

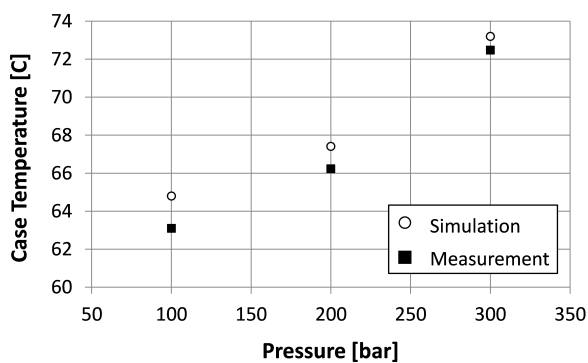


Figure 15: Comparison of the predicted and measured case temperature for maximum displacement, 2000 rpm and different operating pressures.

Also in this case the maximum error between the simulation and measurements is limited to 2 °C. This not only further confirms the validity of the thermal model, but also highlights the ability of the fluid structure interaction model for the lubricating interfaces to predict with high accuracy the mechanical losses. If this was not the case, major discrepancies would have been observed between simulation and measurements.

## 5 Conclusion

A thermal model for the prediction of the temperature in the case and outlet port of axial piston machines under steady state operation was described. The thermal model was coupled with simulation models for the estimation of the effective flow rate of the machine and for the prediction of the performance of the three main lubricating interfaces.

The prediction of the overall machine efficiency and the working temperature in the outlet and case volumes was in very good agreement with the measurements, for many different operating conditions. The developed model has confirmed that the accuracy required for virtual prototyping of axial piston pumps and motors has been successfully achieved.

## References

- [1] Matteo Pelosi and Monika Ivantysynova. Surface Deformation Enables High Pressure Operation of Axial Piston Pumps. In *ASME/Bath Symposium on Fluid Power and Motion Control*, Arlington, VI, USA, 2011.
- [2] Marco Zecchi and Monika Ivantysynova. A novel approach to predict the cylinder block / valve plate interface performance in swash plate type axial piston machines. In *ASME/Bath Symposium on Fluid Power and Motion Control*, pages 13–28, 2012.
- [3] Frank P Incropera, David P DeWitt, Theodore L Bergman, and Adrienne S Lavine. *Fundamentals of Heat and Mass Transfer*, volume 6th of *Dekker Mechanical Engineering*. John Wiley & Sons, 2007.
- [4] Uwe Wiecek and Monika Ivantysynova. Computer aided optimization of bearing and sealing gaps in hydrostatic machines - The simulation tool CASPAR. *International Journal of Fluid Power*, 3(1):7–20, 2002.
- [5] Matteo Pelosi and Monika Ivantysynova. The Influence of Pressure and Thermal Deformation on the Piston/Cylinder Interface Film Thickness. In *52nd National Conference on Fluid Power*, 2011.
- [6] Matteo Pelosi. *An Investigation on the Fluid-Structure Interaction of Piston/Cylinder Interface*. Phd thesis, Purdue University, 2012.
- [7] Andrew Schenk and Monika Ivantysynova. An Investigation of the Impact of Elastohydrodynamic Deformation on Power Loss in the Slipper Swashplate Interface. In *8th JFPS International Symposium on Fluid Power*, Okinawa, Japan, 2011.
- [8] Andrew Schenk and Monika Ivantysynova. The influence of swashplate elastohydrodynamic deformation. In *7th FPNI PhD Symposium*, Reggio Emilia, Italy, 2012.
- [9] Marco Zecchi and Monika Ivantysynova. Cylinder block/valve plate interface - A novel approach to predict thermal surface loads. In *8th IFK International Conference on Fluid Power*, pages 285–298, Dresden, Germany, 2012.

- [10] Marco Zecchi and Monika Ivantysynova. An investigation of the impact of micro surface shaping on the cylinder block/valve plate inter-face performance through a novel thermo-elasto-hydrodynamic model. In *7th FPNI PhD Symposium*, pages 589–610, 2012.
- [11] James Vlkzncik. Prediction of windage power loss in alternators. Technical Report October, NASA, WASHINGTON, D. C., 1968.
- [12] Carl Gazley. Heat-Transfer Characteristics of the Rotation and Axial Flow Between Concentric Cylinders. *Trans. ASME*, 80(1):79–90, 1958.
- [13] Robert Rahmfeld, Marsch Siinje, Wilhelm Giillner, Thorsten Lang, Thomas Dopichay, and Johannes Untch. Mehr Effizienz bei hydrostatischen Einheiten. *O+P Ölhydraulik und Pneumatik*, 7(8):22–27, 2012.
- [14] ISO. Hydraulic fluid power - Positive motors and integral transmissions steady-state performance. Technical report, International Organization For Standardization, 2005.
- [15] Jaroslav Ivantysyn and Monika Ivantysynova. *Hydrostatic Pumps and Motors*. Akademia Books International, New Delhi, India, 2001.

## Nomenclature

Symbols	Denotation	Unit
$z$	number of pistons	[]
$\dot{m}$	mass flow rate	[kg/s]
$\dot{Q}$	rate of heat flow	[J/s]
$\dot{W}$	rate of work	[J/s]
$P$	power	[J/s]
$p$	pressure	[Pa]
$n$	rotational velocity	[rpm]
$\omega$	angular velocity	[rad/s]
$\Delta p$	pressure differential	[Pa]
$T$	temperature	[°C]

$\mu$	dynamic viscosity	[Pa s]
$\nu$	kinematic viscosity	[m <sup>2</sup> /s]
$\rho$	density	[kg/m <sup>3</sup> ]
$h$	enthalpy	[J/kg]
$c_p$	specific heat capacity	[J/kg°C]
$\alpha$	convection coefficient	[W/m <sup>2</sup> °C]
$\gamma$	volumetric expansion coeff.	[]
$\beta$	swash plate angle	[%]
$V_0$	displacement volume	[m <sup>3</sup> /rev]
$V_d$	derived displacement volume	[m <sup>3</sup> /rev]
$Q$	volumetric flow rate	[m <sup>3</sup> /s]
$A$	area	[m <sup>2</sup> ]
$K$	isothermal bulk modulus	[Pa]
$V$	volume	[m <sup>3</sup> ]
$\Phi_d$	mechanical dissipation	[W]
$C_d$	drag coefficient	[]
$L$	cylinder block length	[m]
$R_B$	cylinder block outer radius	[m]
$R_S$	slippers outer radius	[m]
$t$	radial gap between cylinder block and housing	[m]
$Re$	Reynolds number	[]

Subscripts	Denotation
$i$	inlet
$o$	outlet
$c$	case
$h$	housing
$a$	ambient
$th$	theoretical
$l$	loss
$mh$	mechanical
$ci$	compressibility and internal leakage
$DC$	displacement chamber
$PC$	piston / cylinder interface
$CV$	cylinder / valve plate interface
$SS$	slipper /swash plate
$ch$	churning
$ncv$	natural convection
$fcv$	forced convection



# Performing and Interpreting Experiments Towards Understanding Noise Generation in Displacement Machines

T. Opperwall, A. Vacca

Maha Fluid Power Research Center, Purdue University, West Lafayette, Indiana, USA  
E-mail: tjopperwall@gmail.com, avacca@purdue.edu

## Abstract

Noise generation in fluid power systems remains an important problem in current applications, and in the expansion of fluid power to new lighter applications such as passenger vehicles. The current research looks to understand noise generation from two main angles, experimental measurements and numerical modeling. This activity shows the experimental procedures and results towards better understanding the noise performance in the particular case of external gear pumps. Sound intensity measurements and analysis of the frequency characteristics of these machines are used to characterize the air-borne noise generated. Better understanding of the key sources and transmission paths of the noise can lead to a better understanding of how to improve the noise performance from a design standpoint. The method of measuring and interpreting the noise performance of several different displacement machines is explained along with the significance of the results pertaining to the design of new quieter hydraulic solutions. This research serves the more general goal as a validation reference for modeling noise generation and propagation from the sources inside the machine and out to the environment.

**Keywords:** Fluid power, Air-borne noise, Fluid-borne noise, External gear machines

## 1 Introduction

Positive displacement machines are the prime movers of energy in most fluid power systems. They convert the mechanical energy from an engine or motor shaft into a pressurized fluid which is used in many applications for moving heavy loads. The primary applications of these machines are currently in construction and agriculture equipment, aircraft systems, and heavy industrial equipment.

In typical hydraulic pumps, delivery of fluid is caused by a displacing action of moving mechanical parts. This displacing action is also responsible for generating flow oscillation at the outlet port of the machine and the attached hydraulic lines due to the limitation of a finite number of displacing chambers spread out over each machine cycle. These flow oscillations cause pressure fluctuations when acting against a load, and this is a source of noise in the system called fluid-borne noise (FBN). This FBN propagates through the structure and the system as structure-borne noise (SBN) and then out into the environment as air-borne noise (ABN) as described by Fiebig [1]. Due to the high pressures and forces involved, the sources of FBN and SBN in the displacement machine tend to make them significant sources of noise and vibration in fluid power systems. High noise and vibration is undesirable as it decreases system stability, wastes energy, and reduces comfort of the nearby environment. Even more, the noise

and vibration can reduce machine lifetime and introduce more costly maintenance. All of these downsides are present to some degree in most commercial displacement machines, and limit the applications where fluid power systems can be used. In particular, this causes fluid power solutions to be unsuitable to spread to some new applications such as light passenger vehicles.

Previous research has developed advanced models to simulate the physical phenomena in external gear pumps in general such as Vacca and Guidetti [2], Vacca, Dhar, and Opperwall [3], and Dhar and Vacca [4]. In particular, the predictions of these advanced models are used to simulate the noise generation in this type of displacement machine as in Opperwall and Vacca [5].

Many researchers have tried to reduce the radiated noise by minimizing the pressure ripples in the lines of hydraulic systems. This has been done using targeted attenuators such as Helmholtz resonators and expander mufflers demonstrated by Ortwig [6]. Other concepts relating to attenuating line pressure ripple were presented by Earnhart [7]. Edge [8] demonstrated how to take into consideration the system specifications in order to reduce the generated noise. Hartmann [9] optimized an internal gear pump to reduce the FBN. Negrini [10], Lätzel [11], and others have completed work to reduce the noise in external gear pumps through new gear designs. Among others, Ericson,

Johansson, and Palmberg [12] designed optimized axial piston machines.

Bonano [13] compared the frequencies of the SBN to the measured data. Also, Klop and Ivantysynova [14] used sound intensity measurements to match trends between the noise sources and the measured noise for axial piston machines. A similar work was completed by Ngah and Edge [15] using acoustic measurements on components of hydraulic transmissions. Additionally, some work has been done on determining transfer functions and other relationships between noise sources and the radiated ABN such as that done by Pettersson, Weddfelt and Palmberg [16].

The present work seeks to understand the sources and transmission of noise from displacement machines through interpreting measurements of the ABN under a wide range of operating conditions. These measurements were completed in the semi-anechoic chamber at Maha Fluid Power Research Center (Maha).

For the purposes of this research, a reference type of displacement machine is chosen. Four different external gear machines with 38cc/rev displacement were chosen to study the ABN generation. Example gear geometry is shown in Fig. 1. One of the gears is typically driven by an electric motor or combustion engine. This gear then drives the second gear through contact in the meshing zone. Fluid is taken into the volumes of the teeth at the inlet side and carried around the periphery of the machine to the outlet side by the rotation of the gears. The displacing action is achieved by the meshing of the gears where the fluid is forced to move to the outlet port as each tooth volume meshes with the corresponding tooth on the opposite gear. It is this finite number of displacing chambers that causes oscillations in the flow and pressure at the outlet of the pump at frequencies corresponding to the shaft speed and the number of teeth.

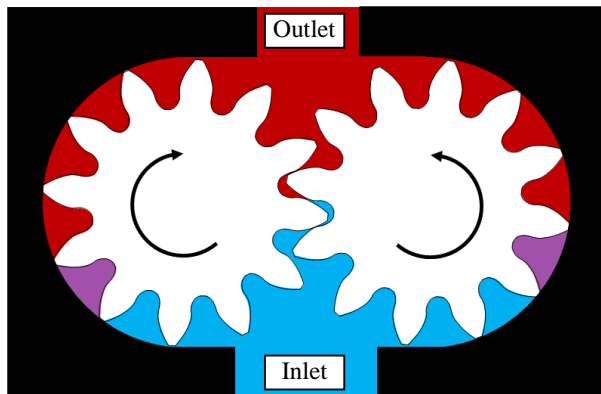


Figure 1: Example geometry and principle of operation of a typical external gear pump.

Three reference pumps of different designs from different manufacturers are compared and are referred to as Pumps 1,2,3. For Pump 2, two different designs are considered, which will further be referred to as Pump 2A and Pump 2B.

The noise characteristics of the different pumps will be compared so that additional insight may be gained. The pumps are physically very similar in terms of overall dimensions and features. All three pumps contain pressure compensated lateral plates or bearing blocks. They all feature identical port sizes and shaft couplings/flanges. The pumps are different from each other in a way which is of interest to noise generation. First, Pumps 1 and 3 contain gears with 10 teeth each. Pumps 2A and 2B contain gears with 14 teeth, but with slightly different part geometry that results in a reduced flow ripple generation by pump 2B with respect to Pump 2A. The differing numbers of teeth and the different flow/pressure ripples will result in differing ABN frequency content and magnitudes if the different pumps are compared at the same speed. Finally, Pumps 1, 2A, and 2B share very similar specified operating condition ranges while Pump 3 is limited to a lower pressure range. A description of the measurement techniques and results can be read in the following sections.

## 2 Methods of Measuring Noise

The first step in the measurement of the ABN is to ensure an accurate measurement technique and calibrated sensors. To complete this, a known sound power source was measured at 62 grid points chosen on a cube of 1.4m by 1.4m by 1m in the semi-anechoic chamber at Maha Fluid Power Research Center of Purdue University (Maha) shown in Fig. 2 and Fig 3.



Figure 2: Semi-anechoic chamber at Maha, from outside the chamber with the doors open.

The semi-anechoic chamber was built to the requirements of ISO 16902-1 [17]. The acoustic insulation is realized by 0.305m acoustic foam wedges attached to walls and ceiling

excluding inside of the measurement frame. The noise floor is 42dB above 150Hz and a reverberation time of 0.11s as reported by Klop [14]. A pump can be mounted to the test rig electric motor, which is isolated from the pump and the chamber by the staggered-stud reflecting wall shown in Fig. 2. An example pump on the test bed is shown in Fig. 3.



Figure 3: Example pump detail image.

A main use for measurements of ABN in hydraulic systems is through a sound intensity technique for the purpose of calculating total sound power level (SWL). A description of sound intensity calculations can be found in Bendant and Peirsol [18]. This method has previously been applied to fluid power applications by Klop and Ivantysynova [14]. A short summary of the sound power calculations will be included here.

The basis of calculating sound power is measuring the sound intensity at discrete points on a surface surrounding a source. Intensity can be simply stated as the pressure times the velocity in a sound field. As a result, the experiment is completed using at least one pair of microphones along with suitable signal acquisition equipment as shown in Tab. 1. A microphone pair is needed since a means of approximating the velocity field must be used.

Table 1: Description of noise measurement equipment.

Item Type	Description
Sound intensity probe	GRAS, three microphones Type 40A0 – Sensitivity 0.2 dB ref 2·10 <sup>-5</sup> Pa, ½“ diameter
Pre-amplifier	GRAS, Type 26CB, ¼“ diameter
Signal acquisition module	NI 9234, 4 channels, 51.2 kS/s per-channel maximum sampling rate, ±5 V input
High speed USB Carrier	NI USB 9162 – bus powered carrier for portability

The microphone pairs are spaced at a fixed distance  $\Delta r$ , with one pair separated by 12mm, and a second pair separated by 32mm. Considering a single microphone pair, two separate time signals of pressure are recorded at 50kHz sampling rate for each  $n$  discrete point on the measurement grid for  $N$  total points.

$$x(t) = x(n\Delta t) \quad (1)$$

$$y(t) = x(n\Delta t) \quad (2)$$

The time signals are divided into segments of 8000 points and zero padded, with 23 total segments for each time signal after the noise sample has been recorded. Each segment is windowed using a Hanning window  $w(n\Delta t)$  which requires a scaling factor of  $\sqrt{8/3}$  to account for energy loss due to windowing.

$$w(n\Delta t) = 1 - \cos^2\left(\frac{\pi n}{N}\right) \quad (3)$$

The Fast Fourier Transform (FFT) is completed in Matlab on each windowed segment.

$$X_i(k) = \Delta t \cdot \sqrt{8/3} \sum_{n_i=0}^{N_{\text{seg}}-1} (x_i(n\Delta t) - \bar{x}_i(n\Delta t)) \quad (4)$$

$$\cdot w(n\Delta t) \cdot \exp\left[-\frac{j2\pi kn}{N_{\text{seg}}}\right]$$

$$Y_i(k) = \Delta t \cdot \sqrt{8/3} \sum_{n_i=0}^{N_{\text{seg}}-1} (y_i(n\Delta t) - \bar{y}_i(n\Delta t)) \quad (5)$$

$$\cdot w(n\Delta t) \cdot \exp\left[-\frac{j2\pi kn}{N_{\text{seg}}}\right]$$

Finally, the sound intensity average taken across all of the segments and summed over the discrete measurement points can be calculated using the two-sided estimate of the cross-spectral density.

$$I(k) = \frac{\text{Im}\left(\frac{1}{N_{\text{seg}}} \cdot \sum_{i=0}^{N_{\text{seg}}-1} \frac{2}{N \cdot \Delta t} [X_i^*(k) \cdot Y_i(k)]\right)}{2\pi f(k) \cdot \rho \cdot \Delta r} \quad (6)$$

The total sound power is found by multiplying the calculated sound intensities by the area discrete measurement element. The total sound power level is calculated based on  $W_{\text{ref}} = 10^{-12}$  Watts.

$$SWL = 10\log_{10}\left(\frac{W}{W_{\text{ref}}}\right) \text{ dB} \quad (7)$$

Once the measurement technique and signal processing algorithm is confirmed, the calibrated sound power source can be replaced by the displacement machine.

A hydraulic test rig circuit was developed for this study as shown in Fig. 4 and Tab. 2. The test rig layout is designed to reproduce the normal open circuit operation of the tested pumps. In particular, a proportional valve is used in closed loop to establish a constant level of pressure at the pump inlet (1 bar), using the hydraulic power supply system present at Maha. Pressure in the inlet lines was measured to examine the pressure fluctuations introduced by the supply and the ripples were found to be in the magnitude of less than 0.2bar, which is within the magnitude of the inlet ripples caused by the pump flow oscillations.

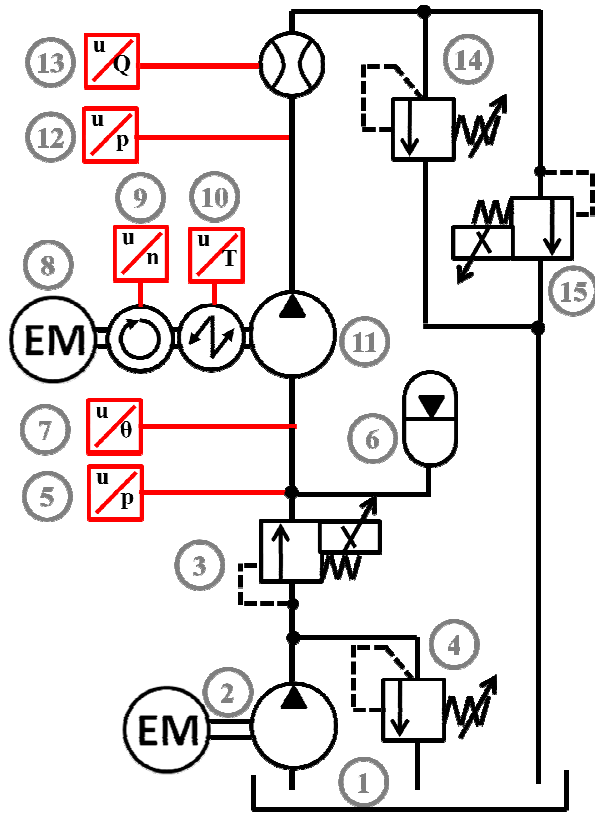


Figure 4: Test rig schematic

Details of the components shown in Fig. 3 are listed in Tab. 2.

Table 2: Details of test rig components.

#	Description	Details
1	Oil Reservoir	Shell Tellus 32 oil, held to 52° C at inlet for 20cSt
2	Maha hydraulic supply	Delivery unit, 80cc/rev, 1185rpm axial piston machine
3	Proportional valve	Hydraforce TS10-26C-8T-N-12DR proportional orifice for pressure reducing to 1bar
4	Pressure relief valve	For setting inlet line pressure from supply pump
5	Inlet pressure sensor	WIKA, 0-100bar, accuracy 0.25% FS
6	Hydraulic accumulator	2 L accumulator to damp inlet, no added precharge
7	Inlet temperature sensor	Omega K-type resistive thermocouple, range 0-120° C, accuracy 1% FS
8	Electric motor	SSB, 500Nm, speed +/-3000rpm
9	Shaft speed sensor	HBM MC60, max 5000rpm, 0.05 Accuracy class
10	Shaft torque sensor	HBM MC60, scale 0-500Nm, 0.05 Accuracy class
11	Test pump	Only feature included inside of noise measurement grid.
12	Line pressure sensor	WIKA, 0-400bar, accuracy 0.25% FS
13	Flow meter	VS 4 by VSE, gear type, 0-400L/min, accuracy 1% FS
14	Pressure relief valve	Safety feature only, set to 300bar.
15	Proportional valve	Hydraforce TS10-26A-8T-N-12DR proportional orifice

### 3 Sound Pressure and Power Results

The measurement procedure for sound pressure level (SPL) and sound power level (SWL) is similar to that presented by Klop [14]. In order to accurately visualize the sound field generated by the pump, a much finer grid would be required; this may be explored in the future similar to the method of Cho and Bolton [19] in the near field of the pump. An example of the measurement planes for the experimental setup is shown in Fig. 5.

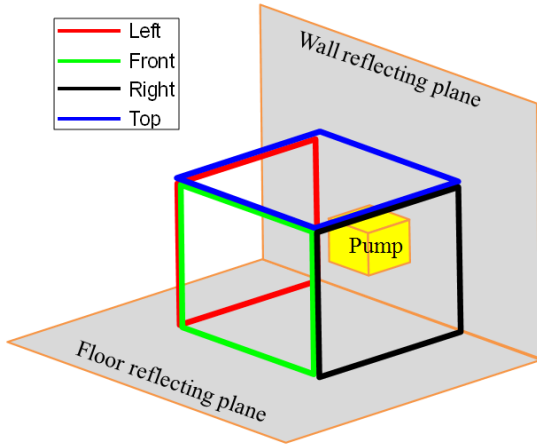


Figure 5: Surfaces for sound measurement.

The measurement volume is a box with six sides. Four of the six sides of the cube are measurement surfaces as shown in Fig. 5. The bottom surface and back surface are reflecting planes of the floor and wall of the chamber respectively. Note that sound pressure level measurements suffer from doubling effects near the main boundaries with the reflecting floor of the chamber. This effect is not seen to a great extent where the top surface meets the reflecting plane since the pump is fixed to the reflecting surface and hence most of the sound is travelling parallel to the surface in that location with little reflection off the surface.

To better understand why noise measurements must be made at many discrete points instead of at just a single point, notice Fig. 6. Considering just one discrete point on each of the four measuring surfaces gives insight onto the varying pressure field surrounding the pump. The FFT of the sound pressure is shown in Fig. 6 for one representative point from each of the four measurement surfaces shown in Fig. 5 at an operating condition of 1000rpm with 100bar outlet pressure for Pump 1. The pump primary frequency occurs at 167Hz for Pump 1 based on the shaft speed and the number of chambers. The higher integer multiples are also present.

$$f_1 = \frac{\text{speed} * nc}{60} \quad (8)$$

The higher multiples of the pump primary frequency feature can be clearly seen as they dominate the frequency spectrum. Furthermore, while the frequency content occurs in basically the same locations on the spectrum across all four discrete measurement points, it does not contain the same magnitudes at those frequencies. In particular, the left and top sides have generally larger magnitude frequency content at the primary pump frequency and around 1000Hz (the 6<sup>th</sup> multiple of the primary frequency). The right and front sides have generally smaller magnitude frequency components except the right side is fairly large at the 3<sup>rd</sup> and 7<sup>th</sup> multiples of the pump primary frequency.

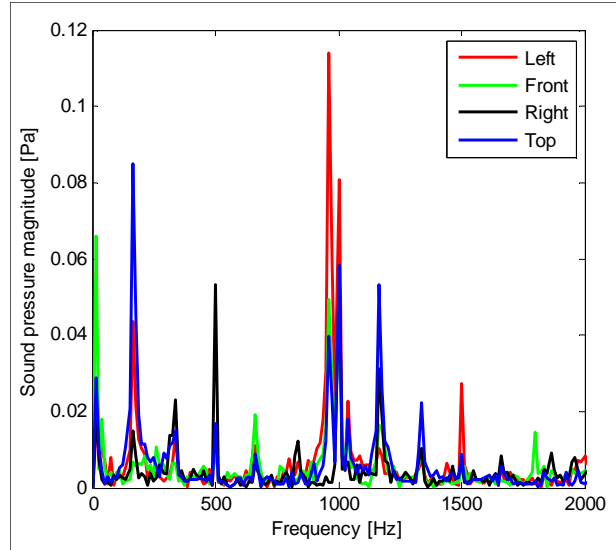


Figure 6: Four points of ABN sound pressure frequency content for Pump 1.

If the sound pressure were to be measured at only a few points, the magnitudes of the various frequency components cannot be considered in terms of absolute value, but only in terms of trends since the set of measurement points is not adequate to calculate an accurate average. Section 4 of this paper will explore the value of other kinds of considerations using fewer discrete points.

The calculated sound intensity map is shown in Fig. 7, along with the total summed SWL. It is shown that the sound intensity also varies over the surface from around 65dB to over 80dB. When these are multiplied by their corresponding areas and summed, the total SWL of 81.49dB is calculated.

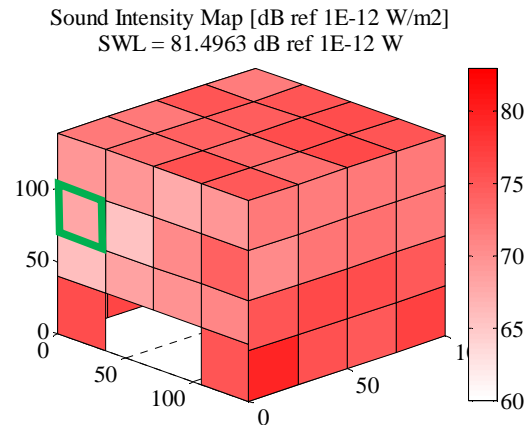


Figure 7: Example sound intensity map with representative point highlighted.

Total SWL measurements for all four pumps is shown in Fig. 8. Each data point in Fig. 8 represents the sum of a set of 62 noise measurements taken over the measurement grid. Total SWL measurements were completed for the operating

ranges of 1000rpm to 2500rpm and 50bar outlet pressure to 250bar outlet pressure except for Pump 3 where its specifications limited it to 200bar. An interesting feature of the pumps is shown in Fig. 8. The pump which is designed to operate at a lower operating condition produces the lowest SWL at 1000rpm across all three measured pressures.

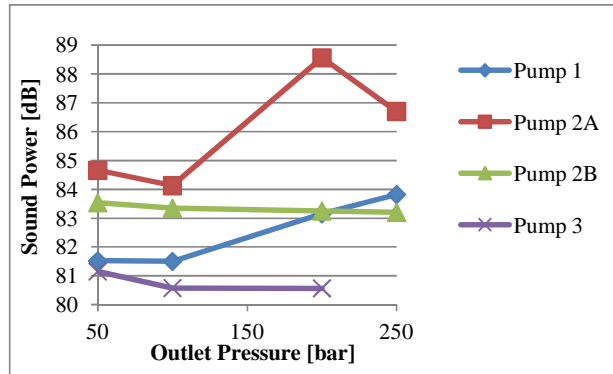


Figure 8: Total SWL for 1000rpm operating speed.

This result shows that while the original Pump 2A was the noisiest at 1000rpm, Pump 2B achieved a reduction in SWL across the pressure range which brought it into line with Pumps 1 and 3. The improvement in Pump 2B can be fully attributed to the reduced pressure ripple generation. It has been shown by other authors as well, as in the modeling work done in parallel with this project, that the frequencies of the FBN can be predicted or measured via various approaches such as in Vacca and Guidetti [2]. It is also shown and can be perceived in the experimental tests that the main frequencies of the ABN are mainly the same frequencies as present in the FBN area inside the outlet volume of the pump and the attached hydraulic lines. According to that understanding along with the experimental results shown in Fig. 8, the conclusion can be made that the reduction in FBN can have a large positive effect on the ABN. Furthermore, the main difference in SWL between various commercial pump products can likely be attributed to how well the pump design handles the generation of FBN.

#### 4 Representative Point Measurements

The noise measurements completed in the previous section involved holding the pump to a steady-state condition while manually moving the sound probe to 62 distinct locations on the microphone grid. The advantage of this method is that the total sound power of the pump can be accurately measured without an impact of the structures and equipment outside of the grid volume. Also, this results in a much higher accuracy estimation of the total sound power of the pump, which can be used to compare various difference pumps on a level playing field without the interference from other sources. The main disadvantage to the SWL method over the discrete grid is the time required for each operating condition. This leads to a very coarse grid of operating points which is not good for spotting trends related to small changes in speed or pressure. In order to make comparisons

at a finer set of operating points, a single representative point highlighted in Fig. 7 is chosen. This point was selected as it reflects the average value of sound pressure level at many speeds across all of the different combinations of pumps and operating conditions tested for SWL. The magnitudes of the sound pressure measured at the reference point cannot be reliably used for characterizing specific features about the total noise generated by the pump, but the frequency content can be analyzed on a much finer set of operating points in order to spot trends or features in the frequency domain.

First, at a single speed and pressure of 1000rpm and 100bar, the FFT of the sound pressure can be analyzed comparing all four pumps simultaneously as shown in Fig. 9. This comparison shows several interesting features of the different pump operations. The frequency range is limited to 1200Hz in order to highlight the differences between the various pumps in this range. First, the primary pump frequencies can be interpreted from this graph. Additionally, the number of teeth on the gears in each pump can be inferred as long as the speed is known, or vice versa. From this graph (and confirmed by the pump catalog specifications) it can be stated that the primary pump frequency corresponding to Pump 1 and Pump 3 is 167Hz as was previously stated in Fig. 6. This corresponds to a 10 tooth pump at 1000rpm. Likewise, for Pumps 2A and 2B, the primary pump frequency is 233Hz which corresponds to a 14 tooth pump at 1000rpm. Looking closer at the FFT in Fig. 9, the frequencies shown for Pumps 1 and 3 correspond very closely to each other despite being different designs from different manufacturers. This occurs mainly because the main features relating to noise generation are very similar. Namely, the number of teeth, the relative size of the pump, and the pressure compensated design. The close SWL results in Fig. 8 also suggests the different designs are operating in a very similar manner. Similarly, the FFT results at the representative point for Pumps 2A and 2B are very similar, with a small decrease in the overall magnitude seen for Pump 2B with respect to Pump 2A.

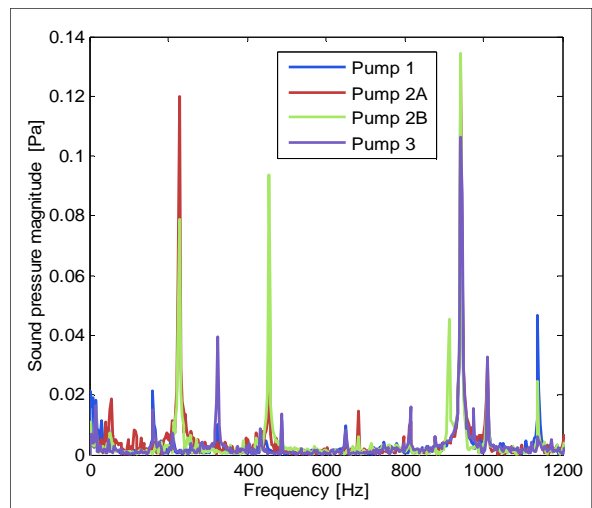


Figure 9: ABN at representative point for all pumps

The peak at 1000Hz for all four pumps see in Fig. 9 indicates that the structure, the system, or features of the geometry of the measurement location are contributing to the sound pressure frequency content. A peak at 1000Hz would be expected for the 10 tooth pumps as that corresponds closely with the sixth multiple of the pump primary frequency. However, a peak at 1000Hz would not be expected based on the FBN of Pumps 2A and 2B since the nearest multiples of the primary pump frequencies are at the 4<sup>th</sup> multiple at 933Hz, and the 5<sup>th</sup> multiple at 1167Hz. However, at 1000Hz, all four pumps have a strong peak in frequency. The ability to detect these kinds of features is simultaneously one of the best things and one of the most difficult things about these kinds of measurement comparisons.

In order to better understand what is happening in the frequency domain, a wider range of frequencies and operating conditions must be considered. The method for this study selected was to hold the outlet pressure constant at 50bar while adjusting the speed across the operating range and recording the sound pressure at the representative measurement point shown in Fig. 7. This results in a fine definition of the pressure spectra across a wide range of operating conditions. The results for Pump 1 are shown in Fig. 10.

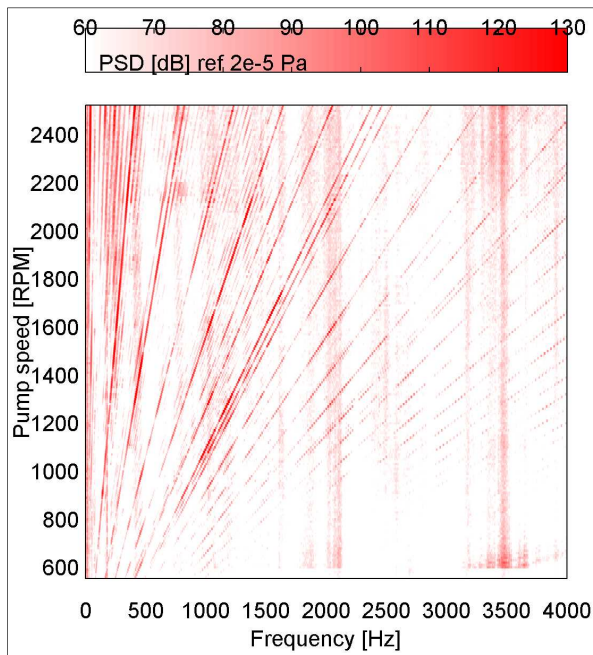


Figure 10: Representative point power spectral density for Pump 1 at 50bar outlet pressure.

The angled lines in Fig. 10 are created by the relationship between the pump speed and the primary pump frequency. The slope of each line is determined by the integer multiples of the pump speed times the number of teeth divided by sixty as shown in Eqn. 8. Figure 10 in particular highlights the fact that the vast majority of the energy in the sound pressure is centered at the multiples of the primary pump frequency. Additional energy content is shown at the shaft

frequency represented by the farthest left line in Fig. 10. System/structural frequencies can also be seen in the image represented by vertical lines; that is, frequency content that is independent of the pump speed and present for all of the displayed operating conditions. Also to be noted is that the frequencies with the most power all occur at relatively low frequencies under about 2000Hz.

An alternate way of looking at the information is to take the integral at each pump speed and sum from left to right while displaying the total value of the PSD. For Pump 1, this alternate display is shown in Fig. 11. This method of looking at it allows for the different noise results to be considered in terms of their contribution to the overall PSD. The frequency range here is cut to 2000Hz since the integral sum was nearly constant after that point for all speeds. Of particular interest to understanding the generation of noise in displacement machines is looking at the dominating frequencies at each speed. In particular, in the speed range of 1000rpm to 1800rpm, the PSD of the ABN is dominated by the same frequencies that are present in the FBN.

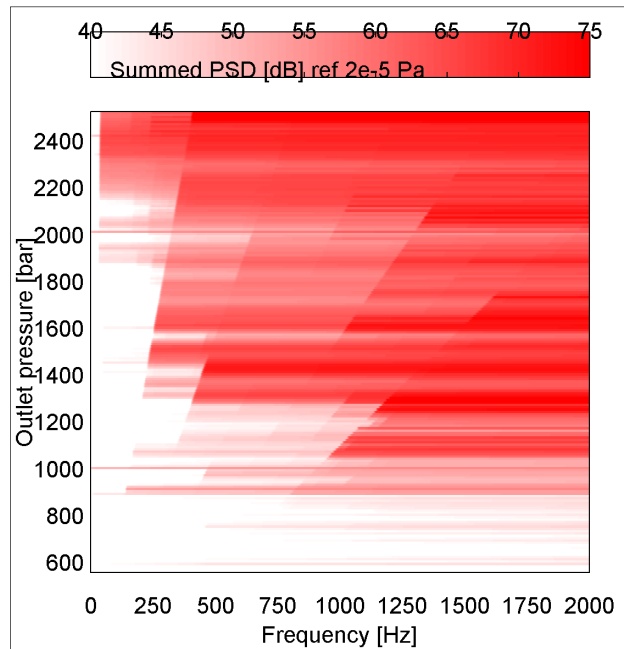


Figure 11: Summed PSD of representative point measurements for pump 1 at 50bar outlet pressure.

Figure 13 shows the same PSD map for Pump 2B. It can be said that there is remarkable similarity between Figs 10 and 11. Everything that was said about Fig. 10 can thus be repeated for Fig. 12.

Of interest after comparing both results in Figs. 10 and 12 together is that the same system/structural frequency features are present in both images, in particular at about 2000Hz and 3500Hz.

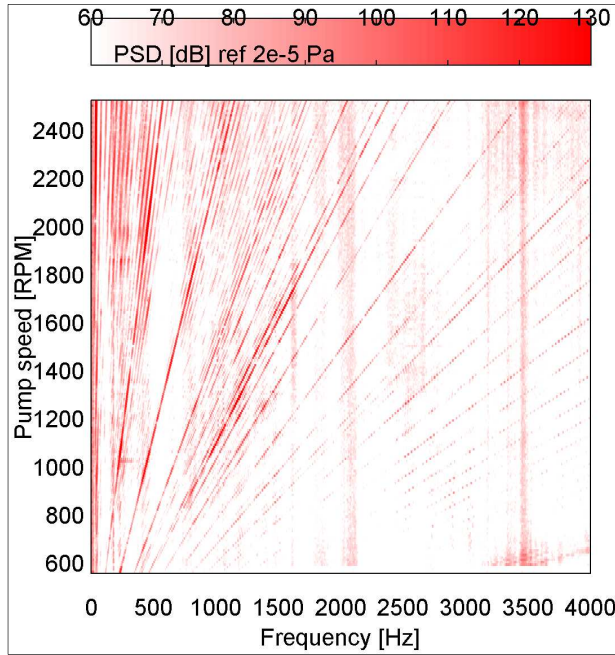


Figure 12: Representative point power spectral density for Pump 2B at 50bar outlet pressure.

For further comparison and completeness, the summed PSD for Pump 2B is shown in Fig. 14.

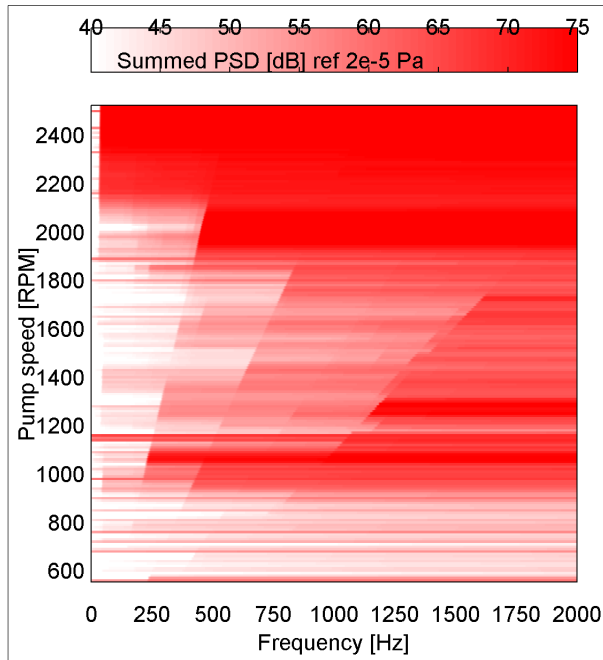


Figure 13: Summed PSD of representative point measurements for pump 2B at 50bar outlet pressure.

The results for Pumps 2A and 3 were omitted as the similarities to the already presented data were very strong.

A final result of the representative point measurements is to compare the average sound pressure level of all four pumps across the same speed range. This result is shown in Fig. 15.

This once again shows the remarkable similarity in the results for all four of the pumps. In particular, the peaks around 1000rpm and 1250rpm in the SPL. This demonstrates a possible bias in all of the measurements. The shape of this function across all four pumps is very nice to describe both the influence that the acoustic environment has on the sound pressure, and also the similarity in the performance of the different models of external gear pump.

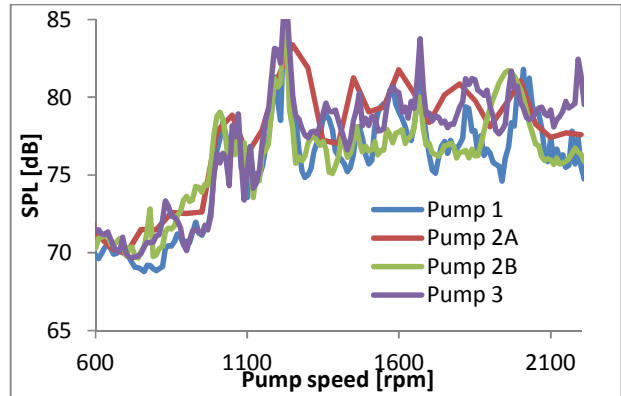


Figure 14: Representative point SPL at 50bar outlet pressure.

## 5 Conclusions

From the experimental results for total sound power, the total ABN generated by each pump can be measured. The frequency spectra for the representative point measurements for Pumps 1 and 2B shown in Figs. 10-14 demonstrate that for the region of 1000rpm through 1800rpm, the dominating frequencies in the ABN match the main frequencies in the FBN. Thus, since the dominating effect in that speed range can be declared to be the FBN. The lower pressure ripple Pump 2B should be expected to have an improvement in the radiated noise in this range over its counterpart Pump 2A, and this expectation was confirmed. The representative point measurements are very helpful in understanding the important features in the ABN, and can be used to aim further design improvements. Also, the procedure is general and can be completed for different pumps. For very similar styles of pump (all are 38cc/rev external gear pumps), the results of these experiments show clues to the most important sources of FBN and SBN in different speed ranges. Optimal speed ranges could also be measured or designed for based on the measurement data. Additionally, the human factor should be taken into account when considering design changes to the effect that decreasing the magnitude of the primary pump frequency in the FBN with no regard for the higher frequency noise may result in a pump that is perceived to be noisier, instead of quieter, despite a lower total sound power. All of the sound power measurements and representative point measurements shown previously in this work are good for understanding important components in the ABN, but future work will be done to better apply how humans in contact with these systems will actually be affected by changes to the pump performance.

As better understanding of the effect of FBN on ABN is gained, the possibility of using an experimental approach in combination with the design process could lead to new methods of designing better displacement machines. The main future work of these experiments is closing the loop and reconciling measured noise with the fluid dynamic model of the pump and developing coupled acoustic model.

## Nomenclature

Designation	Denotation	Unit
FBN	Fluid-borne noise	
SBN	Structure-borne noise	
ABN	Air-borne noise	
$x(t)$	Sound pressure signal 1	[Pa]
$y(t)$	Sound pressure signal 2	[Pa]
$n$	Number for current measurement	
$N$	Total number of points	
$X_i(k)$	FFT for sound pressure signal 1	[Pa]
$Y_i(k)$	FFT for sound pressure signal 2	[Pa]
$N_{seg}$	Number of points in each segment	
$I(k)$	Sound intensity	[W/m <sup>2</sup> ]
$f(k)$	Frequency range	[Hz]
$\rho$	Density of air	[kg/m <sup>3</sup> ]
$\Delta r$	Distance between mics	[m]
$f_1$	First pump frequency feature	[Hz]
nc	Number of chambers in pump	

## References

- [1] Fiebig, W., 2007, "Location of Noise Sources in Fluid Power Machines," *International Journal of Occupational Safety and Ergonomics*, 13 (4), 441-450.
- [2] Vacca A., Guidetti M., 2011, *Modeling and Experimental Validation of External Spur Gear Machines for Fluid Power Applications*, Elsevier Simulation Modeling Practice and Theory, 19 (2011) 2007-2031.
- [3] Vacca A., Dhar S., Opperwall T., 2011, A Coupled Lumped Parameter and CFD Approach for Modeling External Gear Machines, SICFP2011 The Twelfth Scandinavian International Conference on Fluid Power, May 18-20, 2011, Tampere, Finland.
- [4] Dhar S., Vacca A., 2012, A Novel CFD- Axial Motion Coupled Model for the Axial Balance of Lateral Bushings in External Gear Machines, Elsevier Simulation and Modeling Practice and Theory. 2012; 26: 60-76.
- [5] Opperwall T., Vacca A., "A combined FEM/BEM model and experimental investigation into the effects of fluid-borne noise sources on the air-borne noise generated by hydraulic pumps and motors." *Proceedings of the Institution of Mechanical Engineers, Part C: Journal of Mechanical Engineering Science*, First published online on April 22, 2013. (Print publication pending)
- [6] Ortwig, H., 2005, "Experimental and Analytical Vibration Analysis in Fluid Power Systems," *International Journal of Solids and Structures*, 42, 5821-5830.
- [7] Earnhart, N., Marek, K., and Cunefare, K. Novel, compact devices for reducing fluid-borne noise. in *SAE 2011 Noise and Vibration Conference and Exhibition*. 2011. Grand Rapids, MI.
- [8] Edge, K. A., 1999, "Designing Quieter Hydraulic Systems – Some Recent Developments and Contributions," *Proceedings of the Fourth JHPS International Symposium on Fluid Power*, Tokyo, Japan, 3-27.
- [9] Hartmann K., Harms H.H, Lang T. 2012 A Model Based Approach to Optimize the Noise Harmonics of Internal Gear Pumps by Reducing the Pressure Pulsation, 8th International Fluid Power Conference (IFK), March 26-28, 2012, Dresden, Germany.
- [10] Negrini, S. "A Gear Pump Designed for Noise Abatement and Flow Ripple Reduction" *International Fluid Power Exposition and Technical Conference*. 23-25 April 1996.
- [11] Lätzel, M. Schwuchow, D., "An innovative external gear pump for low noise applications" 8th International Fluid Power Conference (IFK), March 26-28, 2012
- [12] Ericson L, Johansson A and Palmberg J-O. Noise reduction by means of non-uniform placement of pistons in fluid power machines. In: *Proceedings of the 2009 ASME dynamic systems and control conference and bath/ASME symposium on fluid power & motion control theme: system engineering*, Hollywood, CA, USA, 12-14 October 2009.
- [13] Bonanno, A., and Pedrielli, F., 2008, "A Study of the Structure borne Noise of Hydraulic Gear Pumps," 7th JFPS International Symposium on Fluid Power, 641-646.
- [14] Klop, R. and Ivantysynova, M. 2010. Sound Intensity Measurements to Investigate Noise Generation of Hydrostatic Transmissions *Proceedings of the 7th*

International Fluid Power Conference Aachen 2010  
(7IFK), Vol. 2, 229-242

- [15] Ngah, Z. and Edge, K.A., "The measurement of positive displacement pump and motor noise using sound intensity techniques." Off-highway Powerplant Congress and Exposition, SAE, Warrendale, USA, pp. 1-6, September, 2001
- [16] Pettersson, M., Weddfelt, K., and Palmberg, J.-O., "Prediction of structural and audible noise from axial piston pumps using transfer functions." In Proc. Of Eighth Bath International Fluid Power Workshop, 1995
- [17] ISO 16902-1:2003 Hydraulic fluid power -- Test code for the determination of sound power levels of pumps using sound intensity techniques: Engineering method - Part 1: Pumps, 2003.
- [18] Bendant J.S. and Peirsol, A.G., "Random Data – Analysis and Measurement Procedures." John Wiley & Sons, INC, ISBN 0-471-31733-0, 2000
- [19] Cho, Y. T., and Bolton, J. S., 2004, "Acoustical Visualization of a Refrigeration Compressor by using Statistically Optimized Nearfield Acoustical Holography in Cylindrical Coordinates," NOISE-CON, 175-182.

## **Optimization of process parameters in series hydraulic hybrid system through multi-objective function**

Somashekhar S. Hiremath\*, R. Ramakrishnan and M. Singaperumal

Department of Mechanical Engineering, Indian Institute of Technology Madras, Chennai, INDIA  
E-mail: somashekhar@iitm.ac.in, ramakrishnan20@gmail.com, msingam@iitm.ac.in

### **Abstract**

Rising demand, scarcity and lower production rate of crude oil has made fuel an unaffordable for a public passenger vehicle. In this scenario, an energy or fuel efficient system called hybrid system is the hardcore requirement of the automotive industry. The latest gasoline-electric hybrid and hydraulic hybrid systems are significantly more energy and fuel efficient than conventional vehicles. Strength of electric hybrids is its high energy density of electric batteries, allowing for large storage in relatively compact and lightweight batteries. Hydraulic hybrid is the potential technological solution for the limitations in the electric hybrid vehicle. Scalability of hydraulic hybrid system to larger, more powerful vehicles like garbage trucks, passenger bus and delivery trucks when compared to its counterparts. In this paper, a new configuration of the series hydraulic hybrid system has been proposed. The dynamic response of the system is studied using simulation results of the system model in AMESim tool. Sizing of key components in the system involves a parametric optimization with objective function as maximize system energy delivered. However, A trade-off prevails between the system energy consumed and energy delivered. Hence, the process parameters of the system are optimized through multi-objective function. The system simulation results after optimization apparently show that, optimal system parameters significantly improve energy efficiency.

**Keywords:** Series hydraulic hybrid, Multi-objective function, Energy efficiency, Optimization

### **1 Introduction**

The American petroleum institute has estimated that, world's crude oil resources (2 trillion barrels or 320000 m<sup>3</sup>) would deplete between 2062AD and 2094 AD at a consumption rate of 80 million barrels per day [1,2]. The high cost and shortage of crude oil have created an alarm to the crude oil dependent industries such as automobile, construction machinery and agriculture machinery industries to design and develop the energy saving, energy efficient and environmental friendly system. Hence, these companies replace their conventional systems by energy efficient hybrid systems to overcome the current fuel crisis. A hybrid system is a combination of two source of power. The possible combinations include gasoline/hydraulic, gasoline/electric, and fuel cell/battery. Typically, one source is used for conversion of fuel into energy and another source is used as the storage unit. In a conventional vehicle, kinetic energy in the wheel during mechanical friction braking is converted into heat energy and dissipated into atmosphere. But, hybrid system has the capability to regenerate the available kinetic energy for braking into useful energy. This method of regeneration is generally called regenerative braking and it is quite possible in various fields like automobile, construction machinery, and agriculture

machinery. Thus, hybrid systems turn out to be a hot topic for research in automotive companies and research institutes all over the world [3].

Generally, these systems can be classified into two categories- electric hybrids and hydraulic hybrids. The most promising hybrid system today is the electric hybrid system, which has two power sources, namely electric battery and internal combustion engine in series or parallel configuration. However, it has a relatively low charging/discharge rates and also poor regeneration energy saving in contrast to the hydraulic hybrid system [4]. Electric hybrids have their own advantages over their counterparts. This hybrid system has better energy density than hydraulic hybrid system but it has relatively poor power density when compared to its counterpart. Hence, electric hybrid systems can't be potentially used in construction and agriculture machinery, where, power requirements are immense. Hydraulic hybrid system meets high power demand in case of heavy vehicles. These systems can be classified based on configurations into two, namely, parallel and series hydraulic hybrid system [5].

In parallel hydraulic hybrids, input power from prime-mover takes a parallel path via mechanical transmission as well as

hydraulic transmission to reach the output shaft. These systems have better power transmission efficiency but it has poor controllability of power in the system due to power transmission in two different domains. In case of series hydraulic hybrid system, the input power takes purely a hydraulic domain of power transmission, in spite of this; better controllability of system is possible when compared to parallel configuration [6, 7].

Series Hydraulic Hybrid System (SHHS) has got great potential to save the regenerated hydraulic energy as potential energy by compressing the nitrogen gas in the hydro-pneumatic accumulators, hence, creating a relatively higher power density than its counterparts. Moreover, high rates of charging/discharging and lower charging time of regenerated energy makes the SHHS a most energy efficient system [8]. SHHS is a highly non-linear and non-continuous system in which designing physical and process parameters are a complex and tedious process. However, a conflict exists between the input and the output energy which leads to conflicting multiple objective function, that is, maximize energy delivered and minimize energy consumed [9]. In order to design such a system, a multi-objective optimization process is an essential method to achieve optimal physical and process parameters, which results in maximum energy delivered for the minimum energy consumed. In addition to that, it augments the vehicle performance, downsizes the engine, reduce the fuel consumption and also pollution. The multi-objective optimization based on multi-membered multi-criteria evolutionary strategy (MMES) algorithm can effectively decide the optimal system parameters, substantially improve the vehicle performance, and also reduce the power consumption of SHHS in a vehicle.

MMES is one type of evolutionary algorithm used to solve the multiple objective problems and it implements a family of population-based (or: multi-membered) evolution strategies with the mutative self-adaptation of step-size variances. It includes a multi-objective extension of evolution strategies using the non-dominated/crowding distance sorting technique. Furthermore, it is capable of dealing with mixed integer problems by employing specialized variation operators for different parameter types. Main features of MMES include self adaptive refinement of step sizes, handles user defined constraints by objective function penalization, supports mixed discrete/continuous optimization, supports multi objective pareto optimization, allows concurrent evaluation of independent individuals. These features are not commonly found in other methods like gradient-based optimization, simulated annealing and genetic algorithm [10,11,12]. In this paper, a multi-objective design optimization procedure based on MMES algorithm, is proposed, which is used to improve the energy efficiency in SHHS is presented. With energy efficiency as a composite function, this procedure decides the process parameters of the system with maximum energy delivered for the given minimum energy consumed. Multi-objective design optimization based on MMES algorithm is discussed in the following paragraphs.

## 2 Series hydraulic hybrid system

Series Hydraulic Hybrid Vehicle (SHHV) is propelled by a system which includes sub-systems such as prime mover (gasoline engine), hydraulic motor/pump, and hydro-pneumatic accumulator. During braking of vehicle, transmission efficiency of vehicle is enhanced by regenerating the kinetic energy in the wheel into useful hydraulic energy using a hydraulic motor/pump. This regenerated hydraulic energy is stored in the high pressure hydro-pneumatic accumulator and used during the subsequent acceleration of vehicle [13, 14]. A modeling methodology for a hybrid vehicle was proposed in 1997 and then a computer model of series hydraulic hybrid vehicle was developed and investigations focused only on urban passenger vehicle. This study shows that hydraulic hybrid power-train is a feasible concept and fuel economy in addition to emission reduction can be done considerably [15, 16].

Figure 1 shows the proposed configuration of the SHHS, which consists of subsystems such as a prime-mover, master hydraulic pump, a hydraulic traction motor, a hydraulic regeneration pump and a hydro-pneumatic accumulator arranged in a series configuration. The prime-mover is directly coupled to a master hydraulic pump, which converts the mechanical energy into hydraulic energy. According to the operating mode, the hydraulic traction motor is driven by the hydraulic energy from the master hydraulic pump as well as hydro-pneumatic accumulator. The hydraulic regeneration pump and hydraulic traction motor are coupled together through a gearbox, which is connected to wheel via a differential.

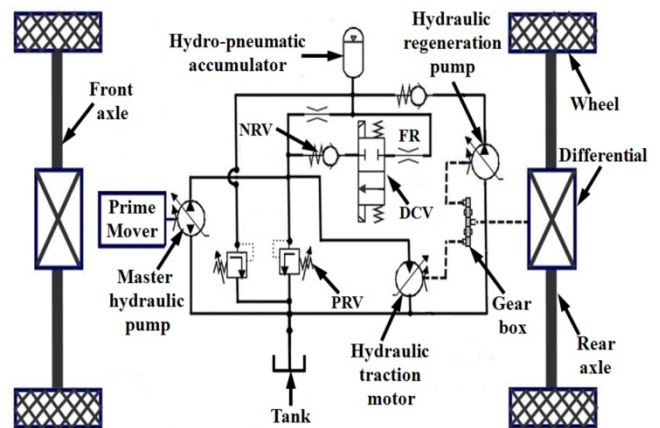


Figure 1: Configuration of series hydraulic hybrid system

The system is divided into three operating modes namely acceleration, cruising and braking mode in a vehicle. When the vehicle is in acceleration mode, energy from two power sources (prime-mover and hydro-pneumatic accumulator) are used to propel the vehicle, that is, hydraulic energy from two sources are supplied simultaneously to power the hydraulic traction motor. During the cruising mode of the vehicle, hydraulic energy from hydro-pneumatic accumulator is cut off and the power from the prime-mover is only used to drive the vehicle. Moreover, the hydro-pneumatic accumulator is also charged with hydraulic

energy from the master hydraulic pump. In the braking mode, hydraulic energy from prime-mover and hydro-pneumatic accumulator is cutoff. An energy recovery method called hydraulic regenerative braking is applied to convert the useless kinetic energy into hydraulic energy. In this method, a new approach called displacement factor control is proposed. It is a process of changing the displacement factor of hydraulic regeneration pump, that is, the increasing in displacement factor proportionately increases the applied torque or load on the hydraulic traction motor. As a result, hydraulic regenerative braking offers resistance to wheel rotation in the vehicle leading to the braking. In addition to that, this method converts kinetic energy in the wheels (usually lost as heat energy due to mechanical friction braking) into useful hydraulic energy.

### 2.1 System modeling and simulation

In order to study the system dynamic characteristics of SHHS, a system model was developed in LMS AMESim tool as shown in Fig. 2.

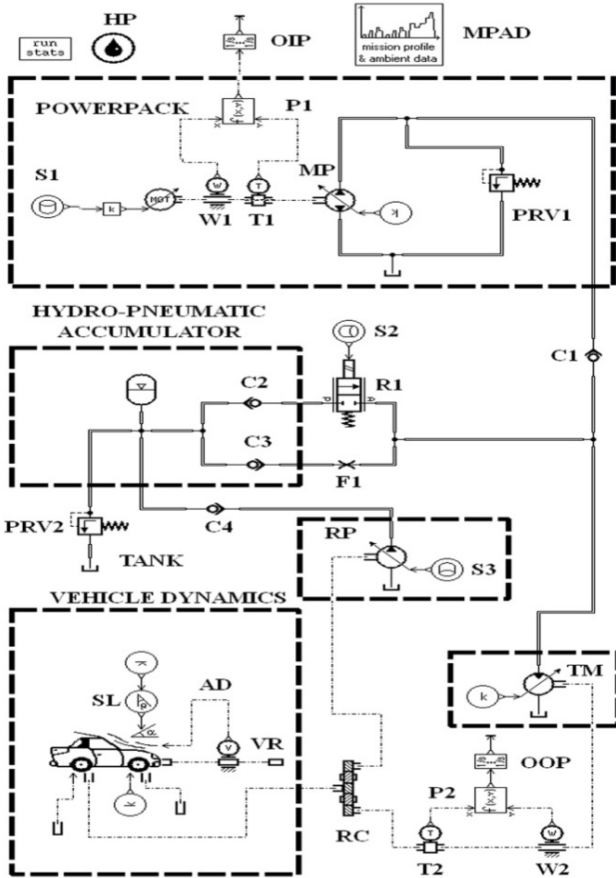


Figure 2: AMESim model of series hydraulic hybrid system

System simulation is carried out with federal urban driving cycle as input to the system [17]. The dynamics characteristic curves of system parameters are plotted as shown in Fig.3. The acceleration mode of the vehicle occurs between 134<sup>th</sup> and 164<sup>th</sup> second in the driving cycle. During this acceleration phase, the hydraulic traction motor is powered by the hydraulic energy from the master hydraulic pump and hydraulic accumulator to meet the high power

requirements in the vehicle. It is apparent from Fig. 3(a) that, the master hydraulic pump speed increases from 0 to 1620 rpm which enables it to deliver hydraulic energy to hydraulic traction motor. Meanwhile, Hydraulic energy from the hydro-pneumatic accumulator is also discharged, which is noticeable from accumulator flow rate between 134<sup>th</sup> and 164<sup>th</sup> second as shown in Fig. 3(b). Furthermore, accumulator hydraulic oil volume decreases from  $7.4 \times 10^{-3} \text{ m}^3$  to  $7.0 \times 10^{-3} \text{ m}^3$  as shown in Fig. 3(c) for the corresponding change in accumulator oil pressure from 13.1 MPa to 12.3 MPa as shown in and Fig. 3(d). It is also observed from Fig. 3(e) that hydraulic traction motor speed increases from 0 to 1180 rpm for the corresponding power from the two sources. Therefore, this substantiates that, the prime-mover as well as hydro-pneumatic accumulator simultaneously delivers the power to the hydraulic traction motor in the acceleration mode of system.

In the braking phase of the vehicle between 460<sup>th</sup> and 495<sup>th</sup> second of the driving cycle time, hydro-pneumatic accumulator volume compresses adiabatically from  $0.4 \times 10^{-3} \text{ m}^3$  to  $5.8 \times 10^{-3} \text{ m}^3$  as shown in Fig. 3(c). At the same time, pressure also rises from 5.2 MPa to 10.1 MPa as shown in Fig. 3(d). It is observed from the above response that,  $5.4 \times 10^{-3} \text{ m}^3$  of hydraulic oil volume is stored in to the hydro-pneumatic accumulator.

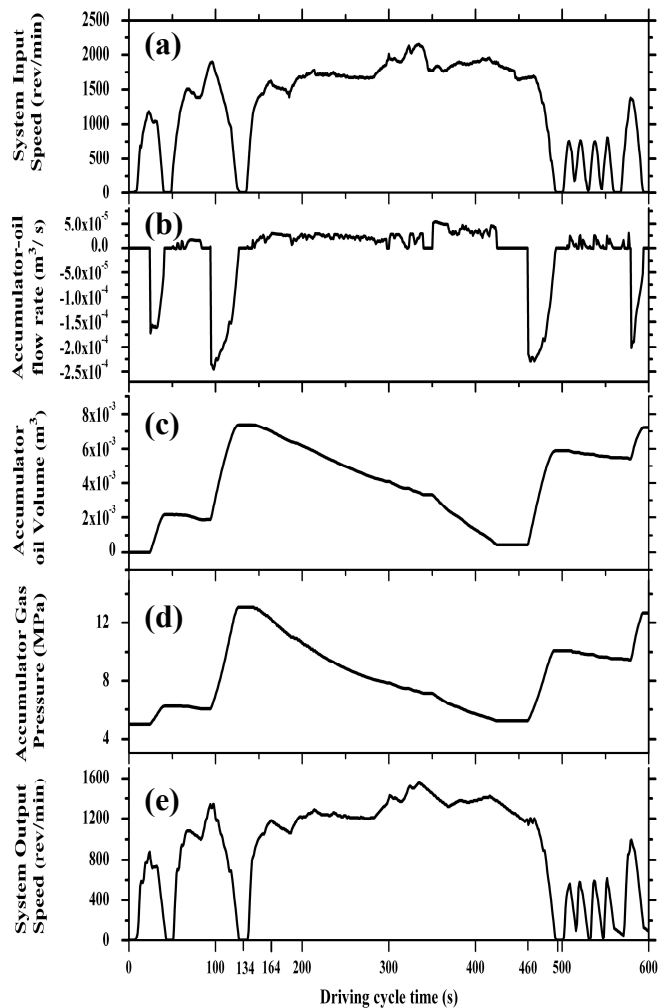


Figure 3: Variation of system parameters Vs driving cycle

### 3 Multi-objective optimization of system process parameters

In case of SHHS, non-optimal physical/process parameters like accumulator size, accumulator pre-charge pressure volumetric displacement of traction motor, master hydraulic pump and regeneration hydraulic pump have an effect on system energy efficiency [18]. Apart from this, losses due to hydraulic leakage, mechanical friction losses and poor controllability reduce the system output energy or energy efficiency. In spite of these factors, vehicle performance becomes very poor. Even though, the energy delivered by the system can be enhanced by increasing the system energy consumed, but the objective is to reduce the power consumption or energy consumed by the system, so that, potential downsizing of a prime-mover can be attained. However, when the energy consumed by the system is reduced, subsequently there will be a decline in the delivered energy by the system. Therefore, reciprocity exists between energy consumed and energy delivered by the system. Here, an attempt is made to design the system in order to maximize the energy delivery and also subsequently minimize the energy consumed by optimizing the system physical/process parameters.

Figure 4 shows the energy distribution in the SHHS. Energy consumed and energy delivered are the cumulative energy available at the input and output of the system respectively. Energy delivered by the system includes the energy used to drive the vehicle or work done and regeneration energy from hydraulic regenerative braking. Energy consumed for hydraulic regenerative braking and vehicle driving are shown in Eq.1 and Eq.2. The output power at traction hydraulic motor is equivalent to sum of power consumed for driving the vehicle and hydraulic regenerative braking as shown in Eq. 3. The multi-objective functions are shown in Eq 4 and Eq.5.

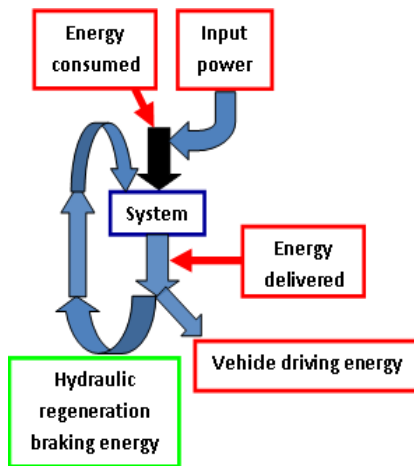


Figure 4: System energy distribution

The composite function is formulated as the energy efficiency as shown in Eq.6, which is a ratio of system energy delivered to the system energy consumed. Energy efficiency parameter is used to select the optimal Design ID (ID corresponds to design parameter set and their value) or global optimum point from the pareto optimal front.

$$\text{Maximize regeneration energy, } E_{RP} = \int_0^T P_{RP} dt \quad (1)$$

$$\text{Maximize vehicle driving energy, } E_{DE} = \int_0^T P_{DE} dt \quad (2)$$

$$P_{TM} = P_{RP} + P_{DE} \quad (3)$$

$$\text{Maximize energy delivered, } E_{TM} = \int_0^T P_{TM} dt \quad (4)$$

$$\text{Minimize energy consumed, } E_{MP} = \int_0^T P_{MP} dt \quad (5)$$

$$\text{Maximize energy efficiency, } \eta_{EE} = \left( \frac{E_{TM}}{E_{MP}} \right) \times 100 \quad (6)$$

Figure 5 shows the schematic of multi-objective architecture of SHHS. Accumulator pre-charge pressure, accumulator size, master hydraulic pump displacement, hydraulic traction motor displacement and regeneration pump displacement are considered as input variables to the mathematical model in the AMESim. A set of random values (design ID) of these parameters with lower, upper boundaries and step size are sent from the Design of Experiments (DOE) to the MMES scheduler in the process loop as shown in the schematic diagram. The MMES scheduler in turn schedules the order of design ID's to the mathematical model.

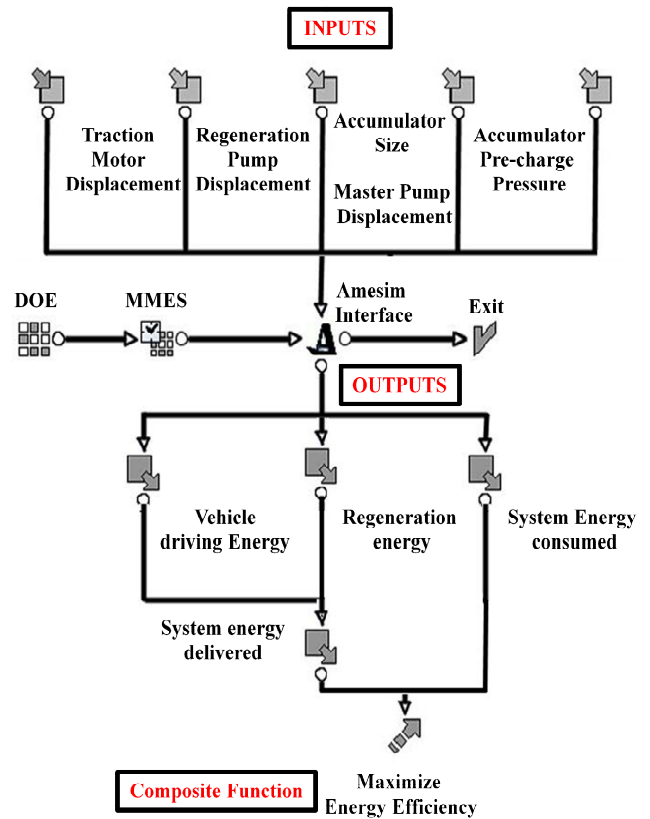


Figure 5: Input-Output architecture of SHHS in multi-objective optimisation

The system simulations are carried out for each set of input variables (design variables) to determine the output

variables, that is, input and output energy of the system. Pareto optimization of SHHS is carried out using Mode Frontier tool [19, 20] with lower and upper limit of input variables considered for optimization as shown in Table 1.

Table 1: Lower and upper limit of input variables considered for optimization.

Input variables	Lower limit	Upper limit	Step size
Accumulator size (m <sup>3</sup> )	0.01	0.02	0.001
Initial accumulator gas pressure (MPa)	9	11	0.2
Accumulator pre charge pressure (MPa)	8	10	0.2
Master hydraulic pump-displacement (m <sup>3</sup> /rev)	$3.5 \times 10^{-5}$	$5.5 \times 10^{-5}$	$2 \times 10^{-6}$
Regeneration hydraulic pump-displacement (m <sup>3</sup> /rev)	$1 \times 10^{-5}$	$2 \times 10^{-5}$	$1 \times 10^{-6}$
Hydraulic traction motor - displacement (m <sup>3</sup> /rev)	$5.2 \times 10^{-5}$	$7.2 \times 10^{-5}$	$2 \times 10^{-6}$

Multi-criteria optimization results are highlighted and discussed in the following paragraphs. The results of multiple objective functions are plotted in pareto optimal front, which consists of pareto optimal points denoted as design ID. Figure 6 shows the pareto optimal front of multi-objective functions (energy delivered and energy consumed) of system. The selection of global optimum from a pareto optimal front is a complex process because all the points in pareto front are optimal solutions, however selecting the best solution out of all optimal solution is intricate. In order to select the global optimum, a composite function called maximize energy efficiency is considered, which satisfies the multi-objective functions in order to determine the best solution out of all optimal solutions.

Figure 7 shows the energy efficiency of the system versus design ID. Design ID - 119, which as maximum energy efficiency of 94 % is selected as the global optimum point from the pareto optimal front. It is apparent from the pareto optimal front that multi-objective optimization based on MMES converges the pareto optimal points towards a global optimum point, where in, the system delivers 4606 kJ of energy for the 4900kJ of energy consumed. This pareto optimal point satisfies the multiple objective functions as maximum energy delivered for minimum energy consumed. Parameter values of design variables as shown in Table 2

are incorporated in to the AMESim model and system simulation is repeated.

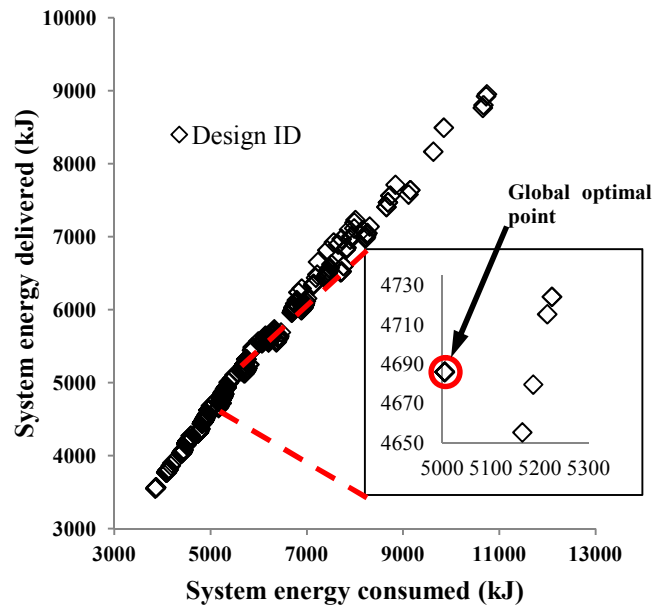


Figure: 6 Pareto optimal front of multi-objective functions

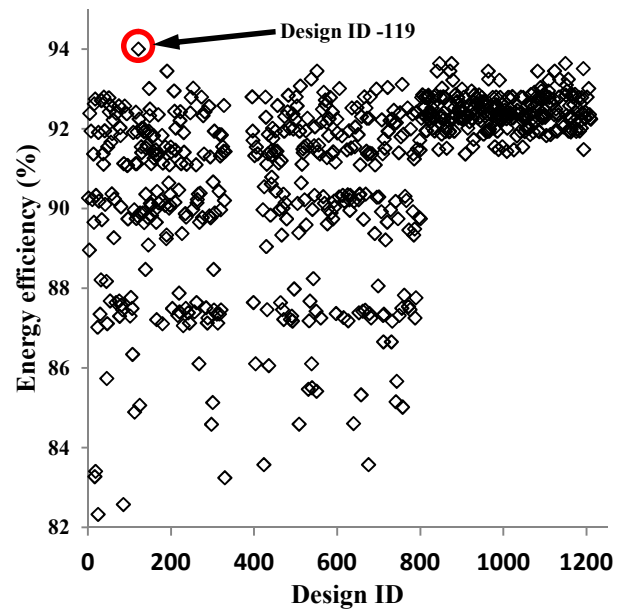


Figure: 7 System energy efficiency Vs design ID

Figure 8 shows the difference of system energy between before and after optimization of series hydraulic hybrid system. It is observed from the plot that, the system energy efficiency after optimization has increased by 4 % from the initial value of 90 % before optimization to 94% after optimization. Due to the increase in energy efficiency, It is clear that, it will facilitate better vehicle performance in optimized SHHS. Moreover, it also facilitates potential downsizing of prime-mover, reduction in power consumption and environmental pollution is possible due to lower energy consumption. Thus, a multi-objective design optimization of process parameters determines the optimal process parameters of series hydraulic hybrid system, which is used to improve the energy efficiency of SHHS.

Table 2 Optimal design parameters values in optimal design ID 119

Design Variables	Optimum value	Before optimization
Accumulator volume (m <sup>3</sup> )	0.013	0.015
Accumulator pre charge pressure (MPa)	3	3
Master hydraulic Pump- displacement (m <sup>3</sup> /rev)	$4.0 \times 10^{-5}$	$4.5 \times 10^{-5}$
Regeneration hydraulic Pump- displacement (m <sup>3</sup> /rev)	$1.75 \times 10^{-5}$	$2.5 \times 10^{-5}$
Hydraulic traction motor - displacement (m <sup>3</sup> /rev)	$9.3 \times 10^{-5}$	$8.8 \times 10^{-5}$

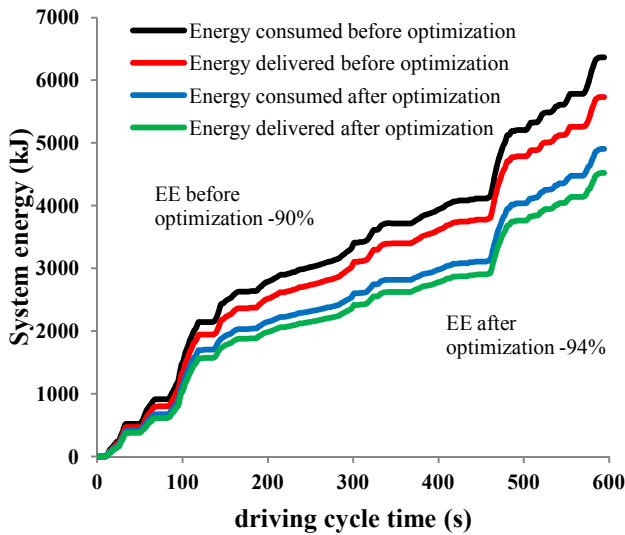


Figure: 8 System energy before and after optimization

## Conclusions

The need for series hydraulic hybrid system arises from world's concern about non-availability of natural resources. In this paper, a multi-objective design optimization of process parameters based on multi-membered multi-objective evolutionary strategy has been carried out to attain better energy efficiency and energy saving. The optimal design ID with maximum energy efficiency of 94% is obtained as global optimum point in the pareto optimal front and it corresponds to 4606 kJ of energy delivered for 4900 kJ of energy consumed. The system simulation with optimal parameters shows that 4 % increase in energy efficiency in comparison with non-optimized system. As the four-wheelers majorly contribute to the world's vehicle population, implementation of series hydraulic hybrid system in these vehicles enhances performance, hydraulic regeneration energy saving, dramatic reduction in power

consumption (downsize the prime-mover) and environmental pollution.

## Nomenclature

Designation	Denotation	Unit
$E_{TM}$	Energy delivered from the system	[kJ]
$P_{TM}$	System output power or actual power delivered by motor	[kW]
$P_{MP}$	System input power or actual power delivered to master hydraulic pump	[kW]
$T_{MP}$	Actual torque delivered to the pump	[Nm]
$T_{TM}$	Actual torque delivered by the motor	[Nm]
$\eta_{OTM}$	Overall efficiency of hydraulic traction motor	[%]
$\eta_{OMP}$	Overall efficiency of master hydraulic pump	[%]
$V_0$	Hydraulic accumulator volume or size	[m <sup>3</sup> ]
$p_0$	Hydraulic accumulator pre-charge pressure	[Pa]
$D_{MP}$	Volumetric displacement of master hydraulic pump	[m <sup>3</sup> /rev]
$D_{TM}$	Volumetric displacement of hydraulic traction motor	[m <sup>3</sup> /rev]
$\omega_{in}$	System input speed	[rad/s]
$\omega_{out}$	System output speed	[rad/s]
$\eta_{vMP}$	Volumetric efficiency of master hydraulic pump	[%]
$\eta_{vTM}$	Volumetric efficiency of hydraulic traction motor	[%]
$p_{gas}$	Hydraulic accumulator gas pressure	[Pa]
$p_{atm}$	Atmospheric pressure	[Pa]
$\rho_o$	Density of hydraulic oil	[kg/m <sup>3</sup> ]
$\rho_{gas}$	Density of hydraulic accumulator gas	[kg/m <sup>3</sup> ]
$D_{RP}$	Volumetric displacement of hydraulic regeneration pump	[m <sup>3</sup> /rev]
$\eta_{vRP}$	Volumetric efficiency of hydraulic regeneration pump	[%]
$t$	Driving cycle time	[s]
$MP$	Master hydraulic pump	
$RP$	Hydraulic regeneration pump	
$FR$	Flow restrictor	
$DCV$	Directional control valve	
$NRV$	Non return valve	
$TM$	Hydraulic traction motor	
$S1$	Prime-mover control signal	
$S2$	Control signal to R1	
$S3$	Braking signal	
$W1, W2$	Angular velocity sensor 1 & 2	
$T1, T2$	Torque sensor 1 & 2	

$C1, C2, C3, C4$	Non return valve 1, 2, 3 & 4
$F1$	Flow control valve 1
$R1$	2/2 Directional control proportional valve
$PRV1$	Pressure relief valve 1
$PRV2$	Pressure relief valve 2
$P1$	System input power
$P2$	System output power
$OIP$	Energy input
$OOP$	Energy output
$AD$	Aerodynamic resistance
$SL$	Slope of the road
$VR$	Linear velocity sensor
$RC$	Rotary node (T-Bevel gear box)
$HP$	Hydraulic oil properties
$MPAD$	Driving cycle
$\eta_{EE}$	System energy efficiency

## References

- [1] Allen E. Fuhs. *Hybrid vehicles and the future of personal transportation*, CRC Press, 2009.
- [2] Davis S C, Diegel S W. *Transportation Energy Data book*. Center for transportation analysis engineering science and technology division. 24<sup>th</sup> ed. Oak Ridge National Laboratory; 2004.
- [3] Karden E., S. Ploumen, B. Fricke, T. Miller and K. Snyder. Energy storage devices for future hybrid electric vehicle, *Journal of Power Sources*, 168:2-11, 2007.
- [4] Clement-Nyns K. *Impact of plug-in hybrid electric vehicles on the electricity system*. PhD Thesis. Katholieke Universiteit Leuven ; 205, 2010.
- [5] Baseley, S., Ehret, C., Greif, E., and Kliffken, M., Hydraulic Hybrid Systems for Commercial Vehicles, *SAE Technical Paper 2007-01-4150*, 2007, doi:10.4271/2007-01-4150.
- [6] Hui, S., Jihai, J. and Xin, W. Torque control strategy for a parallel hydraulic hybrid vehicle, *Journal of Terramechanics*, 46(6): 259–265, 2009.
- [7] Wu, B., Lin, C.-C., Filipi, Z., Peng H., Assanis, D. Optimal Power Management for a Hydraulic Hybrid Delivery Truck, *Journal of Vehicle System Dynamics*, 42(1): 23-40, 2004..
- [8] Van de Ven J D, Olson M W; Li P Y. Development of a hydro-mechanical hydraulic hybrid drive train with independent wheel torque control for urban passenger vehicle. *Proceedings of the International Fluid Power Exposition*, Las Vegas, Nevada; 2008.
- [9] Filipi, Z. and Kim, Y. J. Hydraulic Hybrid Propulsion for Heavy Vehicles: Combining the Simulation and Engine-in-the-Loop Techniques to Maximize the Fuel Economy and Emission Benefits, *Les Rencontres Scientifiques de l'IFP, Advances in Hybrid Powertrains*, 2008.
- [10] Hui S, "Multi-objective optimization for hydraulic hybrid vehicle based on adaptive simulated annealing genetic algorithm", *Engineering Applications of Artificial Intelligence*, 23:27-33, 2010.
- [11] Black T, An overview of parameter control methods by self-adaptation in evolutionary algorithms, *Fundamenta Informaticae*, 35:51-66, 1998.
- [12] Ajith Abraham, Lakhmi Jain and Robert Goldberg (Eds.), *Evolutionary Multiobjective Optimization-Theoretical Advances and Applications*, Springer, Berlin, 2005. ISBN 978-1-84628-137-2.
- [13] Ramakrishnan R., Somashekhar S. Hiremath and M. Singaperumal. Power bond graph modeling of series hydraulic hybrid system, *International Conference on Fluid Mechanics and Fluid Power*, IIT Madras, Chennai, 608:1-8, 2010.
- [14] Young Jae Kim and Zoran Filipi, "Series Hydraulic Hybrid Propulsion for a Light Truck –Optimizing the Thermostatic Power Management, *Society of Automobile Engineerings*, 24:1597-1609, 2007.
- [15] Elder F.T. and D.R. Otis. Simulation of a hydraulic hybrid powertrain, *American Society Of Mechanical Engineers*, 73-ICT-50, 1973.
- [16] Young Jae Kim and Zoran Filipi, "Simulation Study of a Series Hydraulic Hybrid Propulsion System for a Light Truck", *SAE 2007-01-4151*, University of Michigan, 2007.
- [17] R. Ramakrishnan, Somashekhar S. Hiremath and M. Singaperumal. Theoretical investigations on the effect of system parameters in series hydraulic hybrid system with hydrostatic regenerative braking. *The Journal of Mechanical Science and Technology*, 26(5):1321-1331, 2012.
- [18] Kruse R.E., T.A. Huls, "Development of the Federal Urban Driving Schedule," *SAE Paper No. 730553*, 1973.
- [19] ModeFRONTIER, Version 3.1.0, ESTECO, Trieste, Italy.
- [20] Bäck T., Evolution Strategies Module R1.1 for ModeFRONTIER., *Technical Report 2004-05*.



# Aerospace Applications



# **A Robust Adaptive Hydraulic Power Generation System for Jet Engines**

G. Jacazio, A. Mornacchi, P. Ronco, and M. Sorli

Department of Mechanical and Aerospace Engineering, Politecnico di Torino, Italy

E-mail: giovanni.jacazio@polito.it, andrea.mornacchi@polito.it, pierantonio.ronco@polito.it, massimo.sorli@polito.it

## **Abstract**

The paper presents an innovative hydraulic power generation system able to enhance performance, reliability and survivability of hydraulic systems used in military jet engines, as well as to allow a valuable power saving. This is obtained by a hydraulic power generation system architecture that uses variable pressure, smart control, emergency power source and suitable health management procedures. A key issue is to obtain all these functions while reducing to a minimum the number of additional components with respect to the conventional hydraulic power generation systems. The paper firstly presents the state-of-art of these systems and their critical issues, outlines the alternative solutions, and then describes architecture, characteristics and performance of the hydraulic power generation system that was eventually defined as a result of a research activity aimed at moving beyond the present state-of-art in this field.

**Keywords:** Hydraulic power generation, adaptive pressure, energy saving, jet engines, health management

## **1 Problem statement**

Jet engines of several military aircraft are equipped with hydraulically powered actuation systems controlling the angular position of the stator blades of the high pressure compressor (VIGV = Variable Inlet Guide Vanes actuators) and actuation systems controlling the throat and exhaust areas of the nozzle (VEN = Variable Exhaust Nozzle actuators). Furthermore, the engines of some recent military aircraft are also capable of vectoring the thrust, which is typically obtained by individually controlling the positions of the VEN actuators placed around the engine nozzle. The nozzle actuators outputs are connected to a linkage mechanism which moves the nozzle petals such to orientate the flow of the exhaust gases, and hence the thrust, in the required direction.

The hydraulic power necessary for the operation of these actuators is obtained by a hydraulic power generation unit (HPGU) whose pump is driven by a shaft of the engine accessory gearbox, and an autonomous hydraulic circuit is thus created in the engine, which is separated from the aircraft hydraulic system. The engine hydraulic system uses a different oil, better suited for high temperature operation.

A few critical issues are associated to engine hydraulic systems and to their operation. Firstly, the system components operate in a severe temperature environment. The internal heat generation associated to the system operation, in combination with high temperatures of the surrounding air and of the components mounting points, creates a heavy thermal burden on the fuel cooled oil heat

exchanger, with a resulting high temperature of the hydraulic fluid. This makes the system components (in particular the seals) more prone to damages, and reduces the bulk modulus of the hydraulic fluid with an ensuing worsening of the servoloops stability margins. Secondly, a loss of the hydraulic pressure leads to a loss of system operation. A loss of the system pressure may have several origins, but the most likely ones are by far: a pump failure, or a lack of hydraulic fluid due to a progressive depletion of the hydraulic reservoir resulting from external leakages. The engine design is normally such that in case of loss of system pressure, the VIGV and VEN actuators are driven by the aerodynamic loads to a fail-safe position preventing catastrophic consequences, but at the same time leading to a loss of engine thrust. This is a major, but still acceptable failure for a two-engine aircraft, but it becomes hazardous for a single-engine aircraft. A possible way of mitigating the loss of system pressure is to use the hydraulic power supply only for the VEN actuators, while using fuel as a working fluid for the VIGV actuators; this would leave the VIGV actuators operational in case of failure of the hydraulic pump, thereby allowing the engine to still be partially controlled and develop sufficient thrust. It is a viable solution which however brings about a heavier system due to the relatively low pressure of the fuel system and the resulting large size of the VIGV actuators.

A research activity was therefore conducted with the intent of mitigating the criticality of the issues outlined above. In particular, the main objectives of the research were to define a hydraulic power generation and actuation system for a jet engine able to provide control of variable inlet guide vanes,

nozzle exhaust area and thrust orientation with the following characteristics:

- Use of high pressure hydraulic power source for all actuators
- Minimize the internal heat generation by making the system pressure adaptive to the actuators loads. It must be noticed that maximum loads occur for a very small fraction of the aircraft mission, thus unnecessary energy is generated and converted into heat by a constant pressure system
- Establish components characteristics and control laws such to ensure a dynamics of thrust vector control equivalent to that typical of the primary flight controls of a military aircraft
- Ensure a limited back-up power supply for allowing VIGV operation and controlled recentering of the nozzle actuators in case of loss of the system pump
- Implement prognostics and health management algorithms into the engine electronic control unit able to identify the precursors of critical system failures, thereby creating an alert before the failure develops

A hydraulic power generation and actuation system was hence defined to attain the above characteristics, and to do that while keeping the number of sensors to a minimum. The objective was not to add any sensor to those already present in the existing systems, and to take advantage of signals provided by sensors external to the hydraulic power generation system, but available in the engine electronic control unit. The system uses an engine driven variable delivery / variable pressure pump and an auxiliary, electrically driven, variable speed fixed displacement pump to assist the engine driven pump in ensuring the required frequency response for the actuators and as an emergency power source in case of failure of the main pump. In this latter case, a priority valve in the hydraulic distribution system favours the flow passage to the VIGV actuators that retain full performance while the nozzle actuators operate in a degraded mode. The system discharge pressure is established by an appropriate law embedded in the engine control electronics as a function of engine rating and nozzle actuators position; a pressure transducer located on the high pressure line provides the pressure signal necessary to close a pressure servoloop that operates by modulating the setting of the pressure compensator of the engine driven pump and the speed of the electrically driven pump. The modulation of the system pressure as a function of the actuators loads is a very effective way of reducing the heat generation, hence minimizing the power consumption and limiting the maximum temperature of the hydraulic fluid.

The signals provided by all system sensors (reservoir oil level quantity, temperature, filters differential pressure, pumps speeds, servovalves currents, actuators positions) are fused together and managed by appropriate algorithms in order to get a continuous indication of the system health and identify possible degradation patterns of its components.

All together, when compared with existing engine flow control systems, the one defined and thoroughly analyzed in the research activity looks more robust, less power

demanding and better maintainable. The system concept, architecture, characteristics and performance are outlined in the proposed paper.

## 2 State-of-Art

Jet engines are required to operate at different conditions during the aircraft flight and some sort of control of the airflow must be provided in order to ensure an optimal engine performance over the entire range of operating conditions. This section of the paper briefly outlines the main features relevant to the airflow control.

### 2.1 Variable inlet guide vanes

Most of military jet engines are provided with an actuation system that controls the angular position of the stator vanes of the compressor. By doing so, the airflow leaving the stator vanes impinges the rotor vanes of the subsequent compressor stage with the most suitable angle of attack, thereby ensuring a good aerodynamic efficiency, averting the compressor stall and enabling a wider range of engine operating conditions. The compressor vanes provided with the capability of changing their orientation are known as variable inlet guide vanes (VIGV). The stator vanes are actually equipped with levers rotating about a fixed hinge and connected at one end to a unison ring placed around the compressor [1]. By modulating the position of the unison ring, the stator vanes levers are rotated and the vane angle is hence varied.

### 2.2 Variable exhaust nozzle

A second feature used in several military jet engines to optimize the airflow is the variation of the nozzle flow area (VEN = Variable Exhaust Nozzle). The nozzle is the engine component where the gas jet accelerates from moderate speed in the turbine to the higher velocity of ejection from the engine to generate the thrust. A variable exhaust nozzle requires an actuation system to control the position of a mechanical element driving a series of linkages connected to the nozzle petals. The variation of the actuators output position eventually causes the variation of the nozzle area,

### 2.3 Thrust vectoring

In addition to variable geometry, some modern military jet engines are provided with thrust vectoring capability (TVN = Thrust Vectoring Nozzle), which allows to vary the direction of the thrust, thereby enhancing the aircraft maneuverability. Thrust vectoring technology has been successfully demonstrated on several programs to provide tactical maneuvering advantages in the very slow speed, very high angle-of-attack flight regime. This technology has matured to the extent that it is being incorporated into present day fighter aircraft designs [2-7].

### 2.4 Actuation systems

To accomplish VIGV, VEN and TVN functions actuation systems are required to control the position of the inlet guide vanes unison ring and of the nozzle petals such to obtain the

desired guide vanes angle of attack, nozzle area and thrust direction. Three different actuation technologies can in principle be used:

- **Hydraulics:** A dedicated hydraulic power generation unit with an engine driven pump provides high pressure hydraulic power supply to the actuators
- **Fueldraulics:** The actuators are supplied by pressurized fuel drawn from the engine fuel system
- **Electrical:** Electromechanical actuators accept the controlled electrical power supply from the engine electrical system

Aircraft engines that are provided only with VIGVs, but do not have nozzle variable exhaust area control typically use fueldraulic actuators because the loads are small and the size of the actuators is acceptable and can be accommodate in the engine envelope also if the fuel system pressure as low as 6-7 MPa.

Studies have been recently conducted on VIGVs controlled by electromechanical actuators [8] within the research activities on a more electric engine, but no application has so far followed. When nozzle control is required, fueldraulics is not any longer a viable technology because the low pressure of the engine fuel system would lead to an unacceptable large size of the actuators.

Electromechanical actuation technology, though appealing for several reasons, still falls short of meeting the envelope and safety requirements for the nozzle actuators performing either VEN or combined VEN + TVN functions. The critical issues of electromechanical actuation for these applications are the envelope constraints in the nozzle area, the thermal management and the possibility of actuators seizure, that could lead to a hazardous condition for a single engine aircraft.

For these reasons, hydraulic actuation is the only technology presently used in engines with VEN, or VEN+TVN capability. The research activity presented in this paper was focused to engines featuring a VEN, or a VEN+TVN in addition to the VIGVs, thus hydraulic actuation was the technology being considered.

## 2.5 Hydraulic power generation

Different architectures of hydraulic power generation systems can be considered for providing the hydraulic power supply to the engine actuators. Firstly, the overall hydraulic actuation system architecture can be based on a valve controlled system in which the actuators flows are controlled by throttling the flows by means of servovalves, or on a pump controlled system in which individual overcenter variable delivery pumps interface with the corresponding actuators. Although this second concept has the merit of automatically adapting the pumps delivery pressures to the actuators loads, it leads to a too heavy and expensive system because of the large number of pumps; moreover, the continuous tare flow of the servovalves controlling the variable delivery mechanisms of the pumps reduces the overall energy saving achievable from the pump control concept.

The solution typically used for the hydraulic power generation units (HPGU) of engine hydraulic systems is thus to have a pressure compensated, variable delivery pump providing the constant pressure variable flow required to move the actuators, plus the flow necessary to compensate the internal leakages. These HPGUs are sized on the basis of the maximum actuators speed and load determining the maximum flow and pressure to be provided by the HPGU. This sizing ensures that the actuators performance is attained, but does not optimize the energy consumption. The combination of actuators maximum speed and load typically occurs for a very limited portion of the aircraft flight envelope and may last only a few percent of the total aircraft flight time. When loads lower than maximum act upon the actuators, energy is lost through the control valves and heat is generated. Heat is rejected from the engine hydraulic system to a fuel cooled heat exchanger, but there are flight conditions in which the fuel entering into the heat exchanger is already at high temperature, which thwarts the cooling of the hydraulic fluid. Minimizing the heat generation is therefore paramount for the engine hydraulic systems.

## 2.6 Existing solution for heat load reduction

A load sensing hydraulic system seems the logical solution for reducing the heat generation. These systems have been extensively used in industrial and earth moving machinery applications, but are less suitable for the requirements typical of the jet engine hydraulic systems that supply servoactuators requiring a high frequency response. A viable solution for reducing the heat generation of a jet engine hydraulic system was however developed for the air flow control system installed on a reheated turbofan engine for a front-line fighter aircraft and is described in [9]. An analysis of this system is presented in [10]. This hydraulic system supplies the VIGV and the VEN actuators, and uses a variable delivery / variable pressure pump in which a modified pump pressure compensator changes the compensation pressure as a function of the load acting upon the VEN actuators, which are mechanically synchronized and controlled by a single servovalve.

The flow required for the VEN actuators operation is an order of magnitude greater than that required for the VIGV operation; therefore, this hydraulic system was designed to make the pump delivery pressure dependent only on the VEN actuators load. The pump delivery pressure varies in a well defined range depending on the VEN actuators loads and the VIGV actuators were sized to be capable of providing full performance also for the minimum pressure condition. This architecture of the hydraulic system has the merit of allowing a great reduction of heat generation with a very simple design; it leads to a slight greater size of the VIGV actuators, which is however acceptable due to their low absolute dimensions. When all internal losses of the hydraulic system are accounted for, including the pump frictional losses, the heat generation of a variable delivery / variable pressure system for a typical flight mission is well below that obtained from a conventional constant pressure system.

This variable delivery / variable pressure hydraulic system is therefore a good solution for a reheated turbofan engine equipped with VEN and VIGV actuators, and when the aircraft is provided with two engines. For the case of a single engine aircraft this system becomes critical since the loss of the hydraulic power supply resulting from a pump failure would lead to the inability of controlling the VIGVs, which could result in an engine shutdown and thus to a flight safety critical condition.

Moreover, this same hydraulic system is good for an air flow control system in which four VEN actuators are mechanically synchronized and controlled by a single servovalve, but it falls short of optimizing the delivery pressure for engines with TVN capability, in which four servoactuators are independently controlled by four servovalves.

Devising a new architecture for an engine hydraulic system suitable for single engine operation and for TVN control, which is also minimizing the heat generation was hence the objective of the research activity described in this paper.

### 3 Smart adaptive system architecture

#### 3.1 Objectives

While defining the new HPGU architecture, the following main objectives were addressed:

- The engine driven pump is the component with the highest failure rate in the existing systems
- Minimizing the heat generation is paramount
- It is desirable that TVN control meets the dynamic response requirements of primary flight controls in order to enhance the aircraft maneuverability and also provide a backup in case of primary flight controls failure
- Control of the VIGV has priority over VEN/TVN control because loss of VIGV control could lead to a loss of engine thrust and to a flight safety critical condition for a single engine aircraft
- Probability of loss of hydraulic power supply to either VIGV or VEN/TVN servoactuators must be lower than  $1 \times 10^{-7}$  per engine operating hour, whilst probability of total loss of operation of VIGVs must be lower than  $1 \times 10^{-9}$  per engine operating hour
- Maintainability improvement over existing systems is desired
- HPGU operation is controlled and monitored by a dual Digital Engine Control Unit (DECU)

The new HPGU architecture was hence defined such to meet the above objectives

#### 3.2 HPGU architecture

The architecture of the HPGU is shown in the diagram of Fig. 1. The overall system is single hydraulic with dual electrical control, but an electrical backup actuation is

provided to the VIGVs to ensure that the flight safety target is met.

The hydraulic fluid is stored in a bootstrap type self-pressurizing reservoir, consisting of a differential area piston in which the high pressure delivered by the pumps is provided to the low area side of the piston. The resulting force is balanced by an equal force acting in the opposite direction on the large area side of the piston, which determines the value of the pressure of the hydraulic fluid stored in the reservoir. With a ratio of 40 between the large and low areas of the differential piston, a reservoir pressure of 0.5 MPa is obtained for a delivery pressure of 20 MPa. That reservoir pressure is sufficient to avoid cavitation at the pumps suction for any operating condition, including start up at very low temperature. The reservoir accepts the return fluid from the hydraulic system and has an additional port for connection to an overfill/overtemperature relief valve that opens in case of inadvertent overfilling the hydraulic circuit, or of excessive volumetric expansion of the hydraulic fluid caused by abnormal high temperature resulting from HPGU internal failures. Opening of the relief valve prevents a fracture of the reservoir with the loss of the hydraulic system. It must be noticed that when the system is filled up on ground with the hydraulic fluid the plug placed soon downstream the overfill/overtemperature relief valve is removed and the corresponding port is connected to the reservoir of the ground support hydraulic unit. Therefore, if the reservoir is inadvertently overfilled and the reservoir piston is forced against its mechanical stops, the relief valve opens and the hydraulic fluid is returned back to the external reservoir, thereby preventing any external spillage. When the hydraulic system is operating, if an abnormal volumetric expansion forces the reservoir piston against its mechanical stops and the relief valve opens, the plug is now in place and the pressure increase causes a safety disc to fracture and the hydraulic fluid is vented overboard. After the excess volume has been vented, the pressure in the reservoir is reduced and the relief valve closes preventing any further passage of the hydraulic fluid and thus a depletion of the hydraulic system. Operation can then continue unabated. A visual indicator placed in the overboard vent line allows the maintenance crew to detect that hydraulic fluid spillage has occurred in flight and take the necessary maintenance actions.

The reservoir is provided with a hydraulic fluid level sensor, a low hydraulic fluid level switch and a temperature sensor. The signals provided by these sensors and switches are used by the health usage and monitoring system outlined at the end of the paper.

Hydraulic pressure is generated by two pumps: an engine driven pump and an electrically driven pump. The flows delivered by the two pumps are eventually summed upstream of the high pressure filter unit.

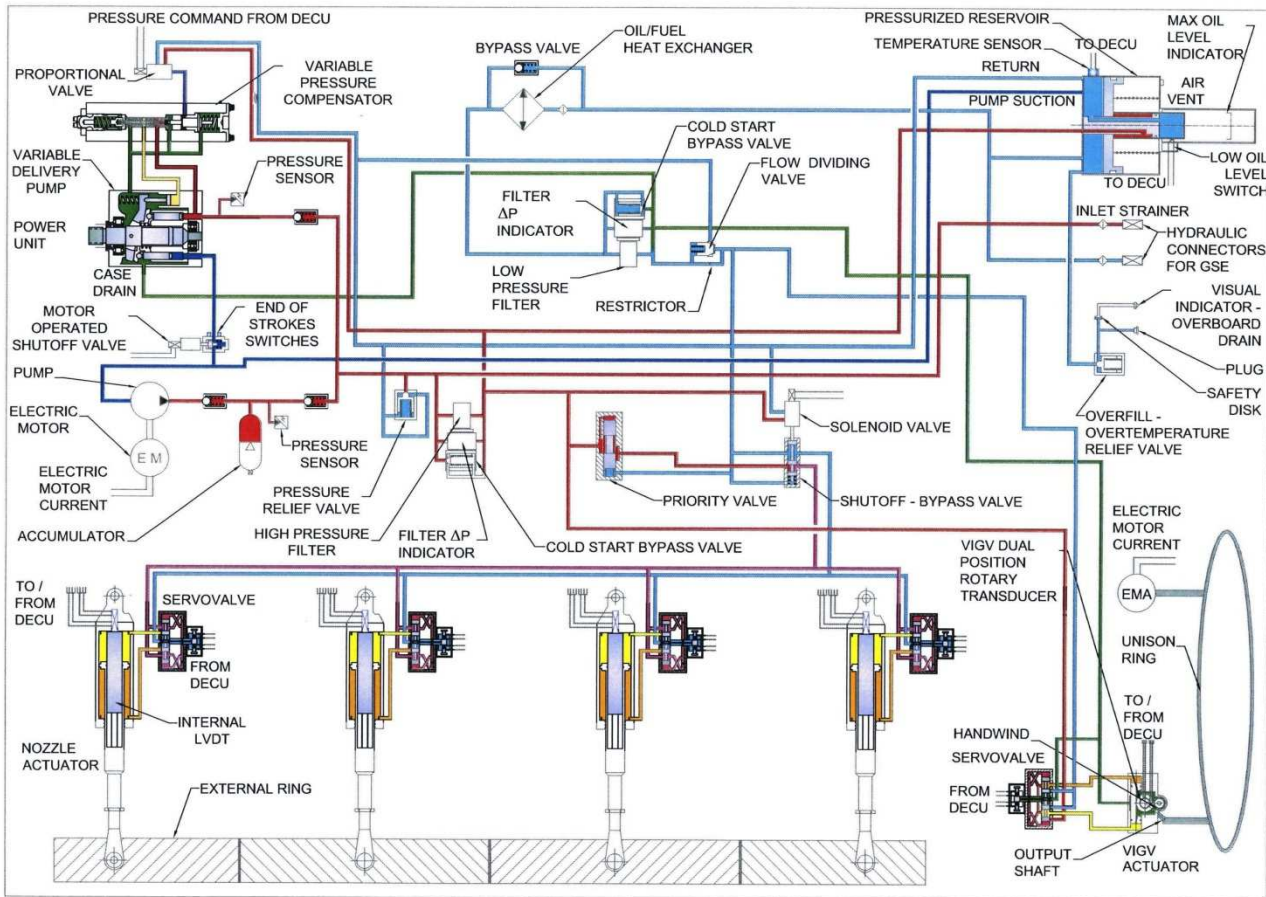


Figure 1: System block diagram

The engine driven pump is the primary pump of the hydraulic system; it is an axial piston variable delivery, pressure compensated pump mechanically connected to a shaft of the engine accessory gearbox. An important feature of the engine driven pump is that it uses a modified pressure compensator able to change the compensation pressure according to the actuators loads. The variable pressure compensator is a modified version of the conventional pressure compensator. A pilot pressure signal acts on an auxiliary piston which in its turn exerts a force on the compensator spool that is a function of the pilot pressure. The end result is to change the preload of the pressure compensator spring, thereby making the pump discharge pressure a function of the pilot pressure.

A pressure transducer located on the pump discharge line measures the pump discharge pressure and provides this information to the DECU. The pump compensator pilot pressure is generated by a 3-way pressure control valve accepting the electrical command from the DECU. This arrangement enables the DECU to vary the pump discharge pressure according to the actuation system needs as it will be described in the following section 4. A check valve downstream of the pressure transducer prevents a reverse flow from the hydraulic system to the engine driven pump.

The electric driven pump acts as an auxiliary unit for the hydraulic system; it is an axial piston, fixed displacement

pump driven by a speed controlled brushless dc electric motor. A gas charged accumulator is placed on the delivery line of the electric driven pump; the delivery line downstream of the accumulator is then connected to the delivery line of the engine driven pump upstream of the high pressure filter unit. A check valve prevents a reverse flow from the hydraulic system back to the accumulator. A pressure transducer measures the accumulator pressure and provides this information to the DECU that eventually controls the electric motor speed to maintain the accumulator pressure at the required value.

The control of the hydraulic fluid cleanliness is performed by high pressure and low pressure filter units. The high pressure filter unit consists of a filter element with a  $\beta_{200} = 3 \mu\text{m}$  and a differential pressure transducer. The high filtering grade is recommended to protect the actuators servovalves and ensure their correct operation over the entire system life. The differential pressure transducer provides indication of the pressure drop through the filter enabling the DECU to monitor the HPGU health as it will be outlined in section 5. No bypass valve is used for the high pressure filter unit because of the high sensitivity of the actuators servovalves to contamination. If the filter creates a large pressure drop, also if temporary, it is preferable to accept a reduction of the actuation systems performance rather than risk to contaminate the actuators servovalves.

The low pressure filter unit consists of a flow dividing valve, a filter element with a  $\beta_{200} = 10 \mu\text{m}$ , a differential pressure transducer and a bypass valve. The flow dividing valve consists of a spring loaded pressure relief valve and a restrictor placed in parallel. The flow dividing valve accepts the return flow from the actuators at its inlet and divides it into two output flows. If the inlet flow is small, as it is for most of the operating time, the flow passes entirely through the restrictor because the pressure drop created by the passage of this flow through the restrictor is lower than required to open the relief valve. If the actuators are commanded to move such to create a large flow, the pressure drop through the restrictor exceeds the limit of the relief valve that then opens bypassing the excess flow directly to the oil/fuel heat exchanger. In this case, part of the hydraulic fluid is not filtered by the low pressure filter, but this is not detrimental for the hydraulic system operation. The purpose of the low pressure filter is in fact to protect the pump from excessive wear, which is a progressive process. The passage of a limited quantity of unfiltered hydraulic fluid from the return line to the reservoir and eventually to the pump suction does not harm the pump operation, nor contribute significantly to the pump wear since the contaminants entrained by this flow will be eventually captured by either the high or low pressure filters as the fluid continues to circulate through the hydraulic system. Moreover, the contamination level of the flow returning from the actuators is normally low, and it is thus acceptable that occasional return flow spikes are not filtered. On the contrary, the drain flows from the two pumps are routed directly at the return filter inlet since they carry most of the contaminants generated by the wear of the pumps moving parts.

A differential pressure transducer senses the pressure drop through the filter element and provides the relevant signal to the DECU for monitoring the HPGU health status. A bypass valve is placed in parallel to the filter element to prevent an excessive backpressure in the return line in case of actuators operation during a very cold start, or of filter element clogging. An excessive backpressure in the return line could lead to a damage of the return line components of the hydraulic system, including the servovalves return paths. Opening of the low pressure filter bypass valve is signalled by a visual indicator to alert the maintenance crew; the visual indicator is provided with a thermal lockout to avoid its activation at low temperature since opening of the bypass valve in that condition is not an abnormal behaviour.

The above described configuration of the low pressure filter unit offers the advantage of ensuring an efficient control of the hydraulic fluid cleanliness with a low size filter element, which entails lower HPGU size, weight and reduced maintenance costs. The mean flow through the hydraulic system during a flight is typically lower than 10% of the maximum flow, hence a much greater filter would be required if designed to accept the rated system flow.

The total return flow leaving the low pressure filter unit passes through a fuel cooled oil heat exchanger which is also provided with a bypass valve to prevent excessive pressure drop in case of system operation during a cold

start-up. It must be noticed that the fuel used as a coolant for the hydraulic fluid of engine hydraulic system has already been used to cool other aircraft system and may enter into the heat exchanger at a relatively high temperature; this makes highly important to minimize the energy losses in the engine hydraulic system to limit insofar as possible the maximum temperature of the hydraulic fluid.

A system pressure relief valve is placed upstream of the high pressure filter unit with the purpose of protecting the hydraulic system from abnormal pressures that could arise as a result of abnormal transients of the actuation systems, or of a failure of any of the two pumps. Section 5 will describe the recovery actions in case of a pump failure.

A motor operated shutoff valve is placed on the suction line of the engine driven pump. When open, this valve has a large enough passage to create minimum pressure drop, thereby avoiding any risk of cavitation at the pump suction. The purpose of this valve is to isolate the engine driven pump in case of its failure. The shutoff valve is provided with end-of-travel switches to allow a periodical check of its operation, thereby avoiding dormant failures.

The clean high pressure fluid leaving the high pressure filter is directed to a priority valve whose purpose is to ensure that the VIGV servoactuator always has the hydraulic supply fluid necessary for its operation. The priority valve is a 3-way valve accepting the hydraulic fluid from the high pressure line and directing it toward the VIGV and the VEN/TVN actuators. The hydraulic system is sized such that under normal conditions both VIGV and VEN/TVN actuators receive all necessary flow for their operation. However, in case of reduced flow delivery, the priority valve progressively closes the passage of the VEN/TVN actuators line, hence throttling the flow to these actuators while leaving the VIGV flow unabated. This function is obtained by sensing the pressure in the hydraulic line connected to the VIGV servoactuator pressure supply. If this pressure decreases below 20 MPa, the priority valve spool moves in the direction of closing the port of the hydraulic line connected to the VEN/TVN actuators pressure supply.

A solenoid operated shutoff/bypass valve is placed on the supply line to the VEN/TVN actuators which consist of servovalve operated linear hydraulic actuators, each provided with a position transducer. The purpose of this valve is to cut off the hydraulic power supply to these actuators in case of a failure, thereby inhibiting their operation and isolating the VEN/TVN part of the entire system from the hydraulic power supply. At the same time, the supply and return lines downstream of the shutoff/bypass valve are interconnected, which allows the aerodynamic loads acting on the nozzle to bring back the actuators to an aligned, fail safe position..

The HPGU has two hydraulic fittings for connection to an external ground support equipment which is used to fill the system with the hydraulic fluid and circulate it through system passageways, pipes and components to ensure a complete air removal.

### 3.3 Nozzle servoactuators

Four linear hydraulic servoactuators placed around the engine nozzle are used to perform VEN and TVN control. Each of the four servoactuator is comprised of a slightly unbalanced area linear hydraulic actuator whose flow is controlled by an electrohydraulic servovalve. A small bypass orifice placed across the servovalve control ports allows the actuator recentering under the external pressure loads in case of loss of hydraulic pressure, and helps the position servoloop stability. The two servovalve coils are independent and accept the control current from the two separate sections of the DECU. A dual electrical position transducer placed inside the piston rod provides a dual redundant position indication to the DECU, which is used both to close the position servoloop and to monitor the system operation.

The unbalanced area configuration for the nozzle actuators entails more reservoir volume, but on the other hand it greatly reduces the actuators length and allows the installation of the position transducer inside the actuator, which is beneficial for the transducer because of the hot environment around the engine nozzle.

### 3.4 VIGVs servoactuators

It was stated in paragraph 3.1 that one of the system objectives is to keep the probability of total loss of VIGVs operation lower than  $1 \times 10^{-9}$  per engine operating hour. This will allow the applicability of this system to a single-engine aircraft. Although the HPGU architecture is based on two pumps, meeting the  $1 \times 10^{-9}$  probability of total loss of the VIGVs operation is not possible unless the two VIGV actuators are connected to two separate HPGUs. A possibility could be to connect one VIGV actuator and the VEN/TVN actuators to the main HPGU, and the other VIGV actuator two an auxiliary HPGU. Although this second HPGU could be miniaturized, still its weight, envelope and cost would be unacceptable, because it would anyhow be a complex unit made up by several components to simply provide the hydraulic power supply to a small servoactuator using a limited amount of flow.

The most logical solution is to have a VIGV actuator connected to the HPGU acting as a master actuator, and a second VIGV actuator consisting of a fuelraulic, or of an electromechanical actuator, acting as a backup actuator. The author preferred choice for the backup actuator is for an electromechanical actuator because it will eventually lead to lower size and weight. In case of failure of the master actuator, it is necessary to control the position of the VIGVs, and the actuator must be able to develop the full load, but the actuation rate could be reduced. There are engine operating conditions in which the fuel pressure is low, which requires a large area of a fuelraulic actuator to balance the VIGV load. On the contrary, an electromechanical actuator can be designed as a geared system in which a small motor torque is amplified by a compact gear reducer, while speed is reduced. An optimum compromise can eventually be reached between motor size, gear ratio and output speed such to make the actuator able to

operate against the maximum load at a reduced, albeit still acceptable, rate.

The solution eventually considered in this research activity was hence to have a hydraulic master actuator and an electromechanical backup actuator. The hydraulic master actuator is a servovalve controlled actuator with a rotary output and a dual electrical rotary position transducer. The servovalve has configuration and operational characteristics identical to those of the nozzle actuators servovalves, and a small bypass orifice is also placed across the servovalve control ports.

The electromechanical actuator consists of a brushless dc motor with its electric motor drive and a gear reducer. A resolver on the motor shaft provides rotor position information to the electric motor drive to perform the appropriate switching of the motor currents and close a motor speed loop. An absolute dual electrical position sensor provides position indication to close the position servoloop. The electric motor power supply is automatically switched to the active electrical lane.

### 3.5 System architecture summary

The architecture of the entire system described in the above paragraphs is then:

- Single hydraulic HPGU with dual pressure supply generation and pressure adaptiveness to the actuators loads
- Nozzle servoactuators consisting of servovalve controlled linear hydraulic actuators, each provided with an internal position transducer for VEN/TVN control
- Master and auxiliary VIGV servoactuators for VIGV position control. The master servoactuator is a servovalve controlled hydraulic actuator with a rotary output, the auxiliary servoactuator is an electromechanical actuator. The actuators are provided with a rotary position transducer
- System control is performed by a DECU consisting of two independent, mutually isolated, lanes operating in an active-standby mode
- All sensors and switches are dual electrical interfacing with the two DECU lanes
- The electrical power supply to the electric motors of auxiliary pump, engine pump suction shutoff valve and auxiliary VIGV servoactuator is automatically switched to the electrical supply of the active DECU lane

## 4 System operation

### 4.1 Hydraulic power generation

Under normal operating conditions the hydraulic power is simultaneously provided by the engine driven and by the electric driven pumps. The engine driven pump is a variable delivery unit whose input shaft speed depends on the engine speed and is not a controlled variable. The pump is hence designed with a maximum displacement such to provide the maximum flow also for the minimum speed condition that occurs when the engine is in ground idle.

The electric driven pump is a fixed displacement unit whose shaft speed is controlled by regulating the electric motor speed. The pump is sized to provide the flow necessary for full rate operation of the VIGV servoactuator and for 10% rate of the VEN/TVN servoactuators.

The hydraulic fluid side of the gas charged accumulator is connected to the portion of the electric pump discharge line between two check valves. In this way, the liquid side of the accumulator can be filled only by the hydraulic fluid delivered by the electric motor pump and not by the engine driven pump. This is instrumental in allowing a good dynamic operation of the VEN/TVN servoactuators under certain operating conditions as it will be described later in this section. The accumulator can then provide pressurized fluid flow to the system pressure line when this pressure falls below the pressure prevailing in the accumulator.

## 4.2 System pressure control

One of the key features of the HPGU is the adaptation of the system pressure to the loads acting on the VEN/TVN actuators. The loads acting on these actuators are not related to the loads acting on the VIGV master actuator; therefore, this actuator is sized to develop the full load when the system pressure is at the minimum of its variation range. A tradeoff analysis led to the conclusion to set the variation range of the system supply pressure from a minimum of 21 MPa to a maximum of 35 MPa. Pressures lower than 21 MPa would have led to a too large VIGV master actuator, while the upper limit of 35 MPa is the present state-of-art for aircraft hydraulic systems.

The value of the required system supply pressure is not determined by measuring the loads acting on the VEN/TVN actuators, or by measuring the pressure differentials across the control lines of those actuators. That solution is in principle possible, but would have led to a very complex system, with a large number of components and a large number of wires, with added weight and reduced reliability. The solution devised for this system is to implement an engine model in the DECU that computes the values of the loads acting on the VEN/TVN actuators based on the engine conditions. In fact, the DECU has all the necessary information to perform that calculation. It has available the engine rating, the aircraft speed and altitude, the fuel flow rate as well as command and position of all actuators. An appropriate algorithm can thus perform real time computation of the actuators loads and hence generate the value of the optimum system supply pressure for that operating condition. A similar concept is proposed for the hydraulic system of high-speed tilting trains [11].

When the loads on the VEN/TVN actuators are below a limit, the system pressure is kept constant at 21 MPa; this pressure is sufficient to ensure the full performance VIGV operation up to the maximum load and for full performance VEN/TVN operation up to the limit load, which normally occurs for more than 90% of the flight time. When the VEN/TVN loads grow higher than the limit, the DECU issues an appropriate signal to increase the system pressure as necessary. This is accomplished by creating two pressure control loops: one for the engine driven pump and one for the electric driven pump.

The pressure control loop of the engine driven pump uses as a feedback signal the pressure transducer of that pump discharge line; the pressure error is processed by a proportional control law to generate the electrical input signal to the pressure control valve modulating the pilot pressure for the pump pressure compensator. As a result, the pressure compensator setting is changed and the engine pump discharge pressure is accordingly modified.

A pressure control loop is also created to control the discharge pressure of the electric driven pump. Again, the pressure transducer of that pump discharge line provides the feedback signal to close the pressure servoloop and generate the pressure error which is processed by a proportional control law. The resulting control signal is accepted as a speed signal by the pump electric motor drive; the pump speed is hence adjusted such to maintain the discharge pressure at the required value.

Since the output flows of the two pumps are eventually merged, a concern is the possible insurgence of a hunting effect between the two parallel pressure control loops. To avoid that, the pressure command for the engine driven pump is set by the DECU to a value slightly greater than that for the electric driven pump. For the prevailing load conditions the pressure command for the engine driven pump is then set at 21 MPa, while that for the electric driven pump is set at 20.5 MPa. Therefore, in these conditions the main function of the electric driven pump is to keep the accumulator pressurized at 20.5 MPa, while the actuators flow is provided by the engine driven pump. However, should the system pressure temporarily fall below 20.5 MPa, the accumulator will deliver the pressurized fluid volume necessary to maintain the system pressure at 20.5 MPa and ensure the actuators dynamic response. It must in fact be noted that the time required by the variable delivery mechanism of the engine driven pump to go from zero to full displacement could be 30 to 40 milliseconds. Without the reserve fluid provided by the accumulator, this would result in some initial delay of the VEN/TVN actuators response following a large step command, while the presence of the accumulator ensures a fast dynamic response.

If conditions are detected by the DECU requiring a system pressure above the 21 MPa base threshold, the pressure command computed by the DECU algorithms is provided to the two pressure control loops. As it was mentioned before, the flow delivered by the engine driven pump cannot be directed to the accumulator, that can only be replenished by the flow delivered by the electric driven pump. The reason for this solution is that if no check valve were present downstream of the accumulator, if a command is issued by the DECU to the VEN/TVN servoactuators simultaneously to the variation of the pressure set, the actuators response could suffer from a large delay because a large portion of the engine driven pump flow would be drawn to replenish the accumulator. It is therefore much better to allow all the engine driven pump flow to be available to the actuators while leaving to the electric driven pump the task of providing the amount of fluid volume necessary to bring the accumulator pressure to the required value. Of course, the

VEN/TVN actuators dynamic response for this particular operating condition might fall short of entirely meeting the requirements because of the time response of the variable delivery mechanism of the engine driven pump. However, this shortfall is negligible in most of the cases, and has some effect only when a very large step command is given to the nozzle actuators either for VEN or TVN operation.

Figure 3 shows the most critical condition of a nozzle initially aligned along the engine axis, which receives a full deflection command for which the actuators will be subjected to the maximum load and hence to the maximum pressure. When the DECU receives from the aircraft flight control system the new position demand, it converts it into a position command varying in time with a rate equal to the maximum design speed of the actuators and it simultaneously issues the new pressure command. The nozzle position command  $x_{setN}$  and response  $x_N$  for this severe condition, as well as the variation of the actuators and of the supply pressure are shown in Fig. 2. The actuator response has an initial maximum transient delay of about 100 ms due to the combined time delay of the supply pressure control system and variable delivery mechanism of the pump; the delay of the actuator response progressively reduces as the pump reacts. The 100 ms initial delay is large, but it is still acceptable for this type of command.

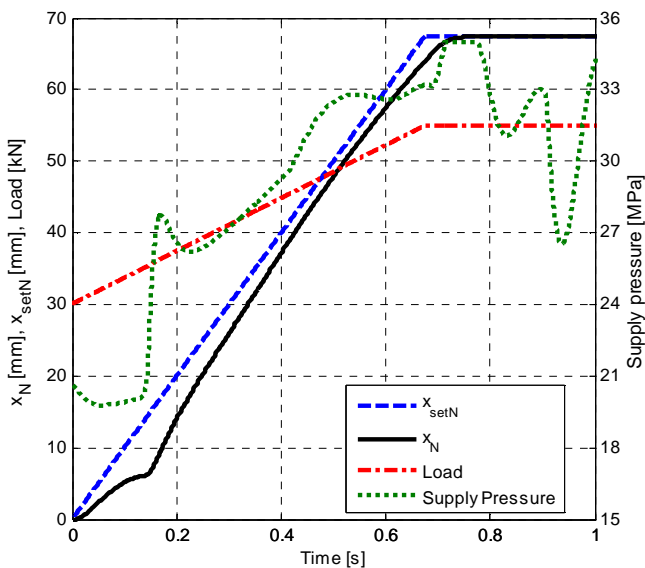


Figure 2: TVN transient following a full deflection command with associated actuators load increase from minimum to maximum

## 5 Performance

### 5.1 Mathematical model

The system performance was assessed for all range of operating conditions with the help of a dedicated mathematical model representative of the entire air flow control system. PI control laws with a small dead band and a saturation on the integrator path were used for VIGV and VEN/TVN position servoloops, while a simple proportional control was used for the pressure control loops.

The mathematical model was a "physical type" model and was implemented as a Matlab/Simulink software code. The model is of non-linear type and provides the values of the all state variables versus time. The independent variables are:

- Nozzle actuators position commands
- Variable inlet guide vanes actuators position command
- Nozzle and VIGV actuators loads
- Engine rating (pump speed)

The model accepts the oil temperature as a parameter and will thus compute the relevant characteristics of the resistance and capacitance of the hydraulic components. The model is essentially organized in different blocks. A *master block* reads the input variables and data, and then manages the simulation. At definite intervals of the simulation time the *master block* prints the value of all the main variables and stores most of them in a file for subsequent plotting. The other blocks are each dedicated to one of the subsystems and interface with the master block. A very detailed model was of each of the subsystem components was developed in order to obtain an accurate simulation. An example of the simulation accuracy reached by mathematical models of hydraulic components is presented in [12]. The DECU characteristics such as A/D converter resolution, recursion rate, computation time were duly addressed by the mathematical model.

### 5.2 Dynamic response

The results of the simulations showed the ability of the system to meet the time and frequency response requirements typical for a primary flight control of a front line aircraft. As an example, Fig. 3 shows the time response to a small step command to the nozzle actuators in VEN mode equal to 3% of the full actuators travel. The time required to reach the commanded position is equal to 25 ms in agreement with the specifications.

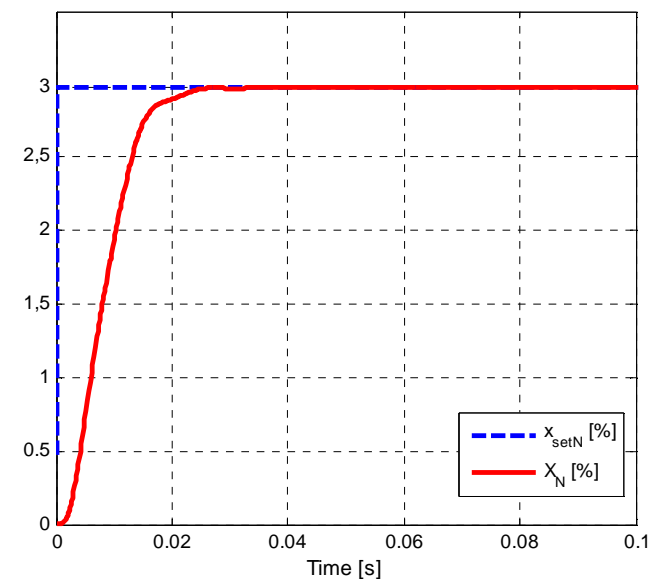


Figure 3: VEN transient for a small step position command

Figure 4 shows the time response to a large step command, equal to 30% of the full actuators travel. The time required

to reach the commanded position is in this case equal to 160 ms, which shows the ability of the nozzle actuators to operate very fast.

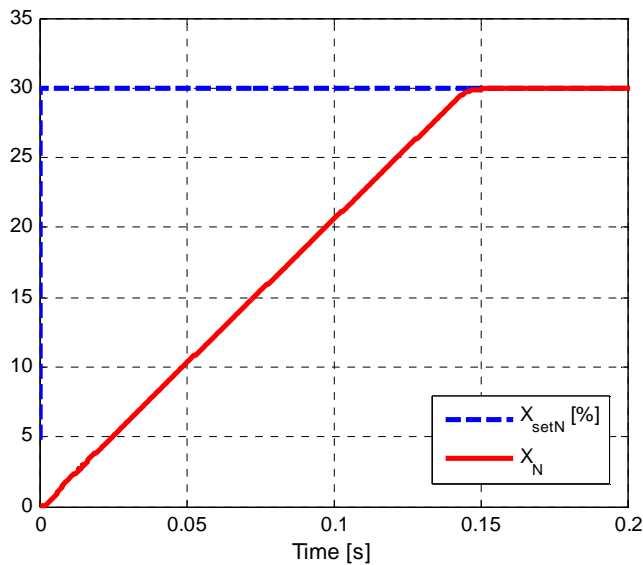


Figure 4: VEN transient for a large step position command

The following Fig. 5 shows the nozzle servoactuators frequency response when commanded in TVN mode. As it can be seen from the figure, the TVN servoloop has a 3 dB attenuation at 10 Hz and a 45° phase lag at 7 Hz, which are characteristics in line with primary flight control actuators requirements.

An even better dynamic performance is presented by the VIGV subsystem, both when commanded by the hydraulic master servoactuator (normal operating mode), or when commanded by the backup electromechanical actuator. Figure 6 shows the VIGVs frequency response for the case of operation with the backup electromechanical actuator.

### 5.3 Heat generation

Heat is generated in the hydraulic system from hydraulic and mechanical sources. Pressure losses of the fluid flow through the hydraulic lines, passageways and metering ports, as well as the leakage flows from high to low pressure side through the hydraulic components generate heat. Windage and tare losses originated by the pumps rotation are a second source of heat generation. Most of these power losses are dependent on the system supply pressure; in particular, the losses associated to the internal leakage are almost proportional to the square of the supply pressure.

Simulations were run to assess the average heat generation during different types of aircraft missions and an average heat generation for the variable pressure system equal to 60% of that for a constant pressure system was found. This reduction of heat generation is highly significant because it greatly reduces the average temperature of the hydraulic fluid with ensuing longer life and improved system reliability.

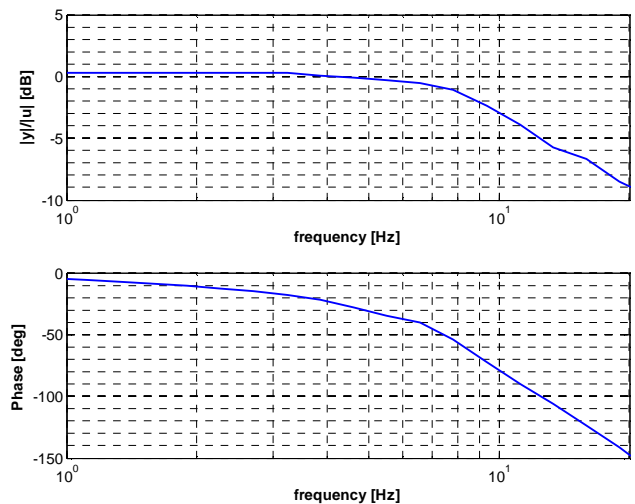


Figure 5: Nozzle servoactuators frequency response in TVN mode

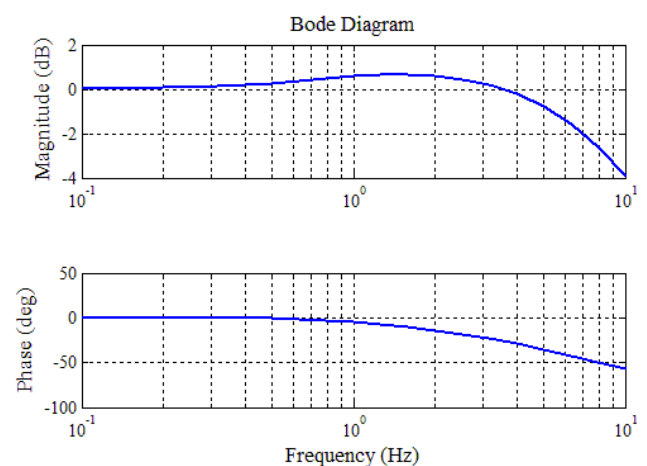


Figure 6: VIGVs frequency response when commanded by the backup electromechanical actuator

## 6 Failure behaviour

### 6.1 In-flight monitoring

The DECU uses the available information of the system status to perform a continuous monitor of the system behaviour in flight, detect failures that could impair the system performance and lead to potentially flight safety critical failures. If any of such failures is detected, the DECU takes the appropriate actions to isolate the failed component and reconfigure the system operating mode to allow a continued safe flight. The main failure cases are described hereunder. It must be emphasized once more that in case of failure ensuring the VIGVs operation is the primary objective.

### 6.2 Failure of a flow control component

All electrically operated valves and all sensors are dual electrical with the two electrical lanes interfacing with the two sections of the DECU. The two electrical lanes of the sensors are always active and the signals acquired by the

two sections of the DECU are mutually exchanged between them, so that each DECU section has available the information coming from both sensor lanes. The electrically operated valves work in an active/standby mode; if the active section fails, the control is switched to the other DECU section.

The functionality of the electrical parts of the control valves is continuously verified by performing the current wrap-around: the actually measured control current is compared with the current command. If an error is detected, the control is switched to the other electrical lane and the operation continues with full performance.

If a failure occurs of any of servovalves controlling the VEN/TVN actuators position, this is recognized as an abnormal, or uncommanded movement, or lack of movement of the VEN/TVN. In this case the solenoid operated shutoff/bypass valve is de-energized, which causes the valve to block the connection of the servovalves supply lines and to create a bypass and a connection with the return line for the actuators. In this condition, the internal pressure forces acting on the nozzle will eventually recenter the nozzle and lead it to a fail-safe position. It must be noticed that the VEN/TVN actuators, as well as the VIGV actuator, have a small bypass orifice across their control lines, which allows a slow movement under the external loads without compromising the dynamic response.

If the same type of failure occurs to the servovalve controlling the VIGV, there is no shutoff/bypass valve to isolate the VIGV servoactuator. The recovery action thus consists of totally removing the hydraulic power supply by switching off the electrically driven pump and by commanding the shutoff valve on the suction port of the engine driven pump to close. This will starve the pump and after the accumulator will be emptied by the internal leakages, there will no longer any supply pressure available. Together with these commands, the VIGV backup electromechanical actuator will be activated and will take control of the VIGV operation, while the VEN/TVN actuators will recenter as for the previous failure case. Of course, it would be possible to place a solenoid operated shutoff/bypass valve also on the VIGV supply line and allow a full system operation after a failure of the VIGV hydraulic servoactuator. However, the probability of failure of the VIGV hydraulic servoactuator is small and does not justify the additional weight, complexity and cost of another electrically operated shutoff/bypass valve.

The priority valve is a flow divider throttling the flow to the VEN/TVN actuators when necessary in order to keep full flow capability to the VIGV hydraulic actuator. It could fail in two ways: unnecessary throttling the flow to the VEN/TVN actuators, or not doing it when needed. In this second case, the VIGVs will not respond with the required dynamics and the DECU will activate the electromechanical actuator. The correct VIGV operation can thus be ensured, and appropriate troubleshooting on ground will allow to detect whether the root cause of the anomalous behaviour was a failure of the priority valve, or of the VIGV hydraulic servoactuator.

### 6.3 Failure of a pump

The engine driven pump can fail in several ways, however, all type of failures will eventually end up in:

- Lack of providing the pressurized fluid flow (could be for instance the case of fracture of the drive shaft)
- Uncontrolled flow delivery (could be the case of the pump hanger plate stuck in the maximum displacement position)
- Large internal leakage (could be the result of abnormal wear of the pump pistons)

The first of the above three failures cases is detected by a lack of pressure signaled by the relevant pressure transducer. If this failure takes place, the DECU will still provide commands to the VEN/TVN actuators, but at a greatly reduced rate to be compatible with the flow delivered by the electrically driven pump.

The second failure case will lead to an excess flow, an uncontrolled pressure increase and the consequent opening of the pressure relief valve. A large heat generation will occur very likely leading to an abnormal temperature increase. As long as the hydraulic fluid temperature remains below a safe limit, no action will be taken. When the temperature grows above the limit, the shutoff valve on the suction port is commanded to close, thereby starving the pump and the operation will continue with the electrically driven pump alone as for the previous failure case. A similar occurrence is for the third failure case of abnormally high internal leakage.

If the electrically driven pump fails, the same possible occurrences outlined above for the engine driven pump can eventually show up, though they can be originated from other causes, such as a failure of the electric motor or of its drive. Lack of providing the pressurized fluid flow will prevent the accumulator from being replenished, which could reduce to a minor degradation of the VEN/TVN servoactuators dynamic response, but leave full performance to the VIGV servoactuator. This failure is detected by a lack of pressure signaled by the relevant pressure transducer. An uncontrolled fluid flow, or an excessive internal leakage will likely remain undetected in flight because the low maximum flow rate deliverable by the electrically driven pump would probably does not entail an abnormal temperature increase for the hydraulic fluid. Should a too high temperature be actually reached, the same recovery action described for the engine driven pump failure will be taken. It could at first seem wrong to starve the engine driven pump, which is normally working, as a consequence of a failure of the electrically driven pump, but this action is effective because the internal leakage of the engine driven pump is a large source of heat generation. Therefore, bringing to zero that heat source is effective in limiting the temperature rise.

### 6.4 Failure of the filter units and of the heat exchanger

Filter units and heat exchanger are the system components contributing in maintaining a good condition of the hydraulic fluid. High pressure and low pressure filters have

a certain dirt holding capacity; when this is exceeded the pressure drop through the filter increases rapidly, which is signalled by the relevant differential pressure transducer. Since the dirt accumulation in the filters is not a sudden event, but a progressive phenomenon, when the pressure drop grows above the acceptance limit a warning is generated by the DECU, but enough pressure differential is left for the actuators, allowing a reliable operation for the remainder of the flight. In the very remote possibility of a complete sudden clogging of the high pressure filter, VEN/TVN will not be possible, but the VIGVs could still be operated by the electromechanical actuator. Sudden filter clogging of the return filter does not impair the actuators operation because its bypass valve will open allowing direct passage of the return fluid to the heat exchanger.

It was outlined in paragraph 3.2 that the low pressure filter unit includes a flow dividing valve that bypasses part of the return flow to the heat exchanger when this flow is greater than an established limit. If this valve fails closed, then a temporary larger than normal pressure develops in the return line during rapid VEN/TVN actuators movements, which could result in a reduction of the actuation speed. No corrective action is taken by the DECU, but a warning is generated for the maintenance crew to signal the anomalous behaviour. If the valve fails open, most of the return flow will not be filtered by the low pressure filter. Although undesired, this failure normally has limited consequences because the mostly contaminated hydraulic fluid flow is the drain flow from the pumps, which does not pass through the flow dividing valve and it is routed directly to the low pressure filter. A failed open failure of the flow dividing valve can be detected by the health usage and monitoring system mentioned in section 7 of this paper.

A reduction of the heat transfer capability of the heat exchanger is very unlikely; it could occur as a result of a partial or full clogging of the heat exchanger passageways, or of an anomalous condition on the fuel side, such as a very high temperature of the cooling fuel. Whatever that failure, the end result is an abnormal temperature increase of the hydraulic fluid. The corrective action is the same as for a pump failure: firstly, close the suction line of the engine driven pump; if this is not enough, shut down the electric driven pump and operate the VIGVs with the electromechanical actuator.

## **6.5 Failure of pressure and direction control components**

The pressure relief valve protecting the system from overpressures could fail in two modes: remaining closed in case of overpressures, or opening at low pressures. If the first failure mode (failed closed) occurs, this will anyhow be a second system failure: firstly there must be a component failure yielding an overpressure, and secondly the pressure relief valve failure. This combination of failures has a remote probability of occurrence, well below  $1 \times 10^{-9}$  per engine operating hour because the latency period between two check of the pressure relief valve operation must be duly taken into account. It must be in fact considered that the functionality of the pressure relief valve can be

periodically tested on ground by commanding a slow increase of the discharge pressure for the electrically driven pump. When the pressure corresponding to the relief valve setting has been attained, no further pressure increase should be measured because the relief valve will open. If a pressure increase above the relief valve setting is signaled by the pressure transducer, the test is immediately stopped and a relief valve failure is then signaled. However, should this combination of the above mentioned failures actually take place in flight, the pressure sensor of the failed pump which is the root cause of the excessive pressure build up will signal the abnormally high pressure and the flow from that pump will be brought to zero, either closing the pump suction (for the engine driven pump), or cutting off the electrical power supply (for the electrically driven pump).

If the pressure relief valve fails open, this will result in a decrease of the supply pressure below the normal minimum of 21 MPa and in an increase of the temperature of the hydraulic fluid. Depending on whether the pressure relief valve fails partially or fully open two different scenarios are possible. If the pressure relief valve is only partially open, then the priority valve will adjust the control areas for the VIGVs and VEN/TVN actuators such to ensure full performance of the VIGVs. A slower than commanded movement of the VEN/TVN actuators will be detected by the DECU and an alert signal is generated. If the pressure relief valve fails fully open, then the system supply pressure falls to a very low value and no further operation is possible with the hydraulic actuators. Operation of the VIGVs is then performed by the electromechanical actuator.

The HPGU includes two check valves that can fail either closed, or open. If any of the two fails closed there could be conditions in which not enough flow can be provided to the actuators. In this case, the priority valve will limit the VEN/TVN flow and the slower than commanded actuation will be detected by the DECU, thereby generating an anomalous behaviour alert. If the check valve of the engine pump delivery line fails open, this will allow a reverse flow from the system supply line back to the engine driven pump in case of simultaneous failure of that pump. The probability of combination of these two failures in flight is extremely remote because of the low failure probability of a check valve and because the check valve functionality can be tested during periodical pre-flight checks by looking at the indication of the pressure transducer of the engine pump discharge line when only the electric driven pump is activated on ground. Anyhow, should this remote combination of failures occur in flight, VIGVs operation can be ensured by their electromechanical actuator.

If the check valve on the accumulator output line fails open, this will lead to a partial degradation of the VEN/TVN dynamic response if they are commanded during a phase of increasing system pressure because part of the fluid flow delivered by the engine driven pump will be drawn by the accumulator, hence reducing the flow available to the actuators. The functionality of this check valve can also periodically verified in pre-flight after the engine has been started and the engine driven pump is running. A high pressure level can be commanded to the pressure control

loop of this pump, while a low pressure level is commanded to the pressure loop of the electric driven pump. If the accumulator pressure increases, that will be an indication of a failed open check valve.

## 6.6 Failure of the reservoir

The reservoir is provided with temperature and hydraulic fluid quantity transducer and with a low hydraulic fluid level switch. It also has a visual level indicator that can be used for a further check by the maintenance personnel. Aside of a structural failure, or of a seal failure that are discussed in the following paragraphs, a possible reservoir failure is the seizure of its piston that remains stuck in one position. In this case, if the system operation and the temperature variations would bring about a volume increase of the hydraulic fluid in the reservoir, such volume increase cannot be accommodated and the reservoir relief valve will first open, then the safety disc will spill the excess fluid volume overboard. This failure will eventually be detected by the health usage and monitoring system because no variation of hydraulic fluid level in the reservoir will be sensed in association with the VEN/TVN actuators movements. Those actuators are unbalanced area actuators and their movement entails a variation of the hydraulic fluid volume in the reservoir.

If the reservoir piston is stuck, but the operating conditions would bring about a decrease of the hydraulic fluid in the reservoir, there will be a decrease of the pressure at the suction ports of the pumps. This might lead, or not, to cavitation of one or both pumps and to anomalous actuators operation. If rapid variations of the actuators position are commanded, and hence large flows required, not enough flow could be available due to pumps cavitation. The priority valve will ensure the correct operation for the VIGVs actuator, but the VEN/TVN actuators will move at a slower than commanded speed. An alert signal is thus generated by the DECU, and the health usage and monitoring system will then identify the cause of the anomalous behaviour by analyzing the system response to the commands that the DECU will continue generating for the remainder portion of the flight.

## 6.7 Failure of the accumulator

A possible failure of the accumulator is the partial or total loss of the gas charge. If this happens, the accumulator function is lost, which results in a possible reduction of the actuators dynamic performance because the pumps dynamics comes into play when the actuators receive a new position command. The amount of dynamic performance reduction depends on the type of command generated by the DECU; deviations from the expected response are recognized and analyzed by the health usage and monitoring system, which provides a warning and a clue for troubleshooting to the maintenance personnel. A loss of the gas charge can be further confirmed by measuring the time necessary to rise the pressure at the system start-up when the electric driven pump is activated before the engine is started. If the gas charge is lost, there will be a noticeable reduction of the time needed to rise the pressure.

The same behaviour happens in case of a fracture of the membrane separating the gas from the liquid side of the accumulator. A possible additional consequence of this failure is the origin of an instability of the VIGVs and VEN/TVN servactuators caused by a large quantity of gas mixed with the hydraulic fluid. If an persistent actuators position oscillation is recognized by the DECU, the solenoid operated shutoff/bypass valve of the VEN/TVN actuators is first de-energized. If the oscillation persists in the VIGVs hydraulic servomotor, the supply pressure is removed by closing the shutoff valve on the engine driven pump suction port and stopping the electric driven pump. At the same time, the VIGVs electromechanical actuator is activated.

## 6.8 Failure of the components seals and components fractures

All hydraulic components have seals preventing internal and external leakages. A seal failure causing an internal leakage would eventually lead to more heat generation and some reduction of the maximum flow available for the actuators operation. If the additional internal leakage generated by a seal failure is small, that might remain undetected, but it will also not directly affect the system operation. However, in general a failure of an internal seal leads to a very large internal leakage with great reduction of the system capabilities and large temperature rise. For instance, if a 15 mm diameter cylinder seal fails and a 0.05 mm radial clearance is left open between piston and cylinder, a leakage flow of about 20 l/min develops for 21 MPa pressure differential. This is a huge amount of flow that will cause a very fast temperature rise, and the same recovery actions will be taken as for the case of the failed open pressure relief valve discussed in paragraph 6.5.

If there is a failure of an external seal, this will eventually lead to a depletion of the hydraulic fluid. A rapid depletion in flight will lead to the inability of the hydraulic system to operate, but the VIGVs can still be operated by the electromechanical actuator. A slow depletion can be signalled by the health usage and monitoring system, that will generate an alert signal allowing the maintenance personnel to check the system, identify the fault and repair it before the fault grows into failure during the following flights.

The same consequences of a large external leakage are caused by a fracture of any component of the hydraulic system.

## 6.9 Failure of the actuators

The most likely failure of a hydraulic actuator is a failure of any of its seals, which has been addressed in the above paragraph 6.8. A structural failure of its cylinder will lead to a loss of hydraulic fluid, which also has been addressed in paragraph 6.8, and eventually to a mechanical disconnection. This is also the case of a fracture of the piston rod, or of the actuator eye ends. A structural failure will thus be detected by a loss of VEN/TVN operation, or of VIGVs operation. However, if there is a failure of the

hydraulic VIGVs actuator, operation will continue under the action of the electromechanical actuator.

Failures of the servovalves controlling the actuators flows have been addressed in paragraph 6.2.

The VIGVs electromechanical actuator is used as a backup unit and its functionality is regularly checked in pre-flight to make sure that there are no dormant failures and that this actuator is thus able to ensure VIGVs operation if required to do so in flight.

### 6.10 Failure of transducers and switches

All transducers and switches are dual electrical and interface with the two sections of the DECU. The VEN/TVN and VIGVs position control loops operate in an active/standby mode, but the two electrical sections of the transducers are always active and provide the relevant signals to the two sections of the DECU that mutually exchange the informations. An individual monitoring of the transducers is continuously performed during the system operation. An effective monitoring is possible by analyzing the output signals of the individual transducers, by comparing the signals of the two sections of the same transducers, and by correlating the values of mutually related quantities.

## 7 Health usage and monitoring system

The Health Usage and Monitoring System (HUMS) has three main tasks:

- Detect failures in flight
- Check in pre-flight that all components are properly operating, including those that cannot be continuously monitored in flight
- Collect all available information and process it through dedicated algorithms to recognize possible slow degradations of the system components

If a failure is detected in flight, then the DECU takes the appropriate corrective actions to allow a continued safe flight, as outlined in the paragraphs of section 6.

Appropriate pre-flight checks are performed before flight initiation to ensure that no failures are present, and built-in-tests are run to discover potentially dormant failures, such as a failure of the pressure relief valve to open. Another pre-flight check consists of closing and opening the motor operated shutoff valve placed on the engine driven pump suction and verify that the end position are reached, which is signaled by the closing and opening of the end-of-travel switches. If a failure is detected in pre-flight, the maintenance crew is alerted and the required maintenance action is taken.

In addition to detect failures, either in flight, or in pre-flight, thereby ensuring the system safety and preventing the occurrence of flight safety critical conditions, the DECU has available all information of the system state variables that allow the implementation of algorithms able to detect if a degradation is under way. If this happens, an alert signal is generated to warn that the system characteristics are drifting

away from nominal, and that a maintenance action must be taken in due time before the fault develops into a failure.

## 8 Conclusions

The hydraulic power generation system and the associated actuators described in this paper make up a possible evolution beyond the state-of-art in the thrust control of military jet engines. The main features of the system described in the paper that provide an advancement over the existing systems are:

- Implementing a thrust vector control capability able to provide pitch and yaw control of the aircraft with dynamic performance equivalent to that of the primary flight control actuators
- Allow a safe flight condition after any single failure also for the case of a single-engine aircraft
- Improve the system maintainability by implementing an effective health usage and monitoring system capable of detecting failures, faults and degradations by performing appropriate in-flight monitoring, pre-flight checks and degradations detection. This will result in a maintainability enhancement, with an ensuing reduction of the maintenance costs and an increase of the aircraft availability. A further work is under way to fully define the health usage and monitoring system algorithms, identify the fault-to-failure mechanisms of all system components and establish the optimal values of the alert thresholds for a reliable signaling of the degradation process without generating false alarms.

## References

- [1] Rolls-Royce. *The Jet Engine*. The Technical Publication Department - Rolls-Royce plc, Derby, England, 1992. ISBN 0-902121 04-9.
- [2] M. Puttre. Thrust vectoring nozzles give pilots an edge. *Mechanical Engineering* 115(3): 64-67, 1963.
- [3] S. Ashley. 1995. Thrust Vectoring: A new angle to air superiority. *Mechanical Engineering* 117(1), 1995.
- [4] B. Flynn, R.E. Smith, and E. Schneider. Thrust vectoring: a new dimension. *Canadian Aeronautics and Space Journal*, 41 (4), 1995.
- [5] G.B. Gilyard, and A. Bolonkin. Optimal Pitch Thrust-Vector Angle and Benefits for all Flight Regimes. *NASA/TM-2000-209021*, 2000, available at URL <http://www.nasa.gov>.
- [6] F.J. Lallman, J.B. Davidson, and P.C. Murphy. A Method for Integrating Thrust-Vectoring and Actuated Forebody Strakes With Conventional Aerodynamic Controls on a High-Performance Fighter Airplane. *NASA/TP-1998-208464*, 1998 available at URL <http://www.nasa.gov>.

- [7] C. Rausch, and K. Lietzau. Integrated Thrust Vectored Engine Control. *Proceedings of the RTO AVT Symposium on Active Control Technology for Enhanced Performance Operational Capabilities of Military Aircraft, Land Vehicles and Sea Vehicles*: 12/1-12/9, Braunschweig, Germany, May 8-11, 2000
- [8] G. Jacazio, D. Ferrara, and M. Sorli. Actuation systems for the control of the engine variable inlet guide vanes: a tradeoff study. *Proceedings of the AST2009 Conference on Aviation Systems Technology*: 121-130, Hamburg, Germany, March 26-27, 2009
- [9] G. Bardone, S. Marchetti, and A. Trovati. Actuation system for variable exhaust nozzle and inlet guide vanes on an advanced gas turbine engine. *Proceedings of the RTO AVT Symposium on Design Principles and Methods for Aircraft Gas Turbine Engines 7/1 - 7/17*, Toulouse, France, May 11-15, 1998
- [10] G. Jacazio. Steady state and transient analysis of an adaptive fluid system. *International Journal of Mechanics and Control*. 3-12, Vol. 02, No. 02, 2001
- [11] G. Jacazio, D. Risso, M. Sorli and L. Tomassini. Adaptive control for improved efficiency of hydraulic systems for high-speed tilting trains. *Proceedings IMechE.*, Vol. 226 Part F: Journal of Rail and Rapid Transit; 272-283, May 2012
- [12] M. Dalla Vedova, G. Jacazio, P. Maggiore and M. Sorli. Identification of Precursors of Servovalves Failures for Implementation of an Effective Prognostics. *Proceedings of the 4th International Conference on Recent Advances in Aerospace Actuation Systems and Components*: 111-126, Toulouse, France, May 5-7, 2010



# The Influence of Fuel Pressure Ripple on Performances of Engine Control System

V. Shorin, A. Gimadiev and V. Sverbilov

Samara State Aerospace University, Samara, Russian Federation  
E-mail: [aseu@ssau.ru](mailto:aseu@ssau.ru), [gimadiev\\_ag@mail.ru](mailto:gimadiev_ag@mail.ru), [v.sverbilov@mail.ru](mailto:v.sverbilov@mail.ru)

## Abstract

Pressure and flow ripple generated by a fuel pump have essential impact on static and dynamic performances of an engine control system. It is especially dangerous for open-loop control used at a turbojet starting mode. The fuel consumption deviation at the engine starting caused by nonlinear averaging of fluctuations over throttling elements can reach up to 25% of a nominal value and provoke engine stopping. In the paper, the method for calculation of the hydro mechanical system characteristics in the presence of fluid born noise and its application for the turbojet start control system are developed. The harmonic analysis and the least mean square (LMS) method for the restrictor performance linearization is used. To avoid influence of fuel flow disturbances on the engine static performance it is proposed to increase system accuracy at the starting mode by placing the hydraulic *RL*-filter into the control unit. The effect of the device was surely verified by the engine test results.

**Keywords:** Fuel flow ripple, turbojet control system, performance accuracy

## 1 Introduction

The problem of high flow ripple level generated in hydraulic systems is well known [e.g., 1]. The fluctuations of a working fluid caused by non-uniformity in delivery of hydraulic and fuel pumps, instability of separate system circuits, have essential impact on static and dynamic performances of aircraft power and control systems. Working fluid ripple is especially dangerous for turbojet open-loop control systems at a start mode. The fuel consumption deviation at the engine starting caused by nonlinear averaging of fluctuations across resistive elements can reach up to 25% of a nominal value. Therefore research of characteristics of engine control systems taking into account high-frequency noise to develop measures for increasing their static and dynamic accuracy is very important and actual.

The problem of calculation of control system static and dynamic characteristics in the presence of fluid born noise is generally reduced to searching of the solution of system of the nonlinear differential equations with variable parameters. Variable parameters are hydraulic resistances of throttling elements evaluated as a result of solution of an equation subsystem in relation to high-frequency fluctuations. Such decision is possible at an assumption that a characteristic time of dynamic process of a desired signal is much more (at least by 5... 10 times) than the greatest period of oscillation components.

In the paper, the generalized scheme of a turbojet control system containing in its structure sources of fluid

oscillations is considered. The fluctuation sources are presented in the form of equivalent flow sources, the system parameters - in the form of the sums of slow variable and high-frequency components.

The calculation models of the throttling elements are presented separately for a slow useful signal and a high-frequency noise in the form of two interconnected equation systems. The high-frequency model of the control system is considered as distributed parameters system with circuit elements described in the form of acoustic two-port network. The system parts containing moving elements are presented in the form of six-pole network, which matrix coefficients depend on the frequency of fluctuations, parameters of connecting channels and damping properties of the element.

The simultaneous solution of the nonlinear differential and algebraic equations is made by a numerical method. On an initial step of iterations the slowly changing system parameters are calculated without high-frequency fluctuations, then, having used an impedance method, complex amplitudes of pressure/flow oscillations in the allocated sections and pressure drops across restrictors are determined. The calculation by such iterative method is conducted till ensuring the required accuracy.

The realization of the stated technique is presented to estimate influence of high-frequency fluctuations of a working fluid on static performances of the turbojet at the starting mode and to develop measures for increase system accuracy under conditions of fuel flow pulsations.

## 2 Modeling

Consider hydraulic circuit having some source of FBN, which can be presented as equivalent flow source

$$Q(t) = Q_0 + \sum_{r=1}^{r=R} q_r \exp(j\omega_r t) \quad (1)$$

where  $Q_0$  – steady flow component;  $q_r$  - complex amplitude of flow rate for  $r$ -component of spectrum;  $\omega_r$  – circular frequency of  $r$ -component;  $r=1 \dots R$  – harmonic number.

Then pressure, flow rate at a cross section  $ij$  and displacement of a moving element  $n$  of the circuit can be presented by sums of slow varying and high-frequency components

$$\left. \begin{aligned} P_{iy}(t) &= P_{i,0} + \sum_{r=1}^{r=R} p_{iy}^{(r)} \exp(j\omega_r t); \\ Q_{iy}(t) &= Q_{i,0} + \sum_{r=1}^{r=R} q_{iy}^{(r)} \exp(j\omega_r t); \\ H_n(t) &= H_{n,0} + \sum_{r=1}^{r=R} h_n^{(r)} \exp(j\omega_r t), \end{aligned} \right\} \quad (2)$$

where  $P, Q$  and  $H$  – corresponding pressure, flow rate and displacement;  $i=1 \dots I$  – number of circuit segment;  $\gamma=1$  – corresponds to inlet of circuit segment;  $\gamma=2$  – corresponds to outlet of circuit segment;  $n=1 \dots N$  – number of moving element.

Since the control system nonlinear properties are mainly defined by throttling elements, for calculation of the poly harmonic oscillatory process it is expedient to use harmonic analysis and the least mean square (LMS) method for the throttle performances linearization.

Model of hydraulic resistance  $k$  can be presented according to (2) for a slow varying useful signal by

$$\Delta P_k = L_k \frac{dQ_k}{dt} + \zeta_{ln,k} Q_k + \zeta_{nln,k} (Q_k - Q_{kr,k} \text{sign} Q_k)^2 \text{sign} Q_k + \delta P_k \quad (3)$$

and for high frequency components by

$$\Delta p_k^{(r)} e^{j\omega_r t} = jL_k \omega_r q_k^{(r)} e^{j\omega_r t} + b_k q_k^{(r)} \quad (4)$$

where  $\Delta P_k$  - slow varying component over nonlinear resistance  $k$ ;  $L_k$  - inductance of throttle element;  $\zeta_{ln,k}, \zeta_{nln,k}$  - coefficients of linear and non linear hydraulic losses over throttling element;  $Q_{kr,k}$  - critical flow rate till linear law of hydraulic losses exists;  $\delta P_k$  - pressure drop increment over throttle element due to non linear averaging of pressure fluctuations;  $\Delta p_k^{(r)}, q_k^{(r)}$  - complex amplitudes of pressure drop and flow rate over throttling element  $k$  for a spectrum component  $r$ ;  $b_k$  – linearization coefficient for pressure/flow curve of the throttle  $k$ .

Linearization coefficient  $b_k$  and shift function (or systematic error)  $\delta P_k$  are determined using LMS method (flow oscillation as input signal).

A typical system part where the mean pressure shift occurs is presented in Figure 1.

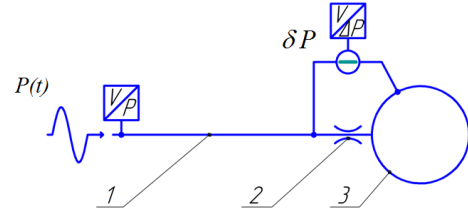


Figure 1: Diagram of a lateral pipeline: 1 – pipe ( $d=7.8\text{mm}$ ,  $L=3.3\text{m}$ ), 2 – restrictor (an orifice plate)  $d=1.04\text{mm}$ , 3 – vessel  $V=0.5\text{l}$

A restrictor 2 is located close to capacity input 3 at the pipe end. The restrictor has a sharp front edge and a rear edge angle  $120^\circ$ . Working fluid viscosity is  $20 \cdot 10^{-6} \text{ m}^2/\text{s}$ , density is  $780 \text{ kg/m}^3$ .

An input signal

$$P(t) = P_0 + p_1 \exp(j\omega_1 t) \quad (5)$$

where  $P_0=40 \text{ bar}$ ,  $p_1=4.2 \text{ bar}$ .

Theoretical and experimental research shows that pressure oscillations close to harmonic signal give a constant component of pressure difference over such asymmetrical restrictor (Figure 2). The similar phenomenon is observed at polyharmonic oscillations so over symmetric as asymmetric restrictors.

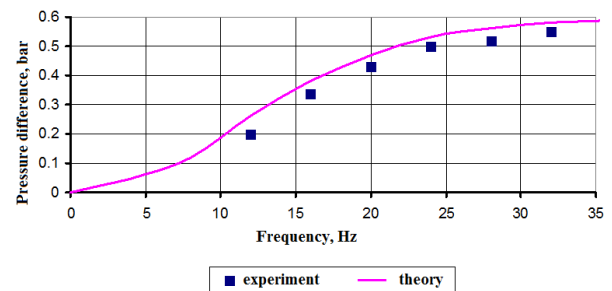


Figure 2: Dependence of a constant component of pressure difference on the frequency of fluctuations

Thus, if hydraulic system has a closed volume with a throttling element at the input, pressure pulsations can lead to emergence of pressure difference on a throttle which value changes depending on a spectrum of pulsations. Thus mean pressure in the cavity will drift relatively mean pressure in the system. In some systems it can have critical consequences.

## 3 Application example

Efficiency of the outlined method can be demonstrated on the example of turbojet control unite shown in Figure 3 pressure ripple being generated by fuel gear pump 4.

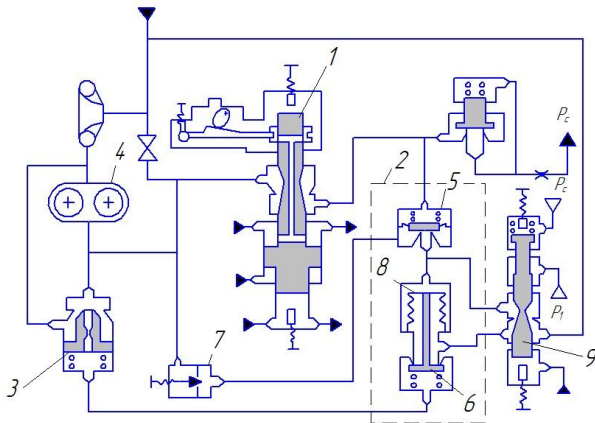


Figure 3: Diagram of the engine fuel control unit: 1- metering pin; 2- pressure drop control valve; 3- pressure relief valve; 4- gear pump; 5- sensing element (pilot valve); 6- slave valve; 7- throttle; 8- bellows; 9- pressure drop compensator

At a starting mode of operation a desired fuel rate determines by a control handle and a compressor pressure ratio. Fuel variation is carried out by moving metering pin 1 and changing its flow area. The pressure drop across the metering pin 1 is stabilized by the control valve 2 acting on the relief valve 3. If pressure drop across the pin 1 increases then the sensing element 5 moves upwards causes the valve 6 to open and to lower pressure in the spring chamber of the relief valve 3. The latest goes down increasing by-pass flow from the pump output to the input thus recovering pressure differential across the pin 1 and the fuel flow rate too.

The fuel flow rate must increase with the compressor pressure ratio  $P_c/P_1^*$  increasing. This task is carried out by the pressure drop compensator 9. As the ratio  $P_c/P_1^*$  increases, the needle valve of the compensator 9 moves down in Figure 3, thus increasing the fuel discharge flow from the chamber outside bellows 8 leading to the valve 6 closing. Then pressure in the spring chamber of the valve 3 increases, the latest moves upwards closing flow area, thus increasing pressure at the input of the metering pin 1 that consequently results in the fuel flow  $Q_d$  increase.

In the case of the fuel overflow the protection system can interrupt engine starting because of thermal overload. The possible reason of the excess fuel flow can be an increase of the pressure drop across the metering pin 1 as a result of non linear averaging of pressure fluctuation generated by the pump 4 over the restrictor 7. It leads to an unwarranted change of pressure drop over the membrane 5 and consequently to changes in pressure drop across the metering pin 1 and the fuel flow rate.

It was shown in the present research that the fuel flow deviation depends on a speed of the pump rotation, amplitudes of flow ripple spectral components and on the structure parameters of the pipeline between the pump and the controller, volumes and passages of the control unit, resistances of the pin 1 and the throttle 7 and their asymmetry. At the engine starting the most fuel flow

deviation occurs at the rotor speed 5000 RPM and 7600 RPM. At these rotations flow ripple reaches the most intensity, maximum pressure drop is realized across the restrictor 7 and the pin 1, consequently resulting in maximum drift of fuel flow rate from the desired value (see Figure 4).

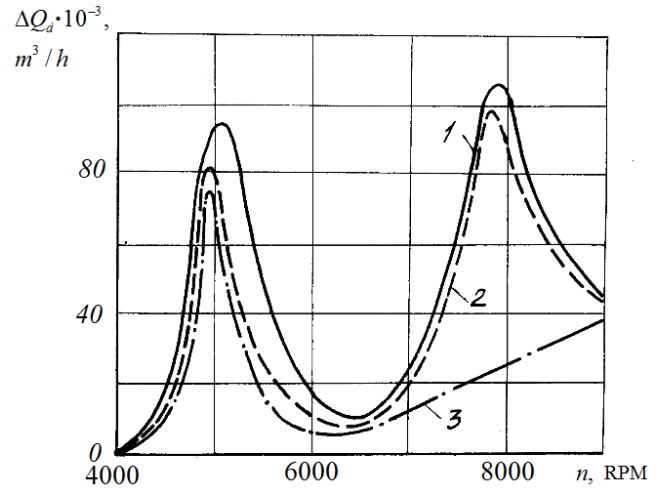


Figure 4: Fuel flow rate fluctuations at the outlet of the metering pin for various spectrum of flow ripple at the pump outlet: 1 -  $A_q^{(1)}=0.125Q_0$ ,  $A_q^{(2)}=0.5A_q^{(1)}$ ,  $A_q^{(3)}=0.3A_q^{(1)}$ ; 2 -  $A_q^{(1)}=0.125Q_0$ ,  $A_q^{(2)}=0.5A_q^{(1)}$ ; 3 -  $A_q^{(1)}=0.125Q_0$

The paper presents some results of analysis of the impact of the structure parameters and the spectral composition on the mean fuel flow rate deviation.

To suppress flow ripple and thus decrease the fuel flow deviation it was proposed to use an acoustic filter. Such approach is well known and described [e.g., 2, 3 and 4]. The acoustic RL-filter was placed in the line of the restrictor 7. The filter presents a composition of hydraulic resistive and inductive elements. The basic issues of the filters and silencers design and application are considered in [2, 5]. Its parameters were determined on the base of a sizing procedure provided avoidance of the flow ripple influence on the engine start response. Experimental results of its application are shown in Figure 5.

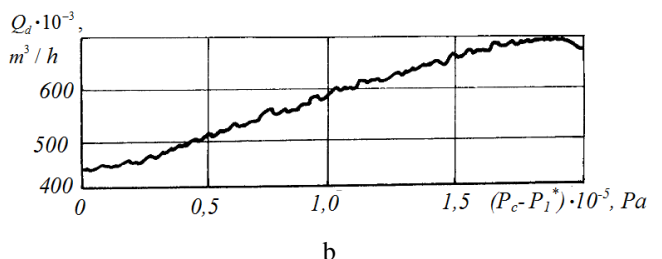
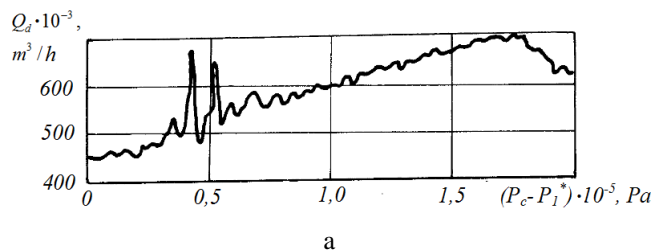


Figure 5: Experimental static performance of engine control system for the altitude starting mode: a – standard version; b – with silencer in form of acoustic RL-filter at the inlet of the restrictor 7

## Conclusion

The effective method for calculation of static and dynamic characteristics of hydro mechanical control systems under the action of flow ripple is presented. On the example of the turbojet controller it is shown that significant deviation of the engine operating regime can be provoked by changes in performances of resistive elements. To avoid influence of high-frequency fuel flow fluctuations on the engine static performances and to increase system accuracy at the starting mode it is proposed to place the hydraulic RL-filter into the control unit. The effect of the device was verified by the engine test results.

## References

- [1] K A Edge. Designing quieter hydraulic system – some recent development and contributions. *Proc. of the Forth JHPS International Symposium*, Japan, Nov., 1999.
- [2] V P Shorin. *Flow pulsations cancelation in aircraft pipelines*. Machine Building, Moscow, 1980. -160 p. (in Russian).
- [3] E Kojima & K A Edge. Experimental determination of hydraulic silencer transfer matrices and assessment of the method for use as a standard test procedure. *Proc. Seventh Bath International Fluid Power Workshop*, Bath, UK, September 1994, pp. 221-241.
- [4] K Lau, D N Johnston & K A Edge. *Fluid borne noise characteristics of hydraulic filters and silencers*. Proc. of Seventh Bath International Fluid Power Workshop, Bath, UK, September 1994, pp. 242-261.
- [5] V P Shorin et al. *Flow ripple and noise reduction in hydro mechanical systems*. SSAU, Samara, 2005. -314 p. ISBN 5-93424-203-2 (in Russian).

# Test Rig Landing Gear Free-Fall System Model Simulation and Design Optimization Using Matlab<sup>®</sup>

Mário Maia Neto and Luiz Carlos Sandoval Góes

Department of Mechanical Engineering, Aeronautical Institute of Technology, São José dos Campos, SP, Brazil  
E-mail: mario.maia.neto@gmail.com, goes@ita.br

## Abstract

In order to comply with the safety level demanded by civil certification requirements and military standards, alternative methods of extending retractable landing gear are provided in practically all airplanes of this type currently flying throughout the world. However, the emergency extension operation system design is not unique and architectures comprising simpler systems like free-fall or spring-assisted up to more complex systems like auxiliary hydraulics-assisted or pneumatics-assisted ones can be found in different airplanes. The airplane landing gear free-fall operation comprises a redundant, dissimilar and independent mechanically operated method of extending airplane landing gear due to a main hydraulic system failure or an electrical system malfunction. This paper aims at describing the modeling and simulation of a general landing gear emergency extension system built in a test rig, for a non-assisted type system, applying only an extension by gravity. Due to the low associated cost, satisfactory results and capability of easily assessing the trade-offs between different systems configurations, modeling applying computational software has become a frequent practice in aeronautical industries with the purpose of reducing product development cycle. Therefore, a parametric model of the landing gear emergency extension system was created in MATLAB<sup>®</sup> Simulink<sup>®</sup> and the system performance at nominal and particular operational conditions could be predicted by running several model simulations. Afterwards, through the assistance of MATLAB<sup>®</sup> tools, discrete and continuous optimization processes were accomplished to illustrate the benefits of applying these techniques to improve system operation response. An optimum damping condition permits the attenuation of the impact effects suffered by aircraft structure when landing gear falls by gravity in an emergency operation, as well as the assurance of sufficient energy for landing gear locking at the end of its downward movement.

**Keywords:** Landing Gear, Free-Fall, Modeling, Optimization

## 1 Introduction

Federal Aviation Regulations Part 23 and Part 25 and MIL-HDBK-516 are examples of civil and military standards frequently applied during the development and certification phases of these types of airplanes throughout the world. In order to guarantee an acceptable degree of safety level on landings, the aforementioned standards present requirements that states the aircraft shall comprise alternative methods of extending retractable landing gear in case of normal operation system failure. Their purpose consists in avoiding a wheels-up landing and it is potentially hazardous condition, as depicted in fig. 1.

According to [1], the landing gear design comprises more engineering disciplines than any other aircraft design topic. Knowledge about materials, manufacturing processes, electrical and hydraulic systems, mechanisms and even airfield strength is required to design the landing gear system.



Figure 1: A wheels-up landing. Source: [2]

The landing gear extension and retraction system choice is also a trade-off issue. For normal landing gear operation system, hydraulic systems consisting of accumulators, tubing, actuators and different types of valves, like restrictor, check and selector ones, represent the most used technology for this purpose. On the other hand, the emergency extension system design encompasses more types of architectures and therefore spring-assisted, auxiliary

hydraulics-assisted, pneumatics-assisted or non-assisted free-fall design can be found in different airplanes of a same category.

The emergency free-fall system presents the simplest configuration, in which a lever or a knob installed in the cockpit is used by the pilot to unlock the landing gear and associated doors up locks, by means of cables, allowing the landing gear to fall by gravity. Basically, it consists in a redundant, dissimilar and independent mechanically operated method of extending airplane landing gear due to a main hydraulic system failure or an electrical system malfunction.

In aeronautical industries, the use of test rigs to accomplish systems operational tests has become a common practice before installing them in an aircraft prototype and running ground and flight tests. The systems integration test bench, usually known as ‘iron bird’, permits the execution of isolated and integrated systems tests, allowing the engineering team to predict deviations in a system operational performance when functioning lonely or simultaneously with other aircraft systems. Figure 2 illustrates an example of landing gear test rig.



Figure 2: A landing gear test rig. Source: [3]

On the other hand, performing system architecture changes during the rig test phase may lead to additional costs to the aircraft development program. Aiming to mitigate this risk, system modeling and optimization applying computational software have become a frequent practice in industries with the purpose of also reducing product development cycle. Due to the low associated cost, satisfactory results and capability of easily assessing the trade-offs between different systems configurations, the virtual modeling allows the predict of system performance at different operational conditions and facilitates the application of optimization techniques, hence reducing the possibility of a necessary system redesign in advanced stages of new aircraft development processes.

The free-fall system to be modeled is associated with a general landing gear emergency extension system built in a test rig. Due to the commonly restrictive operational envelope applicable to the landing gear emergency extension capability, merely a 1g flight test campaign is generally required by advisory circulars like [4] to show compliance with related certification regulations. Therefore, the current model could be further improved to take into

consideration the aerodynamic and maneuver inertial effects occurring during flight in order to define and even expand the landing gear emergency operation envelope to be included in aircraft flight manual.

Finally, the provided model would be worth as a simple and quick evaluation tool to design the main components of the related hydraulic system and to define the variables to be measured during the system operational tests accomplished in production line applying hydraulic bench and aircraft lift on jacks.

Figure 3 presents the free-fall system schematics under evaluation. As depicted in the hydraulic diagram, the elements that make up the system are: nose landing gear, main landing gear (right and left), restrictor valves, tubing, selector valve, free-fall valve, uplocks and emergency lever. However, since the simulations are considered to initiate with the emergency lever pulled and all uplocks released, and the landing gear legs are assumed to be down locked after reaching a predetermined extension angle, the uplock and downlock mechanisms will not be modeled.

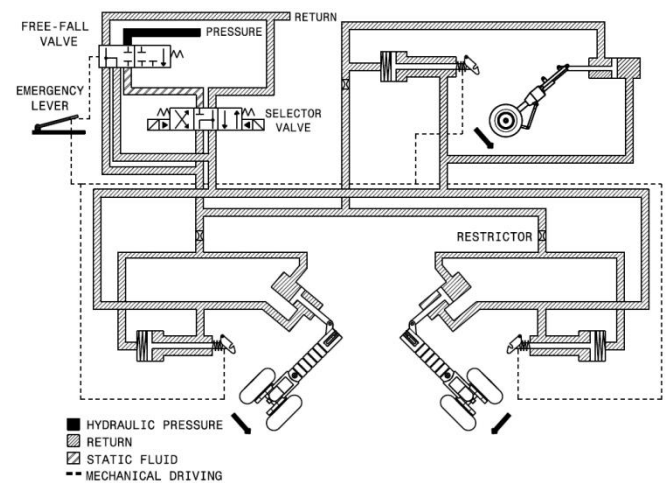


Figure 3: Landing gear free-fall system. Source: adapted from [5]

## 2 Formulation

The basic formulation that composes the free-fall system model will be divided into two separated topics: the hydraulic system equations and the landing gear dynamics ones.

### 2.1 Hydraulic System Modeling

A lumped element model is applied to the landing gear associated hydraulic system, which is characterized by the segregation of system important behavior effects like compliance, inertance and pressure drop, as well as the isolated components installed in the system such as valves and actuators, as discrete elements connected by means of the continuity law or specific pressure conditions. Nowadays, this methodology is embedded in modeling computational pieces of software like MATLAB® Simulink® Simscape library and allows the user a good comprehension of the relation between system components and their main effects.

Assuming at first no significant temperature variations in the system, constant values for fluid viscosity and density are used. However, the fluid density also exhibits a pressure-dependence variation, whose effect can be represented by a discrete element called “system compliance”. The ideal compliance is related to fluid flow and line pressure through eq. (1) [6]. Besides the fluid compressibility, the effects of entrapped air in hydraulic line and the tubing flexibility can also be considered in the calculation of the “effective bulk modulus” by means of eq. (2) [3][7].

$$C_f = \frac{AL}{\beta_e} \triangleq \frac{\int Q dt}{P} \quad (1)$$

$$\frac{1}{\beta_e} = \frac{1}{\beta_c} + \frac{1}{\beta_L} + \frac{V_G}{V_T} \left( \frac{1}{\beta_G} - \frac{1}{\beta_L} \right) \quad (2)$$

Due to its kinetic energy, the fluid flow exhibits another effect known as “fluid inertance”. Represented as another lumped element, the relation between pressure variation and fluid flow in the fluid inertance element is given by eq. (3) [6].

$$\Delta P \triangleq I_f \frac{dQ}{dt} \quad (3)$$

A typical value used for the inertance parameter is present in eq. (4). This formulation is more applicable for turbulent flow regime, when the Reynolds number, calculated by eq. (5), is greater than 4000 [6][7].

$$I_f = \frac{\rho L}{A} \quad (4)$$

$$Re = \frac{\rho V D}{\mu} \quad (5)$$

The last effect observed in the flow dynamics through hydraulic pipes consists in the fluid resistance, also referred to as “pressure drop”. Again, the fluid pressure drop can be modeled as a discrete element, whose semi-empirical equation for horizontal straight tubing and completely developed flow is described by eq. (6). The first term in the right-hand side of the equation is called the “friction factor” and is dependent on tubing relative roughness and also on Reynolds number [7].

$$\Delta P = f \frac{L \rho V^2}{D} \quad (6)$$

Components like restrictor and selector valves result in locally situated pressure drops. The relation between the fluid flow and the pressure drop through their orifices can be expressed by a non-linear equation for turbulent flows, as shown in eq. (7), or by a linear equation for laminar flows, given by eq. (8) [7].

$$Q = C_d A_o \sqrt{\frac{2}{\rho} (\Delta P)} \quad (7)$$

$$Q = \frac{2\delta^2 D_o A_o}{\mu} \Delta P \quad (8)$$

The hydraulic actuators shown in fig. 3, responsible for performing the connection between the hydraulic system and the landing gear mechanism, are of double-acting,

single-rod type. The continuity equations applied to the actuator chambers yield to the formulation presented in eq. (9) and eq. (10). As it can be seen, internal and external leakages are being taken into account as linearly dependents to the pressure differences between the chambers and between each chamber and the external environment, respectively [7].

$$Q_1 - C_{ip}(P_1 - P_2) - C_{ep}P_1 = \frac{dV_1}{dt} + \frac{V_1}{\beta_e} \frac{dP_1}{dt} \quad (9)$$

$$C_{ip}(P_1 - P_2) - C_{ep}P_2 - Q_2 = \frac{dV_2}{dt} + \frac{V_2}{\beta_e} \frac{dP_2}{dt} \quad (10)$$

## 2.2 Landing Gear Dynamics Modeling

The own landing gear weight comprises the main responsible for the extension torque in a free-fall system. For a ground test, the weight torque is basically a function of the landing gear mass, the distance between its center of gravity and the landing gear-to-aircraft attachment (landing gear rotation axle), and the landing gear extension angle. Therefore, substituting the landing gear mechanism mass for an equivalent mass located in the center of gravity of the landing gear leg, the weight torque for each landing gear becomes defined as in eq. (11).

$$T = m g a \cos(\alpha) \quad (11)$$

On the other hand, during this type of operation, some resistant forces act against landing gear downward rotation, decreasing the gravitational potential energy used by the landing gear to extend.

The first resistant torque is consequence of the friction existing in the landing mechanism bearings. In order to simplify the model, this effect is summarized in a term called “viscous friction torque”. Proportional to the extension velocity by a constant factor known as damping coefficient, the viscous friction torque can be expressed by eq. (12).

$$F = B \cdot \dot{\alpha} \quad (12)$$

During the landing gear free-fall extension, another resistant torque appears in the system as a result of the internal flow created in the hydraulic system due to actuator piston movement. Assuming the piston mass and its friction as negligible, the actuator force is caused by the pressure difference existing between its chambers applied to the area of each side of the piston. Equation (13) denotes the actuator force.

$$h = P_1 A_{p1} - P_2 A_{p2} \quad (13)$$

Therefore, the hydraulic actuator torque is defined as in eq. (14). Since the torque arms and piston displacements are functions of the landing gear extension angles, the nose landing gear and main landing gear CAD drawings were used to determine the relationship between them by doing simulated measurements at some extension angle values. Applying the obtained data, parametric curves were then defined making use of cubic polynomial regression techniques.

$$H = \pm h \cdot r \quad (14)$$

Finally, combining in Newton's second law the sum of the torques that act on each landing gear leg during free-fall extension, eq. (15) is obtained.

$$I \ddot{\alpha} = T - F + H \quad (15)$$

### 2.3 Block Diagram

Figure 4 presents the block diagram of the free-fall system shown in fig. 3. Due to system symmetry, the same parameters values were considered for main landing gear 1 and 2, that is, left-side and right-side.

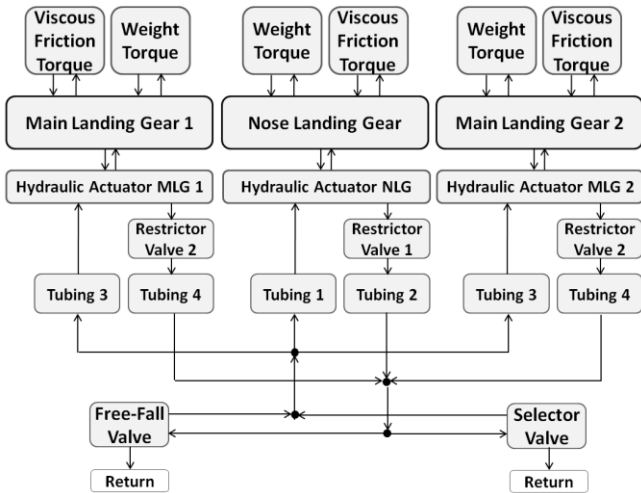


Figure 4: System block diagram. Source: adapted from [8] and [9]

Meanwhile the hydraulic system blocks are depicted in the bottom portion of the diagram, the applicable external torques are represented in the upper part, being the landing gear blocks the connection between them by means of Newton's second law. Regarding the system return pressure, which was assumed equal to the hydraulic fluid reservoir pressure, it basically represents the unique model boundary condition.

For all landing gear legs, it was adopted an extension angle range from  $0^\circ$  to  $90^\circ$  ( $\pi/2$  radians). Since the downlock mechanism was not modeled, it was assumed as a particular criterion that, at an extension angle of  $89^\circ$  (1.533 radians), the landing gear is instantaneously locked supposedly by means of a mechanical lock, which brings it immediately to the final extension angle of  $90^\circ$  ( $\pi/2$  radians).

Figure 5 illustrates the MATLAB<sup>®</sup> Simulink<sup>®</sup> model of the system. For the representation of tubing, restrictor valves, actuators and selector valve, as well as hydraulic fluid properties, the respective blocks from SimHydraulics<sup>®</sup> software were applied. Based on the Physical Network approach, SimHydraulics<sup>®</sup> comprises a modeling environment within Simulink<sup>®</sup> that is appropriate for hydraulic system design and control [10].

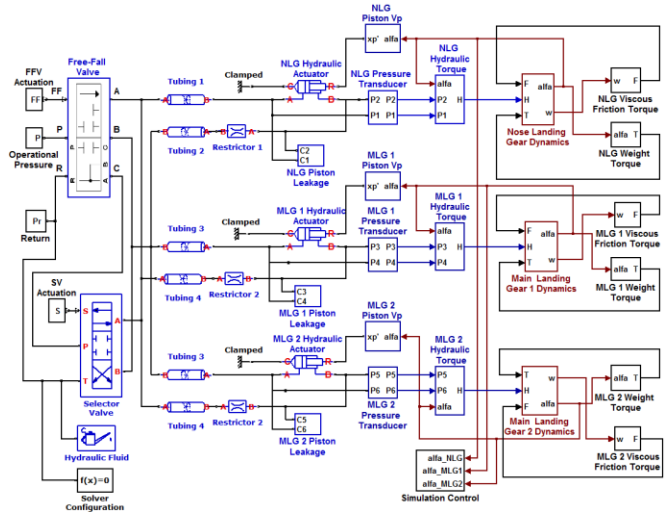


Figure 5: MATLAB<sup>®</sup> Simulink<sup>®</sup> model

A more detailed view of the hydraulic portion of landing gear operation system is shown in fig. 6. Taken from the SimHydraulics<sup>®</sup> pipeline library, the segmented pipeline block comprises all hydraulic important behavior effects like fluid compliance, inertance and resistance in a unique block. Concerning the internal and external leakages of the hydraulic actuators, their representation was accomplished by means of fixed orifice blocks located inside subsystem blocks referred to as "piston leakages", whose parameters were adjusted to maintain a laminar flow that kept the linear proportionality described in eq. (9) and eq. (10).

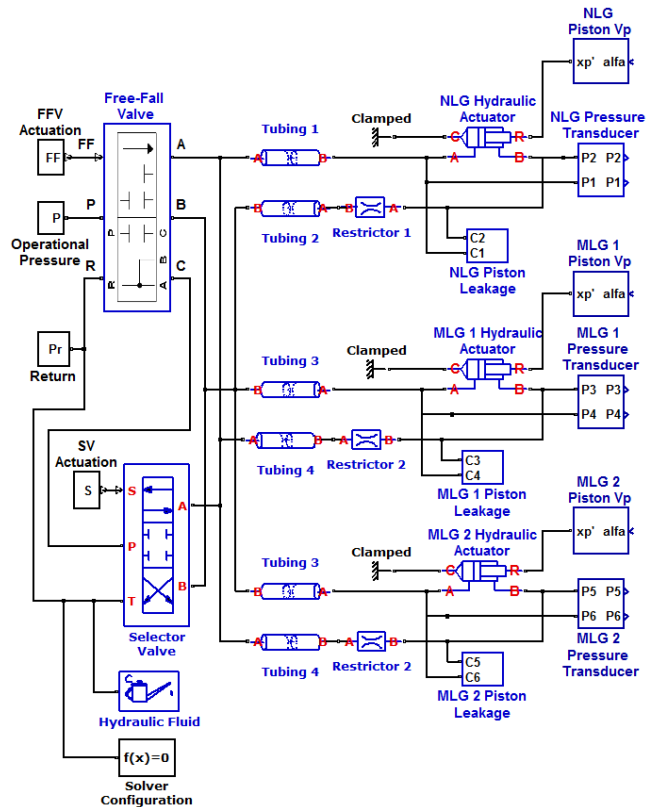


Figure 6 – Detailed view of landing gear system hydraulic components

### 3 Simulation Results

The simulation of the MATLAB® Simulink® model shown in fig. 5 was run applying the system parameters nominal values. To integrate the model differential equations, the simulation was configured to use a fixed-step solver known as “ode14x”. This implicit algorithm is a combination of Newton’s method and extrapolations from the current values [11]. The simulation step size was then adjusted in order to avoid convergence problems.

Figure 7 through fig. 10 present the development of the landing gear extension angles  $e$  respective velocities for nose and main landing gear. As illustrated especially by the velocities graphs, all landing gear legs demonstrated a similar extension profile for the ground test condition. However, the higher rotational velocity values during the first seconds of landing gear extension are consequence of the weight torque magnitude originated when the landing gear legs are practically in a horizontal position.

According to simulation results, the nose landing gear described a faster movement, taking 6.7 seconds to extend by free-fall. On the other hand, the main landing gear extension occurred in a slower manner, requiring 8.7 seconds to reach its final position.

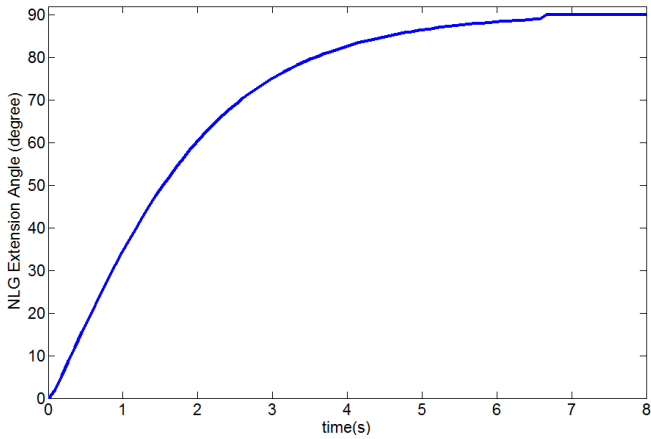


Figure 7: Nose landing gear extension angle: nominal simulation

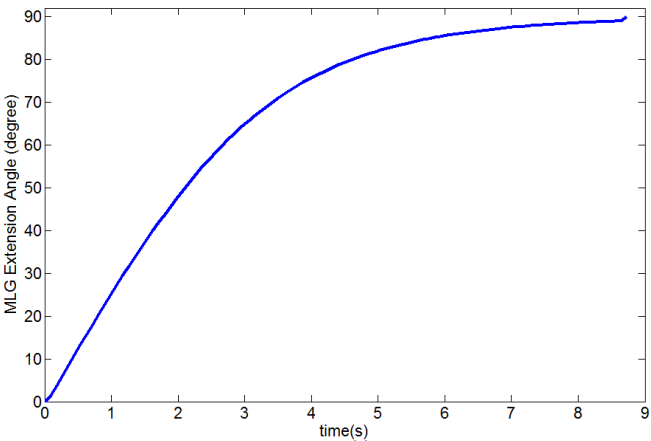


Figure 8: Main landing gear extension angle: nominal simulation

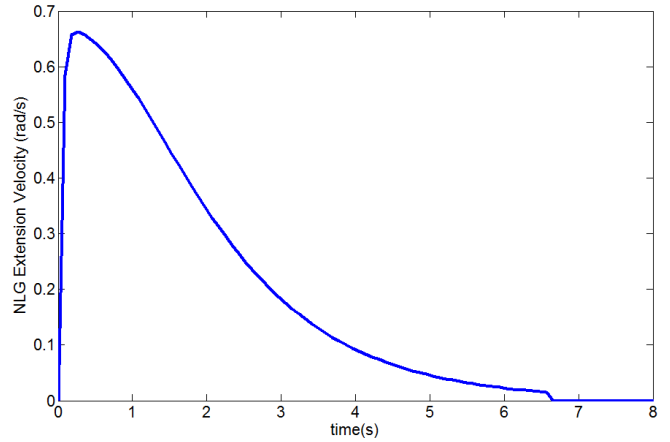


Figure 9: Nose landing gear extension velocity: nominal simulation

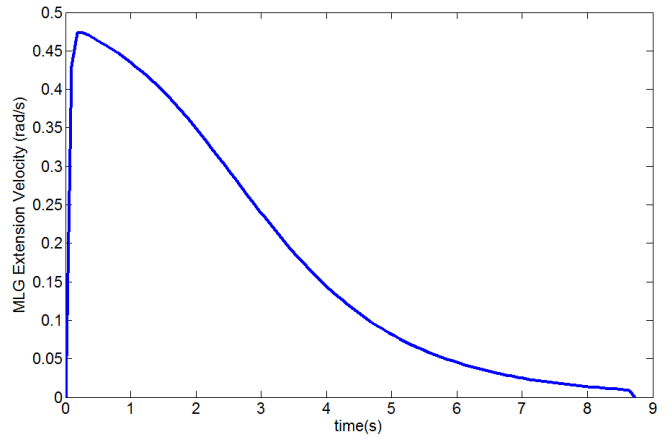


Figure 10: Main landing gear extension velocity: nominal simulation

The fluid temperature effect on landing gear extension times can be evaluated by means of fluid properties variation throughout hydraulic fluid temperature envelope. Assuming a fluid temperature range from  $-40^{\circ}\text{C}$  ( $-40^{\circ}\text{F}$ ) to  $66^{\circ}\text{F}$  ( $150^{\circ}\text{F}$ ), the increase of landing gear emergency extension times at significant low fluid temperatures may be noticed in fig. 11, especially for main landing gear actuation.

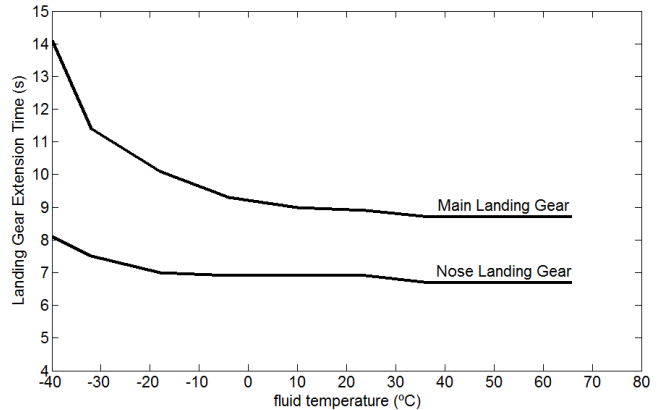


Figure 11: Fluid temperature effect on landing gear extension times

The impact of hydraulic fluid entrapped air on landing gear emergency extension performance can also be estimated using model simulation. For the present system, the consequence of a trapped air relative amount equal to 0.1 on main landing gear emergency extension is shown in fig. 12. Besides increasing extension time in approximately 0.5 second, the presence of a considerable quantity of trapped air in hydraulic fluid led to more oscillations in main landing gear velocities up to about 2 seconds as a result of the fluid capacitance rise. Finally, the existence of entrapped air in hydraulic system can affect not only the emergency extension system, but also landing gear normal retraction and extension operation, especially for those systems whose uplock and downlock mechanisms are very dependent on components synchronism.

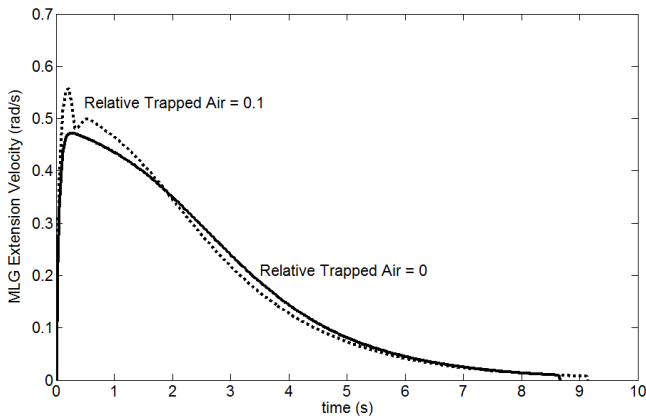


Figure 12 – Main landing gear extension velocities for two trapped air configurations

#### 4 Model Optimization

Generally associated with competitive issues, quality assurance and manufacturing costs reduction, the aerospace design was among the earliest disciplines to significantly apply optimization processes in their product design due to the critical necessity of reducing weight in this type of vehicle. Nowadays, the success of applying an optimization process in engineering design demands not only a good mathematical model describing quantitatively the design problem, but also some specific knowledge from the designer like computer programming and optimization techniques [12].

The nominal simulation results shown in fig. 7 to fig. 10 present in such a way an example of what can be found in terms of free-fall operation. Not even the time delay between the final extensions of the landing gear legs, but also the impacts their movements may have on aircraft structure and landing safety are among the main concerns landing gear engineers have during the system design. While one landing gear leg may reach the lowest point with a considerable amount of energy, which eventually can cause structural damage to its attachment point, other landing gear leg may hardly get down and locked due to the small energy it has at the end of its movement, putting at risk the aircraft integrity in the subsequent landing.

The purpose of the following steps is to illustrate a practical optimization process in order to reduce the time delay between the extension of nose and main landing gear and, consequently, better adjusting the behavior they present at the end of their movements. For this purpose, it is assumed a rig test requirement for free-fall extension time of 7.0 seconds minimum and 8.2 seconds maximum at nominal environmental temperature.

The first example of system optimization considers a discrete optimization method. Although several continuous optimization algorithms are available nowadays in software like MATLAB®, the discrete optimization is also fundamental for engineering design problems, since in many situations the parameter value choice is associated with the standard dimensions provided by the suppliers in their catalogs or for some reason restricted due to manufacturing issues [12].

The “exhaustive enumeration” method comprises a discrete optimization technique, in which all solutions in search space are evaluated [12]. Its main drawback regarding the exponential increase in calculations as more variables are considered may not be a limitation at the present time due to the high memory and fast data processing capabilities of current computers. Moreover, this methodology allows the designer to observe the system response sensibility on parameter value variations throughout the optimization process.

Therefore, tab. 1 presents the parameters evaluated during the system discrete optimization process, as well as their nominal, minimum and maximum values considered in the algorithm. After running the iterative optimization, the parameter optimum values were obtained and are described in the last column of tab. 1.

Table 1: System parameters discrete optimization

Parameter	Nominal Value	Minimum Value	Maximum Value	Optimum Value
Restrictor 1 ( $A_0$ )	$2.54 \times 10^{-6}$	$1.96 \times 10^{-7}$	$7.07 \times 10^{-6}$	$1.96 \times 10^{-7}$
Restrictor 2 ( $A_0$ )	$2.54 \times 10^{-6}$	$1.96 \times 10^{-7}$	$7.07 \times 10^{-6}$	$7.07 \times 10^{-6}$
Tubing 1 ( $D$ )	$8.00 \times 10^{-3}$	$4.00 \times 10^{-3}$	$1.50 \times 10^{-2}$	$4.00 \times 10^{-3}$
Tubing 2 ( $D$ )	$8.00 \times 10^{-3}$	$4.00 \times 10^{-3}$	$1.50 \times 10^{-2}$	$8.00 \times 10^{-3}$
Tubing 3 ( $D$ )	$8.00 \times 10^{-3}$	$4.00 \times 10^{-3}$	$1.50 \times 10^{-2}$	$1.50 \times 10^{-2}$
Tubing 4 ( $D$ )	$8.00 \times 10^{-3}$	$4.00 \times 10^{-3}$	$1.50 \times 10^{-2}$	$8.00 \times 10^{-3}$
NLG Actuator ( $A_{p1}$ )	$1.50 \times 10^{-3}$	$1.30 \times 10^{-3}$	$2.00 \times 10^{-3}$	$1.30 \times 10^{-3}$
NLG Actuator ( $A_{p2}$ )	$1.00 \times 10^{-3}$	$8.50 \times 10^{-4}$	$1.25 \times 10^{-3}$	$1.25 \times 10^{-3}$
MLG Actuator ( $A_{p1}$ )	$3.20 \times 10^{-3}$	$2.60 \times 10^{-3}$	$3.80 \times 10^{-3}$	$2.60 \times 10^{-3}$
MLG Actuator ( $A_{p2}$ )	$1.70 \times 10^{-3}$	$1.40 \times 10^{-3}$	$2.51 \times 10^{-3}$	$2.51 \times 10^{-3}$

Table 2 illustrates the discrete optimization process applied in the present example. In order to reduce the simulation time, the landing gear emergency extension times were evaluated for each parameter configuration, starting from the nominal values denoted by a gray background in tab. 2, and switching the value of only a unique parameter to its maximum and minimum values at a time, in a cascade, successive matter. The optimum solution was found in line 18 of tab. 2.

On the other hand, aiming to assure the obtained result comprised the global optimum solution for the applicable search space, every allowable parameter value combination should have been analyzed, which would have led to more than 59,000 simulations. However, since the landing gear locking times after the proposed discrete optimization became 7.09 seconds for nose landing gear and 8.19 seconds for main landing, it was possible to meet the established requirements only making use of the 21 simulations shown in tab. 2.

Table 2: Discrete optimization process

Case	Restrictor 1	Restrictor 2	Tubing 1	Tubing 2	Tubing 3	Tubing 4	NLG Actuator	NLG Actuator	MLG Actuator	MLG Actuator	NLG time (s)	MLG time (s)
	$A_{\theta}$	$A_{\theta}$	$D$	$D$	$D$	$D$	$A_{p1}$	$A_{p2}$	$A_{p1}$	$A_{p2}$		
1	2.54x10 <sup>-6</sup>	2.54x10 <sup>-6</sup>	8.00x10 <sup>-3</sup>	8.00x10 <sup>-3</sup>	8.00x10 <sup>-3</sup>	8.00x10 <sup>-3</sup>	1.50x10 <sup>-3</sup>	1.00x10 <sup>-3</sup>	3.20x10 <sup>-3</sup>	1.70x10 <sup>-3</sup>	6.73	8.73
2	1.96x10 <sup>-7</sup>	2.54x10 <sup>-6</sup>	8.00x10 <sup>-3</sup>	8.00x10 <sup>-3</sup>	8.00x10 <sup>-3</sup>	8.00x10 <sup>-3</sup>	1.50x10 <sup>-3</sup>	1.00x10 <sup>-3</sup>	3.20x10 <sup>-3</sup>	1.70x10 <sup>-3</sup>	6.82	8.73
3	7.07x10 <sup>-6</sup>	2.54x10 <sup>-6</sup>	8.00x10 <sup>-3</sup>	8.00x10 <sup>-3</sup>	8.00x10 <sup>-3</sup>	8.00x10 <sup>-3</sup>	1.50x10 <sup>-3</sup>	1.00x10 <sup>-3</sup>	3.20x10 <sup>-3</sup>	1.70x10 <sup>-3</sup>	6.73	8.73
4	1.96x10 <sup>-7</sup>	1.96x10 <sup>-7</sup>	8.00x10 <sup>-3</sup>	8.00x10 <sup>-3</sup>	8.00x10 <sup>-3</sup>	8.00x10 <sup>-3</sup>	1.50x10 <sup>-3</sup>	1.00x10 <sup>-3</sup>	3.20x10 <sup>-3</sup>	1.70x10 <sup>-3</sup>	6.82	9.63
5	1.96x10 <sup>-7</sup>	7.07x10 <sup>-6</sup>	8.00x10 <sup>-3</sup>	8.00x10 <sup>-3</sup>	8.00x10 <sup>-3</sup>	8.00x10 <sup>-3</sup>	1.50x10 <sup>-3</sup>	1.00x10 <sup>-3</sup>	3.20x10 <sup>-3</sup>	1.70x10 <sup>-3</sup>	6.82	8.55
6	1.96x10 <sup>-7</sup>	7.07x10 <sup>-6</sup>	4.00x10 <sup>-3</sup>	8.00x10 <sup>-3</sup>	8.00x10 <sup>-3</sup>	8.00x10 <sup>-3</sup>	1.50x10 <sup>-3</sup>	1.00x10 <sup>-3</sup>	3.20x10 <sup>-3</sup>	1.70x10 <sup>-3</sup>	6.64	8.46
7	1.96x10 <sup>-7</sup>	7.07x10 <sup>-6</sup>	1.50x10 <sup>-2</sup>	8.00x10 <sup>-3</sup>	8.00x10 <sup>-3</sup>	8.00x10 <sup>-3</sup>	1.50x10 <sup>-3</sup>	1.00x10 <sup>-3</sup>	3.20x10 <sup>-3</sup>	1.70x10 <sup>-3</sup>	6.73	8.55
8	1.96x10 <sup>-7</sup>	7.07x10 <sup>-6</sup>	4.00x10 <sup>-3</sup>	4.00x10 <sup>-3</sup>	8.00x10 <sup>-3</sup>	8.00x10 <sup>-3</sup>	1.50x10 <sup>-3</sup>	1.00x10 <sup>-3</sup>	3.20x10 <sup>-3</sup>	1.70x10 <sup>-3</sup>	6.73	8.55
9	1.96x10 <sup>-7</sup>	7.07x10 <sup>-6</sup>	4.00x10 <sup>-3</sup>	1.50x10 <sup>-2</sup>	8.00x10 <sup>-3</sup>	8.00x10 <sup>-3</sup>	1.50x10 <sup>-3</sup>	1.00x10 <sup>-3</sup>	3.20x10 <sup>-3</sup>	1.70x10 <sup>-3</sup>	6.73	8.55
10	1.96x10 <sup>-7</sup>	7.07x10 <sup>-6</sup>	4.00x10 <sup>-3</sup>	8.00x10 <sup>-3</sup>	4.00x10 <sup>-3</sup>	8.00x10 <sup>-3</sup>	1.50x10 <sup>-3</sup>	1.00x10 <sup>-3</sup>	3.20x10 <sup>-3</sup>	1.70x10 <sup>-3</sup>	6.73	9.72
11	1.96x10 <sup>-7</sup>	7.07x10 <sup>-6</sup>	4.00x10 <sup>-3</sup>	8.00x10 <sup>-3</sup>	1.50x10 <sup>-2</sup>	8.00x10 <sup>-3</sup>	1.50x10 <sup>-3</sup>	1.00x10 <sup>-3</sup>	3.20x10 <sup>-3</sup>	1.70x10 <sup>-3</sup>	6.73	8.37
12	1.96x10 <sup>-7</sup>	7.07x10 <sup>-6</sup>	4.00x10 <sup>-3</sup>	8.00x10 <sup>-3</sup>	1.50x10 <sup>-2</sup>	4.00x10 <sup>-3</sup>	1.50x10 <sup>-3</sup>	1.00x10 <sup>-3</sup>	3.20x10 <sup>-3</sup>	1.70x10 <sup>-3</sup>	6.73	8.82
13	1.96x10 <sup>-7</sup>	7.07x10 <sup>-6</sup>	4.00x10 <sup>-3</sup>	8.00x10 <sup>-3</sup>	1.50x10 <sup>-2</sup>	1.50x10 <sup>-2</sup>	1.50x10 <sup>-3</sup>	1.00x10 <sup>-3</sup>	3.20x10 <sup>-3</sup>	1.70x10 <sup>-3</sup>	6.73	8.37
14	1.96x10 <sup>-7</sup>	7.07x10 <sup>-6</sup>	4.00x10 <sup>-3</sup>	8.00x10 <sup>-3</sup>	1.50x10 <sup>-2</sup>	8.00x10 <sup>-3</sup>	1.30x10 <sup>-3</sup>	1.00x10 <sup>-3</sup>	3.20x10 <sup>-3</sup>	1.70x10 <sup>-3</sup>	6.91	8.37
15	1.96x10 <sup>-7</sup>	7.07x10 <sup>-6</sup>	4.00x10 <sup>-3</sup>	8.00x10 <sup>-3</sup>	1.50x10 <sup>-2</sup>	8.00x10 <sup>-3</sup>	2.00x10 <sup>-3</sup>	1.00x10 <sup>-3</sup>	3.20x10 <sup>-3</sup>	1.70x10 <sup>-3</sup>	6.55	8.37
16	1.96x10 <sup>-7</sup>	7.07x10 <sup>-6</sup>	4.00x10 <sup>-3</sup>	8.00x10 <sup>-3</sup>	1.50x10 <sup>-2</sup>	8.00x10 <sup>-3</sup>	1.30x10 <sup>-3</sup>	8.50x10 <sup>-4</sup>	3.20x10 <sup>-3</sup>	1.70x10 <sup>-3</sup>	6.73	8.37
17	1.96x10 <sup>-7</sup>	7.07x10 <sup>-6</sup>	4.00x10 <sup>-3</sup>	8.00x10 <sup>-3</sup>	1.50x10 <sup>-2</sup>	8.00x10 <sup>-3</sup>	1.30x10 <sup>-3</sup>	1.25x10 <sup>-3</sup>	3.20x10 <sup>-3</sup>	1.70x10 <sup>-3</sup>	7.09	8.37
18	1.96x10 <sup>-7</sup>	7.07x10 <sup>-6</sup>	4.00x10 <sup>-3</sup>	8.00x10 <sup>-3</sup>	1.50x10 <sup>-2</sup>	8.00x10 <sup>-3</sup>	1.30x10 <sup>-3</sup>	1.25x10 <sup>-3</sup>	2.60x10 <sup>-3</sup>	1.70x10 <sup>-3</sup>	7.09	8.19
19	1.96x10 <sup>-7</sup>	7.07x10 <sup>-6</sup>	4.00x10 <sup>-3</sup>	8.00x10 <sup>-3</sup>	1.50x10 <sup>-2</sup>	8.00x10 <sup>-3</sup>	1.30x10 <sup>-3</sup>	1.25x10 <sup>-3</sup>	3.80x10 <sup>-3</sup>	1.70x10 <sup>-3</sup>	7.09	8.55
20	1.96x10 <sup>-7</sup>	7.07x10 <sup>-6</sup>	4.00x10 <sup>-3</sup>	8.00x10 <sup>-3</sup>	1.50x10 <sup>-2</sup>	8.00x10 <sup>-3</sup>	1.30x10 <sup>-3</sup>	1.25x10 <sup>-3</sup>	2.60x10 <sup>-3</sup>	1.40x10 <sup>-3</sup>	7.09	8.28
21	1.96x10 <sup>-7</sup>	7.07x10 <sup>-6</sup>	4.00x10 <sup>-3</sup>	8.00x10 <sup>-3</sup>	1.50x10 <sup>-2</sup>	8.00x10 <sup>-3</sup>	1.30x10 <sup>-3</sup>	1.25x10 <sup>-3</sup>	2.60x10 <sup>-3</sup>	2.51x10 <sup>-3</sup>	7.09	8.19

Another example of an optimization process in order to improve landing gear emergency extension performance, yet comprising continuous optimization, is demonstrated as follows.

As shown in fig. 11, the overall time for main landing gear to lock down at low hydraulic fluid temperatures can increase considerably if compared to a nominal operational temperature of about 37°C (100°F). Therefore, a continuous optimization technique is applied aiming to reduce the main landing gear extension time in at least 1.5 seconds at a hydraulic fluid operating temperature of -32°C (-25°F). According to fig. 11, the main landing gear took about 11.4 seconds to completely extend at the corresponding temperature.

For a MATLAB® Simulink® model, the use of a "Signal Constraint Block", taken from the Simulink Response Optimization library, facilitates significantly the user's workload when accomplishing a continuous optimization process. In order to optimize a variable response, the aforementioned block shall be linked to the respective signal of the Simulink® model and, by means of a graphical

interface representation, have the signal amplitude limits defined by the user. As a result, by running the optimization algorithm, the selected design parameters values are adjusted to make the output signal obey the imposed bounds. Moreover, it is also possible to require that the variable response track a reference signal defined in the "Signal Constraint Block" user's interface [11].

Figure 13 presents the "Signal Constraint Block" applied to optimize the main landing gear emergency extension performance of the present model. The combination of the external torques in the left-side of fig. 13 are divided by the landing gear moment of inertia and then integrated twice to lead to the main landing gear extension angle. By means of a "Signal Constraint Block" linked to the main landing gear extension velocity signal, the respective variable response over the time can be enhanced through the application of the optimization process.

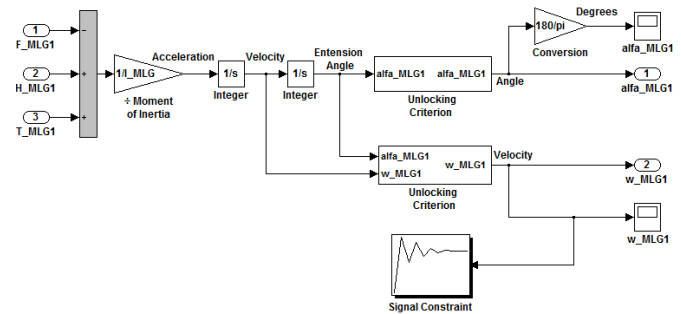


Figure 13 – Use of the "Signal Constraint Block" in main landing gear emergency extension optimization

For the present simulation, the "Signal Constraint Block" default optimization algorithm method called "gradient descent", applying a "medium scale" model size, was selected. The gradient descent algorithm makes use of MATLAB® Optimization Toolbox "fmincon" function to find the minimum of a nonlinear multivariable scalar function, subjected to predefined constraints in response signal and in design variable values, starting at an initial estimate. The "fmincon" function consists in a gradient-based method that applies finite difference techniques for calculation of function gradients. Concerning the option for a medium-scale model, it represents the solution of a quadratic programming subprogram and the use of a quasi-Newton approximation to calculate the Hessian of the Lagrangian at each iteration. Finally, the algorithm also allows the possibility of looking for the maximally feasible solution, which represents the finding of an optimal solution that is generally located further inside the constraint region instead of just closely satisfying the constraints [11].

The continuous system optimization was accomplished applying as design parameters three of the five component features associated with main landing gear actuation shown in tab. 1. Therefore, the orifice area of the restrictor valve located in main landing gear extension line and the tube diameters of both legs operation lines had their dimensions optimized in order to improve main landing gear emergency performance at low hydraulic fluid temperature. These parameters were selected due to the apparent convenience in

updating their respective components, that is, restrictor valve and tubes, without more significant impacts.

As a result, the parameters evaluated during the system continuous optimization process, as well as their nominal and limit values, are present in tab. 3. The parameter optimum values obtained through the application of the "Signal Constraint Block" optimization algorithm are informed in the last column of tab. 3.

In order to obtain the optimum solution, the algorithm performed 4 iterations, accomplishing 28 objective function evaluations. The iteration results and the response signal imposed bounds applied during the optimization process are displayed in fig. 14. The white background area represents the allowable region for the output signal to stay within during the extension time interval.

Table 3: System design parameters applied in continuous optimization

Parameter	Nominal Value	Minimum Value	Maximum Value	Optimum Value
Restrictor 2 ( $A_0$ )	$2.54 \times 10^{-6}$	$1.96 \times 10^{-7}$	$7.07 \times 10^{-6}$	$7.07 \times 10^{-6}$
Tubing 3 (D)	$8.00 \times 10^{-3}$	$4.00 \times 10^{-3}$	$1.50 \times 10^{-2}$	$9.40 \times 10^{-3}$
Tubing 4 (D)	$8.00 \times 10^{-3}$	$4.00 \times 10^{-3}$	$1.50 \times 10^{-2}$	$1.38 \times 10^{-2}$

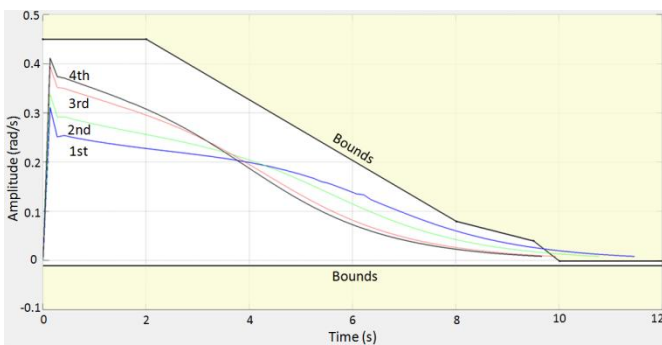


Figure 14 – "Signal Constraint Block" optimization result

Finally, considering the enhanced values obtained by means of the current optimization process for low hydraulic fluid temperature, the new landing gear free-fall extension times were 7.4 seconds and 9.7 seconds, for nose landing gear and main landing gear, respectively. Meanwhile for nose leg practically no improvement in extension time was achieved, which was expected since the design parameters chosen do not have direct effects on its performance, for main landing gear a reduction of 1.7 seconds in extension time was successfully obtained. Moreover, no degradation in landing gear emergency extension performance was observed through the use of the continuous optimized parameter values if compared with the nominal simulation results shown in fig. 7 to fig. 10, for a hydraulic fluid operational temperature of 37°C (100°F). For this condition, the extension times of nose and main landing gear are 6.7 seconds and 8.4 seconds, respectively.

## 5 Conclusions

The objective of the present work was to provide an example of modeling and simulation of a test rig airplane landing gear free-fall system applying MATLAB® software. In spite of the modeling assumptions considered, the formulation applied to construct the model yielded results that seemed to be satisfactorily representative of an airplane landing gear typical free-fall extension operation. Nowadays, the hydraulics formulation presented herein can be found implemented in several pieces of simulation software that apply a Physical Network approach, hence facilitating significantly the design process frequently performed by landing gear system engineers.

Besides running nominal simulations, the effects of hydraulic fluid low temperature operation and the presence of entrapped air in landing gear system could also be evaluated through complementary model simulations. The use of a landing gear free-fall system model to predict the impacts of these particular conditions during later aircraft operation is important to assure an acceptable system performance throughout the required flight envelope or for unusual system operational characteristics.

The impact a landing gear leg downward movement may cause to aircraft structure and the safety-related issue comprising the system capability of assuring landing gear downlocking at all foreseeable operational conditions are among the main concerns landing gear engineers have during the design of this type of system.

Therefore, a discrete optimization process, representative of the situation commonly dealt with by system designers, was firstly used to determine the best values for some model parameters in order to improve both nose and main landing gear system performance. Afterwards, an example of the application of a continuous optimization procedure was also introduced to illustrate the facilities of using the optimization algorithms currently found in simulation software like MATLAB®. Although the feasibility of the optimum solutions provided by these algorithms still needs to be validated by an engineering analysis, they might represent a good sight of the global optimum solution for the design problem, as well as being applied as a starting point for a subsequent discrete optimization process.

Consequently, the benefits of applying a virtual modeling and optimization process to reduce the possibility of system redesign in advanced stages of the product development, especially in system test rig phase, could be observed in the present work. The adoption of these processes and techniques shall be interpreted not only as a costly saving attitude, but also as a way of shortening airplane development cycle.

On the other hand, in a next step of the development process, the system model will need to be improved to consider the aerodynamic effects and eventual maneuver inertial effects expected to occur in flight. For flight conditions, other extension time values requirements might be applicable.

Finally, since aeronautical system design commonly represents a trade-off between several aspects like system performance, weight, cost, maintenance and manufacturing issues, requirements from these fields may also be considered in any optimization process.

## Nomenclature

A list of the variables and parameters referred to in this article is present below.

Designation	Denotation	Unit
$a$	Distance between landing gear center of gravity and landing gear-to-aircraft attachment	[m]
$A$	Tube internal sectional area	[m <sup>2</sup> ]
$A_o$	Restrictor orifice or valve port area	[m <sup>2</sup> ]
$A_{p1}$	Piston area at actuator chamber 1	[m <sup>2</sup> ]
$A_{p2}$	Piston area at actuator chamber 2	[m <sup>2</sup> ]
$B$	Damping coefficient	[N.m.s/rad]
$C_d$	Discharge coefficient	
$C_{ep}$	Actuator external leakage coefficient	[m <sup>3</sup> /s.Pa]
$C_f$	Ideal compliance	[m <sup>3</sup> /Pa]
$C_{ip}$	Actuator internal leakage coefficient	[m <sup>3</sup> /s.Pa]
$D$	Tube inside diameter	[m]
$D_o$	Restrictor orifice diameter	[m]
$f$	Tube friction factor	
$F$	Viscous friction torque	[N.m]
$g$	Gravitational acceleration	[m/s <sup>2</sup> ]
$h$	Hydraulic actuator force	[N]
$H$	Hydraulic actuator torque	[N.m]
$I$	Landing gear moment of inertia	[kg.m <sup>2</sup> ]
$I_f$	Inertance parameter	[kg.m <sup>4</sup> ]
$K$	Landing gear kinetic energy	[J]
$L$	Tube length	[m]
$m$	Landing gear mass	[kg]
$P$	Line pressure	[Pa]
$P_1$	Pressure in actuator chamber 1	[Pa]
$P_2$	Pressure in actuator chamber 2	[Pa]
$Q$	Fluid flow	[m <sup>3</sup> /s]

$Q_1$	Fluid flow in the actuator chamber 1	[m <sup>3</sup> /s]
$Q_2$	Fluid flow in the actuator chamber 2	[m <sup>3</sup> /s]
$r$	Hydraulic actuator torque arm	[m]
$Re$	Reynolds number	
$t$	Time	[s]
$T$	Weight torque	[N.m]
$V$	Fluid velocity	[m/s]
$V_G/V_T$	Relative amount of trapped air	
$V_1$	Volume of actuator chamber 1	[m <sup>3</sup> ]
$V_2$	Volume of actuator chamber 2	[m <sup>3</sup> ]
$\alpha$	Landing gear extension angle	[rad]
$\dot{\alpha}$	Landing gear extension velocity	[rad/s]
$\ddot{\alpha}$	Landing gear extension acceleration	[rad.s <sup>2</sup> ]
$\beta_C$	Container bulk modulus	[Pa]
$\beta_e$	Effective bulk modulus	[Pa]
$\beta_G$	Gas bulk modulus	[Pa]
$\beta_L$	Fluid bulk modulus	[Pa]
$\delta$	Laminar flow coefficient	
$\Delta P$	Pressure variation	[Pa]
$\mu$	Fluid dynamic viscosity	[Pa.s]
$\rho$	Fluid density	[kg/m <sup>3</sup> ]

## References

- [1] N S Currey. *Aircraft Landing Gear Design: Principles and Practices*, AIAA Education Series, Washington, 1998, p. 373. ISBN 0930403-41-X.
- [2] E Kelly. Pictures: Australian General Dynamics F-111 approved for service re-entry after June wheels-up landing. *Global International*. July, 2006. < <http://www.flightglobal.com/news/articles/pictures-australian-general-dynamics-f-111-approved-for-service-re-entry-after-june-wheels-up-landing-208102/>>.
- [3] Liebherr. *Landing Gear Sub System: Extension / Retraction*. <[http://www.liebherr.com/AE/enGB/products\\_ae.wfw/id-14726-0](http://www.liebherr.com/AE/enGB/products_ae.wfw/id-14726-0)>.
- [4] Federal Aviation Administration. *Flight Test Guide for Certification of Transport Category Airplanes*. AC 25-7C. Washington: U.S Department of Transportation, 2012.

- [5] M Maia Neto. *Modelagem, simulação e otimização de sistemas de extensão emergencial de trem de pouso de aeronaves*. 2011, p. 241. Dissertação de Mestrado em Sistemas Aeroespaciais e Mecatrônica – Instituto Tecnológico de Aeronáutica, São José dos Campos.
- [6] E O Doebelin, *System Dynamics: Modeling, Analysis, Simulation, Design*. Marcel Dekker, New York, 1998, pp. 54-75, 206-255. ISBN 0-8247-0126-7
- [7] H E Merritt. *Hydraulic Control Systems*. John Wileys and Sons, Cincinnati, Ohio, 1967. ISBN 0-471-59617-5.
- [8] M Maia Neto, L C S Góes and R C M Furtado. Landing gear free-fall simulation and damping optimization using Matlab. *Inverse Problems, Design and Optimization Symposium*. João Pessoa, pp. 55-62, 2010.
- [9] M Maia Neto, L C S Góes and R C M Furtado. Landing gear free-fall simulation and kinetic energy optimization. *SAE Technical Paper Series*. São Paulo, 2010, p. 14. ISSN 0148-7191.
- [10] Mathworks. *SimHydraulics: User's Guide*. Natick: The MathWorks Inc, v. 1.8, 2010. <[http://www.mathworks.com/help/pdf\\_doc/physmod/hydro/hydro\\_ug.pdf](http://www.mathworks.com/help/pdf_doc/physmod/hydro/hydro_ug.pdf)>.
- [11] Mathworks. *Matlab: The Language of Technical Computing (Matlab Help)*. Natick: The MathWorks Inc, 2007.
- [12] P Venkataraman. *Applied Optimization with MATLAB® Programming*. New York: John Wiley & Sons, 2002. p. 398. ISBN 0-471-34958-5.

# Valve Technology 1



# Investigation on the Dynamic Behavior of a Solenoid Hydraulic Valve for Automotive Semi-Active Suspensions Coupling 3D and 1D Modeling

Matteo Pelosi, Kashyap Subramanya\*, and Jonas Lantz\*\*

Öhlins Racing AB, Jönköping, Sweden

\*Linköping University, Linköping, Sweden

\*\*Applied Thermodynamics and Fluid Mechanics Division, Linköping University, Linköping, Sweden

E-mail: matteo.pelosi@ohlins.se, kassu303@student.liu.se, jonas.lantz@liu.se

## Abstract

The aim of this paper is to investigate the influence of the internal fluid flow characteristics of a special hydraulic solenoid valve, developed by Öhlins Racing AB, on its overall dynamic behavior. This valve is a two stage hydraulic pressure control valve and is typically mounted on each shock absorber of an on-road vehicle, allowing the implementation of semi-active suspension functionality. This technology is referred as CES (Continuously Controlled Electronic Suspension). The CES valve allows continuously controlling the vehicle shock absorbers damping characteristic by proportionally adjusting the metering geometry offered to its damping element, i.e. hydraulic oil. The electronic valve actuation and control, obtained through an electromagnetic solenoid, is based on the input from several vehicle dynamics sensors, such as accelerometers, gyroscopes and other displacement sensors. The CES valve's unconventional design significantly influences the fluid flow, making the use of numerical modeling essential to discover its physical behavior and to support further product development. In this paper, a CFD (Computational Fluid Dynamics) analysis on the main and pilot stages of the hydraulic valve is discussed. This 3D numerical analysis is used to extract critical physical variables, affecting the valve behavior, such as flow coefficients and pressure distributions on the moving elements, i.e. flow forces. This information is coupled with a detailed lumped parameter model of the hydraulic valve, which solves for the valve moving element dynamics considering the action of the main external forces. Moreover, the 1D model allows predicting the valve critical pressure/flow characteristics. It is shown how the coupling of 3D modeling results with the CES valve 1D model strongly improves the whole valve dynamics numerical predictions over traditional methods for considering the effect of fluid inertia and discharge in lumped parameter simulations. Comparisons with measurement both on single regions of the CES hydraulic valve and on the entire valve are discussed in order to validate the various phases of numerical modeling.

**Keywords:** Semi-active suspensions, shock absorber, hydraulic valve, flow forces, CFD

## 1 Introduction

Several aspects influencing the behavior of two-wheel or four-wheel vehicles, both on-road and off-road, are significantly influenced by their shock absorbers characteristics. In particular, the vehicle comfort, handling, grip and stability are a direct consequence of the shock absorber performance and they have to be carefully tuned by a vehicle manufacturer in order to meet the customer demands.

Most of the vehicles today are equipped with passive shock absorbers, which, by connecting the vehicle chassis to the wheels, perform a critical damping function on the overall vehicle dynamics, leading to an improved ride quality. Referring to conventional shock absorbers, the damping

characteristic is typically obtained by metering hydraulic oil through a set of special internal valves mounted in the damper. The damper kinetic energy is dissipated through fluid friction and the shock absorber damping response depends on the passive valves tuning. Different damping behavior for the shock absorbers compression (wheel moving towards the chassis) and rebound (wheel moving away from the chassis) cycles can be implemented, by mounting valves with different metering characteristics.

Öhlins Racing AB (Sweden) is a worldwide leader in the design and development of passive shock absorbers for a variety of on-road and off-road applications. These state of the art shock absorbers fulfill the vehicle damping requirements, by allowing the end customer a wide range of discrete settings while preserving a superior level of

performance. However, a passive damper is unable to change its damping characteristics in real-time. The behavior of the shock absorber is determined by the hydraulic valving fixed metering settings and cannot continuously adapt to the changing driving conditions.

A hydraulic semi-active suspension overcomes this limitation, by allowing a continuous electronic control of the shock absorber damping characteristics. This is obtained by continuously varying the metering geometry offered to hydraulic oil within the damper. The semi-active shock absorber can adapt its behavior during the compression and rebound cycles, considering several driving aspects, i.e. vehicle roll, pitch and yaw attitudes, vehicle accelerations, wheel displacements and throttle position. A simplified depiction of a semi-active suspension system is shown by Figure 1.

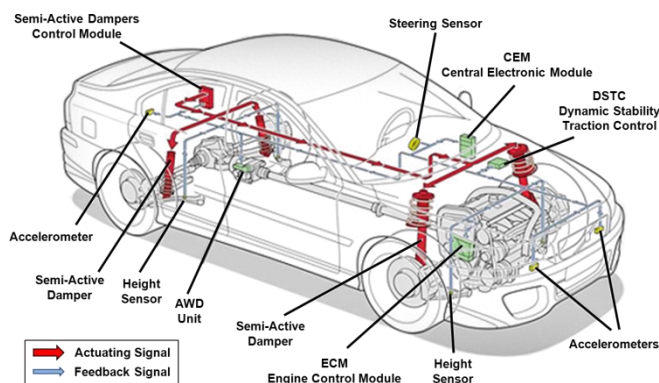


Figure 1: Semi-active suspension technology schematic

Öhlins CES Technologies is dedicated to the research and development of semi-active suspensions technology, named CES (Continuously Controlled Electronic Suspension). In particular, the core of Öhlins semi-active suspensions is represented by the hydraulic control valve responsible for continuously controlling the shock absorber fluid flow and damping performance. This hydraulic valve, is a two stage proportional control valve, actuated by an electromagnetic solenoid. It represents a state of the art component, in use by the several major automotive manufacturers to offer semi-active suspensions as standard or optional features in their vehicles. The special hydraulic valve design allows obtaining a smooth pressure-flow characteristic at different input currents, which is ideal for implementing efficient damper control strategies. To obtain such performance characteristics, the CES valve presents unique design features, which strongly influences the internal fluid flow behavior. In addition, the small dimensions of this component, coupled with high operating pressure and flow rates, make several design details critical for a proper valve performance. Therefore, only through advanced computer simulation it is possible to capture the physical phenomena taking place in the valve, to exactly predict its behavior, to study novel design changes and to shorten the product development leading to a better performance by supporting Öhlins Racing engineers during the design phase.

For these reasons, in this paper a CFD (Computational Fluid Dynamics) analysis on the most critical regions of the CES valve is presented. The numerical results obtained by this

extensive 3D modeling analysis are discussed and used to improve the predictions of a detailed lumped parameter model of the CES valve. In fact, if the steady state CFD studies allow capturing the internal fluid behavior at different boundary conditions and moving elements positions, only with a 1D numerical model it is possible to predict the overall valve dynamic performance, both when studied singularly or coupled with a shock absorber model. In particular, the CFD results allow defining the correct flow regime and flow coefficients at different operating conditions for the critical metering elements of the valve. In addition, the prediction of the flow field static pressure distribution on the moving element surfaces is a key to determine their correct force balance [1]-[3]. Hence, the results from CFD analysis are used to consider the effect of flow inertia on the moving elements dynamic equilibrium solved by the lumped parameter model.

The numerical results obtained by the coupled 3D and 1D numerical modeling are validated both by using special measurements on specific regions of the valve and by testing the complete CES valve over its typical working range.

## 2 The CES8700 Solenoid Hydraulic Valve

In this study, one of the CES valves designed by Öhlins CES Technologies, named CES8700, is analyzed and is shown in Figure 2.



Figure 2: Öhlins Racing CES8700 hydraulic control valve compared to 1 Swedish Krona

The CES8700 is a pilot operated pressure control valve composed by two hydraulic stages, a main stage and a pilot stage, and continuously controlled by an electromagnetic linear actuator, a solenoid.

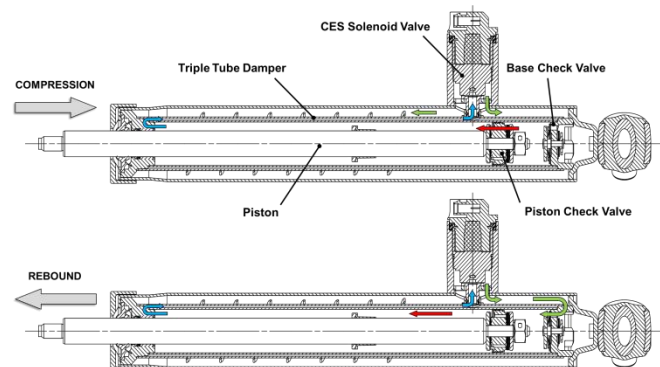


Figure 3: CES8700 valve operation in triple tube damper

The CES8700 valve is externally mounted on triple tube type shock absorbers and, thanks to the triple tube design, receives flow only in one direction through the main stage inlet port, as depicted by Figure 3.

The pilot operated solenoid valve allows controlling the damper fluid pressure through the main stage poppet using small solenoid forces. The pilot stage moving element, connected to the solenoid rod, by regulating the main stage pilot pressure, determines the main poppet metering effect on the damper fluid flow. Hence, a continuously controllable damper stiffness is achieved by adjusting the pressure forces acting on the piston of the shock absorber.

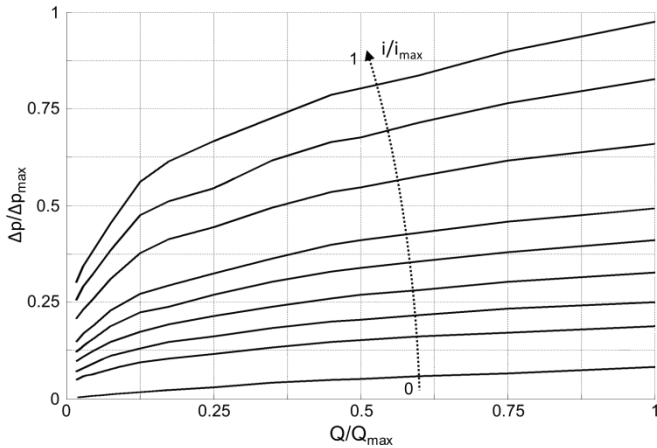


Figure 4: CES  $p$ - $Q$  characteristic over a range of currents

A typical CES pressure/flow characteristic is shown in Figure 4. It can be noticed how increasing levels of input current generate a progressively higher pressure level across the valve. This is due to the higher solenoid force acting on the pilot poppet, determining higher pilot pressure and increasing the main poppet metering effect.

The understanding of the physical phenomena within the main stage and pilot stage is critical to predict the hydraulic valve behavior. Hence, the numerical modeling is focused on capturing the behavior of the critical features of these two stages. In particular, the key components of main and pilot stages are presented in Figure 5.

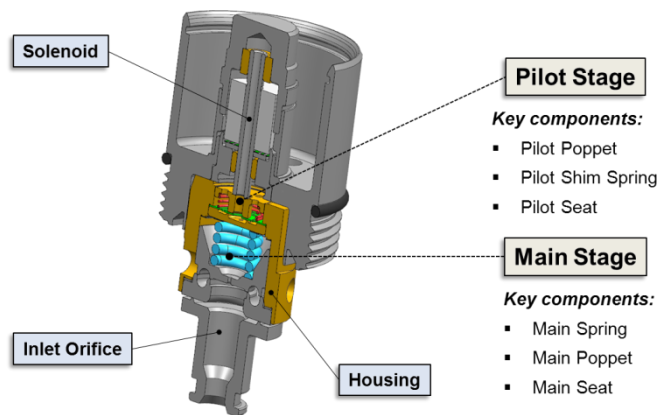


Figure 5: CES8700 detailed view of key mechanical components

The pilot stage metering element is also an essential elastic element, being a specially designed shim spring. The pilot

shim spring, always in contact with the pilot poppet, alters its shape during the stroke due to the spring elastic deformation. The main poppet presents two annular orifices in series separated by a unique toroid shaped volume, which provides the CES valve with a smooth metering characteristic and additional stability.

Due to the unconventional geometrical design of the CES valve, numerical simulation is used to understand the hydraulic valve behavior over a wide range of operating points. A 1D AMESim model solves the second order dynamics of the hydraulic system, considering the mutual influence of several external forces on the moving elements and the hydraulic volumes transient pressure build-up. Springs, viscous, hydro-static and hydro-dynamic forces are calculated by the lumped parameter simulation model, as well as instantaneous flow rates and pressures. Steady-state distributed parameters analysis on the main and pilot stages of the valve, based on Ansys Fluent solver, is used to improve the prediction of this detailed 1D simulation model, concerning in particular flow discharge and hydrodynamic forces behavior [4]. In the next sections, the numerical analysis and the methods introduced to couple 3D and 1D simulations are discussed.

### 3 The 3D Ansys Fluent Simulations

In order to capture the fluid flow behavior in one of the key variable metering regions of the CES8700 valve, RANS (Reynolds Averaged Navier-Stokes) CFD analysis have been performed. The Ansys Fluent solver has been used to run a set of steady-state simulations for the main stage and pilot stage geometries [5]-[10]. The two geometries have been analyzed in two separate environments, assigning proper boundary conditions. Velocity inlets/pressure outlets boundaries are chosen in order to cover the known operating range. In addition, knowing the pilot and main poppet maximum strokes, several CFD studies have been completed at discrete values of progressively higher poppet positions. The main settings for the performed steady-state CFD analysis on the two valve stages are grouped in Table 1.

<b>Fluid model</b>	Newtonian, incompressible
<b>Turbulence model</b>	RANS, realizable $k$ - $\epsilon$
<b>Near wall model</b>	Enhanced Wall Treatment
<b>Schemes Accuracy</b>	Second order
<b>Mesh type</b>	Hybrid (Teth + Prism + Hex)
<b>Mesh size</b>	~2 million cells

Table 1: CFD analysis general settings

The fluid is hydraulic oil, considered Newtonian in its shear properties and incompressible in the considered operating range. The turbulence is captured by using a typical two equations model, the *realizable  $k$ - $\epsilon$*  type [11]. This model is used in many practical engineering flow calculations, thanks to its robustness, economy and accuracy for a wide range of turbulent flows. Additionally, the *realizable* version, compared to *standard  $k$ - $\epsilon$*  models, improves the mathematical formulations around the definition of the critical Reynolds stresses, leading to a better prediction over

flows characterized by strong streamline curvature, vortices and rotations. The CES8700 valve geometry induces these types of flow features. Near-wall turbulence modeling is another critical aspect of RANS CFD simulations, strongly dependent on the grid resolution. The Enhanced Wall Treatment (EWT) available in Ansys Fluent, makes the turbulence model relatively insensitive to the first cell wall distance parameter,  $y^+$ , combining a two-layer model with wall functions. Where the mesh is fine enough,  $y^+ \approx 1$ , a traditional two-layer zonal model is used to predict boundary layer behavior; while where the near-wall mesh is coarser an enhanced wall function formulation is implemented [12]. This method allows overcoming the computational requirements imposed by a standard near-wall resolving turbulence model, which imposes a mesh sufficiently fine everywhere. In order to further reduce the computational expense, hybrid meshes have been generated, combining different meshing methods. In particular, hex dominant meshes have been used wherever possible, to strongly reduce the element count and enhance numerical schemes discretization. Only the most geometrically complex zones have been meshed using tetrahedrons. The near-wall fluid shear layers have been discretized using 12 prism cells normal to the layers.

In the next sections, additional details on the performed CFD analysis for the CES8700 main and pilot stages are provided together with the most significant numerical results.

### 3.1 Main Stage

The main stage fluid domain accurately replicates the 3D inlet geometry and, due to some internal non-symmetrical features, an axisymmetric analysis could not be performed. Hence, the fluid domain is studied in a half symmetric condition, in order to reduce the computational burden. Figure 6 provides a depiction of the main stage geometry and fluid domain. The hole connecting the inlet volume with the main poppet chamber is removed to isolate the analysis to the main stage restrictions.

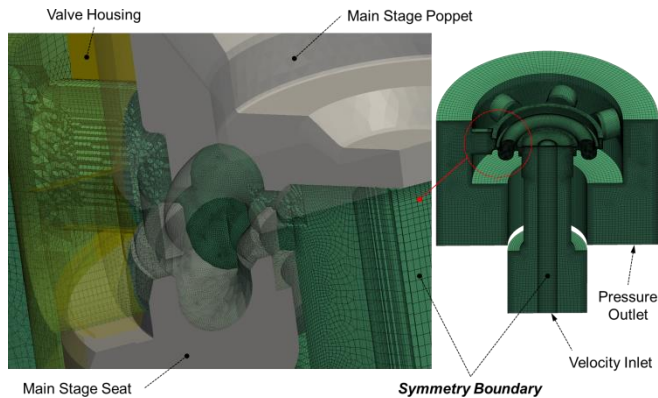


Figure 6: Main stage hybrid fluid mesh with symmetric boundary and zoomed clipped view on critical region

The accuracy and quality of the CFD analysis is validated against flow-bench experiments replicating exactly the CFD model setup. In particular, simulations with the poppet at fixed discrete positions have been compared with

measurements, as shown by Figure 7. The pressure-flow characteristic of the main stage is represented by the total pressured drop between inlet and outlet boundaries. It should be noticed how the accuracy of the CFD modeling is strongly improved by the introduction of a multi-phase model, which models the gas entrainment in the fluid and its impact on the inlet pressure build-up. In particular, the Zwart-Gerber mixture model is used, with a saturation pressure of  $1.0e4$  Pa. Gas entrainment effects are amplified by the unconventional main stage geometry: high speed vortical flows in the toroidal regions induce local static pressure drops, influencing the fluid phase volume fractions and the overall main poppet dynamics.

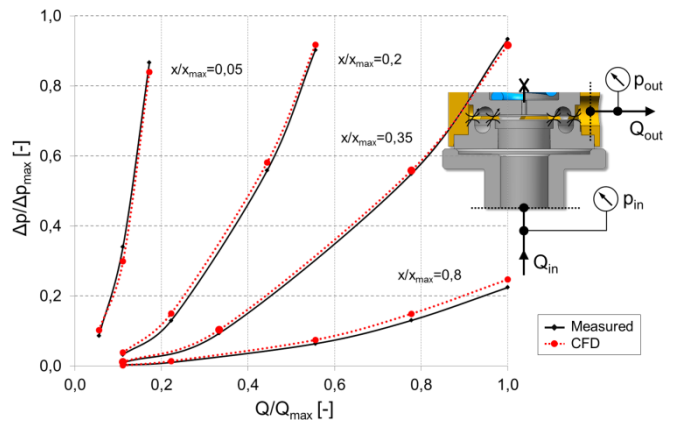


Figure 7: CFD and measured total  $p$ - $Q$  characteristics across the main stage at different fixed positions

Typical CFD analysis results from a main stage simulation are shown by Figure 8, where the complexity of the fluid field and its influence on the variable hydraulic volumes pressure build up can be noticed.

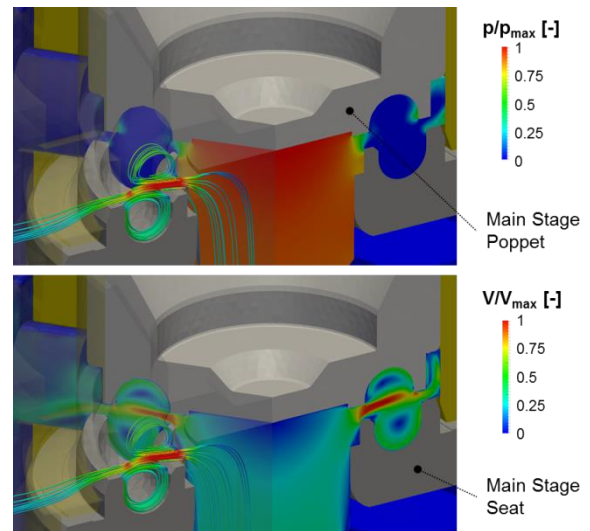


Figure 8: Main stage CFD static pressure (top) and velocity (bottom) fields for one opening position

A combination of vortical flow fields, pressure stagnation regions and fluid jet interference on the moving element surfaces make CFD studies necessary to improve the lumped parameter model. In the main stage AMESim lumped parameter model, the flow rate calculations for each

annular metering orifice are based on the Bernoulli turbulent equation, as shown by Equation 1.

$$Q = C_q(x)\Omega(x)\sqrt{\frac{2|\Delta p|}{\rho}}\text{sign}(\Delta p) \quad (1)$$

Where the flow coefficient  $C_q$  is expressed as an hyperbolic tangent dependent on the main poppet lift,  $x$ , as follows:

$$C_q(x) = C_q^\infty \tanh\left(\frac{2x}{x_{\text{crit}}}\right) \quad (2)$$

The infinite flow coefficient  $C_q^\infty$  corresponds to the Von Mises asymptote or fully turbulent flow, while the critical poppet lift,  $x_{\text{crit}}$ , represents a value at which separation between laminar and turbulent flow occurs [13]. The use of a hyperbolic tangent allows a smooth transition between the two separate regimes.

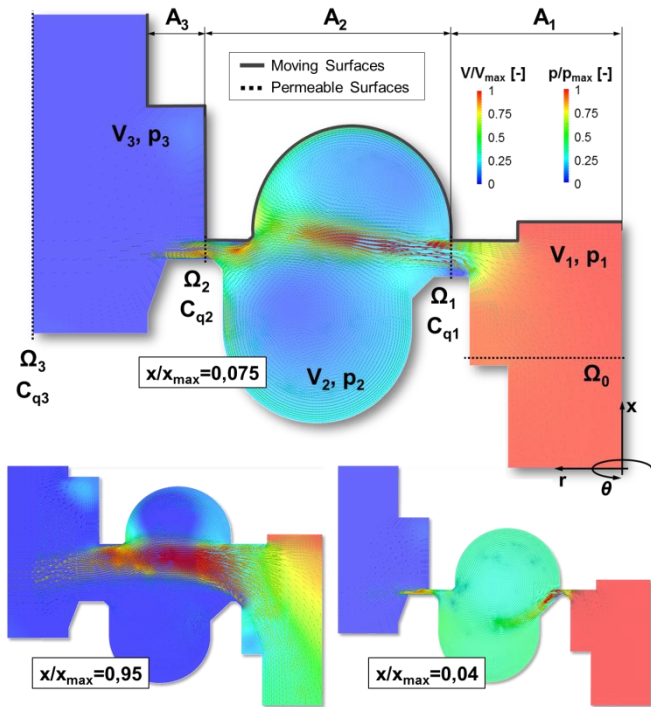
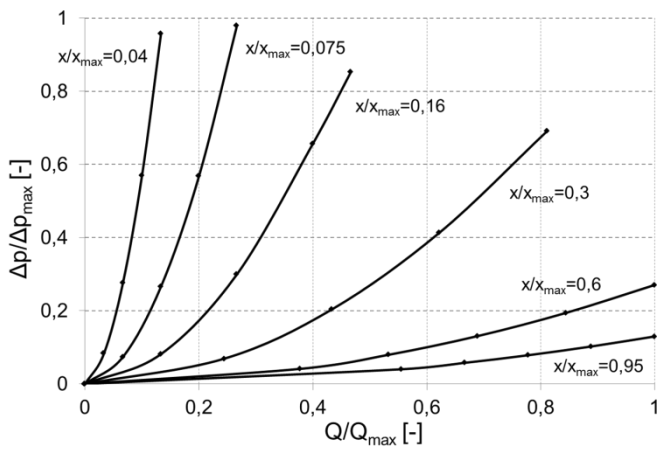


Figure 9: Main stage  $p$ - $Q$  curves from CFD analysis (top), critical parameters on 1D control volumes (center) and CFD flow fields at different openings (bottom)

Using the pressure-flow CFD simulation results as a reference and studying the flow field properties, shown by Figure 9, the values of the flow coefficients on the inner and outer restrictions are extracted for different poppet positions. Being the pressure-flow characteristics turbulent at all openings, the critical poppet lift number is kept constant at  $1.0e-6$ . Referring to Figure 9, the AMESim model considers the pressure build-up in the separate control volumes characterizing the main stage. Hence, the inner and outer annular restrictions are treated separately. The main stage flow coefficients are expressed as a function of the main poppet lift, as depicted by Figure 10.

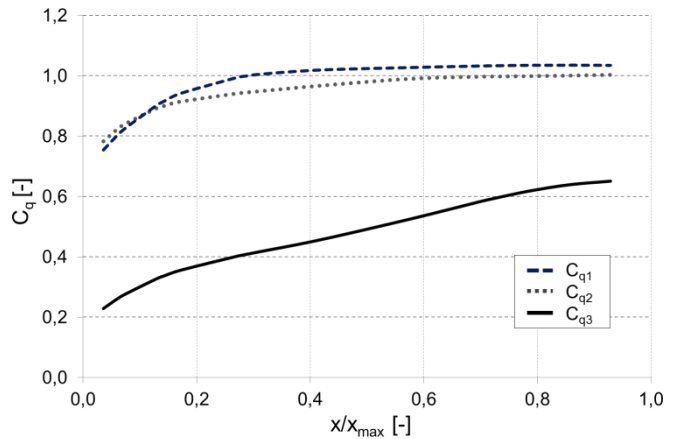


Figure 10: Main stage flow coefficients as a function of the main poppet lift

The flow coefficients curves are implemented in the 1D AMESim model to fit the pressure-flow characteristics predicted by the CFD analysis. The enhancement of the main stage lumped parameter 1D model in the pressure-flow calculations after the introduction of the CFD derived flow coefficients is shown by Figure 11.

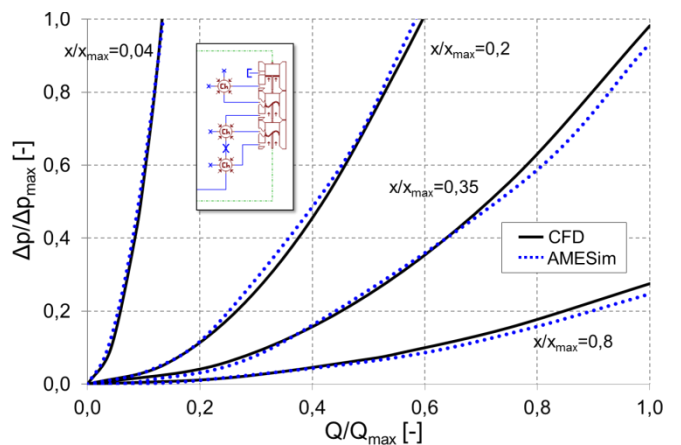


Figure 11: Main stage AMESim model pressure-flow characteristics compared with CFD results

Another critical aspect related to the lumped parameter modeling of hydraulic components is the influence of fluid inertia on the static pressure distributions, which ultimately govern the moving elements second order dynamics. The pressure stagnation phenomena, the non-homogenous 3D flow fields and the real separation between the control volumes pressure distributions, significantly affect the moving element active surfaces. For clarity, the method

implemented for the determination of the hydrodynamic forces acting on the moving elements, based on the discussed CFD analysis, is outlined in the next section concerning the pilot stage modeling.

### 3.2 Pilot Stage

The pilot stage fluid domain is simplified taking advantage of the cyclical geometric design. In particular, a three-dimensional arc of  $120^\circ$  is considered. A single phase modeling of the fluid is considered, hence no air release and/or cavitation models are used. A pictorial representation of the fluid domain within the pilot stage geometry is given by Figure 12. It should be noticed how the pressure regulation is performed by a special shim spring, which simultaneously performs elastic and metering functions.

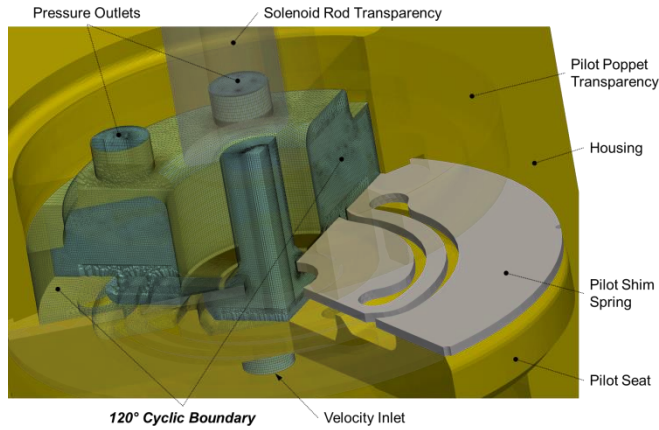


Figure 12: Pilot stage fluid hybrid mesh with cyclic periodicity clipped view for one opening position

Typical results from the CFD study at a given pilot poppet/shim spring position are shown in Figure 13, where the static pressure distribution on the pressurized shim surface, the pressure build-up upstream the annular metering region and the velocity field have to be considered in the coupling between 3D and 1D models.

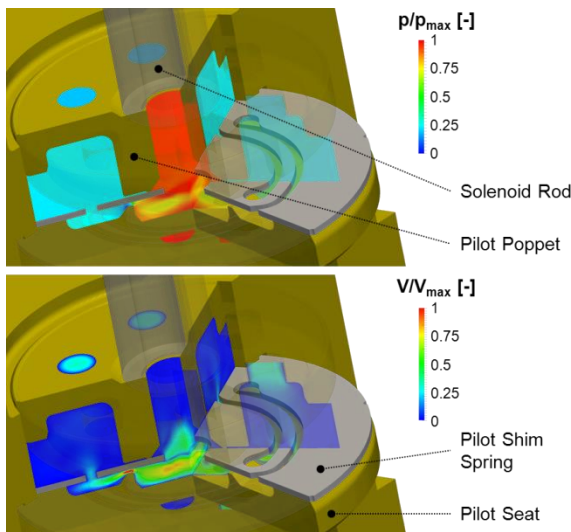


Figure 13: Pilot stage CFD static pressure (top) and velocity (bottom) fields for one opening position

Several operating points are considered in terms of poppet/shim positions, i.e. metering openings, and inlet flow rate, to extract the most critical fluid flow variables to be implemented in the 1D model. Similarly to the main stage analysis, pressure-flow characteristics for the pilot stage can be extracted from the CFD simulations, as depicted by Figure 14.

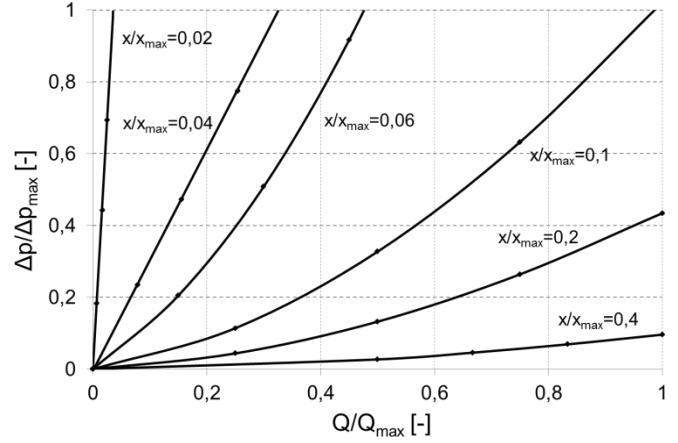


Figure 14: Pilot stage  $p$ - $Q$  curves from CFD analysis in the small stroke range

Referring to Figure 14, due to the long overlap between pilot shim and pilot seat generating a thin annular gap, the transition between laminar to fully turbulent flow characterizes at least the first part of the stroke. Laminar CFD simulation in this range have been performed to confirm this behavior. This working area is critical for the pilot stage and overall valve dynamics, hence a correct modeling of the transition is a key element to predict the CES8700 physical behavior. For this reasons, in the pilot stage 1D model the Bernoulli orifice equation, Equation 1, is modified to better approximate the  $p$ - $Q$  characteristics predicted by the CFD analysis. In particular, the following relationship is implemented:

$$Q = K_q(x) \Omega(x) \eta \sqrt{\frac{2|\Delta p|}{\rho}} \text{sign}(\Delta p) \quad (3)$$

Where  $K_q$  and  $n$  are a special flow coefficient and a flow exponent respectively.

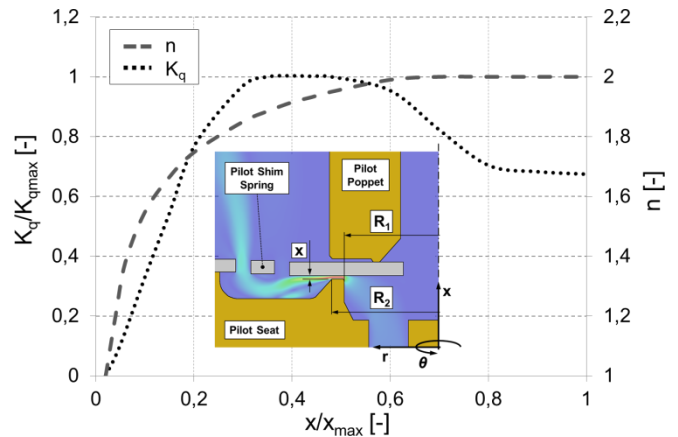


Figure 15: Pilot stage flow coefficient and flow exponent function of poppet/shim position

Their behavior over the poppet/shim stroke is derived from the CFD simulations results and is represented in Figure 15.

Referring to Figure 15, it can be noticed how in the laminar region the flow exponent reaches the value of 1, while the flow coefficient strongly reduces its value, approximating Equation 3 to the typical laminar Poiseuille flow equation for an annular metering gap, shown by Equation 4.

$$Q_{lam} = \frac{\pi}{6\mu \ln(R_2/R_1)} x^3 \Delta p \quad (4)$$

The flow parameters derived from CFD are fed as input to a special AMESim in-house developed model, which replicates the pilot stage flow behavior predicted by the CFD analysis, as shown by Figure 16.

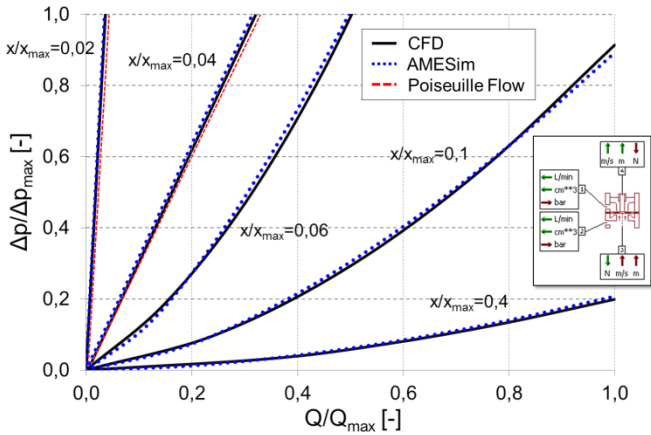


Figure 16: Pilot stage 1D-3D AMESim model pressure-flow characteristics compared with CFD results

As already mentioned in the previous section on the main stage, a critical aspect of lumped parameter modeling of hydraulic valves is represented by the prediction of the hydrodynamic forces acting on the moving elements. In fact, the pressure in each control volume is not uniform, since the fluid momentum causes local variations of static pressure distribution. Hence, the real hydraulic pressure forces acting on the moving bodies can be derived with the contribution of CFD analysis. In the pilot stage, the significant overlap characterizing the shim spring/pilot seat annular orifice together with the 3D fluid jet interactions with the shim body make the static pressure fields and the consequent opening pressure forces a critical physical parameter to be determined. Referring to Figure 17 and focusing on the annular metering orifice region, where the flow field approximates axisymmetric conditions, part of the hydrodynamic forces evaluation is can be based on the classic flow force expression, deriving from the integration of the momentum equation over the system control volume. Assuming incompressible, steady-state conditions, the general expression for the active hydraulic force acting on the poppet/shim assembly leads to:

$$\vec{F}_{hyd}|_x = p_0 A_0 + p_1 A_1 - \rho Q (\vec{U}_1 \cos \delta_1 - \vec{U}_0 \cos \delta_0) \quad (5)$$

Where  $\vec{U}$  is the fluid velocity vector and  $\delta$  is the fluid jet angle formed with the  $x$ -axis. Thanks to the overlapped

design on the restriction, the jet angle is not varying significantly over the stroke, being  $\delta_1$  consistently close to  $90^\circ$ , especially at the smaller openings. However, the impact of fluid momentum on the effective hydraulic forces is known to be significant, hence the equivalent representation of the separation between the two static pressure fields upstream and downstream the pilot restriction has to be improved [14].

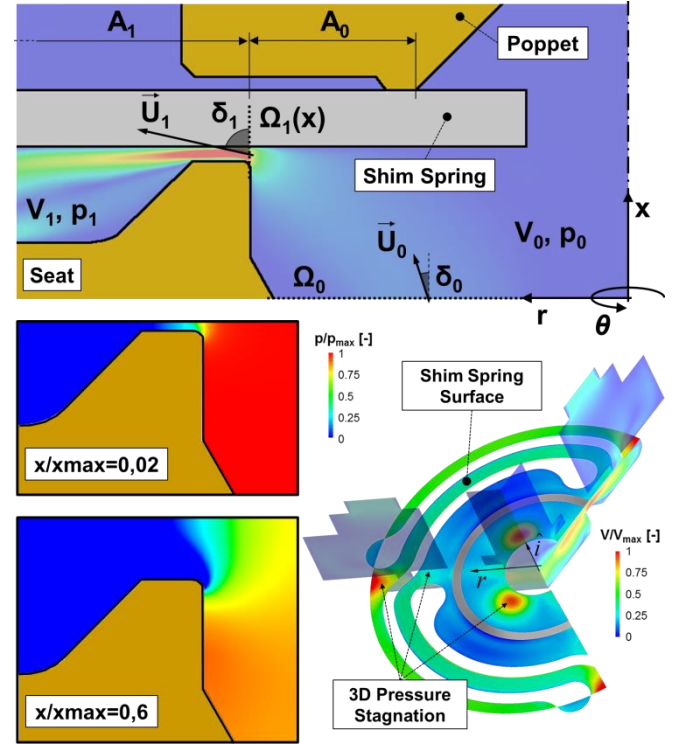


Figure 17: Pilot stage critical parameters on 1D control volumes (top) and different critical CFD flow field characteristics (bottom)

The active pressurized areas are not the nominal ones and as shown by Figure 17, 3D pressure stagnation effects varying over the poppet stroke influence the poppet/shim dynamics. The equivalent upstream and downstream active areas are derived from the CFD analysis performed on the pilot stage. In particular, simplifications on Equation 5 are made, by considering gauge pressure  $p_1$  as 0 [Pa], by neglecting the inlet velocity  $\vec{U}_0$  and by focusing on the inertia driven turbulent flow, since at the smallest openings  $\delta_1 \approx 90^\circ$ . Based on these assumptions, it is possible to derive an equivalent shim pressurized area as follows:

$$A^* = \frac{\int p_{shimCFD} \cdot \hat{i} dA + 2K_q(x)\Omega(x) \cos \delta_1}{p_0} \quad (6)$$

Thanks to the CFD simulation campaign performed it is possible to study the variation of  $A^*$  as a function of the poppet stroke and the pilot stage pressure differential, as shown by Figure 18. Referring to Figure 18, the unique shape of the shim active pressurized area does not depend strongly on the pressure difference, but mostly on the stroke. Hence, to remove one degree of freedom in the 1D model, it

is assumed that the static pressure distribution on the shim spring is purely a function of the geometrical characteristic of the restriction and an average  $A^*$  curve is implemented. Referring to Figure 17, at the smallest openings the upstream pressure enters the annular orifice, maximizing the pressurized area. However, as the increment of the stroke opens the annular restriction, the pressure drop takes place further away from it, reducing the effective pressurized region. At the higher stroke values, the 3D pressure stagnation phenomena contribute to an increment of the equivalent active area.

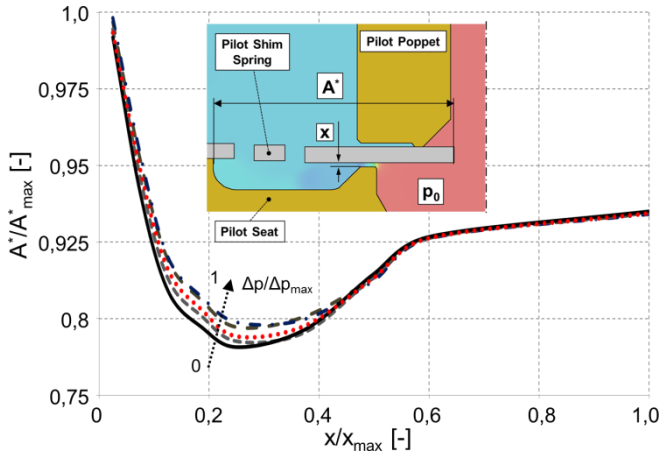


Figure 18: Effective shim spring pressurized area function of pilot poppet position at different pressure drops

The effective shim active area curve is an input to the pilot stage AMESim model, so that the coupling of 3D extrapolated data with the 1D model allows a precise prediction of the hydraulic pressure forces acting on the pressurized surfaces, as shown by Figure 19.

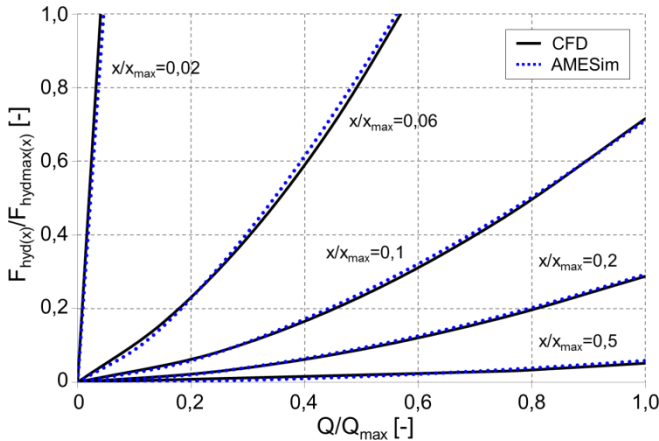


Figure 19: Pilot stage custom 1D-3D coupled AMESim model hydraulic forces compared with CFD results

#### 4 The 1D AMESim Model

Lumped parameter modeling with AMESim allows capturing the dynamics of the CES8700 physical system. The main external forces acting on the inertial equilibrium of the pilot stage and main stage moving elements are considered, i.e. friction forces, pressure forces, spring forces, solenoid forces, etc. An overview of the CES8700 AMESim model is given in Figure 20.

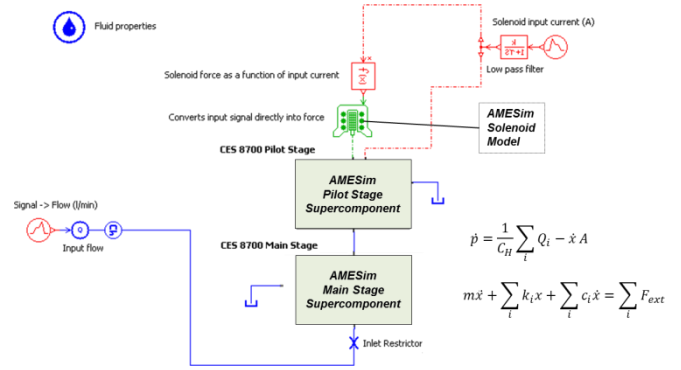


Figure 20: The CES8700 LMS AMESim model

AMESim super-components are implemented; lumping customized components to include the numerical results from 3D modeling. In particular, the customized components allow solving for the variable volumes pressure build-up equation, while considering the flow coefficients derived from CFD analysis in the turbulent flow orifice equations. Furthermore, a critical variable for the correct equilibrium of the moving elements is represented by the flow force. The flow forces acting on the pressurized surfaces are considered by implementing the CFD results as a function of the moving elements position. The 1D model replicates the experimental flow-bench setup of the CES8700 valve during testing, where the inputs to the system is a saw tooth inlet flow rate signal, corresponding to progressively increasing levels of solenoid current.

#### 5 Coupled Numerical Results

The aim of this paper is to show how, by coupling 3D numerical data with a 1D lumped parameter model, a more accurate prediction of the whole dynamic behavior of the CES8700 hydraulic valve can be achieved. In particular, by extracting turbulent flow coefficients and information about static pressure distributions on the moving elements, further understanding on the valve dynamics is reached.

Numerical results are compared with measurements, in order to assess the accuracy of the developed 1D-3D coupled model. In particular, inputs to the 1D lumped parameter model are a flow rate signal and a solenoid current signal, as shown by Figure 21.

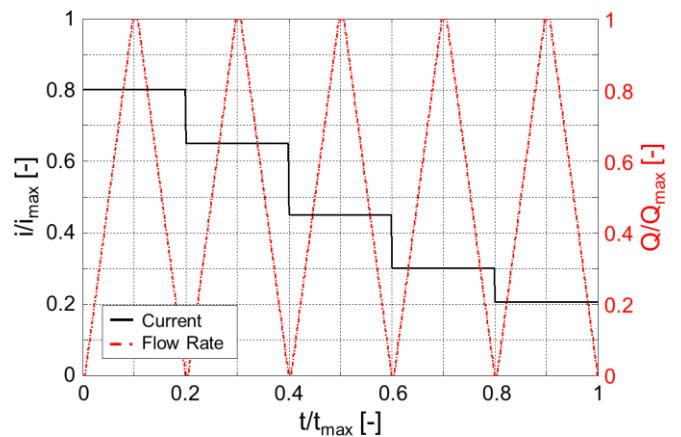


Figure 21: Input signals to 1D simulation models

Additionally, the flow benches available at the Öhlns CES Technologies facilities allow testing the pilot stage alone as well as the full assembled valve, composed by main and pilot stages. Hence, in the next paragraphs an overview of the numerical results compared with measurements is given, both for the pilot stage and the full CES8700 valve.

### 5.1 Pilot Stage

Referring to Figure 22, comparison between measurements on the CES8700 pilot stage and two different 1D model combinations is shown. In particular, the 1D-3D coupled model presented in this paper and a similar AMESim model based on standard components, implementing optimized constant flow coefficients and constant flow force jet angles, are considered. It can be noticed how the numerical results of the 1D model enhanced by CFD data are more accurate over the entire range of flow rates and input currents. The remaining discrepancies between measured and simulated data are affected by measurements scatter and complex friction hysteresis phenomena, not yet precisely considered in the 1D model.

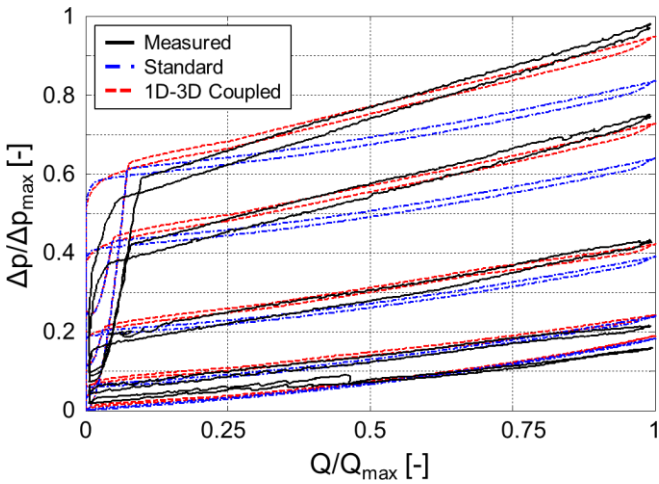


Figure 22: Pilot stage pressure levels from the two 1D models compared with flow bench measurements

Referring to Figure 22, each pressure level corresponds to a specific solenoid current step, in particular the higher the current the higher the pressure drop across the pilot stage.

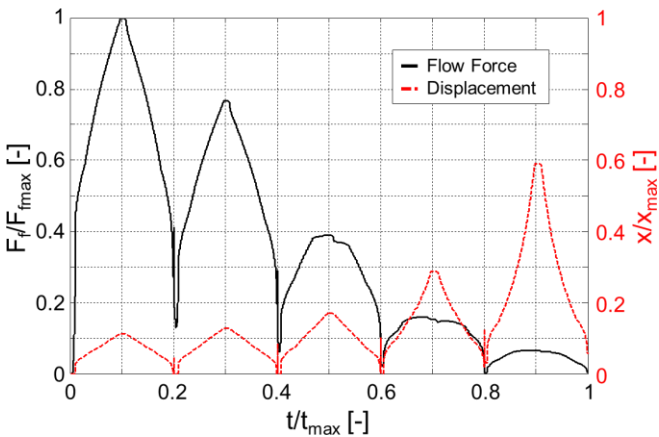


Figure 23: Pilot stage predicted flow forces and pilot poppet displacement for 1D-3D coupled model

Insights on the pilot stage dynamics can be extracted from the lumped parameter modeling. For example, accurate predictions on the total flow forces magnitude, i.e. difference between nominal and effective pressure forces, as well as the corresponding pilot poppet displacement are calculated by the 1D-3D coupled model, as shown by Figure 23. Referring to Figure 23, the pilot poppet/shim assembly displacement increases as the solenoid current progressively decreases, allowing a higher efflux area for the flow rate and consequently a lower pressure level upstream the pilot stage. The gradually lower pressure drop across the pilot metering orifice induces a lower flow force.

### 5.2 Full Valve

Similarly to the pilot stage, the lumped parameter model of the complete CES8700 valve is compared with measurements. Thanks to the flow-bench measurements comparisons, the accuracy of the developed simulation model and of the numerical strategies presented in this paper is validated.

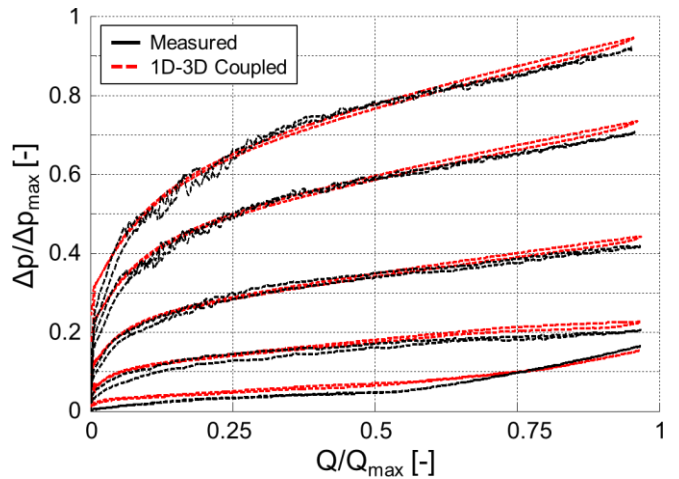


Figure 24: CES8700 p-Q characteristics from 1D-3D model and flow-bench measurements

Referring to Figure 24, the comparison between measured CES8700 p-Q characteristics at different current levels and the predicted valve behavior from the 1D-3D coupled model is shown.

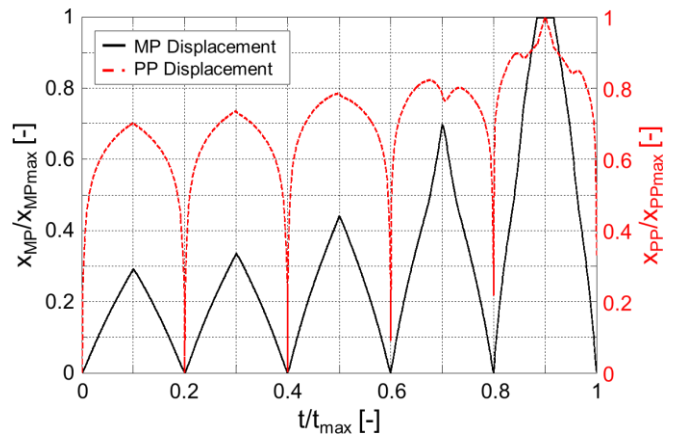


Figure 25: Main poppet and pilot poppet displacement from 1D-3D coupled model

Following the pilot stage behavior, higher pressure levels correspond to higher input solenoid currents. The lumped parameter model of the solenoid valve allows calculating physically inaccessible parameters, impossible to measure, such as the main and pilot poppets simultaneous displacements, depicted by Figure 25. It can be noticed how the poppets

## 6 Conclusions

A numerical analysis on a special solenoid hydraulic valve for semi-active suspensions is presented in this paper. The valve, designed by Öhlins CES Technologies, is in use by several major automotive manufacturers to implement semi-active shock absorbers technology in their vehicles. The unconventional design of the valve, named CES8700, requires advanced computer simulation to predict its hydraulic dynamic behavior. An extensive CFD analysis on the most critical regions of the CES valve is discussed, providing experimental validation on specific regions of the hydraulic valve. The distributed parameter modeling is not only necessary to understand the impact of key design features, but also to extract physical variables associated with the fluid flow. In particular, flow coefficients and static pressure distributions on the moving elements are studied. These parameters are coupled with a 1D numerical model of the valve, used to predict the whole system dynamic behavior. The influence of the CFD results on the 1D model numerical results is discussed. It is shown, comparing simulation results with experimental measurements, how the information from a detailed CFD analysis strongly improves the ability to fully capture the CES hydraulic valve behavior. In the future, 2-way and flow-driven rigid body FSI (Fluid-Structure Interaction) analysis will be developed; in order to understand the impact of the elastic components interaction with the fluid flow and to capture the effects of localized fluid flow phenomena on the poppet dynamics.

## References

- [1] Blackburn, J. F., Reethof G., Shearer, J. L. 1966. *Fluid Power Control*, USA: MIT Press.
- [2] H E Merritt. 1967. *Hydraulic Control Systems*. John Wileys and Sons, Cincinnati, Ohio, ISBN 0-471-59617-5.
- [3] Nervegna, N. 2003. *Oleodinamica e Pneumatica: Sistemi, Componenti, Esercitazioni*. Politeko, Turin, Italy.
- [4] Borghi, M., Cantore, G., Milani, M. and Paoluzzi, R. 1998. Analysis of hydraulic components using computational fluid dynamics models. *Proceedings of the Institution of Mechanical Engineers*, Vol. 212 (7) Part C, pp. 619–629.
- [5] Vacca, A., Greco M., Fornaciari, A. 2008. New concept for the development of a relief, anti-shock and anti-cavitation cartridge valve. *Proceedings of the 2008 IFK*, Dresden, Germany.
- [6] Amirante R, Del Vescovo G, Lippolis A. 2006. Evaluation of the flow forces on an open centre directional control valve by means of a computational fluid dynamic analysis. *Energy Conversion & Management* 47, pp. 1748–1760.
- [7] Amirante R, Del Vescovo G, Lippolis A. 2006. A flow forces analysis of an open center hydraulic directional control valve sliding spool. *Energy Conversion & Management* 47, pp. 114–131.
- [8] Amirante, R., Moscatelli, P. G., and Catalano, L. A. 2007. Evaluation of the Flow Forces on a Direct (Single Stage) Proportional Valve by Means of a Computational Fluid Dynamic Analysis. *Energy Conversion & Management* 48, pp. 942–953.
- [9] Del Vescovo G, Lippolis A. 2003. CFD analysis of flow forces on spool valves. *Proceedings of the 1<sup>st</sup> International Conference on Computational Methods in Fluid Power Technology*, Melbourne, Australia.
- [10] Valdés, J. R., Miana, M. J., Núñez, J. L., and Pütz, T. 2008. Reduced Order Model for Estimation of Fluid Flow and Flow Forces in Hydraulic Proportional Valves. *Energy Conversion & Management* 49, pp. 1517–1529.
- [11] Ansys Fluent User's Guide, Release 14.0, November 2011.
- [12] Ansys Fluent Theory Guide, Release 14.0, November 2011.
- [13] LMS Imagine AMESim Rev. 11 Reference Manual 2012.
- [14] Clavier, A., Alirand, M., Vernant, F. and Sagot, B. 2003. Local Approach to Improve the Global Approach of Hydraulic Forces in Ball Poppet Valves. *Proc. of the 4<sup>th</sup> International Symposium on Fluid Power*, Wuhan, China.
- [15] Baudry X, Mare JC. 2000. Linking CFD and lumped parameters analysis for the design of flow compensated spool valves. *Proceedings of the 1<sup>st</sup> FPNI-PhD symposium*, Hamburg, Germany, pp. 249–258.
- [16] Borghi M, Milani M, Paoluzzi R. 2005. Influence of notch shape and number on the metering characteristics of hydraulic spool valves. *International Journal of Fluid Power*, Vol.6 (2), pp. 5–18.
- [17] Borghi M, Milani M, Paoluzzi R. 2000. Stationary axial flow force analysis on compensated spool valves. *International Journal of Fluid Power*, Vol. 1(1), pp. 17–25.

# Cylinder Pressures in a Position Controlled System With Separate Meter-in and Meter-out

G. Rath and E. Zaev\*

Department for Product Development, University of Leoben, Leoben, Austria

E-mail: gerhard.rath@unileoben.ac.at, emil.zaev@mf.edu.mk

\*Faculty of Mechanical Engineering, Ss.Cyril and Methodius University in Skopje, Skopje, Macedonia

## Abstract

Hydraulic servo system driven with separate meter-in and meter-out valves provide more flexibility with respect to energy efficiency and dynamic properties. In the current problem the operation of such a configuration involves to keep a desired position constant, while an external load force is applied. The position control cannot compensate for fast load fluctuations beyond a certain frequency limit. For this case it can be desired to adjust the static pressures in the cylinder chambers to defined values. The paper describes how to influence this pressures giving weights to the control signals for both moving directions for each valve. With the help of a simulation model the design results are verified. Higher pressure levels decrease the danger of cavitation and inhibit lowering the bulk modulus of the oil volume. The asymmetric control of the valves even lead to better energy efficiency during position control.

**Keywords:** Servo control, smismo, energy efficiency

## 1 Introduction

### 1.1 Control of Hydraulic Actuators

The main component for proportional velocity and position control of industrial or mobile hydraulic systems traditionally is a spool valve applied to each actuator. Analysis of the dynamic behaviour of such a system was done very early [1], and fast servo-valves were developed [2]. For a long time complex control algorithms were reserved for dedicated signal processors [3]. In the last decade programmable logic controllers (PLC) provided more and more computing power and enabled also working with non-linear models of hydraulic systems [4]. The control of the oil flow with valves causes energy loss due to pressure drop. Better efficiency can be obtained by including the pump in the control strategy, either without any additional valve or combining proportional valve with a load-sensing (LS). The dynamic behaviour of such a system was studied in [19].

The most important goal in the recent time is the development of energy efficient systems, which is a major topic for separate meter-in, separate meter-out control (SMISMO) hydraulics [8]. Development of robust sensors and new hydraulic designs for SMISMO enabled more sophisticated control of hydraulic drives, a higher degree of freedom is offered to control engineers. The analysis of the additional working modes provided by such a system can be found in [6] or [13]. It is even possible to recuperate energy, which may be important for heavy machinery [18].

SMISMO control may be combined with classical elements for hydraulic control, such as electronic load-sensing (ELS). Switching strategies for energy optimisation including multiple actuators in an ELS system are presented in [9]. Also over centre valves in SMISMO systems are considered [10].

Another important issue is vibration and oscillation damping. For large-scale machinery the energy efficiency is also a major topic for such applications [11]. With separate meter-in and meter-out extended with a crossport valve, active damping can be accomplished efficiently [12].

The separate meter-in and meter-out system increases the amount of variables to be influenced by electronic control, which requires to apply more sensors. Those are still expensive and not highly dependable. Methods to reduce the amount of sensors are also a research topic, for example in [5].

Sometimes it is desired to simplify the control strategy in order to influence certain variables of the hydraulic and mechanical system more specifically. For example, a decoupled control of variables in a multiple-input/multiple output (MIMO) system, can be found in [7]. The work presented in this paper describes how to influence the chamber pressures during constant position control without the need of an additional control loop.

Most work about separate meter-in and meter-out is done on how to control the motion in an energy efficient manner. Here in contrast a situation is investigated, where the position is regulated to be constant. A solution for a two-valve configura-

ration in a position control application is shown, that allows to influence the pressures within certain limits. Beside for position, no additional sensors are used.

### 1.2 System Description

The hydraulic machine considered here is equipped with a milling head driven with an electric motor. Motion and positioning of the head is done with two hydraulic axes for two degrees-of-freedom. Each of them is controlled with two proportional valves in a SMISMO configuration. When one axis is moving for the milling operation, the other axis stands still and is subjected to load fluctuations caused by the milling process. The purpose of the regulator is to keep the passive axis in a constant position. The goal of the design process proposed here is to optimise the pressure levels in the cylinder chambers so, that maximum force impacts can be caught without the occurrence of cavitation. The hydraulic power supply is a load-sensing system. Since the active cutting axis usually needs the full pressure provided by the pump, the passive axis, which holds its position, is not included in the load-sensing loop. Consequently the maximal, or at least a high pressure level is available for position control. The most im-

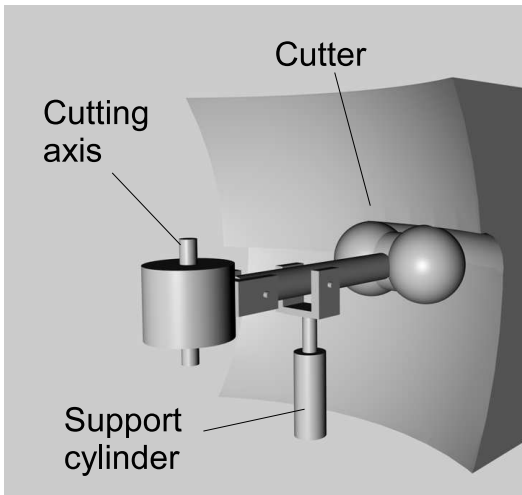


Figure 1: Hydraulic scheme

portant components for the control of the passive hydraulic axis, which is considered, are shown in Fig. 2. It is assumed for the investigations, that the pump provides a constant high pressure during the milling process for the active axis. Two four-land-four-way spool valves are applied to establish separate meter-in and meter-out control. Some auxiliary hydraulic elements of minor relevance are not sketched in Fig. 2.

### 1.3 Problem Description

The actual system is equipped with separate meter-in and meter-out control to allow energy efficient control of motion during several working situations. One strategy for example is to control speed with the meter-in valve while keeping the pressures at a reasonable level with the meter-out valve to avoid high power losses on the one hand, and to avoid cavitation in the case of overrunning load on the other [6].

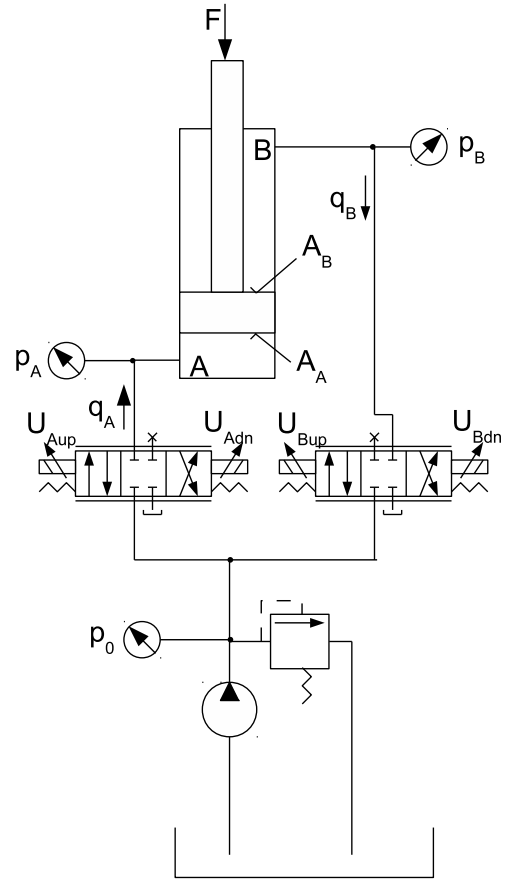


Figure 2: Hydraulic scheme

Cutting operation of the system investigated here requires an additional operating mode, where the support cylinder should not move, but hold its position subject to external forces. For this purpose, a position control loop is required. Now the separate meter-in and meter-out system allows an additional degree of freedom, which is utilised in this work. It is investigated how to improve the performance of position control without adding further sensors or control loops.

## 2 Electronic Control

The scheme for the electronic position regulator of the cylinder is displayed in Fig. 3. This control loop will ensure,

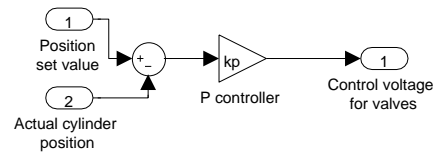


Figure 3: Basic position control

that the mean value of the position is held constant independently from the magnitude of the load force generated by the cutting process. A simple proportional (P) controller is assumed here. From the authors' experience, a more sophisticated algorithm, see [17], does not influence the result of the considerations made here. The control error is multiplied with the

gain and provided as output signal. If both the valves are driven with this signal and have identical characteristics, the result is equivalent to the control of the cylinder with a single servo or proportional valve.

The individual metering valves provide an additional degree of freedom that is utilised here. A factor  $\lambda$  is introduced that provokes asymmetric control voltages for the valves dependent on the moving direction. These motions around a desired setvalue of the cylinder displacement are caused by the external load force and not due to a change of the set value (regulator case). Fig. 4 shows the function block inserted between the position controller and the outputs for the proportional valves.

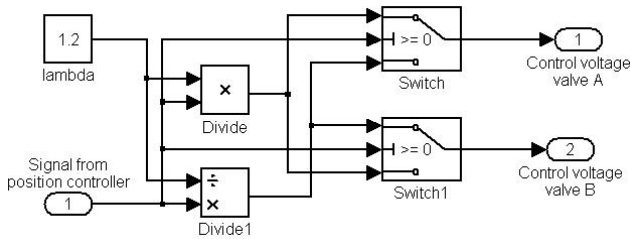


Figure 4: Signal flow for pressure adjustment

The effect of this interception is to introduce a virtual imbalance of the proportional valves. The effect of the electronic imbalance can be understood easier studying a mechanical equivalent in Fig. 5. A thick arrow represents an increased orifice multiplied with the factor  $\lambda$  greater than one. Small

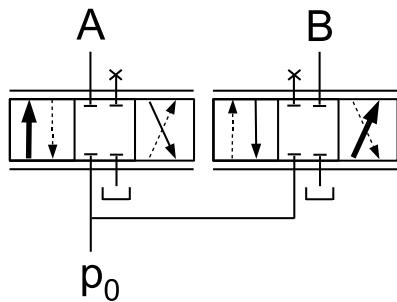


Figure 5: Mechanical equivalent for electronic pressure adjustment

arrows indicate a reduced opening by multiplication with  $\frac{1}{\lambda}$ . Dotted arrows are not active in this configuration. Looking at this model makes clear that the paths to the supply pressure are wider than those to the tank. Hence higher pressure levels are to be expected in the cylinder chambers.

The advantage of the electronic imbalance over a fixed mechanical asymmetry is that a change for other working conditions is easy. For example, if the axis should move over a distance, a different concept for individual metering can be used to optimise the energy efficiency.

### 3 Pressure Levels

The procedure how to calculate the pressure levels in the cylinder chambers of a hydraulic system under electronic control for a constant piston displacement controlled with a single servo or proportional valve was already presented and verified in [14]. Here the scope is extended to separate meter-in and meter-out valves including the method according to Fig. 4 for introducing an imbalance. The scheme with a factor  $\lambda$  was chosen in order to get a simple result in the following procedure.

An external force is applied that fluctuates. As intended, position control will hold the mean values of the oil volumes constant. From this follows, that the mean values of the oil flows to and from of the cylinder chambers to zero. The output of the proportional controller follows the control error with the factor  $k_p$ . Normally the integrating behaviour of the cylinder forces the mean value of the control error to zero. Since the oil flows to and from the cylinder depend on the pressures and hence are different for each chamber, the control error has to assume an offset (Fig. 6). This offset,

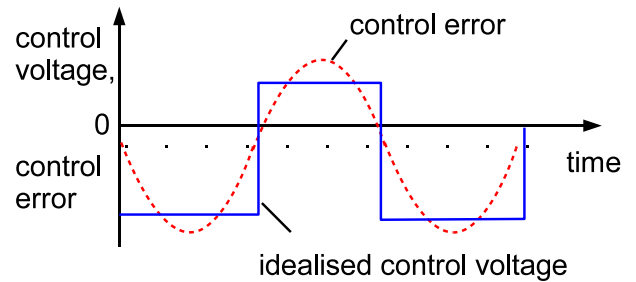


Figure 6: Small oscillations of displacement and controller output

which will be very small in a typical system, can be used to find conditions for the pressures in the cylinder. Approximating now the controller output with square oscillations yields two levels  $U_{up}$  and  $U_{dn}$ .

These oscillations may have the natural frequency of the system or the frequency of the external force. Oil flows are small, consequently pressures do not change much. At this point it should be mentioned that the law of continuity of the oil flows does not apply here, since the flows are mainly contributed by charging and discharging the chamber capacities.

A cylinder is moving 'up' when an oil flow  $q_A$  enters chamber A (Fig. 2). The valve connected to A is supplied with a pressure  $p_0$  from the pump. Chamber B is opened by a separately controlled valve to the tank. During motion 'down', chamber B is connected with the supply and A with the tank. In the first step, both valves accept the same control voltage  $U$  from the position controller in Fig. 3.

For a small motion down we get

$$\begin{aligned} q_{Bdn} &= U_{Bdn} k_B \sqrt{p_0 - p_B} \\ q_{Adn} &= U_{Adn} k_A \sqrt{p_A} \end{aligned} \quad (1)$$

For a small motion up we get

$$\begin{aligned} q_{Bup} &= U_{Bup} k_B \sqrt{p_B} \\ q_{Aup} &= U_{Aup} k_A \sqrt{p_0 - p_A} \end{aligned} \quad (2)$$

What is important here, is the fact, that the position will be held with the exception of a small offset. This is the desired behaviour of the control loop. From this follows, that the oil flow coming out of one chamber must be the same going in during the next half period of the oscillation, which means

$$\begin{aligned} q_{Bdn} &= q_{Bup} \\ q_{Adn} &= q_{Aup} \end{aligned} \quad (3)$$

And further, with Equ. 1 and 2, follows

$$\begin{aligned} U_{Bdn} k_B \sqrt{p_0 - p_B} &= U_{Bup} k_B \sqrt{p_B} \\ U_{Adn} k_A \sqrt{p_A} &= U_{Aup} k_A \sqrt{p_0 - p_A} \end{aligned} \quad (4)$$

and

$$\begin{aligned} \frac{U_{Bdn}}{U_{Bup}} &= \frac{\sqrt{p_B}}{\sqrt{p_0 - p_B}} \\ \frac{U_{Adn}}{U_{Aup}} &= \frac{\sqrt{p_0 - p_A}}{\sqrt{p_A}} \end{aligned} \quad (5)$$

As depicted in Fig. 6, the position controller is assumed to deliver two discrete output levels, a positive voltage  $U_{up}$  and a negative voltage  $U_{dn}$ . Now the circuit in Fig. 4 is intercepted between the controller and the valves. Positive and negative control output values are weighted differently for both valves in the following way

$$\begin{aligned} \frac{U_{Bdn}}{U_{Bup}} &= \frac{\lambda \cdot U_{dn}}{\frac{1}{\lambda} \cdot U_{up}} = \lambda^2 \frac{U_{dn}}{U_{up}} \\ \frac{U_{Adn}}{U_{Aup}} &= \frac{\frac{1}{\lambda} \cdot U_{dn}}{\lambda \cdot U_{up}} = \frac{1}{\lambda^2} \frac{U_{dn}}{U_{up}}, \end{aligned} \quad (6)$$

hence Equ. 5 turns to

$$\begin{aligned} \lambda^2 \frac{U_{dn}}{U_{up}} &= \frac{\sqrt{p_B}}{\sqrt{p_0 - p_B}} \\ \frac{1}{\lambda^2} \frac{U_{dn}}{U_{up}} &= \frac{\sqrt{p_0 - p_A}}{\sqrt{p_A}}, \end{aligned} \quad (7)$$

from which we get

$$\frac{p_B}{p_0 - p_B} = \lambda^8 \frac{p_0 - p_A}{p_A} \quad (8)$$

Pressures A and B depend on the mean value of the cylinder load

$$F = p_A A_A - p_B A_B \quad (9)$$

Consequently pressure  $p_B$  becomes

$$p_B = p_A \frac{1}{\eta} - F' \quad (10)$$

with  $F' = \frac{F}{A_B}$  and  $\eta = \frac{A_B}{A_A}$ . Finally follows

$$\begin{aligned} p_A^2 \frac{1}{\eta} (1 - \lambda^8) + p_A \left[ \lambda^8 p_0 \left( 1 + \frac{1}{\eta} \right) - F' (1 - \lambda^8) \right] - \\ - \lambda^8 p_0 (F' + p_0) = 0. \end{aligned} \quad (11)$$

This is a quadratic equation that delivers the solution for  $p_A$ . Pressure  $p_B$  follows from Equ. 10. Of course Equ. 11 has two solutions. For  $\lambda < 1$  one solution has negative pressures, which is not possible for the physical system. For  $\lambda > 1$  one solution exists with all pressures higher than the supply, which is also not possible. Sign information was lost after squaring Equ. 7. For  $\lambda = 1$  Equ. 11 turns into a linear equation, a case, which was already treated and verified by measurements in [14].

Consequently there exists only one solution for a physical system. It is the result with the positive sign in the solution formula for the quadratic equation. The pressure levels during a constant position control dependent on the load force can be found in Fig. 7. An arbitrary cylinder with equal areas is chosen. It can be seen that by selecting  $\lambda$  the pressures

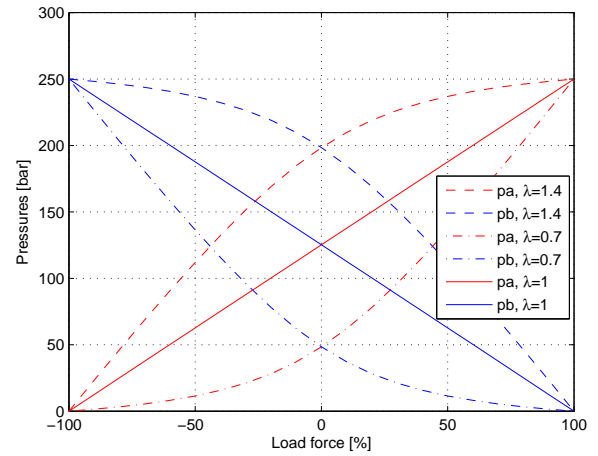


Figure 7: Quiescent pressures depend on load force

in the cylinder may be varied. With the imbalance factor  $\lambda$  greater than one the levels can be drawn towards the supply pressure, or vice versa. Of course at positive or negative force maximum, there is no chance to influence the pressures.

Remarkable is, that different characteristics of the valves, i.e. the ratio of  $k_A/k_B$ , does not contribute to the pressure levels. Of course there is an influence when the cylinder is moving at a desired speed, but this case is not a topic in this considerations.

Fig. 4 represents the implementation of Equ. 6, and Equ. 11 evaluates the resulting pressure levels dependent on the mean external load force.

## 4 Simulation Model

In order to verify the pressure predictions in the previous section and to study the behaviour in various situations, a simulation example is carried out here. The properties of the system are studied applying load forces to the model, first following an idealised step function. Then a force progression is chosen that is typical for the physical system under investigation.

The data that are used for the simulation model are listed in Tab. 1. The fully opened orifices of the valve spool deliver

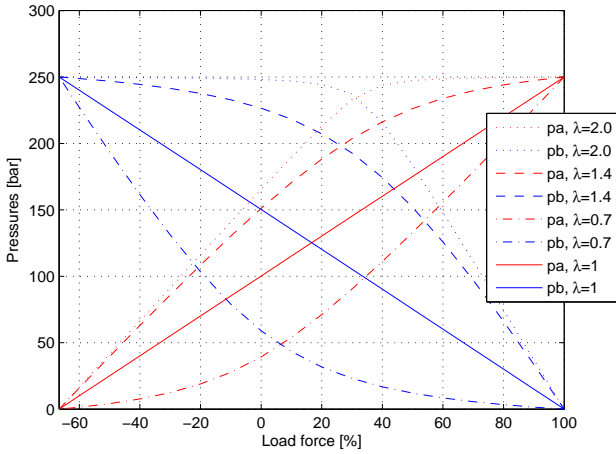


Figure 8: Pressures for  $\eta = 0.7$

$1701 \text{ min}^{-1}$  at a pressure difference of 70 bar.

Designation	Denotation	Value
$A_A$	Area piston side	$0.06 \text{ m}^2$
$A_B$	Area rod side	$0.04 \text{ m}^2$
$p_0$	Supply pressure	$250 \cdot 10^5 \text{ Pa}$
$k_A$	Valve A characteristic	$1.07 \cdot 10^{-6} \text{ m}^3 \text{ s}^{-1} \text{ V}^{-1} \text{ Pa}^{-1/2}$
$k_B$	Valve B characteristic	$1.07 \cdot 10^{-6} \text{ m}^3 \text{ s}^{-1} \text{ V}^{-1} \text{ Pa}^{-1/2}$
$\eta$	Ratio $A_B/A_A$	0.7
$m$	Cutter head mass	11500 kg
$l$	Lever ratio	5
$C_A, C_B$	Hydr. capacities	$8.44 \cdot 10^{-12} \text{ m}^3 \text{ Pa}^{-1}$
$U_{Adn}, U_{Adn}$	Valve A control voltage dependent on direction	max. $\pm 1 \text{ V}$
$U_{Bdn}, U_{Bdn}$	Valve B control voltage dependent on direction	max. $\pm 1 \text{ V}$

Table 1: Data used for modelling

The pressure levels for this system obtained with Eqs. 11 and 10 are shown in Fig. 8. Numerical simulation will yield the same results. Simulation experiments were carried out with Matlab<sup>TM</sup>/Simulink<sup>TM</sup>. After starting the simulation, the system needs some time to settle, before the actual experiment can begin. This time is not displayed in the diagrams of the following simulations.

#### 4.1 Response to Load Force Step

After creating a simulation model, a step response allows to verify the solution of Equ. 11 and to study some basic behaviour. In this experiment, load steps of  $\pm 40\%$  ( $\pm 600 \text{ kN}$ ) are applied. Starting with load zero, the positive step is applied at time  $t = 5 \text{ s}$  and taken back at  $t = 10 \text{ s}$ . The negative pulse follows at  $t = 20 \text{ s}$  until  $t = 25 \text{ s}$ . Fig. 9 shows the results for

$\lambda = 1.0$ , Fig. 10 for  $\lambda = 1.4$ .

Increasing  $\lambda$  shifts the pressure levels towards the supply pressure, as seen also in Fig. 8. Sudden force changes can make a pressure exceed the supply level. This is acceptable until a certain limit, an obligate relieve valve will protect the system from overpressure. On the other hand, a pressure falling to zero, like in Fig. 9 without imbalance, is not acceptable since cavitation occurs. This is the main advantage of introducing an imbalance with  $\lambda$  greater than one.

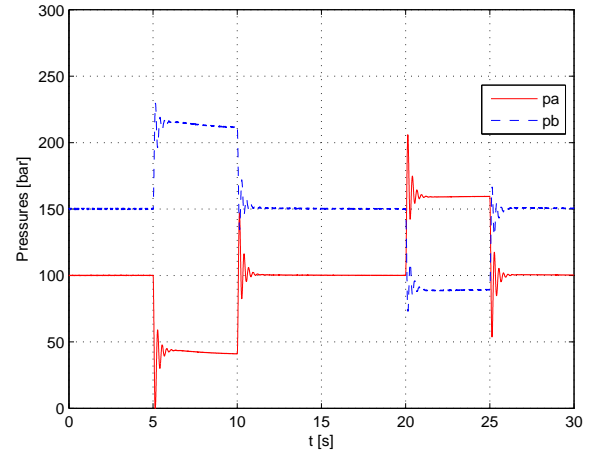


Figure 9: Pressure changes due to force steps,  $\lambda = 1.0$

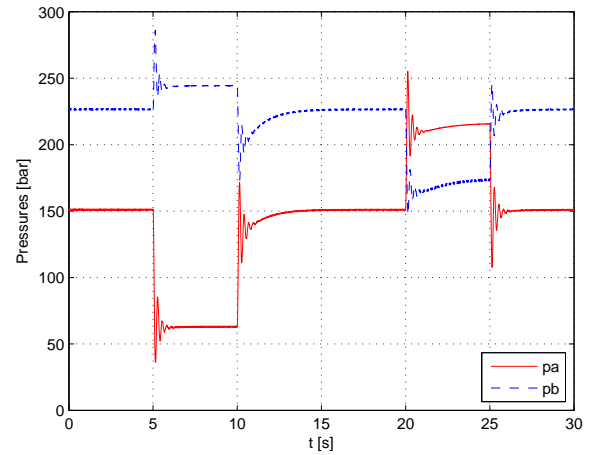


Figure 10: Pressure changes due to force steps,  $\lambda = 1.4$

#### 4.2 Response to Forces During Operation

The hydraulic system considered here is a positioning system for a milling device with external electrical drive. One hydraulic axis is used to move the cutter (active axis). The second cylinder, which is the item of interest here, is used to hold one coordinate of the tool constant (passive axis). In such a configuration, the cutting force is primarily generated by the external cutter drive, and the hydraulic cylinder has to hold its position constant. Hence a position regulator is required like the one shown in Fig. 3.

While in the previous section the response to sudden load changes (step or Heaviside function) was studied, the behaviour under realistic conditions is of interest here. For this purpose, force data are used that are to be expected in practical operation, see Fig. 11. The maximal value displayed on the y-axis is the maximal force the cylinder can exert at the operating pressure of 250 bar. Fig. 12 shows the pressures

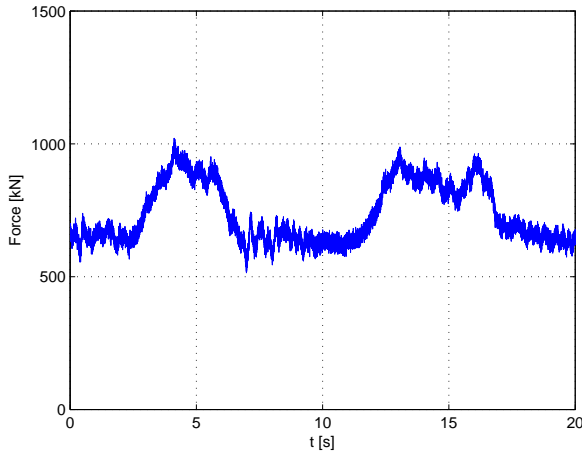


Figure 11: Force applied to the mass

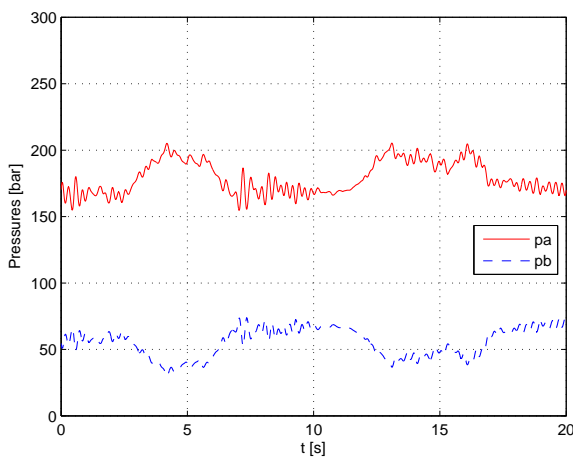


Figure 12: Cylinder pressures with  $\lambda = 1.0$

from simulation experiment with symmetrical excitation of the meter-in and the meter-out valve, which means,  $\lambda$  is set to one in the circuit in Fig. 4. Alternatively, Fig. 13 displays the results for  $\lambda = 1.4$ . As expected, the pressure levels are higher.

### 4.3 Advantages

Low pressure values decrease the bulk modulus of the oil due to entrained air [15] and [22]. Measurements in [16] show that particularly values below 50 bar are of disadvantage. Datasheets of rubber hoses also show higher compliance at low pressures. Furthermore, the danger of cavitation due to force peaks is increased.

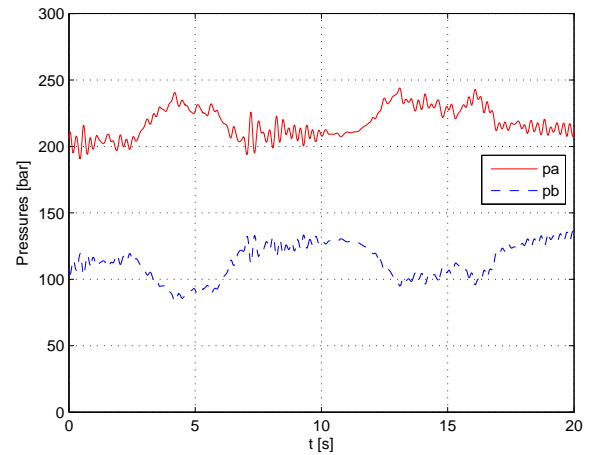


Figure 13: Cylinder pressures with  $\lambda = 1.4$

Using a control loop with an artificial imbalance  $\lambda$  increases the pressure levels and improve the situation in this special operating mode, where the position should be held constant at a desired value.

### 4.4 Control Gain and Energy Efficiency

A position controller was a precondition for evaluating the pressure levels ending up in Equ. 11. Looking at this equation, it is remarkable that the gain has no influence to the long-term quiescent pressure levels. Engineers might tune the controller in order to optimise some property of the closed loop, for example as described in [20] for hydraulic systems. In the case of heavy machinery the energy efficiency is of primary interest to design the controller [21].

To keep the desired position, the controller will open the valves and thus consume oil from the high-pressure supply. The power related to the control action is not to be neglected and must be regarded in the design. Reducing the gain will lower the system's resistance against position change and lower the power consumption. Mean value of the position are kept as well as the steady-state pressure levels. Hence control gain is an important design parameter with respect to power requirement. As an extreme value, a gain of zero is equivalent to closed cylinder chambers, but then position and pressures will drift away due to leakage and possible opening of protective pressure relief valves. Consequently the choice of the gain is a trade-off between loss of energy and position accuracy.

Fig. 14 displays the power required during the operation subject to the forces in Fig. 11 and shows the importance of a proper gain design. Simultaneously the diagram shows that increasing  $\lambda$  can improve the efficiency. When pressure levels in the cylinder are higher, the loss due to incoming oil is expected to be lower.

Stating that a low gain is better concerning power consumption, the influence of the gain to the loop behaviour must be investigated. Assuming, that the cylinder should change its position, the time behaviour usually is a measure for the quality of the design. Fig. 15 shows the time required for a po-

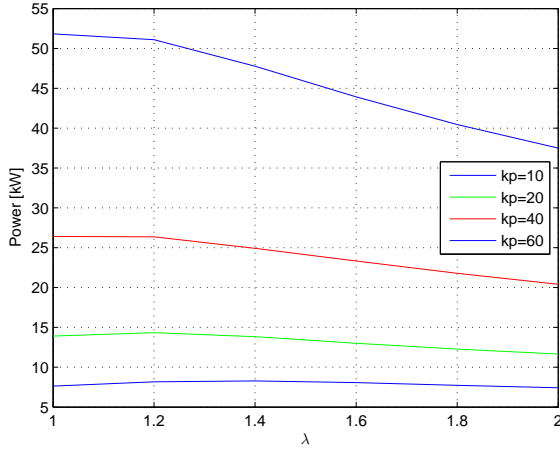


Figure 14: Power drawn from supply by position regulator

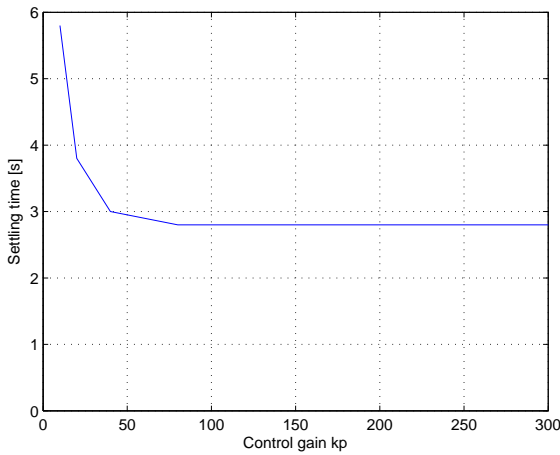


Figure 15: Settling time for a large motion of 100 mm

sition change of 100mm in the simulated system. From this diagram follows that the system is explicitly non-linear. Nevertheless a proper value for the gain can be found, which is as low as possible but does not increase the time constant. Further experiments that are not included in this paper show that the choice of  $\lambda$  has almost no influence to this time behaviour. Motions with the position controller active will be only useful for small changes. For larger distances of course one of the strategies utilising the advantage of separate meter-in and meter-out control is to be preferred.

When the aim is to hold a constant position, the remaining question is how the design influences the position control error during operation. Fig. 16 shows the results from experiments with the simulation model. The root-mean-square (RMS) control error is defined as

$$e_{rms} = \lim_{T \rightarrow \infty} \sqrt{\frac{1}{T} \int_0^T e^2(t) dt}, \quad (12)$$

where the time  $T$  was 20 seconds in the experiment. Fig. 16

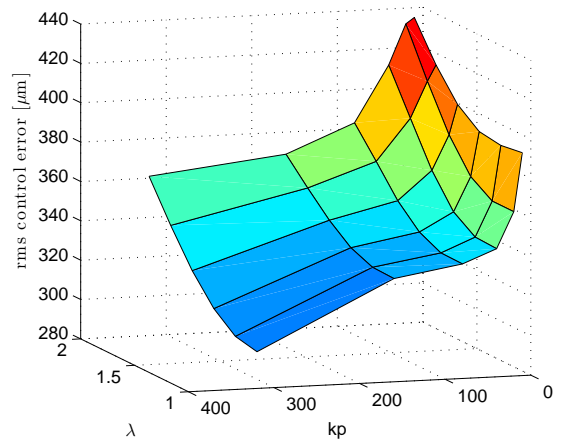


Figure 16: Root-mean-square control error

also shows a slight influence of the factor  $\lambda$ .

Furthermore it can be seen, that the RMS value starts rising at nearly the same low gain values, at which the settling time in the previous experiment was increased. Both design approaches lead to the similar results.

This relationship is not compulsory. In the first case the valves are opened fully and the systems gets non-linear. In the regulator mode, where the RMS errors are taken, the elongations and valve control voltages are very small. It is recommended to repeat both design steps for a specific machine.

## 5 Conclusion

A hydraulic cylinder, which supports a cutting tool head and is subject to high load fluctuations, is controlled with two individual metering valves. In order to hold the position constant a proportional regulator is used. Separate meter-in and meter-out concept usually is applied to improve the energy efficiency during motion. In this work the additional degree of freedom is used to influence the pressure levels at a constant piston displacement during the cutting operation. With the help of electronic control an artificial imbalance is induced to flow control valves.

The effect is modelled with a single factor that allows to calculate the pressure levels in the cylinder in the closed position control loop. The loop is tested in a simulation model first with force steps, then with a set of force data that are typical for practical operation.

Tuning the imbalance factor allows to gain higher pressure levels in the cylinder chambers and hence to be less susceptible to cavitations and to avoid lowering the effective bulk modulus at low pressures. The imbalance slightly increases the control error and has no effect to the time behaviour of the loop. Since the proportional gain of the position controller has a great influence to the power consumption, the design of this gain is discussed.

As an additional effect it turns out that the imbalance also improves the energy efficiency of the system. The proposed

method requires no additional sensor. Furthermore it is an open loop method, so the stability of the position control loop or possible other control loops is not influenced.

## Nomenclature

Designation	Denotation	Unit
$A_A$	Area piston side	$m^2$
$A_B$	Area rod side	$m^2$
$p_0$	Supply pressure	Pa
$k_A$	Valve A characteristic	$m^3s^{-1}V^{-1}Pa^{-1/2}$
$k_B$	Valve B characteristic	$m^3s^{-1}V^{-1}Pa^{-1/2}$
$\lambda$	Factor of signal unbalance for pressure adjustment	
$\eta$	Ratio $A_B/A_A$	
$U_{dn}, U_{up}$	Controller output dependent on direction	V
$U_{Adn}, U_{Adn}$	Valve A control voltage dependent on direction	V
$U_{Bdn}, U_{Bdn}$	Valve B control voltage dependent on direction	V

## Acknowledgement

The authors would like to thank the engineers of the *Sandvik Mining and Construction GmbH* in Zeltweg, Austria, for inspiration and fruitful discussions and further Prof. Paul O'Leary, head of the Chair of Automation at the University of Leoben, for enabling this project.

## References

- [1] H E Merritt. *Hydraulic Control Systems*. John Wileys and Sons, Cincinnati, Ohio, 1967. ISBN 0-471-59617-5.
- [2] W. J. Thayer. Transfer functions for moog servovalves. In *Technical Bulletin 103*. Moog Inc., East Aurora, NY, 1965.
- [3] R. Poley. Dsp control of electro-hydraulic servo actuators. In *Application Report SPRAA76*. Texas Instruments, 2005.
- [4] M. Jelali and A. Kroll. *Hydraulic Servo-systems: Modeling, Identification and Control*. Springer, London, 2003.
- [5] C.C. DeBoer and B. Yao. Energy-efficient motion control of a digital hydraulic joint actuator. In *Proceedings of IMECE'01 2001 ASME International Mechanical Engineering Congress and Exposition*, pages DSC-2B-3, New York, USA, 2001. Japan Fluid Power System Society.
- [6] K.A. Tabor. Velocity based method of controlling an electrohydraulic proportional control valve. United States patent application No. 20040055453, 2004.
- [7] B.K. Nielsen. *Controller Development for a Separate Meter-in Separate Meter-out Fluid Power Valve for Mobile Applications*. PhD thesis, Institute of Energy Technology, Aalborg University, Aalborg, Denmark, 2005.
- [8] B. Eriksson. *Mobile Fluid Power Systems Design with a Focus on Energy Efficiency*. PhD thesis, Institute of Technology, Linköping University, Linköping, Sweden, 2010.
- [9] A.H. Hansen, H.C. Pedersen, T.O. Andersen, and L. Wachmann. Design of energy efficient smismo-els control strategies. In *2011 International Conference on Fluid Power and Mechatronics (FPM)*, pages 522–527, Aug. 2011.
- [10] H.C. Pedersen, T.O. Andersen, Hansen R.H., and S. Stubkier. Investigation of separate meter-in separate meter-out control strategies for systems with over centre valves. In *Proc. of the ASME Symposium on Fluid Power and Motion Control, FPMC 2010*. American Society of Mechanical Engineers, 2010.
- [11] B. Eggers, R. Rahmfeld, and M. Ivantysynova. An energetic comparison between valveless and valve controlled active vibration damping for off-road vehicles. In *Proceedings of the 6th JFPS International Symposium on Fluid Power*, pages 276–283, Tsukuba, Japan, 2005. Japan Fluid Power System Society.
- [12] E. ZaeV. 'Hardware-In-The-Loop' for real-time simulation of complex mechanical systems and their control. PhD thesis, Faculty of Mechanical Engineering, SS. Cyril and Methodius University, Skopje, Macedonia, 2013.
- [13] A. Shenouda. *Quasi-Static Hydraulic Control Systems and Energy Savings Potential Using Independent Metering Four-Valve Assembly*. PhD thesis, Woodruff School of Mechanical Engineering, Georgia Institute of Technology, Georgia, 2006.
- [14] G. Rath. Dynamics of high precision position controlled hydraulic cylinder subjected to elastic load. In K.T. Koskinen and M. Vilenius, editors, *The Eighth Scandinavian International Conference on Fluid Power, Proceedings*, pages 383–396, Tampere, Finland, 2003.
- [15] W. Backé and H. Murrenhof. *Grundlagen der ölhydraulik*. Lecture notes, RWTH Aachen, Germany, 1994.
- [16] R. Forsberg. Cut profile accuracy of roadheaders: Influence of different components and measures for improvements. Master's thesis, KTH Machine Design, Stockholm, Sweden, 2005.
- [17] G.F. Franklin, M.L. Workman, and D. Powell. *Digital Control of Dynamic Systems*. Addison-Wesley Longman Publishing Co., Inc., Boston, MA, USA, 3rd edition, 1997.
- [18] K. Heybroek. *Saving Energy in Construction Machinery using Displacement Control Hydraulics, Concept Realization and Validation*. PhD thesis, Institute of Technology, Linköping University, Linköping, Sweden, 2008.

- [19] P. Krus. *On Load Sensing Fluid Power Systems, With Special Reference to Dynamic Properties and Control Aspects*. PhD thesis, Department of Mechanical Engineering, Linköping University, Linköping, Sweden, 1988.
- [20] T. Shang. *Improving Performance of an Energy Efficient Hydraulic Circuit*. PhD thesis, Department of Mechanical Engineering, University of Saskatchewan, Saskatoon, Canada, 2004.
- [21] M. Linjama and M. Vilenius. Energy-efficient motion control of a digital hydraulic joint actuator. In *Proceedings of the 6th JFPS International Symposium on Fluid Power*, pages 640–645, Tsukuba, Japan, 2005. Japan Fluid Power System Society.
- [22] Y. Jinghong, C. Zhaoneng, and L. Yuanzhang. The variation of oil effective bulk modulus with pressure in hydraulic systems. *Journal of Dynamic Systems, Measurement, and Control*, 116(1):146–150, 1994.



## **Structural design of independent metering control systems**

A. Sitte, J. Weber

Institute of Fluid Power, Technical University Dresden, Dresden/Germany  
E-mail: sitte@ifd.mw.tu-dresden.de, weber@ifd.mw.tu-dresden.de

### **Abstract**

This paper regards to design and examination of electrohydraulic control systems with separate metering edges for mobile applications. Although the idea of individual metering has existed for some time, this promising technology has yet to be applied in field. One reason for the missing prevalence is the lack of understanding regarding the complex control requirements. Furthermore, expected additional expenses regarding components such as valves and transducers hinder the acceptance. This work outlines a systematic analysis of possible circuit concepts. The obtained solution space contains a large number of elements that must be evaluated based on functional and economical criteria. Therefore, it is advantageous to divide the control system into its functional fractions. The clear distinction of the functional fractions enables a systematization of the different drive and control tasks, which then can be combined freely. The selection of appropriate control signals can be supported by the usage of a multivariable system modeling approach. Physical interactions, inherent to electrohydraulic systems, have a strong impact on the behavior of the control loops. By analyzing the coupling elements, conclusions regarding control concepts and structures can be drawn.

**Keywords:** electrohydraulic control systems, separate metering, MIMO, valve structures

### **1 Introduction**

In mobile machinery it is very common that multiple hydraulic drives are supplied by one single pump. The actuators shall be operated independently and simultaneously. The hydraulic control system has to distribute the hydraulic power among the actuators depending on their flow and pressure requirements. Process forces mostly appear in both positive and negative direction. Negative load forces in direction of movement occur for example during lowering of loads or when decelerating moving masses. This typically leads to an overrunning load and thus an uncontrolled acceleration of the hydraulic motor. Moreover negative pressures may occur, since the pump flow is not sufficient for the filling of the cylinder. In order to prevent damage resulting from cavitation phenomena usually suction valves are used. Furthermore overcentre valves are utilized to prevent uncontrolled movement. The throttling cross section is varied as a function of the inlet pressure and thus limits the actuator's velocity. Disadvantages of this setup are increased power consumption, especially at partial loads, and the dynamic behavior of the drive system, which tends to oscillate in an unfavorable manner. Modern systems meet most of the requirements concerning controllability but system limits are increasingly reached in terms of efficiency and dynamics. A reasonable and promising way to overcome this issue is the use of hydraulic systems with independent

metering edges [4], [24] and [10]. By doing so, the opening cross section of the meter-out edges can be adapted to the load situation and can be manipulated independently from the inlet. By influencing the pressure level, regeneration and recuperation modes become possible. A separate control of the tank edge also opens up for minimal pressure losses at all working conditions. Cavitation during pulling load situations can be avoided without extensive control edge design. Furthermore, the distributed valve arrangement allows the use of decentralized control architectures.

### **2 State of the Art**

A natural approach to derive systems with independent metering properties is to add one control input in order to control an additional state variable. As a result, a hardware layout with two 3/3-valves is obtained. These circuit variants are preferred in [11], [4], [27], and [5]. Pressure sensors are used for controlling the main valve [14], [15]. The design of those systems differs considerably. [14] uses the idea of classic load sensing with primary pressure compensation. Although a load-independent actuator movement is implemented, at least two additional pressure transducers are needed. Analogue solutions are published in numerous patents and scientific contributions [16], [17], [18], [19], and [28]. Industrial applications by Eaton [1] and Wessel [8] have come to attention as well. In [20] a valve arrangement with independently controlled metering edges

and the use of secondary pressure compensators is proposed. Thus, a typical flow divider setup is provided. In case of saturation of the pump flow, the flow will still be distributed proportionally in correlation to the valves opening area ratios. The resulting component effort is affected negatively, since two additional pressure compensators are needed. In addition to system solutions utilizing 3/3-valves, especially concepts with 2/2-valves are in the scope of research. These valve types are often simpler and more cost effective. Configurations with 2/2-valves are introduced in [9], [25], and [26] [21], [22], [12]. Eriksson and Palmberg present a system without pressure sensors [6], [23]. Each main valve is equipped with a pressure compensator. The load conditions are determined by measuring the position of the pressure compensators. Among others, Linjama and Villenius deal with stability and control issues [10].

### 3 Derivation of circuit structures for control systems with independent metering edges

Based on today's control systems, the demands in individual metering control can be described as follows:

- Lowering the energy consumption by reducing the losses at the tank edges
- Simplifying the design of control edges in comparison to conventional systems
- Simple control strategies for operating the individual metering elements and thus achieving at least as good dynamic performance as existing control systems
- Reduction of components expense (solenoids, valves, sensors) compared to previously known system solutions with separate control edges
- Control on the basis of the latest electrohydraulic load-sensing systems
- Load compensation for parallel operation of several actuators
- Simple implementation of float functionality
- Simple implementation of circuits to exploit recuperation and regeneration potentials

The approach for finding new solutions comprises a systematic analysis of possible circuit concepts.

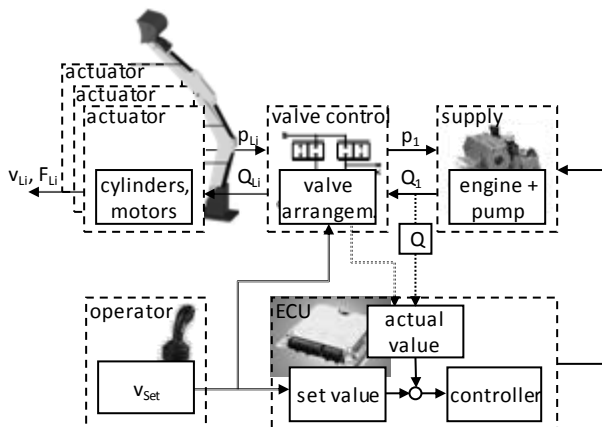


Figure 1: General electrohydraulic structure of working hydraulics for mobile machinery

The obtained solution space contains a large number of elements that must be evaluated based on functional and economical criteria. Therefore, it is advantageous to divide the control systems into its functional areas, see **Figure 1**. For each of these areas a number of solutions are possible. The clear distinction of the functional areas (operator, supply, valve control system, ECU and actuator) enables a systematization of the different drive and control tasks, which can be combined freely.

### 3.1 Main valve architectures

In order to develop circuit principles two design aspects are considered. The first one concerns the valve type combinations while the second one regards the arrangement of elements. Serial arrangements of two proportional metering edges result in redundant structures, which are unfavorable in terms of component expense. Likewise, parallel assemblies of a proportional edge and a switching edge are not applicable, since the control feature of the proportional edge is short circuited, see **Figure 2**.

		Valve Type Combination		
		Prop. & Prop.	Prop. & Switch	
Valve Arrangement	Serial			Proportional Valve 
	Parallel			Switching Valve 
				Hydraulic Connection 

Figure 2: Methodology of determining fundamental circuit principles

The essential requirement of an individual metering layout for a single consumer port corresponds to a 3/3-valve-type design. Under this premise, only circuit principles with at least 3/3-valve functionality are suitable. To determine whether a circuit principle meets the necessary functioning condition, mathematical formulations are used to calculate the equivalent valve functionality. On the basis of an electrical circuit analogy, parallel elements may be added, whereas elements connectec in series are multiplied. A parallel and a serial arrangement of two 2/2-way proportional metering edges serves as an example. Each of the elements contains one independent connection per switch position and two switching positions including null. Adding the number of independent connections i.e. the number of switching positions, which corresponds to a parallel arrangement, results in a 3/3-valve functionality. For a serial arrangement, it is necessary to multiply the characteristic numbers. As expected, the result shows a 2/2-valve functionality.

The systematic de-/coupling of the mechanical constraints starting from 4/3-valve design results in different hardware layouts. In general, the circuit principles can be classified in

symmetric and asymmetric circuits. Symmetric circuits only use one valve type for implementation of basic working functions, whereas asymmetric circuits use at least two different proportional valve types. The functionally and mechanically coupled metering cross section can be allocated either at the working ports ( $p_A$  or  $p_B$ ) or at the supply ports ( $p_0$  or  $p_T$ ) see **Figure 3**.

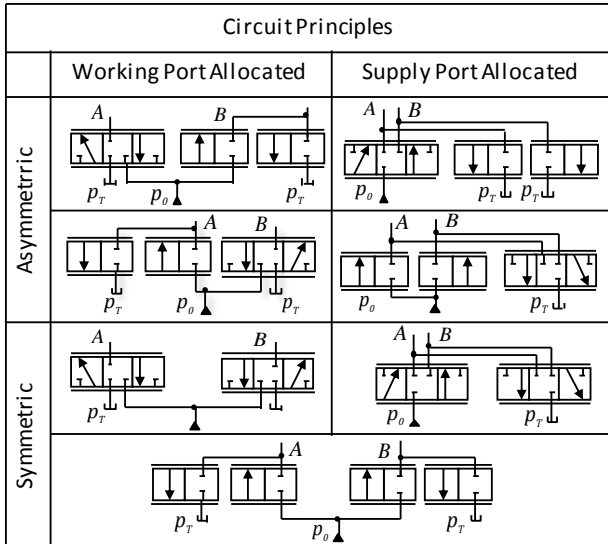


Figure 3: Fundamental circuit principles with parallel arrangement of proportional valve elements

The basic circuit principles can be compared based on criteria like the number of necessary valves or flexibility of arrangement. Also the type of solenoid, whether proportional or switching type, influences the choice. An adoption of 2/2-valves enables the usage of poppet type valves. There are several benefits in using poppet type valves, for example the much simpler valve design or nearly leakage-free characteristic. Furthermore, it is possible to mount these valves directly to the actuator. Enhanced dynamics can be achieved because hose and pipe volumina between valve and cylinder are kept small. Instead of connecting each individual consumer to the supply, pressure and tank line can be connected from one actuator to another. With the introduced combination methodology, several thousand possible valve arrangements are conceivable. But only a handful of them are of relevance for application.

### 3.2 Individual flow control

To attain load independent actuator motion, a constant flow at varying operating pressures over the control valves is necessary. This is accomplished by individual flow control. A circuitry implementation can be performed mechanically by individual pressure compensators or by means of electronics with appropriate sensors, see **Figure 4**. In contrast to sensors, mechanical solutions react directly and rapidly on disturbance variables in the system. However, system performance is influenced because damping might be reduced. The combination of the different possible solutions for the different sub-divisions gives an overview of the results in their entirety.

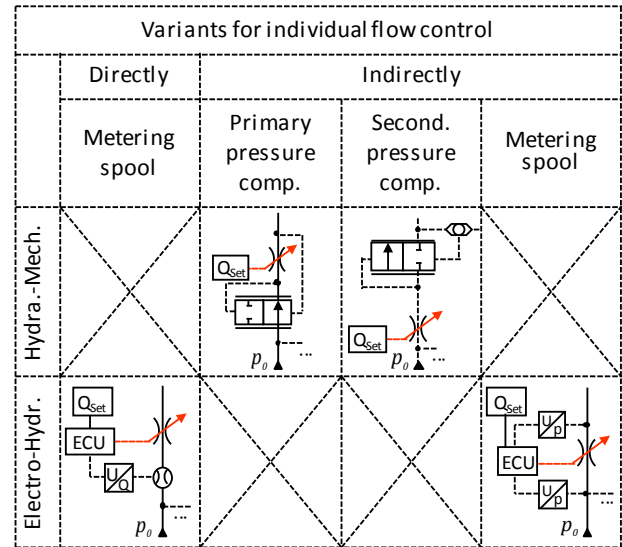


Figure 4: Variants of individual flow control

A conventional pressure compensated hydromechanical load sensing-system serves as a basis of comparison. The result of the evaluation is a ranked list of structures. Some of the solutions are presented in the following.

### 3.3 Determining circuitry concepts

In literature mostly symmetric and parallel arrangements of proportional valves as shown in Figure 3 are suggested, since this reflects the intuitive approach of separating the metering edges. A further aspect that correlates with the separation-thought is the disunion of metering and directing function. A circuit principle that implements such a task has been introduced in Figure 2 by a serial arrangement of a proportional and switching valve. A low-pressure drop and applicability of a simple and therefore low priced actuating solenoid are only some of the benefits of switching valves. By systematically combining different valve types and control circuit principles, a solution space is identified. In **Figure 5** an extract from the resulting set of possible solutions is presented. These novel structures are characterized by an economical use of components. In comparison to known structures, the component effort in terms of complexity and number is reduced. The proposed system layouts utilize two 2/2-proportional valves for metering and two 3/2-switching valves for flow directing functionality. Depending on the configuration, one or two pressure compensators are required. In that way pre- or post compensation can be implemented. To fully use the potentials concealed in the control concept, additional pressure sensors or displacement sensors are necessary. Along with dynamic and functional issues, there are safety issues to consider.

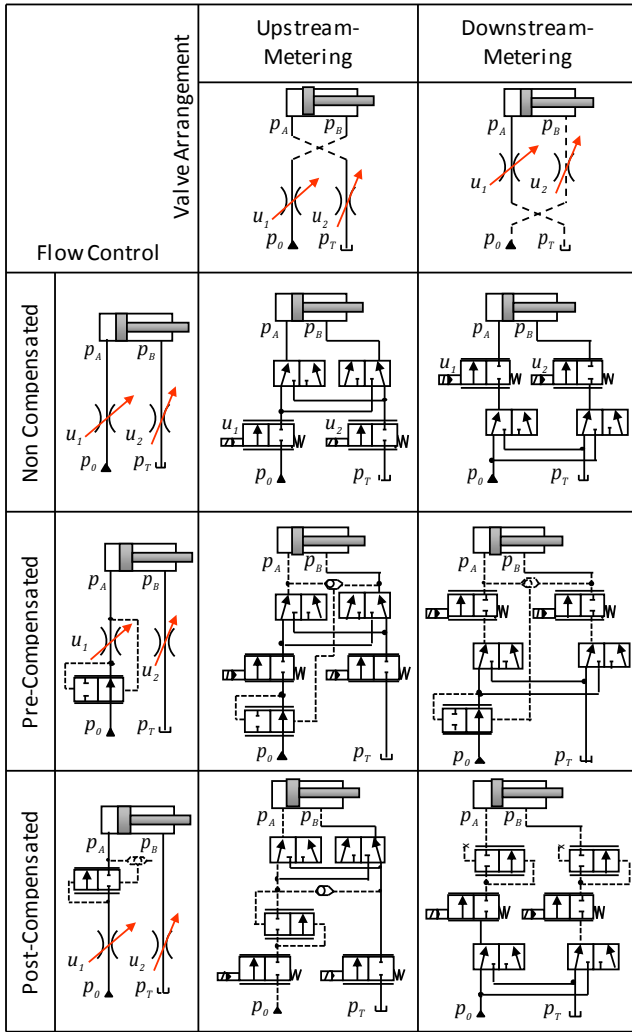


Figure 5: Extract of combination matrix containing novel structures

## 4 Modeling and simulation of systems with independent metering edges

In this chapter, general mathematical models of the individual metering systems are derived. Linearized models are used for analysis of the systems behavior. The investigations are exemplarily conducted on the non-compensated and the primary-compensated system layout, see Figure 5.

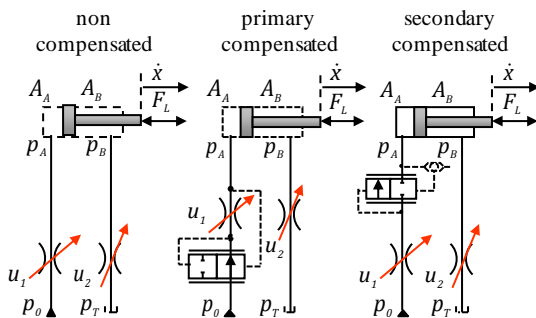


Figure 6: Simplified system layouts

To simplify analysis, the presence of only one actuator is assumed. The pump supply can be modeled using a transfer function with second order dynamics. The spool dynamics of the individual pressure compensator (IPC) as well as the dynamics of the cylinder can be described with a second order transfer function. However, the spool dynamics of the IPC can be modeled statically, since the corresponding inertias are small in comparison to the dynamics of the actuator line. The pressure build-up in hydraulic capacities is of first order. Experimental data of the static flow characteristic of the control valve are plotted in Figure 7 along with simulation results of the non-linear model.

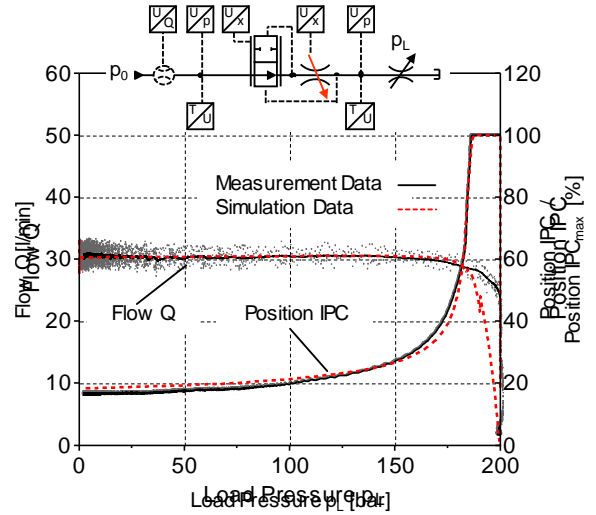


Figure 7: Static flow characteristic, stroke of individual pressure compensator of control valve

The model has been verified in the same manner for different operating points. In general the model showed a good quality match for the static behavior. However, there are deviations concerning certain dynamic phenomena, like excess flows, which are well known effects in two-way flow control valves. Since these deviations result in slight differences in the overall system performance, they may be neglected for further analysis.

### 4.1 Generalized linear models

Linearizing a non-linear model always leads to a compromise, because the resulting system is only valid locally around a specific operating-point. One of the possibilities to overcome this problem is provided by an operating-point tracing. All operating-point-dependent terms are being updated within each simulation run, to obtain model validity.

A minimal set of equations is needed to describe the systems behavior. The linearized flow equation is used to describe turbulent flow through a cross section

$$Q_A = K_{qu1} \cdot u_1 + K_{qp1} \cdot (p_0 - p_A) \quad (1)$$

$$Q_B = K_{qu2} \cdot u_2 + K_{qp2} \cdot (p_B - p_T) \quad (2)$$

where  $K_{Qui}$  is the constant flow coefficient and  $p_i$  are the system pressures. The continuity equation in hydraulic lines

describes the pressure build-up with the corresponding hydraulic capacitances  $K/V_i$

$$Q_A - A_A \cdot \dot{x} = \frac{K'}{V_A} \cdot \dot{p}_A \quad (3)$$

$$Q_B - A_B \cdot \dot{x} = \frac{K'}{V_B} \cdot \dot{p}_B \quad (4)$$

In combination with the motion equation of a differential cylinder, it represents the dynamics of the system

$$m \cdot \ddot{x} = p_A \cdot A_A - p_B \cdot A_B - F_L \quad (5)$$

Leakage effects, which mainly results in damping, is neglected. The resulting system block diagram is shown in **Figure 8**.

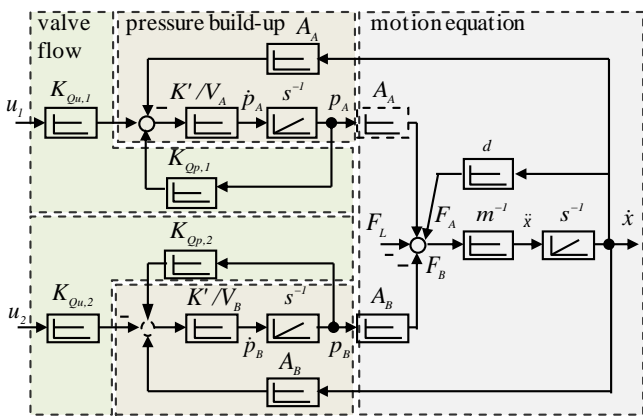


Figure 8: Linearized and simplified model of non-compensated hydraulic control system

The extension of the system with an individual pressure compensator in a pre-compensation layout is shown in **Figure 9**. As noted before, the spool dynamics of the IPC can be modeled statically, since the dynamic is much higher than the cylinder dynamics.

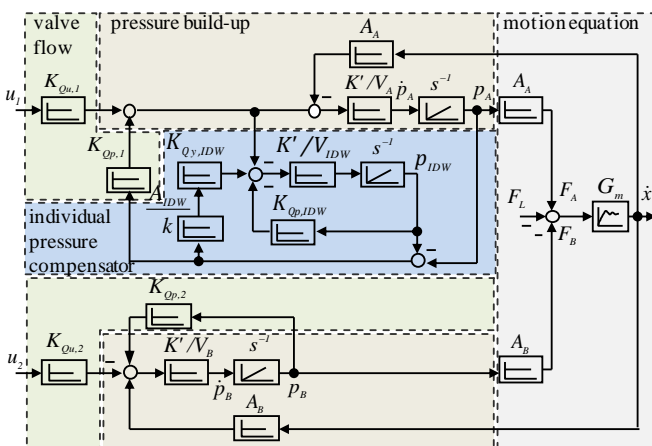


Figure 9: Linearized and simplified model of pre-compensated hydraulic control system

The static motion equation and pressure built-up are noted in Eq. (6) and Eq. (7)

$$y_{IDW} = \frac{A_{IDW}}{k} \cdot (p_{IDW} - p_A) \quad (6)$$

$$Q_{IDW} - Q_A = \frac{K'}{V_{IDW}} \cdot \dot{p}_{IDW} \quad (7)$$

The individual pressure compensator controls the pressure difference across the measuring orifice by throttling the cross sectional flow. In case of load or speed variations, the IPC changes its position in a closed loop characteristic, keeping the pressure difference  $\Delta p = (p_{IDW} - p_A)$  constant. The resulting flow through the control valve can be written as

$$Q_{IDW} = K_{Qy,IDW} \cdot y_{IDW} + K_{Qp,IDW} \cdot (p_0 - p_{IDW}) \quad (8)$$

$$Q_A = K_{Qu1} \cdot u_1 + K_{Qp1} \cdot (p_{IDW} - p_A) \quad (9)$$

It is obvious that the resulting systems with more than one input can no longer be considered as single input systems. In fact, it was the goal all along to control more than one output value, by introducing another input value. In order to continue using linear control design methods, a transformation of the system defining equations becomes necessary. The multivariable system analysis is presented in the following section.

## 4.2 Multivariable system approach

For the solution of analysis and design tasks, it is sometimes important to know which subsystems the multivariable system consists of. Structural information can be used to recognize internal feedbacks in the control system or to identify interactions between several control loops. Two important model forms are the p-canonical and v-canonical representation of multivariable systems, see **Figure 10**. It is a major objective of structured representation to distinguish main-couplings and cross-couplings. Therefore, these structures are mainly utilized for systems with the same number of input and output variables.

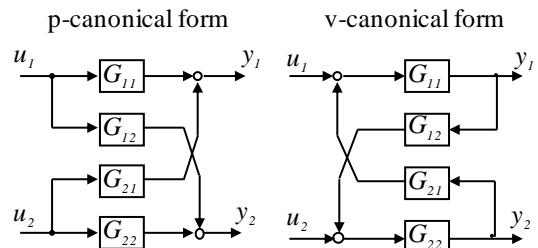


Figure 10: General description of multiple-input multiple-output systems (MIMO)

Multivariable systems can be classified in positively and negatively coupled systems. In case of equal signs (positive or negative), there is a positive coupling. Diverse signs indicate a negative coupling. These types of systems are generally associated with less damping. The influence of the coupling elements becomes particularly clear if the respective other transmission element represents a transfer function parallel to the main transfer function.

The p-canonical structure can be considered as the "natural" structure, which is derived out of the matrix representation

of the system. However, it is not "natural" in the sense of the physical structure. The individual transmission elements  $G_{ii}$  do not describe separate physical processes, but only cover different signal couplings within the same system. This fact becomes particularly obvious when certain system parameters occur in several transfer functions simultaneously.

The resulting p-canonical representation of the multivariable system is shown in **Figure 11**.

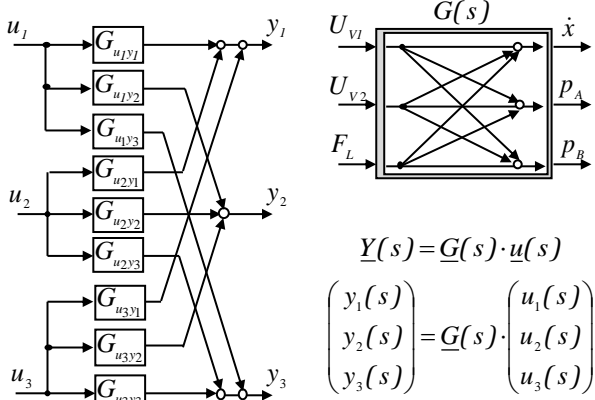


Figure 11: Representation of considered MIMO system with independent metering edges

The matrix containing the transfer functions can be written as

$$\begin{pmatrix} y_1 \\ y_2 \\ y_3 \end{pmatrix} = \begin{pmatrix} 1 \\ N(s) \end{pmatrix} \cdot \begin{pmatrix} G_{u_1,y_1} & G_{u_2,y_1} & G_{u_3,y_1} \\ G_{u_1,y_2} & G_{u_2,y_2} & G_{u_3,y_2} \\ G_{u_1,y_3} & G_{u_2,y_3} & G_{u_3,y_3} \end{pmatrix} \begin{pmatrix} u_1 \\ u_2 \\ u_3 \end{pmatrix} \quad (10)$$

The aforementioned equation neglects operation point dependent terms, which result from calculation of the Taylor series. The equations (11) to (22) evaluate the transfer functions.

$$G_{B1} = K_{Qp1} + \frac{V_A}{K_{\dot{O}l}} \cdot s \quad (11)$$

$$G_{B2} = K_{Qp2} + \frac{V_B}{K_{\dot{O}l}} \cdot s \quad (12)$$

$$N(s) = ms \cdot G_{B1} \cdot G_{B2} + A_A^2 \cdot G_{B2} + A_B^2 \cdot G_{B1} \quad (13)$$

$$G_{u_1,y_1}(s) \cdot N(s) = G_{B2} \cdot K_{Qul} \cdot A_A \quad (14)$$

$$G_{u_2,y_1}(s) \cdot N(s) = G_{B1} \cdot K_{Qu2} \cdot A_B \quad (15)$$

$$G_{u_3,y_1}(s) \cdot N(s) = -G_{B1} \cdot G_{B2} \quad (16)$$

$$G_{u_1,y_2}(s) \cdot N(s) = K_{Qu1} (G_{B2} \cdot m \cdot s + A_B^2) \quad (17)$$

$$G_{u_2,y_2}(s) \cdot N(s) = -K_{Qu2} \cdot A_A \cdot A_B \quad (18)$$

$$G_{u_3,y_2}(s) \cdot N(s) = G_{B2} \cdot A_A \quad (19)$$

$$G_{u_1,y_3}(s) \cdot N(s) = K_{Qu1} \cdot A_A \cdot A_B \quad (20)$$

$$G_{u_2,y_3}(s) \cdot N(s) = -K_{Qu2} (G_{B1} \cdot m \cdot s + A_A^2) \quad (21)$$

$$G_{u_3,y_3}(s) \cdot N(s) = -G_{B1} \cdot A_B \quad (22)$$

The transfer functions  $G_{ii}$  for a variation of cylinder stroke  $x=(Min \dots Max)$ , which mainly results in different capacities, are plotted in **Figure 12**. There is a peak in all the transfer functions for the chosen operating point. This resonance is the hydraulic resonance frequency of the spring-mass system.

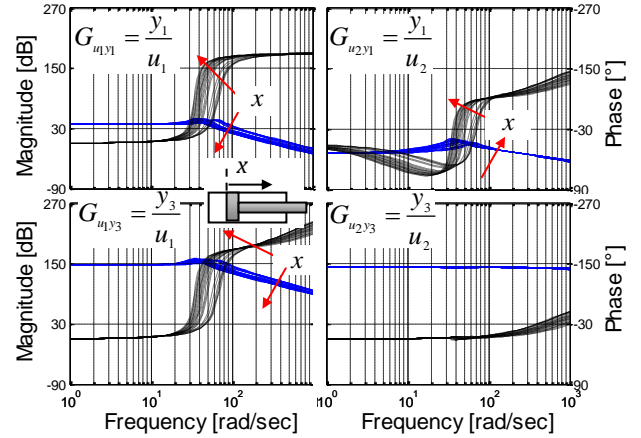


Figure 12: Open loop transfer function of multiple-input multiple-output system (MIMO) without IPC

The Eigenfrequency of the system shifts towards lower values, since the piston side volume increases. As there is no substantial resistance at the meter out edge, which would cause a pressure built up, the frequency of the system does not increase like it would in conventional hydraulic systems with one single spool. The corresponding pole-zero-map is plotted in **Figure 13**. For a decreasing signal at the meter-in valve  $u_I=U_{V1}$  the poles tend to move towards the right complex half plane with decreasing flow across the main valve.

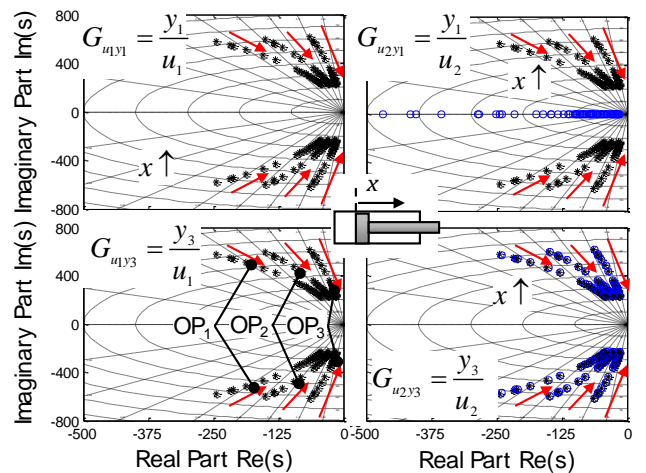


Figure 13: Pole zero map of open loop transfer function without IPC

The arrows indicate the variation of the frequency along the piston stroke. Whereas the operating points  $OP_1$  to  $OP_3$  stand for different actuator velocities. The damping is mainly dependent on viscous friction and flow characteristic of the system. By introducing sensors to feed back state variable information, the dynamics of main-couplings as well as cross-couplings are affected. That is when stability issues have to be taken into account.

Analogous to the model description of the non-compensated system, the equations (23) to (28) are introduced to model a system with primary pressure compensator.

$$G_{B1} = \frac{K_{\dot{O}l}}{V_A} \cdot \left( 1 + \frac{K_{Qp,1} \cdot G_3}{1 - G_{cIDW} \cdot G_3} \right) \cdot s + K_{Qp,1} \cdot \left( 1 + \frac{1}{1 - G_{IDW} \cdot G_{B3}} \right) \quad (23)$$

$$G_{B2} = K_{Qp2} + \frac{V_B}{K'_{\dot{O}l}} \cdot s \quad (24)$$

$$G_{B3} = \frac{k}{A_{IDW} \cdot K_{Qy,IDW}} \quad (25)$$

$$G_{IDW} = \frac{V_{IDW}}{K'_{\dot{O}l}} \cdot s + K_{Qp,IDW} \quad (26)$$

$$F_1 = \frac{1}{1 + \frac{K_{Qp,1} \cdot G_{B3}}{1 - G_{cIDW} \cdot G_{B3}}} \quad (27)$$

$$N(s) = ms \cdot G_{B1} \cdot G_{B2} + \frac{A^2}{F_1} \cdot G_{B2} + A_B^2 \cdot G_{B1} \quad (28)$$

The entries of the matrix  $\underline{G}(s)$ , which represent the transfer functions of the subsystems, are equivalent to the equations (14) to (22). The corresponding dynamics are plotted in **Figure 14**.

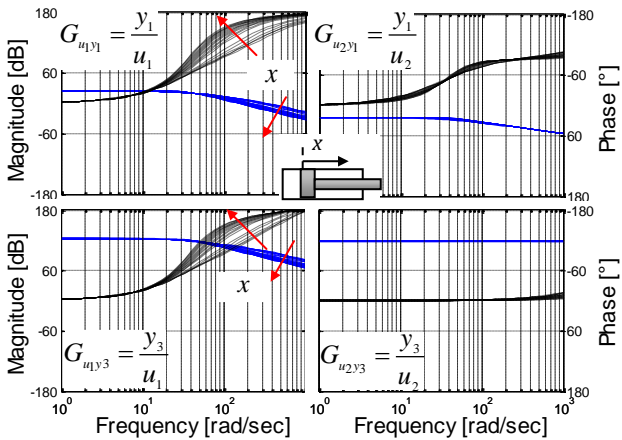


Figure 14: Open loop transfer function of multiple-input multiple-output system (MIMO) with IPC

Analyzing the systems pole-zero-map, see **Figure 15**, it is apparent, that varying the cylinder stroke  $x$  has huge impact

on the locations of the roots. The damping is significantly reduced with increasing piston stroke. The angular frequency however is not affected as severely as in the non-compensated system.

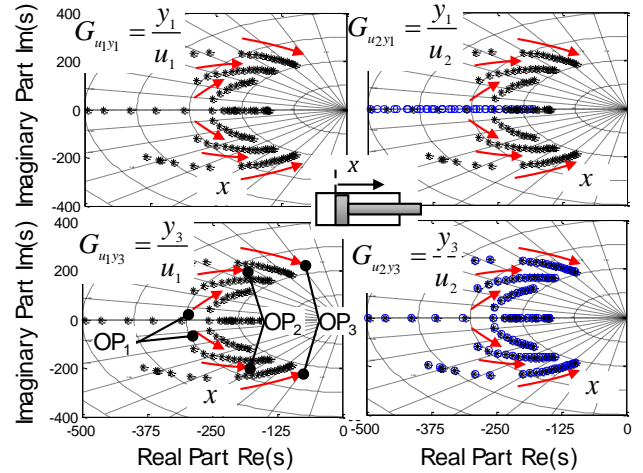


Figure 15: Pole zero map of open loop transfer function with IPC

The cross talk between input variable  $u_1$  and  $u_2$  is decreased. This is because the pressure difference across the measurement orifice is kept constant by the pressure compensator. While the pressure compensator's position is located in the control range, load variations do not influence the flow through the control valve.

### 4.3 Multivariable system analysis

The selection of appropriate control signals is a question of structural nature, since it is not only dependent on specific system parameters but on fundamental transmission properties of the controlled system. Accordingly, the structural properties of the controlled system are the primary factors in determining appropriate control signals. The decision on a certain control structure is significantly affected by the properties of dynamic systems. These properties are as follows:

- In order to stabilize an unstable system path, the control signals and controlled variables must be selected in a way that the unstable eigenvalues of the system become controllable and observable.
- The selected control signals and the controlled variables must not be linearly dependent. This condition is violated when the matrix B or C of the state space model do not meet a certain rank criterion.
- There must always exist at least as many control signals as controlled variables.
- All-pass behavior of the system path and the corresponding control signal complicates the control task.
- All-pass behavior may be eliminated by introducing additional control signals.

The preliminary decision, whether a multivariable controller is necessary or several single loop control circuits are

sufficient mainly depends on the strength of the couplings. In the literature, various empirical coupling measures are proposed. The question, which remains, is the strength of the cross-coupling elements  $G_{12}$  and  $G_{21}$  on the behavior of the control loop. In particular, it is interesting to know the range of values these elements may reach without affecting the stability of the control loops. In the following section, an assessment of the couplings is made to come to a decision whether a multivariable control is required or not.

#### 4.4 Definition and analysis of coupling-factor

To evaluate the couplings, a distinct assignment of input and output variables is necessary. Furthermore, a preliminary control structure must be assumed. Since the problem of input-output assignment is trivial for the system considered, following control structure is obtained, see **Figure 16**.

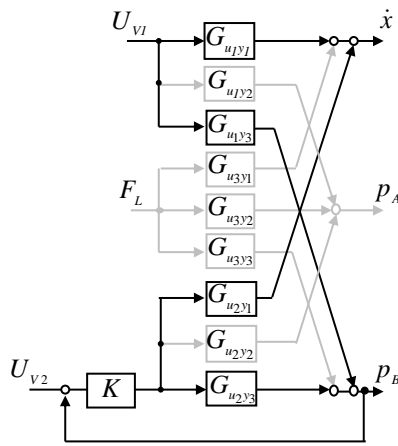


Figure 16: Block Diagram of reference behavior of the controlled MIMO system

The illustration above shows the familiar structure of the MIMO system, which has been extended with a pressure feedback on the meter-out side. The meter-in valve is still responsible for velocity control in an open loop manner. This would be a common and simple approach to control a system with independent metering edges.

The determinant of the feedback matrix  $\underline{F}(s)$  is of major importance for the stability analysis. Internal couplings of the system may be evaluated by examining the cross-coupling-elements  $G_{12}$  and  $G_{21}$ . Computing the determinant of  $\underline{F}(s)$ , one partial result is the so called coupling factor noted in equation (29)

$$\kappa(G(s)) = \left( \frac{G_{12}(s) \cdot G_{21}(s)}{G_{11}(s) \cdot G_{22}(s)} \right) \quad (29)$$

If there were no cross-couplings,  $G_{12}$  and  $G_{21}$  would be equal to zero and two decoupled transmission lines would exist. The absolute value of the expression  $\kappa(s)$  provides information on the strength of the couplings. If the absolute value of  $\kappa(s)$  is much smaller than one, there is a low coupling. Any value close to or greater than one implies strong couplings. The coupling coefficient  $\kappa(s)$  describes the strength with which the first control loop influences the transmission behavior of the second main control line. If

$\kappa(s)$  is very small, the controller  $K(s)$  may be designed only according to the behavior of the second main control path  $p_B(s) = G_{u2y3}(s)U_{V2}(s)$ . However, if  $\kappa(s)$  is large the transmission behavior of the cross- and main-couplings influences the controller design. The term  $\kappa(s)$  only states an empirical coupling-measure and therefore it only provides a guide value. The resulting couplings of the considered system layout are plotted in **Figure 17**. Displayed are two system layouts with- and without individual pressure compensator at two different load conditions.

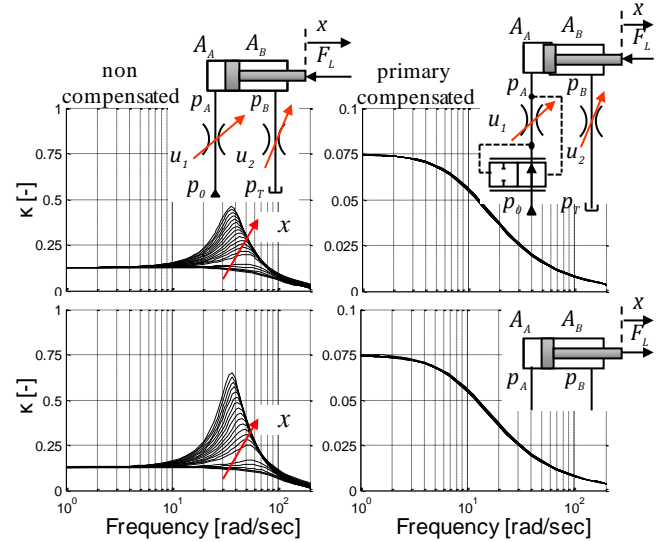


Figure 17: Couplings of the considered system with and without IPC

The top left diagram shows the gradient of the coupling factor, which has a maximum value of 0.5. In the figure below, the equal variations are displayed in case of pulling load characteristics. The value of  $\kappa(s)$  even increases. Since these values are relatively high, the system has to be considered a multivariable system. By introducing the individual pressure compensator to the system, the couplings between the main control lines are reduced significantly, see Figure 17 top-right. Since the coupling factor does not increase when pulling loads occur, a decentralized and therefore single input controller may be designed. A similar behavior can be observed when utilizing post-compensation. While the pressure compensator of the flow divider circuit is working within its control range, it shares likewise characteristics. Since it is one demand to implement simple and robust control methods, the use of individual pressure compensators appears to be desirable.

## 5 Conclusion and outlook

The paper started with a brief review on the state of the art for control systems and valve concepts with independent metering edges. In the following a systematic approach for determining circuitry principles was introduced. In the next paragraph a parametrised non-linear model of a non-compensated and a pre-compensated system have been presented. Some effects like rigid friction, leakage and spool dynamics have been neglected for the purpose of simplification. In order to obtain a canonical model structure

of the multivariable input output system, a linearization has been conducted. The models of both system layouts have been applied to an analysis of the systems couplings. The decision on a certain control structure is significantly affected by the properties of dynamic systems, which can be described with the help of the system couplings. The analysis showed that utilizing mechanical pressure compensators is favourable in terms of the necessary control effort. System couplings are reduced over a wide range of operation. Based on that knowledge, a single input controller layout may be used in order to keep implementation and commissioning effort low.

Since the control system design is highly dependent on the application and the machine structure, it is necessary to take different machines and working functions into consideration. Relevant application areas are primarily in the field of working hydraulics of construction machinery. These machines cover a wide range of applications and load conditions. A comprehensive analysis of machines and their associated application spectrum has to be carried out to develop suitable control system solutions. In combination with an operating strategy this will be the next step to be investigated.

## Acknowledgements

The work reported in this paper was performed within the project: "New Electrohydraulic Control Systems with Independent Metering Edges" funded by the DFG (German Research Society GZ: WE 4828/1-1). The permission for publication is gratefully acknowledged.

## Nomenclature

Designation	Denotation	Unit
$A_i$	Cylinder area	[m <sup>2</sup> ]
$d$	Viscous friction coefficient	[Ns/m]
ECU	Electronic control unit	[-]
$F_{Li}$	Load force	[N]
$G_{ii}$	Transfer function	[-]
$\underline{G}$	Matrix of transfer functions	[-]
$K$	Feedback gain	[-]
$k$	Spring rate	[N/m]
$K'$	Effective bulk modulus	[bar]
$K_{Qp,i}$	Lin. flow-pressure coefficient	[l/min/bar]
$K_{Qu,i}$	Lin. flow coefficient	[l/min/mm]
$\kappa$	coupling coefficient	[-]
$p_{Li}$	Pressure	[bar]
$\dot{p}_{Li}$	Pressure build-up	[bar/s]
$Q_{Li}$	Flow	[l/min]
$s$	Laplace operator	[-]

$u_i$	Input	[-]
$U_{Vi}$	Valve voltage	[V]
$v_{Li}, \dot{x}$	Velocity	[m/s]
$V_i$	Volume	[m <sup>3</sup> ]
$y_i$	Output	[-]

## References

- [1] Lunze, J., *Regelungstechnik 2 Mehrgrößensysteme Digitale Regelung*, Springer, 2005.
- [2] Anon, *Eaton Ultronics Management System*, Brochure No. E-VLDI-MR003-E2 Eaton Cooperation, 2005.
- [3] Djurovic, M., *Energiesparende Antriebssysteme für die Arbeitshydraulik mobiler Arbeitsmaschinen „Elektrohydraulisches Flow Matching“* Dissertation TU Dresden, 2007.
- [4] Eriksson, B.; Larson, J.; Palmberg J.-O *Study on Individual Pressure Control in Energy Efficient Cylinder Drives*, 4th FPNI-PhD Symposium, Sarasota USA, 2006.
- [5] Elving, M; Palmberg, J.-O. *Distributed Control of Fluid Power Actuator – A Load-Sensing Application of a Cylinder with Decoupled Chamber Pressure Control* 5th Scandinavian International Conference on Fluid Power, Linköping, 1997.
- [6] Eriksson, B; Rösth, M.; Palmberg, J.-O. A, *High Energy Efficient Mobile Fluid Power System – Novel System Layout and Measurement*, 6<sup>th</sup> International Fluid Power Conference, Dresden, 2008.
- [7] Finzel, R; *Elektrohydraulische Steuerungssysteme für mobile Arbeitsmaschinen*, Dissertation TU Dresden, 2010.
- [8] Jongebloed, H.; Fees, G. *Proportional Directional Valve with Autonomous Spools (PAS) for Mobile Applications*, 6<sup>th</sup> International Fluid Power Conference 6.IFK, Dresden, 2008.
- [9] Jansson, A.; Palmberg, J.-O. *Separate Controls of Meter-in and Meter-out Orifices in Mobile Hydraulic Systems*, Intenational Off-Highway & Power Plant Congress and Exposition, Milwaukee (USA), 1990.
- [10] Linjama, M.; Huova, M.; Vilenius, M. *Online Minimisation of Power Losses in Distributed Digital Hydraulic Valve Systems*, 6<sup>th</sup> International Fluid Power Conference 6. IFK, Dresden, 2008.
- [11] Matilla, J., *On Energy Efficient Motion Control of Hydraulic Manipulators*, PhD Thesis, Tampere University of Technology, 2000.

- [12] Meilicke, D., *Rough Terrain Lift Truck Efficiency and Control Improvement through Electronically Controlled Distributed Valves*, CFP, Las Vegas (USA), 2008.
- [13] German Patent DE 10200705403536A1, *Energierückgewinnungs- und Wiedernutzungsverfahren für ein Hydrauliksystem*, HUSCO International, 2008.
- [14] United States Patent 5568759 *Hydraulic circuit having Dual Electro-hydraulic Control Valves*, Caterpillar Inc., 1996.
- [15] European Patent EP 1710446A2, *Hydraulische Steueranordnung und Steuerblock*, Bosch Rexroth AG, 2006.
- [16] United States Patent 005947140, *System and method for controlling an independent metering valve*, Caterpillar Inc., 1999.
- [17] United States Patent 006976418, *Hydraulic System with an actuator having independent meter-in and meter-out control*, Caterpillar Inc., 2006.
- [18] Europeans Patent 0809737, *Electrohydraulic proportional control valve assemblies*, Eaton Ultronics, 1996.
- [19] International Patent WO 2007/015814, *EH Metering valve with integral flow control*, Caterpillar, 2007.
- [20] International Patent WO 02/075162 A1, *Control Valve*, Bucher Hydraulics GmbH, 2002.
- [21] United States Patent 002770046, *Integrated valve assembly and computer control for a distributed hydraulic control system*, Husco International Inc., 2007.
- [22] Pfaff, J.; *Distributed Electro-hydraulic Systems for Telehandlers*, 50th National Conference on Fluid Power, Las Vegas (USA), 2005.
- [23] United States Patent 6073652, *Pilot Solenoid Control Valve with Integral Pressure Sensing Transducer*, Husco International Inc., 2000.
- [24] Shenouda, A.; *Quasi-Static Hydraulic Control Systems and Energy Savings Potential using Independent Metering Four-Valve Assembly Configuration*, PhD studies, Georgia Institute of Technology, USA, 2006.
- [25] Shenouda, A.; Book, W.; *Selection of Operating Modes of a Multi-Functional Hydraulic Device*, ASME International Mechanical Engineering Congress and Exposition, Orlando (USA), 2005.
- [26] Tabor, K.; *A Novel Method of Controlling a Hydraulic Actuator with four Valve Independent Metering using Load Feedback*; SAE Commercial Vehicle Engineering Conference, Chicago (USA), 2005.
- [27] Yuan, Q.; Lew, J.; *Modelling and Control of Two Stage Twin Spool Servo-Valve for Energy-Saving*, American Control Conference; Portland, USA, 2005.
- [28] Zhang, J.; *Pressure Compensated Independent Metering Valve for EH System*; NCFP, Las Vegas (USA), 2008.

# Innovative Studies



## **Electrostatic charge measurement in hydraulic circuits**

M. Kühnlein, T. Wendel and H. Murrenhoff

RWTH Aachen University, Institute for Fluid Power Drives and Controls (IFAS), Aachen, Germany  
E-mail: Michael.Kuehnlein@ifas.rwth-aachen.de

### **Abstract**

Electrostatic charging of hydraulic circuits is recently becoming an issue as low conducting hydraulic fluids are increasingly in use. Charge generation is more likely to accumulate and build up large voltages. These high charge accumulations are hazardous as they can damage system components such as filters, which can eventually lead to system failure. In order to develop appropriate counter measures, a precise knowledge of influencing parameters is strongly beneficial. In this paper the causes for charge generation are discussed. Furthermore, methods for charge measurement of hydraulic fluids are presented. As the researched measurement methods are considered inappropriate, a new charge measurement method is developed. The development based on the principles of Faraday-cup and Faraday-cage are discussed in detail. Moreover, the integration of the developed charge sensors into an also developed experimental setup is described. The test rig in combination with the charge sensor allows the quantitative measurement of charged fluid without influencing the fluid to be investigated. It also enables measurements under pressure, meaning that the fluid can be pressurised up to 140 bar. The experimental setup is destined to obtain a large data basis. This data basis allows the validation of a charging model for which the modelling approach is also presented in this paper. This will lay the basis for a charging model to predict the charging tendency of a hydraulic system.

**Keywords:** Electrostatic charging, electro-chemical double layer, charging of hydraulic fluids, flow through filters, charge measurement.

### **1 Introduction**

Electrostatic charging is a well known phenomenon in many areas, one may think of experiencing a small flash of lightning while closing an automobile car door. An area of technical interest includes charging issues in electric power transformers of large scale, which were reported to explode due to electrostatic charging [1]. In these power transformers cooling fluid flows through long and small channels. The reason for electrostatic charging of fluids can be reduced to friction occurring between the flowing fluid and the wall. With unavoidable friction being present, electro-chemical double layers are built up at the wall [2] and the charges are separated by the flow of the liquid [3]. Thereby, charge is being accumulated. Charging of electric power transformers has been extensively analysed.

Charge accumulation is not challenging if the fluid is well conducting and the electric charge can be transported. Therefore, electrostatic charging has not been reported a major issue in hydraulic industry until recently. However, currently hydraulic oils with reduced ash and zinc concentrations are deployed to a greater extent [4]. These oils are less conducting and so lead to an increased charge accumulation.

As a result of the current trend towards low conducting hydraulic fluids, the topic of electrostatic charging becomes more important in the hydraulic industry. This paper gives an overview of the mechanisms responsible for charging and presents selected theories. Furthermore, a modelling approach for hydraulic systems is introduced. Another chapter deals with measurement principles and a new charge sensor, which was developed at the Institute for Fluid Power Drives and Controls (IFAS) of RWTH Aachen University. The presented measurement method is deployed in a hydraulic test circuit, which allows a detailed investigation of the phenomenon in order to expand the base of knowledge on electrostatic charging in hydraulic circuits.

In the later course of the project, for which some results are presented in this paper, a lot of experimental data will be generated. This data will serve as a knowledge base for the development of a charging model which should allow predicting the charging tendency of a hydraulic system. The current focus of the project is the investigation of the influence of hydraulic filters. Because of the large surface and its non-conducting material the filter element of a hydraulic circuit can naturally be regarded as the main source of charging. Until now, quantifiable data for hydraulic circuits regarding various influencing system

parameters is not sufficient and the project under discussion is aimed to close this gap.

## 2 Electrostatic charging of fluids

The electrostatic charging process is mainly caused by two materials with differing work function being situated close together. Friction is not necessary but facilitates a small distance of the two partners [5]. Figure 1 illustrates the charging and its separation for solid bodies.

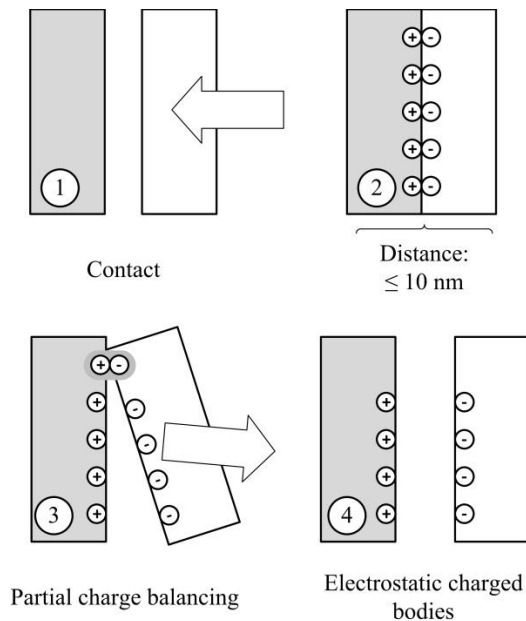


Figure 1: Charge separation for rigid bodies, based on [5]

If two bodies with different work functions are moved together (1) and the distance of the two bodies is less than 10 nm (2) electrons move from the material with the lesser work function towards the material with the higher work function. The reason for the charge transfer is the potential difference. An electrical double-layer builds up and the potential is in the range of millivolts. If the bodies are separated (3) the charge quantity stays constant. During the separation process the capacity of the setup decreases and so the previously low voltage can reach a voltage in the range of kilovolts (4). The duration of the separation process has a major influence on the potential generated. In general, a fast separation process leads to a high voltage, a slow separation process allows for charge compensation processes to take place so that only low voltage is generated.

For explanation of the charging process in fluids Figure 2 is introduced, which shows oil in a pipe.

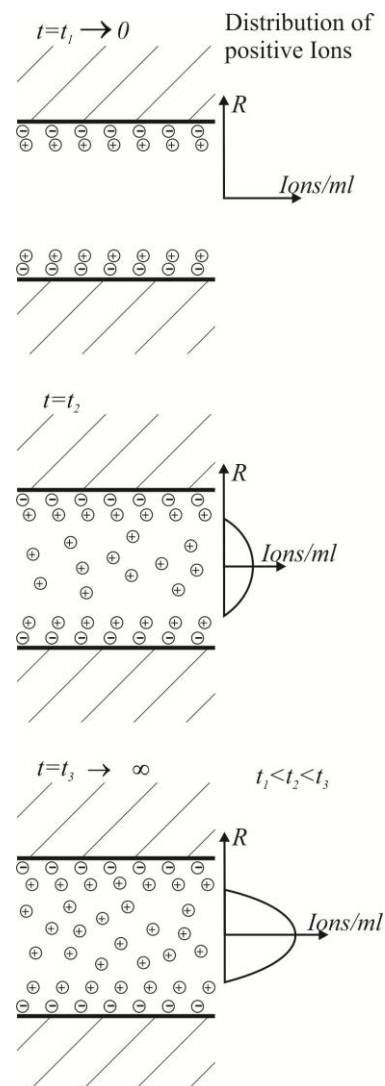


Figure 2: Electrostatic charging process

The charge separation takes place at the Helmholtz double layer [2]. The double layer builds up in the surface area of the wall. Assuming non-flowing fluid, negative ions adsorb on the boundary layer between pipe and oil on the pipe wall. For equilibrium reasons positive ions are in the adjacent layer. Hydraulic fluids are charged positively in most cases [6]. If the fluid flows through the pipe positive ions are carried away from the double layer and agglomerate in the fluid. With increasing time and volume flow a higher charge density is reached in the fluid.

Besides this basic flow electrification mechanism, more sophisticated flow electrification models have been developed. One of these is the nonlinear corrosion double-layer model shown in Figure 3.

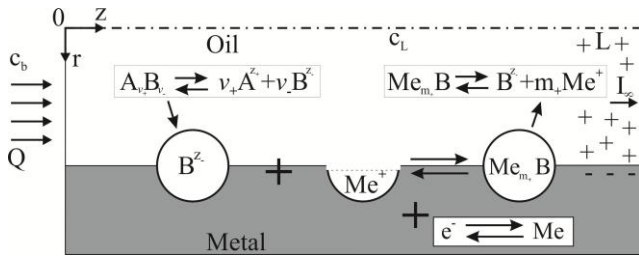


Figure 3: Corrosion double-layer model [3]

In this theory, oil has neutral molecules AB which dissociate into ions  $A^+$  and  $B^-$ . The  $B^-$  ions mainly adsorb at the metal surface and start the metal corrosion with positive  $Me^+$  ions. The  $MeB$  molecules are electrically neutral. As the  $B^-$  ions are thereby neutralised, the positive  $A^+$  ions remain in the fluid and thus charge the fluid positively [3].

Another theory focusses on the interaction between a cellulose material, also used in hydraulic filters, and oil. A description of the model shall be attained with Figure 4.

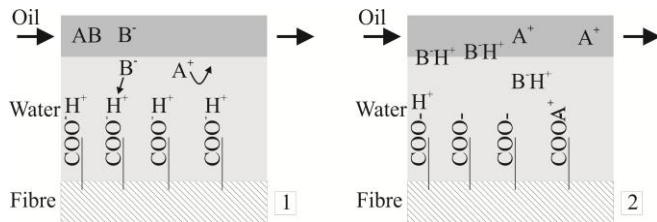


Figure 4: Cellulose fibre theory [7]

The theory states that the fibre structure has carboxy groups  $COOH$  in its boundary and the fibre surface is covered by a thin water layer. In the oil there are neutral molecules  $AB$  which can dissociate into  $A^+$  ions and  $B^-$  ions. The  $A^+$  ions are assumed to have a lower mobility than the  $B^-$  ions. Therefore, the mobile  $B^-$  ions combine with the  $H^+$  ions of the carboxy groups and constitute the neutral molecule  $BH$ . This leads to a neutralisation of the negative ions and so the oil is charged positively with  $A^+$  ions.

The project discussed in this paper has a system view on electrostatic charging. Therefore, the whole charge caused by the system is being considered. To allow a prediction of the charging tendency of a hydraulic system, a charging model is set up. The model will be based upon the data obtained later within the course of the project. As a system consists of many components, the charging model is formulated as a charging model of individual components or system parts. As the focus of the project is on hydraulic filters, the charge  $Q_{Filter}^{el}$  caused by filters is considered vital. Charge  $Q_{Pipe}^{el}$  caused by pipes is another part of the model. These individual “sub-charges” are summed up to yield the overall charge  $Q_{Overall}^{el}$  of the system. The factors  $P_{Pipe}$  and  $P_{Filter}$  are utilised as weighting factors, to account for different pipe length and various filter sizes.

$$Q_{Overall}^{el} = Q_{Pipe}^{el} P_{Pipe} \sum_{i=1}^n K_{i,Pipe} + Q_{Filter}^{el} P_{Filter} \sum_{i=1}^m K_{i,Filter} \quad (1)$$

The sub-charge  $Q_{Pipe}^{el}$  will be predicted with a charging model for pipes. The model from Klinkenberg seems promising, as it distinguishes between laminar flow and turbulent flow [1]. For the charge caused by the filter  $Q_{Filter}^{el}$  the electrification model from Washabaugh seems appropriate [8]. This model describes the flow through the area between two pipes where the outer pipe is metal and the inner pipe is non-conducting. In Equation (1) there are  $K_i$  factors included, which are used to describe the dependency of the charging quantity on influencing factors such as volume flow, temperature, particle contamination, filter material and so on. If for example the volume flow is doubled and the resulting charge quantity is twice as high as the charge quantity obtained with the standard parameter set, the corresponding  $K_i$  factor is 2. However, the sub-models which can be applied will be determined as soon as measurement data is available.

As the charging process and the modelling approach have been discussed, the question arises how the charge could be measured in an experimental setup. Considered measurement methods and the development of a charge sensor meeting the requirements of the challenging project are presented in the next chapter.

### 3 Measurement methods

In electrostatics, the physical value voltage cannot be measured with classical measurement instruments. This is due to the fact, that in electrostatic systems there is no constant voltage source and the amount of charges is limited. Therefore, special attention needs to be paid to isolation in order not to remove any charges from the object to be measured.

In Figure 5 electrostatic voltmeters are outlined, which have a very high resistance and despite that an extremely low tendency to discharge metal parts. Both instruments are strictly mechanical and utilise the force action of electric fields on charge carriers. The instrument shown on the left is basically a parallel-plate capacitor and the distance of the field plates changes depending on the applied voltage and the return spring. A scale allows the quantification of the measured voltage. The instrument shown on the right is an angle dependent rotary capacitor; the measured voltage is in linear relation to the torque  $M$ .

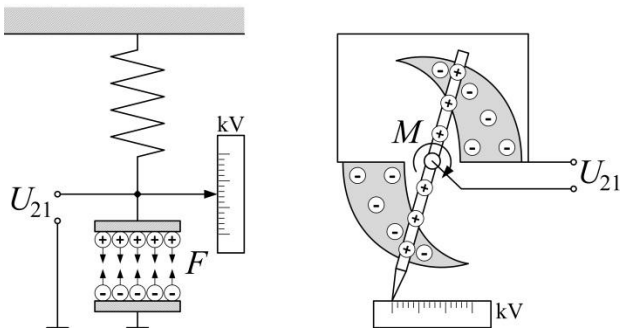


Figure 5: Electrostatic voltmeters, adapted from [5] and [9]

Figure 6 shows another instrument, which allows the measurement of electric fields. A grounded impeller wheel rotates with constant speed above fixed induction electrodes.

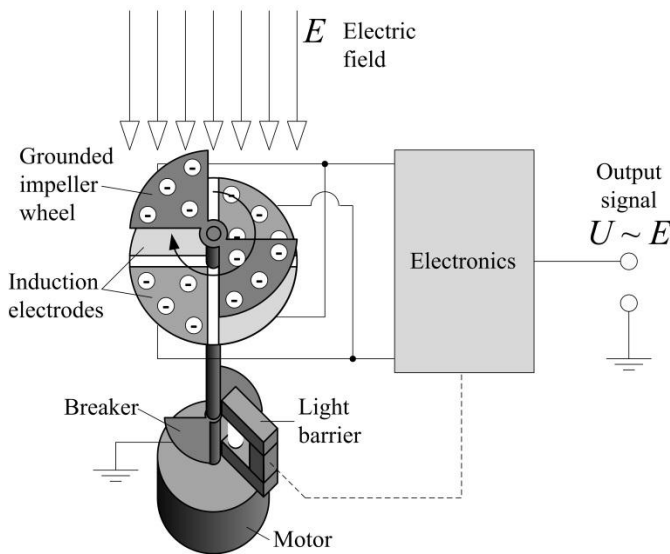


Figure 6: Electro field meter, adapted from [10] and [11]

As an electric field is present, the impeller wheel either exposes or shields the induction electrodes and with amplifying and conditioning electronics the output voltage  $U$  is proportional to the field strength  $E$ . If the electro field meter shown in Figure 6 is used with the voltage measuring head illustrated in Figure 7 voltages can be measured. The voltage measuring head is mounted to the electro field meter and adds a field plate, so that a parallel-plate capacitor is build. The object to be measured is connected to the measurement socket and the charge on the field plate causes an electric field between field plate and the induction electrodes. The grounded impeller wheel rotates in-between field plate and induction electrodes.

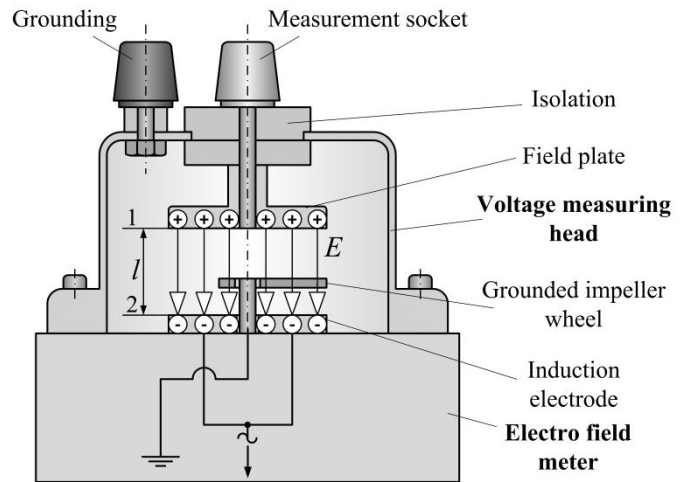


Figure 7: Voltage measuring head, adapted from [5]

For a homogeneous electric field the voltage  $U_{21}$  is a product of the field strength  $E$  and the distance  $l$ .

$$U_{21} = E l \quad (2)$$

The distance  $l$  in the voltage measuring head is precisely known and the field strength  $E$  is measured with the electro field meter, so the voltage of any object connected to the measurement socket can be measured. As the combination of electro field meter and voltage measuring head are in principal a plate capacitor, the isolation against discharge as well as the accuracy is very high. It therefore qualifies as an appropriate method to measure the voltage.

### 3.1 Measuring charges in fluids

To investigate the electrostatic charge of fluids, some methods have been developed in the past. The most relevant of these are presented in short in this chapter.

Figure 8 shows the Mini-Static Tester, which was initially developed by Oomen [12] to allow a detailed investigation of transformer oils.

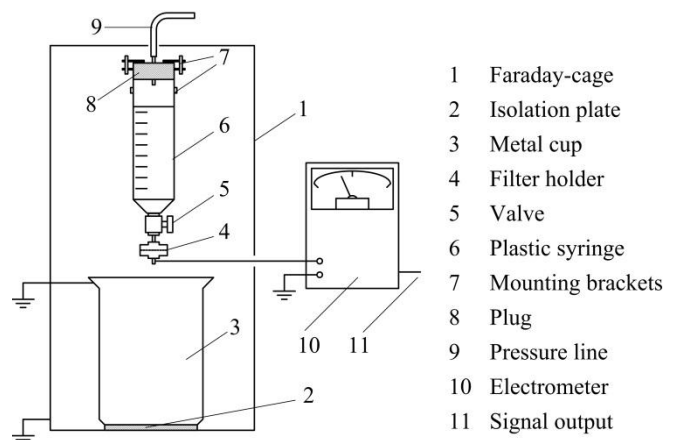


Figure 8: Mini-Static Tester, adapted from [12]

An oil test volume is pressed through a filter (4), where a charge separation takes place. A metal cup (3) collects the filtered oil and the charging current of the filter holder is detected with an electrometer (10). The amount of charge transferred to the filter holder is equivalent to the amount of charge generated in the fluid [12].

With consideration of the volume flow the volume charge density  $\eta$  can be calculated from the charging current measurement. Later, improvements have been made to the Mini-Static Tester in Japan, where the plastic syringe has been replaced by a glass container and a heating system was added. Furthermore, the charging current was measured at the metal cup instead of the filter holder. The volume charge density was then determined from the difference of a measurement with filter material and a measurement without filter material. Thereby, the non-identifiable influence of the cup on the charging process is omitted [13]. The Mini-Static Tester is not appropriate for measurements under higher pressure and the results obtained are charging tendency instead of absolute values.

The Absolute-Charge-Sensor (ACS) uses the Faraday-cup principle, see Figure 9.

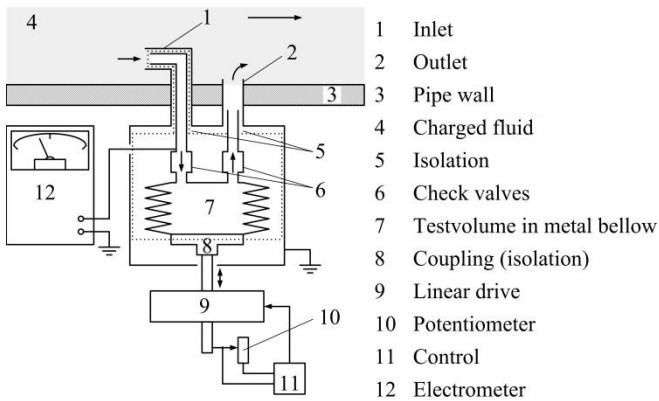


Figure 9: Absolute-Charge-Sensor, adapted from [14]

The charged fluid flows into a metal bellow (7), and the volume of the bellow can be altered with a linear drive (9). By means of influence the charge of the fluid causes a charge on the outside of the metallic bellow. This charge is measured with an electrometer (12). A grounded housing shields the instrument from surrounding electric fields. The volume charge density is calculated from the measured current and the fluid volume flow [14]. The Absolute-Charge-Sensor (ACS) is not suitable for measurements at higher pressure, as the material strength of the metal bellow is limited.

Another method to determine the volume charge density is the Tandem-chamber Charge Density Monitor shown in Figure 10. It uses the relaxation behavior of the electrostatically charged fluid and consists of two identical measurement chambers (5), the housings of the measurement chambers are separated by an isolating flange (6).

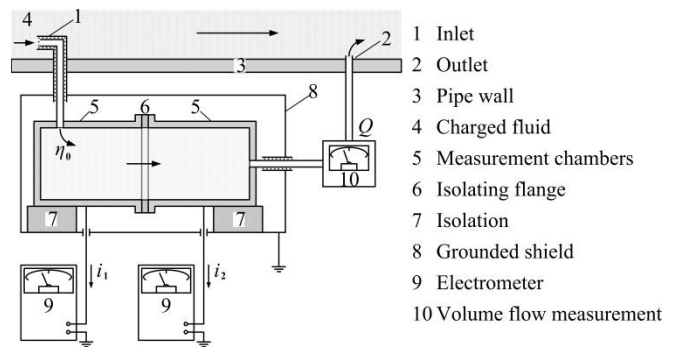


Figure 10: Tandem-chamber Charge Density Monitor, adapted from [15]

The volume charge density is approximated from the differential current measurement of the two electrometers (9), taking the volume flow into account. The Tandem-chamber Charge Density Monitor is not suitable, if higher volume flows are to be investigated, as charges could be dragged from the first chamber to the second. Furthermore, it is very likely to be affected by perturbations.

None of the researched possible measurement principles are considered suitable to investigate charged fluid in a hydraulic system, either because of only low pressure applicability or questionable repeatability due to perturbation affection. Therefore, a new measurement method, which can easily be integrated into hydraulic circuits, needs to be developed. This development is described in the next chapter.

### 3.2 Development of a charge sensor

The main challenge of the required charge sensor is that no hydraulic pipe should be opened to extract charged fluid. This implies the need of a contact-free measurement principle. As charged fluid is surrounded by an electric field, this is considered a starting point. By integrating the electric field strength  $E$  over its enveloping area  $A$ , the charge quantity  $q$  on the enveloping area can be calculated [9]:

$$\iint_A \epsilon_0 \epsilon_r E dA = q \quad (3)$$

This equation is based on Maxwell's equation on enveloping flow. The electrical field constant  $\epsilon_0$  is a natural constant and has a value of  $8.8452 \cdot 10^{-12} \text{ As/(Vm)}$ .  $\epsilon_r$  is the dimension-free relative permittivity, which is material dependent and always greater than zero. Equation (3) shows, that if the field strength  $E$  is known on every point of the enveloping area  $A$ , the enveloping charge quantity can be derived without a physical contact with the charged fluid. Thinking in practical terms, it would allow a direct detection of the charged fluid, even if the fluid is pressurised. Furthermore, no charge would be withdrawn and an accurate measurement could be carried out. The field strength could be measured with the electro field meter described in chapter 3.1.

The determination of the electric field could prove to be challenging, as in reality there are always interfering fields which influence the measurement. Moreover, the measured field strength depends on the localisation of the measurement. However, if one considers a Faraday-cup, the charge is equally distributed on the cup surface and thereby the electric field is also equally distributed. As an electrically conducting cup is an equipotential surface, the electric field lines are perpendicular with regard to the surface. Then the vector product  $\mathbf{E} \cdot d\mathbf{A}$  from Equation (3) simplifies to a scalar product  $E \cdot dA$ . If the relative permittivity is constant it follows:

$$\epsilon_0 \epsilon_r E \iint_A dA = q \quad (4)$$

For surface geometries which are mathematically easy to describe, it is possible to give the charge quantity enclosed in a Faraday-cup if the electric field strength at one point of the surface and the relative permittivity are known.

To account for interfering fields which would perturb the measurement, an electrical capacitor could be used. Capacitors with a simple geometry allow an analytical determination of the charge density and thus the field strength.

The ideal solution therefore would be a combination of a Faraday-cup and a capacitor. Such a combination is drafted in Figure 11.

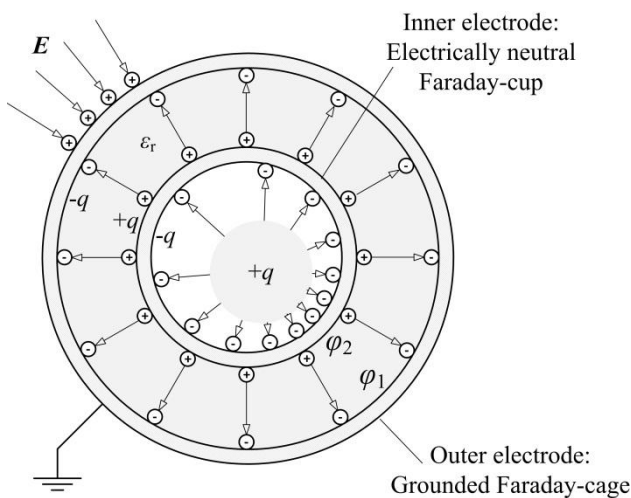


Figure 11: Electrical capacitor as a combination of a Faraday-cup and a Faraday-cage

The Faraday-cup itself is electrically neutral, meaning that the quantity of negative charge on its inner surface equals the quantity of positive charge on its outer surface. The neutrality is always prevalent. If a charge  $+q$  is present in the middle of the cup, an electric field builds up and consequently the inner surface of the cup holds a negative charge. Caused by influence, positive charge is moved to the outer surface of the cup. This causes an electric field between cup and outer electrode. Depending on the field weakening influence of the dielectric, a potential difference

$U = \phi_1 - \phi_2$  develops between the outer surface of the cup and the inner surface of the outer electrode. From the potential difference  $U$  the charge quantity  $q$  can be calculated if the capacity  $C$  is known.

$$q = C U \quad (5)$$

Another possibility is the measurement of the charge. The charge could be conducted from the Faraday-cup and the conducting current could be measured. This method would have the disadvantage, that the Faraday-cup would not be electrically neutral after the measurement. Another possibility is the measurement of the field strength within the capacitor. This would necessitate inserting the measuring device into the capacitor and thereby influencing the measurement itself.

The most promising approach is to measure the potential difference  $U = \phi_1 - \phi_2$  and calculate the charge quantity with Equation (5). The potential difference can be measured with the voltage measuring head in combination with an electro field meter shown in Figure 7. Advantages are that the capacitor setup is not perturbed by inserting a measuring device and the Faraday-cup can be kept electrically neutral.

Considering the test rig, a cylindrical capacitor is best suited because the charged fluid can be easily brought into the capacitor. Figure 12 shows a sectional view of a cylindrical capacitor with charged fluid inside.

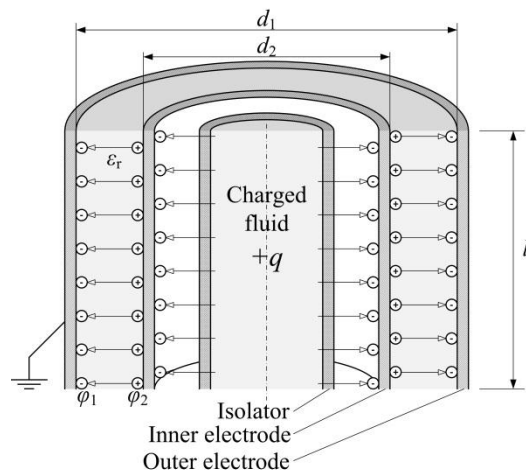


Figure 12: Sectional view of a charged cylindrical capacitor

The electric field caused by the charged fluid ( $+q$ ) leads to a charge movement on the inner electrode. On the inside surface of the inner electrode negative charge accumulates. As the inner electrode is electrically neutral, positive charge accumulates on its outer surface which is the potential  $\phi_2$ . Charged fluid and inner electrode are aligned collinear so that the field lines are perpendicular to the fluid and impinge on the inner electrode without deflection. The whole displacement current caused by a fluid column with the length  $l$  is taken up by the inner electrode of the same length. Field deflections in the edge areas of a practical cylinder capacitor can be reduced to a minimum by a proper design.

The outer electrode is grounded and so shields the capacitor against surrounding interfering fields. The potential  $\phi_2$ , which for the grounded outer electrode is equal to the potential difference  $U$ , is measured without charge loss with the voltage measuring head. The volume  $V$  holding the fluid charge quantity is given by the geometric properties of the fluid column.

As the volume  $V$  is known, the mean charge density  $\eta$  can be determined.

$$\eta = \frac{q}{V} = \frac{C U}{V} \quad (6)$$

The capacity  $C$  of a cylindrical capacitor, where  $d_2$  is the outer diameter of the inner electrode and  $d_1$  is the inner diameter of the outer electrode, is:

$$C = \frac{2 \pi \varepsilon_0 \varepsilon_r l}{\ln(d_2/d_1)} \quad (7)$$

Inserting Equation (7) into (6) yields:

$$\eta = \frac{2 \pi \varepsilon_0 \varepsilon_r l}{V \ln(d_2/d_1)} U \quad (8)$$

To calculate the mean charge density  $\eta$  the relative permittivity  $\varepsilon_r$  of the medium in the capacitor needs to be known. As a medium either air or an isolation gas could be used, for which the permittivity can be found in literature or can be calculated [16].

For dimensioning it is important to specify the parameters. The chosen voltage measuring head has a maximum detectable voltage of 2000 V. The volume  $V$  of the charged fluid is given by:

$$V = \frac{d_{fl}^2 \pi}{4} l \quad (9)$$

Inserting Equation (9) into (8) yields:

$$\eta = \frac{2 \pi \varepsilon_0 \varepsilon_r}{\frac{d_{fl}^2 \pi}{4} \ln(d_2/d_1)} U \quad (10)$$

It is clear, that the charge density  $\eta$  does not depend on the length of the fluid column. Sizing parameters are the diameter of the fluid column  $d_{fl}$ , and the electrode diameters  $d_1$  and  $d_2$ . As a fluid column a non-conducting hydraulic hose is used, which has an inner diameter  $d_{fl}$  of 25.4 mm. In order to allow a dimensioning of the electrode diameters, it is necessary to estimate the expected charge density. Data for the charge density is hard to find. From Sasaki's data a mean charge density of  $2.7 \cdot 10^{-3} \text{ C/m}^3$  can be derived [6]. However, the measuring method of Sasaki is different and the stated value is calculated from transformer oil data where hydraulic mineral oil should be investigated in the case discussed in this paper. The "Technical Rules for Operation Safety" states values of  $5.0 \cdot 10^{-3} \text{ C/m}^3$  as typical values of the charge density downstream of micro filters [17]. The circumstances leading to these values are not further specified. As no other relevant data is available, the data from Sasaki is considered most applicable.

To account for unexpected higher charging, a 20% safety margin is added so that the capacitor is dimensioned for a measuring range of  $3.24 \cdot 10^{-3} \text{ C/m}^3$ . An outer diameter  $d_2$  of the inner electrode of 160 mm is chosen and so the inner diameter  $d_1$  of the outer electrode, under consideration of Equation (10), is 171 mm.

A simplified view of the measurement setup is shown in Figure 13. If one considers the test procedure another obstacle is to be overcome. The charged fluid does not necessarily lose its charge after the measurement and therefore an electric field would still be present. If the inner electrode was grounded beforehand of each measurement, it would immediately assume the charge according to the prevalent electric field. This would falsify the measurement because the initial potential would not be zero. Therefore, a shielding pipe is added to the setup. As the shielding pipe is grounded, the inner electrode is shielded on either side and is in a field-free space.

In this field-free space the inner electrode can be grounded in it assumes zero potential. The measurement procedure is as follows:

1. Insert shielding pipe
2. Shortly ground inner electrode
3. Expose charged oil to capacitor
4. Remove shielding pipe
5. Start charge measurement

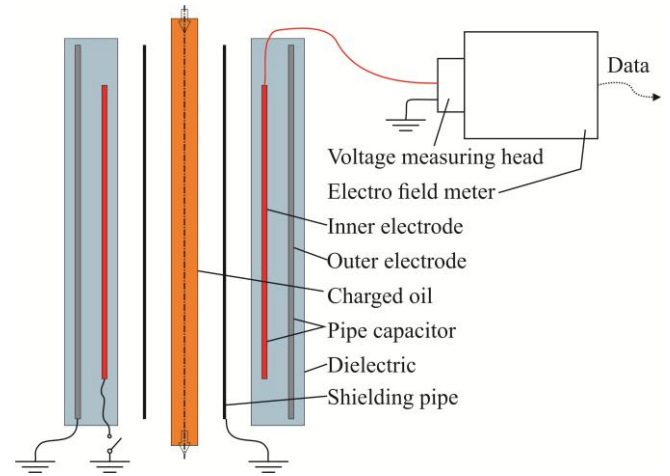


Figure 13: Simplified view of measurement setup

The developed sensor allows a measurement without a loss of charge and does not influence the fluid to be measured. It can easily be integrated into hydraulic circuits and enables measurements under pressure up to 140 bar.

The length  $l$  of the capacitor is set to 200 mm, which is useful in practical terms. Thereby, supplemental electrodes can be added at each end of the inner electrode to minimise deflections of the field lines at both ends of the inner electrode. A sectional view of the developed measurement capacitor is depicted in Figure 14.

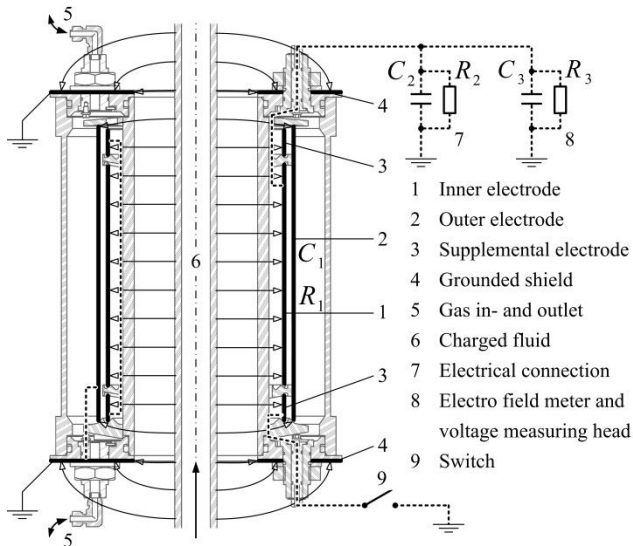


Figure 14: Measurement capacitor

The whole capacitor consisting of the inner electrode, the outer electrode and the two supplemental electrodes is enclosed in isolating polytetrafluoroethylene (PTFE). Thereby, it can be surrounded by a gaseous dielectric. The inner electrode is connected to the voltage measuring head. Outer electrode and supplemental electrodes are grounded during measurements.

The next chapter shows the test rig for the investigation of charged hydraulic fluids caused by filters.

#### 4 Test rig

The hydraulic schematic of the test rig is shown in Figure 15. It consists of a filter module. Pumps provide the oil flow through the filter and the system pressure can be set by a pressure control valve to modify the load. The volume flow of the pumps is 7 l/min or 21 l/min.

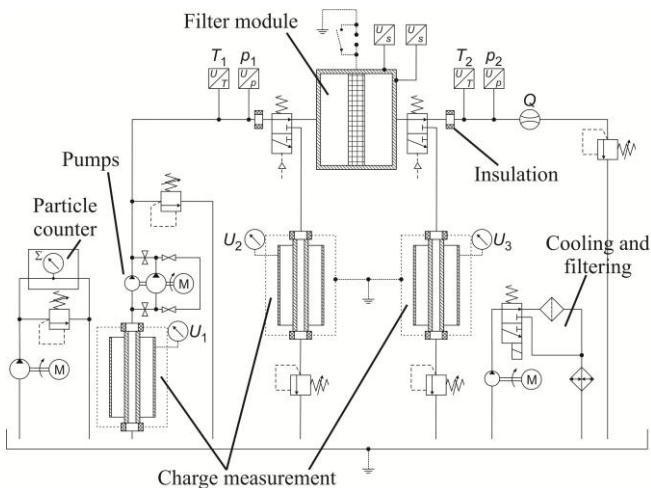


Figure 15: Test rig schematic

Besides the filter, the charge measurement chambers are the core elements of the test rig. These chambers allow the charge measuring of the oil. The fluid is measured before it flows through the filter and after it has passed the filter

module. The charge caused by the filter module is calculated as a difference of up- and downstream measurement. The measurements are carried out intermittent and the necessary flow is taken from the main circuit with pneumatically operated ball valves. A third charge measurement chamber is situated upstream of the pumps to analyse the initial charge of the fluid after leaving the reservoir. Additionally, a cooling and system-filtering sub-circuit is included. A particle counter allows maintaining defined oil cleanliness. To be able to investigate the filter element housing grounded and ungrounded, the housing is completely insulated and can be electrically grounded on purpose.

The physical test rig is shown in Figure 16. The shielding pipe, as a part of the measurement chambers, needs to be inserted and removed during each measurement cycle. To ensure comparable tests, this motion is automated pneumatically. The oil tank holds a volume of 250 l, which accounts for a long relaxation time so the charge should be zero when the oil leaves the tank. To maximise air separation, design recommendations from Weimann are accounted for [18]. The tank is equipped with a spiral-shaped insert which increases the surface area and undissolved air bubbles are expected to rise faster to the surface.

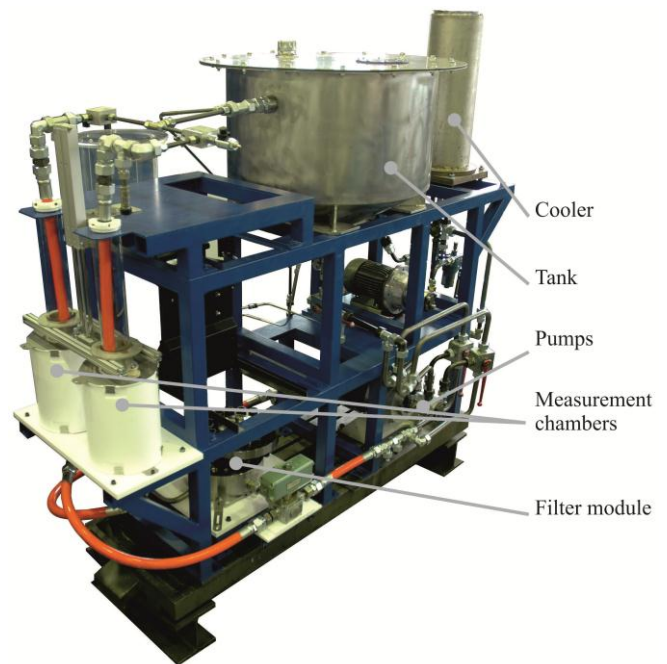


Figure 16: Test rig

Furthermore, the tank is designed cylindrically with a cone shaped bottom to prevent particles from being sedimented at the tank bottom. Another feature is that the test rig is remotely controllable. This is an advantage as the test rig is to be operated under varying temperature conditions.

A detailed view of the filter element housing is shown in Figure 17. The filter material is chosen to be circular and flat in shape to avoid geometry influences on the charge measurement. The filter disk is clamped in the middle of the shown housing. The housing consists of two parts and is connected by screws, which have been dimensioned so that

the housing withstands 350 bar. The dimensioning to 350 bar was verified by simulation and chosen, so that the filter module could also be operated in different hydraulic systems.

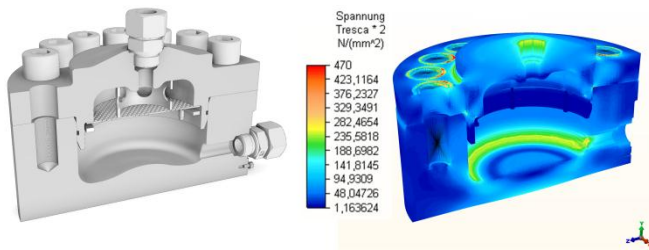


Figure 17: Filter element housing for simplified filter geometries

To allow an optimised and uniform flow through the filter material and account for a sturdy design, the bottom of the housing is designed with an elevation in its middle. As has been pointed out, the filter material is flat in shape. To investigate the influence of the filter material on the charging effect, three different filter media are used as a start. These media are shown in Figure 18.

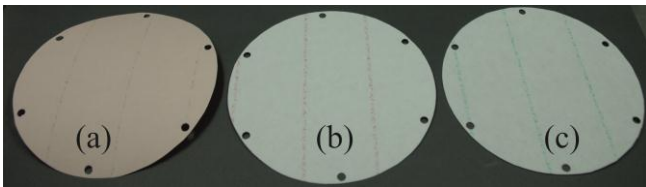


Figure 18: Filter media for filter module

Material (a) is cellulose and has a typical pore size of 15 µm, material (b) is glass fibre with a pore size of 6 µm (according to standard ASTM E 1294) and material (c) is also glass fibre with a typical pore size of 30 µm. The cellulose media is first investigated, as it will allow the validation of the developed charging model. The glass fibre media are investigated as they are closer to filter products widely used in hydraulic industry.

Other parameters to be investigated in the project are the oil temperature, the oil pressure, the oil conductivity, the influence of particles, the water content of the oil, grounded and ungrounded filter housing and volume flow dependency. As this given first parameter set would lead to approximately 30 000 single tests which need to repeatedly measured, a Design of Experiments method (DOE) has been applied to reduce the number of experiments because this huge amount of tests could not be realised. Thereby, a first screening test was set up which necessitates 64 experiments. After the first results, a new test schedule based on the experiences can be set up.

The test rig has another feature with regard to safety. The filter module can be investigated if ungrounded and is therefore electrically insulated from the other components. The “Technical Rules for Operation Safety” give limit values to hinder electrical discharges, which are a danger for persons. An energy content  $W$  of 350 mJ and a charge quantity  $q$  of  $50 \cdot 10^{-6}$  C should never be exceeded [17]. To

account for the safety of persons, a spark gap is designed to the filter module (see Figure 19).

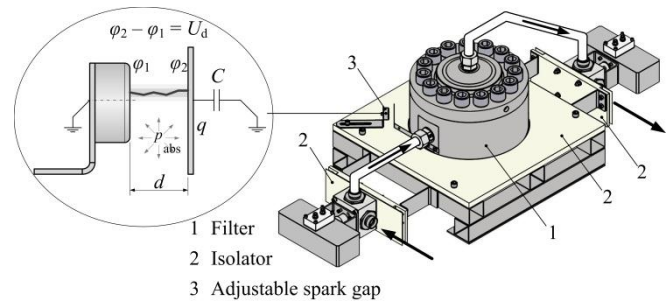


Figure 19: Adjustable spark gap at filter module

With the adjustable spark gap the distance is chosen in such a way, that a discharge occurs before the limit values are reached. The required distance can be calculated based on Paschen’s law [9]:

$$U_d = \frac{B_g p_{abs} d}{\ln\left(\frac{A_g p_{abs} d}{\ln(1 + 1/\gamma)}\right)} \quad (11)$$

It is an analytical approximation equation for the disruptive voltage  $U_d$  in ideal plate capacitors.  $A_g$  and  $B_g$  are gas constants, which have values of 1130 1/(mm bar) and 27.4 kV/(mm bar) respectively for air at a pressure of 1 bar and at room temperature. The coefficient  $\gamma$  for air and steel is  $2 \cdot 10^{-6}$  1/(mm bar) [9].

The energy  $W$  held by a capacitor is:

$$W = \frac{1}{2} C U^2 \quad (12)$$

With the limit of 350 mJ given by [17] and the known capacity of the filter module housing, the distance  $d$  to be set can be determined. Depending on the capacity, a typical value for the distance  $d$  is 8 mm. In a next step the capacity will be measured and so the distance can be set.

## 5 Conclusion

Electrostatic charging is a phenomenon recently occurring more often in hydraulic systems due to hydraulic fluids of low conductivity being applied more widely. As experimental data on the subject is hard to find, aim of the project presented in this article is acquiring such data and developing a model which allows the determination of the charging tendency of a hydraulic system.

The paper discusses the reasons for charging of fluids, which are the build-up of an electrochemical double-layer. If a flow is present, ions are removed from the double-layer and the fluid is charged.

To measure the charged fluid a suitable measurement method is in need. As the researched measurement methods are not considered appropriate, a new charge sensor is developed. It was shown that the electric field of a charged fluid column can be used as a basis for the measurement. A combination of a Faraday-cup and a Faraday-cage were developed and designed as a pipe capacitor. To measure the

charge of the inner measuring electrode an electro field meter in combination with a voltage measuring head was chosen. The advantage is that the voltage of objects can nearly be measured without a loss of charge and thereby preventing a measurement failure. Furthermore, the charge of the fluid is not affected by the measurement.

The whole charge sensor, consisting of the pipe capacitor, the electro field meter and the voltage measuring head, was incorporated into a test setup. The developed experimental setup has a test filter module to investigate various filter types and materials. The fluid is measured up- and downstream of the filter module and by building the difference of the measured charge the influence of the hydraulic filter can be determined. The filter housing design and the safety precautions taken to avoid danger for persons, namely an adjustable spark gap, have been described.

Future work includes the start-up of the developed test rig to obtain the desired experimental data. After data acquisition the focus will be on a further specification and validation of the charging model.

## 6 Acknowledgement

The work and results presented in this article were achieved within the project “Untersuchung der elektrostatischen Aufladung von Hydraulikflüssigkeiten bei der Durchströmung von Filtern”, funded by the German Alliance for Industrial Research (AiF) under grant number 17323/N1.

## Nomenclature

Designation	Denotation	Unit
$A$	Area	[mm <sup>2</sup> ]
$A_g$	Gas constant	[1/(mm bar)]
$B_g$	Gas constant	[kV/(mm bar)]
$C$	Capacity	[F]
$d$	Diameter	[mm]
$d_{fl}$	Fluid column diameter	[mm]
$d_1, d_2$	Diameters	[mm]
$E$	Field strength	[V/m]
$K_i$	Fitting factors	[-]
$l$	Length	[mm]
$M$	Torque	[Nm]
$p_{abs}$	Pressure	[bar]
$P_{Filter}$	Weighing factor filter	[-]
$P_{Pipe}$	Weighing factor pipe	[-]
$q$	Charge	[C]
$Q^{el}$	Charge	[C]
$U, U_{21}, U_d$	Voltage	[V]

$V$	Volume	[mm <sup>3</sup> ]
$W$	Work	[J]
$\gamma$	Gas and material constant	[1/(mm bar)]
$\epsilon_r$	Relative permittivity	[-]
$\epsilon_0$	Permittivity	[A s/(V m)]
$\eta$	Room charge density	[C/m <sup>3</sup> ]

## References

- [1] A Klinkenberg and J L van der Minne. *Electrostatics in the Petroleum Industry*. Elsevier, Amsterdam, 1958.
- [2] H Helmholtz. Studien über electricische Grenzschichten. *Analen der Physik und Chemie*, Neue Folge 7: 337-382, 1879.
- [3] P Fung et al. A Nonlinear Corrosion Double-Layer Model for Laminar Flow Electrification of Hydrocarbon Liquids in Long Metal Pipes. *Journal of Electrostatics*, 1997.
- [4] N N Hydac. Schwerwiegende Folgen vermeiden! *Ölhydraulik und Pneumatik O+P*, 3/2012: 20-23, 2012.
- [5] G Lütgens. Statische Elektrizität begreifen – beherrschen – anwenden. ExpertVerlag, Renningen, 2005.
- [6] A Sasaki and S Uchiyama. Generation of Static Electricity During Oil Filtration. *Lubrication Engineering*, Vol. 55, No. 9: 14-21, 1999.
- [7] A Bourgeois et al. Flow Electrification in Power Transformers: Study of a Potential Remedy. *IEEE Transactions on Dielectrics and Electrical Insulation*, Vol. 13, No. 3, 650-656, 2006.
- [8] A P Washabaugh and M Zahn. A Chemical Reaction-based Boundary Condition for Flow Electrification. *IEEE Transaction on Dielectrics and Electrical Insulation*, Vol. 4, No. 6, 688-709, 1997.
- [9] A Küchler. *Hochspannungstechnik Grundlagen – Technologie – Anwendung*. Springer, Berlin, 2009.
- [10] H Chmela and R Smetana. Feldmühle – Ein Messgerät für elektrische Felder. <http://www.hcrs.at/FELDMU.HTM>, visited October 12, 2012.
- [11] N N. Feldmühle. <http://www.rapp-instruments.de/static-machines/measuring/feldmuehle/feldmuehle.htm>, visited October 12, 2012.
- [12] T V Oommen and E M Petrie. Electrostatic Charging Tendency of Transformer Oils. *IEEE Transactions on*

Power Apparatus and Systems, Vol. 103, No. 7, 1923-1931, 1984.

- [13]K R Stonitsch. Einfluß der hydraulischen Strömungsverhältnisse auf die elektrostatische Aufladung der Kühlkanäle von Hochspannungs-Leistungstransformatoren. Dissertation, TU Graz, 1995.
- [14]A J Morin et al. An Absolute Charge Sensor for Fluid Electrification Measurements. IEEE Transactions on Electrical Insulation, Vol. 26, No. 2, 181-199, 1991.
- [15]J K Nelson and M J Lee. Tandem-chamber Charge Density Monitor. IEEE Transactions on Electrical Insulation. Vol. 25, No. 2, 399-404, 1990.
- [16]H Haken and H C Wolf. Molekülphysik und Quantenchemie. Springer, Berlin, 2006.
- [17]N N. Vermeidung von Zündgefahren infolge elektrostatischer Aufladungen. TRBS 2153, 2009.
- [18]O Weimann. Die Abscheidung von Luftblasen aus Schmierölen durch konstruktive Maßnahmen. Dissertation, TU Darmstadt, 1971.



## Basic Theory and Experiment Study on New Electro-hydraulic Exciter

Dong Han, Guofang Gong, Yi Liu and Huayong Yang

The State Key Lab of Fluid Power Transmission and Control, Zhejiang University, Hangzhou, China  
E-mail: [juebuqingchen@gmail.com](mailto:juebuqingchen@gmail.com), [gfgong@zju.edu.cn](mailto:gfgong@zju.edu.cn), [8303446@qq.com](mailto:8303446@qq.com), [yhy@zju.edu.cn](mailto:yhy@zju.edu.cn)

### Abstract

As important special engineering equipment, tamper is used to complete the work of construction and maintenance in the railway field. In the present market, tampers are mostly mechanically driven and exist technical limitations. A new electro-hydraulic exciter applied on new tamper is proposed. It is mainly composed of new spin valve and new micro-displacement oscillation cylinder. In the paper, new model of spin valve orifice is established based on FLUENT simulation. Theoretical model of exciter is established to early explore the relationship between structure parameters and performance parameters. Experiments are conducted to validate theoretical results. The results show that new model of spin valve and theoretical model of exciter are both accurate. New exciter can realize the flexible adjustment of amplitude and frequency. Therefore, design of new tamper is reasonable and it adapts to all kinds of complex working conditions including hardened ballast and loose ballast. The paper adopts methods of combinations among simulation analysis, theoretical model and testing. The research is very significant and provide theoretical and practical direction for design and optimization of electro-hydraulic exciter.

**Keywords:** tamper, electro-hydraulic exciter, simulation analysis, spin valve port, theoretical model

### 1 Introduction

With the rapid development of railway transport systems and the improvement of people's living standard, requests for comfort and safety by train are growing. So demands of routine maintenance have been considerably growing[1-2]. As large track maintenance machinery, tamping vehicle can obviously improve security, reliability and comfort of high-speed trains. As core equipment of tamping vehicle, the tamper, based on the principle of clamping and vibrating, changes ballast's original permutation and drives them to flow under the sleeper evenly and compactly [3-4]. As we all know, track environment is complex and variable, so it requires tamper having strong adaptability to different working conditions through different kinds of vibration. Vibration with high frequency and low amplitude is fit for hardened ballast. Vibration with low frequency and high amplitude is fit for loose ballast [5].

The current market of tamper is mostly taken by Hasco(America), Matisa(Switzerland) and Plasser(Austria). With multi-functions and high efficiency, their structures are different. Hasco's tamper has a horizontal twisting movement through eccentric linkage[6-8]. Matisa's tamper has a vertical elliptical movement through eccentric linkage[9-11]. and Plasser's tamper has a swing movement through eccentric linkage[12-14]. Therefore, they all use

eccentric shaft to realize mechanical vibration[15-16], which has some technical limitations as follows. First, because of fixed waveform, amplitude and frequency, they can't satisfy complex and variable track conditions. Then, some don't have independent tamping arms, which leads to inconvenience in repair. What's more, mechanical vibration of eccentric linkage accelerates wear.

Compared to tampers of mechanical vibration, hydraulic vibration has advantages of stepless speed, flexible load etc. Therefore, a new tamper of hydraulic vibration(Patent No.: 201010104672.9) is represented. It has independent relationship between squeeze motion and vibration motion. As key parts, a new electro-hydraulic exciter(Patent No.: 201010520147.5) is also presented. It mainly consists of spin valve(Patent No.: 201010100305.1) and micro-displacement oscillation cylinder(Patent No.: 201110229924.5).

The paper introduces working principle of new tamper and electrohydraulic exciter. FLUENT simulation of spin valve orifice indicates special features of spin valve orifice. Based on simulation analysis, revised theoretical model of spin valve port is established. In accordance with numerical analysis, the characteristics and performances of the electro-hydraulic exciter are early explored. At last, experiments results helps validate model and optimize design.

## 2 Operating principle

### 2.1 Principle of new tamper

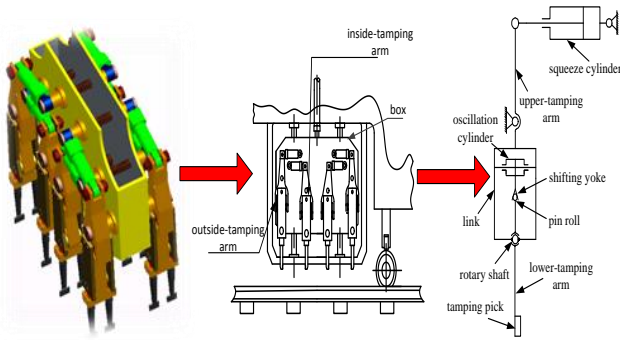


Figure 1: Operating principle of new tamper

As shown in fig.1, the new tamper is composed of box and four same pairs of independent tamping arms, including outside-tamping arms and inside-tamping arms. The box and upper-tamping arm are both hinged with the squeeze cylinder, which controls the upper-tamping arm's squeeze motion. The upper-tamping arm and lower-tamping arm are connected through the link. In addition, the tamping pick and pin roll are fixed on two ends of the lower-tamping arm separately. The vibration cylinder and shafting yoke are joined into a unit, which impels the lower-tamping arm to swing around the rotary shaft through shafting yoke in order to achieve high frequency vibration.

### 2.2 Principle of new exciter

As shown in Figure 2, new electro-hydraulic exciter is made up primarily of rotary valve and micro-displacement double-functioned hydraulic cylinder. In the new designed tamping device [15], the load that shifting yoke drives the lower-damping arm to swing through the rotary shaft is replaced by the load that cylinder body drives the mass to reciprocate on the linear guide rail. The rotary spool which is driven by step motor has two shoulders with the same structure. There are some rectangle grooves on the shoulder, and also the same number of corresponding rectangle windows in the sleeve. The hydraulic cylinder is driven by the rotary valve. As the piston is fixed with moving body, the main oil channel is designed in the piston rod, check valve lying at the end of main channel. There is an inner-leakage channel in the sidewall of body with the renewable damping hole. Besides, with the requirement of micro-displacement, some unique limit holes linked to main channel are applied to achieve automatic displacement limit but also to avoid collision between piston and end cap.

When the step motor impels spool to an specific angle, oil flows from port P to port A, through the main channel, through the right check valve, then through the right check valve and the right limit holes. At the same time, oil flows through left limit holes, through main channel, then from port B to port T. In this case, the cylinder body moves right and gets the outer load to vibrate right. When the step motor impels spool to another angle, similar with the above mentioned, oil flows from port P to port B and from port A

to port T. In this case, the cylinder body moves left and gets the outer load to vibrate left. With the change of step motor's speed, the frequency of rotary spool changes leading to the changes of cylinder's working frequency.

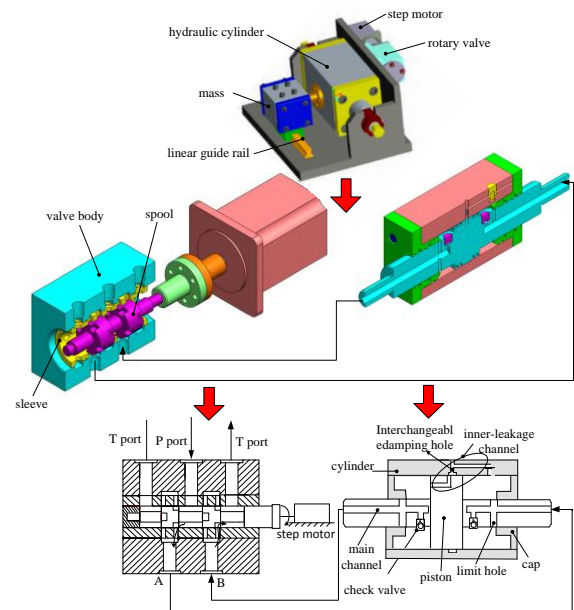


Figure 2: Operating principle of new exciter

The performance comparison of different tamping devices is shown in Table 1. Combined with the Figure 1, Figure 2 and Table 1, we can conclude that the new tamping device has great advantage in excitation since the flexible adjustment of frequency and amplitude can satisfy all kinds of complex working condition.

Table 1 Performance comparison of different tamping devices

Tamping machine	Plasser	Harsco	Matisa	New
Shock mechanism quantity	2	8	2	16
Relevant tamping arms quantity	8	2	8	1
Vibration frequency(Hz)	35	53	45	Adjustable
Amplitude	Fixed	Fixed	Fixed	Adjustable

## 3 CFD simulation of orifice

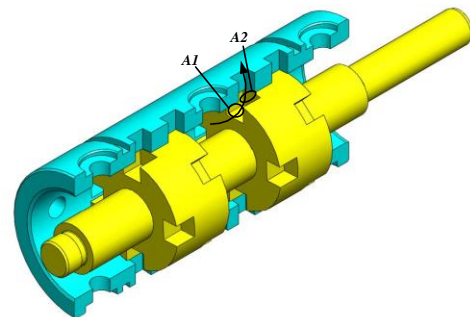


Figure 3: Structure of spool and sleeve

Figure 3 presents the structure of spool and sleeve. Four same rectangle grooves are distributed evenly on each side of every shoulder. Every groove's central angle is  $22.5^\circ$  and central angle of two neighbor grooves is  $90^\circ$ . Figure 4 is the flow field model of inlet orifice. Because of its complex, flexible unstructured mesh is adopted. Figure 5 illustrates the inlet orifice with about 120000 tetrahedron meshes.

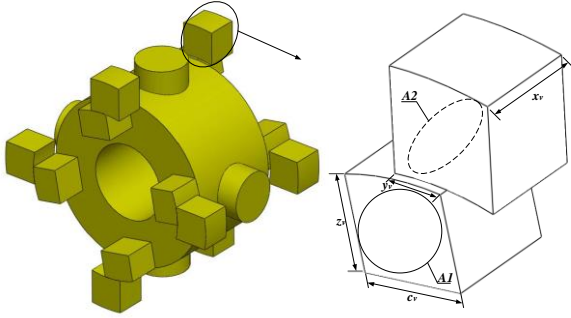


Figure 4: Flow field model of inlet orifice

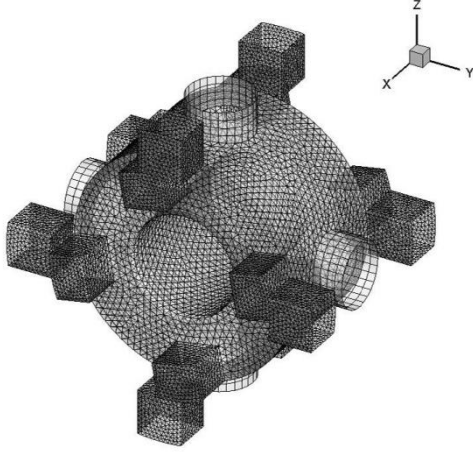


Figure 5: Flow field model of inlet orifice with meshes

Before the dynamic simulation, boundary conditions and initial conditions are set as follows. Assuming that oil is regarded as incompressible and its gravity is negligible. Oil density is  $889 \text{ kg/m}^3$  and kinematic viscosity is about  $4 \times 10^{-5} \text{ m}^2/\text{s}$ . The boundary conditions of inlet and outlet are the very pressure boundary conditions. Considering the dramatic changes in flow field,  $k-\zeta$  turbulent model is adopted.

Assuming that it's zero opening when the angular displacement is at  $\theta=0^\circ$ , Figure 6 shows inlet orifice's pressure distribution under different angular displacement of  $12^\circ$ ,  $22.5^\circ$  and  $33^\circ$ . In Figure (a) and (b), when the angular displacement is at  $\theta=12^\circ$ , the opening is also at  $12^\circ$  with a bigger tendency. Pressure drop is mainly concentrated on  $A1$  and  $A2$  surface. In Figure (c) and (d), when the angular displacement is at  $\theta=22.5^\circ$ , the opening is largest at  $22.5^\circ$ . Pressure drop is also concentrated on  $A1$  and  $A2$  surface, but in less extent than that in Figure (a) and (b). In Figure (e) and (f), when the angular displacement is at  $\theta=33^\circ$ , the

opening is at  $12^\circ$  with a smaller tendency. Pressure drop is also concentrated on  $A1$  and  $A2$  surface in equal extent compared with Figure (a) and (b). According to the above analysis, conclusion can be made that pressure drop is mainly concentrated on  $A1$  and  $A2$  surface. With a rise of orifice opening, unchangeable  $A1$  and bigger  $A2$  made the pressure distribution change. As consequence, pressure drop is less concentrated. Therefore, the rotary valve orifice exists the two throttles phenomena.

## 4 Analysis of mathematic modeling

### 4.1 Flow area model of rotary valve orifice

According to the above dynamic simulation, the two throttles phenomenon happened in the orifice. Therefore, the flow area model of orifice is established based on the two throttles phenomenon. Combined with conduction relationship shown in Figure 3 and geometrical relationship shown in Figure 4, flow area of  $A1$  surface doesn't vary with the spool rotation and can be written as

$$A_{1i} = \frac{\pi r^2}{16} - r^2 \sin \frac{\pi}{16} \cos \frac{\pi}{16} + 2rz_v \sin \frac{\pi}{16} \quad (1)$$

Where  $z_v$  is the radial length of orifice.

Flow area of  $A2$  surface varies periodically with the spool rotation. So it can be describes as

$$A_{2i} (i = 1, 4) = \begin{cases} x_v r \theta & \theta \in \left[ \frac{n\pi}{2}, \frac{(4n+1)\pi}{8} \right) \\ \frac{\pi x_v r}{4} - x_v r \theta & \theta \in \left[ \frac{(4n+1)\pi}{8}, \frac{(4n+2)\pi}{8} \right) \\ 0 & \theta \in \left[ \frac{(4n+2)\pi}{8}, \frac{(4n+3)\pi}{8} \right) \\ 0 & \theta \in \left[ \frac{(4n+3)\pi}{8}, \frac{(n+1)\pi}{2} \right) \end{cases} \quad (2)$$

$$A_{2i} (i = 2, 3) = \begin{cases} 0 & \theta \in \left[ \frac{n\pi}{2}, \frac{(4n+1)\pi}{8} \right) \\ 0 & \theta \in \left[ \frac{(4n+1)\pi}{8}, \frac{(4n+2)\pi}{8} \right) \\ x_v r \theta - \frac{\pi x_v r}{4} & \theta \in \left[ \frac{(4n+2)\pi}{8}, \frac{(4n+3)\pi}{8} \right) \\ x_v r \theta - \frac{\pi x_v r}{2} & \theta \in \left[ \frac{(4n+3)\pi}{8}, \frac{(n+1)\pi}{2} \right) \end{cases} \quad (3)$$

Taking into the two throttles phenomenon into account, the flow area of orifice is calculated in accordance with series connection between  $A1$  surface and  $A2$  surface. So the relation among pressure drop of orifice  $\Delta p_i$ , pressure drop of  $A1$  surface  $\Delta p_{1i}$  and pressure drop of  $A2$  surface  $\Delta p_{2i}$  is given as

$$\Delta p_i = \Delta p_{1i} + \Delta p_{2i} \quad (4)$$

The flow equation through the orifice is shown as

$$q_i = C_d A_i \sqrt{2\Delta p_i / \rho} \quad (5)$$

Where  $C_d$  is flow rate coefficient,  $\rho$  is oil density.

The flow equation through A1 surface is shown as

$$q_{1i} = C_d A_{1i} \sqrt{2\Delta p_{1i} / \rho} \quad (6)$$

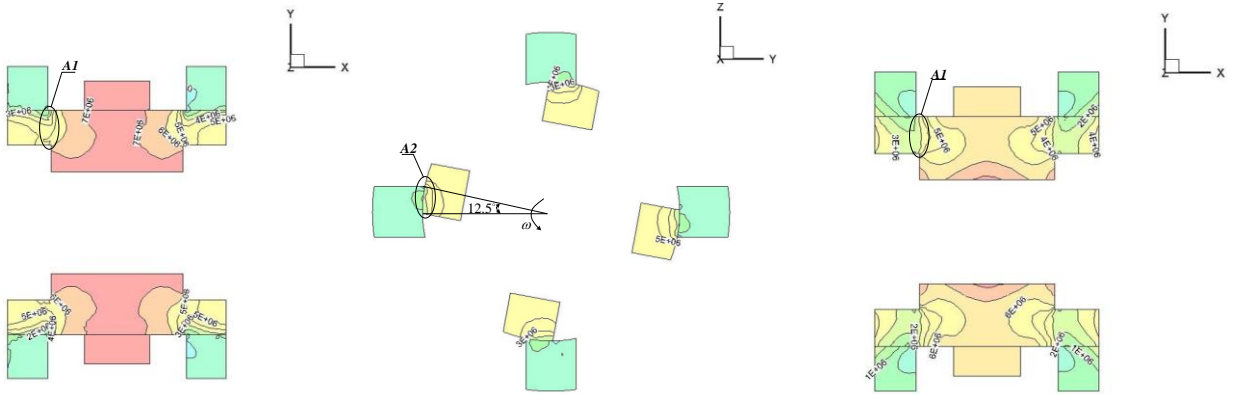
The flow equation through A2 surface is shown as

$$q_{2i} = C_d A_{2i} \sqrt{2\Delta p_{2i} / \rho} \quad (7)$$

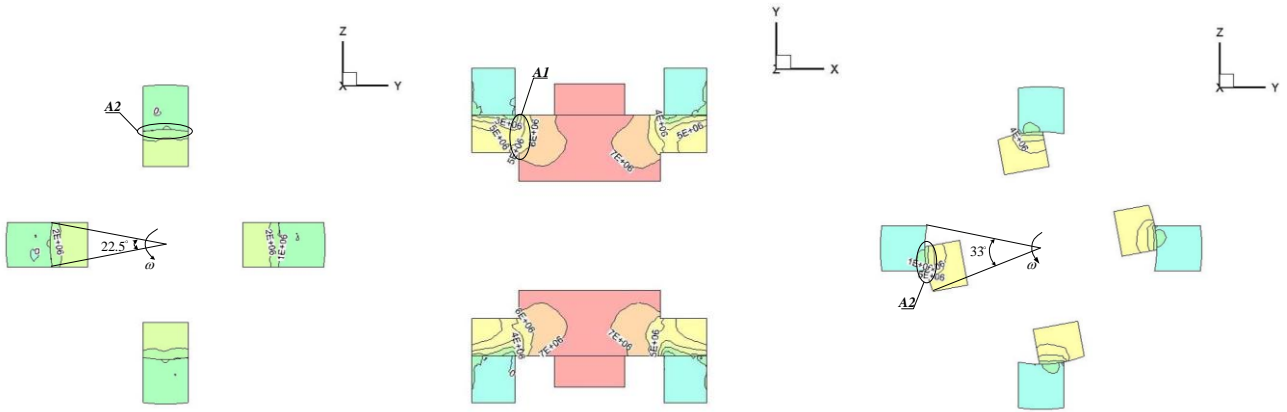
Because of series connection between A1 surface and A2 surface,  $q_i = q_{1i} = q_{2i}$ . Thus, based on the above analysis equations, the flow area of all orifices is calculated as

$$A_i = \frac{4}{\sqrt{\frac{1}{A_{1i}^2} + \frac{1}{A_{2i}^2}}} \quad (8)$$

$$= \begin{cases} \frac{4}{\sqrt{\frac{1}{\left(\frac{\pi r^2}{16} - r^2 \sin^2 \frac{\pi}{16} \cos^2 \frac{\pi}{16} + 2r z_c \sin \frac{\pi}{16}\right)^2} + \frac{1}{(x, r\theta)^2}}} & \theta \in \left[\frac{n\pi}{2}, \frac{(4n+1)\pi}{8}\right) \\ \frac{4}{\sqrt{\frac{1}{\left(\frac{\pi r^2}{16} - r^2 \sin^2 \frac{\pi}{16} \cos^2 \frac{\pi}{16} + 2r z_c \sin \frac{\pi}{16}\right)^2} + \frac{1}{\left(\frac{\pi x, r}{4} - x, r\theta\right)^2}}} & \theta \in \left[\frac{(4n+1)\pi}{8}, \frac{(4n+2)\pi}{8}\right) \\ \frac{4}{\sqrt{\frac{1}{\left(\frac{\pi r^2}{16} - r^2 \sin^2 \frac{\pi}{16} \cos^2 \frac{\pi}{16} + 2r z_c \sin \frac{\pi}{16}\right)^2} + \frac{1}{\left(x, r\theta - \frac{\pi x, r}{4}\right)^2}}} & \theta \in \left[\frac{(4n+2)\pi}{8}, \frac{(4n+3)\pi}{8}\right) \\ \frac{4}{\sqrt{\frac{1}{\left(\frac{\pi r^2}{16} - r^2 \sin^2 \frac{\pi}{16} \cos^2 \frac{\pi}{16} + 2r z_c \sin \frac{\pi}{16}\right)^2} + \frac{1}{\left(x, r\theta - \frac{\pi x, r}{2}\right)^2}}} & \theta \in \left[\frac{(4n+3)\pi}{8}, \frac{(n+1)\pi}{2}\right) \end{cases}$$



(a) Pressure distribution in Z plane,  $\theta=12^\circ$  (b) Pressure distribution in X plane,  $\theta=12^\circ$  (c) Pressure distribution in Z plane,  $\theta=22.5^\circ$



(d) Pressure distribution in X plane,  $\theta=22.5^\circ$  (e) Pressure distribution in Z plane,  $\theta=33^\circ$  (f) Pressure distribution in X plane,  $\theta=33^\circ$

Figure 6 Pressure distribution of inlet orifice

#### 4.2 Modeling of hydraulic exciter

The Principle of new electro-hydraulic exciter is shown in Figure 7. It is assumed that the system pressure  $p_s$  is constant, the total supply flow is  $q_{v3}$ , the flow through the load is  $q_{v1}$  and the pressure drop across the load is  $p_l$ .

If the orifices are both matched and symmetrical, the flows in diagonally opposite arms of the bridge in Figure 7 are equal. The area of valve port is  $A_v$ . Therefore,  $A_{v1} = A_{v3}$ ,  $A_{v2}$

$= A_{v4}$ . Supposing the rotation period of valve spool is  $T$ , the equations of flow through the orifices are shown as follows:

$$\text{For } 0 \leq t \leq \frac{T}{8}, \frac{T}{4} \leq t \leq \frac{3T}{8}, \frac{T}{2} \leq t \leq \frac{5T}{8}, \frac{3T}{4} \leq t \leq \frac{7T}{8},$$

$$\begin{cases} q_{v1} = q_{v3} = C_d A_{v1} \sqrt{\frac{2(p_s - p_l)}{\rho}} = C_d A_{v1} \sqrt{\frac{p_s - p_l}{\rho}} \\ q_{v2} = q_{v4} = 0 \end{cases} \quad (9)$$

For  $\frac{T}{8} \leq t \leq \frac{3T}{8}, \frac{3T}{8} \leq t \leq \frac{T}{2}, \frac{5T}{8} \leq t \leq \frac{3T}{4}, \frac{7T}{8} \leq t \leq T,$

$$\begin{cases} q_{v1} = q_{v3} = 0 \\ q_{v2} = q_{v4} = C_d A_{v2} \sqrt{\frac{2p_1}{\rho}} = C_d A_{v2} \sqrt{\frac{p_s + p_1}{\rho}} \end{cases} \quad (10)$$

Where  $C_d$  is flow rate coefficient;  $\rho$  is oil density;  $p_1, p_2$  are pressure of hydraulic cylinder two cavity respectively.

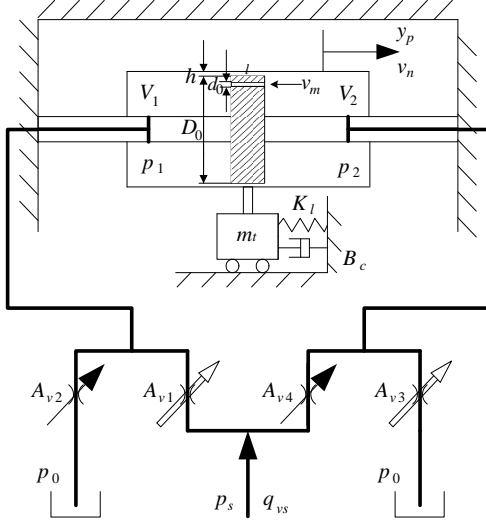


Figure 7 The principle of new electro-hydraulic exciter

The flow rate continuity equation of the left chamber of the cylinder.

$$q_{v1} - q_{v2} = \frac{dy_p}{dt} A_p + \frac{V_1}{\beta_e} \frac{dp_1}{dt} + C_{ep} p_1 + q \quad (11)$$

The flow rate continuity equation of the right chamber of the cylinder.

$$q_{v3} - q_{v4} = \frac{dy_p}{dt} A_p - \frac{V_2}{\beta_e} \frac{dp_2}{dt} - C_{ep} p_2 + q \quad (12)$$

Where  $y_p$  is displacement of cylinder;  $\beta_e$  is effective bulk modulus of oil;  $A_p$  is area of piston;  $V_1$  is volume of forward chamber,  $V_1 = V_{o1} + A_p y_p$ ,  $V_{o1}$  is initial volume of forward chamber;  $V_2$  is volume of return chamber,  $V_2 = V_{o2} - (V_{o1} + A_p y_p)$ ,  $V_i$  is total volume of cylinder chamber;  $C_{ep}$  is the coefficient of external leakage;  $q$  is the internal leakage flow.

If external leakage is zero, the relationship between the load flow of the cylinder is  $q_{vl} = q_{v1} - q_{v2}$ .

That is,

$$q_{vl} = \text{sign}\left(\frac{\pi}{4} - 2\pi ft\right) A_p \frac{C_d}{\sqrt{\rho}} \sqrt{p_s - \text{sign}\left(\frac{\pi}{4} - 2\pi ft\right) p_1} = \begin{cases} C_d A_{v1} \sqrt{\frac{p_s - p_1}{\rho}}, & (0 \leq t \leq \frac{T}{8}); \\ C_d A_{v2} \sqrt{\frac{p_s + p_1}{\rho}}, & (\frac{T}{8} \leq t \leq \frac{T}{4}). \end{cases} \quad (13)$$

General hydraulic system is low damping, increasing hydraulic damping can improve the vibration system performance[17]. Its method is mainly through the interchangeable damping hole in the cylinder barrel to get different damping as shown in Figure 3. Damping hole flow of flow equation is

$$q = A_p v_p = A_p \frac{dy_p}{dt} \quad (14)$$

Where  $v_p$  is speed of cylinder.

The average flow velocity of damping hole is

$$v_d = \frac{4q}{\pi d_0^2} = \frac{4A_p}{\pi d_0^2} \frac{dy_p}{dt} \quad (15)$$

Flow makes pressure difference of hydraulic cylinder two cavity. According to the laminar flow pressure loss formula, the equation of pressure difference of hydraulic cylinder two cavity is :

$$p_{11} = \lambda \frac{l}{d_0} \frac{\rho v_d^2}{2} \quad (16)$$

Where  $\lambda$  is resistant coefficient of pipe,  $\lambda = \frac{75}{R_e}$ ,  $R_e$  is

reynolds number,  $R_e = \frac{v_d d_0}{\nu}$ ,  $\nu$  is kinematic viscosity;  $d_0$  is diameter of interchangeable damping hole;  $l$  is the Piston long.

That is,

$$p_{11} = R_1 A_p \frac{dy_p}{dt} \quad (17)$$

Where  $R_1$  is flowing resistance,  $R_1 = \frac{150\mu l}{\pi d_0^4}$ ;  $\mu$  is absolute viscosity,  $\mu = \nu \rho$ .

The force of the damping hole effect is

$$F_1 = B_1 \frac{dy_p}{dt} \quad (18)$$

Where  $B_1 = R_1 A_p^2$  is damping coefficient.

Oil can also produce damping effect through the gap between cylinder wall and piston. Assume that piston without damping hole, just consider this gap, According to the gap flow formula, the equation of pressure difference of hydraulic cylinder two cavity is:

$$p_{12} = R_2 A_p \frac{dy_p}{dt} \quad (19)$$

Where  $R_2$  is flowing resistance,  $R_2 = \frac{12\mu l}{(1+1.5\varepsilon^2)\pi D_0 h^3}$ ;  $\varepsilon$  is

relative rate of partial core,  $\varepsilon = e/h$ ,  $e$  is eccentricity;  $h$  is gap width between cylinder wall and piston;  $D_0$  is diameter of piston.

The damping force of the gap effect is

$$F_2 = B_2 \frac{dy_p}{dt} \quad (20)$$

Where  $B_2 = R_2 A_p^2$  is damping coefficient.

As a matter of fact, both damping hole and gap influence can be equivalent into a parallel circuit, that is,

$$\begin{aligned} p_{11} &= p_{12} = p_l \\ R_1 q_1 &= R_2 q_2 \end{aligned} \quad (21)$$

Therefore,  $q = q_1 + q_2 = p_l \left( \frac{1}{R_1} + \frac{1}{R_2} \right)$ ,

so  $p_l = \frac{R_1 R_2}{R_1 + R_2} q$ .

Total damping force is

$$F = B \frac{dy_p}{dt} \quad (22)$$

Where  $B = \left( \frac{R_1 R_2}{R_1 + R_2} \right) A_p^2$  is total damping coefficient.

Assuming that the gap minimum, so  $R_2 \gg R_1$ ,

then  $\left( \frac{R_2}{R_1 + R_2} \right) \rightarrow 1$ , that is  $B \rightarrow B_1$ .

Therefore, Total damping force is

$$F \approx B_1 \frac{dy}{dt} \quad (23)$$

Shifting yoke installs the oscillation cylinder with rigid connection, the force of shifting yoke is equivalent to centralize into hydraulic cylinder. The force balance equation for the cylinder barrel is

$$A_p(p_1 - p_2) = m_i \frac{d^2 y_p}{dt^2} + B \frac{dy_p}{dt} + K_l y_p + F_l \quad (24)$$

Where  $m_i$  is equivalent mass;  $B$  is equivalent viscous damping coefficient;  $K_l$  is equivalent stiffness of spring;  $F_l$  is arbitrary load force on cylinder.

### 5 Analysis of vibration waveform

Solving mathematical models in the Simulink can obtained output curves of vibration waveform. The amplitude and acceleration of the excitation cylinder is considered as the main target.

The original position of the cylinder barrel is assumed as the origin of coordinates and forward direction is to the right. It is seen in Figure 8 that the period and displacement of the excitation cylinder, when the rotary frequency of spool is set to 5Hz (excitation frequency is 20Hz), are 2 times the size of that when the rotary frequency of spool is set to 10Hz (excitation frequency is 40Hz). Likewise, the period and displacement of the excitation cylinder, when the excitation frequency is 80Hz, are 1/2 times the size of that when the excitation frequency is 40Hz. The bigger the excitation frequency, the smaller the displacement of the excitation cylinder and the period of motion of  $y_p$ . When the valve orifice becomes wide, the right chamber of cylinder lets in

the oil and left chamber drains the oil. As a result, the cylinder barrel moves right and gets the positive displacement. When we change the valve communication direction by rotating valve spool, the cylinder barrel moves left to the original position and keeps the displacement positive. Reciprocating motion of cylinder barrel is achieved by valve spool rotation.

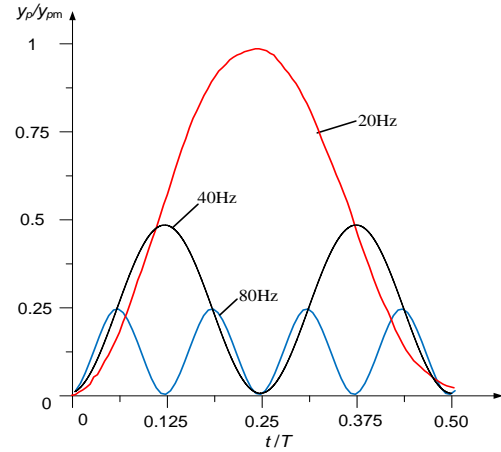


Figure 8 Curves of  $y_p - t$  with different frequency under no damping hole

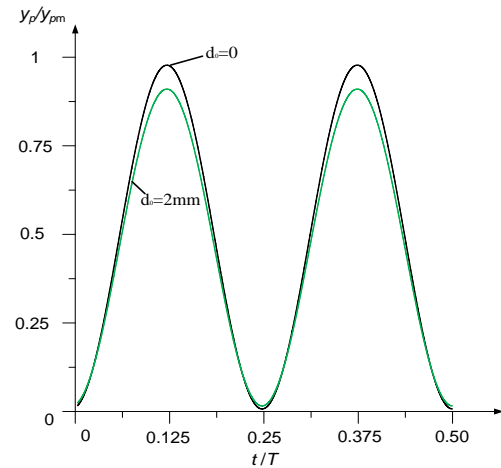


Figure 9 Curves of  $y_p - t$  with different  $d_0$

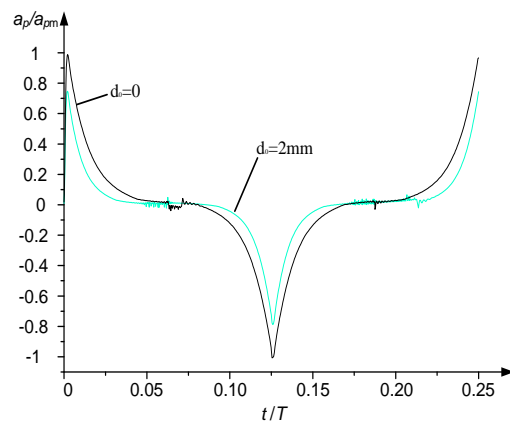
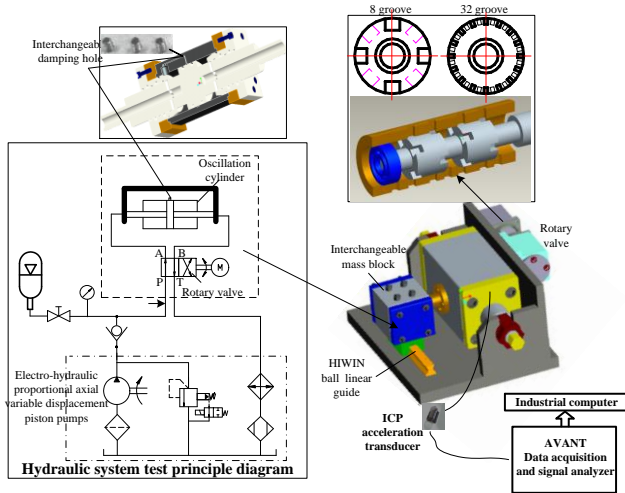


Figure 10 Curves of  $a_p - t$  with different  $d_0$

It is seen in Figure 9 and Figure 10, when  $f_1$  and  $d_0$  are given as 40 Hz, 2mm, the values of  $y_p$  and  $a_p$  is smaller than the one under no damping hole. Furthermore,  $y_p$  and  $a_p$  vary according to the value of  $d_0$ .

## 6 Experiments and discussion



(a) System configuration



(b) Experiment test

Figure 11 Experiment system of the electro-hydraulic vibrator

The experiment system configuration of electro-hydraulic vibrator controlled by spin valve for tamping device is shown in Figure 11. The rotary motion of the valve's spool is driven by stepper motor. Interchangeable mass block on HIWIN ball linear guide is the equivalent mass of lower tamping arm. An ICP acceleration transducer was mounted outside the cylinder barrel to measure the acceleration of the cylinder barrel. The acceleration signals are acquired by AVANT and then are sent to industrial computer. AVANT Data acquisition and signal analyser is an integrated solution for dynamic signal analysis of vibration. It is designed based on distributed processing structure, integrating the up-to-date technology of multi-DSPs computation, vibration control algorithms and data transmission. Its USB2.0 connectivity ensures easy PC connectivity and high-speed disk throughput. AVANT possess functions of integral, quadratic integral and differential and so on. According to the acquired acceleration by accelerometer, the corresponding values of velocity and displacement will be

easy to get. The main parameters of the vibrator structure and the hydraulic system are shown in Table 2.

Table 2 Main parameters of the vibration exciter

Item	Value
Maximum radial opening of the spin valve	6 mm
Maximum axial opening of the spin valve	6 mm
Spool Radius of the spin valve	15.5 mm
Number of grooves on a single spool	8
Diameter of the cylinder	100 mm
Diameter of the piston rod	70 mm
Volumer of the cylinder	$2.9 \times 10^{-4} \text{m}^3$
Interchangeable mass block	16~42kg
System maximum pressure	10 MPa
Maximum flow	100L/min
Natural frequency	267 HZ
Maximum hydrostatic force	40 KN

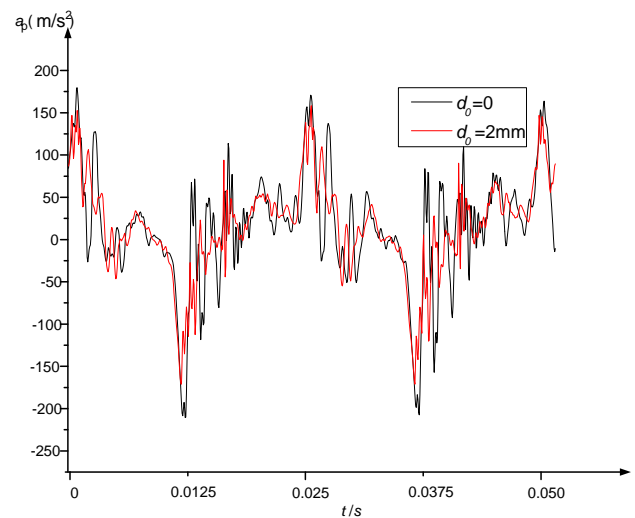


Figure 12 Curves of  $a_p$ -  $t$  with different  $d_0$

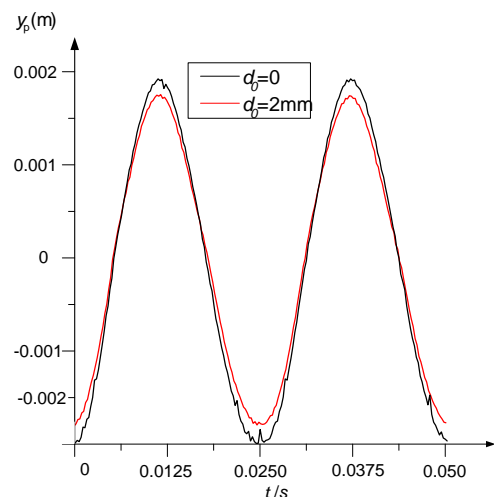


Figure 13 Curves of  $y_p$ -  $t$  with different  $d_0$

When  $n$ ,  $d_0$ ,  $x_v$  and  $y_v$  are set to 600rpm, 0, 6mm, 6mm respectively, the maximal displacement and acceleration of the actuator can reach 4mm and  $210 \text{m/s}^2$  as is shown in Figure 12 and 13. The proportion of the above part and under part of the arm for the new tamping machine is

1:2.1 in terms of design length. Finally, the displacement 8mm and the frequency 40Hz of the tamping end are gotten. When  $d_0$  are given as 2mm, the maximal value of  $y_p$  and  $a_p$  can get to 3.6mm,  $180\text{m/s}^2$  respectively. The maximal values under this condition is smaller than the one under no damping hole. The fluctuate value of  $a_p$  under this condition is also smaller than the one under no damping hole. The Curve of  $y_p$  under this condition is more smooth than the one under no damping hole. Furthermore,  $y_p$  and  $a_p$  vary according to the value of  $d_0$ . The result show that increasing hydraulic damping through the interchangeable damping hole can improve the vibration system performance.

## 7 Conclusion

1) A new tamping device with a hydraulic excitation and independent clamping movement is firstly proposed. It can overcome maintenance difficulty resulting from common shock mechanism and swing problem of the clamping hydraulic cylinder caused by tamping bar vibration. With the new working principle, A new spin valve is designed in order to fulfill dynamic state requirements of the oscillation cylinder.

2) The maximum displacement of the excitation cylinder is 4mm when the rotary spool frequency, the axial area gradient of valve port and the maximum radial guided width of the spool groove are set to 10Hz, 6mm and 6mm respectively. Finally, the vibration of the tamping bar, with the displacement being 8mm and excitation frequency 40Hz, can be achieved. It meets the design requirement.  $y_p$  and  $a_p$  vary according to the value of  $d_0$ . The experimental result show that increasing hydraulic damping through the interchangeable damping hole can improve the vibration system performance.

3) Under the different rotary spool frequency, the size and the changing period of the displacement of the excitation cylinder are different. The bigger the excitation frequency, the smaller the displacement of the excitation cylinder and the changing period of the displacement. As vibration with high frequency and low amplitude is fit for hardened ballast and vibration with low frequency and high amplitude is fit for loose ballast, through setting suitable related parameters in the electrohydraulic exciter, the new tamping device can satisfy all kinds of complex working environment.

4) Ballast characteristics are quite complicated and can not always be seen as invariable. Further research on this project will be conducted by taking into account of uncertain geological conditions and nonlinearities of ballast dynamics and electro-hydraulic system encountered in the tamping process.

## 8 References

[1] Cheng Wenming, "A Retrospect of the Development of Mechanical Equipments for Railway Maintenance in China," Modern Management, 2006(10). (in Chinese)

- [2] Kou C Q, Zhou H L. Machinery on Railway Construction. Beijing: Machinery Industry Press, 2001. (in Chinese)
- [3] Ying Lijun, Zhou Shuwu, Qi Lin, "Development of the Electric Recovery System of the 08-32 Tamper," Journal of the China Railway Society, 26(6). (in Chinese)
- [4] Min Chaoqing, Gong Guofang, Liu Yi, "Design and Simulation Research on New Tamper Based on ADAMS," 2010 International Conference on Digital Manufacturing & Automation(ICDMA 2010), IEEE Press, Dec, 2010, pp. 494-498.
- [5] E Mark Rand, "Effect of Vibration on Ballast," Magazine of British Geography, 1981(09).
- [6] HARSCO TECHNOLOGIES CORP (US) . Split tool tamper[P].EP1172480 , 2002.01.16 .
- [7] HARSCO TECHNOLOGIES CORP (US) . Single shaft tamper with reciprocating rotational output[P].US6386114, 2002.05.14 .
- [8] HARSCO CORP (US) . Split tool tamper[P].DE60125871D , 2007.02.22.
- [9] MATISA MATERIEL IND SA(CH).Railway track ballast tamping device[P]. DE3165697D, 1984.09.27.
- [10]MATISA MATERIEL IND SA (CH) . Railway track tamping device[P]. EP0050889, 1982.05.05.
- [11]MATISA MATERIEL IND SA . Railway ballast tamping machine[P]. EP0424322A1, 1991.04.24 .
- [12]PLASSER BAHNBAUMASCH FRANZ (AT) .Tamping machine for tamping ballast under the sleepers of a railway track[P]. EP1070787, 2001.01.24.
- [13]FRANZ PLASSER BR BAHNBAUMASCHI (AT). Railway track tamping device and method[P]. EP1162309, 2001.12.12.
- [14]FRANZ PLASSERBAHNBAU MASCHINEN (AT) .Ballast Tamping Machine and Method for Tamping a Railway Track[P] . EP1403433 , 2004.03.31.
- [15]Sandsted C A, Moore M J, Delucia A P, et al. Split tool mechanical vibrator:US, 5584248[P]. 1996-12-17
- [16]John M, Peter Y, Single shaft tamper with reciprocating rotational output: US, 6386114[P].2002-05-14
- [17]Merritt H E. Hydraulic Control Systems[M]. New York: John Wiley & Sons, 1967.

## **A Case Study on Quantifying the Workload of Working Machine Operators by Means of Psychophysiological Measurements**

R. Filla<sup>1</sup>, E. M. G. Olsson<sup>2</sup>, B. H. C. von Schéele<sup>3</sup>, and K. Ohlsson<sup>4</sup>

<sup>1</sup>Emerging Technologies, Volvo Construction Equipment, Eskilstuna, Sweden  
E-mail: reno.filla@volvo.com

<sup>2</sup>Department of Public Health and Caring Sciences, Uppsala University, Uppsala, Sweden  
E-mail: erik.olsson@pubcare.uu.se

<sup>3</sup>Stress Medicine AB, Bergvik, Sweden  
E-mail: bo.vonscheele@stressmedicin.se

<sup>4</sup>Department of Management and Engineering, Linköping University, Linköping, Sweden  
E-mail: kjell.ohlsson@liu.se

### **Abstract**

In this study of eighteen wheel loader operators, test-driving a machine in three different traction force settings, we examine if a workload index derived from psychophysiological measurements of heart rate, finger temperature, skin conductance, respiration rate and end-tidal CO<sub>2</sub>-concentration in exhaled air can be easily used to assess operator workload in sufficient detail to use it as a complement to traditional subjective evaluations in machine testing, either of real machines or in a human-in-the-loop simulator. In a longer perspective, such measurements are expected to play a role in a workload-adaptive operator assistance system.

However, the findings do not give support for this vision. Instead they indicate that other types of measurements than what have been used in our study should be employed if ease of use for practitioners such as test engineers is in focus, but also that other factors than just machine operability must be considered to have a great influence on the operator workload.

**Keywords:** operator, working machines, wheel loaders, operator workload, stress, operability, human-machine interaction

### **1 Introduction**

Working machines in construction, mining, agriculture, and forestry are not only becoming ever more sophisticated in terms of digital control, but are also complex in architecture. Many of these machines consist of at least two working systems that are used simultaneously and the human operators are essential to the performance of the machines in their working place.

With their productivity and energy efficiency being linked to the operators' workload, it is essential to make working machines easier to use. The immediate goal of our research is to support product development by complementing the traditional subjective evaluation of a prototype machine's operability (involving asking the operator to rate the machine according to a specific scale) with a less subjective measure based on the operator's workload. In order to be usable in product development projects, such a measure needs to be easy to derive for a test engineer who is not a

trained researcher in the field of psychophysiology. Ideally, this measure would be calculated automatically and online in order to be available during or immediately after testing.

This article will report on the setup and results of a larger study conducted to investigate if common psychophysiological measurements of finger temperature, heart rate, respiratory rate, CO<sub>2</sub> concentration in exhaled air, and galvanic skin response can be used to quantify the workload of wheel loader operators during operation of the machine.

In a longer perspective, such measurements might be employed for giving workload-adaptive assistance to the machine operator.

### **2 Wheel loader application and challenges**

In our on-going research, a wheel loader was chosen as the object of study, although working machines of similar complexity and with similar challenges can be found in construction, agriculture, forestry and mining.

The short loading cycle shown in Figure 1 is highly representative of the majority of a wheel loader's application. Typical of this cycle is bucket loading of granular material (for instance gravel) on an adjacent dump truck (or other load receiver, mobile or stationary) within a time frame of 25-35 seconds, depending on working place setup and how aggressively the operator uses the machine, but also depending on the operator skill. A detailed description with identification of wheel loader working cycles, together with the challenges they present for machine design and operability, can be found in [1].

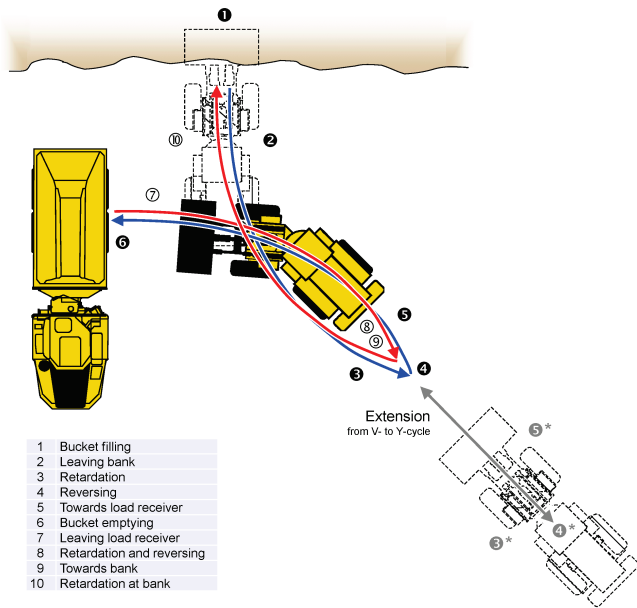


Figure 1: Short loading cycle.

In Figure 1 the short loading cycle has been divided into ten phases, beginning with bucket filling. Visualising test results obtained in earlier studies, Figure 2 shows that the fuel consumption rate (expressed in volume or mass per time unit) is approximately 60% higher during bucket filling than the cycle average. Expressed in absolute values, bucket filling accounts for 35-40% of the mean total fuel consumption per cycle, yet the time spent on filling the bucket is only 25% of the average cycle time.

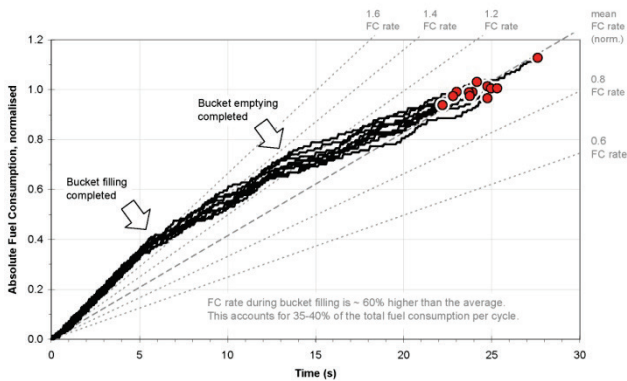


Figure 2: Fuel consumption during short loading cycle.

After bucket filling, the operator drives backwards towards the reversing point and steers the wheel loader to accomplish the characteristic V-pattern of a short loading cycle. The lifting function is engaged the whole time. The operator chooses the reversing point such that having arrived at the load receiver and starting to empty the bucket (phase 6 in Figure 1), the lifting height will be sufficient to do so without delay. Figure 2 shows that the fuel consumption rate for phases 2 to 6 is approximately constant and close to the average fuel consumption rate of the complete short loading cycle.

In the remaining phases, the bucket needs to be lowered and the operator steers the wheel loader back to the initial position in order to fill the bucket again in the next cycle. Phases 7-10 are less energy-demanding and the fuel consumption rate is therefore lower than the average for the complete short loading cycle.

The higher fuel consumption rate during bucket filling (as shown in Figure 2) warrants a closer look at this phase. The inner loop in Figure 3 shows how the human operator interacts with the wheel loader. In order to fill the bucket, the operator needs to control three motions simultaneously: a forward motion that also exerts a force (traction), an upward motion (lift) and a rotating motion of the bucket to load as much material as possible (tilt). This is similar to how a simple manual shovel is used. However, in contrast to a manual shovel, the operator of a wheel loader can only observe, and cannot directly control these three motions. Instead, he or she has to use different subsystems of the machine to accomplish the task. The gas pedal controls engine speed, while the lift and tilt levers control valves in the hydraulics system that ultimately control movement of the linkage's lift and tilt cylinder, respectively.

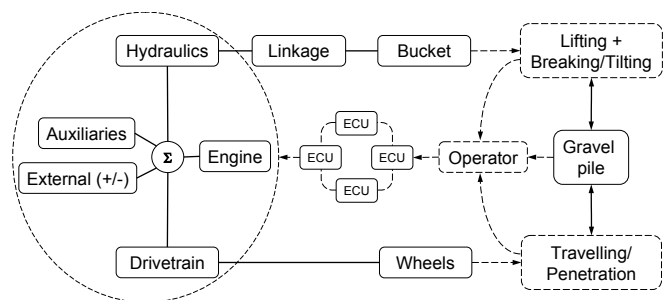


Figure 3: Simplified power transfer and control scheme of a wheel loader.

The difficulty lies in that no operator control directly affects only one single motion. The gas pedal controls engine speed, which affects both the machine's longitudinal motion and via the hydraulic pumps also affects the speeds of the lift and tilt cylinders. The linkage between the hydraulic cylinders and the bucket acts as a non-linear planar transmission and due to its design a lift movement will also change the bucket's tilt angle and a tilt movement affects the bucket edge's height above the ground.

Furthermore, Figure 3 also shows how in the outer loop the primary power from the diesel engine is split up between

hydraulics and drive train in order to create lift/tilt movements of the bucket and traction of the wheels, but is connected again when filling the bucket from for example a gravel pile. Figure 4 shows that in this situation, the traction force from the drive train, acting between wheels and ground, creates a reaction force between gravel pile and bucket edge, which in turn creates a moment of forces around the loading arm's centre of rotation that counteracts the moment of forces created by the push of the lift cylinder.

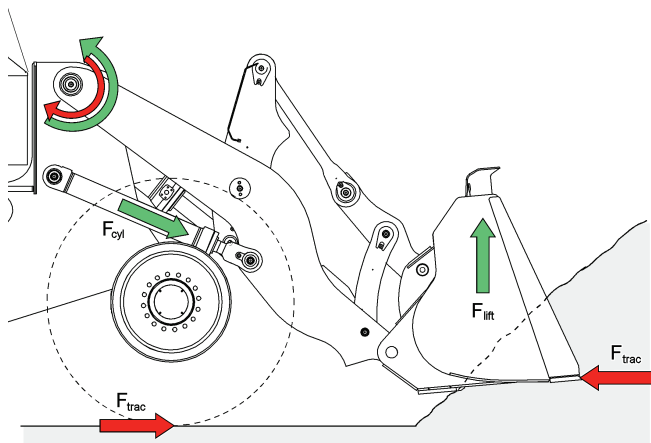


Figure 4: Force balance during bucket filling.

In effect, the traction force, indirectly controlled by the operator through the engine speed, reduces the available lifting force. Depending on lifting height and applied traction force, the lifting force can be completely cancelled out, and the bucket cannot be moved upwards any further. The operator then has to either apply the tilt function or reduce the traction force by reducing the engine speed – which is rather counter-intuitive as a common mental model of vehicle drivers is that an increase in gas pedal deflection leads to more torque from the engine until any external resistance can be overcome.

In our study, the different machine setups (as described in section 4.1) are using this phenomenon to create machines with three different levels of maximum engine speed during bucket filling, translating to different levels of perceived ease of use, depending on the operators' individual skills.

Another general challenge for wheel loader operators exists in that the hydraulic levers control the speed of the hydraulic cylinders, not the force exerted by them. In an old-fashioned less energy-efficient hydraulic system of the Open Centre type a higher external load would result in a lower cylinder speed for the same amount of lever actuation. This would give the operator an indication of the external load acting on the cylinder. This is no longer the case in a modern load-sensing hydraulic system.

In summary, there are many interdependencies and it thus takes a certain amount of training to be able to use a wheel loader efficiently and with high productivity. It is therefore of great interest to investigate machine operability closer and to develop operator-assisting functions.

### 3 Quantifying human workload with psychophysiological measurements

Operating a wheel loader involves both physical and mental workload. Even though the operator sits still and the controls do not demand a large amount of physical strength he/she has to keep balance and be prepared. Mentally the operator has to maintain attention and respond appropriately all the time. Measuring this workload therefore calls for a measure that handles several physiological signals.

As mentioned in the introduction, the short-term goal is to enable test engineers to derive a less subjective measure of how easy a machine is to operate. With the personnel involved in machine testing usually not being trained in performing and analysing measurements of psychophysiological parameters, the scope needs to be limited to signals that are easy to measure and handle.

There are many aspects of how our physiological systems interact with physical and mental workload. Heart rate (HR) and respiration rate (RR) are classical measures of physical workload where a higher HR and RR result in a better supply of oxygen to the working body. Both HR and RR also interact with mental workload.

Other physiological measures involved mainly in mental workload are skin conductance level (SCL) derived from palm sweat gland release and peripheral temperature (typically measured in fingers), derived from smooth muscles constricting the peripheral blood vessels. A higher workload is associated with higher SCL and lower finger temperature. However, the magnitude of changes is dependent on individual vasoconstriction and sweat gland activities.

All physiological parameters are highly influenced by autonomic nervous system (ANS) activity and mainly by the sympathetic branch but heart rate variability (HRV) and respiratory sinus arrhythmia (the portion of HRV that is related to breathing) are associated with both sympathetic and parasympathetic nervous system activity.

Respiration is regulated in a more complex way which includes cognitive, chemical, and metabolic systems as well as the ANS. When subjected to mental or physical challenges, ventilation increases, which in turn results in a drop in plasma  $pCO_2$ . The  $pCO_2$  level can therefore be used to assess whether breathing is in excess of metabolic demands resulting in a low  $pCO_2$ , which is the definition of hyperventilation [2]. A change in  $pCO_2$  level is the result of changes in RR and/or tidal volume. Some researchers have pointed out that  $CO_2$  level can be an advantageous measure of psychosocial stress, since it can differentiate between metabolic and psychosocial demands, which in most other measures generate the same response [3]. The  $pCO_2$ -level is often, as in our study, measured as end-tidal  $CO_2$  ( $EtCO_2$ ) which is satisfactorily correlated to  $pCO_2$  and permits assessment of breath by breath variation. The physiological systems mentioned interact with each other in a complex way, cooperating with and compensating for each other [4]. In case of immense stressful events people tend to stop

breathing, with a direct impact on several regulatory systems as a consequence.

## 4 Method

### 4.1 Machine setup

The wheel loader used was a Volvo L70F equipped with a general purpose bucket with a load capacity of 2.3m<sup>3</sup>. The total operating weight of the machine is approximately 13.4t.

In order to study the effect of the previously mentioned interdependencies during bucket filling, the wheel loader software used in this study was modified to limit engine speed, and thus traction force, whenever the transmission's 1<sup>st</sup> gear was automatically engaged, which occurs only during bucket filling (all machines normally start in 2<sup>nd</sup> gear).

The first limitation of engine speed was chosen so that maximum traction force was reduced to 62% in 1<sup>st</sup> gear, which resulted in a maximum engine speed that was comparable to what expert operators on average used the wheel loader at. This setting also prevented wheel spin. There was a slight impact on the speed of the hydraulic functions (due to the rotational speeds of the engine, torque converter and hydraulic pump being connected, see Figure 3 and the explanation in an earlier section).

In the other condition, engine speed was limited such that maximum traction force was reduced to 47% in 1<sup>st</sup> gear. We deliberately used an engine speed limit below what was needed for the working task planned, which also affected the speed of the hydraulic functions more noticeably. Furthermore, the maximum obtainable traction force in 1<sup>st</sup> gear was even lower than what was available in 2<sup>nd</sup> gear, all of which an operator would experience as clearly negative.

In both conditions the counteracting effect of the traction force is clearly less pronounced so that even at maximum use of the traction force available the lifting force is never cancelled out completely. This should be experienced positively, especially by less experienced operators (but the question is whether this positive aspect outweighs the artificial limitation of maximum available traction force).

The test machine's automatic functions were set to gear-dependent BSS (Boom Suspension System is deactivated when in 1<sup>st</sup> gear), Automatic Power Shift (automatic gear shifting of the transmission) and Auto Kick-down enabled (automatically changing base gear from 2<sup>nd</sup> to 1<sup>st</sup> when needed). We also disabled the function for automatic bucket tilt-in stop at level position.

A more detailed description of the technical setup of our study can be found in [5].

The radio and most of the external displays were turned off in order to not distract the operator from the working task. However, the display for the load weighing system had to stay turned-on and since there were other people and machines present at the proving ground, we also decided to turn on the rear camera monitor for increased safety.

### 4.2 Apparatus and sensor placements

Our study also included another part, reported in [5] and therefore not further presented here, in which the hypothesis was tested that the operator's use of the controls available (gas pedal, lift lever and tilt lever) is indicative of a working machine's operability and that a measure for comparative operability can thus be derived based on the operator's control commands. That study required essentially the same type of data and equipment (and operators) as the one presented in this article, which led to the decision to run both studies concurrently.

During all sessions various data were recorded off the wheel loader's CAN bus, onto which data from externally mounted sensors were also merged (thus providing signals of interest that were not readily available in a standard machine). Vector Informatik's CANcaseXL equipment and CANalyzer software were used for the recording of all traffic on the machine's CAN bus to a laptop placed inside the cab. The need for particular signals required in some cases modification of the software for engine and transmission control, while in other cases an external ECU (Parker IQAN MDL) was used to place calculated signals on the CAN bus. The latter was also used to acquire additional data from externally mounted sensors for lift and tilt cylinder stroke and lever position for lift and tilt. A modified LoadTronic load weighing system from AADI was used to measure the net weight of the bucket. The data were transmitted to the machine controller via SAE J1587 protocol and then merged into the data stream on the CAN bus.

The psychophysiological measurements were conducted using the cStress software from PBM Stressmedicine Systems, running on a second laptop installed in the cab of the wheel loader. Finger temperature, heart rate (via Electrocardiogram, ECG) and skin conductance were acquired using a C2 physiological monitoring system from J&J Engineering and a LifeSense AirPas oxycapnograph handled data acquisition and pre-analysis of the operator's respiration (Figure 5).

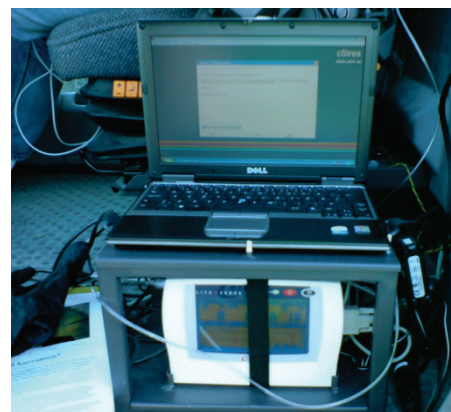


Figure 5: Apparatus for measuring and recording of the psychophysiological data.

The ECG sensors were placed on both wrists (see Figure 6 and Figure 7) using isotonic gel. We knew from earlier

measurements that these sensors need to be secured against relative movement in order to avoid misreadings. Since the operator in a wheel loader cab is exposed to vibrations and accelerations of various frequencies and magnitudes, potentially rendering ECG measurements impossible to perform in this environment, we were pleased to find that good data could be acquired when using the suspended chair's integrated arm rests to support the operator's lower arms and asking the operator to control the machine's articulation angle (for steering) and forward/reverse gear not through the steering wheel and main gear shift lever but by using the controls on the left side of the chair instead (see Figure 7).

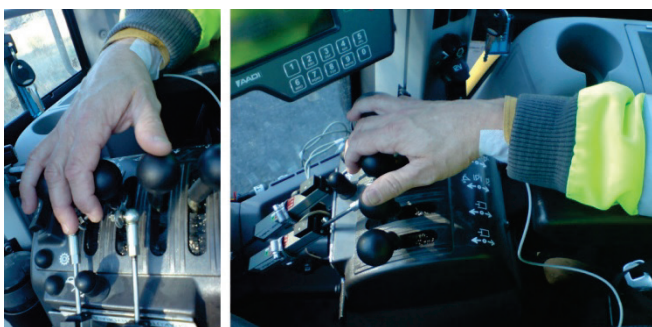


Figure 6: Right hand controls and sensor placement on right wrist.



Figure 7: Left hand controls and sensor placement on left wrist and fingers.

Figure 7 also shows the placement of the other sensors. The operator's finger temperature was acquired by a thermistor taped to the top of the left little finger (the tape did not restrict the blood flow). The sensors for measuring galvanic skin response were attached to the inner phalanges of the ring and middle fingers of the left hand, again using isotonic gel. The operator's respiration was sampled by a nasal sample line, inserted some millimetres into the left nostril; in connection with this the operator was asked to exclusively breathe through the nose.

All tests were also recorded on video using an externally placed digital video camera and later synchronised with all other acquired data. Synchronising video to CAN data was possible by using stationary points in the recorded data for

bucket height and wheel speed. Synchronisation of machine data (recorded in CANalyzer) and psychophysiological data (recorded in cStress) proved a little more challenging. In the end we chose an offline semi-manual approach: at the beginning and end of each test recording we would press two buttons simultaneously, where activation of the first button was logged on the CAN bus and the other logged as an event in cStress. These synchronisation markers were later used to automatically merge both data streams.

A simple kitchen timer counted backwards and sounded an alarm when the required operating time was reached. Both the timer and all measuring equipment were placed so that the operator was unable to look at the displays.

### 4.3 Working cycle

With the intriguing facts visualised in Figure 2 (fuel consumption in a loading cycle), Figure 3 (hydraulics and drivetrain as parallel power systems), and Figure 4 (interaction of traction force and hydraulics) in mind, we specifically wanted to study the wheel loader operator during the bucket filling phase. We therefore chose to modify the short loading cycle such that the operator was instructed to still go through most of the motions, but not to use steering (as mentioned previously) and thus empty the bucket at the same spot where it was filled. Since the material used was sorted gravel which does not stick together like for example clay, and is thus fairly easy to handle, this procedure did not introduce any skewing of the test results as far as the bucket filling phase is concerned.

Not using steering also solved another problem that would have had an impact on the results: inexperienced operators are unused to using the joystick rather than the steering wheel, and forcing them to do so would have introduced additional workload, thus potentially skewing the test results. The decision not to use the steering function at all solved this dilemma.

### 4.4 Psychophysiological Stress Profile

Every human being has an individual response to workload, which means that some sort of reference or calibration is needed in order to be able to correctly evaluate the results of psychophysiological measurements. While not common procedure in the research community, establishing a PSP (Psychophysiological Stress Profile) has proven to be valuable in our (Olsson and von Schéele) clinical work with patients with stress-related dysfunctions.

The PSP shown in Table 1 is essentially taken from [6] and has been implemented in the cStress software. It contains 15 minutes of data recording, guiding the patient (or in our case the wheel loader operator) through six steps.

In step 1 we provided the operator with a neutral text to read, informing him that this was not an exam and while we asked him to read carefully and try to understand the text, he was not required to read all of it or even remember anything. This put some workload on the operator, but far from enough to induce stress. (In our case the text handed out was a newspaper article about the Nobel Prize for Literature and



To the right, Figure 9 shows the division of the scale into four skill groups and how the individual operators are placed in these groups, using their self-reported skill ranks. These turned out to be similar to the author’s preliminary judgement, resulting in nine operators in skill group 1 (inexperienced), six in skill group 2 (experienced) and three in skill group 3 (expert). This also gives the possibility to combine groups 2 and 3 at a later stage into an aggregated “experienced and above” group that matches the “inexperienced” group in size, which would benefit the statistical strength of direct comparisons.

In our pre-selection of potential test operators for this study we chose not to focus on expert operators alone, but to include operators of all skill groups in order to test whether there is any difference in how operators in these groups handle and evaluate the different machine variants. However, we deliberately avoided newcomers in order to guarantee at least a theoretical knowledge of how to operate a wheel loader, and in order to exclude learning effects as much as possible. The ten minutes of self-training before each live testing session would not have sufficed for newcomers, but were deemed sufficient for operators in skill group 1 and above.

#### 4.6 Design of the study and procedure

Each operator was given an exclusive 2.5 hours session after lunch, starting with the Psychophysiological Stress Profile (PSP) described earlier. For this, we took the operator of the day to a secluded place. The PSP was conducted with the operator sitting in working position in the cab of the wheel loader and the person administering the test standing on the ladder, instructing through the open door, and monitoring through the closed door when recording was in progress.

After the PSP, the operator took the machine to the proving ground, where a smaller area was reserved for this study. The testing of all three machine variants was then performed, with the traction force setting as the independent variable. The study design is in essence a three-condition within-subjects setup, with the two limited settings of 47% and 62% tested against the unmodified software version with 100% maximum traction force, in random order, unknown to the operator. The operators were not told what had been modified and how, but most of them, especially the more experienced ones, were able to deduce this fairly quickly.

In order to minimise the skewing influence of learning effects, before testing a machine version each operator was given ten minutes’ self-training just to familiarise himself with the specific characteristics of the current machine version. After the training followed five minutes’ live test-driving, where the operator was asked to make sure to fill the bucket completely and use the machine at a normal production tempo, resulting in a cycle duration of approx. 25 seconds (both of which most of the inexperienced operators did not manage to achieve completely, but at least this demand created a certain pressure). The session ended with a subjective evaluation where, among other things, the operator was asked to judge the tested machine version’s

ease of bucket filling and perceived power on a visual analogue scale (without printed values). The operator was also asked to rank his overall impression of the machine in comparison to all previously tested variants on a nominal scale (“better”, “worse” or “same”). See Figure 10 for the questionnaire used after testing of the third machine variant.

Since the study was performed during the autumn, comparable conditions for the operators were ensured by performing tests only on days with good weather (no rain) and at the time of the highest ambient temperature, at 13:00 local time. The latter also guaranteed that the operators were rested and had eaten recently.

**Evaluation of machine variant #3**

**How do you rank the machine in this setup, especially during bucket filling? (Put an X somewhere on the line.)**

Very hard to fill the bucket                      OK, about normal                      Very easy to fill the bucket

The machine feels powerless, slow                      OK, about normal                      The machine feels powerful, quick

Does the machine feel better or worse than the first one – or the same? (Circle the answer)

Does the machine feel better or worse than the second one – or the same? (Circle the answer)

**How do you evaluate your own performance, did you cope? (Put an X somewhere on the line.)**

It did not go well at all                      OK, as required                      It went very well

I felt very stressed                      OK, no major problems                      I felt no stress at all

Do your hands feel warmer or colder than before – or the same? (Circle the answer)

Estimate your finger temperature: \_\_\_\_\_ °C

Figure 10: Questionnaire, to be filled in after testing of each machine variant.

## 5 Analysis

### 5.1 General setup

The measurements conducted during this study resulted in several gigabytes of data, making at least semi-automated analysis necessary.

The main parts of the calculations were executed in MathCad worksheets that merged data originating from machine and operator by using synchronisation markers

embedded in both data streams. A function then automatically tagged each bucket filling phase within each loading cycle and exported part of the data stream back to cStress for expert review (see next section). This result of this review was a consensus figure for each operator's absolute workload level in each condition. These data and the results from the various questionnaires each operator had to fill in were then imported into MathCad and merged with all other recorded data for further analysis.

### 5.2 Expert review of psychophysiological data

As mentioned in the introduction, our immediate goal is to support product development, in which the operability of prototype machines is traditionally evaluated subjectively by asking the operator to compare the tested machine with a base line and rate it according to a specific scale. Thus, a measure of operator workload is required, ideally calculated automatically either during or immediately after testing.

However, we are aware of the magnitude of this. There exists a relationship between finger temperature and mental workload in that increased workload leads to decreased finger temperature and vice versa [7]. Such relationships can also be found other signals, e.g. heart rate, heart rate variability, respiratory rate etc [8][9][10][11]. However, these data have to be evaluated in context and in relation to the PSP and each other, which today requires expert knowledge. Furthermore, a reliable algorithm to automatically remove measurement artefacts in data for ECG and respiration has yet to be developed.

It is precisely this problem of analysing the output of interacting and compensating systems in context that drives the development of Artificially Intelligence systems for such tasks. The on-going research reported in [12] is promising, but the results cannot yet easily be implemented into a system as described above. Instead, we simulated the output of such an automatic system: three of us (Olsson, von Schéele, and Ohlsson) used their expertise in this field to manually review and analyse the measurement data and derive an absolute workload index for each operator in each of the conditions (PSP and three machine variants), without knowledge of the operator's skill level, his subjective evaluation, and which machine variant (setting of traction force limitation) corresponded to which condition for this particular operator. After each of us analysed the data individually, we compared our results and agreed on a consensus workload index for each operator in each condition.

Our manual analysis uses all of the recorded data (not just from the bucket filling sequences) with the following criteria applied. The ratings ranged between 1 and 5 in every time period. The highest ratings (5) should be applied if all the criteria listed below showed a very functional pattern well within known reference values for each physiological signal. The lowest rating (1) should be applied when the workload seem very high in all signals. If a physiological signal contained many measurement errors, this signal was not used in the rating of that period.

The physiological signals were rated as described below and in the priority order listed:

1. Level of HR, RR, EtCO<sub>2</sub> and peripheral temperature. A HR below 80, RR below 20, EtCO<sub>2</sub> above 4.5% and peripheral temperature above 25°C indicates low workload.
2. Noticeable recovery mainly in HR, RR and SCL between bucket fillings and during relaxation in the PSP indicates a more effort-economic behaviour and therefore low workload.
3. A clear connection between breathing and heart rate variations, RSA (Respiratory Sinus Arrhythmia), indicates low workload.
4. Extreme reactivity or extreme rigidity in mainly HR and SCL indicates high workload

Signs of habituation in any system, with priority to HR by bucket fillings, indicate a more effort-economic behaviour and therefore low workload.

## 6 Results

Table 2 shows the expert's consensus on the operators' workload during the PSP and the three test conditions. To the right this table, sorted by operator skill level, also shows in which individual order the machine variants with their respective traction force setting were tested by the operators.

Table 2: Results, workload index and test order of variants

Skill group	Skill level	Operator #	Workload index (expert consensus) *				Test order of variants **		
			PSP	Cond. 1	Cond. 2	Cond. 3	"100%"	"62%"	"47%"
1	30.8	18	3.8	3.5	3.6	3.7	1	3	2
	32.8	12	4.3	4.0	4.1	4.0	2	1	3
	37.8	8	4.6	3.2	3.4	3.0	1	3	2
	39.3	26	3.4	2.9	2.9	3.3	2	1	3
	39.8	4	4.0	4.0	4.0	4.0	3	1	2
	42.8	5	3.5	2.8	2.5	2.8	3	1	2
	48.8	11	4.5	3.5	3.7	3.7	2	3	1
	49.8	13	3.5	3.4	3.2	3.1	2	3	1
	49.8	29	3.9	3.4	3.4	3.5	2	3	1
2	61.7	14	3.8	3.8	3.6	3.5	1	2	3
	64.2	27	4.0	3.9	3.9	4.0	1	3	2
	66.2	6	4.1	3.0	3.0	2.8	3	2	1
	66.2	20	3.8	3.7	3.5	3.5	2	1	3
	69.7	2	4.0	3.6	3.8	3.9	3	2	1
	70.6	21	4.0	3.8	3.8	3.8	1	2	3
3	87.6	22	3.9	3.8	3.8	3.8	3	2	1
	88.1	25	3.7	3.9	3.9	3.9	3	1	2
	93.0	28	3.8	3.8	3.8	3.9	1	2	3

\* higher = higher workload

\*\* 1 = tested first, i.e. as condition #1

It is peculiar that the four operators with the highest skill levels consistently have a high workload for all machines, not affected by traction force limitation. This is presumably a ceiling effect. It is interesting to note that none of the operators were aware of their high workload. In their opinion, the work performed was little demanding, especially in comparison to other possible tasks such as loading of shot rock.

With the exception of one, all operators show a higher workload during the Psychophysiological Stress Profile than during the first machine test. Comparing the different conditions, it shows that the workload does not vary much within each subject, despite the operators clearly

commenting on experiencing the machine variants differently, as shown in Table 3.

Table 3: Results, questionnaire responses on personal satisfaction and stress-free operation

Skill group	Skill level	Operator #	Personal satisfaction *			Stress-free operation		
			Cond. 1	Cond. 2	Cond. 3	Cond. 1	Cond. 2	Cond. 3
1	30.8	18	39	54	51	50	46	54
	32.8	12	40	45	50	39	50	50
	37.8	8	26	26	36	28	26	37
	39.3	26	40	44	16	54	47	43
	39.8	4	66	46	52	61	55	84
	42.8	5	38	47	66	43	58	67
	48.8	11	50	44	50	59	58	30
	49.8	13	46	46	44	51	53	51
	49.8	29	50	51	72	37	28	49
2	61.7	14	59	50	50	62	38	35
	64.2	27	50	21	50	40	22	48
	66.2	6	42	50	63	50	31	59
	66.2	20	50	37	50	43	35	32
	69.7	2	50	50	32	50	50	50
	70.6	21	63	38	13	74	42	17
3	87.6	22	66	68	89	27	12	89
	88.1	25	49	50	89	50	15	50
	93.0	28	96	90	94	98	91	95

\*) 100% = high, 50% = normal      \*\*) 100% = stress-free, 50% = normal

No clear overall trend emerges when comparing the operators' answers in the questionnaire on how well they felt they had managed ("personal satisfaction") and how stress-free they felt during the operation with the experts' consensus on the operators' workload.

The operators' responses related to the tested machines, evaluated for their ease of bucket filling, overall impression of power and comparative rank are shown in Table 4. Here again, no clear trend is immediately obvious.

Table 4: Results, questionnaire responses on subjective machine evaluations

Operator #	Rank of variants *			Ease of bucket filling **			Machine power ***		
	Cond. 1	Cond. 2	Cond. 3	Cond. 1	Cond. 2	Cond. 3	Cond. 1	Cond. 2	Cond. 3
18	2	1	3	36	46	22	34	50	13
12	2	1	3	50	43	44	50	61	44
8	2	3	1	50	28	36	50	68	35
26	2	1	3	50	61	10	59	55	9
4	2	3	1	60	34	85	65	71	87
5	3	2	1	35	58	90	39	61	89
11	1	3	2	56	28	41	56	29	49
13	3	1	2	49	60	44	20	67	44
29	3	1	1	67	99	99	50	96	100
14	1	2	3	71	19	14	65	20	13
27	1	3	2	50	0	35	51	0	39
6	3	2	1	51	87	92	50	83	86
20	1	2	3	99	39	7	93	49	11
2	3	1	1	50	37	69	44	60	71
21	1	2	3	67	25	5	63	13	5
22	3	2	1	27	59	90	56	61	91
25	2	3	1	35	11	90	23	2	92
28	1	2	3	94	39	32	89	19	0

\*) 1 = best of all tested      \*\*) 100% = very easy, 50% = normal      \*\*\*) 100% = very powerful, 50% = normal

In conclusion, the workload index, derived from the psychophysiological measurements, mostly shows no obvious variation with any of the independent or other dependent variables. Naturally, the next step to take as a researcher interested in discovering any correlation would be to employ sophisticated statistical methods, such as principal component analysis or structural equation modelling.

However, the purpose of our study was not to show whether a correlation between self-assessed ease of bucket filling and measured workload index could be established at all, using such sophisticated statistical methods. Rather, the goal was to study whether such possible correlation was strong

enough for application-oriented test engineers without research background to employ simple statistical methods for converting measured workload indices back to degrees of machine operability, without having the operators performing any self-assessment. In other words, if the possible correlation is that weak and fragile, that in order for it to be discovered sophisticated statistics is required, then no engineer in the field will be able to make any use of it.

Despite this, we do not plan to abandon the data generated by the measurements performed during this study. Further statistical analysis is still planned, but its results will have to be reported in a later paper. As for now, the findings do not give support for our vision of using psychophysiological measurements as a complement to traditional subjective evaluations of a machine's operability and even less for using such measurements for workload-adaptive operator assistance; instead they indicate that also other factors have a great influence on the operator workload.

## 7 Discussion of possible sources of error

While performing the measurements, as well as during analysis and reporting, we significantly improved our knowledge with regard to appropriateness of equipment and procedures. This will be discussed in the following.

### 7.1 Procedure

We were able to secure a specific machine and a dedicated test area for our study, thus ensuring that all operators were operating under the same conditions.

During the testing phase we tried to keep the environmental conditions as similar as possible. We only tested on days with good weather (no rain) and at the time of the highest ambient temperature, i.e. immediately after lunch (which also ensured that the operators were rested). But since this study was performed in mid-autumn, temperatures were generally lower; during the testing around 5-10°C. The machine was parked outside overnight and had therefore cooled quite substantially by the morning. Together with 20-30 minutes' engine warm-up each day (about two hours before testing) and a 1.5km drive to the testing site, the first ten minutes of self-training should provide enough waste heat to warm up the machine (engine, transmission, axles, and hydraulics), so that testing conditions were similar for all cycles, independent of order.

At the proving ground we had a dedicated area, but were at times surrounded by other machines using the same facilities. This may have distracted the operator and generated higher workload.

During testing, the wheel loader's automatic functions were fixed at gear-dependent BSS (Boom Suspension System), automatic APS (Automatic Power Shift), and with Auto Kick-down enabled. Of course, the BSS is only deactivated when in 1st gear, which means it is activated during the first seconds of the bucket filling phase, until the transmission automatically shifts from 2<sup>nd</sup> to 1<sup>st</sup> gear. This is done via an adaptive algorithm, which might differ between operators.

Perhaps one of the pre-defined fixed APS settings L (low power), M (medium power) or H (high power) should have been used instead. Or perhaps the automatic kick-down function might have better been disabled altogether, in order to give the operator the freedom to choose when to shift gear.

The operators were asked to use the machine for three times 10 + 5 minutes, in total 45 minutes. There is a risk of fatigue, especially for the less experienced operators, but we can at best only find weak support for this in the workload index data.

Furthermore, in spite of the ten minutes of self-training before each live testing session, a learning effect might still be present, especially for the less experienced operators.

The significance of a Psychophysiological Stress Profile is to see the individual dynamic variation, as well as record the base line and review the subject's ability to relax. Before testing at the proving ground, we took the operator of the day to a secluded place to establish the PSP. While this location was isolated visually, it was not so audibly, since it was still within hearing distance of the proving ground, a nearby motorway and the R&D workshop's busy prototype parking area (with the backing alarm of a machine driving in reverse being a particularly disruptive sound). This may have influenced the PSP measurement data. A possible improvement may also be to establish a PSP in a non-work place environment for comparison.

## 7.2 Measuring equipment and data acquisition

The measuring equipment used to acquire the psychophysiological data was originally developed for clinical applications, i.e. use in a stationary, stable and clean environment. Using it, as we have done, in a mobile environment, exposed to large and frequent accelerations might have introduced measurement errors other than what is discussed below.

As explained earlier, the operators were instructed to lay their lower arms on the arm rests attached to the suspended chair. This dramatically lowered the amount of measurement artefacts in the ECG signal, yet some still occurred and had to be accounted for manually in the analysis phase.

Many measurement artefacts were found in the respiratory signal, which was acquired with a nasal sample line, inserted some millimetres into the left nostril and secured by a piece of tape. However, in a few cases the operator's facial hair prevented good adhesion, leading to a temporary detachment of the cannula and thus giving erroneous readings. For some operators we therefore used a nasal cannula that could be secured via the operator's ears. With only three such nasal cannulas available, we had to decide in which cases to employ this alternative method.

During both the PSP session and machine operation the operator was asked to exclusively breathe through the nose. However, we suspect that some of the artefacts in the respiratory data are due to the operator unintentionally breathing through the mouth (which itself is a sign of high

workload and stress, but hard to clearly identify in retrospect).

The PSP was conducted with the operator sitting in working position in the cab of the wheel loader and the person administering the test standing on the ladder, instructing him through the open door, and monitoring through the closed door when recording was in progress. With the colder ambient temperatures, yet still strong sunshine, this led to a cooling of the cab's interior while instructing the operator, yet gradual warm-up during execution of the PSP steps – both of which had an impact on at least the finger temperature measurements. In some cases operators complained about low temperature and wanted to turn on the heating and air conditioning system. But since this would have required a running engine, which might have distracted the operator from the required task, the decision was taken to only do so during the instruction phases before each PSP step.

Furthermore, we discovered that the finger temperature readings were affected by heat influx from the sun and by the flow of cold/warm air from the cabin's heating and air conditioning system, both during the PSP sessions and at the proving ground. Some operators even deliberately directed air flow to their hands to cool/warm them during operation of the machine. This discovery discredited the finger temperature readings enough for us to decide to completely disregard them when determining the workload index.

With regard to the above discussed we were still able to obtain satisfactory data from all subjects to estimate their psychophysiological functioning based on ocular analysis.

## 7.3 General considerations

There are several general considerations to make with regard to this study. To begin with, the workload index we derived is a compound measure that does not only reflect the necessary mental effort of the operator to handle different traction force settings of a wheel loader. With the lack of distinct results at hand, it is thus probable that other effects had a larger influence on the psychophysiological data we acquired.

Operators themselves commented on distracting elements, such as poor gear shifting quality of the automatic kick-down function, other machines nearby which required one to look out when driving in reverse, or looking straight into the sun when turning the head in order to check that nobody was standing behind the machine (even though we specifically instructed him to check the rear-view camera monitor). These are normal for a working place, but it might be that the impact of the different traction force settings was too small to be registered in measurements with durations of a mere five to six minutes. Next time we should consider aiming for 30 minutes or more.

Related to this the question arises of when to consider a workload to be different, e.g. whether or not a difference of 0.1 in value is to be considered significant, and how this relates to testing time.

In the future we need to consider measuring other data known to be indicative of workload. The quality of our measurements of finger temperature was too poor to use the data acquired. But as finger temperature is normally an important measure of activity in the sympathetic nervous system, SNS, we should try to vary the sensor placement for increased reliability and validity. Although heart rate and heart rate variability can change within seconds, reliable measurements are obtained for periods with a minimum of 30-40 seconds (i.e. four times longer than a typical bucket filling sequence), and a maximum of 5 minutes. It is warned that sensitivity decreases for shorter or longer periods [9].

Respiratory Sinus Arrhythmia, RSA [13] can be analysed dynamically and is the most sophisticated way to analyse activity in the autonomous nervous system, ANS. This is very complex and at the moment there are no automatic analysis methods available, but we included RSA in our manual estimation of the subjects' workload index, based on our understanding of the problem.

Finally, we need to reassess the working cycle. It could be that the workload index was impacted so little by even the severe traction force limitation in the "47%" machine because there were no immediate consequences of falling behind in pace or bucket load. In reality, for instance at a saw mill or an asphalt processing plant, trucks would be arriving continuously to be filled by the wheel loader. A decrease in productivity is clearly visible in a constantly lengthening line of trucks waiting their turn. Furthermore, when truck and wheel loader are properly matched it takes four buckets to fill a truck. Again, the productivity decrease is clearly visible if an operator needs a fifth run. In our study the operators would have to face none of these stress-increasing consequences. We need to consider either more closely representing the situation at real working places or introducing consequences by artificially adding some productivity-related feedback by visual or acoustic means.

There was also the ambivalence of our instructions to keep "a normal cycle time of 20-25 seconds" (again, without consequences for not doing so) and the conflicting requirements of both keeping pace and completely filling the bucket each time, especially for the "47%" machine variant with severely limited traction force which simply does not permit a bucket to be filled as fast and as much in comparison with the unmodified "100%" machine. Each operator handled this trade-off individually. Some operators chose to keep the bucket fill factor constant, which led them to spend more time at the gravel pile. Others chose to keep the pace with the consequence of less material in the bucket.

## 8 Conclusion and outlook

At the beginning of this article we described our vision of using psychophysiological measurements to assess operator workload in sufficiently detail to use it as a complement to traditional subjective evaluations, but also use such measurements in a workload-adaptive operator assistance system in a longer perspective. Even though the data allow for some interesting observations at both individual and skill group level, the results of this study indicate that measures

other than ones based on heart rate, finger temperature, skin conductance and respiratory air flow should be considered. All of these parameters seem hard to measure reliably in the tough environment of a mobile working machine, but will be less prone to artefacts in the controlled environment of a human-in-the-loop simulator. This of course requires the use of a simulator that has both the fidelity required to produce correct results on the machine side and the immersiveness required to produce correct results on the side of the operator. The research summarised in [14] shows that this is possible in principle.

In a simulator as well as in reality it is important to provide relevant test scenarios. We suspect that the operators in our study did not experience enough pressure, because there were no immediate consequences for not keeping the set cycle pace or not filling the bucket completely. In the future we will try to add this pressure by either more closely representing a real working place or by adding productivity-related feedback artificially, for example by tactile, acoustic or visual means.

We also found that the sensitivity of the psychophysiological measurements conducted appears to be too low for our requirements. On the other hand, promising research is being done on the use of Artificial Intelligence techniques (such as Case-Based Reasoning) to evaluate data from psychophysiological measurements [12][16]. With proper input, perhaps such systems can provide the sensitivity we require and might then also be able to recognise measurement artefacts. The need to automatically analyse all acquired data in context is the major driver for such AI-based analyses, since a manual review of multiple channels with data from interacting and compensating systems can today only be performed by experts, relying on clinical data which cannot very easily be transformed into complex work situations.

We and others, for example [15], also work with the development of new wireless sensors that can be deployed without distracting the operator from the working task, while at the same time being able to acquire data without the amount of measuring artefacts we have to cope with today.

## References

- [1] Filla, R. (2011) "Quantifying Operability of Working machines". Doctoral thesis, Department of Management and Engineering, Linköping University, Sweden. <http://urn.kb.se/resolve?urn=urn:nbn:se:liu:diva-70394>
- [2] Ley, R. (1999) "The modification of breathing behavior. Pavlovian and operant control in emotion and cognition". *Behavior Modification*. Vol. 23(3), pp 441-479. <http://dx.doi.org/10.1177/0145445599233006>
- [3] Schleifer, L. M., Ley, R., Spalding, T. W. (2002). "A hyperventilation theory of job stress and musculoskeletal disorders". *American Journal of Industrial Medicine*. Vol. 41(5), pp 420-432. <http://dx.doi.org/10.1002/ajim.10061>

- [4] Von Schéele, B. H. C. and von Schéele, I. A. M. (1999) "The Measurement of Respiratory and Metabolic Parameters of Patients and Controls Before and After Incremental Exercise on Bicycle: Supporting the Effort Syndrome Hypothesis?". *Applied Psychophysiology and Biofeedback*. Vol. 24(3), pp 167-177.  
<http://dx.doi.org/10.1023/A:1023484513455>
- [5] Filla, R. (2012) "Study of a Method for Assessing Operability of Working Machines in Physical and Virtual Testing". *International Journal of Vehicle Systems Modelling and Testing*, vol. 7, no. 3, pp 209-234, 2012.  
<http://dx.doi.org/10.1504/IJVSMT.2012.048939>
- [6] Begum, S., Ahmed M. U., Funk, P., Xiong, N. and von Schéele, B. (2006) "Using Calibration and Fuzzification of Cases for Improved Diagnosis and Treatment of Stress". Proceedings of the 8<sup>th</sup> European Conference on Case-Based Reasoning, pp 113-122.  
<http://citeseerx.ist.psu.edu/viewdoc/summary?doi=10.1.1.97.4.004>
- [7] Begum, S. (2011) "A Personalised Case-Based Stress Diagnosis System Using Physiological Sensor Signals". Doctoral thesis, Mälardalen University, Västerås, Sweden.  
<http://urn.kb.se/resolve?urn=urn:nbn:se:mdh:diva-12257>
- [8] De Waard, D. (1996) "The Measurement of Driver's Mental Workload". Doctoral thesis, University of Groningen, The Netherlands.  
<http://irs.ub.rug.nl/ppn/297329391>
- [9] Castor, M., Hanson, E., Svensson, E., Nählinder, S., Le Blaye, P., MacLeod, I., Wright, N., Alfredson, J., Ågren, L., Berggren, P., Juppet, V., Hilburn, B., Ohlsson, K. (2003) "GARTEUR Handbook of Mental Workload Measurement", Final Report for Flight Mechanics Group of Responsibilities (FM GoR) of the Group for Aeronautical Research and Technology in Europe (GARTEUR) by GARTEUR Action Group FM AG13.
- [10] Park, B. (2009) "Psychophysiology as a Tool for HCI Research: Promises and Pitfalls". Proceedings of *HCI 2009: New Trends*, LNCS 5610, pp 141-148.  
[http://dx.doi.org/10.1007/978-3-642-02574-7\\_16](http://dx.doi.org/10.1007/978-3-642-02574-7_16)
- [11] Di Stasi, L. L. (2010) "Mental Workload in HMI". Doctoral thesis, Departamento de Psicología Experimental y Fisiología del Comportamiento, Universidad de Granada, Granada, Spain.  
<http://hdl.handle.net/10481/15439>
- [12] Begum, S., Ahmed, M. U., Funk, P., Filla, R. (2012) "Driver's Mental State Monitoring System Using CBR Based on Heart Rate Variability Analysis". Proceedings from the 7th International Symposium Advances in Artificial Intelligence and Applications (AAIA'12).  
<http://fedcsis.org/proceedings/fedcsis2012/pliks/407.pdf>
- [13] Von Schéele, B. H. C. (1995) "Respiratory Sinus Arrhythmia as a Diagnostic Tool, a Treatment Goal, a Rule for Treatment Planning, a Cool Biofeedback, and an Out-Come Variable". *Biofeedback and Self Regulation*. Vol. 20(3), pp 308-309.
- [14] Nählinder, S. (2009) "Flight Simulator Training: Assessing the Potential". Doctoral thesis, Department of Management and Engineering, Linköping University, Sweden.  
<http://urn.kb.se/resolve?urn=urn:nbn:se:liu:diva-17546>
- [15] Voskamp, J. and Urban, B. (2009) "Measuring Cognitive Workload in Non-military Scenarios. Criteria for Sensor Technologies". Proceedings of *HCI 2009: Foundations of Augmented Cognition - Neuroergonomics and Operational Neuroscience*, LNCS 5638, pp 304-310.  
[http://dx.doi.org/10.1007/978-3-642-02812-0\\_36](http://dx.doi.org/10.1007/978-3-642-02812-0_36)
- [16] Begum, S., Barua, S., Filla, R., Ahmed, M. U. (2013) "Classification of Physiological Signals for Wheel Loader Operators Using Multi-Scale Entropy Analysis and Case-Based Reasoning". To be published in *Expert Systems with Applications*.

(Internet links updated and verified on March 11, 2013)

Effective Use



# Optimizing the trajectory of a wheel loader working in short loading cycles

R. Filla

Emerging Technologies, Volvo Construction Equipment, Eskilstuna, Sweden  
E-mail: reno.filla@volvo.com

## Abstract

A study into alternative trajectories for wheel loaders working in short loading cycles has been conducted, examining other patterns than the traditional V- or Y-cycle. Depending on workplace setup and target function of the optimisation other trajectories can indeed prove beneficial. The results of this study can be used in operator models for offline simulations as well as for operator assistance or even in controllers for autonomous machines or energy management systems for non-conventional machines like hybrids.

**Keywords:** wheel loader, working cycle, trajectory, work pattern, simulation, operator model, control, operator assistance

## 1 Introduction

Figure 1, published in its first version in [1] and quoted in several publications, shows the classic short loading cycle with the characteristic driving pattern in the shape of a V, possible to extend to a Y, if necessary.

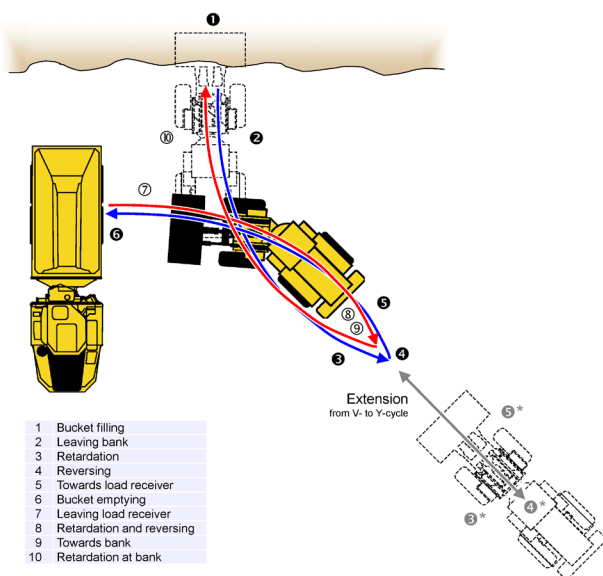


Figure 1: Short loading cycle in classic V- or Y-pattern.

From phase 1 to 6, the wheel loader operator first fills the bucket in the gravel pile, then drives backwards towards the reversing point (phase 4) and steers the wheel loader to accomplish the aforementioned characteristic V-pattern. The lifting function is engaged the whole time. The operator chooses the reversing point such that having arrived at the load receiver and starting to empty the bucket (phase 6), the

lifting height will be sufficient to do so without delay. In case of a bad matching between the machine's travelling speed and the lifting speed of the bucket, the operator needs to drive back the wheel loader even further than necessary for manoeuvring alone. This additional leg transforms the V-pattern into a Y-pattern.

In the remaining phases 7 to 10, the bucket needs to be lowered and the operator steers the wheel loader back to the initial position in order to fill the bucket again in the next cycle.

While the different phases of the depicted loading cycle are generally applicable (even though in other circumstances it might be meaningful to introduce new phases and events or combine some of the phases shown in Figure 1), the driving pattern does not necessarily have to resemble a V or Y. It appears that this pattern has emerged from the operators' desire to minimise the personal workload, rather than maximise energy efficiency, for a required productivity.

For new non-conventional systems like (semi)autonomous machines or hybrids, where the operator's requirements are less dominant or taken out of the loop completely, the traditional cycle in Figure 1 is not necessarily the most productive or the most energy-efficient way, either. Improved energy management for such machines may involve some kind of optimal control scheme along a pre-defined trajectory – so the obvious question would be whether there is optimisation potential in the trajectory itself.

Even if accepting the V/Y-cycle as the trajectory to use, it is an interesting question how to best orient the load receiver for a given position. The traditional recommendations are a 90° or 135° angle, given not only by Volvo but also other players in the industry [2][3]. However, also these recommendations are based on the performance of conventional

systems and might not be valid for autonomous machines or hybrids.

There is therefore a need to examine this in more detail and the results can have various applications, from improved dynamic simulations by adding planning capabilities to operator models [4] over off-line use for education or site planning purposes [5][6], on-line operator assistance functions [7] to autonomous machines [8] and improved energy management in advanced systems [9][10][11][12].

## 2 Problems of the classic V-/Y-cycle

A first attempt at examining different driving patterns has been made by the author in [4] – however the work then focused on a specific variant of the classic V-cycle without further consideration of alternatives. When using this trajectory in various workplace setups it becomes apparent that its use is limited to tight places with loading and unloading spots in close vicinity. For larger distances and other orientations of the load receiver, the classic V-cycle with equal steering to both sides very quickly results in unreasonable long transporting distances (Figure 2 left and right).

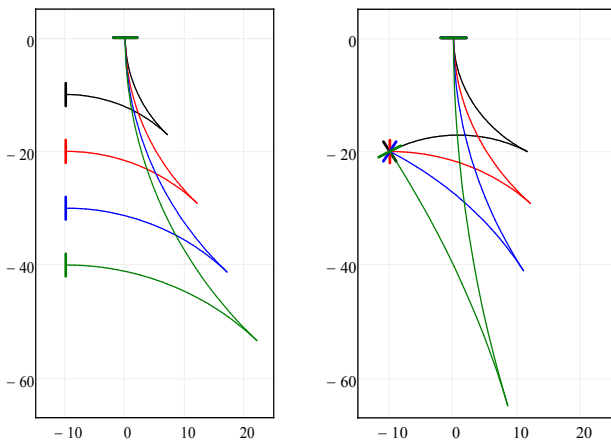


Figure 2: Classic V-cycle for different locations of the load receiver (left) and different orientations (right).

This stems from the cycle being modelled as simply two circular arcs meeting tangential in the reversal point. For larger workplaces an experienced operator would gradually vary the curve radius or at the very least extend the classic trajectory with line segments rather than travel such long distances in a curve with a very large radius.

Furthermore, above a certain transport distance any operator will start using the wheel loader in a Load & Carry cycle instead (Figure 3). In the “grey” area between tight working places and wide ones other shapes of loading cycle trajectories can serve as a smooth transition. Several possible candidates have been examined in this study; equations have been derived for easy implementation both on-line and off-line.

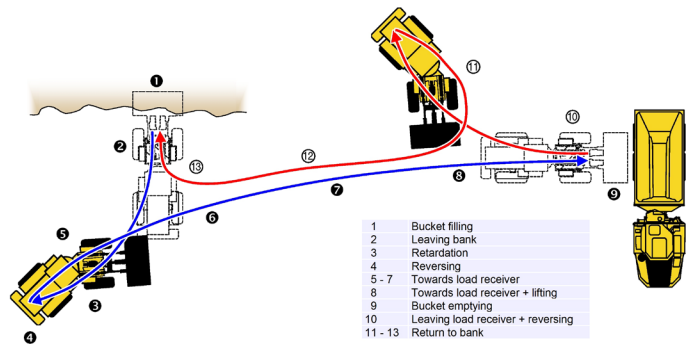


Figure 3: Load & Carry cycle.

## 3 Overview of examined cycle variants

Expanding upon the variants briefly touched upon in [4] Figure 4 shows the main cycle types and their respective sub-variants that have been examined in this study.

		Sub-variant		
		generic (g)	compact (c) (min #sections)	extreme (x) (min turn radius)
Main type	A			
	B			
	C (classic)			
	D			
	E			
	F			
	G			
	H		(same as Cc)	
	I		(same as Cc)	

Figure 4: Main cycle types and sub-variants examined in this study. (Depicted load receiver position and orientation is just an example.)

The first five main types “A” to “E” constitute a systematic exploration of the classic V-/Y-cycle (which is labelled “C”), while “F” and “G” represent a more intricate type with one S-shaped leg and the other one straight. Finally, “H” and “I” are permutations of the “C”-type with reversed order of line and arc section in the second leg (“H”-type), and first leg (“I”-type), respectively.

All cycles types studied can actually be seen as special cases of one unified cycle type with the following properties:

- S-shaped legs with a linear section in between the arc segments
- Length of linear segments can vary in interval  $(-\infty, \infty)$
- Radius of arc segments can vary in interval  $\{[-\infty, -R_{\min\_turn}), [R_{\min\_turn}, \infty]\}$
- Section angle of arc segments can vary in interval  $[0, 360^\circ)$

However, this unified cycle would have seven degrees of freedom and an extremely large search space, due to the parameter intervals also covering negative values. With the current approach and the current tools at hand this seems infeasible to solve in a reasonable amount of time.

Apart from the generic variant (sub-labelled “g”) with the highest amount of degrees of freedom, each cycle type can also be realised either as a compact cycle (sub-labelled “c”) with as few segments per leg as possible or as an extreme variant (“x”) where all curves are executed with highest articulation angle and therefore smallest possible turning radius.

## 4 Analysis

Table 1 shows the amount of degrees of freedom for each cycle variant. While for example “Bc”, the compact variant of the “B”-type, is fully constrained by the three parameters of the workplace setup: orientation of the load receiver and its vertical and horizontal distance from the loading spot, the “Cg” variant has three degrees of freedom left to constrain, which means that a parameter optimisation needs to be performed, for example varying the angle of reversing and the turning radii of both legs.

The equations for all cycle variants have been derived analytically in order to achieve fast calculation. They have been implemented in a collection of MathCad worksheets and verified with parametric profiles in SolidEdge.

The high amount of degrees of freedom for certain cycle variants and thus the necessity of parameter optimisation has an impact on calculation times, however. Even though each individual cycle variant can be calculated fairly quickly, finding the optimal cycle with an optimal load receiver orientation (i.e. an additional degree of freedom) for a given load receiver position takes some seconds nonetheless. Performing a massive workplace sweep as in Figure 15 and Figure 16 takes several days on an average PC.

Table 1: Degrees of freedom for each cycle variant.

		Sub-variant		
		g	c	x
Main types	A	2	1	0
	B	1	0	0
	C	3	1	1
	D	1	0	0
	E	2	1	0
	F	3	2	1
	G	3	2	1
	H	3	(1)	1
	I	3	(1)	1

All cycle variants can be calculated in “strict” and “non-strict” mode. In the former, the wheel loader is forced to always arrive perpendicular to the load receiver, i.e. in a  $90^\circ$  angle. An example from the field for such a scenario is an immobile crusher with a ramp: neither can the crusher be moved or rotated, nor can the wheel loader enter the ramp other than reasonably aligned.

In contrast to this a conveyor belt, a pit or a submerged truck are all fixed in position and orientation, but the wheel loader serving them has some freedom in the approach for unloading. In “non-strict” calculations a permitted interval for the angle of arrival is introduced, which adds an additional degree of freedom and therefore increases calculation time even more.

### 4.1 Delimitations

We only consider the part of the cycle between bucket filling and bucket emptying, i.e. phases 2-5 according to Figure 1.

The intended use of the results of this study for, among others, on-line operator assistance functions, autonomous machines, and improved energy management in advanced systems excludes the possibility to perform detailed dynamic simulations due to a limited time budget. The focus has therefore been on calculations by means of explicit equations for the trajectory parameters and properties.

However, this has the consequence that the effects of the intricate dynamical interaction of engine, drive train and hydraulics cannot be studied. One result is that all curve trajectories are simplified as circular arcs. While circular arcs merging tangential into each other seems smooth to the outside observer, for the wheel loader it is not a smooth manoeuvre at all. Any sudden change of curve radius requires an equally sudden change of articulation angle. With the masses of front and rear frame of a wheel loader, this not only requires a certain amount of energy, but also produces violent jerking. The use of arcs with a constant radius is therefore only correct for a constant articulation angle (Figure 5).

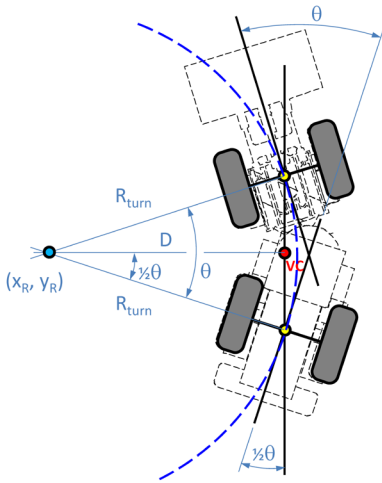


Figure 5: Wheel loader in a turn, fixed articulation.

Any path transition needs to employ smooth changes of radii. In most situations the wheel loader will be in longitudinal motion while the steering function is used to slowly change the frame articulation from a start value to a value that results in the required turning radius (Figure 6)

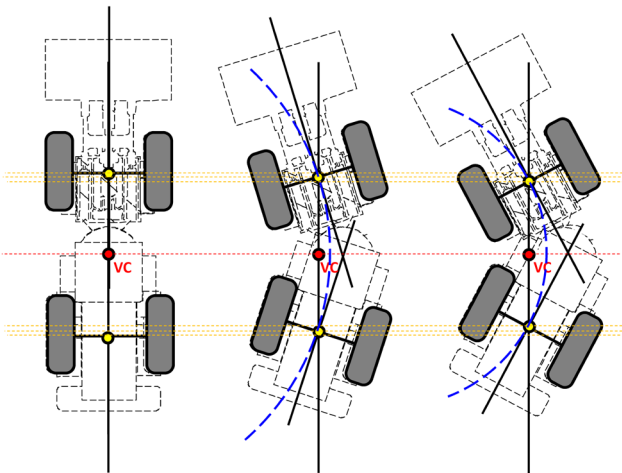


Figure 6: Wheel loader in a turn, several stages from straight to full turn.

This means that instead of following an arc with a constant radius the wheel loader's track will rather resemble a clothoid or Euler spiral (provided that the change in articulation angle is linear). Figure 7 shows in top view how the curvature of a wheel loader's trajectory is affected by different machine speeds: in all traces (simulating a L120G wheel loader model for 20s) the steering angle is increased with a steering speed of 20% of maximum possible, beginning with a straight machine (0° articulation) and a cut-off at the machine's maximum articulation angle. The dashed line represents the theoretical turning circle, which assumes an already established articulation angle of maximum value. It can be seen that the higher the machine speed, the higher the deviation of the actual trajectory from the theoretical turning circle.

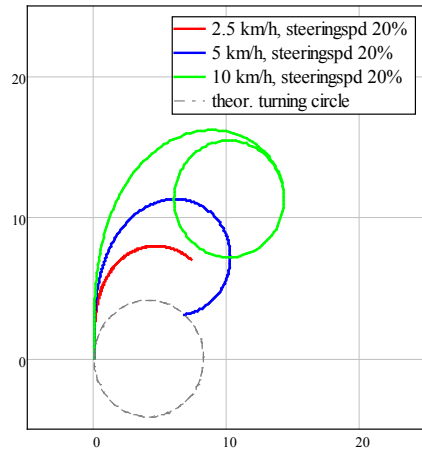


Figure 7: Wheel loader trajectories for different machine speeds at constant steering speed (linearly increasing articulation from 0° with cut-off at maximum).

Figure 8 shows how the curvature of a trajectory is affected by different steering speeds (again simulating a L120G wheel loader model for 20s). Not surprisingly, the lower the steering speed, the higher the deviation of the actual trajectory from the theoretical turning circle.

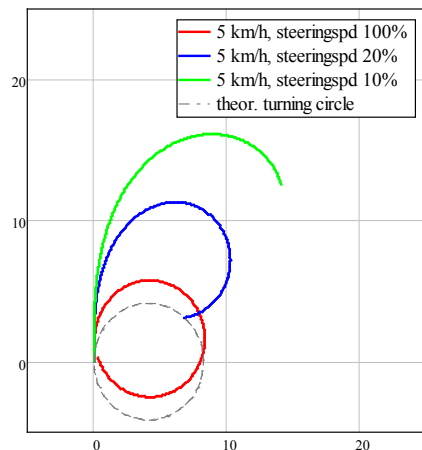


Figure 8: Wheel loader trajectories for different steering speeds (linearly increasing articulation from 0° with cut-off at maximum) at constant machine speed.

Modelling the curve trajectories as clothoids would require a detailed simulation model that provides correct values for machine speed and steering angle over time, which in turn requires detailed modelling of the complete machine system including actuation by the operator, engine dynamics, and how hydraulics and drive train compete for the limited engine power available.

As mentioned before, several of the intended applications of the results of this study do not allow any detailed simulation to be used anyway. In the case of optimal control we also have arrived at a Catch-22 situation, where we would need a detailed simulation in order to optimally control for example energy management of a hybrid machine – in a simulation.

For this study we have therefore chosen to simplify and approximate curves as circular arcs nonetheless. This enables an analytical solution to all cycle variants to be examined, which has a beneficial effect on the calculation time that is required for optimisation.

This simplification leads to quite a significant deviation of the actual machine position from the theoretical turning radius when an established and maintained machine speed of typically 10km/h is considered (Figure 9).

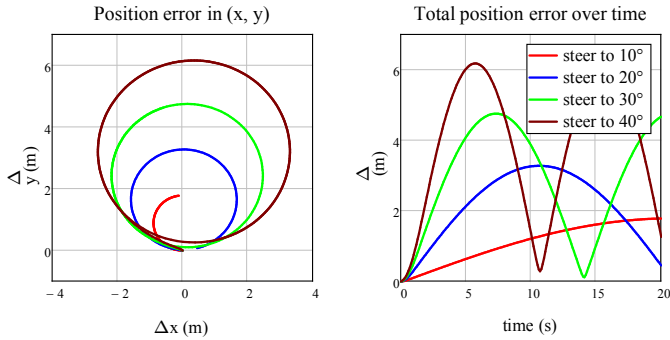


Figure 9: Error in position calculation due to simplification (circular arcs instead of clothoids)

However, if we assume that for the most part a steering action coincides with an acceleration of the machine from stand-still (probably never attaining the typical speed of 10km/h), then the error caused by the simplification of clothoid segments to circular arcs is tolerable, especially for target steering angles of 20° and below (Figure 10).

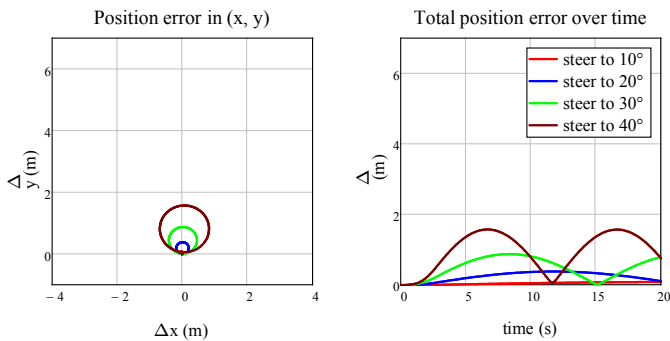


Figure 10: Error in position calculation due to simplification (circular arcs instead of clothoids)

## 4.2 Boundary conditions

The equations for cycle variant are set up so that the wheel loader trajectory always joins perpendicular to the loading spot and load receiver. The non-strict calculation mode, in which the machine’s angle of arrival at the load receiver is allowed within a pre-specified interval, is realised by varying the load receiver orientation within the same interval and perform strict calculations.

The arc segments have to be executed with a radius at least equal to the specified wheel loader model’s minimum turning radius.

Line segments that are enclosed by arcs and connect to the reversing point are allowed to have negative length, so that they can be executed either before or after reversing. This applies to variants of cycle types “A”, “E”, “H” and “I”.

Additional boundary conditions ensure that prohibited territory is not violated. For example, the trajectory is only allowed to approach both load receiver and loading spot from the front. It may also not go behind either one. The left image in Figure 11 shows all such invalid trajectories (in grey) for cycle variant “Cg” in a specific workplace setup. The red trajectory is the optimal one.

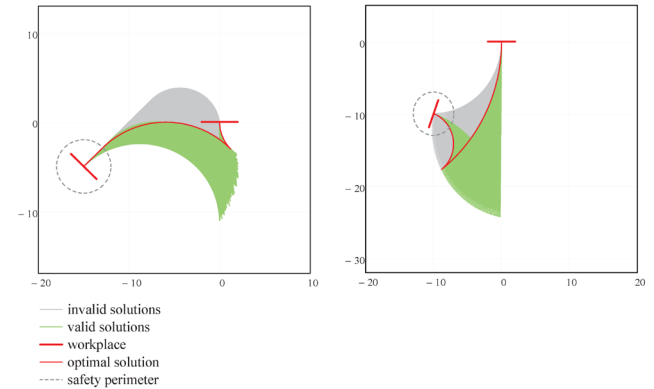


Figure 11: Examples of valid and invalid trajectories

A safety perimeter (dotted circle in Figure 11) is established around the load receiver, ensuring that trajectories do not collide with the dump truck or crusher placed there. The right image in Figure 11 shows all such invalid trajectories (in grey) for cycle variant “Ec” in a specific workplace setup. In the calculations performed in this study the safety radius has been set to 3 meters.

## 4.3 Optimisation of cycle parameters

The degrees of freedom shown in Table 1 for each cycle variant mean that the cycle trajectory is not fully constrained just by knowing the load receiver position and orientation (as discussed previously, these can become additional degrees of freedom). Instead, some cycle parameters need to be set explicitly – not by chance with a random value but through optimisation with a value that maximises or minimises a chosen property of the cycle.

Since most (if not all) optimisation problem in this study are ill-conditioned and also non-smooth due to the boundary conditions, after initial trial runs with different optimisation algorithms it was decided to implement brute force optimisation instead. In most cases the optimisation parameter was an angle that was to be varied in an interval of 180° or less. Sweeping this interval in steps of one degree was easy to do and improved performance noticeably. It was reasoned that this would be precise enough because a human operator is hardly able to perform a turn with even this precision.

But which target function to use for optimisation, i.e. what distinguishes a better cycle in comparison to another variant? The properties listed below are good candidates:

1. driving distance
2. driving time
3. driving time including time for steering
4. productivity
5. energy efficiency
6. operator workload

We will discuss these proposals in the following sections.

#### 4.4 Optimisation for driving distance

This is the most simple target function as it involves only the calculation of the length of each individual segment, which has to be done anyway.

It can be argued that optimising for “driving distance” also covers the fuel consumption caused by energy requirements of the drive train – at least to a certain extent, though not in any greater detail.

#### 4.5 Optimisation for driving time

The case can be made that not the driving distance matters, but the time it takes to travel that distance. Calculating with constant machine speed would just be the same as optimising for driving distance, but the picture changes when both the acceleration and the retardation of the machine, together with a pre-defined maximum travelling speed (Figure 12) are taken into account.

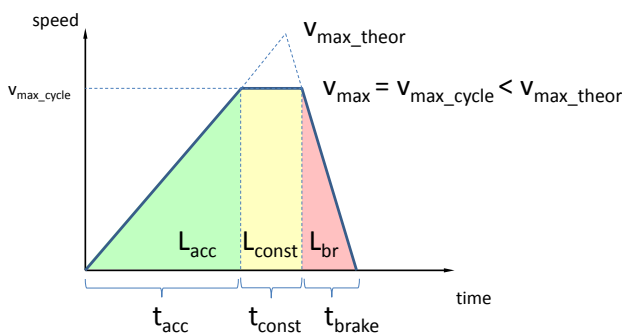


Figure 12: Speed profile over a cycle segment on which the maximum travelling speed is reached.

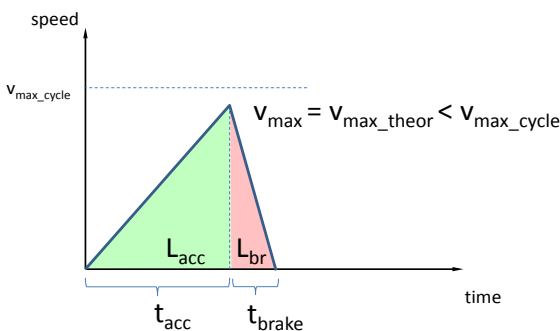


Figure 13: Speed profile over a cycle segment on which the maximum travelling speed is not reached.

When choosing the driving time as the target function for optimisation, it might be an advantage to have one cycle segment longer than the other, on which the machine can be accelerated to maximum driving speed, giving a higher mean speed for the complete cycle, rather than dividing the cycle equally into two segments which are both too short to result in maximum travelling speed until it is time again for retardation (Figure 13).

Measurements from previous machine testing have been used to determine typical acceleration and retardation rates; and the maximum travelling speed is set such that no shift into 3<sup>rd</sup> gear is performed. With a simplified modelling like this there is no need for detailed dynamic simulation, thus calculation time is low as only linear equations are involved.

#### 4.6 Optimisation for driving time including steering

Taking the travelling time due to longitudinal motion into account is a first step but the influence of steering must also be considered. In Figure 14 both trajectories have segments of the same length, yet the turning radii of the curves in trajectory 2 are smaller, which requires larger articulation. In the point of reversing the operator needs to change articulation from right to left, which takes more time for tighter turns as in the second trajectory.

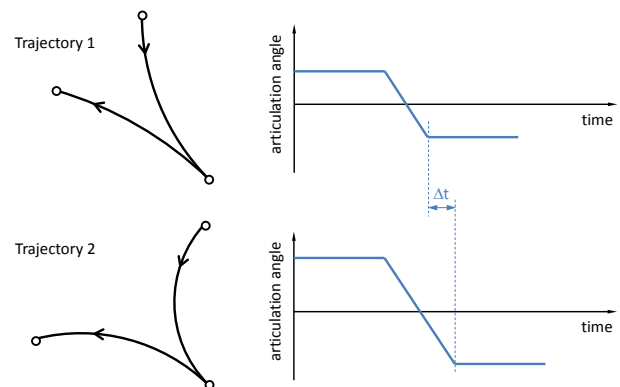


Figure 14: Cycle segments of the same length but different turning radii, thus different steering angles.

We assume that the machine is not moving when steering. In reality this would be the case, but then the curvature would resemble clothoids and the driving distance would increase, somewhat compensating for our simplified assumption. Also, see Figure 10 which shows that the impact of this simplification is minor for realistic machine acceleration and steering speed values, especially for target articulation angles of 20° and below.

#### 4.7 Optimisation for productivity

Any meaningful optimisation for productivity must include the bucket filling phase, because of the trade-off an operator can make between the lifting height achieved when leaving the loading spot (e.g. a pile of gravel) and the driving distance required to achieve a lifting height sufficient for emptying the bucket onto the load receiver.

This means we need to model different bucket filling techniques, which requires a simulation with models of the drivetrain and hydraulics of the machine, as well as models of the operator and the material to be loaded. However, one of the prerequisites for this study was to avoid detailed simulations and employ analytical equations instead, as discussed previously.

#### 4.8 Optimisation for energy efficiency

Basically the same arguments put forth in the previous section are also valid against choosing energy efficiency as optimisation target, however with an even higher emphasis on the model quality since power consumption is in the focus, rather than time required for certain motions. The most problematic requirement is the need for a high-quality (and in terms of computation expense tolerable) model of the material to be loaded. Today, great simplifications would be needed in order to perform these simulations in a reasonable time, which would be abused by the optimisation algorithm to find the most energy-efficient way to fill the bucket according to the (probably over-) simplified model – not according to reality.

The option of only considering power consumption of the drivetrain is not a valid work-around for a complex machine such as a wheel loader [10]. Also, optimising for “driving distance” already covers the drivetrain aspect to a certain extent, though not in any greater detail.

#### 4.9 Optimisation for operator workload

Apart from the difficulty to assess and quantify operator workload in a computer simulation there is the general problem of defining operator workload over a cycle.

If we would reduce it to encompass only control effort, then the optimum would be a cycle variant with the least amount of control input from loading to unloading – which is implicitly already covered by the “driving time including steering” option (section 4.6).

Any closer examination of operator workload would again require detailed simulation however with a greatly improved operator model.

### 5 Results

For any given workplace setup, consisting of orientation of the load receiver and its vertical and horizontal distance from the loading spot, each cycle variant can be calculated without any great computational effort. Implementation in autonomous machines and as assistance functions in wheel loaders controlled by a human operator is therefore feasible.

However, the more degrees of freedom, the longer the calculation time will be. Optimisation of all identified cycle variants in “non-strict” mode requires significantly more time, which might necessitate the implementation of pre-calculated lookup tables. Using the MathCad worksheets developed during this study a complete workplace area can be screened and the optimal load receiver orientation together with the parameters describing the optimal cycle

trajectory for each element in a matrix of load receiver positions can be calculated.

#### 5.1 Complete workplace area

Figure 15 shows the results of such a workplace parameter sweep for a L120G wheel loader, optimised for “driving time including steering”. In this calculation the load receiver orientation was not specified either and added therefore to the number of degrees of freedom – leading to quite a long calculation time (several days, as mentioned previously).

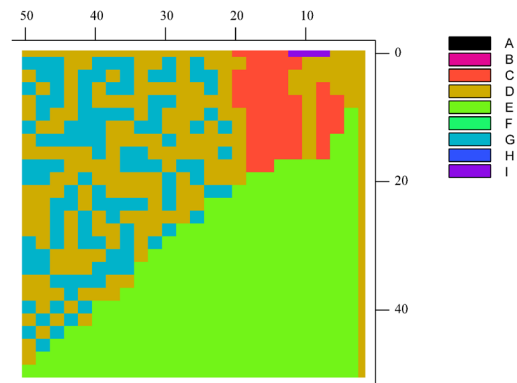


Figure 15: Optimal cycle variant depending on workplace

However, the colour plot of Figure 15 does not reveal the full picture, since the flexibility in several cycle variants enables them to closely resemble the shape of another cycle type – often of much simpler ones (see also Figure 16).

It is therefore more meaningful to examine cycle *shapes* (i.e. the driving directions for the operator) rather than the cycle variants (which are defined by the sets of equations they are calculated from). Figure 16 shows the principle cycle shapes that emerge as “driving time including steering”-optimal within the calculated workplace parameter interval.

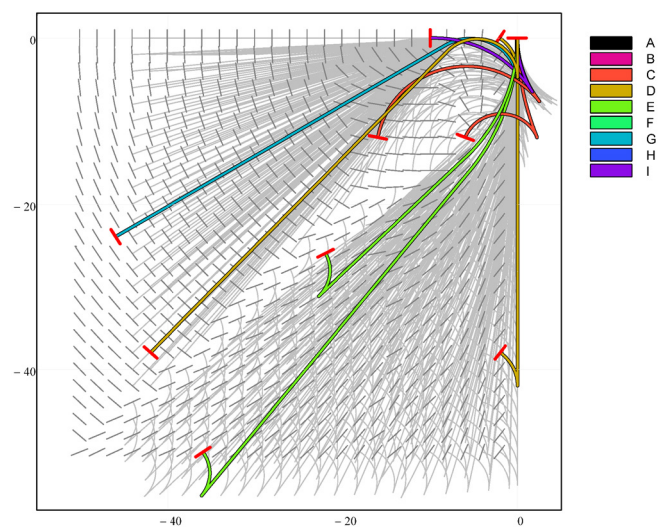


Figure 16: Optimal cycle shapes and optimal load receiver orientations depending on workplace setup (optimised for “driving time including steering”)

Judging from Figure 16 it seems clear that in the lower right half of the workplace it is better to drive in reverse for most of the distance. This is confirmed by plotting the relative performance of single cycle types such as in Figure 17. It can be seen that cycle type “C” is optimal (or very close to) in the entire upper left area of the workplace, but not so in the lower right area where “E” is optimal (except on the very right edge where “E” is restricted by the safety radius around the load receiver, leaving the field open to “C”).

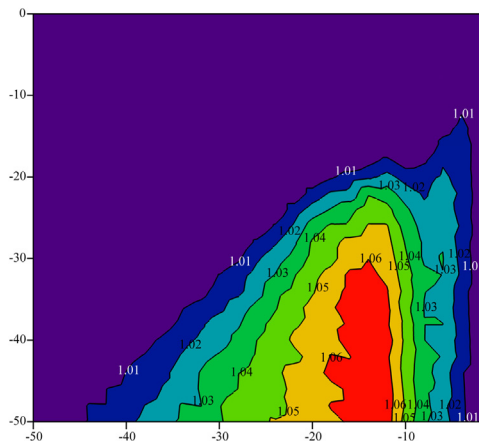


Figure 17: Relative performance of cycle type “C” compared to optimum in each single location (optimised for “driving time including steering”)

Figure 17 also reveals that even though cycles types “D” and “G” were presented as optimal in the upper left area of Figure 15, cycle type “C” is more or less equally good. This is again due to the actual *shape* of cycle types “G” and “C” being optimised to resemble “D” – a sign that the additional degrees of freedom in these cycles are not always needed. However, Figure 18 shows that the area where cycle type “D” is the optimum is not as large as for “C”.

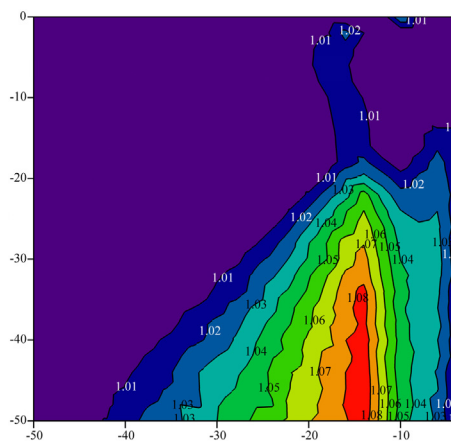


Figure 18: Relative performance of cycle type “D” compared to optimum in each single location (optimised for “driving time including steering”)

Using such plots it can be shown that cycle type “E” is far from being optimal in the upper left area of the workplace, as well as that cycle types “A” and “B” are inferior in

generally all situations, provided the orientation of the load receiver is not fixed.

However, it is difficult to generalise, since the observations made above are valid for a specific wheel loader model and a specific situation (safety radius, variable load receiver orientation, etc.). In another setup with perhaps a more restrictive safety perimeter around the load receiver and a fixed orientation of the latter it might very well be the case that cycles type “A” is superior to all others.

## 5.2 Specific load receiver locations, strict

In order to not use overly academic examples we designed a test case that followed the recommendations given in the literature. Acting upon the advice in [2][3] and others that a tight “C”-type cycle shall be driven with no more than 1.5 wheel revolutions per leg or better  $\frac{3}{4}$  to  $1\frac{1}{4}$  (as experienced professionals do), the load receiver, angled at  $135^\circ$  as recommended, was positioned 3m to the side at 2m distance from the loading spot.

Due to the tight work place setup some cycle variants are prevented from reaching a valid solution. Figure 19 shows that no valid solutions could be found for cycle types “E” and “F” when optimising for driving distance. The optimal cycle in this setup is a “C”-type cycle optimised as variant “Cx” (trajectory and bar in red colour in Figure 19).

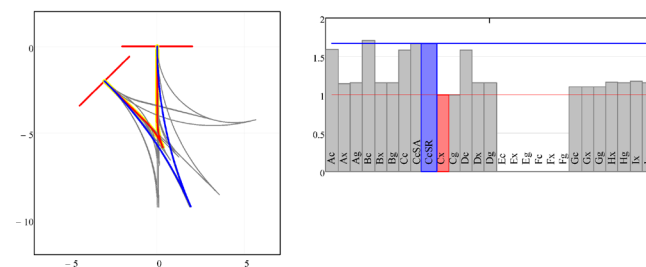


Figure 19: Test case optimised for driving distance

The blue trajectory and bar in Figure 19 belongs to “CcSR”, a special case of a “Cc” cycle with a boundary condition that both arcs shall have the same radius. This gives the same articulation angle right and left for the wheel loaders operator to steer to – probably a workload-minimising way an operator might want to choose. It is presumed that this (or the rather similar “CcSA”) is close to the classic V/Y-cycle as depicted in Figure 1, where both legs are clearly noticeable arcs (whereas a common “Cc” variant has one degree of freedom left and can be optimised into having the radius of one leg as nearly infinite, thus approaching a straight line).

Driving a cycle according to this classic case “CcSR” would have increased driving distance by 70% compared to the optimal solution (blue trajectory and blue bar in Figure 19).

In comparison to the optimum “Cx”, an optimised “Dg” cycle would have increased driving distance by 20%.

Optimising for driving time instead of driving distance does not result in a significantly different outcome. Those cycle variants with degrees of freedom get optimised into

basically the same shape. However, it is interesting to note that the advantage of the optimal variant of “Cx” decreases, so that classic case “CcSR” now only features a 30% higher value for the driving time as opposed to a 70% higher driving distance. The difference is due to the wheel loader using the longer legs to accelerate to higher machine speed, which greatly improves the average cycle speed.

The picture changes more significantly when optimising for driving time including steering. Now there is also a penalty on turning radii which require a lot of steering. Figure 20 shows that this favours a “D”-type cycle (but not “Dc” or “Dx”), presumably because this cycle only requires the wheel loader operator to use the steering function one time during reversing. However, the advantage over, for example the classic case “CcSR” is even smaller than previously: the latter only suffers from a 10% increase in driving time when the effects of steering are included.

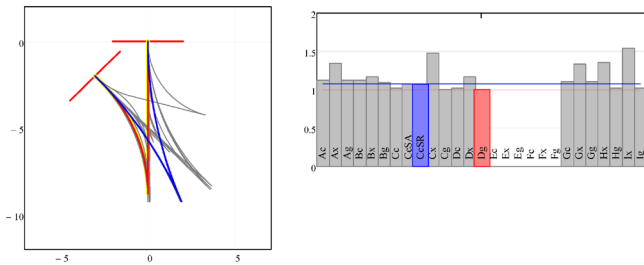


Figure 20: Test case optimised for driving time including steering

It is interesting to examine how the result changes with different machine parameter values. For example, in the calculation to the results in Figure 21 the wheel loader’s steering speed has been reduced to half of its original value. This has a profound negative impact on the “x” variants in which all turns are executed with minimum radius, i.e. maximum machine articulation. Cycle “Cx” takes now twice the time to drive compared to the optimised “Dg”. The latter now requires 17.8s to drive, compared to only 11.6s with the original machine.

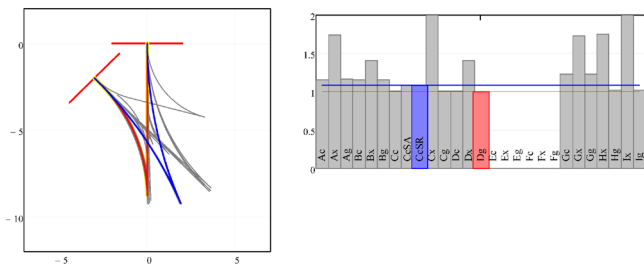


Figure 21: Test case optimised for driving time including steering, machine with halved steering speed

In Figure 22 the machine performance has been boosted by 100% so that the values for typical acceleration, retardation and steering speed are doubled. This favours a “Cg”-variant that almost resembles the shape of a “D”-type cycle, but not quite (though the driving time including steering is stated as 8.7s in both cases, so the difference is marginal). It is

interesting to see that the relative performance of all cycles now varies less than when calculating with the original machine parameters (Figure 20).

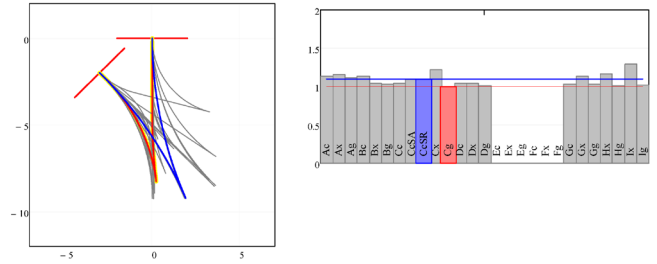


Figure 22: Test case optimised for driving time including steering, machine with doubled acceleration, retardation and steering speed

### 5.3 Specific load receiver locations, non-strict

In “non-strict” mode the wheel loader is permitted to arrive at the load receiver with an angular deviation from the exact 90° that the “strict” scenario stipulates.

In the calculations in this study the interval is set to ±15°. Figure 23 shows that this helps cycle type “F” to find a valid solution when optimising for driving distance. The angle deviation utilised by “Fx” is 11°, meaning that the best value of this cycle type is calculated for arrival at 101°. All other cycle types were able to find valid solutions already in “strict” mode and prefer therefore to arrive at 75° instead.

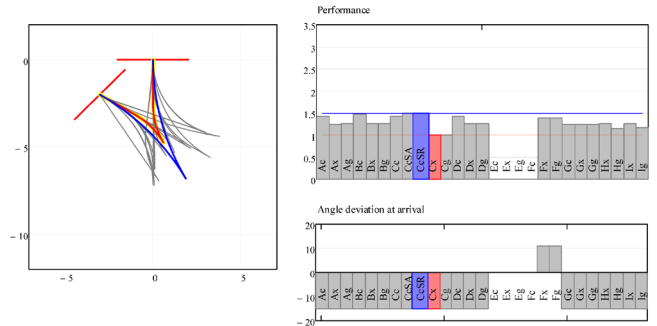


Figure 23: Test case optimised for driving distance, non-strict

In general, Figure 23 shows that “Cx” is still optimal when driving distance is considered – however the classic case “CcSR” now only shows a 50% higher value. It seems that “Cx” profits more from the “non-strict” mode than “Dg”, because the relative performance of the latter is 30% higher than “Cx”, while it was only 20% higher in “strict” mode (for comparison: in “strict” mode the “Cx” cycle resulted in 10.9m driving distance, compared to 9.4m in “non-strict”).

When optimising for driving time including steering, we see that “Dg” is marked as the optimum in Figure 24 (in red), however “Dc”, “Cc” and “Cg” do perform equally well. The conclusion is that in this setup the optimal cycle shape is that of “Dc” and the other cycles resemble that shape in their



## References

- [1] R Filla (2003) "Anläggningsmaskiner: Hydrauliksystem i multidoräna miljöer". Proc. of *Hydraulikdaggar 2003*, Linköping, Sweden.  
<http://urn.kb.se/resolve?urn=urn:nbn:se:liu:diva-13371>
- [2] L Stewart (2005) "Production Heroes: Wheel Loaders. Take-Charge Loader Operators – Fill Trucks Faster". *Construction Equipment*, pp 42-46, no. 3, 2005.  
<http://www.constructionequipment.com/take-charge-wheel-loader-operators-fill-trucks-faster>
- [3] North Pacific Training and Performance, Inc (2008) "Loader Operator Training Manual (Sample Pages) 992G Wheel Loader". Downloaded 2012-12-15.  
<http://www.north-pacific.ca/LoaderManual-Sample-English.pdf>
- [4] R Filla (2005) "An Event-driven Operator Model for Dynamic Simulation of Construction Machinery". Proc. of *The Ninth Scandinavian International Conference on Fluid Power*, Linköping, Sweden.  
<http://www.arxiv.org/abs/cs.CE/0506033>
- [5] J Fu (2012) "A Microscopic Simulation Model for Earthmoving Operations". *World Academy of Science, Engineering and Technology*, issue 67, pp 218-223.  
<https://www.waset.org/journals/waset/v67/v67-38.pdf>
- [6] E Uhlin (2012) "Microsimulation of Total Cost of Ownership in Quarries". Proc. of *17<sup>th</sup> International Conference of Hong Kong Society for Transportation Studies*, Hong Kong.
- [7] B Frank, L Skogh, R Filla, A Fröberg, and M Alaküla (2012) "On Increasing Fuel Efficiency by Operator Assistance Systems in a Wheel Loader". Proc. of *International Conference on Advanced Vehicle Technologies and Integration*, pp 155-161, ISBN 978-7-111-39909-4, Changchun, China.
- [8] J Blom (2010) "Autonomous Hauler Loading". Master Thesis. Dept. of Innovation, Design and Engineering, Mälardalen University, Västerås, Sweden.  
<http://www.idt.mdh.se/examensarbete/index.php?choic e=show&lang=en&id=1019>
- [9] K Heybroek, G Vael, J-O Palmberg (2012) "Towards Resistance-free Hydraulics in Construction Machinery". Proc. of *8th International Fluid Power Conference*, Dresden, Germany.
- [10] R Filla (2009) "Hybrid Power Systems for Construction Machinery: Aspects of System Design and Operability of Wheel Loaders". Proc. of *ASME 2009 International Mechanical Engineering Congress and Exhibition*, Vol. 13, pp 611-620.  
<http://dx.doi.org/10.1115/IMECE2009-10458>
- [11] K Pettersson, K-E Rydberg, P Krus (2011) "Comparative Study of Multiple Mode Power Split Transmissions for Wheel Loaders". Proc. of *The Twelfth Scandinavian International Conference on Fluid Power*, Tampere, Finland.  
<http://urn.kb.se/resolve?urn=urn:nbn:se:liu:diva-72630>
- [12] T Nilsson (2012) "Optimal Engine Operation in a Multi-Mode CVT Wheel Loader". Licentiate thesis, Linköping University, Linköping, Sweden, 2012.  
<http://urn.kb.se/resolve?urn=urn:nbn:se:liu:diva-80838>



# Measurements and Simulations to Evaluate Strategies for Improved Energy Efficiency of a Reach Stacker, Forwarder and Wheel Loader

Olof Noréus , Magnus Hägglund , and Mats Emlén

ITH, Institute of Applied Hydraulics, Örnköldsvik, Sweden  
E-mail: ons@ith.se

## Abstract

As the boom on for example a conventional reach stacker, a forwarder or a wheel loader is retracted and lowered, the entire potential energy of the boom and the load is wasted and converted into fluid heat in the control valves. To reduce the energy consumption and power installation requirements, one possible solution is to compensate for the empty weight, for example by utilising a spring or gas accumulator. By integrating a gas accumulator into the piston rod of the boom cylinder, it is possible to improve the energy efficiency on existing equipment just by changing the boom cylinder. This solution can be used in conventional hydraulic systems but it also has potential to reduce power consumption in more complex electric or hydraulic potential energy recuperation solutions.

A number of load handling sequences have been simulated in SimulationX software using a conventional hydraulic reach stacker load handling simulation model and simulation results have been compared to measurements. The simulation results show a good overall compliance with reality. The simulation model can provide detailed information about how large the losses are in different components of the system. By modifying the model and utilise the measured data to get a relevant loading cycle, it is possible to evaluate strategies for improved energy efficiency. Performed simulations indicate that it is possible to further improve the energy efficiency of the system by adding a cylinder and accumulator to recuperate energy when lowering the boom. That also enables the possibility to downsize and reduce the cost for hybrid solutions.

**Keywords:** Energy Efficient Hydraulics, Mobile Load Handling, Crane, Reach Stacker

## 1 Introduction

Hydraulic actuators are commonly used in mobile load handling systems due to large benefits such as high power density, large force and torque capability and robustness regarding chock loads. In mobile systems it is important to keep the weight down and the hydraulic system is often kept rather simple both to reduce weight and cost.

Although such hydraulic systems are efficient regarding weight and force or torque performance, they tend to be less impressive when it comes to energy efficiency. For systems where the hydraulic actuators only are used a small part of the time, that might not be an issue, since keeping the weight and cost down keeps the complete system efficient.

However, with increased energy costs the motivation to improve the energy efficiency also increases. In particular in applications where the hydraulic actuators are heavily used, it is beneficial to make the hydraulic system more energy efficient.

Methods to improve the energy efficiency are discussed in Section 2. A common energy loss in load handling systems

is that energy is consumed to lift the empty weight, and that energy is then dissipated as the boom is lowered.

### 1.1 Evaluated applications for energy saving

Measurements have been performed on a wheel loader, a reach stacker and a forwarder. Each vehicle is equipped with a hydraulically manoeuvred boom.

The focus in this study is to include a support cylinder that recuperates potential energy from the empty weight when lowering the boom, and then contributes to the energy needed to lifting the empty weight when raising the boom. Such a cylinder is described in Section 2.1 and the application to a wheel loader is discussed as an example. The boom lift cylinder pressure for a conventional cylinder has been measured during full stroke loading cycles. The energy saving potential, when compensating for the empty weight, is estimated by calculations.

Measurements and modelling of a reach stacker to make it possible to analyse the energy saving potential in a simulated environment are described in Section 3 and 4. Pressure and flow have been measured at several positions in the system

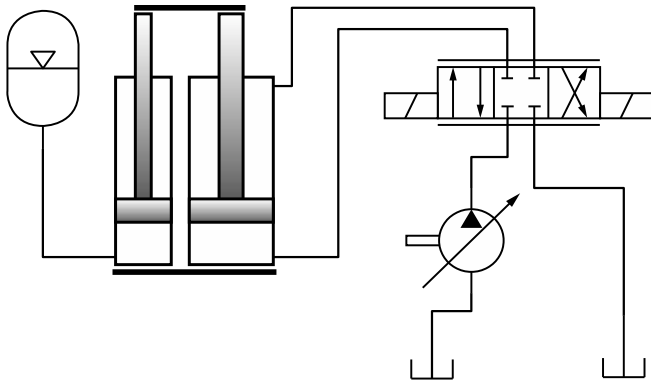


Figure 1: Addition of support cylinder compensating the empty weight for improved energy efficiency.

while using conventional lift cylinders and a dynamic model is validated by comparing simulation results to the measurements. The energy saving potential is estimated by including energy saving cylinders in the model and performing dynamic simulations. Using a dynamic model of the complete system also makes it possible to analyse effects on other parts of the system and potential problems such as oscillations.

Finally, the energy saving potential by applying energy efficient cylinders on the reach stacker and a forwarder, estimated by dynamic simulations, are presented in Section 5. For the forwarder, measurements of lift cylinder pressures and position have been made and a simplified dynamic model, including the lift cylinder and the load, is utilised to estimate the energy saving potential.

## 2 Strategies for improving energy efficiency

The hydraulic system in, for example, the Kalmar DRF450 reach stacker contains energy saving control strategies. The variable pump is controlled using a load sensing signal from the directional control valve in order not to provide more pressure than necessary from the pump. In addition, the regenerative valves enable faster lifting and reduced pump flow demand at moderate loads by leading the oil from the cylinder minus side through a spring biased check valve to the cylinder plus side.

There are several possible strategies to further improve the energy efficiency, e.g. described in [1, 2]. One evaluated example is to add a cylinder and accumulator, according to fig. 1, that acts like a spring and recuperates energy when lowering load and contributes to the force when lifting.

### 2.1 Energy efficient cylinder with gas accumulator

Instead of adding another cylinder with accumulator to compensate for the empty weight as in fig. 1, a solution developed by THORDAB AB is to integrate the accumulator into a cylinder by using a hollow piston rod, as shown in fig. 2. The piston rod is filled with gas and an accumulator piston rod is added inside it. Thus, the piston rod is also acting as a cylinder filled with gas.

Depending on the piston rod length, it may be possible to have

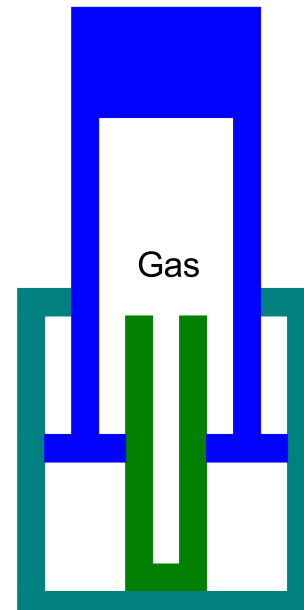


Figure 2: Energy efficient cylinder with integrated gas accumulator developed by THORDAB AB.

a gas volume in the top of the piston rod, above the accumulator piston rod stroke, to ensure that the compressed gas volume is large enough when the accumulator piston rod is pushed fully into the piston rod. Additionally, by letting the seals be mounted inside the piston on the piston rod and using a hollow accumulator piston rod, an additional gas volume is created. Thereby, compressing the gas too much can be avoided.

Both single acting and double acting cylinders are utilised in load handling systems. For equipment with single acting cylinders, it is necessary to not let the accumulator piston rod force exceed the empty weight in order to be able to lower the boom.

When double acting cylinders are used, it may be possible to even out the power demand during the loading cycle by letting the accumulator piston rod provide a force that is higher than the empty weight. It will then be necessary to actively push the boom down, i.e. it is necessary to provide hydraulic power also when lowering the boom without load, but the power demand during the lifting sequence is further reduced.

Depending on the maximum allowable gas pressure and the desired force from the accumulator piston rod, it is possible to determine an appropriate accumulator piston rod outer diameter. In order to eliminate the need to fasten the accumulator piston rod in the cylinder bottom, it is beneficial to never let the gas pressure drop below the hydraulic pressure. To maintain enough gas pressure during the cylinder stroke, a large enough gas volume is needed in the accumulator.

If the accumulator should be fully integrated within the cylinder, that implies that a minimum inner diameter of the piston rod can be determined. In fig. 3, the accumulator piston rod diameter and piston rod inner diameter are shown for varying maximum gas pressures.

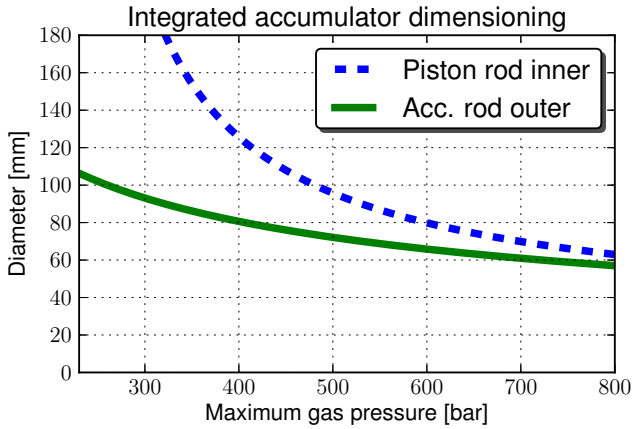


Figure 3: Dimensioning of integrated accumulator in cylinder. The accumulator piston rod outer diameter and the piston rod inner diameter are depending on the maximum desired gas pressure.

The cylinder in this example is appropriate for the Atlas Copco ST14 mining wheel loader. The cylinder is double acting and the accumulator piston rod is chosen such that it compensates for the empty weight, while the piston rod inner diameter is chosen such that the gas pressure never drops below the hydraulic pressure.

Assuming that the normal compressed gas pressure should be 350 bar, fig. 3 indicates that the appropriate outer diameter of the accumulator piston rod is about 85 mm and the corresponding piston rod inner diameter is about 155 mm.

With the chosen accumulator design, the gas pressure is shown in fig. 4. In fig. 5 the measured hydraulic pressure in a standard cylinder when lifting and the corresponding estimated pressure in the accumulator cylinder are shown. Comparing to fig. 4, it can be seen that the hydraulic pressure never exceeds the gas pressure.

In this application the hydraulic pressure increases with the cylinder stroke. Since the gas pressure drops as the gas is expanding, the accumulator will support a larger amount of the load at lower positions. Therefore, the hydraulic pressure for the accumulator cylinder approaches the pressure of the standard cylinder as the stroke position increases. Ideally, the hydraulic pressure demand would be decreasing with the stroke position, allowing the gas pressure to support about the same amount of the load at all stroke positions.

However, although the pressure demand approaches the demand for the standard cylinder at full stroke, the accumulator piston rod reduces the volume in the cylinder. Therefore, the flow to the cylinder is reduced at all positions and thereby also the power demand, which is shown in fig. 6.

The reduced pressure demand for the accumulator cylinder shown in fig. 5 contributes to the reduced hydraulic power consumption for the cylinder, but the global effect on the complete system varies with the configuration.

If the pump pressure cannot be reduced, for example due to other consumers demanding a high pressure in an LS sys-

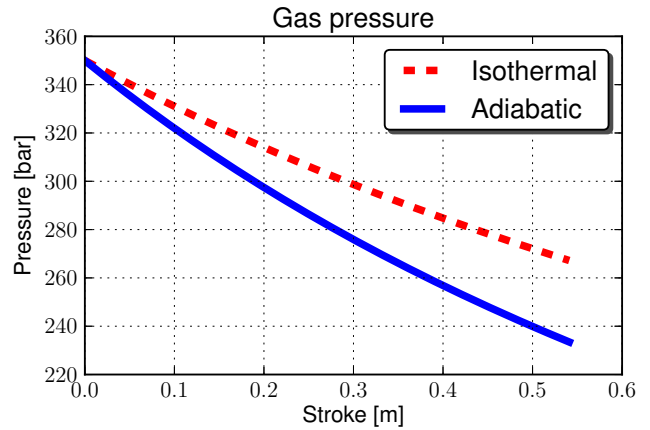


Figure 4: The gas pressure decreases when lifting.

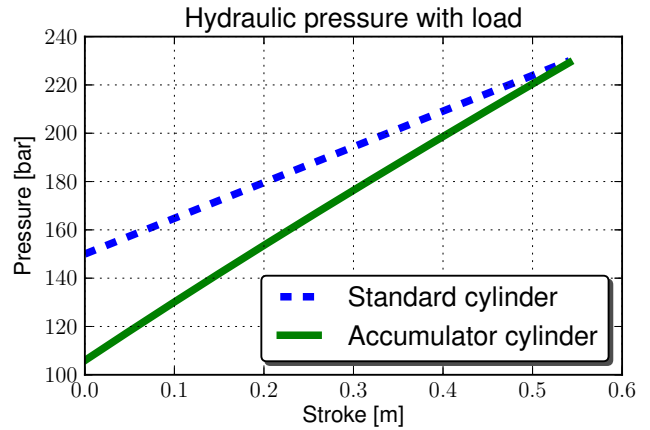


Figure 5: Hydraulic pressure in the cylinder when lifting. The pressure in the standard cylinder is measured during a real loading cycle, while the corresponding pressure for the accumulator cylinder is estimated.

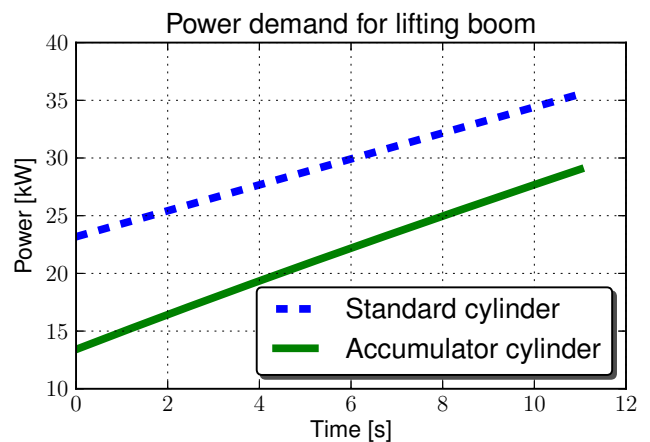


Figure 6: Power demand for each cylinder when lifting the boom, estimated from measured pressure on the standard cylinder, neglecting losses.

tem (described in Section 4.1), the control valve losses are increased instead. Therefore, the reduced pressure demand does not necessarily contribute to a reduced power consumption for the complete system.

On the other hand, if the standard cylinder was the consumer demanding the highest pressure, changing it to an energy efficient cylinder demanding a lower pressure would reduce valve pressure losses also for other consumers. Moreover, the decreased flow demand not only reduces the cylinder power, but also reduces pressure drop losses in the system, regardless of other consumer's demands.

From an energy point of view it is beneficial to increase the gas volume in this case, since the gas pressure is better maintained during the stroke. If it is not possible to increase the piston rod inner diameter, it may be possible to add an external gas bottle.

The maximum possible energy saving would in this case be if the gas pressure could be kept constant during the stroke. In that case 110 kJ per cylinder and stroke would be saved of the total 320 kJ needed from each cylinder to lift the boom. That is, it is not possible to save more than 34 % of the energy when lifting with an accumulator cylinder in this application.

For the accumulator integrated within the cylinder, the reduced power demand shown in fig. 6 corresponds to an energy saving of 88 kJ, corresponding to 27 % for the cylinder, not including losses and effects on the rest of the system.

### 3 Measurements on a reach stacker

A reach stacker is a vehicle used for handling cargo containers and are able to quickly transport containers short distances and pile them. When lowering heavy containers, there is a great energy saving possibility, since the potential energy usually is dissipated as heat.

The reach stacker considered in this study is a Kalmar DRF450 reach stacker manufactured by Cargotec and shown in fig. 7. It handles 20 and 40 feet containers with a maximum lift capacity of approximately 45 t.

Measurements have been carried out when lifting the container to full height. All sequences have been made with 0t, 27t and 45t containers resulting in a range of different load handling sequences. In addition, these sequences have all been carried out both for fully and slowly increasing joystick actuation at full engine speed. Also, all measurements were repeated with two flow turbines measuring both pump flows.

Measuring pump speed, flow, pressures in the system and boom angle and extension enables verification of the simulation model for the unmodified system and also gives a relevant driving cycle to use in the simulations.

### 4 Modelling of a reach stacker

A 3D multibody system (MBS) model as well as a load handling hydraulic model of a conventional reach stacker container truck has been built using the SimulationX software, described for example in [3–5].



Figure 7: Kalmar reach stacker.

#### 4.1 Hydraulic model

The hydraulic system, shown in fig. 8, managing the boom lift and boom extension functions of the reach stacker is a so called load sensing (LS) system. This means that the displacements of the variable pumps are controlled in order to match the highest pressure demand. The simulation model consists of standard SimulationX element types such as variable pumps, differential cylinders and valves, as well as a number of element types specially assembled for this system: the M402 directional control valve, the variable pump control block and the regenerative valve block.

For the hydraulic cylinders, a mechanical efficiency of 97 % is assumed. Moreover, they are simulated with a rigid end stop and no internal or external leakages are considered.

In addition to the hydraulic components, there is also a boom assembly multibody system (MBS) connected to lift and extension cylinders.

#### 4.2 Mechanical model

The mechanical model is divided into two submodels; one load handling submodel and one running gear submodel. This way load handling can be simulated separately by the load handling submodel or both load handling and driving can be simulated by connecting the two submodels to each other. It is important that the submodels can be connected when evaluating system solutions where energy is transferred from one subsystem to another. The simulation tool is considered to

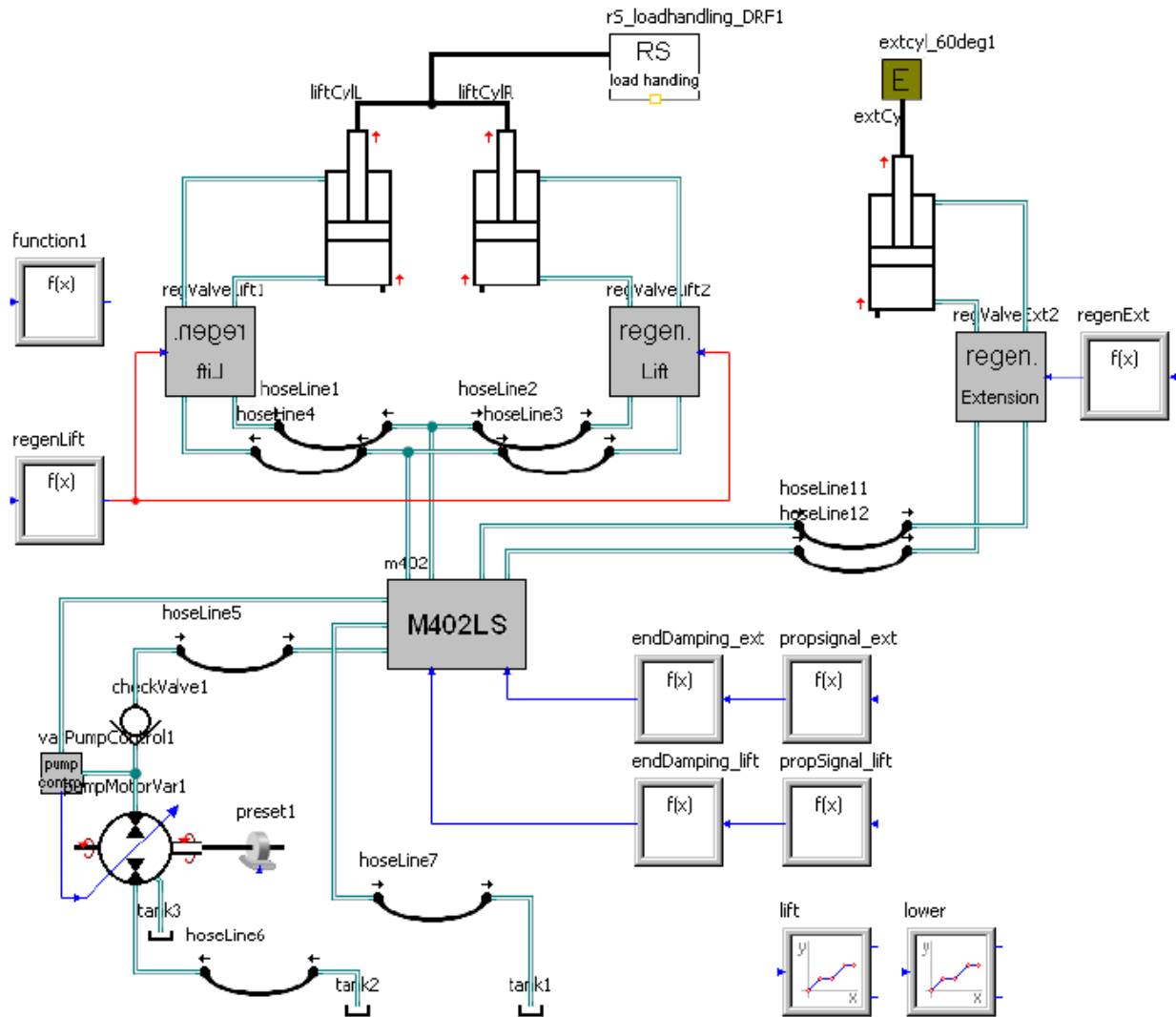


Figure 8: Simplified hydraulic model in SimulationX.

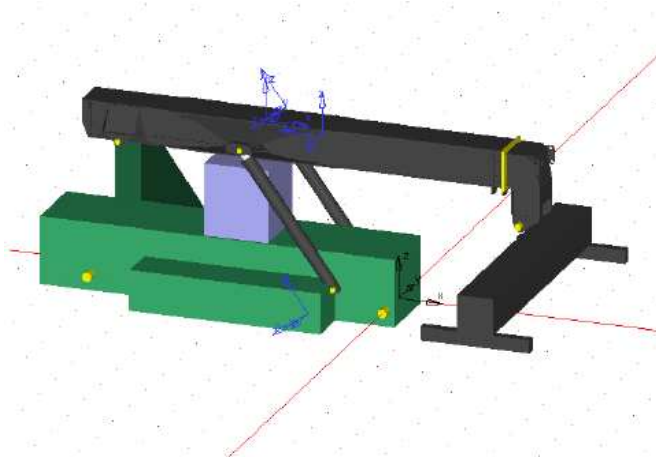


Figure 9: Load handling visualisation of simulation model.

be efficient if the whole system as well as subsystems can be effectively studied. The two submodels are built by rigid bodies, joints and forces from the SimulationX 'MBS Mechanics' library and tire elements from the 'Power Transmission MBS' library.

#### 4.2.1 Load handling model

The load handling model, shown in fig. 9, consists of a number of rigid bodies representing chassis, outer boom, inner boom, spreader, container etc.; each of them with a defined geometry and mass. In addition it has a lift cylinder force, a boom rotational joint, a boom extension joint and a spreader rotational joint.

The boom can be set into lift and extension motion by affecting the lift cylinder force and the boom extension joint by mechanical forces. During simulation, these forces can be determined for example by simply defining a velocity or by connecting a hydraulic cylinder from a hydraulic simulation model.

The rotational and prismatic joints of the lift cylinders are assumed to be frictionless. Rigid friction with continuous

transition is considered for the boom rotational and extension joints as well as for the spreader joint, with the coefficient of slipping friction set to 0.1, the limit angular and linear velocity difference set to  $5 \times 10^{-5}$  rad/s and  $5 \times 10^{-5}$  m/s, respectively, and the friction radius set to 100 mm.

#### 4.2.2 Vehicle running gear model

The driving model consists of rigid bodies with geometries and mass representing rims and tires. It also includes ‘Tire Plane Contact’ elements simulating the tire motions, a force element representing the drag force and rotational as well as translational joints in order to enable the driving motions of the vehicle. The vehicle is set into motion by affecting the left and right front tires by mechanical torques. During simulation, the torques can be determined for example by simply defining an angular velocity or by connecting a differential gearbox from a drive system simulation model.

### 5 Results

The measurements provide both relevant load cycles and data for verification of models. By using the simulation model, it is possible to identify where in the system most energy is dissipated and evaluate possible energy savings by modifying the system.

#### 5.1 Verification of models

The reach stacker load handling system simulation model’s compliance with reality has been evaluated by comparing simulation results with measurement data for different load handling sequences. The evaluation shows a good overall compliance.

#### 5.2 Evaluation of energy losses

Simulating the system according to the driving cycle makes it possible to identify the components that contribute most to the energy losses. Thereby it is clarified what parts in the system it would be most beneficial to further develop in order to achieve an improved energy efficiency.

#### 5.3 Improved energy efficiency

When using an accumulator to recuperate energy, the amount of saved energy is depending on both the gas prefill pressure and the initial oil pressure in the accumulator. When lifting a 27 t container, it is reasonable to save about 10 % to 30 %, which is shown in fig. 10 and fig. 11. This is based on simulations of the lifting phase, i.e. the energy saving is not representative for a complete loading cycle.

#### 5.4 Energy efficient cylinder applied to a forwarder

A forwarder is a forest machine equipped with a crane and grasper used for loading and transporting logs.

A similar energy efficiency simulation, studying the effects of adding an extra cylinder, as described in the reach stacker case was also performed on a forwarder. In this case an El-Forest forwarder with a Cranab FC crane was continuously lifting and lowering the boom without load in the grasper, as shown

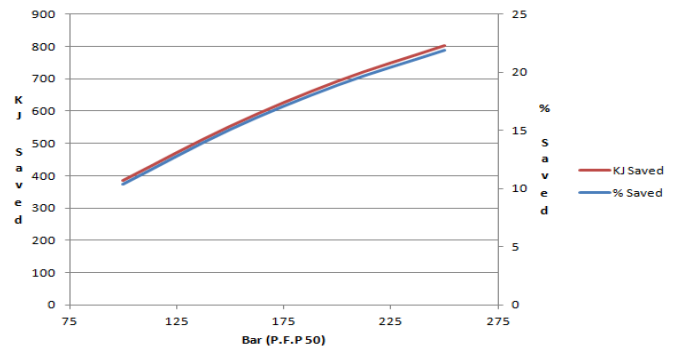


Figure 10: Energy saving vs. initial oil pressure when lifting a 27t container. The prefill pressure in the accumulator is 50 bar.

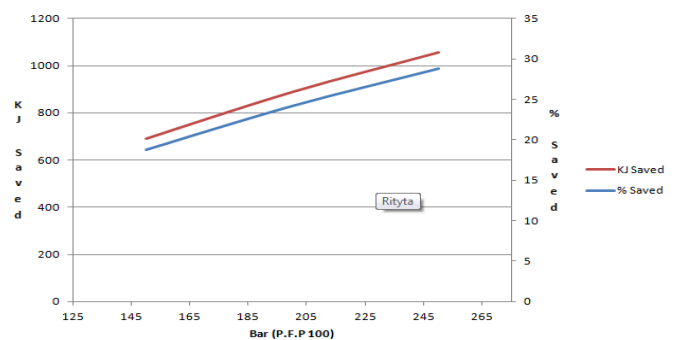


Figure 11: Energy saving vs. initial oil pressure when lifting a 27t container. The prefill pressure in the accumulator is 100 bar.

in fig. 12 and 13. During this time the lift cylinder pressure and position were measured. These measurements were used as input in the simulation.

The model is simpler than in the reach stacker case only focusing on the lift hydraulics. The simulation is supposed to follow the measured lift cylinder motion. Therefore a constant pressure pump is used with a PID controlled proportional direction valve to the lift cylinder. The controller set-points are the measured positions of the cylinder.

The force acting on the cylinder was calculated from the measured pressure. The lift cylinder pressure and motion in the simulation correspond to the measured values, which validates the model. The hydraulic power in the lift cylinder from simulations with and without an additional cylinder and gas accumulator was compared.

The results indicate an improved energy efficiency of about 20 % during lifting, using the additional cylinder. The pressure could be lowered compared to a conventional cylinder. As the pump pressure in an LS system adjusts to the highest pressure demand this could mean less energy loss in pressure drop to other functions during normal driving cycles. Problems during simulation were oscillations, which may or may not occur in reality.



Figure 12: Forwarder with boom in high position without load.



Figure 13: Forwarder with boom in low position without load.

## 6 Conclusions

A validated MBS heavy equipment model can be a very useful tool not only for evaluating energy efficiency but also for a number of additional design work question formulations, in both new design and design modifications. Axle pressure figures could be used for determining the vehicle stability in extreme load positions and/or motions. Power figures could be used for dimensioning hydraulic and propulsion systems out of a vehicle performance specification. MBS simulations are of great value in early design phase as well as a tool for simulation driven design.

The performed simulations and calculations applied to a reach stacker, forwarder and wheel loader indicate that it is possible to further improve the energy efficiency of mobile load handling systems by adding a cylinder and accumulator to recuperate energy when lowering the boom. Since the cylinder reduces the power and energy demand, it also has the potential to reduce the cost and improve the efficiency of more complex electric or hybrid energy recuperating systems. Losses will decrease as less power has to be handled by for example a battery. Moreover, smaller components can be used.

One obstacle when developing electric or hybrid energy recuperating systems might be the increased initial cost for the system. Therefore, the energy efficient cylinder can not only replace a conventional cylinder to improve the efficiency of existing equipment, but it can also enable the development of electric or hybrid energy recuperating systems by reducing the power demand and thereby also the initial cost.

## References

- [1] Xingui Liang and Tapio Virvalo. Energy reutilization and balance analysis. *Proceedings of the Fifth International Conference on Fluid Power Transmission and Control (ICFP)*, 4:306–310, 2001.
- [2] Karl-Erik Rydberg. Energy efficient hydraulic systems and regenerative capabilities. *Proceedings of the Ninth Scandinavian International Conference on Fluid Power, SICFP'05*, 2005.
- [3] Hans Dresig and Franz Holzweißig. *Dynamics of Machinery: Theory and Applications*. Springer-Verlag, Berlin Heidelberg, 2010. ISBN 978-3-540-89939-6.
- [4] Saeed B. Niku. *Introduction to Robotics: Analysis, Control, Applications*. John Wiley & Sons, 2010. ISBN 978-0-470-60446-5.
- [5] Ryszard Jablonski, Mateusz Turkowski, and Roman Szewczyk. *Recent Advances in Mechatronics*. Springer-Verlag, Berlin Heidelberg, 2007. ISBN 978-3-540-73955-5.



# Modeling Hydraulic Accumulators for use in Wind Turbines

Henrik Brun Hansen and Peter Windfeld Rasmussen

R&D/Fritz Schur Energy, Glostrup, Denmark  
E-mail: hbh@fsenergy.dk, pwr@fsenergy.dk

## Abstract

One of the major challenges in numerical simulation of hydraulic systems, is the long computation times of accumulators. In wind power applications, the accumulators must provide necessary hydraulic energy during emergency stops, while the weight of hydraulic equipment must be minimized. Therefore, precise and efficient design tools for accumulators are essential.

This paper addresses the issue of understanding the dynamic phenomena in piston type accumulators, and how this leads to improved numerical accumulator models. Developing a numerical model has two challenges. First, the unsteady heat transfer between the accumulator gas and the wall has to be described. Secondly, a suitable real gas model has to be identified and employed. To verify the model, a series of experiments were conducted at Fritz Schur Energy in Glostrup, Denmark. The experiments were designed to investigate gas dynamical properties at various precharge pressures, maximum pressures, and ambient temperatures. These parameters were varied to obtain parameter independent conclusions. During controlled piston movements, hydraulic and gas pressures were measured together with the piston position and the gas temperature.

It was found that the simple thermal time constant approximation by Rotthäuser was suitable and stable for the application. It was also found that the Soave-Redlich-Kwong equation was overall best suited with experimental data. The Soave-Redlich-Kwong equation is as much as six times faster than the widely used Benedict-Webb-Rubin equation, independent of the ambient temperature, maximum pressure and precharge pressure.

This project concludes that the Soave-Redlich-Kwong equation should be used in simulation of piston type accumulators. It is noted that the pressure available after expansion is some 5-10 bar lower than predicted by any model. Therefore, it is suggested that more research is conducted to obtain an improved model for the heat transfer. Finally, measurement quality was confirmed by comparing measured pressure data by pressure calculations based on measured temperature.

**Keywords:** Hydraulics, Accumulator, Thermodynamics, Modelling, SIMULINK, Matlab, Verification, Thermal time constant

## 1 Problem Introduction

Hydraulic pitch systems in wind turbines require a reliable safety system to enable emergency stop without the presence of electrical power. Figure 1 shows the general system layout for each blade.

The system must supply volumes in the range 10 to 25 liters of oil in less than 10 seconds for each blade. Hence accurate calculation of the accumulator size in a temperature range from  $-30^{\circ}\text{C}$  to  $+50^{\circ}\text{C}$  is essential.

### 1.1 Motivation

Over the years a number of models have been presented and tested. Otis et al presented the Benedict-Webb-Rubin (BWR) model in 1985 [1], as an expansion of the Beattie-Bridgeman

(BB) model from 1974 [4]. However practical experience has shown that these models have limited accuracy at low temperatures. Another aspect in modern computational analysis is the time required to run the simulation. Debugging the system model shows that the accumulator model is the part requiring the smallest time steps. Hence reducing the simulation time will require a faster numerical model of the accumulator.

## 2 Theory

In order to model the phenomena in the accumulator gas, a thermodynamical model is set up using the first law of thermodynamics:

$$\dot{U} = \dot{Q}_{con} - \dot{W} \quad (1)$$

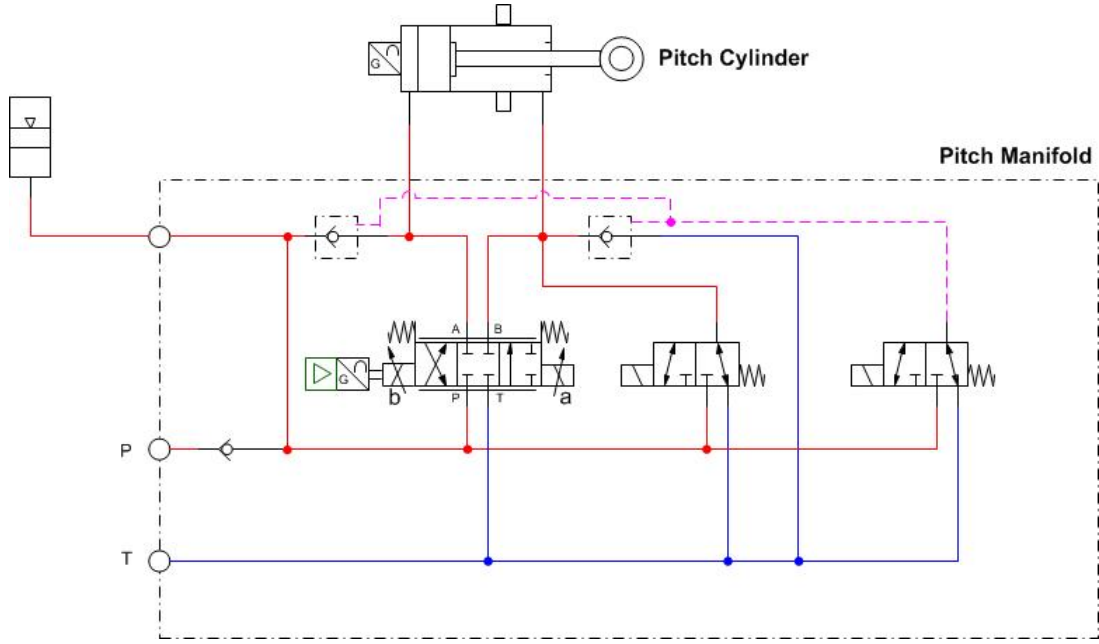


Figure 1: The system layout for each wind turbine blade

All symbols are explained in the nonmenclature (table 1 page 3). This is a simple energy balance on the gas. Consider the differential equation by Otis [2]:

$$\dot{U} = mc_v \frac{dT}{dt} + m \left( T \left( \frac{\partial p}{\partial T} \right)_v - p \right) \frac{dV}{dt} \quad (2)$$

Since:

$$\dot{W} \equiv p \frac{dV}{dt} \quad (3)$$

and the heat transfer from a system can be written

$$\dot{Q}_{con} = hA(T_a - T) \quad (4)$$

Combining equation 1, 2, 3 and 4 yields:

$$hA(T_a - T) - p \frac{dV}{dt} = mc_v \frac{dT}{dt} + m_{gas} \left( T \left( \frac{\partial p_{gas}}{\partial T} \right)_v - p_{gas} \right) \frac{dV}{dt} \quad (5)$$

Which is a first order, heterogeneous partial differential equation. It can be simplified to:

$$\frac{dT}{dt} = \frac{hA}{c_v m} (T_a - T) - \frac{mT}{mc_v} \left( \frac{\partial p_{gas}}{\partial T} \right)_v \frac{dV}{dt} \quad (6)$$

This equation can further be simplified by introducing the thermal time constant,  $\tau$ , which can be written in the form:

$$\tau = \frac{m_{gas} c_v}{hA} \quad (7)$$

Then equation 6 becomes:

$$T = \frac{(T_a - T)}{\tau} - \frac{T}{c_v} \left( \frac{\partial p_{gas}}{\partial T} \right)_v \frac{dV}{dt} \quad (8)$$

This differential equation can be solved when combined with some equation of state for the accumulator gas. The equation should express gas pressure as a function of temperature, volume and gas specific constants, as:

$$p = \mathcal{F}(T, V, C_1, C_2, \dots, C_n) \quad (9)$$

By taking the partial derivative of the equation of state, it can be inserted into equation 8:

$$T = \frac{(T_a - T)}{\tau} - \frac{T}{c_v} \left( \frac{\partial}{\partial T} \mathcal{F}(T, V, C_1, C_2, \dots, C_n) \right)_v \frac{dV}{dt} \quad (10)$$

The problem of determining the gas temperature has now reduced significantly. When the change of gas temperature from a small volume change,  $dV$ , is known, it can be substituted back into the chosen equation of state to determine the pressure change. By doing this, the pressure and temperature development in the accumulator gas can be determined accurately. However, two questions still remain:

1. How to determine the thermal time constant,  $\tau$ ?
2. Which equation of state should be chosen?

These questions frame the main challenge of this article.

## 2.1 The Thermal Time Constant

To answer the question regarding the thermal time constant, it is necessary to physically understand it. As seen in equation 7, it depends on the heat transfer coefficient,  $h$ , gas properties and the exposed wall area,  $A$ . It therefore expresses something about the time it takes for the gas to transfer heat to the accumulator wall. It can be expanded by writing out the heat transfer coefficient:

$$h \equiv \frac{Q}{A\Delta T} \quad (11)$$

Symbol	Explanation	Unit
$\dot{U}$	Rate of internal energy change	$\frac{J}{s}$
$\dot{Q}_{Con}$	Rate of convective heat transfer	$\frac{J}{s}$
$Q$	Heat flow	$\frac{J}{s}$
$\dot{W}$	Rate of work done	$\frac{J}{s}$
$m$	Gas mass	kg
$T$	Gas temperature	K
$t$	Time	s
$p$	Gas pressure	Pa (bar when noted)
$V$	Gas volume	$m^3$
$h$	Heat transfer coefficient	$\frac{W}{m^2K}$
$A$	Exposed wall area	$m^2$
$T_a$	Ambient temperature	K
$c_v$	Specific heat capacity at constant volume	$\frac{J}{kgK}$
$\tau$	Thermal time constant	s
$\mathbb{C}$	Some constant	Some unit
$v$	Specific volume	$\frac{m^3}{kg}$
$R$	The gas constant	$\frac{J}{molK}$
$T_c$	Critical temperature	K
$p_c$	Critical pressure	Pa
$\omega$	Acentric factor	-
$P_0$	Preload pressure	Bar
$T_0$	Preload (initial) temperature	$^{\circ}C$
$A_0, a, B_0, b, C_0, c$	Benedict-Webb-Rubin equation constants	-

Table 1: Nonmenclature

By inserting into equation 7,  $\tau$  becomes:

$$\tau = \frac{m_{gas}c_v}{\frac{Q}{A\Delta T}A} = \frac{m_{gas}c_v\Delta T}{Q} \quad (12)$$

In many applications,  $\tau$  is constant since the heat flux can be assumed constant. Therefore  $\tau$  is called a thermal time *constant*. However, as indicated by [2], it is not constant when examining accumulator dynamics. It must therefore be evaluated as gas temperature and heat flow changes. Equation 12 does not offer easier computations than equation 4. It merely shows that  $\tau$  is independent of exposed wall area. It solves the problem of finding the heat transfer coefficient between the accumulator gas and the accumulator wall, but instead it introduces the heat flow. In hydraulics, this property is often unknown. However, much effort has been put into approximating  $\tau$ , for example [2] and [3]. More and less complicated approximations have been presented. For the scope of this research, the simple approximation by [3] proved sufficient:

$$\tau \approx 0.3pV^{0.33} + 86.2V^{0.49} \quad (13)$$

Note: Only for piston type accumulators.

Even though  $\tau$  physically varies through compression or expansion, the results obtained when applying the presented thermodynamical model, equation 8, are not compromised much by assuming a constant  $\tau$ . This is also noted by [4].

## 2.2 Equation of State

The subject of choosing the equation of state is the main contribution of this article. Parallel models employing equation 8 with different equations of state were made and compared to experimental data.

- The Van Der Waals equation
- The Beattie-Bridgeman equation
- The Benedict-Webb-Rubin equation
- The Redlich Kwong extension to the Van Der Waals equation
- The Soave extension to the Redlich Kwong extension to the Van Der Waals equation (The Soave-Redlich-Kwong equation)

However, since the Benedict-Webb-Rubin equation is an improvement of the Beattie-Bridgeman equation, and since the Soave-Redlich-Kwong equation is an improvement of the other Van Der Waals based equations, the analysis can be reduced to the comparison between the two. They are explained in the following.

### 2.2.1 The Benedict-Webb-Rubin Equation

This model offers greater complexity than the others. It is like the Beattie-Bridgeman equation based on empirical data and it is widely recognized for being very accurate. It can be written:

$$p = \frac{RT}{V} + \frac{B_0RT - A_0 - \frac{C_0}{T^2}}{V^2} + \frac{bRT - a}{V^3} + \frac{a\alpha}{V^6} + \frac{c(1 + \frac{\gamma}{V^2})e^{-\frac{\gamma}{V^2}}}{V^3T^2} \quad (14)$$

### 2.2.2 The Soave-Redlich-Kwong equation

Soave [5] improved the Redlich-Kwong equation by introducing the acentric factor,  $\omega$ . In short, the acentric factor is a measure of how non-spherical a molecule is. It thereby takes the shape of the molecules of interest into account. The equation is especially useful in chemical engineering where phase transitions are of great importance. Since nitrogen is efficiently described by a cubic equation of state, it is expected to model accumulator gas dynamics accurately. It can be written:

$$p = \frac{RT}{V - b} - \frac{a(T)}{V(V + b)} \quad (15)$$

Where:

$$a(T) = 0.4274 \frac{R^2 T_c^2}{p_c} \left[ 1 + \kappa \left( 1 - \left( \frac{T}{T_c} \right)^{\frac{1}{2}} \right) \right]^2 \quad (16)$$

With:

$$\kappa = 0.480 + 1.57\omega - 0.176\omega^2 \quad (17)$$

and:

$$b = 0.08664 \frac{RT_c}{p_c} \quad (18)$$

Because the Soave-Redlich-Kwong equation is much simpler than the Benedict-Webb-Rubin equation, it is as much as six times faster to evaluate numerically.

## 3 Experimental Approach

The hydraulic set-up for the experiment is simple. A six liter piston type accumulator is connected to a proportional valve which in turn is connected to a pressure source. Pressure and temperature is measured on both sides of the accumulator. A sketch of the set-up is shown in figure 2.

As the purpose of the research is to compare simulated data, using the thermodynamical model from section 2, to experimental data. The data has to span different temperatures and pressures. Furthermore, as the model must predict the dynamics of accumulators fitted in wind turbines, conclusions regarding validity of the model must also hold for a wide span

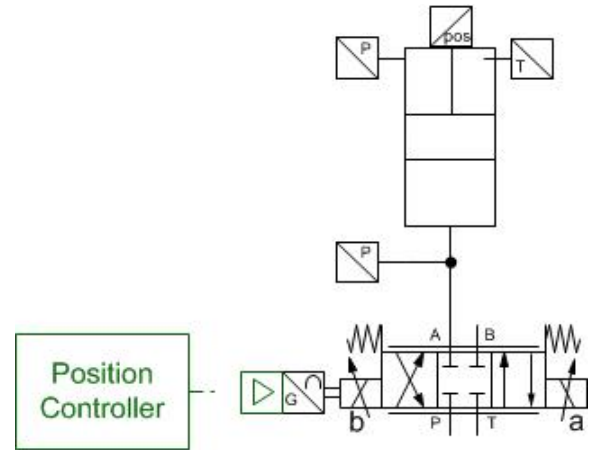


Figure 2: Overview of the experimental set-up

of ambient temperatures. The experiments conducted fall in the parameter-window illustrated in table 2 .

Maximum pressure			
Ambient Temperature	Preload Pressure		
	Low	Medium	High
Low	H, M, L	H, M, L	H, M, L
Medium	H, M, L	H, M, L	H, M, L
High	H, M, L	H, M, L	H, M, L

Table 2: Parameter window. H=High, M=Medium, L=Low.

The table illustrates that all combinations of low, medium and high ambient temperatures, preload pressures and maximum pressures. This is a total of  $3 \cdot 3 \cdot 3 = 27$  combinations. The limits of the parameters tested are listed in table 3.

Ambient Temperature	
Low	-20 C°
Medium	20 C°
High	60 C°
Preload Pressure	
Low	50 bar
Medium	100 bar
High	150 bar
Maximum Pressure	
Low	180 bar
Medium	220 bar
High	250 bar

Table 3: Limits of parameters tested

To obtain this parameter window, the piston was, for each of the preload pressures and ambient temperatures, moved to different minimum gas volumes. The minimum volumes were estimated using a steady state model and the ideal gas equation. Relatively small deviation on the maximum pressure from the estimated is expected. It is assumed that these small deviations does not influence the validity of the overall conclusions.

The desired ambient temperatures were reached by construct-

ing an insulated chamber. Using solid carbon dioxide, cold ambient temperatures was obtained (table 3 gives an estimate of about  $-20\text{ C}^\circ$ ). A heat source was used for creating the high ambient temperature environment. Figure 3 shows how a well insulated heat chamber can be constructed. Pictures of the set-up are shown in figure 4.

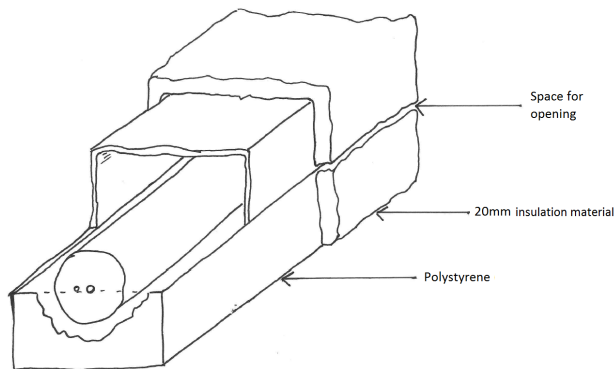


Figure 3: Sketch of how to insulate an accumulator from the environment

In order to stress the numerical models, steep pressure gradients are experimentally obtained. Practical experience has shown that it is easier to predict the behaviour at small pressure and temperature gradients than the opposite. To obtain high gradients, the gas was compressed and expanded by a realistic in application rate. An example of the expansion and compression time series is given by figure 5.

In the following, the measured temperatures and pressures are plotted versus simulation results with the experimentally obtained volumes as input. In this way, it is easy to see which real gas model best fits experimental results.

#### 4 Results

A limited portion of the generated results are presented. However, results from both low, medium and high ambient temperatures are shown. Also, both temperature and pressure measurements are compared to calculated results. Please note that a first order filter was used on the temperature data to limit noise. Of course this results in phase transition which should be ignored.

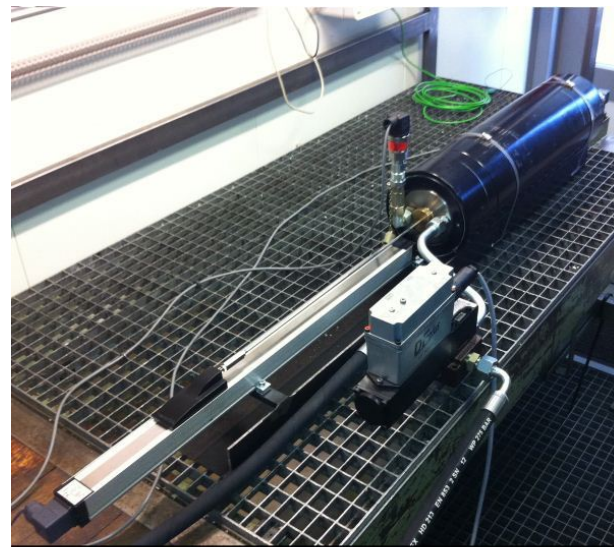


Figure 4: The setup from two angles.

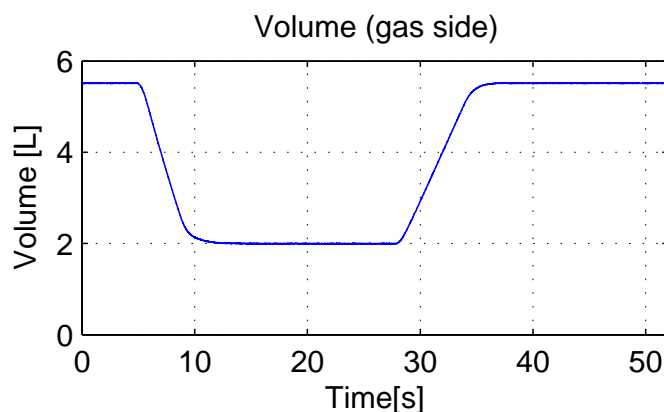


Figure 5: An overview of the experimental compression and expansion of the accumulator gas.

By driving the real gas model with the measured temperature, that is, using the data from the right hand side plots to drive the calculations in the left hand side plots, plots like figure 12 can be created.

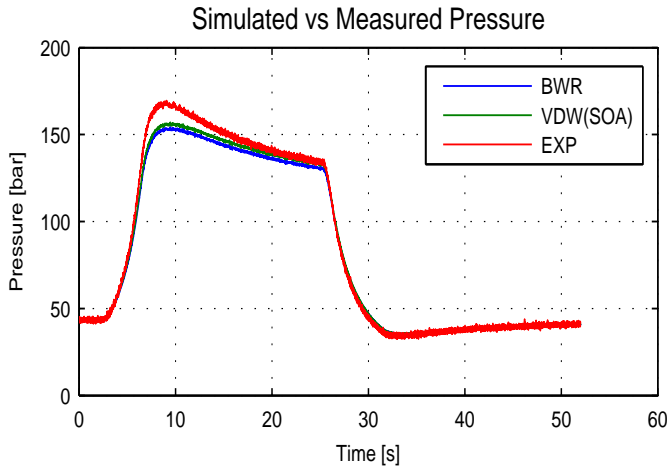


Figure 6:  $p_0 = 48 \text{ bar}$ ,  $T_0 = 30^\circ\text{C}$

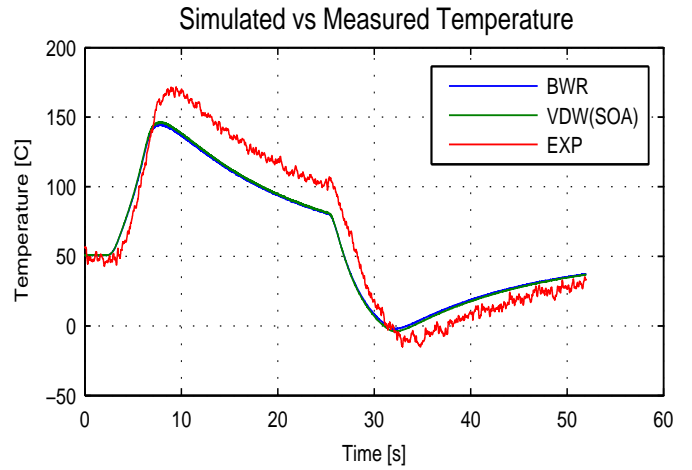


Figure 9:  $p_0 = 48 \text{ bar}$ ,  $T_0 = 30^\circ\text{C}$

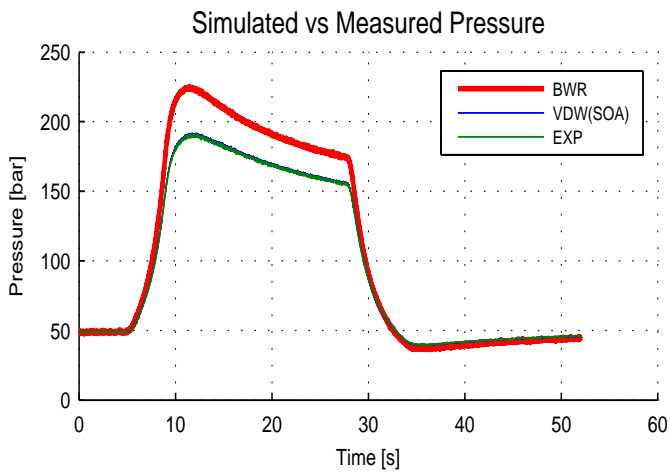


Figure 7:  $p_0 = 48 \text{ bar}$ ,  $T_0 = -5^\circ\text{C}$

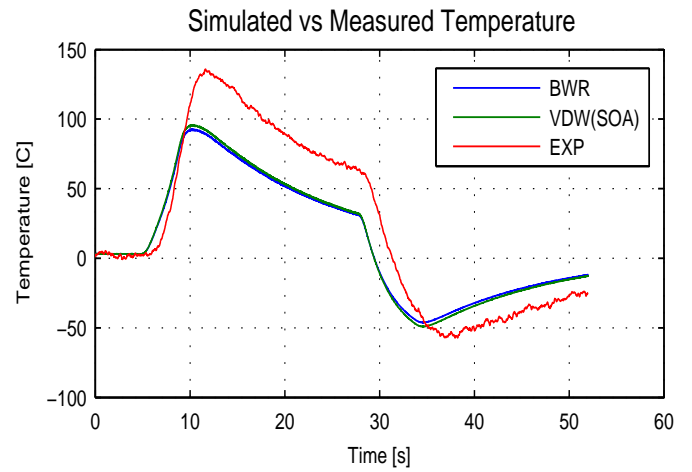


Figure 10:  $p_0 = 48 \text{ bar}$ ,  $T_0 = -5^\circ\text{C}$

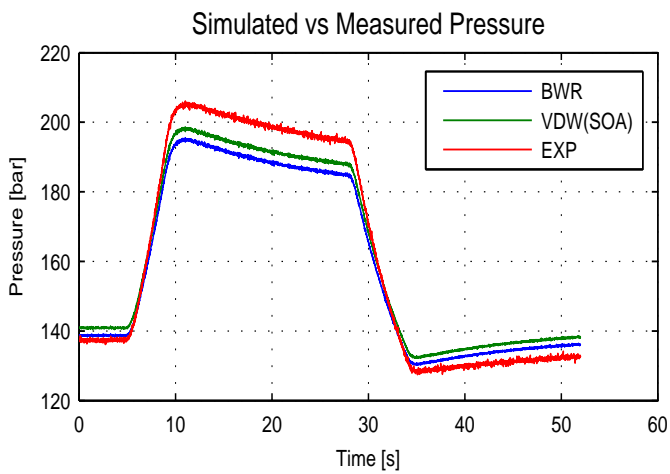


Figure 8:  $p_0 = 140 \text{ bar}$ ,  $T_0 = 80^\circ\text{C}$

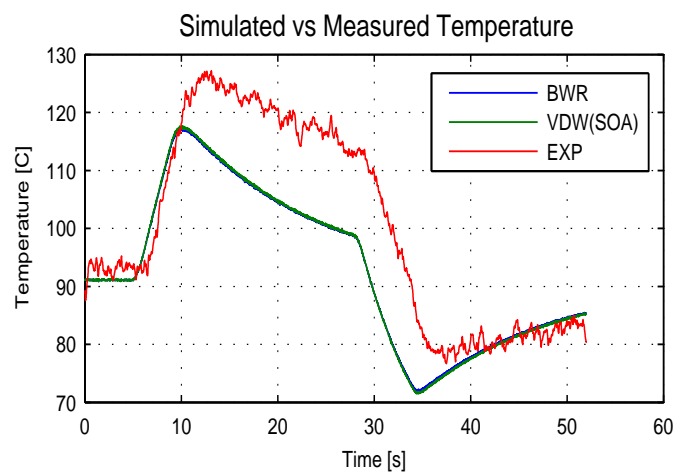


Figure 11:  $p_0 = 140 \text{ bar}$ ,  $T_0 = 80^\circ\text{C}$

## 5 Discussion

There are two clear observations from the presented results: Firstly, the two real gas models resemble in comparison to

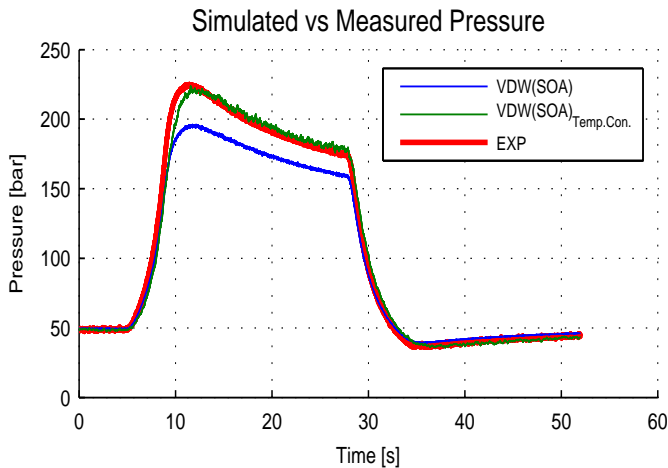


Figure 12:  $p_0 = 48 \text{ bar}$ ;  $T_0 = -5^\circ\text{C}$ , pressure calculations with calculated versus measured temperature input.

the experimental results. They both predict pressures that are some 5-10 bar lower than measured. At higher compression and expansion ratios, the calculation error is higher. Secondly, there are some clear deviations between the simulated data and the measured data. The first observation enlightens the benefits of the Soave-Redlich-Kwong equation. While maintaining the overall accuracy, it greatly reduces computation times.

The second observation requires some examination. Clearly, some error sources have to be identified. Several such error sources could be suggested:

- Bad measurements
- Inaccurate real gas model
- Incorrect or inaccurate unsteady model

In the following, each of these suggestions are examined. Great effort has been put into validating and calibrating the temperature measurement devices in controlled environments prior to the research investigations. If the temperature measurements were bad despite the validation attempts, bad pressure calculations would be a result. However, as seen in figure 12, the pressure calculations are much more accurate if the real gas model is evaluated using the measured temperature.

Figure 12 is data from the same experimental run as figure 7. It can be seen that much more accurate pressure calculations can be performed if the measured temperature is used as input to the real gas model. Similar results are obtained for all other parameters, though not presented here. This serves to validate:

- The real gas model
- The pressure measurements
- The temperature measurements

It can therefore be concluded that the primary source of error is the limited accuracy in the thermodynamical model, equation 8. By analysing the presented data, this work serves to suggest the need for a better thermodynamical model, in order to precisely determine the dynamical behaviour of accumulators. The presented thermodynamical model has limited accuracy, because it does not model the accumulator wall. It merely suggests that the heat is transferred from the accumulator gas to the surroundings. Instead, a more precise model would employ a thick wall solution for the accumulator wall. Also, the heat conduction from the hydraulic oil to the accumulator gas (and vice versa) is not modelled. Especially when the ambient temperature are very different from the oil temperature, this will have a significant contribution.

Aside from these major issues, minor error sources in the thermodynamical model can be identified. One minor error source is the absence of the heat generated by the viscous oil in the model and also of gas flow at the accumulator wall. Especially the viscous gas flow heat contribution is a challenge to model as a function of volume change. It is likely to have negligible effect at low rate of volume change, since flow phenomena are unimportant to the problem compared to compressibility effects.

The model may be constructed by employing a heat transfer model for the accumulator wall. The model should include heat convection from the gas to the wall, heat conduction through the wall (such that temperature in the wall changes with the wall depth), heat conduction from the wall to the surroundings and also radiation from the accumulator to adjacent surfaces. Also, the model should include heat contribution from the accumulator oil by conduction through the piston to the gas. This should all serve to enlarge the insulation properties of the accumulator with respect to the gas, thus increase the peak temperature after compression.

As can be seen in the results, the presented model predicts temperature- and pressure changes better after the expansion than after the compression. As accumulators are loaded during wind turbine operation at much slower rates than conducted in this experiment, the need for performance predictions here vanishes. As the accumulators empty very rapidly during emergency stops of the turbines, the crucial performance phase of the accumulator is during gas expansion. The need for a better thermodynamical model, as discussed above, may therefore have greater importance for areas in hydraulics where accumulators are loaded at high rates of volume change.

## 6 Conclusion

The presented thermodynamical model has limitations at high rates of volume changes. This is most likely due to the inaccurate modelling of the insulation properties of the accumulator. The inaccuracies are some 5-10 bar difference between measured and calculated data just after compression and expansion. The difference is higher for higher compression/expansion ratios and the difference approaches zero for infinitely slow rates of volume changes.

A better thermodynamical model can maybe be established by implementing a heat balance on the accumulator wall in the model.

The two presented real gas models; The Benedict-Webb-Rubin equation and the Soave-Redlich-Kwong equation are almost similarly accurate. The Soave-Redlich-Kwong model suggests a slightly higher pressure after compression compared to the Benedict-Webb-Rubin equation. Since the Soave-Redlich-Kwong equation is much more efficient than the Benedict-Webb-Rubin equation, this work concludes that the Soave-Redlich-Kwong equation should replace the Benedict-Webb-Rubin equation in future simulations.

The quality of the measurements were confirmed by calculating the pressure using the Soave-Redlich-Kwong equation with the measured temperature, and then comparing the calculations to measured pressures. Since the calculated data matched the measured data extremely well, it is concluded that the measurements are accurate, dynamic and reliable. Also, it is concluded on this basis that the Soave-Redlich-Kwong real gas model is accurate enough for any application within the wind turbine technology.

## References

- [1] Pourmovahed A. Otis, D. R. An Algorithm for Computing Nonflow Gas Processes in Gas Springs and Hydropneumatic Accumulators. *Journal of Dynamic Systems, Measurement, and Control*, 107:93–96, 1985.
- [2] A Pourmovahed and D. R. Otis. An Experimental Thermal Time-Constant Correlation for Hydraulic Accumulators. *Journal of Dynamic Systems, Measurement and Control*, 112:116–121, 1990.
- [3] S. Rotthäuser. *Verfahren zur Berechnung und Untersuchung hydropneumatischer Speicher*. Fakultät für Maschinenwesen der Rheinisch-Westfälischen Technischen Hochschule Aachen, Essen, Germany, 1993.
- [4] D. R. Otis. New Development in Predicting and Modifying Performance of Hydraulic Accumulators. *National Conference on Fluid Power*, 1974.
- [5] G. Soave. Equilibrium Constants from a Modified Redlich-Kwong Equation of State. *Chem. Eng. Sci.*, 27:1197–1203, 1972.

# Valve Technology 2



# **Numerical and Experiential Study of Motion Control Using Pressure Feedback**

M. B. Kjelland and M. R. Hansen

Department of Engineering, University of Agder, Grimstad, Norway  
E-mail: magnus.b.kjelland@uia.no, michael.r.hansen@uia.no

## **Abstract**

This paper is concerned with the inherent oscillatory nature of pressure compensated motion control of a hydraulic cylinder subjected to a negative load and suspended by means of an overcenter valve. A pressure feedback scheme that indirectly eliminates the oscillations is investigated. The indirect control scheme utilizes pressure feedback to electronically compensate the metering-out allowing for the removal of the compensator and, subsequently, elimination of the oscillations. The suggested electronic compensation scheme is implemented and examined in a single degree-of-freedom test rig actuated by means of a double acting hydraulic cylinder. The control scheme is compared with other control schemes and the importance of measurement filtering and controller cycle time are investigated.

**Keywords:** Overcenter valve, pressure feedback, negative load, experimental verification

## **1 Introduction**

The use of overcenter valves or counterbalance valves are widely used in hydraulics on such applications as cranes, telehandlers and winches as an integrated part in the actuator control. They are distributed to each actuator (degree of freedom) depending on the type of external loading. They are multi-functional and, normally, they serve at least the following functions:

- leak tight load holding
- shock absorption
- cavitation protection at load lowering
- load holding at pipe burst
- no drop before lift

It is, however, well known that they tend to introduce instability in a system, especially when the flow supply is pressure compensated. This is the case when the directional control valve that supplies flow to the actuator suspended by the overcenter valve is equipped with an internal compensator in series with the main spool; a so-called flow control valve. As the latter is frequently asked for by system manufacturers a major problem in present day hydraulics is to design pressure compensated systems containing overcenter valves that offer stable load lowering performance without unnecessarily compromising system efficiency and response.

Naturally, this problem has attracted a lot of attention with emphasis on modeling and parameter variation [1..16] revealing a number of common stabilizing characteristics. They include increased volume between directional valve and actuator, reduced pilot area ratio as well as reduced pay

and inertia load, whereas the influence by a number of other design variables remain less obvious.

As pointed out in [7] the operation of the over-center valve is application sensitive, greatly increasing the complexity of choosing/designing it. Adding to the difficulties is the fact that hard to control quantities such as friction and hysteresis in the overcenter valve also are sources of instability [8]. Finally, it should be noted that stability only is one of several performance parameters for an over-center valve system. The different functionalities constitutes a set of design constraints whereas power consumption, stability, response time, load dependency, manufacturability and costs represents performance criteria.

The popularity of the pressure compensation is mainly due to basic functionality: it allows several actuators to be driven simultaneously with minimal influence between the different active circuits. However, it does also provide an important advantage in closed loop motion control because the valve flow is a well-defined function of the control signal removing the disturbing influence from fluctuating loads.

Therefore, this paper is concerned with the removal of the oscillatory nature of an overcenter valve system taking into account that the above mentioned design criteria cannot be ignored. In [16] an alternative approach that simply moves the main throttling from the overcenter valve to the return orifice of the main directional control valve is introduced. In that case the overcenter valve is piloted open during lowering and the system is stable, however, it is limited with respect to the load variations that can be handled. In [17] a pressure feedback scheme that has as target to maintain the high pass filtered pressure gradient equal to zero is adopted with a view to reduce oscillations while maintaining other

performance criteria related to the motion control. It yields lead compensation with a markedly improved performance, however, it requires a valve with a bandwidth that is significantly higher than the mechanical-hydraulic system. Alternatively, if at least two pressure transducers are available it is possible to abandon the mechanical-hydraulic compensation and, subsequently, the source of the oscillations, by using the measured metering-out pressure drop to compensate variations in pressure drop via the spool position. In that case the overcenter valve is maintained with unaltered functionality and the ability to share flow between actuators and reject load disturbances is maintained. The extra use of pressure transducers is easily motivated by the increasing level of instrumentation and computational power in hydraulically actuated machinery today.

However, the experimental implementation is needed. The main contribution of this paper is the practical implementation of the proposed electronic pressure compensation scheme on a single degree-of-freedom test rig with nonlinear dynamic characteristics using typical commercially available valves.

## 2 Considered system

In fig. 1 the main components of a pressure compensated overcenter valve circuit are shown. They comprise a 4/3 way directional control valve (in lowering position) with a compensator in series that maintains the pressure drop across the main spool metering orifice approximately constant. Further, the circuit contains an actuator (here a double acting cylinder) and the overcenter valve. Finally, a shock valve and a suction valve (not shown) are typically inserted so that cavitation and pressure peaks caused by the dissipation of the kinetic energy of the payload inertia are avoided.

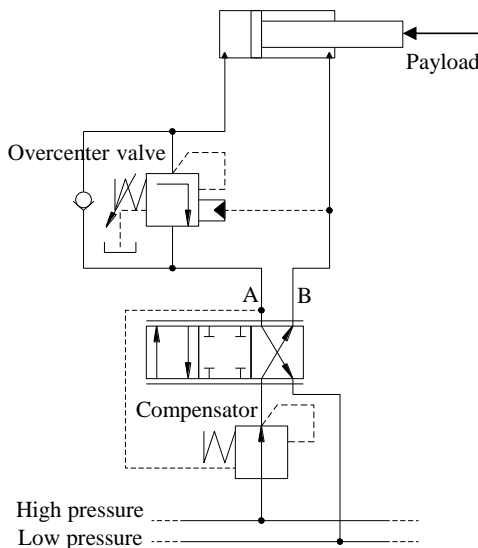


Figure 1: Single overcenter valve circuit with compensator.

In fig. 2 a simplified circuit is shown including the core components and parameters.

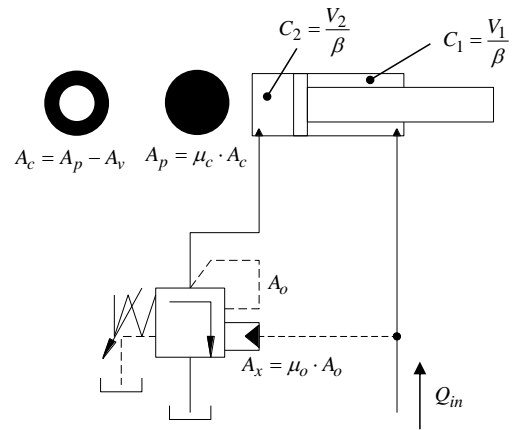


Figure 2: Simplified circuit.

Linearizing the governing equations for this system and formulating the transfer function between input signal and output velocity it is possible to utilize the Routh-Hurwitz stability criterion yielding:

$$\frac{C_1}{C_2} > \frac{\mu_o}{\mu_c} \cdot \frac{K_{qo}}{K_{qo} + K_{qp}} \quad (1)$$

In eq. (1) the flow gains of the overcenter valve with respect to valve opening pressure,  $K_{qo}$ , and valve pressure drop,  $K_{qp}$ , appear together with the capacitances and the area ratios of the overcenter valve and the cylinder, respectively. Normally,  $K_{qo} \gg K_{qp}$ , hence, for normal operation and typical values for  $\mu_o = 2.8$  the stability criteria is impossible to satisfy in the major part of the cylinder stroke. The expression in (1) is based on hard parameters, i.e., damping, friction, and viscosity do not enter into these equations.

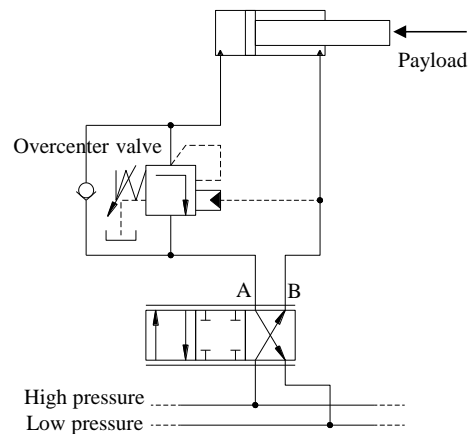


Figure 3: Single overcenter valve circuit without compensator.

The parameters that exhibit the strongest uncertainties are probably the capacitances via the influence of the bulk modulus of the fluid. However, it is clear that the basic overcenter valve circuit is prone to instability and oscillatory behavior. Removing the compensator, see fig. 3, eliminates the possible instability of the simplified circuit, in fact, the Routh-Hurwitz criterion now yields:

$$\mu_c \cdot C_l > 0 \quad (2)$$

Which is always fulfilled for physical meaningful parameters. Another important stabilizing factor is that the non-compensated circuit will have more throttling across the return orifice yielding higher pressure levels and quite often a fully piloted open overcenter valve. In order to benefit from this it is, however, necessary to use a 4-port vented overcenter valve as indicated in figs. 1..3.

### 3 Electronic pressure compensation

The challenge with the circuit in fig. 3 is to facilitate flow sharing with several circuits active simultaneously and to reject load disturbances during motion control. The proposed electronic pressure compensation is based on an electro hydraulically actuated directional control valve with closed loop spool position control, see fig. 4.

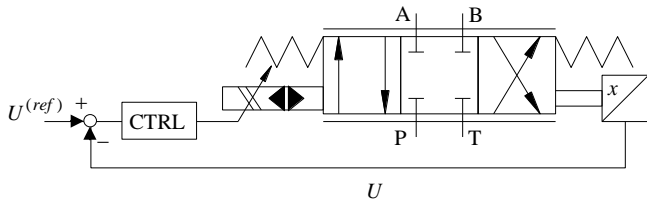


Figure 4: Inner spool position control loop.

For such a valve, we can assume that the steady state spool position will be a linear function of the input signal:

$$x = K_{xU} \cdot U^{(ref)} = K_{xU} \cdot U \quad (3)$$

Also, the flow through the valve may be expressed using the orifice equation as:

$$Q = C_d \cdot A_d(x) \cdot \sqrt{\frac{2}{\rho} \cdot \Delta p_{mo}} \quad (4)$$

Combining eqs. (3) and (4) yields:

$$Q = C_v(U) \cdot \sqrt{\Delta p_{mo}} \quad (5)$$

where

$$C_v(U) = C_d \cdot A_d(K_{xU} \cdot U) \cdot \sqrt{\frac{2}{\rho}} \quad (6)$$

The variation of the discharge area is, in general, not a linear function, hence, some effort must be devoted to set up the inverse of eq. (6) yielding some functional relationship between the input signal,  $U$ , to the valve and the orifice parameter,  $C_v$  :

$$U = f(C_v) \quad (7)$$

This functional relationship may be implemented in an electronic pressure compensation together with a continuous measurement of the pressure drop across the metering orifice to meet a flow reference, see fig. 5.

Obviously, this is a purely open loop control of the valve flow, however, that corresponds to the classical pressure compensated system in fig. 1.

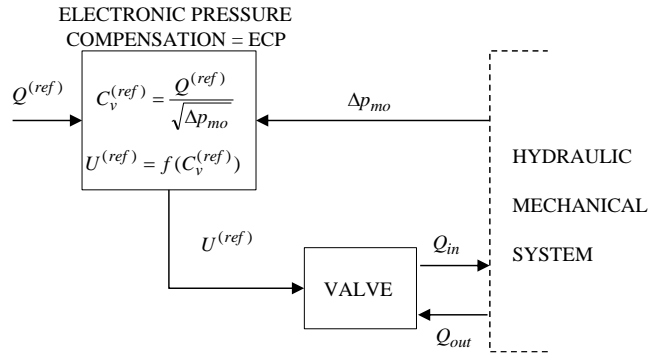


Figure 5: Basic components of electronic pressure compensation.

The electronic pressure compensation easily fits into a typical motion control scheme with a velocity feed forward term and a position feedback term, see fig. 6.

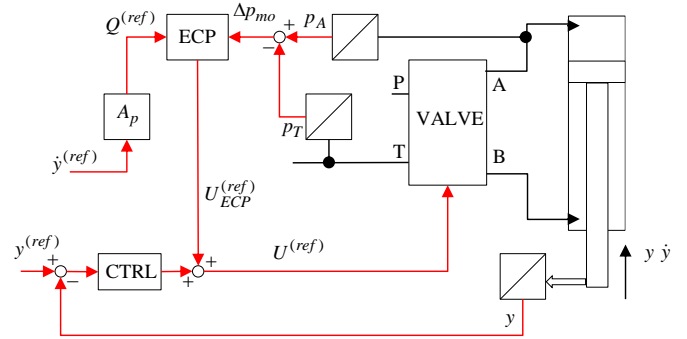


Figure 6: Electronic pressure compensation implemented in the feed forward path of a motion control scheme.

With position feedback from the actuator it is also possible to do the motion control without a variable feed forward term, i.e., without the electronic pressure compensation. This gives a simpler setup, however, it will be less efficient handling load disturbances or, in general, large load variations.

### 4 Experimental setup

In fig. 7 the experimental setup is shown in diagram form, and the mechanical dimensions are shown in fig. 8.

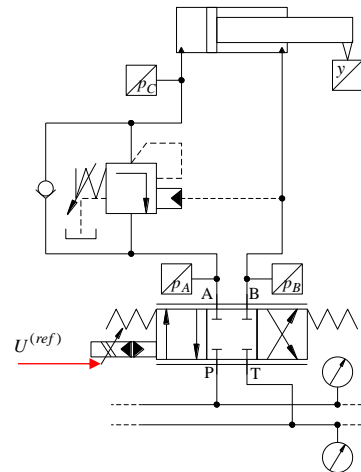


Figure 7: Hydraulic diagram of experimental setup.

The directional control valve is part of a Sauer-Danfoss PVG32 valve group with several valve units both with and without pressure compensation. In fig. 7 is shown a valve with no compensator. The overcenter valve can be chosen from a range of Sun Hydraulics vented overcenter valves with pilot area ratio ranging from 1 to 5.

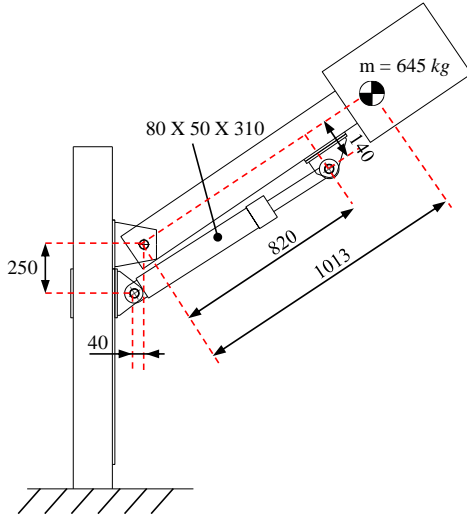


Figure 8: Mechanical system with all measurements in mm.

The experimental setup is inserted in a ring line system with the fluid power being supplied by a pressure controlled HPU that maintains a pressure of 207 bar.

The electronic pressure compensation was only developed for the load lowering because this is where the system potentially becomes unstable or highly oscillatory. Also, the metering orifice is chosen as the return orifice A-T, for two reasons: it has a higher pressure drop during lowering thereby and the internal pressure drops are expected to be smaller in the outlet line of the valve as compared to the inlet thereby reducing the uncertainties associated with the actual pressure drop across the metering orifice.

For the main spool and the 24V electrohydraulic actuation the curves in fig. 9 apply, as adopted from the PVG32 catalogue [18].

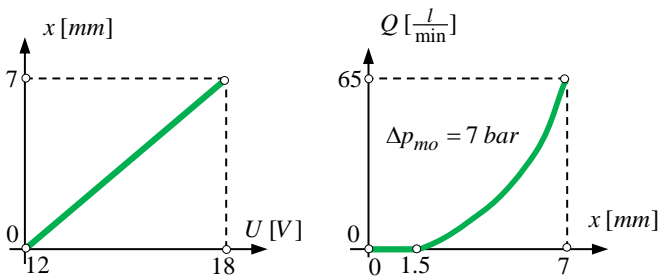


Figure 9: Spool travel vs. input signal (left) and volume flow vs. spool travel (right) for the main spool.

The mathematical expression for the flow as a function of the spool travel is expressed in eq. (8).

$$Q(x) = 0.327 \cdot x^3 - 2.236 \cdot x^2 + 10.716 \cdot x - 12.319 \quad (8)$$

$$[Q] = \frac{l}{min} \quad [x] = mm$$

From this a curve fit was developed to describe the variation of the input signal vs. the orifice parameter because this is what is ultimately needed in the electronic compensation, see fig. 5. In parallel, the same correlation was obtained experimentally by measuring the volume flow through the A-T orifice for four different pressure drops at different input signals. In fig. 10 the resulting curves are shown, and clearly there are some deviations around the smallest openings including a difference in actual dead band. The curve fit based on the measurements were used in the electronic compensation scheme since they easily produced better motion control performance than those derived from the catalogue. The entire valve characteristics were not mapped in this work since only the portion displayed in fig. 10 was used

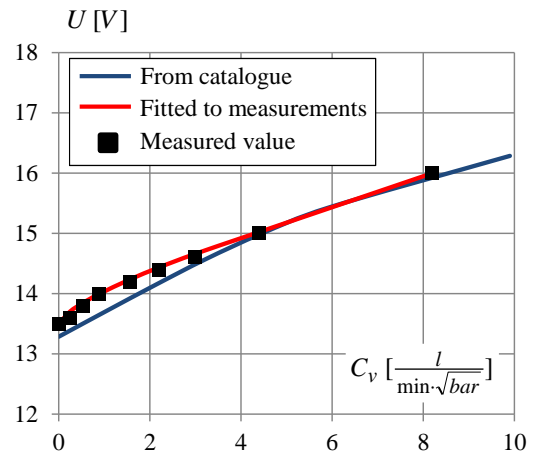


Figure 10: Input signal vs. orifice parameter as derived from catalogue data and from measurements.

The mathematical expression for the curve fitted to the measurements is given in eq. (9)

$$U(C_v) = 13.45 + 0.538 \cdot C_v^{0.699} + 1.302 \cdot 10^{-6} \cdot C_v^{5.544} \quad (9)$$

$$[U] = V \quad [C_v] = \frac{l}{min \cdot \sqrt{bar}}$$

Continuous pressure measurements were only carried out for  $p_A$  because the tank pressure outside the valve consistently was read to  $p_T = 0 \text{ bar}$ . The actual back pressure at the metering orifice, however, was estimated based on the current flow to be as high as  $\Delta p_{ret} = 1.5 \text{ bar}$ . This was included in the electronic pressure compensation and had some correcting influence for situations with small  $p_A$  values.

## 5 Experimental results

For the experimental investigations emphasis has been on lowering. In fig. 11 the inlet pressure,  $p_B$ , is plotted when lowering the arm by retracting the cylinder. In both cases an overcenter valve with pilot area ratio  $\mu_o = 3$  is used and the cylinder is retracted a distance  $\Delta y = 0.2 \text{ m}$  in  $\Delta t = 5 \text{ s}$ .

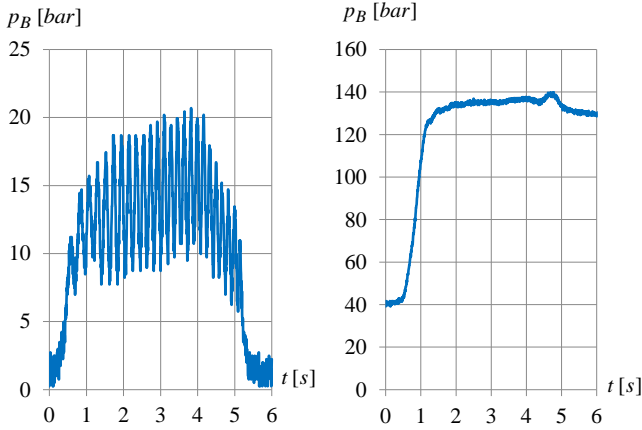


Figure 11: Inlet pressure,  $p_B$ , vs. time during cylinder retraction for a compensated (left) and a non-compensated (right) system.

It is apparent that removing the compensator eliminates the oscillations. In this case, the overcenter valve is simply piloted open yielding a very stable system.

Next, the control scheme in fig. 6 is implemented, however, in two versions: variable feed forward gain with continuous measurement of  $\Delta p_{mo}$  and constant feed forward gain based on a fixed value of  $\Delta p_{mo}$  which is estimated. The latter approach basically corresponds to tuning the feed forward gain to handle a range of pressure levels as good as possible. The pressure level is adjusted by means of the overcenter valve to three typical values and the reference motion is derived from a trapezoid shaped velocity profile that retracts the cylinder  $\Delta y = 0.3\text{ m}$  in  $\Delta t = 5\text{ s}$ , see fig. 12.

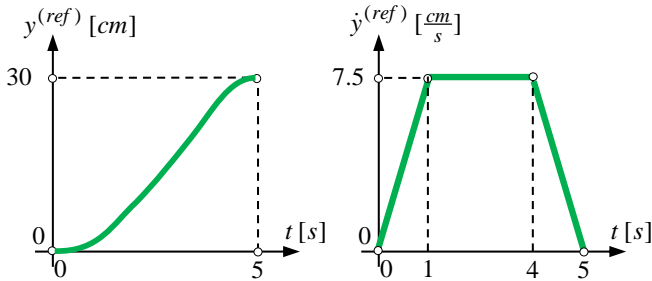


Figure 12: Reference position and velocity for cylinder.

In figs. 13 and 14 the resulting position error is shown for the variable and the constant feed forward gain. The errors are logged for three different load cases that are characterized by an average value for  $p_A$  of 15, 60 and 125 bar, respectively. The back pressure is adjusted by means of the crack pressure of the overcenter valve while draining the pilot line.

The position error at the end of the 5 s travel is eventually removed by means of the position feedback control. As can be deduced from figs. 14 and 15 the constant feed forward gain was calibrated to yield the best possible result for a pressure drop of  $\Delta p_{mo} = 60\text{ bar}$  across the metering orifice.

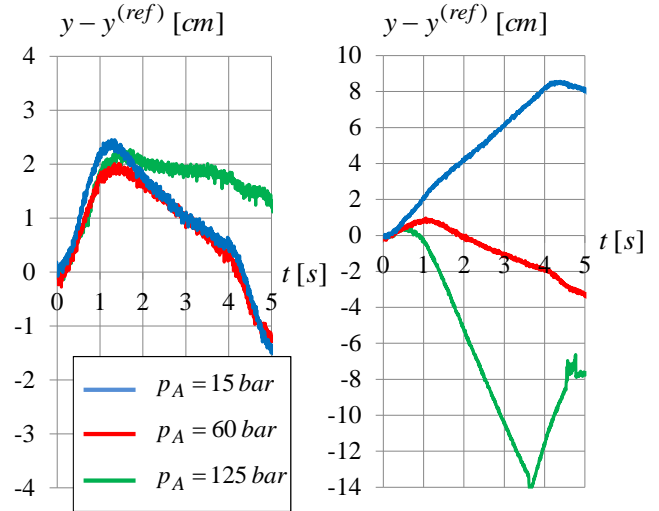


Figure 13: Position error for variable (left) and constant feed forward gain (right) without pressure feedback control.

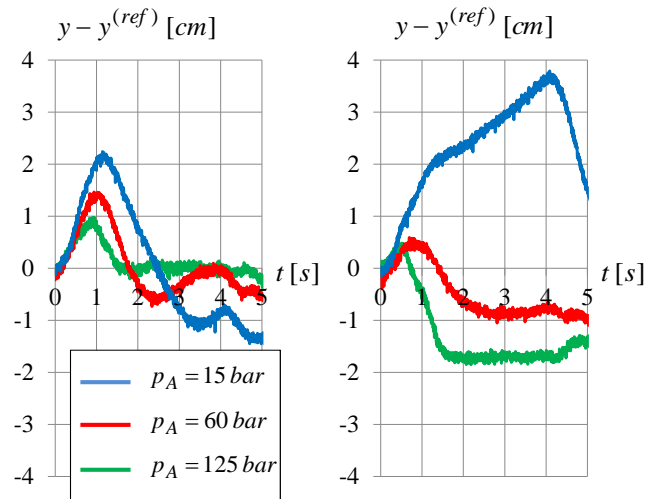


Figure 14: Position error for variable (left) and constant feed forward gain (right) with pressure feedback control.

In fig. 15 the input signal (subtracted the 12V offset) and its contributions from the feed forward and the feedback path of the control scheme are shown for  $p_A = 125\text{ bar}$ .

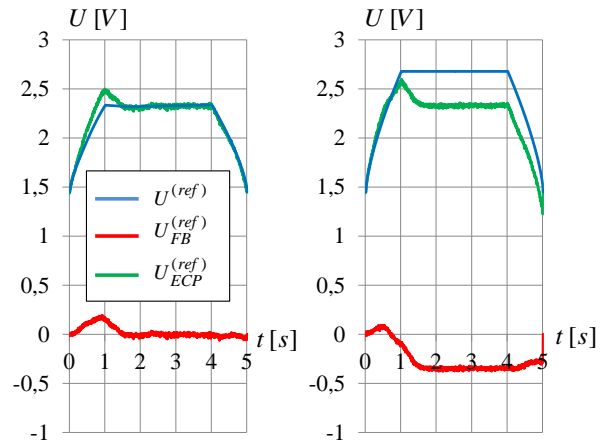


Figure 15: Valve input signal for variable (left) and constant feed forward gain (right).

In general, the use of variable feed forward gain, i.e., electronic pressure compensation, reduced the demands on the closed loop controller. The price for this improved robustness is the introduction of pressure transducers and a somewhat more complex computation of the input signal. The main task may easily lie in the development of expressions like eqs. (8..9) that are needed in order for the proposed control scheme to work better than the constant feed forward.

In practice, the proposed control scheme may depend on the type of filtering of the pressure measurements as well as the cycle time of the controller. In the current implementation the filtering of the measurements is done via moving average and investigations clearly show that the method is quite robust towards the time span of the moving average. This reflects that it is not a rapidly varying parameters that is needed for the electronic pressure compensation but only a relatively slow varying steady state pressure level.

The influence of the cycle time is shown in fig. 16 where the position error is plotted vs. the cycle time.

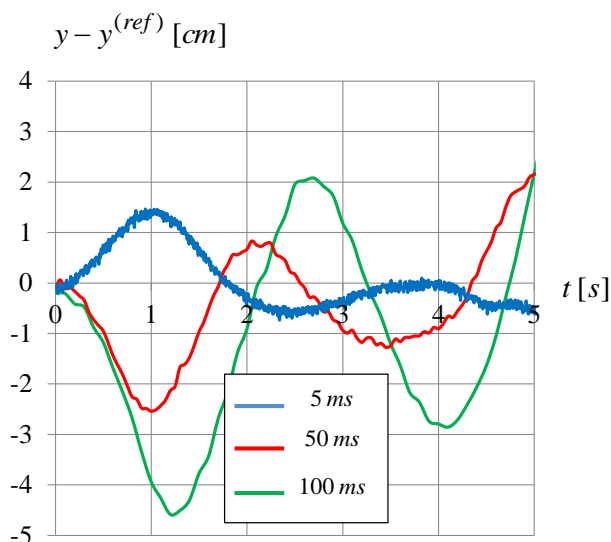


Figure 16: Position error vs. cycle time.

It seems that at a cycle time around 50 ms the performance begins to deteriorate.

## 6 Conclusions

An electronic pressure compensation control scheme is put forward that allows the use of non-compensated directional control valves in closed loop motion control is presented and implemented in a practical system consisting of commercially available components. The control scheme measure the pressure drop across the metering-out orifice and continuously adjusts a feed forward gain that is computed based on a preprocessing of the valve characteristics. The main purpose of introducing the scheme is to reduce the inherently oscillatory nature of a pressure compensated valve in series with an overcenter valve. The experimental implementation reveals that abandoning the compensator eliminates the oscillatory nature of the hydraulic circuit. The electronic pressure compensation can

be introduced in motion control via a velocity feed forward term but the valve catalogue data may not be adequate to represent the valve characteristics in a sufficiently precise manner. This seems to be most predominant at small openings of the valve. From the investigations conducted in this paper the proposed scheme gives a better performance than a pressure compensated circuit (difference in oscillation level) and a better performance than a non-compensated circuit with constant feed forward (less sensitive to load variations). In general, the proposed scheme seems to be a realistic alternative within motion control of hydraulic actuators.

## References

- [1] S Miyakawa. Stability of a Hydraulic Circuit With a Counterbalance-Valve, *Bulletin of the JSME*, 21(162), 1978.
- [2] G. Overdiek, Dynamisches Verhalten von Senkbremms-Sperrventilen im Hydraulik-Hubwerk. *Ölhydraulik und Pneumatik*, 24(11), 1980 (in german).
- [3] G Overdiek. Design and Characteristics of Hydraulic Winch Controls by Counterbalance Valves, *European Conference on Hydrostatic Transmissions for Vehicle Applications*, Aachen, 1981.
- [4] T Persson, P Krus, and J O Palmberg. The Dynamic Properties of Over-Center Valves in Mobile Systems. Proc. of *2nd International Conference on Fluid Power Transmission and Control*, Hangzhou, China, 1989.
- [5] Y Ramli, P J Chapple, D G Tilley. An Application of computer aided design (CAD) in Hydraulic Systems Using Counterbalance Valves. Proc. of *4th International Conference on CAD and CG*, Wuhan, China, 1995.
- [6] B Zähe. Stability of Load Holding Circuits with Counterbalance Valves. Proc. of *8th International Bath Fluid Power Workshop*, Bath, UK, 1995.
- [7] P J Chapple and D G Tilley. Evaluation Techniques For The Selection of Counterbalance Valves. Proc. of *The Expo and Technical Conference for Electrohydraulic and Electropneumatic Motion Control Technology*, Anaheim, USA, 1994
- [8] H Handroos, J Halme and M Vilenius. Steady State and Dynamic Properties of Counterbalance Valves. Proc. of *3rd Scandinavian International Conference on Fluid Power*, Linköping, Sweden, 1993.
- [9] H. Zoebel. Senkbremssventile und Ventilkombinationen zur Steuerung der Bewegungsgeschwindigkeiten. *Ölhydraulik und Pneumatik*, 42(11-12), 1998 (in german).

- [10]F Weingarten. Aufbau Hydraulischer Zeitglieder und Ihr Einsatz im Signalzweig hydraulisch-mechanischer Regelungen. Dissertation Dr.-Ing., *Fakultät für Maschinenwesen der Rheinisch-Westfälischen Technischen Hochschule, Aachen*, 1983 (in german).
- [11]T Persson, P Krus, and J O Palmberg. The Dynamic Properties of Over-Center Valves in Mobile Cranes. Proc. of *9th AFK Conference for Hydraulics and Pneumatics*, Aachen, West Germany, 1990.
- [12]M R Hansen, and T O Andersen. A Design Procedure for Actuator Control Systems Using Optimization. Proc. of *The 7th Scandinavian International Conference on Fluid Power*, Linköping, Sweden, 2001.
- [13]T O Andersen, M R Hansen, P Pedersen, and F Conrad. The Influence of Flow Force Characteristics on the Performance of Over Centre Valves. Proc. of *The 9th Scandinavian International Conference on Fluid Power*, Linköping, Sweden, 2005.
- [14]M R Hansen, and T O Andersen. Performance of Mobile Cranes Using Pressure Feedback. Proc. of *2001 Drives and Controls/Power Electronics Conference*, London, UK, 2001.
- [15]B Zähe, Allt under kontroll, *Fluid Scandinavia*, 2, 2009, (in swedish).
- [16]P A Nordhammer, M K Bak and M R Hansen. A Method for Reliable Motion Control of Pressure Compensated Hydraulic Actuation With Counterbalance Valves. Proc. of *2012 ICCAS12 12th International Conference on Control, Automation, and Systems*, Jeju, Korea, 2012.
- [17]M R Hansen and T O Andersen. Controlling a negative loaded hydraulic cylinder using pressure feedback. Proc. of *IASTED International Conference Modelling, Identification, and Control : Proceedings* Innsbruck, Austria, 2010.



## Lubricity of new Tailor-Made Fuels from Biomass

A. Weinebeck, H. Murrenhoff

IFAS, RWTH Aachen University, Aachen, Germany  
E-mail: Alexander.Weinebeck@ifas-rwth.aachen.de,  
Hubertus.Murrenhoff@ifas-rwth.aachen.de

### Abstract

The interactions of new biofuels and standard engine components are being investigated at the Institute for Fluid Power Drives and Controls (IFAS) at RWTH Aachen University as part of the research of the cluster of excellence “Tailor-Made Fuels from Biomass”. Since modern common rail fuel pumps are fuel lubricated special interest lays on the lubricity of new fuels. At IFAS a High Frequency Reciprocating Test Rig (HFRR) is used to screen possible biofuel candidates with regard to this property. Most of these substances show lubricating abilities similar to those of modern diesel fuels. Nevertheless with 2-Methyltetrahydrofuran a remarkable outlier can be found among the favoured fuel candidates. To unravel the influences of certain molecule structures additional substances were included into the experimental research. By comparing the wear scars of linear alkanes, alkenes and alcohols produced in the HFRR the influence of the molecules chain length and functional group is analysed. This paper gives an introduction to the HFRR test set up and presents the experimental results of the recently screened biofuel candidates.

**Keywords:** Biofuel, Lubricity, HFRR, Tailor-Made Fuels from Biomass

### 1 The Cluster of Excellence “Tailor-Made Fuels from Biomass”

Due to the exploitation of non-renewable resources in modern times some significant effort is put in the development of alternative concepts of mobility. One approach to this task is the usage of the highly sophisticated technology of combustion engines in combination with fuels based not on mineral oil but on renewable biological materials such as food wastes or wood. Within the cluster of excellence “Tailor-Made Fuels from Biomass” at RWTH Aachen University such new biofuels are being developed and tested in an interdisciplinary approach, see *Figure 1*.

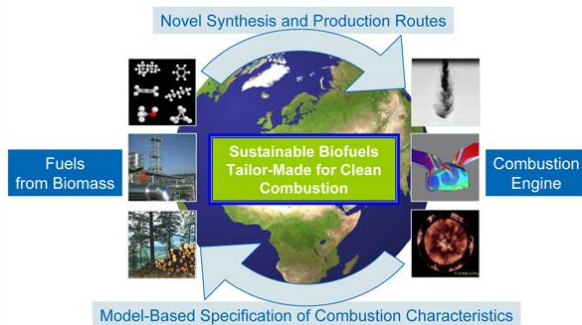


Figure 1: The cluster of excellence Tailor-Made Fuels from Biomass

### 2 The Research at the Institute for Fluid Power Drives and Controls

Viscosity, bulk modulus and lubricity are important properties concerning the handling of a fuel within a combustion engine and its periphery. All of these properties are being investigated at the Institute for Fluid Power Drives and Controls (IFAS), as part of the cluster of excellence. Since modern common rail systems operate with self-lubricating fuel pumps (see *Figure 2*) the fuel lubricity and viscosity are critical criteria judging the possibility of a future usage of a proposed biofuel.



Figure 2: Common rail pump. Source: Robert Bosch GmbH

The so far investigated biofuel candidates tend to have significantly lower viscosities against temperature and

pressure compared to modern diesel fuels. Since most of the candidates also perform badly as lubricants the safe and reliable combination of these biofuels and modern engine equipment such as common rail fuel pumps becomes a difficult task. In spite of this the usage of these substances as part of a future biofuel could be favourable or even necessary due to their performance or properties in other fields of interest such as combustion.

To enable the widespread usage of new biofuels in the future, the cluster's research has covered the compatibility related topics from the very beginning of the fuel development. The research at IFAS is part of this branch of the cluster with two subprojects:

On the one hand, closely linked experimental and theoretical studies are performed to unravel potential modifications of the standard components (micro and macro geometry, materials, coatings, etc.) to ensure a safe and efficient use of these in combination with the new biofuels [1].

To do so the tribologically relevant fluid properties need to be known. Consequently all substances that emerge from the research within the cluster are systematically being screened. Beside the investigations of the fluid's lubricity these tests include measurements of the density, the bulk modulus and the dynamic viscosity as functions of pressure and temperature. Another important research topic at IFAS is the compatibility of the biofuel candidates and sealing materials. Furthermore models to calculate or predict the fluid's behaviour are being developed. First measurements indicate that good lubricating fuel-candidates also perform well as lubricating additives in other fuels including biofuels. Consequently the performances of selected fuel-blends are investigated [2].

This paper deals with the performance of unblended biofuel candidates in a standardised fuel-lubricity test.

### 3 The High Frequency Reciprocating Test Rig

The importance of a sufficiently high lubricity of fuels became a topic of increased research after the introduction of low sulphur diesel fuels during the mid-nineties of the last century. Due to the hydrotreatment used in the production of these fuels most of the fuel inherent lubricants were removed. This led to increased friction and wear within the tribological contacts of the fuel-lubricating pumps and therefore drastically decreased the life expectancies of such systems. To prevent the lubricity based failures tests such as the High Frequency Reciprocating Test Rig (HFRR) were developed and standardised (see [3], [4]). At IFAS such a test rig is used to measure the lubricity of different fluids including biofuel candidates (see *Figure 3*).



Figure 3: The HFRR at IFAS

The *Figure 4* shows the principal design of the HFRR as given in [3]. A disk made of 100Cr6 steel (Vickers hardness "HV30" of 190 to 210) is mounted in a basin containing a sample of 2 ml fuel to be investigated. Against the surface of the disk a 100Cr6 steel ball (Rockwell hardness in "C-scale" 58 to 66) is pressed. The ball is mounted in the reciprocating arm and the contact force is delivered by an external weight of exactly 200 g that is attached to the arm (see *Figure 3* and *Figure 4*).

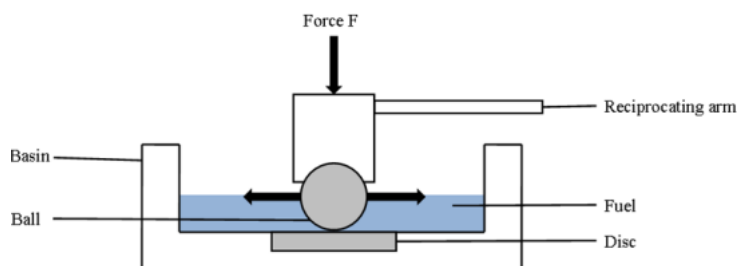


Figure 4: Test setup of the HFRR [1]

Prior to the experiment's start the investigated fluid sample is heated up to 60°C and kept at this temperature until the test ends. Some of the investigated substances have boiling points relatively close to 60 °C. To include these in the research, the described set up needs to be altered. Hence for all substances with a boiling point lower than 100 °C an increased fuel sample of 10 ml was used.

During each test the arm oscillates for a given time and frequency in a reciprocating stroke rubbing the two probes against each other. DIN EN ISO 12156-1 gives the test duration as 75 minutes with a frequency of 1 Hz for the stroke.

This process leads to typical wear scars on the surfaces of the ball and the disc (see *Figure 5*).

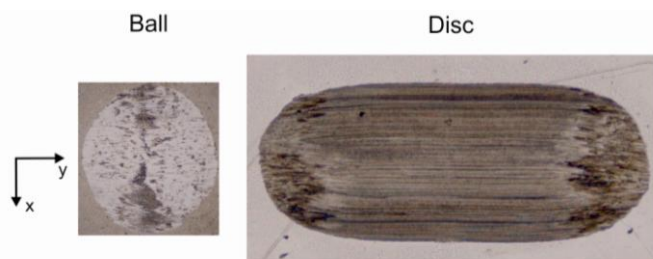


Figure 5: Wear scars of the lower (Ball) and upper (Disc) specimen after a test with cyclohexanone

After each test the probes need to be evaluated with an optical microscope as shown in Figure 6.

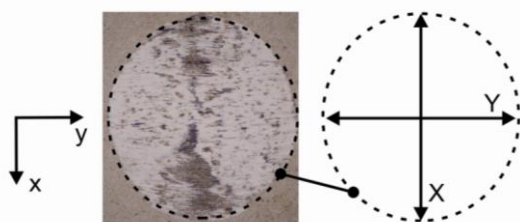


Figure 6: Determination of the wear scar diameter on the ball

The wear scar diameter (*WSD*) value of the specimen, ball and disc alike, is determined by averaging the latitude of the scars in direction of the oscillation (*Y*) and vertical (*X*) to it as given in eq. 1 (see Figure 6).

$$WSD = \frac{X + Y}{2} \quad (1)$$

Both DIN EN ISO 12156-1 and ASTM D6079 use the averaged wear scar diameter of the ball to determine the fluid's lubricity. However Fatemimoughari et al. have reported that for substances with very good lubricating abilities no measurable wear could be found on the ball [8]. To avoid such problems while investigating the highly unknown tribological properties of the substances proposed by the cluster, it was decided to include the wear scars of the discs into the evaluation.

Varying levels of temperature and humidity can influence the measured *WSD* value. To compensate this, a corrected wear scar diameter - the *WSI.4* - was developed. The *WSI.4* is widely used and a maximum value of 460  $\mu\text{m}$  has been proposed by the European Committee for Standardization as an acceptable value for safe field performances [3]. However, as Lacey and Howel have shown this correction is not valid for different types of (diesel) fuels [4]. Since the investigation of the biofuel candidates proposed by the cluster requires screening a vast number of non-similar substances the uncorrected *WSD* value is used for the research at IFAS [2].

To minimize statistical errors due to uncertainties each test is repeated at least two times. Each of the *WSD* values

presented in this paper gives therefore the arithmetical mean value of three specimens.

Fatemimoughari has shown that small amounts of a substance with good lubricating properties can drastically reduce the measured wear scar in other fluids [2]. Consequently impurity in the investigated sample of a fluid can have a huge effect on the measured lubricity. An analysis of the composition of each fuel sample provided to our lab is not feasible. Therefore the experimental results of all investigated fluids will be listed with their minimum purity as given by the producer.

#### 4 Previous research on Biofuel Lubricity at IFAS

At the beginning of the research on the lubricity of biofuel candidates at IFAS the list of proposed substances was limited. About ten substances were available at the clusters start or shortly after. Consequently these were screened. To gain a more detailed understanding of the properties influencing a fuels capability to reduce wear and friction in the HFRR several additional substances were also tested ([2], [8]). In Figure 7 some of these early results are shown.

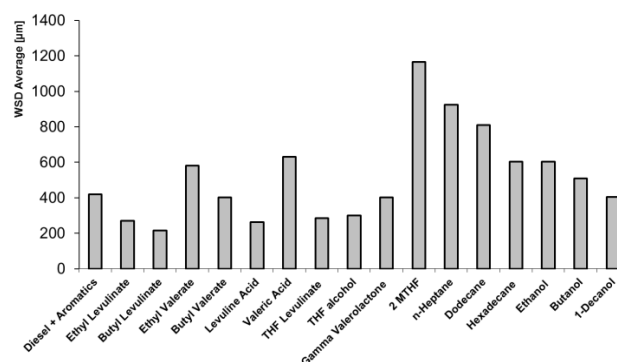


Figure 7: Wear scar diameters of the fluids previously investigated by Fatemimoughari [2]

The research performed by Fatemimoughari et al. showed that although quite different to conventional diesel fuel most biofuel candidates would pass the critical mark of 460  $\mu\text{m}$  or produce only slightly more severe wear scars. There are however some remarkable outliers such as 2-Methyltetrahydrofuran and (2-MTHF) and Butyl-Levulinate. With a *WSD* value of 216,5  $\mu\text{m}$  for the ball the latter performs outstandingly well in protecting the specimen and can be used as a lubrication additive in other fuels [2]. 2-MTHF on the other hand, favoured by some institutions within the cluster due to its good performance as a fuel, has produced the highest wear (Ball *WSD* = 1165,4  $\mu\text{m}$ ) of all fluids so far recorded. Please note that this value differs from the one presented in Table 2 at the end of the paper. The reason for this mismatch is most likely caused by the different purities of the investigated samples. We used a fluid with 99.0% purity whereas Fatemimoughari was provided with a sample of 99.8% purity 2-MTHF. Since the 99.0% sample is going to be used in several upcoming investigations dealing with fuel blends its *WSD* value is presented as well.

The effect of low viscosity (bio)-fuels on conventional fuel equipment is a topic of on-going scientific research (e. g. see [1], [2]). Without further knowledge of the tribological system and underlying processes a suitable pass/fail criteria to judge a fuel's compatibility can hardly be specified at this point. Therefore the experimentally determined lubricities will be listed without relating them to any prediction on the usage of these substances as fuels.

In the past five years the list of proposed substances with favourable properties with regard to their potential as a biofuel has steadily increased. As a matter of fact the number of candidates and complementary substances being investigated within the cluster has come close to the number of tests that can be performed economically. This raises the need to screen substances in an even faster and more efficient way than performing experiments with the HFRR. Such a predictive model is even more desirable taking into account that the production of the necessary volume (approximately 10 ml) of an exotic fuel-candidate can take up to several weeks. Therefore the available amount of the fluid is limited.

Consequently a prediction-method for the lubricity of biofuel candidates has been developed during the first phase of the cluster of excellence. By correlating the experimental data with quantum chemical calculations, based on the chemical structure of the substance, a QSPR-Model was set up ([2], [8]). The model has been trained with an external data-set dealing with substances similar to those investigated in the cluster [16]. The necessary calculations were performed with the chemical simulation software *COSMO-RS* in cooperation with the Institute of Technical Thermodynamics (*LTT*) at RWTH Aachen University.

Fatemimoughari et al. have shown that the established QSPR-model can be used to give a first estimation of a molecule's lubricating abilities (e.g. *Figure 8*). A comparison of some experimental and predicted wear scar diameters of a selection of investigated substances is given in [8].

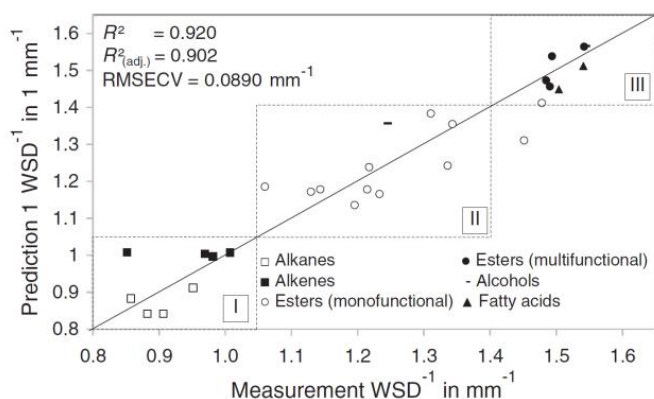


Figure 8: Plot of the predicted vs. measured WSD [8]

Since the QSPR-model only enables a preliminary evaluation of the fuel candidates experimental screening of

the more favourable ones is still necessary and has been performed continuously.

To gain a better understanding of the lubricating progress and to increase the accuracy of the prediction model several additional experimental studies with different kinds of substance have been performed at IFAS and will be presented in the next paragraph. These results will be used to further increase the prediction capabilities of the QSPR model. This is especially important since the progress in the cluster has and will shift the focus of its research towards new types of substances.

## 5 Lubricity of selected biofuel candidates and similar substances

The protection of the metal surface by the lubricant is a highly complex procedure which cannot be ascribed to a single property of the fluid's molecules. Nevertheless we have arranged the HFRR test results of all recently screened fluids in Table 2 and Table 3 into groups of molecules with similar structures (The tables are put at the end of the paper to increase the readability). The presented results include the averaged wear scars of both specimens as explained above. In case of 2-Butylfuran and Di-n-Butylether one of the three ball specimens could not be evaluated and the presented *WSD* values therefore give the arithmetical mean of the remaining two probes. However the corresponding discs could be analysed.

Taking into account that the so far proposed biofuel candidates are taken from very different types of organic substances such as alcohols, ethers, ketones and furans, the understanding of their lubricating abilities by comparing their *WSD* values becomes a rather difficult task. To overcome this hindrance several additional substances were included into our research. These fluids were chosen due to certain similarities or differences they show when compared to a biofuel candidate. One example for this is the investigation of 1-Octanol, which has been added to the clusters research due to its favourable properties as a fuel. To analyse the lubricity of this substance other linear molecules such as alkanes and other alcohols were screened. Screening results are discussed in the next chapter. Due to the high variation of the chemical and physical properties of the selected biofuel candidates such comparative experiments cannot be performed for all of them. To illustrate the influence of certain properties a discussion on selected molecules from the list will be given. For complementary reasons five measurements performed by Fatemimoughari are included lubricity in the following discussion (see Table 4 at the end of the paper).

### 5.1 Lubricity of linear molecules

By adsorbing to the metal surfaces the molecules of a lubricant can reduce the friction and wear occurring in a contact (see *Figure 9*) [15].

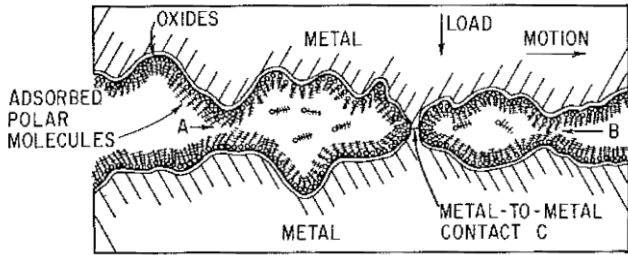


Figure 9: Protective layers of adsorbed polar molecules [15]

The formation of the protective layer of adsorbed molecules is complex and influenced by all characteristics of the tribological system such as the structure of the lubricants molecules and those of the surface material ([14], [15]). Since the set up of the HFRR test, including the material of the specimen, is given only the lubricants properties influence the built up and performance of the protective layers present during the lubricity experiments.

The functional groups of linear molecules are known to influence tribological phenomena such as friction [15]. To investigate whether such an influence is present in the performed HFRR experiments as well, similar molecules with different functional groups need to be investigated. The molecules of n-dodecane, n-dodecene and 1-dodecanol are all composed of twelve carbon atoms (see Figure 10).

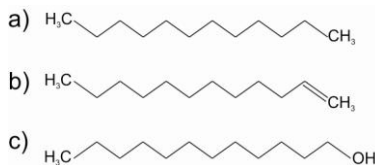


Figure 10: Molecule structures of a) n-dodecane, b) n-dodecene and c) 1-dodecanol

Since they have a similar size the influence of their functional groups can be derived by comparing their WSD values (see Table 1).

Formula	Substance	WSD Ball [ $\mu\text{m}$ ]
$\text{C}_{12}\text{H}_{26}$	n-Dodecane	810,0
$\text{C}_{12}\text{H}_{24}$	1-Dodecene	635,0
$\text{C}_{12}\text{H}_{26}\text{O}$	1-Dodecanol	344,5

Table 1: The Wear scar diameters of the investigated  $\text{C}_{12}$  molecules

The alcohol group (-OH) of the linear alcohols, such as 1-dodecanol, has a relatively high “polarity” when compared to the functional groups of alkanes and alkenes. In [19] Hsu defines this “polarity” as a function of several molecule properties such as the reactivity of the functional group and molecules shape. In the presences of other polar molecules such as metal oxides these molecules therefore will form stronger bonds with the atoms of the specimen’s surface. As sketched in Figure 11 the combination of a long carbon chain and a polar head group leads to a perpendicular

alignment of the molecules on the surface which further increases the protection of the metal [14].

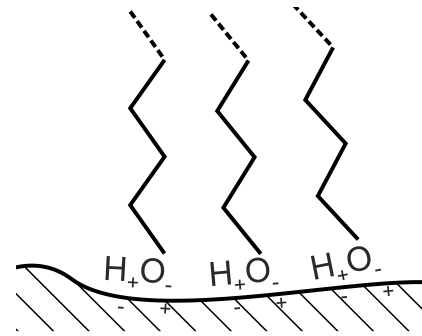


Figure 11: Alignment of adsorbed polar molecules

Since the molecules of alkanes and alkenes do not possess a head group with a high polarity the bonds between the surface and the lubricant’s molecules will be weaker and the molecules will adsorb to the surface in a more or less random fashion. Consequently such substances provide a less effective protection from wear in the HFRR as can be seen in Table 1.

In Figure 12 the WSD values of three alkanes, four alkenes and six alcohols form Table 2 are given as function of the amount of carbon atoms in each molecule. In the graph the averaged values of three specimens are presented including the maximum and minimum WSD measured. Please note that for comparative reasons some measurements performed by Fatemimoughari were included into the graph (see Table 4). The geometrical forms of these molecules are quiet similar since all of them have a chain structure without branches (see Figure 10). The simple linear structure of these molecules can be used to analyse the influence of the molecule elongation.

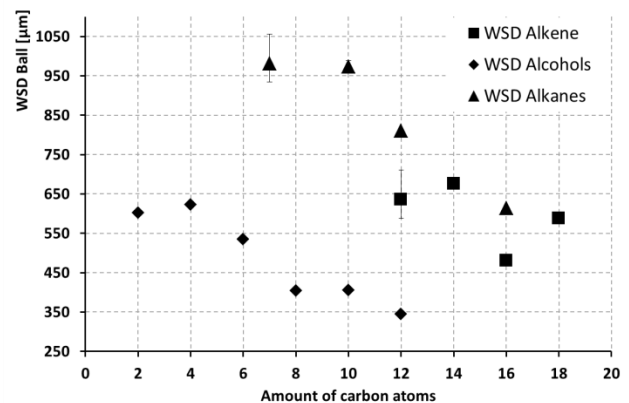


Figure 12: Wear scar diameters of the investigated alcohols, alkenes and alkanes

The investigated alcohols and alkanes show a clear tendency towards a better lubricity with increasing chain-length. The experimental results of the presented alkenes did not produce such pronounced behaviour. Although the WSD values increase from 1-Dodecene to 1-Tetradecene and from 1-Hexadecene to 1-Octadecene the overall trend also shows a decreasing wear over the increasing chain length. The

decrease of wear in the tribological system of the HFRR in the presence of long chain molecules with a polar head group is in compliance with the results of Studt [18]. By studying the influence of the chain length of polar molecules on the friction between metal and ceramic surfaces, he found that for metal surfaces molecules with polar head groups and long carbon chain could decrease the friction the most.

### 5.2 Lubricity results of more complex molecules

Some of the linear molecules discussed above are among the favoured candidates of potential biofuels within the cluster of excellence. However most of the proposed candidates have far more complex structures such as the molecule of 2,2'-Oxybis(methylene)bis(tetrahydrofuran) given in Figure 13.

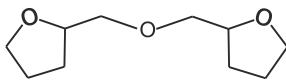


Figure 13: The molecule structure of 2,2'-oxybis(methylene)bis(tetrahydrofuran)

The shortage of experimental data concerning these and similar molecules limits investigation of their specific properties. However the lubricating performance of these fuels is still important and needs to be taken into account when dealing with them in test rigs or combustion engines. Among the investigated fluids 2,5-Dimethylfuran and Benzyl alcohol performed best in protecting the metal surface by producing a  $WSD_{Ball}$  of only 300,5  $\mu m$  respectively 303,0  $\mu m$  on the upper specimen. In contrast the two worst lubricating abilities were measured for 2-Methyltetrahydrofuran with a  $WSD_{Ball}$  of 855,1  $\mu m$  and n-Heptane with a  $WSD_{Ball}$  of 925,0  $\mu m$  (see Figure 14).

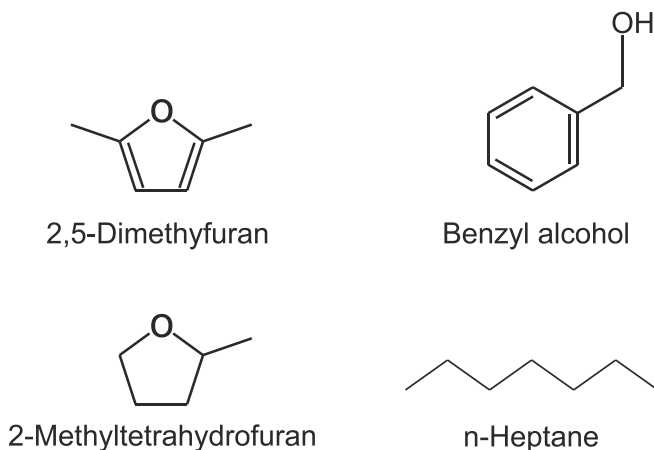


Figure 14: Molecule structure of the best (top) and worst (bottom) lubricants

The bad performance of n-Heptane, which is the shortest of the investigated alkanes, follows consequently from the phenomena discussed above. In the case of 2-MTHF Fatemimoughari et al. have suspected that the steric hindrance of the methyl group prevents a good surface

coverage [9]. Considering the similar molecule structure of 2,5-Dimethylether and its outstandingly good lubricating properties this explanation seems to be implausible. Consequently the unsatisfactory performance of 2-MTHF and its understanding will be part of future research.

### 5.3 The influence of the fuel viscosity

In the Figure 15 the lubricity values of the investigated alkenes and alcohols are combined with the dynamic viscosities of the investigated alkenes and alcohols at 25 °C. Please note that these are taken from literature (see [17]) due to small amount of fluid available. For both groups the viscosities increase over the chain length and the wear decreases. However the changes do not follow a similar trend.

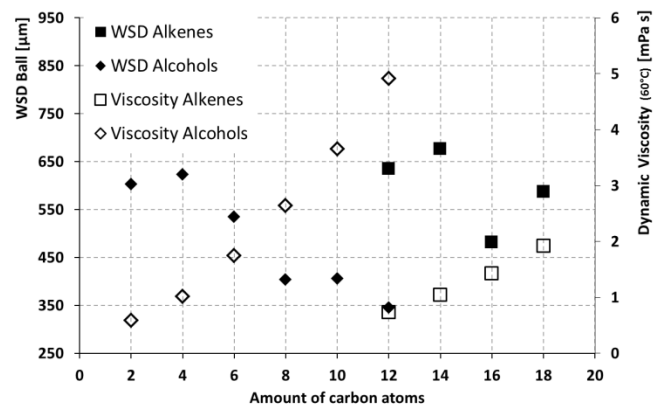


Figure 15: Comparison of the lubricity and dynamic viscosity

Wei et al. published a hypothesis that the decrease of the  $WSD$  values among alkanes with longer chain length is due to the increase of the dynamic viscosity and its influence in the built up of an hydrodynamic film between the two specimen [11].

Sivebaek et al. have investigated the performance of alkanes in the regime of boundary lubrication theoretically with molecular dynamic simulations ([12], [13]). Contrary to Wei et al. they do not ascribed the reduced wear mainly to the increase in the dynamic viscosity. In their simulations they found that a longer chain-length resulted in a higher surface density of the investigated fluid molecules which would lead to a better protection of the metal atoms. Considering the steep rise in the viscosity from 1-Octanol ( $C_8H_{18}O$ ,  $\eta = 2,643 mPa s$ ) to 1-Decanol ( $C_{10}H_{22}O$ ,  $\eta = 3,565 mPa s$ ) and the nearly constant lubricities of the two substances the hypothesis presented by Sivebaek seems to give a more suitable description of the present phenomena.

A more detailed discussion on the theoretical effects of the molecule chain length and the influence on the fuels viscosity is given in [2].

## 6 Conclusion and Outlook

The experimental procedure to screen biofuel candidates with regard to their lubricity at the Institute for Fluid Powers and Controls (IFAS) with a HFRR test rig has been presented. The *WSD* values of 27 investigated fluids were given. This group includes alkanes, alkenes, alcohols, aldehydes, furanes and ketones. By comparing the results of selected substances the influence of molecules chain length and polar head groups have been investigated. In case for linear molecules such as alkanes the lubricity increases with the length of carbon chain. Molecules with polar head groups, such as the investigated linear alcohols, perform better in protecting a metal surface than molecules of similar size that do not feature such structures. Among the screened substances 2,5-Dimethylfuran showed the best and 2-Methyltetrahydrofuran the worst lubricating abilities.

Due to the novel and fundamental character of the research performed within the cluster of excellence a wide spread and steadily increasing selection of possible biofuel candidates are being investigated. These will be screened and evaluated according to the procedures described in this paper.

In addition to this a set of favourable biofuel blends has been formulated by some of the cluster's researchers. The lubricating performance of binary blends is highly nonlinear [2] and cannot be derived by averaging the pure substances *WSD* values. Therefore the behaviour of fuel-blends will be investigated by experimental and theoretical research.

To develop and improve fast screening methods is important when dealing with a vast number of possible fuel candidates. Consequently the lubricity data presented in this paper will be used to improve the QSPR prediction model that has been developed by Fatemimoughari et al.

Since the lubricity of fuel blends will be an essential part of the upcoming experimental research, the QSPR-Model will be extended to cover these as well.

## Nomenclature

Designation	Denotation	Unit
<i>X</i>	Wear scar diameter vertical to the direction of oscillation	[ $\mu\text{m}$ ]
<i>Y</i>	Wear scar diameter in the direction of oscillation	[ $\mu\text{m}$ ]
<i>WSD</i>	Averaged wear scar diameter	[ $\mu\text{m}$ ]
<i>WSI.4</i>	Corrected wear scar diameter	[ $\mu\text{m}$ ]
$\eta$	Dynamic viscosity	[Pa s]

## References

- [1] Heitzig, S., Leonhard, L., Drumm, S., Murrenhoff, H., Lang, J. & Knoll, G. (2013), Simulative Analysis of the Tribological Contacts of Common Rail InjectionPumps Lubricated by Tailor-Made Biofuels, *Tribologie und Schmierungstechnik*, 6, 17-22.
- [2] Fatemimoughari, A. Analysis of Tribological Properties for the Design of Synthetic Biofuels. *Shaker*, Aachen, 2012.
- [3] DIN EN ISO 12156-1
- [4] ASTM D6079
- [5] Nikanjam, M., Crosby, T., Henderson, P., Gray, C., Meyer, K., Davenport, N. ISO diesel fuel lubricity round robin program. *SAE Transactions*, 104, 1995.
- [6] DIN EN 590.
- [7] Lacey, P.I., Howell, S.A., Fuel lubricity reviewed. *Society of Automotive Engineers*, 1998
- [8] Masuch, K., Fatemimoughari A., Murrenhoff, H. and K Leonhard. A COSMORS based QSPR model for lubricity of petro- and biodiesel components. *Lubrication Science*, online, 2011.
- [9] Fatemimoughari, A., Masuch K., Murrenhoff, H., Leonhard, K., Experimental investigation and theoretical prediction of the lubricity of biofuel components, *Fluid Power and Motion Control Symposium*, Bath, 2010
- [10] Barbour, R., Rickeard, D., and Elliott, N., Understanding Diesel Lubricity. *SAE Technical Paper* 2000-01-1918, 2000
- [11] Wei, D., Spikes, H., Korcek, S., The lubricity of gasoline. *Tribology transactions*, 42, 1999
- [12] Sivebaek, I. M., Samoilov, V.N., Persson, B.N.J., Squeezing molecular thin alkane lubrication films between curved solid surfaces with long-range elasticity: Layering transitions and wear, *Journal of chemical physics*, 119, 2003
- [13] Tartaglino, U., Sivebaek, I. M., Persson, B. N.J., Tosatti, E., Impact of molecular structure on the lubricant squeeze-out between curved surfaces with long range elasticity, *Journal of chemical physics*, 125, 2006
- [14] Czichos, H., Habig, KH., *Tribologie-Handbuch; Reibung und Verschleiss*, Vieweg, Wiesbaden, 1992.
- [15] O'Connor, J. J (editor)., *Standard handbook of lubrication engineering*, McGraw-Hill, New York, 1968
- [16] Knothe, G., Evaluation of ball and disc wear scar data in the HFRR lubricity test. *Lubrication Science*, 20, 2008
- [17] Wohlfarth, C. and Wohlfarth, B., *Viscosity of Pure Organic Liquids and Binary Liquid Mixtures, Subvolume B: Pure Organic Liquids*, Springer-Verlag: Berlin, Heidelberg, New York, 2001
- [18] Studt, P., Boundary lubrication: adsorption of oil additives on steel and ceramic surfaces and its influence on friction and wear, *Tribology international*, 22, 1989
- [19] Hsu, S., Molecular basis of lubrication, *Tribology International*, 37, 2004

Formula	Substance	Purity	Ball specimen		
			Averaged WSD [µm]	Maximum WSD [µm]	Minimum WSD [µm]
C <sub>7</sub> H <sub>16</sub>	n-Heptane	99,0%	980,8	933,8	1055,8
C <sub>10</sub> H <sub>22</sub>	n-Decane	99,0%	972,7	963,4	988,24
C <sub>16</sub> H <sub>34</sub> O	n-Hexadecane	99,0%	613,2	610,2	615,39
C <sub>12</sub> H <sub>24</sub>	1-Dodecene	99,0%	635,0	633,8	636,71
C <sub>14</sub> H <sub>28</sub>	1-Tetradecene	99,0%	676,1	669,8	681,56
C <sub>16</sub> H <sub>32</sub>	1-Hexadecene	99,0%	480,9	471,4	489,25
C <sub>18</sub> H <sub>36</sub>	1-Octadecene	99,0%	587,2	578,6	600,69
C <sub>4</sub> H <sub>10</sub> O	1-Butanol	99,9%	622,7	620,5	624,95
C <sub>6</sub> H <sub>14</sub> O	1-Hexanol	99,0%	534,2	527,1	539,85
C <sub>8</sub> H <sub>18</sub> O	1-Octanol	99,0%	403,9	395,3	410,99
C <sub>12</sub> H <sub>26</sub> O	1-Dodecanol	98,0%	344,5	342,9	347,28
C <sub>6</sub> H <sub>12</sub> O	1-Hexanal	99,0%	360,4	352,4	368,4
C <sub>8</sub> H <sub>16</sub> O	1-Octanal	99,0%	236,0	232,6	239,49
C <sub>6</sub> H <sub>12</sub> O	Cyclohexanol	98,0%	312,7	302,5	326,17
C <sub>3</sub> H <sub>8</sub> O	2-Propanol	99,5%	604,4	588,9	593,33
C <sub>7</sub> H <sub>8</sub> O	Benzyl alcohol	98,0%	303,0	290,1	328,72
C <sub>8</sub> H <sub>12</sub> O	2-Butylfuran	98,0%	429,2	424,5	433,92
C <sub>5</sub> H <sub>6</sub> O <sub>2</sub>	2-Furylmethanol	98,0%	419,9	404,4	530,75
C <sub>5</sub> H <sub>8</sub> O <sub>2</sub>	γ-Valerolacton	98,0%	505,6	491,1	525,69
C <sub>5</sub> H <sub>10</sub> O	2-Methyltetrahydrofuran	99,0%	855,1	846,3	869,78
C <sub>6</sub> H <sub>8</sub> O	2,5-Dimethylfuran	98,0%	226,3	252,6	348,37
C <sub>9</sub> H <sub>18</sub> O <sub>2</sub>	2-(butoxymethyl)tetrahydrofuran	98,0%	356,4	354,9	358,57
C <sub>10</sub> H <sub>18</sub> O <sub>3</sub>	2,2'-oxybis(methylene)bis(tetrahydrofuran)	98,0%	308,6	275,2	341,1
C <sub>8</sub> H <sub>18</sub> O	Di-n-Butylether	98,0%	620,5	611,7	629,36
C <sub>9</sub> H <sub>18</sub> O	Nonan-5-one	99,0%	450,8	440,8	456,86
C <sub>11</sub> H <sub>22</sub> O	2-Undecanone	98,0%	478,9	447,0	513,93
C <sub>6</sub> H <sub>10</sub> O	Cyclohexanone	99,0%	512,9	509,6	516,19

Table 2: The Wear scar diameters of the measured substances on the ball specimen

Formula	Substance	Purity	Disc specimen		
			Averaged WSD [ $\mu\text{m}$ ]	Maximum WSD [ $\mu\text{m}$ ]	Minimum WSD [ $\mu\text{m}$ ]
C <sub>7</sub> H <sub>16</sub>	n-Heptane	99,0%	1454,6	1347,9	1542,3
C <sub>10</sub> H <sub>22</sub>	n-Decane	99,0%	1470,7	1434,1	1502,8
C <sub>16</sub> H <sub>34</sub> O	n-Hexadecane	99,0%	1094,5	1081,8	1102,3
C <sub>12</sub> H <sub>24</sub>	1-Dodecene	99,0%	1148,1	1135,9	1165,1
C <sub>14</sub> H <sub>28</sub>	1-Tetradecene	99,0%	1163,7	1154,9	1172,4
C <sub>16</sub> H <sub>32</sub>	1-Hexadecene	99,0%	1008,0	989,7	1024,8
C <sub>18</sub> H <sub>36</sub>	1-Octadecene	99,0%	1064,0	1045,3	1080,3
C <sub>4</sub> H <sub>10</sub> O	1-Butanol	99,9%	1101,3	1080,3	1128,6
C <sub>6</sub> H <sub>14</sub> O	1-Hexanol	99,0%	1016,0	995,6	1030,6
C <sub>8</sub> H <sub>18</sub> O	1-Octanol	99,0%	911,7	903,5	918,1
C <sub>12</sub> H <sub>26</sub> O	1-Dodecanol	98,0%	859,6	852,3	866,9
C <sub>6</sub> H <sub>12</sub> O	1-Hexanal	99,0%	868,4	786,5	929,8
C <sub>8</sub> H <sub>16</sub> O	1-Octanal	99,0%	731,7	729,5	733,9
C <sub>6</sub> H <sub>12</sub> O	Cyclohexanol	98,0%	807,9	801,1	820,1
C <sub>3</sub> H <sub>8</sub> O	2-Propanol	99,5%	1102,3	1067,2	1131,1
C <sub>7</sub> H <sub>8</sub> O	Benzyl alcohol	98,0%	789,4	773,4	798,2
C <sub>8</sub> H <sub>12</sub> O	2-Butylfuran	98,0%	902,5	888,8	918,1
C <sub>5</sub> H <sub>6</sub> O <sub>2</sub>	2-Furylmethanol	98,0%	974,5	782,1	1062,8
C <sub>5</sub> H <sub>8</sub> O <sub>2</sub>	$\gamma$ -Valerolacton	98,0%	989,2	976,6	1010,2
C <sub>5</sub> H <sub>10</sub> O	2-Methyltetrahydrofuran	99,0%	1358,1	1345,0	1369,8
C <sub>6</sub> H <sub>8</sub> O	2,5-Dimethylfuran	98,0%	798,2	769,0	847,9
C <sub>9</sub> H <sub>18</sub> O <sub>2</sub>	2-(butoxymethyl)tetrahydrofuran	98,0%	864,5	855,2	874,2
C <sub>10</sub> H <sub>18</sub> O <sub>3</sub>	2,2'-oxybis(methylene)bis(tetrahydrofuran)	98,0%	806,0	785,0	831,8
C <sub>8</sub> H <sub>18</sub> O	Di-n-Butylether	98,0%	1133,0	1125,7	1137,4
C <sub>9</sub> H <sub>18</sub> O	Nonan-5-one	99,0%	957,1	944,4	969,2
C <sub>11</sub> H <sub>22</sub> O	2-Undecanone	98,0%	960,0	956,1	964,9
C <sub>6</sub> H <sub>10</sub> O	Cyclohexanone	99,0%	998,0	986,8	1010,2

Table 3: The Wear scar diameters of the measured substances on the disc specimen

Formula	Substance	Purity	WSD Ball [ $\mu\text{m}$ ]	WSD Disc [ $\mu\text{m}$ ]
C <sub>12</sub> H <sub>26</sub>	n-Dodecane	98,0%	810,0	1329,1
C <sub>2</sub> H <sub>6</sub> O	Ethanol	98,0%	602,5	1112,7
C <sub>10</sub> H <sub>22</sub> O	1-Decanol	99,0%	405,4	909,1
C <sub>10</sub> H <sub>20</sub> O	1-Decanal	-	205,0	746,0
C <sub>5</sub> H <sub>10</sub> O <sub>2</sub>	Tetrahydro-2-furanylmethanol	99,0%	300,0	806,0

Table 4: The Wear scar diameters measured by Fatemimougharimoughari [2]

## Energy Efficient Active Vibration Damping

E. Zaev, G. Rath\*, and H. Kargl\*\*

Faculty of mechanical engineering, Ss. Cyril and Methodius University, Skopje, Macedonia

E-mail: emil.zaev@mf.edu.mk, gerhard.rath@unileoben.ac.at, hubert.kargl@sandvik.com

\*Institute for automation, University of Leoben, Leoben, Austria

\*\*Sandvik Mining and Construction, Austria

### Abstract

Mining machines are subjected to severe vibrations during their operation. If we succeed to damp some of those vibrations then we have succeed to reduce the dynamic load of the machine and to improve operator comfort and productivity. The main idea for the research done in this paper is to investigate possible improvements in active vibration damping in hydraulic power systems of a mobile machine (mining machine) influencing hydraulic system layout and control strategy. Modelling of a standard and individual metering (separate meter-in separate meter-out SMISMO) load sensing (LS) hydraulic power system of a machine has been done. Model of the individual metering system has been validated with measurements. Those models have been used to study new concepts of active vibration damping. SMISMO system has been used to develop new energy efficient concept for active vibration damping using the third (crossport) valve between meter-in and meter-out lines of the hydraulic cylinder as a damping element. Using simulations has been shown that this new system can improve damping effect, drastically decreasing usage of the energy from the pump.

**Keywords:** fluid power systems, active vibration damping, dynamic pressure feedback, energy efficiency.

### 1 Introduction

The vibrations, which are appearing during working process of the mining machine and are a result from external forces are part of this study. Dampening of those vibrations can be accomplished in two ways. The first way is with passive damping. Passive damping is usually done with the usage of high pressure hydro-pneumatic accumulators [1], [2]. The advantage of this system is that no energy from the pump is used for dampening the vibrations, which makes this system energy efficient. The disadvantage is additional costs, place and maintenance of the high pressure accumulators.

A second way to damp the vibrations on the machine is to use active vibration damping [3], [4], [5], [6], [7]. Active vibration damping is not an energy efficient way for dampening the oscillations, since energy from the pump (or other external sources) is used to damp the oscillations. Still, this is an efficient way to damp the vibration, hence this method is attractive to automotive [8], [9], [10], [11], [12], [13], [14], [15], [16] and construction industry [17], [18], [19]. To damp the oscillations with active vibration dampening, some kind of oscillation source feedback is needed (acceleration feedback, pressure feedback or force feedback) to find out about dynamics of the sources. Then, energy from the pump is used to act against those forces, the proportional control valve is open and the fluid from the pump is brought in the chamber. The advantage of the active vibration damping is that the

same means for controlling the motion (opening of the valve) can be used as well as for damping. Experimental work with using optimal control theory [20], [21], [22] has shown that there is a potential in making active vibration damping more energy efficient. Unfortunately, practical implementation of those principles is still an adventure.

Trends to improve the energy consumptions in heavy machinery are asking for change of the conventional valve system with individual metering systems. This gives possibility for energy regeneration and recuperation and effective deceleration control which leads to energy efficiency improvement of the machine [23–34]. However, the main idea of changing the classical LSPC system with SMISMO system at the SANDVIK machine (Figure 1) is to make the boom more stiff during the cutting process, controlling the pressure in the meter-out side of the active cylinder. The same system can also be used for active damping. Actual trends towards dampening the oscillations of the machine structure is in the area of active oscillation damping technologies [35].

This research explores one simple method to introduce dampening in hydraulic power systems for heavy machinery: dynamic pressure feedback (DPF). First, it is examined the influence of dynamic pressure feedback on the servo hydraulic system with load sensing pressure compensated (LSPC) system. Second, effects from dynamic pressure feedback on a individual metering hydraulic system are analysed. Third, novel

energy efficient dynamic pressure feedback (EE DPF) is proposed.

## 2 Model development

The cutting process of a mining machine SANDVIK Roadheader MT720 (fig. 1) is done by the cutter head. The cutter head is moved in horizontal and vertical direction by hydraulic cylinders (fig. 17).

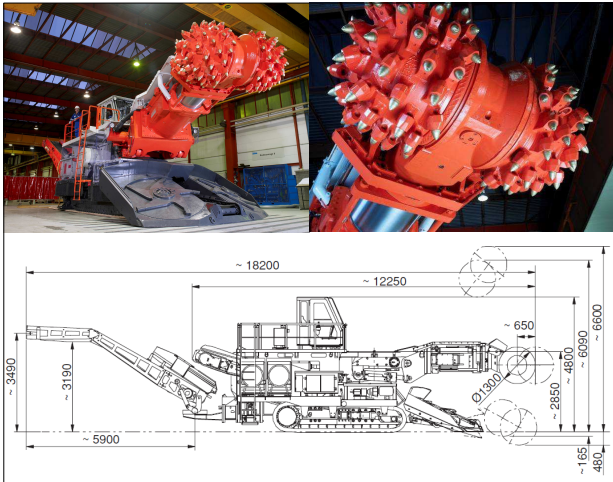


Figure 1: Mining Machine SANDVIK Roadheader MT720 [36].

Hydraulic system which is used in the machine is from LSPC type, as presented on fig. 11.

### 2.1 Model of the servovalve controlled actuator

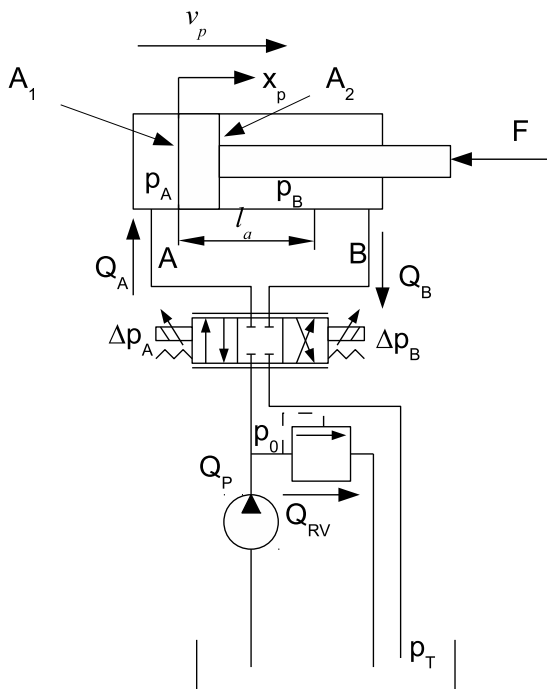


Figure 2: Hydraulic system, servovalve controlled cylinder.

Hydraulic actuators, actually hydraulic cylinders, do most important movements of cutter head during the cutting process. A hydraulic cylinder integrated in the turret (fig. 1) does horizontal movement. Two hydraulic cylinders placed underneath the turret actuate vertical movement and two cylinders on each side of the boom actuate the telescopic elongation.

The cylinder and its servovalve (fig. 2) are presented with non-linear equations derived from basic physical laws. The modelling is performed in graphical environment using Matlab/Simulink.

The dynamics of the valve which has been used in the hydraulic system can be represented with the following equations for standard second order system [37], [38]:

$$G_v(s) = \frac{x_v}{U_v} = \frac{\omega_v^2}{s^2 + 2 \cdot \delta_v \cdot \omega_v \cdot s + \omega_v^2} \quad (1)$$

Where  $x_v$  is the valve spool displacement,  $U_v$  is valve input voltage,  $\omega_v$  is valve undamped natural frequency and  $\delta_v$  is damping ratio coefficient.

Sign convention for cylinder piston displacement  $x_p$  in all equations is chosen to be positive for cylinder elongation. This means that when cylinder is fully extended  $x_p = l_a$ . The rate of pressure increase in the rod and piston side of the cylinder can be described by the rate at which the fluid in the volume  $V$  of the chamber is being compressed ( $\frac{dp}{dt} = \frac{E}{V} \frac{dV}{dt}$ ) as:

$$\frac{dp_A}{dt} = \left( \frac{\beta_e}{V_1 + A_1 x_p} \right) (Q_A - A_1 v_p) \quad (2)$$

$$\frac{dp_B}{dt} = \left( \frac{\beta_e}{V_2 + A_2 (l_a - x_p)} \right) (A_2 v_p - Q_B) \quad (3)$$

Where  $V_1$  and  $V_2$  are dead volumes in the cylinder and volume of the fluid in connected hoses, with the cylinder in retracted position.

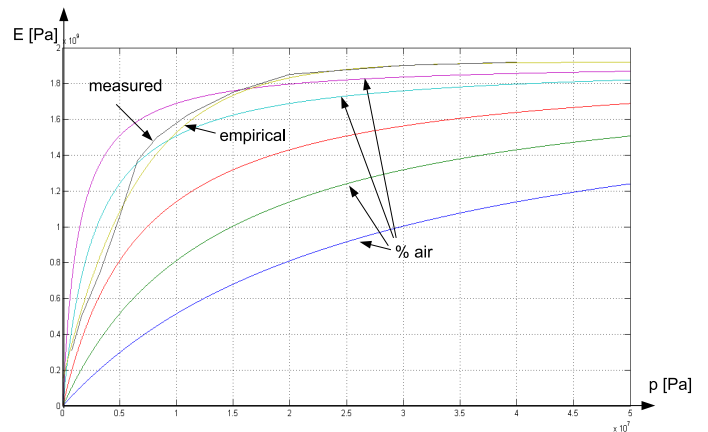


Figure 3: Measured and simulated values of an bulk modulus of the oil. Blue line has highest percentage of air.

It has been identified with comparison of measured and calculated values (fig. 3) that effective bulk modulus of the here used oil  $\beta_e$  can be calculated with the empirical equation:

$$\beta_e(p) = \beta_{\max} [1 - \exp(-k_1 - k_2 \cdot 10^{-7} \cdot p)] [Pa] \quad (4)$$

Where coefficients  $k_1$ ,  $k_2$  and  $\beta_{\max}$  have been identified to be  $k_1 = 0.08$ ,  $k_2 = 1.5$  and  $\beta_{\max} = 1.8 \cdot 10^9 [Pa]$  for here used oil. In simulations, if ideal not air contaminated oil is assumed,  $\beta = 1.4 \cdot 10^9 [Pa]$  can be used.

From Second Newton Low force on the cylinder may be described as:

$$a_p = \frac{dv_p}{dt} = \frac{(p_A A_1 - p_B A_2 - F_f - F_{ext})}{m_p} \quad (5)$$

$$\frac{dx_p}{dt} = v_p \quad (6)$$

Where subscription  $p$  is used for piston mass, displacement, speed and acceleration. Friction force  $F_f$  can be approximated with only viscous friction and  $F_f = B \cdot v_p$  where  $B$  is friction coefficient.

Finally, to describe the flow through the valve, non-linear orifice equation has been used:

$$Q_A = Q_N \cdot \frac{y}{y_{\max}} \cdot \sqrt{\frac{\Delta p_A}{\Delta p_N}} = N \cdot \frac{y}{y_{\max}} \cdot \sqrt{\frac{p_0 - p_A}{\Delta p_N}} \quad (7)$$

$$Q_B = Q_N \cdot \frac{y}{y_{\max}} \cdot \sqrt{\frac{\Delta p_B}{\Delta p_N}} = Q_N \cdot \frac{y}{y_{\max}} \cdot \sqrt{\frac{p_B - p_T}{\Delta p_N}} \quad (8)$$

Where  $Q_N$ ,  $y_{\max}$  and  $\Delta p_N$  are nominal valve parameters.

## 2.2 Model of the vertical mechanical structure

Vertical mechanical structure is given on fig. 4.

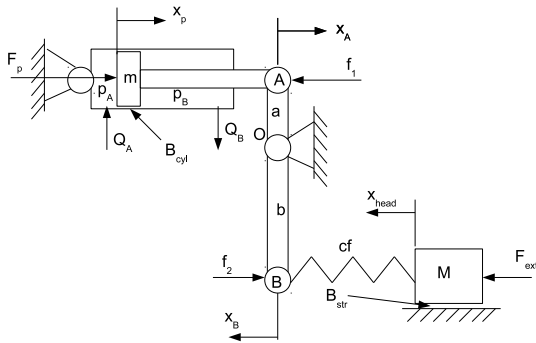


Figure 4: Simplified model of the vertical hydro-mechanical system.

Differential equations which describe the dynamic behaviour of the vertical hydro - mechanical structure are as follows:

$$(mD^2 + B_p D)x_p(t) = F_p - f_1 \quad (9)$$

$$x_B(t) \cdot c_f + x_{head}(t) \cdot c_f = f_2 \quad (10)$$

$$(mD^2 + B_{str} D + c_f)x_{head}(t) - c_f x_B(t) = F_{ext} \quad (11)$$

$$\frac{f_1}{f_2} = \frac{x_B}{x_A} = \frac{b}{a} = i \quad (12)$$

Or, translated in "s" domain:

$$x_p(s) = \frac{1}{m} \frac{1}{s^2} \{F_p - B \cdot x_p(s) \cdot s - [(x_p(s) \cdot i - x_{head}(s))c_f] \cdot i\} \quad (13)$$

$$x_{head}(s) = \frac{1}{M} \frac{1}{s^2} \{F_{ext} - B \cdot x_{head}(s) \cdot s - [(x_{cyl}(s) \cdot i - x_{head}(s))c_f]\} \quad (14)$$

## 2.3 Model of the horizontal mechanical structure

Horizontal mechanical structure together with hydraulic system is given on fig. 5. Simplified model of this structure is given on fig. 6.

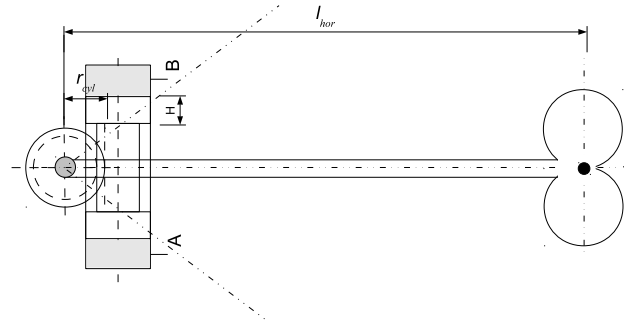


Figure 5: Horizontal hydro-mechanical system. Rodless cylinder (integrated in the turret) and boom with the cutter head.

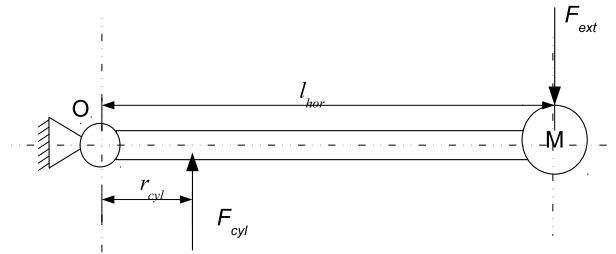


Figure 6: Simplified model of the horizontal structure.

Figure 6 shows how the rodless cylinder is used for operation of a mechanical arm. The total mass of the moving arm is  $M$ . The distance from the gravity center of the mass to the joint ( $O$ ) is  $l_{hor}$ . The lever length for the hydraulic cylinder is  $r_{cyl}$ .

Differential equations which describe dynamic behaviour of the horizontal mechanical system are given as follows:

$$J_{hor} \cdot \ddot{\theta} + B_T \cdot \dot{\theta} = F_p \cdot r_{cyl} - F_{ext} \cdot l_{hor}$$

$$\dot{\theta} = \frac{\dot{x}}{r_{cyl}}$$

$$\dot{\theta} = \frac{\dot{x}}{r_{cyl}}$$

In addition, in "s" domain:

$$\theta(s) = \frac{1}{J_{hor}} \frac{1}{s^2} (F_p \cdot r_{cyl} - F_{ext} \cdot l_{hor} - B_T \cdot \theta \cdot s) \quad (15)$$

## 2.4 Model of the pump

The pump used in the machine is from the LS type. Due to the lack of information for dynamic behaviour of the pump, and because the pump is not under examination but the rest of hydraulic system, the pump can be modelled as ideal load sensing pump. Let us imagine ideal LS pump as pump which always delivers required  $\Delta p$  pressure from the highest load in the hydraulic circuit, or:

$$p_0 = p_{LS} + \Delta p \quad (16)$$

where  $p_0$  represents the pressure delivered from the pump and  $p_{LS}$  represents pressure in the load sensing line. To make the model more realistic, the dynamics of the LS line can be taken in account with first order low pass filter ( $\frac{\omega_{LS}}{s + \omega_{LS}}$ ), designed so that it does not bring instabilities. This can be done in order to check the behaviour of the rest of the system when the LS pump is appropriately chosen and installed, as it is the case with the Roadheader. Good model of LS pump can be found in [39].

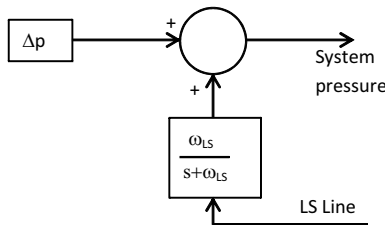


Figure 7: Model of the LS pump.

## 2.5 Valve model adaptation to be used in individual metering system

Special property of SMISMO systems is possibility to control two system parameters, in our case speed of the moving actuator and the pressure in the cylinder chambers. To accomplish this, our individual metering system uses two valves, one on the meter-in and one on the meter-out side. Model of the valve developed in Simulink must adequately represent this special property. Valve in our Simulink model of the individual metering system is modelled with two spools (left and right proportional valve), and has two separate control voltage  $y_A$  and  $y_B$ . Voltage  $y_A$  has been used to produce flow to the chamber A ( $Q_A$ ), and voltage  $y_B$  is used to produce the  $Q_B$  flow. This model is presented on the fig. 8.

## 2.6 Model validation

The model validation can be seen on fig. 9 and fig. 10. Figure 9 shows 24 [s] pressure measurement done on the horizontal hydraulic SMISMO system during cutting process of the machine in comparison with simulated pressures. Input for simulations is external force modelled from measurements on cylinder pressures. In measurements and in simulation PI controller has been used to control back pressure (on the figure pressure  $p_B$ ). On fig. 9 we can see very good matching of the pressures in meter-in side ( $p_A$ ). This can be expected

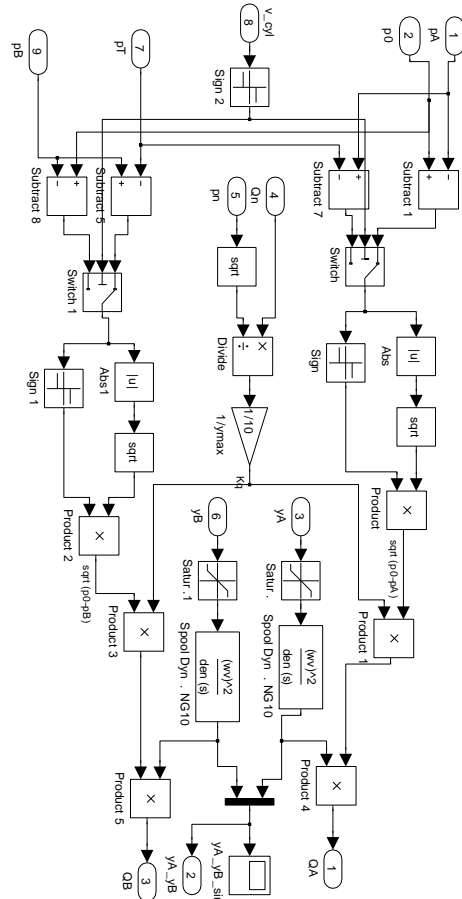


Figure 8: Simulink model of the separate metering system with two valves.

since in measurements and in simulations the opening of the meter-in valve was hold constant (it does not depend from sensor signals). Also, it can be noticed that simulated and measured pressures on the meter-out side ( $p_B$ ) are not matching perfectly. Simulated pressures have smoother values (they are more attenuated) and never go to cavitation. This also is not unusual since in simulations the feedback sensor signal and PI controller are idealized. Simulated and measured values of the horizontal angle of the boom are represented on the fig. 10 and have good confirmation.

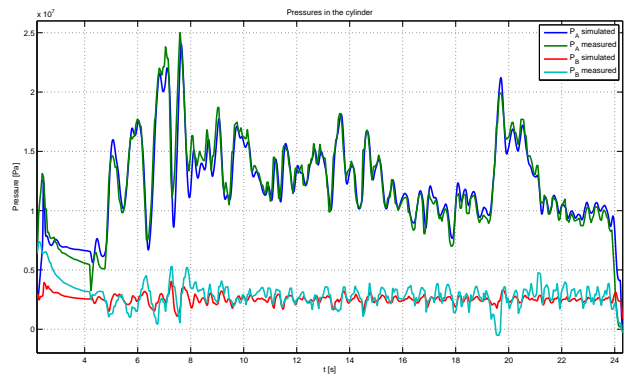


Figure 9: SMISMO model validation. Simulated and measured pressures in cylinder.

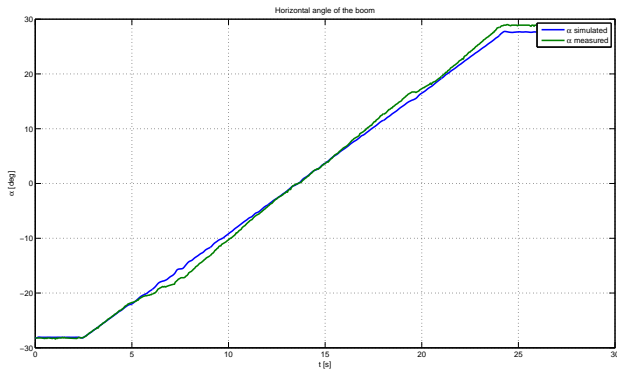


Figure 10: SMISMO model validation. Simulated and measured angle of the boom.

### 3 Active vibration damping with hydraulic servo system

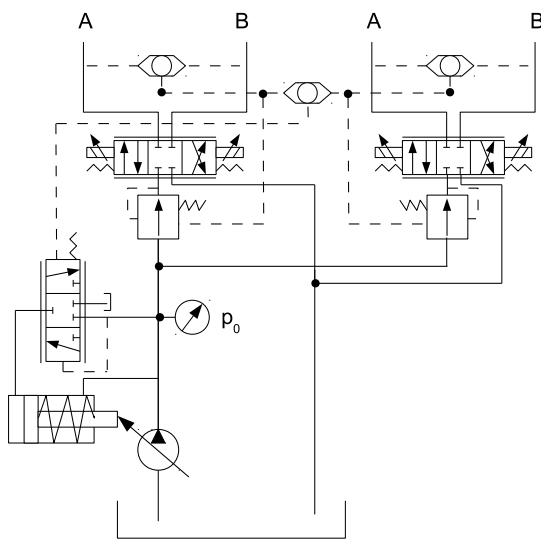


Figure 11: Load sensing pressure compensated systems.

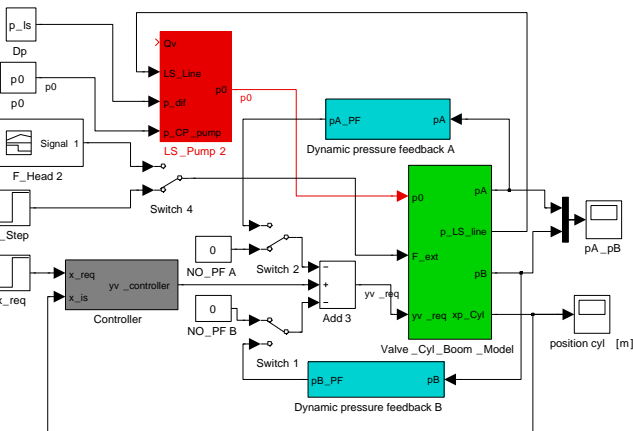


Figure 12: Simulink model of the hydro-mechanical LSPC system.

Investigations on possible damping with dynamic pressure feedback have been done for servo hydraulic system of LSPC

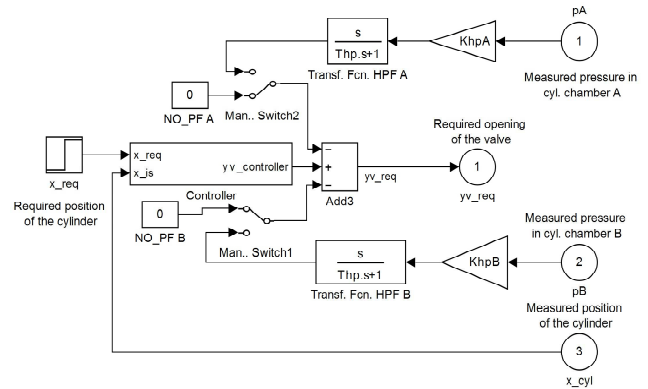


Figure 13: Implementation of the high pass filter in the pressure feedback lines.

type shown on fig. 11. Figure 12 shows the model of this system together with the high pass filter in the pressure feedback lines. Figure 13 zooms out implementation of the high pass filter in the pressure feedback lines. This model has been used to investigate the influence of the dynamic pressure feedback in three cases: (1) if implemented on meter-in (high pressure side), (2) if implemented on meter-out (low pressure side) and (3) if implemented on both sides. It has been determined that the introduction of dynamic pressure feedback on both sides has no advantages. Actually, the introduction of dynamic pressure feedback on the meter-in side (high pressure side) has the biggest influence and contributes to the attenuation of the pressure vibrations on the meter-out side also. That happens because two pressures are coupled through the piston. This also has been reported from other scientists [40]. The idea of using dynamic pressure feedback is that the feedback signal reaches its maximum value at a frequency, which has to be damped (the hydraulic frequency  $\omega_h$ ). In the design of the high pass filter two conditions has been followed:

**First**, the cut-off frequency of the filter  $\omega_{hp} = \frac{1}{T_{hp}}$  is set to be below the resonance frequency of the system [3], [40]. For our system it is chosen to be  $\omega_{hp} = 10 [s^{-1}]$ ;  $T_{hp} = \frac{1}{\omega_{hp}} = \frac{1}{10} = 0.1 [s]$ .

**Second**, the feedback gain  $K_{hp}$  is set to obtain reasonable stability margins [40]. Using this principle the value of  $K_{hp}$  has been determinate to be  $K_{hp} = 0.00000007$ .

To investigate the influence of dynamic pressure feedback on vibration damping, the eq. (5) has been changed, actually the friction  $B$  in the mechanical structure has been neglected. This has been done with the purpose to see more clearly the influence of dynamic pressure feedback on vibration damping. Investigations of the implementation of dynamic pressure feedback on the meter-in side have been done with the following scenario:

The cutting head is moved using the vertical cylinder to reach 400 mm displacement from the starting position (see fig. 14, note vertical axis is in [m]). Simple position feedback and a proportional controller is used to track the position. The desired position is reached in approximately 20 s when the

force of 50 kN is applied in the positive direction (restrictive force). The vibrations in the system can be monitored through the pressure sensors on the cylinder and are shown on fig. 15 and fig. 16). On the fig. 15 the pressure oscillations without dynamic pressure feedback are shown and on the fig. 16 the pressure oscillations with dynamic pressure feedback are shown. The attenuation of vibrations is obvious. It is good to note that when no pressure feedback is used, the oscillations created from a sudden big force (step input 40 kN) are a long time transmitted through the system before they are attenuated.

The analysis done in the previous passages lead to the following conclusions:

1. The implementation of the dynamic pressure feedback will damp the oscillations of the system drastically. However, it is interesting to note that simulations shown that the peak pressure has not been removed, rather in some situations it has been enlarged.
2. The draw-back of this principle is that energy from the pump must be supplied in order to damp oscillations. The pump is supplying flow to the meter out port (lower pressurized port) in order to make the system more stiff which is making this method not energy efficient.

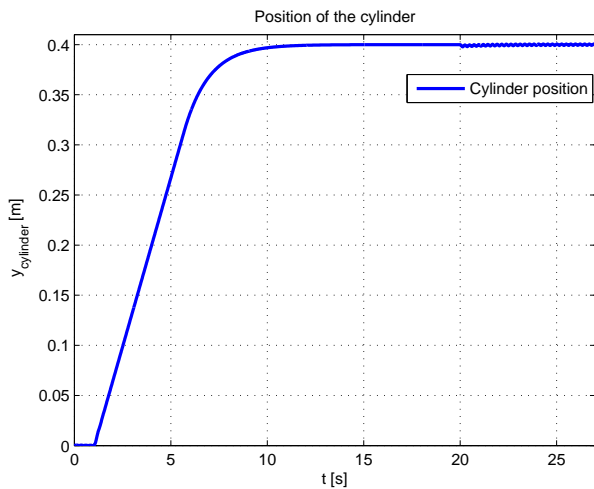


Figure 14: Cylinder position, when force is applied on a LSPC servo system (without DPF).

#### 4 Energy efficient active vibration damping

In this section a novel system for active vibration damping with energy efficient dynamic pressure feedback (EE DPF) is presented. In order to damp vibrations, in the new system it is used third, crossport valve (see fig. 17 and fig. 18). Crossport valve in independent metering systems is usually introduced in order to be used for regenerative purposes as it is shown on fig. 18. When the desired moving direction is the same as the direction of a load force, then the load force can be used as a power supply element in the circuit. In this situation the cross port (third) valve is open and meter-in and meter-out valves are closed (see fig. 18). The speed of the load

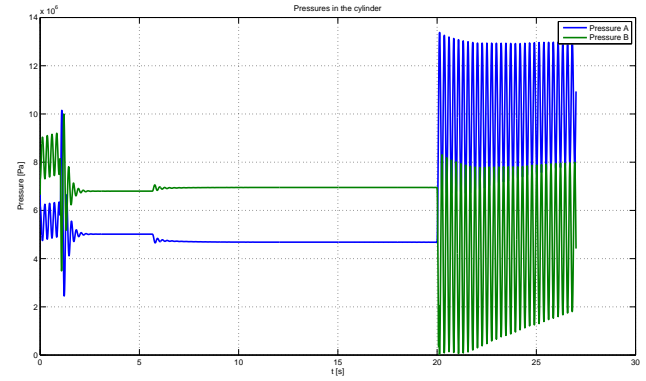


Figure 15: Pressure response without pressure feedback on meter-in side.

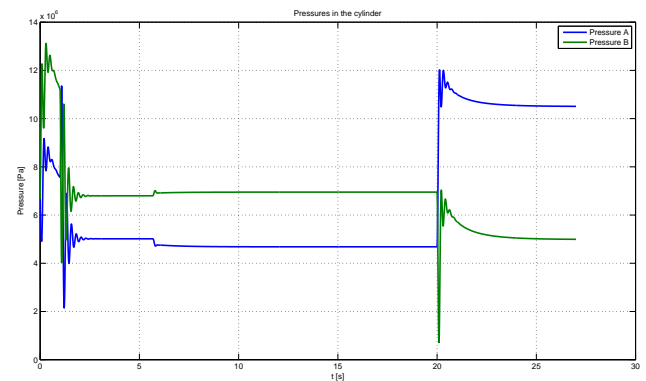


Figure 16: Pressure response with pressure feedback on meter-in side

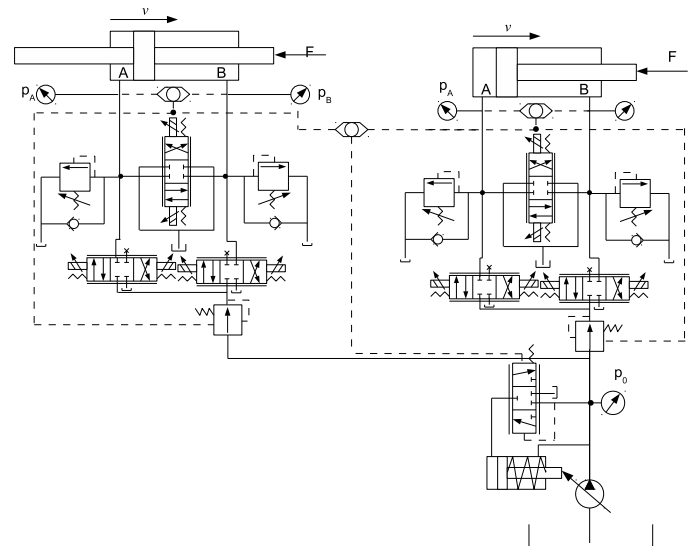


Figure 17: New SMISMO hydraulic system with cross port valve.

is then controlled with the opening of the cross-port valve. The crossport valve works in two modes of operation: (1.) Regenerative extension and (2.) Regenerative retraction.

The idea is to use this crossport valve for energy efficient (EE) active vibration damping with dynamic pressure feed-

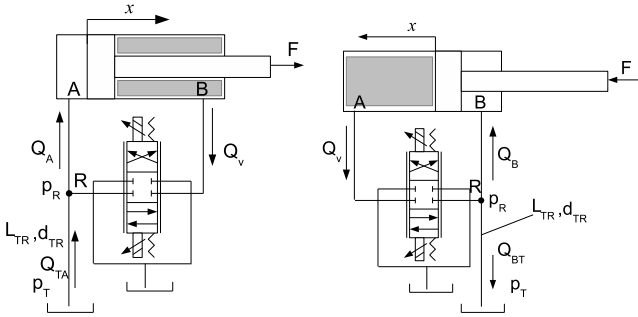


Figure 18: Regeneration with negative force (left) and regeneration with positive force (right).

back (DPF). The third valve for EE DPF can be implemented also in standard servo systems. In order to test this idea, Simulink model of the crossport valve and his controller has been developed (fig. 19 and fig. 20). Simulations have shown that the third valve can be the same type of valve as the other two valves, or with bigger nominal flow.

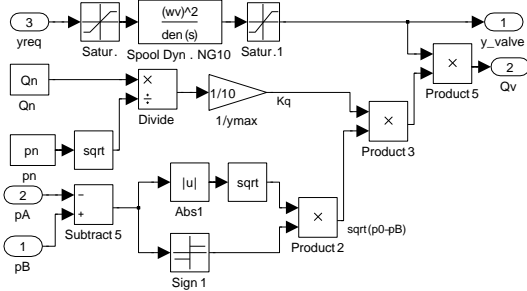


Figure 19: Simulink model of the crossport valve.

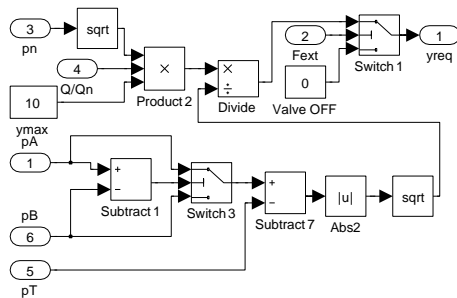


Figure 20: Simulink model of the crossport valve controller.

The following scenario has been examined: cutting head is moved using the vertical cylinder to reach 400 mm displacement from starting position when (in second 20) force of 50 kN is applied in positive direction (restrictive force). The vibrations in the system are monitored trough pressure signals from the cylinder and position signals from the cylinder and cutter head. Since, power represents time derivative of work  $P = \frac{dW}{dt}$  energy can be calculated integrating instantaneous power ( $P = Q_{load} \cdot p_{pump}$ ) over time  $E = W = \int P dt = \int F \cdot v dt = \int p_{sup} \cdot Q_{load} dt$ . The energy spend in period of 10 seconds has been used in comparisons of the suggested strategies, since this period is enough to the system to go back in previous state before the disturbance.

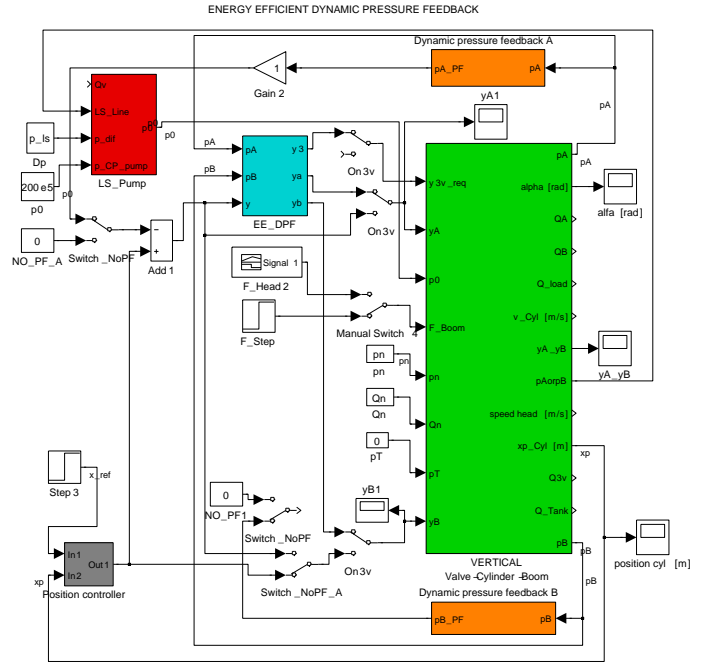


Figure 21: Simulink model of the SMISMO system. Different active damping strategies can be examined using appropriate switches.

Three strategies for active vibration damping have been examined using Simulink model shown on the fig. 21:

**Strategy 1.** Here, DPF has been used as in classical servo systems (fig. 11 and fig. 12). Active damping with dynamic pressure feedback is implemented (only) on the piston side (high pressure side), then signal from pressure oscillations is subtracting the signal from a position controller and then supplying the valve A and valve B (meter-in and meter-out valve) with control signal. Thus, control signals of the valve A and valve B has been influenced from pressure oscillations. Dampening effect in this strategy will be count as best and will be used to compare Strategy 2 and Strategy 3.

On fig. 22 we can see that:

- Pressure oscillations have been attenuated very effectively and in very short period, less then 1 s.
- Unfortunately, for this wonderful work of damping, in 10 seconds, 9840 J of energy have been used from the supply.

**Strategy 2.** In this strategy, DPF is implemented on the piston side, same as in Strategy 1 but now, crossport (3-th) valve is included in control circuit. Control signal to the valves is supplied trough EE DPF controller which decides when will be the third valve turn on. Third valve is activated when the conditions for his activation are fulfilled, actually when  $p_A > p_B$  and control signal from a position controller is negative. For the simulations it is used valve with 20 % bigger nominal flow than other

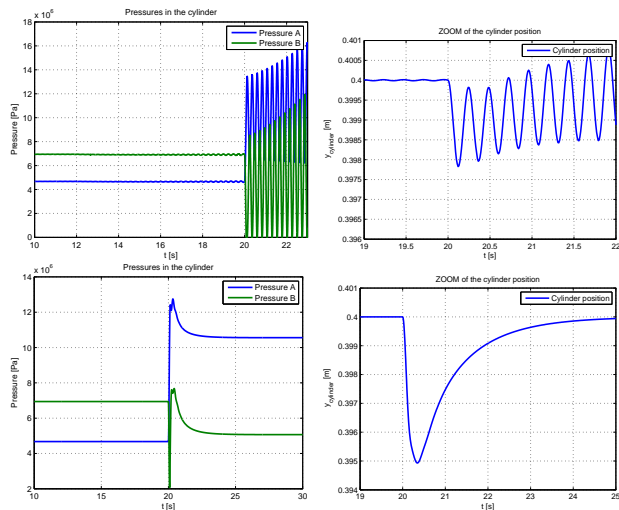


Figure 22: Cylinder pressures and position. SMISMO system without and with DPF.

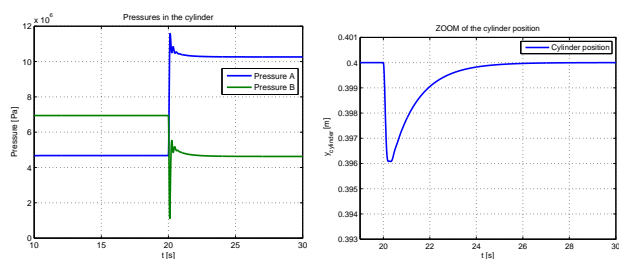


Figure 23: Cylinder pressures and position of the SMISMO system with EE DPF.

two valves, in order to get similar position footprint as in Strategy 1.

Comparing fig. 22 and fig. 23 it can be concluded that with Strategy 2 pressure and position vibrations can be successfully attenuated as well as with Strategy 1, and even better with Strategy 2, pressure in low pressure chamber is not going below 7 bars.

With this strategy for the work of vibration damping, in 10 seconds, 4818 J of energy have been spend from the supply. This means that Strategy 2 is 51% more energy efficient strategy for active vibration damping.

**Strategy 3.** In this strategy, DPF has been implemented on the piston side then signal from pressure oscillations is subtracting the signal from a position controller, then supplying to the valve A. Thus, control signal from a position controller supplied to the valve B has not been influenced. This is not unusual to be done and has been reported as control strategy in [41]. In order to get the same position footprint as in Strategy 1, the signal from DPF had to be 3 times enlarged.

Comparing fig. 22 and fig. 24 it can be concluded that with Strategy 3 position vibrations can be successfully attenuated as well as with Strategy 1. Little pressure vibrations have stayed but they are on satisfactory level. Unfortunately, with Strategy 3, pressure in low pressure

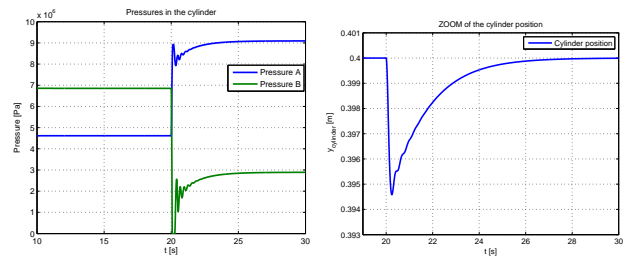


Figure 24: Cylinder pressures and position of the SMISMO system with DPF only on high pressure side.

chamber is falling deep to cavitation. For the work of vibration damping in 10 s with this strategy 6892 J have been spend from power supply.

This means that this strategy has better energy efficiency than Strategy 1 (30%), but one must have in mind that with this strategy pressure control on a low pressure side must be implemented. This strategy can not be implied in standard servo systems.

## 5 Conclusion

Research done in this paper had intention to investigate possible improvements in a hydraulic power system of a mobile machine (mining machine), hydraulic system layout and control strategy, and with this contribute to better vibration damping of the machine.

Investigations has been done using simulations and measurements. Appropriate models of the standard and individual metering load sensing (LS) hydraulic system have been developed. Model of the individual metering system has been validated with measurements. This model has been used to study new control concepts of active vibration damping.

As a result from those investigations, innovative system layout with three independent metering valves has been proposed. The third valve (called also crossport valve) is introduced in order to improve active vibration damping.

The idea to use this crossport valve for active vibration damping with dynamic pressure feedback (DPF) proved to be energy efficient concept. In investigations three strategies has been compared, in first an standard dynamic pressure feedback has been used, in second DPF on only one valve has been used and in third DPF with third valve has been used. Novel concept and control strategy of DPF with third valve proved to be superior in comparison with the other two methods according to their energy efficiency and damping. In comparison, energy efficiency of the novel concept proved potential for 50 % savings with same or better damping effect.

## References

- [1] J. Hosseini. Automatic ride control, 1992.
- [2] S.T. Ufheil et al. Programmable ride control, 1996.
- [3] P. Krus and J.O. Palmberg. Dampening of fluid power systems in machines with high inertia loads. In *Proc. SICFP*, Sweden, 1998.

- [4] S. Mizui et al. Device and method for suppressing vibration of a working machine, 1998.
- [5] K. Moon. Control system for suppression of boom or arm oscillations, 2007.
- [6] K. Yoshino. Vibration control method and vibration control system for fluid pressure control circuit, 2007.
- [7] A.D. Borger et al. Electronic ride control system for off-road vehicles, 1999.
- [8] Lei Zuo et al. Model reaching adaptive control for vibration isolation. 13(4), 2005.
- [9] Lei Zuo, Jean-Jacques, and E. Slotine. Robust vibration isolation via frequency-shaped sliding control and modal decomposition. 2005.
- [10] I. Fialho et al. Road adaptive active suspension design using linear parameter-varying gain-scheduling. 10(1), 2002.
- [11] Toni Lieder. *Improving The Performance Of The Semi-Active Tuned Mass Damper*. PhD thesis, Univ. of OULU, Finland, 2009.
- [12] Jyh-Chyang Renn and Tsung-Han Wu. Modeling and control of a new 1/4t servo-hydraulic vehicle active suspension system. 15(3), 2007.
- [13] C. A. Pare. Experimental evaluation of semiactive magneto-rheological suspensions for passenger vehicles. Master's thesis, Virginia Polytechnic Institute and State University, Virginia, 1998.
- [14] Mark D. Donahue. Implementation of an active suspension, preview controller for improved ride comfort. Master's thesis, B.S. Boston University, Boston, US, 1998.
- [15] Yuyou Liu. *Semi-Active Damping Control For Vibration Isolation Of Base Disturbances*. PhD thesis, University of Southampton, Southampton, UK, 2004.
- [16] K.S. Hon et al. Modified skyhook control of semiactive suspensions: A new model, gain scheduling, and hardware-in-the-loop tuning. In *Proc. of ASME*, 2002.
- [17] A. Preumont. *Active Vibration Control*. Lecture Notes in Active Vibration Control. University Libre de Bruxelles, Brussels, Belgium, 2000.
- [18] T.K. Datta. A state-of-the-art review on active control of structures. 40(1), 2003.
- [19] Kan Shimizu, Toshikazu Yamada, Jun Tagami, and Haruhiko Kurino. Vibration tests of actual buildings with semi-active switching oil damper. In *Proc. of 13th World Conference on Earthquake Engineering*, Vancouver, B.C., Canada, 2004.
- [20] H. Ivanov et al. Optimal control of electrohydraulic power transmission. In *International summer school of automation*, Maribor, Slovenia, 2001.
- [21] J. Leavitt, F. Jabbari, and J. E. Bobrow. Optimal control and performance of variable stiffness devices for structural control. In *Proc. of the American Control Conference*, Portland, OR, USA, 2005.
- [22] P. Holobut. Time-optimal control of hydraulic manipulators with path constraints. 43:523–538, 2005.
- [23] J.A. Aardema et al. Systems and method for controlling an independent metering valve, 1999.
- [24] B. Eriksson. *Mobile Fluid Power Systems Design with a Focus on Energy Efficiency*. PhD thesis, Univ. of Linköping, Linköping, Sweden, 2010.
- [25] B. Eriksson. Control strategy for energy efficient fluid power actuators utilizing individual metering. Master's thesis, Univ. of Linköping, Linköping, Sweden, 2007.
- [26] K. Heybroek. Saving energy in construction machinery using displacement control hydraulics-concept realization and validation. Master's thesis, Univ. of Linköping, Linköping, Sweden, 2009.
- [27] Q.H. Yuan and Jae Y. Lew. Modeling and control of two stage twin spool servo-valve for energy-saving. In *American Control Conference*, Portland, OR, USA, 2005.
- [28] B.S. Turner. Electrohydraulic proportional valve assemblies, 1996.
- [29] B. Yao and S. Liu. Energy-saving control of hydraulic systems with novel programmable valves. In *Proc. of the 4th World Congress on Intelligent Control and Automation*, Shanghai, P.R. China, 2002.
- [30] S. Liu and B. Yao. Energy-saving control of single-rod hydraulic cylinders with programmable valves and improved working mode selection. In *Proc. of the NCFP*, 2002.
- [31] J.A. Crosser. Hydraulic circuit and control system therefor, 1992.
- [32] T. Hajek et al. Hydraulic system with an actuator having independent meter-in meter-out control, 2005.
- [33] C. Dixen and B. Nielsen. Hydraulic valve arrangement, 2006.
- [34] M. Linjama and M. Vilenius. Energy-efficient motion control of a digital hydraulic joint actuator. In *Proceedings of the 6th JFPS International Symposium on Fluid Power*, SUKUBA, 2005.
- [35] B. Eggers, R. Rahmfeld, and M. Ivantysynova. An energetic comparison between valveless and valve controlled active vibration damping for off-road vehicles. In *Proc. Symposium on Fluid Power*, TSUKUBA, 2005.
- [36] Sandvik Mining and Construction G.m.b.H., Sandviken, Sweden. *Sandvik Tunneling Roadheader MT720 in Action*, 2009.

- [37] E. Zaev, G. Rath, A. Tuneski, and D. Babunski. Non-linear modeling and hil simulation of hydraulic cylinder for hydro turbine governing system. In *Proc. ZE-MAK2010*, Ohrid, Macedonia, 2010.
- [38] W. J. Thayer. *Transfer Functions for Moog Servovalves*. Moog Inc., East Aurora, NY, 1965.
- [39] P. Krus. *On Load Sensing Fluid Power Systems with Special reference to Dynamic Properties and control Aspects*. PhD thesis, Univ. of Linkoping, Linkoping, Sweden, 1988.
- [40] H.C. Pedersen, T. O. Andersen, et al. Investigation of separate meter-in separate meter-out control strategies for systems with over centre valves. In *Proc. FPMC2010*, 2010.
- [41] T. O. Andersen. Evaluation of velocity control concepts involving counter balance valves in mobile cranes. In *Proc. IEEE*, 2008.

# Geometrical Design and Operability Verification of a Proportional Pressure Relief Valve

M. Erhard, J. Weber, and G. Schoppel\*

Institut für Fluidtechnik, Technische Universität Dresden, Germany

E-mail: erhard@ifd.mw.tu-dresden.de, weber@ifd.mw.tu-dresden.de, georg.schoppel@boschrexroth.de

\*Bosch Rexroth AG, Germany

## Abstract

This paper demonstrates a novel numerical procedure for a synthesis of electro-hydraulic pressure relief valve performance starting with the performance requirements from a functional specification. Results of this methodological approach are the unknown demands for the solenoid with regard to control orifice concepts and the solenoid geometry itself fulfilling the requirements.

The developed modeling approach comprises two major solution steps. At the beginning the displacement-dependent solenoid-spring force characteristic is calculated from the intended pressure-flow rate characteristic map without the use of optimization tools. This new algorithm performs an inverse simulation of a single stage pressure valve. The next solution step deals with the determination of the geometrical shape of the solenoid. Here steady state FEM computations are used in combination with response surface methodologies to predict the desired geometrical shape. At the end robustness verification is done by means of Monte-Carlo simulation for the uncertainties of the valve assembly.

Starting point for the inverse calculations are different control orifice concepts causing varying demands on the solenoid. As a result of this benchmark the most favorable control orifice concept is used for determination of the solenoid geometry. This is performed within several iterations also considering the spring force. Afterwards the robustness of the valve assembly is examined. The verification of the modeling attempt is done on the basis of prototype parts for the solenoid and the control orifice. Measurements confirm the accuracy of the novel simulation strategy for a standalone virtual product development.

**Keywords:** pressure relief valve, inverse simulation model, solenoid, CFD, FEM

## 1 Introduction

Nowadays, simulation techniques in virtual product development are more and more efficient and reliable offering the possibility for the prediction of valve performance by using only simulation methods. The different simulation techniques cover a wide range of applications, whereby the temporal and spatial distribution of the inner field variables as well as the overall system behavior is in the focus of the investigations. The acquired transparency of the inner field variables in combination with the resulting component performance establishes a basis for a knowledge-based further development of these electro-hydraulic components.

Nevertheless, the complex and nonlinear character of electro-hydraulic valves and its physical-based description were already part of previous scientific work not all fields of application are considered until now. In particular, this includes without limitation the prediction of the geometrical shape of the different physical subsystems of an electro-

hydraulic valve outlined in fig. 1 with respect to an intended and predefined valve performance, respectively. Although modern simulation techniques, e.g. finite-element-methods (FEM) or computational fluid dynamics (CFD), establish a relation between the geometrical shape and the subsystem performance including solenoid force, pressure drop or pressure distribution, in general no explicit formulation of these linkages is possible.

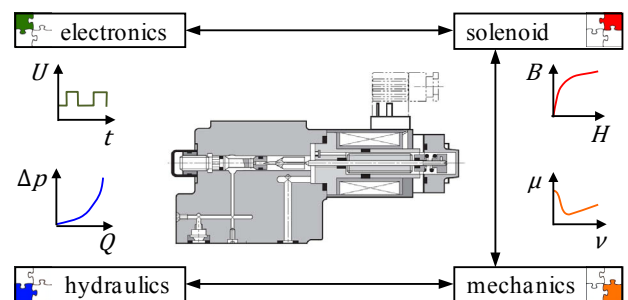


Figure 1: Physical subsystems of electro-hydraulic valves

This describes the well known problem of inverse simulation techniques. Normally, the so called "forward simulation" or "analysis" gives a suitable solution whereas the "inverse simulation" or "synthesis" requires particular solution strategies. Leaving the subsystem level, see fig. 2, the same problem exists on the component level. Starting from an intended valve performance the unknown subsystem characteristics have to be determined initially followed by the estimation of an appropriate geometrical shape.

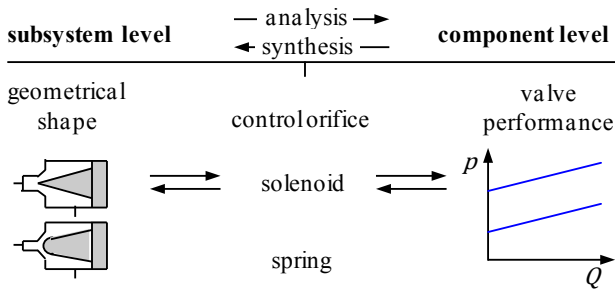


Figure 2: Simulation inputs and outputs (schematic)

As outlined above, the simulation techniques presented in literature predominantly focus on the analysis of existing systems, the verification of the methodological approach or the failure analysis. The mathematical analysis of a direct-operated pressure valve [1, 2] reveals fundamental relations, especially concerning the dynamic valve behavior. Because no detailed parameters for the flow region are taken into consideration, no linkage between the geometrical shape and the valve performance can be established. An extension of this initial analysis approach is given through the involvement of detailed field simulation techniques for parameter extraction, namely FEM and CFD. Current papers [3] illustrate the modeling approach for electro-hydraulic proportional valves using FEM for parameterization of the solenoid and simplified parameters for the hydraulic and mechanical subsystem. Other authors [4, 5] use CFD calculations for the hydraulic part of the valve, gaining a deeper insight of the internal flow and the force on the valve spool. This enables more detailed simulation models and broadens its range of application such as a failure analysis based on the geometrical tolerances of the flow region. A combination of both modeling strategies is presented in [6] predicting the whole component performance without measurements using a holistic approach. Recent developments [7, 8] merge the advantage of a detailed flow simulation with the possibility of component performance predictions. These so called fluid-structure interaction simulations create new opportunities for the investigation of significant more complex problems.

However, there is a similarity between these modeling approaches: each focuses on the analysis of an existing system. The more interesting issue primarily in industrial applications deals with the inverse problem. Here, the functional specification defines the valve performance and the necessary subsystem characteristics as well as the associated geometrical shapes are unknown. Usually, this is done by a trial&error process but simulation techniques become more and more important in this field of application. The imple-

mentation of these techniques on the component level for the hydraulic subsystem is presented in [9] optimizing the relief valve performance based on a holistic simulation approach. Because no linkage between the geometrical shape of the flow region and the describing parameters exist radical changes of the flow region aren't permissible.

This paper takes up this gap by establishing an inverse simulation approach for a direct-operated proportional pressure relief valve. An initial approach for this idea was already presented by the authors in a preceding paper [10]. The inverse simulation is carried out in two major steps starting on the component level with the calculation of the unknown subsystem characteristics. Afterwards, the geometrical shape fulfilling the subsystem requirements is predicted. Because of the multi-dimensionality of this task a simplification step is introduced. The problem dimension is reduced by replacing the degrees of freedom of the control orifice in a way that predefined concepts are investigated.

The simulation model developed by the authors demonstrates the conceptual and geometrical design of a pressure valve starting from the intended valve performance. Since the expected valve performance is predicted only using nominal values of the influencing parameters a further robustness analysis is implemented. The additional information facilitates the interpretation of the prototype performance. Final measurements of solenoid and valve characteristics verify the quantitatively accurate predictions and show the potentials of this novel methodology.

## 2 Proportional pressure relief valves and its modeling

The component analyzed in this work is a direct-operated proportional pressure relief valve with its main elements illustrated in fig. 3. Increasing demands in power-density are the driving factors for new solutions for these valves, whereby further enhancement in valve performance is restricted through the limits determined by physical laws. Decreasing component sizes simultaneously linked with increasing nominal flow rates result in higher energy losses and actuator forces. In conjunction with minimized electric power consumption valve operability strongly depends on highly-adapted flow conditions and actuator concepts. Pressure relief valves are generally used for pressure limitation or pressure setting, whereas the pressure-flow rate characteristic curve is a crucial property. Additionally, the dynamic behavior has an important role especially the stability in all operating points. Dynamic analyzes of this valve aren't part of this paper, neglecting all derivatives with respect to time.

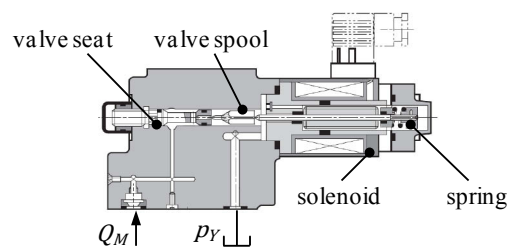


Figure 3: Assembly structure of investigated pressure valve

Electro-hydraulic valves, just as the proportional pressure relief valve outlined in fig. 3 are characterized through complex interactions between the different physical subsystems. Special emphasis should be placed on the influence of the valve seat/valve spool combination in conjunction with the solenoid-spring force characteristics on the system performance. Therefore, a well-coordinated geometrical shape of both subsystems offers the possibility for great performance enhancements. Hence, knowledge and transparency of the spatial distribution of the inner field variables as well as understanding the major interactions between these different subsystems are essentially for a successful valve design.

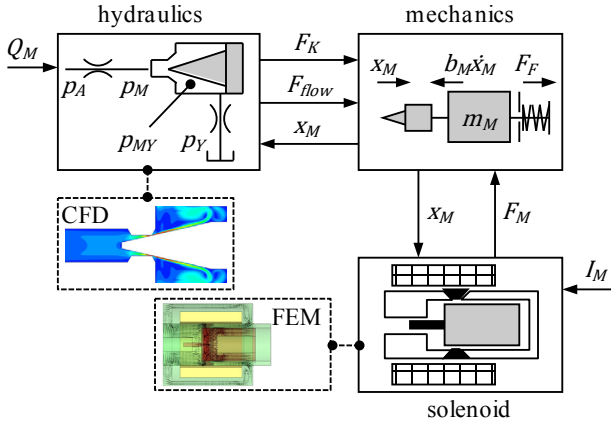


Figure 4: Modeling structure

The modeling structure, see fig. 4 is directly derived from the element structure of the valve assembly; the electronics is not part of the investigations. A detailed description of the remaining subsystems is outlined in the following subsections.

## 2.1 Hydraulic subsystem

Irreversible energy losses and the force reaction on the valve spool are considered in this subsystem. In case of pressure valves these losses occur predominantly at the control orifice, additional losses are in the upstream and downstream flow region. The loss coefficient  $\zeta$  for hydraulic resistances with cross-section  $A_{flow}$  is calculated with eq. (1). Therein  $\Delta p$  represents the pressure loss over a given system length with closest cross-section  $A_{flow}$  at flow rate  $Q_M$ . For more complicated control orifice designs the application of an alternative modeling approach in form of characteristic maps following eq. (2) is also conceivable.

$$\zeta = \frac{\Delta p}{\frac{\rho}{2} \left( \frac{Q_M}{A_{flow}} \right)^2} \quad (1)$$

$$\Delta p_{M-MY} = f(Q_M, x_M) \quad (2)$$

With the knowledge of pressure losses the static pressures  $p_A / p_M / p_{MY}$  in the valve as well as the force reactions on single boundaries of the flow region can be calculated. Here, the valve spool is the element of interest. The static pressure on the valve spool decreases continuously once the fluid is accelerated in proximity to the control orifice, see fig. 5. The

resulting valve spool force is influenced through the appearing pressure profile making and adjustment of the force equation necessary. Therefore, eq. (3) concerning the force reaction  $F_{spool}$  is split into a theoretical pressure force  $F_K$  and a corrective term  $F_{flow}$  called flow force. The model eq. (4) for the flow force is determined by conservation of momentum, whereas  $k_{GF}$  represents a preliminary unknown coefficient characterizing the control orifice design.

$$F_{spool} = F_K - F_{flow} \quad (3)$$

$$F_{flow} = \frac{\rho Q_M^2}{A_{flow}} k_{GF} \quad (4)$$

$$F_{flow} = f(Q_M, \Delta p_{M-MY}) \quad (5)$$

If the results for the geometrical coefficient show no clear allocation, an adequate description of the flow force also requires the use of characteristic maps according to eq. (5). In contrary to the previous equation the displacement  $x_M$  of the valve spool isn't explicitly included any more.

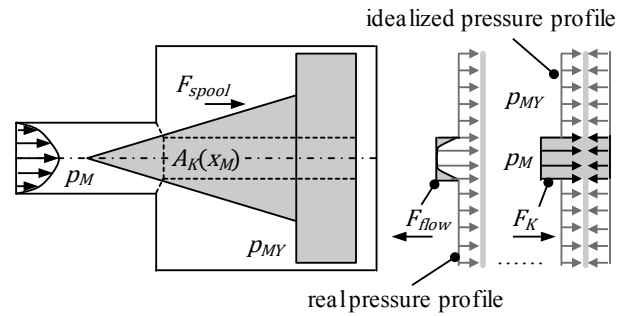


Figure 5: Force on the valve spool

## 2.2 Mechanical subsystem

The valve performance of pressure valves is governed by flow-induced force effects which are in mechanical equilibrium with the solenoid  $F_M$  and spring force  $F_F$ . The equation of motion (6) summarizes all force effects dependent on valve displacement  $x_M$ , time  $t$  and solenoid current  $I_M$ . In general, frictional and damping forces are present, their implementation is simplified and reduced to a viscous friction coefficient  $b_M$ . However, this simplification has no influence on the static valve performance.

$$m_M \ddot{x}_M + b_M \dot{x}_M - F_K + F_{flow} + F_M - F_F = 0 \quad (6)$$

Since the design of the static valve performance is the major focus of this paper all derivatives with respect to time  $\partial/\partial t$  are neglected later.

## 2.3 Solenoid subsystem

The solenoid depicted in fig. 6 is an electromechanical transformer. The current  $I_M$  in the coil causes a magnetic flux in the magnetic circuit consisting of armature, yoke and pole tube. In the residual air gap arises an attractive solenoid force  $F_M$  between armature and pole tube. Their dependence on the current  $I_M$  and the armature displacement ( $x_M + x_{M0}$ ) is determined by the geometrical shapes of the elements in the magnetic circuit as well as their nonlinear material proper-

ties. The solenoid's force-displacement curves are represented in the following modeling steps by a characteristic map; see also eq. (7). A time dependence of the solenoid's force is neglected because the dynamic performance of typical actuators is sufficient for applications in pressure valves.

$$F_M = f(x_M + x_{M0}, I_M) \quad (7)$$

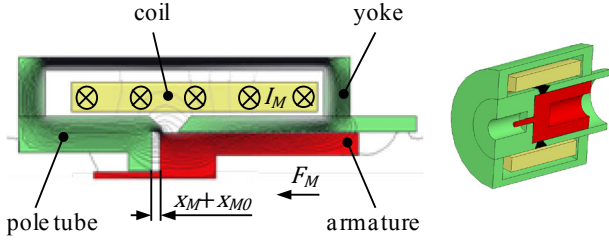


Figure 6: Setup of the electromechanical transformer

### 3 Inverse simulation model

As explained recently the static valve performance is an important property for this valve type. It results from the force interactions of the different physical subsystems outlined in short in fig. (4). System inputs are the flow rate  $Q_M$  and the solenoid current  $I_M$ , the valve displacement  $x_M$  and the pressure  $p_A$  result from the geometrical shape of the involved elements and the other system parameters. Here, the geometrical shape of the control orifice is represented through the loss and geometrical coefficient or the associated characteristic maps. The solenoid's geometry is included by its force-displacement curves.

#### 3.1 Forward problem formulation

Starting point for the inverse simulation is the mathematical description of the pressure-flow rate characteristics, because these curves represent the subsequent inputs later. The pressure  $p_A$  is the sum of three pressure drops eq. (8), whereas the important term is the pressure loss  $p_M - p_{MY}$  at the control orifice. The computation of the other pressure losses in dependence of the flow rate is a simple problem.

$$p_A = \Delta p_{A-M} + \Delta p_{M-MY} + \Delta p_{MY-Y} + p_Y \quad (8)$$

After combining the equation of motion with the equation for the hydraulic resistance a new transcendent equation (9) establishes the linkage between the valve functionality and the subsystem properties.

$$Q_M^2 = \frac{F_M - F_F}{\zeta_{M-MY} \frac{\rho}{2} \frac{A_K}{A_{flow}^2} - \frac{\rho}{A_{flow}} k_{GF}} \quad (9)$$

The above equation forms the basis for the following considerations. It defines an implicit relation between the flow rate and the valve displacement. With the knowledge of the flow rate all pressure drops are computable and the static valve performance curves result from the  $p_A = f(Q_M)$  linkage. Without the use of the coefficients  $\zeta_{M-MY}$  and  $k_{GF}$  another solution strategy is required. Therefore, the flow rate becomes an additional iteration parameter. Now, the equivalent root problem eq. (10) needs to be solved in a proper

way. The major difficulty lies in the transcendent character of this equation and that the convergence is evaluated in the pressure drop at the control orifice while the iteration parameter is given through the flow rate. With the help of an iterative problem-solving approach a feasible solution was found.

$$\Delta p_{M-MY}(Q_M, x_M) = \Delta p(x_M, F_{flow}(Q_M, \Delta p_{M-MY}), F_M - F_F) \quad (10)$$

Equations (9, 10) illustrate how modifications of the geometrical shape influence the valve performance. This happens through changes in the coefficients or in the characteristic maps for the control orifice and the solenoid.

#### 3.2 Inverse problem formulation

Based on the mathematical formulation of the static valve performance an inverse solution strategy is developed. Here, the new inputs for the simulation model are the characteristic curves  $p_A = f(Q_M)$  for  $I_M = \text{const.}$  Furthermore, these inputs form the basis for a subsequent solenoid design in combination with the already mentioned predefined control orifice concepts.

The mathematical solution involves several solution steps. First, the hydraulic resistances for the upstream and downstream flow region have to be subtracted from the input curves according to eq. (8) remaining the pressure drop-flow rate relation for the control orifice. The next step is indispensably for the calculation of the force-displacement curves. Here, the essentially needed linkage between pressure drop, flow rate and valve displacement have to be determined. Therefore, the resistance equation is transformed into a root problem eq. (11). Because of the predefined control orifice concepts only the smallest cross-section  $A_{flow}$  is unknown. The geometrical shape of the control orifice directly connects the flow area with the valve displacement. An equivalent solution is possible when the characteristic map  $\Delta p = f(Q_M, x_M)$  is used instead of the model equation.

$$0 = \zeta_{M-MY} \frac{\rho}{2} \left( \frac{Q_M}{A_{flow}(x_M)} \right)^2 - (p_M - p_{MY}) \quad (11)$$

If the valve displacement is known the sum of solenoid and spring force  $F_M - F_F$  can explicitly be computed according to eq. (9). The use of characteristic maps yields to a similar equation.

$$F_M - F_F = Q_M^2 \left( \zeta_{M-MY} \frac{\rho}{2} \frac{A_K}{A_{flow}^2} - \frac{\rho}{A_{flow}} k_{GF} \right) \quad (12)$$

$$F_M - F_F = A_K \Delta p_{M-MY} - F_{flow}(Q_M, \Delta p_{M-MY}) \quad (13)$$

Equations (12, 13) summarize the two different solution opportunities. They offer a possibility to compute the force characteristics for the solenoid-spring combination without any optimization algorithm. The solution strategy bases on the idea that different geometrical control orifice concepts require various counter forces for realization of the intended valve performance. Hence, the choice of a control orifice put requirements on the solenoid's force-displacement characteristics whose achievement by a geometrical design remains

unanswered so far. The next logical step includes the calculation of the force demands for the different predefined control orifice concepts and their benchmarking with respect to a general feasibility. The following section focuses on these issues.

## 4 Geometrical valve design

### 4.1 Control orifice concepts

As explained in the previous sections every control orifice concept can be described with four characteristic curves. The geometrical values are the closest cross-section  $A_{flow}(x_M)$  and the theoretical pressure area  $A_K(x_M)$ . The energy losses are modeled with the loss coefficient  $\zeta_{M-MY}$  and the force reactions with the geometrical coefficient  $k_{GF}$ . Alternatively, characteristic maps are used instead of the coefficients describing the fluid flow. For the pressure relief valve three different geometrical concepts were investigated; see fig. 7. These include a valve seat with a chamfer and a valve spool shaped in a cone-/piston-/sphere-like manner. This selection ensures geometric similarity meanwhile all other differences result from the flow-dependent model parameters.

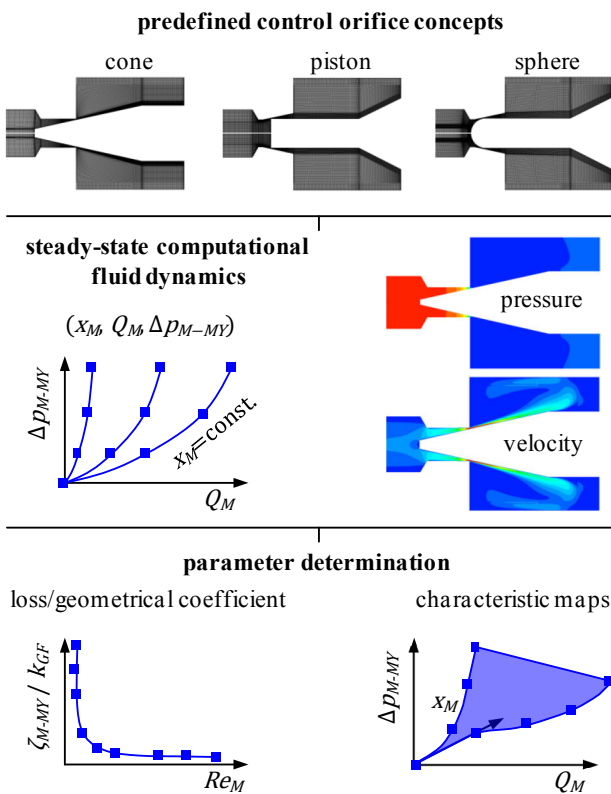


Figure 7: Determination of the hydraulic parameters

The numerical CFD simulations are carried out for several valve displacements analyzing the pressure drop at the control orifice and the force reaction on the valve spool. Assuming similar flow conditions at different valve displacements, a reduction of the obtained results to a 1-dimensional model description is possible. Otherwise, the complex 3-dimensional fluid flow is expressed in terms of characteristic maps.

Figure 8 illustrates the results for the hydraulic resistance and the flow force depending on the Reynolds' number  $Re_M$ .

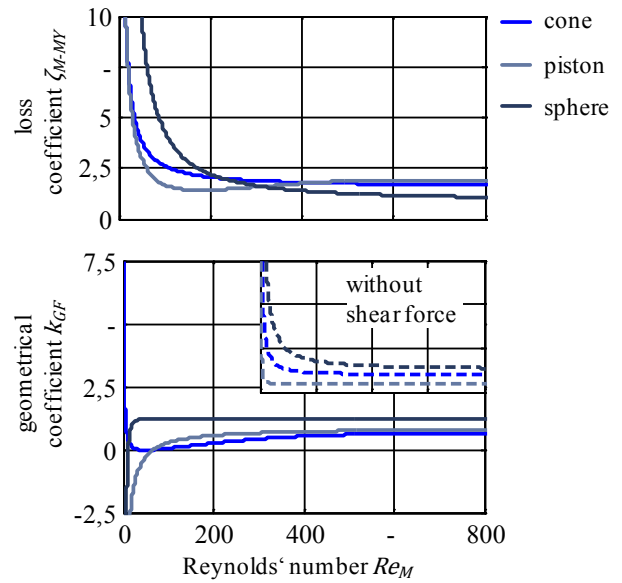


Figure 8: Control orifice characteristic curves

The results of fig. 8 show the different hydraulic behavior of the investigated control orifice concepts. The differences in the laminar region of the loss coefficient  $\zeta_{M-MY}$  can easily be explained through the geometrical shape of the control orifice. Neglecting the shear forces at the valve spool lead to similar characteristic curves for the geometrical coefficient  $k_{GF}$ . Since the shear forces support the valve opening the acting flow forces are reduced and the geometrical coefficient displays these distinctions. Especially for the cone- and sphere-shaped orifice geometry there exist large differences in the remaining flow forces.

### 4.2 Determination of counterforce characteristics

In this subsection, the previously computed characteristic curves for the control orifice concepts are combined with the intended valve performance. For reasons of simplification the whole pressure difference should operate at the control orifice, thus no additional upstream and downstream resistances exist. The results outlined in fig. 9 indicate various differences between the control orifice concepts. For the same static valve performance there exist different demands on the valve displacement. The reason, of course, lies in the varying loss coefficient. In contrast to this, the slopes of the force characteristics dominantly result from the hydraulic forces, in particular the flow force. Additionally, the force slopes differ between a low and high pressure setting entailing a spreading dependent on the applied orifice design.

The benchmark of the different orifice concepts leads to a favorable design. As a result, the cone-shaped control orifice remains for the following considerations because of its advantageous counterforce slopes. The decreasing force slope at maximum pressure setting ensures that almost the whole solenoid force is used for closing the valve seat. This supports the development of a smaller actuator. Furthermore,

the convenient spreading of the force slopes facilitates the realization through a solenoid.

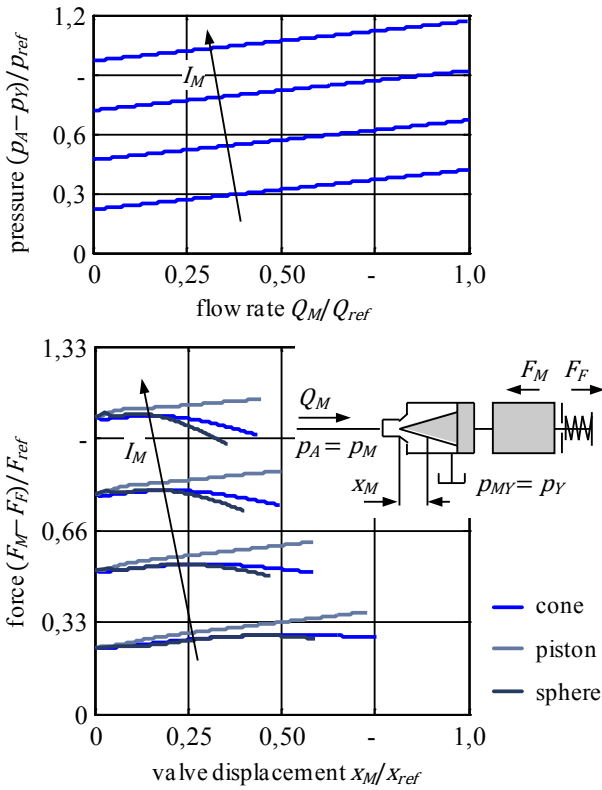


Figure 9: Pressure-flow rate demands and computed counterforce maps

Against the backdrop of a subsequent geometrical solenoid design the required counterforce map contains features of a proportional and switching solenoid. In combination with a spring the realization of this force demands appears possible. How accurate the implementation succeeds is presented in the subsequent section for the solenoid design.

### 4.3 Solenoid design

Starting from the preliminary draft the force requirements have to be fulfilled by a derived solenoid and its geometrical design. As already mentioned the force characteristics combine a switching and proportional behavior. The idea behind the solenoid design is to realize the force spreading inside the actuator and modify the force level with a linear spring. This strategy shows fig. (10). Here, the three governing demands are the maximum force to achieve the highest pressure setting, the necessary operating range the counterforce have to be present and the spreading in the force slopes to obtain a uniform pressure rise independent of the pressure setting. A backward calculation of the solenoid force from the counter forces is nontrivial, because additional parameters characterizing the spring are introduced. These parameters are the spring rate and the spring preload. Furthermore, the used armature displacement range defined through the residual air gap is also of interest. For simplification, the design demands for the solenoid are formulated without the spring force. This allows further adjustments after the geometrical design of the solenoid.

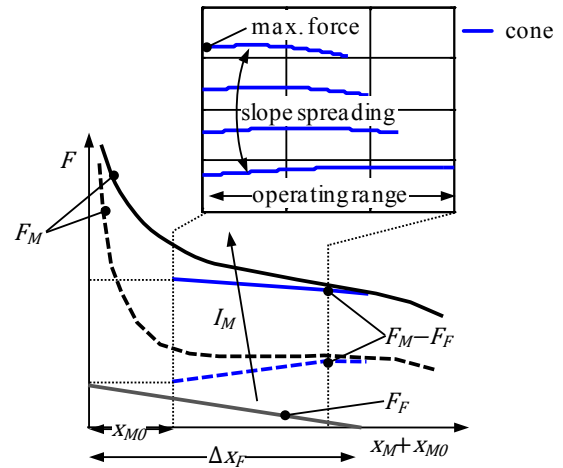


Figure 10: Analysis of the required force characteristics

Based on the requirements the design of the force-influencing air gap in the pole tube was done by means of response surface methodology. Afterwards, different combinations of the solenoid's force characteristics including the spring force were compared until an adequate solution was reached. A final comparison clarifies fig. (11). There, the results agree well at low pressure settings, at higher pressure settings only the average slope is reached. The affect of these differences on the overall valve performance in contract to the preliminary design is discussed in the following sections.

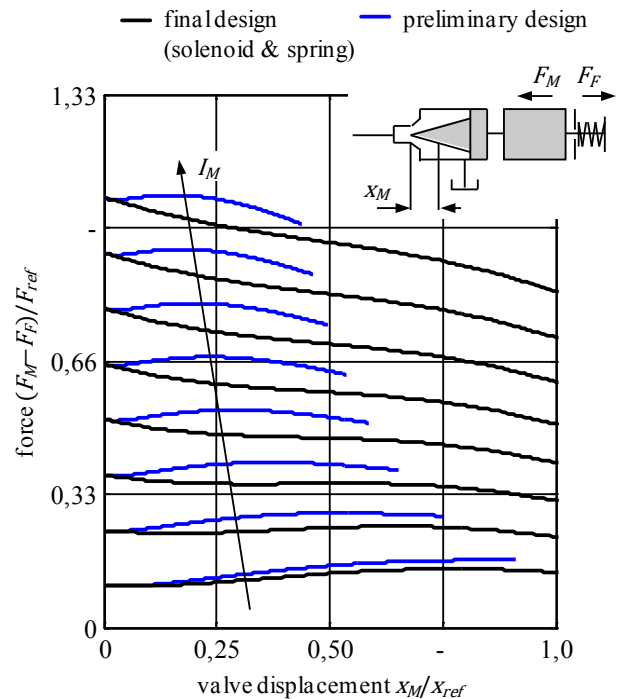


Figure 11: Achieved force characteristics: solenoid-spring combination

In taking a deeper insight into the resulting counterforce map, the force slopes reveal as source of uncertainties. This means, that a deviation of the valve adjustment can cause force errors, even if the compensation of the pressure setting

through spring preload modifications is generally possible. However, additional errors due to the different reference position may exist. The answer of this question is explained in the second last section.

### 5 Measurement and simulation results

After the fundamental preliminary design of the solenoid on the basis of control orifice concepts with the help of the inverse simulation model the real prototype valve and its subsystem characteristics are considered in a simulation model. Therefore, the already presented solenoid force-displacement characteristics are compared with measurement results of the manufactured solenoid. The characteristic curves of the solenoid are measured without the hydraulic elements of the valve assembly. Here, the armature of the solenoid acts against a force transducer, their displacement is measured contactless via laser triangulation meanwhile the coil is set under direct current.

The measurement results in fig. 12 show a good agreement with the simulation at high solenoid currents. At lower magnetic potentials the differences between measurements and simulation rise slowly approving the used simulation methods for a geometrical solenoid design. Anyway, the most influencing factors and crucial simulation parameters in this designing stage are the material properties of the elements in the magnetic circuit. The accuracy of the FEM simulation results is very sensitive to this parameter making intensive foregoing considerations necessary. After the actuator verification the next steps involve the evaluation of the hydraulic subsystem and of the whole component performance.

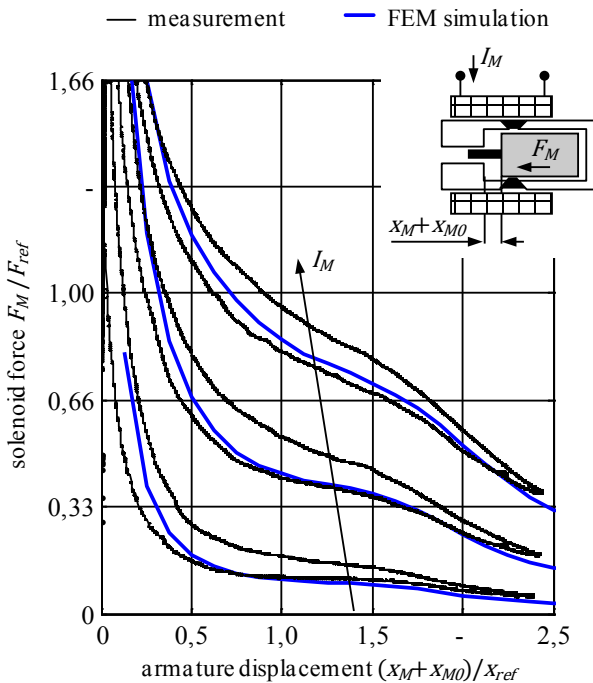


Figure 12: Solenoid force-displacement characteristics: measurement vs. simulation

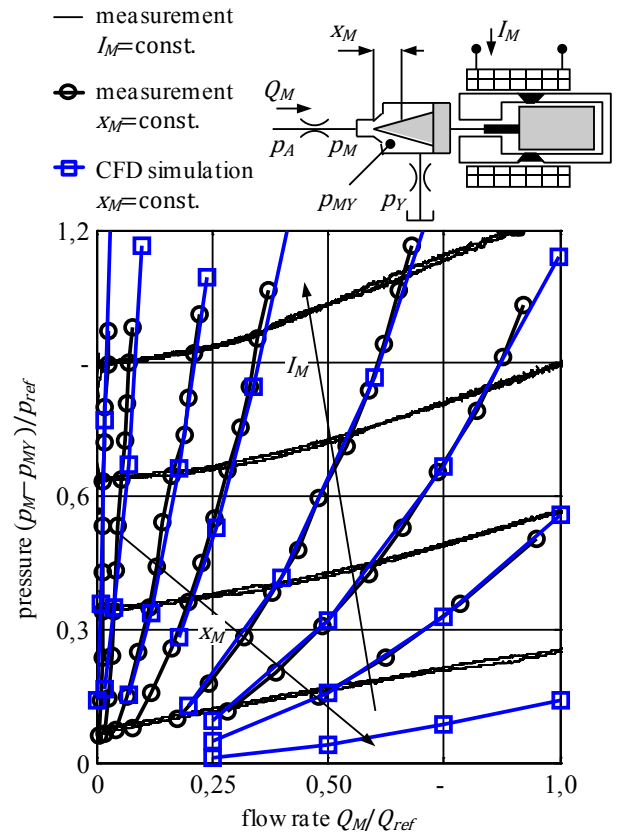


Figure 13: Control orifice pressure drop-flow rate characteristics: measurement vs. simulation

The verification of the hydraulic subsystem is done through the comparison of the pressure drop-flow rate characteristics of the control orifice. The force reaction on the valve spool isn't measured directly, for what reason the validation of the flow forces can only be done indirectly by comparing the valve performance curves. In accordance to the CFD simulation the pressure loss have to be evaluated for a constant valve displacement. Thus, the static valve performance is measured quasi-statically and the desired values are extracted from these results as illustrated in fig. 13 subtracting the upstream and downstream pressure loss before. The measurement of the valve displacements during valve operation is quite complex, because no additional leakage or friction should be incorporated into the system. For this reason, an optic measurement method was chosen and the armature displacement was captured with a laser vibrometer. The presented measurement results are in very good agreement with the simulation results and acknowledge the applied parameter description according to fig. 8. Because no direct force reaction estimation is possible the next step includes comparisons of the whole valve performance.

For verification of the valve performance, there are several issues to take into account, especially the valve adjustment. Here, the valve setting inclusive spring preload has to be identically in measurement and simulation, which requires special efforts in measurement preparation. After this, the static valve performance is validated through the three state variables pressure drop/flow rate and valve displacement. Because the functional specification is given as a function of

flow rate all characteristic curves in fig. 14 are plotted against the flow rate.

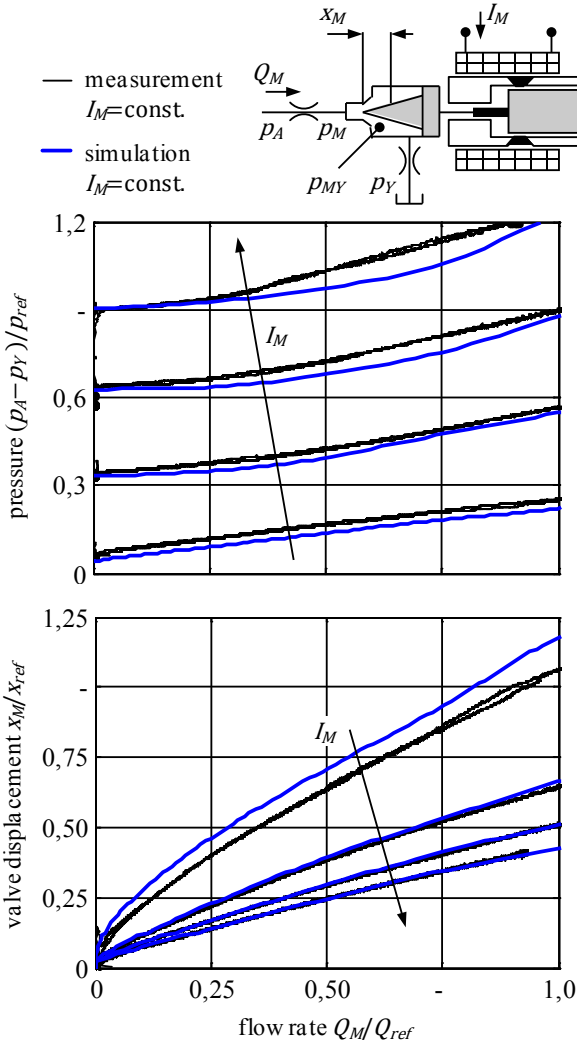


Figure 14: Static valve performance: measurement vs. simulation

The valve displacements in measurement and simulation agree very well with each other. The reason for this was already explained in the verification of the hydraulic subsystem, see also fig. 13. Therefore, the existing differences result only from the slight deviations in the opening pressures. Another situation illustrates the pressure-flow rate characteristic curves. The correlation between measurement and simulation differs increasingly with the opening pressure and the flow rate. A detailed investigation of these deviations inside the CFD simulation shows the formation of a stagnation point within the downstream flow region. This disturbs the force balance at the valve spool and as a consequence the valve performance. At this point, no further investigations are done.

The comparison between the intended and achieved static valve performance confirms the applicability of this simulation strategy for valve design. The differences at low flow rates and high pressure settings can be explained with the counterforce map according to fig. 11. The additional pres-

sure rise at higher flow rates and opening pressures is the result of a stagnation point. Its effect on the force balance can be suppressed through further modifications not discussed in detail here.

Besides the static valve performance pressure relief valves tend to instability requiring additional considerations during the designing stage. The equations for the physical-based description of the valve performance include parameters that only act on the dynamic valve performance. These variables introduce enough degrees of freedom to perform a dynamic valve design in parallel to the static one. No dynamic simulations in the time domain for the whole valve assembly were done, but further measurements to confirm the desired system damping. Figure 15 summarizes some of the measurement results for a nominal current jump at the solenoid at different flow rates.

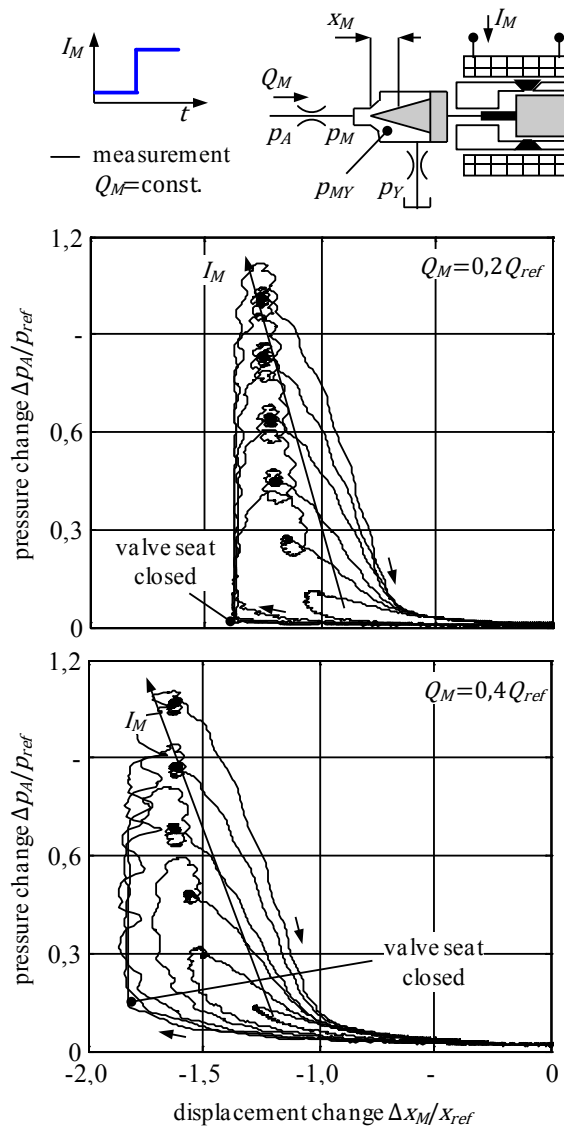


Figure 15: Dynamic valve performance: measurement

The measurements show, that in dependence of the size of the current jump the valve seat is temporarily closed by the solenoid. This tendency decreases with increasing flow rates. Furthermore, the system damping increases with the

flow rate and decreases with the size of the current jump. However, the system damping is more than sufficient in every operating point sometimes characterized by slight overshoots in the pressure. The primary causes of these overshoots are the small slopes of the pressure-flow rate characteristic curves at higher opening pressures and small flow rates, because the system damping is contrarily to the pressure-flow rate slopes. All in all, the geometrical design of the proportional pressure relief valve provides good results for the overall valve performance without integration of measurements during the virtual design process. Finally, the robustness of this valve assembly is investigated. The reason for this originates from the existing uncertainties within the valve assembly and the related adjustment effort.

### 6 Sensitivity and robustness analysis

The sensitivity and robustness analysis contain of several solution steps outlined in fig. 16. The computation is done with the so called Monte-Carlo simulation. First, a simulation model for the system must be available including the system parameters and their uncertainties. For every random parameter, the variance has to be described in an appropriate manner. After that, random samples of the valve are generated and computed within the simulation model. Finally, the extraction of relevant parameters from a set of random characteristic curves yields information about mean value, distribution and dependences of the output variables. Different evaluation possibilities for the massive set of simulation data exist, whereby histogram plots and first-order and total-effect sensitivity indices are suitable for general nonlinear systems like the proportional pressure relief valves.

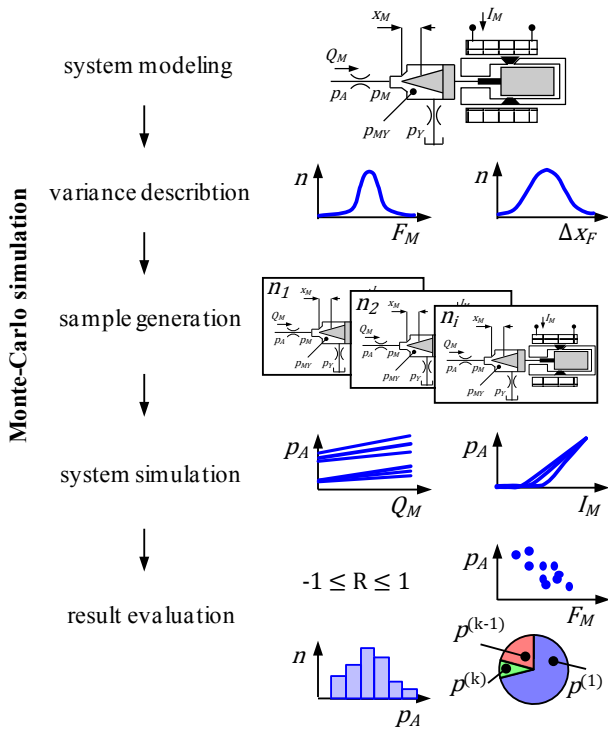


Figure 16: Probabilistic analysis: Monte-Carlo simulation

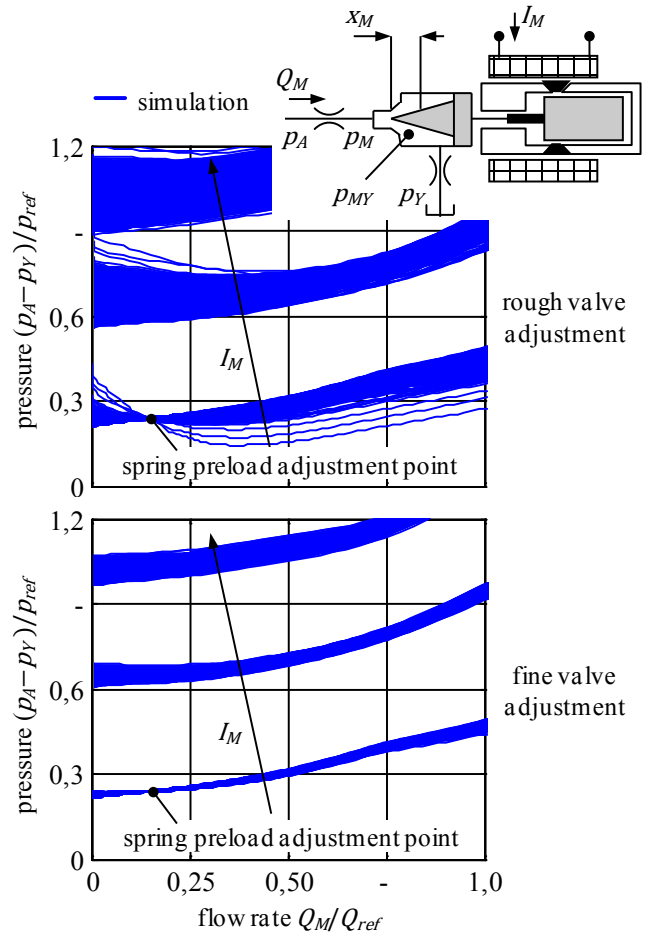


Figure 17: Monte-Carlo simulation: influence of valve adjustment on valve performance

The basis for the Monte-Carlo simulation is the simulation model for the whole valve assembly. Therein, the geometrical tolerances and other uncertainties are integrated. The characteristic curves for the control orifice are held constant during the simulations. In contrast to this, force variations of the solenoid are incorporated in a proper way. A major problem during sample generation is the determination of the spring preload because the adjustment point is a simulation point and a priori not known. Assuming a definite valve displacement and flow force for this operating point, the solution of the balance of forces is possible resulting in a distribution for the spring preload. Figure 17 depicts some results of these simulations for two different adjustment accuracies. The results verify the setup procedure for the valve assembly during sample generation. Additionally, the results provide an insight into the massive set of data and the expected pressure distributions.

As illustrated in fig. 17, it would be very helpful to estimate the influence of a single parameter uncertainty onto a particular output distribution. In the linear case, this can be realized with correlation coefficients. Otherwise, the variance-based sensitivity analysis is an appropriate solution strategy. The computation of correlation coefficients eq. (14) is known from basic mathematics. For two random samples  $A, B$  the correlation coefficient is in the range of  $R = -1$

to 1. No correlation exists if the coefficient is approximately zero; otherwise a partial linear relationship is present. By transferring these basics to the Monte-Carlo simulation correlation coefficients can be calculated for every output variable in relation to every input uncertainty. These values describe, among others, the arrangement of the simulation points in the so called scatter plots.

$$R(A, B) = \frac{\text{Cov}(A, B)}{\sqrt{\text{Var}(A) \cdot \text{Var}(B)}} \quad (14)$$

Another possibility is the computation of first-order and total-effect indices using the variance-based sensitivity analysis. Here, the single influences and their interactions with each other are calculated from two sets of independent random samples. For that reason, the two sets of samples have to be computed as well as several resampling matrices of the independent inputs. Together with the necessary sampling length for achieving statistical convergence, computation effort increases intensely. Various formulas published in literature exist for the computation of these indices, whereby the calculation method presented in [11] is used; see also eq. (15, 16). Therein,  $S_i$  denotes the first-order and similarly  $S_{Ti}$  the total-effect indices.

$$S_i = \frac{1}{N-1} \sum_{r=1}^N f_{B,r} \cdot (f_{A_{B,r}^i} - f_{A,r})^2 \quad (15)$$

$$S_{Ti} = \frac{1}{2N} \sum_{r=1}^N (f_{A,r} - f_{A_{B,r}^i})^2 \quad (16)$$

Based upon the evaluation basics the simulation results for a proper adjusted valve assembly stated at the bottom of fig. 17 are used for further investigations. Thus, the distribution of the pressure and pressure rise for a constant flow rate is extracted for different solenoid currents and outlined in fig. 18. The flow rate at the spring preload adjustment operating point is chosen as reference for these studies.

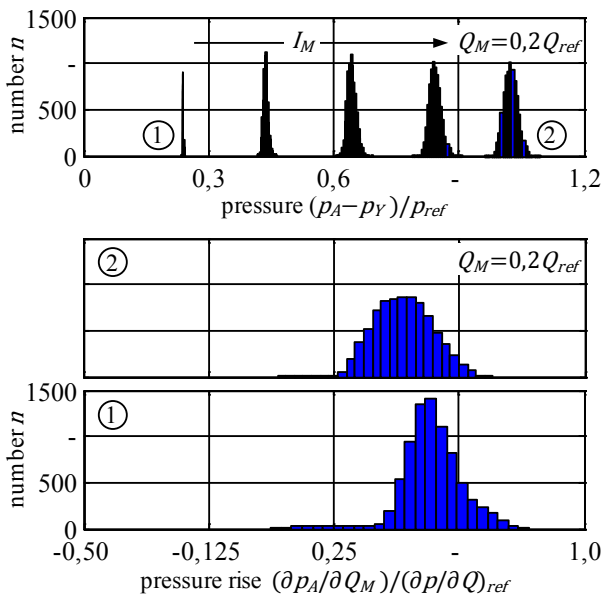


Figure 18: Histogram plots for selected operating points according to fig. 17

Subsequently, the following two issues have to be discussed in detail. In particular, this includes the questions whether the valve performance is robust under the existing uncertainties and to what extent the several influencing parameters contribute to the output variances. This paraphrases in short a robustness and sensitivity analysis. The results indicate an increasing pressure variance with growing pressure setting. This behavior arises predominantly from the valve adjustment and the underlying mounting tolerances of the valve assembly. However, the existing deviations remain within the permissible tolerance. Thus, the designed valve performance fulfills on the one hand the intended mean performance and on the other hand remains rather constant under the influence of parameter uncertainties. This is typically for a robust design generally characterized by a bi-objective optimization problem. The same situation occurs for the pressure rise. The slope variations of the solenoid force-displacement curves cause a flattening of the pressure rise at low flow rates. As shown at the top of fig. 17 an insufficient adjustment of the valve can entail decreasing pressure-flow rate curves resulting in instability at low flow rates. This behavior was observed in measurements too. Anyhow, the pressure rise also seems to be robust, additional deviations with higher flow rates arise from flow force differences as a result of the stagnation point influence. In conclusion, the Monte-Carlo simulations confirm some inconsistencies during first measurements and verify the robustness of the valve performance. The next investigations contain a discussion about the composition of the output variations.

The sensitivity analysis is carried out with the help of correlation coefficients and sensitivity indices. The obtained results for the operating points out of fig. 18 are depicted in fig. 19. The correlation coefficients clarify linear tendencies between the inputs and outputs. In contrast to the sensitivity indices these results contain directional information expressed by its sign. The pressure variations are primarily determined by the valve adjustment and the solenoid. The effective direction is different between these two influencing parameters that compensation effects are possible. An identical situation exists for the pressure rise only the acting directions are reversed. The other sources of uncertainty seem to have no significant influence on the output variations. One look at the sensitivity indices indicates a similar situation. Because no larger differences between the first-order and total-effect indices are present the result interpretation is reduced to first-order indices. The equality of these values points towards the absence of interactions between the input parameters in the range of their single uncertainties. Here, the situation is clearly equivalent to the correlation coefficients. The uncertainties of the valve adjustment and of the solenoid affect primarily the output variances. The partial values depend on the pressure setting and are in this parameter combination nearly evenly distributed. As a result, the first-order indices clearly show the principal influential parameters. Further enhancements of the robustness of the valve performance should begin with modifications of these uncertainties. With this, the simulation-based design of the valve performance and its robustness is completed showing the applicability of the acquired and existing simulation methods for an entire and successful virtual valve design.

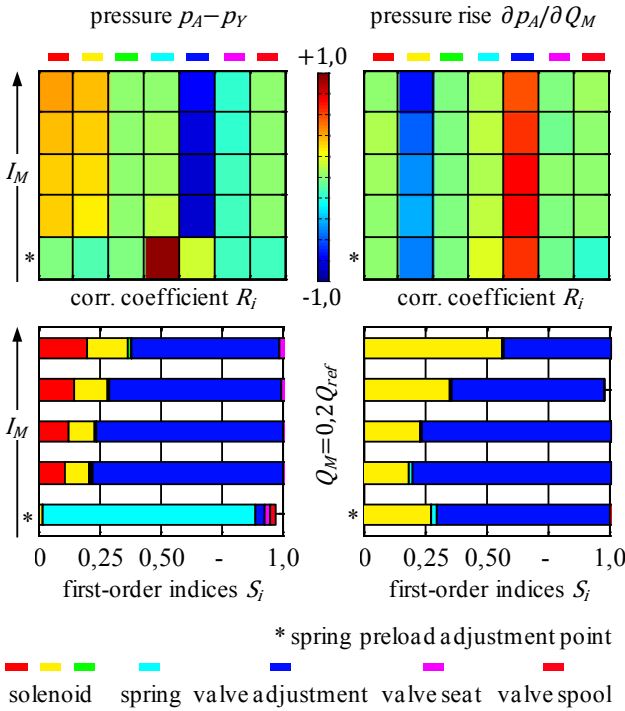


Figure 19: Correlation coefficients and first-order sensitivity indices according to fig. 18

## 7 Conclusion and Outlook

This paper explains an entire solution strategy in virtual valve design starting with a functional specification of the intended valve performance of a proportional pressure relief valve. Based upon these requirements a novel numerical procedure is developed enabling a direct computation of the necessary solenoid force-displacement characteristic curves. Afterwards, the implementation of these requirements is realized through a specifically designed geometrical shape of the solenoid. In parallel, different control orifice concepts are benchmarked resulting in a favorable solution for the whole valve assembly. The virtual designed valve basically consisting of a control orifice and a solenoid is built up and its operability is verified on a test rig. The qualitative and quantitative correlation between measurement and simulation results confirms the chosen simulation strategy and its applicability in virtual product design. Finally, a robustness analysis reinforces the whole valve design regarding uncertainties at the control orifice, the solenoid and the compounded valve assembly. The sensitivity and robustness analyses support the understanding of measurement observations arising from varying valve adjustments as well as the identification of important parameters for further enhancements of the valve operability.

Furthermore, this inverse simulation attempt can be extended to a geometrical design of the control orifice on the subsystem and component level instead of using predefined geometrical concepts. With it, the whole design process of a proportional pressure valve is covered through simulation methods greatly supporting the virtual product developing starting from a functional specification.

## Nomenclature

Designation	Denotation	Unit
$A, B$	random input variables/matrices	[-]
$A_K$	pressure area	[mm <sup>2</sup> ]
$A_{flow}$	smallest flow cross-section	[mm <sup>2</sup> ]
$b_M$	viscous damping coefficient	[m/s]
$f_A, f_B, f_{AB}$	random output variables/matrices	[-]
$F_{flow}$	flow force	[N]
$F_F$	spring force	[N]
$F_K$	pressure force	[N]
$F_M$	solenoid force	[N]
$I_M$	solenoid current	[A]
$k_{GF}$	geometrical coefficient	[-]
$m_M$	mass	[g]
$n$	number	[-]
$\Delta p$	pressure drop/pressure loss	[bar]
$p_A$	operating pressure	[bar]
$p_M$	upstream pressure	[bar]
$p_{MY}$	downstream pressure	[bar]
$p_Y$	tank pressure	[bar]
$Q_M$	flow rate	[l/min]
$R$	correlation coefficient	[-]
$S_i$	first-order sensitivity index	[-]
$S_{Ti}$	total-effect sensitivity index	[-]
$\Delta x_F$	spring preload	[mm]
$x_M$	valve displacement	[mm]
$x_{M0}$	residual air gap	[mm]
$\zeta$	loss coefficient	[-]
$\rho$	density	[kg/m <sup>3</sup> ]

## References

- [1] G Licskó, A Champneys, and C Hős. Nonlinear Analysis of a Single Stage Pressure Relief Valve. *International Journal of Applied Mathematics*, 39(4), 2009.
- [2] C Bazsó, and C Hős. An experimental, numerical and theoretical study on valve chatter. *Proc. of the Fluid Power and Motion Control*, Bath, 2010
- [3] D Cristofori, and A Vacca. The Modeling of Electrohydraulic Proportional Valves. *Journal of Dynamic Systems, Measurement and Control*, 134, 2012

- [4] T D Spegar et al. An Analytical and Experimental Study of a High Pressure Single Piston Pump for Gasoline Direct Injection (GDi) Engine Applications. *SAE Technical Paper*, 2009-01-1504, 2009
- [5] J Faulkner, N Johnston, and S Weber. Computer Modeling of a Pressure Relief Cartridge Valve. *Proc. of the 52<sup>nd</sup> National Conference on Fluid Power*, Las Vegas, 2011
- [6] D Wehner. *Modellbasierter Systementwurf am Beispiel vorgesteuerter Druckbegrenzungsventile*. Dissertation, Technische Universität Dresden, 2008
- [7] M Erhard, D Wehner, and J Weber. Numerische Strömungsberechnung (CFD) im Ventilentwurf. Fluid-Struktur-Interaktion (FSI) und deren Anwendungspotenzial. *Ölhydraulik und Pneumatik*, 11-12, 2011
- [8] M Petzold et al. Analysis of the flow conditions in a dosing pump with regards to new fuels. *Proc. of the 8<sup>th</sup> International Fluid Power Conference*, Dresden, 2012
- [9] P Casoli, and A Vacca. Design Optimization of a special relief valve with Response Surface Methodology. *Proc. of the Power Transmission and Motion Control*, Bath, 2007
- [10] M Erhard, G Schoppel, and J Weber. Simulation-Based Design of a Direct-Operated Proportional Pressure Relief Valve. *Proc. of the 8<sup>th</sup> International Fluid Power Conference*, Dresden, 2012
- [11] S Han. *Varianzbasierte Sensitivitätsanalyse als Beitrag zur Bewertung der Zuverlässigkeit adaptiver Systeme*. Dissertation, Technische Universität Darmstadt, 2011

# Diagnostics



# Recognition of Operating States of a Medium-Sized Mobile Machine

T. Krogerus, M. Hyvönen, K. Raivio\* and K. Huhtala

Department of Intelligent Hydraulics and Automation, Tampere University of Technology, Tampere, Finland

E-mail: tomi.krogerus@tut.fi, mika.hyvonen@tut.fi, kalevi.huhtala@tut.fi

\*Department of Information and Computer Science, Aalto University School of Science, Espoo, Finland

## Abstract

In this study the main goal was to study the operating states of a medium-sized mobile machine. The measured time series data were analysed to find frequent episodes (sequences of operating states) to which the conditional probabilities were then calculated. The time series data were first segmented to find events. One or more segments build up an event which can be interpreted to be an operating state. The segments were then clustered and classified. The segment class labels were interpreted as events. As a result, a list of rules was established. The rules describe causal connections between consecutive operating states and transition probabilities from 1<sup>st</sup> state to 2<sup>nd</sup> state. The recognized operating states were further analysed to be used in diagnosis of the operation of the machine and focusing the diagnostics on certain operating states.

**Keywords:** Mobile machine, analysis, diagnostics, operating state, hydraulics, time series, segmentation, episode, event, piecewise linear regression, clustering, classification, association rules, quantization error

## 1 Introduction

Technological development has produced mobile machines that are remotely operated [1] directly or work autonomously [2] while only being supervised remotely. These machines demand increased monitoring and analysis [3] of the performance and operating states of these machines when there is no person present inside the machine. If the operating states of the machine can be recognized during work tasks, causal connections between consecutive operating states can be determined and furthermore, diagnostics can be focused on specific operating states.

Typically, in a modern mobile machine there is already a lot of information available about the operation of the machine, e.g. process and control data through communication buses, which can be used in analysis. In addition to this, condition monitoring specific sensors can also be added to the system. When all this information from communication busses and additional sensors are recorded, it leads to the generation of a huge amount of data. High dimensionality complicates the processing of time series data especially from the pattern recognition point of view [4]. A time series is defined as a collection of observations made sequentially in time [5].

In order to analyse the time series data of mobile machines, detectors of events to find frequent episodes need to be first created, and after that some higher level description, for example probability distributions or quantization error method [3] should be used. Finding frequent episodes from

the measured time series data of a mobile machine requires segmentation of the time series data to find the events. Time series segmentation is often used as a pre-processing step in time series analysis applications. An episode is again defined as a collection of events that occur relatively close to each other in a given partial order [6]. Causal connections are then searched for by analysing the consecutive episodes.

The operation of the machine can be further analysed using the recognized operating states. Diagnostics can be focused on certain operating states. Usually these are the ones that have the biggest changes in the analysed variables. Most information in regard to the detection of anomalies is obtained from these operating states.

## 2 Description of the studied mobile machine

The studied mobile machine, called IHA-machine [7], was engineered at the Department of Intelligent Hydraulics and Automation at Tampere University of Technology. It was designed to serve as a platform where different types of research could be conducted concurrently. The research platform is shown in fig. 1.

An overview of the hydraulic systems of IHA-machine, which are related to the analysis performed in this study, is given here. More details are presented in [7]. Figure 2 shows a simplified hydraulic circuit of the closed loop hydrostatic transmission (HST) of IHA-machine. It also shows the added sensors and most important auxiliary components that provide safety and maintenance functions.



Figure 1: Studied mobile machine [7].

The main source of power is a 100 kW four-cylinder diesel engine. The HST pump has a displacement of 100 cm<sup>3</sup>/r and contains various integrated hydraulic components, sensors and electronics to implement the closed-loop control of the swivel angle and the data communication.

Both the diesel engine and the pump are connected to the main PLC (Programmable Logic Controller) of the machine via the CAN bus. They also have separate control units, which are connected to the CAN bus, offering data from integrated sensors. Therefore, via the CAN bus several parameters related to the operation of these components, e.g. diesel load and HST pump angle, can be monitored and recorded for later analysis.

Every wheel of the machine is equipped with a slow speed hydraulic hub motor, with a displacement of 470 cm<sup>3</sup>/r. Each motor has a pressure controlled holding brake and an integrated sensor for measuring rotational speed. A separate hydraulic gear pump provides the power needed by the steering system. The steering of the machine can be controlled using proportional flow control valve and two symmetrically placed hydraulic cylinders. The work hydraulics of the IHA-machine are based on digital hydraulics [7,8], but this part of the machine is not studied here.

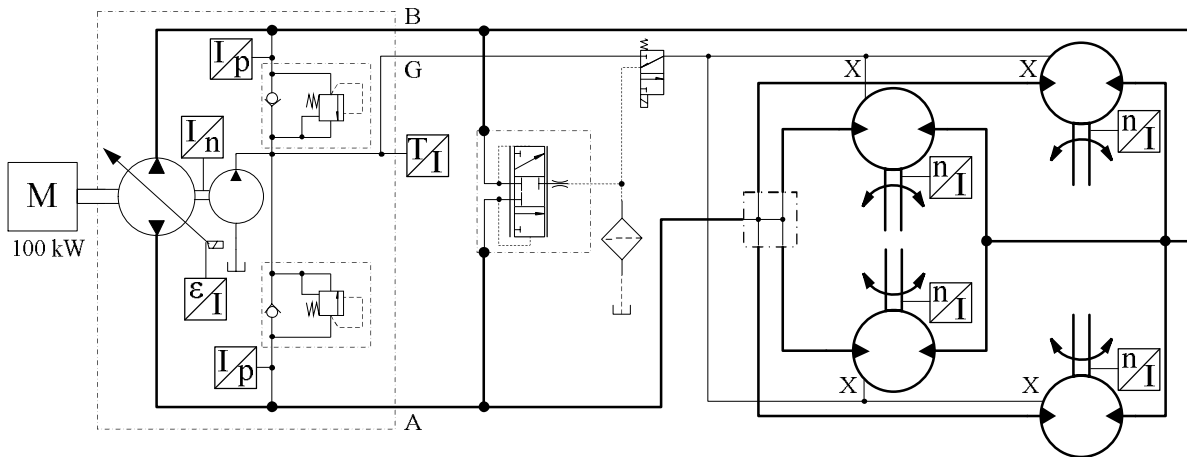


Figure 2: Hydrostatic transmission of studied mobile machine [7].

### 3 Events and causal connections from time series

In the method used in this study to find causal connections from the time series data, the data have been segmented to extract operating states. One or more segments build up an event which can be interpreted to be an operating state. A state is defined as a combination of the patterns of the selected variables. The sequences of operating states can then be further analysed to discover association rules from the sub-sequences. The method depicted in fig. 3 will be explained in more detail in the following sections.

#### 3.1 Pre-processing

The data have to be scaled before segmentation. This guarantees that all variables have an equal effect on the segmentation result. Representative statistics of the data are needed in order to be able to scale the measurements. To do that, all the variables of the data should have enough variation. The data range and distribution used to compute the statistics should correspond to those of the whole data set. Pre-processing also includes the elimination of outliers

and noise reduction and possibly down sampling using moving average filtering for each measurement.

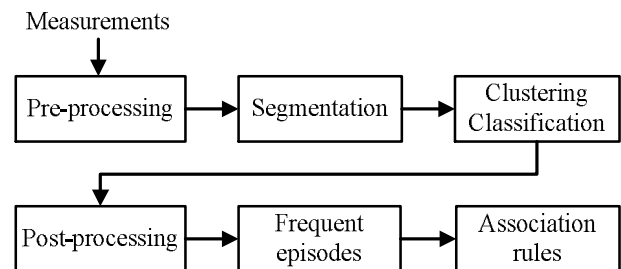


Figure 3: Events and causal connections from time series.

#### 3.2 Segmentation

In segmentation, the time series data are transformed into piecewise linear representation. A segment is a contiguous subset of a time series. In this study, the time series data is segmented using the sliding window method with piecewise linear regression [5]. In this method, curves are approximated with lines: see fig. 4.

New samples are added to the segment until cumulative squared estimation error exceeds a predefined threshold. Another possible criterion is the maximum of squared error in the segment. Several measurements can be segmented together. Thus, they have common cost function and the cost is computed by summing all the measurements. The measurements define together the edges of segments.

The sliding window segmentation method is well suited to online segmentation, because only the preceding samples are needed to define the edges. However, the method can be quite slow if the sampling rate is high. There are several modifications of the sliding window segmentation algorithm and there are other more efficient segmentation methods, but unfortunately most of them are not very suitable for online analysis. This is because the methods expect that the whole sequence is available at the time of segmentation.

### 3.3 Classification of segments

Pre-processed segments are then clustered and classified. Clustering is the process of organizing objects into groups whose members are similar in some way. A cluster is therefore a collection of objects which are similar between them and are dissimilar to the objects belonging to other clusters. Clustering can be performed using hierarchical methods or k-means algorithm [9].

The parameters of piecewise linear regression lines are used as features. One choice is to use the slopes of lines as features. Also, the offset and the length of segment can be used as additional features. The number of segment clusters has to be defined, or a validation index should be used to select a suitable amount of clusters [10]. It is not necessary to cluster all the available segments, as some of them can be classified using cluster prototype vectors defined using a representative set of segments. Each cluster is presented by a d-dimensional prototype vector (also known as: weight, codebook, model, reference)  $m = [m_1, \dots, m_d]$ , where d is equal to the dimension of the input vectors. It is useful to save these prototype vectors, to classify another set of segments or to analyse classes or classification results later.

### 3.4 Post-processing segmentation results

Segment classes can be analysed using their prototype vectors. In case slope coefficients are used as segment features, prototypes can easily be visualized to find interpretation for classes or states: see fig. 5.

When the classified segments are converted to events, it is possible to remove non-interesting segments or events. Events describe the behaviour and actions of the system. For example, a segment class with around zero slope coefficients for all measurements can be considered unusable. Events built from these segments can be removed before further analysis, because later analysis will be focused on those operating states where changes in the analysed variables are at their biggest which means that the slopes of the feature vectors are steep. It is also possible to combine subsequent segments with the same class labels if a lower number of detected states are wanted or a high probability of transitions from states to themselves is

undesirable. Of course, the above post-processing methods will change single state distributions and transition probabilities.

The sequence of segment classes will be interpreted as a sequence of states. Each state has a discrete label and a time stamp. Sequences from multiple sources can be combined into one sequence. Possible sources for sequences are the segmentation results of two separate measurement groups. Different methods or features can be used in each segmentation.

### 3.5 Search for frequent episodes

Frequent episodes can be searched from the sequences using the Apriori algorithm [6,11]. The algorithm finds the most probable sub-sequences from a sequence starting from the sub-sequence of length one. The length of the sequence is increased by one every round. The effectiveness of method is based on the principle that only those episodes which have had all their sub-episodes frequent enough in the previous round are possible candidates for frequent episodes.

The algorithm has two possibilities for initial search of length of two episodes. It is possible to search for serial or parallel episodes from the sequence. In the case of serial episodes, the order in which the states have occurred on the time scale is important, but in the case of parallel episodes the primary interest is to find out if the states occurred in the same time window or not. When longer episodes are searched for, it is, of course, possible to search for more complicated combinations of parallel and serial episodes if desired.

The algorithm has several parameters, which have to be defined. These are the minimum frequency for an episode to be considered as interesting, the length of window used in the search, maximum length of episode and minimum confidence. The last one is actually a threshold for the conditional probability of a sequence.

The sequence occurrence rates are converted to probabilities by dividing the rate by the number of all search windows. The sequence probabilities  $P(A, B)$  are further converted to conditional probabilities  $P(B|A)$  using single state probabilities: see eq. 1.

$$P(B|A) = \frac{P(A, B)}{P(A)} \quad (1)$$

Here, state A precedes state B, and  $P(A)$  is the probability of state A. The target is to find causal connections between states which occur frequently enough compared to other sequences in which either one of the two states occur.

## 4 Measured data for analysis

Different test cases were defined and 79 different test drives were carried out to obtain measurement data from different operating states, which were then analysed. These test cases consist of a combination of different work tasks: driving straight, turning, going uphill, downhill, over obstacles, emergency braking, reversing, different driving speeds, and

slow and fast rise time of driving speed. Two different ground types were used: asphalt and gravel. The machine was driven with either a test person on-board, or remotely using a laptop computer. An added load of 1000 kg was also used in some of the test drives. Some combinations of task scenarios were driven several times. Table 1 shows cases of

these test drives on gravel. Table 2 shows the measured variables during these test drives which were then used in the analysis. Measured time series data were analysed using two different data sets, namely variables of machine driving behaviour (velocity/turnings) and hydrostatic transmission.

*Table 1: Cases of test drives on gravel.*

Case id	Description	Speed	Control	Load	Special definitions
6-1	Uphill	40 %	Person	X	
6-2	Downhill	20 %	Person	X	
6-3	Uphill-stop-uphill start	40 %	Person	X	
6-4	Uphill	40 %	Person	-	
6-5	Downhill	20 %	Person	-	
6-6	Uphill-stop-uphill start	40 %	Person	-	
7-1	Turn right - over obstacle	20 %	Computer	-	Obstacle: block of wood (right tyre)
7-2	Turn right - over obstacle	40 %	Computer	-	Obstacle: block of wood (right tyre)
7-3	Turn right - over obstacle	20 %	Computer	-	Obstacle: block of wood (left tyre)
7-4	Turn right - over obstacle	40 %	Computer	-	Obstacle: block of wood (left tyre)
8-1	Driving straight	40 %	Computer	X	Slow: rise time 1.5 s to max. speed
8-2	Driving straight	40 %	Computer	X	Fast: rise time 0.5 s to max speed
8-3	Driving straight	40 %	Person	X	Slow: rise time 1.5 s to max. speed
8-4	Driving straight	40 %	Person	X	Fast: rise time 0.5 s to max speed
8-5	Driving straight	40 %	Computer	-	Slow: rise time 1.5 s to max. speed
8-6	Driving straight	40 %	Computer	-	Fast: rise time 0.5 s to max speed
8-7	Driving straight	40 %	Person	-	Slow: rise time 1.5 s to max. speed
8-8	Driving straight	40 %	Person	-	Fast: rise time 0.5 s to max speed
9-1	Driving straight	40 %	Person	-	Emergency braking
10-1	Straight-right-straight-left-straight	20 %	Person	-	
10-2	Straight-right-straight-left-straight	40 %	Person	-	
10-3	Straight-right-straight-left-straight	20 %	Person	X	
10-4	Straight-right-straight-left-straight	40 %	Person	X	
10-5	Straight-right-straight-left-straight	20 %	Computer	X	
10-6	Straight-right-straight-left-straight	40 %	Computer	X	
10-7	Straight-right-straight-left-straight	20 %	Computer	-	
10-8	Straight-right-straight-left-straight	40 %	Computer	-	
11-1	Directly reversing	40 %	Computer	-	Slow: rise time 1.5 s to max. speed
11-2	Directly reversing	40 %	Computer	-	Fast: rise time 0.5 s to max speed
12-1	Simulation of normal operation		Person	-	

Table 2: Measured variables during test drives.

	Signal	Range	Unit
Driving behaviour	Steering reference	-16384...16383	-
	Frame angle	193,1...117,1	°
	Rotational speed of front left tyre	$-\infty \dots \infty$	r/s
	Rotational speed of front right tyre	$-\infty \dots \infty$	r/s
	Rotational speed of rear left tyre	$-\infty \dots \infty$	r/s
	Rotational speed of rear right tyre	$-\infty \dots \infty$	r/s
Hydrostatic transmission	Diesel rotational speed reference	0...2200	rpm
	HST pump angle reference	-1000...1000	%
	Diesel rotational speed	0...2200	rpm
	Diesel load	0...100	%
	HST pump measured angle	-1000...1000	%
	Pressure at port A	0...500	bar
	Pressure at port B	0...500	bar

## 5 Recognition of operating states from measurement data

Measurements were scaled to zero mean and unit variance before the analysis. For this, measurement statistics from eleven representative test drives were collected. Moving average filtering was also used to get rid of situations when segment is intercepted by noise in measured variables.

Next, the pre-processed measurements were segmented using sliding window segmentation with piecewise linear regression. Cumulative squared error function with the threshold 0.3 was used to define the edges of segments. Data from all the test drives were segmented similarly using two groups of measurements. An example of segmentation of one test drive in the case of driving behaviour related measurements (frame angle and rotational speed of front left) is shown in fig. 4.

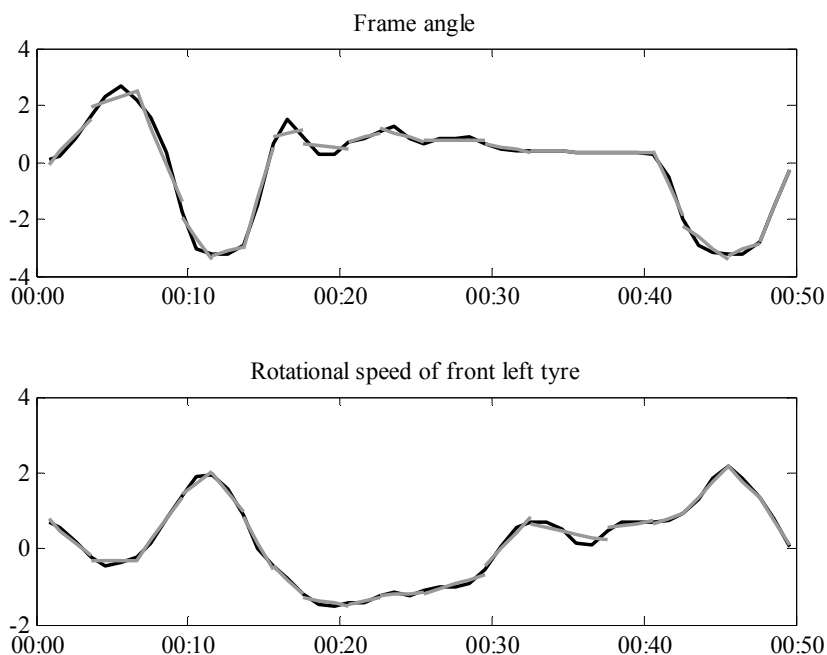


Figure 4: Time series segmentation of case 12-1. Frame angle and rotational speed of front left tyre are shown as examples. The measurements are normalized to zero mean and unit variance for segmentation and the length of time series is 50 s.

The segments of eleven representative test drives were clustered using k-means clustering with Davies-Bouldin validation index [10] and segment slopes as features. In tab. 3 is defined the basic steps of k-means algorithm.

Table 3: Steps of K-means clustering.

K-means clustering
1. Initialize: select a set of K candidate cluster centres
2. Assign each data point to the closest cluster centre
3. Set the cluster centres to the mean value of the points in each cluster
4. Repeat Steps 2 and 3 for a fixed number of iterations or until there is no change in cluster assignments

The grouping in k-means algorithm is done by minimizing the sum of squares of distances between data and the corresponding cluster centres according eq. 2, where K is the number of groups and N is the number of sample/feature vectors,  $\mathbf{x}_n$  is sample/feature vector and  $\mathbf{m}_i$  is the mean of the data points in set i, i.e. prototype of cluster i and it is calculated according eq. 3.

Clustering was repeated five times for every number of clusters and the result with minimum quantization error was selected. The number of clusters was varied from 10 to 30

clusters and the one giving minimum validation index value was selected. In this study, the optimal number of clusters for driving behaviour variables was found to be 27, and for hydrostatic transmission variables 29.

As a result of clustering, the segments of representative test drives were clustered and a prototype vector for each cluster was computed. These models were used to classify the segments of other test drives. Prototype vectors of clusters for driving behaviour measurements are shown in fig. 5. The lines in the subplots describe the behaviour of the signal in a particular state. The signal is constant or increases or decreases at a certain rate. A state is a combination of the patterns of the selected variables. For example, in state 27 (the far right column) the values of the 1<sup>st</sup> and 6<sup>th</sup> variable increase and the others decrease.

$$J = \sum_{i=1}^K \sum_{n=1}^{N_i} \|\mathbf{x}_n - \mathbf{m}_i\|^2 \quad (2)$$

$$\mathbf{m}_i = \frac{1}{N_i} \sum_{n=1}^{N_i} \mathbf{x}_n \quad (3)$$

The segmentation results were further processed by combining consecutive segments belonging to the same class. The segment class labels generate an event sequence. For each event a time stamp is computed by averaging sample time stamps of the segment.

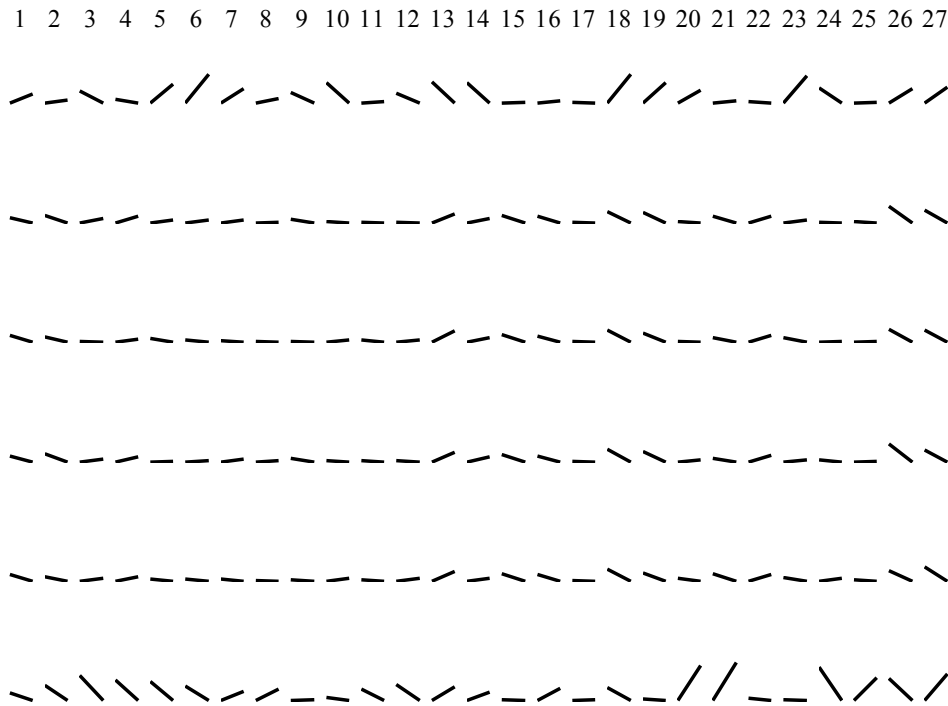


Figure 5: Prototype segments for 1st variable set. The rows correspond to variables and columns to operating states.

Two event sequences were built for each test drive. Event labels generated using hydrostatic transmission related measurements are shifted by the number of segment classes for driving behaviour measurements to obtain event labels

which are unique over both measurement sets. As a result, hydrostatic transmission related events are labelled between 28 and 56. In fig. 6 classified segments with the event labels of one test drive are shown.

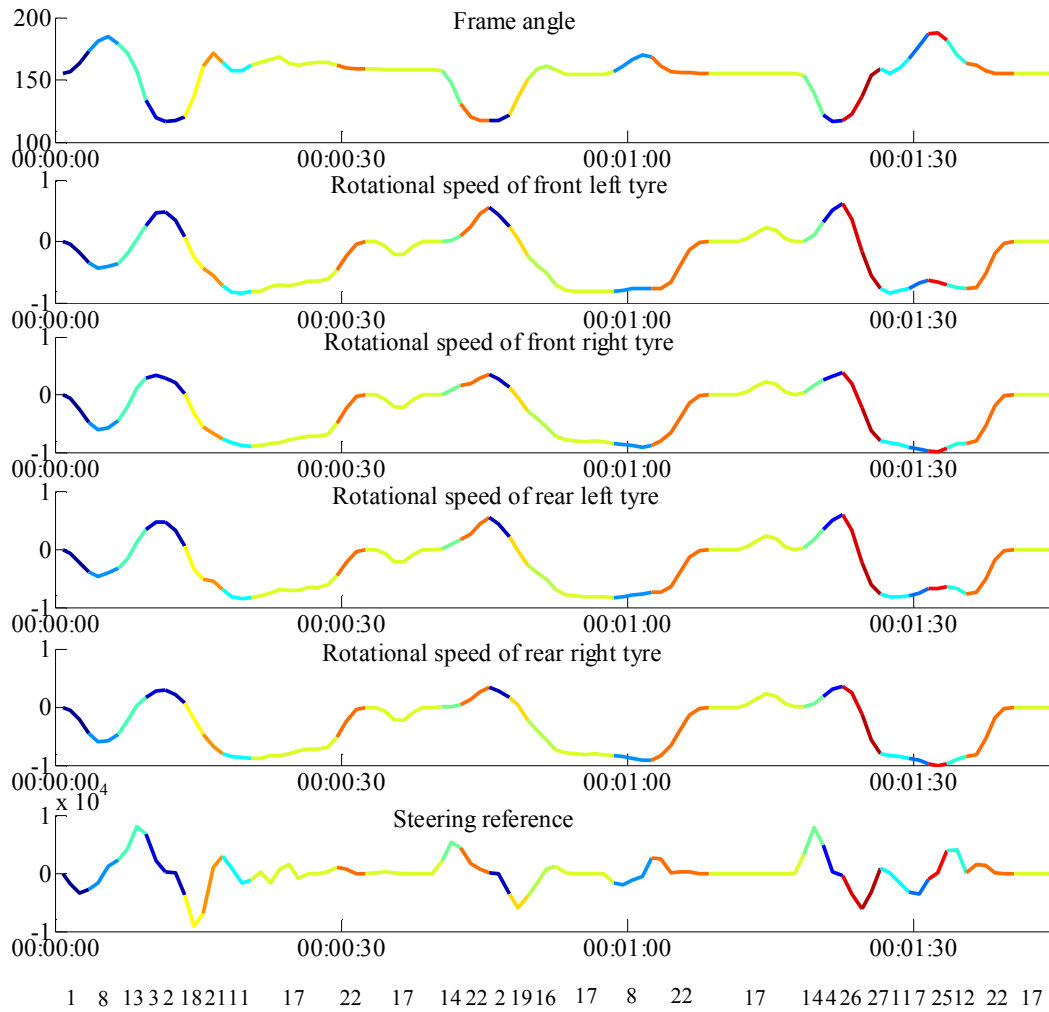


Figure 6: Time series (case 12-1) of length 1min 45s are plotted using different colours for each event. The labels of events are shown on the bottom row.

The probabilities of the events which occur in the test drives are shown in fig. 7. Some of the segment classes are more probable than others. Usually, the slopes of segments in such classes or states are near zero. Thus, the classes correspond to constant movement or operation without any changes.

For each test drive two sequences corresponding to the measurement sets were combined. The new sequence has events with labels from 1 to 56.

Frequent serial episodes of length 2 were searched for from these sequences. The time stamps were converted to discrete values, because the original algorithm is designed to process these.

Serial episodes with a certain probability were found. The probabilities were further converted to conditional probabilities using eq. 1 to find out how probable it is that one state occurs when a certain state has already occurred. In tab. 4 serial episodes with the highest conditional probability are shown. The probability of an episode in the studied sequences is also shown, as well as the overall probability of the first events of episodes.

According to the first rule in the table, state 45 occurs nine times and there is an over 88% probability that state 15 will follow.

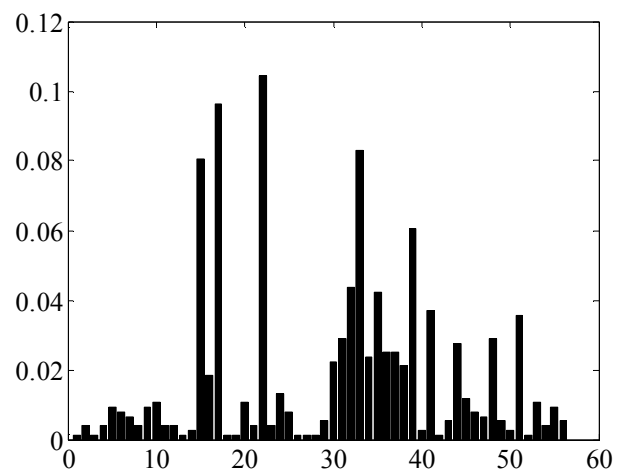


Figure 7: Probabilities of all events over all cases. There are total 56 different events: 27 for 1<sup>st</sup> variable sets and 29 for 2<sup>nd</sup> variable sets.

Table 4: Serial episodes and the event probabilities used to compute episode conditional probabilities. There are in total 758 events. Episodes with first event occurring three times or less are left out as well as episodes with conditional probability of less than 0.3.

A → B	P(A,B)	P(A)	n(A)	P(B A)
45 → 15	0.01055	0.01187	9	0.8889
46 → 15	0.00660	0.00792	6	0.8333
31 → 22	0.02243	0.02902	22	0.7727
44 → 15	0.02111	0.02770	21	0.7619
53 → 22	0.00792	0.01055	8	0.7500
43 → 22	0.00396	0.00528	4	0.7500
55 → 22	0.00660	0.00923	7	0.7143
30 → 22	0.01583	0.02243	17	0.7059
51 → 15	0.02243	0.03562	27	0.6296
20 → 10	0.00660	0.01055	8	0.6250
48 → 17	0.01715	0.02902	22	0.5909
41 → 22	0.02111	0.03694	28	0.5714
5 → 33	0.00528	0.00923	7	0.5714
6 → 20	0.00396	0.00792	6	0.5000
6 → 33	0.00396	0.00792	6	0.5000
34 → 37	0.01187	0.02375	18	0.5000
22 → 39	0.04881	0.10422	79	0.4684
37 → 31	0.01055	0.02507	19	0.4211
24 → 33	0.00528	0.01319	10	0.4000
39 → 17	0.02375	0.06069	46	0.3913
10 → 41	0.00396	0.01055	8	0.3750
17 → 33	0.03430	0.09631	73	0.3562
35 → 17	0.01451	0.04222	32	0.3438
25 → 32	0.00264	0.00792	6	0.3333
35 → 32	0.01319	0.04222	32	0.3125
15 → 48	0.02507	0.08047	61	0.3115

## 6 Analysis of operation using recognized states

After recognition of the operating states, these can be further analysed to study the operation of the machine. On the basis of earlier research results [3] it was noticed that the biggest effects of different fault states were at the transient stages of the hydraulic system in which the changes in the pressure and volume flows were at their highest. Therefore analysis will be focused on operating states where the slopes of the feature vectors are steep and when changes in the analysed variables are at their biggest.

The quantization error method [3,12,13] was used to study the operation of the machine, and it is based on the distance calculation, Euclidian distance, which is shown in eq. 4.

Here, the neuron whose weight vector is closest to the input sample vector  $x$  is called the BMU, denoted by  $c$ .

$$e_q = \|x - m_c\| = \min_i \{\|x - m_i\|\} \quad (4)$$

After this, a certain threshold can be set which determines the greatest distance on which recognition occurs. So when the method is tested the distances between the sample vectors from the testing data and all the cluster prototype vectors are calculated. If the minimum distance is bigger than the threshold value set beforehand, then this sample vector is treated as an anomaly, which can be either a new operating or a fault state.

After anomalies have been detected and proved to be faulty operating states, data from these states can be used to detect and identify them in the future. However, in this study there were no data available from faulty states.

Figure 8 shows the quantization error of all the classified segments of the 1<sup>st</sup> data set. There are altogether 302 segments. In turn, fig. 9 shows the quantization error of the 2<sup>nd</sup> data set. There are altogether 377 segments. Based on these quantization errors, thresholds can be set to separate possible anomalies from normal states. In these figures few larger quantization errors can be seen, which complicates the detection of anomalies. In this case, some of the anomalies could be mixed with normal states. This could perhaps still be improved by selecting a different number of clusters or even another clustering method. Only the k-means clustering method was used in this study. But also longer and more versatile test drives than those which are used here would improve the situation and reduce the number of spikes in the quantization error.

Figure 10 shows the quantization error of state number 22, which is the most probable state in the test drives: see fig. 7. 84 segments were classified as state 22. Here, only a few of the quantization error values are significantly larger than the rest of the values. Thus, in case of state number 22 the definition of the threshold to detect anomalies is more straightforward.

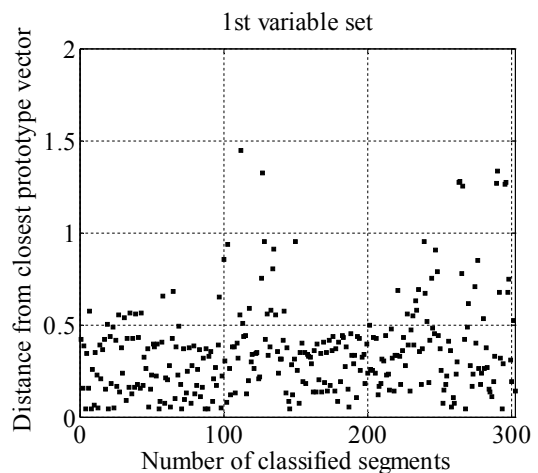


Figure 8: Quantization error of all classified segments of 1<sup>st</sup> data set.

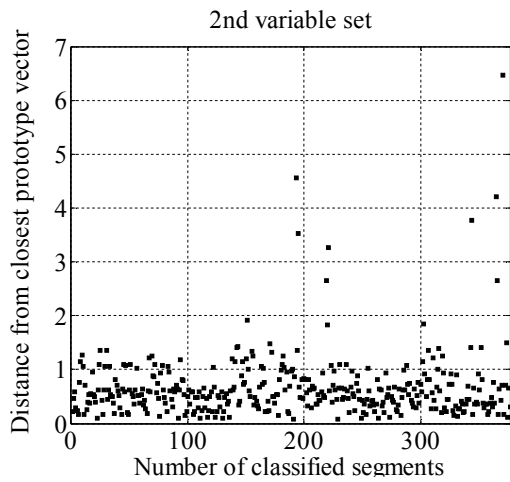


Figure 9: Quantization error of all classified segments of 2<sup>nd</sup> data set.

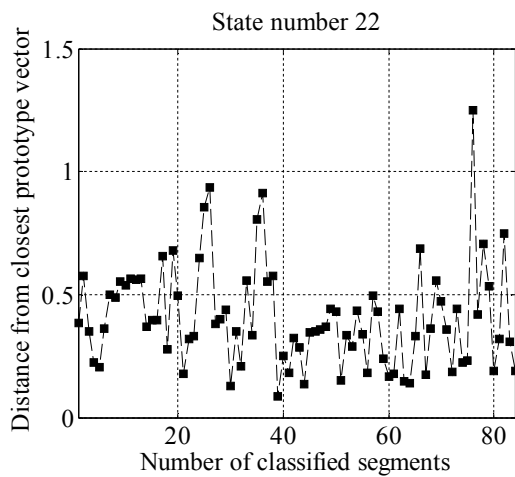


Figure 10: Quantization error of state number 22.

## 7 Conclusions

The operating states of a medium-sized mobile machine were studied to find causal connections between consecutive operating states and transition probabilities from 1<sup>st</sup> state to 2<sup>nd</sup> state, and to focus the analysis of operation on certain operating states.

Altogether 56 different operating states were found from measurement data using sliding window method with piecewise linear regression for time series segmentation and k-means algorithm for clustering and classification of pre-processed segments. The analysed data were comprised of two different data sets (machine driving behaviour and hydrostatic transmission).

Causal connections between consecutive operating states were found, using the Apriori algorithm, to which transition probabilities were then calculated. In this study consecutive serial operating states of length 2 were searched for from the recognized operating states. If desired, also longer and/or more complicated sequences can be searched for.

The operating states that have the steepest slopes of the feature vectors were found and these can be further analysed

to study the operation of the machine using the quantization error method. It is noted that this is an on-going work.

The data-driven methods described in this study can be implemented to different kinds of mobile machines. Insufficient sensor information may limit the number of applications, but the analysis methods in general are not restricted to a specific machine type. The thresholds in segmentation and anomaly detection need be defined based on specific applications and need specific knowledge about the operation of the system. The selection of critical measurement signals describing the operation of the machine also requires knowledge about the machine.

## Nomenclature

Designation	Denotation	Unit
A	1 <sup>st</sup> state	[-]
B	2 <sup>nd</sup> state	[-]
c	Best-matching unit (BMU)	[-]
$e_q$	Quantization error	[-]
J	Sum of squares clustering function	[-]
K	Number of groups/clusters	[-]
<b>m</b>	Prototype vector	[-]
$m_c$	Prototype vector chosen as BMU	[-]
N	Number of sample vectors	[-]
n(A)	Number of state A	[-]
P(A)	Probability of state A	[-]
P(A, B)	Sequence probability	[-]
P(B A)	Conditional probability	[-]
$x$	Data/feature vector	[-]

## References

- [1] Uusitalo, J. 2011. A Case Study on Effects of Remote Control and Control System Distribution in Hydraulic Mobile Machines. Dissertation. Tampere, Finland. Tampere University of Technology. Publication 960. 111 p.
- [2] Durrant-Whyte, H. 2005. Autonomous Land Vehicles. Proc. IMechE., Part I: Journal of Systems and Control Engineering, 1, vol. 219, no. 1, pp. 77-98.
- [3] Krogerus, T. 2011. Feature Extraction and Self-Organizing Maps in Condition Monitoring of Hydraulic Systems. Dissertation. Tampere, Finland. Tampere University of Technology. Publication 949. 126 p.
- [4] Ruotsalainen, M., Jylhä, J., Vihonen, J. and Visa, A. 2009. A Novel Algorithm for Identifying Patterns from Multisensor Time Series. In Proceedings of the 2009 WRI World Congress on Computer Science and Information Engineering, CSIE 2009, Los Angeles, California, USA, 31 March - 2 April, 2009, vol. 5, pp. 100-105.

- [5] Keogh, E., Chu, S., Hart, D. and Pazzani, M. 2011. An Online Algorithm for Segmenting Time Series. In Proceedings of *IEEE International Conference on Data Mining*, 2001, pp. 289-296.
- [6] Mannila, H., Toivonen, H. and Verkamo, I. 1997. Discovery of Frequent Episodes in Event Sequences. *Data Mining and Knowledge Discovery*, vol. 1, no. 3, pp. 259-289.
- [7] Backas, J., Ahopelto, M., Huova, M., Vuohijoki, A., Karhu, O., Ghabcheloo, R. and Huhtala, K. 2011. IHA-Machine: A Future Mobile Machine. In Proceedings of *The Twelfth Scandinavian International Conference on Fluid Power, SICFP'11*, Tampere, Finland, May 18-20, 2011, Vol. 1, No. 4, pp. 161-176.
- [8] Huova, M., Karvonen, M., Ahola, V., Linjama, M. and Vilenius, M. 2010. Energy Efficient Control of Multiactuator Digital Hydraulic Mobile Machine. In Proceedings of *7<sup>th</sup> International Fluid Power Conference Aachen*, Aachen, Germany, March 22 -24, 2010, vol. 1, 12 p.
- [9] Theoridis, S. and Koutroumbas, K. 1999. Pattern Recognition, Academic Press, USA.
- [10] Davies, D. and Bouldin, D. 1979. A Cluster Separation Measure. *IEEE Transactions on Pattern Analysis and Machine Intelligence*, vol. 1, no. 2, pp. 224-227.
- [11] Agrawal, R. and Srikant, R. 1994. Fast algorithms for mining association rules. In Proceedings of the *20th VLDB conference*, 1994, pp. 487-499.
- [12] Ahola, J., Alhoniemi, E. and Simula, O. 1999. Monitoring Industrial Processed Using the Self-Organizing Maps. In *Proceedings of the 1999 IEEE Midnight-Sun Workshop on Soft Computing Methods in Industrial Applications, Kuusamo, Finland*, June, 1999. pp. 22-27.
- [13] Alhoniemi, E., Hollmén, J., Simula, O. and Vesanto, J. 1999. Process Monitoring and Modeling Using the Self-Organizing Map. *Integrated Computer-Aided Engineering*, vol. 6, no. 1, pp. 3-14.

## **Model-Based Fault Detection for Hydraulic Servoproportional Valves**

José Roberto Branco Ramos Filho\* and Victor Juliano De Negri

LASHIP, Mechanical Engineering Department, Federal University of Santa Catarina, Florianópolis, SC, Brazil

E-mail: robertobrancofilho@gmail.com, victor.de.negri@ufsc.br

\*Institute of Engineering and Geosciences, Universidade Federal do Oeste do Pará, Santarém, Pará, Brazil

### **Abstract**

This paper presents a mathematical model for online fault detection on single solenoid servoproportional spool valves. The most common failures as well as its effects on the valve behavior are studied and took into account for the model representation. Servoproportional valves are used in industry, aerospace, and military fields. Some of these uses are critical-mission, where the valve must not fail without previous warning to prevent or mitigate financial losses, equipment damage, and risk to personnel. Even in less demanding applications, it is very useful to be able to quickly locate a failure in the hydraulic circuit, which is a task that may demand up to 80% of the time used in corrective maintenance. Total failure can readily be detected using the signals available on the valve electronics. However, since the spool positioning is on closed loop on these valves, incipient failures that can be overcome by the controllers cannot be easily detected. In this paper, an experimentally validated analytical model is used as a reference model such that the solenoid actual current can be compared with the theoretical current. Since the valve hysteresis is considered, the model calculates maximum and minimum current values that correspond to an undamaged valve. Experimental results with a standard valve and a damaged valve show the effectiveness of the model for fault detection.

**Keywords:** hydraulics, proportional valves, fault detection.

### **1 Introduction**

Electrically modulated hydraulic control valves [1], particularly servoproportional spool valves, are used in several applications in industry, aerospace, and military fields. Some of these applications are critical-mission, where the valve must not fail without previous warning to prevent or mitigate financial losses, equipment damage, and risk to personnel. Even in less demanding applications, it is very useful to help quickly locating a failure in the hydraulic circuit, which is a task that may demand up to 80% of the time used in corrective maintenance. Also, a valve who has not lost its function, but is not operating at its best may affect the entire hydraulic system performance, making it hard for engineers to locate and solve the problem [2].

A fault detection process isolates the source of a system malfunction through the gathering and the analysis of information about the current state of the system obtained through measurement, testing and other sources of information, such as the user [3]. Since the detection is usually performed in embedded systems with other functions, such as control, the fault detection process should be as simple as possible. The attempt to detect all possible failures would make the process unnecessarily complex and would increase its response time. That is why embedded fault detection systems are made to quickly detect the most common faults. On the other hand, running complex tests periodically would not compromise the system safety [4].

The evaluation of the acquired data from the system is important to the decision making process and it can be done using techniques such as artificial intelligence, behavior or failure models, signal analysis, process history, statistical methods and others [3], [5]. The model based approach requires extensive effort during the development phase, and is computer intensive when used on-line, but is adaptable to other similar equipment through parameter and model adjustments. The model development process also adds knowledge over the system under study [5]. For these reasons, the model approach has been chosen by the authors to generate the necessary information for decision making.

### **2 Common failures in spool valves**

Electrically modulated hydraulic control valves should have a service life of several million cycles when operated with adequate filtered fluid within the boundaries of its nominal specifications. However, its service life is greatly influenced by operational conditions such as the environment where it is installed, fluid contamination, the use of dither, pressure and voltage spikes, etc.

Among the most common failures are the ones caused by contaminated fluid and degraded components due to excessive wear [2]. In order to gain some knowledge on how these failures affect the valve and what should be monitored to detect such a situation, the most common faults are discussed below [2], [6].

## 2.1 Solenoid fault

After the solenoid reaches the magnetic saturation current level, additional current through the solenoid will only cause it to generate heat. This increases its impedance and therefore decreases the current through the solenoid for a certain voltage. This also reduces its ability to generate mechanical force. In extreme cases the core may fracture or the coil inductance may be permanently altered. When the solenoid burns it becomes an open circuit, and no current goes through no matter the voltage applied. This causes the valve not to respond to the command signal, and therefore no spool movement will be possible.

## 2.2 Spring fault

A broken or fatigued spring may cause the spool to drift, since it is subject only to both the solenoid and to the steady-state flow forces. A valve with a broken spring is not able to comply with the command signal, even though the solenoid is working properly.

## 2.3 Fluid fault

According to [7], up to 75% of the failures in hydraulic systems are caused by contamination generated or added to the system. The undesirable effects include frequent component replacement, loss of movement repeatability, parameter alteration, fluid degradation and others. Among the most common contaminants are those presented below.

### 2.3.1 Solid particles

The gap between the spool lands and the sleeve of control valves ranges from 1 to 25  $\mu\text{m}$  according to the valve size and design. Particles around that size can silt or become wedged in the spool or sleeve, leading to erratic movements, jamming, and permanent damage to lands, orifices and sleeve [8]. Contaminants such as sand, metal particles, polish compound, and other residues can cause wear and premature failure, making this kind of contaminant one of the critical factors to affect the service life and the reliability of hydraulic systems [9], [10], [11]. These contaminants may come from the external environment or may come from the wear of components of the system.

How long it will take for this to occur depends on the amount and size of particles, and on the pressure differential, varying from a few seconds to a few hours if the valve is centered [9], [8]. Particles ranging from 5  $\mu\text{m}$  to 40  $\mu\text{m}$  may quickly jam a valve, and occurrences even during the commissioning of the machine have been reported [8].

In the long run, particle contamination may cause increased friction between the spool and the sleeve, increasing hysteresis, scratching the spool surface and eroding edges, increasing flow and non-linear behavior in the center position. This state demands more from the solenoid, who has to operate at higher current levels to move the spool, increasing both threshold and flow gains, and decreasing pressure gains. When the valve is extremely damaged its responses may become slower, unstable or fail completely

due to the clogging of orifices or to the failure of the solenoid [9], [8].

### 2.3.2 Water

Water may be dissolved in the fluid up to the saturation point, and then the excess presents as a second phase (free water) or an emulsion. Water contamination can lead to failures such as corrosion of surfaces, accelerated abrasive wear, metal fatigue, and increased friction due to viscosity loss among others. These effects will lead to the increase of the force necessary to move the spool. Even greater complications may occur when the temperature decreases, since the fluid holds less dissolved water under these conditions, and when the freezing point is reached, the formation of ice crystals may affect the system functions [12].

### 2.3.3 Air

The air may be dissolved or free in the hydraulic fluid. Though it causes less trouble when dissolved, it may cause jamming, erratic functioning and other undesirable effects when it is trapped inside a valve [13]. The air may come from leaks in the system, from maintenance interventions, or from fluid turbulence in the reservoir.

### 2.3.4 Varnish and slug

Varnish and slug are generated by the degrading of the hydraulic fluid, which may happen as a result of natural aging, overheating, or the presence of contaminants such as water, air, solid particles, among others. It may be dissolved or free in the fluid. The fluid capacity to hold them dissolved depends greatly on the fluid temperature [9]. The varnish may accumulate in low flow and low temperature areas of the system, while areas with a high flow or high temperature are not affected. This kind of contaminant affects particularly valves that are not used for a certain period of time, like the ones used in emergency systems or during the cold start of a machine with degraded fluid [14].

These residues may clog orifices and grooves making the valve sluggish. In such a state the valve experiences jamming and performance loss. Also, solid particles may accumulate on the sticky surface, creating an abrasive surface that accelerates the wear of the moving parts of the system [14].

## 2.4 Other factors

Other factors may cause problems, such as pressure spikes, electrical surges, fatigue and manufacturing defects. Pressure spikes and electrical surges may be generated by accidents or design problems. When pressure spikes occur, damage to internal components, valve manifold an leaks may affect the valve, causing alterations in its behavior. Electrical surges may damage the electronic components of a servoproportional valve, rendering it useless. Fatigue and manufacturing defects such as problems in the valves surfaces, component alignment, geometry of chambers and drains, or even broken mechanical components, who may be

noticed on valve commissioning of after a period of operation, will affect greatly the valve behavior.

As seen above, in electrically modulated hydraulic control spool valves, the most common failures may cause the increase of friction between the spool and the sleeve due to wear, abrasion, varnish and particle accumulation, that end up altering the valve frictional characteristics [15]. Those may increase the stick and slip phenomenon, where the spool moves and stops several times during its trajectory, causing the actuator to move irregularly, and may even jam the valve spool. Some failures, such as damaged electronic components or broken mechanical components may affect the valve ability to control the forces on the spool. For that reason it is important to have some estimate of the forces that would normally be present. Since the force applied on the valve by the solenoid is fairly proportional to the current through its coil, an estimate of normal current levels can be used for comparison with the actual current levels through the solenoid to detect faults. Knowing the current that should be applied at the solenoid at each spool position at a certain operating condition may help the operator or monitoring system to realize when the valve is not working properly even before the fault could be noticed through other of the valve signals, such as spool position.

### 3 Servoproportional valve modeling

#### 3.1 Force and current equations

From the previous section one can realize that the magnitude of the forces involved in the spool movement is affected in most of the failures mentioned in the researched literature. Servoproportional valves are built with solenoids stronger than the needs to overcome the valve internal forces in order to be able to move even in the presence of certain contaminants or at higher pressure differentials. This is why the difference between the current levels of a healthy valve are so different from the levels of a contaminated or damaged valve, since the controller uses the extra power when it is not able to move the spool. Therefore, a model to estimate the internal forces through the magnitude of the current that should be applied at each spool position at certain operation conditions was developed [16]. In order to do so, a closer look at the forces involved in the spool movement is required.

The axial force required to move the spool is a consequence of the necessary forces to accelerate the spool and anything else that moves with it, to overcome friction, and the forces due to the flow through the valve, also called flow induced forces or Bernoulli forces [9]. There is also the force necessary to overcome springs used to center or return the spool valve.

Regarding the flow forces, the most significant is the steady-state flow force that is related to the variation of the quantity of motion of the fluid in the valve chambers (fig. 1). The jet angle is typically at around  $69^\circ$  from the center axis of the spool if the radial clearance between the spool and the sleeve is neglected [9]. Therefore, the resulting force has a lateral component that pushes the spool against the sleeve or

body of the valve, and an axial component that tends to shut the valve closed. Commonly the ports of the valve are located symmetrically around the spool, leading the components of the lateral force to compensate each other. However, the axial forces are not compensated except the valve has a flow force compensation design.

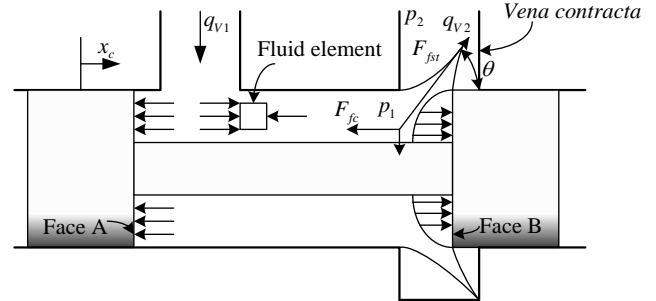


Figure 1: Flow forces on a spool valve due to flow leaving a valve chamber [9].

The steady-state flow force can be expressed for each valve chamber as [9], [17], [18]

$$F_{fst} = \frac{\rho \cdot q_v^2}{cc \cdot A_0} \cdot \cos \theta \quad (1)$$

where:

$F_{fst}$  is the steady-state flow force in axial direction [N];

$\rho$  is the fluid mass density [kg/m<sup>3</sup>];

$q_v$  is the volumetric flow rate through the valve [m<sup>3</sup>/s];

$A_0$  is the metering orifice area [m<sup>2</sup>];

$\theta$  is the jet angle at the *vena contracta* [no dimension].

$cc$  is the contraction coefficient that relates the area at the metering office to the area at the *vena contracta* [no dimension].

This force is applied over the fluid. Consequently, the reaction force on the spool ( $F_{fc}$ ) has the same module but inverse signal.

Using the valve flow coefficient defined in [19], the flow rate can be expressed by [20]

$$q_v = Kv \cdot \frac{x_c}{x_{cn}} \cdot \sqrt{(p_1 - p_2)} \quad (2)$$

where:

$x_c$  is the valve spool displacement [m];

$x_{cn}$  is the nominal spool displacement, at which the  $Kv$  is obtained [m];

$Kv$  is the valve flow coefficient [m<sup>3</sup>/s.√Pa];

$p_1$  is the inlet pressure [Pa];

$p_2$  is the outlet pressure [Pa].

Since that the flow coefficient can be expressed by [20]

$$Kv = cd \cdot A_{0n} \cdot \sqrt{\frac{2}{\rho}} \quad (3)$$

where:

$A_{0n}$  is the nominal metering orifice area [m<sup>2</sup>];

$cd = cv \cdot cc$  is the discharge coefficient [no dimension];

$cv \approx 1$  is the velocity coefficient [no dimension];

the reaction force  $F_{fc}$  can be written combining eq. (1), eq. (2), and eq. (3):

$$F_{fc} = \frac{Kv \cdot x_c \cdot \sqrt{2 \cdot \rho \cdot (p_1 - p_2)} \cdot \cos \theta}{x_{cn}} \quad (4)$$

The force above contributes significantly to the force required to stroke the valve spool [9]. One can notice that the reaction force ( $F_{fc}$ ) is proportional to the spool displacement and therefore it can be represented by  $F_{fc} = K_{esc} \cdot x_c$  where  $K_{esc}$  [N/m] is a variable stiffness.

Therefore, the necessary force to move the valve spool can be expressed as

$$F_c = m_e \cdot \ddot{x}_c + B_e \cdot \dot{x}_c + K_{me} \cdot x_c \quad (5)$$

where:

$F_c$  is the force necessary to move the valve spool [N];

$m_e$  is the equivalent moving mass [kg];

$B_e$  is the equivalent viscous friction coefficient [N.s/m];

$K_{me} = K_m + K_{esc}$  is the effective spring rate [N/m];

$K_m$  is the spring rate [N/m].

The inertial force is related to the effective moving mass that consist the mass of the valve moving parts plus fluid contained in the valve chambers and drain ports at the spool ends. The dampening forces are a consequence of the transient flow forces related to flow acceleration and the viscous friction forces caused by the fluid adjacent to the valve moving parts. These forces are in general considerably smaller than the spring and steady-state flow forces and can be neglected in the model for simplicity sake. Their effect, however, is important, since they limit the valve performance and response time and may demand the solenoid maximum available force during the initial acceleration of the spool when changing the area of the

metering orifices. For this reason measures must be taken in the fault detection process to avoid false detections [16].

This yields a much simpler, easier to calculate model, allowing a reduced processing time for on-line fault detection. In a solenoid valve all these forces must be overcome by the solenoid(s). Since the force generated by the solenoid(s) can be described in a simplified way by [18]

$$F_s = K_{Fi} \cdot i_s \quad (6)$$

where:

$F_s$  is the force produced by the solenoid [N];

$K_{Fi}$  is the solenoid force - current coefficient [N/A]

$i_s$  is the current on the solenoid [A].

Substituting eq. (6) in eq. (5) and considering steady-state conditions one obtains:

$$i_s = \frac{K_{me}}{K_{Fi}} \cdot x_c \quad (7)$$

### 3.2 Model applied to the studied valve

The Hydrus, HR01 servoproportional single solenoid valve is a prototype valve designed at LASHIP/UFSC. Since there is no failure field data and the magnitude of the internal forces at such operational conditions, the choice for the model based approach was reinforced, since it could be based on the in lab valve behavior [16].

Being a single solenoid valve, the HDR01 has only one spring, as seen in Fig. 2. This spring counteracts the solenoid and to this force the steady-state flow force is added. At the beginning of the solenoid displacement, when the current and the force yielded by the solenoid is zero, the valve port A is fully open and connected to the supply port, while the port B is connected to the return port. Following the center position, where all ports are closed, the valve connects the port B and the supply port at the same time it connects the port A and the return port. Since the steady-state flow forces tend to close the valve, while the port A is connected to the supply port the steady-state flow forces help the solenoid against the spring. After the center position, the steady-state flow forces act against the solenoid along with the spring.

As it typically occurs, the proportional solenoid has non-linear regions at the beginning and at the end of its displacement. These regions were avoided to make the valve proportional, but the non linearity offsets the force curve from zero, since the solenoid only starts generating force after a certain current is applied. Also, the solenoid presents hysteresis on its force versus current relation, as a result of the remanence phenomenon, which is the residual magnetization of a ferromagnetic material in the absence of external magnetic fields. Therefore it is necessary to add a linear coefficient to eq. (7) in order to compensate the force offset. This coefficient has two values in order to account

for the hysteresis of the solenoid, delimiting the maximum and minimum force yielded for a given current level.

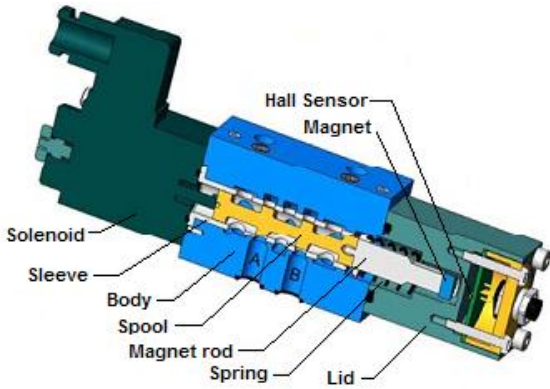


Figure 2: HR01 servoproportional valve

The force actually generated by the solenoid at a certain current will depend on its previous movements and on which way it is moving. Hence

$$F_s = K_{Fi} \cdot i_s + b_s \quad (8)$$

where:

$b_s$  is the solenoid force x current curve linear coefficient [N].

Therefore, associating eq. (4), eq. (7) and eq. (8), regarding the characteristics of the valve one has, for  $x_{c\min} \leq x_c \leq x_{c\max}$ ,

$$i_s = \left[ \frac{\sqrt{2} \cdot \rho \cdot Kv \cdot \cos \theta \cdot \Delta p}{x_{cn} \cdot K_{Fi}} + \frac{K_m}{K_{Fi}} \right] \cdot x_c + \left[ \frac{-\sqrt{2} \cdot \rho \cdot Kv \cdot \cos \theta \cdot x_{c0} \cdot \Delta p}{x_{cn} \cdot K_{Fi}} + \frac{K_m \cdot x_{m0} - b_s}{K_{Fi}} \right] \quad (9)$$

where:

$x_{c0}$  is the spool center position [m];

$x_{c\min}$  is the minimum spool displacement for which the valve is linear [m];

$x_{c\max}$  is the maximum spool displacement for which the valve is linear [m].

$x_{m0}$  is the valve spring initial displacement [m];

Equation (9) can be rearranged into:

$$i_s = a_i \cdot x_c + b_i \quad (10)$$

where:

$a_i$  is the angular coefficient of the current estimate model [A/m];

$b_i$  is the linear coefficient of the current estimate model [A].

These coefficients can be expressed as

$$a_i = \left[ \frac{\sqrt{2} \cdot \rho \cdot Kv \cdot \cos \theta}{x_{cn} \cdot K_{Fi}} \right] \cdot \Delta p + \left[ \frac{K_m}{K_{Fi}} \right] \quad (11)$$

and

$$b_i = \left[ \frac{-\sqrt{2} \cdot \rho \cdot Kv \cdot \cos \theta \cdot x_{c0}}{x_{cn} \cdot K_{Fi}} \right] \cdot \Delta p + \left[ \frac{K_m \cdot x_{m0} - b_s}{K_{Fi}} \right] \quad (12)$$

Both eq. (11) and eq. (12), however, can be further divided in angular and linear coefficients regarding  $\Delta p$  forming the equations below

$$a_i = a_{a_i} \cdot \Delta p + b_{a_i} \quad (13)$$

$$b_i = a_{b_i} \cdot \Delta p + b_{b_i} \quad (14)$$

where:

$a_{a_i}$  is the angular coefficient that adjusts  $a_i$  to the pressure drop on the valve [A/m.Pa];

$b_{a_i}$  is the linear coefficient that adjusts  $a_i$  to the pressure drop on the valve [A/m];

$a_{b_i}$  is the angular coefficient that adjusts  $b_i$  to the pressure drop on the valve [A/Pa];

$b_{b_i}$  is the linear coefficient that adjusts  $b_i$  to the pressure drop on the valve [A].

From eq. (10), eq. (13), and eq. (14) a Simulink block diagram has been designed as shown in fig. 3. This block diagram estimates the maximum and the minimum current at the solenoid at a certain spool position for a given pressure drop on the valve. It is supposed to estimate the steady-state current, but since the effective spring forces are considerable, it can be used too to estimate with a reasonable margin of error the transient current that occurs when the solenoid and valve are accelerating, since the estimates change as the spool moves. Under steady-state conditions the current value is to be around the range delimited by the two estimated limits, or slightly above or below if hunting occurs due to the static friction of the spool, which is a non-linear characteristic not accounted for in the model.

The model expressed in Fig. 3 is fit for a symmetrical proportional valve. For an asymmetrical valve, two of these block diagrams should be used in order to change the  $KV$  value as the valve changes the flow direction.

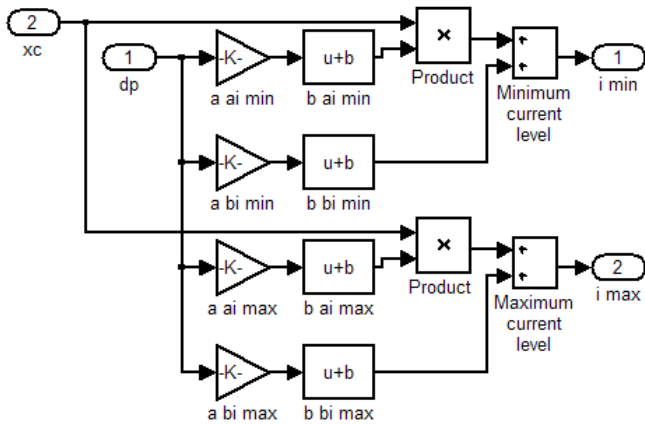


Figure 3: Solenoid current estimation model

Signals obtained from sensors that measure spool position, supply pressure, return pressure, chamber A pressure, and chamber B pressure are used by the model to output two current estimates, the maximum and the minimum current levels expected for that spool position at those operating conditions. Running in parallel with the valve, as shown in fig. 4, the model generates real time estimates that can be compared to current on the valve solenoid to detect discrepancies, and therefore, potential faults. Depending on the characteristics of those discrepancies, a certain type of fault is more likely to be happening, information that is valuable for diagnosis and to narrow down maintenance actions to solve the problem.

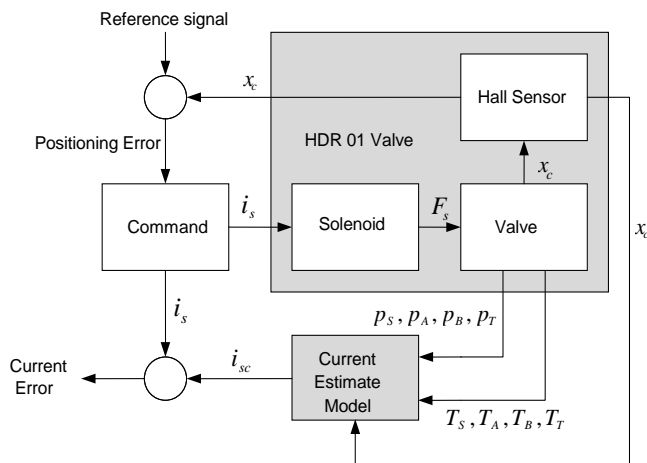
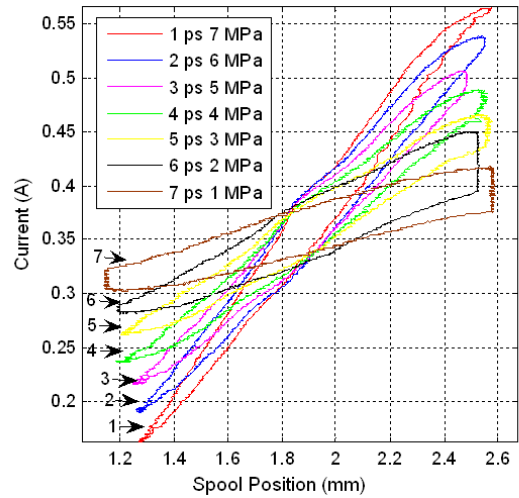


Figure 4: Current on the solenoid estimate model running in parallel with the actual valve

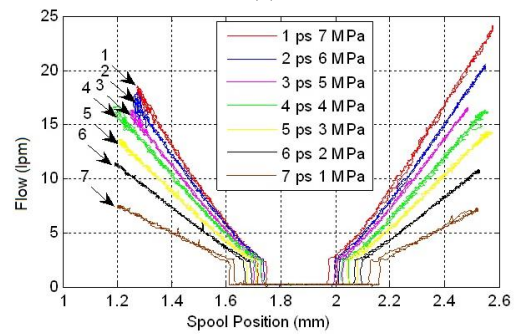
### 3.3 Experimental results

Firstly, experiments were made to check the modeling hypothesis and evaluate the need for models that account for temperature changes. In fig. 5a the valve behavior under different supply pressure levels can be seen, showing that current changes relatively linearly with spool displacement, and the rate of this change varies with the supply pressure on the valve. This is a consequence of the changing of valve flow rate with pressure, as shown in fig. 5b. Notice that flow rates below to 2.5 l/min are out of the measuring range of the flow transducer used in these experiments, and the sudden drop in the flow rate close to the valve center does

not occur. During these experiments the ports A and B were interconnected and the temperature controlled at  $40 \pm 2^\circ\text{C}$ .



(a)



(b)

Figure 5: Results with different  $p_s$  at  $40^\circ\text{C}$ : (a) Current on the solenoid  $x$  spool position; (b) Flow rate  $x$  spool position

Figure 6a shows that flow rate does not change within the temperature range such that there is a small variation in the current levels necessary to move the spool (fig. 6b). For greater temperature changes further compensations may be needed on the model. In figures 5a and 6b the effect of hysteresis and threshold can be noted, since two different current levels are seen for the same spool position, depending on the spool moving direction.

Based on these results, the temperature effect was not included in the model. However, a model using temperature sensors to estimate the pressure drop between the supply port and port A (or B, depending on the flow direction) and the other working port and the return port was developed to replace the pressure measurements. That would make the hardware necessary to feed the model cheaper. However, the temperature sensors readings were too slow to keep up with the spools movements, and that could lead to false detections.

The model was validated using both parameters extracted from the product catalog and experimental parameters, extracted from fig. 5a. Good results were achieved with both approaches however the use of experimental parameters resulted in a more accurate current estimation, as expected.

Merritt [9] discusses about the uncertainty of the flow force theoretical models, especially when the spool is close to the center, due to the changes in the jet angle at the *vena contracta* and other simplifications as the orifice geometry. Experimental parameters can reduce the influence of these simplifications and variations that occur from valve to valve. However, the model with theoretical values is still good enough for estimate due to the considerable differences in current observed when the valve is contaminated or worn.

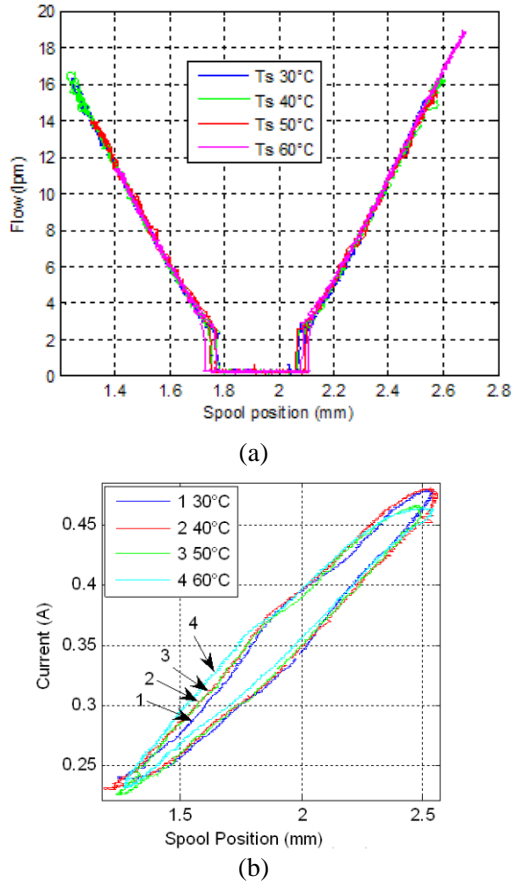


Figure 6: Results with different  $T_S$  at  $p_s = 4$  MPa: (a) Flow rate  $\times$  spool position; (b) Current  $\times$  spool position.

The experiments were carried out on a test rig according to recommendations from ISO 10770-1 [1]. Valve port A was connected to port B and supply temperature  $T_S$  adjusted from 30°C to 60°C. Supply pressure  $p_s$  ranged from 3 to 5 MPa. Step inputs ranging from 1.32 to 2.43 mm and sinusoidal inputs from 1.32 to 2.43mm with periods ranging from 1 to 20 s were used [16]. Figure 7a shows the solenoid current  $i_s$  response for a position step input from 1.85 to 1.635 mm compared with the minimum and maximum current estimates using experimental values and catalog/theoretical values to obtain the coefficients  $a_{a_i}$ ,  $b_{a_i}$ ,  $a_{b_i}$ , and  $b_{b_i}$ .

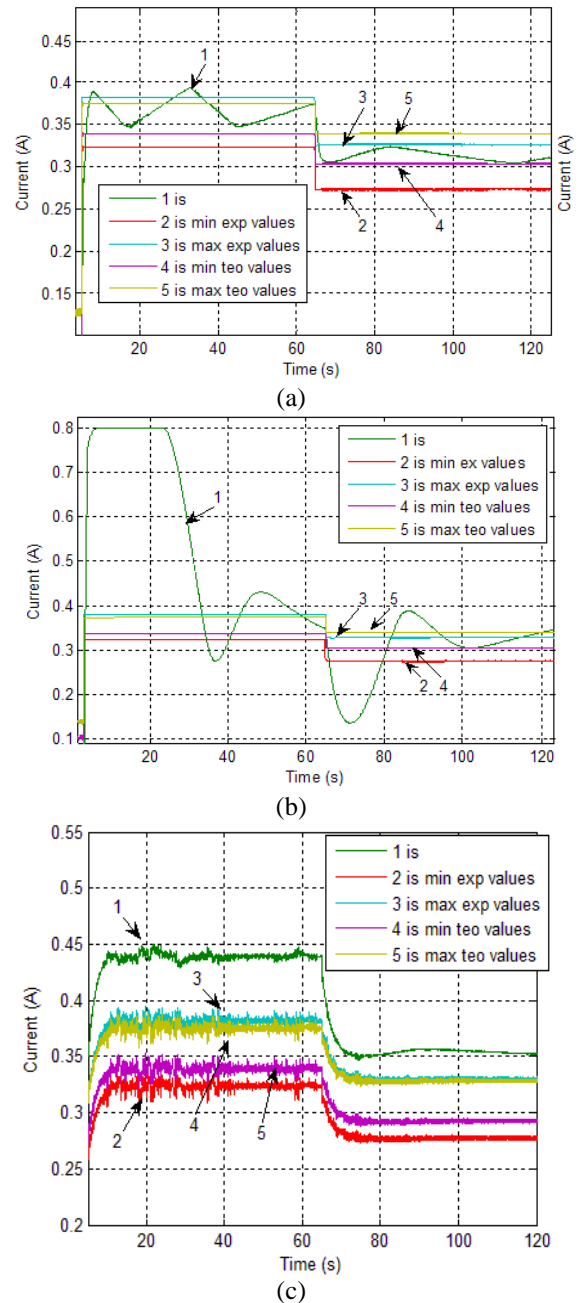


Figure 7: Current for step inputs of 1.85mm and 1.635 mm at  $p_s = 4$  MPa and  $T_S = 40^\circ\text{C}$ : (a) healthy valve (b) degraded valve (c) contaminated valve

The greatest difference between the estimated and the actual current for a healthy valve was observed during the first 10% of the settling time after a step input. Since the estimate is based on a steady state model, the difference between the estimated and the actual current is maximum when the spool is being accelerated or decelerated. During steady-state conditions the current remained within the boundaries of the estimates for most of the time, except when hunting occurred. Here some error was noticed due to the spool static friction, which forced the controller to raise the current to move the spool while the spool remained still.

The sinusoidal response is presented in fig. 8a where the error corresponds to the percentage difference between the

actual and estimated current. When considering the minimum estimate value, the error must be positive or very close to zero which means that the actual current is higher than the minimal estimated value. In the same way, for maximum estimate currents the error must be negative or very close to zero for a healthy valve. It is not accomplished when the movement direction of the spool changes since that the dynamic effects are not computed by the model.

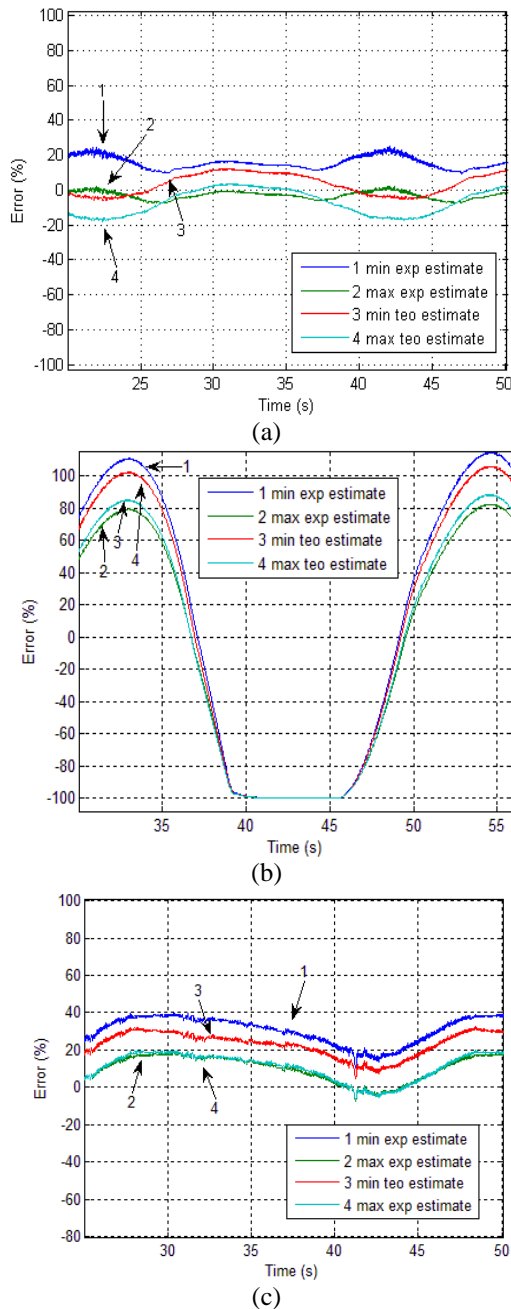


Figure 8: Current error for sinusoidal signals with amplitude of 1.74 mm and period of 20 s at  $p_S = 4 \text{ MPa}$   $T_S = 40^\circ\text{C}$ : (a) healthy valve (b) degraded valve (c) contaminated valve

Aiming to verify the effectiveness of the estimate model for fault detection three from twelve valve grooves were contaminated with diesel engine adhesive as shown in fig. 9.

This emulates the accumulation of dirt or varnish on the grooves. As can be seen in fig. 7b and fig. 8b, the valve did not lose its function and the controller was still able to be positioning the spool, even though it did it with increased error. However, the valve settling time was increased and the solenoid demanded more current yielding great differences between the estimates and the actual current even after the spool accelerating. In fig. 8b one can notice the saturation of the solenoid current during the spool displacement. The error between actual and estimate current was greater than 100% during a considerable amount of time. Under these conditions a fault detection system would be able for fault detection and warning the operator before a valve jam occurred.

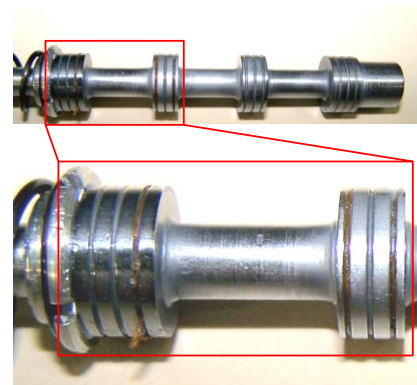


Figure 9: Valve with obstructed grooves

The spool valve without contaminants but with eroded control surfaces was also analyzed (fig. 10). The valve parameters such as the null spool position and the flow coefficients changed, and also the internal forces. As shown in fig. 7c, the current difference was higher than 20% even during steady state conditions. Figure 8c shows that with sinusoidal signals the error for the maximum estimate models (using theoretical or experimental parameters) was positive almost all the time indicating that the demanded current was greater than the estimated values indicating a potential fault. Even though with an eroded control surface the controller was still able to position the valve spool.



Figure 10: Valve with eroded control surfaces

## 4 Conclusions

The proposed model estimates adequately the solenoid current of a servo-proportional valve establishing minimum and maximum limits for an undamaged valve. Along with pressure measurement on valve ports and signals commonly available on the embedded electronic controller of servoproportional valves, an effective fault detection system can be designed using, for example, a simple rule based system. Although the model is based on steady-state equations, a difference between the actual and estimated current greater than the specified value taking into account the transient forces will be occurring when the valve is in poor conditions. Therefore, the model can be used for diagnosis under transient conditions as well, provided the estimates made during the initial spool acceleration are disregarded.

The sensibility of the system will depend upon the quality of the transducers, on the quality of the valve and on the user's tolerance to faults. If the transducers have a low uncertainty, the valve is linear and well balanced, the fluid is well filtered, and the application has little tolerance to changes in valve behavior, the user can set the system to warn after small errors between the estimates and the actual current are detected. However, if some of those conditions are not met, a higher error level should be tolerated before a fault is considered detected.

## Nomenclature

Designation	Denotation	Unit
$F_{fst}$	Steady-state flow force in axial direction	[N]
$\rho$	Fluid mass density	[kg/m <sup>3</sup> ]
$q_v$	Volumetric flow rate	[m <sup>3</sup> /s]
$A_0$	Metering orifice area	[m <sup>2</sup> ]
$\theta$	Jet angle at the <i>vena contracta</i>	[no dimension]
$cc$	Contraction coefficient	[no dimension].
$F_{fc}$	Reaction force on the spool	[N]
$x_c$	Valve spool displacement	[m]
$x_{cn}$	Nominal spool displacement	[m]
$K_V$	Valve flow coefficient	[m <sup>3</sup> /s.√Pa]
$p_1$	Inlet pressure	[Pa]
$p_2$	Outlet pressure	[Pa]
$A_{0n}$	Nominal metering orifice area	[m <sup>2</sup> ]

$cd$	Discharge coefficient	[no dimension]
$K_{esc}$	Valve spring rate due to $F_{fc}$	[N/m]
$F_c$	Force necessary to move the valve spool	[N]
$m_e$	Equivalent moving mass	[kg]
$B_e$	Equivalent viscous friction coefficient	[N.s/m]
$K_m$	Spring rate	[N/m]
$K_{me}$	Effective spring rate	[N/m]
$F_s$	Force produced by the solenoid	[N/m]
$K_{Fi}$	Solenoid force - current coefficient	[N/A]
$i_s$	Current on the solenoid	[A]
$b_s$	Solenoid force x current curve linear coefficient	[N]
$x_{c0}$	Spool null position	[m]
$x_{c\min}$	Minimum spool displacement for which the valve is linear	[m]
$x_{c\max}$	Maximum spool displacement	[m]
$x_{m0}$	Valve spring initial displacement	[m]
$a_i$	Angular coefficient of the current estimate model	[A/m]
$b_i$	Linear coefficient of the current estimate model	[A]
$\Delta p$	Valve pressure drop ( $p_1 - p_2$ )	[Pa]
$a_{a_i}$	Angular coefficient of $a_i$	[A/m.Pa]
$b_{a_i}$	Linear coefficient of $a_i$	[A/m]
$a_{b_i}$	Angular coefficient of $b_i$	[A/Pa]
$b_{b_i}$	Linear coefficient of $b_i$	[A]
$T_S$	Temperature at supply port	[°C]
$T_A$	Temperature at A port	[°C]
$T_B$	Temperature at B port	[°C]
$T_T$	Temperature at return port	[°C]

## References

- [1] International Organization for Standardization, 1998, "ISO 10770-1 Hydraulic fluid power - Electrically modulated hydraulic control valves – part 1: test methods for four way directional flow control valves", Switzerland.
- [2] Bhojkar, A., 2004, "Fault simulator for proportional solenoid valves". Thesis (Master of Science), Department of Mechanical Engineering of the University of Saskatchewan, Saskatoon, Canada. 115p.
- [3] Fenton, B., McGinnity, M., Maguire, L., September 2002, "Fault diagnosis of electronic systems using artificial intelligence". IEEE Instrumentation & Measurement Magazine, 1094-6969-02. pp. 16-20.
- [4] Bowers, M., Arnold, D. Crew, A. W., Gibson, R. J., Ghrist III, W. D., February 1989, "Diagnostic software and hardware for critical real-time systems", IEEE Transactions on Nuclear Science, Vol. 36, No.1. pp. 1291-1298.
- [5] Grimmeliuss, H. T., Meiler, P. P., Maas, H. L. M. M., Bonnier, B., Grevink, J. S., van Kuilenburg, R. F., April 1999, "Three state-of-the-art methods for condition monitoring", IEEE Transactions on Industrial Electronics, vol. 46, no. 2. pp. 407-416.
- [6] Parker Hannifin, 2005, "The handbook of hydraulic filtration", Metamora, USA. 38 p.
- [7] Vijlee, A., January 2003, "Roll-off cleanliness of hydraulic systems", Machinery Lubrication Magazine, no. 200301.
- [8] Park, R. W., August 1997, "Contamination control – a hydraulic OEM perspective", Workshop on Total Contamination Control Centre for Machine Condition Monitoring, Monash University. 18 p.
- [9] Merrit, H. E., 1967, "Hydraulic control systems", New York: John Wiley and Sons. 368p.
- [10] Tessman, R. K., Hong, I. T., 1998, "Contamination control of aircraft hydraulic systems", Stillwater: FES/BarDyne Technology Transfer Publication, no.10.
- [11] Doddannavar, R., Barnard, A., 2005, "Practical hydraulic systems: operating and troubleshooting for engineers and technicians". London: Elsevier. 232p.
- [12] Parker Hannifin, June 1999, "Tecnologia hidráulica industrial", M2001-1 BR, Jacareí, Brazil. 158 p.
- [13] ATOS Electrohydraulics, 2006, "KT Master catalog – KT06/E". Italy.
- [14] Atherton, B., 2007, "Discovering the root cause of varnish formation – the hidden issues beyond heat", Practicing Oil Analysis Magazine, Issue 200704, Noria Corporation, Tulsa, Oklahoma, EUA. pp. 22-25.
- [15] Fey, C., 1987, "Identifying Component Wear through Metallurgical Analysis", Proceedings of the 42<sup>nd</sup> National Conference on Fluid Power, Chicago, Illinois, USA, pp. 221-232.
- [16] Ramos Filho, J. R. B., 2009, "Análise teórico-experimental de falhas em válvulas direcionais servoproporcionais" Dissertation (Master in Mechanical Engineering) - Universidade Federal de Santa Catarina, Florianópolis, Brazil. 138 p.
- [17] Linsingen, I. v., 2003, "Fundamentos de sistemas hidráulicos" 2. ed., Florianópolis: Editora da UFSC. 399 p.
- [18] Stringer, J. D., 1976, "Hydraulic Systems Analysis", Macmillan. 192 p.
- [19] Johnson, J. L., "Design of Eletrohydraulic Systems for Industrial Motion Control". Parker Hannifin. USA, 1995.
- [20] Furst, F. L., 2001, "Sistematização do projeto preliminar de circuitos hidráulicos com controle de posição". Dissertation (Master in Mechanical Engineering) – Universidade Federal de Santa Catarina, Florianópolis, Brazil. 132 p.

# Guidelines for modeling hydraulic components and model based diagnostics of hydraulic applications

Sebastian Adén<sup>1</sup>, Kenny Stjernström<sup>2</sup>

<sup>1</sup>Linköping University, Department of Management and Engineering, Linköping, Sweden  
E-mail: sebad028@student.liu.se

<sup>2</sup>Combitech AB- Technical Information Solutions, Linköping, Sweden  
E-mail: [kenny.stjernstrom@combitech.se](mailto:kenny.stjernstrom@combitech.se)

## Abstract

Model based diagnosis is a very hot topic right now in the world of system engineering, through RODON the user is provided with the necessary tools to accomplish this. With this software one can model a hydraulic system and auto-generate fmea (failure-mode-effect-analysis). The old fashioned way for solving this procedure is with pen and paper and that's a very time-demanding activity. In addition to previous attributes of traditional failure-mode-effect-analysis: The complexity-grade is increasing fast in large machinery. Due to the origin of the paper, i.e. as a product of a master thesis; a huge effort has been put in to understand how RODON works, and how hydraulics best should be modeled to provide the user with as much information and accuracy as possible.

**Keywords:** System, modeling, auto-generated fmea, diagnostics, non-causal interface.

## 1 Introduction

### 1.1 Background to paper and objectives

This paper is a milestone in one of the authors' master thesis. It should be considered as a method suggestion for auto-generating fmea of hydraulic machinery. The main goal of the thesis is to develop an expansion of RODONs standard component library, with aim of hydraulic and pneumatic components. The results from this paper are the same as the results from the thesis; up to the deadline-date of submission for full paper to SICFP (April 14, 2013).

### 1.2 Introduction to paper

FMEA is a conventional tool for the investigation; how effects of component fault modes propagating the system [1]. Often it is used in an early state of production, to find construction-critical areas, but as well for maintenance work in the field. With RODON such analysis are auto-generated, in the terms of: system behavior is simulated with activated failure modes. With this information one can evaluate construction-concept and also find the candidate failure mode that's consistent with the shown behavior.

Modeling in RODON is built on the idea that systems can be described in terms of intensity- and flow-variables. Such observations are often represented in bond graphs.

In autonomous diagnostics methods, where diagnosis is stated by sensors and microcontrollers, the diagnostic engineer got harsh requirements for constructing accurate models; off-

line diagnosis can be run on much more simplified diagnosis models.

## 2 Background

The paper assumes basic knowledge of system engineering techniques, failure-mode-effect-analysis, logic and control theory. In some parts more, advanced theory is used, but for overall understanding basic knowledge is enough.

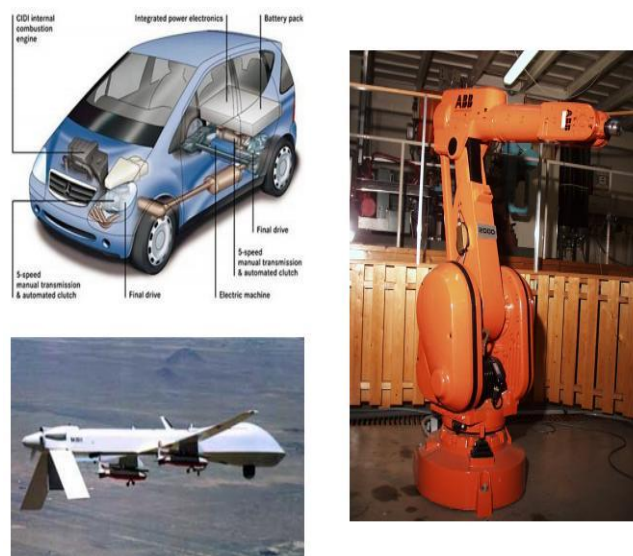


Figure 1 Different areas where diagnose is a common tool, photo: ISY, LinköpingsUniversity

## 2.1 Diagnosis

For the uninitiated, the term diagnosis is often only associated with medical diagnosis. But a diagnosis can also be stated for a technical system that got a headache. In this case the diagnose-algorithm is the doctor and the system is the patient.

The aim of a diagnosis is to decide whether the system is in a fault mode or not and in case of fault, identify the root cause [4]. There are many types of diagnosis and methods for generate them. This paper will focus on how to achieve diagnosis study on hydraulic applications, with help of stationary conditions. The concept is evaluated off-line. I.e. the analysis is not automated by sensor, in the sentence of; compare sensor readings with a threshold. If the sensor signal exceeds the threshold level, the system is considered faulty and the user should be warned.

Traditional diagnosis methods and the original version of fmea are to use a set of diagnostic rules, based on experience. A diagnostic rule could look something like: “If the lamp is not lit when the switch is turned on, either the switch is stuck in open position or the lamp is broken or both components are defect”. The diagnosis method that’s been used in this paper is of the type model-based and will be explained in the following sections.

## 2.2 RODON

Combitech develop and market products and services in model based diagnosis, on the platform of their own software; RODON. In RODON it is possible to create system models from existing component-libraries and from those generate different kinds of failure-analysis, like Failure-Mode-Effect-Analysis (FMEA) and diagnosis in form of Decision Trees (DT). RODON can also do the opposite; state diagnosis based on symptoms given by the user.

For mechatronic systems, typical in automotives, there are well developed experiences in terms of methods and component-library for how these systems best should be modeled in RODON and to get a FMEA that’s satisfies the demands from the industry. An important aspect for successfully find the right method of modeling a system for auto-generated FMEA, is to investigate on which “level of detail” previous work is done. Shortly; the failure-analysis in RODON should generate the same system-information, as a manual made FMEA but as a considerably less time consuming activity and with an increased quality.

Today RODON is used in the automotive industry, with the work performed in this paper; the ambitions are that RODON should be able to perform diagnosis on hydraulic machinery as well.

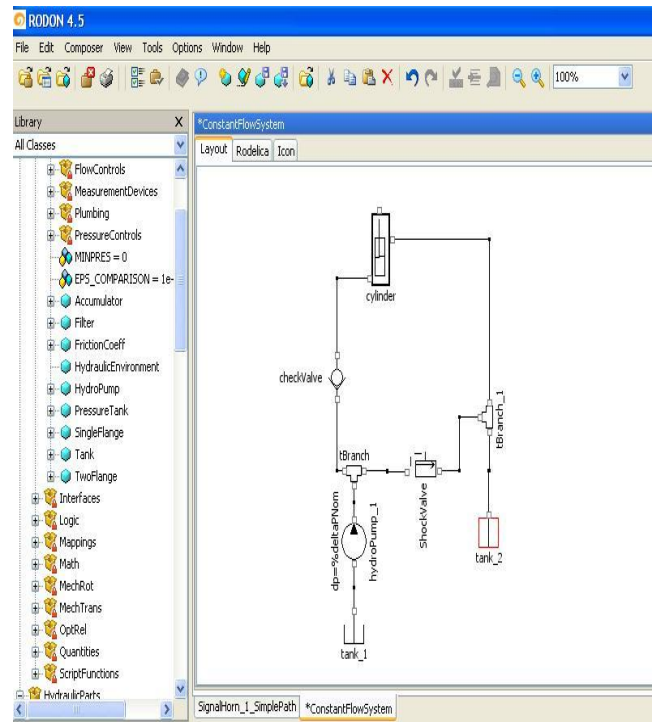


Figure 2 RODON's Graphical User Interface, Simple hydraulic system

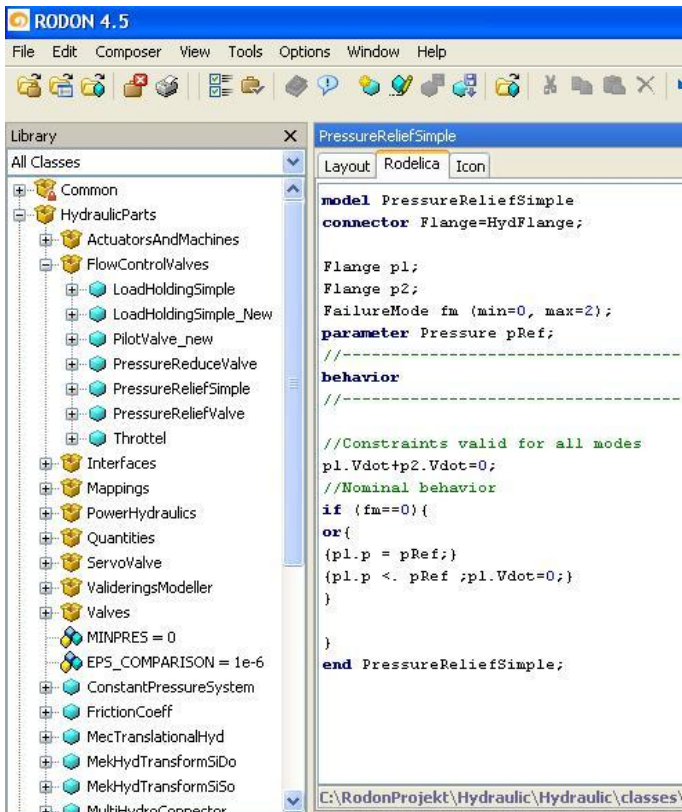
RODON provides an equation-based object orienting language called Rodelica [2]. The syntax is related to Modelica [3]. Some of the Rodelica features are:

- It is based on interval-arithmetic, instead of sharp values.
- It supports non-causal interface, i.e. the user is not in need of propagate calculations order.
- Simulation routine with activated failure modes.
- Or-statement. This operator compare a set of conditions during simulation and executing only the one that could be valid for the whole system.

The auto-generating fmea-routine in RODON can be dived into some main steps:

- The Composer (figure 2). Where the user creates a class of the system.
- The Analyzer (figure 4), for investigation of implemented equation.
- SDBView for generate fmea
- DtGen, evaluation of decision trees.

Editing and creation of a class can be constructed in a graphical way (drag-and-drop from a component-library) or in pure Rodelica-code, as for the case in figure 3.



```
//-----
behavior
//-----
//At SystemLevel
//Implemented condition for the case of considering
symptom signalHornNoSound to be true:
```

```
signalHornNoSound:=(switchOnOff1.posNom==1 &
signalHorn1.sound==0);

connect(gnd.pHarness, wireGnd.p2);
connect(wireGnd.p1, signalHorn1.p2);
connect(signalHorn1.p1, switchOnOff1.p1);
connect(switchOnOff1.p0, wireBattSwitch.p2);
connect(wireBattSwitch.p1, batterySimple1.p);
```

Figure 3 RODON's Graphical User Interface, Rodelica code for pressure relief-class

In figure 3 the Rodelica-interface for a pressure relief-valve is presented. Development of a component in general, consists basically of two steps; Instructions for nominal behavior and component behavior when a fault-mode is active. For the case in figure 3, no behavior for defect mode has been implemented yet.

The next step in the fmea-routine is to import the model into the Analyzer, like in figure 4. In Analyzer-mode, the user can simulate the system and evaluate the implemented equations. But foremost; in the Analyzer-mode, the user have access to what RODON call AutoSim. With this tool a simulation-routine can be initiated and for every single/multiple fault, the effect can be evaluated by the RODON- engine. This comes in handy when a diagnostic engineer, wants to find out candidates to debilitating/defect behavior. Symptoms of this kind are implemented in Composer-mode on system-level. To draw a parallel to the situation in figure 4 (horn system); a symptom could be implemented based on the statement "the horn is not sounding, although the nominal value of switch-position is turned to position on". This is realized by the following Rodelica code-snippet.

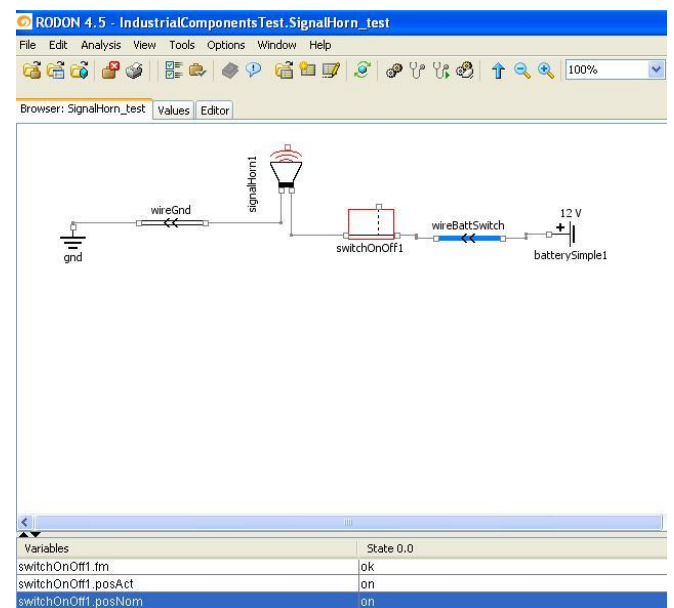


Figure 4 Graphical User Interface, Analyzer-mode of a horn-system

During AutoSim-routine, every combination of component-status, for which the system generates outputs that satisfy the symptom-condition; RODON will store information like this in a special database. Concrete; RODON have found candidates, which can explain system behavior and state a diagnosis.

As been said before, RODON can present diagnosis in form of Decision Trees (DT). In the case of defect horn-system, this could look something like figure 5. From this view a user can navigate through the remaining candidates to find the root cause of the debilitating behavior.

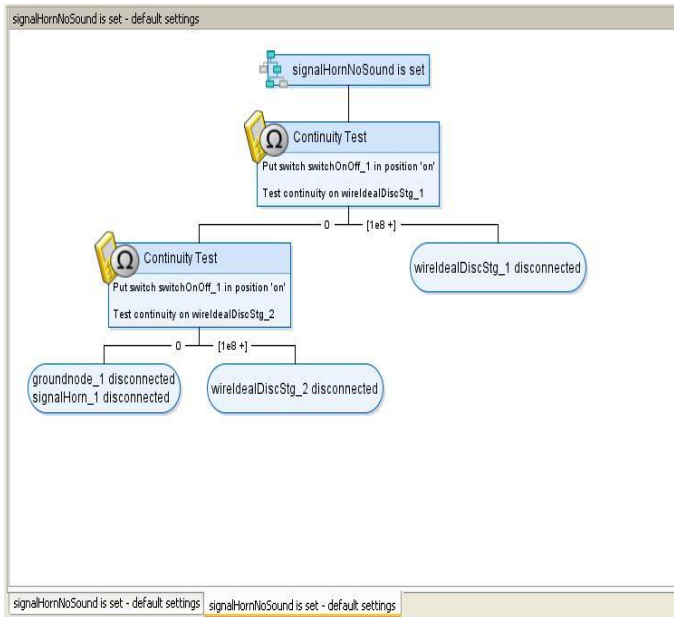


Figure 5, Decision Tree for guided diagnostic of horn system

### 2.3 Diagnosis system

Diagnosis systems are implemented in a wide area of technical system [4]. For example:

- Electrical motors
- Industrial robots
- Automotive

The reason and argument for implementing a diagnosis system are foremost:

- Safety
- Environment/Machine protection
- Maintenance work

With incorporate diagnosis system of an off-line approach, an ease of maintenance work is likely the goal of implementation. This is how RODON is used today; from generic component models, join into large mechatronic systems (with multiple physical domains), make statements of possible candidate(s) which is/are consistent with observed symptoms.

### 2.4 Diagnosis model

The definition of model-based diagnosis is: the diagnosis is based on an explicit formal model of the system. The first research reports of the subject were published in the beginning of the 1970s. [4].

A model that is used for diagnosis analysis is called a diagnosis model. It is used for evaluating presence of fault, given observation(s). In practice that means: A diagnostic

model doesn't necessarily need to calculate the exact physical behavior, as long as it represents the behavior of interest for making statements regarding component health.

The simplest form of model based diagnostics is to model the system for nominal behavior and compare with observations. Results from such test are then evaluated against a threshold, in diagnose theory terms; one have created a residual, i.e. the numerical difference between system output and model output based on the same input, that's ideal zero (no fault). The computation routine is explained graphically in figure 6.

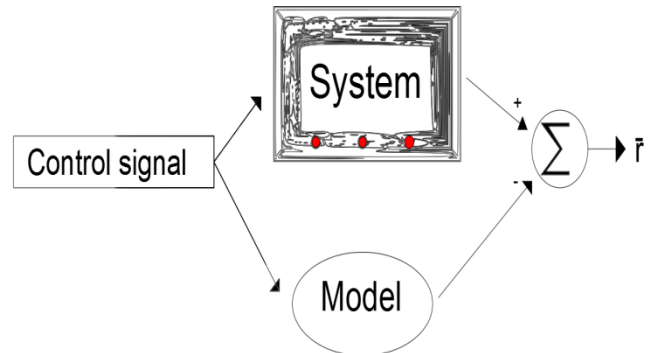


Figure 6 generating residual for diagnosis purpose

The size of absolute residual ( $r$ ) -value is compared against a threshold ( $J$ ).

In the case of  $r$  is larger than the threshold, the system is considered faulty. Due to the well-known nonlinear nature of hydraulics as well as the diagnostic engineers possibilities to accurate measure flow and pressure in arbitrary areas, adequate models for online diagnosis are rather hard to establish.

In a component-based reasoning approach (like the one in RODON), outputs from a faulty system can not have completely arbitrary values. It is the application engineer's assignment to construct components with well-defined nominal and faulty behavior.

A simple system is shown in figure 7, it contains two adders and three multiplies and illustrates the model-based reasoning for evaluating of error.

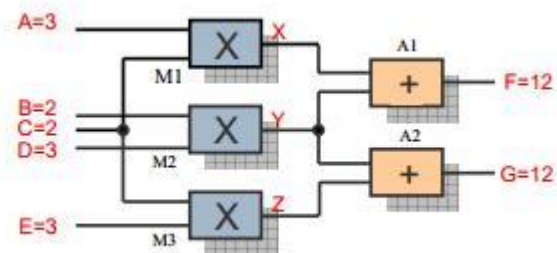


Figure 7 Multiplier- and Adder circuit, photo: Kleer and Kurien [6]

Inputs to the system are A, B, C, D and E, while F and G are the outputs. X, Y and Z can be considered as probing points. In the case of hydraulic environment, this corresponds to pressure and flow transducers. If the system is provided with the input of A=3, B=2, C=2, D=3, E=3, the expected output signal should become F=12 and G= 12, i.e. for system in nominal behavioral mode. A conflict is every value that differs from the nominal.

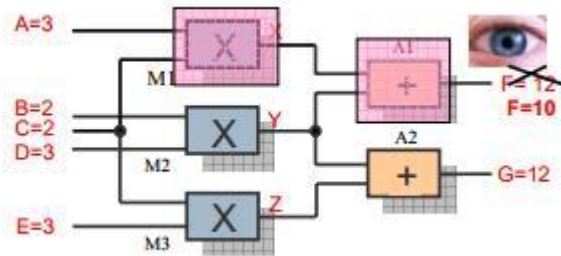


Figure 8 Multiplier- and Adder circuit with inconsistent behavior, photo: Kleer and Kurien [6]

Possible candidates to explain the behavior shown in figure 8 are: multiplier M1 or adder A1 is defect. This diagnosis-statement is based on logic reasoning, due to output G still acting consistent with predicted behavior. From figure 8, one can evaluate that G is decoupled from M1 and A1, and for the case of only single fault (defect M2 and A2 can also explain above observations) there could not be any other candidates than M1 or A1. For isolating one candidate and state a minimal diagnosis, the probing points needs to taking into account as well.

### 2.5 Level of detail

From above discussion about reasoning approach to diagnosis, the natural extension of that subject is; on which level of detail should components be developed, so they could be used both for nominal- as well as for faulty-behavior in a generic way. It should be noted that the main task of a diagnosis model is not to perform a simulation.

For example: When modeling a relay, from a diagnosis point of view. It's not relevant that equations corresponding to current-flow through the coil are implemented in the model (if not the interesting symptoms expects to depend on that specific behavior). An easier approach is to represent the relay with a resistance and a discrete switch, the function of the "simple-relay" is then emphasized from knowledge according to effect flow in the resistance-element.

### 2.6 Simple hydraulic modeling

The interface between components in Rodelica [2] is built on the idea that many systems can be described in terms of flow- and intensity-variables. Such observations are often represented in bond graphs [5]. For modeling work in RODON, no account needs to be taken to maintain conflict-free causality. The solver deals with this during its simulation-routine.

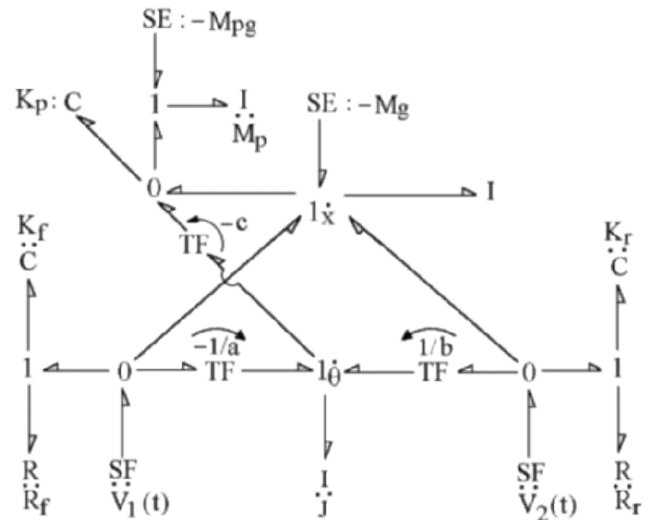


Figure 9 Bond graph of a mechatronic system, photo: bondgraph.org

For hydraulic environments these flow- and intensity variables are directly translated to flow and pressure respectively.

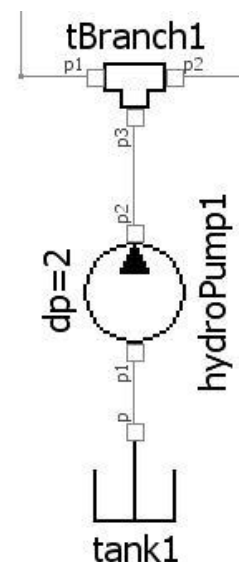


Figure 10, component-interface in RODON

Since Rodelica is built on interval-arithmetic, the only sharp value that has been declared for a hydraulic environment is tank-pressure (apart from parameters). Value-assignment for the rest of the hydraulic circuit is done by simulation-routine.

### 3 Results

In the following subsections results from the thesis to present day will be presented.

#### 3.1 Components

As been described; the master thesis that this paper is based on, aims to develop a standard component-library in RODON.

Hydraulic components can rather rough be divided into following classes:

- Hydraulic machines (pumps and motors)
- Actuators
- Directional valves
- Pressure-control valves
- Flow-control valves
- Check-valves
- Pipes

For which objects can be instantiated. With different attributes e.g.:

- Proportional control
- Servo control
- Linear/non-linear characteristics

#### 3.2 Hydraulic modeling in RODON

In the world of interval arithmetic and diagnostic approach; programming of component-classes can become quite confusing at first glance. Since one not normally propagates calculation order in RODON, the function-structure differs from a conventional simulation-program (e.g. MATLAB/Simulink). The easiest way of illustrate above statement is to look in to the Rodelica-code of a throttle valve.

```

model Throttlet
/** Hydromechanical connectors*/
connector Flange=HydFlange;
Flange p1, p2;
parameter FrictionCoeff kFriction = 1;
FailureMode fm (max = 1, mapping = "ok, blocked");
// -----
behavior
//-----
// Constraints valid for all modes:
// Volume flow balance:
p1.Vdot + p2.Vdot = 0;
// Definition of pressure drop:
deltaP = p1.p - p2.p;

// Basic constraints for nominal case:
if (fm == 0)
{
    deltaP = kFriction * p1.Vdot;
}
// Constraints for failure mode "blocked":
if (fm == 1)
{
    // No volume flow through pin 1:
    p1.Vdot = 0;
}
end Throttlet;

```

In the Rodelica-code for a throttle; no propagation is taken place for input/output signal, nor which of the ports that acting input/output. Depending of components, more or less sophisticated failure-modes have been implemented. A failure-mode can be considered as a state-machine; whenever a fault is present, the component should act in a predefined way.

As a first approach in component-modeling of hydraulics; only trivial failure modes are implemented, e.g. clog (as in the case of throttle-model) or pressure drain to atmosphere.

Verbal defined functions:

- If the clog- failure mode is active, then set flow through component to zero
- If component suffer from leakage to atmosphere, then set component pressure to atmosphere pressure.

Due to diagnosis purpose, modeling can be done with different abstraction-level (2.5 level of detail). Consider a load holding-valve like the one in figure 11.

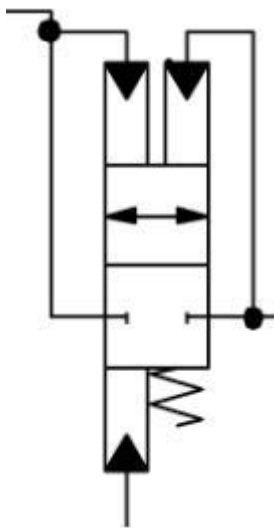


Figure 11 Schematic view of a conventional load holding-valve, photo: used with permission from Volvo CE

A Newtonian force balance of the component in figure 11 exhibit at least four well-defined forces. These are all relevant for simulation purpose, due to the study of dynamic/static behavior. Suppose now that the purpose of modeling is to investigate the health of the load holding-valve; an abstraction of component-function becomes:

- Depending on flow direction; No effect-losses on the high-pressure side, i.e. free flow. On the low-pressure side, a small pressure build up is propagated, i.e. component acting like a throttle. If a local or global fault is active, then the behavior will change.

An implementation of an abstracted load holding-valve in RODON is presented in figure 12. One demand in the master thesis is that all components should be constructed in a generic way; when the component classes are created, additional features are implemented as well. For the case of the load holding-valve in figure 12, an extra port (p3) has been added. Due to this one can e.g. let the valve function depend on a pilot valve or some other external components. For diagnosis this is very important; Consider the load holding-valve in figure 11, internal failure modes could be {always open, spring broken}. But system behavior will also be affected if a pilot valve suffer from leakage or sticks in closed position, the effects of these modes are spread to load holding-valve through port p3. In this case the pilot valve should be considered as an information port, i.e. the simplest way for modeling a pilot valve is to assign it carateristics of a discrete switch.

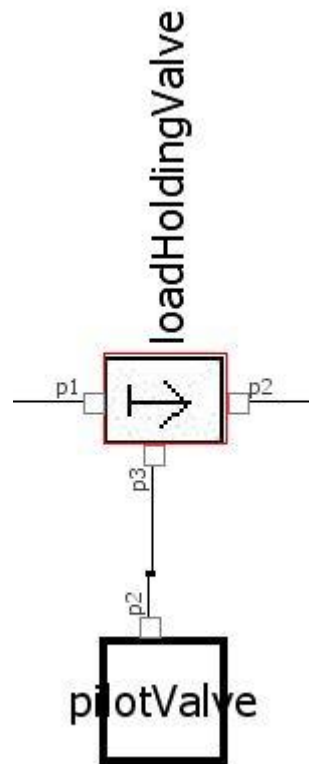


Figure 12 Schematic representation of a load holding-valve

In summary the discussion according to the load holding-valve ends up in the following Rodelica-code:

```
model LoadHoldingValve
/** Hydromechanical connectors*/
connector Flange=HydFlange;

/**Connector prepared for connection with pilot valve*/
connector actPos= Discrete;
```

```

/**Declare connector for pilotvalve*/
actPos p3;

FailureMode fm (max = 0, mapping = "ok,
stucksClosed, stucksOpen");
Discrete modeNom (min=0, max=1, mapping =
"closed, open");
Discrete modeAct (min=0, max=1, mapping = "closed,
open");
/**user defined parameters*/
parameter Interval fricNom;
parameter Interval fric2;
parameter Interval fricLeak;
parameter Interval fric1;
//-----
behavior
//-----
deltaP = p1.p - p2.p;
p2.Vdot + p1.Vdot = 0;
or
{
    {
        //Behavior is not propagated from pilot valve
        p3=0;
        modeNom = 0;
    }
    {
        //Behavior is propagated from pilot valve
        p3> 0;
        modeNom = 1;
    }
}
if (modeAct==0)
{
    p1.Vdot * fric2 = deltaP;
}

```

```

if (modeAct==1)
{
    //Nominal behavior
    if(p3==1){
        p1.Vdot * fric1 = deltaP;
    }
    // Leakage over pilotValve
    if(p3==2){
        p1.Vdot * fricLeak = deltaP;
    }
    // PilotValve stuck in closed position
    if(p3==3){
        //only leakage flow over loadholding valve
        p2.Vdot= 0;
    }
}
// nominal case:
if (fm==0)
{
    modeAct = modeNom;
}
end LoadHoldingValve;

```

### 3.3 Effects due to failure

Throughout the standard library that has been developed in the thesis, a certain level of abstraction has been used. In this section some of the component will be used for modeling the working hydraulics in a wheel loader and auto-generated decision trees for guided diagnostics will also be presented.



Figure 13 Volvo Wheel loader, photo: used with permission from Volvo CE

The working hydraulics of the tilting function in a wheel loader is represented in figure 14.

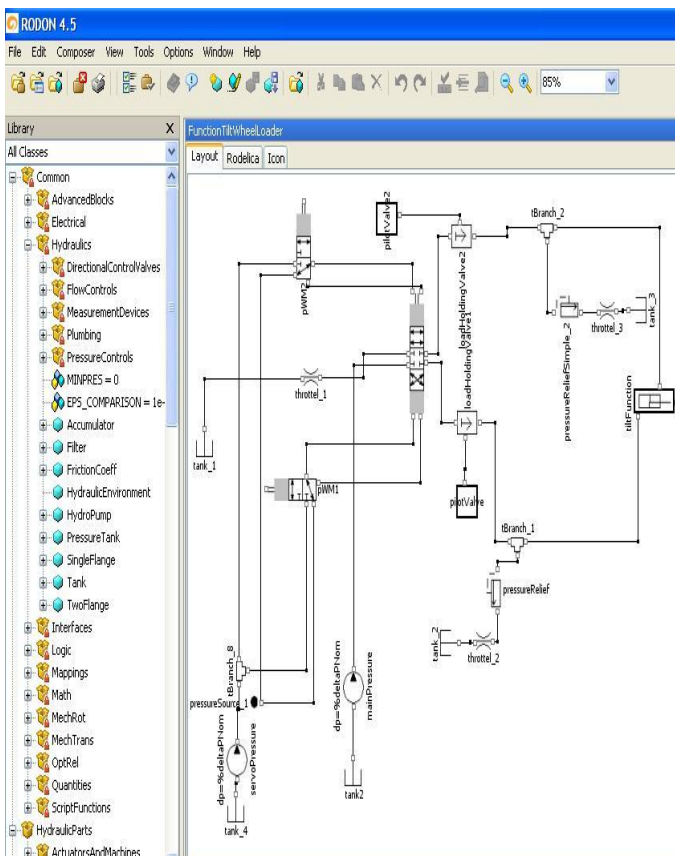


Figure 14, Tilt function in a wheel loader, modeled in RODON

Assume the diagnostics engineer got interest in finding all candidates that can explain performance problems within the tilting cylinder.

A symptom-variable is implemented, as explained in section (2.2), in this case:

- lowTransmissionPower (Boolean)
- tiltFunctionOutOfService (Boolean)

Conditions to satisfy the symptoms -->

lowTransmissionPower:=(tiltFunction.p1.Vdot>0 & tiltFunction.p1.p< 1.42) | (tiltFunction.p2.Vdot>0 & tiltFunction.p2.p< 1.95);

tiltFunctionOutOfService := (pWM1.PWMposNom == 0 & pWM2.PWMposNom == 0 & tiltFunction.isMoving != 0) |

(pWM1.PWMposNom == 1 & pWM2.PWMposNom == 0 & tiltFunction.isMoving != 2) |

(pWM1.PWMposNom == 0 & pWM2.PWMposNom == 1 & tiltFunction.isMoving != 1);

Based on the symptoms in the Rodelica Code; stated above, a decision tree has been computed (figure 15). The decision tree contains all the possible failure modes that can explain the faulty behavior; also it shows a guided diagnostic to ease maintenance work. Within the decision tree, the thought is to do the suggested tests. The final goal is to find the candidate on component level that can explain the debilitating behavior on system level.

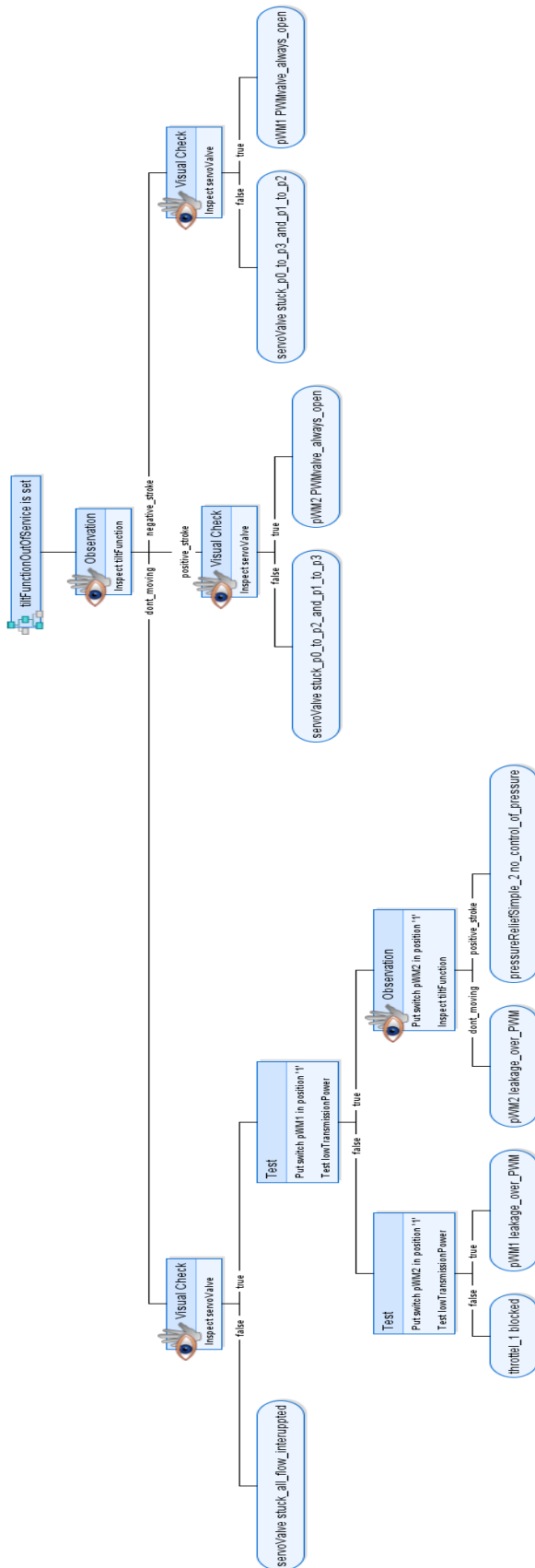


Figure 15, an auto generated Decision Tree for defect tilt-function

## 4 Conclusions

By the work of this paper; a component-library has been developed, for diagnostics use. It has been shown that the root cause for debilitating behavior can be found, through a model based diagnostic approach. By the end of the thesis, the expectations are that more sophisticated symptoms could be diagnosed; as well as more attributes should be implemented in the beta models, so that the decision trees will be more informative. Such additives could be an ECU. This work can be considered as a method evaluation, with the ultimate goal to find an artificial intelligence method for locate arbitrary failure modes in hydraulic machinery.

## References

- [1] National Aeronautics and Space Administration (NASA), 2007, NASA Systems Engineering Handbook, Tech.Rep, [http://ntrs.nasa.gov/archive/nasa/casi.ntrs.nasa.gov/2008008301\\_2008008500.pdf](http://ntrs.nasa.gov/archive/nasa/casi.ntrs.nasa.gov/2008008301_2008008500.pdf)
- [2] Peter Bunus, Olle Isaksson, Beate Frey, Burkhard Munker (2009), RODON- A Model-Based Diagnosis Approach for the DX Diagnostic Competition, Uptime Solutions AB.
- [3] The Modelica Association (2007). Modelica- a unified object-oriented language for physical systems modeling
- [4] Mattias Nyberg, Erik Frisk, 2012, Model Based Diagnosis of Technical Processes
- [5] Lamb, J.D., Woodall, D.R. Asher, G.M (1997c), Bond graphs ii: Causality and singularity
- [6] Johan de Kleer and James Kurien (2003). Fundamentals of Model-Based Diagnosis. In Proceedings of IFAC SafeProcess, Washington USA, June 2003

# Comparison of optical and magnetic particle detection systems for detection of pitting damage in low speed hydraulic motors

E. Sjödin, P-O. Westin

Institute of Applied Hydraulics, Örnköldsvik, Sweden  
E-mail: Per-Oskar.Westin@ith.se

## Abstract

In this study two systems for detection of pitting damage in low speed hydraulic motors were compared. These systems were based on an optical particle detector and a magnetic plug respectively. The purpose of the comparison was to determine the relative effectiveness of two methods for detecting pitting damage in a low speed hydraulic motor. In order to do this extensive testing was conducted in Bosch Rexroth Mellansel AB laboratory in Mellansel, Sweden. In the course of the project two post-processing algorithms were developed to enable automatic triggering of alarms based on measurement values from the optical sensor. The optical sensor showed earlier indication of damage than the magnetic plug and the algorithms produced automatic alarms, but there was also a higher false alarm rate when using the optical sensor compared to the magnetic plug.

**Keywords:** Condition Monitoring, Particle Counting, Failure Detection

## 1 Introduction

This project originated at Bosch Rexroth Mellansel AB with the realization that there was a need for an automated and continuous condition monitoring system capable of detecting the onset of pitting damage in their hydraulic motors. Pitting wear is typically characterized by an accelerating generation of wear particles. For a detailed review of wear and fatigue in rolling contacts, see [1]. While wear of components is in itself an issue, it becomes all the more important since the generation and distribution of wear particles in e.g. a hydraulic motor can be a root cause for catastrophic seizure brought on by trapping of particles in clearances between moving parts [2]. If pitting wear can be detected early, maintenance intervention can replace failing parts either during a previously planned stop or at the very least under conditions of controlled system shutdown. Generally speaking, it makes more economic sense to replace a failing bearing or roller than to risk sudden seizure and complete system stoppage.

The reasoning described above is essentially the strategy of *Condition Based Maintenance* (CBM), a branch of *Preventive Maintenance* (PM) strategy. Another PM strategy is *Time Based Maintenance* (TBM) which involves part replacement at intervals based on statistically determined lifetimes. A comparison of CBM and TBM strategies is given in [3]. One issue with TBM that arises with hydraulic drives running under high torque/low speed conditions is that statistical calculations of component lifetimes can be unreliable [4].

Monitoring oil condition as a means to evaluate system health and provide maintenance personnel with valuable information is not a new idea [5]. Typically, oil analyses are performed in laboratory on samples taken from the system on a regular basis. Using filtration and microscopy techniques, oil contaminants can be characterized and information can be extracted about the wear situation in the system [6]. The reliability of *off-line* analyses will depend greatly on oil sampling practices and some working environments are so unforgiving as to render oil sampling impractical for the purpose of debris monitoring, particularly if the level of contamination is low [7].

A common approach for *on-line* monitoring of oil debris is the use of *magnetic chip detectors* (MCD) or *magnetic plugs* [8]. MCDs are simple and cheap and are used for monitoring drive systems. The method is based on regular visual inspection of a magnetic plug in the oil drainage line [9]. Magnet based particle detectors/collectors have been used extensively to detect damage in rolling contact applications and machinery [10-12]. The magnetic particle detector (magnetic plug) used in this study was an Eaton Tedeco model 3A7690-1 magnetic chip collector. This is the magnetic plug currently in use by Bosch Rexroth Mellansel AB and it is designed in such a way that it can be removed for inspection while the test is running. Disadvantages of the magnetic chip detector approach are that it does not provide continuous monitoring and requires an experienced on-site analyst.

When considering methods for continuous on-line or in-line monitoring of oil debris, light blocking or inductive particle counting emerge as attractive alternatives. Dempsey et al.

have shown the applicability of inductive particle counting on gear box systems [13-16]. They found that cumulative particle counting can be used to indicate the onset and progression of pitting damage in gears. A similar approach has been shown effective for damage detection in bearings [17]. These earlier studies all used inductive in-line sensors for particle detection. The advantage of an in-line sensor is that it effectively monitors the entire oil flow in the system. A major drawback is that these inductive sensors have a high detection threshold, limiting the method to studying particles of size 100  $\mu\text{m}$  and larger. In a more recent study, Craig et al. found that particle counters gave early detection of bearing wear [18]. In this case, while the on-line inductive particle counter only registered a single particle, an off-line, light-blocking particle counter showed significant increase in the 5-15  $\mu\text{m}$  range. Research on light-blocking type particle counters is not widely published to the best of the authors' knowledge. When used for off-line analysis industry publications have criticized the method due to problems with repeatability and reproducibility [7][19]. A comparative test from the same publication used portable particle counters that could be attached directly to the system, eliminating the problem related to bottle sampling, transport and delays. In this case, all particle counters showed good performance with the caveat that it takes some time to reach a stable measurement. A very clean system can require flushing for several hours before stable values are reached [20]. For the study covered in this paper an on-line optical particle sensor delivering ISO 4406:1999 codes for fluid particle contamination was used in combination with signal post processing of the produced ISO trend curves. This type of sensor was chosen due to its high availability in the industry and if proven effective it could provide a simple yet cost effective transition to automated condition monitoring by introducing post processing algorithms in the data collection.

The purpose of this study was to compare two condition monitoring systems with respect to their effectiveness in detecting pitting damage in a low speed hydraulic motor. These two systems are based on an optical particle sensor and a magnetic plug respectively. The magnetic plug system is an existing solution and its performance will be used as a baseline in the comparison. In this comparison effectiveness will be considered in terms of *Early detection of damage*, *False alarm rate* and *Ease of use*. Using these points of comparison the optical sensor system would have to provide earlier detection (greater sensitivity) of damage, lower false alarm rate and require less operator training and experience to be considered as better than the existing magnetic plug system.

It is acknowledged that there exist a number of techniques that can monitor the wear situation in rotating machinery without involving oil analysis, notably vibration analysis and acoustic emission methods. Oil analysis as a means of condition monitoring was chosen based on the express research interest in debris particles as well as the availability

of in-house expertise and equipment. Furthermore, there are many more oil analyses that could be considered, in particular for off-line sampling, notably LNF particle counting and classification, FTIR, SOAP/ICP or RULER®. It is beyond the scope of this work to comment in detail on each of them.

## 2 Experimental

All experimental testing in this study was done in the hydraulic laboratory at Bosch Rexroth Mellansel AB in Mellansel, Sweden. An on-site roller bearing test rig (described below) was used. It was deemed suitable as it was built specifically for fatigue testing of roller bearings.

### 2.1.1 Roller bearing test rig

The basis for the roller bearing test rig (Figure 2) used in this project is a modified Hågglunds Viking hydraulic motor (A). The Viking motor is an internal radial piston motor with stationary center (cylinder block) and rotating case (housing). This means the pistons are arranged radially and when the cylinders are pressurized the pistons apply force radially outwards against the inside of a cam ring. The piston assemblies in the Viking motor consist of a piston with integral piston rod and attached cross pin. On the cross pin there are roller bearings that during operation press against, and rotate with, the cam ring. There are also guide bearings that via slots in a guide plate keep the piston assembly in line with the cylinder, for a schematic illustration see Figure 1. These roller bearings use the cross pin as inner race. For more in-depth information on the Viking motor please refer to [www.boschrexroth.se](http://www.boschrexroth.se) and the Viking product manual.

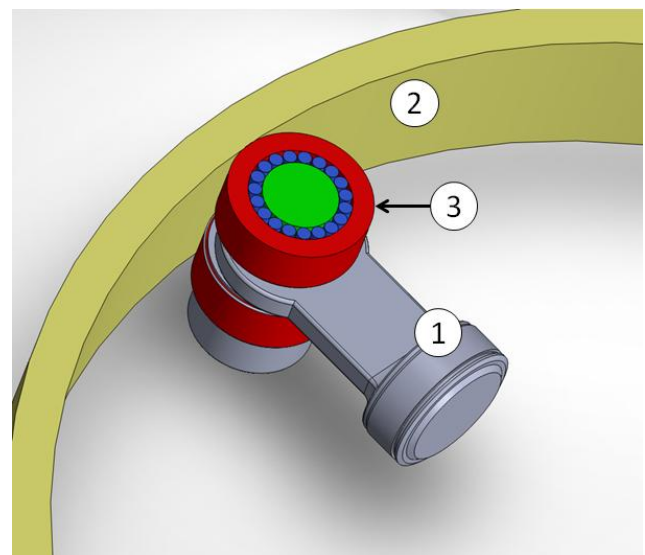


Figure 1: Cross section drawing of piston assembly in test rig where 1: piston 2: rotating cam ring with cylindrical inner surface. 3: roller bearing with outer ring (red), roller (blue) and cross pin (green).

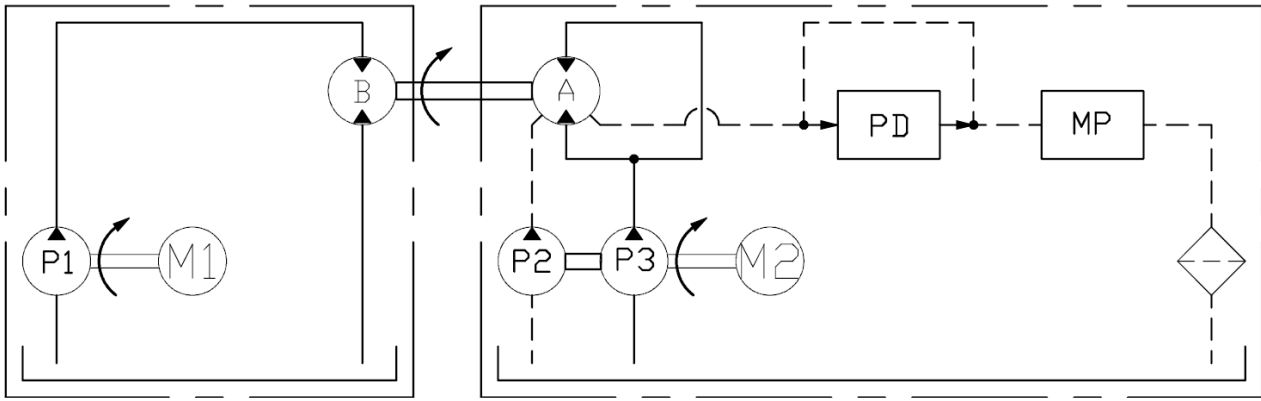


Figure 2: Schematic drawing of the test setup. The modified Viking Motor (A) is pressurized by a pump (P3). In parallel, another pump (P2) provides the flushing flow to the Viking Motor. An optical particle detector (PD) and a magnetic plug (MP) are fitted on the drain line. A separate system (M1, P1 and B) applies the rotational motion.

The modification of the Viking motor consists of the cam ring having a circular inner surface instead of the normal “wavy” profile. This modification causes the pistons to be stationary in their respective cylinders during rotation of the housing. With this modification pressurizing the cylinders and rotating the housing causes the piston roller bearings to be loaded and rotated. This rotation is provided by a second hydraulic motor (B) attached axially to the housing of the modified Viking motor.

The Viking motor and additional drive motor is mounted to a stand as to allow rotation of the housing and to keep the cylinder block stationary. Additionally there are two sets of electric motors (M1-2) and pumps (P1-3) to drive the rotation, pressurize cylinders and provide flushing flow through the housing of the Viking motor. Both in- and out-flow ports on the Viking motor are pressurized during testing, this in combination with the circular cam ring results in zero flow in the pressure line due to rotation of the housing. There will however be leakage flow from the cylinders out into the housing. Through the housing there is a flushing flow which is introduced and drained from the housing via the stationary center. Thus both cylinder leakage flow and flushing flow (all flow going into the motor) leaves the motor via the housing drain line, and any particles leaving the housing will do so via the drain line flow. Therefore the drain line is the main measurement point. All

tests were run under equal conditions. The running parameters are found in Table 1 below.

The maximum allowed particle contamination (ISO 4406) level at startup was 16/13, measured in the housing drain line. The rig was run without pressurizing the cylinders until this level was achieved before starting the test with load on the bearings.

Table 1: Operating conditions

Metric	Value	Tolerance
Cylinder pressure	175 bar	+/-2
Flushing oil temperature	50°C	+/-1
Housing rotation	20 RPM	+/-0,5

### 2.1.2 Measurement equipment

For data recording a Hydac CMU1000 was used. To it an array of sensors were connected, these are accounted for in Table 2 below.

Data from all sensors were collected every 5 minutes and saved as a .txt file. This file was then downloaded from the CMU1000 and exported to Microsoft Excel for evaluation and post processing. The sampling interval was chosen based on the duration of earlier test in the rig and the maximum number of data points in a 2D data series in Excel, based on these considerations a 5 minute interval was chosen to achieve adequate resolution without the amount of data causing problems with post processing.

The magnetic plug was checked daily. The checks followed the routine normally used at Bosch Rexroth Mellansel hydraulic laboratory and consisted of removing the plug and inspecting it visually for debris and then wiping it clean before reinstallation. The plug used was designed to allow removal without stopping the test. The interpretation of the magnetic plug was complicated by the presence of wear debris even under normal operating conditions. The ability to distinguish normal wear particles from particles caused



Figure 3: Actual piston assembly consisting of piston, cross pin and bearings.

by the onset of pitting damage is based on practical experience on the part of the operator.

The CS1000 is an on-line, light blockage type sensor; it works by leading a small (30-300 ml/min) portion of the system flow between a light source and a light sensor and detecting the shadows cast by the particles in the fluid. From the detected shadows ISO contamination levels and flow through the sensor is calculated. The lowest contamination level that the CS1000 can measure is ISO 9/8/7, below that there is simply too few particles to make an accurate measurement.

Table 2: Metrics and associated measurement equipment

Metric	Equipment	Signal type	Measurement point
Particle contamination	Hydac MCS1000 and CS1000	HSI (Hydac Smart Interface)	Drain line
Oil condition	Hydac lab sensor HLB1300	HSI	Drain line
Temperature	JUMO 0-100 °C	4...20 mA	Pressure, flushing and drain line
Pressure	Hydac HDA 4745 0-16 and 0-400 bar	4...20 mA	Pressure, flushing and drain line
Flow	VSE vs 0,2 EP012V 5000 pulses/liter	0-5 pulse	V Flushing line
RPM	Lenord Bauer, 2500 pulses/rev.	0-5 pulse	V Motor housing
Magnetic plug	Tedeco 3A7690-1	n/a, ocular inspection	Drain line (downstream of other sensors)

### 3 Results

Tests were run for a total of 4301 hours, in this time the test was stopped 6 times and produced 7 instances of identified pitting damage. The time from start of test to failure of the individual piston assemblies ranged from 839 h to 3166 h, with median and mean time being 1808 h and 1770 h respectively. At the end of testing two piston assemblies remained from the original set of eight present in the rig at the start of testing, the others having suffered damage and been replaced. This wide range exemplifies the complexity in calculating expected component lifetime.

#### 3.1.1 Measurement data

Measurement data was imported to Microsoft Excel where it was analyzed and compiled into trend curves after each stop

in testing. Studying these trend curves it was clear that the only measurement values that showed changes correlating to pitting damage was the ISO levels reported by the CS1000, and under certain circumstances the flow value measured by the CS1000. A typical trend curve showing the ISO levels is shown in Figure 4 where a complete test cycle from filtering and startup through steady state operation to stopping the test due to damage is shown.

At the start of the test, after filtering, there is a large spike in the ISO levels before settling at steady state operation. Similar spikes were generated when the test was stopped and restarted again. Such spikes in ISO values correlating with surges in flow has been observed by [21] and [22] when using optical particle counting in fluids. Detecting the transition between steady state operation and phase of increasing ISO levels due to damage is complicated both by these spikes and by the noise in the signal. Automation of the detection is desirable since it makes damage detection independent of operator judgment. To achieve this, post processing algorithms were developed in order to obtain a more easily interpreted trend curve and to trigger alarms based on that curve. As the algorithms for detecting damage were intended for use in the CMU1000 in real time during testing they had to be kept as simple as possible. Therefore more advanced methods such as fuzzy logic or neural nets were not used. The algorithms that were developed are described in the section below.

#### 3.1.2 Data post processing

In order to achieve automatic triggering of alarms based on the ISO levels measured by the CS1000 two post processing algorithms were developed, the first for converting the ISO levels trend curve into a more easily interpreted form, the second algorithm then uses the shape of this new trend curve to trigger alarms.

The first algorithm is based on the steady state ISO values found during testing and the cumulative time these steady state values are exceeded. At each sampling interval the algorithm is evaluated and the cumulative sum  $C$  taken according to the conditions in the algorithm. Applying this algorithm to the data series showed in Figure 4 and trending the  $C$  value produces the blue curve showed in Figure 5 (the green alarm curve is described below).

This curve has less noise than the ISO curves and a characteristic behavior when damage occurs. The absolute value of  $C$  is not of particular interest, as it can vary widely as a result of spikes in the ISO values caused by for example stopping and restarting the test, instead the shape of the curve is used for indication of damage. The characteristic behavior of the curve when damage occurs is an accelerating increase that starts off slowly, as opposed to an increase caused by a spike in the ISO levels which produces a decelerating increase that starts out very steep. In order to detect this accelerating increase a second algorithm was developed. It works by comparing the increase in  $C$  over consecutive periods of time to determine if the value is accelerating. The length and number of these consecutive

periods of time were found iteratively by applying the algorithms to measurement data in post processing.

A warning variable was introduced, which was set to 1 if accelerated cumulative wear was detected and 0 if otherwise. This variable was then plotted together with the C trend curve and thus produced the green alarm curve in Figure 5. As can be seen in the figure the alarm triggers when the curve starts accelerating upwards from its slow steady state increase, but does not trigger as a result of the spike in ISO values at the start of the test. However there were some false alarms during filtering. The performance of this alarm as compared to the magnetic plug will be discussed under method comparison below.

### 3.1.3 Method comparison

The purpose of this study was to compare the effectiveness of a light blockage type particle sensor with an existing magnetic plug particle detector. Effectiveness was considered in terms of early detection, false alarm rate, and ease of use.

*Early detection:* on all but one occasion of pitting damage the CS1000 responded before the magnetic plug, that is; increasing levels of particles were detected before the test was stopped.

*False alarm rate:* during all of the testing done in this study the magnetic plug system produced only one false alarm, as opposed to the CS1000 and post processing that produced numerous false alarms.

*Ease of use:* the magnetic plug requires experienced operators that are able to interpret the growth in the amount

of debris on the magnet; this will also cause interpretations to vary with different operators. The output from the post processing of ISO levels is digital, damage or no damage, and thus is not dependent on the experience or judgment of the operator.

In summary the CS1000 with post processing is capable of earlier detection and is easier to use, but is also affected by significantly higher false alarm rates when compared to the magnetic plug being used by experienced operators.

## 4 Discussion

Earlier studies [13-16] have used cumulative particle counting with inductive particle sensors in combination with fuzzy logic post processing to detect pitting damage in gears. Results indicated that cumulative mass was a good predictor of pitting damage, and that fuzzy logic was a good technique for setting alarm thresholds. A similar approach to damage detection was used in this study.

During initial testing it became clear that the only measurement value which showed changes corresponding to pitting damage occurring was the ISO class and flow values measured by the CS1000 particle counter. An effort was therefore made to have the system automatically trigger alarms based on the ISO class values. To achieve this, measured values had to be post processed to produce a trend curve that more clearly indicated when changes started to occur in the ISO class values. A means of automatically interpreting this new trend curve was also necessary. Two algorithms, one for post processing and one for automatic interpretation, were developed.

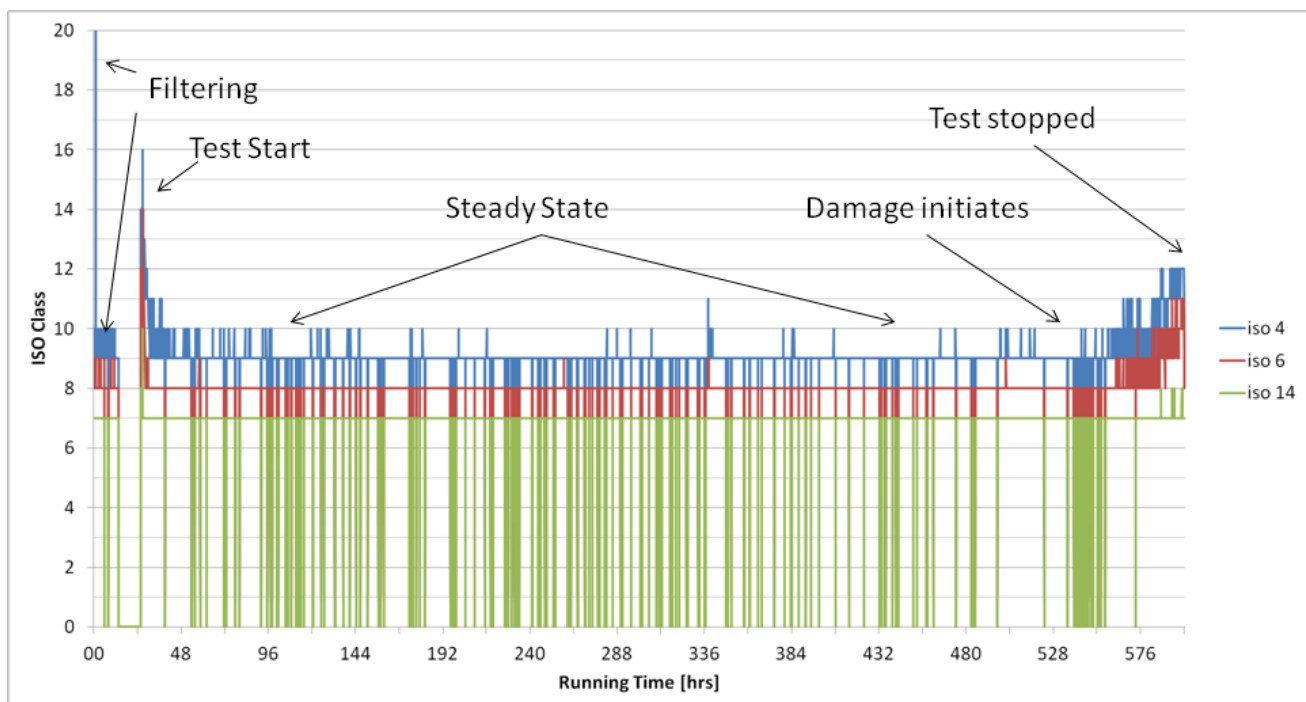


Figure 4: ISO levels trend curve by optical particle counting.

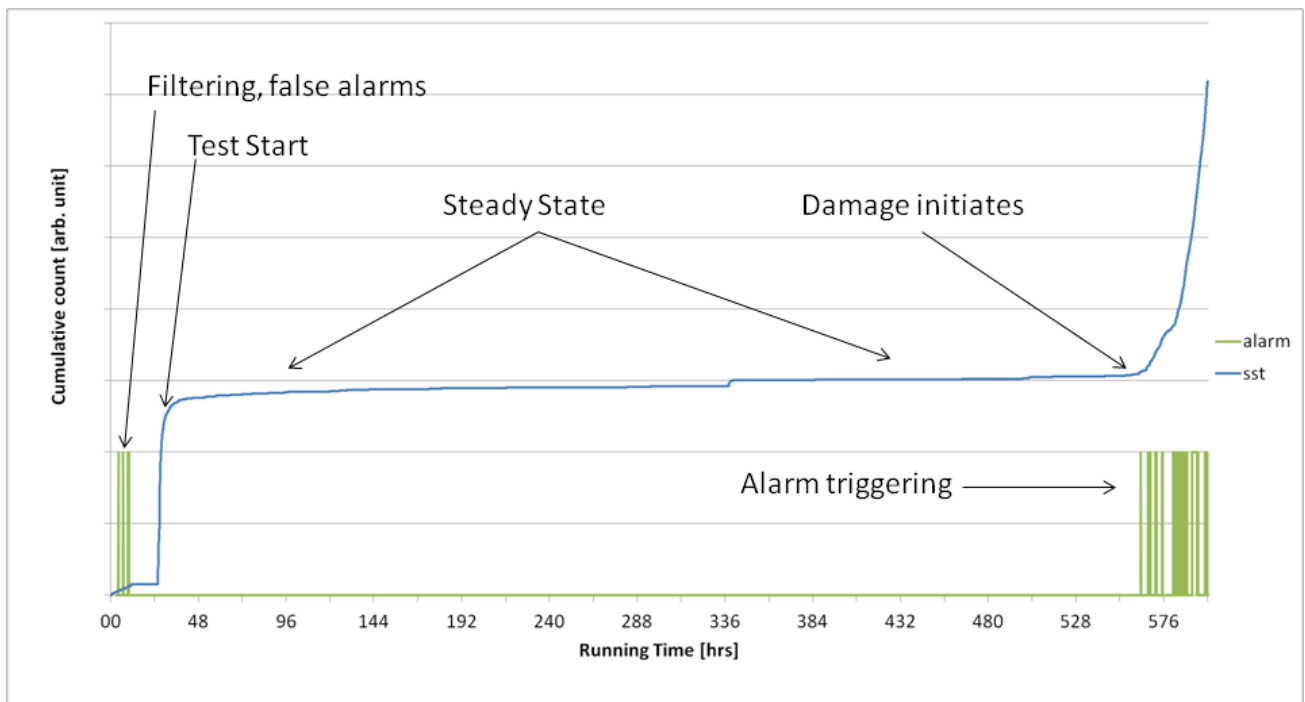


Figure 5: Cumulative counting trend curve and triggered alarms

The post processing algorithm developed in this study produces a trend curve with behavior similar to cumulative counting. But the absolute value can vary widely as a result of spikes in the ISO values caused by stopping and restarting the test. Using the absolute value to trigger alarms would therefore be problematic. Instead the algorithm for triggering of alarms uses the shape of the trend curve to detect when particle levels start to increase from a steady state value, thus avoiding the problems with widely varying absolute values by looking at differences over time instead. Both algorithms developed in this study are very simple mathematical and logical operations; this should make it possible to incorporate in most data collection systems.

It should be noted that all testing in this study was done under constant conditions such as temperature, flow, RPM, load etc. Stopping and starting the test caused large spikes in the ISO levels, and it seems likely that running the test under varying conditions would cause the ISO levels to vary accordingly. This would make damage detection more difficult, as the method presented here relies on steady state ISO values as limits for the cumulative counting. In principle, the method is valid for any hydraulic system, regardless of size or speed, provided that a) a drainage line exists which carries particle contaminants from the wear location and b) a suitable pre-processing of the signal is available which can aid in establishing steady state wear during working conditions. More testing is therefore required to investigate how varying conditions affect ISO trend curves, and how to compensate for such variation. Also, a rig made specifically for this type of testing should be built, as it has not been investigated if the design of the piston assemblies used in this study affect the release of wear particles from the loaded components out into the oil. A means to determine remaining useful component life based on the ISO values would also be desirable.

## 5 Conclusions

Extensive testing of wear detection was performed using a light blockage type particle sensor and a magnetic plug particle detector. Methods were developed for particle sensor signal processing and automatic alarm generation. When comparing the particle sensor system to the magnetic plug system in terms of early detection, false alarm rate, and ease of use some conclusions can be drawn.

1. *Early detection*: the optical sensor reacts before the magnetic plug.
2. *False alarm rate*: with experienced operators the magnetic plug has significantly lower false alarm rate than the optical sensor and post processing algorithms.
3. *Ease of use*: with the post processing algorithms used the optical sensor does not require an experienced operator, and output is independent of operator experience.

The optical sensor in combination with signal post processing has shown promise as a means of automatic early detection of pitting damage, but the high false alarm rate is a major problem and more work is needed to reduce this without compromising measurement sensitivity. More work is also needed to investigate how ISO levels behave in a system with varying operating conditions.

## 6 Acknowledgements

This work was performed in close collaboration and with support from Bosch Rexroth Mellansel AB. Financial support for the project was provided by Tillväxtverket as part of EU funding for regional development.

## 7 References

- [1] J. Halme and P. Andersson, "Rolling contact fatigue and wear fundamentals for rolling bearing diagnostics - state of the art," Proceedings of the Institution of Mechanical Engineers, Part J: Journal of Engineering Tribology, no. 224, pp. 377-393, 2010.
- [2] D. Nilsson, "Investigations for Enhanced Tribological Performance of a Hydraulic Motor," Doctoral Thesis, Luleå University of Technology, 2011.
- [3] R. Ahmad and S. Kamaruddin, "An overview of time-based and condition-based maintenance in industrial application.," Computers & Industrial Engineering, vol. 63, no. 1, pp. 135-149, 2012.
- [4] D. Nilsson and S. Berg, "Wear and life of roller bearings under low speed and clean environment, a comparison of Me-C:H coated and uncoated rollers," in Nordic Symposium on Tribology, 2002.
- [5] J. A. Briggs, "Determining contamination levels in hydraulic systems," in Annual Meeting, American Society of Lubrication Engineers, 1969.
- [6] F. D. Norvelle, "Contamination control — the key to reliability in fluid power systems," Wear, vol. 94, no. 1, pp. 47-70, 1984.
- [7] L. Arvidsson, "Partikelräkning eller gravimetri vid föroreningsanalys av hydraulolja," Fluid Scandinavia, no. 3, 1997.
- [8] C. Evans, "Wear debris analysis and condition monitoring," NDT international, no. June, pp. 132-134, 1978.
- [9] R. Sjölund and E. Söderkvist, "Tillståndskontroll av hydraulmotorer med hjälp av magnetindikator," Master's Thesis, Luleå University of Technology, Luleå, 2006.
- [10] S. Dory and T. Hansen, "Magnetic plug inspection enhances condition-based maintenance," Practicing Oil Analysis, no. September, 2003.
- [11] M. H. Jones, "Particle Transfer from Magnetic Plugs," Swansea Tribology Services Ltd., University of Wales Swansea, 1998.
- [12] S. Raaduni, "Magnetic Chip Detector (MCD) Wear Particle Analysis," King Mongkut's University of Technology, Bangkok, 2002.
- [13] P. J. Dempsey, "Gear Damage Detection Using Oil Debris Analysis," NASA, Glenn Research Center, Cleveland, Ohio, 2001.
- [14] P. J. Dempsey and A. A. Afjeh, "Integrating Oil Debris and Vibration Gear Damage Detection Technologies Using Fuzzy Logic," in International 58th Annual Forum and Technology Display, Montreal, 2002.
- [15] P. J. Dempsey, G. Kreider and T. Fichter, "Investigation of Tapered Roller Bearing Damage Detection Using Oil Debris Analysis," Power transmission engineering, february 2007.
- [16] D. G. Lewicki, P. J. Dempsey, G. J. Heath and P. Shanthakumaran, "Gear Fault Detection Effectiveness as Applied to Tooth Surface Pitting Fatigue Damage," National Aeronautics and Space Administration, Washington, DC, 2009.
- [17] J. L. Miller and D. Kitaljevich, "In-line oil debris monitor for aircraft engine condition assessment," in IEEE Aerospace conference proceedings, 2000.
- [18] M. Craig, T. J. Harvey, R. J. K. Wood, K. Masuda, M. Kawabata and H. E. G. Powrie, "Advanced condition monitoring of tapered roller bearings, Part 1," Tribology International, vol. 42, no. 11-12, pp. 1846-1856, 2009.
- [19] S. Sjöberg, "Partikelräkning eller gravimetri för föroreningsbestämning av hydraulolja," Fluid Scandinavia, no. 1, 1997.
- [20] B. Andersson, "Jämförande utvärdering av partikelräknare," Fluid Scandinavia, no. 5, 1996.
- [21] A. Östgren, "Mätning av föroreningar i hydraulolja med automatisk partikelräknare," LTU, Luleå, 1996.
- [22] B. Verdegan, A. True-Dahl, W. Haberkamp, N. Blizard, D. Genter and E. Quillen, "Filtration Solutions for High Pressure Common Rail Fuel Systems," Cummins Inc., 2008.



Low Viscosity



# Investigation on Velocity Response and Energy Saving Performance of Water Hydraulic Systems Without Using Servo Valve

Pha N. Pham , Kazuhisa Ito , and Shigeru Ikeo\*

Department of Machinery and Control Systems, Shibaura Institute of Technology, Saitama, Japan

\*Department of Engineering and Applied Sciences, Sophia University, Tokyo, Japan

E-mail: phamngocpha@gmail.com; kazu-ito@shibaura-it.ac.jp; s\_ikeo@sophia.ac.jp

## Abstract

In recent years, water hydraulics has been getting more and more attention from the fluid power society because of its inherent merits, including environmental friendliness, high safety against fire hazards, running cost reduction, and easy availability. However, water hydraulics still has two main problems to make it popular in application; first one is the much higher price of water hydraulic devices in comparison with the conventional one and the other is energy loss because of more leakage and larger friction than oil hydraulics due to its low viscosity. Water hydraulic systems without using servo valve such as a water hydraulic fluid switching transmission (FST) and a water hydraulic pump motor transmission (PMT) that can recover energy in deceleration period are good solutions for these difficulties.

This paper investigates two most important points on velocity response and energy saving performance consisting of recovery energy and energy consumption of water hydraulic FST and PMT. The comparison between the experimental results of these two transmissions also will be presented in this research to get the conclusion for the advantages and disadvantages of each transmission. The PMT system has proved its many advantages such as reducing noise because of smooth operation, lengthening the life duration of the devices, and the drastic reducing of both steady state error in a working phase and energy consumption. The recovered energies of the both systems are almost same and get the values from 26.3 to 31.7% of the kinetic energy of flywheel.

**Keywords:** Water hydraulic, fluid switching transmission, hydraulic pump motor transmission, velocity performance, energy saving, energy consumption

## 1 Introduction

In modern society, using safe and clean systems is the one of the most important requirements for technical fields; from this point, water hydraulics that uses pure tap water as pressure medium emerges as an excellent solution and it is considered as the fourth driving source beside electricity, pneumatics, and conventional oil hydraulics, especially in the fields of food and medicine processing, steel and glass production, nuclear power generation, ocean exploration, underwater robotics [1], and underwater gait training orthosis. Water hydraulic has a very long story as mention in [2]; however, water hydraulic systems was only paid much attention by researchers from late 1990s, when advances in materials and machining technology realized the longer life times and higher flow rate and pressure for water hydraulic components [3]. Today, water hydraulics tends to divide into two branches: water hydraulic servo systems and water hydraulic systems without using servo valve.

For water hydraulic servo systems, researches mainly concen-

trated on precise control such as simple adaptive control [3] and [4], robust control [5], and sliding mode control combined with disturbance observer in [6] for dealing with nonlinearities in water hydraulic component, *e.g.* high friction, leakage, dynamic dead zone character, and so on. The control response is getting better day by day; conventional systems using servo or proportional valves, however, remain inhere restrictions consist of expensive devices [7], especially for water hydraulics, lower energy efficiency in comparison with the system using ON/OFF valve shown in [8], and the difficulties in recovering energy in deceleration period because of conflict in control algorithm. Thus, servo valve mainly uses for the systems that require highly precise control performance and quick response.

To make water hydraulics more popular to protect environment as its original purpose, reducing cost of such systems is primary requirement. In recent years, some researches introduced hydraulic fluid switching transmission [9] or water hydraulic fluid switching transmission (FST) [7], [10], and [11],

that is a good method to reduce the original price of the system because of using ON/OFF valve that is much cheaper than servo valve. Moreover, FST system also can recover kinetic energy of load in deceleration period to become high pressure fluid energy stored in accumulator and it can be reused in the acceleration process in next cycle [7]. The two properties of FST system are very important and make it be useful in real application.

However, FST system inherently exposes limitations that need to be improved. First, FST system uses the fast switching logic to control the velocity; hence, the ON/OFF valves of the system switch many times in the condition of high fluid pressure that makes the hydraulic motor to change the state of working and breaking for each switching. It causes unendurable noise and the duration of the motor to be reduced. Second, to control the velocity of the load, it needs setting a velocity threshold to make the velocity theoretically work inside the bounds, but in fact, the steady state error goes beyond the bounds because of the time delay of devices. The methods to reduce the error are using the quick response devices and the restricting the velocity threshold as mentioned in [7] and [11]; however, the restriction has its limit depending on the characteristic of the ON/OFF valves, that means the steady state error inherently remains in the control logic. The first method will bring the price of the system up and the second one will make the number of switching of ON/OFF valves increase, that leads to shorten the lifetime of the valves. Last, in working phase, FST system operates in condition of high pressure that acts as the load of hydraulic pump; thus, the system dissipates large amounts of energy, because an amount not less losses via relief valves and other amount stores in shock absorbed accumulator and then disappears after action cycle.

To deal with the limitations of FST system, this research studied on a new water hydraulic transmission that is the directly connection of a water hydraulic pump and a motor, it can be called a water hydraulic pump motor transmission (PMT). In the past, there are very few research concerned with the system that is the direct connection between a hydraulic pump and an actuator such as in [12] and [13]; however, all the researches worked for controlling the displacement of a cylinder and the systems cannot recover energy in the deceleration period. PMT system mentioned in this paper is an improvement of FST system. It can work smoother and reduce noise drastically because ON/OFF valves only switch one time in all cycle consist of acceleration, working or constant, and deceleration phases. By this way, the durations of the hydraulic motor and ON/OFF valves will be lengthened due to stable working pressure and much fewer states changing.

The main objectives of this study are twofold:

1. To examine the velocity responses of FST and PMT systems and then compare the results to prove the advantage of PMT in experiments.
2. To evaluate the saved energies of FST and PMT systems based on energy consumption in all a working cycle and recovered energy in deceleration period. From these results, compare the consumption of each system.

The remainder of the paper is organized as follows. In Section 2, the introductions of FST and PMT systems including the structures, operations, and specifications of experimental devices are shown. Then, the control logics of FST and PMT system are presented in Section 3. Sections 4 and 5 are the experimental results of velocity responses and energy saving for FST and PMT systems, and at the end of each section is the comparison of results of FST and PMT system to draw conclusions.

## 2 FST and PMT Systems

In this section, the structures, operations, and specification of experimental devices of the two water hydraulic transmissions, FST and PMT, will be presented and discussed.

### 2.1 FST System

A simple FST circuit used for experiments in this research will be introduced in fig. 1. The system consists of following main elements: a fixed displacement pump (P) that is connected with an electric motor (M), a fixed displacement pump/motor (PM), two accumulators (ACC<sub>*i*</sub>, *i* = 1, 2), three ON/OFF valves (VS<sub>*i*</sub>, *i*=1,...,3). The two accumulators ACC<sub>1</sub> and ACC<sub>2</sub> are used as a pressure surge absorber and an energy storage, respectively. The fluid energy with the pressure  $p_s$  generated by the pump P is considered as the input energy, kept as 12 MPa in all experiments. The flywheel (FW) connected to PM is considered as a working load. The specifications of main experimental devices will be shown in tab. 1.

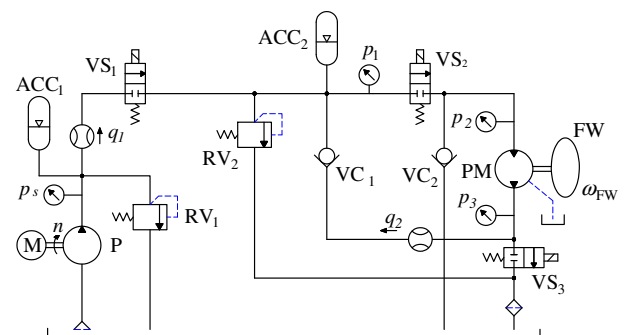


Figure 1: Schematic of water hydraulic FST system.

The goal is to control the flywheel velocity to meet the desired constant velocity at the working time. An operational cycle can be divided into three phases: an acceleration phase, a working or constant phase, and a deceleration phase as shown in fig. 4 (a). In the acceleration phase, there is no control for ON/OFF valves, they are opened to make the water flow directly from the pump P to the pump/motor PM. After once getting the desired constant velocity, the state of the system is changed to the working phase. At this time, the control logics for ON/OFF valves are used to force the flywheel velocity to oscillate around the constant value. When the working finishes, the system turns to the deceleration phase, the electric motor M is stopped and all the ON/OFF valves are in close state; however, the pump/motor PM still works because

Table 1: Specifications of experimental devices.

Symbols	Specifications	Values
P	Displacement volume	$15 \times 10^{-6} \text{m}^3$
PM	Displacement volume	$15 \times 10^{-6} \text{m}^3$
ACC <sub>1</sub>	N <sub>2</sub> gas volume	0.005 m <sup>3</sup>
	Precharge pressure	5.0 MPa
ACC <sub>2</sub>	N <sub>2</sub> gas volume	0.01 m <sup>3</sup>
	Precharge pressure	7.8 MPa
FW	Moment of inertia	1.58 kgm <sup>2</sup>
	Mass	78.9 kg
	Diameter	0.4 m
	Thickness	0.08 m
Electric motor	Revolution	1200 min <sup>-1</sup>

of kinetic energy of flywheel and it acts as a hydraulic pump to convert the kinetic energy into high pressure fluid that is stored in the accumulator ACC<sub>2</sub>, it supplies the water via the suction line that contains the check valve VC<sub>2</sub>. This energy is called recovery energy and will be reused in the next action cycle in the acceleration phase to make the transient time of the acceleration phase shorten, and also to reduce the energy consumption in this cycle.

## 2.2 PMT System

A new water hydraulic pump motor transmission PMT will be introduced in this subsection, fig. 2 is the schematic of the system. The PMT system is set on the basis of the FST system, only some devices was changed and the control algorithms for the ON/OFF valves and the electric motor M are different. Note that, the same symbols of devices of the FST and PMT systems in figs. 1 and 2 represent for the same devices in the real systems, and the specifications of the experimental devices of the PMT system can be seen in the tab. 1. In the PMT system, the ON/OFF valve VS<sub>1</sub> was replaced by the check valve VC<sub>3</sub>, the accumulator ACC<sub>1</sub> was eliminated, and the accumulator ACC<sub>2</sub> was used for both tasks: pressure surge absorber in acceleration and constant phases and energy storage for recovered energy in deceleration phase.

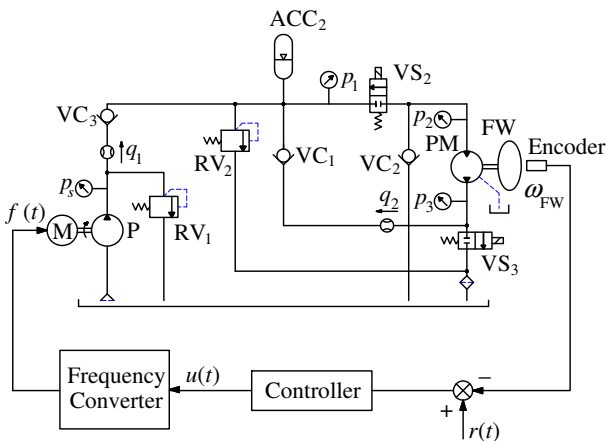


Figure 2: Schematic of water hydraulic PMT system.

The most important point of the PMT system is control logic for the two ON/OFF valves VS<sub>2</sub>, VS<sub>3</sub>, and the electric motor M. In the acceleration and constant phases, all the two ON/OFF valves VS<sub>2</sub> and VS<sub>3</sub> are opened and they will be closed for all time of the deceleration phase. The controller receives the reference signal  $r(t)$  as in fig. 2 and the feedback of the flywheel velocity that is provided by an encoder to generate the control signal  $u(t)$ . The hardware for controller is dSPACE and the software is MATLAB; thus the control signal  $u(t)$  is limited by  $\pm 10$  Voltage. The rotational velocity of an electric motor can be calculated via following equation [14]

$$n = 120 \frac{f}{P}, \quad (1)$$

where  $n$  is the rotational velocity of the electric motor,  $f$  the frequency of electrical power supply, and  $P$  the number of poles of the motor, in this case  $P = 4$ . Thus, the control signal that is delivered to the electric motor M is frequency. A frequency converter is used for converting the control signal out of dSPACE in voltage to frequency signal supplied to the electric motor M. The specification of the frequency converter can be derived by doing some tests on it. The experimental data of the tests will be shown in tab. 2, the results are the average of five times of experiments; for more detail, fig. 3 shows the input-output mapping of the frequency converter.

Table 2: Test data of the frequency converter.

Input (V)	Output (Hz)
0.1	0.70
0.2	1.30
0.4	2.60
0.8	5.08
1.0	6.30
1.5	9.40
2.0	12.50
2.5	15.50
3.0	18.70
3.5	21.75
4.0	24.80

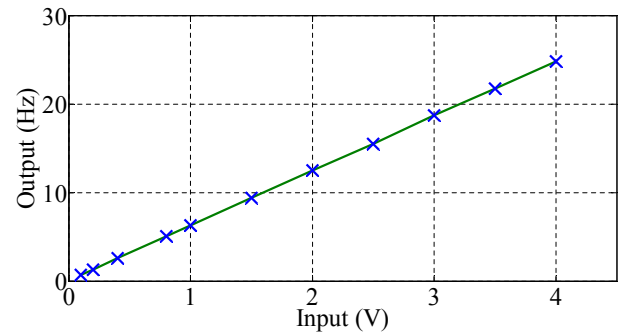


Figure 3: Frequency converter input-output mapping.

From the experimental results, it is easy to realize that, the relationship of the input and output of the frequency converter

can be considered as linear mapping, and it can be written approximately as following equation

$$f = \varepsilon u, \quad (2)$$

where  $\varepsilon$  is the frequency coefficient and get the value of 6.1817 Hz/V.

In the deceleration phase, all the ON/OFF valves are closed as mentioned above, and the electric motor M are also stopped. Thus, there is no energy supply to the hydraulic pump/motor PM but it still works same as FST system and also converts the kinetic energy of the flywheel FW into high pressure fluid stored in the accumulator ACC<sub>2</sub>.

### 3 Control Logics of FST and PMT Systems

#### 3.1 FST System

The drive pattern of the flywheel shown in fig. 4 (a) consists of three simple phases: an acceleration phase (Phase 1), a constant speed phase (Phase 2), and a deceleration phase (Phase 3). This section will explain the logic to control the ON/OFF valves, depending on the flywheel drive pattern and the variable reference velocity of the flywheel (fig. 4 (b)). The valve VS<sub>1</sub> is opened in both Phase 1 and Phase 2, and only closed in Phase 3. The two valves VS<sub>2</sub> and VS<sub>3</sub> received the same control signal depending on the flywheel rotational velocity  $\omega_{FW}$ . The electric motor M is operated with the constant velocity in all Phases 1 and 2, it is stopped in Phase 3 for saving energy. Following, the valve switching algorithms corresponding to the three phases will be introduced.

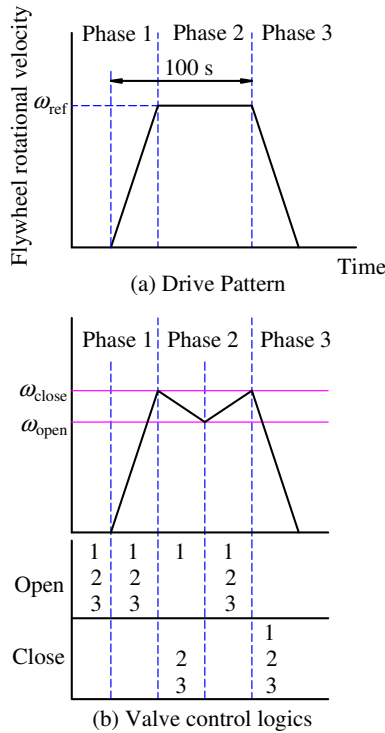


Figure 4: Control logic of ON/OFF valves.

#### 3.1.1 Acceleration Phase (Phase 1)

In this phase, the FST accelerates the flywheel FW from stationary state to a given reference rotational velocity. Once reached to the reference rotational velocity, the control system is switched to Phase 2. In this phase, all of the ON/OFF valves are opened full time and the electric motor is operated with the velocity of 1200 min<sup>-1</sup>.

#### 3.1.2 Constant (Working) Phase (Phase 2)

This phase maintains the rotational velocity of the flywheel FW between  $\omega_{open}$  and  $\omega_{close}$  as in fig.4 (b). Two Phases 1 and 2 take 100 seconds. Tables 3 presents the control logics of the three ON/OFF valves. In the control logic, when the velocity of flywheel reaches out of  $\omega_{close}$ , the both ON/OFF valves VS<sub>2</sub> and VS<sub>3</sub> are changed the state from open to close to brake the flywheel. Inversely, when the velocity downs less than  $\omega_{open}$ , the state of the both ON/OFF valves VS<sub>2</sub> and VS<sub>3</sub> are altered from close to open. By this control logic, the velocity of the flywheel will oscillate theoretically inside  $\omega_{open}$  and  $\omega_{close}$ ; however, in fact, the steady state error of the flywheel velocity is larger because of the effect of the time delay of the real devices in the system.

Table 3: Valve operation logic in Phase 2.

Valves	Open	Close
VS <sub>1</sub>	Open	
VS <sub>2</sub>	$\omega_{FW} < 795 \text{ min}^{-1}$	$\omega_{FW} > 805 \text{ min}^{-1}$
VS <sub>3</sub>	$\omega_{FW} < 795 \text{ min}^{-1}$	$\omega_{FW} > 805 \text{ min}^{-1}$

#### 3.1.3 Deceleration Phase (Phase 3)

In the final phase, the speed of the flywheel is decelerated to zero and note that also in this phase, no velocity control is executed. In this phase, all the ON/OFF valves are closed, the closing of ON/OFF valve VS<sub>3</sub> is to brake the flywheel FW and also induce energy recovery process, ON/OFF valve VS<sub>1</sub> is closed to cut the supply energy, and ON/OFF valve VS<sub>2</sub> is closed to keep the recovery energy inside the accumulator ACC<sub>2</sub>. The recovery energy is mainly produced in this Phase; at this time, the pump/motor PM is act as a pump to convert kinetic energy of the flywheel into high pressure fluid that is stored in the accumulator ACC<sub>2</sub>.

#### 3.2 PMT System

The controller of PMT system that is depicted in fig. 5 is a feedback control that aims to make the velocity of the flywheel track a desired reference velocity  $r(t)$  as shown in fig. 2. The controller in this study is conventional PID control that was tuned manually to attenuate the steady state error and overshoot. The PID controller has the transfer function

$$G_c(s) = K_P + \frac{K_I}{s} + K_D s, \quad (3)$$

where  $K_P$ ,  $K_I$ , and  $K_D$  are the proportional, integral, and derivative gains; in the experiment, they get the value of 0.002,

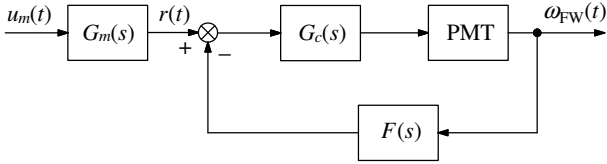


Figure 5: Control structure of PMT system.

0.001, and 0.001, respectively.

In the feedback loop, a first order low-pass filter that can be described by eq. (4) was used to eliminate the high frequency noise caused by measurement devices that consist of an encoder and a frequency-velocity (FV) converter.

$$F(s) = \frac{10}{s+10}. \quad (4)$$

The reference  $r(t)$  was generated after a reference model  $G_m(s)$  as in eq. (5) by a rectangular input signal  $u_m(t)$ .

$$G_m(s) = \frac{1}{2s+1}. \quad (5)$$

## 4 Velocity Response

In this section, the velocity response of the flywheel FW for both FST and PMT systems will be shown and compared.

### 4.1 FST System

In the drive pattern as shown in fig. 3 (a) consists of three phases; however, Phase 2 is the most important for velocity response because the system will work and do its function mainly in this phase. Phase 2 is also called constant (velocity) phase or working phase and its reference velocity  $\omega_{wr}$  in this research is constant for the values from  $600 \text{ min}^{-1}$  to  $1000 \text{ min}^{-1}$ . Table 4 is bounds of the velocity responses at Phase 2 of FST system when reference velocity  $\omega_{wr}$  varies from  $600 \text{ min}^{-1}$  to  $1000 \text{ min}^{-1}$  and fig. 6 has a more detail view about the velocity response when the reference velocity  $\omega_{wr}$  is  $800 \text{ min}^{-1}$ .

Table 4: Experimental velocity response of FST system.

Reference velocity $\omega_{wr} [\text{min}^{-1}]$	$\omega_{\min}$ [ $\text{min}^{-1}$ ]	$\omega_{\max}$ [ $\text{min}^{-1}$ ]	$e_{\min}$ [%]	$e_{\max}$ [%]
1000	968	1028	3.20	2.80
900	869	927	3.44	3.00
800	767	827	4.13	3.38
700	669	726	4.43	3.71
600	570	625	5.00	4.17

As showing in tab. 4 the flywheel velocity errors was regulated in a range from  $-33 \text{ min}^{-1}$  to  $28 \text{ min}^{-1}$  corresponding with the bound of percentage errors  $e_{\min}$  and  $e_{\max}$  that will be defined in eqs. 6 and 7 to 5% and 4.17%, respectively, when the reference velocity changes from  $600 \text{ min}^{-1}$  to  $1000 \text{ min}^{-1}$ . Note that these bounds of the flywheel velocity errors are almost same when the reference velocity varies,

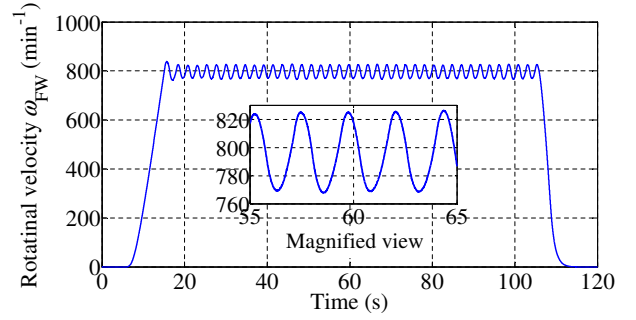


Figure 6: Experimental velocity response of FST system ( $\omega_{wr} = 800 \text{ min}^{-1}$ ).

they depend mainly in the range of the threshold and the time delay of the devices as mentioned in [7],

$$e_{\min} = \frac{\omega_{wr} - \omega_{\min}}{\omega_{\min}}, \quad (6)$$

$$e_{\max} = \frac{\omega_{\max} - \omega_{wr}}{\omega_{\max}}, \quad (7)$$

where  $\omega_{\min}$  and  $\omega_{\max}$  are the minimum and maximum velocity in the working phase.

Another property of the flywheel velocity response in Phase 2 needs to be noticed is that the velocity response of FST system oscillates around the reference velocity. Figure 7 shows the control signal of the ON/OFF valves  $VS_2$  and  $VS_3$  that presents for the ON or OFF state of the valves. With the working time of 100 seconds, the number of switching of the valves is 80 times. The oscillation of the velocity is not good for operation of the system, so it should be improved. The excessive changing states of the ON/OFF valves make the lifetime of not only the ON/OFF valves but also the hydraulic pump/motor PM decrease.

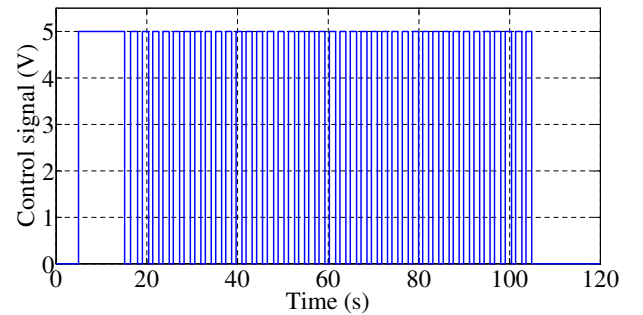


Figure 7: Control signal of ON/OFF valves  $VS_2$  and  $VS_3$ .

### 4.2 PMT System

PMT system was controlled by a conventional PID as mentioned above, the target of the control is to make the velocity of the flywheel converge to a reference signal  $r(t)$ . To compare with the velocity response of FST, the reference signal is also divided into three parts: an acceleration phase, a constant (working) phase, and a deceleration phase. The acceleration phase can be calculated when the velocity is the stationary state to get the constant value of the reference signal  $\omega_{wr}$ , the

constant and working phase is defined same as FST system, the acceleration and constant phases also took 100 seconds for each cycle.

The velocity responses in working phase of PMT system corresponding with the reference velocity  $\omega_{wr}$  from  $600 \text{ min}^{-1}$  to  $1000 \text{ min}^{-1}$  are shown in tab. 5, and fig. 8 shows the velocity response in case of reference velocity  $\omega_{wr} = 800 \text{ min}^{-1}$ . Base on the tab. 5, it is easy to realized that the limit of the bounds of the velocity errors is  $3.92 \text{ min}^{-1}$  and  $4.18 \text{ min}^{-1}$  corresponding with the bound of percentage errors  $e_{\min}$  and  $e_{\max}$  that also will be defined in eqs. 6 and 7 to 0.49% and 0.52%, respectively, when the reference velocity changes from  $600 \text{ min}^{-1}$  to  $1000 \text{ min}^{-1}$ . As showed in fig. 7, the transient time (in the acceleration phase) of the response takes longer time than the reference, it can be improved by using larger gains of PID controller, however, it will bring the larger overshoot. Thus, finding a method to reduce the transient time and still keep a small overshoot is a requirement of this research in the future.

Table 5: Experimental velocity response of PMT system.

Reference velocity $\omega_{wr}$ [ $\text{min}^{-1}$ ]	$\omega_{\min}$ [ $\text{min}^{-1}$ ]	$\omega_{\max}$ [ $\text{min}^{-1}$ ]	$e_{\min}$ [%]	$e_{\max}$ [%]
1000	996.85	1003.20	0.32	0.32
900	896.88	904.18	0.35	0.46
800	796.08	802.99	0.49	0.37
700	697.22	704.10	0.40	0.59
600	598.34	603.13	0.28	0.52

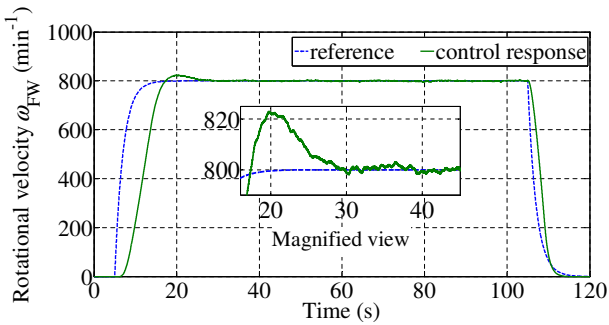


Figure 8: Velocity response of PMT system ( $\omega_{wr} = 800 \text{ min}^{-1}$ ).

Figure 9 shows the control signal of the electric motor M. In the working phase, the controller sent to the motor a signal that is not changed much. This is really good for the duration of the motor. For all the time of the acceleration and working phases, the ON/OFF valve  $VS_2$  and  $VS_3$  were opened, that made the supply pressure for hydraulic pump/motor PM was steady; therefore, the lifetime of the both ON/OFF valves and also the hydraulic pump/motor is not affected.

### 4.3 Comparison

This subsection aims to analyse and compare the velocity response between FST and PMT to derive the advantage and disadvantage of each transmission. The percentage errors  $e_{\min}$

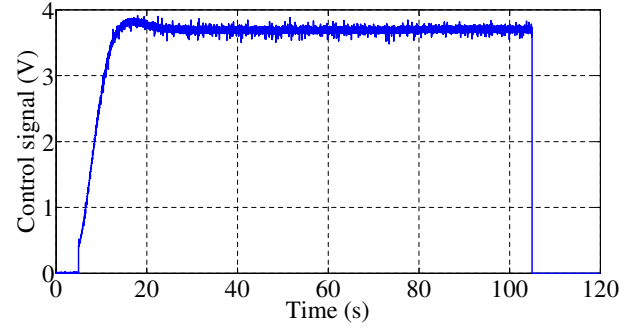


Figure 9: Control signal of electric motor.

and  $e_{\max}$  are shown in figs. 10 and 11, respectively. Base on the figures and tabs. 4 and 5, it can be concluded that the steady state error of PMT system is much smaller than FST system in both percentage errors  $e_{\min}$  and  $e_{\max}$  and the maximum difference is nearly 18 times and the minimum one is approximately 6 times.

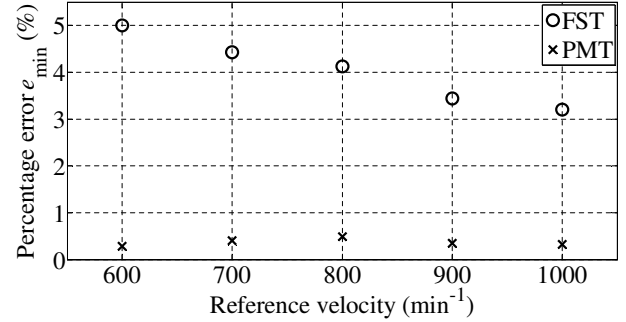


Figure 10: Percentage error  $e_{\min}$ .

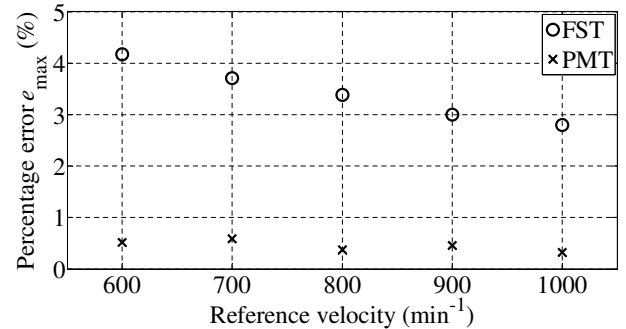


Figure 11: Percentage error  $e_{\max}$ .

Figure 12 shows the velocity responses of both FST and PMT systems in case of reference velocity  $\omega_{wr} = 800 \text{ min}^{-1}$ . At the beginning of the acceleration phase, the control performances of the both transmissions are almost same; only the end of this phase, the PMT responded slower than FST a little bit however it is smoother. In the most important phase, working phase, the flywheel velocity of PMT system not only much more precise but also is smoother and does not oscillate rapidly in comparison with FST system.

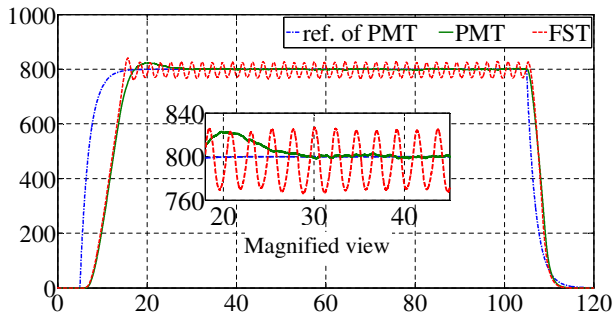


Figure 12: Velocity responses of FST and PMT ( $\omega_{wr} = 800 \text{ min}^{-1}$ ).

## 5 Energy Saving

Energy saving is one of most important property of water hydraulic systems without using servo valve. The energy saving of both FST and PMT systems that concerns with recovered energy in deceleration process and energy consumption in acceleration and working phase will be presented in this section.

### 5.1 Energy Consumption

Because of the energy loss of the water hydraulic transmissions is considerably higher than conventional one; thus, taking into account of the energy consumption is an important requirement of the water hydraulic systems in general and the water hydraulic systems without using servo valve in particular.

#### 5.1.1 FST system

Energy consumption of the FST system is only for Phase 1 and Phase 2, because in Phase 3, the electric motor M is stopped. Table 6 shows the energy consumptions of the system in a cycle when the reference velocity varies from  $600 \text{ min}^{-1}$  to  $1000 \text{ min}^{-1}$ . The energy consumptions are almost same and decrease if the reference velocity increases. The reason for this can be explained as follows. The velocity of the electric motor M is constant for all the reference velocities and gets the value of approximately  $1200 \text{ min}^{-1}$  to force the system to complete full cycle when the reference velocity gets the highest value of  $1000 \text{ min}^{-1}$ . The energy consumption for the acceleration phase is higher if the reference velocity is bigger; however, in phase 2, when the reference velocity is bigger, the flow rate flows through the hydraulic pump/motor is also bigger and the supply flow rate from the hydraulic pump P is almost constant, it leads to the working pressure that can be considered as load of the hydraulic motor is smaller and the energy consumption of the electric motor will decrease in this phase. The energy consumption is the combination of the both phases. Thus the energy consumption of the system depends on both the working time of the system and the reference velocity.

#### 5.1.2 PMT system

Energy consumption of PMT system is only for the acceleration and working phases same as FST system, because the electric motor M is also stopped in the deceleration phase.

Table 6: Energy consumption of FST system.

Reference velocity $\omega_{wr} [\text{min}^{-1}]$	Energy consumption [Wh]
1000	137
900	138
800	140
700	140
600	141

Energy consumption of the system when the reference velocity is from  $600 \text{ min}^{-1}$  to  $1000 \text{ min}^{-1}$  will be shown in tab. 7. The energy consumptions of PMT system decreases if the reference velocity goes down. It is not difficult to understand because the velocity of the electric motor M also varies depending on the reference velocity.

Table 7: Energy consumption of PMT system.

Reference velocity $\omega_{wr} [\text{min}^{-1}]$	Energy consumption [Wh]
1000	28.5
900	26.0
800	23.0
700	20.8
600	18.4

### 5.1.3 Comparison

The comparison of the energy consumption between FST and PMT is one of the major purposes of this research. Figure 13 shows the energy consumption of FST and PMT systems. Based on the figure and tabs. 6 and 7, the advantage in the energy saving of PMT is displayed clearly. The minimum difference between FST and PMT is 4.8 times and the maximum one is 7.7 times corresponding with the reference velocities of  $1000 \text{ min}^{-1}$  and  $600 \text{ min}^{-1}$ , respectively. The difference is because of the energy loss of FST system via relief valve, stored in  $ACC_1$  that will disappear after the cycle. Moreover, the energy lose when the ON/OFF valves change its state that contributes the bigger part and the energy stored in accumulator  $ACC_2$  which can be reused same as the recovered energy.

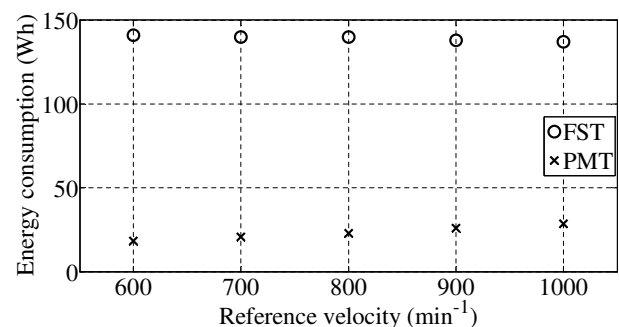


Figure 13: Energy consumption of FST and PMT.

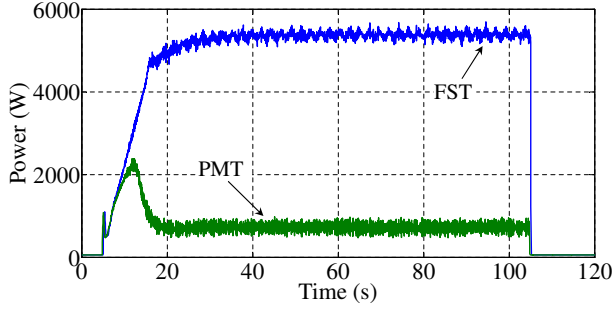


Figure 14: Electric motor supply power of FST and PMT ( $\omega_{wr} = 800 \text{ min}^{-1}$ ).

Figure 14 shows the instantaneous value of the supply power to the electric motor M of FST and PMT system in experiment. At the beginning of the acceleration phase, the energy consumption of FST and PMT is similar; however, at the end of the phase, energy consumption of FST still increase and the energy consumption of PMT reduces, because the velocity of the electric motor M increases rapidly for FST case and slower for PMT case that make the velocity response of PMT is slower. In the working phase, the energy consumption of FST is much higher than PMT because the pressure in the output line of the hydraulic motor of FST system is higher than PMT system.

## 5.2 Energy Recovery Efficiency

Energy recoveries of both FST and PMT systems were produced in the deceleration phase. The deceleration phases of FST and PMT systems were exactly same, all ON/OFF valves were closed, the electric motor M was stopped. ON/OFF valve VS<sub>3</sub> was closed to break the flywheel; at that time, the hydraulic pump motor PM acted as a pump and converted the kinetic energy of the flywheel FW that caused by high speed of the flywheel into high pressure water and it was stored in the accumulator ACC<sub>2</sub>. The recovered energy would be reused in the next cycle of the systems. The ON/OFF switching valve VS<sub>2</sub> was closed to cut the supply energy to the hydraulic pump/motor PM directly and preserve the recovered energy. The recovered energy stored in the accumulator ACC<sub>2</sub> is defined as follows

$$E_{\text{recovery}} = \int_{t_{\text{start}3}}^{t_{\text{end}3}} p_{\text{ACC}2} \cdot q_{\text{ACC}2} dt, \quad (8)$$

where  $E_{\text{recovery}}$  is the recovered energy to the accumulator ACC<sub>2</sub> during the deceleration phase,  $p_{\text{ACC}2}$  the pressure of the accumulator ACC<sub>2</sub>,  $q_{\text{ACC}2}$  the flow rate stored in the accumulator ACC<sub>2</sub>, and  $t_{\text{start}3}$ ,  $t_{\text{end}3}$  the times at the beginning (the time of 105 second) and the end of Phase 3, respectively. Because the pressure  $p_{\text{ACC}2}$  and the flow rate  $q_{\text{ACC}2}$  are same as the pressure  $p_1$  and the flow rate  $q_2$ , eq. (9) can be written as

$$E_{\text{recovery}} = \int_{t_{\text{start}3}}^{t_{\text{end}3}} p_1 \cdot q_2 dt. \quad (9)$$

To estimate the recovered energy, the efficiency index  $\eta$  will be introduced as the ratio of the recovered energy and the

maximum kinetic energy of the flywheel FW in the deceleration phase as follows

$$\eta = \frac{E_{\text{recovery}}}{E_{\text{FW}}}, \quad (10)$$

where  $E_{\text{FW}}$  is the maximum kinetic energy possessed by the flywheel in Phase 3. This evaluates how much energy will be recovered from the kinetic energy of the flywheel dissipated in conventional operations and can be reused in next action cycle in real application. In this case,  $E_{\text{FW}}$  is calculated by following equation

$$E_{\text{FW}} = \frac{1}{2} I \omega_{\text{max}}^2, \quad (11)$$

where  $\omega_{\text{max}}$  is the maximum rotational velocity of the flywheel in the deceleration phase.

Table 8: Recovered energy of FST system.

Reference velocity $\omega_{wr}$ [min <sup>-1</sup> ]	$E_{\text{recovery}}$ [kJ]	$E_{\text{FW}}$ [kJ]	$\eta$ [%]
1000	3.17	8.65	36.7
900	2.49	7.16	34.8
800	1.88	5.67	33.2
700	1.27	4.22	30.1
600	0.86	3.27	26.3

Table 9: Recovered energy of PMT system.

Reference velocity $\omega_{wr}$ [min <sup>-1</sup> ]	$E_{\text{recovery}}$ [kJ]	$E_{\text{FW}}$ [kJ]	$\eta$ [%]
1000	3.21	8.66	37.1
900	2.48	7.02	35.3
800	1.85	5.54	33.4
700	1.29	4.25	30.4
600	0.83	3.12	26.6

Tables 8 and 9 shows the recovered energies of FST and PMT systems in the deceleration phase, all the results are the average of five times experiments. From the tables, it is easy to realize that the recovered energy of the FST and PMT systems are almost same; however, they still exist a minor difference because the maximum rotational velocities of the flywheel in the deceleration phase  $\omega_{\text{max}}$  of the FST and PMT systems are not the same and the measurement devices have its deviations. The recovered energies of the both systems increased when the reference velocities raised and got the maximum values of 3.17 and 3.21 corresponding with the energy recovery efficiency index  $\eta$  of 36.7% and 37.1% for the FST and PMT systems, respectively.

## 6 Conclusion

This paper is an investigation on the FST and PMT systems that do not use servo valve. The easiest advantage of the systems is cheap and the energy loss can be reduced.

The FST system is good at recovering energy in the deceleration period, it is almost same as the PMT system, and it can save from 26.3 to 26.7% of the kinetic energy of the flywheel. However, the steady state error of the flywheel velocity in the working period is still large, it is from 2.8 to 5% and it is very difficult to be reduced because the error exists in the control logic. The energy consumption of the system is quite high because of lossing via the relief valves, the accumulator ACC<sub>1</sub>, and the process of changing state of ON/OFF valves. It needs from 137 to 141 Wh for all acceleration and working phases that last 100 seconds when the reference velocity changes from 600 to 1000 min<sup>-1</sup>.

The PMT system displayed more advantage than FST system. First, the system can reduce the noise because of smooth operation and enlarge the duration of the devices such as the ON/OFF valves VS<sub>2</sub>, VS<sub>3</sub> and the hydraulic motor. Second, the steady state error in the working phase decreased dramatically in the PMT system, from 6 to 18 times, it is from 1.66 to 4.1 min<sup>-1</sup> corresponding with the percentage errors of 0.28 to 0.59%. Following, The energy consumption of PMT system reduced much, it was only from 4.8 to 7.7 times less than energy consumption in FST system.

However, PMT system remains some restrictions that need to be improved consist of long transient time in acceleration phase and taking time to tune the gain of PID controller.

## References

- [1] F L Yin, S L Nie, and J Ruan. Research on the reliability of sliding bearing support in a swash-plate type axial piston water hydraulic pump. *Proc. of 2011 International Conference on Fluid Power and Mechatronics (FPM)*, 2011.
- [2] B Hollingworth. The past, present and future of (water) hydraulics. *Proc. of 12<sup>th</sup> Scandinavian International Conference on Fluid Power, SICFP'11*, 2011.
- [3] P N Pham, K Ito, and S Ikeo. The application of simple adaptive control for simulated water hydraulic servo motor system. *Proc. of International Conference on Industrial Technology IEEE ICIT*, 2013.
- [4] K Ito. Control performance comparison of simple adaptive control to water hydraulic servo cylinder system. *Proc. of 19<sup>th</sup> Mediterranean Conference on Control and Automation (MED)*, 2011.
- [5] K Ito and S Ikeo. Robust velocity control of a water hydraulic servomotor system with parameter uncertainty. *Proc. of SICE Annual Conference in Fukui*, 2003.
- [6] K Ito, H Takahashi, S Ikeo, and K Takahashi. Robust control of water hydraulic servo motor system using sliding mode control with disturbance observer. *Proc. of SICE-ICASE International Joint Conference*, 2006.
- [7] P N Pham, K Ito, W Kobayashi, and S Ikeo. Analysis of velocity control performance and energy recovery efficiency of water hydraulic fluid switching transmission. *Proc. of International Journal of Automation Technology*, 6(4):457–467, 2012.
- [8] M Linjama, M Huova, P Boström, A Laamanen, L Siivonen, L Morel, M Waldé, and M Vilenius. Design and implementation of energy saving digital hydraulic control system. *Proc. of The Tenth Scandinavian International Conference on Fluid Power, SICFP'07*, 2007.
- [9] K Sanada. A study on hils of fluid switching transmission. *Proc. of SICE-ICASE International Joint Conference*, 2006.
- [10] K Ito, W Kobayashi, P N Pham, and S Ikeo. Control and energy saving performance of water hydraulic fluid switching transmission. *Proc. of 12<sup>th</sup> Scandinavian International Conference on Fluid Power, SICFP'11*, 2011.
- [11] P N Pham, K Ito, W Kobayashi, and S Ikeo. Research on velocity error and energy recovery efficiency of water hydraulic fluid switching transmission. *Proc. of 11<sup>th</sup> International Conference on Automation Technology*, 2011.
- [12] S Habibi and A Goldenberg. Design of a new high performance electrohydraulic actuator. *Proc. of 1999 IEEE/ASME International Conference on Advanced Intelligent Mechatronics*, 1999.
- [13] Y Lin, Y Shi, and R Burton. Modeling and robust discrete-time sliding-mode control design for a fluid power electrohydraulic actuator (eha) system. *Proc. of IEEE/ASME Transaction on Mechatronics*, 18(1):1–10, 2013.
- [14] H W Beaty and J L Kirtley. *Electric Motor Hand Book*. McGRAW-HILL, 1998.



# **Effect of Design Parameters on Response Characteristics of Water Hydraulic Proportional Control Valves**

F. Yoshida and S. Miyakawa

Basic Technology R & D Center, KYB Corporation,  
1-12-1 Asamizodai, Minami-ku, Sagamihara-shi, Kanagawa-ken, Japan  
E-mail: yoshida-fut@kyb.co.jp, miyakawa-shi@kyb.co.jp

## **Abstract**

Water hydraulic proportional control valves using “tap water” as the working fluid are suitable for systems that require high levels of environmental friendliness and safety. Particularly, there are high expectations for their application to mining machinery, wave and wind power generation systems, and ocean development machinery, including underwater drilling machinery. In the previous report, the authors defined the transfer functions of three components of the water hydraulic proportional control valve, namely the compensation circuit, the solenoid, and the pilot valve, and experimentally and analytically examined the effects of design parameters on valve performance. In water hydraulic proportional control valves that use tap water, with its poor lubricating properties, as the working fluid, the hydrostatic bearings and damping orifices, which comprise the structural characteristics of the valve, function to ensure friction/wear prevention and stable operation of the spool. Moreover, the hydrostatic bearings and damping orifices structurally constitute a meter-in circuit that is effective in improving the response characteristics of the spool and a meter-out circuit that is effective in improving the damping characteristics of the spool; their functions are determined depending on the purpose of the valve. This report focuses on the open loop transfer function represented by the solenoid and the pilot valve and how that function effects the characteristics of the entire valve; more specifically, the effect of the geometric parameters of the hydrostatic bearings and damping orifices is examined; then, the effect of these parameters on the step response characteristics of the entire valve is analytically verified.

**Keywords:** Water hydraulic proportional control valve, tap water, response characteristics

## **1 Introduction**

Water hydraulic proportional control valves using “tap water” as the working fluid are suitable for systems that require high levels of hygiene and safety; they can be used in a wide range of applications, including foods, beverages, semiconductors, medicines, pharmaceuticals, cosmetics, chemicals, natural energy technologies, and underwater applications. In particular, there are high expectations for their application to systems that require high levels of safety and environmental friendliness, for instance, mining machinery, wave and wind power generation systems, and ocean development machinery, including underwater drilling machinery, as well as systems requiring high levels of hygiene and washing performance in the automation of meat/seafood processing, which has been conventionally performed manually.

In the previous report, the authors defined the transfer functions of three components of the water hydraulic proportional control valve, namely the compensation circuit, the solenoid, and the pilot valve, and experimentally and

analytically examined the effects of design parameters on valve performance [2], [3], [4]. A water hydraulic proportional control valve using tap water with low lubricating properties as the working fluid has a structure in which hydrostatic bearings support the spool at both ends for friction/wear prevention; damping orifices generate damping force for stable spool operation by guiding fluid flowing from the hydrostatic bearings to the pressure chambers at the both ends of the spool. From their positional relationship, the hydrostatic bearings and damping orifices constitute a meter-in circuit and a meter-out circuit for spool operation, respectively. Since the meter-in circuit effectively improves the response characteristics of the spool and the meter-out circuit effectively improves the damping characteristics of the spool; their functions are determined depending on the purpose. Their dimensions need to be optimally set for stable valve operation; however, consideration of the dimensions has been conducted only empirically, not theoretically.

This report focuses on the open loop transfer function that is represented by the solenoid and the pilot valve and how it

affects the characteristics of the entire valve; more specifically, the effect of the geometric parameters, is examined. Then, the effect of these parameters on the entire valve in terms of its response characteristics is verified. Specifically, the dimensional ratio of the damping orifice diameter  $D_n$  against the hydrostatic bearing equivalent orifice diameter  $D_b$ , is defined as  $Cr = D_n/D_b$ , the effect of changes in  $Cr$  on the first-order lag time constant of the pilot valve  $T_L$  and on the second-order lag damping coefficient of the solenoid and the pilot valve  $\zeta$ , and the effect of  $Cr$  on the step response of the loop transfer function of the entire valve including the compensation circuit are analytically examined.

## 2 Overview of the water hydraulic proportional control valve

This section describes the structural characteristics and control method of the water hydraulic proportional control valve.

### 2.1 Structure

Figure 1 shows the structure of the water hydraulic proportional control valve. Table 1 shows its major specifications. Low-viscosity tap water used as the working fluid makes it difficult to form water film in the clearance of the sliding member. For this reason, the water hydraulic proportional control valve has a structure in which hydrostatic bearings support the spool at both ends so that the spool can be displaced without contacting the sleeve to reduce friction/wear caused by sliding. Damping orifices are provided at both ends of the spool between the pressure chambers and the return line. This allows stable valve operation by providing damping force for spool operation. The spool is set in place by balancing between the solenoid thrust and the spring force. While a typical solenoid valve has a structure in which the solenoid and a compression spring support the spool at both ends, the water hydraulic proportional control valve instead uses an extension spring. The use of the extension spring frees the other end of the spool, allowing more effective hydrostatic bearing operation for reduced moment and lateral force.

Table 1 Specifications

Item		Specification
Rated flow rate	[L/min]	20
Rated pressure	[MPa]	14
Operating pressure range	[MPa]	3.5 to 14
Operating temperature range	[deg C]	2 to 50
Working fluid		Tap water
Input voltage	[V]	+/-10

### 2.2 Functions of the hydrostatic bearing orifices and damping orifices

Figure 2 schematically shows the positional relationship between the spool, hydrostatic bearing orifice, and damping orifice. Since the hydrostatic bearing orifices function to support the spool in the sleeve so that it does not make contact with the sleeve and thus prevent friction/wear, the design dimensions of the orifices are determined by the load capacity required to retain the spool [1]. Fluid passing through the hydrostatic bearing orifices is guided to the pressure chambers at the ends of the spool; then, it passes through the damping orifices, generating damping force. The design dimensions of the damping orifices depend on the design dimensions of the hydrostatic bearing orifices; therefore, they cannot be uniquely determined. In addition to supporting the spool without coming into contact with it, as is apparent from the orifices positional relationship with the spool, the hydrostatic bearing orifices function as a meter-in circuit that effectively improves the response characteristics of the spool. Meanwhile, the damping orifices function as a meter-out circuit that effectively improves the damping characteristics of the spool. Which of the meter-in circuit or the meter-out circuit has a larger effect on spool operation depends on the relative relationship between the two types of orifices, the hydrostatic bearing orifices and the damping orifices. That is, if the hydrostatic bearing orifices are relatively smaller than the damping orifices, the effect as a meter-in circuit becomes larger; if the damping orifices are relatively and sufficiently larger than the hydrostatic bearing orifices, the effect as a meter-out circuit becomes larger. When the two circuits have an equal relationship, the effects of the meter-in and meter-out circuits are combined and considered to affect the spool.

Generally, the viscosity of water is very small (one thirtieth that of oil); thus, it is assumed that when water is used as the working fluid, the damping orifice diameter needs to be very small to generate sufficient damping force. From a practical point of view, making the damping orifice diameter smaller may increase the effect of contamination; however, almost no quantitative study has been made to such effect. In this regard for the water hydraulic proportional control valve, we studied the friction factor required to calculate the damping force of the damping orifices by comparing it with a case in which oil is used as the working fluid, instead of water. First, the relationship between the orifice diameter  $D$  and the Reynolds number  $Re$  is calculated by using the orifice

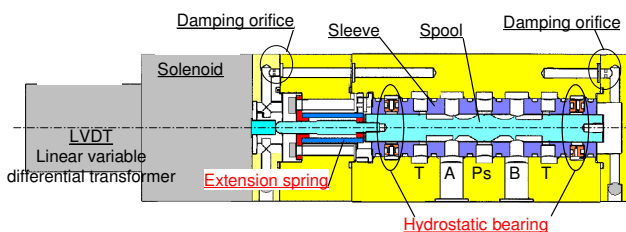


Figure 1: Structure



the solenoid, and the pilot valve. The compensation circuit is defined by eq. (1) with a standard PI controller.

$$C(s) = \frac{k_p T_I s + k_p}{T_I s} \quad (1)$$

Since it has been experimentally verified that the transfer function of the solenoid  $S(s)$  can be approximated by a standard first-order lag transfer function in the previous report, it is defined by the transfer function in eq. (2). Figure 7 shows a comparison of the experimental results of the frequency characteristics of the solenoid thrust with the analytical results of the transfer function in eq. (2).

$$S(s) = \frac{K_{SOL}}{\tau_{SOL} s + 1} \quad (2)$$

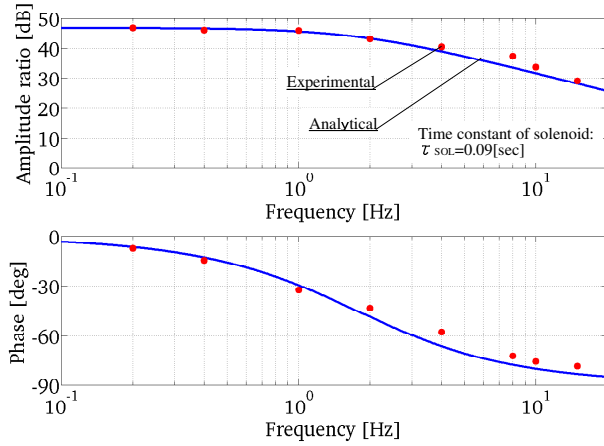


Figure 7: The frequency characteristics of the solenoid thrust

The transfer function of the pilot valve  $P(s)$  can be obtained as the first-order lag transfer function in eq. (3) by Laplace, transforming the mathematical model that linearizes the pressure and flow rate of each component in the vicinity of experimental points. Parameters in eq. (3) are defined by eq. (4) to eq. (19). In eq. (15),  $C_r$  is the ratio of the damping orifice diameter against the hydrostatic bearing orifice diameter. Since four hydrostatic bearings are provided in the circumferential direction of the spool, they are expressed as the hydrostatic bearing equivalent orifice diameter  $D_b$ , as one orifice defined by eq. (14), and the ratio is expressed as  $C_r = D_N/D_b$ . From the measured flow rate and the Reynolds number calculated from the geometry, the flow from the hydrostatic bearing orifice was assumed to be laminar flow, and therefore, the orifice is modeled as a choke orifice by eq. (12). The friction factor  $\lambda$  that determines the damping force of the damping orifices is modeled by eq. (19) by applying the Blasius equation for turbulent flow, as described above.

The transfer characteristics of the solenoid and the pilot valve (excluding the compensation circuit) of the three components defined above are expressed as the open loop transfer function  $V(s)$  of the valve shown in the block diagram (fig. 8) by the second-order lag transfer function in eq. (20). The damping coefficient  $\zeta$ , the natural frequency  $\omega$ , and the proportionality constant  $K$  are defined by eq. (21) to eq. (23), respectively. Further, as shown in fig. 3, the loop transfer function of the feedback control valve system, including the compensation circuit,  $V_{SYS}(s)$  is a third-order lag transfer function as shown in eq. (24).

$$P(s) = \frac{x(s)}{F_{SOL}(s)} = \frac{K_L}{T_L s + 1} \quad (3)$$

$$T_L = \frac{\Gamma - \xi}{K_{SP} + \beta} \quad (4)$$

$$K_L = \frac{1}{K_{SP} + \beta} \quad (5)$$

$$\Gamma = (L_{bn} + L_{bT}) \frac{2\pi \cdot D_{SPL} \cdot \mu}{\delta} \quad (6)$$

$$\xi = \frac{2A_{SPL}^2}{\alpha \cdot \alpha_{bN}} \quad (7)$$

$$\beta = 8 \cdot C \cdot L_W \cdot (P_S - P_L) \cot(\theta) \quad (8)$$

$$\alpha = \frac{\alpha_{bN}}{\alpha_{bN} + \alpha_{bT} - \alpha_b} - \frac{\alpha_N}{\alpha_{bN}} - 1 \quad (9)$$

$$\alpha_N = \frac{\pi^2 2^5 D_b^5}{16 \rho L_{NT} Q_{NT0} \cdot \lambda} C_r^5 \quad (10)$$

$$\alpha_{bN} = \frac{\pi \cdot D_{SPL} \cdot \delta^3}{12 \cdot \mu \cdot L_{bN}} \quad (11)$$

$$\alpha_b = \frac{\pi \cdot D_b^4}{32 \cdot \mu \cdot L_b} \quad (12)$$

$$\alpha_{bT} = \frac{\pi \cdot D_{SPL} \cdot \delta^3}{12 \cdot \mu \cdot L_{bT}} \quad (13)$$

$$D_b = 2D_b \quad (14)$$

$$C_r = \frac{D_N}{D_b} \quad (15)$$

$$D_N = 2C_r D_b \quad (16)$$

$$Re = \frac{2wD_b}{\nu} C_r \quad (17)$$

$$w = \frac{4Q_{NT0}}{\pi \cdot 2^2 D_b^2} \frac{1}{C_r^2} \quad (18)$$

$$\lambda = 0.3164 \cdot \left( 2 \frac{wD_b}{v} \right)^{0.25} C_r^{-0.25} \quad (19)$$

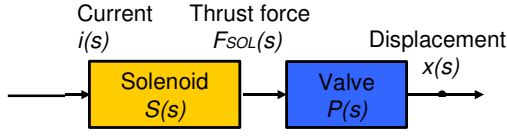


Figure 8: Block diagram of valve components excl. the compensation circuit

$$V(s) = \frac{K\omega^2}{s^2 + 2\zeta\omega s + \omega^2} \quad (20)$$

$$\omega = \sqrt{\frac{1}{T_L \cdot \tau_{SOL}}} \quad (21)$$

$$\zeta = \frac{1}{2} \left( \frac{1}{\tau_{SOL} \omega} + \tau_{SOL} \omega \right) \quad (22)$$

$$K = \frac{K_{SOL}}{K_{SP} + \beta} \quad (23)$$

$$V_{SYS}(s) = \frac{k_p K \omega^2 \left( s + \frac{1}{T_i} \right)}{s^3 + 2\zeta\omega s^2 + (1 + k_p K) \omega^2 s + \frac{k_p K \omega^2}{T_i}} \quad (24)$$

## 4 Results and discussion

Before finding out the characteristics of the entire valve, it is important to know the relationship between the transfer characteristics of the open loop transfer function shown in fig. 9 and  $Cr$  defined as the equivalent diameter ratio of the damping orifice diameter against the hydrostatic bearing orifice diameter.

This section discusses the relationship between the time constant  $T_L$  of the first-order lag transfer function  $P(s)$  of the pilot valve in eq. (3) and the damping coefficient  $\zeta$  of the second-order lag transfer function  $V(s)$  of the solenoid and the pilot valve in eq. (20), with changes in  $Cr$  defined as the equivalent diameter ratio of the damping orifice diameter against the hydrostatic bearing orifice diameter. Figure 9 shows the relationship between the damping coefficient  $\zeta$  and  $Cr$  that affects the time constant  $T_L$ .

### 4.1 Effect of $Cr$ on the transfer function $P(s)$ of the pilot valve

A  $Cr$  larger than 1 suggests that the damping orifice diameter is relatively larger than the hydrostatic bearing orifice diameter. A  $Cr$  smaller than 1 suggests that the damping orifice diameter is relatively smaller than the hydrostatic bearing orifice diameter.

Based on the above facts, the following relationship between the time constant  $T_L$  of the transfer function of the pilot valve and  $Cr$  are considered to be true.

- The smaller the  $Cr$ , the larger the time constant  $T_L$  and the slower the pilot valve response. This suggests that the damping orifices have an effect as a meter-out circuit on spool operation.

- The larger the  $Cr$ , the smaller the time constant  $T_L$  and the faster the pilot valve response. This suggests that the effect of the hydrostatic bearing orifices as a meter-in circuit is larger than the effect of the damping orifices as a meter-out circuit.

- As a general trend, in inverse proportion to an increase in the  $Cr$ , the time constant  $T_L$  decreases, and the effect as a meter-out circuit on spool operation decreases rapidly. When the  $Cr$  is larger than 1.2, the effect of the damping orifices is almost zero.

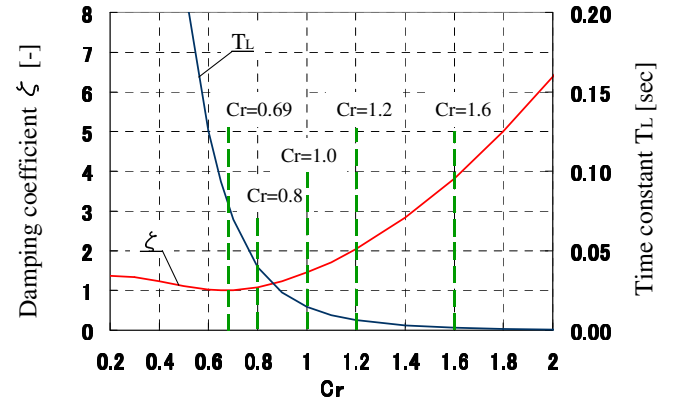


Figure 9: Relationship between the damping coefficient  $\zeta$  and  $Cr$  that affects the time constant  $T_L$

### 4.2 Effect of $Cr$ on the transfer function $V(s)$ that is expressed as the product of the pilot valve and the solenoid

In fig. 9, the following relationship between the  $Cr$  and the damping coefficient  $\zeta$  of the open loop transfer function  $V(s)$ , expressed as the product of the pilot valve and the solenoid in eq. (4), are considered to be true.

- Regardless of the value of the  $Cr$ ,  $\zeta$  is always positive. Thus, the transfer characteristics of the solenoid and the pilot valve (excluding the compensation circuit) are basically stable.

- When the  $Cr$  is 0.69, the damping coefficient  $\zeta$  becomes the minimum value 1, which is the critical damping for a response that does not generate overshoot in the transient response.

- When  $\zeta$  is larger than 1, overdamping occurs, and the response slows down.

- In an exponential increase in the  $Cr$ , the damping coefficient  $\zeta$  increases, and the level of the overdamping effect increases.

### 4.3 Effect of $Cr$ on the step response characteristics of the open loop transfer function, excluding the compensation circuit

Figure 10 shows the effect of the  $Cr$  on the step response characteristics of the open loop transfer function when the  $Cr$  is in the range from 0.69 to 1.6.

The smaller the  $Cr$ , the larger the time constant  $T_L$  of the transfer function  $P(s)$ , and the rise time tends to be fast.

The larger the  $Cr$ , the smaller the time constant  $T_L$  of the transfer function  $P(s)$ , and the rise time is fast. However, overdamping occurs due to increase in the damping coefficient  $\zeta$  of the transfer function  $V(s)$ , not necessarily providing improvement in the response characteristics. When the  $Cr$  is 1 or more, there is no significant difference in the stabilization time.

Based on the relationship described above, when the  $Cr$  is small, the effect of the damping orifices as a meter-out circuit slows down the pilot valve response; when the  $Cr$  is large, overdamping due to increase in the damping coefficient  $\zeta$  slows down the response. Thus, the appropriate value of the  $Cr$  is considered to be in the range from 0.69 to 1.6.

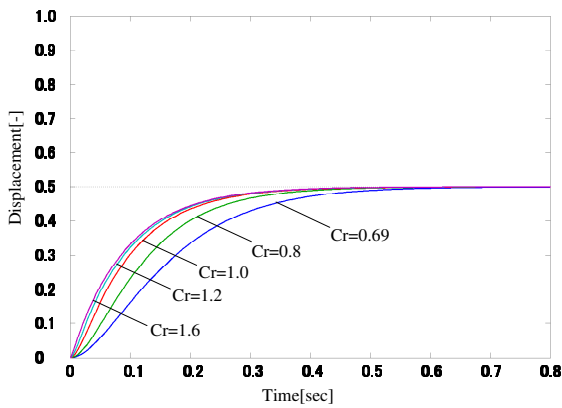


Figure 10: Effect of  $Cr$  on the step response characteristics of the open loop transfer function

### 4.4 Effect of $Cr$ on the step response characteristics of the loop transfer function

The above results indicate that the  $Cr$  has an appropriate range. It also indicates that the transfer characteristics that can be obtained from the thrust characteristics of the solenoid and the geometric structure of pilot valve are always stable. Overall, the water hydraulic proportional control valve constitutes a feedback control system, including the compensation circuit; the overall loop transfer function indicates the characteristics of the third-order lag transfer function in eq. (25). Figure 11 shows the effect of the  $Cr$  on the step response characteristics of the loop transfer function. Based on this result, the effect of the compensation circuit was examined in terms of the step response characteristics of the valve system. Here, the  $Cr$  is in the range from 0.69 to 1.6; the proportional gain of the compensation circuit  $K_P$  is 1.9; the integral time  $T_I$  is 0.1 sec.

When the  $Cr$  is 0.69, the rise time is slow, damped oscillation occurs, and convergence is slow. As the  $Cr$  increases from 0.69 to 1, both the rise time and convergence tend to be faster. Further, comparing the case where the  $Cr$  is 1.2 with the case where the  $Cr$  is 1.6, in the case of  $Cr = 1.6$ , the rise time is faster, but damping occurs rapidly, and the stabilization time is longer than in the case of  $Cr = 1.2$ . Thus, the effect of the time constant  $T_L$  on the rise time is considered to be large, and rapid damping occurs with the inflection point affected by the damping coefficient  $\zeta$  when approaching the target value.

Figures 12 and 13 show the effect of the  $Cr$  under different conditions of the proportional gain and integral time. In fig. 12, the proportional gain  $K_P$  is 4, and the integral time  $T_I$  is 0.1 sec. In fig. 13, the proportional gain  $K_P$  is 1.9, and the integral time  $T_I$  is 0.05. Based on these results, the smaller the  $Cr$ , the slower the rise time under different conditions of the proportional gain and integral time; convergence proceeds as damped oscillation occurs. When the  $Cr$  is too large, the rise time is fast, but the stabilization time tends to be lengthened.

Generally, the faster the rise time, the more likely overshoot occurs. However, this is not the case with the water hydraulic proportional control valve. As shown in fig. 10, the fast rise time is assumed to be achieved by the effect of the time constant  $T_L$  of the transfer function  $P(s)$  of the pilot valve; the characteristics in the course of accessing the steady-state value and reaching convergence are assumed to be achieved by the effect of the damping coefficient  $\zeta$  of the transfer function  $V(s)$  of the solenoid and the pilot valve.

From the above results, in terms of rise time and damping characteristics, the  $Cr$  is considered to have an optimum value in the range from 0.69 to 1.6. Appropriate values for the proportional gain and integral time of the compensation circuit need to be set in a certain range by considering both stable valve operation and good response characteristics.

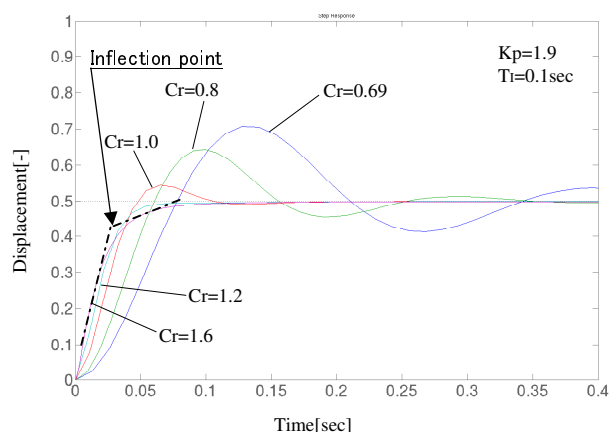


Figure 11: Effect of  $Cr$  on the step response characteristics of the loop transfer function of the valve incl. the compensation circuit ( $K_P = 1.9$ ,  $T_I = 0.1$  sec)

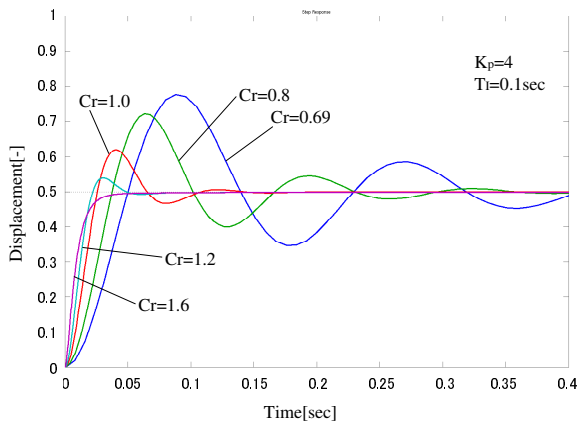


Figure 12: Effect of  $Cr$  on the step response characteristics of the loop transfer function of the valve incl. the compensation circuit

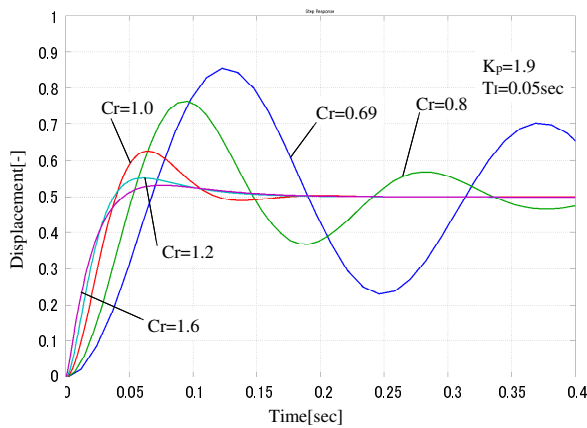


Figure 13: Effect of  $Cr$  on the step response characteristics of the loop transfer function of the valve incl. the compensation circuit ( $K_P = 1.9, T_I = 0.05 \text{ sec}$ )

## 5 Experimental verification

From analytical verification in the previous section, it is found that the  $Cr$  has a value that optimizes the step response characteristics in the range from 0.69 to 1.6 in terms of rise time and damping characteristics. This analytical result was experimentally verified.

### 5.1 Experimental methods

Figure 14 shows the schematic diagram of the experimental apparatus for step response characteristic verification. The experimental procedure is as follows. With the stop valve closed, the neutral point of the valve was adjusted. The difference between the load pressures at Port A and Port B  $P_L$  was adjusted to 7 MPa while opening the stop valve with an input signal of 50% input to the controller for experimental equilibrium. After adjusting the load pressure,

the input signal was set to 0%. For the waveform, stepwise input signals of 0% to 50% were input into the valve. The input signal  $u$  and the spool displacement  $x$  were chronologically recorded by the data logger. The experiment was conducted with supply pressure  $P_s$  at 14 MPa and water temperature at  $25 \pm 5 \text{ }^\circ\text{C}$ .

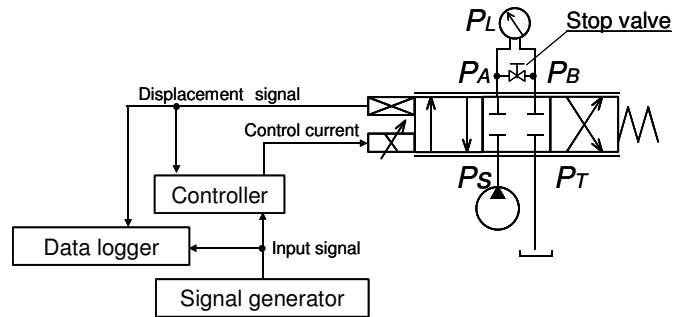


Figure 14: Schematic diagram of the experimental apparatus for step response characteristic verification

### 5.2 Experimental results

Figure 15 shows an example of the experiment where the effect of the  $Cr$  on the step response characteristics was examined. Here, the parameters of the compensation circuit were adjusted to indicate the effect of the  $Cr$  more clearly, and the spool displacement was normalized by removing steady-state errors. When the  $Cr$  is 0.9, the rise time to reach the steady-state value is relatively slow (50 msec). When the  $Cr$  is 2, the rise time is faster than for  $Cr = 0.9$ ; once about 95% of the target value is achieved, the slope of the curve becomes small at the inflection point before reaching the target value. It is assumed that the rise time is fast since the time constant  $T_L$  is small when the  $Cr$  is large, and at the inflection point and beyond, there is a damping effect of overdamping due to a large damping coefficient  $\zeta$ . The smaller the  $Cr$ , the slower the rise time; the larger the  $Cr$ , the faster the rise time, but the stabilization time is lengthened due to the damping effect of overdamping. These experimental results are similar to the analytical results.

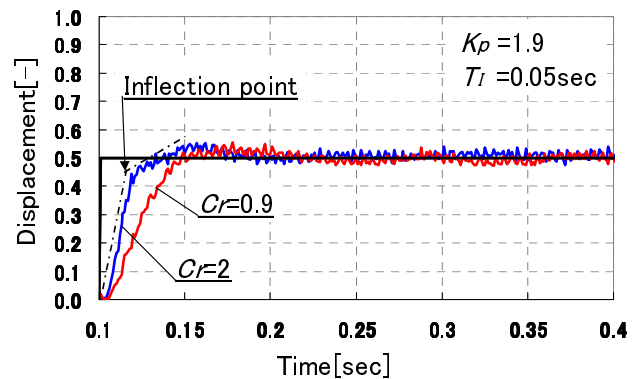


Figure 15: Experimental verification for the effect of  $Cr$  on the step response characteristics ( $K_P = 1.9, T_I = 0.05 \text{ sec}$ )

## 6 Conclusions

When the  $Cr$  is small, the effect of the damping orifices as a meter-out circuit slows down the pilot valve response. When the  $Cr$  is large, overdamping due to an increase in the damping coefficient  $\zeta$  slows down the response. Thus, the  $Cr$  has an appropriate value in the range from 0.69 to 1.6.

In step response characteristics, when the  $Cr$  is too small, the slow rise time slows down convergence toward the target value. On the other hand, when the  $Cr$  is too large, overdamping due to fast rise time slows down convergence toward the target value. When the  $Cr$  is within a certain range, both the rise time and convergence tend to be fast.

The findings obtained from our analytical verification as described above have also been verified by our experimental results.

## Nomenclature

Designation	Denotation	Unit
$A_{SPL}$	Spool Cross-sectional area	[m <sup>2</sup> ]
$D_b$	Pressure	[Pa]
$D_{SPL}$	Spool diameter	[m]
$D_n$	Damping orifice diameter	[m]
$F_F$	Flow force	[N]
$F_{SOL}$	Solenoid thrust	[N]
$K_{SP}$	Spring constant	[N/m]
$K_{SOL}$	Constant of solenoid thrust	[N/A]
$L_W$	Control orifice width	[m]
$L_{bn}, L_{bT}, L_{NT}$	Annular clearance length	[m]
$P$	Supply pressure	[Pa]
$Q$	Flow rate	[m <sup>3</sup> /s]
$\zeta$	Damping coefficient	[-]
$\lambda$	Friction factor	[-]
$\theta$	Jet angle	[degree]
$\delta$	Radial clearance	[m]
$\mu$	Viscosity	[Pa s]
$\nu$	Kinetic viscosity	[m <sup>2</sup> /s]
$\rho$	Working fluid density	[kg/m <sup>3</sup> ]
$k_P$	Proportional gain	[-]
$T_I$	Integral time	[sec]
$\tau_{SOL}$	Time constant	[sec]
$\beta$	Coefficient of flow force	[N/m]
$\Gamma$	Coefficient of viscosity	[Ns/m]
$C$	Flow constant	[-]

$F_i$	Force	[F]
$p$	Pressure	[Pa]

## References

- [1] S Miyakawa, C Yamashina, and T Takahashi. Development of Water Hydraulic Proportional Control Valve. *The Fourth JHPS International Symposium on Fluid Power*, ISBN4-931070-04-3, © Copyright JHPS, 1999 All rights reserved. Japan.
- [2] F Yoshida, and S Miyakawa. Characteristics of Proportional Control Valve Using Tap Water. *The 7th International Fluid Power Conference, Group H*, 445-456, 22-24 March 2010, Aachen , Germany.
- [3] F Yoshida, and S Miyakawa. Dynamic Characteristics of Proportional Control Valve Using Tap Water - Experimental Examination-. *The Twelfth Scandinavian International Conference on Fluid Power*, Vol. 2 469-480, 18-20 May 2011, Tampere, Finland.
- [4] F Yoshida, and S Miyakawa. Effect of Parameters on Frequency Characteristics of Proportional Control Valve Using Tap Water. *The 8th JFPS international Symposium on Fluid Power* in Okinawa, Japan, on October 25-28, 2011, CD-ROM.

# Simulative Analysis and experimental Investigation of Common Rail Injection Pumps lubricated with tailor-made Biofuels

S. Heitzig, S. Drumm and H. Murrenhoff

Institute for Fluid Power Drives and Controls (IFAS), RWTH Aachen University, Aachen, Germany  
E-mail: Stefan.Heitzig@ifas.rwth-aachen.de,  
Hubertus.Murrenhoff@ifas.rwth-aachen.de

## Abstract

In the scope of the cluster of excellence “*Tailor-Made Fuels from Biomass*” new biofuels are developed within an interdisciplinary research approach at *RWTH Aachen University*. The most promising fuel candidates so far tend to have a low viscosity and a low lubricity compared to diesel fuel. It is the task of the authors to develop a guideline for designing injection systems that are especially adapted to these fuels. The main focus is on high pressure pump within common rail systems. In this paper, the effects of those fuel candidates on the tribological contacts in standard common rail pumps are investigated by means of experiments and simulations. On the experimental side a test rig is presented, which allows the measurement of the transversal force on a piston and the friction force, which occur in the piston/bushing-contact. On the simulation side, elastohydrodynamic simulation models of several tribological contacts within the standard pump are presented. Results of simulation and measurement are presented.

**Keywords:** Elastohydrodynamic simulation, friction forces, tribological contacts, common rail pump, fuels, journal bearings

## 1 Introduction and Motivation

### 1.1 Tailor-made Fuels from Biomass

Environmental pollution and the exploitation of non-renewable resources of modern times force the development of new sustainable biofuels. One approach to find such biofuels is pursued within the cluster of excellence “*Tailor-Made Fuels from Biomass*” at *RWTH Aachen University*. Within the cluster, new biofuels are developed and tested in an interdisciplinary approach, see fig. 1.

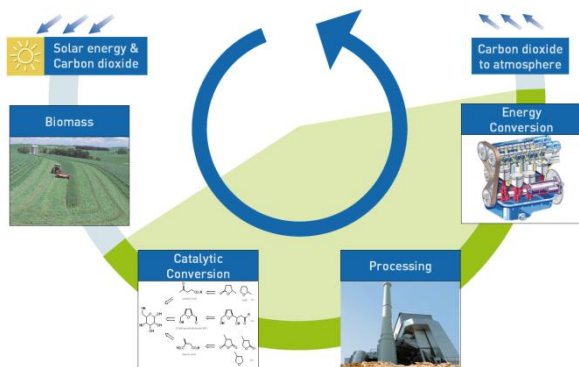


Figure 1: Tailor-made Fuels from Biomass

The fluids are evaluated regarding their suitability for use as a biofuel on the basis of their conversion, combustion and tribological characteristic. A lot of the investigated fuels

have an excellent combustion and conversion characteristic but poor tribological properties. They can differ severely from conventional fuels in their lubrication and viscosity characteristics. Therefore, tribological problems and higher efforts to pressurise the fuel to the injection pressure level have to be expected in fuel-lubricated common rail pumps when operated with the new fuel candidates. In order to facilitate a widespread usage of potential new biofuels, research at the *Institute for Fluid Power Drives and Controls (IFAS)* focuses on two approaches to ensure a proper functioning of the tribological systems. On the one hand, low-lubricity biofuels can be blended with high-lubricity biofuels in order to enhance their lubrication characteristics in the boundary lubrication regime [1, 2]. On the other hand, research on the components reveals what extent modifications of those components (micro and macro geometry, materials, coatings, etc.) can contribute reducing the effort that is necessary in order to pressurise the fuel candidates.

### 1.2 Common Rail Injection Pump

Diesel injection systems of modern passenger cars are nowadays generally designed as so-called common rail systems. In those systems the pressure build-up is decoupled from the injection process by means of the so-called rail, which functions as a hydraulic accumulator. In this paper the focus is on the common rail pump, which is used to pressurise the fuel to the injection pressure level. From the

hydraulic point of view this is a challenging task for several reasons. Firstly, the pressure level of common rail systems is much higher than in standard hydraulic applications. Systems of the first generation started with a maximum pressure level of 1350 bar. In the second and third generation the maximum pressure level was increased in order to achieve a more efficient combustion and fewer emissions. To fulfill the upcoming regulation regarding future emission limits, the next generation of common rail systems will operate at even higher pressures from 2500 up to 3000 bar. Secondly, from a tribological point of view the fluid properties of diesel are worse in comparison to standard hydraulic fluid. According to DIN EN 590, at 40 °C diesel has a viscosity within the range from 2,0 up to 4,5 mm<sup>2</sup>/s. This leads to more leakage losses in pumps and more operation of the tribological contacts in the mixed and boundary lubrication regime. And thirdly, those pumps are for the rather cost sensitive automotive sector.

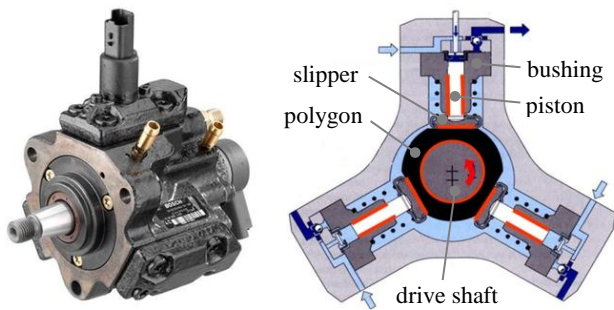


Figure 2: Common rail pump CPI. Source: Robert Bosch GmbH

As a starting point the effects of the fuel candidates on a standard common rail pump of the first generation are studied in this paper. This kind of pump, a BOSCH CP1 [3], is a radial piston type design and consist of three pistons, see fig. 2. Via a metal sheet clamp, each piston is connected to a piston slipper, which is sliding on a planar surface of the polygon ring. This ring is connected via a rotational journal bearing to the eccentric shoulder of the pump drive shaft. All tribological contacts in this pump are lubricated by the fuel itself.

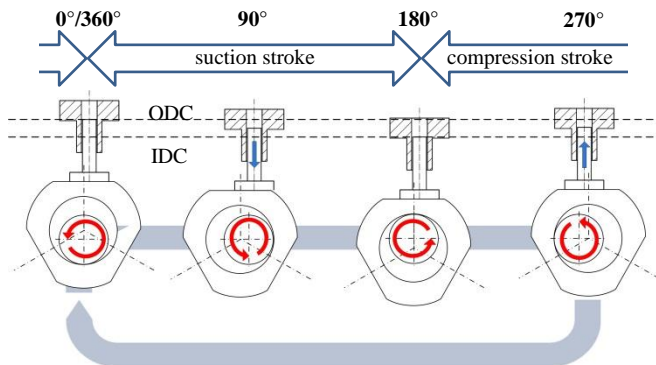


Figure 3: Sequence of one revolution

In fig. 3 the kinematics of this kind of pump are illustrated for the movement of one piston unit. The revolution starts at 0° drive shaft angel with the transition from the compression

stroke to the suction stroke. The piston is at the outer dead center (ODC) and hence its velocity is zero. From 0° to 180° the suction stroke is continuous and the piston moves downwards. At 90° the direction of the relative motion in the sliding contact between slipper and polygon changes its direction. At 180° the piston is at the inner dead center (IDC) of its movement. From 180° to 360° the compression stroke is continuous and the piston moves upwards again.

At closer inspection of cross section of the pump in fig. 2 it becomes obvious that there is a slight displacement  $d$  between the axis of each piston and the axis of the drive shaft. This detail in design, which can be found in every common rail pump of this type, is exemplified in fig. 4.

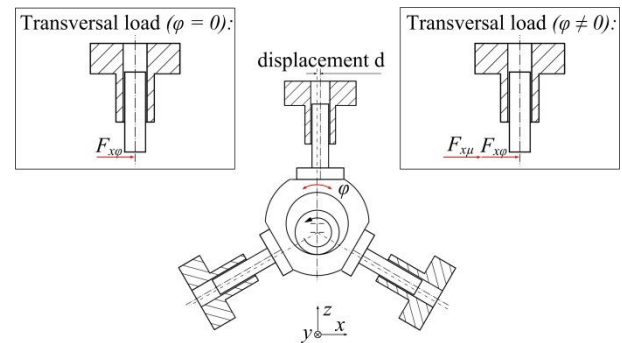


Figure 4: Tilting of the polygon ring

The motivation for this displacement  $d$  is a reduction of the tilting  $\varphi$  of the polygon ring. This tilting is determined by the forces acting on the polygon ring. In the investigated pump type each piston axis has a displacement  $d$  to the drive axis of half the eccentricity  $e$  of the drive shaft. With this displacement the tilting of the polygon ring is reduced and hence the transversal load  $F_x$  on each piston, see eq. 1.

$$F_x = F_{x\varphi} + F_{x\mu} = F_z \cdot \tan(\varphi) + F_\mu \cdot \cos(\varphi) \quad (1)$$

If no tilting occurs ( $\varphi = 0$ ), the transversal load  $F_x$  is equal to the friction force  $F_\mu$  in the polygon/slipper-contact, because the bearing surface on the polygon is orthogonal to the axis of the piston. As soon as the polygon is tilted ( $\varphi \neq 0$ ), a transversal force  $F_{x\varphi}$  due to the inclined plane has to be taken into account.

### 1.3 Focus of this Paper

Within the scope of this paper simulative and experimental approaches investigating the effects of the new fuel candidates on standard common rail pumps are discussed. The presented experimental approach tries to cover the operating characteristic and conditions of standard pumps as realistic as possible. But nevertheless, a few differences occur between the operating characteristic and conditions in the test rig and in a standard pump. This experimental approach allows the measurement of the friction force in the piston/bushing-contact as well as the transversal load on the piston. In the simulative approach further contacts are taken into consideration to reach a better comparability of measurement and simulation. As this paper will demonstrate, there are several specific reasons why a satisfying comparability of measurement and simulation is

difficult to reach at this point. Improvements on the experimental side will be exposed, which will enable a better comparability in the future.

## 2 Experimental Approach

### 2.1 Test Rig Set-Up

Over the past decades several test rigs were designed to measure the friction forces in tribological contacts within hydraulic pumps [4] [5] [6] [7] [8]. The basic principle chosen for this test rig is comparable to the one developed by Breuer [9].

The design of the test rig is shown in fig. 5 (a). This design allows the measurement of the friction force (z-direction) and the transversal load (x-direction) of one piston unit. All tribologically relevant parts are taken from standard pumps (piston, bushing, piston slipper, polygon ring, drive shaft). One bushing is separated from the housing and connected to the force measurement platform. In order to compensate the huge forces occurring because of the pressure build-up in the piston chamber, a compensation piston with the same diameter is installed. This piston transmits the pressure forces directly to the base frame so that these forces are not measured by the force sensors.

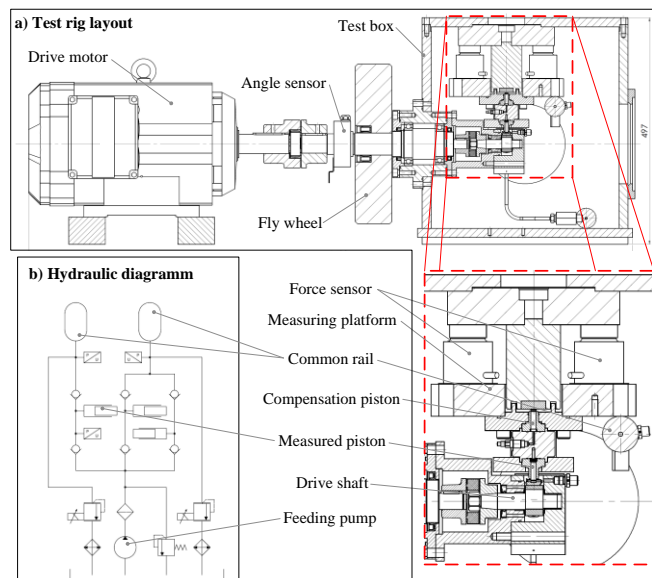


Figure 5: Test rig, layout (a) and hydraulic diagram (b)

Figure 5 (b) shows the hydraulic diagram of the rig. A simple external gear pump is used as a fuel feeding pump. To achieve a constant supply pressure of 6 bar a pressure relieve valve is installed. Two check valves at each piston are used for commutation. The flow of the pistons is pumped to two different common rails (accumulators). One rail is connected to the measured piston while the other rail is supplied by the unmodified pistons. The pressure in each common rail is controlled by a pressure relieve valve. By means of the use of two common rails it is achieved that only low pressure connections are installed between the platform measuring the force and the base frame of the test rig. That is how no additional forces develop because of

pressure pulsation in the high pressure system are induced to the force measuring system.

A more detailed description of the test rig can be seen in [10].

### 2.2 Comparison of Test Rig and Standard Pump

Even though operating conditions of the tribological contacts in the test rig are similar to those in standard pumps, there are a few differences. In the following, these differences will be discussed.

In order to separate the pressure forces from the friction forces a compensation piston is added to the test rig. This will slow down the pressure build-up in the piston chamber, because additional leakage occurs at this piston/bushing-contact. In addition to that, friction forces will occur in this contact as well. Even if there is no relative motion between the surfaces in this contact, hydrodynamic friction forces due to the leakage will occur at the bushing and will be measured by the force sensors. In order to be able to install a dynamic pressure sensor and the compensation piston, dead volume is added to the piston chamber of the measured piston unit. Like the additional leakage due to the compensation this will slow down the pressure build-up as well.

For the reasons explained above, two separated common rails are used in the rig. Thus, the pressure level in the measured piston/bushing unit is completely decoupled from the pressure level in the other two piston units. The pressure levels in the two rails are adjusted by manually adjustable pressure relief valves. Slightly different pressure levels as well as different dynamic characteristics will occur in the two rails. Furthermore, in a standard pump the housing is pressurised (roughly 3 – 6 bar) and flushed by the flow of the feeding pump. At this point this is not the case in the rig. In order to avoid a force shunt between the pump housing and the force measurement platform, no sealing is installed between the housing and the bushing. As a consequence it is not possible to pressurise the housing of the rig. The flushing of the housing in the rig is only achieved by the leakage of the three piston units and not by the total flow of the supply pump. A further difference between pump and test rig is that the fuel in the rig is pressurised several times. In a common rail system the pressurised fuel is burned after compression. Only a small amount is pressurised several times. In the rig an aging of the diesel can occur during the measurement, because it is pressurised and throttled several times.

Some of those differences will be eliminated in future measurements, see Chapter 5 of this paper.

### 2.3 Measurement Results

In a first step, measurement with standard diesel were conducted to prove the functioning of the rig and to detect weaknesses. Measurement results at a selected point of operation (rail pressure: 1800 bar; revolution: 200 1/min) are shown in fig. 6.

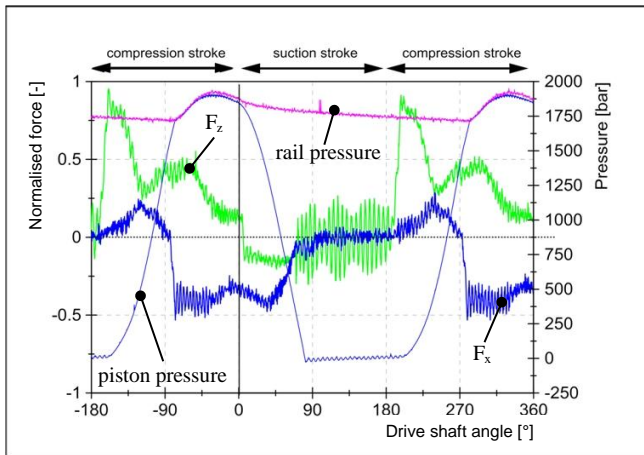


Figure 6: Measurement results

The revolution starts at the outer dead center of the piston with a rotation angle of  $0^\circ$ . From  $0^\circ$  to  $180^\circ$  the piston is moving downwards (suction stroke) and from  $180^\circ$  to  $360^\circ$  upwards (compression stroke). Forces during the suction stroke are on a low level due to the low level of the piston pressure of just a few bars. Just at the very beginning of the suction stroke there is still a higher piston pressure level and hence a higher level of forces. This higher level of piston pressure is due to the compressibility of the fuel and the elasticity of the components. At roughly  $80^\circ$  the decompression is completed and the piston pressure stays on the pressure level of the feeding pump. As soon as the compression stroke is entered, the pressure in the piston chamber raises. Due to a great amount of leakage in the piston/bushing-contact of the measured piston unit and the compensating piston as well as due to the compressibility of the fuel and the elasticity of the solid bodies, the raise of the pressure takes some time. At roughly  $270^\circ$  the piston pressure reaches the pressure level of the rail. From then on, fuel is delivered to the rail. A few degrees before the suction stroke is entered the pressure level in the piston chamber decreases. At this point the piston movement is not fast enough to compensate the leakage losses. The transversal forces on the piston  $F_x$  are submitted to a change in direction at  $270^\circ$ , because at that point the relative motion in the polygon/slipper-contact changes. This is also the case at  $90^\circ$ , but at that point the change of direction is not visible in the plots due to the low level of the force.

As exemplified before, the transversal load on the piston is not just the friction force in the polygon/slipper-contact. The transversal load of the cylinder  $F_x$  is equal to that friction force  $F_\mu$  only if the surface of the polygon ring is orthogonal to the piston axis, see eq. 1. To detect the influence a tilting of the polygon may have on the transversal load, measurements with different displacements of the axis of the measured piston unit to the drive shaft axis were conducted. The test rig allows the variation of the displacement of the measured piston unit from  $-2,5$  mm up to  $+2,5$  mm. The results of these measurements are shown in fig. 7 (rail pressure: 1800 bar; revolution: 200 rpm/min).

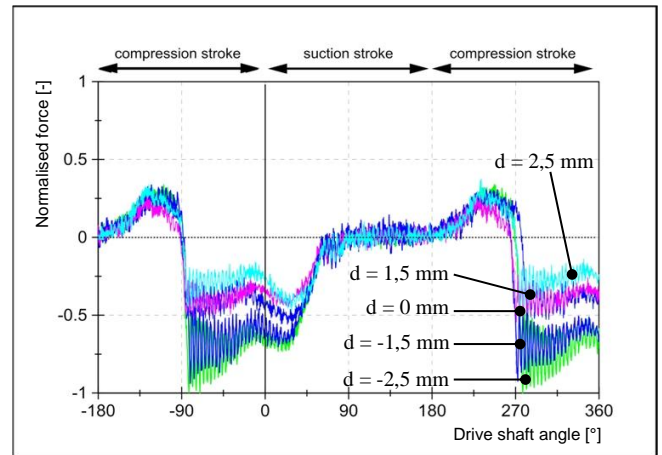


Figure 7: Measurement results for  $F_x$  with different displacements

As it can be concluded from the results the displacement has a huge influence on the transversal load on the piston. The displacement of  $-2,5$  mm leads to the highest transversal load on the piston. The transversal load is reduced with every step the displacement takes towards  $2,5$  mm. It can be assumed that the friction force  $F_{\mu}$  in the polygon/slipper-contact is independent of the displacement and has approximately the same characteristic in all five measurements due to comparable tribological operating conditions of this contact. Hence, the variation in transversal load  $F_x$  on the piston is caused by a different tilting characteristic of the polygon ring.

To draw conclusions from the measurement results concerning the most beneficial displacement  $d$  is not possible due to several reasons. Firstly, in the rig the displacement of only one piston unit is changed. The position of the other two piston units cannot be changed. Secondly, up to now only one operating point is measured, which is not a typical operating point of this kind of pump. It can be expected that the most beneficial displacement is a function of the operating conditions (revolution, pressure, temperature) as well as of the tribological properties of the fuel (lubricity and viscosity characteristic).

### 3 Simulative Approach

In the simulative approach, elastohydrodynamic models of the fuel-lubricated contacts were set up. In the following, a short introduction to the simulation tool will be provided. For more detailed information regarding the simulation tool the reader is referred to Knoll et al. [11, 12].

Solid bodies are incorporated in the simulation by FEM-models. The local deformation and global rigid motion is determined by the integration of a special formulation of Newton's equation of motion, which combines large rigid body motions and small deformations of the elastic bodies, see eq. (2). The properties of the elastic bodies are incorporated in this equation by the mass ( $M$ ), damping ( $D$ ) and stiffness ( $K$ ) matrices, which are obtained from FEM-models. Centrifugal, gyroscopic and coriolis forces arising on the right hand side of eq. 2 besides external

forces. The total acceleration vector ( $\ddot{q} + \ddot{u}$ ) is separated into rigid body ( $\ddot{q}$ ) and elastic accelerations ( $\ddot{u}$ ).

$$\mathbf{M} \cdot (\ddot{\mathbf{q}} + \ddot{\mathbf{u}}) + \mathbf{D} \cdot \dot{\mathbf{u}} + \mathbf{K} \cdot \mathbf{u} = \mathbf{f}_{\text{ext}}(t) + \mathbf{f}_{\text{ce}}(t) + \mathbf{f}_{\text{co}}(t) + \mathbf{f}_{\text{gy}}(t) \quad (2)$$

Prior to the elasto-hydrodynamic simulation, a reduction scheme is applied in order to achieve acceptable computation time by limiting the number of degrees of freedom (DOFs) of conventional finite element models. With the help of the reduction step, the modeling capabilities of the structure are reduced to reasonable deformation modes. It is important to choose relevant DOFs for the reduction step, because all solutions in the reduced system are weighted by superposition of these modes. In this reduction procedure, which is called mixed Guyan/modal reduction scheme, two different kinds of DOFs have to be chosen. The first group, the so-called static Ritz vectors model local deformations in stiff regions. These DOFs are used to cover the local deformations of for example bearing surfaces or surfaces where a load is applied. The second kind of DOFs are the so-called modal Ritz vectors. These DOFs represent the eigenvectors of the structure, which are obtained from a modal analysis. With the help of these DOFs global deformations can be represented by the reduced structures. The static and modal Ritz vectors represent the reduced DOFs and called static and modal DOFs, respectively. The reduction step is done once for each structure before the elasto-hydrodynamic simulation.

Besides standard coupling of different solid bodies by means of springs and dampers the solid bodies can be coupled via nonlinear hydrodynamic reaction forces which represent lubricating films. Those hydrodynamic forces are calculated on a separate 2d-mesh by solving Reynolds equation for thin lubricating films, see eq. 3. Microhydrodynamic effects are incorporated via flow factors according to Patir and Cheng [13], which are gained from measurements of real surface segments.

$$\begin{aligned} \frac{\partial}{\partial x_i} \left( \Phi_{ij}^p \frac{\rho h^3}{12\eta} \frac{\partial p}{\partial x_j} \right) &= \quad ; i \neq 3 \quad (3) \\ &= \frac{v_{i2} + v_{i1}}{2} \frac{\partial(\rho h)}{\partial x_i} - \frac{v_{i2} - v_{i1}}{2} \sigma \sigma^v \frac{\partial(\rho \Phi_{ij}^*)}{\partial x_j} + \frac{\partial(\rho h)}{\partial t} \end{aligned}$$

Cavitation is considered by Reynolds boundary condition. The different fuels are characterised by their viscosity characteristics. Since high pressures and temperatures can occur in injection systems, the temperature and pressure dependency of the viscosity plays a major role. In order to determine the fuel viscosity characteristic, a viscometer for elevated pressure and temperature has been set up at IFAS [14]. Based on these viscosity measurements, models were parameterised and included in the simulation, see eq. 4.

$$\eta = \eta_0 e^{\frac{\sigma \rho_0}{z} \left( \left( 1 + \frac{p}{\rho_0} \right)^z - 1 \right)} \quad (4)$$

As soon as the hydrodynamic forces cannot bear the entire external forces on the lubrication film, solid body contact

occurs. The contact pressure is determined with the help of the contact pressure curve. This curve is calculated based on measurements of real surface segments. If a critical gap height, which depends on the surface roughness of the parts sliding against each other, is reached during the dynamic analysis, solid body contact occurs. Friction forces are calculated according to eq. 5.

$$F_{\text{friction}} = \mu_c \int p_c dA_c + \int \eta \frac{\partial u}{\partial z} dA \quad (5)$$

Up to now an energy equation is not included in the simulation tool and hence local temperatures cannot be calculated by the simulation tool.

## 4 Simulation Models

### 4.1 First Simulation Models

In a first step simple simulation models for the polygon/slipper-contact as well as for the piston bushing contact were set up. In order to reduce simulation time, those two lubricating films were simulated in separate models. The simulated friction force in sliding direction (polygon/slipper simulation) is transferred to the piston in the piston/bushing simulation as transversal load. A more detailed description of the models can be taken from [15].

The viscosity characteristic of the fuels is incorporated according to eq. 4. The parameters are set according to measurement results from a high pressure viscometer, which was set up at IFAS. The results of those measurements for several fuels at  $T = 40^\circ\text{C}$  are displayed in fig. 8. The intensive pressure dependency of some fuels becomes obvious.

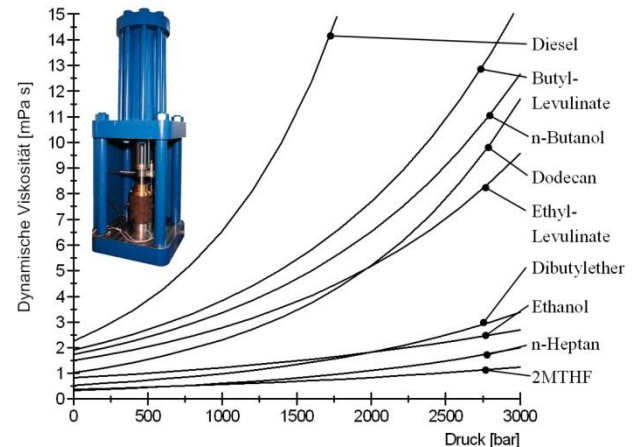


Figure 8: Pressure dependency of the viscosity at  $40^\circ\text{C}$  [16]

Fig. 9 shows the temperature dependency of some TMFB candidates at atmospheric pressure. In Common-Rail-Systems temperatures up to  $120^\circ\text{C}$  and pressures up to 2000 bar have to be expected [17]. Hence, the temperature as well as the pressure dependency cannot be neglected in simulations.

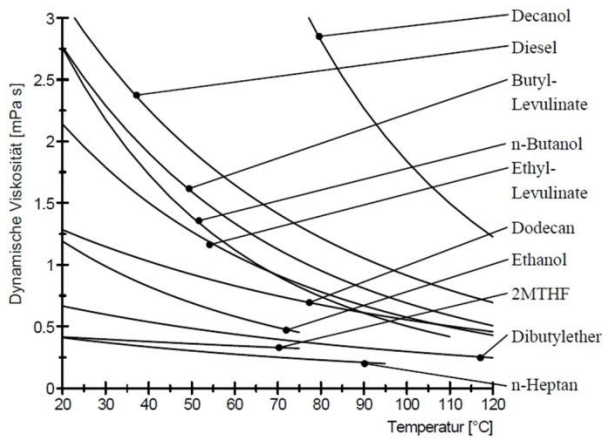


Figure 9: Temperature dependency of the viscosity at atmospheric pressure [16]

For the following simulations the promising fuel candidates dibutylether (DBE), 2-Methyltetrahydrofuran (2-MTHF) and butyl levulinate (BL) were chosen.

In fig. 10 simulation results for the bearing forces of the contact are pictured. At closer inspection of the results for the polygon/slipper-contact (left side of fig. 10) a huge influence of squeeze-effects can be identified, which reduces or even avoids solid body contact at the beginning of the compression stroke at 180°. Those squeeze-effects are viscosity-dependent and hence less distinctive for the fuel candidates like DBE, 2-MTHF and BL with a low viscosity. As a consequence, more solid body contact occurs if this contact is lubricated with those fuel candidates. This leads to higher friction forces in the polygon/slipper-contact and consequently to a higher transversal load on the piston in the piston/bushing simulation. There, because of this higher load and due to the lower viscosity, more solid body contact occurs in this contact as well. All in all these results indicate that this kind of pump design is sensitive to fuel viscosity.

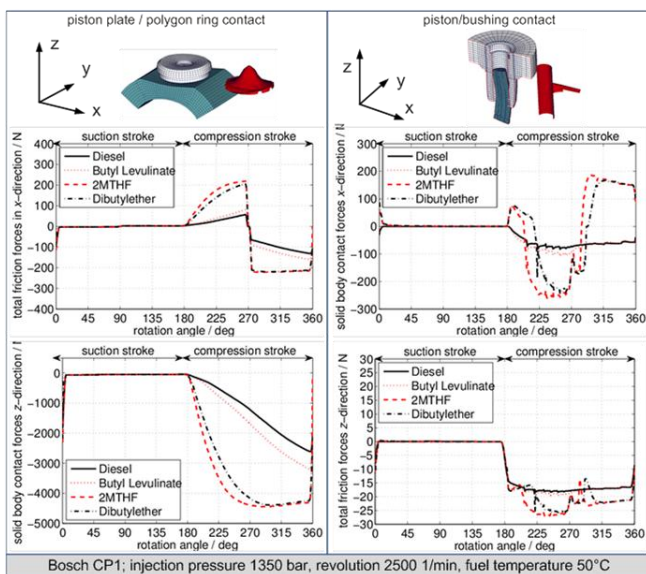


Figure 10: Test rig, layout (a) and hydraulic diagram (b)

The comparability of those models to a real pump is limited. For example the tilting of the polygon ring is not covered by the models and hence the transversal load on the piston is just the friction force  $F_{x\mu}$  of the polygon/slipper-contact. Furthermore, an almost ideal shape of the pressure in the piston chamber was assumed. From 5° to 175° a constant suction pressure level of 3 bar was assumed and from 185° to 355° a constant injection pressure level. From 355° to 5° and from 175° to 185° the commutations in-between the pressure levels were assumed. As measurements at the test rig have shown, the pressure in the chamber raises slowly due to leakage, compressibility and elasticity.

## 4.2 Improved Models

In a next step those models were extended to achieve a better comparability of the measurement and the simulation. In the following these models – all in all three of them - are presented. In a first simulation the tilting  $\varphi$  of the polygon is detected. This tilting  $\varphi$  is an input for the second simulation. In this simulation the contact between polygon and slipper is modelled more accurately. The output of that simulation is the transversal load  $F_x$  on the piston. The piston bushing contact is calculated in the last simulation. The reason for three separate models instead of one model for the whole pump is once again the required computation time.

### 4.2.1 Tilting of the Polygon Ring

As measurements indicated, the tilting  $\varphi$  of the polygon ring has a huge influence on the transversal load  $F_x$  on the piston, see fig. 3. To consider this in the simulation, an additional elastohydrodynamic simulation tool was set up, see fig. 11. The piston pressure input, which is displayed in fig. 11 as well, was determined a priori in a separate hydraulic simulation with the simulation tool DSHplus. This model consists of eight rigid or non-rigid solid bodies:

- piston (three times); rigid (0 DOFs)
- slipper (three times); non-rigid (50 DOFs)
- polygon ring (one time); non-rigid (100 DOFs)
- eccentric shoulder (one time); non-rigid (50 DOFs)

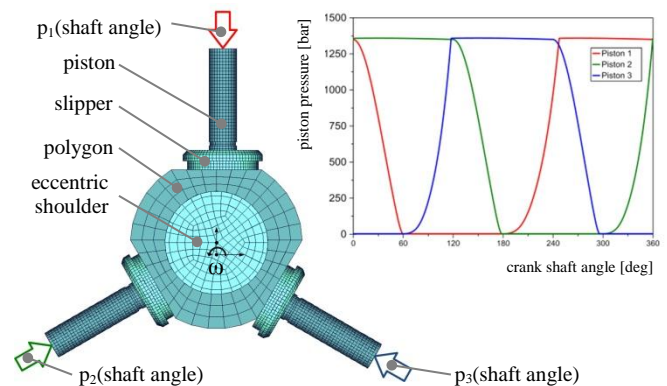


Figure 11: Simulation model for the tilting of the polygon

The eccentric shoulder is coupled with the polygon via a rotational journal bearing (140 nodes) and the three slippers

are coupled to the polygon via axial journal bearings (71 nodes). All bearings are lubricated with fuel. The way the piston is coupled to the slippers has a high influence on the tilting of the polygon. In the pump, the piston is held down to the slipper by a small metal clip, see fig. 12. This clip does not block a tilting up to a tilting angle of  $4^\circ$  in both directions. As soon as piston and slipper axis are not concentric, not the whole bottom surface transfers the load from the piston to the slipper. On one side of the contact a gap arises and on the other side the load is transferred via solid body contact pressure of the contacting surfaces. In the simulation this characteristic could be modelled with the help of a lubricating film. But since the computation effort to solve the Reynolds equation on this film and to determine the contact pressures on the bearing surfaces is huge, this option is not implemented in the simulation model. Instead another solution, which reduces computation time dramatically, is chosen. Each piston is coupled with its slipper via three compression springs, see fig. 12. With this kind of coupling the basic characteristic of the contact between piston and slipper in the pump can be modelled, assuming an adequate parameterisation of those three springs.

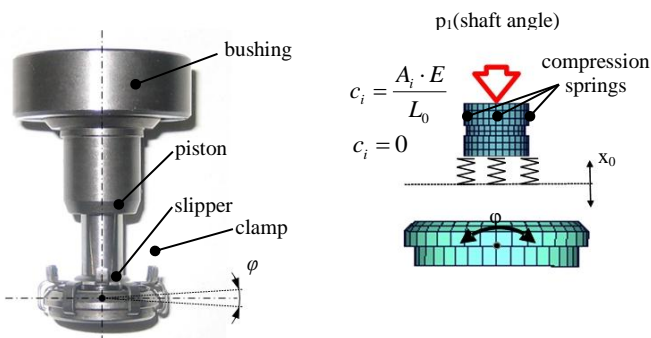


Figure 12: Coupling of piston and slipper

#### 4.2.2 Polygon/Slipper-Contact

The second simulation is a more precise simulation of the polygon/slipper-contact, see fig. 13. In this simulation only one lubricating fuel film is covered and there are only three solid bodies:

- piston; non-rigid (0 DOFs)
- slipper; non-rigid (250 DOFs)
- 1/3 polygon; non-rigid (300 DOFs)

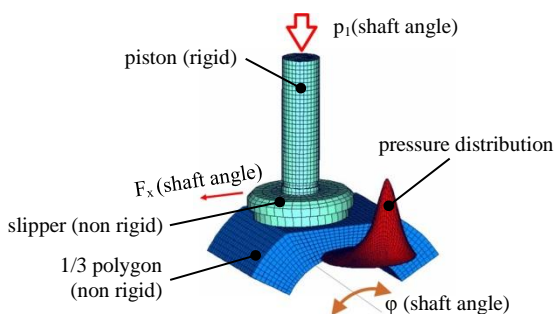


Figure 13: Simulation model for the polygon/slipper-contact

The polygon is tilted as a function of the shaft angle according to the results of the first simulation. In order to get more accurate results the number of DOFs of the slipper and polygon is increased in comparison to the first simulation. Furthermore, the 2d-mesh representing the lubricating film between slipper and polygon is defined more precisely (1871 nodes). The piston is modeled as a rigid body. The coupling between piston and slipper is implemented by three compression springs again. This simulation delivers as a result the transversal load  $F_x$  on the piston as a function of the shaft angle.

#### 4.2.3 Piston/Bushing-Contact

The third and last model is a more accurate model of the piston/bushing-contact, see fig. 14.

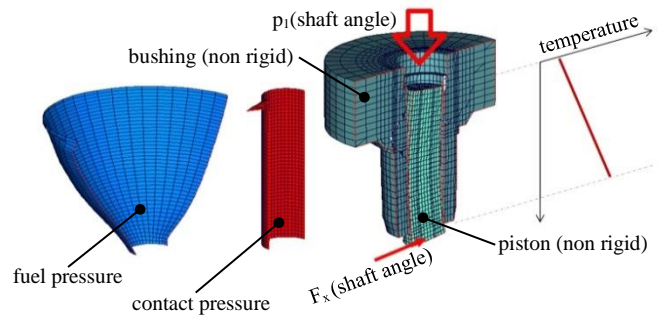


Figure 14: Simulation model for the piston/bushing-contact

The solid bodies, the piston and the bushing, are modeled as non-rigid bodies with 100 DOFs and 300 DOFs respectively. The lubricating film along the piston/bushing-contact is represented by a 2d-mesh with 1936 nodes. Along the gap in axial direction the pressure level is reduced by throttling effects. At the top end of the piston the pressure is on a high level during the compression stroke and at the lower end the pressure level is equal to the pressure level in the pump housing. The fuel is throttled from the piston chamber pressure level to the pressure level in the housing, as it can be seen in the fuel pressure distribution in fig. 13. In real pumps this energy dissipation leads to a heating of the fuel along the gap. Since the energy equation is not implemented in the model, thermal effects are included in a simplified manner. As measurements in literature show [18], the temperature distribution along the bushing is approximately linear. This knowledge is used to define a temperature-dependent reference viscosity  $\eta_0$  along the z-direction of the lubricating gap.

#### 4.3 Simulation Results

In the following some results of the improved models are presented. The simulated operating point is the same like in fig. 10 (rail pressure: 1350 bar; revolution: 2500 1/min, temperature: 50 – 100°C).

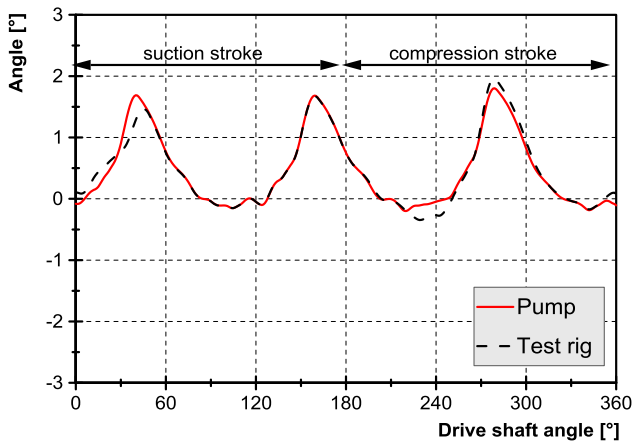


Figure 15: Results regarding the tilting of the polygon

In fig. 15 the simulated tilting of the polygon is plotted. A periodic characteristic is visible. Every 120° a peak up to 1.8° occurs due to the commutation. The dashed line represents the simulation results for the tilting of the polygon in the test rig. This tilting differs from the tilting in a standard pump due to the deviating pressure build-up in the measured piston unit (piston 1) in comparison to the other two piston units in that test rig. As explained before, the pressure build-up in the measured piston unit is slowed down by leakage at the compensation piston and by an increased dead volume.

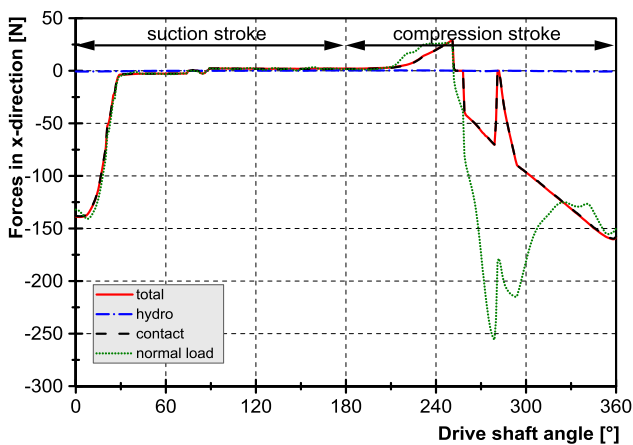


Figure 16: Results regarding friction forces of the polygon/slipper-contact and the transversal load on the piston

Figure 16 shows the friction forces in the polygon/slipper-contact and the transversal load  $F_x$  on the piston. Besides the total friction force  $F_\mu$  its share resulting from solid body friction and its share due to hydrodynamic friction are plotted. The hydrodynamic share is neglectable so that almost all the friction in this contact is due to solid body friction. Because a tilting of the polygon occurs, the transversal load deviates from the total friction force. Only when the tilting angle is zero the transversal force  $F_x$  is identical to the friction force  $F_\mu$ , e.g. at 325°.

Comparing the simulation results for the transversal load on the piston of the first simulation models plotted in fig. 10

(upper left side) to the results of the improved models it is visible that the transversal load simulated with the improved models is oscillating due to tilting of the ring. This characteristic is not visible in the results of the first models in fig. 6. There the transversal load is steadily rising during the compression stroke. In the measurement results plotted in fig. 6 and 7 an oscillating characteristic similar to the results of the improved models is visible, too. Nevertheless, a comparison of measurement and simulation is disputable at this point because of different operating points in the simulation and the measurement.

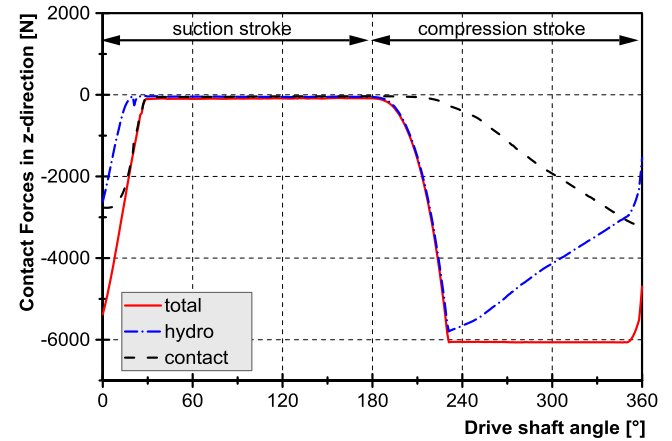


Figure 17: Results regarding contact forces of the polygon slipper-contact

In fig. 17 the contact forces in the polygon/slipper-contact are presented. Again distinctive squeeze-effects at the beginning of the compression stroke are visible. Solid body contact is avoided or reduced by these effects at the beginning and hence the friction force in x-direction starts on a low level. Later on, this effect decreases and consequently more and more of the load is carried by solid body contact.

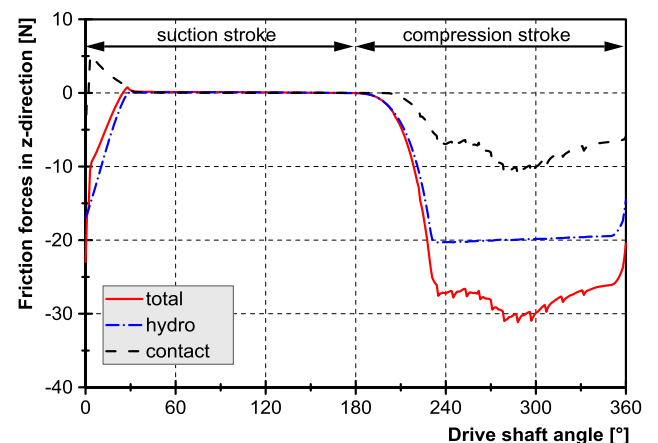


Figure 18: Results regarding friction forces of the slipper/polygon-contact

Figure 18 presents the friction forces in the piston/bushing-contact. Again, the total friction force is divided into its hydrodynamic friction share and its contact friction share. In contrast to the polygon/slipper-contact, the hydrodynamic

friction share is not negligible. Because of the huge pressure difference during the compression stroke of 1350 bar an intensive poiseuille flow leads to a hydrodynamic friction force of roughly 20 N. Because of the transversal load on the piston solid body contact occurs and hence a solid body friction force.

## 5 Conclusion and Outlook

In this paper an experimental and simulative approach for investigating the impact of new biofuels on the tribological contacts in common rail pumps was presented. Potential for further improvements on the experimental side and first results were discussed. These results are indicating a huge influence of the tilting  $\varphi$  of the polygon on the transversal load  $F_x$  on the piston. On the simulative side first simulation models and results for different fuels were presented. Those first models do not capture the tilting of the ring. In order to achieve a better compatibility with the measurements, the simulation models were improved and extended. The results for diesel show a better compatibility to the measurements, but a validation of the simulation by the measurement is not possible at this time, because there are several drawbacks mainly on the experimental side. To further increase comparability, improvements of the test rig will be done. This includes improvements of the pressure control in the rail, a better capturing of local temperatures and leakage measurements at the piston or at the compensation piston. After those modifications, testing of more typical operating points at higher speeds of more than 1000 rev/min will be possible as well as testing of different fuels.

## 6 Acknowledgement

This work was supported by the *Deutsche Forschungsgemeinschaft* (German Research Foundation) within the cluster of excellence 236 "Tailor-made Fuels from Biomass" [EXC 236].

## Nomenclature

Designation	Denotation	Unit
$A$	Area	[m <sup>2</sup> ]
$f_{ce}$	Centrifugal force	[N]
$x$	Coordinate	[m]
$f_{co}$	Coriolis force	[N]
$D$	Damping matrix	
$\rho$	Density	[kg/m <sup>3</sup> ]
$d$	Displacement	[m]
$e$	Eccentricity	[m]
$E$	E-module	[N/m <sup>2</sup> ]
$f_{ext}$	External force	[N]
$\Phi$	Flow factor	[-]
$F_i$	Force	[N]

$\mu$	Friction coefficient	[-]
$h$	Gap height	[m]
$f_{gy}$	Gyroscopic force	[N]
$L$	Length	[m]
$M$	Mass matrix	
$p$	Pressure	[bar]
$c$	Spring stiffness	[N/m]
$K$	Stiffness matrix	
$T$	Temperature	[°C]
$\varphi$	Tilting angle	[°]
$t$	Time	[s]
$v$	Velocity	[m/s]
$\eta$	Viscosity	[(N s)/m <sup>2</sup> ]

## References

- [1] A Fatemi, K Mausch, H Murrenhoff, K Leonhard. *Experimental investigation and theoretical prediction of the lubricity of biofuel components*. In: Fluid power and motion control: (FPMC 2010). Basildon : Hadleys, 2010. – ISBN 978–0–86197–181–4, pp. 39–51
- [2] K Mausch, A Fatemi, H Murrenhoff, K Leonhard. *A COSMO-RS based QSPR model for the lubricity of biodiesel and petro-diesel components*. In: Lubrication Science 23 (2011), Nr. 6, pp. 249–262. – ISSN 1557–6833
- [3] K Reif. *Moderne Diesel-Einspritzsysteme*. Wiesbaden : Vieweg + Teubner Verlag / GWV Fachverlage GmbH, 2010. – ISBN 978–3834813121
- [4] K-Th Renius. *Untersuchungen zur Reibung zwischen Kolben und Zylinder bei Schrägscheiben-Axialkolbenmaschinen*. In: VDI Forschungsheft 561, VDI-Verlag, Düsseldorf, 1974
- [5] O Koehler. *Anlaufreibungsverluste eines Schrägscheiben-Axialkolben-Motors*. In: Ölhydraulik und Pneumatik Nr. 31, Jahrgang 11, 1987
- [6] S Donders. *Kolbenmaschinen für HFA-Flüssigkeiten – Verlustanteile einer Schrägscheibeneinheit*. Verlag Mainz, Aachen, 1998
- [7] A Kleist. *Berechnung von Dicht- und Lagerfugen in hydrostatischen Maschinen*. Shaker Verlag, Aachen, 2002
- [8] R Lasaar. *Eine Untersuchung zur mikro- und makrogeometrischen Gestaltung der Kolben-/Zylinderbaugruppe von Schrägscheibenmaschinen*. VDI Verlag, Düsseldorf, 2003

- [9] D Breuer. *Reibung am Arbeitskolben von Schrägscheibenmaschinen im Langsamlauf*. Shaker Verlag, Aachen, 2007
- [10] S Drumm, S Heitzig, H Murrenhoff. *Friction measurement of plunger bushing contact in fuel injection pumps*. Proc. of Bath/ASME Symposium on Fluid Power & Motion Control, ISBN: 978-0-86197-187-9, S./Art.: 51-58
- [11] G Knoll, R Schönen, K Wilhelm. *Full Dynamic Analysis of Crank-shaft and Engine Block with Special Respect to Elastohydrodynamic Bearing Coupling*. In: Proceedings of the ASME Internal Combustion Engine (ICE) Division Meeting Bd. 28, 1997, pp. 1–8
- [12] R Schönen. *Strukturdynamische Mehrkörpersimulation des Verbrennungsmotors mit elastohydrodynamischer Grundlagerkopplung*. Kassel: Kassel Univ. Press, 2003 (Fortschrittsberichte Strukturanalyse und Tribologie, Teil 15). – ISBN 3–89958–507–0
- [13] N Patir, H S Cheng. *Application of Average Flow Model to Lubrication Between Rough Sliding Surfaces*. In: Journal of Lubrication Technology 101 (1979), Nr. 2, pp. 220–229
- [14] S Drumm, A Wohlers, A Fatemi, H Murrenhoff. *Viscosity and bulk modulus measurements under high pressure conditions*. In: Society of Tribologists and Lubrication Engineers annual meeting and exhibition 2010: Las Vegas, Nevada, USA, 16 - 20 May 2010. Red Hook, NY : Curran, 2010. – ISBN 978–1–61738–727–2, pp. 413–416
- [15] S Heitzig, S Drumm, L Leonhard, H Murrenhoff, J Lang, G Knoll. *Simulative Analysis of the Tribological Contacts of Common Rail Injection Pumps Lubricated by Tailor-Made Biofuels*. In: Tribologie und Schmierungstechnik
- [16] S. M. Drumm. *Entwicklung von Messmethoden hydraulischer Kraftstoffeigenschaften unter Hochdruck*. Shaker Verlag, Aachen, 2012
- [17] T. Illner,. *Oszillierendes kippbewegliches Axialgleitlager bei Grenzreibung und Kraftstoffschmierung*. Shaker Verlag, Aachen, 2010
- [18] J Blume. *Druck- und Temperatureinfluß auf Viskosität und Kompressibilität von flüssigen Schmierstoffen*, RWTH Aachen, Diss., 1987

# Hydraulic Fluid Properties and their Impact on Energy Efficiency

Karl-Erik Rydberg

Division of Fluid and Mechatronic Systems, Department of Management and Engineering

Linköping University, Linköping, Sweden

[karl-erik.rydberg@liu.se](mailto:karl-erik.rydberg@liu.se)

## Abstract

To meet the increased requirements on higher efficiency and better functionality of hydraulic systems, new components and system concepts have been developed over the years. However, the most important component in a hydraulic system, which has a major impact on system efficiency and wear are the fluid itself. The last decades, major attention on hydraulic fluid development, have been set upon environmental adaption. Today, energy efficiency has been a hot topic and a number of energy efficient fluids have been launched on the market. Besides energy efficiency, environmental adaption of fluids, are extremely important in mobile applications.

In this paper the focus is set on hydraulic fluid properties and its impact on system efficiency. Environmental adapted fluids will also be discussed. Synthetic saturated esters are analysed and compared with mineral oils. The main question that will be tried to answer is - "How to select the best fluid for a specific application?".

**Keywords:** Hydraulic fluids, Synthetic esters, Fluid properties, Viscosity, Energy efficiency.

## 1 Introduction

The pressure media is the most important component in the hydraulic system because it takes care of the energy transfer in the whole system from pump to cylinder / motor. Additionally the hydraulic fluid has to provide lubrication and cooling. Especially in mobile applications it is of great importance to minimize the negative environmental influence from hydraulics.

### 1.1 Environmental adapted fluids

In order to make hydraulic fluids environmentally adapted a number of synthetic fluids have been developed. One of the most promising fluids is saturated synthetic esters. This type of fluid has many interesting properties to explore. Synthetic saturated esters have been on the market for more than 10 years, but the evaluation of their properties is still limited. However, the results so far about the lubrication properties, viscosity index, and stability etc are very positive, see **Fig. 1**. There is no doubt that the synthetic esters can be considered as a

future product with a high development potential.

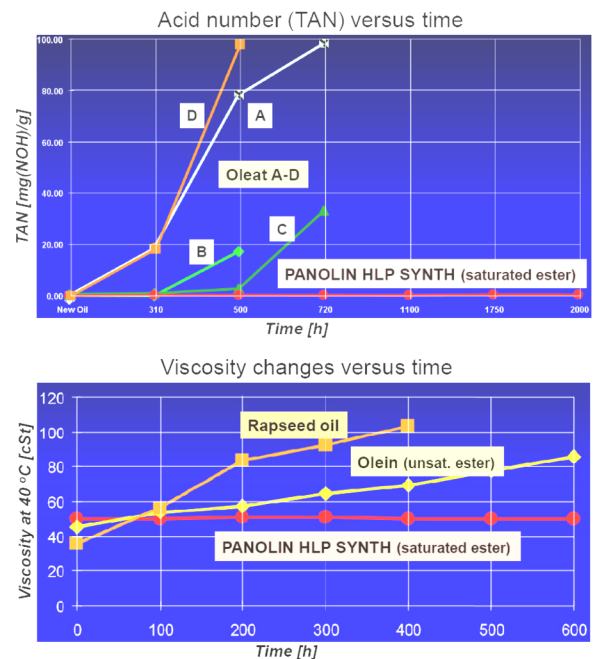


**Fig. 1:** Acid number and viscosity stability of saturated ester, Panolin HLP Synth, [2].

From Fig. 1 it can be seen that the saturated ester (Panolin HLP Synthetic) has extremely stable acid number (TAN) and viscosity compared to unsaturated esters. In comparison with mineral oil the saturated ester also shows impressive shear stability over the time.

## 1.2 Energy efficient fluids

In order to maximize energy efficiencies in hydraulic systems, mechanical and volumetric losses must be balanced so the sum of these losses is minimized. Since the mechanical losses in sealing gaps are proportional to the fluid viscosity and volumetric losses inverse proportional to viscosity, it is clear that an optimal viscosity exists.

Fluid viscosity is not the only parameter that improves energy efficiency. Also, friction coefficient provided by the fluid in sealing gaps as well as the viscosity index (VI) of the fluid is very important parameters. Looking at the development of engine lubricants for cars it can be noted that today's fluids are low viscosity oils with friction modifiers and VI improvers. It has been proven that this kind of fluids have a significant impact on fuel consumption.

The fluid properties impact on hydraulic system energy efficiency has been clearly validated in a NSF-sponsored project at *Center for Compact and Efficient Fluid Power (CCEFP)* in US. An excavator has been selected as a primary vehicle for a test bed, [3]. As a member of this project, Evonik RohMax has developed a new multi-grade fluid, optimized with high-tech polymer additives and friction modifiers. Field tests, performed by Evonik RohMax, on excavators show efficiency gains between 18 and 26%, depending on work cycle, [4]. The importance of high viscosity index (VI>160) and good shear stability has also been stated.

## 1.3 Fluid viscosity grade and viscosity index

Selection of an energy efficient fluid for a specific hydraulic application is highly associated with a proper viscosity grade and the viscosity index (VI) of the fluid.

The standard viscosity grade, ISO VG gives the fluid viscosity in cSt at the temperature 40 °C. In mobile applications the most commonly used viscosity grade is VG 46. However, if the hydraulic system contains high speed pumps and motors as well as long lines a lower

VG-value will boost the efficiency. Using fluids with low VG-value (VG 32 or VG20) in mobile machines it is very important to take the viscosity index into account. The lower VG-value the higher VI-value is required.

In mobile applications where the fluid temperature variations can be very high the viscosity index (VI) has a high impact on energy efficiency. RohMax in US, a leading manufacturer of hydraulic fluid additives, has investigated the impact of VI on hydraulic pump efficiency in mobile application, [5]. They have developed a fluid with very high shear stability and tested the fluid in Eaton-Vickers vane pumps. The efficiency improvements versus fluid temperature at different VI-values are shown in **Fig. 2**. The 0-level stays for VI=100.

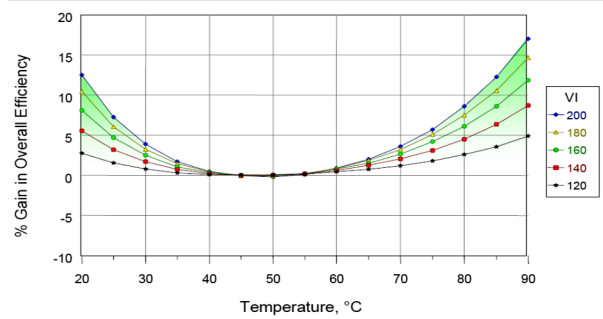


**Fig. 2:** Gain in pump efficiency versus fluid temperature with VI as parameter, [5].

The above figure shows that VI > 160 is needed if the fluid temperature rang is bigger than 50 °C. It is also worth to be mentioned that these figures belongs to one specific pump. In practice, the required VI-value depends upon the type of pump, the pump speed range and the system pressure range.

## 2 Viscosity dependent losses in hydraulic pipes

Hydraulic systems are commonly included long pipe. The pressure losses in a straight pipe are theoretically calculated as follows:

$$\text{Laminar flow: } \Delta p_{lam} = \frac{32 \cdot L \cdot \eta}{d^2} \cdot v_m \quad (1)$$

$$\text{Turbulent flow: } \Delta p_{turb} = \frac{0,068 \cdot L}{d^{1.25}} \cdot \rho^{0.75} \cdot \eta^{0.25} \cdot v_m^{1.75} \quad (2)$$

where  $d$  = pipe diameter [m],  $L$  = pipe length [m],  $\eta$  = dynamic viscosity [Ns/m<sup>2</sup>],  $\rho$  = fluid density [kg/m<sup>3</sup>],  $v_m$  = average flow velocity [m/s].

Calculated pressure drop across a 15 m long pipe with

two different viscosities of the fluid (VG 46), are illustrated in **Fig. 3**.

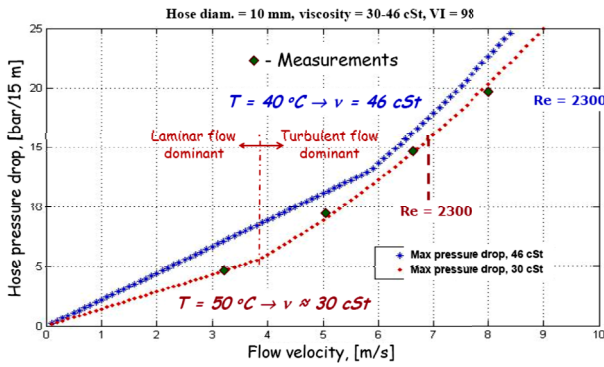


**Fig. 3:** Pressure drop in a 15 m long pipe ( $\phi=10$  mm) versus flow velocity for the viscosity 30 and 46 cSt.

Comparison with measurements in Fig. 3, shows that the real pressure drop follows the theoretical values if this is calculated as,

$$\Delta p = \max\{\Delta p_{lam}, \Delta p_{urb}\} \quad (3)$$

From the figure it can be observed that the turbulent flow starts to increase the pressure drop at a much lower Re-number than the critical value (2300). In Fig 4,  $\Delta p_{urb}$  is bigger than  $\Delta p_{lam}$  for all  $Re > 0,56 \cdot 2300$ . In practice, the transition from laminar to turbulent stage is very smooth and not as an immediate switch at  $Re = 2300$ .

### 2.1 Pressure drop measurements

Pressure drop measurements have been performed at the division of Fluid and Mechatronic Systems in Linköping, Sweden. The principle layout of the used test-stand is illustrated in **Fig. 4**.

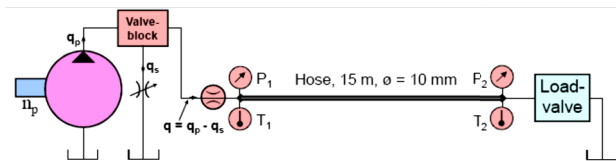


**Fig. 4:** Test-stand for measurements of pressure drop in pipes.

The test object is 15 m long hose with an inner diameter of 10 mm. The fluids that have been tested are one mineral oil (VG 46), four different synthetic saturated esters (three VG 32 fluids and one VG 12) and one low viscosity fluid an eco-diesel (VG 3). Measured hose pressure drop versus fluid velocity for these six fluids are shown in **Fig. 5**. More details about the pressure drop tests and fluid examinations are presented in ref. [6].

The test results demonstrated in Fig. 5, are all following the theoretical calculations according to eq. (3).

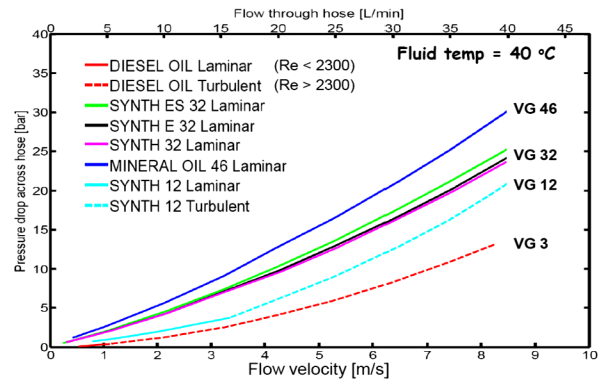


**Fig. 5:** Measured pressure drop in a 15 m long hose ( $\phi=10$  mm) versus flow velocity for 6 different fluids.

### 3 Energy efficiency of pumps and motors

All hydraulic systems are containing at least one pump. The pump is a primary system unit that has to transform mechanical energy into hydraulic energy. Therefore, the pump efficiency has a significant impact on the overall system efficiency. The pump efficiency is related to the dominant losses, which are volumetric (leakage) and mechanical (friction) losses. These losses are mainly affected by the fluid viscosity. In order to analyse the viscosity impact on pump efficiency a model can be used.

Based on a semi-empirical efficiency model for axial piston machines, [1], **Fig. 6** shows simulated pump efficiencies as a function of fluid viscosity.

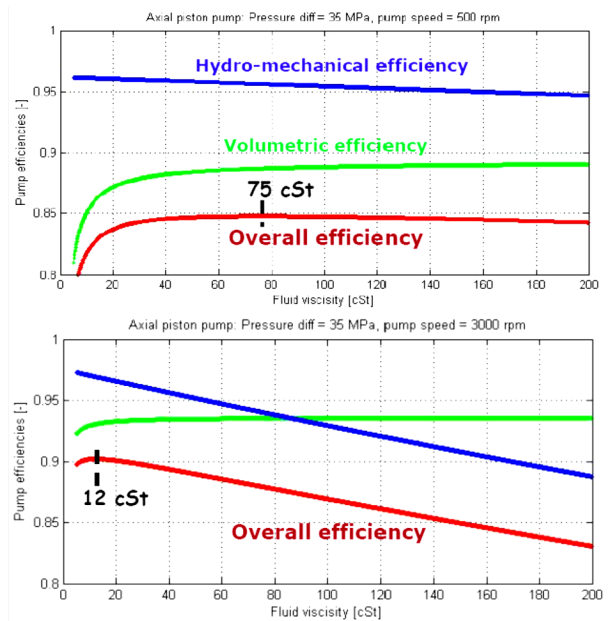


**Fig. 6:** Efficiencies versus fluid viscosity for an in-line axial piston pump at two speeds, 500 and 3000 rpm.

Fig. 6 shows that the viscosity, which maximize the pump overall efficiency is related to operation conditions, pressure and speed.

From the efficiency model the dynamic viscosity ( $\eta$ ) that gives max efficiency can be expressed as,

$$\eta_{opt} = \frac{p_p}{n_p} \cdot \sqrt{\frac{C_v}{k_v}} \quad (4)$$

where  $C_v$  and  $k_v$  are machine constants,  $p_p$  = pump pressure and  $n_p$  = pump speed.

Equation (4) is applicable on both pump and motors, but it has to be observed that the machine constants can varies in a wide range, depending on the type of machines.

### 3.1 Hydrostatic transmission efficiency

Hydrostatic transmissions are widely used in drive train for working machines. In a wheel loader or forwarder (forest machine) the drive transmission stays for more than 50% of the energy consumption. Therefore, it is highly important to make an analyses of how the fluid properties will affect the transmission overall efficiency.

The transmission investigated in this study is schematically depicted in *Fig. 7*.

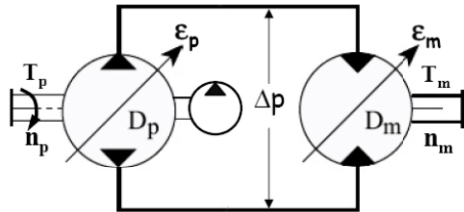


*Fig. 7: Schematic drawing of the test transmission.*

The transmission concept is traditional, with variable displacement axial piston units as pump (In-line) and motor (Bent-axis). The main pump is supported with a fixed displacement boost pump.

For theoretical examination of transmission efficiency the pump and motor loss models, developed for axial piston units, reference [1], is used.

The variable pump, volumetric and hydro-mechanical efficiencies are expressed as.

$$\eta_{vp} = 1 - a_{0p} - \left( \frac{a_{1p} + a_2}{\epsilon_p} \right) \frac{\Delta p}{\beta_e} - a_{3p} \frac{\Delta p}{2\pi\eta\epsilon_p n_p} - a_{4p} \frac{\Delta p^2}{\epsilon_p n_p} \quad (5)$$

$$\eta_{mp} = \frac{1}{1 + \frac{b_{0p}}{\epsilon_p} + b_{1p} + \left( \frac{b_{2p} + b_{3p}}{\epsilon_p} \right) \frac{p_L + b_{4p}}{\Delta p} + b_{5p} \frac{p_H + \delta_p p_L}{1 + \left( \frac{n_p}{n_{0p}} \right)^{\gamma_p}} + b_{6p} \frac{2\pi\eta n_p}{\epsilon_p \Delta p} + b_{6p} \frac{\epsilon_p^2 n_p^2}{\Delta p}} \quad (6)$$

The efficiencies of the variable motor are,

$$\eta_{vm} = \frac{1}{1 + a_{0m} + \left( \frac{a_{1m}}{\epsilon_m} \right) \frac{\Delta p}{\beta_e} + a_{2m} \frac{\Delta p}{2\pi\eta\epsilon_m n_m} + a_{3m} \frac{\Delta p^2}{\epsilon_m n_m}} \quad (7)$$

$$\eta_{hmm} = 1 - \frac{b_{0m}}{\epsilon_m} + b_{1m} + \left( \frac{b_{2m} + b_{3m}}{\epsilon_m} \right) \frac{p_L + b_{4m}}{\Delta p} + b_{5m} \frac{p_H + \delta_p p_L}{1 + \left( \frac{n_m}{n_{0m}} \right)^{\gamma_m}} + b_{6m} \frac{2\pi\eta n_m}{\epsilon_m \Delta p} + b_{6m} \frac{\epsilon_m^2 n_m^2}{\Delta p} \quad (8)$$

In equation (5) - (8),  $a$  and  $b$  are machine dependent loss coefficients,  $\eta$  = fluid dynamic viscosity,  $\Delta p$  = transmission pressure difference,  $n$  = shaft speed and  $\epsilon$  = displacement setting.

The overall transmission efficiency, with exclusion of the boost pump, is calculated as,

$$\eta_{t,o} = \frac{T_m \cdot n_m}{T_p \cdot n_p} = \eta_{vp} \cdot \eta_{hmp} \cdot \eta_{vm} \cdot \eta_{hmm} \quad (9)$$

Including the boost pump power, the overall efficiency is expressed as,

$$\eta_{t,bp,o} = \frac{T_m \cdot n_m}{(T_p + T_{bp}) \cdot n_p} \quad (10)$$

where  $T$  = shaft torque.

### 3.2 Theoretical analysis of transmission efficiency

In the analysed transmission (see Fig 7), the main pump and motor have max displacement of  $D_p = 110 \text{ cm}^3/\text{rev}$  and  $D_m = 150 \text{ cm}^3/\text{rev}$ , respectively. The boost pump displacement is  $D_{bp} = 0,2D_p$ . Simulated efficiency characteristic of the sequence controlled transmission, without boost pump, is presented in *Fig. 8*.

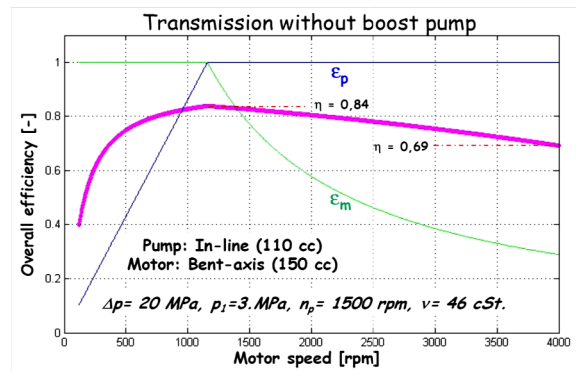


*Fig. 8: Simulated transmission overall efficiency versus motor speed, without boost pump,  $v = 46 \text{ cSt}$ .*

The transmission efficiency characteristic in Fig. 8 is calculated for operation conditions of constant pump

speed,  $n_p = 1500$  rpm, constant pressure difference,  $\Delta p = 20$  MPa, constant low pressure (boost pressure),  $p_1 = 3$  MPa and a fluid viscosity of 46 cSt. Max efficiency (84%) is reached, as expected, when the pump and motor have max displacement stroking ( $\epsilon_p = \epsilon_m = 1.0$ ). When the motor speed is increased from 1000 rpm to 4000 rpm the efficiency goes down, mainly because of viscosity and speed dependent friction and pressure losses. At the motor speed, 4000 rpm the transmission efficiency is reduced to 69%.

If the boost pump is included in the efficiency calculations (Eq. 10), the efficiency graph became as in **Fig. 9**. At constant pump speed the boost pump power is constant, around 3 % of the main pump power, when  $\epsilon_p = 1.0$  and  $\Delta p = 20$  MPa. Therefore, the boost pump will reduce the transmission overall efficiency approximately 3% (when  $\epsilon_p = 1.0$ ), compared to the case in Fig. 8.

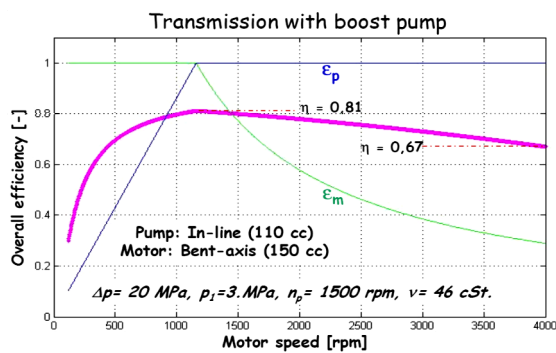


**Fig. 9:** Simulated transmission overall efficiency versus motor speed, with boost pump,  $v = 46$  cSt.

According to equation (4), the fluid viscosity that maximizes the efficiency of a hydraulic machine, depends upon pressure and speed. By using a low viscosity fluid (VG 12) in the transmission, it can be expected that its efficiency will be mostly gained at high motor speed. This is confirmed by the characteristics shown in **Fig. 10**.

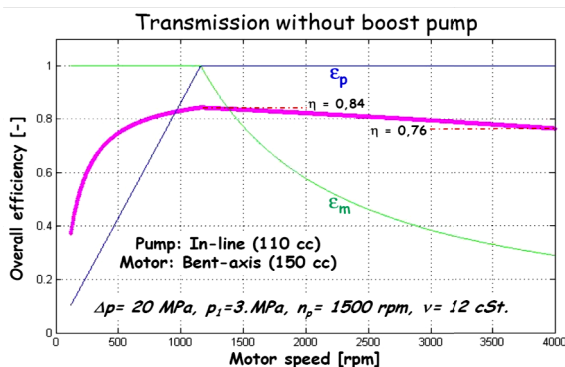


**Fig. 10:** Simulated transmission overall efficiency versus motor speed, without boost pump,  $v = 12$  cSt.

Energy efficient hydraulic fluids, is the commonly used name for fluids containing specific friction modifiers. For mobile applications these fluids also have high viscosity index ( $VI > 150$ ) and high shear stability, [7].

Focusing on the friction modifiers impact on transmission efficiency, this can be evaluated by reduction of the friction coefficient values in the efficiency model (eq. 5 – 8). In **Fig. 11**, the transmission efficiency characteristics (boost pump included) are shown for  $\Delta p = 40$  MPa, but two friction cases - original friction coefficients and with reduced friction, 25% of original values.

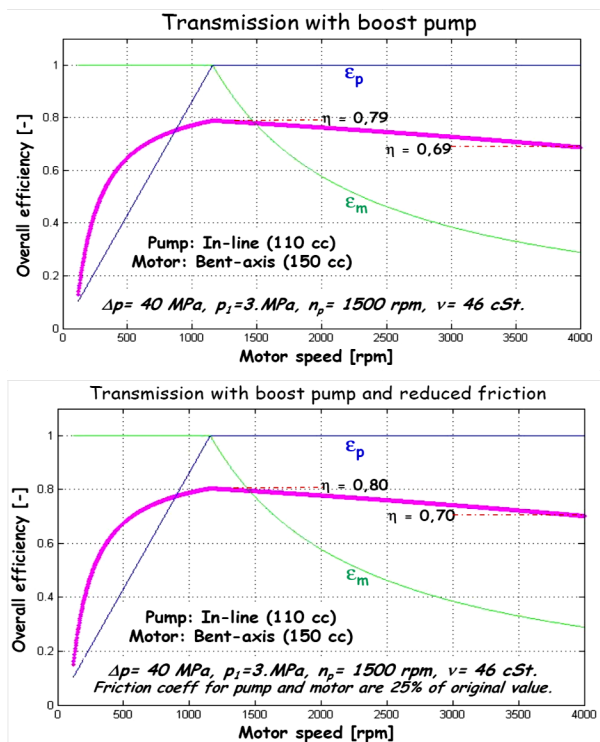


**Fig. 11:** Simulated transmission overall efficiency versus motor speed, with boost pump, without and with reduced friction.

The figure above shows that this dramatic reduction of friction only will increase the efficiency about 1%. This example demonstrates that, to reach an efficiency gain around 20%, according to reference [4] and [7], it is not enough to use fluids with friction modifiers, VG- and VI-values as well as shear stability must be adjusted for the application.

It has to be noted that the conducted work presented above is just a theoretical analyses based on semi-empirical efficiency models validated for axial piston units, [1].

### 3.4 Experimental validation of efficiencies

In a transmission test-stand at FluMeS lab in Linköping, some efficiency measurements have been conducted. The test object is similar to the transmission shown in Fig. 7. The tests have been performed at max displacement setting of pump and motor ( $\epsilon_p = \epsilon_m = 1,0$ ). Test results are presented in Fig. 12-14.

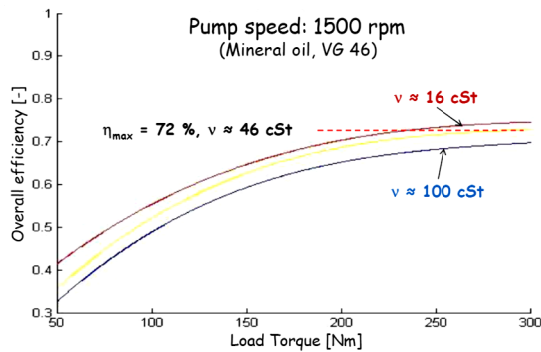


Fig. 12: Measure transmission overall efficiency versus Load Torque, (boost pump incl.), mineral oil VG 46.

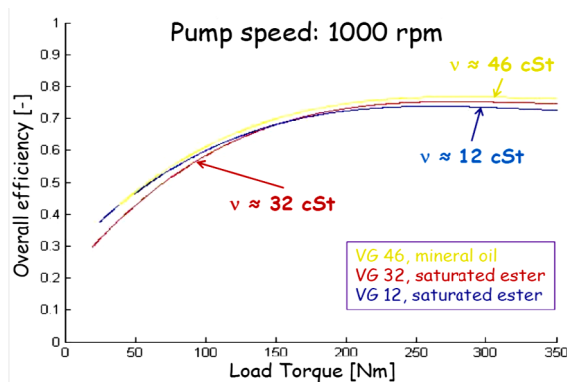


Fig. 13: Measure transmission overall efficiency versus Load Torque, (boost pump incl.), for three different fluids.

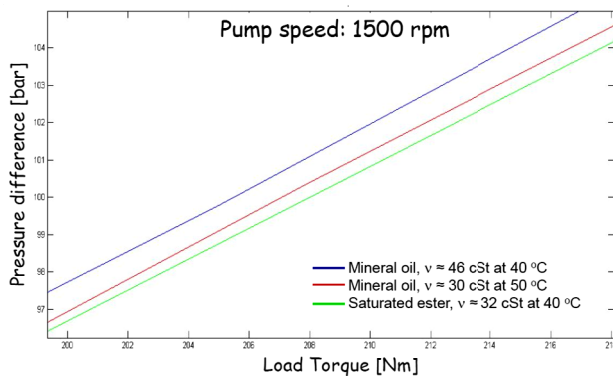


Fig. 14: Measured transmission pressure difference versus Load Torque, (boost pump incl.).

Fig. 12 illustrates the transmission efficiency for

mineral oil, at three different fluid temperatures and thereby three different viscosities, 16, 46 and 100 cSt. From the lowest to the highest viscosity the change in efficiency is about 5 %. It can be noted that this viscosity impact on efficiency corresponds quite well to simulation results presented in this paper (see Fig. 9 and 10).

In Fig. 13 two saturated esters (VG 12 and VG 32) are compared with a mineral oil (VG 46) at low pump speed (1000 rpm). The figure shows that optimal fluid viscosity is load dependent. Increased transmission pressure requires higher viscosity to maximize the efficiency. Also the lubrication property of saturated esters is better than for mineral oil. Fig. 14 demonstrates that the ester creates lower friction losses than mineral oil.

## 4 How to select the best fluid?

The hydraulic fluid is one of the most important design factors in a hydraulic system and should be considered as a machine element, possible to develop as well as the other hydraulic components in a system.

Fluid selection must be based on a detailed system specification - containing type of components, system pressure range, pump and motor speed range and operation temperature range. Also, expected operation time and reliability must be included in the specification.

Optimal VG-value for the specified system can be found by using theoretical models, which are validated by practical tests. The estimated temperature range for maximum power operation gives the requirement on viscosity index (VI).

Especially in high pressure systems the fluid lubricity is of high importance. It is a well known fact that synthetic esters, gives lower friction and wear than mineral oil. Ester fluids also have higher heat capacity than mineral oils, which results in lower temperature variations. Field tests conducted by the Forestry Research Institute of Sweden, confirms that the steady state fluid temperature in a forest machine, will be reduced 5-10 °C with use of synthetic esters instead of mineral oils.

Several decades of documented experience shows that the lifetime of a hydraulic system (including the fluid) depends mainly on the cleanliness of the fluid, stability and working temperature. A clean fluid (low amount of particles, low water and air content) with good stability regarding viscosity and acid number that can work in a

suitable temperature gives a very long system lifetime. It is also a very well known fact that there is a clear connection between the cleanliness, stability and temperature of the fluid. The reason is that particles and water, in combination with high temperature give an accelerating oxidation of the fluid and a faster brake down of the additives.

## 5 Conclusions

The theoretical and practical results presented in this paper, demonstrates that the efficiency of a system is strongly dependent on the viscosity of the hydraulic fluid. The “optimal” viscosity is however, dependent on the pressure level and speed. In an application the viscosity should be selected so that the efficiency is maximized within the pressure and speed where the biggest amount of energy is transferred so that one can reduce the energy losses.

The viscosity index is highly important in mobile systems. It is also stated that synthetic ester fluids gives lower friction losses than standard mineral oil. The shear stability of saturated esters is extremely good compared to mineral oil and unsaturated esters.

However, these facts just represent a part of the information needed to find the “optimal” fluid for a specific application. Besides theoretical facts a solid experience is needed for a satisfactory fluid selection. Finally, this paper demonstrate, that there is no simple answer of the question “How to select the best fluid?”. To find a relevant answer, a good choice is to start with a detailed system specification and try to convert the specification into fluid requirements.

## Acknowledgement

This work has been supported by the *Swedish Fluid Power Association* (IFS).

## References

- [1] Rydberg K-E.: *On performance optimization and digital control of hydrostatic drives for vehicle applications*. Ph.D. thesis no 99, Linköping University, Sweden, 1983.
- [2] K Eriksson: *Environmental adapted pressure media versus mineral oils*, (in Swedish). Presentation at National Hydraulic Days, Linköping, May 30-31, 2007.

- [3] *High Efficiency Excavator*. Info\_CCEFP\_Excavator. Center for Compact and Efficient Fluid Power, US, March 16, 2011.
- [4] A Presher: *New Hydraulic Fluids Aimed at Energy Savings*. Design News, October 2009.
- [5] C K Dustman, Rohmax USA. *Performance Benefits of High Viscosity Index Hydraulic Fluids*. Lubricants-Russia – 2006, Moscow, November 24, 2006.
- [6] S Javalagi, S Singireddy: *Hydraulic fluid properties and its influence on system performance*. Master’s Thesis, LIU-IEI-TEK-A--12/01284—SE, Linköping Univ., 2012.
- [7] S Herzog: *Improving Fuel Economy and Productivity of Mobile Equipment through Hydraulic Fluid Selection*. Evonik Rohmax USA, 2011.
- [8] TechBulletin: *HYDREX<sub>TM</sub> Energy Efficiencies in Mobile Equipment*. Petro-Canada, 2010.



# Pneumatics



## **Fast switching pneumatic valves: experimental bench for flow and pulsed air jet characterizations**

T. Ferreira, S. Sesmat, E. Bideaux, F. Sixdenier

Laboratoire Ampère, Université de Lyon, Lyon, France

E-mail: Thiago.caetano-ferreira@insa-lyon.fr, Sylvie.sesmat@insa-lyon.fr, Eric.bideaux@insa-lyon.fr, Fabien.sixdenier@univ-lyon1.fr

### **Abstract**

This paper presents a new experimental bench which allows the characterization of different fast switching valves in terms of flow rate and free air jet generation. By using this new bench, it is possible to study the different phenomena that may occur in the inner and outer circuits from the source up to the free jet. The different sensors positioned at key points along the air circuit allow the determination of the flow characteristics as well as the dynamic behavior of the different components during the generation of the pulsed air jets. By the tests performed with a fast spool-sleeve valve, it was possible to determine its flow characteristics (sonic conductance and critical pressure ratio). These values were used to build an average mass flow rate curve which is compared to the one measured by using a flowmeter during dynamic tests. This comparison enables to evaluate the limit frequency up to which the steady state flow characteristics can be used to estimate the average mass flow rate during dynamic operation. The next step consists in exploring the jet in a 3D space by using a 5-hole probe which provides the information on pressure, temperature and velocity necessary to determine the most suitable zone to perform object sorting with the jet. Also its unsteady behavior can be observed allowing the identification of the limit frequency at which the jet efficiency starts to decrease.

**Keywords:** Fast switching, pneumatic valve, pulsed air jet, mass flow rate characterization

### **1 Introduction**

The development of new fast switching pneumatic devices is an important challenge for the fluid power industry [1][2][3]. The use of these elements on power transmission provides benefits in terms of power density, compactness, possibility to work in harsh environments, reliability and low cost.

The market for fast switching pneumatic valves with high flow capacity is in growth. Most manufacturers offer these components for pulsed air jets generation and the applications can be in the automotive industry, food processing, sorting elements and so forth. They also announce their products can achieve response time on the order of a few milliseconds, which leads to the generation of jets at frequencies up to 1 kHz, for flow rates about 150 NI/min (ANR).

First of all, for the food processing and sorting applications, the distance between the generated jets is highly constrained in a way the sorting operation can be precisely executed. Due to this fact, the miniaturization of the valve is also a major problem for these components, once the product must

keep the small dispersion on response time and flow, good energy efficiency and long lifetime.

Also to perform the sorting operation it is necessary to know the jet coming from the valve and understand how is it affected by the dynamic behavior of the mechanical elements.

Some theoretical and simulation studies have been already carried out [4][5] and present theories and analytical formulation for air jets under certain conditions. However, steady state and dynamic behaviors of the whole circuit (valve, inner and outer circuit and free air jet) are being studied recently. [6][7][8][9].

Motivated by this problematic, an experimental bench was designed and built in order to evaluate the mechanical and pneumatic performances on air jet generation by fast switching valves. This bench enables the evaluation of the flow along the entire path from the source up to the free air jet and under different working conditions.

## 2 Objective

This paper presents the experimental bench designed to study the mechanical and pneumatic behavior of the system used in sorting applications. The steady state flow characteristics of a system composed by an inner circuit, fast switching valve and nozzle can be determined with no need of disassembling the different elements. In a same way, the study of their performances in dynamic applications can also be performed.

From the steady state mass flow rate characteristics of the valve, and its dynamic response, it becomes possible to determine the average mass flow rate according to the working frequency of the system.

The analysis carried out enables the determination of the mechanical limitation of the system as well as the pneumatic behavior of the air flow in the inner circuit.

Also, a first study of a steady jet is presented. Its complete characterization using a multi-hole probe will be performed in the next steps and also the influence of the system's dynamics on pulsed air jet generation.

## 3 Experimental procedure

### 3.1 Test bench

The experimental bench was developed in a way to study and understand the different phenomena occurring along the flow path from the source up to the free jet. The bench is presented in Figure 1.

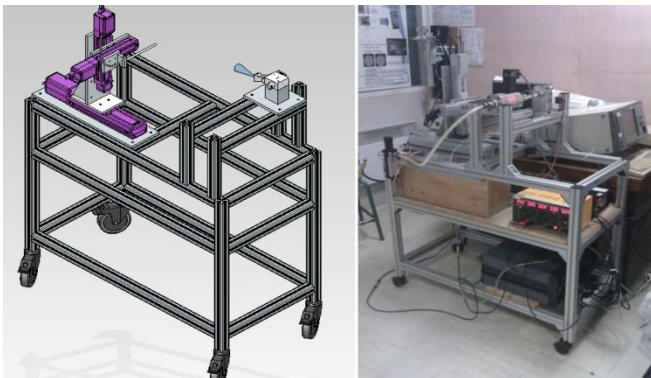


Figure 1: Experimental bench.

The pressures along the circuit upstream to the nozzle are measured using miniature pressure sensors to be able to measure dynamic pressure with a high bandwidth. In order to obtain the position of the pneumatic shutter of the valve, a magnetic displacement sensor is used. The average air mass flow rate is measured by a mass flowmeter placed between the inlet and a tank used to filter the pressure oscillations induced by the frequency operation of the valve.

A 3-axis robot is used to precisely move a 5-hole probe (Figure 2), designed by Aeroprobe [10]. This enables the determination of the total and static pressures, total temperature and velocity (module and orientation) at

different points in the free air jet. It is done by measuring the pressures and temperature at the tip of the probe. [11][12]

This device allows having a better understanding of the jet in order to optimize the energy required to eject different objects by using a pulsed air jet.



Figure 2: 5-Holes probe [10]

### 3.2 Steady State characterization

The scheme in Figure 3 shows the complete pneumatic circuit and the location of the sensors.

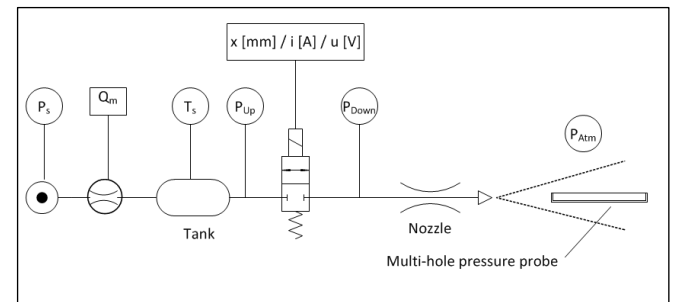


Figure 3: Pneumatic circuit scheme

In order to determine the flow rate characteristics of the different parts of the circuit upstream to the nozzle, it is necessary to build for each part the pneumatic conductance curve function of the downstream to upstream pressure ratio. Considering the flow as being adiabatic, the conductance can be calculated from the measurement of steady state mass flow rate, pressures upstream and downstream the element and temperature measured at the source  $T_s$  (equation 1).

$$C_e \left( \frac{P_d}{P_u} \right) = \frac{q_m \left( \frac{P_d}{P_u} \right)}{\rho_0 P_u} \sqrt{\frac{T_s}{T_0}} \quad (1)$$

Usually the sonic conductance and the critical pressure ratio of the valve are determined in steady state flow for the completely opened flow section according to ISO 6358 standard [13]. In this way, during simulations of pneumatic behavior of solenoid valves, it is of common sense to use, for intermediate positions, a conductance value proportional to the sonic conductance by a factor  $x$  ( $0 < x \leq 1$ ) which takes into account the intermediate flow sections. The

critical pressure ratio is supposed to be constant for all positions.

In this particular studied valve, due to its functioning way and the present sensors, it is possible to obtain one flow rate measurement for each intermediate position of the spool, which leads to intermediate points for the conductance curve.

In order to complete the steady state characterization, measurements with the 5-Holes probe were performed in a steady jet issued from the system.

### 3.3 Dynamic characterization

As the valve is used to generate pulsed jets, the understanding of its dynamic behavior is mandatory. In such mechanical systems different phenomena may occur (resonance, blocking, shocks) which may lead to a misuse and degradation of their performance. It is expected that these events have a direct influence on the pulsed jet generation. However, the real relation has yet to be determined.

Assuming that the flow rate is instantaneously established the dynamic mass flow rate  $q_m(t)$  for a given time, can be calculated using the steady state flow characteristics depending on the mobile part position  $x(t)$  with equation 2 [14].

$$q_m(t) = C(x(t)) \cdot \rho_0 \cdot P_u(t) \sqrt{\frac{T_0}{T_s}} \cdot \left( 1 - \left( \frac{P_d(t) - b(x(t))}{P_u(t) - b(x(t))} \right)^2 \right)^m \quad (2)$$

By integrating  $q_m(t)$  on one cycle, one can obtain the average mass flow rate  $Q_m$  flowing through the valve and compare it with the measurement performed by the mass flowmeter after stabilization for a given frequency.

## 4 Results

### 4.1 – Steady state characterization

The tests were performed with a 2 stage spool and sleeve valve. The opening operation is performed by turning its electromagnetic actuator on, which allows the air to flow and push a spool inside a sleeve opening the flow section of the valve. To close, the electric circuit is turned off and the spool is returned to its initial position by means of a flat spring.

The displacement of the spool is measured as well as the voltage and current on the electrical circuit of the actuator. Also the mass flow rate is obtained by using the mass flowmeter as shown in Figure 3.

First of all, in order to identify the working pressure range of the valve first measurements were performed. In this test, the upstream pressure  $P_{Up}$  was progressively increased

whilst the spool displacement and the flow rate were measured. The resulting curve is presented in Figure 4.

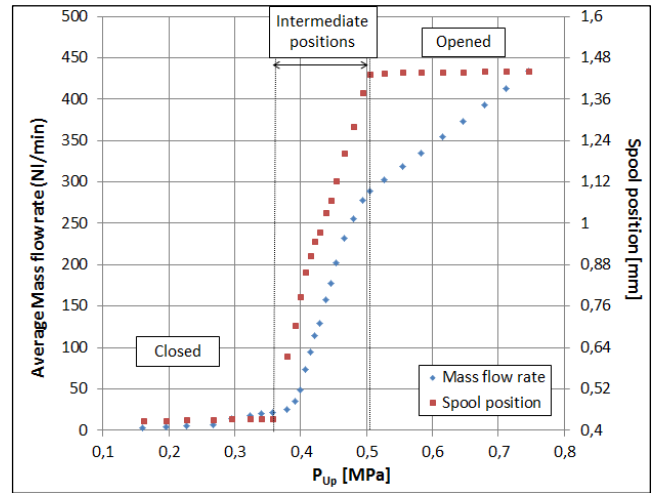


Figure 4: Flow rate and spool position function of the upstream pressure  $P_{Up}$ .

Three different zones can be distinguished in this figure. Up to an upstream absolute pressure of 0,35 MPa the valve remains closed. The slight rising on the flow rate is due to the functional leakage of the system. From 0,35 to 0,5 MPa, the spool is in an intermediate position and the flow section is not completely opened. Above the pressure of 0,5 MPa the spool reaches its maximum displacement and the flow increases proportionally to the upstream pressure.

For the steady state characterization of the components present in the circuit, the upstream pressure  $P_S$  is set in intermediate values up to 0,7 MPa to vary the pressure ratios. During the tests, different pressures along the circuit are measured (see Figure 3). From the values obtained the different conductance curves of the components can be drawn according to equation 1.

In Figure 5 an unusual conductance curve of the valve is presented. In a similar way as in Figure 4, it is possible to identify 3 different zones. The first points (red diamond shaped) represent the rising upstream pressure with the valve still closed. As the pressure keeps rising whilst the spool still in its initial position, we observe a saturation behavior which could indicate a choked leakage flow even before its opening. This hypothesis seems not to be equivocal once the minimal pressure to open the component is already at 0,35 MPa.

Another important zone is the points with maximum opening where the flow is certainly choked (purple circles) once they all have the same conductance and pressure ratio values. The pressure ratio is blocked to its critical value whatever is the upstream pressure.

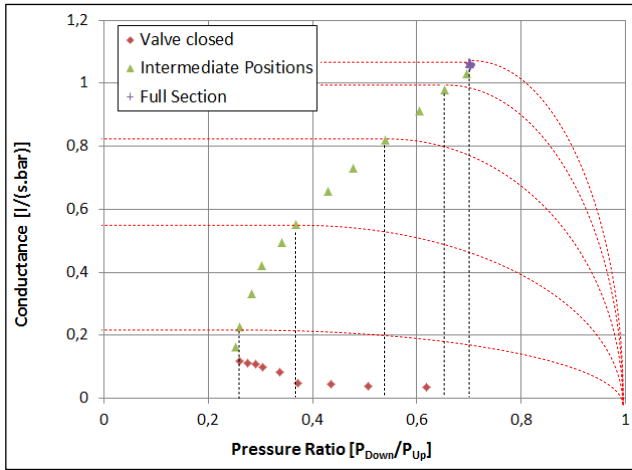


Figure 5: Measured Conductance curve of the Valve for different positions ( $P_{Up}$  to  $P_{Down}$ ).

These facts lead to a strong hypothesis: considering all the intermediate points as being critical flows for intermediate flow sections (see dotted lines in Figure 5).

Due to the assumptions, it is then possible to determine a relation of the sonic conductance (Figure 6a) and critical pressure ratio of the valve (Figure 6b) for different spool positions. Using these curves and having the position and pressure values measured during the dynamic tests, it is possible to recover the information about the dynamic mass flow rate and its average value for one cycle during its operation.

The experimental conductance curve for the entire pneumatic circuit from the valve upstream pressure up to atmosphere is presented in the Figure 7. Its unusual shape comes logically from the flow section variation of the valve according to the circuit upstream pressure. Also the three zones already discussed for the valve (functional leakage – progressive opening – full opening) appear clearly.

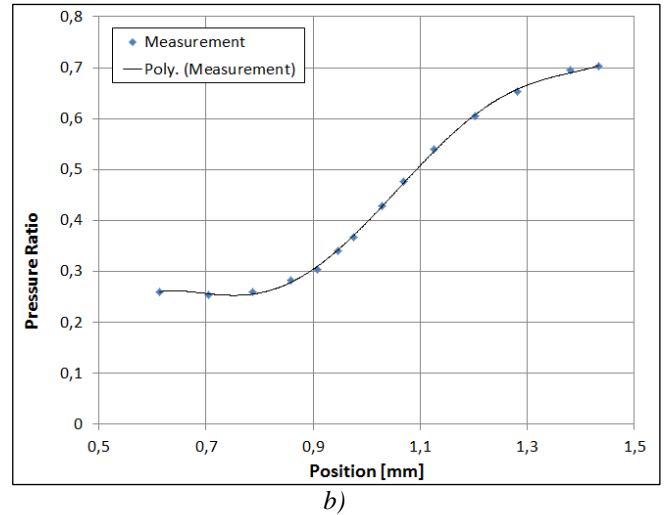


Figure 6: Measured flow characteristics of the valve for intermediate positions and their polynomial approximation  
a) Sonic conductance; b) Critical pressure ratio.

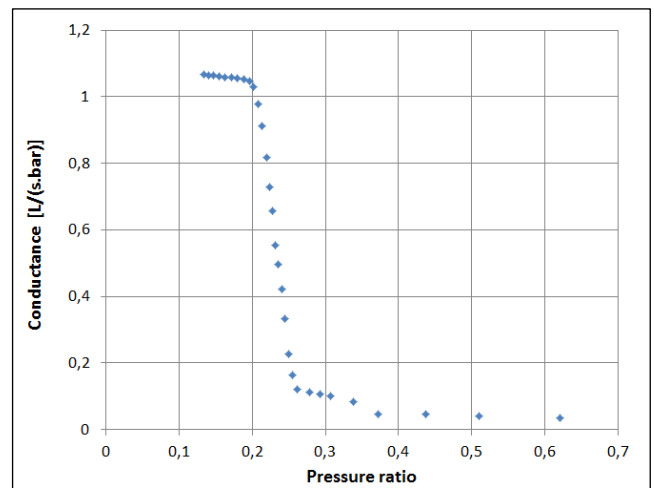
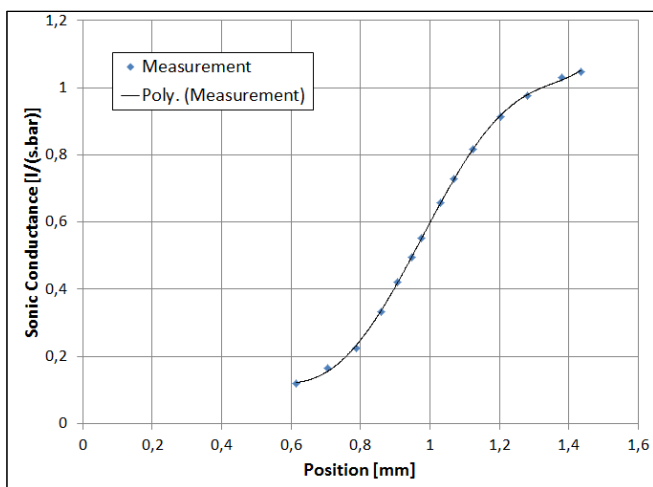


Figure 7: Conductance curve for the whole circuit (From  $P_{Up}$  to  $P_{Atm}$ )



a)

## 4.2 Dynamic behavior

As the valve under study has a minimal pressure value in order to achieve its maximal displacement and consequently its maximal flow section, the dynamic tests have to be performed with upstream pressures above this value. In the following, the absolute working pressure is set to 0,7 MPa.

Once having the flow characteristics of the valve, the dynamic study can be performed. In this part the opening-closing frequency is controlled and the average mass flow rate in the circuit, the pressures, the solenoid current and the spool position are measured.

Having an electromagnetic actuator in the first stage of the valve, it is expected to obtain a set of well-known curves for the measured variables frequently present in the published works as in [8] where the characteristics of an

electromagnetic flapper disk valve were investigated. Its switching time characteristics are presented in Figure 8.

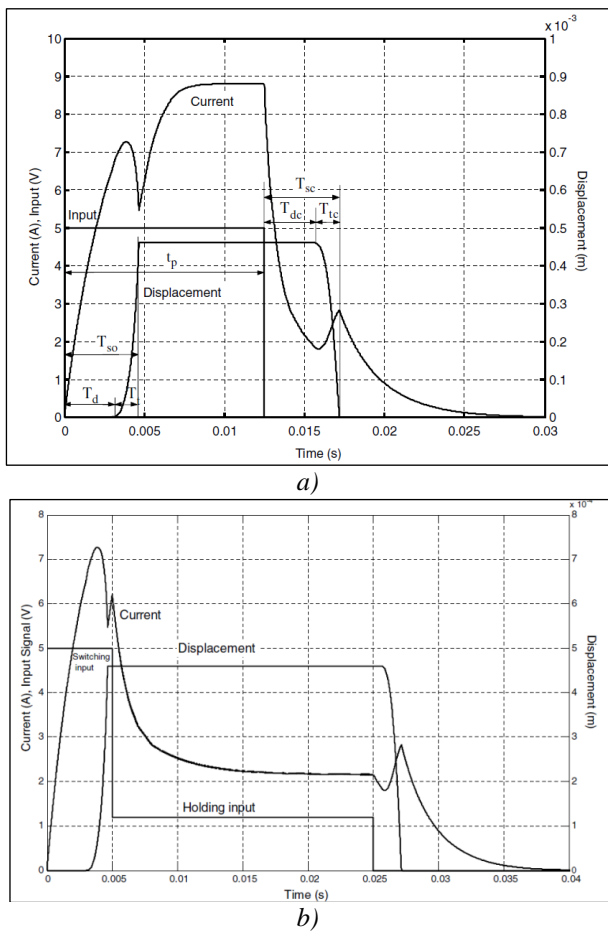


Figure 8: a) Switching time characteristics ; b) Effects of holding current. [8]

In order to minimize the influence of the dynamic behavior of the electrical system on the final results, a different input was set to minimize the rising time of the current in the coil. In this way, the delayed time measured on opening is mostly due to the moving mass on the mechanical system. In the other hand, to accelerate the closing movement of the valve, a negative voltage is set in the coil. The input voltage profile is shown in Figure 9.

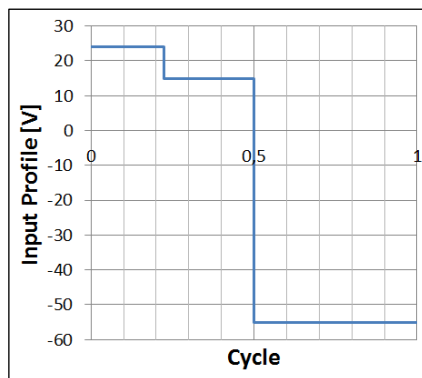


Figure 9: Input voltage profile per cycle

The dynamic tests were performed for frequencies from 10 Hz to 100 Hz with an increasing step of 10 Hz. The results for a low frequency (20 Hz) and a higher frequency (80 Hz) are presented in Figure 10.

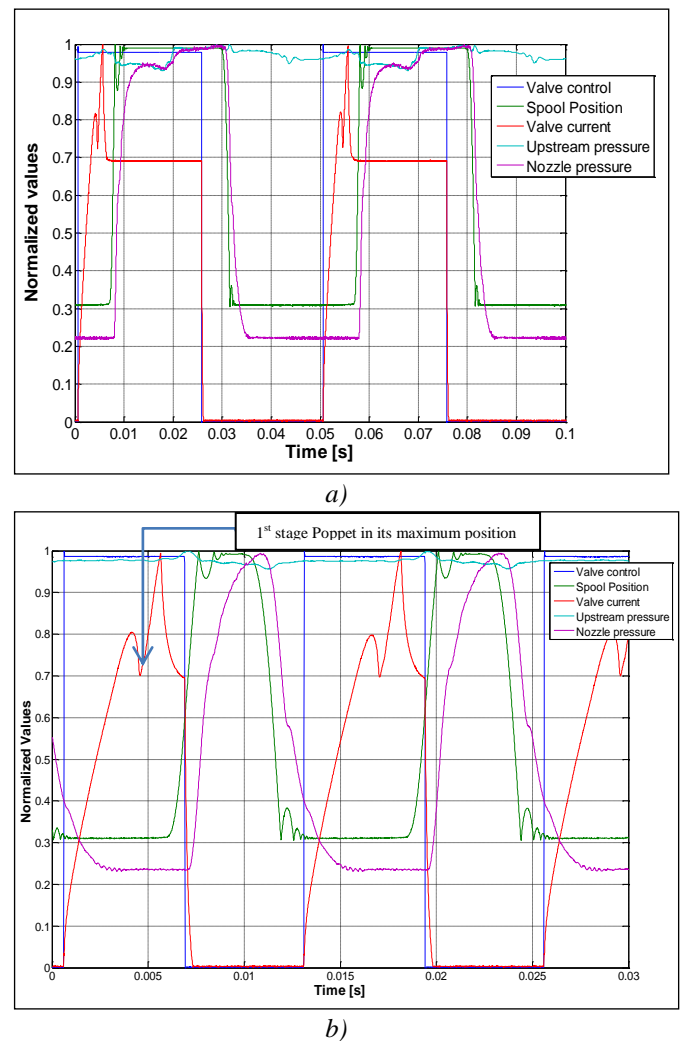


Figure 10: Measurements for: a) 20Hz; b) 80Hz;

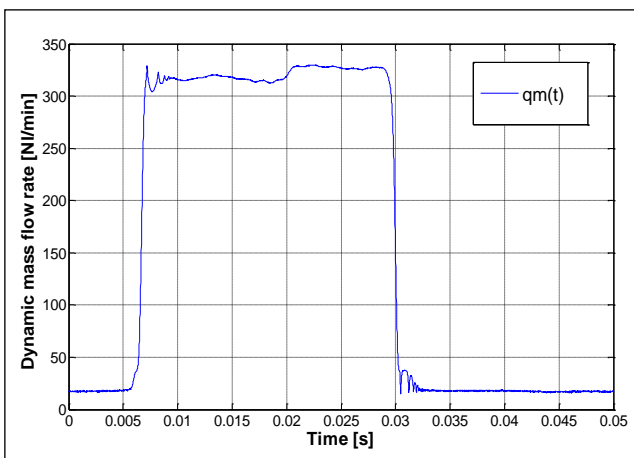
It is possible to notice a similar behavior to the one presented on Figure 8. For low frequencies (Figure 10a), the spool starts to move after a short delayed time and stays in its maximum position (opened) during almost the complete ON period of the input. The nozzle upstream pressure starts to increase after the spool starts to move and almost reaches the value of the upstream pressure, following its oscillations.

As the frequency is increased (Figure 10b), it is possible to observe that the spool starts to move almost the input is set to OFF and current starts to decrease. The electric system, even with the improvements in the input, spends a long time to establish the current in coil. In the other hand the valve has 2 stages with a pneumatic actuation, where the electromagnetic actuator moves the poppet of the first stage that reaches its maximum position at the point where the current has a local minimal value indicated in the Figure 10b. The delayed time from this point and the time where

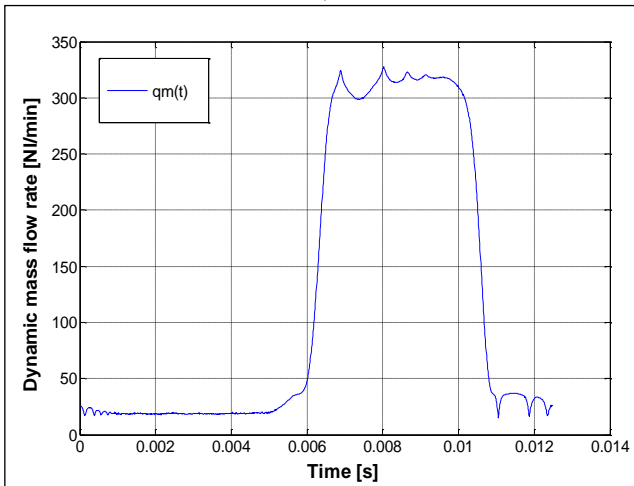
the spool starts to move is due to the pneumatic chamber being filled.

For frequencies higher than 120 Hz the spool cannot return to its initial position. Even with the poppet opening and closing normally, the pneumatic chamber does not have time to fill out, and the valve remains opened.

As the spool position and pressures along the circuit were acquired during the dynamic tests for the different frequencies and using the results of the steady state flow characterization, the instantaneous mass flow rate of the valve can be reconstructed for different frequencies by using equation 2 and the flow parameters of the valve shown in Figure 7. The results are shown in Figure 11 for one period and two frequencies.



a)



b)

Figure 11: Reconstruction of the dynamic mass flow rate for: a) 20Hz; b) 80 Hz

By integrating the results obtained for each measurement during one cycle (duty cycle 50%), it is possible to determine an average mass flow rate curve function of the frequencies and compare it with the average mass flow rate measured by the mass flowmeter. The measured and calculated values are presented in the Figure 12.

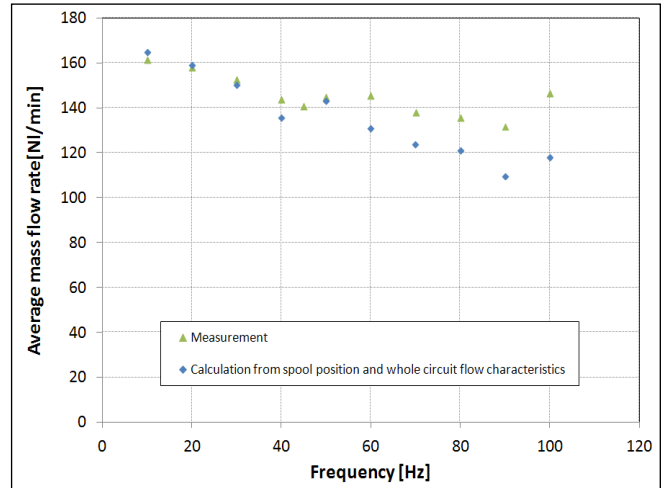


Figure 12: Average mass flow rate.

The results show a good parity for the estimated and measured average mass flow rate curves. For low frequencies up to 50 Hz, the values have smaller discrepancies when compared to the higher ones. This is due to the fact the valve remains a longer time in its completely opened position, where its flow characteristics are well-known, and also because this calculation has been conducted assuming the flow as instantaneously established. This is a correct approximation for low frequencies, but no longer for the higher ones where the transient effects are more important, which can be a source of errors. However, having the characteristics of the valve for some intermediate positions, and assuming a critical flow during the whole opening range of the valve, gives a good approximation for the average mass flow rate for high frequencies.

These transient effects will certainly be higher when using very fast switching valves. This is also the aim of this test bench to identify at which frequency the transitory effect of the flow establishment will become non negligible.

### 4.3 Jet exploitation

Another important part of the work consists in the characterization of the air jet coming from the system. As discussed before, the understanding of its characteristics in terms of velocity, pressure and temperature in the space and how they evolve in a dynamic operation of the system is crucial for the aim of optimizing the sorting operation.

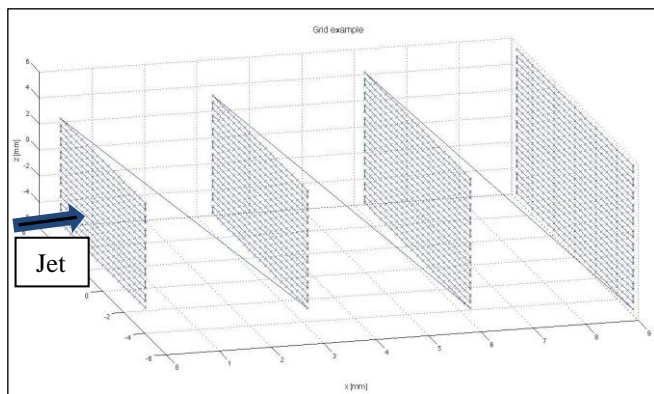
Leonhard [9] presents the topology of the jet. Thus, it is known the jet has, at its origin, the same diameter as the nozzle orifice, which is 3 mm in the studied case. In this way, it is expected to have a jet with a conical geometry with an increasing diameter following its centerline and moving away from the nozzle.

For a first characterization of the jet, different parallel square measurement grids as shown in Figure 13a, perpendicular to the jet axis and spaced of 3 mm, are set.

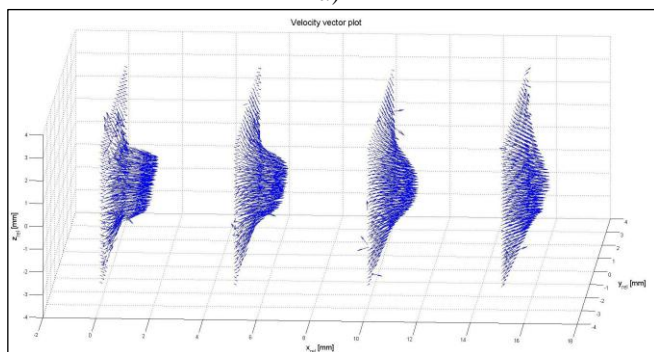
These square grids have an increasing length as they distance the nozzle orifice in order to ensure the jet stays in the measuring zone.

However, as the probe used in this work is suitable for measurements in subsonic jets, the upstream pressure was reduced in order to prevent permanent damage to the probe.

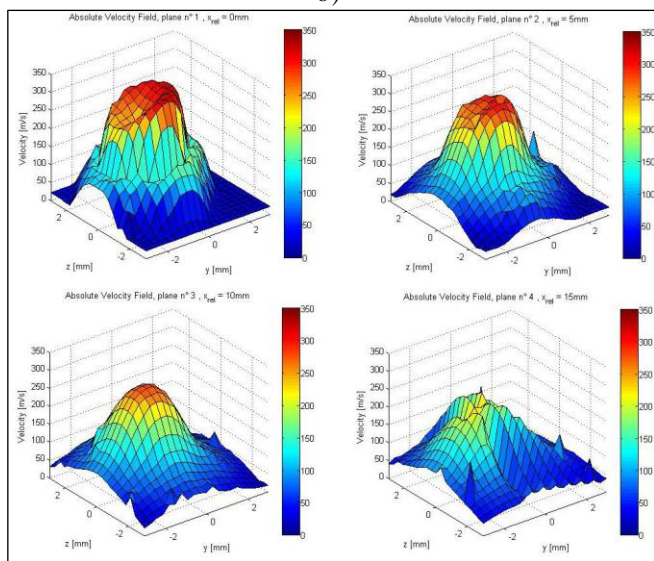
The first validation tests with a steady state jet with the 5-hole probe are presented in Figure 13.



a)



b)



c)

Figure 13: a) Measurement grids; b) Normalized velocity vectors; c) Absolute Velocity Field

In Figure 13b the spatial evolution of the steady air jet is presented. In the plane close to the nozzle one can notice the potential core of the jet surrounded by a region where a mixing between the jet and the freestream air takes place. Inside this region, the jet keeps its maximum velocity magnitude, as well as pressure and temperature.

In a farther distance from the nozzle, the mixing region has spread inward and reaches the center line of the jet. In this point the diameter of the jet continues to increase and the potential core disappears.

A more detailed study of the jet in steady state and dynamic behavior is being carried out in order to determine the influence of the mechanical system on the jet generation. The goal is to identify the parameters which have more influence on the jet properties. In this way, one can optimize their system since the design of the elements (valve-nozzle and circuit between them) in order to have a more efficient sorting operation.

## 5 Conclusion

The development of the experimental bench as well as its instrumentation leads to a useful tool for the characterization of fast switching valves. By its use, it becomes possible to determine the flow characteristics of the valve without the need to disassembly the components and identify different phenomena that can occur along the inner and outer circuit from source to free air jet.

The possibility to drive the valve up to high frequencies and perform accurate measurement and analysis, allowed the determination of the working zone of the element in which the mechanical and pneumatic performance still achieve its nominal value suitable for the different applications.

The valve tested has a maximum operation frequency of 120 Hz, which is still far from the faster valves already used in sorting applications. Thus, during tests with these faster elements, the transient effects will be more important and the need of a complete characterization of the elements shows to be a new challenge in order to reconstruct the average mass flow rate more accurately.

A first 3D analysis in terms of velocity of the air jet was performed in steady state and presented in this paper. The next step is to conduct a similar analysis in terms of pressure and temperature, and also in transient conditions to identify its dynamic behavior. This will enable to determine the different zones in the air jet in order to optimize the object sorting and evaluate the possible efficiency degradation of jets generated in high frequencies.

The future results could help the design of new valves taking into account the mechanical parameters which have more influence on the jet properties. This will deliver valves more adapted for sorting applications.

## Nomenclature

Designation	Denotation	Unit
$q_m$	Mass flow rate	[m <sup>3</sup> /s (ANR)]
$P$	Pressure	[Pa]
$P_u$	Upstream pressure of element under characterization	[Pa]
$P_d$	Downstream pressure of the element under characterization	[Pa]
$C$	Sonic conductance	[m <sup>3</sup> /s/Pa (ANR)]
$C_e$	Conductance	[m <sup>3</sup> /s/Pa (ANR)]
$T$	Temperature	[K]
$T_0$	Temperature at standard reference atmosphere (273.15)	[K]
$\rho_0$	Mass density at standard reference atmosphere (1,185)	[kg/m <sup>3</sup> ]
$b$	Critical pressure ratio	-
$T_d$	Delayed time to start the opening movement	[s]
$T_t$	Opening traveling time	[s]
$T_{so}$	Opening switching time	[s]
$T_{sc}$	Closing switching time	[s]
$t_p$	Switching pulse time	[s]
$T_{dc}$	Delayed time to start the closing movement	[s]
$T_{tc}$	Closing traveling time	[s]

## References

- [1] H. Yamada, S. Tsuchiya, T. Muto, Y. Suematsu. Development of a low cost high-speed on/off Digital valve using a bimorph PZT actuator. *4th JHPS International Symposium*, 591-596, 1999.
- [2] S.N. Yun, Y.B. Ham, J.H. Park, D.Y. Ham, L.Y. Lee. Pressure control characteristics of Electro-Pneumatic Regulator with Two multilayered PZT Valves. Proceeding to the *7th JFPS International Symposium on Fluid Power*. 449-452. 2008.
- [3] S.N. Yun, Y.B. Ham, J.H. Park, H.H. Kim, H.J. So. Design Strategy of a Piezoelectric Valve for a Color Sorter. *Journal of the Korean Physical Society*, Vol. 57, No. 4, 913-917. 2010.
- [4] J. Dubois. Etude expérimentale de jets libres compressibles ou en présence d'un obstacle. *PhD Thesis*. Marseille. 2010.
- [5] C. Donaldson and R. Snedeker. A study of free jet impingement part 1: mean properties of free and impinging jets. *Journal of fluid Mechanics*, 45, Part 2. 281-319. 1971.
- [6] D.T Branson, F.C Wang, D.N Johnston, D.G Tilley, C.R Bowen, P.S Keogh. Piezoelectrically actuated hydraulic valve design for high bandwidth and flow performance. *Proc. IMechE* Vol. 225(3). 345-359. 2011.
- [7] G.J Wilfong, M.A Bardorff, J.H Lumkes. Design and dynamics analysis of high speed ON/OFF Poppet Valves for digital pump/motors. *Proc. 6<sup>th</sup> FPNI-PhD Symposium*. 259-269. 2010.
- [8] E.E. Topçu, I. Yüksel, Z. Kamis. Development of electro-pneumatic fast switching valve and investigation of its characteristics. *Journal Mechatronics* 16. 365-378. 2006.
- [9] A. Leonhard. Untersuchungen zum pneumatischen Sortieren von Schüttgütern mittels Freistrahlen. *PhD Thesis*. Dresden. 2010.
- [10] Aeroprobe documentation.
- [11] S.S. Truong. Conical Probe Calibration and Wind Tunnel Data Analysis of the Channeled Centerbody Inlet Experiment. *Bachelor Thesis. California Polytechnic State University*. 2011
- [12] E.S. Johansen, O.K. Rediniotis, G. Jones. The Compressible Calibration of Miniature Multi-Hole Probes. *Transactions of the ASME*. Vol 123. 128-137. 2001.
- [13] ISO Standard 6358. International standard, Pneumatic fluid Power Components using compressible Fluids - Determination of flow rate characteristics. 1989.
- [14] Kagawa, T., Cai, M., Kawashima, K., Wang, T., Nagaki, T., Hasegawa, T., and Oneyama, N. Extended representation of flow-rate characteristics for pneumatic components and its measurement using isothermal discharge method. *Power Transmission and Motion Control, PTMC'04*. 271-282. 2004.

## **Statistical Approach To Energy Efficiency Issue In Industrial Pneumatic Systems**

Jyrki Parkkinen, Kai Zenger and Joonas Ollila

Aalto University, School of Electrical Engineering,

Department of Automation and Systems Technology, Helsinki, Finland

E-mail: , [jyrki.parkkinen@aalto.fi](mailto:jyrki.parkkinen@aalto.fi) , [kai.zenger@aalto.fi](mailto:kai.zenger@aalto.fi), [joonas.ollila@aalto.fi](mailto:joonas.ollila@aalto.fi) ,

### **Abstract**

In this paper, some statistical methods to the energy efficiency issue in industrial pneumatic systems are presented. Since all compressed air (CA) systems are different, in industrial applications it may be difficult to analyse energy efficiency of a single CA system from a theoretical model-based viewpoint. Instead of modeling the industrial pneumatic system from first principles the energy efficiency of the system is analyzed based on time series measurements. The dependency between energy consumption, potential variable pressure and flow variable mass flow makes possible to draw conclusions of the energy efficiency based on the measurements of pressure and power/energy.

In woodworking industry, e.g. sawmills, the functioning of the assembly line is relatively monotonic from day to day. Typically, CA is almost entirely used for linear motions. A double acting cylinder is the most common actuator in these applications. The length of the impact, the radius of the piston and radius of the cylinder are the essential key figures of this cylinder type. From these figures and basic dynamics of the cylinder, the air volume per impact can be obtained. When the average values and standard deviation of the air flow in each consumption point (cylinder) is known, statistical methods can be implemented for the total consumption of CA. According to the Central Limit Theorem, the total air consumption, i.e. the sum of consumptions in different consumption points approaches a normal distribution. Since the consumed air flow is proportional to the compressor's energy consumption, the trend of energy can also be approximated as a sum of regression curve and normally distributed deviation component. By this result, a confidence interval for energy consumption can be determined. The result is also ready to be used in energy saving calculations in the future.

Also, the adjustable pressure-difference in a two-point controlled compressor has an essential effect on the overall energy efficiency of the system. When this pressure difference is large, the system is not optimal from the viewpoint of energy efficiency. Typically the time series measurements of pressure are somewhat noisy, but some kind of conclusions of stationary behavior can be done. After possible pre-filtering process of the data, it becomes evident that the measurement data signal is typically a periodic shape with strict minimum and maximum values. The consumption of CA is typically dependent on pressure i.e. higher pressure increases consumption making the shape of pressure curve exponential. A stationary time series described by its mean, variance and autocorrelation function makes possible to identify the essential features of the dynamics of the CA system and the type of consumption.

With the appropriate statistical methods, the results of short-time measurements can be applied for predicting the energy consumption trend in a long run. The combination of first principle modeling with measurements opens new methods in energy efficiency techniques especially when designing new pneumatic systems or the improving of existing designs.

**Keywords:** Pneumatics in woodworking industry, time series analysis, estimate, confidence interval, autocorrelation

## 1 Introduction

The subject of the energy efficiency of pneumatic systems has taken a growing interest during the last ten years. Actually, CA systems are major consumers of electric energy and there is plenty of room for improvement. Many comprehensive investigations by research institutes including Fraunhofer[1], University of Cape Town [2] have been made. These investigations list several practical methods to improve energy efficiency in compressed air (CA) systems.

In a comprehensive review on the energy efficiency on pneumatic production [3] several viewpoints on the issue have been taken into consideration. The issue can be approached both energy efficiency use in the generation and treatment of CA and its consumption by end-users (actuators). The analysis of energy efficiency can be based on exergy, i.e. the useful energy, which can be converted to mechanical work. Alternatively, a life cycle costing analysis from product users perspective can be made [3]. Optimization can be made in different levels including pneumatic device and circuit level, condition monitoring and system level.

Also, many theoretical models have been under development lately. In an investigation [4], simulations to form predictive models in industrial applications have been presented. In the model, all types of cylinders, cylinder-based actuators, grippers and blowers are taken into the model. The dynamic modeling approach enables a greater understanding of CA consumption by production machines and lines.

Recently, many simulation models including a Matlab/Simulink model of pneumatic transmission line based on a detailed mathematical descriptions of pneumatic drive components have been developed. In addition to previous models, essential phenomena in CA piping networks like delay and dead time are taken into consideration [5],[6].

For large systems like an industrial pneumatic line, it may also be useful to model the CA system with subsystems. For example, a pneumatic system can be divided into production and consumption subsystems. From the practical viewpoint, since all CA systems are different, in industrial applications it may be difficult to analyze energy efficiency of a single CA system from a theoretical model-based viewpoint since processes involved with the consumption of CA have often stochastic nature.

In this paper, instead of focusing on the models of pneumatic systems, the used method is black-box based. Using measurement data and statistical methods it is relatively simple to form a suggestive general view of the

consumption of CA system. The essential parameters affecting the consumption of CA and energy efficiency are the pressure difference of an adjustable two-point compressor.

In his licentiate thesis and paper [7], [8] the author (J.P) has pointed out, that in many industrial pneumatic systems, especially when a two-point compressor is used, the energy efficiency of a CA system can be analyzed based on pressure values. In a simplified form, the duty cycle of a compressor consists of two parts, the compressor is either switched on, when it produces compressed air with full power or it is totally switched off. On the other hand, in some cases, the compressor is still idle running when not producing CA. Typically, in industrial woodworking applications, the idle running power is 20-30 % of the maximum power of the system.

From the viewpoint of energy consumption, the question is the profile of a duty cycle. The pressure difference and the minimum and maximum values of compressor inlet pressure determine the shape and length of the pressure curve. Roughly, the bigger the proportion of the rising time of the total cycle time, the more energy consuming the system.

In practice, an industrial pneumatic system is typically large. The length of a pneumatic line is often hundreds of meters and it has dozens of consumption points. Usually, these consumption points are actuators. The main actuator type in woodworking industry is a double acting cylinder. The dynamics of the air consumption in a single consumption point may be modeled starting from first principles when dimensions of the cylinder are known.

The structure of the paper is as follows. In Ch. 2 the essential factors and features of a typical industrial CA system are classified by their nature. The starting point is the presumption, that the consumption of CA is typically pressure-dependent. In Ch. 3 suitable statistical approach methods for the results are considered. These methods include Central Limit Theorem with an assumption that the sum of regular consumptions approaches a normal distribution. Also, tools for the time series analysis of the pressure measurements are presented. In Ch.4 a case study of a typical woodworking plant in Finland is presented in detail with suggestion for predicting the energy consumption. Ch.5 presents the variables to be measured (pressure, energy) and technical details of the measurement process. Also an interpretation of the measurement results is presented. Final conclusions are presented in Ch.6.

## 2 The factors affecting on energy efficiency of CA system of an assembly line

In two-point controlled compressor systems, the consumption can be classified in two main types: the pressure-dependent and independent consumption [7] (Fig. 1).

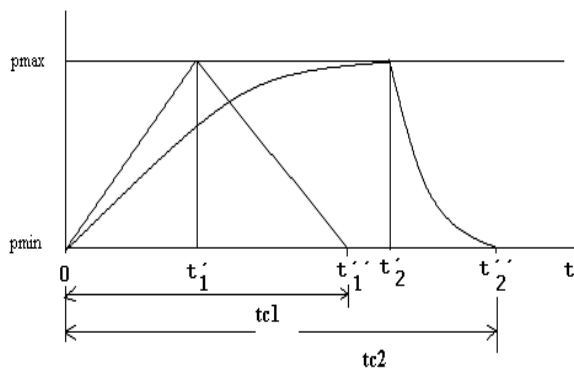


Figure 1: Typical pressure curves in industrial applications in two consumption-types: the pressure-dependent (cycle time =  $tc2$ ) and pressure-independent (cycle time =  $tc1$ ) consumptions

The function of the CA network is periodic in both cases. The compressor either works with full when turned on or is switched totally off (2-point control) the volume flow being constant when turned on and 0 when turned off. However, in some applications the compressor is also idle running when not producing CA.

In the case of pressure-independent consumption, the pressure grows linearly when the compressor is switched on and also drops linearly when the compressor is switched off. In that case, it is also possible to determine the consumption of the electrical energy easily.

In practice, the pressure-dependent consumption is much more common than the pressure-independent. In that case, the consumption of compressed air increases as the pressure grows. The pressure profile is an periodical exponential curve between minimum and maximum values. The length of the rise time depends on the adjustable pressure difference.

While basic consumption types in Fig. 1 are ideal consumption models, one can also identify from Fig 2. (measurement of an actual compressor) that the typical consumption is pressure-dependent. Actually, the measurement data of Fig.2 is smoother than most pressure measurement data series (see Fig.4) and pre-filtering is needed required.

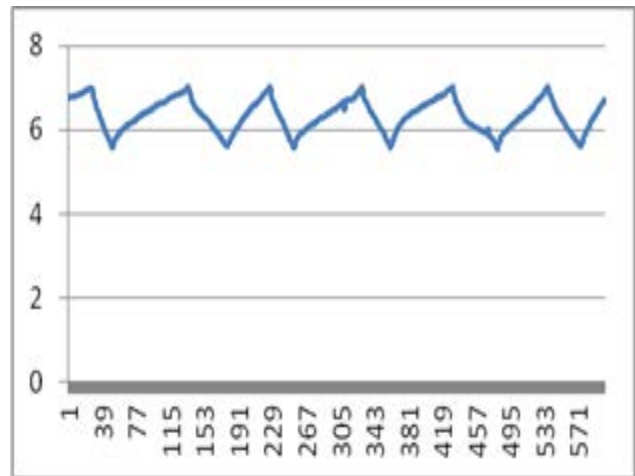


Figure 2: An example of a pressure (bars) time series (duty cycle) of an actual two-point controlled compressor

CA consumption in industry is characteristically less regular. The after treatment and leaks cause pressure losses between production and consumption points.

In the energy efficiency analysis of a manufacturing/assembly line system, it is reasonable to classify parameters by their nature. The parameters can be identified of constant (nominal scale), adjustable and statistical nature. The parameters affecting on the consumption of the CA in a sawmill system in production and consumption by nature are dealt in detail in Chapter 4 and listed in the tables 1 and 2.

The factors that have an effect on the consumption of the CA in a system, can be classified on the factors in production and consumption.

### 2.1 Production of CA

From a purely statistical viewpoint, the units of production systems are of nominal scale and they cannot be changed. Such factors are for example the type of compressor, number and type of filters and type of after treatment system. Usually, the pressure loss caused by a filter type are well known. In a typical CA system, the total pressure losses in the after treatment system are [7]

- Drier 0.1-0.5 bar
- Prefilter 0.35 bar
- Fine filter 0.35 bar
- Dust filter 0.1-0.5 bar
- After cooler and piping 0.2 bar

On the other hand, many parameters, especially the pressure difference of the compressor can be adjusted to satisfy the consumption of CA optimally. Typically the pressure difference is about 0.3-1 bar. The control of a compressor can also be changed by user (two-point/inverted control)

and may have a major effect on the consumption of compressed air.

## 2.2 Consumption of CA

In many industrial applications, the consumption points of CA have many similarities. Industrial systems are typically transport systems of bulk material. For example in sawmills, the assembly line starts from the debarking unit and continues via one or more sawing phases. Typically most of these phases have cylinder-based actuators and the operation of the line is quite similar from day to day.

The three main types of cylinders are single-acting, double-acting and rotating cylinder. In a typical assembly line, the double-acting cylinder is the dominating actuator. The consumption of CA in a single consumption point can be determined from the mechanics and dimensions of the cylinder.

## 3 Statistical methods to be applied

### 3.1 Central Limit Theorem

In probability theory, the **Central Limit Theorem (CLT)** states that, given certain conditions, the mean of a sufficiently large number of independent random variables, each with a well-defined mean and well-defined variance, approaches a normal distribution. According to the Central Limit Theorem, independent, identically distributed random variables having mean  $\mu$  and nonzero variance  $\sigma^2$ , for the sample variance  $s_n$

$$\lim_{n \rightarrow \infty} P \left( \frac{s_n - n\mu}{\sigma\sqrt{n}} \leq x \right) = \Phi(x) \quad (1)$$

in which  $\Phi(x)$  is the probability that a standard normal random variable is less than  $x$ .

#### 3.1.1 Key figures of a double acting cylinder

In a typical industrial system, the actuator is a double acting cylinder. The piston motion cycle consist of two motions, the piston first moves to the +direction consuming air according to the equation

$$\pi R^2 s (1 + I) \quad (2)$$

in which

length of the impact =  $s$ ,

radius of the piston =  $r$ ,

Radius of the cylinder =  $R$ .

For the relative pressure notion  $p/p_0$  notation  $\Pi$  is used

and returns to the -direction when the air consumption is

$$\pi(R^2 - r^2)s(1 + I) \quad (3)$$

making the total air consumption as a sum of (2) and (3)

$$\pi s(1 + I)(2R^2 - r^2) \quad (4)$$

The consumption rate per time unit can be further obtained from (4) by observing the actuator. If the number of cylinder movements per minute is  $N$ , the air volume consumed by the cylinder per time unit is

$$q = N\pi s(1 + I)(2R^2 - r^2)/t \quad (5)$$

For example if  $t = 60$  min,  $N = 100$ ,  $s = 50$  cm,  $R = 10$  cm,  $r = 2$  cm,  $p = 9$  bar, makes the total air consumption of 0.5 normal cubic meters per minute.

The consumptions of other cylinder-like actuators can be determined in a similar fashion when the dimensions are known.

#### 3.1.2 CLT applied to the industrial pneumatic system

From the basic structure and key figures of the double acting cylinder, it can be easily observed that the air consumed in a impact of the cylinder can be characterized by a well-defined mean and variance. In the common form of the theorem, the random variables are independent and identically distributed (i.i.d), but the theorem can also be used when they are not.

For example, in industrial applications, the variables related to the cylinders may vary according to the size of cylinder. Usually the length of the impact is full, but in some cases may also be incomplete (See also Ch. 5).

The air consumption of cylinders is predictable, near constant in most consumption points. This makes the variance in most consumption points small resulting that the variance of the sum of consumptions is also small.

If  $M$  is the number of consumption points with an actuator (cylinder), the total consumed volume flow  $Q$  is

$$Q = \sum_{i=1}^M q_i \tag{6}$$

in which air consumption of cylinder  $i = q_i$

Since one cylinder consumes the same amount of CA per impact, the consumption of CA per time unit can be obtained by observing how many impacts per time unit the cylinder moves.

The behavior of the assembly line is quite stationary from hour to hour. Since energy consumption is strongly, almost linearly dependent on the volume flow, it is therefore reasonable to assume that the trend of the cumulative energy consumption is linear.

Also, it is possible to include stochastic consumptions (blowing purposes) to the model. However, usually the role of these consumptions is minor and they have no significant effect on the overall consumption trend.

### 3.2 Time series analysis of pressure measurements

As can be seen from Fig. 4, the actual pressure curve is far from ideal models in Fig. 1-2. From Fig.4 only the essential figures (pressure difference, min/max pressures) can be easily identified.

It is seen that the curve includes noise, which makes the determination of the duty cycle much more elaborate than in the cases shown in Fig. 2. However, since off-line analysis is possible, a practical method for the estimation of the (changing) period and (changing) duty cycle can be described as follows. The minimum and maximum points in the time series sequence are determined by considering continuously the sign between two successive data points. The change negative to positive means minimum and the change positive to negative means maximum. The period is the time between two minima, and the duty cycle is the time between minimum and maximum divided by the period.

To prevent clear mistakes caused by the noisy signal it is possible to introduce security checks by using the standard

deviation for example to give the minimum limits to minimum and maximum.

## 4 Case study

On the following, a typical example of a industrial pneumatic system is presented. The system is a woodworking plant (sawmill) in northern Finland. The products of the sawmill include building materials, dimensionally accurate boards and planks and lining material for various purposes. The material of the products is pine.

CA of the sawmill line is produced by three compressors. The compressors are oil-injected two-point controlled screw compressors. The compressors produce about 10, 4 and 3 normal cubic meters of CA in a minute respectively. Usually, inlet power of compressor is 6-7 kW per normal cubic meter making the powers of compressors about 70, 30 and 20 kW. The energy needed to produce the necessary CA usually depends on the outlet pressure and adjustable pressure-difference of the compressors.

The total number of cylinder-based actuators in the system is about 300, while the number of working stages is about 100. Almost all of the cylinders are double-acting. Usually almost all these actuators are on use at the same time, the total CA consumption on the assembly line can be obtained by summing these consumptions. Usually, the cylinders are supplied from the same manufacturer to make the maintenance simpler.

Beside actuators, a small portion of CA is used for blowing and other random purposes. It is noteworthy, that in the system there are tanks with a magnitude of  $1\text{m}^3$  for CA soon after compressors. The tanks act like an integrator, which filters the peaks in the consumption. Random consumptions are thus not noticeable.

Table 1: Compressor parameters affecting on the consumption of CA (production)

	Constant/ Class- scaled	Adjustable	Statistical
Idle running power	x	x	
Type of the compressor	x		

Filters of after treatment system	x		x
Control/regulation method of the compressor	x	x	
Pressure difference of the compressor		x	

Typical adjustable parameters of the system (Table 2) are the velocity of the assembly line and the feeding rate of the system. Actually, the feeding rate is usually constant.

The first phases of the assembly line, mainly barking unit are more of stochastic nature than other parts of the line. The typical statistical factor is the size of a trunk. Key figures are the length and the diameter of a trunk. Profile of a typical stem is presented in figure 3. The length and diameter of a trunk may vary considerably depending on the cargo of wood. Total CA consumption in barking unit can be estimated when information of wood and from figure 3 are available.

Also it is possible that on the same sawmill, the species of tree varies from day to day. Different species of trees have different properties [11]. However, on the case study plant, only pine was used.

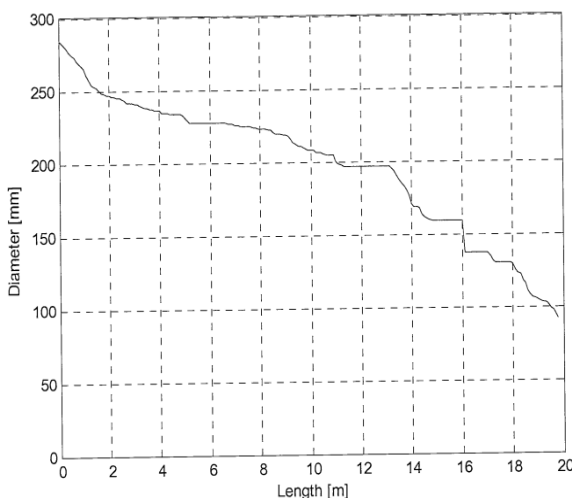


Figure 3: Typical diameter profile of a trunk [11]

Usually, a large trunk effects on the length of the impact of the cylinder, which is in turn proportional to the air consumption. After the debarking unit, the trees typically go through several sawing phases. In these phases the cylinders typically work predictably with full impact.

In most phases, the type of actuator is a double acting cylinder. Also, in a couple of working phases, when movement of the load is done to the upward direction, a single acting cylinder is used.

Table 2: System parameters affecting on the consumption of CA in a woodworking plant (consumption)

	Constant/Class-scaled	Adjustable	Statistical
Species of a tree	x		x
Length of the trunk			x
Thickness of the trunk			x
Velocity of the assembly line of the unit		x	
Feeding rate of the assembly line of the unit		x	x
Type of actuators (cylinder)	x		
Number of working shifts (1/2/3)	x	x	

In an energy efficiency analysis of a woodworking plant, regular seasonal properties of the system must also be taken into account. These seasonal properties can be classified into short time and long-time nature. Typically they are periods when the assembly line is stopped.

Usually the working day consists of two 8-hour shifts. Depending on economic situation, the number of shifts may also be one or three. In case of two shifts, the pneumatic line is typically switched off in the night time (12p.m-

8.a.m). Shorter breaks on regular basis typically occur on lunch time and during the change of shift.

In the long run, a longer standstill (of magnitude of 1 month) at the plant typically takes place on summer time. Also during public holidays, a break of a few days may take place.

Temporarily, the functioning of the assembly-line may stop due to blockages on the line. However, these breaks occur seldom and are short-time. Usually, on a woodworking plant, there are also reserve parts for defective actuators (cylinders).

## 5 Measurements in compressed air systems

During the last few years, measurements in several woodworking industrial plants in Finland have been made. The overall strategy of the measurements was to compare the energy consumption of different consumption network configurations by collecting data from one relatively long period – e.g. working with one configuration, repeat the same measurements with another configuration and compare results.

### 5.1 Pressure measurements

A time series of pressure values were measured. The measurements typically include pressure (bar) with sampling frequency of 1Hz.. The pressure measurement equipment consists of radio controlled data loggers. With SMS-commands, the measurement could be controlled remotely. These commands included start/stop/pause/continue qualities.

The most essential figures of the system are the maximum, minimum and average values of pressure. These values depend mostly on the pressure difference of the compressor. Since the measurement point is usually located behind the after-treatment system of the compressor, the losses cause that the measured values are typically 0.5-1 bar lower than in the compressors outlet.

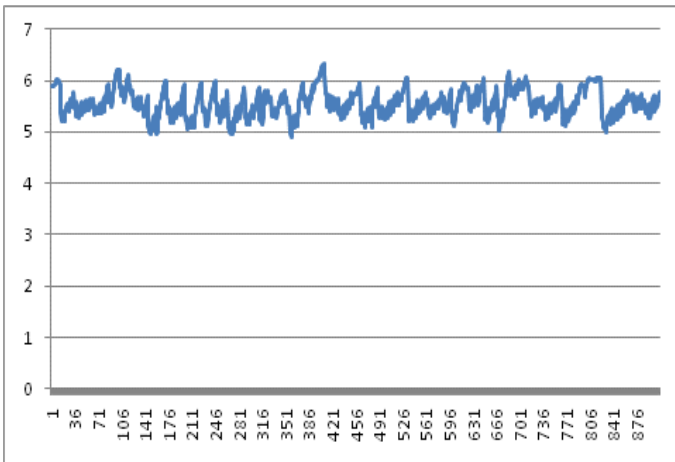


Figure 4: An example of pressure measurements(bars)

The measurements are usually performed at the consumption point. When the actual adjustable pressure-difference of the compressor is known, it is simple to get the pressure losses between production and consumption. However, in order to get the idea about the consumption type (pressure-dependent/independent consumption) the raw data requires some preparation.

Since compressors in many industrial applications usually work with on/off-basis, from the viewpoint of energy efficiency, the most essential factor is the proportion of the rise time of the total cycle time.

In some industrial applications, during the unloading period the compressor is idle running.

In a case, when a compressor runs with idle-power, the total energy can be obtained from (6) The idle running power of the motor is constant  $P_0$  during the unloading period.

Total energy during the cycle is

$$W_{tot} = P't' + P_0(t'' - t') \tag{7}$$

The average power during the period is respectively

$$P_{ave} = \frac{t'}{t''}P' + \left(1 - \frac{t'}{t''}\right)P_0 \tag{8}$$

Typically  $P_0$  is of magnitude 20-30% of the average power.

### 5.2 Energy and power measurements

Simultaneously with the pressure measurements, energy and power measurements were carried out. The frequency of the measurements was 1/30s. Since the sampling frequency is much slower than in pressure measurements, the results are not compatible. From the measurements, certain equivalencies between the potential variable (pressure), flow variable (mass flow) and energy/power consumption can be notified. For example, energy consumption is proportional to the production of compressed air (normal cubic meters).

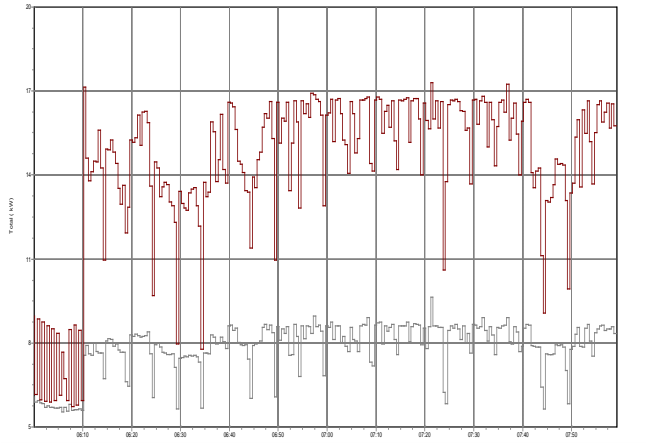


Figure 5: An example of power measurement.(maximum and average power consumption)

The quantities to be measured included minimum, maximum and average values of three-phase current, voltage, apparent and active power/energy in three phases and total. However, only minimum, maximum and average power are relevant from viewpoint of energy efficiency. In Fig.4 time series of minimum and average power consumption are presented. Since every measurement is discrete and the sampling frequency is high, the time series is not very smooth, but certain homogeneous behavior can be identified (maximum active power correspondence the nominal power of the compressor). In practice, it is more reasonable to examine the cumulative energy consumption (Fig.6,7), which can be directly integrated from the power.

### 5.3 Interpretation of the measurements

#### 5.3.1 Pressure measurements

The measurement data of a two-point controlled compressor is in many applications typically noisy (Fig.4) A naturally arising question is whether periodicity in the pressure changes can be identified.

A standard widely-used filtering method for continuous time series is sliding average method. If the filtering method is successful, from the pressure time series the length of the total time cycle and the proportion of rise/fall time can be identified..

An autocorrelation plot of the pressure measurements during a reasonable long period e.g. one hour may be very informative (Fig.6).

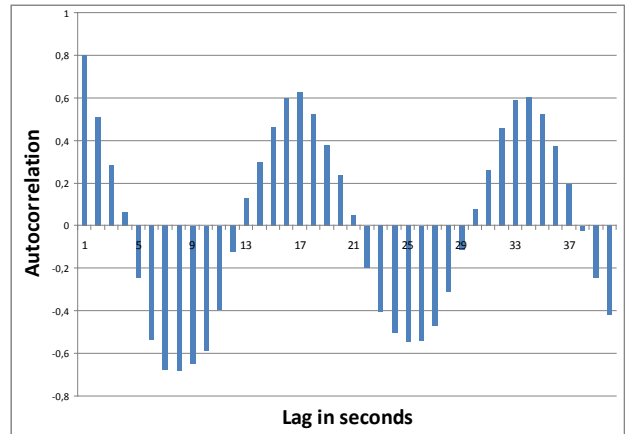


Figure 6: An example of an autocorrelation plot

For example, from figure 6, it can be inferred, that the pressure values between 15-20 seconds are quite strongly dependent. Combining the autocorrelation method with the approaching described in Ch. 3.2, the shape of the actual pressure curve can be estimated and proportion of the rise time (compressor on) of the total time determined.

#### 5.3.2 Energy and power measurements

The trend of the cumulative energy consumption can be revealed by various regression methods [9].

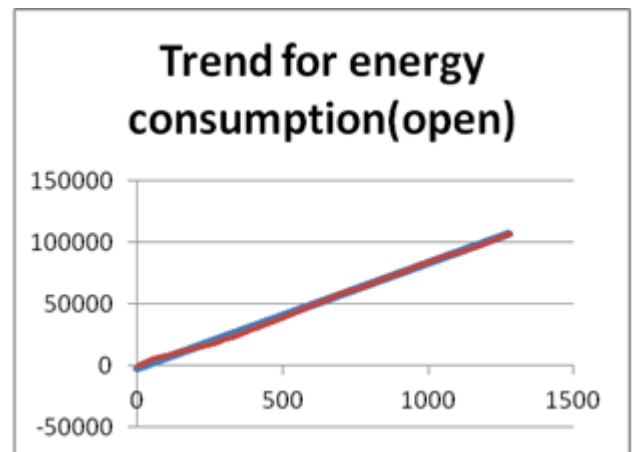


Figure 7: An example of an actual cumulative energy consumption (in kW) trend(red) and regression estimate for prediction (blue)

Figure 7 presents a measurement data of cumulative energy consumption from the period of one working day while a regression estimate based on a short time (1-2 hours) From the figure, one can make a conclusion, that energy consumption trend can be modeled with simple linear regression.

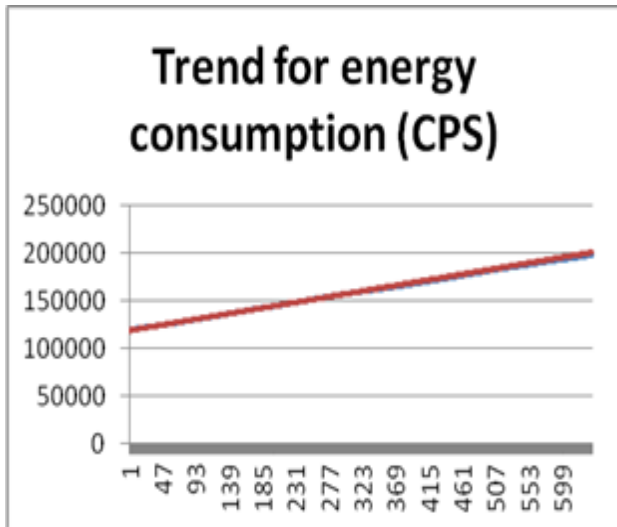


Figure 8: An example of an actual cumulative energy consumption trend (red) and regression estimate for prediction (blue)

The same energy/power measurements were repeated with different configuration on next day (Fig.7). The system in this measurement was CPS (Closed Pneumatic System), based on the recycling of CA [10]. Since the slope of the closed system is much lower than that of open system, the closed system evidently consumes less energy per time unit. From viewpoint of statistics, it is noteworthy that the trend remains linear even when the configuration is changed.

With certain reservations, one can generalize the results and make the normality assumption. In practice, the statistical properties affecting on the consumption of compressed air are often of mechanical reason and follow normal distribution. In that case, a confidence interval (95%) for the energy consumption can be determined.

## 6 Conclusions

Since energy consumption of a compressor is strongly, almost linearly dependent on the consumption of CA, it is reasonable to analyze the energy efficiency issue by analyzing consumption points by their nature. In a typical manufacturing/assembly line process the most of the CA is used by actuators, the main actuator type being a double-acting cylinder. From the physical principles and dimensions of the cylinder, the consumption of CA in a single consumption point can be determined analytically. The behavior of these consumptions is quite similar even for cylinders with different dimensions. According to the Central Limit Theorem, the sum of consumptions can be assumed to approach a normal distribution. Measurements of a relatively short time (one working day) can be generalized and a forecast of energy consumption with confidence interval be obtained.

In addition to regular consumptions, some consumptions on the manufacturing line, like blowing purposes are of stochastic nature. However their role is usually insignificant and has minor or no effect on the overall trend.

Furthermore, leaks have a permanent deteriorating effect on energy efficiency of industrial systems. Since the consumption of CA usually strongly depends on the pressure [7], the effect of the leaks on the overall energy efficiency becomes more evident when the pressure is high. In such CA systems, it is important to detect leaks in time. In practice, when the pressure measurements are performed during a stoppage when there is no natural CA consumption by keeping compressor on, even the proportion of leakage can be easily approximated from the pressure curve.

In practice, the energy consumption in an industrial pneumatic system is often a monotonic function, which can be approximated as a sum of a regression line and a normally distributed deviation component. In order to predict the energy consumption in the future an estimate in a certain confidence level can be calculated from the regression line combined with the stochastic component. The result is then ready to be used in energy saving calculations regarding the design of new pneumatic systems or the improvement of existing designs.

On workdays, from Monday to Friday, the consumption of CA typically follows some similar trend. However, on weekends, the trend may be quite different. Also, there may be certain seasonal components in the consumption of CA (e.g. in the summer the production in some branches of industry is lower than in the winter). Fitting seasonal components [9] to the overall consumption trend is a subject of further investigation.

Also, it is possible to model the CA system starting from first principle physical modeling, and then combining it with measurements added with stochastic component. The estimation of model parameters can be computed on-line by using the numeric model. The described approach opens new methods in energy saving techniques in the future.

## Nomenclature

Designation	Denotation	Unit
$\Phi(x)$	Probability function	
$\mu$	Mean	
$N$	Number of cylinder movements	
$p$	Pressure	[bar]
$p_0$	Atmospheric pressure	[bar]
$P$	Nominal power	[kW]
$P_{ave}$	Average power	[kW]
$P_0$	Idle running power	[kW]
$\Pi$	Relative pressure	
$q_i$	Consumption	[m <sup>3</sup> /min]
$Q$	Total consumption	[m <sup>3</sup> /min]
$r$	Radius of the piston	[mm]
$R$	Radius of the cylinder	[mm]
$s$	Length of the impact	[mm]
$\sigma^2$	Variance	
$t_c$	Cycle time	[s]
$t'$	Rise time (loading)	
$t''$	Fall time (unloading)	
$W_{tot}$	Total Energy	[kJ]

## References

- [1] P Radgen, E Blaustein. (Eds) *Compressed Air Systems in the European Union: Energy, Emission, Savings Potential and Policy Actions 2001*
- [2] The Energy Research Institute, Department of Mechanical Engineering, University of Cape Town *How to save energy and money: Guide Book 3: Compressed Air Systems 2007*
- [3] Paul H Harris, Garret O'Donnell, Tim Whelan *Energy Efficiency in Pneumatic Production Systems: State of the Art and Future Directions Leveraging Technology in a Sustainable World Proceedings of the 19th CIRP Conference on Life Cycle Engineering, University of California at Berkeley, Berkeley, USA 2012*
- [4] Paul H Harris, Garret O'Donnell, Tim Whelan. *Predictive Consumption Models for Electro-Pneumatic Production Systems. IEEE Transactions on Mechatronics 2011*
- [5] Susanne V Krichel, O Savodny. *Analysis and optimization of compressed air networks with model-based approaches, Ventil 17/2011*
- [6] Susanne V Krichel, O Savodny. *Dynamic modeling of pneumatic transmission lines in MATLAB/SIMULINK Proceedings of the International Fluid Power and Mechatronics Conference, Beijing/China 2011*
- [7] J Parkkinen. *Energy Efficiency in Industrial Pneumatic Systems Helsinki University of Technology Control Engineering Laboratory Espoo 2007 (lic.thesis)*
- [8] J Parkkinen, K Zenger. *A new Efficiency Index for Analysing and Minimising Energy Consumption in Pneumatic Systems Int. Journal of Fluid Power 2008*
- [9] G.E.P Box, G.M. Jenkins, G.C. Reinsel: *Time Series Analysis: Forecasting and Control John Wiley & Sons, Inc 2008*
- [10] J Parkkinen. *Improving Energy Efficiency in Industrial Pneumatic Systems by Structural Means The Twelfth Scandinavian International Conference on Fluid Power 2011, Tampere, Finland*
- [11] V.Hölttä: *Analysis of stem diameter measurement in forest harvester (diploma thesis) 2004*

## **Energy saving measures on pneumatic drive systems**

J. Hepke, J. Weber

Institute of Fluid Power (IFD), Dresden University of Technology, Dresden, Germany  
E-mail: hepke@ifd.mw.tu-dresden.de, weber@ifd.mw.tu-dresden.de

### **Abstract**

In this article two different energy saving measures are presented. The possible savings potential and the effort of realizing these methods are described. Using these measures it was shown, that up to 55 % energy saving could be achieved for a single drive.

The paper presents the thermodynamic principles that are needed to determine the energy consumption of pneumatic drives, which consist of the compressed air and the exergy analysis calculations. Further on, the influence of the design parameters on the energy consumption has been studied. Possible savings solutions have been arranged and brought together to provide an exemplary overview. In this case two savings methods were realized on a single cylinder drive of a pneumatic handling system.

These selected energy saving solutions aim at the optimization of the design parameters of pneumatic cylinder drives and on the use of exhaust air recovery circuits. The use of these saving measures is first tested via simulation and then implemented on an example cylinder drive. For each saving measure the influence on the energy consumption and on the motion profile of the drive is investigated in detail. Focus was especially directed to the question, whether the original motion profile of the example drive remained the same after applying the saving measures.

**Keywords:** pneumatic drive systems, energy saving measures, optimization of the design parameters, exhaust air recovery circuit, pay-back period

### **1 Introduction**

The field of industrial automation requires the realization of complex handling tasks. In order to solve them, handling systems with pneumatic and electric drives are being used. Pneumatic drives require only low investment and maintenance costs and distinguish themselves through a flexible and robust design. They have to handle different operating tasks with a large range of forces, strokes and operating times.

In most cases handling tasks can be realized using pneumatic as well as electric drives. In this competition energy costs of the drive technology become more and more important. Compressed air is an expensive source of energy. To increase the competitiveness of pneumatic drives the compressed air consumption has to be reduced.

There are several energy saving measures, however only a few give a concrete statement about the correlation between potential energy savings and implementation costs.

The paper gives an overview about possible energy saving measures for pneumatic drives. Two of these saving measures will be investigated experimentally and

simulation-based. Drawing on the example of a standard exhaust-air-flow-controlled cylinder drive the achieved energy saving, the effort for implementing these measures as well as the resulting pay-back period will be shown in the following chapters.

### **2 Theoretical approaches for determining energy consumption of pneumatic drives**

There are different methods known for quantifying the energy demand of pneumatic drive systems, i.e. a compressed air consumption calculation and an exergy analysis. Moreover a calculation based on the "air power" can be performed [1]. This approach can be derived from the formula of the technical work at a cylinder as well as from the exergy flow under the assumption of isothermal conditions (instant temperature equalization). This method is excluded from this paper.

#### **2.1 Compressed air consumption calculation**

The first approach is a compressed air consumption calculation [2], which is a simplified method for calculating the energy consumption of pneumatic drives. It can only be

used for standard systems like an exhaust-air-flow-controlled cylinder drive. This method considers the compressed air that is needed for filling the different volumes. This compressed air is required for the compression processes within the tube and dead volumes and for the realization of the cylinder's stroke. To calculate the energy consumption for a double stroke of a standard cylinder drive by using the first method, fig. 1 shows the required equations.

**Method 1: Compressed air consumption calculation**

Assumptions: - Isothermal system behaviour  
- No Leakage

$$V_{cylinder} = \frac{\pi}{4} (d_p^2 + d_c^2 - d_r^2) \cdot h \cdot \frac{p_1}{p_0}$$

$$V_{dead\ volume} = (V_{dead,A} + V_{dead,B}) \cdot \frac{p_1}{p_0} - (V_{dead,A} + V_{dead,B})$$

$$V_{tubes} = (V_{t,A} + V_{t,B}) \cdot \frac{p_1}{p_0} - (V_{t,A} + V_{t,B})$$

$$V_{double\ stroke} = V_{cylinder} + V_{dead\ volume} + V_{tubes}$$

$$V_{double\ stroke} = \frac{\pi}{4} (d_p^2 + d_c^2 - d_r^2) \cdot h \cdot \frac{p_1}{p_0} + (V_{dead,A} + V_{dead,B}) \cdot \frac{p_1}{p_0} - (V_{dead,A} + V_{dead,B}) + (V_{t,A} + V_{t,B}) \cdot \frac{p_1}{p_0} - (V_{t,A} + V_{t,B})$$

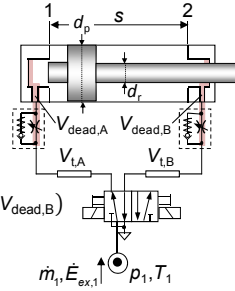


Figure 1: Compressed air consumption for a double stroke (1→2 + 2→1) of a standard cylinder drive

The calculation formula is based on a summation of the filling volumes and the pressure levels. Hence this equation compares the initial thermodynamic state, within the filling volumes, with the thermodynamic state after completing the motion of the piston. Therefore this method isn't suitable for quantifying energy losses during the thermodynamic processes.

The tube and dead volumes are filled with compressed air starting at ambient pressure level  $p_0$  whereas the cylinder chambers are filled starting at the null volume. Under the assumption of isothermal system behaviour (instant temperature equalization with the ambient air) and no leakage occurrence the compressed air consumption only depends on the filling volumes and pressure levels. However technical thermodynamic systems typically show polytropic changes in values of state variables. Compression processes that are occurring during such a state change are characterized by a temperature increase, which is accompanied by a pressure increase. As a result less mass flow is required for the pressure build-up within the filling volume.

The neglect of the temperature behaviour is an error in the air calculation, which can be estimated by investigating the air consumption of a drive with shifting heat exchange conditions. This experiment can be virtually done. The heat exchange conditions depend on the thermal transmittance of the cylinder wall as well as tube walls and on the operating times of the drive. A drive with short operating times and for this reason short dwell times will show approximately adiabatic thermal behaviour, since there is no time for heat transfer with the surroundings. In the next step the heat

transfer condition of the cylinder wall and tube walls is varied from isothermal ( $n = 1$ , instant heat exchange with the ambience) to polytropic ( $n = 1,1$ ) and finally to adiabatic ( $n = 1,4 = \kappa$ , no heat exchange with the ambience). This experiment shown in fig.2 demonstrates that the compressed air consumption of a system with isothermal and adiabatic thermodynamic changes differs about 16 %. Thus this error normally causes differences between the calculated and the actually consumed compressed air.

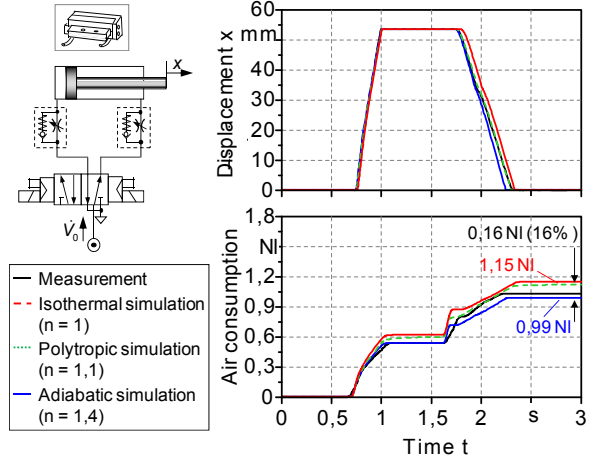


Figure 2: Compressed air consumption for a cylinder drive with changing heat transfer conditions

In case of an energy saving drive structure with a modified circuit structure (exhaust-air recovery circuit) or a modified valve control strategy the volumes are filled with compressed air up to an unknown pressure level that is lower than the working pressure. For these drive structures a compressed air calculation cannot be performed. For this purpose a system simulation that is more complex has to be done for the determination of the energy consumption.

In contrast to the second method a compressed air calculation is less complex and more practical than determining the exergy.

**2.2 Exergy analysis**

The second method represents an exergy analysis [3]. For this analysis equations are needed, that are based on the first and second law of thermodynamics. This method is much more complex than the compressed air consumption calculation, but implies all forms of energy (heat etc.) and enables a self-contained energy balancing within a system. Figure 3 shows the equations that are required for calculating the exergy flows at certain observation points and the exergy consumption for a double stroke of a standard cylinder drive.

## Method 2: Exergy analysis

- Observation point

Exergy flow at a certain observation point

$$\dot{E}_{ex,i} = \dot{m}_i \cdot (c_p \cdot T_0 - c_p \cdot T_i) - \dot{m}_i \cdot T_0 \cdot \left( -c_p \cdot \ln \frac{T_i}{T_0} + R \cdot \ln \frac{p_i}{p_0} \right)$$

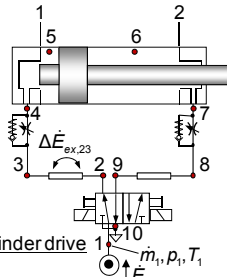
Exergy consumption for a double stroke of the cylinder drive

$$E_{ex,1} = \int_{double\ stroke} \dot{m}_i \cdot (c_p \cdot T_0 - c_p \cdot T_i) \cdot dt - \int_{double\ stroke} \dot{m}_i \cdot T_0 \cdot \left( -c_p \cdot \ln \frac{T_i}{T_0} + R \cdot \ln \frac{p_i}{p_0} \right) \cdot dt$$

Exergy flow difference between certain observation points (including leakage)

$$\Delta \dot{E}_{ex,ij} = \dot{m}_i \cdot c_p \cdot T_j - \dot{m}_i \cdot c_p \cdot T_i + \dot{m}_i \cdot T_0 \cdot c_p \cdot \ln \frac{T_j}{T_0} - \dot{m}_i \cdot T_0 \cdot c_p \cdot \ln \frac{T_i}{T_0} - \dot{m}_i \cdot T_0 \cdot R \cdot \ln \frac{p_j}{p_0} + \dot{m}_i \cdot T_0 \cdot R \cdot \ln \frac{p_i}{p_0}$$

Figure 3: Exergy flows and exergy consumption for a double stroke (1→2 + 2→1) of a standard cylinder drive



Based on the determined single exergy flows an exergy flow difference between several observation points can be calculated. With regard to a defined operating task the exergy loss of each component can be determined.

The analysis of the required equations of the first and second method shows the influence of the design parameters of the drive system on the energy consumption. In particular the working pressure and the volumes of the cylinder and the tubes have a large influence.

The working pressure should be adapted on the individual requirements of each drive. In general a high pressure level increases the occurrence of leakage and total leakage mass flow. Drive systems with low requirements on the load force should be supplied with a corresponding low pressure level. The pressure level can be reduced by using a pressure regulator and increased by using a pressure booster.

The dimensioning of the components especially the choice of the piston and tube diameter has a large influence on the energy consumption. Furthermore unneeded filling volumes cause a slow dynamic behaviour.

## 3 Energy saving measures

For pneumatic single drives and multi-axes systems three categories for energy saving solutions can be distinguished. These categories concern dimensioning as well as pneumatic structures, valve technologies and control strategies. Within these categories different energy saving solutions are known [4] that are shown in the scheme in fig. 4.

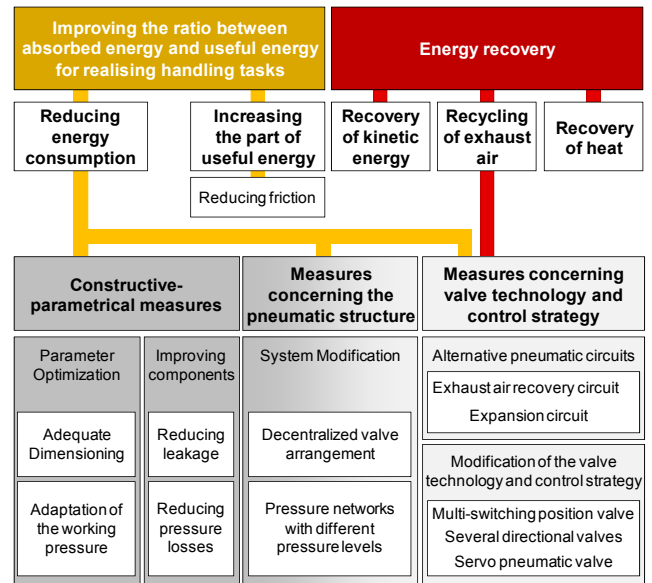


Figure 4: Energy saving measures on pneumatic drive systems

The first category <Constructive-parametrical measures> contains methods for optimizing the design parameters of a drive structure or improving components meaning constructive modifications. The parameter optimization aims at the reduction of the energy consumption by modifying the design parameters of the drive. The improving of components requires the minimization of leakage and the reduction of preventable pressure drops. In most cases component modifications can be realised without any constraints but that often means a large effort concerning costs.

The second category <Measures concerning the pneumatic structure> contains saving solutions that target on the modification of the system structure consisting of several drives. This involves for example decentralized valve arrangements or the implementation of pressure networks with different pressure levels. For the dimensioning of different drives only a few standardized components can be used. In consequence these drives are often oversized. So it is very important to supply these drives with an appropriate pressure level. The usage of a multi-level pressure network enables an adapted compressed air supply of different drives.

The third category is “Measures concerning valve technology and control strategy”. Some of these solutions with regard to valve technology are energy-saving circuit concepts like expansion- and exhaust-air recovery circuits as described in [5] and [6]. These pneumatic circuit configurations serve to utilize exhaust air which in case of standard configurations is vented unused. Further circuit- and control-based solutions aim at the modification of control- and valve technology. Their goal is to minimize fundamental losses at cylinder drives. Some examples are pressure losses due to the use of exhaust-air flow control, energy emitted through exhaust air or wasted heat during the compression processes at high pressure levels. Some studies focus on circuit configurations consisting of several 2/2-

switching valves [7]. The energy requirements of a drive system can be significantly improved, by using an optimized control strategy in combination with these switching valves. The main energy saving of this circuit structure is achieved by closing the supply valve and using the expansion energy of the compressed air during motion of the piston.

In the following potential saving measures will be implemented on a single cylinder drive of a handling system. The handling system is an automatic placement machine which is used for the placement and quality check of plug housings. The example drive system is a typical standard exhaust-air-flow-controlled cylinder drive in the field of small-part handling. The structure of the drive and some important design parameters concerning energy consumption and motion behaviour are shown in fig. 5. The drive has a pressure supply (1), tubing (3), different valves (2), (4) and a pneumatic cylinder (5).

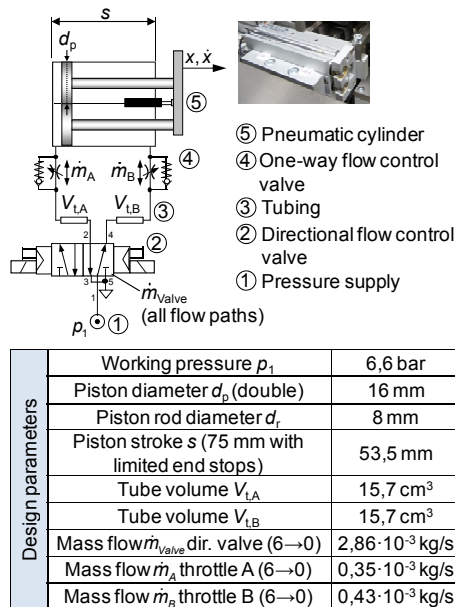


Figure 5: Structure and design parameters of the example drive

The drive is designed as a double piston cylinder with an oil brake. According to its operating task the standard configuration of the cylinder drive is oversized.

The automatic placement machine including the chosen example drive was energetically analyzed in [8]. In this process an exergy analysis according to method 2 was performed. Thereby the balancing with the exergy enables the detection of exergy losses and appropriate saving potentials. This analysis had shown that a significant energy saving potential of the machine lies in an optimized dimensioning and in the utilization of the exhaust-air of the cylinder drives. The potential of recovering the exhaust-air is even greater when an exhaust-air flow control is not used for the purpose of speed control.

After analyzing the saving potentials, a benchmark of possible energy saving measures was performed. Therefore the characteristics of these saving measures were compared

to the detected energy saving potentials and the attributes of the automatic placement machine. Based on this benchmark two potential saving measures were identified i.e. the optimization of the design parameters and the use of an exhaust-air recovery circuit.

## 4 Realization of energy saving measures

In the first instance these saving measures are tested and implemented in a simulation model individually.

A lumped parameter model of the drive is created (*SimulationX*). The simulation model consists of different physical domains. Table 1 gives an overview of important parameters, which are required for modelling.

Tab. 1: Required parameters for the simulation model

Component	Required parameters for modelling
Pneumatic cylinder	Dimensions ( $\varnothing$ piston/rod, stroke, clearance of the sealing)
	Mass of the load (Moving mass)
	Friction Force
	Heat transfer coefficient $k_{cylinder}$
One-way flow control valve	Throttle position
	C-b-characteristics
	Cracking pressure
Tubing	Dimensions ( $\varnothing$ , length)
	C-b-characteristics
	Heat transfer coefficient $k_{tube}$
Directional flow control valve	C-b-characteristics
	switching time
Pressure supply	Opening performance
	Working pressure $p_1$

The parameterisation of the components is based on data sheets, pneumatic schematics and the measurement data. Some characteristics like the throttle position of the one-way flow control valves or the friction force of the cylinders have to be calculated. For example the sliding friction of the cylinder is determined by the equilibrium of forces at the piston, when it moves with constant speed. The heat transfer coefficients at the tubing and at the cylinders can be calculated with an approximation formula [8]. The amount of leakage of the drive is relatively small and can therefore be neglected.

Firstly the optimization of the design parameter is performed at the example drive. Design parameters of the drive structure are i. e. the working pressure, the piston diameter, the length of the tubes or the flow rate of the metering throttles.

### 4.1 Optimization of the design parameters

The objective of the optimization is to reduce the energy consumption for a double stroke of the cylinder drive while sustaining the motion profile. In the first instance the range of nominal values of the design parameters will be set. The piston stroke and the flow rate at the directional valve will not be changed, since the value of the piston stroke is directly coupled to the operating task and the directional valve is part of a valve terminal with specified dimensions. The variation range of each design parameter is  $\pm 25\%$ . For

example, a reduction of the tube volume  $V_{t,a}$  of 25% means to trim the tube length about 25%. In most cases a reduction of the tube length is possible, despite constructional constraints. The definition of a variation range generally constrains the considered values of the design parameter. Thus it is possible that the parameter configuration with the lowest energy consumption of the cylinder drive (global optimum) could no longer be found. However on the basis of the suggested approach drive configurations with lower energy consumption and sufficient robustness can be found which is important for the usage in an industrial application.

In addition to the variation range of the design parameters some restrictions will be determined for the optimization process. These are obtained from the original motion profile. The cylinder drive has to fulfil its operating task according to the original operating times. The example drive is linked with other drives within the handling system. The drive's operating times have to remain constant to keep the total cycle time of the entire machine. The acceleration, the maximum velocity and the velocity at the end of the stroke are limited. In general there are different constraints with regard to manufacturer-specific limit values and the transport of handling objects. Generally the restrictions make sure that the motion profile of the modified drive is similar to the original one. The variation range of the design parameters and the restrictions are listed in tab. 2.

Tab. 2: Variation range of the design parameters and restrictions for the optimization process

Design parameter	Working pressure $p_1$	4,8 bar	<	6,6 bar	<	8,4 bar
	Piston diameter $d_p$	12,0 mm	<	16,0 mm	<	20,0 mm
	Tube volume $V_{t,A}$	11,8 cm <sup>3</sup>	<	15,7 cm <sup>3</sup>	<	19,8 cm <sup>3</sup>
	Tube volume $V_{t,B}$	11,8 cm <sup>3</sup>	<	15,7 cm <sup>3</sup>	<	19,8 cm <sup>3</sup>
	Mass flow $\dot{m}_A$ throttle A (6→0)	$0,26 \cdot 10^{-3}$ kg/s	<	$0,35 \cdot 10^{-3}$ kg/s	<	$0,44 \cdot 10^{-3}$ kg/s
	Mass flow $\dot{m}_B$ throttle B (6→0)	$0,32 \cdot 10^{-3}$ kg/s	<	$0,43 \cdot 10^{-3}$ kg/s	<	$0,54 \cdot 10^{-3}$ kg/s
Restrictions	Extending time $t_{ex}$	500 ms	<	512 ms	<	520 ms
	Retracting time $t_{re}$	238 ms	<	242 ms	<	248 ms
	Max. extending speed $\dot{x}_{ex,max}$	0,09 m/s	<	0,11 m/s	<	0,13 m/s
	Max. retracting speed $\dot{x}_{re,max}$	0,25 m/s	<	0,3 m/s	<	0,35 m/s
	Max. acceleration $\ddot{x}_{max}$	25 m/s <sup>2</sup>	<	32 m/s <sup>2</sup>	<	40 m/s <sup>2</sup>

The optimization is done by linking the lumped parameter model with an optimization tool (*OptiY*). The optimization tool realizes different simulation runs with varying design parameters within the defined range. For every simulation run the amount of energy consumption after a double stroke of the drive and violations of the specified restrictions are benchmarked. Because the number of design parameters is low a gradient-based optimization strategy (*Hooke-Jeeves*) is chosen [9]. A nominal optimization with 500 steps is performed.

The optimization process leads to a modified cylinder drive configuration with reduced energy consumption. The final resulting design parameters are shown in tab. 3.

Tab. 3: Design parameters of the optimized cylinder drive configuration

	Standard	Optimized	
Design parameters	Working pressure $p_1$	6,6 bar	5,0 bar
	Piston diameter $d_p$	16 mm	16 mm
	Tube volume $V_{t,A}$	15,7 cm <sup>3</sup>	11,8 cm <sup>3</sup>
	Tube volume $V_{t,B}$	15,7 cm <sup>3</sup>	11,8 cm <sup>3</sup>
	Mass flow $\dot{m}_A$ throttle A (6→0)	$0,35 \cdot 10^{-3}$ kg/s	$0,36 \cdot 10^{-3}$ kg/s
	Mass flow $\dot{m}_B$ throttle B (6→0)	$0,43 \cdot 10^{-3}$ kg/s	$0,46 \cdot 10^{-3}$ kg/s

The optimized drive structure has a reduced working pressure, reduced tube volumes and the flow rate at the metering throttles is raised. For the implementation on the actual drive the working pressure has to be reduced by using a pressure regulator. Furthermore the tubes have to be trimmed and the throttle position of metering throttles has to be increased. The piston diameter remains unchanged because a change of this parameter would have a weighty influence on the motion profile and often leads to a violation of the restrictions. The simulated modified drive structure shows energy savings up to 44 % (see fig. 6).

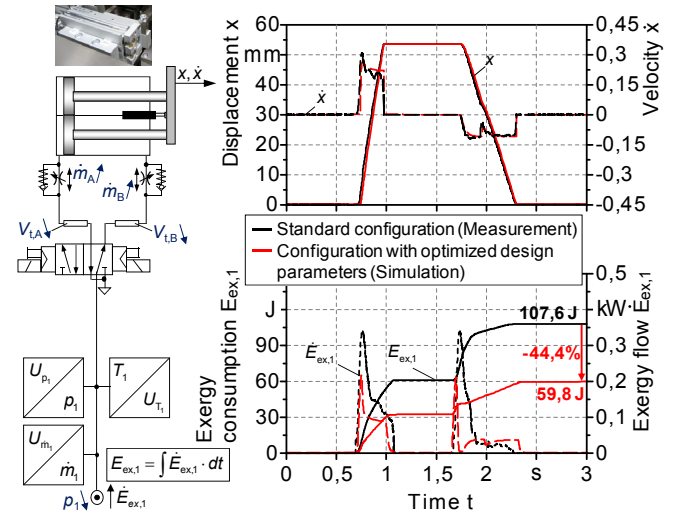


Figure 6: Energy savings using a design parameter optimization for a standard cylinder drive

As depicted in fig. 6 the motion profile with the modified design parameters meets the original profile very well. This result shows that the restrictions were observed during the optimization process.

#### 4.2 Implementation of an exhaust-air recovery circuit

An exhaust air recovery circuit can be used for drives that require only a small cylinder force for the backward stroke. For the implementation of the exhaust-air recovery system a storage circuit is added to the original configuration of the drive. There are different structural possibilities for implementing a recovery circuit. One of these circuit

structures including its necessary valve control strategy is depicted in fig. 7.

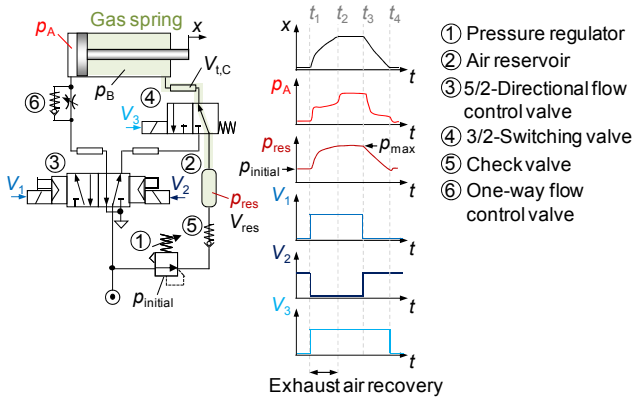


Figure 7: Structure and control strategy of the used exhaust-air recovery circuit

The circuit structure shown in fig. 7 is suitable for upgrading a standard drive that is connected to a valve terminal. In general a pressure regulator (1) and an air reservoir (2) have to be installed. The initial pressure of the air reservoir is set by the pressure regulator. The control of the movement direction is executed by the 5/2-directional flow control valve (3). The 3/2-switching valve (4) connects the air reservoir to the cylinder chamber B. When the piston extends, the compressed air within the gas spring is compromised and the pressure  $p_{res}$  rises. The check valve (5) prevents the saved compressed air of returning to the pressure regulator. At the same time the rising counterforce at the piston causes a limitation of the piston speed that eliminates the need for a metering throttle. After completing the extending stroke the saved energy is used for the backward stroke. The one-way flow control valve (6) realises the speed regulation for the backward stroke.

The initial pressure, the volume of the air reservoir and the flow rate of the metering throttle have a large influence on the motion profile of the cylinder drive. The volume of the air reservoir strongly depends on the piston diameter and the stroke. These appropriate operating parameters can be determined with the help of the simulation model with the coupled optimization tool. Table 4 lists the determined parameters for the recovery circuit.

Tab. 4: Determined design parameters of the recovery circuit

Initial pressure $p_{initial}$	4,5 bar
Volume of the air reservoir $V_{res}$	50 cm <sup>3</sup>
Mass flow $\dot{m}_A$ throttle A (6→0)	0,39 · 10 <sup>-3</sup> kg/s

Another way to determine the suitable volume of the air reservoir  $V_{res}$  can be realised by an approximate calculation.

The volume of the gas spring  $V_{gas}(x)$  is:

$$V_{gas}(x) = \left( \frac{\pi}{4} (d_p^2 - d_r^2) \cdot (s - x) + V_{dead,B} + V_{t,C} + V_{res} \right) \quad (1)$$

The volume of the tube  $V_{t,C}$  and the dead volume  $V_{dead,B}$  are very small and can be neglected.

Under isothermal conditions the states of the gas spring at the time  $t_1$  with  $V_{gas}(x = 0 \text{ mm})$  and  $t_3$  with  $V_{gas}(x = 53,5 \text{ mm})$  are given with:

$$t_1: \quad p_{initial} \cdot \left( \frac{\pi}{4} (d_p^2 - d_r^2) \cdot s + V_{res} \right) = m \cdot R \cdot T \quad (2)$$

$$t_3: \quad p_{max} \cdot V_{res} = m \cdot R \cdot T \quad (3)$$

During the time the stroke extends, the piston has to reach the end stop safely. As a conclusion the maximum pressure  $p_{max}$  of the gas spring has to be limited. A useful restriction for the maximal counterforce  $F_B$  is:

$$F_B \leq \frac{2}{3} \cdot p_1 \cdot \frac{\pi}{4} \cdot d_p^2 \quad (4)$$

In this case the maximal pressure  $p_{max}$  is:

$$p_{max} \leq \frac{2}{3} \cdot p_1 \cdot \frac{d_p^2}{(d_p^2 - d_r^2)} \quad (5)$$

The result for the calculation of  $V_{res}$  is obtained by equalizing formula (2) and (3) and using condition (5).

$$V_{res} = \frac{p_{initial}}{\frac{2}{3} \cdot p_1 \cdot \frac{d_p^2}{(d_p^2 - d_r^2)} - p_{initial}} \cdot \frac{\pi}{4} (d_p^2 - d_r^2) \cdot s \quad (6)$$

On the basis of eq. (6) the volume of the air reservoir  $V_{res}$  can be calculated as a function of the geometric parameters of the cylinder, the working pressure  $p_1$  and the chosen initial pressure  $p_{initial}$ .

The use of a recovery circuit includes higher investment costs due to the additional components. The switching valve can be excluded when using a decentralized valve arrangement. However the pressure regulator, the check valve and the air reservoir increase the investment as well as the maintenance costs.

Besides the parameters of the recovery circuit have to be adapted in case of changing operating times, load masses or cylinder parameters.

The simulation of this modified drive structure shows energy savings amounts of 43 % (see fig. 8). The motion profile of the modified drive structure basically matches the original profile. The operating times are a bit higher ( $\Delta x_1$  and  $\Delta x_2$ , fig. 8) but don't leave the specified range. These extended operating times don't restrict the functionality of the drive.

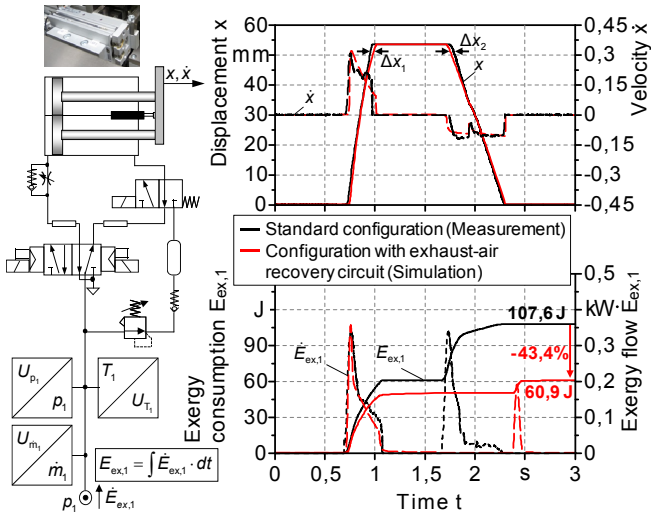


Figure 8: Energy savings using an exhaust-air recovery circuit for a standard cylinder drive

As shown in fig. 6 and fig. 8 both saving measures, e.g. the design parameter optimization and the exhaust-air recovery circuit, can reduce the energy consumption of the example drive about 44 % without changing the motion profile.

### 4.3 Combination of an exhaust-air recovery circuit and a design parameter optimization

In the next step both energy saving solutions are implemented in combination at the example cylinder drive. Figure 9 compares the system behaviour of the drive, as well as the energy flow and energy consumption before and after the modification. The resulting energy savings are proven experimentally.

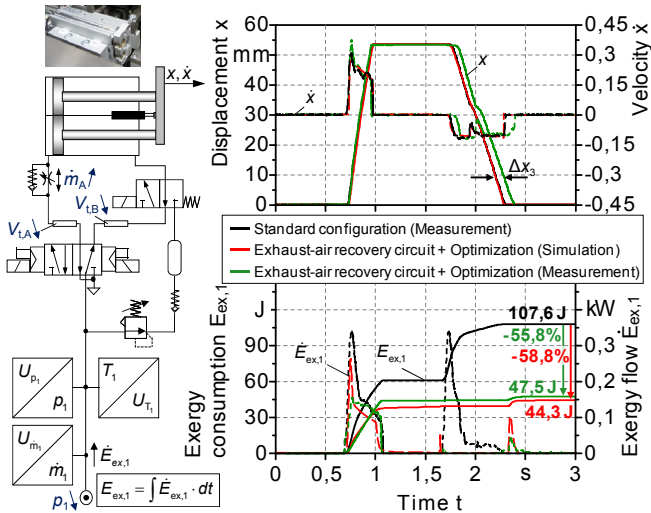


Figure 9: Resulting energy savings using an exhaust-air recovery system and a design parameter optimization for a standard cylinder drive

After the modification the motion profile shows a delay  $\Delta x_3$  in the backward stroke of the cylinder. This will not restrict the functionality of the drive within the machine, since the backward stroke is not time-sensitive. As depicted in fig. 9

the energy saving determined by measurement data corresponds to the results of the simulation.

## 5 Determination of the pay-back period

In order to benchmark the used energy saving solutions the pay-back period has to be determined. Therefore the investment costs and the cost savings due to reduced energy costs have to be compared.

### 5.1 Operating scenario and costs for compressed air

For calculating the energy costs the number of double strokes within one year has to be specified. The selected drive is part of an entire handling system that has a total cycle time of 6 seconds. During this period the drive realises one double stroke. The handling system operates 16 hours per day. During the weekend and on maintenance days the machine remains at stand still. All in all the handling system runs 250 days per year. The number  $N_1$  of double strokes per year is calculated in tab. 5.

Tab. 5: Calculation of the number of double strokes per year

Cycle time for one double stroke	6 s
Operating time per day	16 h
Number of double strokes per day	57.600
Operating time per year	250 days
Number of double strokes $N_1$ per year	14.400.000

The compressed air consumption  $D_1$  of each drive structure per double stroke can be determined via the exergy consumption under the assumption of isothermal conditions:

$$D_1 = \frac{E_{ex,1}}{T_0 \cdot R \cdot \rho_0 \cdot \ln(p_1/p_0)} \quad (5)$$

In the next step the costs for generating the compressed air have to be considered. At this point an abstracted approach for the compressed air costs is chosen. The compressed air costs are  $C_{air}$  €/Nl (Nl ... litre under ambient conditions). The Compressed air costs within one year can be calculated on the basis of eq. (6).

$$\text{Compressed air costs} = N_1 \cdot D_1 \cdot C_{air} \quad (6)$$

All costs will be referred to the compressed air costs  $C_{standard}$  of the standard configuration (see tab.6).

Tab. 6: Calculated compressed air costs and savings

Drive configuration	Standard configuration	Design parameter optimization	Exhaust-air recovery circuit	Recovery circuit and parameter optimization
Compressed air consumption $D_1$ per double stroke [Nl]	0,570	0,317	0,323	0,235
Compressed air costs per year [€]	$C_{standard}$	$0,56 \cdot C_{standard}$	$0,57 \cdot C_{standard}$	$0,41 \cdot C_{standard}$
Compressed air savings per year [€]		$-0,44 \cdot C_{standard}$	$-0,43 \cdot C_{standard}$	$-0,59 \cdot C_{standard}$

## 5.2 Investment costs

The investment costs of each drive configuration are calculated as the sum of all single component investment costs. This includes the cylinder, valves, the air reservoir and end stop switches. The additional used 3/2 switching valve of the exhaust-air recovery system increases the functionality of the drive structure, but can be dropped to reduce investment costs. In the next step the additional investment costs in relation to  $C_{\text{standard}}$  are determined. The results are shown in tab. 7.

Tab. 7: Calculated investment costs

Drive configuration		Standard configuration	Design parameter optimization	Exhaust-air recovery circuit	Recovery circuit and parameter optimization
Components	Cylinder	1	1	1	1
	5/2-valve	1	1	1	1
	3/2-valve			1	1
	One-way valve	2	2	1	1
	Pressure Regulator		1	1	2
	Check valve			1	1
	Air reservoir			1	1
	End stop switches	2	2	2	2
Investment costs [€]		$2,97 \cdot C_{\text{standard}}$	$3,17 \cdot C_{\text{standard}}$	$3,80 \cdot C_{\text{standard}}$	$4,00 \cdot C_{\text{standard}}$
Additional investment costs [€]			$+0,20 \cdot C_{\text{standard}}$	$+0,83 \cdot C_{\text{standard}}$	$+1,03 \cdot C_{\text{standard}}$

Finally the pay-back period for each configuration can be determined. Figure 10 displays the investment costs and compressed air costs versus the operating time of the drive. The break-even point is signed with the cross. No maintenance costs as well as costs due to installation are considered.

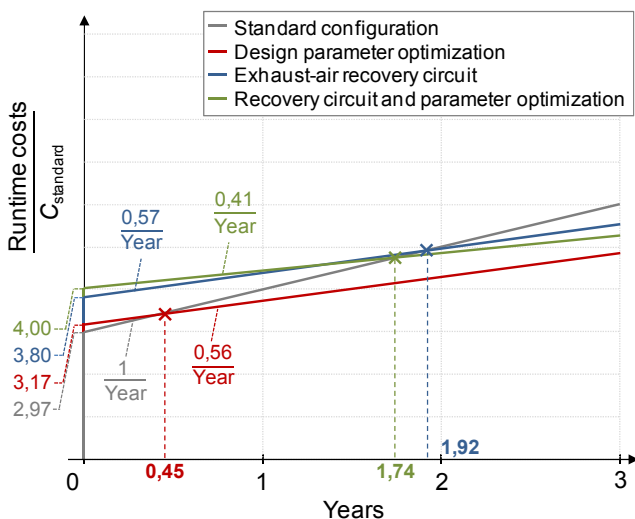


Figure 10: Determination of the pay-back periods

As shown in fig.10 the drive configuration with the optimized design parameters has the shortest pay-back period of 0,45 years. This configuration only needs an additional pressure regulator, so the investment costs are comparable to the standard configuration. The effort on additional components for the exhaust-air recovery system is very high. The pay-back period of these drive configurations with exhaust-air recovery system lies between 1,75 to 2,00 years.

## 6 Conclusion

This article proposes energy saving measures on pneumatic drive systems. Normally investigations on energy saving measures only deal with saving potentials and functional issues. This paper presents the saving potential, the effort for implementation and the calculation of the pay-back period for two chosen energy saving solutions.

For the determination of the energy consumption two methods are presented, i.e. a compressed air consumption calculation and an exergy analysis. An exergy analysis is the preferred method because it considers all forms of energy and enables the quantification of energy losses as well as a self-contained energy balancing.

This paper shows several different measures for saving energy at pneumatic single drives and multi-axes systems. The implementation of chosen energy saving measures is tested at a representative single example drive.

The energetic analysis of this drive has successfully proven that there are two significant saving potentials. Referring to its operating task the example drive is oversized with tube lengths sized quite generously and the pressure level being too high. So the first saving method targets at an adequate dimensioning of the drive. The second saving potential lies in the utilization of the exhaust-air of the cylinder drive. This potential is even greater when an exhaust-air flow control is not used for the purpose of speed control. Based on these identified energy saving potentials, two suitable energy saving solutions are selected and implemented, i.e. an optimization of the drive's design operating parameters as well as an exhaust-air recovery system.

The implementation of these two saving measures is tested via simulation. Therefore a lumped parameter model of the drive is created and validated via measurement data. The possible energy savings when implementing the saving solutions individually as well as in combination is shown. When combining both saving measures energy savings up to 56% can be proven.

For the validation the saving measures are implemented at the example drive. In this process the effort of implementing each measure is demonstrated. The results of the experimental investigations match the results gained by simulation.

Finally the pay-back period of each saving measure is determined based on an operating scenario. The pay-back period for the design parameter optimization is 0,45 years because only one additional pressure regulator is needed.

However the optimization process can only be done by using a coupled optimization tool. The calculated pay-back period of the drive structures with exhaust-air recovery system is less than 2 years.

As shown in this article pneumatic drive systems often hold significant saving potentials. Drive systems with energy saving solutions can utilize these potentials within a manageable pay-back period.

## 7 Acknowledgement

The content of this article was developed within the project „Verbesserung der Energieeffizienz pneumatischer Handhabungssysteme“, that was funded by the Fluid Power Research Fund of VDMA, the German Engineering Federation, FKM Nr. 702520.

## Nomenclature

Designation	Denotation	Unit
$c_p$	Specific isobare heat capacity	[J/kg·K]
$d$	Diameter	[m]
$E$	Energy	[J]
$E_{ex}$	Exergy	[J]
$\dot{E}_{ex}$	Exergy flow	[J/s]
$k$	Thermal transmittance	[W/m <sup>2</sup> ·K]
$m$	Mass	[kg]
$\dot{m}$	Mass flow	[kg/s]
$n$	Polytropic coefficient	-
$p$	Pressure	[Pa]
$p_0$	Ambient pressure	[Pa]
$R$	Specific gas constant	[J/kg·K]
$s$	Stroke	[m]
$T$	Temperature	[K]
$T_0$	Ambient temperature	[K]
$V$	Volume	[m <sup>3</sup> ]
$x$	Displacement	[m]
$\dot{x}$	Velocity	[m/s]
$\kappa$	Isentropic coefficient	-
$\rho_0$	Density of the ambience	[kg/m <sup>3</sup> ]

## References

[1] M CAI, and K Kawashima, T Kagawa. *Power Assessment of Flowing Compressed Air*. Published in Journal of Fluids Engineering, Transactions of the ASME, Vol.128, No.2, 2006.

[2] J Hepke, and J Weber. *Energiesparende Pneumatik*. fluid Markt 2013, 83-89, 2012.

[3] W T Bader, and J K Kissock. *Exergy Analysis of Industrial Air Compression*. Proc. from the 22th National Industrial energy Technology Conference, Houston, 2000.

[4] N N. *EnEffAH - Energy Efficiency in Production in the Drive and Handling Technology Field*. final report, 37-44, 2012.

[5] C Ferraresi, and W Franco, and G Quaglia, and M Scopesi. *Energy Saving in Pneumatic Drives: An Experimental Analysis*. Proc. from the 9th International Workshop on Research and Education in Mechatronics, Bergamo, 2008.

[6] E Köhler, and E Zipplies. *Pneumatische Antriebskonzepte unter dem Gesichtspunkt der Energieoptimierung und der Verbesserung der Dynamik*. Proc. from Viertes Deutsch-Polnisches Seminar: Innovation und Fortschritt in der Fluidtechnik, Chemnitz, 2001.

[7] M Doll, and O Sawodny. *Energy Efficient Adaptive Control of Pneumatic Drives with Switching Valves*. Proc. from the 7th International Fluid Power Conference, Dresden, 2012.

[8] J Hepke, and J Weber. *Improving Energy Efficiency of Pneumatic Handling Systems*. Proc. from the 7th International Fluid Power Conference, Dresden, 2012.

[9] K-H Grote, and J Feldhusen. *Dubbel – Taschenbuch für den Maschinenbau*. 22th Edition, Springer-Verlag Berlin Heidelberg New York, D 29, 2007.

[10] H P Schwefel. *Numerische Optimierung von Computer-Modellen mittels der Evolutionsstrategie*, Birkhäuser Verlag, Basel und Stuttgart, 1977.



# A Scheme for Compressed Air Saving in Pneumatic Positioning Systems for High Loads

Luciano Endler, Victor Juliano De Negri, and Eugênio B. Castelan\*

Laboratory of Hydraulic and Pneumatic Systems, Mechanical Engineering Department, Federal University of Santa Catarina, Florianópolis, Santa Catarina, Brazil

E-mail: lucianoka@ibest.com.br, victor@emc.ufsc.br, eugenio@das.ufsc.br

\*Automation and Systems Department, Federal University of Santa Catarina, Florianópolis, Santa Catarina, Brazil

## Abstract

A problem with pneumatic positioning systems is the low energetic efficiency. This paper presents a structure of a compressed air saving for pneumatic positioning systems with capacity to move high loads. This structure use the loading to save compressed air and thus to increase the energetic efficiency of these systems. This configuration adds a fast switching on/off valve in a feedback between the cylinder chambers. This type of valves is low cost, compared with a proportional valve, but the system can achieve the same performance. Experimental results show that with this type of configuration up to 58 % of compressed air saving can be achieved in comparison to classical pneumatic positioning system.

**Keywords:** Pneumatic system, fast switching valve, energetic efficiency, position control.

## 1 Introduction

Pneumatic servo positioning systems are very attractive for industrial applications because they have a good power/weight ratio and easy maintenance, when compared with electric positioning systems, and are low cost when compared to hydraulics. Pneumatic positioning systems can be used, for example, in the metal mechanical industry, in the medical area, in the brakes of heavy vehicles, in the agricultural area and others.

Pneumatic systems are considered as having a low energy-efficiency [1], and also present some control difficulties due to nonlinear characteristics of the system, such as air compressibility, nonlinear behavior mass flow rate through the valve orifice [2] and dead zone [3], besides the friction in the seals of the cylinder [4]. Table 1 presents some advantages and disadvantages between the positioning systems mentioned above.

As mentioned before, one of the major problems in the pneumatics systems is the low energetic efficiency, because the compressed air is exhausted to atmosphere after use. Several authors deals with energy saving or consumption of compressed air in pneumatic systems, what can be seen in [5], [6], [7], [8] and [9].

Specifically, [5] uses an auxiliary on/off valve in a feedback between the chambers of an asymmetrical cylinder. Figure 1 shows this scheme. When the piston moves from the left to the right with constant speed, the pressure  $p_B$  in chamber B is greater than the pressure  $p_A$  in chamber A. If the auxiliary valve is opened in this case, some exhaust air of  $p_B$  will be

Table 1: Advantages and disadvantages of positioning systems.

Positioning system	Advantages	Disadvantages
Pneumatic	Easy maintenance, clean, high confiability, does not generate sparks, low cost.	Very low energetic efficiency, difficulties in control, separate power supply, low stiffness.
Hydraulic	High force density, accumulators for peaks load, easy control, keep high forces, stiffness, low velocity, does not generate sparks.	Hard installation of power supply, noisy, leakage, fire risk, high cost.
Electric	Easy maintenance, flexibility, easy control, clean.	Low force density, problems with water, sparks, high cost.

reused. To guarantee that the system is working in case  $p_A > p_B$ , a check valve is placed in this path. When the piston moves from the right to the left, the by-pass valve is closed. A PID controller to control the proportional valve in closed-loop is used. The experimental results show that for 10 work cycles 12 % of compressed air is saved using this system strategy

In [6], a similar configuration as the one in fig. 1 is present.

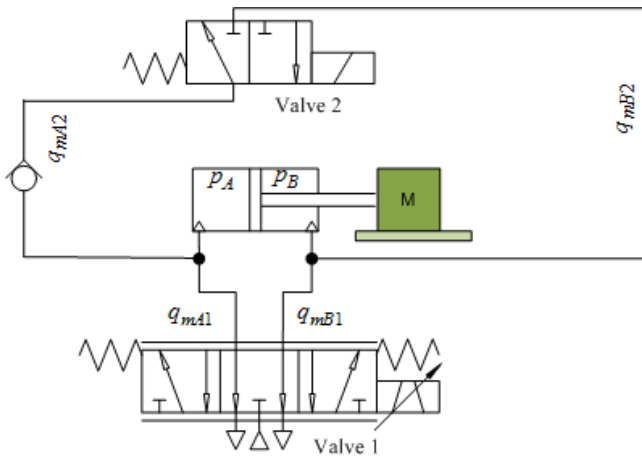


Figure 1: Pneumatic scheme with auxiliary valve (Adapted from [5]).

ted, but in this case the feedback between the chambers of an asymmetrical cylinder is carried out by one proportional valve 2/2 positions (auxiliary valve). An energy saving controller was developed to save compressed air. When the pressure in the depressurized chamber is greater than the pressure in the pressurized chamber, the required mass flow rate can be supplemented via the auxiliary valve. The proposed controller was firstly developed by calculating the control effort required for tracking, and, secondly, by calculating the extent to which the feedback can contribute to the differential mass flow rate. The sliding mode control was utilized to control the two valves. Experimental results present reduced energy consumption by 25-52 % to different desired sinusoidal trajectories and for a step input.

Another concept is proposed in [7]. A typical pneumatic system with a 5/3 proportional valve is replaced by one using two 3/2 proportional valves, such that the mass flow rate on the cylinder chambers can be controlled separately. The idea was to develop two control modes to modified system: an active mode, that uses only compressed air from supply, and a passive mode, that uses only the control of the mass flow rate from the exhaust of the cylinder chamber. Experimental results indicate an energy saving from 10 % to 46 % depending on the desired tracking frequency.

In a similar way, [8] shows a system with two 3/2 proportional valves, using a nonlinear multivariable control law developed for tracking position and energy saving. The system configuration allows to control two different trajectories, position and to control pressure. The control strategy is related to tracking the desired position with minimum energy consumption. The results presented show an improvement of 29 % in terms of energy delivered inside the cylinder with this multivariable nonlinear control.

Finally, [9] shows an analysis not only based on the compressed air consumption of pneumatic systems but also on the balancing of energies. This strategy enables the continuous balancing of all fractions of energy and energy losses. After balancing, as a first step to energy saving, the parameter of

optimization is selected and, secondly, the implementation of exhaust-air recovery system is suggested. An exhaust-air recovery system is made by means of installing two additional directional valves as well as a compressed-air reservoir. Thus, the utilization of the exhaust air of a cylinder chamber is possible when the piston moves from the right to the left. The experimental results show energy savings around 23 % in comparison with the energy consumption of the standard and modified system.

The aim of this paper is the study of a structure for pneumatic positioning systems for compressed air saving in systems which need move high loads. This structure consists of adding a fast switching on/off valve in a feedback between the cylinder chambers. These types of valves are low cost, when compared to proportional valves, but the same system performance can be achieved. This scheme will be presented in next section.

This paper is organized as follows. In Section 2 the pneumatic positioning system with and without an auxiliary valve is described. Section 3 is dedicated to the presentation of the technique for compressed air saving and the model for the estimate of the mass of compressed air consume. The control design is shown in Section 4. In Section 5 the results and discussions are presented. The main conclusions are presented in the last section.

## 2 Description of the pneumatic positioning system

The proposed scheme was implemented in one experimental setup to verify the air compressed saving. This experimental setup was used for tests whose purpose is to control the position of the turbine blades of speed governors of small hydroelectric power plants [10] - [11]. Figure 2 shows a diagram of the typical pneumatic positioning system.

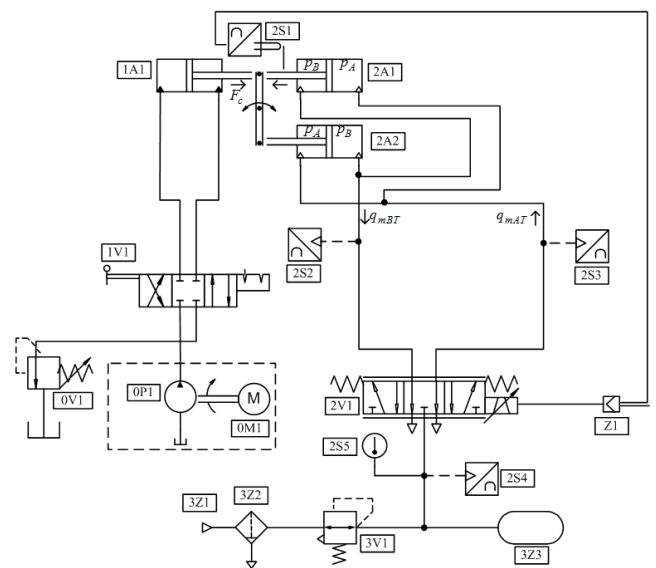


Figure 2: Diagram of the typical test setup (Adapted from [10]).

The components of the typical pneumatic positioning system consist of one 5/3 proportional valve (2V1) for control of mass flow rate, two pneumatic asymmetric cylinders (2A1 and 2A2) in a symmetric configuration, position transducer (2S1), three pressure transducers (2S2, 2S3 and 2S4), thermocouple (2S5), filter (3Z2), compressed air source (3Z1), air reservoir (3Z3), pressure reducing valve (3V1) and valve controller (Z1). The loading system is composed of an asymmetric hydraulic cylinder (1A1), a 4/3 directional hydraulic valve (1V1), a hydraulic power unit (0P1 and 0M1) and a hydraulic pressure reducing valve (0V1).

In this specific study a fast switching on/off valve was added to reuse the compressed air. Figure 3 shows a diagram of the pneumatic positioning system with feedback between chambers with an auxiliary 3/2 fast switching on/off valve configured as a 2/2 valve. In both figures the arrows indicate the positive direction.

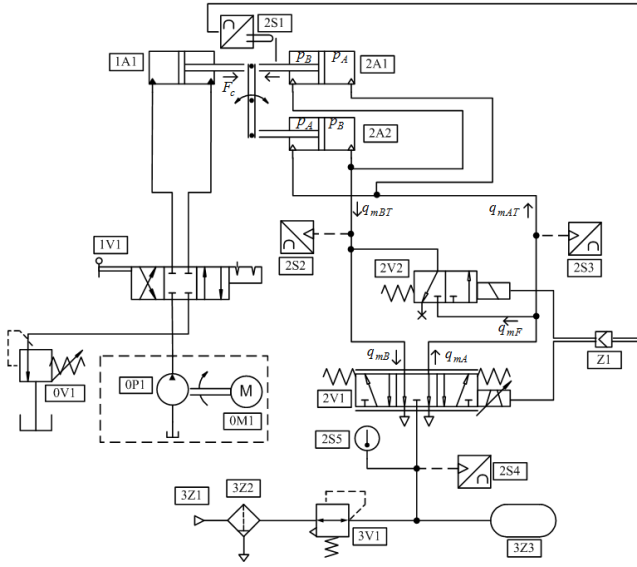


Figure 3: Diagram of the test setup with feedback between the chambers of the cylinder.

The compressed air is supplied to the proportional valve through a pressure reducing valve. The proportional valve spool opens the supplying orifice of compressed air to one chamber of the cylinder and allows the air to be released to the atmosphere. After the variation of the pressure in the cylinder chamber happens, it results in a force that moves the cylinder rod in positive or negative way, depending on the input signal. When the system has a positive load ( $F_c$ ) and is moving in the opposite direction, compressed air can only be saved using the auxiliary valve, as well as when the system as a negative load.

### 3 Compressed Air Saving

As previously described, with a fast switching on/off valve in a feedback between the cylinder chambers, compressed air can be reused. To guarantee the system performance and also provide operating conditions for the system an algorithm was proposed, which is shown in the subsection 3.1. To estimate

the mass of air consumption an equation was developed. This equation is presented in subsection 3.2.

#### 3.1 Technique for compressed air saving

The loading system imposes a difference in the pressure in the cylinder chambers. This difference will be used for the operation of the auxiliary valve. Three cases of operation will be considered as shown below:

Case 1 :

If  $\Delta p > \alpha$

When  $U > 0$  2V1 operating and 2V2 closed

When  $U \leq 0$  2V2 operating and 2V1 closed

Case 2 :

If  $-\alpha \leq \Delta p \leq \alpha$

2V1 operating and 2V2 closed

Case 3 :

If  $\Delta p < -\alpha$

When  $U > 0$  2V2 operating and 2V1 closed

When  $U \leq 0$  2V1 operating and 2V2 closed

where  $U$  is the control signal, 2V1 and 2V2 are the proportional valve and the auxiliary valve, respectively,  $\Delta p$  is the difference between the pressure in the cylinder chambers, and  $\alpha$  is the tolerance of pressure difference, that is the pressure difference required to insure the feedback of the compressed air between the cylinder chambers and also to achieve the performance requirements.

#### 3.2 Mass of compressed air consumed

The mass of compressed air consumed ( $M_P$ ) can be calculated by the integral of the mass flow rate  $q_m$  into the cylinder chamber from the start to stop of piston movement. This is described in the following equation:

$$M_P = \int_{t_i}^{t_f} q_m dt. \quad (1)$$

In the pneumatic servo positioning in study, the pneumatic mass of compressed air consumed should be calculated by consumption of total mass flow rate through the supply. When there is flow from  $S$  to  $A$  or from  $S$  to  $B$ , there is compressed air consumption. In this way, the mass consumption of pneumatic positioning system can be computed by eq. (2):

$$M_P = \int_{t_i}^{t_f} (q_{mA+} + |q_{mB-}|) dt. \quad (2)$$

In the eq. (2),  $q_{mA+}$  and  $q_{mB-}$  can be computed by using the following equation, whose parameters are obtained according to ISO 6358 [12]:

$$q_{mA+} = K_u U_{czm} C_{PS} \rho_0 \omega \left( \frac{P_A}{P_S} \right) \quad \text{if } U \geq 0 \quad (3)$$

$$q_{mB-} = K_u U_{czm} C_{PS} \rho_0 \omega \left( \frac{P_B}{P_S} \right) \quad \text{if } U < 0 \quad (4)$$

Replacing  $qm_{A+}$  and  $qm_{B-}$  in the eq. (2) gives

$$M_P = K_u C \rho_0 p_S \int_{t_i}^{t_f} (U_{czm} \omega \left( \frac{p_A}{p_S} \right) + |U_{czm}| \omega \left( \frac{p_B}{p_S} \right)) dt. \quad (5)$$

The used parameter values are the following constants:  $C = 16.5 \times 10^{-9} \text{ m}^5/\text{Ns}$ ,  $b = 0.12$ ,  $\rho_o = 1.205 \text{ kg/m}^3$  and  $p_S = 8 \times 10^5 \text{ Pa}$ . This equation will be used to calculate the mass of compressed air consumed in pneumatic positioning systems.

## 4 Control Design

The control strategy that will be used in this system consists in using PI controller. However, since there are two different valves, the control strategy for the proportional valve and the fast switching on/off valve are different. In [13] the authors describe a control scheme with a PWM (pulse width modulation) technique associated with a PI control. Thereby, the gains of the controller do not need to be modified, since that the two PID controllers differentiate only by PWM. The PI controller for both valves will be presented in the next subsection.

### 4.1 PI Controller

The PI controller is one of the most used controllers in the industry. The PI controller can be seen in [14]. It is a simple method for implementation and the control law is given by:

$$U(t) = k_P e(t) + k_I \int_{t_0}^t e(t) dt, \quad (6)$$

where  $e(t)$  is the difference between the desired input and the actual output, that is the system error,  $k_P$  is the proportional gain to error and  $k_I$  is the gain proportional to integrative part of the system error. In general, the proportional gain is used to improve the time performance and the integrative term is responsible for reducing the steady state errors.

This control signal was already used in the subsection 3.1, to give the conditions for compressed air saving in the pneumatic positioning system. At this point, the control signal will be split into two signals,  $U\_V1$  and  $U\_V2$ . One will be used to compose the signal sent to the proportional valve and the other to compose the signal sent to the auxiliary valve. In the signal sent to the proportional valve, a dead zone compensation will be used and the signal sent to fast switching on/off valve shall be applied the PWM technique associated with PI control. In the following subsection the dead zone will be identified and compensated by the methodology employed in [3].

### 4.2 Dead zone

The dead zone in the proportional valve is an important non-linearity which should be considered. This nonlinearity happens when the spool width is greater than the orifice valve width. The dead zone presence in a pneumatic positioning system is among the factors that limit the performance of feedback control loops.

Dead zone is a static input-output relationship, that for a range of input values gives no output, where  $U$  is the input and  $U_{zm}$

is the output. In general, the right ( $zmd$ ) and left ( $zme$ ) limits, and the slopes ( $md$  and  $me$ ) are not equal. Figure 4 shows a graphical representation of the dead zone [3].

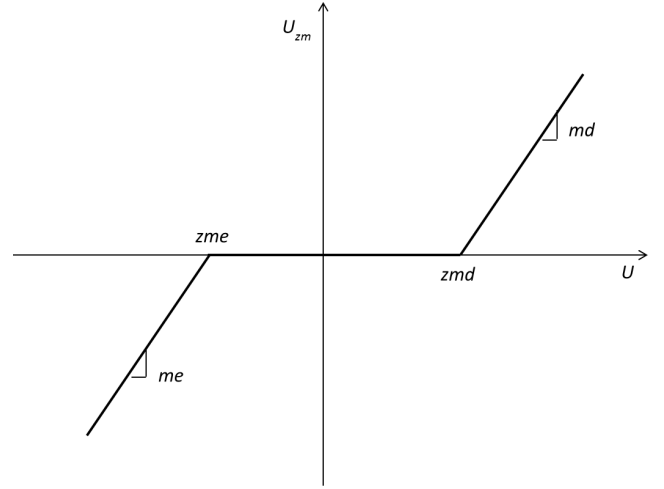


Figure 4: Graphical representation of the dead zone (Adapted from [3]).

The dead zone analytical expression is given by:

$$U_{zm}(t) = \begin{cases} md(U(t) - zmd) & \text{if } U(t) \geq zmd \\ 0 & \text{if } zme < U(t) < zmd \\ me(U(t) - zme) & \text{if } U(t) \leq zme \end{cases} \quad (7)$$

The dead zone compensation is carried out through an inverse function. If the inverse is exact and the parameters are known ( $zmd$ ,  $zme$ ,  $md$  and  $me$ ) the cancelation of the dead zone would be perfect. Therefore, it is necessary to use the smoothed inverse to avoid the discontinuity as near to the zero position and an abrupt switching between  $zme$  and  $zmd$ .

Figure 5 shows the graphical representation of the dead zone compensation with smoothing near to zero position,

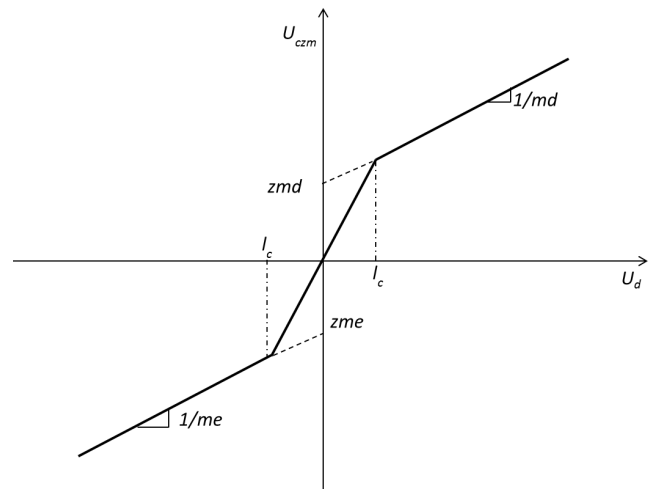


Figure 5: Graphical representation of the dead zone compensation (Adapted from [3]).

where  $U_d$  is the desired signal control in the default of the

dead zone,  $U_{czm}$  is the compensated output signal and  $l_c$  is the smoothness width used in compensation. The inverse function used to compensate the dead zone is described by

$$U_{czm} = \begin{cases} \frac{U_d(t)}{md} + zmd & \text{se } U_d(t) \geq lc \\ \frac{U_d(t)}{me} + |zme| & \text{se } U_d(t) \leq -|lc| \\ \left(\frac{zmd+lc/md}{lc}\right)U_d(t) & \text{se } 0 \leq U_d(t) < lc \\ \left(\frac{|zme|+|lc|/me}{|lc|}\right)U_d(t) & \text{se } -|lc| \leq U_d(t) < 0 \end{cases} \quad (8)$$

To identify the dead zone, an open loop test of actuator system (proportional valve and pneumatic actuator) is proposed with a slow sine control signal with 10 volts amplitude and 50 seconds period according to eq. (9). This methodology was presented in [3].

$$u(t) = -10 \cos\left(\frac{2\pi}{50}t\right), \quad (9)$$

Experimental tests consist of the acquisition of the pressure and control signal of the sine wave given by eq. (9). The graphical control signal as a function of the pressure is presented in 6. At this point, the pressures variation as a function of control signal are analyzed.

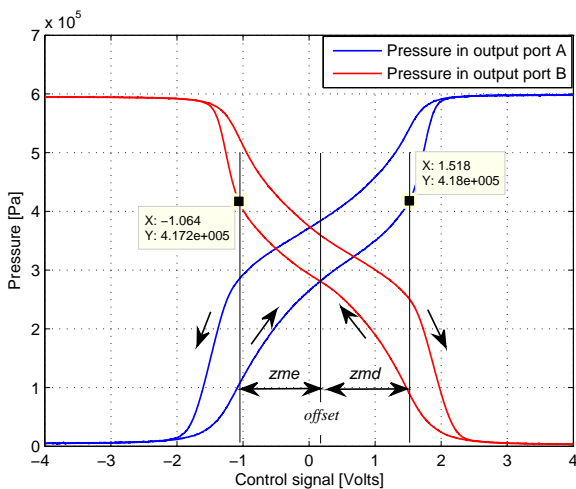


Figure 6: Graphical representation of the dead zone values.

According to fig. 6, for the pressures A and B, when the control signal exceeds the right or left limits of dead zone a pressure change sudden occurs. The offset identification of the proportional valve is through the determination of the midpoint of the pressure variation due to internal leaks. The values achieved from fig. 6 were the right dead zone  $zmd = 1.064$  V, the left dead zone  $zme = 1.518$  V and the offset was considered  $offset = 0$  V because it is very near the center. The values of  $md = me = 1$  and  $l_c = 0.4$  were used. The  $l_c$  value represents a trade-off between control signal quality and effective dead zone compensation. According to [3], if  $l_c$  is large, dead zone compensation is poor. If  $l_c$  is

too small, oscillations in the control signal can occur near of origin.

### 4.3 PWM associated with PI control

This previously mentioned control technique can be applied directly to the proportional valve, but to apply to an on/off valve we should associate the PWM technique. The PWM technique consists in the use of a particular frequency switching in the directional control on/off valve and the duty cycle control. The duty cycle is the time that the signal control is “on” in relation to total cycle time [15]. Figure 7 describes the duty cycle through two examples: a system with a duty cycle of 50% and another with 20%, both with a period of 10 s.

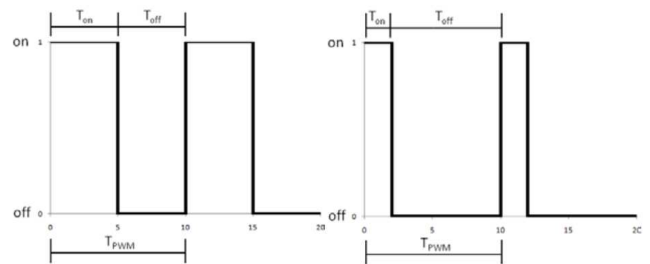


Figure 7: PWM Signal [15].

The control signal from PI control is changed for the duty cycle of the valve according eq. (10)

$$\begin{cases} \text{if } \Delta p > \alpha \text{ and } U \leq 0 \text{ then } U_{dc} = |U_{V2}|/3 \\ \text{if } \Delta p < -\alpha \text{ and } U > 0 \text{ then } U_{dc} = |U_{V2}|/3 \end{cases} \quad (10)$$

Figure 8 shows the implementation of the PWM in Matlab/Simulink.

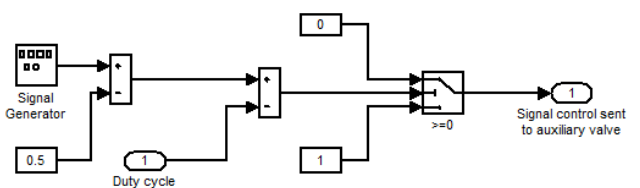


Figure 8: PWM implementation in Simulink.

There is a pulse generator that generates a sawtooth signal with amplitude of -0.5 to 0.5 in a specific frequency (PWM frequency, see fig. 9(a)). This signal is summed with a value of 0.5. This results in a signal with a value ranging from 0 to 1 that is subtracted from the duty cycle (see fig. 9(b)). From the switching block there is a signal sent to the valve (see fig. 9(c)), where 1 is valve “on” and were 0 is valve “off” [15].

## 5 Results and Discussions

The experiments were based in a test bench of a servo-pneumatic system whose purpose is to control the position

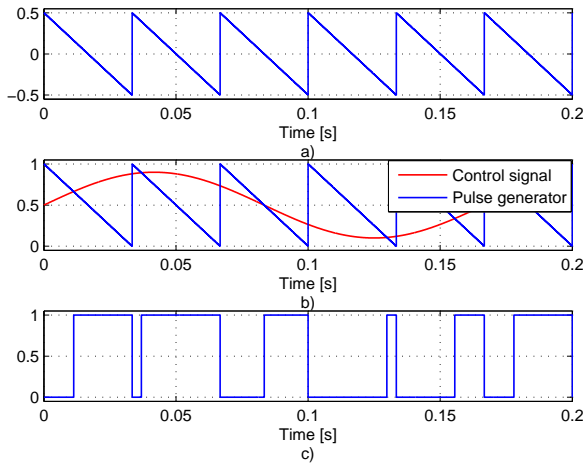


Figure 9: PWM signal generation. a) Pulse generation. b) Pulse and duty cycle. c) Signal sent to the valve (Adapted from [15]).

of the turbine blades used in hydroelectric power plants (see fig. 10). The diagrams of the setup with and without feedback between the chambers of the cylinder were already shown in Chapter 2. Table 2 presented the key components of the test bench.

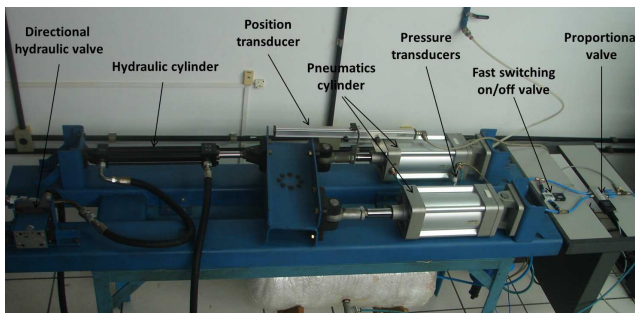


Figure 10: Test bench.

Results for a sinusoidal trajectory with amplitude of 8 mm at a frequency of 0.05 Hz and step inputs of 16 mm and 8 mm will be presented. These trajectories are used in the position control of turbine blades. A dSPACE system was used for data acquisition and control, working together with Simulink/Matlab and ControlDesk software. For the experiments, an integration step of  $1 \times 10^{-3}$  sec and PI controller gains  $K_p=850$  and  $K_i=40$  were used. A period of 0.033 sec for the PWM signal was used. The experiments were obtained with a positive load around 5000 N.

First-order low pass digital filters were used, due to the considerable electromagnetic noise in the position and pressure signals. For the position signal a cut-off frequency of 50 Hz was used and for the pressure signals a 250 Hz were used. The simulink model used in the experimental tests is presented in Appendix A.

Table 2: Main components of test bench.

Component	Maker	Code	Specification
Proportional valve	Festo	MPYE 5-1/8	5/3, 350 l/m.
Fast switching on/off valve	Festo	MHE3-MS1H-3/2G-QS-6	3/2, 200 l/m.
Pneumatics cylinder	Dover	CNGPS125D-B160	Stroke=160 mm, Diameter=125 mm
Hydraulic cylinder	Parker	38.1CBB2HL U29AC-0300	Stroke=300 mm, Diameter=38.1 mm
Directional hydraulic valve	Rexroth	4WMM10 E 10/F	4/3
Pressure transducers	HBM	HDM P8AP	0 - 10 Bar
Position transducer	Balluff	BTL5-A11-M0400-P-S 32	Stroke=400 mm

Figure 11 presents the comparison between the displacement (fig 11(a)) and the error (fig. 11(b)) with and without an auxiliary valve for sinusoidal input. Both responses demonstrate a good trajectory tracking, but both systems present small steps over the sinusoidal trajectory. These small steps are mainly caused by the static friction at the actuator and there are also influences of the flow control valve.

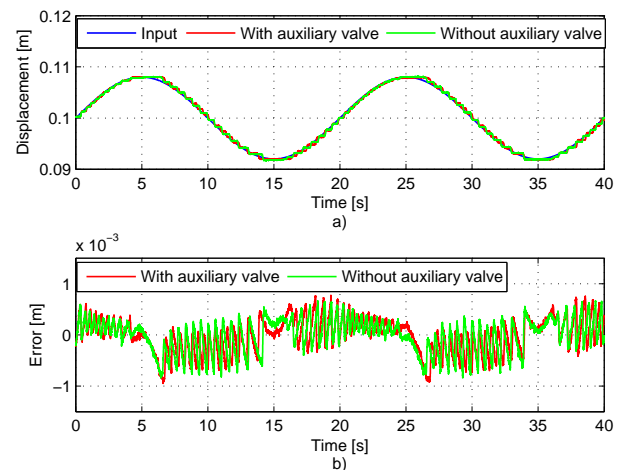


Figure 11: Sinusoidal trajectory tracking (a) and tracking error (b).

Both trajectory tracking errors are between  $\pm 0.9$  mm. Both trajectories, with and without auxiliary valve, did not present significant deviation. The pressures in chambers A and B for the system with and without an auxiliary valve are presented

in fig. 12.

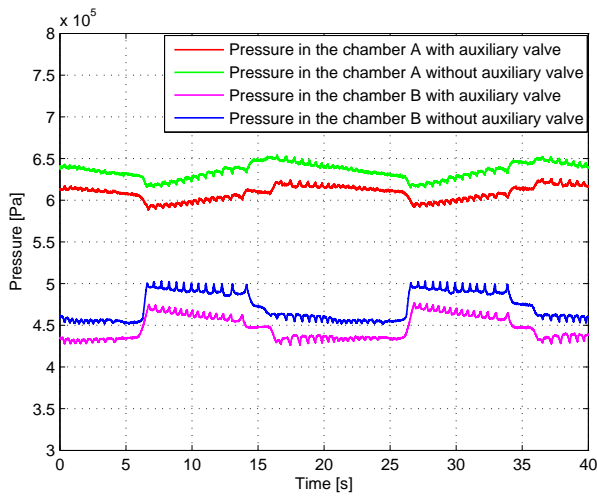


Figure 12: Pressures  $p_A$  and  $p_B$  for sinusoidal trajectory.

The pressures into the cylinder chambers are relatively lower in the system with an auxiliary valve. This occurs because when the system has feedback, the supply is closed and the pressures have a slight decrease.

When the pneumatic positioning system is moving in the positive direction, the auxiliary valve is activated and the proportional valve is closed, and thus there is not any consumption of compressed air. Figure 13 shows the mass of compressed air consumed by the system with and without an auxiliary valve related to the sinusoidal input shown in fig. 11(a). In this case, the compressed air saving is around 58 % for two work cycles.

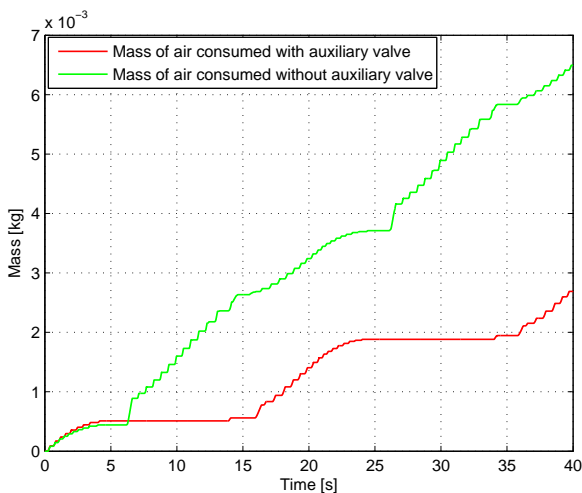


Figure 13: Mass of compressed air consumed for sinusoidal trajectory.

Figure 14 presents the comparison between the displacement (fig. 14(a)) and the error (fig. 14(b)) with and without an auxiliary valve for step inputs.

Both trajectories present position errors that are lower than

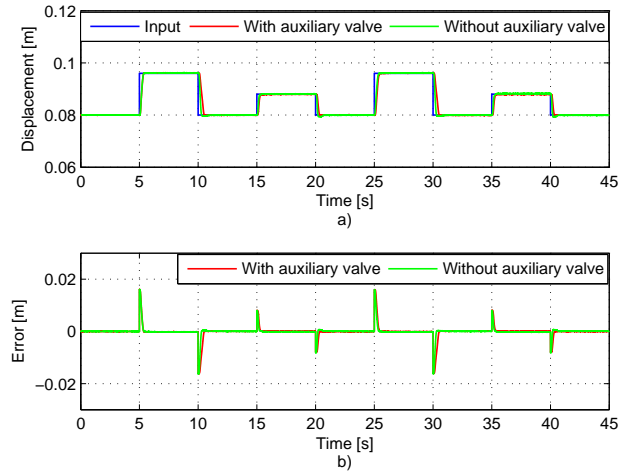


Figure 14: Step responses (a) and position errors (b).

$\pm 0.25$  mm for the steady state. This steady state behavior can be seen in the fig. 15 that shows a zoom of the position error. The experiment with and without an auxiliary valve did not presented significant deviation. Figure 16 presents the signal control sent to the valves with (fig. 16(a)) and without (fig. 16(b)) auxiliary valve for a steps trajectory.

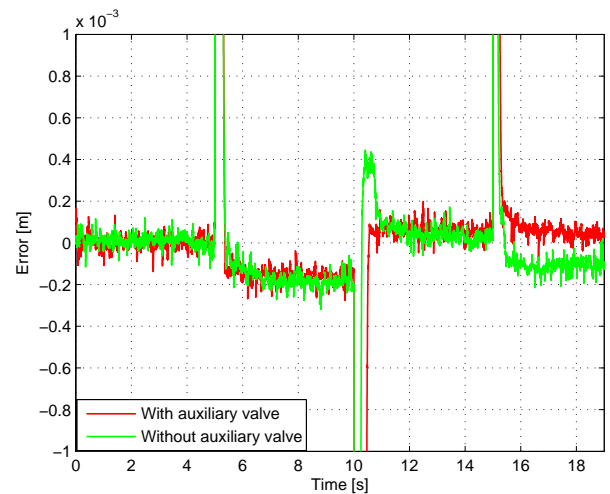


Figure 15: Zoom of the position error.

One can observe the contribution of the auxiliary valve because at the instant that it is acting the proportional valve is closed. This occurs because the load imposes the pressure difference enough to activate the auxiliary fast switching on/off valve. At this moment there is no consumption of compressed air and therefore there is compressed air saving.

Figure 17 shows a zoom of the switching of the on/off valve signal. It can be observed that at the beginning the auxiliary valve is "on" and then it begins to switch. This switch occurs because the piston is decelerating and positioning itself in steady state.

The pressures in the chamber A and B for the system with

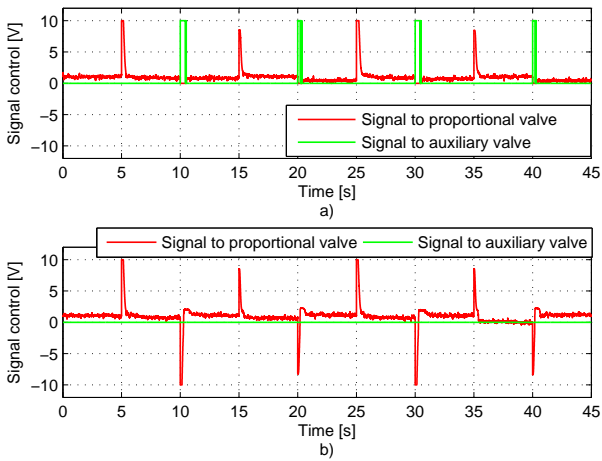


Figure 16: Control signal sent to the valves with and without an auxiliary valve.

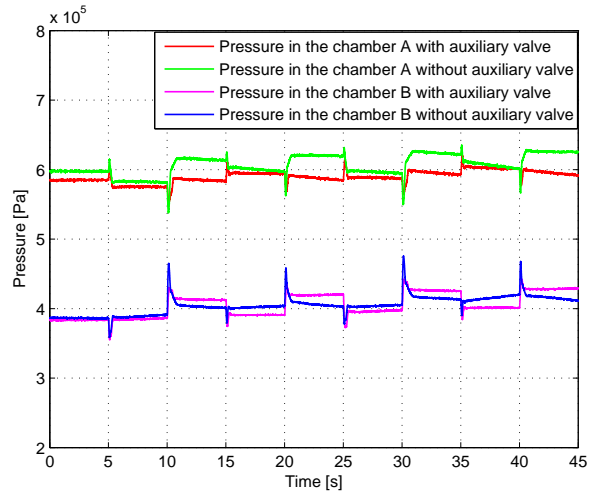


Figure 18: Pressure  $p_A$  and  $p_B$  for steps input.

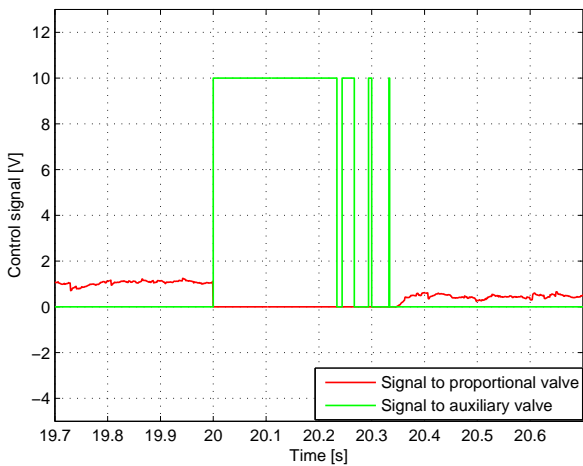


Figure 17: Zoom of the control signal sent valves.

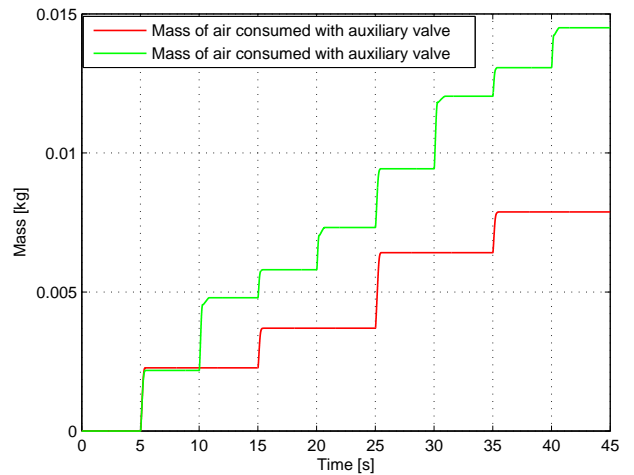


Figure 19: Mass of compressed air consumed for steps input.

and without an auxiliary valve are presented in fig. 18. The pressure in the chambers A and B of the cylinder show similar behaviors and are in the same range values. In the steady state the tendency is to stabilize the pressures through of the supply because the auxiliary valve is closed.

Figure 19 shows the mass of compressed air consumed by system with and without auxiliary valve related to the steps input shown in fig. 14(a). In this case, the compressed air saving is around 46 % for two work cycles.

The feedback between the cylinder chambers helps to increase the energetic efficiency. The equations used to calculate the mass of the compressed air consumed were presented in Section 3.

## 6 Conclusion

This paper presented a structure for a pneumatic positioning systems for compressed air saving in systems which need to move high loads. A comparison was made between the typ-

ical pneumatic positioning system and a system with an auxiliary fast switching valve in a feedback between the cylinder chambers.

For both step and sinusoidal inputs there were low position errors demonstrating that the fast switching on/off valves in a feedback between the cylinder chambers can be a promising solution. Experimental tests show it is possible to combine fast switching on/off valves with proportional valves without difficulties of control and performance losses. Their price can be as low as 10 % when compared to proportional directional valves.

The experimental results showed that with this type of configuration, up to 58 % of compressed air saving can be achieved in comparison to a typical pneumatic positioning system. This increases the energetic efficiency of studied pneumatic positioning system.

## Acknowledgments

The authors are grateful to CNPq (Brazilian National Council for Scientific and Technological Development) for the financial support.

## Nomenclature

Designation	Denotation	Unit
$C$	Sonic conductance	$[m^5/N.s]$
$e$	Error	$[m]$
$F_c$	Load force	$[N]$
$l_c$	Smoothness width	$[V]$
$M_P$	Mass of compressed air consumed	$[kg]$
$md$	Right slope of output	
$me$	Left slope of output	
$p_A$	Pressure in chamber A	$[Pa]$
$p_B$	Pressure in chamber B	$[Pa]$
$p_B$	Supply pressure	$[Pa]$
$q_m$	Mass flow rate	$[kg/s]$
$q_{mA}$	Mass flow rate in line A	$[kg/s]$
$q_{mB}$	Mass flow rate in line B	$[kg/s]$
$q_{mAT}$	Mass flow rate in chamber A	$[kg/s]$
$q_{mBT}$	Mass flow rate in chamber B	$[kg/s]$
$q_{mF}$	Mass flow rate in feedback between cylinder chambers	$[kg/s]$
$U$	Signal control	
$U_{czm}$	Compensated output signal	$[V]$
$U_d$	Desired signal without dead zone	$[V]$
$U_{dc}$	Duty cycle at auxiliary valve	
$U_{zm}$	Signal control with dead zone	$[V]$
$zmd$	Right dead zone value	$[V]$
$zme$	Left dead zone value	$[V]$
$\alpha$	Tolerance of pressure difference	$[Pa]$
$k_P$	Proportional gain	
$k_I$	Integral gain	
$\Delta P$	Pressure difference	$[Pa]$
$\rho_0$	Density at the STP <sup>1</sup> ,	$[kg/m^3]$

## References

- [1] S V Krichel, O Sawodny, S Hülsmann, S Hirzel, and R Elsland. Exergy flow diagrams as novel approach to discuss the efficiency of compressed air systems. In *Proceedings 8th International Fluid Power Conference Dresden*, 2012.
- [2] R Guenter, E A Perondi, E D DePieri, and A C Valdiero. Cascade controller pneumatic position systems with lugre model based friction compensation. *Journal of the Braz. Soc. of Mech. Sci. & Eng.*, 28:48–57, 2006.
- [3] A C Valdiero, D Bavaresco, and P L Andrighetto. Experimental identification of the dead in proportional directional pneumatic valves. *International Journal of Fluid Power*, 27:27–34, 2008.
- [4] P L Andrighetto, A C Valdiero, and L Carlotto. Study of the friction behavior in industrial pneumatic actuator. *ABCM Symposium Series in Mecatronics ed Rio de Janeiro*, 2:369–376, 2006.
- [5] A Yang, J Pu, C B Wong, and P Moore. By-pass valve control to improve energy efficiency of pneumatic drive system. *Control Engineering Practice*, 17:623–628, 2009.
- [6] X Shen and M Gouldfard. Energy saving in pneumatic servo control utilizing interchamber cross-flow. *Journal of Dynamic Systems, Measurement, and Control*, 129:303–310, 2007.
- [7] K A Al-Dakkan, M Gouldfard, and E G Barth. Energy saving control for pneumatic servo systems. In *Proceedings of the 2003 IEEE/ASME International Conference on Advanced Intelligent Mechatronics (AIM 2003)*, volume 1, pages 284–289, 2003.
- [8] X Brun, D Thomasset, and E Bideaux. Influence of the process on the control strategy: application in electropneumatic field. *Control Engineering Practice*, 10:727–725, 2002.
- [9] J Hepke and J Weber. Improving energy efficiency of pneumatic handling systems. In *Proceedings 8th International Fluid Power Conference Dresden*, 2012.
- [10] Y E Assaf and V J De Negri. Development of a high power pneumatic servo-positioning system for speed governors of hydraulic turbines. In *Proceedings of the 19th International Congress of Mechanical Engineering, COBEM*, Brasilia, Brazil, 2007.
- [11] Y E Assaf and L G Oliveira V J De Negri. Applicability of servo-pneumatic positioning systems for high loads. In *Bath/ASME Symposium on Fluid Power and Motion Control (FPMC 08)*, Bath, UK, 2008.
- [12] ISO 6358. Pneumatic fluid power - component using compressible fluids. determination of flow rate characteristics. 1989.
- [13] C C Locateli, V J De Negri, and E R De Pieri. A servo-pneumatic positioning system driven by fast switching on/off valves. In *Proceedings of the ASME 2011 Dynamic Systems and Control Conference and Bath/ASME Symposium on Fluid Power and Motion Control*, volume 2, pages 303–310, 2011.
- [14] G F Franklin, J D Powell, and A Emani-Naeini. *Feedback Control of Dynamic Systems*. Prentice Hall, 1994.
- [15] C C Locateli. Modelagem e desenvolvimento de um sistema de controle de posição pneumático com acionamento por válvulas on/off. Master's thesis, Universidade Federal de Santa Catarina, Florianópolis, 2011.

<sup>1</sup>STP = Standard Condition for Temperature and Pressure adopted by ISO 6358



# Digital Hydraulics



## Control of a fast switching valve for digital hydraulics

N. P. Sell , D. N. Johnston , A. R. Plummer , and S. Kudzma

Dept. of Mechanical Engineering, University of Bath, Bath, UK

E-mail: N.P.Sell@bath.ac.uk

### Abstract

The success of digital hydraulics is dependent on the ability to produce digital hydraulic valves that can supply both high flows and high switching rates. This paper will elucidate the control scheme of, and results obtained from, such a valve which has been developed at the University of Bath. It will be shown that through the combination of iterative learning control and state variable feedback control it is possible to accurately follow a 100Hz PWM signal on a valve designed for high flow rates (65l/min at 10bar), making it well suited to use in a Switched Reactance Hydraulic Transformer.

**Keywords:** Digital Hydraulics, Learning Control, System Identification, Complimentary filters.

## 1 Introduction

The field of digital hydraulics is seen as pivotal to the on-going success and applicability of fluid power as a whole, as it can offer significantly more efficient hydraulic circuit designs in many applications. The realisation of these savings is, however, currently limited by hardware and more specifically the fast switching valves required.

This reliance on high speed switching valves has resulted in numerous papers on the subject, these take one of two routes. The first is looking into using commercially available valves. This approach was shown to be successful, though not ideal in many cases, for example controlling a three camber cylinder [1], for use in a digital hydraulic transformer [2] and the creation of a higher flow rate switching valve by modifying existing 4/2 directional valves [3]. The second route is to develop valves specifically for use in digital hydraulics. Many novel designs have arisen to meet the contrary demands of high flow and fast switching, these have included a bistable hammer design [4], a small needle valve [5] and a rotating valve [6]. There also exists a commercial solution [7]. All of these valves all have different applications in mind and as such have a range of switching frequencies, flow rates and package sizes.

There is however, currently, no valve that combines the high flow rate and switching speeds needed for us in a Switched Reactance Hydraulic Transformer (SRHT). The Centre for Power Transmission and Motion Control at the University of Bath is currently developing such a valve. A SRHT works on a similar premise to the buck converter in power electronics, as can be seen in Figure 1, though frequently a buck converter utilises a diode in the ground connection in place of the switch.

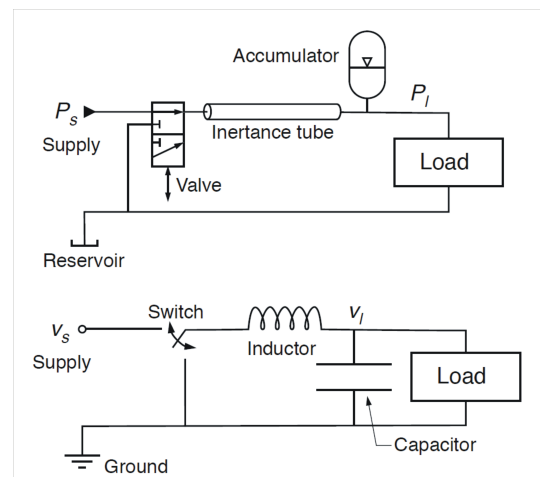


Figure 1: Comparison between SRHT and buck converter

By switching between low pressure and high pressure sources quickly it is possible to generate a range of different pressure and flow rates without the need for throttling and the associated losses. In order for the SRHT to work the fast switching valve must be able to track pulse width modulated (PWM) signals of at least 100Hz [8]. A brief overview of the valve's design, simulation and modelling will be given below, before describing the development of the control scheme used with the valve. Finally experimental results showing the valve's ability to reproduce a 100Hz square wave will be presented.

## 2 Valve Design

In order to meet the high speed requirements of an SRHT, whilst maintaining the high flow rate (65L/min at 10bar pressure drop) needed to make the SRHT practical, a novel three

stage design has been adopted. The primary stage is a Moog high speed servo valve which is used to direct high pressure flow (up to 200bar) into an equal area actuator. This is directly attached to the main spool with its multiple grooves. These multiple grooves have the advantage of exposing a large flow area,  $37.7\text{mm}^2$ , for a small spool displacement,  $0.1\text{mm}$ . It is this high flow gain that makes the valve suited to digital hydraulics, giving both a high frequency of switching and a high flow rate. Due to the nature of the primary stage it is also possible to operate the valve as a simple proportional control valve if this proves more efficient in a specific circumstance. To aid with the control of the valve an accelerometer and position sensor are also incorporated into the valve housing, the former at the top and the latter the bottom of the valve as shown in Figure 2 below.

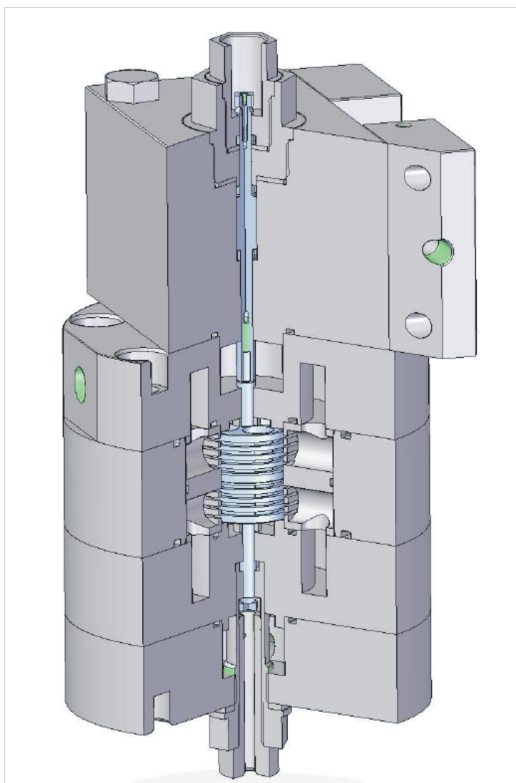


Figure 2: CAD model of the fast switching linear valve

More detailed explanation of the valve’s design and construction can be found in a previous paper [9].

### 3 Experimental Set-up

In order to validate the valves design and control strategy the test rig shown in Figure 3 was created. It uses two power packs, one to supply flow to the main stage and the other to supply high pressure flow to the pilot stage. Currently the pressures and flow rates in the main stage are not being controlled but instead are being used to provide lubrication, therefore the pressure difference between the two ports is currently not in excess of 10bar and the high pressure not above 40bar.

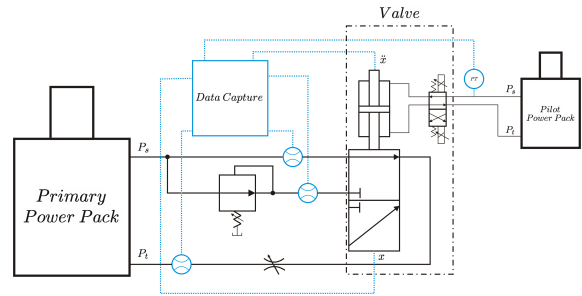


Figure 3: Experimental Set-up

The data provided by the pressure transducers and flow meters is currently used for monitoring purposes only, whilst the Keyence EX-110 position sensor and Kistler 8730AE500 accelerometer housed within the valve body are used for control. Both of these sensors are band limited with the position sensor accurate between  $0\text{-}400\text{Hz}$  and the accelerometer between  $20\text{-}2\text{kHz}$ . It is desirable to have a larger bandwidth for the position measurements to enable faster and more accurate control. This is achieved by low pass filtering the position data and then combining it with high pass filtered acceleration data which has been integrated twice. The high and low passed signals are simply added together, this can be done as the two filter designs were made complementary [10]. Complementary filters are filters whose sum in the frequency domain is unity at all points. The magnitude of the two filters is shown in Figure 4.

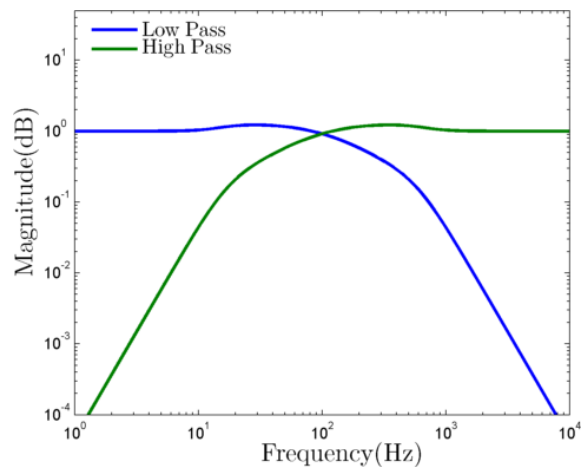


Figure 4: Magnitude of complementary filters

Therefore at the point of crossover ( $100\text{Hz}$  in this case) the signal is an equal combination of the two sources, at frequencies below this point the position signal makes a greater contribution. A similar technique can be used to improve the bandwidth of the acceleration data and also to provide high bandwidth and accurate velocity measurements. It is necessary to differentiate the position data in both of these cases which is achieved by increasing the order of the numerator in the low pass filter.

## 4 Simulation and Modelling

The first stage in the development of the spool position control system was to create a mathematical model of the valve for use in simulation. Figure 5 shows a block diagram of the model developed.

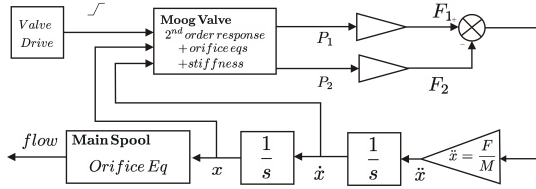


Figure 5: Block diagram of valve model

### 4.1 Model Validation

In order to validate the valve model an empirically tuned PID controller was used to stabilise the valve and provide some data for comparison purposes. A comparison between the simulated and measured results can be seen in Figures 6 and 7.

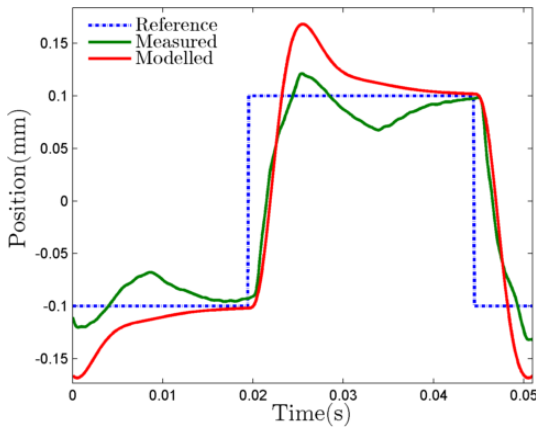


Figure 6: Comparison of simulated and actual response under PID control at 20Hz

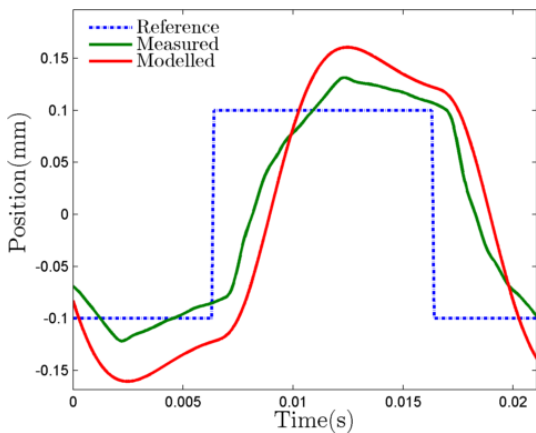


Figure 7: Comparison of simulated and actual response under PID control at 50Hz

The mismatch between the simulated and recorded response is believed to be mainly the result of leakage between the lower chamber of the second stage and the main stage. Therefore system identification methods were used to estimate an improved linear model of the valve, the step response of this new model can be seen in Figure 8 along with the response of the originally derived system.

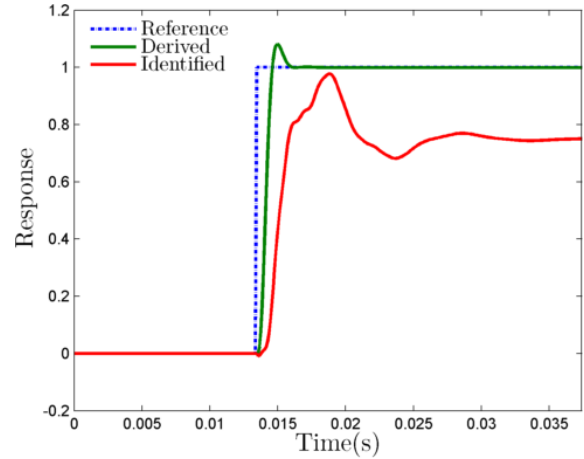


Figure 8: Comparison of empirical and identified models step response

## 5 State Variable Feedback Control

Whilst it is apparent that a classic PID controller could be used with the valves there are two characteristics of the state-space model that make the use of State Variable Feedback (SVF) appealing. Firstly high bandwidth and accurate data for the valves position, velocity and acceleration is available courtesy of the complementary filter network outlined in section 3, meaning that the system is fully observable. Secondly it is possible to prove that the state space model is fully controllable as the controllability matrix is of full rank [11]. This combination of observability and controllability means that it is possible to move all the open-loop poles to any arbitrary closed-loop location using SVF [12]. The block diagram of the SVF system can be seen in Figure 9.

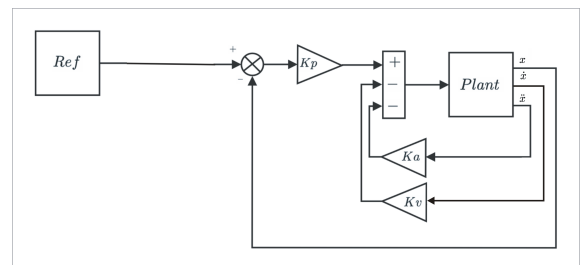


Figure 9: SVF system block diagram

Ackerman's method [12] was used to set the three SVF gains such that the closed loop system had poles at  $(s + 250 \pm 4.33i)$  and  $(s + 500)$ . This produced very high feedback gains which would cause stability issues in real time application.

Therefore they were scaled down and then empirically tuned slightly to allow for the non-linear nature of the leakage which was not modelled. This produced the tracking results seen in Figure 10 and 11.

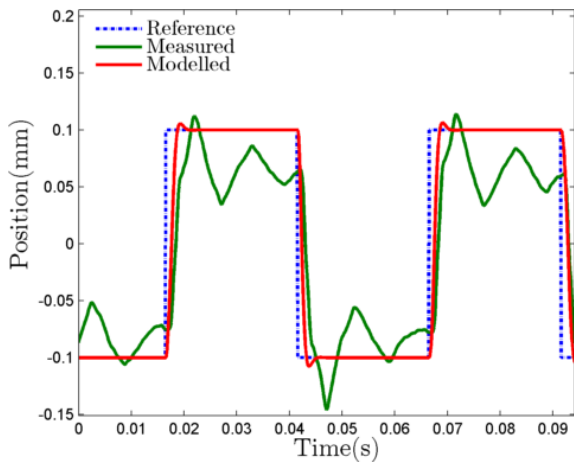


Figure 10: Comparison of valves actual and simulated response to SVF control at 20Hz

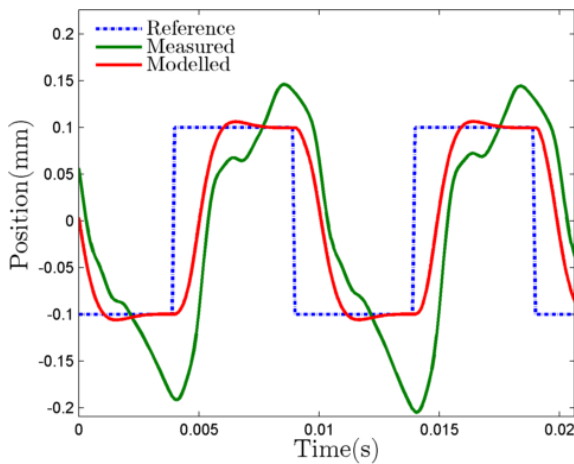


Figure 11: Comparison of valves actual and simulated response to SVF control at 100Hz

There is a large discrepancy between the simulated and obtained results. The lack of symmetry in the response of the valve at 100Hz implies that the linear model is not able to account for the non-linear leakage. As with the comparison of the original model and experimental results the transient appears to be reasonably well modelled, but overshoot and beyond differ significantly. This is to be expected as it is during this period that the leakage will be most prevalent. Figure 11 makes two things clear. Firstly that a non-linear model of the valve is required and secondly that linear feedback control is not likely to prove sufficient to obtain a suitable response at 100Hz.

## 6 Iterative Learning Control

An Iterative Learning Controller was therefore used as a feed-forward controller. Iterative Learning Control (ILC) first found widespread acceptance in 1984 with the publishing of a seminal paper by Arimoto *et al* [13]. Since then it has become one of the more popular forms of adaptive control due to its inherent simplicity. Consider a linear time invariable (LTI), single input single output (SISO) system.

$$y_k = G(s)u_k \quad (1)$$

$$e_k = y_d - y_k \quad (2)$$

Where  $y_d$  is the desired output, ILC works by modifying the input from the last iteration by some function of the error.

$$\begin{aligned} u_{k+1} &= u_k + L(s)e_k \\ &= u_k + L(s)(y_d - G(s)u_k) \\ y_{k+1} &= y_k + G(s)L(s)(y_d - y_k) \end{aligned} \quad (3)$$

Where  $L(s)$  is the learning function. The block diagram for a simple ILC circuit is shown in Figure 12.

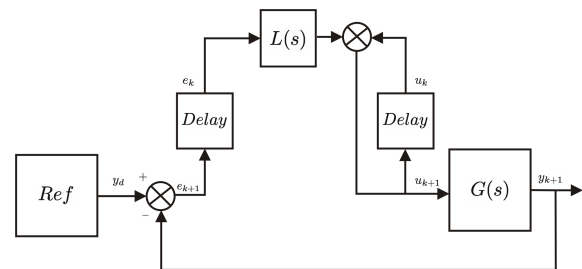


Figure 12: ILC Block Diagram

The success or failure of the controller is dependent only on the design of  $L(s)$ . It is apparent that the ideal learning function is a perfect inversion of the plant, as this would converge to a perfect solution after one iteration:

$$\begin{aligned} L(s) &= G(s)^{-1} \\ \therefore G(s)L(s) &= 1 \\ y_{k+1} &= y_k + G(s)L(s)(y_d - y_k) \\ &= y_k + y_d - y_k \\ &= y_d \end{aligned} \quad (4)$$

Effectively ILC works by passing the error from the current iteration through an inverse model of the plant, then removing this from the input signal of the current iteration. The resulting signal is then used as the input for the next iteration. This means that if the inverse model were perfect then after a single iteration it would provide perfect tracking. It is however not possible to obtain a perfect inverse as no real plant is perfectly time invariant. It is also not possible to directly invert a non-minimum phase model, or to invert most non-linear models. However if the inverse is sufficiently close to the 'perfect' inverse it can be proved that the ILC will monotonically converge to an ideal solution [14] [15].

Classically the inverse model is derived by, either, modelling or identifying the system and then inverting the result, which can cause result in non-realisable or unstable inversions. Consequently the inverse models require the addition of fast poles or other modifications, reducing their accuracy. This also limits the inverse model to being linear in general, as most non-linear models cannot be inverted. In order to avoid this extra step, and the extra inaccuracies it produces, it was proposed that instead an inverse model should be identified. This was achieved by using the high bandwidth position signal as the input for identification purposes and the input to the SVF loop as the output. This means that non-linear models can be used, though only with a modification to the classic ILC system. To ensure correctness it is necessary to pass the feedback signal through the inverse model and then subtract from the inverted desired signal to find the correction, rather than subtracting then passing through the model. The modification to the classic ILC block diagram can be seen in Figure 13 below.

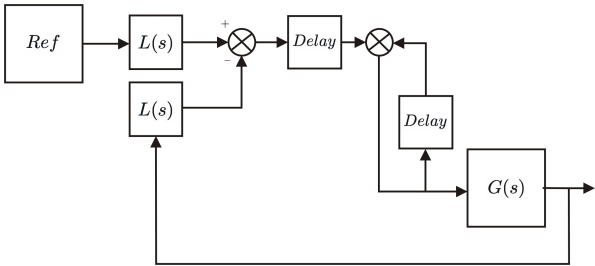


Figure 13: Block diagram for ILC with non-linear inverse model

The data used to identify the inverse model was a sine sweep between 10Hz and 200Hz. This was to ensure that there would be sufficient data around the critical 100Hz area without attempting to model higher order effects. The experimental data used can be seen below in Figure 14.

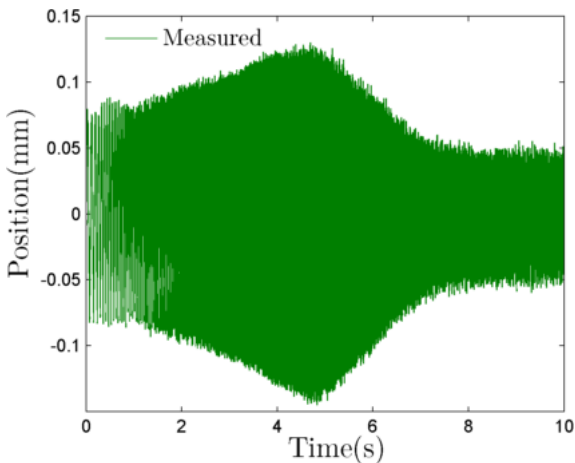


Figure 14: Valves response to a 0.1mm 10-200Hz sweep under SVF control

In order to account for the non-symmetrical leakage in the second stage of the valve a Hammerstein-Wiener model [16]

was identified. This models input and output non-linearities and uses a linear model for the transient response, an example can be seen in Figure 15.

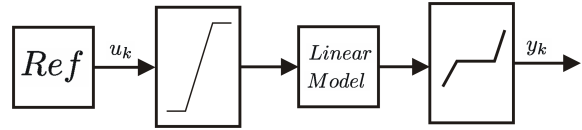


Figure 15: Example Hammerstein-Wiener model

The input and output non-linearities were modelled as piecewise linear functions. With the input function acting as a saturation block and the output block attempting to model the non-symmetrical valve leakage. The frequency response of the linear model can be seen in Figure 16.

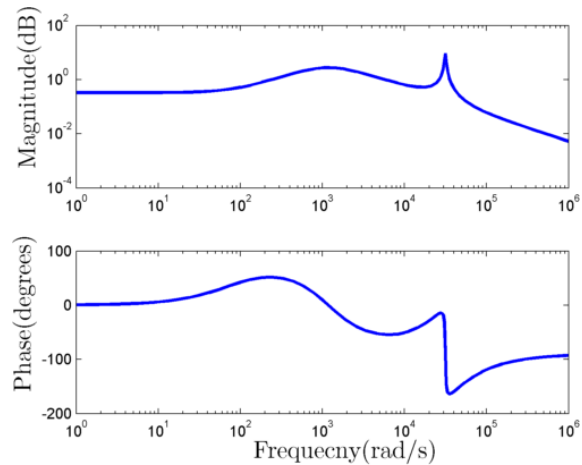


Figure 16: Frequency response of linear inverse model

For validation purposes the model was run on the position signal from a 100Hz square wave experiment, Figure 17 shows that the model was effective at recreating the input square wave but with a pure time delay of 1ms. This delay can be accounted for in the ILC scheme by reducing the amount of delay on the corrective arm (before  $L(s)$ ). Therefore this offset will not present under ILC.

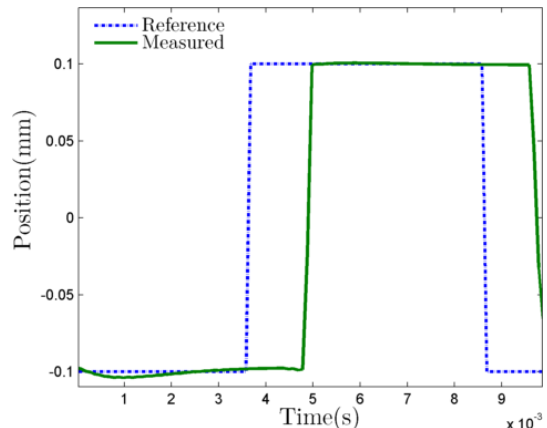


Figure 17: Validation of Inverse Model

This inverse model was then used in the non-linear ILC scheme depicted in Figure 13. The convergence of the solution can be seen in Figure 18. A single cycle taken post convergence can also be seen in Figure 19. The input signal which generated this result is compared to the SVF input signal in Figure 20.

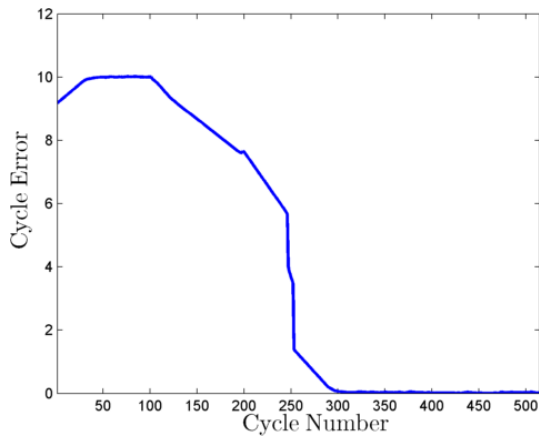


Figure 18: Smoothed cycle error of non-linear ILC

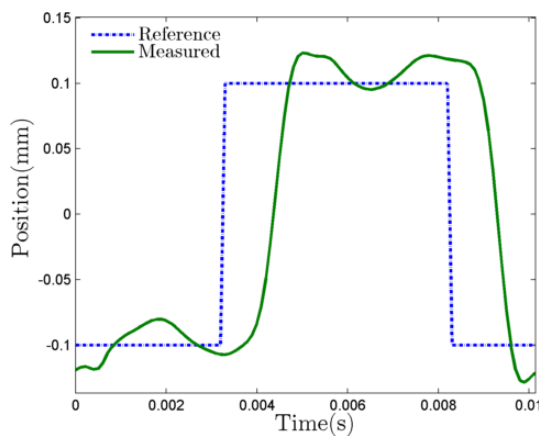


Figure 19: Valve response to ILC at 100Hz

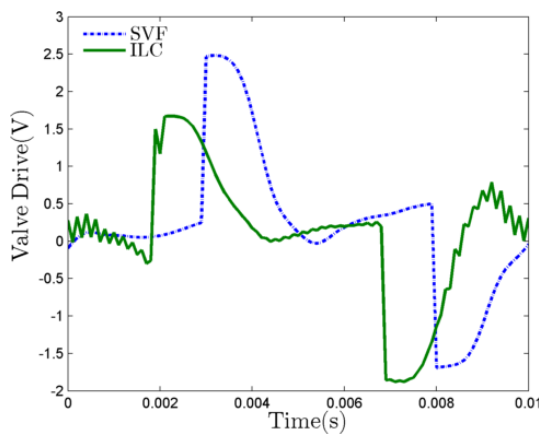


Figure 20: Comparison of input under ILC and SVF control

The solution takes around 300 cycles to converge, this is unacceptable for use in a SRHT, as the required response could be changed every second or less. The inclusion of the ILC dropped the rise time from 0.65ms to 0.58ms. This is a small increase but the larger benefit can be seen in the difference of response post rise. Comparing the input from the SVF and ILC tests it can be seen that the ILC doesn't drive the pilot stage as hard as the SVF, meaning that it produces a smaller overshoot. However the ILC has a faster rise time than the SVF system. This is believed to be the result of not having to move from a stationary position and thus not needing to overcome the static friction in the valve. There is also a preemptive downturn at 2ms that assists with reducing the overshoot. The sharp oscillations in the ILC response should be noted however.

The over long convergence time is the result of a low learning gain (only 1% of the calculated correction was applied each cycle) that was required to ensure stability in the basic ILC scheme. In order to allow for higher learning gains it is necessary to build a more robust correction arm that is able to stop learning, once a sufficient response has been obtained. This will stop it from continuing to increase the initial transient once saturation has been reached. A low pass filter could also be added to stop the model trying to correct high frequency errors above the range of the valves response, such as can be seen in the input signal above (Figure 20).

## 7 Conclusion

The field of digital hydraulics is set to be pivotal in the future development of power transmission. It has the ability to compete with the on going advance of electrical drives by significantly improving the efficiency of hydraulic drives. Currently, however, the benefits of digital hydraulics have been realised on paper more than in reality. A SRHT is now closer to becoming a reality as it has been shown that it is possible to switch a high flow rate digital hydraulic valve at the 100Hz required to make the concept viable.

Such a frequency was achieved by using a combination of SVF control and an ILC in the feed-forward path. Full state control by using a series of complementary filters to combine data from the position sensor and accelerometer to give high bandwidth position, velocity and acceleration measurements. SVF was sufficient to follow a 20Hz square wave but suffered from significant undershoot. Therefore it was determined to use a feedforward controller to compliment the SVF. An inverse model ILC was used, with this inverse model being identified from empirical data using a non-linear Hammerstein-Wiener framework. This required a slight modification to the standard ILC circuit but proved effective up to 100Hz.

Since these results were recorded the next design iteration of the valve has been developed to solve the non-symmetric leakage in the second stage. The Hammerstein-Wiener inverse model has also been exchanged for an auto-regressive neural network. This allows for a recursive inverse model that is able to adjust to a wide range of frequencies and pulse widths. Both of these changes are yet to be tested experi-

mentally but it is believed that they will improve the dynamic response further.

## Acknowledgements

This work is supported by UK Engineering and Physical Sciences Research Council (EPSRC EP/H024190/1), together with Instron, JCB and Parker Hannifin.

## Abbreviations

Abbreviations	Definition
SRHT	Switched Reactance Hydraulic Transformer
PWM	Pulse Width Modulation
PID	Proportional Differential & Integral
SVF	State Variable Feedback
SISO	Single Input Single Output
LTI	Linear Time Invariable
ILC	Iterative Learning Control

## References

- [1] M. Huova and A. Laamanen. Control of three-chamber cylinder with digital valve system. In *Proceedings of The Second Workshop on Digital Fluid Power*, Tampere, Finland, 2009.
- [2] E. Bishop. Linearization of quantized digital hydraulic transformer output. In *Proceedings of The Third Workshop on Digital Fluid Power*, Tampere, Finland, 2010.
- [3] I. Hyöty. Commercial high flow on/off-valves for digital hydraulics. In *Proceedings of The Fifth Workshop on Digital Fluid Power*, Tampere, Finland, 2012.
- [4] J. P. Uusitalo, V. Ahola, L. Söderlund, M. Linjama, M. Juhola, and L. Kettunen. Novel bistable hammer valve for digital hydraulics. In *Proceedings of The Second Workshop on Digital Fluid Power*, Tampere, Finland, 2009.
- [5] M. Karvonen, M. Ketonen, M. Linjama, and V. Puumala. Recent advancements in miniture valve development. In *Proceedings of The Fourth Workshop on Digital Fluid Power*, Tampere, Finland, 2011.
- [6] H.C. Tu, M.B. Rannow, M. Wang, P. Y. Li, and T.R. Chase. Modeling and validation of a high speed rotaryt pwm on/off valve. In *Proceedings of the ASME Dynamic System and Control Conference*, 2009.
- [7] M. Ketonen. Impementation of a digital hydraulic valve system with bosch rexroth sec valves. In *Proceedings of The Fifth Workshop on Digital Fluid Power*, Tampere, Finland, 2012.
- [8] D.N Johnston. A switched inertance device for efficient control of pressure and flow. In *Proceedings of the Bath/ASME conference of Fluid Power and Motion Control*, Hollywood, 2009.
- [9] S. Kudzma, D.N. Johnston, A.R. Plummer, and N.P. Sell. A high flow fast switching valve for digital hydraulic systems. In *The Fifth Workshop on Digital Fluid Power*, Tampere, 2012.
- [10] A.R. Plummer. Optimal complementary filters and their application in motion measurement. *Journal of syst. & contr. engineering*, 220(6), 2006.
- [11] K. Ogata. *Modern Control Engineering*, chapter 9, pages 686–692. Pearson, 2010.
- [12] K. Dutton, S. Thompson, and B. Barraclough. *The Art of Control Engineering*, chapter 5. State Variable Feedback. Addison-Wesley, 1998.
- [13] S. Arimoto, S. Kawamura, and F. Miyazaki. Bettering operation of robots by learning. *Journal of Robotic Systems*, 2:123–140, 1984.
- [14] K. L. Moore. An observation on monotonic convergence in discrete-time -p-type iterative learning control. In *Proc.IEEE Int. Symp. Intell. Contr.*, Mexico City, 2001.
- [15] N. Amman, D. H. Owens, and E. Rogers. Iterative learning control for discrete time systems with exponential rates of convergence. In *IEE Proc Cntr. Thr. & Appli-cat.*, 1996.
- [16] A. H Falkner. 1988. *International Journal of Control*, 48(1):385–396, 1988.



# **Investigation of a Digital Hydraulic Actuation System on an Excavator Arm**

Alessandro Dell'Amico , Marcus Carlsson , Erik Norlin , and Magnus Sethson

Division of Fluid and Mechatronic Systems, Department of Management and Engineering, Linköping University, Linköping, Sweden

E-mail: alessandro.dellamico@liu.se, magnus.sethson@liu.se

## **Abstract**

Digital hydraulics is an ongoing trend that offers many interesting advantages and possibilities. Digital refers to that the system output is discrete, e.g. using an on/off valve with only discrete values or a finite amount of flow steps available. The advantages mentioned when compared to analogue systems are better performance, robust and fault tolerant, and amplitude independent bandwidth. On the other side noise and pressure pulsations must be handled, the physical size can be a problem, and the system requires complicated control. When considering control of linear motion, there are mainly two branches, controlling the flow with several parallel connected on/off valves, which generates discrete output flow values, or switching valves, which in theory can generate any mean output flow. The latter only requires one valve for each flow path but the demand for fast valves is very high, while the former requires many valves but avoids high frequent switching. With the introduction of a multi-chamber cylinder, secondary control is now also possible for linear motion. This paper is a first step in the investigation of the system applied to an excavator arm. The cylinder has four chambers, each with different area. Three pressure lines are used and a valve-pack of 27 on/off valves. The valve-pack connects the three pressure lines with each chamber generating 81 available force steps. The scope has been to start out with relative simple control of the velocity of the cylinder. To handle unnecessary switching of valves, different penalty strategies were tested. The results are promising where relatively smooth control could be achieved at the same time challenges with the system were identified. Next step is to investigate the force transients due to different capacitance in all four chambers as well as mode control for better accuracy. Energy potential compared to original system remains to investigate as well.

**Keywords:** Digital hydraulics, secondary control, excavator, on/off-valves

## **1 Introduction**

Digital hydraulics is a promising technology for flow control. It has gained extensive research efforts over the latest years. Digital refers to the output of the system being discrete. For valve flow control there are two main branches, one is the use of several parallel configured on/off valves replacing each and one of the control edges in an conventional proportional valve. The other strategy makes use of a modulating technology. Both technologies are based on on/off valves but the latter only requires one valve for each control edge, [1]. However, there is a demand for very fast and durable valves. These are challenges that need to be handled as well as parasitic losses due to large capacitances of the hydraulic system and pressure peaks. The former technique avoids fast continuous switching of valves but the physical size of the unit becomes large due to the many valves involved, [2]. In this case each Digital Flow Control Unit (DFCU) generates a discrete flow output. The benefits are a robust and possible fault tolerant solution, amplitude independent opening, and

flexibility. The flexibility of the system allows for different control modes and when compared to traditional load sensing system, high energy savings are reported, [3]. However, the solution should also be compared to other solutions with distributed valves, like in [4]. The main challenges with parallel configured valves are; system size and cost, complex control strategies and noise and pressure pulsations. The pressure pulsations are due to the uncertainty in valve timings and is dependent on the coding of the DFCU [5]. The performance of the system is dependent on the characteristics of the on/off valves, among others. In many cases commercial valves are not sufficient and research has been focused on development of high performance valves, [6]. The need for fast valves and advanced controllers is shown in [7] and [8], where a digital hydraulic system is compared to a servo valve system for different applications.

With the development of a multi-chamber cylinder, [9], secondary control is now possible for linear actuator control. Secondary control has previously been restricted to displace-

ment machines only. The technique has a high potential of being a very energy efficient system [10], since no valve throttling takes place. The system uses a constant pressure supply line and if an accumulator is connected to the system, energy can be recovered during retardation of the load. Several secondary control units can be added to the same supply thereby simplifying the piping. A secondary controlled swing drive of an excavator was investigated in [11] and showed upon a possible 60 % energy consumption reduction. The challenge with secondary control is however the need for advanced controllers, [12]. For linear motion a multi-chamber cylinder is used together with constant pressure supply lines. A valve-pack with on/off valves combines the supply lines with the different chambers. In this way the cylinder delivers discrete force steps. In [13] a four chamber cylinder is investigated with two pressure lines for position control. That system has 16 possible force levels to control the movement of a load. A PI-controller is used together with a switch strategy that minimizes unnecessary switching. The results showed a good controllability of high inertia loads and a reduction of 60 % in energy consumption compared to a traditional LS system for the same application.

The scope of this paper is to investigate a four chamber cylinder with three pressure lines, generating 81 force levels, applied to an excavator arm. This is a first attempt in trying to understand the system characteristics of digital hydraulics, studying the advantages and the challenges. At first only the boom of the arm is installed and a simple control structure for velocity control is tested.

## 2 System setup

A test system has been formed to provide a realistic environment for laboratory tests. In the beginning, only the inner arm is installed. It is going to be extended with the complete excavator arm. With two arms later installed, the system can also be tested for over-centre loads as well as energy recovery from two actuators.

An overview of the system is seen in fig. 1. The main components of the system is the excavator arm, the hydraulic supply system with its three pressure lines, the 27-valves block, and the multi-chamber cylinder. The cylinder is controlling the motion of the the boom of the excavator arm. The supply system is at this point rather simple with focus only on functionality. Three pressures are used, 200, 110, and 20 bars. The highest pressure is set by a pressure relief valve (Bosch Rexroth DBDS10K1X/315) and the pump running at constant speed. The medium and low pressure are in turn set by two pressure reducing valves (Bosch Rexroth DR20G5-4X/200YM and DR20G5-4X/100YM). Two relief valves are also installed for security at medium and low pressure line (Bosch Rexroth DBDS10G1X/200 and DBDS10G1X/100). The actual pressures in the three lines are of course affected by the characteristics of the relief and reducing valves. Three accumulators of 4 litres each are installed at the three pressure lines. They are not sufficiently large for energy recovery operation but will smoothen out the supply pressures.

The valve-pack consists of 27 on/off valves with 50 ms rated

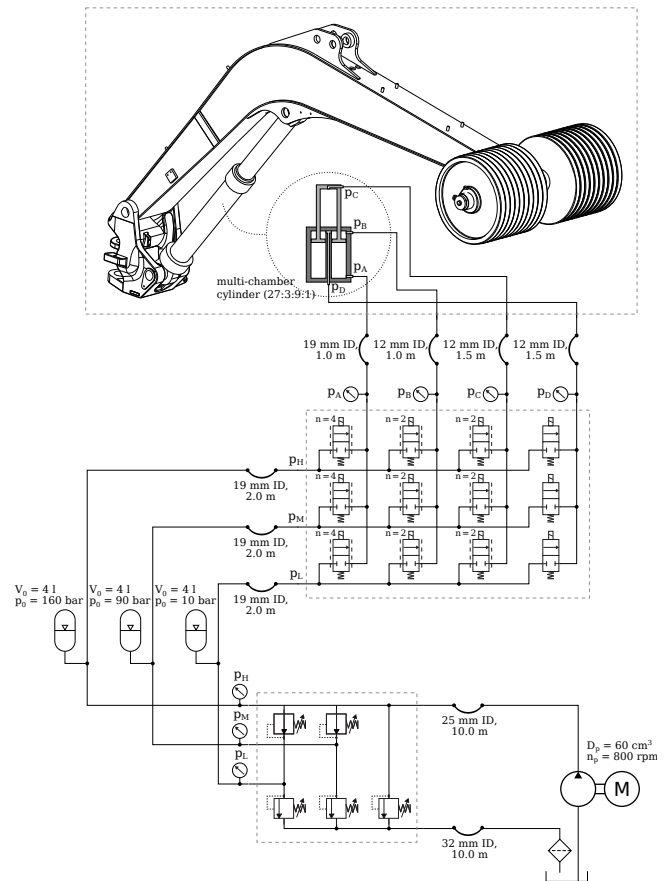


Figure 1: System overview.

response time. The valve-pack connects the pressure lines to each chamber of the cylinder. The connection between each pressure line and each chamber is done by several parallel configured valves. The largest chamber has four valves in parallel for each pressure line and smallest has only one valve for each pressure line. The other two chambers have two valve each for each pressure line. To use several parallel connected valves for the chambers is beneficial in several ways. The flow demand for a given velocity of the piston is different for each chamber. To decrease the pressure drop a larger effective area is achieved by several valves. Another advantage is the possibility to control the pressure build up in a more effective way. The pressure build up is dependent on the flow in or out of the chamber and the capacitance of the chamber. A more robust solution is also achieved with several valves. If one valve breaks the arm can still be operated, at least for the three larger cylinder areas.

The cylinder consists of four chambers with different areas with relative relation 27:9:3:1. Two chamber extends the cylinder and two chambers retracts it. By combining the three pressures in the four chambers of the cylinder  $3^4 = 81$  force steps can be applied by the cylinder. An overview of the cylinder is seen in fig. 2. Figure 3 shows the available force distribution. The maximum available force is 129.9 kN and the maximum retraction force is 2.1 kN. Since only one arm is in place at the moment an axle is installed at the tip of the boom.

In this way the boom can be loaded with up to 400 kg.

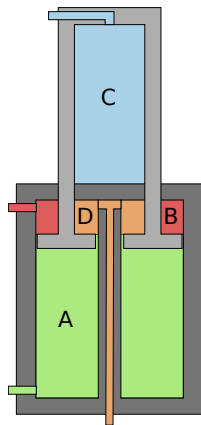


Figure 2: An overview of the multi-chamber cylinder.

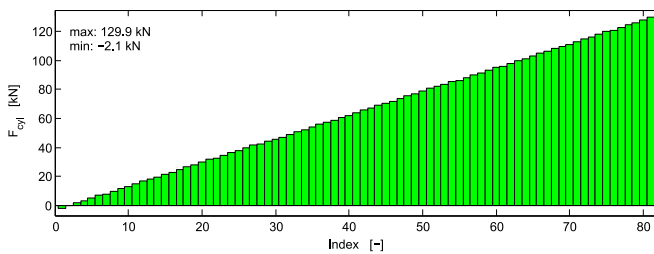


Figure 3: Available force spectrum for  $HP = 200$  bar,  $MP = 110$  bar, and  $LP = 20$  bar.

The valve-pack is controlled by an prototype Exertus HCM-series unit which communicates with the industrial computer MPL PIP8 via a CAN bus. The controller software is developed in Matlab/Simulink and downloaded to the industrial PC through xPC Target. The valve control unit also provides analogue input channels for sensor data. Sensors used are pressure sensors for the three pressure lines and each chamber of the cylinder. In this way the pressure drop over the valve-pack can be measured. The position of the piston is measured with a potentiometer multi-turn wire sensor. The derivative of the position signal is filtered with a second order low pass filter to get the velocity of the piston.

Future work of the test rig involves the installation of the outer arm as well. This will further extend the possibilities of the elaborative studies of the system characteristics. The multi-chamber cylinder for the outer arm will use the same three pressure lines as the installed boom cylinder. The amount of hoses is reduced compared to a traditional system. Also, energy can be recovered from both actuators. The future test rig is shown in fig. 4.

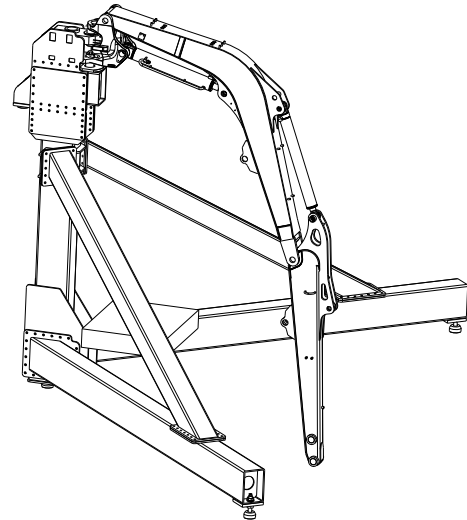


Figure 4: Future test rig of the crane.

### 3 Control structure

A traditional hydraulic system gives the operator a way to control the velocity of the piston. The system studied is secondary controlled and is therefore force controlled. Some kind of external controller is therefore required in order to control the velocity. In order to investigate the system and its behaviour a simple control approach has first been tested. The actual force applied by the cylinder is calculated as:

$$F = p_A A_A - p_B A_B + p_C A_C - p_D A_D \quad (1)$$

#### 3.1 Control Strategy A

The controller is a PI-controller that compares a reference velocity of the piston with the actual velocity. The output from the controller is the required force to follow the reference. Since the system is digital and therefore discrete, only a finite amount of force steps are available and the closest available force compared to the reference force needs to be chosen. This is done by comparing the reference force with each available force and the combination that gives the smallest error is chosen according to 2.

$$u = \min (|F_{ref} - \hat{F}(u_i)|) \quad i = 1 : 81 \quad (2)$$

The actual available force steps depends on the pressure in the three supply lines. As they will fluctuate during movement of the crane, the supply pressures are measured and the force distribution updated each time step. The control structure is seen in fig. 5. The measured supply pressures are quantized to avoid influences from measurement noise.

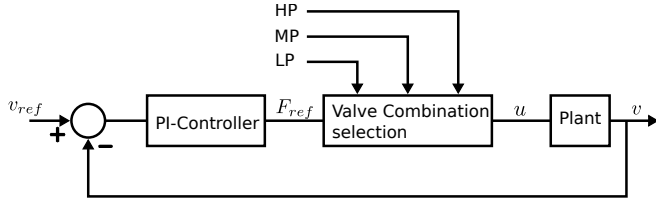


Figure 5: Controller structure.

Due to the discrete nature of the system, unnecessary switching between different force states might occur. To avoid this a penalty for switching can be introduced. The controller is only allowed to change force state if changing state has big enough effect. The penalty is added to every force level except the previous one. This is according to [13]. The selection of combination can now be updated as follows.

$$u = \min (|F_{ref} - \hat{F}(u_i)| + Pj) \quad i = 1 : 81 \quad (3)$$

$$j = \begin{cases} 1 & \text{if } u_i \neq u_{previous} \\ 0 & \text{if } u_i = u_{previous} \end{cases}$$

where  $P$  is the penalty and is a tuning variable together with the PI-controller gains.  $u$  and  $u_{old}$  are the new and old control combination respectively.

### 3.2 Control Strategy B

The other strategy also tested uses a score-based system to avoid frequent switching of high amplitude pressure changes. High amplitude changes will have biggest effect on the smoothness, especially if it occur on all chambers at the same time. A high amplitude change is rated high in score and a low amplitude change rated low. For each change in force step a total score can be calculated as the sum of the scores from all chambers. If the total score is high a penalty is added to the previous force step in order avoid changing back to it. Again, this mimics eq. 3.

## 4 Experimental setup

Several tests are conducted in order to evaluate the system's ability to be controlled by a velocity reference. For all tests the input signal is a pulse train with an amplitude of  $3\text{cm/s}$ . The tests are carried out in both directions of the cylinder. Before changing direction the arm is set to stand still for 2 seconds. The input reference signal is somewhat smoothen by limiting the maximum allowed acceleration and jerk. For each control structure two load cases are tested, 200 kg and 400 kg. All controller parameters are tuned experimentally and a penalty of 2000 N is used.

## 5 Results

Figure 6 and fig. 9 show the results of the test with 200kg and 400kg respectively. For the 200kg weight only the B and D chambers switch pressure. They are small which results in a quiet smooth movement. For the heavier weight all chambers changes pressure. This occurs frequently during acceleration.

Since also the larger chambers changes pressure the movement is less smooth. Figure 7 shows the result of the test with 200kg and penalty function A. Frequent switching is no longer taking place but accuracy has become worse which affected the smoothness. Figure 10 shows the same run with 400kg. Here it is even more obvious that the frequent switching no longer takes place. The movement is smoother due to the larger inertia but since no functionality is implemented to handle zero velocity input, the resolution is not high enough to find force equilibrium for those cases. Figure 8 shows the test with strategy B. No difficult pressure changes occur and the result is similar as in the case with no penalty function implemented. The effect of strategy B is seen in fig. 11, where frequent switching of all chambers at the same time is avoided.

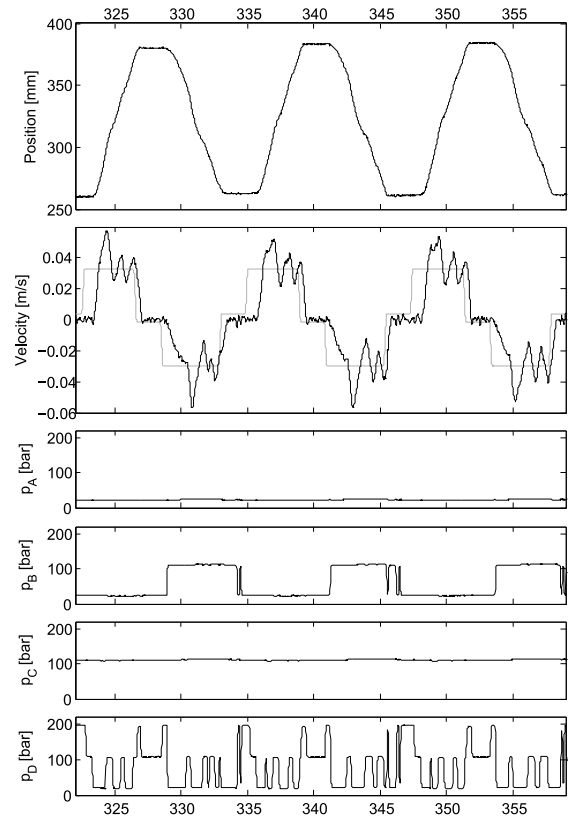


Figure 6: 200 kg with no penalty.

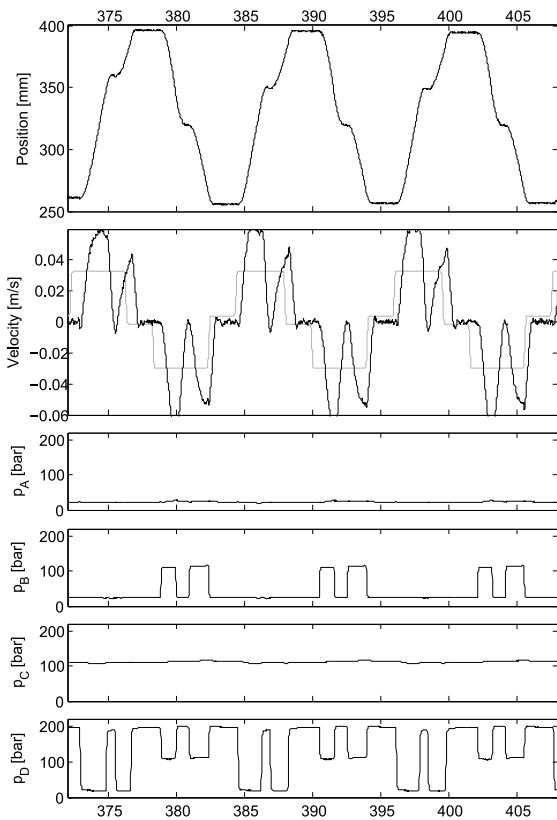


Figure 7: 200 kg with penalty strategy A.

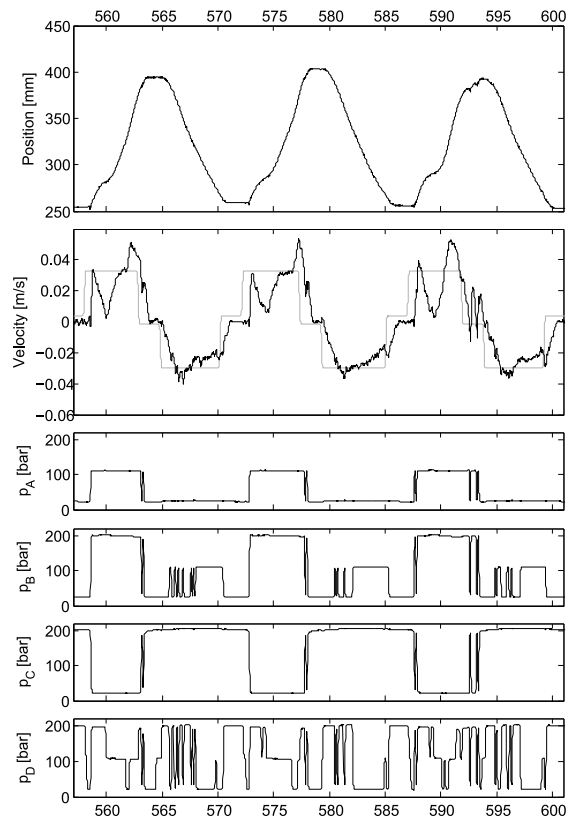


Figure 9: 400 kg with no penalty.

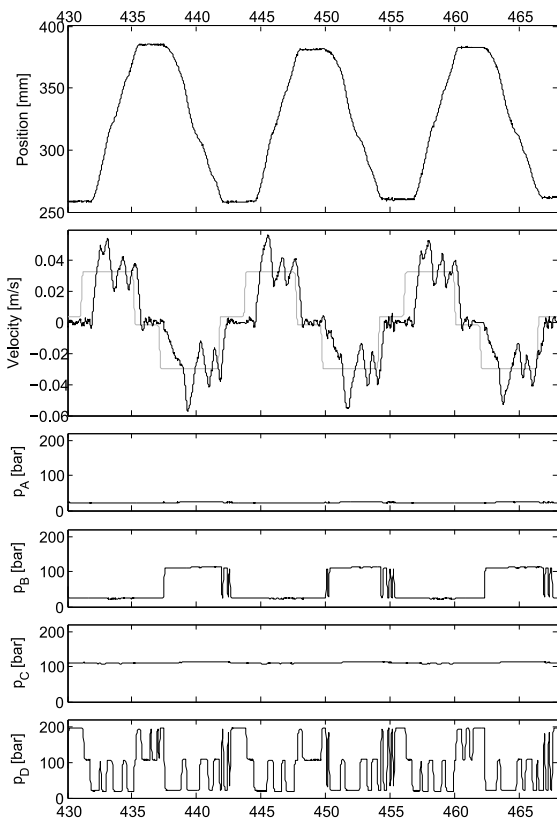


Figure 8: 200 kg with penalty strategy B.

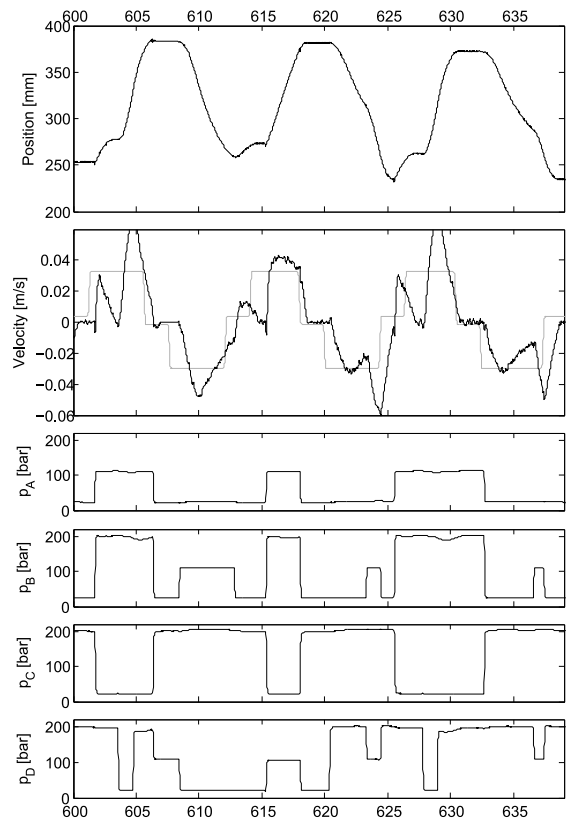


Figure 10: 400 kg with penalty strategy A.

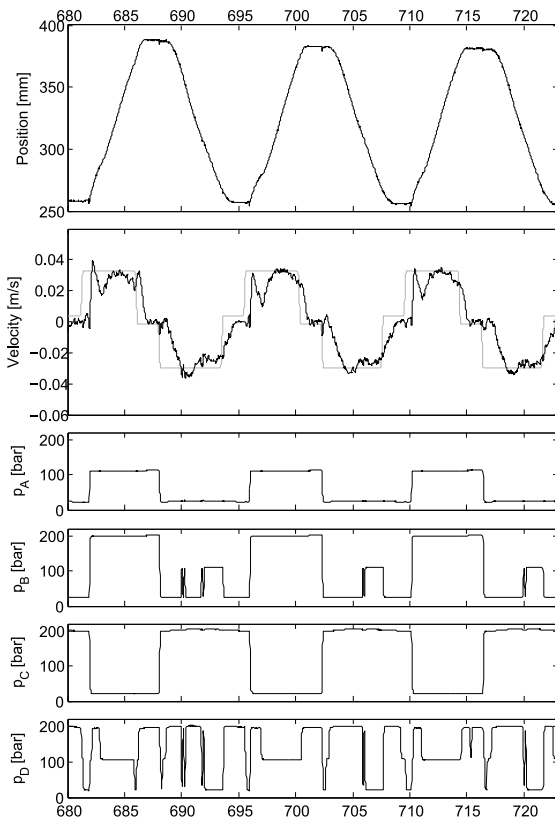


Figure 11: 400 kg with penalty strategy B.

## 6 Discussion and future work

The results from the tests are promising. They show that with simple control a relatively smooth operation of the arm is possible. Due to the nature of the system frequent switching between force steps can occur and must be handled in some way. The different strategies tested showed that there is a compromise between accuracy, smoothness of the arm and frequent switching. Another factor is the energy efficiency. This has not been studied in this work but it was shown in [13] that the biggest losses are the compressibility losses and this should be considered as well when selecting switching strategy. Next step is to add the outer part of the excavator arm and study the energy consumption compared to the original system to get an idea of the energy saving potential. Another thing to be studied is the effect of different pressure rates in the chambers due to different capacitances. This could lead to force transients that counteracts the movement of the arm. Noise is another concern that should be studied and is related to the pressure build up in the chambers and frequent switching.

## 7 Conclusions

A test rig of an excavator arm actuated by a secondary controlled multi-chamber cylinder has been built and tested. At this first stage only the boom is installed and simple control strategy is implemented and evaluated. For a lighter load the big chamber do not switch anything and the effect of switching in the smaller chambers is negligible on the smoothness. For the heavier weight all chambers switches pressure more

frequent which affected the smoothness of the arm. Two different strategies were tested to avoid this behaviour, both affecting the switching of the valves. By adjusting the control and switching strategies it is potentially possible to adjust operation conditions, controller trajectory performance and noise generation.

## References

- [1] Rudolf Scheidl and Bernhard Manhartgruber. State of the art in hydraulic switching control - components, systems, applications. In *The Ninth Scandinavian International Conference on Fluid Power*, Linköping, Sweden, June 1-3 2005.
- [2] Matti Linjama. Digital fluid power - state of the art. In *The Twelfth Scandinavian International Conference on Fluid Power*, Tampere, Finland, May 18-20 2011.
- [3] Matti Linjama, Mikko Houva, Pontus Boström, Arto Laamanen, Lauri Siivonen, Lionel Morel, Marina Waldèn, and Matti Vilenius. Design and implementation of energy saving digital hydraulic control system. In *The Tenth Scandinavian International Conference on Fluid Power, SICFP'07*, Tampere, Finland, May 21-23 2007.
- [4] Björn Eriksson. *Mobile Fluid Power Systems Design*. PhD thesis, Linköping University, 2010.
- [5] Arto Laamanen, Matti Linjama, and Matti Vilenius. On the pressure peak minimization in digital hydraulics. In *The Tenth Scandinavian International Conference on Fluid Power, SICFP'07*, Tampere, Finland, May 21-23 2007.
- [6] Matti Linjama and Matti Vilenius. Digital hydraulics - towards perfect valve technology. In *The Tenth Scandinavian International Conference on Fluid Power, SICFP'07*, Tampere, Finland, May 21-23 2007.
- [7] Matti Linjama, Juho Seppälä, Jouni Mattila, and Matti Vilenius. Comparison of digital hydraulic and traditional servo system in demanding water hydraulic tracking control. In *Fluid Power and Motion Control*, 2008.
- [8] Ville Ahola, Matti Linjama, and Matti Vilenius. High performance digital hydraulic servo system for linear cyclic motion. In *The Tenth Scandinavian International Conference on Fluid Power, SICFP'07*, Tampere, Finland, May 21-23 2007.
- [9] Ari Sipola, Hannu-Pekka Vihtanen, Matti Linjama, and Arto Laamanen. Digital hydraulic system, 2010.
- [10] Göran Palmgren and Karl-Erik Rydberg. Secondary controlled hydraulic systems - energy aspects and control strategies. In *International Conference on Fluid Power*, Tampere University of Technology, Finland, March 24-26 1987.

- [11] Karl Pettersson and Seppo Tikkanen. Secondary control in construction machinery - design and evaluation of an excavator swing drive. In *The 11th Scandinavian International Conference on Fluid Power, SICFP'09*, Linköping, Sweden, June 2-4 2009.
- [12] H. Berg and M. Ivantysynova. Design and testing of a robust controller for secondary controlled hydraulic drive. *Proceedings of the Institution of Mechanical Engineers*, 213:375–386, 1999.
- [13] M. Linjama, H-P. Vihtanen, A. Sipola, and M. Vilenius. Secondary controlled multi-chamber hydraulic cylinder. In *The 11th Scandinavian International Conference on Fluid Power, SICFP'09*, Linköping, Sweden, 2009.



# Hydraulic Energy Recovery in Displacement Controlled Digital Hydraulic System

M. Heikkilä and M. Linjama

Department of Intelligent Hydraulics and Automation, Tampere University of Technology, Tampere, Finland  
E-mail: mikko.heikkila@tut.fi, matti.linjama@tut.fi

## Abstract

Digital hydraulic power management system (DHPMS) is a solution based on the digital pump-motor technology but has multiple outlets. The outlets are independent of each other and several system pressure levels are allowed. The DHPMS is also capable of transferring energy between the outlets. In this study, the hydraulic energy recovery is analyzed by simulations of a small excavator crane. One outlet of a 6-piston DHPMS is directly connected to a single-acting lift cylinder while a high pressure accumulator is attached to the other outlet. The results show that the energy can be recovered to the accumulator when the load is lowered. In addition, the peak power of the prime mover reduces significantly when the accumulator energy is utilized.

**Keywords:** Digital hydraulic power management system, displacement control, energy recovery

## 1 Introduction

### 1.1 Energy efficiency in hydraulics

Despite a good efficiency of hydraulic components the overall efficiency of hydraulic systems has been generally very low. Load sensing hydraulics, which is widely used in mobile applications, can have the total efficiency as low as 4 % [1]. Due to environmental issues and the tightening legislation, more energy efficient hydraulic systems have been studied increasingly.

Inderelst et al. [2] compared a conventional LS-system to five alternative system layouts introduced for excavator work hydraulics. Their simulations showed that most energy was saved in the system where the actuators were controlled by variable displacement pumps. Significant reduction in energy consumption was also achieved when the actuators were controlled by using hydraulic transformers connected to a constant pressure rail also.

Huova et al. [3] have used a digital hydraulic valve system (DVS) in a wheel loader instead of a traditional LS-system and successfully reduced the energy losses. Potential for a 33-63 % reduction in losses in multi-actuator systems was shown by simulations. In addition, it was shown in [4] that the energy efficiency of the DVS can be further improved by utilizing a pressurized tank line. All in all, the trend is clear in modern-day hydraulic research, i.e. to minimize losses while investigating methods for energy recuperation [5], [6], [7] and [8].

### 1.2 Displacement controlled hydraulic systems

Displacement controlled hydraulic systems are potential solution for more energy-efficient mobile machinery;

energy-wasting throttling of the flow can be discarded when actuators are controlled directly using variable displacement pumps and motors. Pump displacement control was compared to traditional LS-valve control by Williamson et al. [9]. They constructed dynamic models for both systems and simulated a trench-digging cycle for a mini-excavator. Compared to the traditional system 39 % less energy was consumed when the displacement-controlled excavator was used. In their study, the energy savings were achieved solely through the elimination of flow throttling losses because power recovery was not considered.

Zimmerman and Ivantysynova [10] have developed the displacement control of multi-actuator systems even further. They presented two hybrid hydraulic architectures (parallel hybrid and series-parallel hybrid), which allowed energy to be stored in hydraulic accumulators. Furthermore, the approach enabled the engine load to be controlled actively. Their simulations showed that the rated engine power could be reduced to 50 % when the hybrid systems were used, compared to the rated engine power of the non-hybrid system. They also stated that a parallel hybrid system would reduce the fuel consumption of the non-hybrid displacement controlled system by 18.5 % and the series-parallel hybrid by a corresponding 20.3%.

### 1.3 Digital hydraulic power management system

Digital hydraulic power management system (DHPMS) is one solution towards more energy efficient hydraulic systems [11]. The DHPMS can be considered as a digital pump-motor but in addition, independently controlled outlets enable highly efficient power transfer [12]. There are several applications where the technique can be adapted to and a couple is studied in [13], [14] and [15].

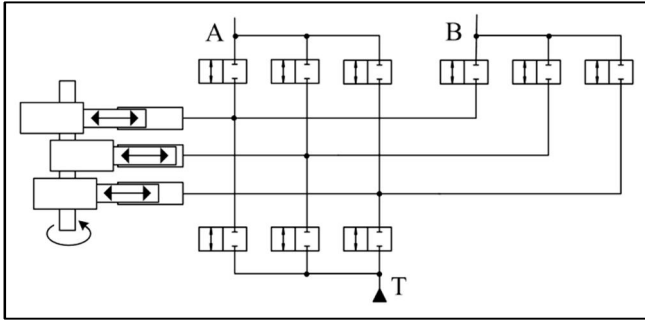


Figure 1. Schematic of 3-piston DHPMS with two outlets

Figure 1 shows a schematic of a 3-piston DHPMS with two independent outlets. Every piston can be connected to each outlet or to the tank via actively controlled on/off valves. The decision for each piston can be made twice in a revolution of the crankshaft; once for the suction phase and once for the pumping phase. Active valve control also enables optimal pre-compression and pressure release functions; valve timing can be adjusted such that the pressure losses are minimized [12].

Figure 2 shows all periodic pumping and suction cycles of a piston in the case of two independent outlets. Arrows in the drawings stand for flows. Drawings on the first row describe idling when the mean power required from the prime mover is zero (ideal case). However, cases (a2) and (a3) are usually avoided. Drawings (b1) and (b2) shows a normal pumping cycle; fluid is sucked from the tank and pumped to either outlet. Drawings (c1) and (c2) are the motoring cycles respectively. Last two drawings depict the power transfer between the outlets i.e. the fluid is received from one outlet and pumped to another. Of course, it is possible to shift from whichever cycle to any other cycle and, because the pistons are independent of each other the DHPMS can function also as a transformer. It was first shown in [11] that the prime mover power reduces significantly when an accumulator is used as energy source/sink in one outlet of the DHPMS.

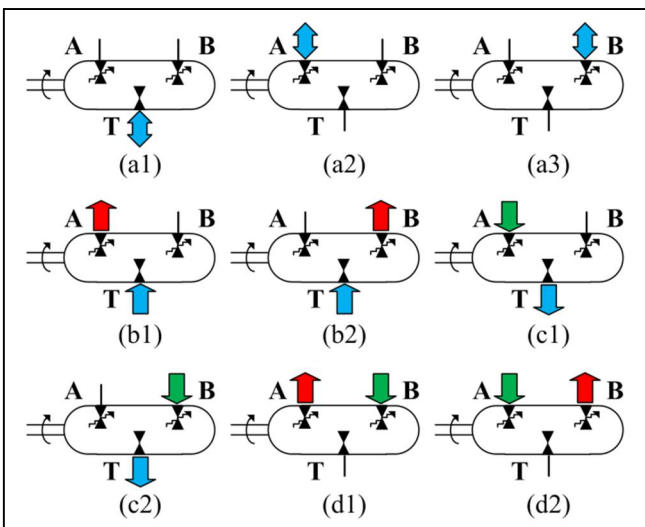


Figure 2. Possible fluid flows in DHPMS

## 2 Simulated system

### 2.1 Hydraulics and mechanics

Figure 3 shows a schematic and CAD-drawing of the studied system. The DHPMS is driven by an electric motor with rotational speed of 750 rpm. A flywheel is attached to the DHPMS axis to smooth the motor torque. The outlet B of the DHPMS is connected to the cylinder B-chamber while the A-chamber is connected to a pressurized tank. A static volume with port orifice in the actuator line is used as a damping element. A 4-liter accumulator attached to the DHPMS outlet A is used as energy storage. The tilt cylinder is hydraulically locked close to its minimum length whereas the bucket cylinder and the mechanics have been ignored in the model.

System model is created using MATLAB/Simulink and SimMechanics and the principle of the modeling procedure is similar that presented in [13] and [14]. Induction motor is modeled as a torque source and angular acceleration is calculated considering the moment of inertia of the flywheel. Angular velocity and angle of the motor shaft are the first and the second integrals of the angular acceleration respectively.

Chambers of the DHPMS are modeled as volumes which change according to sinusoidal motion of the crankshaft. Every chamber can be connected to a tank line or either one of the outlets via on/off control valves. The valves ( $Q_n = 23$  l/min @  $\Delta p_n = 0.5$  MPa) are modeled using a square root equation of flow and linear spool movement is assumed after the command delay. Ideal model of the DHPMS is used in the study i.e. neither leakages nor torque losses are considered.

Supply line B is modeled as a volume and is connected to a cylinder B-chamber via port orifice ( $Q_n = 100$  l/min @  $\Delta p_n = 0.5$  MPa). Port orifice of the A-chamber connects the cylinder to a pressurized tank which is modeled as a constant pressure source. Outlet A of the DHPMS is connected to an accumulator model through a volume and orifice ( $Q_n = 100$  l/min @  $\Delta p_n = 0.5$  MPa). Accumulator is modeled based on an adiabatic change of state by using equations

$$p_0 V_0^\kappa = p_1 V_1^\kappa = p_2 V_2^\kappa \quad (1)$$

Where  $p_0$  is the gas pre-charge pressure,  $p_1$  the gas initial pressure,  $p_2$  the instantaneous gas pressure and  $V_0$ ,  $V_1$  and  $V_2$  the corresponding gas volumes. Adiabatic exponent is a constant  $\kappa = 1.4$ .

Model of the crane consists of five bodies: base, two-part lift boom, tilt boom and load mass. Parts of the lift boom are joined together using a weld while the base and the tilt boom are connected to the lift boom parts through revolute joints. Finally, ball-shaped load mass is welded to the tip of the tilt boom. The booms are modeled as slender rods when calculating the moment of inertia tensors.

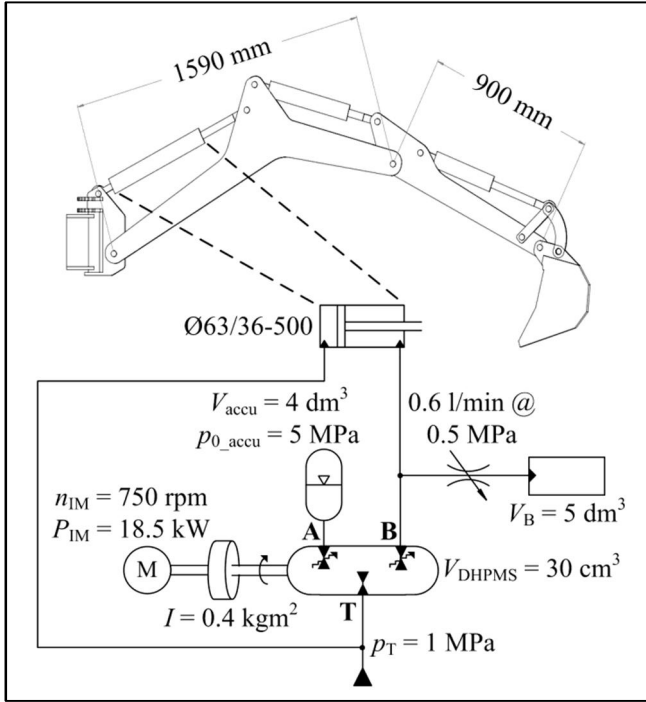


Figure 3. Schematic and CAD-drawing of studied system

## 2.2 Control logic

### 2.2.1 Fluid volume control

Fluid volume control in a direct connection approach is based on stroke-to-stroke control of the DHPMS and is explained in detail in [14]. The piston velocity reference is converted into the fluid volume target and the controller minimizes the error by pumping to or sucking from the actuator line. Of course, the DHPMS can also be left to idle.

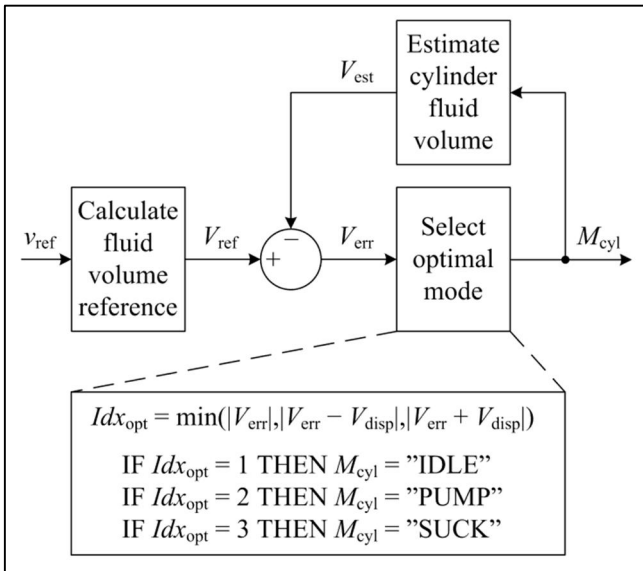


Figure 4. Block diagram of fluid volume control

Figure 4 shows a block diagram of the cylinder mode selection logic. First, the fluid volume reference is calculated from the velocity reference when a piston area is

a known parameter. Error in the cylinder fluid volume is further calculated by subtracting the estimated fluid volume from the target value. In this study, the total fluid volume produced by the DHPMS is estimated without utilizing pressure feedback. The piston displacement used by the volume controller is manually adjusted such that positioning accuracy is good enough.

The optimal mode is selected such that the fluid volume error minimizes. There are three mode options for cylinder volume control at every mode selection instant: pumping, suction or idling. Hence, the cylinder volume control is always prioritized over accumulator energy control.

### 2.2.2 Accumulator energy control

Accumulator energy control logic is shown in Figure 5. First, hydraulic total energy in a cylinder outlet is estimated according to a mode outputted from the volume controller. The energy is calculated as a product of theoretical DHPMS piston displacement and measured cylinder pressure. Hydraulic total energy of the DHPMS is further calculated by adding accumulator energy which is estimated similarly that of the cylinder.

At every mode selection instant, the optimal mode for accumulator energy control is determined to minimize consumed hydraulic energy in the outlets of the DHPMS. However, the mode for accumulator control is always selected after the selection of cylinder mode thus the optimal mode cannot be realized every time. Idle-mode is selected for the accumulator whenever the mode of volume control and the optimal accumulator mode conflicts.

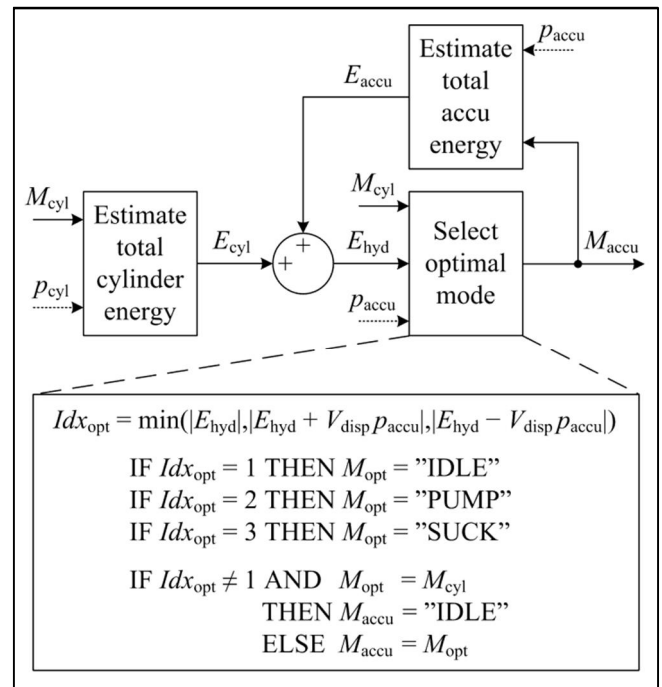


Figure 5. Mode selection logic of accumulator control

Logic for charging the accumulator and controlling the pressure is separate from the energy control. The logic can be realized by using three parameters for the accumulator:

target pressure, minimum pressure and maximum pressure. The accumulator is charged if the pressure is below the target and the actuator does not require power. However, the optimal target pressure is not studied here. The pressure limits instead are set to prevent too high or low pressure in the accumulator.

### 3 Simulation results

#### 3.1 Charging of accumulator

Figure 6 shows power consumption and require energy when the accumulator is charged from 15 to 21 MPa as shown in graph (a). It can be seen that the peak power during charging is over 6 kW when the maximum flow capacity of the DHPMS is used (blue solid line in graph (b) of Figure 6). The peak power halves when every other piston of the DHPMS is used (red dash line in graph (b) of Figure 6). On the other hand, the charging time doubles respectively. When only one piston in revolution is used for charging the accumulator, the mean power decreases significantly but the peak power is still over 2.5 kW at maximum (black dot-and-dash line in graph (b) of Figure 6). In this case, 6 MPa increase in accumulator pressure takes over seven seconds. Required input energy is independent of the charging rate in the studied accumulator model as can be seen in graph (c) of Figure 6.

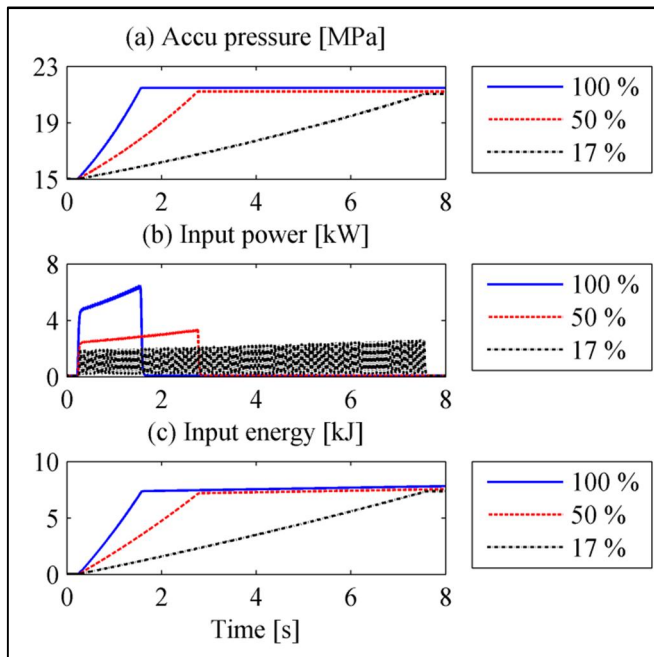


Figure 6. Power consumption during accumulator charging

#### 3.2 Energy recovery potential of the system

##### 3.2.1 Reference simulation

First, a test trajectory used in the study is simulated without utilizing accumulator energy. Load mass of 400 kg has been added to a tip of the tilt boom and open-loop fluid volume control is used to drive the lift boom cylinder. Retracting

movement of 0.2 m is performed to lift the boom upward and after that extending movement is done such that the original position is achieved.

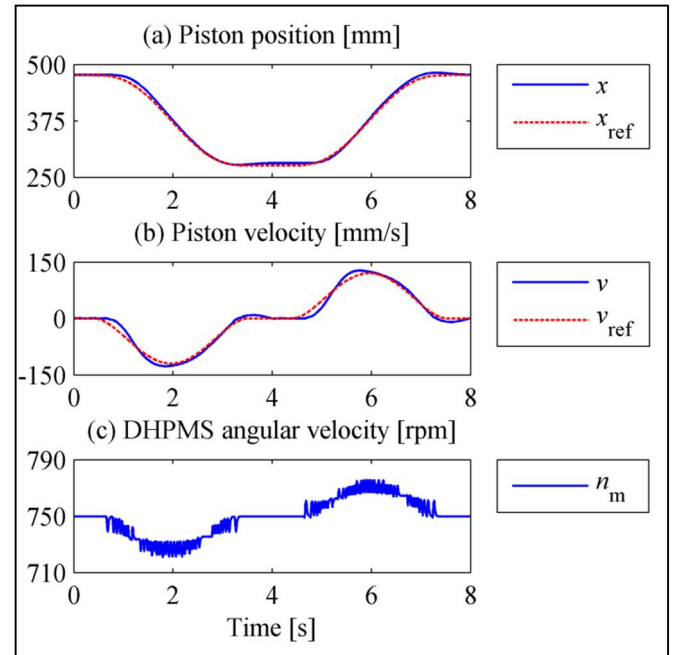


Figure 7. Test trajectory and tracking accuracy

Position tracking is good as shown in graph (a) of Figure 7. However, the effect of large inertial load can be seen during the movement especially in piston velocity (graph (b) of Figure 7). Building up the pressure causes a delay in the beginning of the movement and after that the piston accelerates rapidly to its maximum speed. Natural damping of the displacement controlled system is quite low despite of the attached damping elements. Graph (c) of Figure 7 shows rotational speed of the induction motor. Rotational speed decreases when the DHPMS requires torque and increases when the DHPMS is motoring i.e. the electric motor functions as a generator.

Graph (a) of Figure 8 shows the lift cylinder pressure and accumulator pressure during the simulated trajectory. Pressure in the chamber B varies between 15.2 and 20.5 MPa when the load mass is 400 kg. The highest and the lowest pressure occur at the beginning of the movements when the inertial load is accelerated. Output power of the system is calculated as a product of generated cylinder force and piston velocity. The power is about 4.5 kW at maximum when lifting the boom and -4.2 kW at minimum during lowering as shown in graph (b) of Figure 8 (red dash line). A blue solid line in the graph (b) of Figure 8 is an input power of the system which is calculated as a product of the motor torque and angular velocity. Required peak power of the electric motor is close to 5.5 kW and the minimum about -5.0 kW correspondingly.

Graph (c) of Figure 8 shows input and output energies during the test trajectory (blue solid line and red dash line). The energies are integrals of the presented input and output powers. It can be seen from the curves that the system can

recover the energy. The losses are produced solely in on/off control valves of the DHPMS because the torque losses are not considered in the model. However, if the negative input power cannot be utilized by the prime mover the losses are about 7 kJ which is described by the black dot-and-dash line in graph (c) of Figure 8 (saturated input energy).

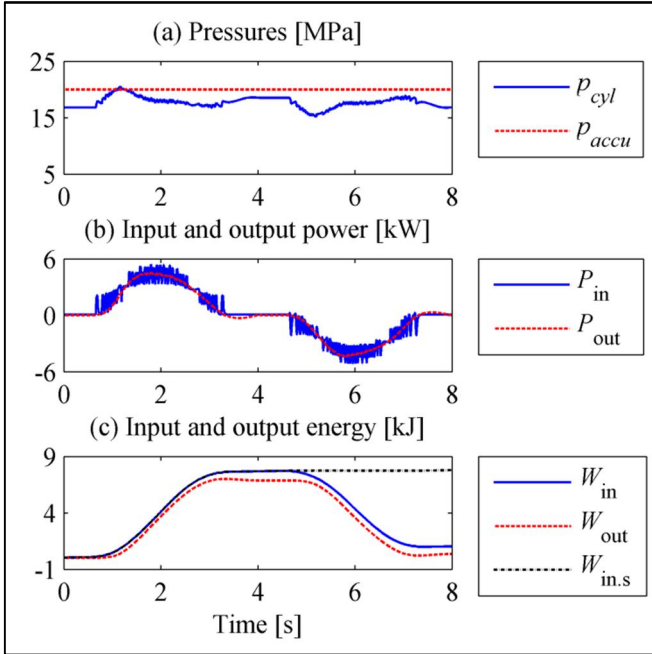


Figure 8. System characteristics without accumulator

### 3.2.2 Hydraulic energy recovery

Figure 9 shows a simulation where the hydraulic energy recovery is enabled and the load mass is 400 kg. The trajectory used is the same that the one in the reference simulation. Initial pressure of the accumulator is 20 MPa as shown in graph (a) of Figure 9 (red dash line). First, the accumulator energy is utilized in lifting the boom and the pressure decreases. On the contrary, the energy is stored in the accumulator when the load is lowered and the pressure rises. Cylinder pressure (blue solid line in graph (a) of Figure 9) is similar than in the reference simulation because the fluid volume control is separate from the accumulator energy control.

Output power shown in graph (b) of Figure 9 is identical to the one in the reference simulation but the peak power required from the induction motor, however, is significantly smaller when accumulator energy is utilized. It can be seen that when the pressures are close in, the input power is smooth and near zero because the ratio of pumping and motoring cycles equals one. Peaks in the power curve are caused by uneven pumping and motoring cycles due to divergent pressures in the outlets of the DHPMS. In this case, the accumulator energy controller chooses the ratio of pumping and motoring cycles such that the mean power of the electric motor is zero which means that the DHPMS functions as a transformer.

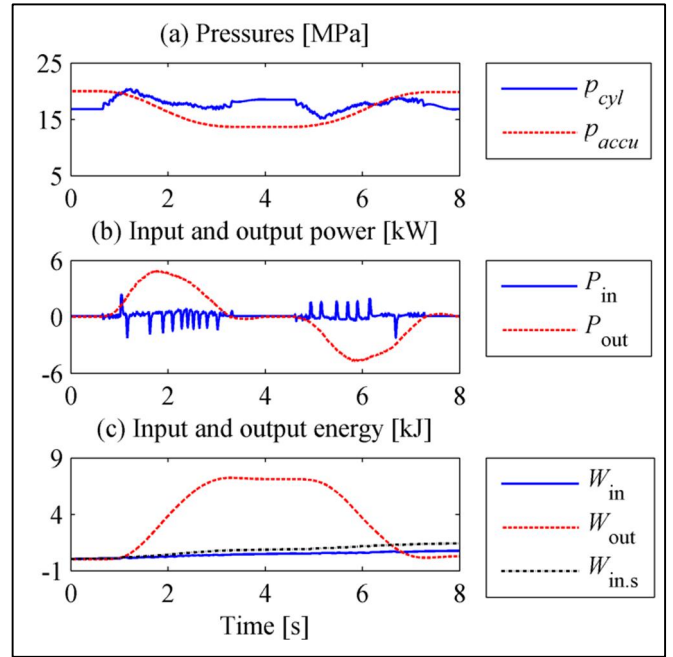


Figure 9. Test cycle with load mass of 400 kg

Graph (c) of Figure 9 shows that the difference between consumed input energy (blue solid line) and its saturated value (black dot-and-dash line) is about 0.5 kJ at the end of the simulation which means that hydraulic energy recovery possesses good efficiency. It can be seen that the final value of the input energy is somewhat smaller than the one in the reference simulation. Hence, slightly more energy has been taken from the accumulator during lifting than the energy is stored in while motion in the opposite direction. In this paper, however, the object is not to study total losses of the system but the functionality of hydraulic energy recovery.

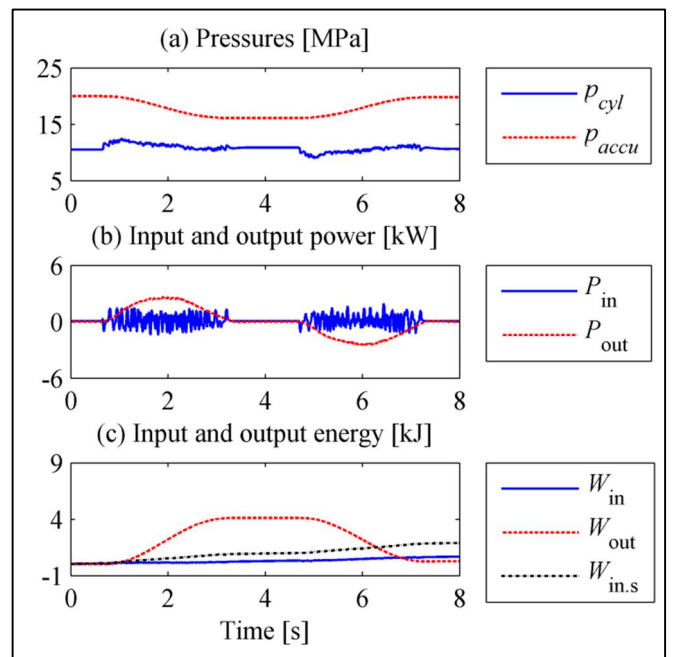


Figure 10. Test cycle with load mass of 200 kg

Figure 10 shows the result of a simulation with the load mass of 200 kg. Pressure level of the cylinder is about 11 MPa (blue solid line) and initial pressure of the accumulator 20 MPa as shown in graph (a) of Figure 10. Compared to the previous case, the change in accumulator energy is smaller during the trajectory due to larger difference between the cylinder pressure and accumulator pressure. In this case, uneven pumping and motoring cycles cause significant ripple in the input power curve, although the mean value is close to zero. Output power instead is between -2.6 and 2.6 kW in this case.

Graph (c) of Figure 10 shows lower efficiency of the hydraulic energy recovery compared to the previous case. Saturated input energy is now about 2.0 kJ (black dot-and-dash line) at the end of the trajectory and is 1.1 kJ greater than the total energy of the electric motor (blue solid line). With a load mass of 200 kg, lifting requires about 4 kJ while lowering returns the same amount of energy (red dash line).

### 3.2.3 Improving efficiency of energy recovery

Simulation examples in the previous chapter show that the hydraulic energy recovery can be realized using the DHPMS. However, peaks in the input power are quite high during uneven pumping and motoring cycles. The reason is a large displacement volume of the pistons; hence the performance can be further improved by diminishing the displacement of the DHPMS.

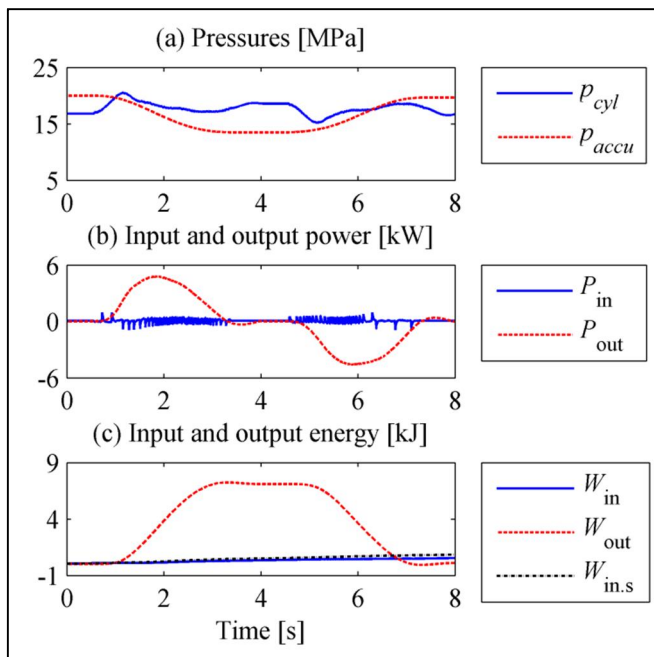


Figure 11. Test cycle with load mass of 400 kg

Figures 11 and 12 show simulations where the piston displacement is a quarter of the original one but the rotational speed of the DHPMS is 3000 rpm. Figure 11 shows the pressures, powers and energies when the load mass is 400 kg. It can be seen in graph (a) that the ripple in the cylinder pressure has diminished significantly. Pressure curve of the accumulator has not changed compared to the simulation in the previous chapter. Instead, the difference

can be clearly seen in power (blue solid line); the peak power of the electric motor is about one-fourth of the original one. Difference between the end value of input energy (blue solid line) and saturated energy (black dot-and-dash line) is only 0.3 kJ as shown in graph (c) of Figure 11 which means better efficiency of hydraulic energy recovery.

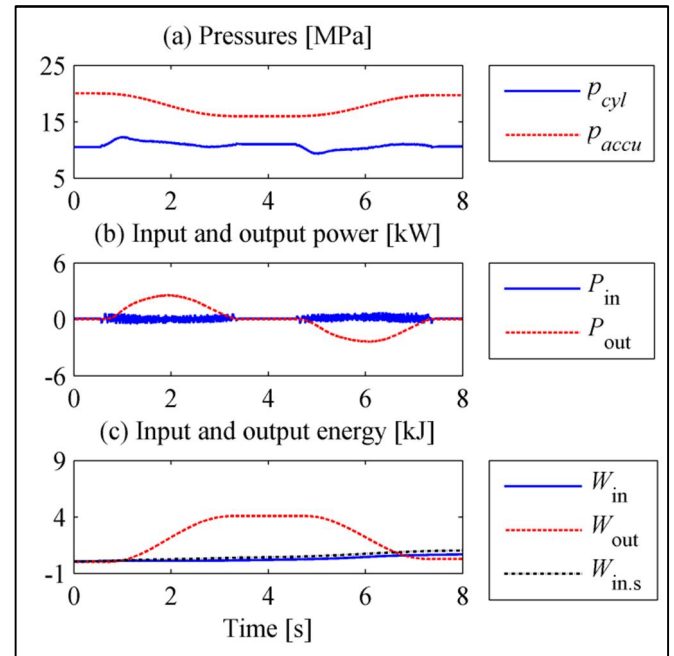


Figure 12. Test cycle with load mass of 200 kg

The effect of smaller displacement volume can be seen even better in Figure 12 which shows a simulation with a load mass of 200 kg. Graph (a) shows smoother cylinder pressure curve and graph (b) diminished ripple in the input power. Efficiency of the hydraulic energy recovery increases considerably compared to the original case. Here, the difference between the total input energy (blue solid line) and saturated energy (black dot-and-dash line) is no more than 0.3 kJ as shown in graph (c) of Figure 12.

## 4 Conclusions and further research

### 4.1 Recovering energy

In this study, hydraulic energy recovery using a digital hydraulic power management system and high pressure accumulator was tested by simulations. An excavator crane was controlled using a single acting cylinder connected to one outlet of the DHPMS, and the accumulator attached to another outlet was used as energy source/sink. The principle of accumulator energy control was to minimize hydraulic power consumption of the system.

The results show that the hydraulic energy recovery is possible in the displacement controlled digital hydraulic system. Potential energy of the load mass can be efficiently stored into the accumulator during the lowering movement. Noteworthy is that the DHPMS can handle different ratios of pressure levels thanks to the transformer function. Hence, the mean of the input power stays close to zero regardless of the load mass in the tested cases.

## 4.2 Prime mover downsizing

Instantaneous power required from the prime mover also reduces significantly when the accumulator energy is utilized. Simulations show that the size of the piston displacement has a great effect on the peak power. The system without the hydraulic energy recovery had input power of 5.5 kW at maximum in the studied trajectory with a load mass of 400 kg. When the accumulator was used the corresponding power was 2.4 kW or 0.9 kW depending on the piston displacement. According to the simulations, the highest power is needed when the accumulator is charged to the high pressure; however, the peak power can be controlled by limiting number of the pumping pistons.

## 4.3 Next step in study

In this study, initial pressure of the accumulator was set to 20 MPa regardless of the load pressure. The simulations show that the accumulator can be effectively used as an energy source/sink at different pressure levels. However, optimal pressure level control should be further researched to be able to minimize the input power and to maximize the recovered energy for the most of loadings and duty cycles. In the future, the hydraulic energy recovery will be also tested and the losses analyzed in a real system similar to the one presented in this study.

## Acknowledgement

The research was funded by the Doctoral Program in Concurrent Mechanical Engineering (DPCME) and the Academy of Finland (Grant No. 139540).

## References

- [1] Virvalo, T. and Vilenius, M. The Influence of Pumps and Valves on the Efficiency of a Hydraulic Boom. Development in Fluid Power Control of Machinery and Manipulators, Cracow, Poland, 2000.
- [2] Inderelst, M., Losse, S., Sgro, S. and Murrenhoff, H. Energy Efficient System Layout for Work Hydraulics of Excavators. The Twelfth Scandinavian International Conference on Fluid Power, SICFP'11, Tampere, Finland, 2011.
- [3] Huova, M., Karvonen, M., Ahola, V., Linjama, M., Vilenius, M. Energy Efficient Control of Multiactuator Digital Hydraulic Mobile Machine. The 7<sup>th</sup> International Fluid Power Conference (IFK), Aachen, Germany, 2010.
- [4] Huova, M. and Linjama, M. Energy Efficient Digital Hydraulic Valve Control Utilizing Pressurized Tank Line. The 8<sup>th</sup> International Fluid Power Conference (IFK), Dresden, Germany, 2012.
- [5] Bishop, E. Digital Hydraulic Transformer - Approaching Theoretical Perfection in Hydraulic Drive Efficiency. The 11<sup>th</sup> Scandinavian International Conference on Fluid Power, SICFP'09, Linköping, Sweden, 2009.
- [6] Kogler, H., Scheidl, R., Ehrentraut, M., Guglielmino, E., Semini, C. and Caldwell, D. A. Compact Hydraulic Switching Converter for Robotic Applications. Bath/ASME Symposium on Fluid Power and Motion Control (FPMC 2010), Bath, UK, 2010.
- [7] Juhala, J., Kajaste, J. and Pietola, M. Improving Energy Efficiency of Hydraulic Accumulator. The Twelfth Scandinavian International Conference on Fluid Power, SICFP'11, Tampere, Finland, 2011.
- [8] Linjama, M., Vihtanen, H-P., Sipola, A. and Vilenius M. Secondary Controlled Multi-Chamber Cylinder. The 11th Scandinavian International Conference on Fluid Power, SICFP'09, Linköping, Sweden, 2009.
- [9] Williamson, C., Zimmerman, J., and Ivantysynova, M. Efficiency Study of an Excavator Hydraulic System Based on Displacement-Controlled Actuators. Bath/ASME Symposium on Fluid Power and Motion Control (FPMC 2008), Bath, UK, 2008.
- [10] Zimmerman, J., and Ivantysynova, M. Hybrid Displacement Controlled Multi-Actuator Hydraulic Systems. The Twelfth Scandinavian International Conference on Fluid Power, SICFP'11, Tampere, Finland, 2011.
- [11] Linjama, M., Huhtala, K. Digital Pump-Motor with Independent Outlets. The 11<sup>th</sup> Scandinavian International Conference on Fluid Power, SICFP'09, Linköping, Sweden, 2009.
- [12] Heikkilä, M., Tammisto, J., Huova, M., Huhtala, K., Linjama, M. Experimental Evaluation of a Piston-Type Digital Pump-Motor-Transformer with Two Independent Outlets. Bath/ASME Symposium on Fluid Power and Motion Control (FPMC 2010), Bath, UK, 2010.
- [13] Karvonen, M., Heikkilä, M., Huova, M., Linjama, M., Huhtala, K. Simulation study - Improving Efficiency in Mobile Boom Using Digital Hydraulic Power Management System. The Twelfth Scandinavian International Conference on Fluid Power, SICFP'11, Tampere, Finland, 2011.
- [14] Heikkilä, M., Linjama, M. Direct Connection of Digital Hydraulic Power Management System and Double Acting Cylinder – A Simulation Study. The Fourth Workshop on Digital Fluid Power (DFP'11), Linz, Austria, 2011.
- [15] Heikkilä, M., Linjama, M. Improving Damping Characteristics of Displacement Controlled Digital hydraulic System. The Fifth Workshop on Digital Fluid Power (DFP'12), Tampere, Finland, 2012.



Control



# **Robustness Study on the Model-Free Control and the Control with Restricted Model of a High Performance Electro-Hydraulic System**

Yaozhong Xu , Eric Bideaux , and Daniel Thomasset

Laboratory AMPERE - UMR CNRS 5005, INSA Lyon, University of Lyon, Villeurbanne, France  
E-mail: yaozhong.xu@insa-lyon.fr, eric.bideaux@insa-lyon.fr, daniel.thomasset@insa-lyon.fr

## **Abstract**

In industry, some unexpected or unpredicted effects make difficult to apply certain control techniques which show good performances in laboratory. In this paper, we introduce two new control methods, called the model-free control and the control with restricted model [1–3], in the case of position tracking of an electro-hydraulic test rig. For an industrial point of view, these methods present many advantages as they are closed to the classic PID control and do not required an intensive modelling work. However, an accurate differentiation of the output has to be done on-line at high sampling frequency in order to estimate accurately the evolution of the state function. Experiments are conducted to estimate the sensibility of these control strategies to the system parameter perturbations. The results illustrate that the proposed controls have a good robustness performance, and that the tracking performance is sensitive to the velocity estimation precision.

**Keywords:** Model-Free Control, Control with Restricted Model, Robustness Analysis, Non-linear System, Eletro-Hydraulic System

## **1 Introduction**

Hydraulic technology has been developed in industry for long ago. Despite the large use of hydraulic system, it is still difficult to achieve an accurate position tracking on a large frequency range due to its nonlinearities [4], such as friction force, servovalve dynamic and flow rate characteristics. These nonlinearities make difficult a precise modelling of the hydraulic system. In previous research, some researchers tend to solve this problem by linearizing the nonlinear state equations to degrade it into a high-order linear model [5]. However, this kind of model is not accurate in a large operating range and is valid only on the neighbourhood of an operating point. Some nonlinear control strategies, such as the technique of backstepping [6, 7], and sliding mode [8, 9], have been developed in order to realize the precise control of such a nonlinear system. Nevertheless, they are rarely employed in industry because of their requirement of a precise mathematical modelling to achieve an accurate control and their complexity of implementation and controller gains tuning.

In this paper, we will explore the application of the model-free control method [1–3] which can realize an accurate position control without considering a precise system model. This method introduces a common ultra-local model which can approximate the unknown system dynamics on a very short time interval, rather than to develop a global system model. Moreover, the system parameters are estimated rapidly by gathering the system state information from sensors, and is automatically updated at every time interval. This means it can work

automatically without manual interruption once well configured, and then provides a new approach to deal with a complex nonlinear system. It has the advantage to be easy to implement and the tuning of the control law coefficients is simplified compared to other nonlinear methods. To improve the control performance, it is possible to use a limited model, for example without all dynamics developed and nonlinearities, while the unknown part is estimated by the model-free method. This evolution of the model-free control is called the control with restricted model. Since more information is known about the system, this method could provide a better control performance.

Because of its independence for the system model and ease of implementation, the model-free control is a convenient approach for application in industry where systems are much more complex than models in laboratory due to some unpredictable effects, such as changes of the environment. The model accuracy is possibly degraded due to the model misadjustment, or unavailability of some measurements, or also because of the difficulty of the system parameters tuning. When a control strategy is applied in practice, problems may occur and lead to a degraded even unpredictable result. The robustness of a control strategy is thus an important criterion of the performance evaluation. Of course, one of the main difficulty of the robustness analysis is to define properly the parameters to check and their range of variation.

Following this introduction, section 2 will give a brief introduction to the implementation of the model-free on our test

rig. Experiments will be conducted for the robustness analysis with different loads and precisions of the estimated velocity in section 3. Finally, section 4 will give some conclusions and perspectives.

## 2 Control strategy design

The system under study is a high performance electro-hydraulic test rig developed specifically for research purposes. The configuration of the test rig is shown in fig. 1. This test rig is equipped with two high bandwidth servovalves (MOOG D765) used as a 3-way component for driving each actuator chamber. They are both installed on an intermediate block [10] equipped with accumulators and solenoid valves, which conduct the modulated flow rates from the servovalves to a low friction actuator. The implementation of the model-free control in this rig and the experimental validation has been carefully investigated in [11].

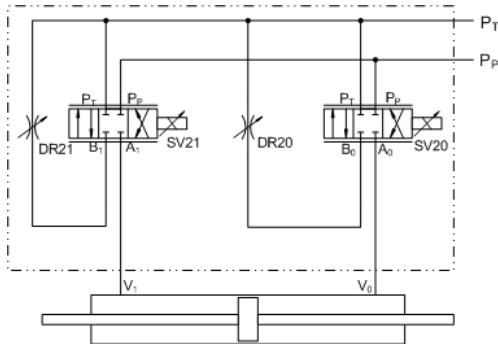


Figure 1: Simplified diagram of electro-hydraulic system

### 2.1 Model-Free control

The electro-hydraulic system is here considered as a SISO (single input single output) system by taking the opposite command condition for the servovalves, namely,

$$u = u_1 = -u_2. \quad (1)$$

The output of the system is the actuator piston displacement. According to the model-free method, we do not need any information about the system model. In a very short time step (in practice, the sampling period  $\Delta T$ ) the system is modelled by

$$\dot{y}(t) = F(t) + \alpha u(t) \quad (2)$$

where  $F$  represents the unmodelled or time-varying part of the system and will be updated automatically;  $\alpha$  is a parameter chosen by the user such that  $\alpha u$  and  $F$  have the same magnitude.

Then, the value of  $F$  is evaluated from  $u$  and  $\dot{y}$  at any time step as the following:

$$\hat{F}_k = \hat{y}_k - \alpha u_{k-1} \quad (3)$$

where  $\hat{F}_k$ ,  $\hat{y}_k$  are the estimated values of  $F$  and  $\dot{y}$  at time step  $k$ ;  $u_{k-1}$  is the command at time step  $k-1$ . Moreover,  $\hat{y}_k$  is obtained from position differentiation by applying an adaptive high-order sliding modes differentiator [12].

The controller is then developed from equation (2) as follows:

$$u_k = -\frac{\hat{F}_k}{\alpha} + \frac{\dot{y}_k^d}{\alpha} + K_P e_k + K_I \sum (e_k \cdot \Delta T) \quad (4)$$

where  $u_k$  is the command at time step  $k$ ;  $\dot{y}_k^d$  is the desired velocity at time step  $k$ ;  $e_k = y_k - y_k^d$  is the tracking error;  $K_P$ ,  $K_I$  are the classic PI tuning gains.

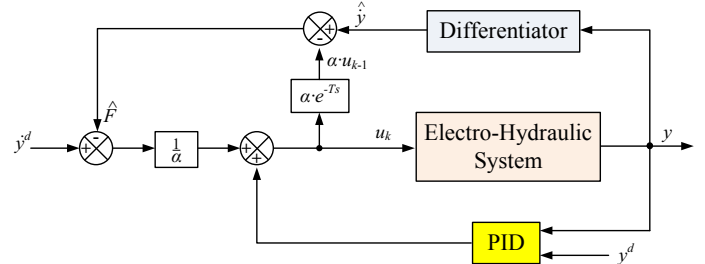


Figure 2: Scheme of the model-free control

The block diagram of the model-free control is presented in figure 2. This controller is called intelligent PI controller or i-PI in [1, 2]. The last PI part is required to assure the stability of the system and better performances. Compared with a classic PI controller, the i-PI controller contains a part involving the system structure information represented by the estimation of  $F$ . Therefore, the i-PI can improve the system robustness and tracking performance even for highly nonlinear systems in comparison with the classical PI or without requiring a complex tuning of the parameters as it is the case for nonlinear control laws.

### 2.2 Control with restricted model

A restricted model or an approximate model can be used to improve the pre-calculation of the open-loop command which is applied according to the desired position. In our case, the following assumptions are considered:

- 1) the internal and external leakages are ignored;
- 2) the fluid inertia and gravity in each chamber are neglected;
- 3) the dynamics of the servovalves is neglected;
- 4) the flow rates are considered proportional to the command.

Since the dynamics of the servovalve has been neglected in the dynamic model for the control design, the servovalve model consists therefore only in a static characteristic described by (6). This formulation is proposed by [13] for simplifying the flow rate calculation. It is related to the supply pressure  $P_P$ , tank pressure  $P_T$ , actuator chamber pressure  $P_1$  or  $P_2$ , and input command  $u_1$  or  $u_2$ . In order to get a unified control model, we use an operator  $sign(\cdot)$  to couple the inlet and outlet flow in (6). While handling the approximation of the control model, the focus is given on the dynamic of the actuator.

The compressibility of the fluid gives the pressure dynamics in each actuator chamber according to the piston velocity and the flow provided by each servovalve ( $\phi_1 u_1$  and  $\phi_2 u_2$ ). The

Newton's law gives the dynamics of the moving load. Dry friction  $F_{fs}$  calculated by (7), as well as the viscous friction term and gravity, are taken into account. The dynamic model of the actuator is then as follows:

$$\begin{cases} \frac{dy}{dt} = v \\ \frac{dv}{dt} = \frac{A}{M} (P_1 - P_2) - g - \frac{b}{M} v - \frac{F_{fs}(v)}{M} - \frac{F_{ext}}{M} \\ \frac{dP_1}{dt} = -\frac{\beta}{V_1(y)} \cdot A \cdot v + \frac{\beta}{V_1(y)} \cdot \phi_1(P_1, P_P, P_T, \text{sign}(u_1)) \cdot u_1 \\ \frac{dP_2}{dt} = \frac{\beta}{V_2(y)} \cdot A \cdot v + \frac{\beta}{V_2(y)} \cdot \phi_2(P_2, P_P, P_T, \text{sign}(u_2)) \cdot u_2 \end{cases} \quad (5)$$

$$\phi_i = \frac{Q_n}{u_n} \cdot \sqrt{\frac{|P_P - P_i|}{\Delta P_n} \cdot \frac{\text{sign}(u_i) + 1}{2}} + \frac{Q_n}{u_n} \cdot \sqrt{\frac{|P_i - P_T|}{\Delta P_n} \cdot \frac{\text{sign}(u_i) - 1}{2}} \quad (6)$$

$$F_{fs}(v) = (F_C + (F_{s_{dyn}} - F_C) e^{-C|v|}) \tanh(v) \quad (7)$$

For the design of the control with restricted model, a diffeomorphism is firstly required from the initial system coordinates (5)  $(y, v, P_1, P_2)$  to the new coordinates defined as  $(y, v, a, P_1)$ . The new system equations are written straightforwardly as

$$\begin{cases} \frac{dy}{dt} = v \\ \frac{dv}{dt} = a \\ \frac{da}{dt} = \frac{1}{M} \left( -b \cdot a - \frac{\partial F_{fs}(v)}{\partial v} \cdot a - A^2 \beta \left( \frac{1}{V_1(y)} + \frac{1}{V_2(y)} \right) \cdot v \right. \\ \quad \left. + A \beta \left( \frac{\phi_1(\cdot)}{V_1(y)} \cdot u_1 - \frac{\phi_2(\cdot)}{V_2(y)} \cdot u_2 \right) \right) \\ \frac{dP_1}{dt} = -\frac{\beta}{V_1(y)} \cdot A \cdot v + \frac{\beta}{V_1(y)} \cdot \phi_1(P_1, P_P, P_T, \text{sign}(u_1)) \cdot u_1 \end{cases} \quad (8)$$

As we consider only a SISO system with the model-free based controls, the pressures are not directly controlled. Instead, the opposite command condition as given by equation (1) is taken into account. Then, this system is degraded to a SISO one with an input command  $u$  and a position output  $y$  as described in (9).

$$\begin{cases} \frac{dy}{dt} = v \\ \frac{dv}{dt} = a \\ \frac{da}{dt} = \frac{1}{M} \left( -ba - \frac{\partial F_{fs}(v)}{\partial v} \cdot a - A^2 \beta \left( \frac{1}{V_1(y)} + \frac{1}{V_2(y)} \right) v \right. \\ \quad \left. + A \beta \left( \frac{\phi_1(\cdot)}{V_1(y)} + \frac{\phi_2(\cdot)}{V_2(y)} \right) \cdot u \right) \end{cases} \quad (9)$$

By inverting the dynamics model (9), an open-loop nominal command is given by

$$u^* = \frac{M \cdot j^d + b \cdot a^d + \frac{\partial F_{fs}(v^d)}{\partial v^d} \cdot a^d + A^2 \beta \left( \frac{1}{V_1(y^d)} + \frac{1}{V_2(y^d)} \cdot v^d \right)}{A \beta \left( \frac{\phi_1(\cdot)}{V_1(y^d)} + \frac{\phi_2(\cdot)}{V_2(y^d)} \right)} \quad (10)$$

As the system model is incomplete and there exists some unknown effects, the control law can then be defined as

$$u = u^* + \Delta u \quad (11)$$

where  $\Delta u$  represents the compensation command of the unknown phenomena or unmodelled parts of the system and also the feedback controller.

We assume that the compensation command complies with the following relationship (12) with the system output.

$$\dot{y}(t) = F(t) + \alpha \Delta u(t) \quad (12)$$

Similarly to what was done with the model-free control, the function  $F$  is given by

$$\hat{F}_k = \hat{y}_k - \alpha \Delta u_{k-1} \quad (13)$$

$$\text{where } \Delta u_{k-1} = u_{k-1} - u_{k-1}^* \quad (14)$$

$u_{k-1}^*$  is the nominal command at time step  $k-1$ .

The compensation command at time step  $k$  is then calculated by

$$\Delta u_k = -\frac{\hat{F}_k}{\alpha} + \frac{\dot{y}_k^d}{\alpha} + K_P e_k + K_I \sum (e_k \cdot \Delta T) \quad (15)$$

Finally, the controller with restricted model is given in the following equation (16):

$$u_k = u_k^* - \frac{\hat{F}_k}{\alpha} + \frac{\dot{y}_k^d}{\alpha} + K_P e_k + K_I \sum (e_k \cdot \Delta T) \quad (16)$$

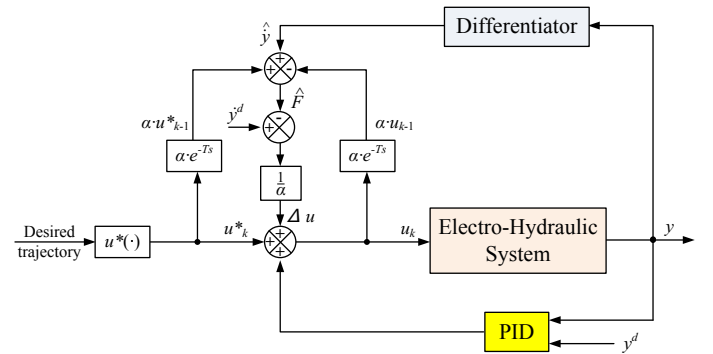


Figure 3: Scheme of the control with restricted model

The block diagram of the model-free control is presented in figure 3. With more information about the system, we will show that the control with restricted model can achieve better control performances than the model-free control, the i-PI being dedicated to the regulation along the tracked trajectory in this case. Some simulation and experimental results are presented in the following sections.

### 3 Experimental results

Experiments are conducted with different loads and different precisions of the estimated velocity in order to study the robustness performance with respect of the mass perturbation of the moving part and the velocity error. The piston position is measured by a LVDT sensor. This position signal is collected into dSPACE acquisition board (DS1104) at a sampling frequency of 1 KHz. The velocity information is evaluated by an on-line 2nd-order adaptive differentiators (DAO2) [12]. The desired trajectory is defined by a 7th-order polynomial function which has a smooth velocity, acceleration, and jerk profile.

Some parameters of the test bench are given in table 1.

Table 1: Test bench characteristics

Actuator	
Total stroke	300 mm
Mass of the moving part (rod+piston): $M$	5.8 Kg
Active section area: $A$	9.456 cm <sup>2</sup>
Dead volume at each end	14.184 cm <sup>3</sup>
Servovalve Moog D765	
Rated flow	19 L/min
Rated input signal	±10 V
Response time	2 ms
LVDT sensor installed on the rod of the actuator	
Measurement range (MR)	300 mm
Sensibility	4.4 mV/V/mm
Precision	< 0.1% of the MR

### 3.1 Experiments with different loads

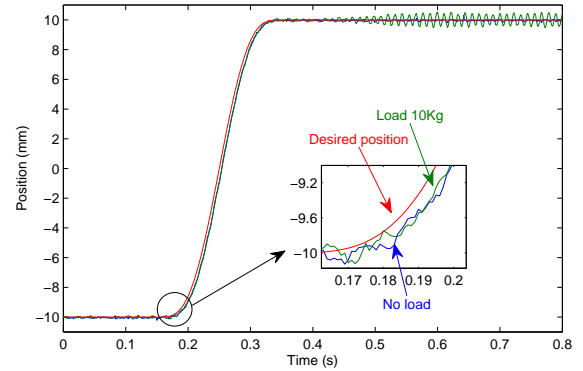
In practice, the operating situation is always changing according to the task requirements, e.g. the loads, the environmental conditions corresponding to different tasks. A good control strategy with high performance should show insensitivity to these changes. In this section, we will mainly discuss the influence of the payload change on the control performances. Experiments are conducted with different loads in order to investigate the robustness performance with respect to the mass perturbation. The load will vary from 0 to 20 kg, while the other experimental configurations remain unchanged.

In order to make a comparison with the classic linear control strategy, we present firstly the experimental results obtained by a proportional control with different loads in figure 4. The experimental results of the proportional control with a load of 20 kg are not presented in the figure as its behaviour becomes unstable when the load reaches 20 kg. From this figure, we can observe that the position tracking curve in the experiment with a load of 10 kg presents already oscillations with an important amplitude up to 1 mm, which implied that the control tended to make the controlled whole system unstable.

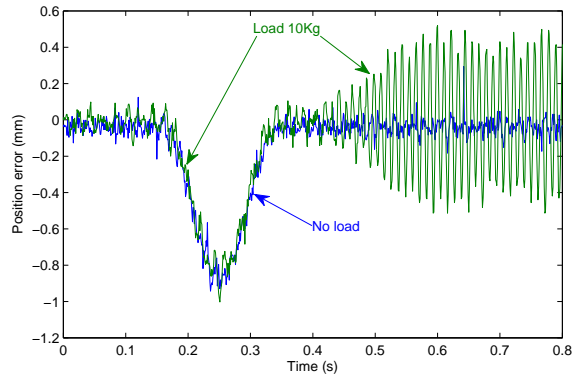
Since the static error is very low, only the gain  $K_P$  is really required. The loads are 0, 10, and 20 kg, and a value of 30 V/m is used for the tuning gain  $K_P$ . Figures 5 and 6 present the experimental results obtained respectively by the model-free control and the control with restricted model.

Compared to the results obtained with the proportional control (figure 4) which becomes unstable at the end of the transient phase, the model-free based control strategies are keeping a good behaviour despite the load changes. Especially, it can be noticed that the accuracy of the position tracking is conserved with the control with restricted model when the payload is increased. No notable changes in the results with the different loads can be observed, which implies that the mass change has little influence on the tracking performance of the proposed strategies. This is due to the self-adjustment of the control strategies according to the estimation of the uncertain ultra-local parameter  $F$ .

Table 2 gives a summary of the position errors obtained with both the model-free control and the control with restricted



(a) Position tracking



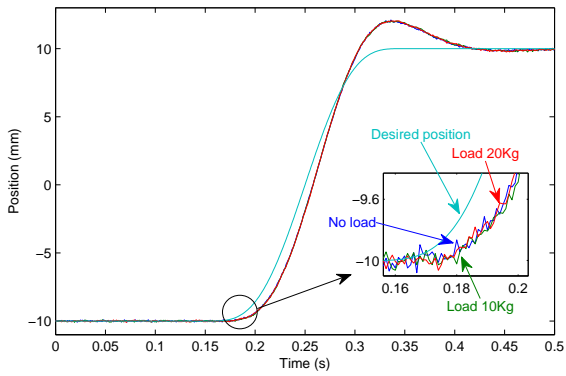
(b) Position error

Figure 4: Robustness experiment results obtained by the proportional control

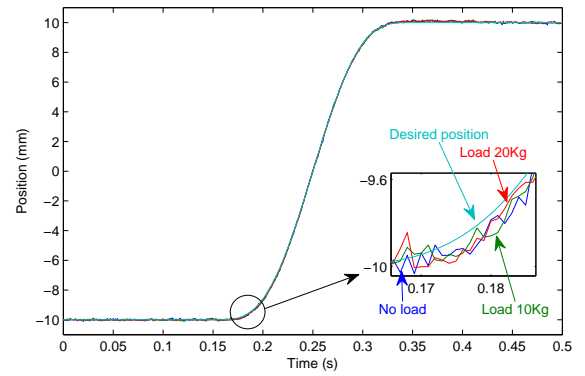
Table 2: Comparison summary of the position error ( $\mu\text{m}$ ) with different loads in model-free control (MFC), control with restricted model (CRM), and proportional control (Prop.)

Control strategy	Load (kg)	Transient phase		Steady state	
		Max.	STD <sup>a</sup>	Mean	STD <sup>a</sup>
MFC	0	2122	1344	0.06	39
	10	2082	1370	-0.2	40
	20	2079	1372	-0.02	34
CRM	0	192	71	0.2	41
	10	189	77	-0.4	40
	20	184	66	0.02	33
Prop.	0	943	304	-41	35
	10	1003	315	-10	52

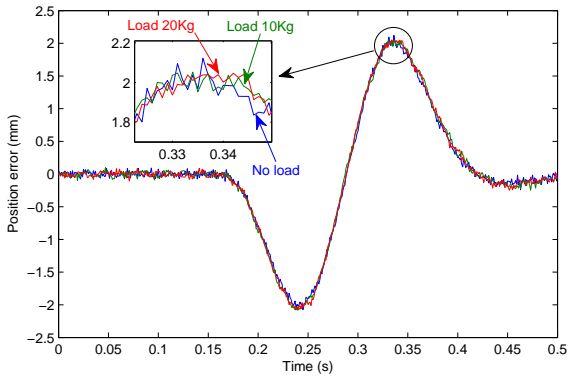
a) STD: Standard deviation



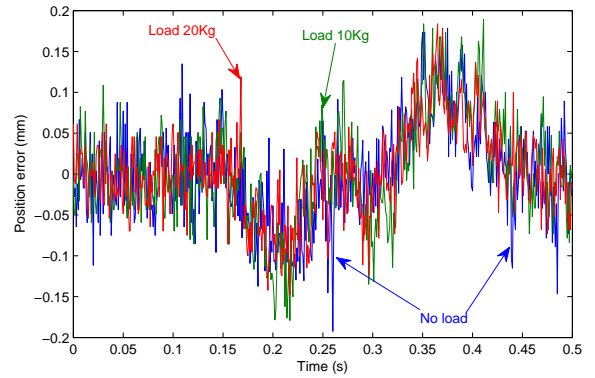
(a) Position tracking



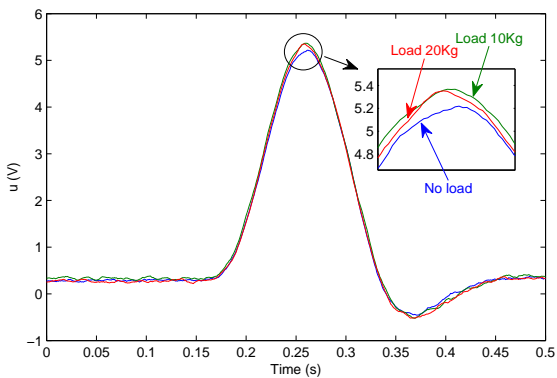
(a) Position tracking



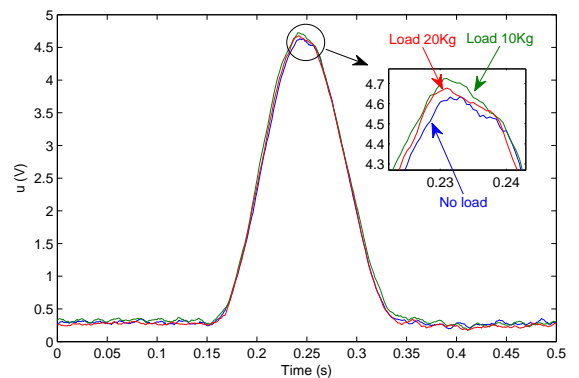
(b) Position error



(b) Position error



(c) Command  $u$



(c) Command  $u$

Figure 5: Robustness experiment results obtained by the model-free control

Figure 6: Robustness experiment results obtained by the control with restricted model

model when the load is changed. According to table 2, in all cases, the control with restricted model shows a higher precision in transient phase. In all cases, the average static error obtained from the two model-free based methods can be neglected. In conclusion, according to the experimental results, the controls based on the model-free method show very good robustness performances against the mass perturbation of the moving part.

### 3.2 Experiments with different precisions of the estimated velocity

The calculation of the uncertain ultra-local parameter  $F$  (3) and (13) uses the estimated value of velocity obtained from the DAO2 algorithm. Hence, the control performances are associated with the estimation precision of the numeric differentiator which is influenced by the tuning gains of the DAO2. The phase shift of the estimated velocity becomes significant when the DAO2 gains are decreased, this leads actually to the precision degradation. However, the noise is obviously reduced. Unfortunately, as no direct measurements of velocity are available on the test rig, we are limited here to a qualitative analysis of the estimation precision and it is difficult to conclude on the estimation accuracy.

Figures 7, 8, and table 3 show the experimental results obtained with different precisions of the tuning gains of the DAO2 which is used here for velocity estimation. When these gains decrease, the estimated velocity will be less precise but will be less noisy. The other experiment parameters remain the same as those in section 3.1.

Table 3: Comparison summary of the experimental position error ( $\mu\text{m}$ ) with different precisions of DAO2: model-free control (MFC), control with restricted model (CRM), and proportional control (Prop.)

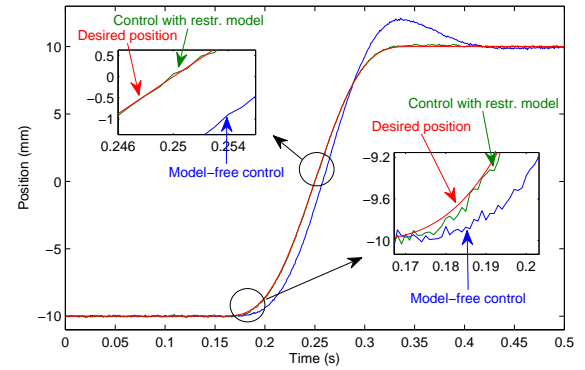
Control strategy	Transient phase		Steady state	
	Max.	STD <sup>c</sup>	Mean	STD <sup>c</sup>
MFC (HG-DAO2 <sup>a</sup> )	2122	1344	0.06	39
CRM (HG-DAO2 <sup>a</sup> )	192	71	0.2	41
MFC (LG-DAO2 <sup>b</sup> )	1301	582	0.06	38
CRM (LG-DAO2 <sup>b</sup> )	1429	627	-0.3	44

a) HG-DAO2 : low gain values of DAO2

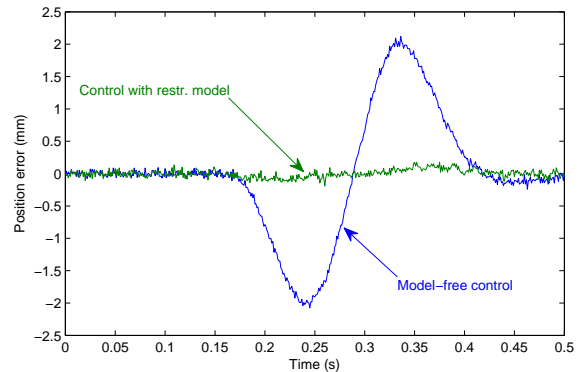
b) LG-DAO2 : high gain values of DAO2

c) STD: Standard deviation

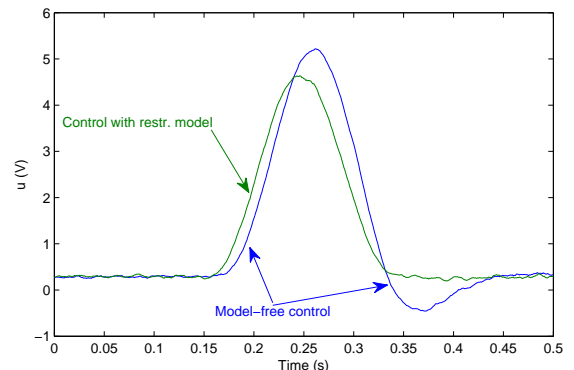
For the model-free control (figure 8(a)), it can be noticed that the system needs more time to reach the high level position due to the degradation of the velocity precision. Some oscillations at low frequencies occur at the steady state. By comparing figures 7(d) and 8(d), it can be observed that the estimated velocities have less noise as the gains of the DAO2 decrease, but the phase shift becomes significant, which leads to fluctuations in the command calculations (figures 7(c) and 8(c)). Decreasing the estimated velocity precision leads to a more significant degradation on the tracking performance for the control with restricted model because this control law uses an approximate system model involving a term function



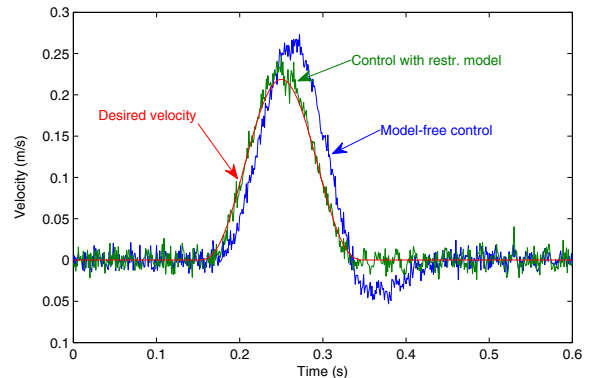
(a) Position tracking



(b) Position error

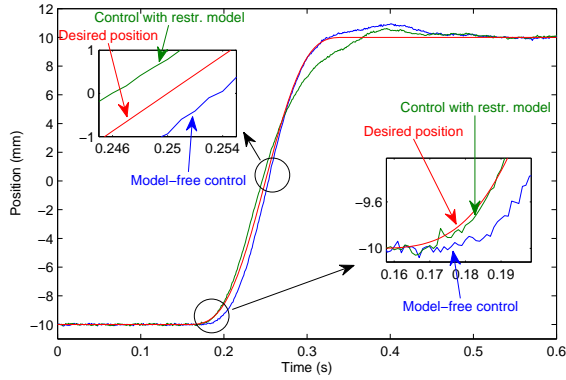


(c) Command  $u$

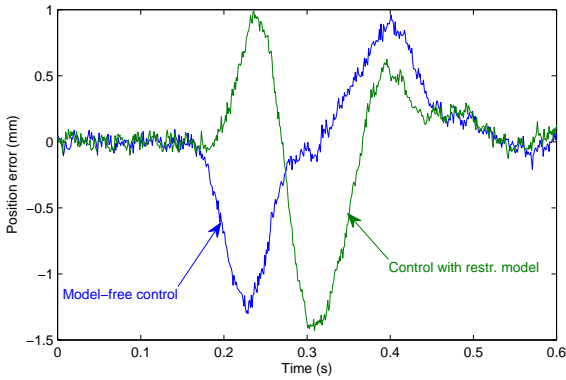


(d) Velocity evolution

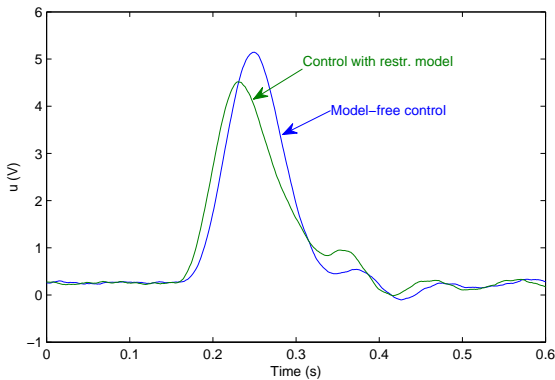
Figure 7: Experimental results of the methods based on model-free control with high gain values of DAO2



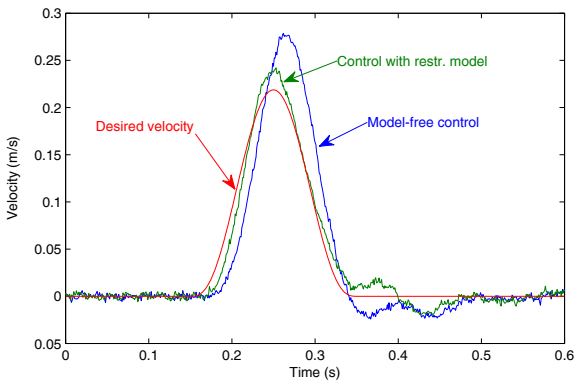
(a) Position tracking



(b) Position error



(c) Command  $u$



(d) Velocity evolution

Figure 8: Experimental results of the methods based on model-free control with low gain values of DAO2

of the velocity. On the other hand, although the tracking error of the model-free control decreases for low gain values of the DAO2, the control performance is actually degraded according to the fluctuations in the command (figure 8(c)) which implies a degradation of the system stability. In conclusion, for the two proposed control strategies, the tracking performances are degraded as the velocity becomes inaccurate. The precision of velocity estimation is then a critical factor to improve the performances of this kind of control strategies.

## 4 Conclusion

In this paper, the robustness performance of controls based on the model-free method has been studied throughout some experiments. These experiments results show that compared to the proportional control, the proposed control strategies have a good robustness performance against the mass change of the moving part. However, with the model-free based controls, it should be noticed that in order to get accurate tracking, the velocity estimation accuracy is an essential factor. To conclude, the model-free based control methods are easy to implement as they do not require a precise model of the system and have good robustness performances with high position tracking precision. This shows its high potential for application in industry.

## Nomenclature

Designation	Denotation	Unit
$y$	Piston position	[m]
$v$	Actuator velocity	[m/s]
$a$	Actuator acceleration	[m/s <sup>2</sup> ]
$u_{1,2}$	Control input 1 or 2	[V]
$P_{1,2}$	Pressure in chamber 1 or 2	[Pa]
$P_T$	Tank pressure	[Pa]
$P_P$	Supply pressure	[Pa]
$\Delta P_n$	Rated valve pressure drop	[Pa]
$u_n$	Rated control input	[V]
$Q_n$	Rated flow	[m <sup>3</sup> /s]
$A$	Piston active area	[m <sup>2</sup> ]
$b$	Viscous coefficient	[N/(m/s)]
$\beta$	Bulk modulus	[Pa]
$V_{1,2}$	Volume in chamber 1 or 2	[m <sup>3</sup> ]
$F_{fs}$	Dry friction	[N]
$F_{s\text{dyn}}$	Dynamic dry friction	[N]
$F_C$	Coulomb friction	[N]
$C$	Friction index	[-]

## References

- [1] M. Fliess and C. Join. Commande sans modèle et commande à modèle restreint. *e-STA*, 5(4):1–23, 2008.
- [2] M. Fliess and C. Join. Model-free control and intelligent pid controllers: Towards a possible trivialization of nonlinear control. In *Proceeding of 15th IFAC Symp. System Identif., Saint-Malo*, 2009.
- [3] M. Fliess, C. Join, and S. Riachy. Nothing is as practical as a good theory: Model-free control. In *JN-JD-MACS, Marseille*, 2011.

- [4] H.E. Merritt. *Hydraulic Control Systems*. John Wileys and Sons, Cincinnati, Ohio, 1967. ISBN 0-471-59617-5.
- [5] D.H. Kim and T.-C. Tsao. A linearized electrohydraulic servovalve model for valve dynamics sensitivity analysis and control system design. *Journal of Dynamic Systems, Measurement, and Control*, 122(4):179–187, 2000.
- [6] M. Smaoui, X. Brun, and D. Thomasset. A study on tracking position control of electropneumatic system using backstepping design. *Control Engineering Practice*, 14(8):923–933, Aug. 2006.
- [7] Y. Xu, L. Sidhom, E. Bideaux, and M. Smaoui. Multivariable backstepping controls of a high bandwidth electro-hydraulic actuator. In *Proceeding of Bath/ASME Symposium on Fluid Power & Motion Control, Bath, UK*, pages 397–410, Sep. 2012.
- [8] A. Levant. Universal siso sliding-mode controllers with finite-time convergence. In *IEEE Transaction on Automatic Control, Barcelona*, volume 46, pages 1447–1451, 2001.
- [9] G. Bartolini, A. Pisano, and E. Usai. A survey applications of second-order sliding mode control to mechanical systems. *International Journal of Control*, 76(9):875–892, June 2003.
- [10] Y. Xu, E. Bideaux, S. Sesmat, and J.P. Simon. Dynamic effect of the intermediate block in a hydraulic control system. *Journal of Mechanical Engineering and Automation*, 2(6), Nov. 2012.
- [11] Y. Xu, E. Bideaux, and D. Thomasset. Model-free control and control with restricted model of a high performance hydraulic system. In *8th International Conference on Fluid Power Transmission and Control, Hangzhou, China*, 2013.
- [12] L. Sidhom, M. Smaoui, D. Thomasset, X. Brun, and E. Bideaux. Adaptive higher order sliding modes for two-dimensional derivative estimation. In *Proceeding of 18th World Congress of the International Federation of Automatic Control (IFAC), Milano*, 2011.
- [13] MOOG. Servovalves with integrated electronics d765 series. Technical report, MOOG Inc.

## **Contribution on Control Strategies of Flow-On-Demand Hydraulic Circuits**

M. SCHERER, M. GEIMER and B. WEISS\*

Karlsruhe Institute of Technology, Chair of Mobile Machines, Karlsruhe, Germany  
E-mail: martin.scherer@kit.edu, marcus.geimer@kit.edu, bweiss@weiss-can-sps.de

\*Weiss Mobiltechnik GmbH, Rohrdorf, Germany

### **Abstract**

The development of an innovative flow-on-demand electrohydraulic system for mobile forestry cranes is described in the present paper. To overcome functional principle related weaknesses of conventional hydraulic-mechanical Load-Sensing systems, this work breaks up the control pressure difference related dependence of the delivered oil flow. Rather the swiveling angle of the displacement pump is calculated by summing up the single consumer oil flows corresponding to the velocity requests of the machine operator. For the electrohydraulic spool valves, several advanced control strategy concepts are discussed, each of which leading to an energy efficient artificial but controlled undersupply. The energy saving potentials are derived from a characteristic forestry crane duty cycle via dynamic simulation methods. Further on, the system shall be set up in a prototype crane to validate simulation results and to pave the way to the market by demonstrating the system performance.

**Keywords:** flow-on-demand, flow control, Load-Sensing, electrohydraulic, forestry crane, dynamic simulation, control strategy, energy efficiency, operability

### **1 Introduction and Objectives**

Electrohydraulic systems offer new possibilities regarding energy efficiency and operability. A rising number of electrohydraulic components available on the market leads to their advancing application in mobile machines, as manufacturers, machine owners and operators show increasing confidence in the reliability of these complex systems. In recent years an interest shift from pressure controlled hydraulic systems to directly flow controlled systems, requiring electrohydraulic components, may be identified from academic publications. Despite being a relatively young field of research, nevertheless these flow controlled systems themselves have shown a slight evolution over the last few years [1] [2] [3] [4] [5]. With researchers from internationally distributed institutions taking up the issue and adding their ideas [6] [7] [8] (cf. chap. 2.2 and 2.3) flow controlled systems have reached a sophisticated status. Nevertheless these systems still play a negligible role in the industry of mobile hydraulics. Merging the most promising flow sharing solutions from relevant publications with own approaches, at the Karlsruhe Institute of Technology (KIT), a public funded, application-oriented research project is conducted to investigate the benefits of an electrohydraulic flow-on-demand control. This innovative hydraulic system for a forestry crane is compared to a conventional hydraulic-mechanical Load-Sensing (LS) system in terms of energy efficiency. In a first step, the system is represented using simulation methods and later validated with a hydraulic test

bench and a prototype. To ensure a smooth introduction on the market, especially for small batch applications like forestry machines, an unique characteristic of the project is the sole use of components available off-the-shelf.

### **2 Theoretical Considerations**

The motivation for research on flow-on-demand systems is based on the omnipresent striving for improved energy efficiency in general as well as on considerations concerning operability improvements in particular. To understand the advantages of flow controlled applications, initially hydraulic-mechanical Load-Sensing systems are discussed, representing the state-of-the-art in a wide range of mobile hydraulic applications as of today.

#### **2.1 Technical Reference - Load-Sensing**

Load-Sensing hydraulic control systems adjust the pump pressure and/ or the flow rate to the demand of the consumer loads. The first Load-Sensing systems were developed in the mid-seventies in the US [9]. The intention was to reduce the power losses of constant flow or constant pressure systems.

In principle Load-Sensing systems can be divided in two categories, the Open-Center (OC) and the Closed-Center (CC) systems. Open-Center Load-Sensing systems use a fixed displacement pump and regulate the pump pressure by

an inlet pressure compensator in the valve assembly. This unloading valve is operative to bypass excess pump flow to the tank. Thus the efficiency is related to the ratio of the pump flow rate  $Q_p$  to the summation  $\Sigma Q_L$  of the flow rates that are demanded by the hydraulic loads [10]. Therefore the OCLS systems generate high losses when the load pressure is high but flow rate demand is relatively small [5]. For equally loaded consumers, the best point of the degree of efficiency is calculated by eq. (1):

$$\eta_{th} = \frac{1}{1 + \frac{\Delta p_{LS}}{p_L}} \cdot \frac{\Sigma Q_L}{Q_P} \quad (1)$$

Due to this disadvantage, OCLS systems have de facto lost their market relevance to CCLS systems. To reduce the losses and improve the efficiency, these hydraulic systems are provided with variable displacement pump. The pump is regulated by a pressure controller as well as a flow rate controller. The control pressure margin  $\Delta p_{LS}$  between the highest load pressure  $p_L$  and the pump pressure  $p_p$  is held constant over all operating points (see eq. (2)).

$$\Delta p_{LS} = p_p - p_L \quad (2)$$

Therefore the efficiency is not related to the flow rate [10]. The degree of efficiency is calculated by eq. (3), again the losses related to minor loaded consumers remain unconsidered in the equation:

$$\eta_{th} = \frac{1}{1 + \frac{\Delta p_{LS}}{p_L}} \quad (3)$$

To provide load independent flow rates and therefore consumer velocities and to prevent load interference between the hydraulic consumers, individual pressure compensators are installed either up- or downstream to the directional control valves. These pressure compensators ensure a constant pressure drop  $\Delta p = const$  over the metering orifice, thus the flow rate is nothing but dependent on the restriction area  $A_0$ , corresponding to the valve spool position. This relation is described via the universal orifice formula (see eq. (4)).

$$Q = \alpha_D \cdot A_0 \cdot \sqrt{\frac{2 \cdot \Delta p}{\rho}} \quad (4)$$

The so called pre- or post compensators show similar system behavior in normal operating mode, but differ in case of pump saturation. In these undersupply situations, the pre compensator layout causes only the consumer with the momentarily highest load to slow down or even stop, leaving the other consumers undisturbed. Whereas the technically complexer post compensators divide the flow rate in ratio to the nominal flow of the main valves, slowing down each consumer proportionally.

Exemplary, the hydraulic circuit of a LS system with two linear motors is shown in Figure 1.

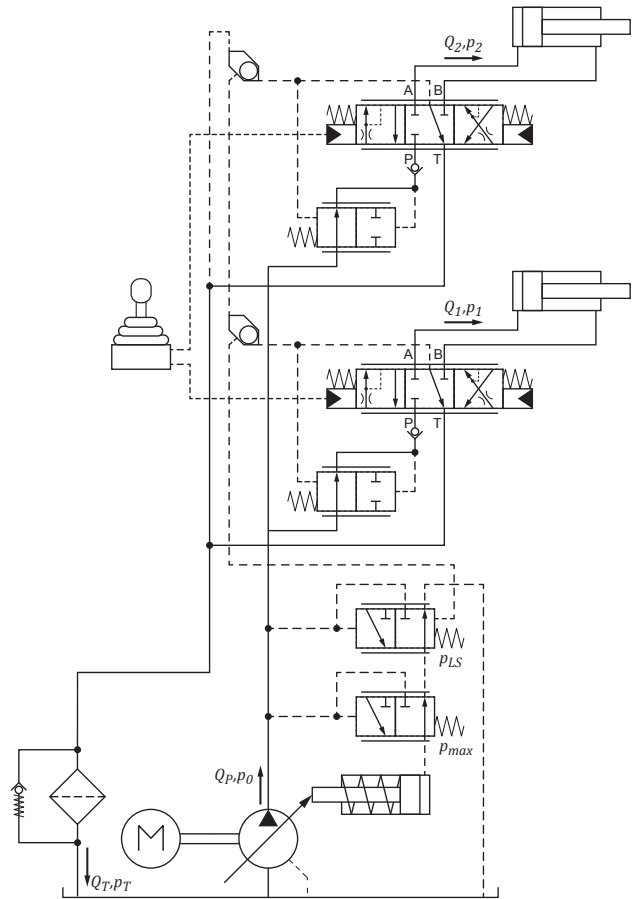


Figure 1: circuit layout of a CC hydraulic-mechanical Load-Sensing system with pre compensator

To ensure sufficient control performance and quick response times the control pressure margin  $\Delta p_{LS}$  between pump pressure and highest load pressure in conventional Load-Sensing systems is set to at least 20 bars, easily reaching 30 bars in systems with remote consumers entailing long load signal lines. As those signal lines form a closed hydraulic control loop, LS systems show a disturbing oscillation tendency.

Especially in partial load situations where the constant control pressure margin accounts for considerable ratios of the total energy demand, Load-Sensing hydraulic systems face efficiency disadvantages. The throttling losses are mainly linked to the pressure drop  $\Delta p_{PC}$  over the metering orifice of the highest loaded consumer, set by the related individual pressure compensator. This constant pressure drop is usually tuned in at ratios of  $\frac{2}{3}$  up to  $\frac{3}{4}$  of the total Load-Sensing functional principle pressure difference  $\Delta p_{LS}$ , set by the flow rate controller of the pump. Thus, the pressure difference related power losses consist of throttling losses  $P_{Loss,thr}$  and an additional functional principal share  $P_{Loss,fp}$ . In Figure 2 these losses are represented for the exemplary LS system with two consumers.

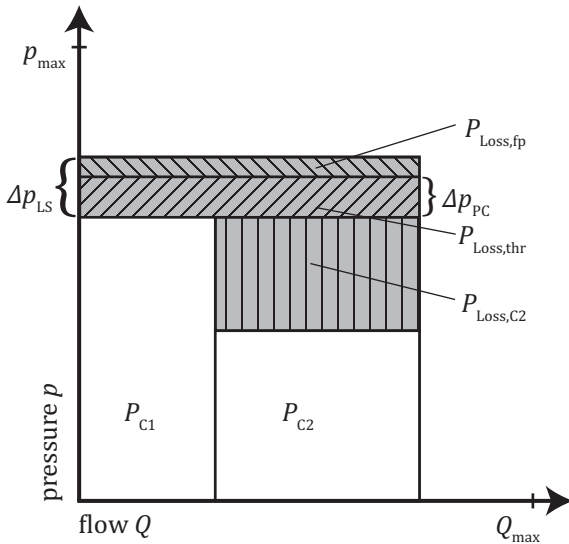


Figure 2: power losses of Load-Sensing systems

The throttling losses are made up by line resistances and pressure drops over the control edges of the directional control valve and pressure compensator of the consumer with the highest load. These losses are inherent in valve controlled hydraulic systems. In contrast, the functional principal losses may be omitted by changing from a pressure controlled system to a flow controlled system.

Another drawback of Load-Sensing systems is their poor cold start performance, also related to the signal lines and the hydraulic-mechanical controllers, a deficit that also becomes obsolete with the proposed flow-on-demand control.

## 2.2 Flow-On-Demand Principle

The basic idea behind the flow-on-demand principle is to calculate the required oil flow through the consumer velocity inputs of the electronic joysticks or by reading back the valve spool positions with the integrated displacement sensors. The aggregate flow, delivered by an electrohydraulic displacement pump, is to match the single flow demands precisely. The pump pressure settles itself according to the highest load pressure plus the pressure drop over the metering orifice and the inevitable line resistances. In comparison to Load-Sensing systems, a significant reduction of the pressure level may be achieved (see Figure 3). To ensure load independence of the system and accurate flow distribution, individual pressure compensators are installed. For smooth ease of control the pressure compensators are setup to keep a constant pressure drop of 7 bars over the metering orifices [5]. Together with the line resistances, this pressure drop accounts for the power loss margin  $P_{\text{loss,thr}}$  of the flow-on-demand system, which makes up about 30-40 % of the Load-Sensing principle related power losses of comparable LS systems. The decreased pressure level accounts for the saving potential of the power consumption  $P_{\text{sp}}$ . Thus the degree of efficiency is calculated by eq. (5):

$$\eta_{th} = \frac{1}{1 + \frac{\Delta p_{PC}}{p_L}} \quad (5)$$

The losses related to the obligatory throttling of minor loaded consumers (eg.  $P_{\text{Loss,C2}}$ ) remain as weakness of valve controlled systems with shared pump usage, but are yet accepted as displacement controlled systems where each function has a dedicated pump [11] [12] [13] [14] have other drawbacks, especially concerning differential cylinder actuation, partial load situations and control dynamics.

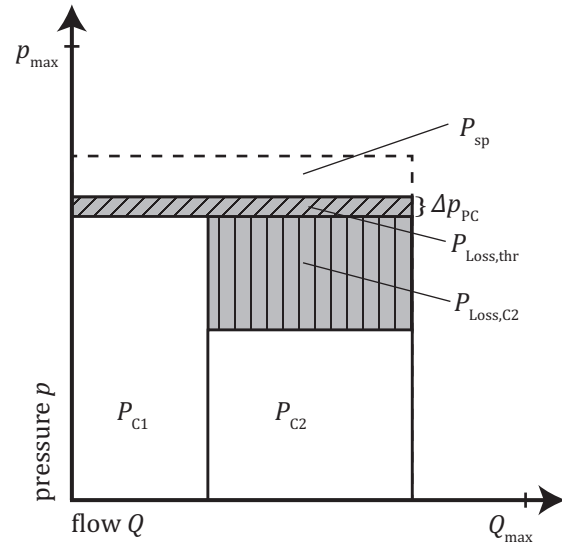


Figure 3: power losses of flow-on-demand system

To compare and to differentiate the proposed flow-on-demand system from related publications and from the current state-of-the-art, a preliminary discussion on terminology of hydraulic systems with direct pump displacement control is necessary. While the described functional principle differs only marginally, a wide variety of designations has been established. As development started in Germany, many expressions are in German language, where attention is to be paid to the marvelous linguistic distinction between ‘Steuerung’ and ‘Regelung’, which translate as ‘open-loop’ and ‘closed-loop’ control. Initial considerations were published by ZÄHE [15] in 1993 under the expression ‘Summenstromregelung’, roughly ‘aggregate flow control’. DJUROVIC [1] refined the issue in 2007 under the proprietary Bosch Rexroth brand name ‘EFM - Electronic Flow Matching’, when suitable electrohydraulic components were finally available. In the same year, FEDDE [2] came up with his interpretation of the subject and named the system ‘Bedarfsstromsteuerung’ which contains the denotation ‘Bedarf’, meaning ‘demand’, for the first time. Following up on DJUROVIC’s work, FINZEL [5] frequently switched between ‘Bedarfsstromregelung’ and ‘Flow Matching’ but finally applied the acronym ‘ELS’ for ‘Electrohydraulic Load-Sensing’. Which he explains with the preserved load-sensing functionality at least in the flow distribution section because the pressure compensators still compare the highest load pressure to the system pressure. In absence of the pressure

dependency of the displacement control in the flow generation section, meaning the position of the swiveling angle of the pump has no pressure related closed-loop control, the denotation ‘ELS’ appears rather confusing. In international publications AXIN [7] and ERIKSSON [6] coined the most suitable phrase ‘Flow Controlled System’, with the latter likewise using ‘Flow Sharing System’ alongside.

Being linked to a single company or implying ambiguities, the authors resign from applying any of the identified expressions from literature and introduce the term ‘flow-on-demand’ control to characterize the presented hydraulic system for a forestry crane application.

As indicated, DJUROVIC laid the basics for following interpretations of flow controlled system. He settled his research on ideas of HESSE [16] and HELDUSER [17] and developed an extensive classification for the design of directly displacement controlled hydraulic systems with multiple consumers per pump. He distinguished systems with open-loop control of the pump flow rate and directly or indirectly closed-loop controlled versions. Furthermore he groups pre- and post-compensated systems. In the assembled matrix, practical solutions are identified and studied in detail. Figure 4 shows the schematic of the previously described, principle Flow Matching application with open-loop flow rate control. The simplified illustration dispenses with representing the consumers. The directional valve is displayed as adjustment meter-in orifice, the return flow is not shown. The system gets along without any sensors and therefore depicts the simplest version of a flow control implementation. Unfortunately, the system shows inadequate behavior during operating states of under- or oversupply, that may occur due to erroneous flow rate aggregation, leakages or operating errors. Analogous to Load-Sensing hydraulics with pre compensators (cf. chap. 2.1), undersupply or rather unforced pump saturation, causes the consumer with the highest load

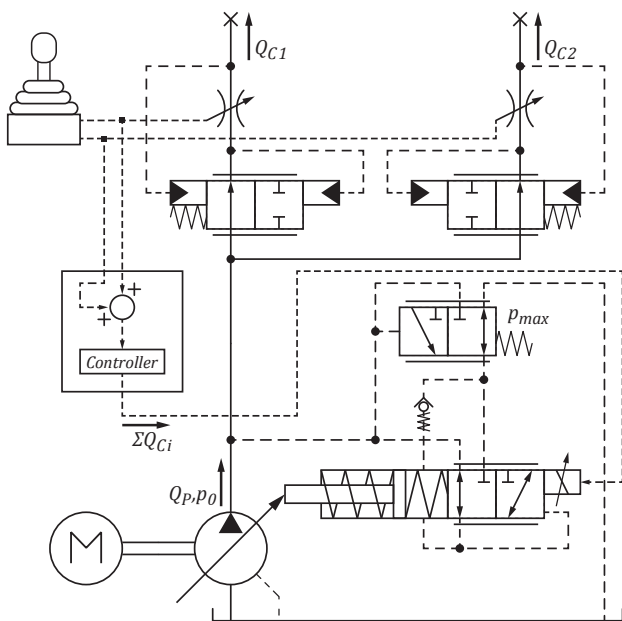


Figure 4: Open-loop control type Electrohydraulic Flow Matching with pre compensator [1]

pressure to slow down or even stop. This behavior may be compensated by the operator. Recognizing the deviation, he will simply increase the velocity target-setting with the joystick. The major drawback arises from situations of flow oversupply. In this case the pressure drop over the metering orifice increases and the pre compensator shuts completely, preventing further consumer movement. The pump pressure increases to its maximum. A simple but energy inefficient workaround is the introduction of an inlet pressure compensator in the valve assembly, operative to bypass excess pump flow to the tank.

To maintain the efficiency advantage and to ensure a well tuned and distributed flow rate, DJUROVIC developed several closed-loop control strategies. A direct flow control is depicted in Figure 5. The introduction of a pump flow rate sensor serves to evade the over- and undersupply issues on the one hand. On the other hand, these sensors are expensive, fragile and generate throttle losses themselves.

Thus, indirectly controlled systems appear to be the better alternative. If the previously mentioned inlet pressure compensator is equipped with a translational sensor, the controlled variable for the pump flow rate is a straight shut compensator. A common disadvantage herewith, is the reintroduction of a hydraulic-mechanical closed-loop controller, entailing the drawbacks of a conventional Load-Sensing system. Another indirect control solution is to fit the individual pre compensators with translational sensors. Inherent to the functional principle, the compensator of the load-leading consumer opens the farthest. Consequently, the controlled variable for the pump flow rate is the completely opened position of the relevant compensator.

As flow controlled systems with conventional pre compensators require additional components and sensors to regulate flow distribution and keep up functionally in case of oversupply, the development of systems with flow sharing post

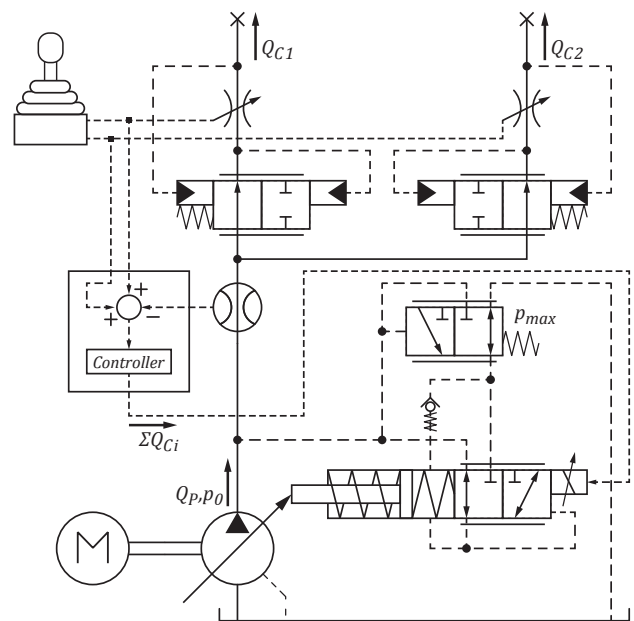


Figure 5: Closed-loop control type Electrohydraulic Flow Matching with pre compensator and flow rate sensor [1]

compensators seems reasonable. Availability of the obligatory electrohydraulic directional valves, let to research on the topic by FINZEL [3] [5]. The corresponding schematic of an exemplary flow controlled hydraulic system with two consumers is shown in Figure 6.

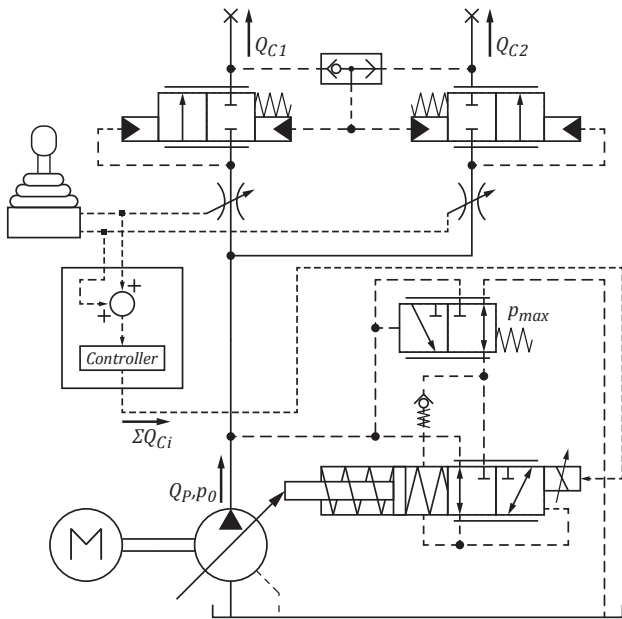


Figure 6: Open-loop control type Electrohydraulic Flow Matching with post compensator [5]

Not at all utilizing any hydraulic signal lines nor any sensors or electronic closed-loop controls, a robust and reliably system is achieved.

### 2.3 Advanced Control Concepts

To further improve the energy efficiency of flow controlled systems, the electronic control unit allows for several advanced control strategies. Without the LS-inherent pressure dependence of the oil flow delivered by the displacement pump, the system may be operated in a state of controlled undersupply. For this undersupply, different operating strategies are conceivable, all affecting control precision but further enhancing efficiency. DJUROVIC resigns from compensating leakages in valves and consumers into the pump flow rate calculation [1]. Generating a rather tad small oil flow the machine operator is to balance out inaccuracies by adjusting his flow demand. As FINZEL deploys post compensators with flow sharing properties, these compensators distribute the entire pump flow relative to the individual valve openings. This gives the control system one extra degree of freedom, that may be used to minimize the pressure drop across the metering orifices. FINZEL suggests to open the orifice of the load-leading consumer completely and to adjust the opening of the remaining orifices according to the demanded flow shares [5]. A similar approach is presented by FEDDE, only that the orifice openings of the minor loaded consumers are derived from a characteristic diagram by means of the pressure differences of the consumers currently in action [2]. AXIN comes up with a similar argumentation but uses the maximum restriction area of the consumer with

the highest momentary flow demand. The other actuators use an increased restriction area in proportion to their flow requests [4]. The potential additional energy savings of those four advanced control concepts are investigated in a dynamic simulation model of the forestry crane (cf. chap. 4).

A novel control concept is being introduced to prevent flow oversupply in case of consumers reaching cylinder end stops. In this case the consumer velocity inputs and the actual consumer oil flows do not match any more. If the aggregate flow of the pump is solely calculated through addition of these consumer velocity inputs, the pump delivers too much oil into the systems, accelerating the residual consumers in an undesirable manner. To overcome the issue, the control valves are equipped with additional pressure transducers and electronic pressure limiting functions. Reaching an end stop, causes the consumer pressure to rise to its preset maximum. In turn the related control valve switches from flow control mode to pressure control mode, ignoring the joystick input and controlling the pressure by reducing the control edge opening. The respective closed-loop control is displayed in Figure 7.

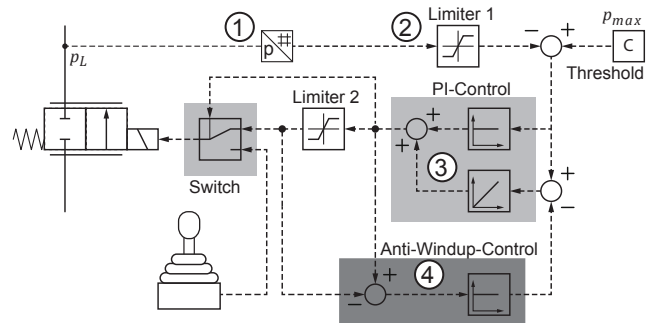


Figure 7: electronic pressure control

The load pressure  $p_L$  behind the valve is measured by a pressure transducer (1) and compared to a threshold. Due to a limiter (2), which sets the minimum value of the load pressure to the threshold, the comparator just passes a signal unequal to zero if the pressure is above the threshold. In this case, the error is conducted to a proportional-integral (PI) control. This provides accurateness for the maximum pressure values. The value behind this control switches, once it has reached a threshold, the command of the valve from the user to the pressure-control of the valve (3). Another limiter restricts the signal of the proportional-integral control, so the valve closes if the maximum pressure is reached. Due to the fact, that the valve is not constantly following the values of the PI-control, the stability of the system requires an anti-windup control (4). The anti-windup control subtracts the difference of the values before and after the limiter from the value leading to the integral part of the PI-control. Through the feedback of the anti-windup control, the value of the integral part of the PI-control will not grow through the limitation. To calculate the aggregate pump oil flow, no longer the velocity input is utilized but the flow corresponding with the valve spool position.

A further issue is the poor damping characteristic of a standard meter-out orifice, being firstly addressed by AXIN [8].

Especially concerning dragging loads, unwanted aftereffects may occur. As elaborated orifice design is the decisive factor, but not being detailed in the simulation models, the authors have included an innovative directional valve into the hydraulic test bench layout (cf. chap. 5). The concerned device has a segmented valve spool, which allows for independent activation of the control edges  $P-A$  from  $B-T$ , respective  $P-B$  from  $A-T$ . The flow rate is calculated according to the meter-in orifice position, which is related directly to the desired consumer velocity. To avoid too fast consumer movement induced by dragging loads, the meter-out orifice may be used to throttle the outlet flow appropriately. Therefore the valve is equipped with two integrated pressure transducers. A closed-loop control shuts the meter-out orifice as narrow that negative pressure and thus cavitation on the inlet side are prevented.

### 3 Reference Application

Loading cranes represent one of the most delicate applications in mobile hydraulics, as they call for fast and precise response on operator inputs. On this account, as reference basis for the flow-on-demand control, a forestry crane with conventional hydraulic-mechanical Load-Sensing system with pre compensators is selected. Being state-of-the-art, these hydraulic systems however suffer from the known disadvantages (cf. chap. 2.1). Especially crane movement anticipation and positioning precision are difficult when a state of pump saturation ends abruptly because a consumer

with high flow rate is stopped and another consumer simultaneously being fine positioned, gets a flow peak as reaction.

The selected reference application, the feeder crane of a mobile log debarker (see Figure 9) is equipped with measurement technology to record hydraulic pressures and flow rates as well as cylinder strokes and velocities. The measurement results are used to parametrize and validate the LS simulation model (cf. chap. 4), consisting of five main consumers, namely crane slewing, boom- and bucket cylinders, gripper and associated rotation unit. The consumers are divided into two decoupled hydraulic circuits with variable displacement pumps being powered by a diesel engine. Additionally the machine has several auxiliary consumers, e.g. the telescopic arm and the hydraulic outriggers, not taken into account for the derived characteristic duty cycle (see Figure 8). The crane starts in position 1, grips the log a first time in position 2 and places it in position 3. Being gripped a second time in position 4, the log is fed to the debarker from position 5 on. The log is released, leaving the crane in its initial position 1, ready for the next cycle. The specific consumer movements, namely cylinder strokes and rotation angle, are displayed in Figure 10. The corresponding consumer loads are illustrated in Figure 11. For better appreciation, the numbers (1 - 2 - 3 - 4 - 5 - 1) in those two figures indicate the slewing position of the crane, analogue to Figure 8.

Selected by availability and moreover its high workload and daily hours of service, the sample application represents

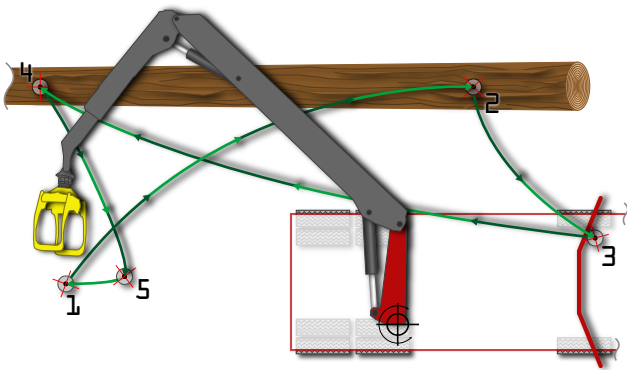


Figure 8: characteristic forestry crane duty cycle



Figure 9: reference application - feeder crane of a mobile log debarker

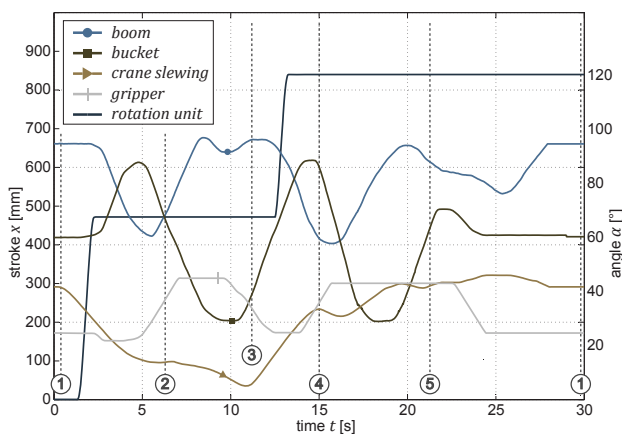


Figure 10: duty cycle - consumer movements

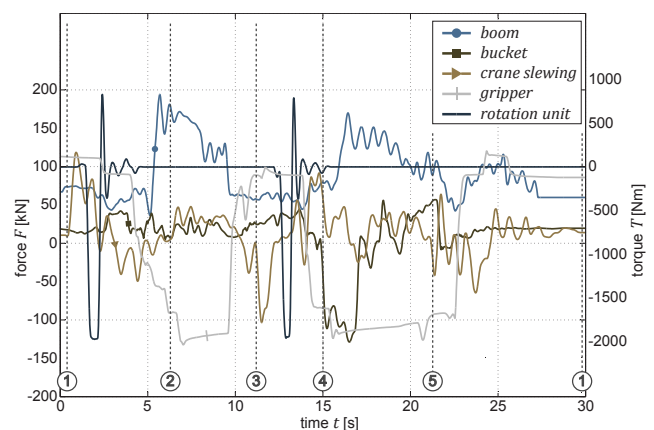


Figure 11: duty cycle - consumer loads

other forestry crane applications with similar duty cycles like timber transporters, forwarders and wood chippers, implicating potential energy savings in the same range, at least concerning their cranes. The duty cycle of a timber transporter crane is exactly the same, also having two pick-up points and two release points, only that the overall workload is wane due to major driving shares in the complete duty cycle of the transporter. Apart from usually only gripping a log once, duty cycles of forwarder and wood chipper cranes also correspond, despite the latter frequently using its telescopic arm to feed the chipper.

#### 4 Dynamic Simulation

Simulation software is applied to develop suitable flow-on-demand concepts for the selected forestry crane application. The energy saving potentials are determined via dynamic simulation to evaluate whether the concepts are able to maintain the required performance. A dual circuit system with two hydraulic pumps and five actuators represents the main functions of the forestry crane (cf. chap 3). In the first instance the real Load-Sensing reference application is re-modeled in the simulation environment. Followed by the

build-up of the simulation model of the flow-on-demand concept crane. To assure comparable simulation outcomes, the directional control valves of both systems are equally parametrized with the data of a series proportional valve with downstream pressure compensators and CAN communication, intended to be used in the latter prototype.

Comparing the flow-on-demand system to the LS reference, the simulation results reveal promising efficiency improvements. Figure 12 depicts the pressure histories of the two hydraulic pumps, clearly showing the pressure level of the flow-on-demand system lying always at least 10 bars beneath the LS-pump pressure. Analogous, the flow rate histories over the characteristic duty cycle are displayed in Figure 13. The flow rate margin between the two systems has a smaller magnitude than the pressure differences, but is anyhow existent. The reason is, LS systems require a small but constant signal oil flow that is bled off to the reservoir. The fact, that LS systems keep up the pressure difference  $\Delta p_{LS}$  even in idle duty cycle states, further decreases their energy efficiency. Contrary, in Flow-on-demand systems, the pressure drops to the minimum pump pressure in those situations. Additionally, the swiveling angle of the pump retreats to its minimum position. Figure 14 and Figure 15

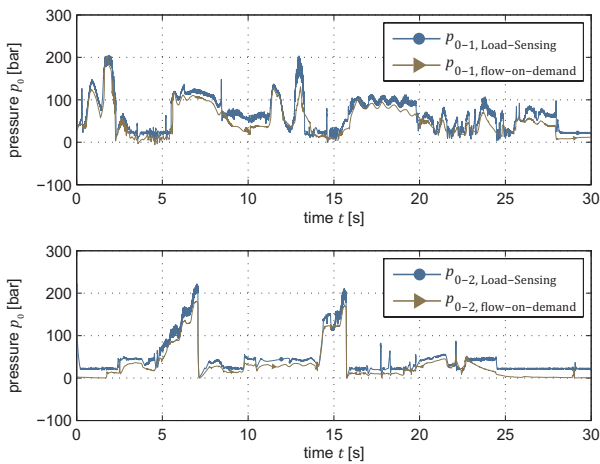


Figure 12: pressure history over duty cycle

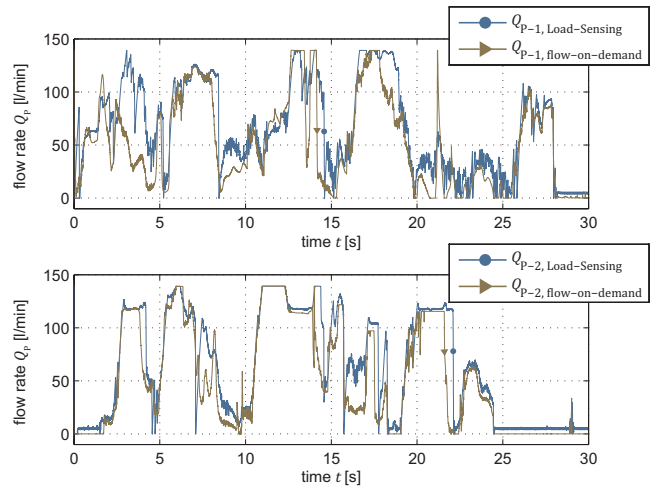


Figure 13: flow rate history over duty cycle

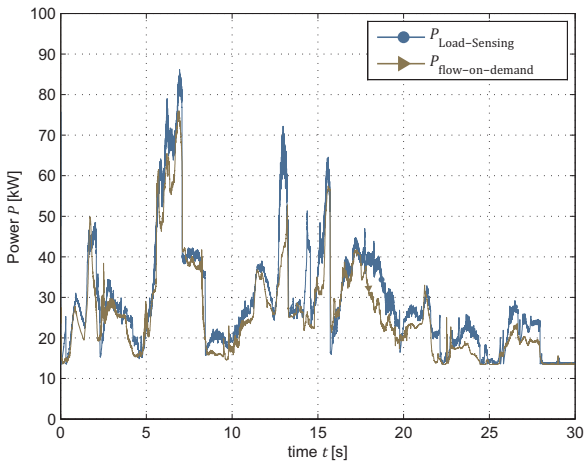


Figure 14: power consumption over duty cycle

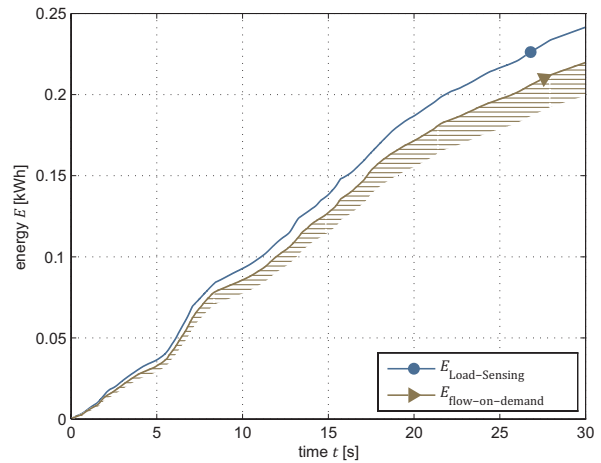


Figure 15: energy demand over duty cycle

indicate the power consumption and energy demand of the entire system, calculated by eq. (6) and eq. (7):

$$P_{mech} = \frac{1}{\eta_{hm} \cdot \eta_{vol}} \cdot P_{hyd} = \frac{1}{\eta_{hm} \cdot \eta_{vol}} \cdot p_0 \cdot Q_p \quad (6)$$

$$E_{mech} = \int P_{mech} dt \quad (7)$$

The hatching in Figure 15 represents further decreased energy demand by applying the advanced control concepts, introduced in chapter 2.3. Related simulation outputs show energy saving potentials of 8 to 15 percent, depending on the regarded concept.

## 5 Hydraulic Test Bench

The operator in the simulation models is represented by a PI-controller. Apart from monitoring, that actuators are able to follow their theoretical path target, no qualitative feedback on system performance is given. Furthermore, not every single effect may be reproduced by simulation. Those arguments call for a hydraulic test bench. Especially the artificial undersupply may bear a trade-off between energy efficiency and system performance which has to be evaluated on a real system rather than in a simulation environment.

The layout of the hydraulic test stand (see Figure 16), being installed at the testing facilities of the Chair of Mobile Machines, includes an electrohydraulic displacement pump and three hydraulic consumers. Namely two differential cylinders (2) and (3) and a pressure adjustment orifice in bridge connection (1). The latter is used to represent loads of hydraulic motors. The bridge of four check valves enables flow reversion. The pressure adjustment orifices in the return flow lines of consumer (2) likewise represent hydraulic loads corresponding to external forces. Consumer (3) drives a mass mounted on a sled. To enable imprinting of dragging loads, consumer (2) and (3) may be coupled. The valve discs have pressure transducers integrated into their actuation units. Hence the presented electronic pressure limitation functions (cf. chap. 2.3) are easily implemented. A unique feature is included with the directional valve of consumer (3) as it has a segmented valve spool. Besides realization of a floating position, eventually occurring aftereffects concerning dragging loads may be addressed by controlling the meter-out orifice independently.

This setup allows for careful fine tuning and profound testing of the developed flow-on-demand control. Moreover the dynamic performance of the advanced control concepts, evolved from simulation, may be validated on the real system.

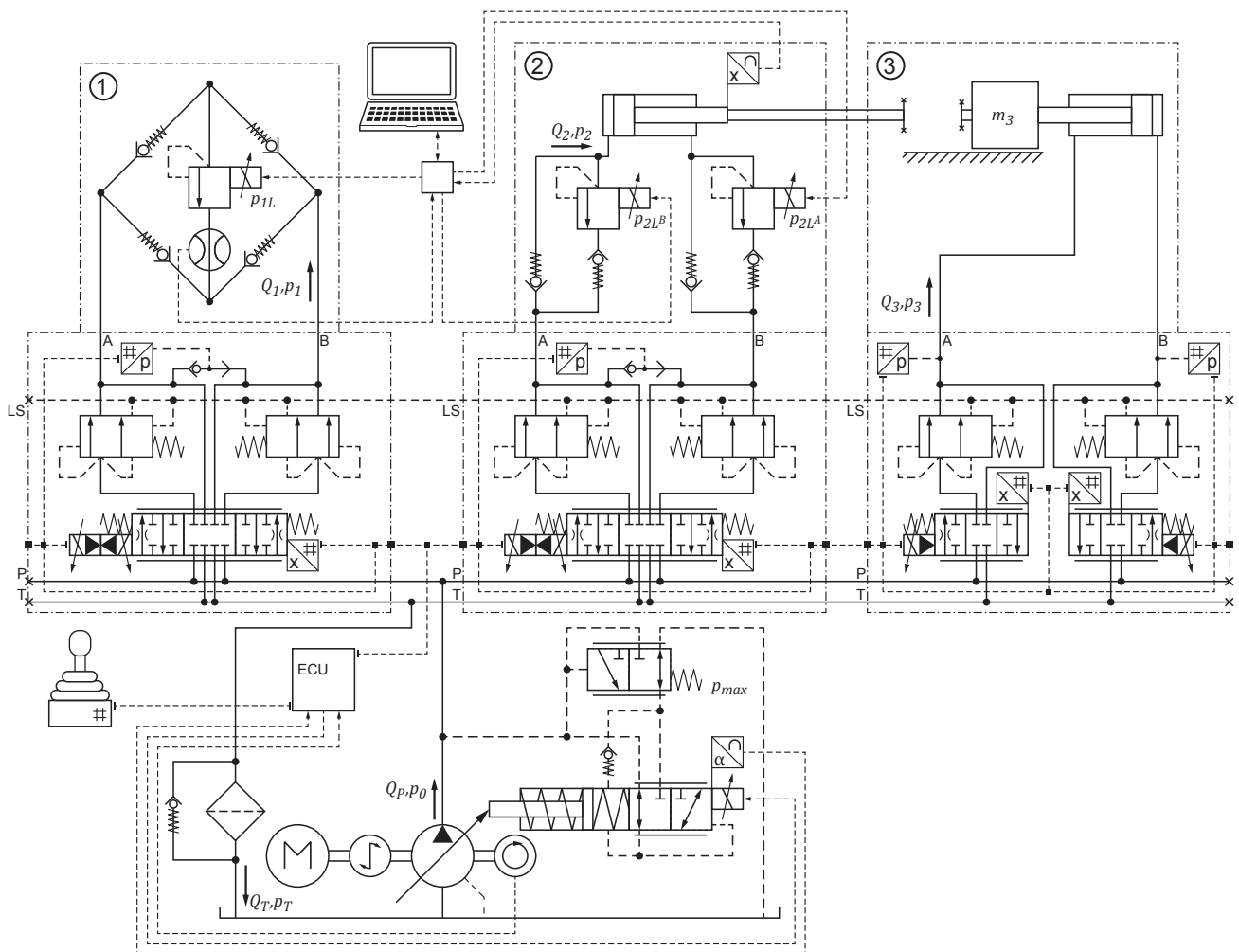


Figure 16: Flow-on-demand control hydraulic test bench layout

## 6 Outlook

Flow-on-demand hydraulic systems offer the prospect of a sustainable reduction of energy demand and fuel consumption. In the course of the presented project a prototype will be build up to verify the potential. At large further enhancements and functional combinations are thinkable and call for future research.

### 6.1 Forestry Crane Prototype

The reference machine is equipped with the related electrohydraulic components and control unit to complete intensive field tests of the flow-on-demand concept. Comparison to the Load-Sensing measurements will reveal its true energy savings. The machine operators shall evaluate the improved operability in terms of oscillation avoidance, cold start performance and maneuverability. The prototype serves as demonstration object for forestry machine manufacturers and will lead the path for the introduction of electrohydraulics into an anyway innovation friendly branch of industry.

### 6.2 Recuperation

The breakup of the flow dependence between consumers and displacement pump allows for a facile integration of recovery units for potential energy. Furthermore the pump may be used to charge hydraulic accumulators in otherwise idle states or partial load situations.

## 7 Acknowledgments

The presented research is funded by the Deutsche Bundesstiftung Umwelt (DBU) with the goal to improve the energy efficiency of forestry machinery. The authors are pleased to thank for the endorsement of the project and the cooperation. The hydraulic simulation software DSHplus is provided by the company Fluidon GmbH free of charge. A communication interface for the Software-in-the-Loop development of the ECU is provided by the company Vector Informatik GmbH. The components for the hydraulic load equipment of the test bench are donated by HAWE Hydraulik SE. Special thanks are directed to Bucher Hydraulics GmbH for the support on the valve block, which is the key feature of the presented flow-on-demand hydraulic system.

## Nomenclature

Designation	Denotation	Unit
$A_0$	restriction area	[mm <sup>2</sup> ]
$A, B$	consumer port	-
$\alpha_D$	flow coefficient	-
$C$	consumer	-
CAN	Controller Area Network	-
CC	closed center	-
$E$	energy	[Wh]

Designation	Denotation	Unit
ECU	electronic control unit	-
fp	functional principle	-
hm	hydraulic-mechanical	-
$L$	load	-
LS	Load-Sensing (port)	-
$\eta_{th}$	degree of efficiency	-
OC	open center	-
$P$	power	[kW]
$P$	pump (port)	-
$p$	pressure	[bar]
PC	pressure compensator	-
$Q$	flow rate	[l/min]
$\rho$	density	[kg/m <sup>3</sup> ]
sp	saving potential	-
$T$	tank port	-
$th$	theoretical	-
$thr$	throttling	-
vol	volumetric	-

## References

- [1] M Djurovic. *Energiesparende Antriebssysteme für mobile Arbeitsmaschinen „Elektrohydraulisches Flow Matching“*. PhD thesis, Techn. Univ., Dresden, 2007
- [2] T Fedde. *Elektrohydraulische Bedarfsstromsysteme am Beispiel eines Traktors*. PhD thesis, Techn. Univ., Braunschweig, 2007
- [3] R Finzel. and S Helduser. *Energy-Efficient Electro-Hydraulic Control Systems for Mobile Machinery / Flow Matching*. Proc. of 6<sup>th</sup> International Fluid Power Conference, Dresden, 2008
- [4] M Axin, B Eriksson and J-O Palmberg. *Energy Efficient Load Adapting System without Load Sensing - Design and Evaluation*. Proc. of the 11<sup>th</sup> Scandinavian International Conference on Fluid Power, Linköping, 2009
- [5] R Finzel. *Elektrohydraulische Steuerungssysteme für mobile Arbeitsmaschinen*. PhD thesis, Techn. Univ., Dresden, 2010
- [6] B Eriksson and J-O Palmberg. *How to Handle Auxiliary Functions in Energy Efficient, Single Pump, Flow Sharing Mobile Systems*. Proc. of 7<sup>th</sup> International Fluid Power Conference, Aachen, 2010
- [7] M Axin, B Eriksson, J-O Palmberg and P Krus. *Dynamic Analysis of Single Pump, Flow Controlled Mobile Systems*. Proc. of the 12<sup>th</sup> Scandinavian International Conference on Fluid Power, Tampere, 2011

- [8] M Axin, J-O Palmberg and P Krus. *Optimized Damping in Cylinder Drives Using the Meter-out Orifice - Design and Experimental Verification*. Proc. of 8<sup>th</sup> International Fluid Power Conference, Dresden, 2012
- [9] US3866419. *Integrated Pressure Compensated Load Sensing System*. Parker-Hannifin Corp. United States Patent, 1975
- [10] K Steindorff. *Untersuchungen zur Energierückgewinnung am Beispiel eines ventilgesteuerten hydraulischen Antriebs*. PhD thesis, Techn. Univ., Braunschweig, 2010
- [11] R Rahmfeld. *Development and Control of Energy Saving Hydraulic Servo Drives for Mobile Systems*. Fortschr.-Ber. VDI Reihe 12 Nr. 527. Düsseldorf: VDI Verlag, 2002
- [12] R Rahmfeld, M Ivantysynova and J Weber. *Displacement Controlled Wheel Loader – a simple and clever Solution*. Proc. of 4<sup>th</sup> International Fluid Power Conference, Dresden, 2004
- [13] K Heybroek, J-O Palmberg, J Lillemets, M Lugnborg and M Ousbäck. *Evaluating a Pump Controlled Open Circuit Solution*. Proc. of 51<sup>st</sup> National Conference on Fluid Power, Las Vegas, NV, 2008
- [14] D Peitsmeyer. *Elektrifizierung der Arbeitsausrüstung mit Zylinderantrieben*. Proc. of 7. Kolloquium Mobilhydraulik, Karlsruhe, 2012
- [15] B Zähe. *Energiesparende Schaltungen hydraulischer Antriebe mit veränderlichem Versorgungsdruck und ihre Regelung*. PhD thesis, RWTH Aachen, 1993
- [16] DE 103 42 037 A1. *Steueranordnung und Verfahren zur Druckmittelversorgung von zumindest 2 hydraulischen Verbrauchern*. German Patent, 2003
- [17] M Djurovic, S Helduser and G Keuper. *Neue Lösungen zum elektrohydraulischen Load-Sensing*. Proc. of 4<sup>th</sup> International Fluid Power Conference, Dresden, 2004

# **Novel Energy-Saving Steer-by-Wire System for Articulated Steering Vehicles: A Compact Wheel Loader Case Study**

Naseem Daher, Chuang Wang, and Monika Ivantysynova

School of Mechanical Engineering, Purdue University, West Lafayette, Indiana, USA  
Email: [ndahe@purdue.edu](mailto:ndahe@purdue.edu), [wang1310@purdue.edu](mailto:wang1310@purdue.edu), [mivantys@purdue.edu](mailto:mivantys@purdue.edu)

## **Abstract**

Improving energy efficiency remains a priority in the industrial and academic communities given the ever increasing demand on fossil fuels and their skyrocketing prices. Pump displacement controlled (DC) actuation is an energy efficient alternative to traditional valve controlled actuation. The technology has shown significant fuel savings on mobile machinery when applied to the working hydraulics (implement) functions of such machines. However, DC actuation has never been investigated for use on mobile machinery chassis systems, namely power steering. In this paper and for the first time, a novel closed-circuit pump DC system architecture is devised to perform the power steering system function of a compact wheel loader. A dynamic model of the new system was generated to corroborate concept feasibility, perform system sizing and analysis, and predict performance during standard steering maneuvers. Simulation results showed that a DC power steering system is a feasible, promising, and challenging alternative, which upon further research and development will be brought to life and tested on a prototype machine.

**Keywords:** displacement control, articulated steering, power steering, dynamic modeling

## **1 Introduction**

Demand for power steering originated from the need for providing assistance to operators in achieving their heading directions, especially as transportation vehicles grew in size and mass. While the main requirements of primitive systems were simply adequate assistance levels and acceptable controllability, today's requirements are more stringent. Given the increased awareness and attention paid to energy efficiency, productivity, and safety, researching alternative technologies is underway. Present-day power steering systems include hydraulic, electric, and electro-hydraulic architectures, which vary based on their energy source, energy transmission, and energy management schemes. Hydraulic power steering is plagued with poor energy efficiency mainly due to throttling losses associated with hydraulic control valves. Electric power steering systems offer better energy efficiency with on-demand power supply and result in improved packaging constraints, but suffer from power limitations at larger vehicle segments. State-of-the-art electrohydraulic steering systems take advantage of the high power density and efficiency of fluid power, but use electronically controlled valves that still suffer from energy inefficiency.

This paper introduces a novel electrohydraulic steer-by-wire steering system and uses a compact wheel loader as a case study. The paper details the high-fidelity co-simulation plant model consisting of a coupled hydraulics and dynamics modules. The new system utilizes a proven energy-saving technology, Displacement Control (DC) developed by

Rahmfeld and Ivantysynova (1998), which eliminates hydraulic control valves throttling losses by directly controlling the pump displacement instead.

## **2 Displacement Control Power Steering**

Displacement Control (DC) steering can be classified under electro-hydrostatic power steering, where the steering wheel torque / angle and vehicle speed are sensed and fed back to a controller that adjusts the displacement of a variable displacement pump as opposed to controlling a proportional valve. Figure 1 is provided for identification of components in the proposed circuitry. The actuator (8) velocity is controlled by adjusting the pump (2) speed, displacement, or both. The pump input/output ports are connected to the piston/rod sides of the actuator. The differential fluid flow between the actuator's uneven sides is overcome by means of pilot-operated check valves (6), which keep the low pressure side of the actuator connected to a low pressure source that can either provide or absorb flow to balance the unequal cylinder flow. The low pressure source has its own fixed displacement charge pump (4), driven by the same prime mover (1), providing continuous flow to the cylinder's low pressure side and the pump control system. The low pressure level setting is adjusted via a pressure relief valve (5). An accumulator (not shown) could be used in order to provide high flow rate spikes when sudden high speed cylinder movements are incurred, if the charge pump flow is not sufficient. The system is protected from over-pressurization by means of pressure relief valves (7) installed on both sides of the actuator.

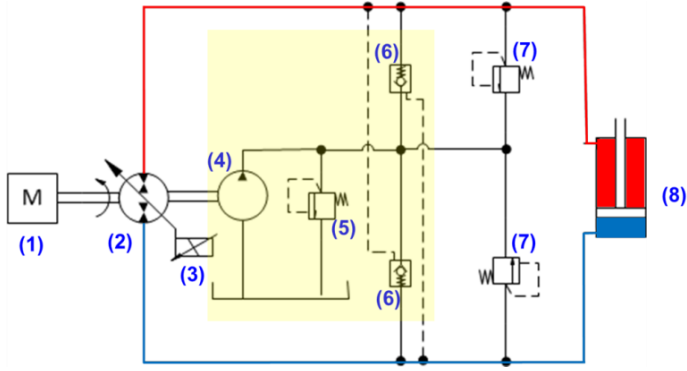


Figure 1: DC Steering Hydraulic Schematic

The pump control system (3), which is detailed in fig. 2, uses a single stage proportional control valve that meters flow to a double rod actuator connected to the pump swash plate. The actuator linear displacement determines the angular position of the swash plate, and therefore the instantaneous pump displacement volume per revolution.

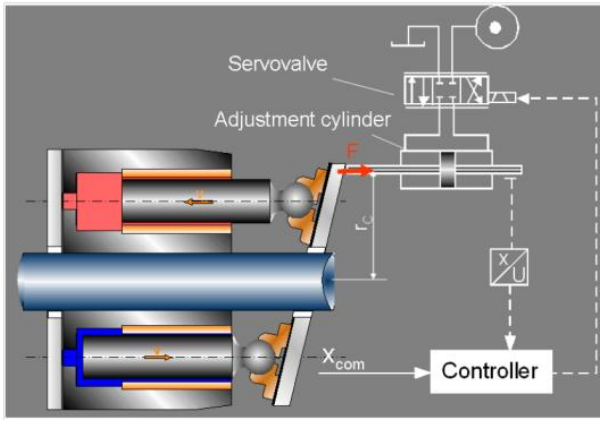


Figure 2: Pump Swash Plate Control System

### 3 System Modeling

In this section, a detailed dynamic model of the DC steering system plant is described. The system level model is composed of two main building blocks: a hydraulics module and a mechanics one. Figure 3 shows a top-level block diagram of the system model structure and setup. The hydraulics module delivers the required flow rates to induce motion in the linear actuators, which translates into vehicle articulation. The pressure levels in the actuator sides are determined by the load computed within the mechanics module mainly due to the opposing loads generated at the ground-tire interface.

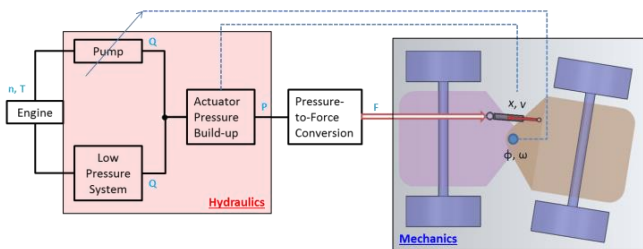


Figure 3: Block Diagram of DC Steering System Model

### 3.1 Hydraulics Subsystem Model

The hydraulics module includes a variable displacement pump / motor unit modeled with its associated volumetric and torque losses, transmission line losses, a pump control system, a low pressure source system, and a pressure-flow model to determine pressure build-up inside the actuator.

#### 3.1.1 Variable Displacement Pump/Motor Model

The variable displacement axial piston machine is modeled with careful consideration to volumetric and torque losses incurred throughout the entire pump operating range. First, the derived (actual) pump displacement volume is determined using the Toet method. Second, steady-state measurements are recorded at various speeds, displacements, and pressures at constant inlet temperature. The measured data is then fitted to a 3<sup>rd</sup> degree polynomial to generate the proper loss coefficients as functions of operating conditions. Following are the governing equations that were used to generate the pump model, provided in *pumping* mode operation.

$$Q_e = \beta V_d n - Q_s \quad (1)$$

where  $Q_e$  is the effective pump flow rate,  $\beta$  is the normalized pump swash plate angle,  $V_d$  is the derived pump displacement volume,  $n$  is the pump speed, and  $Q_s$  is the volumetric loss flow rate given by eq. (2).

$$Q_s(V_d, n, \Delta p)_{T=const.} = \sum_{i_1=0}^{I_1} \sum_{i_2=0}^{I_2} \sum_{i_3=0}^{I_3} K_Q(i_1, i_2, i_3) \cdot V_d^{i_1} \cdot n^{i_2} \cdot \Delta p^{i_3} \quad (2)$$

The pump effective torque,  $T_e$ , is given by eq. (3):

$$T_e = \beta V_d \Delta p + T_s \quad (3)$$

where  $\Delta p$  is the pressure differential across the pump ports, and  $T_s$  is the torque loss given by eq. (4).

$$T_s(V_d, n, \Delta p)_{T=const.} = \sum_{i_1=0}^{I_1} \sum_{i_2=0}^{I_2} \sum_{i_3=0}^{I_3} K_T(i_1, i_2, i_3) \cdot V_d^{i_1} \cdot n^{i_2} \cdot \Delta p^{i_3} \quad (4)$$

The derived pump displacement volume obtained via the Toet method is given in eq. (5).

$$V_d = \frac{1}{n} \cdot \frac{\sum_{j=1}^k Q_{ej} \cdot \sum_{j=1}^k \Delta p_j^2 - \sum_{j=1}^k \Delta p_j \cdot \sum_{j=1}^k \Delta p_j \cdot Q_{ej}}{k \cdot \sum_{j=1}^k \Delta p_j^2 - \left( \sum_{j=1}^k \Delta p_j \right)^2} \quad (5)$$

#### 3.1.2 Pressure-Flow Equations

The pressure build-up inside the actuator chambers is determined from the conservation of mass principle, which leads to the pressure being a function of the sum of flow

rates entering / leaving the chambers multiplied by the reciprocal of the control volumes hydraulic capacitance. In the following equations, the zero-position is assumed to be at mid-stroke, and the actuator displacement / velocity are positive during the compression stroke (fig. 4).

$$p_A = \frac{1}{C_{HA}} \int \left( Q_A + A_A \cdot \dot{x} - Q_{Li} - Q_r \right) dt \quad (6)$$

where  $p_A$  is the piston (A) side pressure,  $C_{HA}$  is control volume A hydraulic capacitance,  $Q_A$  is the net flow entering the piston chamber,  $A_A$  is the piston side area,  $\dot{x}$  is the actuator velocity,  $Q_{Li}$  is the internal leakage flow across the actuator chambers, and  $Q_r$  is the relief valve flow rate.

$$C_{HA} = \frac{1}{K} \left\{ \left( \frac{H}{2} - x \right) A_A + V_{dead} + V_{LA} \right\} \quad (7)$$

Where  $K$  is the fluid bulk modulus,  $H$  is the total actuator stroke,  $x$  is the actuator position,  $V_{dead}$  is the dead volume inside the actuator, and  $V_{LA}$  is the transmission line A volume.

Similarly, the pressure on side B (rod) is determined via eq. (8) and eq. (9).

$$p_B = \frac{1}{C_{HB}} \int \left( -Q_B - A_B \cdot \dot{x} + Q_{Li} - Q_r \right) dt \quad (8)$$

$$C_{HB} = \frac{1}{K} \left\{ \left( \frac{H}{2} + x \right) A_B + V_{dead} + V_{LB} \right\} \quad (9)$$

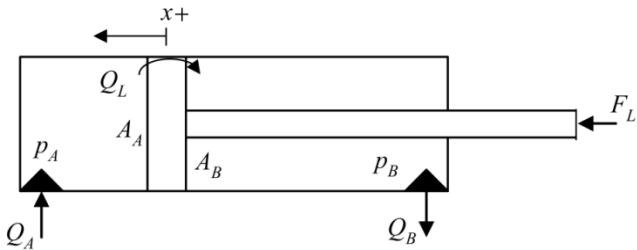


Figure 4: Actuator Pressure-Flow Diagram

### 3.1.3 Actuator Friction Model

The sliding friction behavior between the actuator's rod and cylinder housing is modeled based on the Stribeck curve regime, which accounts for static friction, coulomb friction, and viscous friction effects.

$$F_R(\dot{x}) = d_v \dot{x} + \text{sign}(\dot{x}) \left( F_C + F_H e^{\frac{-|\dot{x}|}{\tau_H}} \right) \quad (10)$$

where  $F_R$  is the resultant friction force,  $d_v$  is the viscous friction coefficient,  $F_C$  is the Coulomb friction force,  $F_H$  is the static friction force, and  $\tau_H$  is the static friction force constant. A sample plot of the actuator friction force is shown in fig. 5.

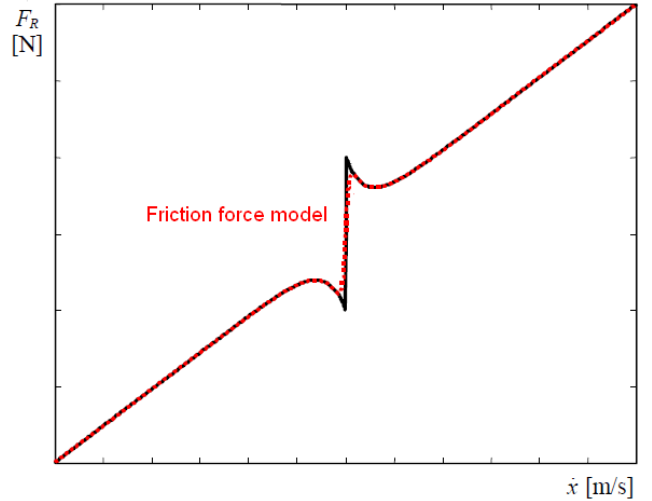


Figure 5: Actuator Stribeck Friction Curve

### 3.1.4 Transmission Line Losses

Transmission line losses are derived from the Navier-Stokes equations by balancing the pressure forces against the viscous forces. Given that the lines configuration and fluid viscosity are virtually constant, the pressure drop in the transmission lines,  $\Delta p_L$ , could be determined by multiplying the effective flow rate by a constant gain per eq. (11).

$$\Delta p_L = \frac{8\mu l_L v}{R_L^2} = \left[ \frac{8\mu l_L}{A_L R_L^2} \right] \cdot Q_e \quad (11)$$

where  $\mu$  is the fluid dynamic viscosity,  $v$  is the fluid kinematic viscosity, and  $l_L$ ,  $R_L$ , and  $A_L$  are the transmission line length, radius, and area respectively.

### 3.1.5 Low Pressure System

The low pressure system consists of a fixed positive displacement charge pump, two pressure relief valves, and two pilot-operated check valves (POCV) shown in fig. 6.

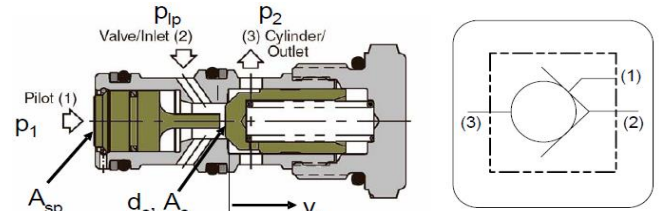


Figure 6: Pilot-Operated Check Valve

The POCV is modeled using a force balance on the pilot spool, which determines both its displacement,  $y_c$ , as well as the mode of operation i.e. normal flow versus reverse flow.

Normal Flow Direction:

$$y_c = \frac{1}{k_0} \left[ A_c (p_{LP} - p_2) - F_{k0} \right] \quad (12)$$

Reverse Flow Direction:

$$y_c = \frac{1}{k_0} \left[ A_{sp}(p_1 - p_{LP}) + A_c(p_{LP} - p_2) - F_{k0} \right] \quad (13)$$

The resulting POCV flow is given by eq. (14).

$$Q_c = \alpha_D \sqrt{\pi A_c} 2y_c \text{sign}(\Delta p) \sqrt{\frac{2}{\rho} |\Delta p|} \quad (14)$$

$$\Delta p = p_{1/2} - p_{LP} \quad (15)$$

where  $A_c$  is the cone orifice area,  $p_{LP}$  is the pressurized low pressure,  $p_1$  is the pilot pressure,  $p_2$  is the cylinder / outlet pressure,  $F_{K0}$  is the spring pre-load force,  $k_0$  is the spring rate,  $A_{sp}$  is the spool area, and  $\alpha_D$  is the discharge coefficient.

### 3.1.6 Pump Control System

The dynamics of the pump control system responsible for adjusting the swash plate angle are dominated by the servovalve dynamics, which are modeled as a linear second order transfer function from the commanded input voltage signal,  $u_{SV}$ , to the output spool position,  $y_{SV}$ , per eq. (16).

$$\frac{Y_{SV}(s)}{U_{SV}(s)} = \frac{\omega_{SV}^2}{s^2 + 2\zeta_{SV}\omega_{SV}s + \omega_{SV}^2} \quad (16)$$

where  $\omega_{SV}$  is the servovalve natural frequency and  $\zeta_{SV}$  is the valve's damping ratio.

## 3.2 Mechanics Module

Two separate mechanics modules were generated to allow for performing simulations of two types of common wheel loader maneuvers. The first model is a 1-DOF model where the loader articulates while stationary, simulating a truck loading cycle where the load is transferred from one side to the other. The second model is a 3-DOF model where the loader articulates as it travels, simulating transferring a load at a work site.

### 3.2.1 1-DOF Dynamic Model

The wheel loader was modeled as two sub-frames connected in the center at the articulation (revolute) joint. For simplicity, the rear sub-frame was fixed to the ground and only the front sub-frame was allowed to rotate, resulting in 1-DOF motion. The linear actuator was modeled as two rigid bodies, rod and cylinder, moving relative to one another along an axial (prismatic) joint. The hydraulic force acts on the rod causing it to translate inside the cylinder, which induces rotational motion of the sub-frame about the articulation (revolute) joint. The rotational motion is a result of the balance of moments about the articulation joint (fig. 7) given in eq. (17).

$$F_{str} * r_j - N_f * \mu_{tf} * \frac{wb}{2} - (d_{AJ} + d_{Tire\_Lat}) * \omega_f = I_f \dot{\omega}_f \quad (17)$$

where  $F_{str}$  is the steering force,  $r_j$  is the normal distance between the articulation joint and the steering actuator force

line of action,  $N_f$  is the front axle normal load,  $wb$  is the vehicle wheelbase,  $\mu_{tf}$  is the friction coefficient between the tire and the ground,  $d_{AJ}$  is the articulation joint damping coefficient,  $d_{Tire\_Lat}$  is the tires lateral damping coefficient,  $\omega_f$  is the front sub-frame articulation angle rate, and  $I_f$  is the front sub-frame moment of inertia.

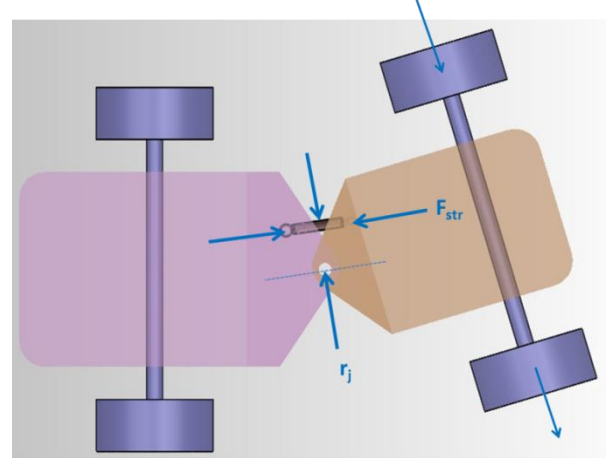


Figure 7: 1-DOF Dynamic Model

### 3.2.2 3-DOF Dynamic Model

The 1-DOF model only allows for simulating static steering maneuvers. In order to simulate a moving vehicle, a multi-DOF model is then required. However, making changes to the steering system of any moving vehicle requires a deep understanding of the vehicle dynamics aspect. The mechanics module primarily consists of a 3-DOF vehicle dynamics model based on the Lagrangian equation. The Lagrangian approach was adopted due to the complexity of forces and constraints associated with articulated vehicles, where the Newtonian approach is strenuous to apply given the vectorial nature and continuous variation of the forces and accelerations at hand.

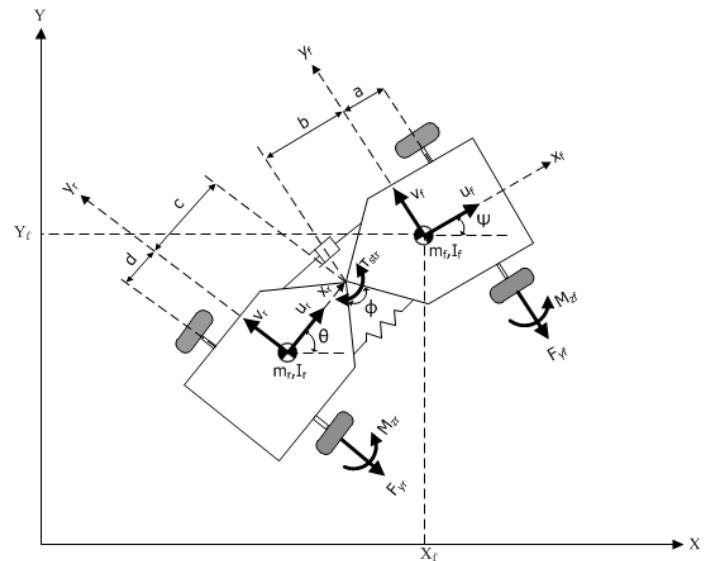


Figure 8: Articulated Vehicle Dynamics

The standard form of the Lagrange equation is given in eq. (18) below:

$$\frac{d}{dt} \left( \frac{\partial L}{\partial \dot{q}_i} \right) - \frac{\partial L}{\partial q_i} + \frac{\partial D}{\partial \dot{q}_i} = Q_i \quad (18)$$

where  $L$  is the Lagrangian function (defined as kinetic energy,  $T$ , minus potential energy,  $V$ ),  $q$  is the set of generalized coordinates,  $D$  is the dissipative function, and  $Q_i$  is the set of generalized forces and moments. The kinetic energy includes the translational and rotational motions of two constrained sub-frames as shown in eq. (19). The potential energy and dissipative function are functions of the (equivalent) torsional spring and damping constants, and the articulation angle / rate as shown in eq. (20) and eq. (22).

$$T = \frac{1}{2} m_f (\dot{X}_f^2 + \dot{Y}_f^2) + \frac{1}{2} I_f \dot{\psi}^2 + \dots \quad (19)$$

$$\frac{1}{2} m_r (\dot{X}_r^2 + \dot{Y}_r^2) + \frac{1}{2} I_r \dot{\theta}^2$$

$$V = \frac{1}{2} K_{aj} (\psi - \theta)^2 \quad (20)$$

$$L = T - V \quad (21)$$

$$D = \frac{1}{2} C_{aj} (\dot{\psi} - \dot{\theta})^2 \quad (22)$$

Given the constraint imposed by the articulation joint, the rear sub-frame motion can be expressed in terms of the front sub-frame motion, yielding the modified kinetic energy expression given by eq. (23).

$$T = \frac{1}{2} m_f (\dot{X}_f^2 + \dot{Y}_f^2) + \frac{1}{2} I_f \dot{\psi}^2 + \dots \quad (23)$$

$$\frac{1}{2} m_r [(\dot{X}_f + b \sin \psi \dot{\psi} + c \sin \theta \dot{\theta})^2 + \dots$$

$$(\dot{Y}_f - b \cos \psi \dot{\psi} - c \cos \theta \dot{\theta})^2] + \frac{1}{2} I_r \dot{\theta}^2$$

The originally selected set of generalized coordinates,  $q$ , consisted of the global  $X$  and  $Y$  coordinates, and the angles,  $\psi$  and  $\theta$ , which the front and rear sub-frames make relative to the global  $X$  abscissa, respectively. However, to allow for performing maneuvers with large deviations from the global axes such as steady-state cornering, and to reduce the order of the system, a coordinate transformation to the local front sub-frame longitudinal and lateral velocities,  $u_f$  and  $v_f$  respectively, is necessary per eq. (24) and eq. (25).

$$u_f = \dot{X}_f \cos \psi + \dot{Y}_f \sin \psi \quad (24)$$

$$v_f = -\dot{X}_f \sin \psi + \dot{Y}_f \cos \psi \quad (25)$$

As a result the Lagrangian equations of the  $X$  and  $Y$  coordinates are replaced with those of  $u_f$  and  $v_f$  respectively.

$$\frac{d}{dt} \frac{\partial T}{\partial u_f} - \frac{\partial T}{\partial v_f} \dot{\psi} = Q_{u_f} \quad (26)$$

$$\frac{d}{dt} \frac{\partial T}{\partial v_f} + \frac{\partial T}{\partial u_f} \dot{\psi} = Q_{v_f} \quad (27)$$

Another substitution that simplifies the system of equations as well as allows for explicitly stating the articulation angle,  $\phi$  (a desired state variable), is to apply eq. (28).

$$\phi = \psi - \theta \quad (28)$$

Consequently, the following set of coordinates was selected:

$$\mathbf{q}(t) = (u_f, v_f, \dot{\psi}, \dot{\phi})^T \quad (29)$$

where  $\dot{\psi}$  is the front yaw angle rate, and  $\dot{\phi}$  is the articulation angle rate.

Next, the rear sub-frame local velocities are expressed in terms of the front sub-frame local velocities assuming small articulation angle approximation.

$$u_r = u_f - v_f \phi + b \dot{\phi} \dot{\psi} \quad (30)$$

$$v_r = u_f \phi + v_f - (b+c) \dot{\psi} + c \dot{\phi} \quad (31)$$

At last, the kinetic energy is now expressed in terms of the desired generalized coordinates,  $u_f$ ,  $v_f$ ,  $\psi$ , and  $\phi$  as shown in eq. (32).

$$T = \frac{1}{2} m_f (u_f^2 + v_f^2) + \frac{1}{2} I_f \dot{\psi}^2 + \frac{1}{2} m_r [u_f^2 + v_f^2 \phi^2 \dots$$

$$+ b^2 \dot{\phi}^2 \dot{\psi}^2 - 2u_f v_f \phi + 2b u_f \phi \dot{\psi} - 2b v_f \phi^2 \dot{\psi} + u_f^2 \phi^2 \dots$$

$$+ v_f^2 + (b+c)^2 \dot{\psi}^2 + 2u_f v_f \phi - 2u_f \phi (b+c) \dot{\psi} \dots$$

$$- 2v_f (b+c) \dot{\psi} + c^2 \dot{\phi}^2 + 2u_f c \phi \dot{\phi} + 2v_f c \dot{\phi} \dots$$

$$- 2c (b+c) \dot{\phi} \dot{\psi}] + \frac{1}{2} I_r \dot{\psi}^2 - I_r \dot{\psi} \dot{\phi} + \frac{1}{2} I_r \dot{\phi}^2 \quad (32)$$

Using the virtual work principle, the right hand sides of the Lagrangian equations are resolved. Referring to fig. 8, the following virtual work equation is arrived at.

$$\delta W = \delta_{y_f} (F_{y_f} + F_{y_r}) + \dots$$

$$\delta \psi [a F_{y_f} - (b+c+d) F_{y_r} + M_{z_f} + M_{z_r}] + \dots \quad (33)$$

$$\delta \phi [(c+d) F_{y_r} - M_{z_r}]$$

For determining the tire lateral forces, it is first necessary to determine the tire lateral slip angles. The tire lateral slip angle is defined as the angle between the actual traveling direction of the tire and the direction of the tire centerline. Using small angle approximation, the average slip angles of the front and rear tires are given by eq. (34) and eq. (35).

$$\alpha_f = \frac{v_f + a\dot{\psi}}{u_f} \quad (34)$$

$$\alpha_r = \frac{v_f - (b+c+d)\dot{\psi} + (c+d)\dot{\phi}}{u_f} + \phi \quad (35)$$

For this paper, the linear tire model is used given its simplicity, linear property, and applicability for the maneuvers under consideration relative to speed, articulation angle, and such. The linear tire model is given by eq. (36) through eq. (39).

$$F_{y_f} = -N_f C_{\alpha_f} \alpha_f \quad (36)$$

$$F_{y_r} = -N_r C_{\alpha_r} \alpha_r \quad (37)$$

$$M_{z_f} = N_f C_{M\alpha_f} \alpha_f = N_f C_{M\alpha_f} \left( \frac{v_f + a\dot{\psi}}{u_f} \right) \quad (38)$$

$$M_{z_r} = N_r C_{M\alpha_r} \left( \frac{v_f - (b+c+d)\dot{\psi} + (c+d)\dot{\phi}}{u_f} + \phi \right) \quad (39)$$

where  $F_{y_f}$  and  $F_{y_r}$  are the front and rear tire lateral forces respectively,  $N_f$  and  $N_r$  are the front and rear axle vertical loads respectively, and  $C_{\alpha_f}$  and  $C_{\alpha_r}$  are the front and rear tires lateral force coefficients respectively.  $M_{z_f}$  and  $M_{z_r}$  are the front and rear tire aligning moments respectively, and  $C_{M\alpha_f}$  and  $C_{M\alpha_r}$  are the front and rear tire aligning moment coefficients respectively. The tire normal loads are determined based on equilibrium analysis of forces and moments leading to the expression of the tire normal forces in terms of the defined vehicle parameters shown in fig. 8.

$$N_f = \frac{m_r g d + m_f g (b+c+d)}{a+b+c+d} \quad (40)$$

$$N_r = \frac{m_f g a + m_r g (a+b+c)}{a+b+c+d} \quad (41)$$

#### EOM for Generalized coordinate $v_f$ :

The EOM for  $v_f$  is obtained after taking time derivatives, partial derivatives, ignoring nonlinear and second order terms, and substituting the generalized force,  $Q_{v_f}$ , in the Lagrange equation.

$$\begin{aligned} & (m_f + m_r) \dot{v}_f + (-b m_r - c m_r) \ddot{\psi} + (m_f + m_r) u_f \dot{\psi} + (c m_r) \ddot{\phi} = \\ & \left( \frac{-N_f C_{\alpha_f} - N_r C_{\alpha_r}}{u_f} \right) \dot{v}_f - \left( \frac{N_r C_{\alpha_r} (c+d)}{u_f} \right) \dot{\phi} - (N_r C_{\alpha_r}) \phi \dots \\ & + \left( \frac{-a N_f C_{\alpha_f} - (b+c+d) N_r C_{\alpha_r} - (m_f + m_r) u_f}{u_f} \right) \dot{\psi} \end{aligned} \quad (42)$$

The EOM for the remaining two generalized coordinates are obtained in a similar fashion and are listed below in eq. (43) and eq. (44) for completeness.

#### EOM for Generalized coordinate $\dot{\psi}$ :

$$\begin{aligned} & \dot{v}_f [-m_r (b+c)] + \ddot{\psi} [I_f + I_r + m_r (b+c)^2] \\ & + \ddot{\phi} (-m_r b c - m_r c^2 - I_r) - \dot{\psi} [m_r (b+c) u_f] = \\ & v_f \left[ \frac{-a N_f C_{\alpha_f} + (b+c+d) N_r C_{\alpha_r} + N_f C_{M\alpha_f} + N_r C_{M\alpha_r}}{u_f} \right] \dots \\ & + \dot{\psi} \left[ \frac{\left( -a^2 N_f C_{\alpha_f} - (b+c+d)^2 N_r C_{\alpha_r} \right)}{u_f} + m_r (b+c) u_f \right] \dots \\ & + \dot{\phi} \left[ \frac{(b+c+d)(c+d) N_r C_{\alpha_r} + (c+d) N_r C_{M\alpha_r}}{u_f} \right] \dots \\ & + \phi [(b+c+d) N_r C_{\alpha_r} + N_r C_{M\alpha_r}] \end{aligned} \quad (43)$$

#### EOM for Generalized coordinate $\dot{\phi}$ :

$$\begin{aligned} & \dot{v}_f (m_r c) + \ddot{\psi} (-m_r c^2 - m_r b c - I_r) \\ & + \ddot{\phi} (m_r c^2 + I_r) = \\ & v_f \left[ \frac{-(c+d) N_r C_{\alpha_r} - N_r C_{M\alpha_r}}{u_f} \right] + \dots \\ & \dot{\psi} \left[ \frac{(c+d)(b+c+d) N_r C_{\alpha_r} + N_r C_{M\alpha_r} (b+c+d)}{u_f} \right] + \dots \\ & \dot{\phi} \left[ \frac{-(c+d)^2 N_r C_{\alpha_r} - N_r C_{M\alpha_r} (c+d)}{u_f} - m_r c u_f \dot{\phi} - C_a \right] + \dots \\ & \phi [-N_r C_{\alpha_r} - N_r C_{M\alpha_r}] \end{aligned} \quad (44)$$

At this point, the equations of motion are expressed in a manner such that the derivatives of the selected generalized coordinates are on the left hand side, whereas the generalized coordinates themselves are on the right hand side of the equations. This format is in accordance with a system of linear first order differential equations. Such formulation lends itself to expressing the system in state space format, which is currently under development for generating a linear model to be used for designing a controller based on modern control theory.

### 3.3 MSC Adams Model

The compact wheel loader under investigation is designated as the baseline test vehicle to be used for model validation, hardware implementation, and controller development. The

generated models in this paper were developed based on the parameters of the baseline vehicle shown in tab. 1.

Parameter	Description	Value	Unit
$m$	Vehicle Mass	4100	kg
$m_f$	Front Sub-frame Mass	1640	kg
$m_r$	Rear Sub-frame Mass	2460	kg
$I_f$	Front Sub-frame Moment of Inertia	1500	kg.m <sup>2</sup>
$I_r$	Rear Sub-frame Moment of Inertia	2500	kg.m <sup>2</sup>
$wb$	Vehicle Wheelbase	2.12	m
$a$	Distance Between Front Sub-frame CG and Front Axle	0	m
$b$	Distance Between Front CG and Articulation Joint	1.06	m
$c$	Distance Between Rear CG and Articulation Joint	1.06	m
$d$	Distance Between Rear Sub-frame CG and Front Axle	0	m
$r_j$	Normal Distance Between the Articulation Joint and the Steering Actuator Force Line of Action	0.2	m

Table 1: Baseline Wheel Loader Parameters

A multi-body dynamics model was generated in MSC Adams software for two purposes. First, it allows for performing accurate simulations of dynamic steering maneuvers when coupled with the hydraulic subsystem. Second, it will provide a platform for validating the derived linear model, which will be used for advancing the research forward relative to control algorithms development. The model's topology comprises two rigid bodies connected at the articulation joint via a revolute joint. When no articulation angle input is present i.e. no flow to/from the actuator and ignoring leakage across the actuator sides, the hydraulic fluid inside the steering actuator creates the effect of a (stiff) torsional spring at the joint, whose stiffness,  $K_{aj}$ , is approximated via eq. (45), which results from the pressure-flow equation.

$$K_{aj} = \frac{K}{V_t} A_A^2 (1 + \alpha^2) \gamma r_j \quad (45)$$

where  $K$  is the fluid bulk modulus,  $V_t$  is the total volume of fluid under compression including actuator chambers and transmission lines,  $A_A$  is the actuator piston area,  $\alpha$  is the area ratio between the actuator sides,  $\gamma$  is a linear conversion factor between the steering actuator linear motion and the vehicle rotational motion, and  $r_j$  is the normal distance between the articulation joint and the steering actuator force line of action. As for damping, the articulation joint friction along with the tires lateral damping play the role of a torsional damper present at the joint. This parameter was estimated based on literature review [1] due to lack of measurements at the present time. The PAC 2002 Magic-Formula tire model was selected, which is suitable for the considered maneuvers involving single-lane change and steady-state cornering. Figure 9 shows the generated Adams model that was used during the simulation run.

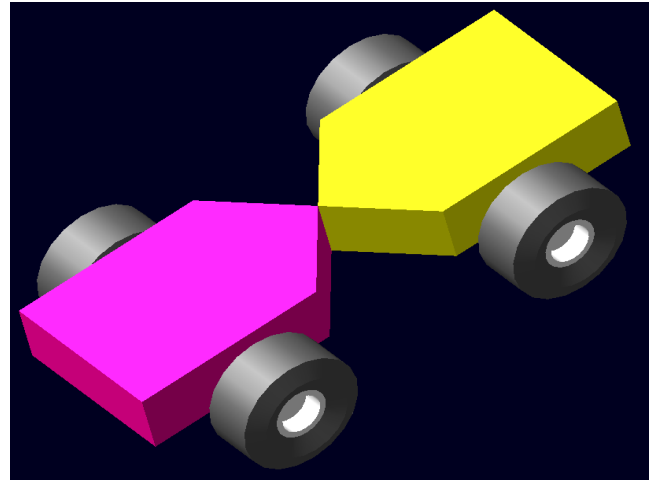


Figure 9: Adams Model of an Articulated Vehicle

### 3.4 MATLAB Simulink SimMechanics™ Model

A 1-DOF dynamic model was designed in MATLAB Simulink SimMechanics™ environment. The main purpose of the model is to generate a load that the hydraulic subsystem must overcome to induce articulation while the vehicle performs static maneuvers i.e. zero forward speed.

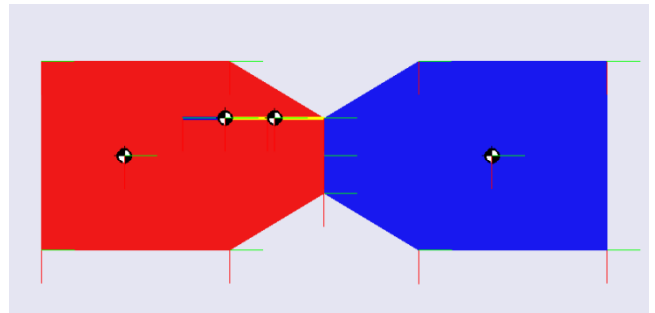


Figure 10: MATLAB Simulink SimMechanics™ Model

## 4 System Model

Inducing an articulation angle requires a steering torque to be exerted about the articulation joint. This requires coupling the hydraulics and mechanics models. For the Adams model to accept steering force as an input, the

steering actuator was modeled as a linear spring / damper element connected to both subframes (fig. 11).

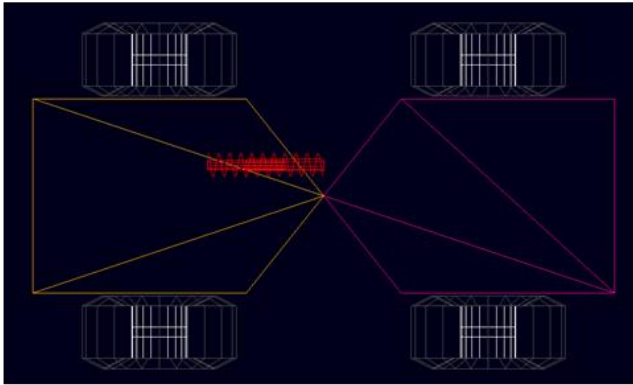


Figure 11: Adams Model Linear Actuator Setup

The Adams plant model was then exported to Simulink in a manner that inputs actuator force and outputs the articulation angle and rate as shown in fig. 12.

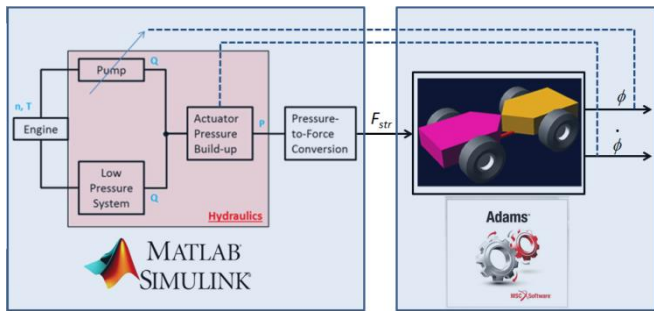


Figure 12: Exported Adams Plant Model into Simulink®

### 5 Simulation Results

Two maneuvers were simulated: a static maneuver where the vehicle speed is set to zero and the articulation angle is varied between +25° and -25° emulating a static loading cycle; second, a dynamic maneuver where the vehicle forward speed is set to 20 km/hr and the vehicle direction changes between ±9° mimicking a lane change maneuver. The maneuvers were realized via a simple proportional controller providing closed-loop position control. The relevant parameters used during the simulation are given in tab. 2.

Description	Value	Unit
Pump Displacement Volume	18	cm <sup>3</sup> /rev
Engine/Pump Speed	1500	rev/min
Actuator Piston Diameter	0.078	m
Actuator Rod Diameter	0.032	m
Fluid Bulk Modulus	1.9e9	N/m <sup>2</sup>
Fluid Density	870	Kg/m <sup>3</sup>

Low Pressure System Pressure	25	Bar
Articulation Joint Damping	350	N.m.s/rad

Table 2: Simulation Parameters

#### 5.1 Static Maneuver

Figure 13 shows the vehicle articulation angle varying between +25° and -25°. The ramp-up and ramp-down rates confirm the sizing of the DC steering pump, which was sized to meet the same cycle requirements as the baseline hydrostatic steering system.

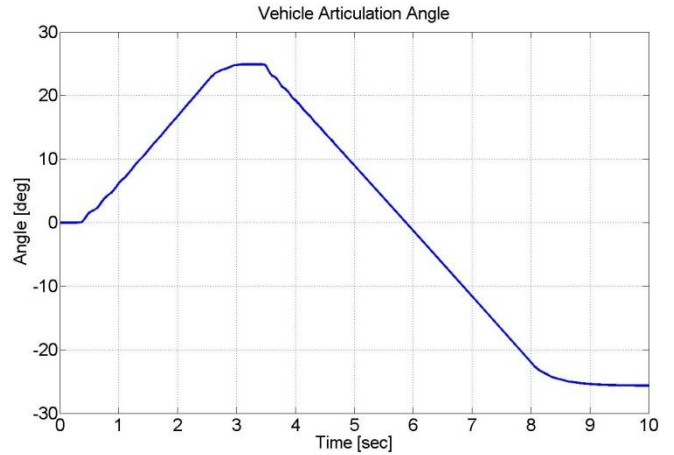


Figure 13: Static Maneuver – Articulation Angle

Figure 14 shows the pressure rise inside the corresponding chambers of the steering actuator. The results serve multiple validation checks. First, given that the steering actuator is mounted with its piston side (A) towards the rear of the vehicle, articulating the vehicle to the left (positive angle) requires the pressure on the rod side (B) to rise and vice versa. Second, the model accurately predicts that higher pressure is needed to articulate the vehicle left than right, since side B has a smaller area than side A. Lastly, the low pressure system successfully kept the low pressure side at the specified setting of 25bar, which confirms the sizing as well as validates the intricate modeling of the low pressure system.

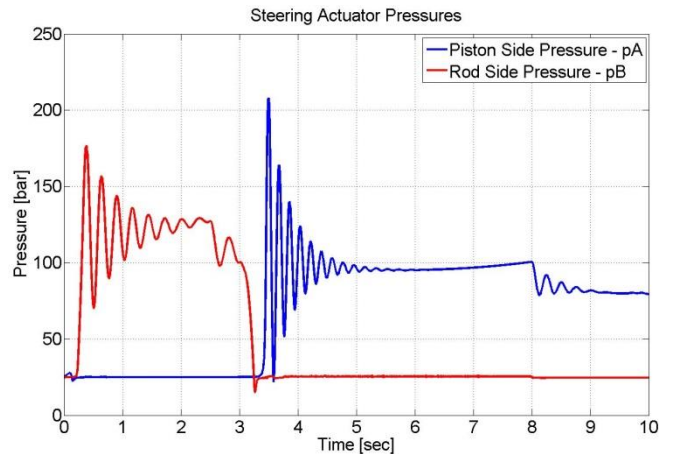


Figure 14: Static Maneuver – Actuator Pressure

Figure 15 shows the net steering actuator force resulting from the pressure differential across the actuator sides.

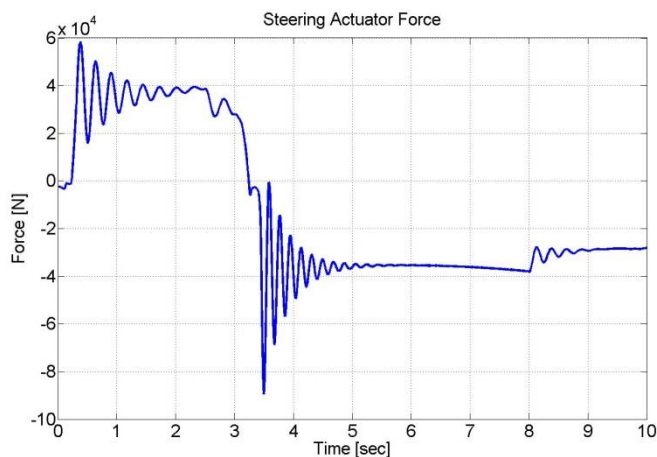


Figure 15: Static Maneuver – Steering Actuator Force

## 5.2 Dynamic Maneuver

Figure 16 shows the articulation angle of the vehicle during the dynamic maneuver. The vehicle executed a lane change maneuver by changing direction in both ways while driving at 20 km/hr.

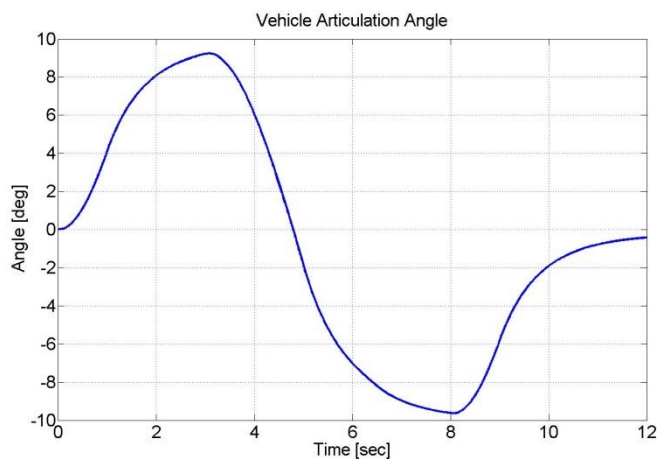


Figure 16: Dynamic Maneuver – Articulation Angle

Figure 17 shows the pressures inside the actuator chambers as the vehicle articulates. Similar results were obtained as in the static maneuver. Articulating the vehicle to the left (positive) requires the pressure on the rod side (B) to rise and vice versa, higher pressure levels are needed to articulate the vehicle left than right since side B has a smaller area than side A, and the low pressure system kept the low pressure side at the specified setting of 25bar.

Figure 18 shows the corresponding steering actuator force resulting from the pressure differential across the actuator chambers. Smaller force magnitudes are observed since the friction coefficient between the tire and ground is lower in dynamic conditions than static ones. When the vehicle reaches the commanded position, the force magnitude returns to zero since no further steering effort is required.

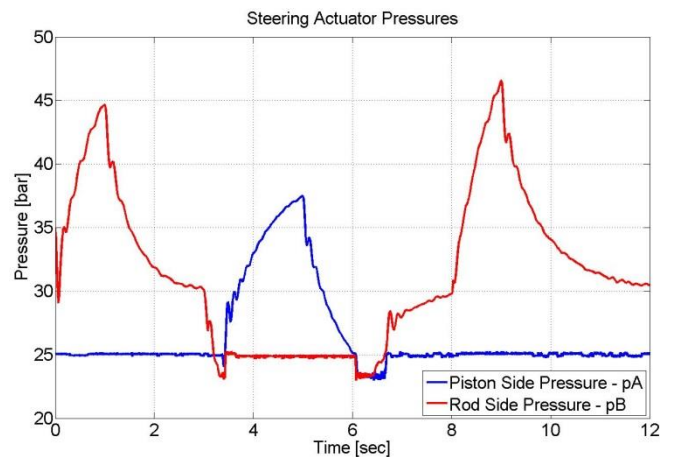


Figure 17: Dynamic Maneuver – Actuator Pressures

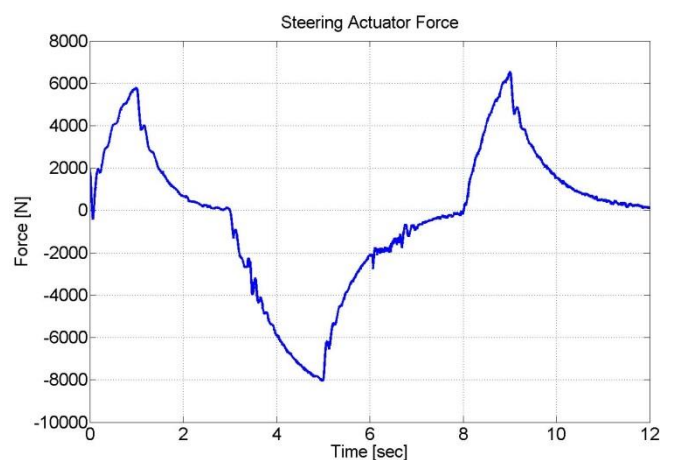


Figure 18: Dynamic Maneuver – Actuator Force

Figure 19 shows the tire lateral slip angles as the vehicle direction deviates from straight-line forward motion. The sign and magnitude of both axes accurately reflect the maneuver at hand, which were verified against manually performed calculations based on eq. (34) and eq. (35). The fact that the slip angles of the tires on the same axle almost overlap, which allows for modeling the vehicle as a bicycle and combining both tires into one.

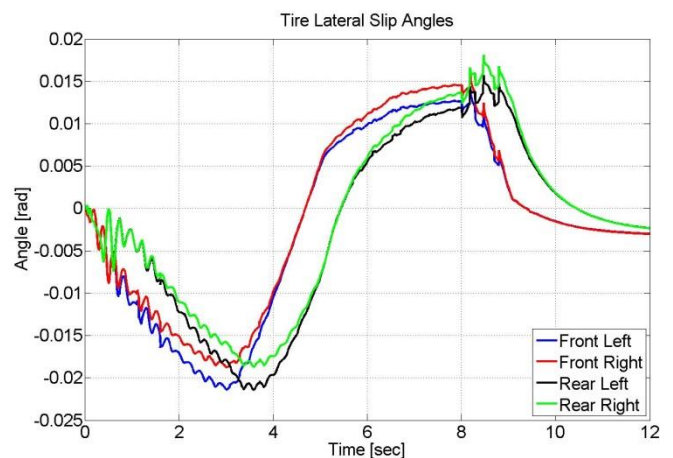


Figure 19: Dynamic Maneuver – Tire Lateral Slip Angles

Figure 20 shows the tire lateral forces resulting from the slip angles shown in fig. 19, the tire normal loads, and the surface type. The sign and magnitude of the tire forces match the theoretical values as computed from eq. (36) and eq. (37).

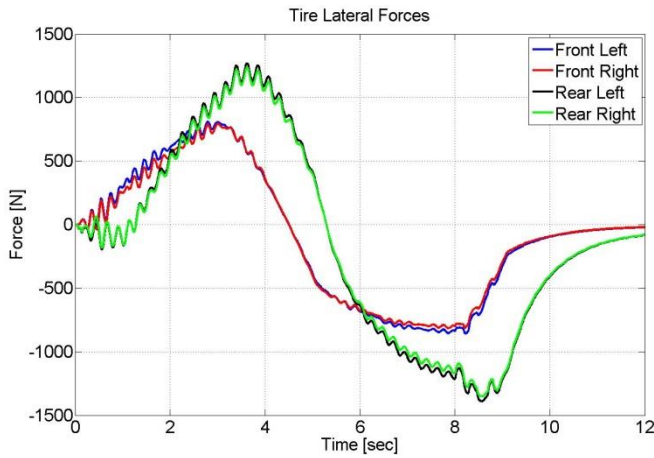


Figure 20: Dynamic Maneuver – Tire Lateral Forces

## 6 Future Work

The results obtained in this paper will be used to aid in both the derivation process as well as the validation process of linearized models for the hydraulic subsystem, the dynamic subsystem, and the entire system. Linear models allow for exploiting modern control theory techniques pertaining to linear time-invariant (LTI) systems. After designing a controller, the generated control algorithms and dynamic models will be validated and fine-tuned based on measurement results obtained from a baseline test vehicle. This requires retrofitting the test vehicle with a renovated steering column assembly, tactile feedback device, a DC axial piston pump, sensors, actuators, electronics, and a real-time controller.

## 7 Conclusion

A novel electro-hydraulic steer-by-wire system realized via DC technology has been proposed. High fidelity nonlinear dynamic models of the two subsystems that are at the heart of the new system, hydraulics and mechanics, were developed and validated. Finally, a sophisticated nonlinear system plant model is now available on hand, which will be used for validating the linearized models under investigation, paving the road in front of the design and development of a robust steer-by-wire system controller.

The technology will be demonstrated on a compact wheel loader. Baseline measurements of the stock loader have been conducted, and will be used to compare against the new measurement results after the implementation of the new steering system.

## Nomenclature

$Q_e$	Pump Effective Flow Rate
$\beta$	Pump Swash Plate Angle (Normalized)

$V_d$	Pump Displacement Volume (Derived)
$n$	Pump Speed
$Q_s$	Pump/Motor Volumetric Loss
$T_e$	Pump/Motor Effective Torque
$T_s$	Pump/Motor Torque Loss
$\Delta p$	Pressure Differential Across Pump/Motor Ports
$K_Q$	Pump/Motor Volumetric Loss Coefficient
$K_T$	Pump/Motor Torque Loss Coefficient
$p$	Pressure
$Q$	Flow Rate
$C_H$	Hydraulic Capacitance
$\dot{x}$	Actuator Velocity
$A$	Area
$V$	Volume
$\alpha$	Actuator Area Ratio
$K_{Li}$	Coefficient of Internal Leakage of Actuator
$K$	Fluid Bulk Modulus
$H$	Maximum Actuator Stroke (End-to-End)
$x$	Actuator Position
$V_{dead}$	Actuator Dead Volume
$\mu$	Fluid Dynamic Viscosity
$\nu$	Fluid Kinematic Viscosity
$\rho$	Fluid Density
$F_R$	Resultant Friction Force
$F_C$	Coulomb Friction Force
$F_H$	Static Friction Force
$\tau_H$	Static Friction Force Constant
$l_L$	Transmission Line Length
$R_L$	Transmission Line Radius
$y_c$	Pilot-Operated Check Valve Spool Displacement
$Q_c$	Pilot-Operated Check Valve Flow Rate
$\alpha_D$	Pilot-Operated Check Valve Discharge Coefficient
$d_c$	Pilot-Operated Check Valve Cone Diameter
$y_c$	Pilot-Operated Check Valve Cone Position
$A_c$	Pilot-Operated Check Valve Cone Orifice Area

$p_{LP}$	Pressurized Low Pressure
$p_1$	Pilot-Operated Check Valve Pilot Pressure
$p_2$	Pilot-Operated Check Valve Cylinder / Outlet Pressure
$F_{K0}$	Pilot-Operated Check Valve Spring Pre-load Force
$K_0$	Pilot-Operated Check Valve Spring Rate
$A_{sp}$	Pilot-Operated Check Valve Spool Area
$\omega_{SV}$	Servo valve Natural Frequency
$\zeta_{SV}$	Servo valve Damping Ratio
$F_{str}$	Steering Actuator Force
$r_j$	Normal Distance Between the Articulation Joint and the Steering Actuator Force Line of Action
$C_{aj}$	Articulated Joint Torsional Damping Coefficient
$N_f$	Front Axle Normal Load
$\mu_f$	Friction Coefficient Between the Tire and Ground
$wb$	Vehicle Wheelbase
$d_{aj}$	Articulation Joint Damping Coefficient
$d_{Tire\_Lat}$	Tires Lateral Damping Coefficient
$\omega_f$	Front Sub-frame Articulation Angle Rate
$L$	Lagrangian Function
$T$	Kinetic Energy
$V$	Potential Energy
$D$	Dissipative Function
$Q_i$	Generalized Forces
$m_f$	Front Sub-frame Mass
$m_r$	Rear Sub-frame Mass
$X_f$	Front Sub-frame Global Abscissa
$Y_f$	Front Sub-frame Global Ordinate
$x_f$	Front Sub-frame Local Abscissa
$y_f$	Front Sub-frame Local Ordinate
$I_f$	Front Sub-frame Moment of Inertia
$I_r$	Rear Sub-frame Moment of Inertia
$\psi$	Front Sub-frame Yaw Angle
$\theta$	Rear Sub-frame Yaw Angle
$\phi$	Articulation Angle
$a$	Distance between Front C.G. and Front Axle
$b$	Distance between Front C.G. and Articulation Joint
$c$	Distance between Rear C.G. and Articulation

	Joint
$d$	Distance between Rear C.G. and Rear Axle
$K_{aj}$	Articulation Joint Equivalent Torsional Stiffness
$C_{aj}$	Articulation Joint Equivalent Torsional Damping
$u_f$	Front Sub-frame Longitudinal Velocity
$v_f$	Front Sub-frame Lateral Velocity
$F_y$	Tire Lateral Force
$M_Z$	Tire Aligning Moment
$\alpha_s$	Tire Slip Angle
$\alpha_f$	Front Tires Slip Angle
$\alpha_r$	Rear Tires Slip Angle
$N$	Axle Normal Load
$C_\alpha$	Tires Lateral Force Coefficient
$C_{M\alpha}$	Tires Aligning Moment Coefficient
$g$	Gravity Constant
$\gamma$	Conversion Factor Between Actuator Linear Motion and Vehicle Articulation Motion
$C_d$	Actuator Viscous Damping Coefficient
$m_r$	Actuator Rod Mass
$F_L$	Actuator Load Force
$DC$	Displacement Control
$POCV$	Pilot-Operated Check Valve
$DOF$	Degree(s) of Freedom
$CG$	Center of Gravity
$EOM$	Equation(s) of Motion

## References

- [1] Azad, N. Dynamic Modelling and Stability Controller Development for Articulated Steer Vehicles. *Ph.D. dissertation, University of Waterloo*. Waterloo, Ontario, Canada. 2006.
- [2] Chen, C. and Tomizuka, M. Modeling and Control of Articulated Vehicles. *Report number UCB-ITS-PRR-97-42, California Partners for Advanced Transit and Highways, Institute of Transportation Studies, Berkeley, California*. 1997.
- [3] Crolla D. *Automotive Engineering: Powertrain, Chassis System and Vehicle Body*. Elsevier Science & Technology Books. Burlington, MA. 2009.
- [4] Daher, N. and Ivantysynova, M. Electro-hydraulic energy-saving power steering systems of the future.

*Proceedings of the 7<sup>th</sup> FPNI PhD Symposium*, Reggio Emilia, Italy, pp. 929 – 952. 2012.

- [5] Greenwood, D. *Principles of Dynamics*. Prentice-Hall, Inc., Englewood Cliffs, New Jersey. 1988.
- [6] Horton D.N.L. and Crolla D.A. Theoretical analysis of the steering behaviour of articulated frame steer vehicles. *Vehicle System Dynamics*, vol. 15, pp. 211—234. 1986.
- [7] Merritt, H.E. *Hydraulic Control Systems*. John Wileys and Sons, Cincinnati, Ohio. 1967
- [8] Milliken, W.F. and Milliken, D.L. *Race Car Vehicle Dynamics*. SAE International. 1995.
- [9] Rahmfeld, R. Development and Control of Energy Saving Hydraulic Servo Drives for Mobile Systems. *Ph.D. Thesis. Dept. of Aircraft Systems, Technical University of Hamburg-Harburg*. Hamburg, Germany. 2002.
- [10] Rahmfeld, R. and Ivantysynova, M. Energy Saving Hydraulic Actuators for Mobile Machines. *Proceedings of 1st Bratislavian Fluid Power Symposium*, pp. 47-57. Častá – Píla, Slovakia. 1998
- [11] Rahmfeld, R. and Ivantysynova, M. Displacement Controlled Wheel Loader – a simple and clever Solution. *4<sup>th</sup> International Fluid Power Conference Proceedings*, pp. 183-196. Dresden, Germany. 2004.
- [12] Williamson, C., Zimmerman, J., and Ivantysynova, M. Efficiency Study of an Excavator Hydraulic System Based on Displacement-Controlled Actuators. *ASME/Bath Workshop on Fluid Power and Motion Control (FPMC08)*. Bath, UK. 2008.
- [13] Williamson, C and Ivantysynova, M. Power Optimization for Multi-Actuator Pump-Controlled Systems. *Proceedings of the 7th International Fluid Power Conference Aachen 2010 (7IFK)*, Vol 1. pp.91 - 102. 2010.
- [14] Wittren, R.A. Power Steering For Agricultural Tractors. *American Society of Agricultural Engineers, Winter Meeting Distinguished Lecture Series*. Chicago, IL, USA. 1975.